14.14 V.I. Aleksandrov, V.V. Osiko, A.M. Prokhorov, V.M. Tatarintsev: Novel method of preparation of refractory single crystals and melted ceramic materials, Herald Rus. Acad. Sci. **12**, 29–36 (1973), in Russian

14.15 V.I. Aleksandrov, V.V. Osiko, A.M. Prokhorov, V.M. Tatarintsev: Synthesis and crystal growth of refractory materials by RF melting in a cold container, Top. Mater. Sci. **1**, 421–480 (1978)

14.16 R.F. Sekerka, R.A. Hartzell, B.J. Farr: Instability phenomena during the RF-heating and melting of ceramics, J. Cryst. Growth **50**, 783–806 (1980)

14.17 R.A. Hartzell, R.F. Sekerka: Mathematical modeling of internal centrifugal zone growth of ceramics and ceramic metal composites, J. Cryst. Growth **57**, 27–42 (1982)

14.18 C. Gross, W. Assmus, A. Muiznieks, G. Raming, A. Muehlbauer, C. Stenzel: Power consumption of skull melting, Part I: analytical aspects and experiments, Cryst. Res. Technol. **34**, 319–328 (1999)

14.19 A. Muiznieks, G. Raming, A. Muehlbauer, C. Gross, W. Assmus, C. Stenzel: Power consumption of skull melting, Part II: numerical calculation of the shape of the molten zone and comparison with experiment, Cryst. Res. Technol. **34**, 329–338 (1999)

14.20 T. Behrens, M. Kudryash, B. Nacke, D. Lopuch, A. Martynow, I. Loginov: Induction skull melting of Y_2O_3–BaO–CuO in a cold crucible, Int. Sci. Coll. Modelling for Electromagnetic Processing (Hannover 2003) pp. 249–254

14.21 B. Nacke, T. Behrens, M. Kudryash, A. Jakovics: Skull melting technology for oxides and glasses, Conf. Fundamental and Applied MHD, Vol. 2 (Riga 2005) pp. 241–244

14.22 A.V. Shkulkov: Attractor formation in induction skull-melting systems and its effect on crystal structure, Bull. Rus. Acad. Sci. Phys. **68**, 1000–1006 (2004)

14.23 V.V. Osiko, M.A. Borik, E.E. Lomonova: Crucible-free methods of growing oxide crystals from the melt, Annu. Rev. Mater. Sci. **17**, 101–122 (1987)

14.24 E.E. Lomonova, V.V. Osiko: Growth of zirconia crystals by skull-melting technique. In: *Crystal Growth Technology*, ed. by H.J. Scheel, T. Fukuda (Wiley, Chichester 2003) pp. 461–484

14.25 Y.S. Kuzminov, E.E. Lomonova, V.V. Osiko: *Refractory Materials from a Cold Crucible* (Nauka, Moscow 2004)

14.26 Y.B. Petrov: *Inductive Melting of Oxides* (Energoatomizdat, Leningrad 1983), in Russian

14.27 V.I. Aleksandrov, A.L. Blinov, M.A. Borik, V.V. Osiko: Investigation of temperature distribution in viscous oxide melts under process of skull melting in a cold crusible, Izv. AS USSR, Inorg. Mater. **19**, 443–447 (1983), in Russian

14.28 V.I. Aleksandrov, S.H. Batygov, V.F. Kalabuhova, S.V. Lavrischev, E.E. Lomonova, V.A. Mizina, V.V. Osiko, V.M. Tatarintsev: Ittria distribution and inhomogenities into cubic ZrO_2–Y_2O_3 crystals, Izv. AS USSR, Inorg. Mater. **16**, 99–104 (1980), in Russian

14.29 V.I. Aleksandrov, S.H. Batygov, V.F. Kalabuchova, S.V. Lavrischev, E.E. Lomonova, V.A. Mizina, V.V. Osiko, V.M. Tatarintsev: Effect SiO_2 on growth and perfection of stabilized ZrO_2, Izv. AS USSR, Inorg. Mater. **16**, 1800–1804 (1980), in Russian

14.30 V.I. Aleksandrov, M.A. Vishnyakova, V.F. Kalabuchova, E.E. Lomonova, V.A. Panov: Growth of zirconia single crystals by direct crystallization in a cold container, Proc. Indian Natl. Sci. Acad. **2**, 133–144 (1991)

14.31 V.I. Aleksandrov, V.V. Osiko, A.M. Prokhorov, V.M. Tatarintsev: Refractory materials preparation by skull melting in a cold container, Rus. Chem. Rev. **47**, 385–427 (1978), in Russian

14.32 V.I. Aleksandrov, V.P. Voitsitskii, E.E. Lomonova, V.V. Osiko, N.P. Khaneev: Study of melting and crystallization processes in a cold container with direct radio-frequency heating, Instrum. Exp. Tech. **3**, 231–234 (1991), in Russian

14.33 V.I. Aleksandrov, V.P. Voitsitskii, E.E. Lomonova, V.V. Osiko, N.P. Khaneev: Study of dielectric materials melting in a cold container with direct radio-frequency heating, Izv. AS USSR, Inorg. Mater. **27**, 983–987 (1991), in Russian

14.34 V.I. Aleksandrov, V.P. Voitsitskii, E.E. Lomonova, V.V. Osiko, N.P. Khaneev: Investigation of melting and crystallization processes in a cold container with direct radio-frequency heating, Izv. AS USSR, Inorg. Mater. **27**, 2167–2171 (1991), in Russian

14.35 V.I. Aleksandrov, V.P. Voitsitskii, E.E. Lomonova, V.V. Osiko, N.P. Khaneev: Control method of melt propogation on a initial stage of direct radio-frequency melting in a cold container, Instrum. Exp. Tech. **4**, 212–217 (1992), in Russian

14.36 V.I. Aleksandrov, V.P. Voitsitskii, E.E. Lomonova, V.V. Osiko, N.P. Khaneev: Monitoring of melt propogation direction on a initial stage of direct radio-frequency melting in a cold container, J. Tech. Phys. **62**, 180–186 (1992), in Russian

14.37 B.T. Melekh, F.F. Andreeva, N.F. Kartenko, I.V. Korkin, V.B. Smirnov: Features of direct induction melting and crystal growth of refractory oxide transition elements, Izv. AS USSR, Inorg. Mater. **18**, 98–101 (1982), in Russian

14.38 R. Aragon, H.R. Harrison, R.H. McCallister, C.J. Sandberg: Skull melting single crystal growth of magnetite (Fe_3O_4)–ulvospinel (Fe_2TiO_4) solid solution members, J. Cryst. Growth **61**, 221–228 (1983)

14.39 V.I. Aleksandrov, A.L. Blinov, M.A. Borik, V.G. Veselago, V.V. Voronov, V.M. Ivanovskaja, V.A. Misina, V.V. Osiko, V.T. Udovenchik, V.A. Fradkov, M.A. Chernikov: Synthesis and crystal growth of $YBa_2Cu_3O_{6.5+x}$ from the melt by direct radio-frequency heating in a cold container, 7 All-Union Conf. on Crystal Growth, Vol. 2 (Moscow 1988), pp. 378–379, in Russian

14.40 M. Hartmanova, E.E. Lomonova, V. Navratil, P. Sutta, F. Kudracik: Characterization of yttria-doped ceria prepared by directional crystallization, J. Mater. Sci. **40**, 5679–5683 (2005)

14.41 L. Mazerolles, D. Michel, M.J. Hÿtch: Microstructures and interfaces in directionally solidified oxide–oxide eutectics, J. Eur. Ceram. Soc. **25**, 1389–1395 (2005)

14.42 W.-J. Jang, K. Imai, M. Hasegawa, H. Takei: Growth and structure of $La_2NiO_{4+\delta}$ ($0.19 \geq \delta \geq 0.12$) single crystals, J. Cryst. Growth **152**, 158–168 (1995)

14.43 V.I. Aleksandrov, V.V. Osiko, V.M. Tatarintsev: Melting of refractory dielectric materials by radio-frequency heating, Instrum. Exp. Tech. **5**, 222–225 (1970), in Russian

14.44 V.I. Aleksandrov, M.A. Vishnyakova, Y.K. Voron'ko, V.F. Kalabuchova, E.E. Lomonova, V.A. Misina, V.V. Osiko: Crystal growth of $SrTiO_3$ by Czochralski method from a cold crusible, Izv. AS USSR, Inorg. Mater. **19**, 104–108 (1983), in Russian

14.45 V.I. Aleksandrov, S.H. Batygov, M.A. Vishnyakova, Y.K. Voron'ko, V.F. Kalabuchova, E.E. Lomonova, V.V. Osiko: Optical properties of $SrTiO_3$ single crystal grown by Czochralski method, Izv. AS USSR, Inorg. Mater. **19**, 265–268 (1983), in Russian

14.46 V.I. Aleksandrov, I.A. Gerasimova, A.V. Kolesnikov, E.E. Lomonova, V.V. Osiko, V.A. Panov, P.A. Makarov, A.V. Archakov, N.G. Gorashchenko, A.A. Mayer: Growth of sillenite (BGO) single crystals from cold container, Russ. J. Inorg. Chem. **35**, 878–883 (1990)

14.47 D. Mateika, R. Lauien, M. Liehr: Czochralski growth by double container technique, J. Cryst. Growth **65**, 237–242 (1983)

14.48 A.M. Balbashov, A.J. Chervonenkis: *Magnetic Materials for Electronics* (Energija, Moscow 1979), in Russian

14.49 O. Ruff, F. Ebert: Contributions on ceramics of high refractory materials. I. The forms of zirconium dioxide, Z. Anorg. Allg. Chem. **180**, 19–41 (1929)

14.50 B.J. Curtis, J.A. Wilkinson: Preparation of mixed oxide crystals by chemical transport, J. Am. Ceram. Soc. **48**, 49–50 (1965)

14.51 V.A. Kysnetsov, O.V. Sidorenko: Crystallization of ZrO_2 and HfO_2 in hydrothermal conditions, Crystallogr. Rep. **13**, 748–749 (1968), in Russian

14.52 A.M. Anthony, V. Loc: Preparation de monocristaux de zircone pure monoclinique, C. R. Acad. Sci. **260**, 1383–1385 (1965), in French

14.53 A.B. Chase, J.A. Osmer: Growth of single crystals of ZrO_2 and HfO_2 from PbF_2, Am. Mineral. **51**, 1811–1888 (1966)

14.54 W. Kleber, L. Ickert, J. Doerschel: Ein Beitrag zum Wachstum von Zirkoniumdioxid-Einkristallen aus Schmelzenlosungen, Krist. Tech. **1**, 237–248 (1966)

14.55 M. Yokoyama, T. Ota, I. Yamai: Flux growth of yttria-stabilized zirconia crystals, J. Cryst. Growth **75**, 630–632 (1986)

14.56 T. Yamakawa, N. Ishizawa, K. Uematsu, N. Mizutani, M. Kato: Growth of yttria partially and fully stabilized zirconia crystals by xenon arc image floating zone method, J. Cryst. Growth **75**, 623–629 (1986)

14.57 M. Yoshimura, T. Hiuga, S. Somiya: Crystal growth of yttria stabilized zirconia (YSZ) under hydrothermal conditions, J. Cryst. Growth **71**, 277–279 (1985)

14.58 T.B. Reed: Growth of refractory crystals using the induction plasma torch, J. Appl. Phys. **32**, 2534–2535 (1961)

14.59 A. Saiki, N. Ishizawa, N. Mizutani, M. Kato: Directional crystal growth of yttria-stabilized zirconia by the arc image floating-zone method, J. Mater. Sci. Lett. **6**, 568–570 (1987)

14.60 D. Michel, M. Perez y Jorba, R. Collongues: Sur l'elaboration de monocristaux de zircone stabiliseret sur certaines proprieles de la solution solide cubique ZrO_2–CaO, C. R. Acad. Sci. C. **266**, 1602–1604 (1968), in French

14.61 D. Michel, M. Perez y Jorba, R. Collongues: Growth from skull-melting of zirconia rare earth oxide crystals, J. Cryst. Growth **43**, 546–548 (1978)

14.62 A.M. Anthony, R. Collongues: Modern methods of growing single crystals of high-melting point oxides. In: *Preparative Methods in Solid State Chemistry*, ed. by P. Hagenmuller (Academic, New York 1972) pp. 147–249

14.63 R.C. Garvi, R.H. Hannink, R.T. Pascoe: Ceramic steel, Nature **258**, 703–704 (1975)

14.64 T.K. Gupta, J.H. Bechtold, R.C. Kuznicki, L.H. Cadoff, B.R. Rossing: Stabilization of tetragonal phase in polycrystalline zirconia, J. Mater. Sci. **12**, 2421–2426 (1977)

14.65 T.K. Gupta: Sintering of tetragonal zirconia and its characteristics, Sci. Sinter. **10**, 205–216 (1978)

14.66 D.L. Porter, A.H. Heuer: Mechanisms of toughening partially stabilized zirconia (PSZ), J. Am. Ceram. Soc. **60**, 183–184 (1977)

14.67 R.H.J. Hannink, P.V. Kelly, B.C. Muddle: Transformation toughening in zirconia-containing ceramics, J. Am. Ceram. Soc. **83**, 461–487 (2000)

14.68 M.E. Mashburg, W.E. Coblenz: Reactio-formed ceramics, J. Am. Ceram. Soc. **67**, 356–363 (1988)

14.69 R. Chaim, M. Hefetz: Effect of grain size on elastic modulus and hardness of nanocrystalline ZrO_2–3 wt %-Y_2O_3 ceramic, J. Mater. Sci. **39**, 3057–3061 (2004)

14.70 K. Tzukuma, K. Heda, M. Shimada: Strength and fracture toughness in isostatically hot pressed composites of Al_2O_3 and Y_2O_3 partially stabilized ZrO_2, J. Am. Ceram. Soc. **68**, C4–C5 (1985)

14.71 M. Hoch, K.M. Nair: Densification characteristics of ultrafine powders, Ceramurg. Int. **2**, 88–97 (1976)

14.72 K.S. Mazdiyasni: Powder synthesis from metal-organic precursors, Ceramurg. Int. **8**, 42–56 (1982)

14.73 C.J. Howard, R.J. Hill, B.E. Reichert: Structures of the ZrO_2 polymorphs at room temperature by

high-resolution neutron powder diffraction, Acta Crystallogr. B **44**, 116–120 (1980)
14.74 G. Teufer: Crystal structure of tetragonal ZrO_2, Acta Crystallogr. **15**, 1187 (1962)
14.75 R.J. Ackermann, S.P. Garg, E.G. Rauh: High-temperature phase diagram for the system Zr-O, J. Am. Ceram. Soc. **60**, 341–345 (1977)
14.76 D.K. Smith, C.F. Cline: Verification of existence of cubic zirconia at high temperature, J. Am. Ceram. Soc. **45**, 249–250 (1962)
14.77 J. McCullough, K. Trueblood: The crystal structure of baddeleyite (monoclinic ZrO_2), Acta Crystallogr. **12**, 507–511 (1959)
14.78 N.V. Belov: Crystallographic structure of baddeleyite, Crystallogr. Rep. **5**, 460–461 (1960), in Russian
14.79 D.K. Smith, H.W. Newkirk: The crystal structure of baddelyite (monoclinic ZrO_2) and its relation to the polymorphism of ZrO_2, Acta Crystallogr. **18**, 983–991 (1965)
14.80 R. Cupres, R. Wollast: Polymorphism conversion of pure zirconia, Ber. Dtsch. Keram. Ges. **40**, 527–532 (1963)
14.81 P. Duwez, F.H. Brown, F. Odell: The zirconia-yttria system, J. Electrochem. Soc. **38**, 356–362 (1951)
14.82 S.P. Ray, V.S. Stubican: Fluorite related ordered compounds in the ZrO_2-CaO and ZrO_2-Y_2O_3 system, Mater. Res. Bull. **12**, 549–556 (1977)
14.83 H.G. Scott: Phase relationships in the yttria-zirconia system, J. Mater. Sci. **10**, 1527–1535 (1975)
14.84 V.S. Stubican, R.C. Hink, S.P. Ray: Phase equilibria and ordering in the system ZrO_2-Y_2O_3, J. Am. Ceram. Soc. **61**, 17–21 (1978)
14.85 V.S. Stubican, G.S. Gorman, J.R. Hellmann, G. Senft: Phase relationships in some ZrO_2 systems. In: *Advances in Ceramics Vol. 12: Science and Technology of Zirconia II*, ed. by N. Claussen, M. Ruhle, A.H. Heuer (Am. Ceram. Soc., Columbus 1984) pp. 96–106
14.86 V.S. Stubican: Phase equilibria and metastabilities in the systems ZrO_2-MgO, ZrO_2-CaO, and ZrO_2-Y_2O_3,. In: *Advances in Ceramics Vol. 12: Science and Technology of Zirconia II*, ed. by N. Claussen, M. Ruhle, A.H. Heuer (Am. Ceram. Soc., Columbus 1984) pp. 71–95
14.87 C. Pascual, P. Duran: Subsolidus phase equilibria and ordering in the system ZrO_2-Y_2O_3, J. Am. Ceram. Soc. **66**, 23–27 (1983)
14.88 M. Rühle, N. Claussen, A.H. Heuer: Microstructural studies of Y_2O_3-containing tetragonal ZrO_2 polycrystals (Y-TZP). In: *Advances in Ceramics Vol. 12: Science and Technology of Zirconia II*, ed. by N. Claussen, M. Rühle, A.H. Heuer (Am. Ceram. Soc., Columbus 1984) pp. 352–370
14.89 A.H. Heuer, M. Rühle: Phase transformations in ZrO_2-containing ceramics. II. The martensitic reaction in t-ZrO_2. In: *Advances in Ceramics Vol. 12: Science and Technology of Zirconia II*, ed. by N. Claussen, M. Rühle, A.H. Heuer (Am. Ceram. Soc., Columbus 1984) pp. 14–32
14.90 C.H. Perry, D.W. Liu, R.P. Ingel: Phase characterization of partially stabilized zirconia by Raman spectroscopy, J. Am. Ceram. Soc. **68**, 184–187 (1985)
14.91 Y.K. Voron'ko, A.A. Sobol, S.N. Ushakov, L.I. Tsimbal: Tetragonal structure formation in partly stabilized zirconia, Izv. AS USSR, Inorg. Mater. **30**, 803–808 (1994), in Russian
14.92 M.A. Aboimov, M.A. Borik, G.A. Gogotsi, V.F. Kalabuchova, E.E. Lomonova, V.A. Mizina: Phase transitions in crystals of partially stabilized zirconia, Inorg. Mater. **33**, 285–291 (1997)
14.93 M. Hillert: Critical limit for massive transformation, Metall. Mater. Trans. A **33**, 2299–2308 (2002)
14.94 H.G. Scott: Phase relationships in the yttria-rich part of the yttria–zirconia system, J. Mater. Sci. **12**, 311–316 (1977)
14.95 C.A. Ànderson, J. Greggi, T.K. Gupta: Diffusionless transformations in zirconia alloys,. In: *Advances in Ceramics Vol. 12: Science and Technology of Zirconia II*, ed. by N. Claussen, M. Ruhle, A.H. Heuer (Amer. Cer. Soc., Columbus, OH 1984), pp.78–85
14.96 A. Rouanet: Diagrams of solidification and diagrams of high temperature phases in the zirconia-erbium oxide, zirconia-yttrium oxide and zirconia-ytterbium oxide systems, C. R. Acad. Sci. Ser. C **267**, 1581–1584 (1968)
14.97 Y. Du, Z. Jin, P. Huang: Termodynamic assessment in the ZrO_2-$YO_{1.5}$ system, J. Am. Ceram. Soc. **74**, 1569–1577 (1991)
14.98 N.S. Jacobson, Z.-K. Liu, L. Kaufman, F. Zhang: Thermodynamic modeling of $YO_{1.5}$-ZrO_2 system, J. Am. Ceram. Soc. **87**, 1559–1566 (2004)
14.99 M. Chen, B. Hallstedt, L.J. Gauckler: Thermodynamic Modeling of the ZrO_2-$YO_{1.5}$ system, Solid State Ion. **170**, 255–274 (2004)
14.100 V. Lantery, A.H. Heuer, T.E. Mitchell: Tetragonal phase in the system ZrO_2-Y_2O_3. In: *Advances in Ceramics Vol. 12: Science and Technology of Zirconia II*, ed. by N. Claussen, M. Rühle, A.H. Heuer (Am. Ceram. Soc., Columbus 1984), pp.118–130
14.101 T. Yagi, A. Saiki, N. Ishizava, N. Mizutani, M. Kato: Analytical electron microscopy of yttria partitioning in the yttria-partially-stabilized zirconia-crystal, J. Am. Ceram. Soc. **69**, C3–C4 (1986)
14.102 G.B. Bokij: *Crystal Chemistry* (Nauka, Moscow 1971), in Russian
14.103 V.P. Gorelov, S.F. Pal'guev: Examination of oxigen vacancy model in solid solution ZrO_2-Y_2O_3, Izv. AS USSR, Inorg. Mater. **13**, 181–182 (1977), in Russian
14.104 H.H. Möbius: Sauerstoffionenleitende Festelektrolyte und ihre Anwendungsmöglichkeiten, Z. Chem. **2**, 101–106 (1962), in German
14.105 S. Fabris, A.T. Paxton, M.W. Finnis: A stabilization mechanism of zirconia based on oxygen vacancies only, Acta Mater. **50**, 5171–5178 (2002)

14.106 E.V. Stefanovich, A.L. Shluger, C.R.A. Catlow: Theoretical study of the stabilization of the cubic-phase ZrO_2 by impurities, Phys. Rev. B **49**, 11560–11571 (1994)

14.107 S. Fabris, A.T. Paxton, M.W. Finnis: Relative energetics and structural properties of zirconia using a self-consistent tight-binding model, Phys. Rev. B **63**, 094101–13 (2001)

14.108 F.F. Lange: Transformation toughness, Part I: Size effects associated with the thermodynamics of constrained transformation, J. Mater. Sci. **17**, 225–234 (1982)

14.109 D. Michel, L. Mazerolles, M. Perez y Jorba: Fracture of metastable tetragonal zirconia crystals, J. Mater. Sci. **18**, 2618–2628 (1983)

14.110 F.R. Chien, F.J. Ubic, V. Prakash, A.H. Heuer: Stress-induced transformation and ferroelastic deformation adjacent microhardness indents in tetragonal zirconia single crystals, Acta Mater. **46**, 2151–2171 (1998)

14.111 J. Lefevre: Fluorite-type structural modifications in system having a zirconium and hafnium oxide based, Ann. Chem. **8**, 117–149 (1963)

14.112 D. Baither, B. Baufeld, U. Messerschmidt, F.H. Foitzik, M. Rühle: Ferroelasticity of t′-zirconia: I, high electron microscopy studies of the microstructure in polydomain tetragonal zirconia, J. Am. Ceram. Soc. **80**, 1691–1698 (1997)

14.113 Y.K. Voron'ko, M.A. Zufarov, B.V. Ignat'ev, V.V. Osiko, E.E. Lomonova, A.A. Sobol': Raman scattering in tetragonal single crystals ZrO_2-Gd_2O_3 and ZrO_2-Eu_2O_3, Opt. Spectrosc. **51**, 569–571 (1981), in Russian

14.114 K.M. Prettyman, J.-F. Jue, A.V. Virkar, C.R. Hubbard, O.B. Cavin, M.K. Ferber: Hysteresity effects in 3 mol % yttria-doped zirconia (t′-phase), J. Mater. Sci. **27**, 4167–4174 (1992)

14.115 D. Baither, B. Baufeld, U. Messerschmidt: Morphology of tetragonal precipitates in Y_2O_3-stabilized ZrO_2 crystals, Phys. Status Solidi (a) **137**, 569–576 (1993)

14.116 A.H. Heuer, V. Lanteri, A. Dominguez-Rodriguez: High-temperature precipitation hardening of two phase Y_2O_3-partially-stabilized ZrO_2 single crystals: A first report, J. Amer. Cer. Soc, **69**, 285–287 (1986)

14.117 V. Lanteri, T.E. Mitchell, A.H. Heuer: Morphology of tetragonal precipitates in partially stabilized ZrO_2, J. Am. Ceram. Soc. **69**, 564–569 (1986)

14.118 V.I. Aleksandrov, M.A. Borik, M.A. Vishnyakova, V.P. Voitsitskii, V.F. Kalabuchova, E.E. Lomonova, V.V. Osiko: Method of single crystal preparation (modification), RF Patent 2133787 (1999), in Russian

14.119 A.G. Merjanov, V.A. Raduchev, E.N. Rumanov: Heat waves of melting in dielectric crystals, Dokl. AS USSR **253**, 330–334 (1980), in Russian

14.120 E.N. Rumanov: *Heat Wave of Elementary Substance Melting* (Preprint OIHF AS USSR, Chernogolovka, 1982) p. 20, in Russian

14.121 B. Chalmers: *Theory of Solidification* (Metallurgija, Moscow 1968), in Russian

14.122 A. Hellawell, P.M. Herbert: The development of preferred orientations during the freezing of metals and alloys, Proc. R. Soc. London Ser. A **269**, 560–573 (1962)

14.123 W.A. Tiller: Preferred growth direction of metals, J. Met. **9**, 845–855 (1957)

14.124 A. Rosenberg, W.A. Tiller: The relationship between growth forms and the preferred direction of growth, Acta Metall. **5**, 565–573 (1957)

14.125 W.A. Tiller: Solute segregation during ingot solidification, J. Iron Steel Inst. **215**, 447–457 (1959)

14.126 G.G. Lemmlein: Geometric selection in growing crystal agregate, Dokl. AS USSR **48**, 177–180 (1945), in Russian

14.127 A.V. Chubnikov: About geometric selection rule during formation crystal agregate, Dokl. AS USSR **51**, 679–681 (1946), in Russian

14.128 A.N. Kolmogorov: On the Issue of "geometric selection" crystals, Dokl. AS USSR **65**, 681–684 (1949), in Russian

14.129 V.V. Osiko, D.L. Penyaz, N.P. Khaneev: Study of directional crystallization process in a cold container with direct radiofrequency heating, J. Cryst. Growth **128**, 1193–1196 (1993)

14.130 R.P. Ingel, D. Lewis, B.A. Bender, P.W. Rice: Temperature dependence of strength and fracture toughnes of ZrO_2 single crystals, J. Am. Ceram. Soc. **65**, C150–C152 (1982)

14.131 R.P. Ingel, D. Lewis, B.A. Bender, P.W. Rice: Room temperature strength and fracture of ZrO_2-Y_2O_3 single crystals, J. Am. Ceram. Soc. **65**, C108–C109 (1982)

14.132 D. Michel: Relation between morphology and structure for stabilized zirconia crystals. In: *Advances in Ceramics, Vol. 24 Science and Technology of Zirconia III*, ed. by S. Somiya, N. Yamamoto, H. Yanahida (Am. Ceram. Soc., Columbus 1988) pp. 455–461

14.133 P. Hartman, W.G. Perdok: On the relations between structure and morphology of crystals, Acta Crystallogr. **8**, 525–531 (1955)

14.134 H. Römer, K.-D. Luther, W. Assmus: Measurement of the distribution coefficient of neodymium in cubic zirconium dioxide, J. Cryst. Growth **130**, 233–237 (1993)

14.135 H. Römer, K.-D. Luther, W. Assmus: The distribution coefficients of rare earth ions in cubic zirconium dioxide, J. Cryst. Growth **141**, 159–164 (1994)

14.136 H. Römer, K.-D. Luther, W. Assmus: Determination of the distribution coefficients of the rare earth ions Er^{3+} and Nd^{3+} in yttria-stabilized c-ZrO_2 single crystals, Z. Kristallogr. **209**, 311–314 (1994)

14.137 V.B. Glushkova, V.V. Osiko, L.G. Shcherbakova, V.I. Aleksandrov, Y.N. Paputskii, V.M. Tatarintsev: Study of features monocrystalline solid solution in

ZrO_2–Y_2O_3 system, Izv. AS USSR, Inorg. Mater. **13**, 2197–2201 (1977), in Russian
14.138 D.B. Zhang, X.M. He, J.P. Chen, J.C. Wang, Y.F. Tang, B.L. Hu: Research on crystal growth and defects in cubic zirconia, J. Cryst. Growth **79**, 336–340 (1986)
14.139 A. Baermann, W. Guse, H. Saalfeld: Characterization of different (Me,Zr)O_2 single crystals grown by the "skull-melting" technique, J. Cryst. Growth **79**, 331–335 (1986)
14.140 W.-S. Kim, I.-H. Suh, Y.-M. You, J.-H. Lee, C.-H. Lee: Synthesis of yttria-stabilized zirconia crystals by skull-melting method, Neues Jb. Miner. Monatsh. **3**, 136–144 (2001)
14.141 E.V. Alekseev, O.N. Gorshkov, E.V. Chuprunov, V.A. Novikov, A.P. Kasatkin, G.K. Fukin: Investigation into the specific features of the changes in the crystal structure of stabilized zirconia upon thermochemical reduction, Crystallogr. Rep. **51**, 632–635 (2006)
14.142 H. Kahlert, F. Frey, H. Boysen, K. Lassak: Defect structure and diffuse scattering of zirconia single crystals at elevated temperatures and simultaneously applied electric field, Appl. Cryst. **28**, 812–819 (1995)
14.143 J.S. Thorp, A. Aypar, J.S. Ross: Electron spin resonance in single crystal yttria stabilized zirconia, J. Mater. Sci. **7**, 729–734 (1972)
14.144 R.I. Merino, V.M. Orera, O. Povill, W. Assmus, E.E. Lomonova: Optical and electron paramagnetic resonance characterization of Dy^{3+} in YSZ single crystals, J. Phys. Chem. Solids **58**, 1579–1585 (1997)
14.145 R.I. Merino, V.M. Orera, E.E. Lomonova, S.K. Batygov: Paramagnetic electron traps in reduced stabilized zirconia, Phys. Rev. B **52**, 6150–6152 (1995)
14.146 D. Gomez-Garcia, J. Martinez-Fernandez, A. Dominguez-Rodriguez: Recent advances in electron-beam-induced damage models in yttria fully stabilized zirconia single crystals, Philos. Mag. Lett. **81**, 173–178 (2001)
14.147 R.P. Ingel, D. Lewis III: Lattice parameters and density for Y_2O_3-stabilized zirconia, J. Am. Ceram. Soc. **69**, 325–332 (1986)
14.148 V.I. Aleksandrov, G.E. Val'jano, B.V. Lukin, V.V. Osiko, A.E. Rautbort, V.M. Tatarintsev, V.N. Filatova: Crystal structure of stabilized zirconia, Izv. AS USSR, Inorg. Mater. **12**, 273–277 (1978), in Russian
14.149 R.H. Ingel, D. Lewis, B.A. Bender, R.W. Rice: Physical, microstructural and termomechanical properties of ZrO_2 single crystals. In: *Advances in Ceramics Vol. 12: Science and Technology of Zirconia II*, ed. by N. Claussen, M. Rühle, A.H. Heuer (Am. Ceram. Soc., Columbus 1984) pp. 408–414
14.150 A. Cheikh, A. Madani, A. Touati, H. Boussett, C. Monty: Ionic conductivity of zirconia based ceramics from single crystals to nanostructured polycrystals, J. Eur. Ceram. Soc. **21**, 1837–1841 (2001)
14.151 M. Hartmanova, J. Schneider, V. Navratil, F. Kundracik, H. Schulz, E.E. Lomonova: Correlation between microscopic and macroscopic properties of yttria stabilized zirconia. 1. Single crystals, Solid State Ion. **107**, 136–137 (2000)
14.152 D.S. Thorp, H.P. Buckley: The dielectric constants of current-blackened single crystal yttria-stabilized zirconia, J. Mater. Sci. **8**, 1401–1408 (1973)
14.153 S.P.S. Badwal: Electrical conductivity of single crystal and polycrystalline yttria-stabilized zirconia, J. Mater. Sci. **19**, 1767–1776 (1984)
14.154 N. Bonanos, E.P. Butler: Ionic conductivity of monoclinic and tetragonal yttria-zirconia single crystals, J. Mater. Sci. Lett. **4**, 561–564 (1985)
14.155 V.I. Aleksandrov, S.H. Batygov, Y.K. Voron'ko, B.I. Denker, E.E. Lomonova, V.V. Osiko, V.M. Tatarintsev: Coloure centres in cubic ZrO_2 single crystals, Izv. AS USSR, Inorg. Mater. **11**, 664–667 (1975), in Russian
14.156 V.I. Aleksandrov, M.A. Vishnyakova, V.P. Voitsitskii, E.E. Lomonova, M.A. Noginov, V.V. Osiko, V.A. Smirnov, A.F. Umiskov, I.A. Shcherbakov: Fianite (ZrO_2–Y_2O_3:Er^{3+}) laser emitting the 3 µm range, Sov. J. Quant. Electron. **19**, 1555–1556 (1989)
14.157 V.I. Aleksandrov, M.A. Vishnyakova, V.P. Voitsitskii, Y.K. Voron'ko, E.E. Lomonova, V.A. Mizina, A.A. Sobol, S.N. Ushakov, L.I. Tsimbal: Spectroscopic properties solid solution ZrO_2–Y_2O_3 single crystals doped with Cr and Nd, Izv. AS USSR, Inorg. Mater. **26**, 1251–1255 (1990), in Russian
14.158 A.V. Prokof'ev, W. Assmus, A.I. Shelykh, I.A. Smirnov, B.T. Melekh: Absorption edge of zirconium dioxide crystals doped with rare earth ions, Phys. Solid State **38**, 2739–2743 (1996)
14.159 H. Römer, K.-D. Luther, W. Assmus: Coloured zirconia, Cryst. Res. Technol. **29**, 787–794 (1994)
14.160 S.E. Paje, J. Llopis: Photoluminescence decay and time-resolved spectroscopy of cubic yttria-stabilized zirconia, Appl. Phys. A **59**, 569–574 (1994)
14.161 V.I. Aleksandrov, N.A. Abramov, M.A. Vishnyakova, V.F. Kalabukhova, E.E. Lomonova, N.R. Miftiahetdinova, V.V. Osiko: High temperature disproportionation of fianit, Izv. AS USSR, Inorg. Mater. **19**, 100–103 (1983), in Russian
14.162 L. Thome, J. Fradin, J. Jagielski, A. Gentils, S.E. Enescu, F. Garrido: Radiation damage in ion-irradiated yttria-stabilized cubic zirconia single crystals, Eur. Phys. J. Appl. Phys. **24**, 37–48 (2003)
14.163 T. Hojo, H. Yamamoto, J. Aihara, S. Furuno, K. Sawa, T. Sakuma, K. Hojou: Radiation effects on yttria-stabilized zirconia irradiated with He or Xe ions at high temperature, Nucl. Instrum. Methods Phys. Res. B **241**, 536–542 (2005)
14.164 R. Mevrel, J.-C. Laizet, A. Azzopardi, B. Leclercq, M. Poulain, O. Lavigne, D. Demange: Thermal diffusivity and conductivity of $Zr_{1-x}Y_xO_{2-x/2}$ ($x = 0$,

0.084 and 0.179) single crystals, J. Eur. Ceram. Soc. **24**, 3081–3089 (2004)
14.165 J. Martinez-Fernandez, A.R. Pínto Gómez, J.J. Quispe Cancapa, A.R. de Arellano López, J. Llorca, J.Y. Pastor, S. Farmer, A. Sayir: High-temperature plastic deformation of Er_2O_3-doped ZrO_2 single crystals, Acta Mater. **54**, 2195–2204 (2006)
14.166 A.H. Heuer: Indentation induced crackes and the toughness anisotropy of 9.4 mol yttria-stabilised cubic zirconia single crystals, J. Am. Ceram. Soc. **74**, 855–862 (1991)
14.167 A. Dominguez-Rodriguez, K.P.D. Lagerlof, A.H. Heuer: Plastic deformation and solid solution hardening of Y_2O_3-stabilized ZrO_2, J. Am. Ceram. Soc. **69**, 281–284 (1986)
14.168 D. Holmes, A.H. Heuer, P. Pirouz: Dislocation structure around Vickers indents in 9.4 mol Y_2O_3-stabilized cubic ZrO_2 single crystals, Philos. Mag. A **67**, 325–342 (1993)
14.169 A. Pajares, F. Guiberteau, A. Dominguez-Rodriguez, A.H. Heuer: Microhardness and fracture toughness anisotropy in cubic zirconium oxide single crystals, J. Am. Ceram. Soc. **71**, C332–C3331 (1988)
14.170 A. Pajares, F. Guiberteau, A. Dominguez-Rodriguez, A.H. Heuer: Indentation-induced cracks and toughness anisotropy of 9.4 mol %-yttria-stabilized zirconia cubic single crystals, J. Am. Ceram. Soc. **74**, 859–862 (1991)
14.171 K.J. McClellan, A.H. Heuer, L.P. Kubin: Localized yielding during high temperature deformation of Y_2O_3-fully-stabilized cubic ZrO_2 single crystals, Acta Mater. **44**, 2651–2662 (1996)
14.172 F. Guiberteau, F.L. Cumbrera, A. Dominguez-Rodrigues, E. Fries, J. Castaing: X-ray Berg–Barrett topography of the deformation substructure of stabilized zirconium oxide single crystals deformed at 1673 K, J. Appl. Cryst. **27**, 406–410 (1994)
14.173 D. Gomez-Garcia, J. Martinez-Fernandez, A. Dominguez-Rodriguez: Recent advances in electron-beam-induced damage models in yttria fully stabilized zirconia single crystals, Phil. Mag. Lett. **81**, 173–178 (2001)
14.174 M. Bartch, A. Tikhonovsky, U. Messerschmidt: Plastic deformation of yttria stabilized cubic zirconia single crystals II: Plastic instabilities, Phys. Status Solidi (a) **201**, 46–58 (2004)
14.175 G.A. Gogotsi, D.Y. Ostrovoi, E.E. Lomonova: Deformation behavior of cubic ZrO_2 single crystals, Refractories **3**, 15–19 (1992), in Russian
14.176 R.P. Ingel, D. Lewis III: Elastic anisopropy in zirconia single crystals, J. Am. Ceram. Soc. **71**, 265–271 (1988)
14.177 I.L. Chistyi, I.L. Fabelinskij, V.F. Kitaeva, V.V. Osiko, Y.V. Pisalevskij, I.M. Sil'vestrova, N.N. Sobolev: Experimental study of the properties of ZrO_2-Y_2O_3 and HfO_2-Y_2O_3 solid solution, J. Raman Spectrosc. **6**, 183–192 (1977)
14.178 C.F. Bolling, W.A. Tiller: Growth from the melt. II. Cellular interface morphology, J. Appl. Phys. **31**, 2040–2045 (1960)
14.179 V.G. Fomin, M.G. Mil'vidskii, R.S. Beletskaja: Study of heavy doped silicon single crystals with cellular structure, Crystallogr. Rep. **13**, 172–173 (1968), in Russian
14.180 A.N. Kirgintsev, L.I. Isaenko, V.A. Isaenko: *Impurity Distribution Under Direct Crystallization* (Nauka, Novosibirsk 1977), in Russian
14.181 A.H. Heuer, V. Lantery, A. Dominguez-Rodriguez: High-temperature precipitation hardening of Y_2O_3 partially-stabilized ZrO_2 (Y-PSZ) single crystals, Acta Metall. **37**, 559–567 (1989)
14.182 G.A. Gogotsi, E.E. Lomonova, V.G. Pejchev: Strength and fracture toughness of zirconia crystals, J. Eur. Ceram. Soc. **11**, 123–132 (1993)
14.183 G.A. Gogotsi, E.E. Lomonova, Y. Furmanova, I.M. Savitskaya: Zirconia crystals suitable for medicine: 1. Implants, Ceramurg. Int. **20**, 343–348 (1994)
14.184 V.I. Aleksandrov, S.H. Batygov, Y.K. Voron'ko, M.A. Vishnyakova, V.F. Kalabuchova, E.E. Lomonova, V.V. Osiko: Effect Pr_2O_3 on ZrO_2 crystal growth frim melt, Izv. AS USSR, Inorg. Mater. **23**, 349–352 (1987), in Russian
14.185 M.A. Borik, E.E. Lomonova, V.V. Osiko, V.A. Panov, O.E. Porodinkov, M.A. Vishnyakova, Y.K. Voronko, V.V. Voronov: Partially stabilized zirconia single crystals: growth from the melt and investigation of the properties, J. Cryst. Growth **275**, e2173–e2179 (2005)
14.186 V.V. Alisin, M.A. Borik, E.E. Lomonova, A.F. Melshanov, G.V. Moskvitin, V.V. Osiko, V.A. Panov, V.G. Pavlov, M.A. Vishnjakova: Zirconia-bazed nanocrystalline synthesized by directional crystallization from the melt, Mater. Sci. Eng. C **25**, 577–583 (2005)
14.187 M.A. Borik, Y.K. Voron'ko, E.E. Lomonova, V.V. Osiko, V.A. Sarin, G.A. Gogotsi: Mechanical properties of the PSZ crystal grown by skull melting technique: influence of technology conditions. In: *Fracture Mechanics of Ceramics, Vol.13, Crack-Microstructure Interaction, R-curve Behavior, Environmental, Effects in Fracture, and Standardization*, ed. by R.S. Bradt, D. Munz, M. Sakai, V.Y. Shevchenko, K. White (Kluwer/Plenum, New York, Boston, London, Moscow 1999), pp.485–496
14.188 G.A. Gogotsi, E.E. Lomonova, V.V. Osiko: Mechanical characteristics zirconia single crystals for constructional applications, Refractories **8**, 14–17 (1991), in Russian
14.189 G.A. Gogotsi, V.I. Galenko, B.A. Ozerskii, E.E. Lomonova, V.A. Mizina, V.F. Kalabukhova: Prochno strength and fracture toughness of zirconia single crystals with yttrum and terbium oxides, Refractories **6**, 2–8 (1993), in Russian

14.190 S.N. Dub, G.A. Gogotsi, E.E. Lomonova: Hardness and fracture toughness of tetragonal zirconia single crystals, J. Mater. Sci. Lett. **1**, 446–449 (1995)
14.191 G.A. Gogotsi, S.N. Dub, B.A. Ozerskii, D.Y. Ostrovoi, G.E. Khomenko, S.H. Batygov, M.A. Vishnjakova, V.F. Kalabukhova, S.V. Lavrishchev, E.E. Lomonova, V.A. Mizina: Zirconia single crystals with yttrum and terbium oxides, Refractories **7**, 2–10 (1995), in Russian
14.192 V.V. Alisin, K. Amosova, V.P. Voitsitskii, V.V. Voronov, V.A. Grinenko, E.E. Lomonova, N.I. Medvedovskaya, V.I. Ustinov: Influence of temperature on oxygen redistribution in nanocrystal-zirconia-based materials with high mechanical characteristics. In: *Perspektivnie Materiali I Tehnologii: Nanokompozity*, Vol. 2, ed. by A.A. Berlin, I.G. Assovsky (Toruss, Moscow 2006) pp. 183–193
14.193 J. Martinez-Fernandez, M. Jimenez-Melendo, A. Dominguez-Rodriguez: Microstructural evalution and stability of tetragonal precipitates in Y_2O_3-partially stabilized ZrO_2 single crystals, Acta Metall. Mater. **43**, 593–601 (1995)
14.194 J. Martinez-Fernandez, M. Jimenez-Melendo, A. Domiguez-Rodriguez, A.H. Heuer: Microindentation-induced transformation in 3.5 mol yttria-partially-stabilized zirconia single crystals, J. Am. Ceram. Soc. **74**, 1071–1081 (1991)
14.195 V.V. Osiko, V.V. Alisin, M.A. Vishnjakova, Z.V. Ignat'eva, E.E. Lomonova, V.G. Pavlov: Tribological properties of nanocrystalline material based on zirconia, Frict. Wear **26**, 285–289 (2005), in Russian
14.196 V.V. Osiko, V.V. Alisin, M.A. Vishnjakova, Z.V. Ignat'eva, E.E. Lomonova, V.G. Pavlov: Effect Y_2O_3 stabilisator content on tribological properties of nanocristalline material based on zirconia, Zavod. Lab. Diagn. Mashin **4**, 47–52 (2006), in Russian
14.197 K.V. Frolov, V.V. Osiko, V.V. Alisin, M.A. Vishnjakova, Z.V. Ignat'eva, E.E. Lomonova, A.F. Melshanov, G.V. Moskvitin, V.G. Pavlov, M.S. Pugachev: Mechanical and tribological properties of nanocrystalline material based on zirconia, Probl. Mashinostr. Nadezn. Mashin **4**, 3–8 (2006), in Russian
14.198 P. Christel, A. Meunir, M. Heller, Y.P. Torre, C.N. Peille: Mechanical properties and short-term in vivo evaluation of yttrium oxide–partially-stabilized zirconia, J. Biomed. Mater. Res. **23**, 45–61 (1989)
14.199 C. Piconi, G. Maccauro: Zirconia as a ceramic biomaterial, Biomaterials **20**, 1–25 (1999)
14.200 V. Nezhentsev, Y. Petrov, A. Zhilin, O. Dymshits: Use of induction furnaces with a cold crucible for melting hard glasses (review), Steklo Keram. **9**, 9–11 (1986)
14.201 V.I. Aleksandrov, M.A. Borik, G.H. Dechev, N.I. Markov, V.A. Myzina, V.V. Osiko, V.M. Tatarintsev, R.Y. Khodakovskaja: Synthesis and investigations of La_2O_3-Al_2O_3-SiO_2 glasses, Glass Phys. Chem. **6**, 170–173 (1980), in Russian
14.202 B.À. Sakharov, Ò.S. Sedyh, Å.P. Rashevskaja: Study of system Y_2O_3-SiO_2-Al_2O_3, Trudy Giredmet **52**, 83–87 (1974), in Russian
14.203 V.I. Aleksandrov, M.A. Borik, V.B. Glushkova, R.E. Krivosheev, N.I. Markov, V.V. Osiko, V.M. Tatarintsev: Synthesis and some properties of refractory glasses in $R_2O_3 - Al_2O_3 - SiO_2$ system, Glass Phys. Chem. **3**, 177–180 (1977), in Russian
14.204 A. Makishima, Y. Tamura, T. Sakaino: Elastic moduli and refractive indices of aluminosilicate glasses containing Y_2O_3, La_2O_3 and TiO_2, J. Am. Ceram. Soc. **61**, 247–249 (1978)
14.205 A. Makishima, T. Shimohira: Alkaline durability of high elastic modulus aluminosilicate glasses containing Y_2O_3, La_2O_3 and TiO_2, J. Non-Cryst. Solids **39/40**, 661–666 (1980)
14.206 G.E. Malashkevich, V.N. Tadeush, V.V. Kuznetsova, A.K. Cherches, N.I. Bliznyuk, V.G. Mikhalevich, M.B. Rzhevskii: Physicochemical and spectral luminescence properties of a glass based on thf SiO_2-Al_2O_3-La_2O_3-Nd_2O_3 system, J. Appl. Spectrosc. **37**, 926–929 (1982)
14.207 J. Shelby, S. Minton, C. Lord, M. Tuzzolo: Formation and properties of yttrium aluminosilicate glasses, Phys. Chem. Glasses **33**, 93–98 (1992)
14.208 J. Kohli, J. Shelby, J. Frye: A structural investigations of yttrium alumosilicate glasses using ^{29}Si and ^{27}Al magic angle spinning nuclei-magnetic resonance, Phys. Chem. Glasses **33**, 73–78 (1992)
14.209 T.T. Basiev, Y.K. Voron'ko, V.V. Osiko, A.M. Prokhorov: Laser spectroscopy doped crystals and glasses. In: *Spectroscopy of Crystals*, ed. by A.A. Kaplyansky (Leningrad, Nauka 1983) pp. 57–82, in Russian
14.210 M. Weber: Laser exited fluorescence spectroscopy in glass. In: *Laser Spectroscopy of Solids*, ed. by W.M. Yen, P.M. Selzer (Springer, Berlin-Heidelberg, New-York 1981) pp. 189–239
14.211 G.E. Malashkevich, N.N. Ermolenko, V.I. Aleksandrov, M.A. Borik, G.M. Volokhov, A.S. Gigevich, G.A. Denisenko, A.V. Mazovko, V.N. Tadeush: Spectral-luminescent and thermomechanical characteristics of silicate-borate glasses activated with Yb^{3+} and Er^{3+} ions, Izv. AS USSR, Inorg. Mater. **6**, 1053–1055 (1987), in Russian
14.212 Y.I. Matunin, A.V. Demin, T.V. Smelova: Behavior of uranium and rare-earth elements in glasses synthesized in an induction melter with a cold crucible, At. Energy **83**, 795–800 (1997)
14.213 N.D. Musatov, V.G. Pastushkov, P.P. Poluektov, T.V. Smelova, L.P. Sukhanov: Compaction of

radioactive thermal-insulation materials and construction debris by melting in a cold crucible, At. Energy **99**, 602–606 (2005)

14.214 K. Guilbeau, A. Giordana, W. Ramsey, N. Shulyak, A. Aloy, R. Soshnikov: Induction-melting technology, Am. Ceram. Soc. Bull. **83**, 38–40 (2004)

15. Crystal Growth of Laser Host Fluorides and Oxides

Hongjun Li, Jun Xu

Following the discovery of the first laser action based on ruby, hundreds of additional doped crystals have been shown to lase. Among those, many crystals, such as Ti:Al_2O_3, Nd:$Y_3Al_5O_{12}$, Nd:YVO_4, Yb:$Y_3Al_5O_{12}$, Yb:$Ca_5(PO_4)_3F$, and Cr:LiCAF have come to practical application, and are being widely used in scientific research, manufacturing and communication industries, military applications, and other fields of modern engineering. These crystals are mainly oxides and fluorides, which are grown from melt. This chapter reviews the major results obtained during recent years in the growth of various crystalline oxides and fluorides for laser operation, with emphasis on crystals doped with the additional ions Ti^{3+}, Nd^{3+}, and Yb^{3+}. On the other hand, special attention is paid to discuss the elimination of growth defects in these crystals. Limited by the length of this chapter, for each crystal, only outstanding defects are considered herein.

15.1 **Crystal Growth of Laser Fluorides and Oxides from Melt** 479
15.1.1 Laser Crystal Growth from the Melt . 480
15.1.2 Czochralski Technique (CZ) 480
15.1.3 Temperature Gradient Technique (TGT) 482
15.1.4 Heat-Exchanger Method (HEM) 483
15.1.5 Vertical Bridgman Technique (VBT) . 484
15.1.6 Horizontal Bridgman Technique (HBT) 485
15.1.7 Laser-Heated Pedestal Growth Method (LHPG) 486
15.1.8 Flux Technique (FT) 487
15.2 **Laser Crystal Defects** 487
15.2.1 Ti:sapphire 487
15.2.2 Nd-Doped Laser Crystals 489
15.2.3 Yb-Doped Laser Crystals 492
15.2.4 Other Activator-Doped Laser Crystals 498
15.3 **Crystal Growth Techniques Characterization** 501
15.3.1 Czochralski (CZ) Process 501
15.3.2 Temperature Gradient (TGT) 501
15.3.3 Heat-Exchanger Method (HEM) 502
15.3.4 Vertical Bridgman Technique (VBT) . 502
15.3.5 Horizontal Bridgman Technique (HBT) 502
15.3.6 Laser-Heated Pedestal Growth (LHPG) 503
15.3.7 Flux Technique (FT) 503
References 503

15.1 Crystal Growth of Laser Fluorides and Oxides from Melt

The development of many advanced fields in modern engineering is, to a large extent, governed by the success achieved in the techniques of crystal growth. On the other hand, the demand for new crystals for advanced technologies has stimulated the improvements in growth techniques of these crystals. Certainly, this concerns only a few very important crystals.

In 1960, laser action was first demonstrated on the basis of a ruby laser rod (or Cr^{3+}-doped Al_2O_3) [15.1], indicating the birth of a new subdiscipline of science: the laser technique. In the 1970s, the discovery of Nd^{3+}-doped yttrium aluminum garnet (Nd:YAG) [15.2] crystal prompted the rapid development of the solid-state laser. In the 1980s, the invention of Ti^{3+}-doped sapphire (Ti:Al_2O_3) [15.3] made it possible to produce ultra-intense and ultrafast lasers, based on which the intralase technique has been employed widely in both basic and applied science fields. In the 1990s, the successful fabrication of Nd:YVO_4 [15.4] led to a new period of development for the laser technique:

the all-solid-state laser. Simultaneously, the advent of cheap diode-laser pump sources brought about the practical application of Yb-doped materials such as Yb:YAG [15.5] and Yb:$Sr_5(PO_4)_3F$ (Yb:S-FAP) [15.6], which have shown great capability in high-power laser systems. Entering the 21st century, research into laser materials is expanding extensively in the forms of single crystal, glass, ceramics, and fiber. Owing to their advantages of simple fabrication processes, lower costs, and greater perfection, laser fiber [15.7] and polycrystalline ceramics [15.8] are challenging the dominant status of traditional materials.

In spite of the hundreds of additional doped crystals that have been shown to lase, few crystals have proven to be useful in practical circumstances. In fact, the gap between demonstration exercises of laser action and the engineering of practical systems is often wide and difficult to bridge.

In order to develop and test new laser crystals, it is first crucial to identify the appropriate means by which to grow and fabricate the crystal. To further optimize the crystal growth conditions, it is necessary to understand the physical properties of the melt and solid. In order to improve the crystal quality, it is important to clarify the formation mechanism of growth defects in the crystal so as to find proper ways to eliminate them. While the methods and issues associated with crystal growth occupy the bulk of this chapter, we begin with a discussion of the important growth techniques and their modifications for laser crystal growth. Our attention is focused on the insights and issues involved in the development, melt-growth, and defect elimination of the main laser oxides and fluorides. Since our approach will entail discussion from the perspective of laser materials, only crystals doped with the most attractive additional ions, such as Ti^{3+}, Nd^{3+}, and Yb^{3+}, will be addressed.

15.1.1 Laser Crystal Growth from the Melt

After the development of the first laser, which was based on a Verneuil-grown ruby, almost all of the classical crystallization techniques have been applied to analyze growth characteristics and provide high-quality laser crystals and the development of new laser crystals. In the 1960s, flux methods were widely used to grow the rare-earth aluminum and gallium garnets, both pure and doped, as well as some of the rare-earth orthoaluminate hosts. The emphasis later was on melt techniques, as they provided both larger crystal size and faster growth rates. Among these, the Czochralski technique (CZ) employing iridium crucibles and radiofrequency (RF) heating was the most adaptable and widely used for the majority of high-temperature laser oxides, while the vertical Bridgman technique (VBT) was commonly used for laser fluorides. On the other hand, static growth techniques, such as the heat-exchange method (HEM) and temperature gradient technique (TGT), have been becoming efficient methods for the growth of large-sized laser crystals, while two other promising techniques, the micro-pulling-down method (μ-PD) and the laser-heated pedestal growth method (LHPG), are especially used for fiber crystal growth.

15.1.2 Czochralski Technique (CZ)

The CZ method is named after *Jan Czochralski* who introduced an early version of the present-day process in 1916, and published it as a method for studying the crystallization rate of metals [15.9]. Further modifications by *Teal* and *Little* [15.10] brought the technique closer to the process known today as the Czochralski, or CZ, method. The application of this technique and its consequent development was stimulated by the invention of the laser in 1960, since when it has been used for oxide crystal production [15.11, 12].

The CZ furnace geometry is relatively simple, as shown in Fig. 15.1, and is usually constructed of either Al_2O_3 or stabilized ZrO_2 ceramics. The crucible can be either Pt or Ir, depending upon the melting point of the material and/or the atmosphere required for the growth process.

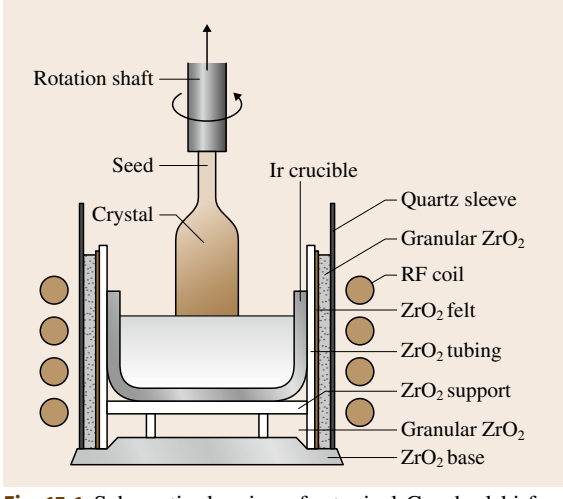


Fig. 15.1 Schematic drawing of a typical Czochralski furnace used for the growth of oxide-based laser crystals

The crucible is heated by means of an RF generator operating in the range of 10–400 kHz. With the development of solid-state RF generators, the trend is toward lower frequencies, preferably in the range 10–30 kHz. These lower frequencies have the distinct advantage of producing more uniform heating of crucible, which is necessary for the growth of large-diameter crystals, and in the case of the higher-melting oxide systems that must use ZrO_2 insulation, avoiding coupling of the RF energy directly into the ceramic parts of the furnace.

The growth and control of the crystal is dependent upon the radial temperature gradient in the liquid and the vertical gradient through the length of the furnace. For smaller growth systems (typically using crucibles less than 75 mm in diameter), the adjustment of the radial and vertical thermal gradients can be easily accomplished by varying the ceramic insulation and its dimension. However, once beyond this size, a suitable liquid radial gradient becomes more difficult to establish, thereby making seeding and the initial cone section of the crystal more difficult to control, hence the need for an automatic diameter control system. Although several methods of diameter control have been developed [15.14–17], the one mostly widely used is that of weighing the crystal while it is growing. In this case, a load cell with a sensitivity of ±0.1 g is placed in line with the rotation shaft to which the seed crystal is attached. As the crystal is pulled from the melt, the change in weight is used to generate a control signal that modifies the generator output power to the crucible, thereby controlling the diameter through small changes in the liquid temperature. Typical systems are easily capable of maintaining a 75 mm-diameter crystal to within ±1 mm.

The CZ growth process is, by far, the most commonly used process for the growth of laser materials and is employed over a wider span of materials and melting points than any other melt-growth method, ranging from mixed compounds such as nitrates, through germinates, fluorides, molybdates, tantalates, and garnets, to single oxides such as sapphire and yttria. To circumvent various kinds of problems encountered during crystal growth, numerous modifications have been made to improve the standard CZ growth process.

During the growth of Nd:YAG crystals, the Nd segregation problem always exists. Nd concentration increases as crystal growth proceeds so that, if we want to keep uniformity of concentration within 0.1 at. %, solidification is restricted to 20–30% of melt in crucible. To achieve higher solidification, *Katsurayama* and coworkers [15.13] developed a double-crucible method with

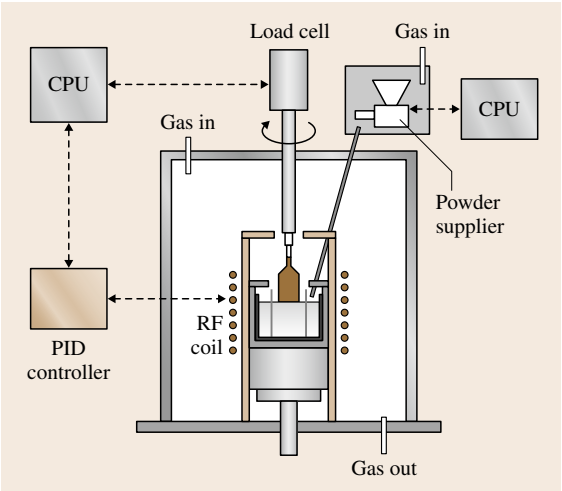


Fig. 15.2 Schematic diagram of crystal growth apparatus with automatic powder supply system [15.13] (CPU – central processing unit, PID – proportional–integral-derivative)

automatic powder supply (Fig. 15.2). In this system, material powder is continuously supplied into the crucible to maintain the concentration of Nd in the melt. As a result, the Nd concentration fluctuation in the grown crystal has been reduced to as low as 0.02 at. % when 30% of melt is solidified. On the other hand, *Kanchanavaleerat* et al. [15.18] modified the growth parameters to grow highly doped Nd:YAG crystals with excellent optical quality, as shown in Fig. 15.3, and the laser testing shows that the highly doped Nd:YAG rods have very good efficiency due to low passive losses.

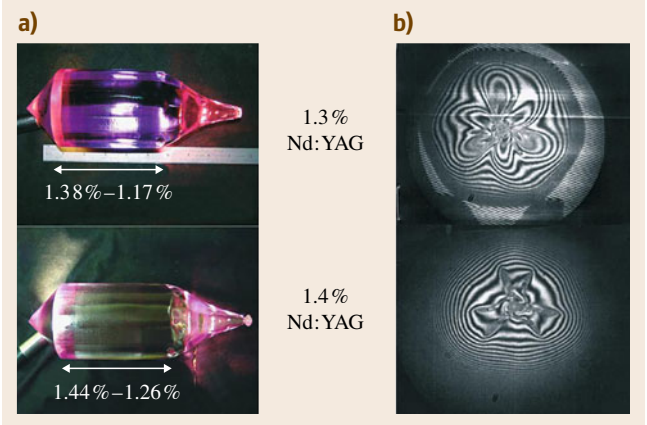


Fig. 15.3 **(a)** Highly doped Nd:YAG crystals, **(b)** Zygo interferogram

Boulon et al. [15.19] indicated that Y_2O_3, Sc_2O_3, and Lu_2O_3 sesquioxides have the highest laser potentialities in the continuous wave (CW) regime. However, due to their high melting points, about 2420 °C, the growth of the sesquioxides is rather difficult. The major problem is that the high temperature restricts the choice of crucible materials, which has to be mechanically stable at the melting point and resistant to chemical reactions with the melt as well as with the surrounding thermal insulation. The results of *Fornasiero* et al. [15.20] reveal that rhenium fulfills these requirements to the greatest extent. Rhenium is sensitive to oxidizing atmospheres but resistant to melts of Al_2O_3 and rare-earth oxides. The melting point of rhenium is 3180 °C. To avoid the react of the hot crucible and the ceramic zirconia insulation at high temperatures, Fornasiero designed a holding construction which consisted of rhenium rods directly welded to the crucible. The crucible was suspended in a thermally insulating tube of zirconia felts so that it was completely surrounded by gas. To reduce the radiation losses from the free melt surface, rings and funnels were inserted into the crucible a few millimeters above the melt. Through the above modifications of the conventional CZ configuration, several crystals with typical length of 5 mm and diameter of 10 mm have been grown [15.20].

Shimamura et al. reported the growth of Ce:LiCAF crystals without either the use of HF gas or the hydrofluorination of raw materials [15.21]. Instead, a growth chamber was evacuated to about 10^{-2} Torr prior to growth, and high-purity Ar (99.9999%) gas was used as a growth atmosphere. Under these conditions, a deposit of a white foreign substance, composed of volatile fluorides and oxyfluoride, was found on the surface of the grown crystals. In order to avoid its formation and to grow high-quality crystals with higher reproducibility, several modifications such as high-vacuum atmosphere prior to growth, use of CF_4 gas instead of Ar, and growth with a low temperature gradient, were required [15.21]. Such modifications are also needed for the growth of other fluorides, e.g., $LiYF_4$ (YLF), $BaLiF_3$, and CaF_2 [15.22, 23].

15.1.3 Temperature Gradient Technique (TGT)

The temperature gradient technique (TGT) is a typical static directional solidification technique, which was invented by *Zhou* et al. [15.24] in 1979; Shanghai Institute of Optics and Fine Mechanics (SIOM) obtained a patent on TGT in 1985 [15.25].

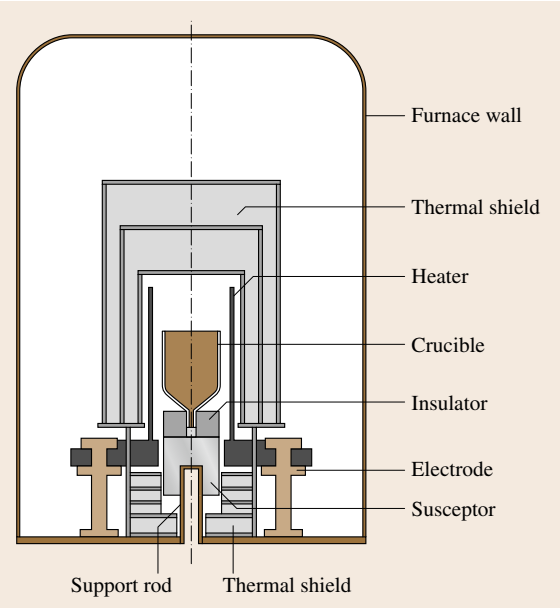


Fig. 15.4 Schematic diagram of a TGT furnace

A schematic diagram of the TGT furnace is shown in Fig. 15.4. It consists of a molybdenum crucible, graphite heating element, and molybdenum heat shields. The cylindrical graphite heating element is designed as an electric circuit with appropriate linear resistance from the top to the middle by making holes with a certain distribution. The cylinder is placed in the graphite electrodes, which are cooled by water. The temperature gradient of the upper part is produced by the linear resistance of the heating element, whereas that in the lower part depends on the extraction of heat by water flowing in the tubes through the electrodes. Besides these, the temperature field near the seed is influenced by the heat conductivity of the water-cooled center rod. In TGT, there are no moving parts. The growth process is accomplished by dropping the temperature at designed rates with a high-precision temperature program controller.

Large-sized laser oxide and fluorides, such as Ti:sapphire [15.26], Nd:YAG [15.27], Yb:$YAlO_3$ (Yb:YAP) [15.28], and Na,Yb:CaF_2 [15.29] shown in Fig. 15.5, have been grown successfully by the TGT method. Taking the growth of Ti:sapphire as an example, the basic growth process of TGT can be described as follows. A cylindrical seed with the selected orientation is placed into the seed hole of the molybdenum crucible, and the high-purity starting materials are placed in the crucible. The furnace is loaded for the

growth process, outgassed to $(2-4)\times10^{-3}$ Pa; when the temperature at the bottom of crucible is about 1400 °C, high-purity Ar is fed into furnace; then the material is melted and kept molten for several hours. After the temperature field has stabilized, crystallization is started by slow cooling (1.3–3 K/h). The solid–liquid interface advances upwards as the temperature drops. The whole crystallization process is completed automatically. During the growth process, it is essential that the temperature and thermal field are very stable, and an important factor is the flow stability of the circulating cooling water so that the solid–liquid interface advances with constant velocity.

The typical size of TGT-grown Ti:sapphire boules is $\varnothing110\times80\,\mathrm{mm}^2$, the titanium doping levels are between 0.05 and 0.52 wt %, the absorption coefficient at 490 nm is from 1 to 7.5 cm^{-1}, the absorption coefficient can be as high as 10 cm^{-1} in some case (the theoretical limit is 11 cm^{-1} for absorption coefficient at 490 nm), and the figure of merit (FOM) of Ti:sapphire crystals is in the range 150–400. Besides the mentioned advantages, there are other advantages of TGT-grown Ti:sapphire, such as low dislocation density, low scattering, and high perfection, which are very important factors determining laser performance [15.31].

For TGT-grown Nd:YAG crystals, high doping concentration of neodymium is a distinct character. Highly doped (2.5 at. %) Nd:YAG shows high absorption coefficients at the 808 nm laser diode (LD)-pumping wavelength up to 7.55 cm^{-1}, nearly three times higher than 1 at. % Nd:YAG [15.32]. Therefore, a short crystal length (e.g., 1 mm) is preferred, and compact microchip lasers can be constructed by using 2.5 at. %-doped Nd:YAG. Almost the same output has been achieved preliminarily in both (111)-cut 1 mm-long Nd:YAG and *a*-cut 1 mm-long YVO_4 microchip lasers with a very short (9 mm) laser cavity. In particular, the broader and smoothly varying absorption bandwidth allows less stringent requirements on temperature control.

In the growth of Yb:CaF_2 crystals, it is notable that a lid was employed to seal the crucible to reduce volatilization of the materials. Sometimes, small amounts of PbF_2 or ZnF_2 acting as scavengers were added to the CaF_2 raw materials to eliminate residual moisture prior to growth.

15.1.4 Heat-Exchanger Method (HEM)

The heat-exchanger method (HEM) for growing large sapphire boules was invented by *Schmid* and *Viechnicki* at the Army Materials Research Lab in Watertown, MA,

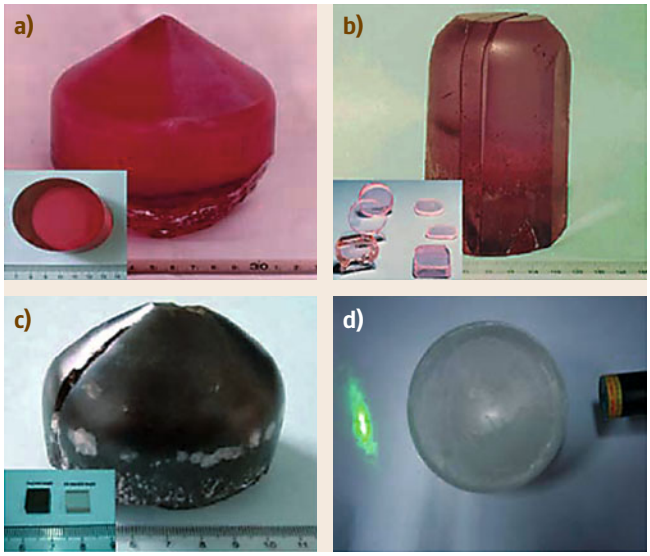


Fig. 15.5a–d Crystal boules and fabricated samples of Ti:sapphire (**a**), Nd:YAG (**b**), Yb:YAP (**c**) and Na, Yb:CaF_2 (**d**) grown by TGT

in 1967 [15.33]. The modern implementation of *Schmid* and *Viechnicki*'s heat-exchanger method at Crystal Systems in Salem, MA, is shown in Fig. 15.6 [15.30].

It consists of a water-cooled chamber containing a well-insulated heat zone. A high-temperature heat exchanger is introduced from the bottom of the furnace

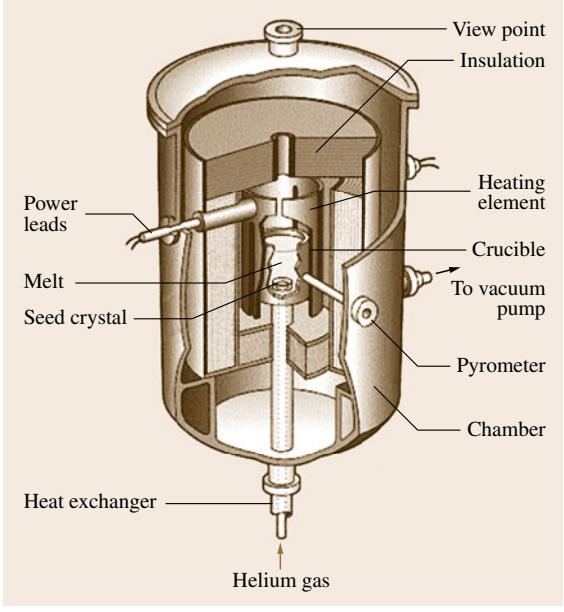


Fig. 15.6 Schematic of a HEM furnace [15.30]



Fig. 15.7 A 10 cm-diameter Ti:Al_2O_3 crystal grown by HEM [15.34]

into the heat zone. The heat exchanger is a closed-end tube with an injection tube through which a controlled flow of coolant gas is introduced. A crucible with a seed crystal positioned at the bottom and loaded with charge is placed on top of the heat exchanger. The furnace chamber can be evacuated with a vacuum pump or backfilled with a gas for controlled atmosphere processing. Heat is supplied by the graphite resistance to melt the charge; the seed is prevented from melting by flowing minimal coolant gas through the heat exchanger. After partial melting of the seed, gas flow is increased to cool the seed and initiate crystallization of melt onto the seed. The furnace is held at constant temperature during growth of the crystal, which proceeds out from the seed in three dimensions. After crystallization is complete, the furnace temperature and the helium flow are decreased and the boule is slowly annealed in situ. The long, slow cool-down produces crystals of the highest quality.

HEM has been successfully utilized for the growth of the world's largest sapphire boules with diameter of 340 mm and mass of 82 kg [15.36]. By this method, more than 95% of the melt can be converted into high-quality crystalline material. HEM was capable of growing laser crystals such as Ti:sapphire (as shown in Fig. 15.7) [15.34], Co:MgF_2 [15.34, 37], Nd:YAG [15.38], and Ti:YAP [15.39].

Recently, a modified HEM technique has been employed in the production of high-melting (about 2400 °C) sesquioxides, such as Yb:Sc_2O_3 and Yb:Y_2O_3 [15.35]. Due to the high melting point (m.p.) of yttria and scandia, rhenium (m.p. 3180 °C) was selected

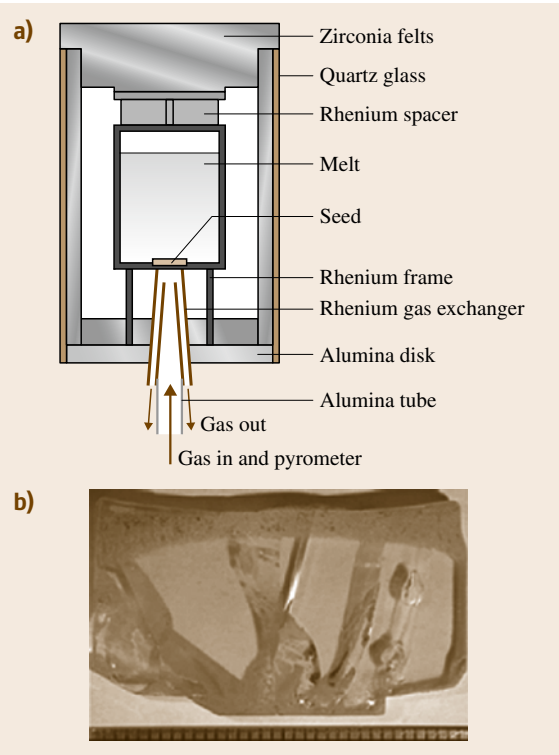


Fig. 15.8a,b Insulation HEM setup for the growth of high-melting sesquioxide crystals **(a)** and the grown Sc_2O_3 crystal **(b)** [15.35]

as the crucible material, and the crucible was completely surrounded by gas since no insulation materials could be found that would be stable when in direct contact with the crucible at the required temperature. The growth setup is shown in Fig. 15.8a. During the growth process, the crucible was heated by an RF generator under an atmosphere of 0.01% O_2, 10–15% H_2, and 85–90% N_2 at pressure of 1 bar. Eventually, crystals with vertical volumes of small, single crystals were obtained (Fig. 15.8b), owing to the use of a polycrystalline seed.

15.1.5 Vertical Bridgman Technique (VBT)

The vertical Bridgman technique (VBT) was first used by *Bridgman* in 1925 [15.40] and especially exploited by *Stockbarger* in 1936 and 1949 [15.41, 42]. This technique is commonly known as the Bridgman–Stockbarger method, although sometimes the names of Tammann (1925) and Obreimov (1924) are associated with the technique. *Buckly* [15.43] discussed the histor-

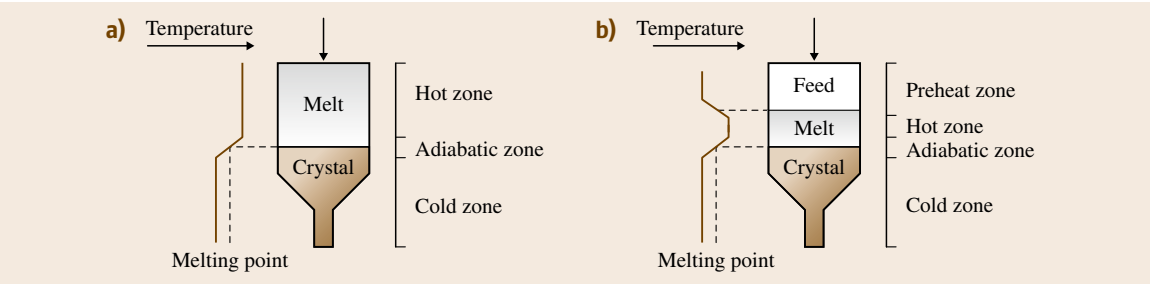


Fig. 15.9a,b A classical (**a**) and a modified (**b**) vertical Bridgman process

ical aspects of the technique and assigned the name to the original researcher.

In the Bridgman process, an ampoule containing the materials to be crystallized is translated from a zone hotter than the melting point, through a temperature gradient, to a zone cooler than the melting point in order to solidify the material (Fig. 15.9a). Equivalently, the temperature can be translated through a stationary ampoule by moving the furnace relative to the ampoule.

The vertical Bridgman technique has been applied to the growth of oxide crystals since the late 1960s [15.44]. In apparatus for this purpose a resistively heated tungsten furnace and crucibles (tubes) fabricated from molybdenum are used. Several complex oxide crystals have been grown by this technique, including Nd:YAG, and the first lasing material Nd:$YAlO_3$. This technique has proved to have great potential in both materials research and in the production of oxide laser crystals. Various Bridgman-grown crystals possessing application quality are now available, including Nd:YAG, Er:YAG, Tm^{3+},Cr^{3+}:YAG, Tm^{3+},Cr^{3+},Ho^{3+}:YAG, Er:LuAG, Pr:$YAlO_3$, Pr:$LuAlO_3$, and Nd:$LuAlO_3$ [15.44]. Improvements of crystalline and chemical perfection of crystals, obtained as a result of better understanding of the basic physical possesses occurring during crystallization in this configuration, have resulted in larger-scale use of this technique for oxide crystal growth. In addition, VBT has been widely used for the growth of large-sized commercial CaF_2 crystals for optical applications [15.45]. Certainly, this technique can be modified for the growth of ion-doped CaF_2 crystals or other fluorides for laser applications.

Figure 15.9b illustrates a modification of the Bridgman technique in which a third zone, cold relative to the melting point, is added to the top of the furnace. This is referred to as the moving melt zone or the traveling heater method. In this case the melt volume is small compared with the ampoule. The advantages of this configuration are twofold. First, steady-state conditions may be established in the small melt volume for growth of crystals with nonunity segregation coefficient to level out changes in dopant concentration along the length of the crystal. Second, the upper interface produces a temperature gradient that drives buoyant convection, thereby increasing mixing in the melt. This can be important for growth of multicomponent systems.

15.1.6 Horizontal Bridgman Technique (HBT)

The horizontal Bridgman technique (HBT), also known as the Bagdasarov method, is a method for refractory single-crystal growth proposed by *Bagdasarov* in 1964 [15.46]. In HBT, presented schematically in Fig. 15.10, the crystallizing material (in the form of powder, crystal crackles or ceramics) is placed in a boat-like crucible, melted by moving the crucible through the heating zone, and then crystallized. To obtain a strictly oriented crystal the single crystal seed is mounted on the top of the crucible (boat) and both the moment of seeding and the formation of the growth front are observed visually.

HBT allows repeated crystallizations to be carried out when additional chemical purification of the raw

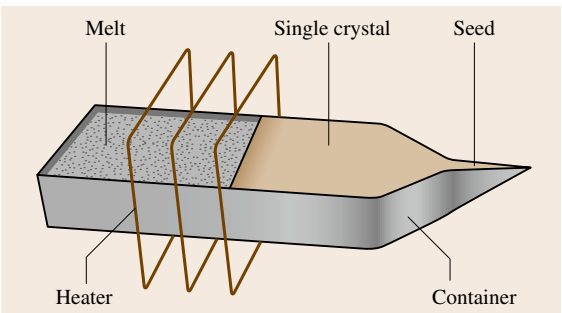


Fig. 15.10 Horizontal Bridgman technique scheme

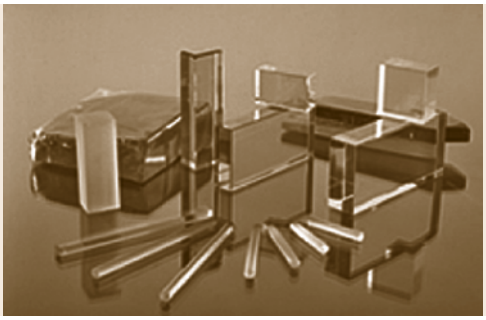


Fig. 15.11 Nd:YAG and Er:YAG crystals grown by HBT [15.46]

material is required. It is also possible to carry out a continuous crystallization process by directed shifting of the crucible echelon through the crystallization zone. With the HBT method it is technically easy to create a controlled temperature field, which is crucial for the growth of high-perfection large-size single crystals. This method makes it possible to obtain large slabs with almost perfect edges and of any given crystallographic orientation.

Initially, this method was designed in order to grow large-size, Nd-doped, high-perfection yttrium–aluminum garnet laser crystals. Later, it turned out to have potential for the growth of yttrium–erbium–aluminum garnet. The crystals have a typical size of $130 \times 130 \times 25\,\mathrm{mm}^3$ as well as high optical homogeneity, as shown in Fig. 15.11. Recently, it is reported that HBT could be used to produce a new type of Nd:YAG crystal with emission property two times higher than from conventional Nd:YAG crystals [15.46].

15.1.7 Laser-Heated Pedestal Growth Method (LHPG)

Poplawsky [15.48] was the first to initiate crystal growth using a pedestal growth process based on melting materials by the energy created by an image furnace. Then, in 1972, *Haggerty* et al. developed the laser-heated pedestal growth method (LHPG), which was improved later by *Feigelson* [15.49] at Stanford University.

Figure 15.12 illustrates LHPG crystal growth. In this technique a float zone is created at the top of a vertical feed rod by using a focused laser beam. Motion of the float zone is generated by vertical displacement of the feed. During this translation, the feed progressively melts and, behind the float zone, a crystallized rod is formed. The float zone remains in equilibrium with the feed and the crystallized rod due to surface tension. The source rod materials containing the desired host and dopant materials can be used as oriented fiber single crystals or polycrystalline reacted materials prepared by solid-state reaction. A seed crystal, once dipped into the molten zone, is withdrawn at some rate faster than the source material is fed in. By conservation of melt volume, this leads to the crystalline fiber

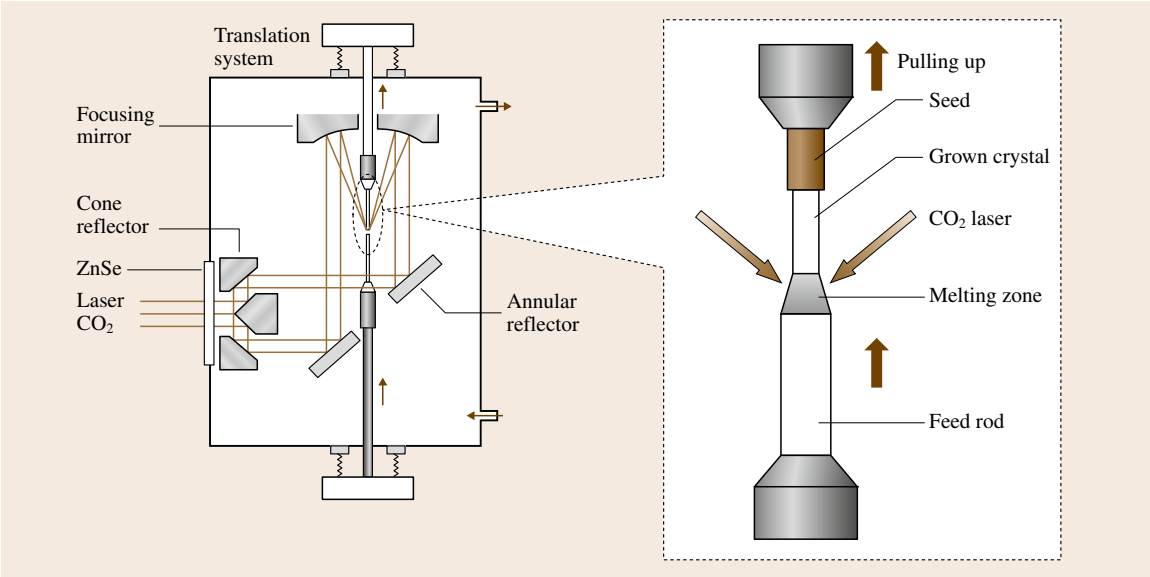


Fig. 15.12 Schematic diagram of the laser optics used in the LHPG technique [15.47]

growing at some constant fraction of the source rod diameter.

A great variety of oxide and fluoride crystal fibers doped with rare-earth and transition metal ion activators in a great range of concentrations have been pulled by the LHPG technique [15.47, 50]. Specially, because of the lack of crucible and the use of a CO_2 laser, the LHPG technique is well adapted to high-refractory crystals such as yttria, scandia, and lutecia sesquioxides, as well as garnets [15.19, 51].

In the combinatorial approach proposed by *Boulon* [15.19], the LHPG technique is applied to a feed rod constituted by two ceramics parts, A and B, with different compositions. When the molten zone moves along the feed rod, there is mutual solubilization of A and B. As the solubilized amounts of A and B vary, the composition of the molten zone changes continuously, inducing a progressive and continuous composition gradient along the crystallized rod. This new approach is an efficient tool for measuring optical, spectroscopic or thermal properties in any type of inorganic optical materials in which either activator ion or nominal composition concentrations can be changed.

15.1.8 Flux Technique (FT)

The flux technique (FT) is based on growth of crystals from a nonaqueous solution. As a rule, a mixture of salts is used as a solvent. In the 1960s, flux methods were widely used to grow the rare-earth aluminum [15.52–54] and gallium [15.55] garnets, both pure and doped, as well as some of the rare-earth orthoaluminate hosts [15.56]. The emphasis later was on melt techniques, as they provided both larger crystal size and higher growth rates. At present, a modified FT method, the top-seeded solution growth method (TSSG), is widely applied to produce those crystals that cannot be grown from melt easily, Nd:YVO_4 [15.57], Yb:$KY(WO_4)_2$ (Yb:KYW) [15.58], Nd:$KGd(WO_4)_2$ (Nd:KGW) [15.59], and Yb:$YAl_3(BO_3)_4$ (Yb:YAB) [15.60]. Sometimes, TSSG is also described as a high-temperature solution growth method or a modified Czochralski technique.

Among the Yb^{3+}-doped oxide crystals for diode-pumped solid-state lasers, KYW and KGW were evaluated to be the hosts with the greatest lasing potential in the CW regime [15.19]. FT is obvious the choice for the growth of single crystals such as KGW, since KGW crystal has a phase transition at 1005 °C (KYW at 1014 °C) below its melting point (1075 °C). A typical growth procedure of such crystals is described as follows [15.58].

The starting materials with flux, such as K_2WO_4 or $K_2W_2O_7$, are mixed and placed into the platinum crucible. The fully charged crucible is then placed into the furnace. It is important that the charged crucible be kept at a constant temperature of 1050 °C for 3–4 days to let the solution melt completely and homogeneously. The saturation temperature of the solution is determined exactly by repeated seeding. The seed contacts the melt at a temperature 5 K above the saturation temperature and is kept at constant temperature for half an hour to dissolve the outer surface of the seed. During the growth period, the crystal is slowly cooled at a rate of 1 K/day and rotated at a rate of 4.5 rpm. When the growth process ended, the crystal is pulled up from the melt surface and cooled to room temperature at a rate of 15 K/h.

15.2 Laser Crystal Defects

The main defects which can degrade the performance of melt-grown crystals are now generally recognized to be any which can absorb, reflect, refract or scatter magnetic, optical, acoustic or electrical energy either generated within or incident upon the material. Thus, dislocations, color centers, facet, striations, twins, voids, cellular structures, precipitates, inclusions, and more destructive defects such as cracks are all important defects that have to be eliminated or controlled. Due to the great variety of defects, only those frequently encountered and those specific to the concerned host materials are discussed herein.

15.2.1 Ti:sapphire

Ti:sapphire single crystal is one of the most attractive broadly tunable solid-state laser materials. Both CW and pulsed lasers have been demonstrated with very high efficiency over a tuning range in excess of 300 nm centered at 800 nm. In order to develop this material to meet the needs of current commercial laser systems a variety of growth techniques, such as HEM [15.34], VGF (vertical gradient freeze) [15.61], CZ [15.62], and TGT [15.26], have been used to grow Ti:sapphire crystals. Residual infrared absorption and

mosaic structure are the main defects in as-grown Ti:sapphire crystals.

Residual Infrared Absorption

The efficiency at which a laser can operate is fundamentally impacted by its gain-to-loss ratio. As a consequence, the presence of absorptive loss at laser wavelengths can potentially reduce the efficiency, or even render the system inoperable. These parasitic losses generally arise from the presence of unwanted impurities or from unanticipated oxidation states of the laser ion. Parasitic absorption losses can be more harmful to laser performance than an equivalent amount of loss resulting from scattering, since the absorption often leads to additional heating of the medium. Since many solid-state amplifiers operate in the grain regime of 3–30%/cm, losses on the order of 1%/cm can seriously impair laser performance [15.63].

In Ti:sapphire, parasitic losses are mainly induced by the presence of a relatively weak, broad infrared absorption band that peaks between 800 and 850 nm [15.64–67]. *Aggarwal* and coworkers [15.68] proposed that the residual absorption in these crystals is largely due to Ti^{3+}/Ti^{4+} ion pairs, and also indicated that annealing such crystals at high temperatures ($\approx 1600\,^{\circ}C$) in a reducing atmosphere (an Ar/H_2 mixture) decreased the residual absorption without significantly changing the main absorption, whereas annealing in an oxidizing atmosphere (Ar/O_2 mixture) increased the residual absorption and simultaneously decreased the main absorption. The decrease in the main absorption, which was also observed in earlier experiments on Ti:sapphire crystals grown by the Czochralski method [15.69–71], results from the oxidation of Ti^{3+} ions to Ti^{4+} ions. *Mohapatra* and *Kroger* [15.71] concluded that charge compensation is probably accomplished by the formation of an A1 vacancy for every three Ti^{3+} ions converted to Ti^{4+}. The main absorption could be restored by annealing oxidized samples in a reducing atmosphere [15.69–71].

As noted above, the residual infrared absorption could be eliminated with careful attention to the redox conditions in the melt and also by postannealing techniques [15.72, 73].

Basal Slip

Because of its rhombohedral structure and its resulting anisotropic properties, sapphire exhibits different crystalline habits and structure perfections when growing along different directions [15.74]. Generally it is difficult to grow high-quality sapphire single crystal along the [0001] direction because this orientation is not preserved in the grown crystal [15.74], due to the weakening action of the main slip systems. The slip systems of sapphire reported so far are $(0001)1/3\langle 11\bar{2}0\rangle$ basal slip, $\{11\bar{2}0\}\langle 1\bar{1}00\rangle$ prism slip, and $\{10\bar{1}1\}1/3\langle\bar{1}101\rangle$ pyramidal slip [15.75, 76]. Among those, basal slip is known to be the easiest slip system at elevated temperatures.

In HEM or CZ systems an interface is developed which is convex towards the liquid. With such an interface a boule grown along the [0001] orientation always exhibits solidification stress. So, typically, sapphire is often grown in $[11\bar{2}0]$, $[10\bar{1}0]$, and $[1\bar{1}02]$ orientations to avoid basal slip. For zero-birefringence optics, the [0001] orientation is required, and components can be obtained from $[11\bar{2}0]$- and $[10\bar{1}0]$-oriented boules by fabricating pieces orthogonal to the growth direction [15.77]. However, this limits the size and homogeneity of fabricated components. As will be discussed in Sect. 15.3.2, the TGT system has a rather more stable thermal field than any other system, and the solid–liquid interface in the TGT system is much flatter (slightly convex). This made it easier to grow [0001]-oriented boules [15.78, 79], thereby enhancing the perfection of fabricated components, which results in a good laser performance, as described below [15.31].

The concentration of titanium along the radius in Ti:sapphire crystal grown by TGT is nearly unity. Figure 15.13 shows the distribution of the absorption coefficient at 514 nm ($\alpha_{514\,nm}$) along the growth axis of Ti:sapphire crystal grown by HEM and TGT. It can be seen that the concentration of Ti^{3+} in HEM-grown Ti:sapphire is not high, and the concentration gradi-

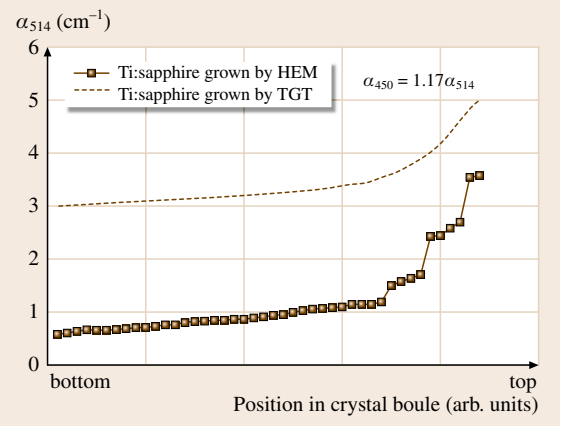


Fig. 15.13 Distribution of the absorption coefficient at 514 nm ($\alpha_{541\,nm}$) along the growth axis of Ti:sapphire crystal grown by HEM and TGT

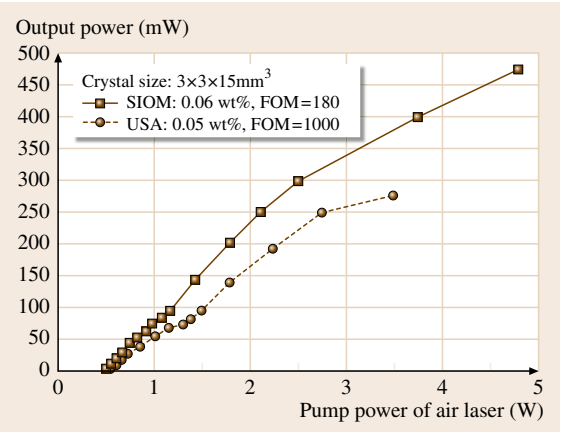


Fig. 15.14 CW laser performance of Ti:sapphire crystals grown by TGT and HEM in the same laser systems without water cooling

ent is large in the highly doped section (1–3.6 cm^{-1}). The concentration of Ti^{3+} in TGT-grown Ti:sapphire is higher, and the absorption coefficient can reach as high as 5 cm^{-1}. Figure 15.14 shows the CW laser performance of Ti:sapphire crystals grown by TGT and HEM without water cooling in the same laser system. Although the FOM, mainly determined by the Ti^{3+}/Ti^{4+} ratio in the crystal, of HEM-grown Ti:sapphire is as high as 1000, 5.5 times higher than that of the TGT-grown one, the laser performance (efficiency and output power) of TGT-grown Ti:sapphire crystal is obviously better. These results show that the laser performance of Ti:sapphire depends not only on the FOM, but more on the crystal perfection. Furthermore, ultrashort pulse performance in China (12 fs) and in other counties (8 fs) was also achieved using TGT-grown Ti:sapphire crystals. High gain was obtained in TGT-grown highly doped Ti:sapphire crystals in RIKEN, Japan in 1994, and was 100 times higher than the data reported for Ti:sapphire crystals grown by HEM at that time [15.31].

15.2.2 Nd-Doped Laser Crystals

Nd-ion-based lasers are among the mostly used solid-state laser systems. They find applications in many areas, including the generation of the highest energy per pulse for laser-induced fusion purpose. Nd:YAG is by far the most useful material, owing to its unique combination of excellent thermomechanical properties and high gain cross section at 1.064 μm. Nd:YLF offers lower thermal lensing and longer storage time compared with Nd:YAG, although it is also a much less robust crystal. The Nd:YAP crystal does not exhibit the thermal birefringence problems experienced by Nd:YAG, but crystal growth of this medium has been hampered by several problems, including a tendency to twin. Nd:FAP and Nd:YVO_4 crystals possess the important properties of very large emission cross sections.

In spite of possessing many advantages, high-quality Nd-doped laser crystals are not easy to obtain due to the presence of many growth defects such as striations, facets, inclusions, the low distribution coefficient of Nd in host materials, etc.

Striations

Temperature fluctuations can give rise to striations in the growing crystal, which are often detrimental to laser performance [15.80]. These fluctuations can arise both from imperfect temperature/power control in the heating elements as well as from periodic or turbulent flows in the melt.

Striations can be eliminated or reduced in a number of ways. In pure compounds, growth at the congruently melting composition is an obvious solution. However, with deliberately doped or slightly impure materials the lowest temperature gradients and smallest melt depths compatible with crystal diameter control and the avoidance of other defects must be employed in order to limit convection.

Striations represent a useful built-in record of the interface shape at any point in the crystal and are thus widely employed in studying defects and morphology changes related to the solid–liquid interface. Figure 15.15 illustrates the striations observed in CZ and TGT-grown Nd:YAG crystals. It shows that the CZ configuration tends to produce a conical interface shape, while TGT has a flatter shape. Such a discrepancy results mainly from differences in the melt geometries, thermal and boundary conditions, and heating methods.

In CZ growth of laser crystals, the time constant of the system is generally set by the melt and the crys-

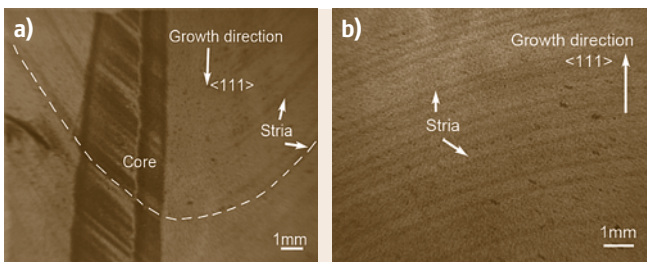


Fig. 15.15a,b Striations in CZ-grown **(a)** and TGT-grown **(b)** Nd:YAG crystals, observed by synchrotron radiation topography

tal, since induction heating of the crucible is usually the method of choice. The thin-walled crucible has a negligible impact on the time constant of the furnace. On the other hand, in TGT, VBT or HEM growth, the furnace time constant is often much longer because of the use of massive heating elements (either inductive or resistive). This large mass dampens the inevitable temperature fluctuations from the power supply. Rather than inductively heating the crucible, a relatively massive resistive heater is used that radiates to crucible. The crucible mass can be as large as required. For inductive heating, a massive susceptor can also be used, even for higher-melting materials such as Nd:YAG. A susceptor is a material used for its ability to absorb electromagnetic energy and convert it to heat.

In TGT, VB or HEM growth, with the melt above the crystal, the vertical temperature gradient is stabilizing with respect to natural convection (hot above cold), as opposed to the CZ configurations, which is destabilizing. In this context, stabilizing and destabilizing refer to the tendency to establish buoyancy-driven flows. For systems in which hotter fluid rests on top of colder fluid, such as in TGT, VB, and HEM growth, the lower density associated with the hotter fluid on top means that it will tend to remain in that position; hence this is stable. For systems in which hotter fluid is below colder fluid, such as for CZ growth, the colder upper fluid will tend to fall due to its higher density; this is unstable with respect to convection. In additional to TGT and HEM growth, keeping the crucible and growing crystal stationary will reduce temperature fluctuations resulting from mechanical vibration, and thus further enhance thermal stability in the melt.

In TGT, VB or HEM systems, the temperature gradient can be as small as practically required, depending on thermodynamic considerations. This can be important for controlling thermal stresses or selective evaporation from multicomponent systems. In Czochralski growth, appreciable temperature gradients are required to control the diameter. In fact, *Surek* [15.81] showed by analysis that, when heat transfer effects are neglected isothermally, the CZ process is unstable; small perturbations will produce large fluctuations in crystal diameter.

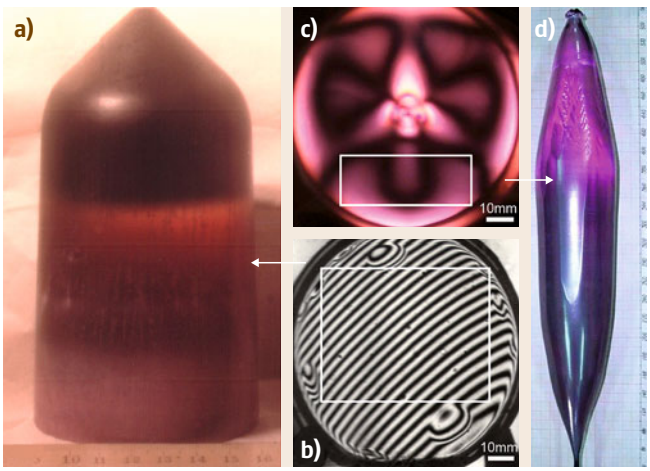


Fig. 15.16a–d Distributions of facet-induced cores in ∅ 75 mm TGT-grown YAG **(a,b)** and in ∅ 80 mm CZ-grown Nd:YAG **(c,d)**; the white frames indicate the available aperture for laser elements

Facets

During the growth of Nd:YAG crystal along [111] crystallographic axis under conditions which produce a deep interface, i. e., the growing end of the crystal has an essentially conical shape, convex into the melt, the interface geometry, combined with {211} facets near the tip, generates a nonhomogeneous central core [15.82] surrounded by a six-lobed strain pattern (Fig. 15.16c). The presence of facets limits the size of the slab that can be harvested from the boule and degrades the uniformity of the crystal.

Ming et al. [15.83] indicated that the core will appear at the region where the facet planes are parallel to the solid–liquid interface. Since the interface shapes in TGT and CZ configurations are commonly different, it is certain that the distribution of cores in crystals grown by these methods will be different: one is at the center, while the other is at the periphery (Fig. 15.16).

In the CZ configuration, Nd:YAG naturally grows with a deep interface because of radiative heat loss through the cooler, upper part of the furnace. In effect, the cold part of the furnace pushes the melt/crystal interface down into the melt via this long-range radiative exchange. In the CZ configuration, the interface shape can be controlled to give an approximately planar surface by increasing the crystal rotation rate to a critical value that depends on the crystal diameter [15.84–87], but this approach increases the risk of temperature fluctuations.

For some garnets, e.g. $Dy_3Al_5O_{12}$, the planar interface shape is produced at lower crystal rotation rats as compared with $Y_3Al_5O_{12}$ [15.88], while at higher rates it transforms to a concave one [15.89]. This behavior has been attributed to intensive absorption in the infrared associated with Dy^{3+} ions that overlaps with the maximum wavelength of spectral density of the thermal radiation used for melting [15.88]. In order to adapt this approach to laser crystal growth, impurity ions that are

spectroscopically indifferent with respect to the lasing ions must be selected. It has been seen, for example, that additions to YAG melts of small amounts of Pr^{3+}, Sm^{3+} or Zr^{3+} [15.90], producing intensive absorption lines in the infrared region, also affect the shape of the interface.

In the TGT or VBT configurations, the low temperature gradients give an approximately planar solid–liquid interface except near the crucible wall, where the interface becomes slightly convex towards the melt and it is here that the facets occur [15.27, 91]. In the case of the ⟨100⟩ axis, which is normally accepted as the most preferable for Bridgman growth of garnets [15.90], the facets are eliminated further to the crystal peripheral region due the lager angle between the growth axis and the facets plane.

Scattering and Inclusions

The sources of scattering and inclusions can be either extrinsic (impurities) or intrinsic, such as solid-state exsolvation of a compound from a congruently melting, nonstoichiometric crystal.

For small intrinsic defects, often nothing can be done to eliminate them. In general, there are two ways in which small intrinsic defects can be eliminated or reduced in number. Point defects can sometimes be quenched before agglomeration take place. However, quenching implies the presence of large temperature gradients that are often problematic, producing either large thermal stresses or intense melt convection. The second means of elimination is solid-state diffusion of species over macroscopic distances. This mechanism is only applicable for small ions such as lithium or sodium, since the diffusion coefficients must be very large for this to be practical. Large defects, on the order of tens or hundreds of microns, of some intrinsic composition are indicative of other problems in the growth process. These can result from temperature fluctuations leading to large undercooling in portions of the melt, or from insufficient mixing in a multicomponent system, leading to localized composition nonuniformities. In these cases significant changes in growth conditions, or a different growth process, may be in order.

Extrinsic defects are generally controlled by a combination of suitable purification of starting materials and atmosphere control. In the growth of fluorides, this generally involves the use of reactive atmosphere processing using either HF, CF_4, SF_6 or other species to react with oxide impurities to form volatile byproducts [15.92, 93]. In addition, fluorides crystals are often grown in either HF, such as YLF, or in vacuum to further minimize contamination. Sometimes gettering compounds such as PbF_2 are employed to react with oxide impurities prior to growth.

The presence of inclusions in oxide crystals is usually a result of the formation and precipitation of a second phase in the primary liquid phase during the crystal growth process. One example is the formation of an oxygen-deficient phase in many of the gallium-containing garnets. In this case, simply increasing the oxygen partial pressure of the growth atmosphere is sufficient to eliminate this source of inclusions. Similar types of oxygen-deficient phases, usually appearing as submicron particles, i. e. smoke, have been observed in YAG, sapphire, and Y_2SiO_5 (YSO) and can be eliminated by appropriate adjustment of the oxygen partial pressure of the growth atmosphere [15.94].

A second source of inclusions can be associated with the dopant ion, as is the case in the growth of Nd:YAG. In the $Y_3Al_5O_{12}$ system, the distribution coefficient for Nd in YAG is relatively low (less than 0.2). Therefore to achieve approximately a 1 at. % Nd doping level in the crystal, the liquid must contain approximately 5 at. % Nd. Furthermore, since the distribution coefficient is much less than unity, as the growth of the crystal proceeds, the concentration of Nd in the liquid increases. Usually, when only about 20% of the liquid is crystallized, approximately a 20% change in the dopant ion concentration through the length of the crystal is produced. Variations in the dopant concentration beyond this amount often have detrimental effects on the laser performance of the material. Thus a low dopant ion distribution coefficient also imposes another limit on the useful amount of material that can be crystallized from the melt. The desire for large fabricated components therefore enforces the use of large quantities of starting material and large crucibles in CZ growth of Nd:YAG using the batch process. However, the batch process introduces complexity into the growth of a crystal through the progressive decrease in melt height. As the melt height decreases, transfer of heating power to the melt is affected and the strength of convective melt flow and mixing is reduced. The thermal environment of the crystal is also altered as the melt level falls, exposing the crystal to a greater area of the hot crucible wall. This tends to lower the temperature gradient in the melt, which enhances the risk of constitutional supercooling [15.87]. In order to circumvent some of the shortcomings of the standard process, development of an automated CZ growth process was initiated to achieve steady-state conditions through addition to the melt to maintain constant melt height and constant concentration of dopant in the melt [15.19, 87].

On the other hand, the compound $Nd_3Al_5O_{12}$ does not exist among the rare-earth aluminum garnets. Consequently, this system is not a solution between two different rare-earth aluminum garnets, but is a solution between $NdAlO_3$ (a perovskite phase) and $Y_3Al_5O_{12}$ [15.63]. Unfortunately at the required Nd liquid concentration, one is very close to the solubility limit of $NdAlO_3$ in YAG. Small temperature fluctuations from external or internal source, e.g., the heating power or a change in the cooling-water temperature, will easily result in constitutional supercooling, thereby exceeding the solubility limit of $NdAlO_3$ in YAG, which causes localized precipitation of the perovskite phase. Once in the crystal, they cannot be removed by subsequent processing such as annealing.

A similar example occurs in the growth of substituted $Gd_3Ga_5O_{12}$ (GGG) [15.95, 96]. In this case, Mg^{2+}, Ca^{2+}, and Zr^{4+} are added to the liquid in a ratio such that the resulting distribution coefficients are nearly equal to unity. However, this results in a Zr^{4+} liquid concentration (0.65 atoms per formula unit) that is very close to the solubility limit of $Gd_2Zr_2O_7$ in GGG (approximately 0.7 atoms per formula unit). Again, local temperature fluctuations near the growth interface can produce an excess of Zr^{4+} that results in the precipitation of submicron $Gd_2Zr_2O_7$ particles in the liquid, which are trapped by the growing crystal.

In both of these examples, not only are scattering sites produced in the crystal, but generally associated with these inclusions are region of strain [15.97]. In some cases, the induced strain is of sufficient magnitude that it can result in the formation of clusters of dislocations that propagate down the crystal axis and are roughly normal to the growth interface. For a crystal of 25–50 mm in diameter, these dislocations will continue down the crystal axis for approximately another 3–7 cm before reaching the crystal surface, thus further degrading its optical quality. Although the formation and subsequent entrapment of a second phase can be localized, its influence on the optical quality of the crystal can extend far beyond the local environment. As in the case of inclusions, subsequent processing such as annealing will have little, if any, effect on this type of defect. Thus the formation of optical-quality oxide materials must be accomplished during the crystal growth of the material and cannot necessarily be achieved after the growth process is complete.

Both of these cases illustrate the fact that a stable thermal environment is necessary for the growth of optical-quality single crystals suitable for laser applications. Thus much of the effort in the growth of many of these materials is devoted to the design of the growth equipment, its power source, and the furnace geometry.

A third source of scattering sites in oxide materials can result from contamination of the liquid by the crucible material, either Pt or Ir. These scattering centers can vary from submicron to tens of microns in size. Unlike inclusions generated by the precipitation of a second phase, these inclusions always appear as either triangular or pseudohexagonal particles with an aspect ratio of at least 10 : 1. Furthermore, these are flat, thin particles, and tend to align themselves parallel to the growth interface when trapped by the growing crystal. Thus the larger cross section of the particle presents itself to the optical path of the resulting laser rods, which greatly increases the possibility of damage. Both Ir and Pt particles can be formed in the liquid by numerous chemical paths [15.98]; for example, the presence of H_2O in either the starting powder or the growth atmosphere usually results in a high density of particles in many oxide systems. Of the two metals usually used for oxide growth, Ir is more prone to oxidation than is Pt. Consequently, for those oxide systems that require iridium as a crucible, the elimination of Ir particles is always a concern. Special attention must be paid to powder preparation, crucible cleaning and charging, and growth atmosphere to avoid any possible set of conditions that could result in the transport via oxidation of the crucible material into the bulk charge.

15.2.3 Yb-Doped Laser Crystals

The most promising ion that can be used in a non-Nd laser in the same range of emission wavelength is Yb^{3+}. The Yb^{3+} ion has some advantages over the Nd^{3+} ion as a laser-emitting center due to its very simple energy-level scheme, consisting of only two levels: the $^2F_{7/2}$ ground state and the $^2F_{5/2}$ exited state. There is no excited-state absorption to reduce the effective laser cross section, no up-conversion, no concentration quenching. The intense Yb^{3+} absorption lines are well suited for laser-diode pumping near 980 nm and the small Stokes shift between absorption and emission reduces the thermal loading of the material during laser operation. The disadvantage of Yb^{3+} is that the final laser level of the quasi-three-level system is thermally populated, increasing the threshold.

Among new directed searches for novel laser crystals, one important approach is the use of Yb^{3+} active ion in an inertial-fusion energy diode-pumped solid-state laser. $Ca_5(PO_4)_3F$ (FAP) and YAG were soon recognized to be favorable hosts for lasing in the

nanosecond pulse regime. This fact was supported by an evaluation of the spectroscopic properties of several Yb^{3+}-doped crystals useful for laser action [15.99,100].

Although, compared with Nd-doped crystals, ytterbium can easily be incorporated into the host materials due to its relatively small ionic radii, many defects induced by doping effects are still present in Yb-doped crystals, and significantly impact on their thermal and spectral properties.

Lattice Distortion

The lattice parameters of YAG and YbAG were measured to be 1.2011597 ± 0.000034 and 1.1937997 ± 0.000054 nm, respectively, and there is only a 1.8% difference in unit-cell size [15.101, 102]. Figure 15.17 shows the Yb^{3+} concentration dependence of lattice parameter. It can be seen that lattice parameter is a linear function of Yb^{3+} concentration, and a linear equation can be obtained as follows:

$$\alpha(x) = 1.20076 - 0.007072x \text{ nm} .$$

From this equation, the densities of crystals with different Yb^{3+} concentration can be estimated from the cell volume and molecular weight of Yb:YAG.

As discussed above, compared with the CZ method, the temperature and thermal field of TGT are very stable and convection that disturbs the solid–liquid interface does not appear. Therefore, Yb^{3+} ions can more easily substitute at the position of Y^{3+} sites. From the results of cell parameters shown in Table 15.1, it can be seen that the effect of Yb^{3+} on the crystal lattice deformation in TGT-grown Yb:YAG crystals is smaller than that in CZ-grown Yb:YAG crystals. The cell structure of TGT-grown Yb:YAG crystals is steadier.

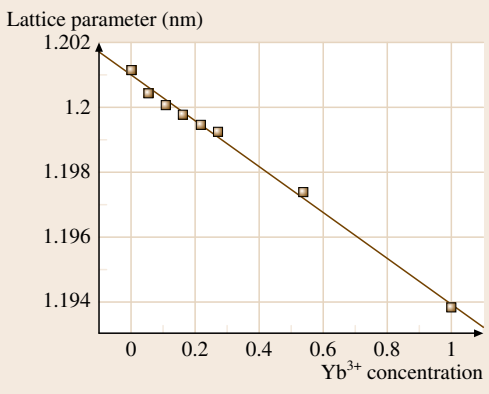


Fig. 15.17 Lattice parameter as a function of Yb^{3+} concentration

Different from the typical four-level Nd:YAG laser, the quasi-three-level nature of Yb:YAG requires high pump density in order to overcome the deleterious effect of the lower laser level reabsorption at room temperature; moreover, the laser performance decreases significantly with increasing temperature [15.103]. So it is favorable to keep the temperature of Yb:YAG crystal as low as possible. Obviously, knowledge of the effect of doping on thermal properties of crystal is helpful for both designing laser systems or improving crystal performance.

Figure 15.18a shows that the thermal diffusivity decreases with increasing Yb^{3+} concentration, and values of thermal diffusivity at 50 °C are 1.72×10^{-6}, 1.62×10^{-6}, and 1.54×10^{-6} m^2/s for single crystals with doping level 5 at. %, 10 at. %, and 25 at. %, respectively. Figure 15.18b shows that the specific heat increases as the temperature increases in the measured range, and the variation of temperature has a strong influence on highly doped Yb:YAG crystals [15.104]. The thermal conductivity was calculated from the thermal diffusivity and specific heat capacity, as displayed in Fig. 15.12c, and we can see the apparent influence of Yb^{3+} doping concentration on the thermal conductivity. In Yb:YAG crystals, the main mechanism of heat transfer is by phonons. Yb doping into YAG crystals inevitably induces structural distortion in crystals. The defects in crystals remarkably reduce the phonon mean free path, and the thermal conductivity decreases as Yb doping concentration increases. The deterioration of thermal properties of highly doped Yb:YAG will more easily lead to thermo-optic aberrations, lensing, and birefringence. Therefore, in order to acquire high beam quality and stable laser output from highly doped Yb:YAG media, an efficient cooling system must be adopted [15.105, 106].

The result of *Chenais* et al. [15.107] shows that the thermal conductivity of Yb:GGG, although lower than that of Yb:YAG at weak Yb^{3+} concentrations, becomes

Table 15.1 Cell parameters of Yb:YAG crystals

Growth method	Yb^{3+} concentration (at.%)	α (nm)	β	V (nm^3)
CZ	5.4	1.200424 ± 0.000063	90.0	1.72983
TGT	5.4	1.200704 ± 0.000052	90.0	1.73104

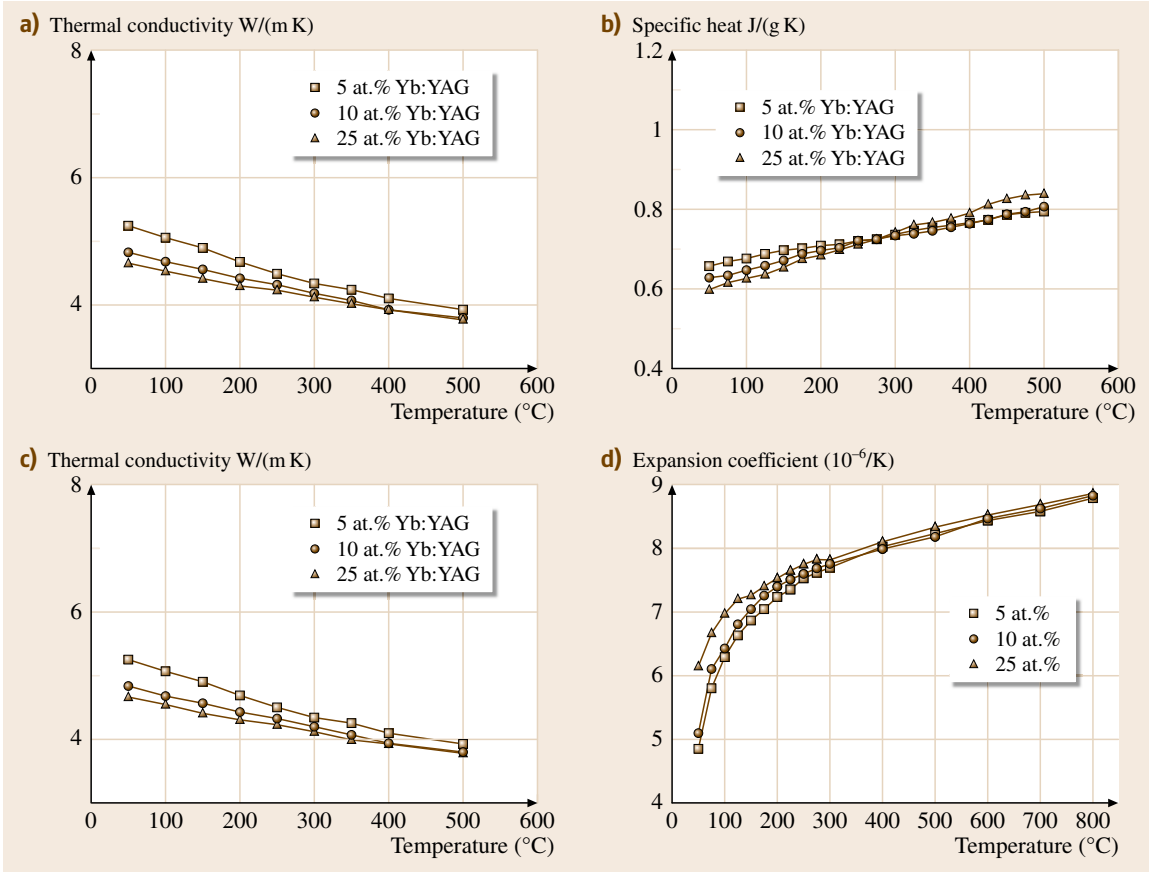


Fig. 15.18a–d Thermal diffusivity (**a**), specific heat (**b**), conductivity (**c**), and expansion coefficient (**d**) of Yb:YAG crystals as a function of temperature for several Yb^{3+} doping concentrations

higher for doping levels above 5×10^{20} ion/cm^3. This means that Yb:GGG exhibits a lower quantum defect and better thermal conductivity, and thermal loading is lower than in Yb:YAG for high doping levels.

Color Centers

Color centers in oxide-based crystals constitute a complex problem, as some centers can be removed by annealing in oxidizing atmosphere [15.108] and others by annealing under reducing or vacuum conditions [15.109, 110]. Color center formation, in general, is attributed to change of lattice defects associated, primarily, with unintentionally introduced impurities.

In CZ-grown Yb:YAG, a particular color center was found [15.111–113], whose absorption spectra are shown in Fig. 15.19. The inert growth atmosphere brought about a lot of oxygen vacancies and formed

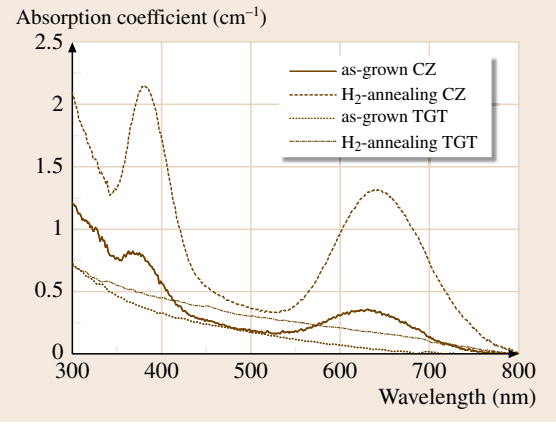


Fig. 15.19 Absorption spectra of color centers in Yb:YAG crystals

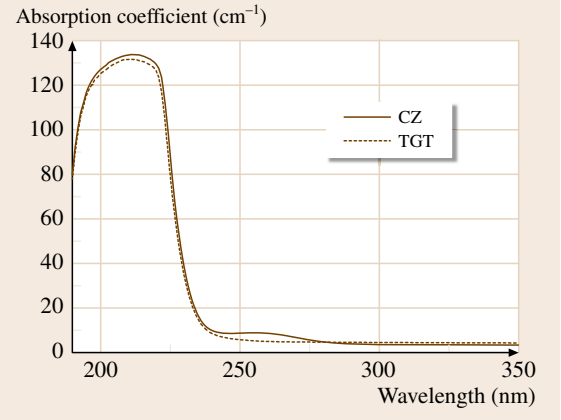


Fig. 15.20 UV absorption spectra of Yb:YAG crystals

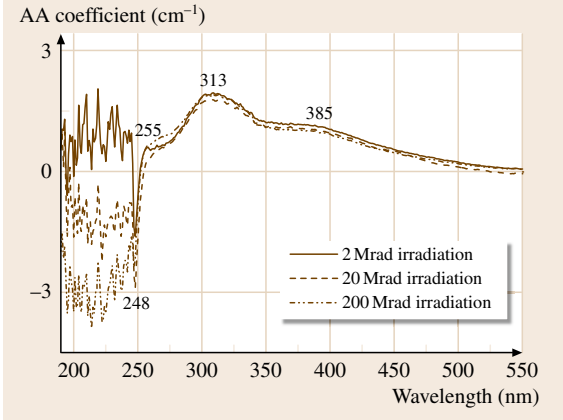


Fig. 15.21 Absorption spectra of color centers in Yb:YAP crystals

Re-F type color centers and Yb^{2+}, which are detrimental to the intrinsic spectroscopic performances of Yb:YAG. They degraded the Yb^{3+} intrinsic absorption at 900–1050 nm and the emission intensity at 1028–1060 nm, and shortened the fluorescence lifetime of Yb^{3+} in YAG host. The color center's two absorption bands are located at wavelengths of 368 and 623 nm, respectively. Each absorption peak increases in intensity after annealing the sample in hydrogen at 1400 °C for 12 h, and the main band positions move from 368 to 381 nm and from 623 to 642 nm, respectively. The absorption spectra of TGT-grown Yb:YAG crystals are also shown in Fig. 15.19. Although also grown in an inert atmosphere, and even when annealing the sample in hydrogen atmosphere, TGT-grown Yb:YAG crystals do not exhibit the same absorption bands. The results indicate that there is no Yb^{2+} and color center absorption in TGT-grown Yb:YAG crystal, which is of great use for the laser performance of Yb:YAG.

The ultraviolet (UV) absorption spectra after annealing in oxygen shows a weak peak around 255 nm in CZ-grown Yb:YAG crystals, as shown in Fig. 15.20. *Chen* et al. [15.114] used optical absorption and electron paramagnetic resonance (EPR) techniques to study iron impurities in YAG crystals and considered that the absorption band at 255 nm was attributable to a Fe^{3+} charge-transfer band that was made up of contributions from substitutional Fe^{3+} ions in octahedral and tetrahedral sites. The role of Fe impurity ions in color center formation has also been demonstrated by other technologists in YAG [15.115], $YAlO_3$ [15.116, 117], and Al_2O_3 [15.118, 119].

For Yb:YAP crystals [15.120], three irradiation-induced color center absorption bands, located at wavelengths 248, 309, and 385 nm, respectively, were observed (Fig. 15.21). The significant additional absorption (AA) peak at 248 nm is believed to be caused by the slight shift of the charge-transfer absorption edge of Yb^{3+} ions induced by the charge density redistribution. Based on the result discussed above, combined with the data reported by *Matkovski* [15.121] for the absorption band at 263 nm corresponding to Fe^{3+} ions in Nd:YAP, Fe^{3+} ions are considered to be responsible for the absorption band at 256 nm in Fig. 15.21. The 313 nm band has been observed by *Matkovski* [15.121] in absorption spectra of Nd:YAP and pure YAP crystals and was attributed to Fe^{2+} in YAP host. Kaczmarek suggested that a 313 nm band in γ-ray-irradiated Cr;Tm;Ho:YAG is most probably correlated to Fe^{2+} ions. Therefore, it is reasonable to

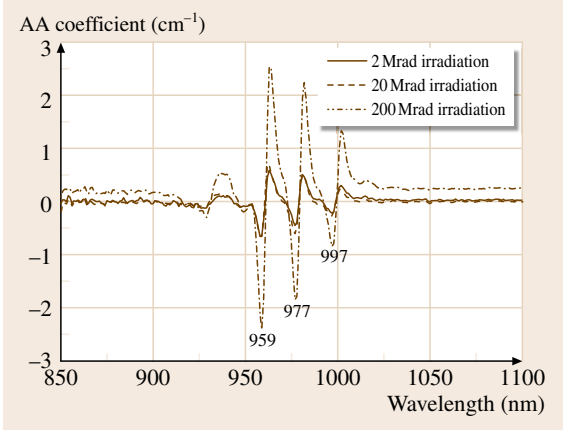


Fig. 15.22 UV absorption spectra of Yb:YAP crystals

believe that the 313 nm bands in Yb:YAP are also associated with the same kind of impurity. The increased AA value of the 313 nm band clearly indicates that the concentration of Fe^{2+} ions increased after γ-ray irradiation. The preexisting Fe^{3+} ions in Yb:YAP captured the electrons produced by γ-ray irradiation and the following interaction takes place: $\gamma + Fe^{3+} \rightarrow Fe^{2+}$. Yb^{3+} ions in Yb:YAP crystal could also capture the free electrons induced by γ-ray irradiation and as a result the transition $Yb^{3+} \rightarrow Yb^{2+}$ takes place, as shown in Fig. 15.22. The broad absorption band centered at about 385 nm shown in Fig. 15.21 has attracted more attention due to its complicated origin. According to the results of *Sugak* et al. [15.122], one broad absorption band located at 385–666 nm occurred in γ-irradiated Nd:YAP and the absorption induced in this region is caused by color centers intrinsic to the YAP lattice. Furthermore, a similar band was also observed in Pr:YAP under γ-ray irradiation [15.123]. *Matkovski* et al. [15.121] found that color centers in this region created in YAP crystals are associated with the crystal host and that their nature does not depend strongly on the type of dopant, even for high dopant concentrations. Because the Yb:YAP crystal was grown in inert atmosphere, a lot of oxygen vacancies are produced in the crystal. In analogy with the charge–recharge process of Fe and Yb ions, these O^{2-} vacancies in Yb:YAP crystal would capture one or two electron(s) to form F^+ or F centers. It has been shown that cation vacancy would be the most common defect intrinsic to the YAP lattice [15.124]. Consequently, it is most probable that the broad AA band centered at 385 nm is correlated with the cation vacancies and F-type center.

Commonly, color centers may be annealed out or reduced in number at high temperature under oxidizing, reducing or vacuum atmosphere depending on the center's origination. In the case of Yb:YAG, it is notable that annealing at high temperature increases the possibility of scattering formation due to a phase transition occurring at 1369.5 °C, as shown in Fig. 15.23, so a relatively lower temperature should be adopted when annealing.

Fluorescence Quenching

The effective stimulated-emission cross section (σ) and radiative lifetime (τ) are two important parameters for the assessment of a laser crystal [15.125]. Knowledge of both σ and τ is essential when evaluating laser system performance parameters such as saturation intensity and threshold pump power; for example, the threshold pump power is inversely proportional to the product of the effective emission cross section and the radiative lifetime of the lasing crystal [15.126].

Figure 15.24 shows the relationship of measured fluorescence lifetime of Yb:YAG crystals with temperature. At higher temperatures (above 200 K), the fluorescence lifetime increases as the Yb^{3+} concentration increases in the YAG host because of radiative trapping and reabsorption effects. The measured lifetime is longer than the radiative lifetime in these cases. At lower temperatures (below 80 K), the measured fluorescence lifetime of Yb in YAG is nearly the same for each concentration, similar to the results reported by *Patel* et al., [15.127] except for the 30 at. % Yb:YAG crystal. The decreased lifetime ob-

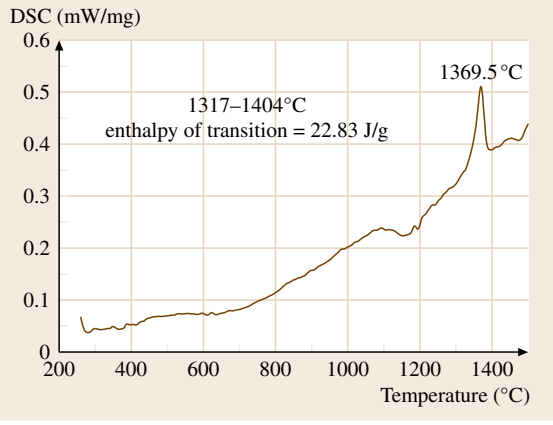


Fig. 15.23 Differential scanning calorimetry (DSC) curve of Yb:YAG

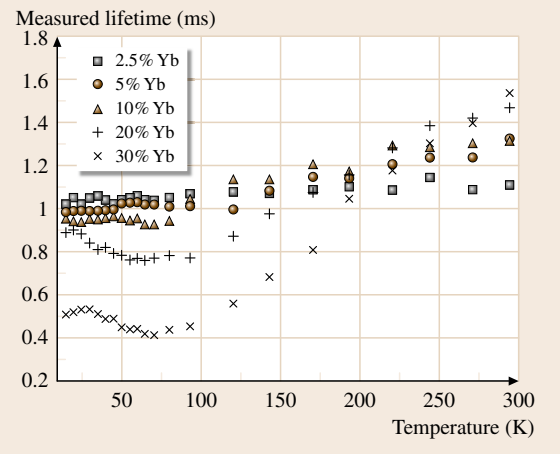


Fig. 15.24 Measured lifetime of Yb:YAG crystals as a function of temperature

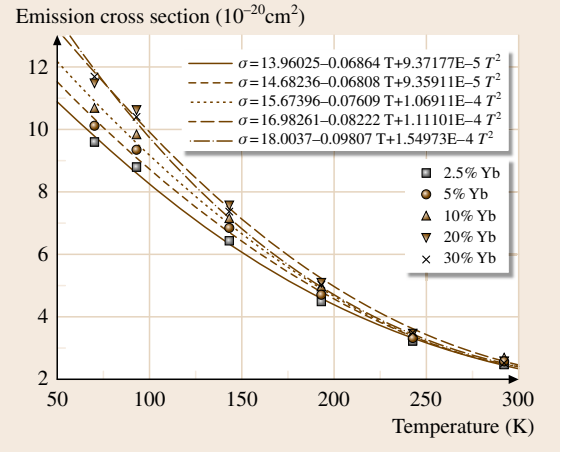


Fig. 15.25 Emission cross sections of Yb:YAG as a function of temperature for five concentrations of Yb; the indicated polynomial fits were obtained by the least-squares method

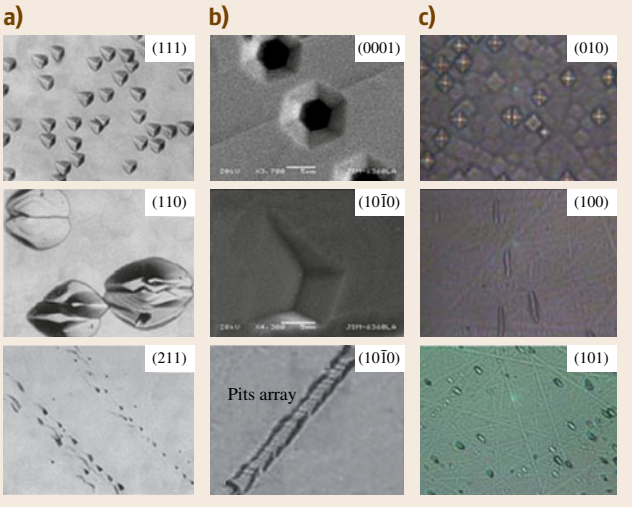


Fig. 15.26a–c Etch patterns formed on different faces of Yb:YAG **(a)**, Yb:FAP **(b)**, and Yb:YAP **(c)**

served for the 30 at. % crystal at the lowest temperatures may be due to the presence of more impurities in the highly doped crystal, which cause significant fluorescence quenching. These impurities may be other rare-earth ions that are hard to eliminate from the Yb starting material.

Using the measured lifetime at the lowest temperature as the radiative lifetime of different concentrations of Yb:YAG crystals, the effective emission cross section of Yb:YAG crystals can be calculated from the Füchtbauer–Ladenburg (F–L) formula [15.125]. Figure 15.25 shows the dependence of the effective emission cross section of these Yb:YAG crystals on temperature. The emission cross section increases as the temperature decreases.

Dislocations

Dislocation structures in oxides etc. have been widely studied using chemical etching procedures to reveal dislocations as individual pits. Such procedures can be misleading as great care is needed to distinguish dislocation etch pits from etch pits caused by inclusion or surface damage. X-ray topography has provided significant information but a useful innovation has been the application of electron microscopy to such studies because of the inherent resolution improvement at shorter wavelengths.

Generally, the symmetry of an etch pit is in accordance with the symmetry of the crystal face, and the shapes of etch pits on different faces are different for the same crystal [15.128]. The change of etching conditions may also affect etch-pit morphology.

For Yb:YAG crystals [15.129], under the same etching conditions, the pits on the (111) face have two

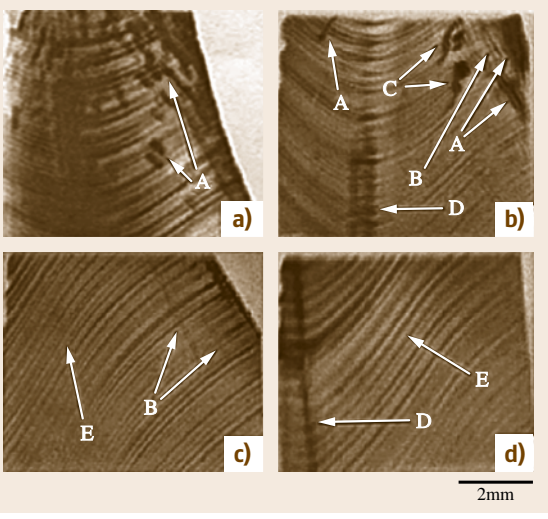


Fig. 15.27a–d Transmission synchrotron topography of (110) slices of Yb:YAG parallel to the [111] growth axis with (121) reflection. **(a–d)** From the upper parts to the middle of the crystal. A: dislocation bundles originated from seed/crystal interfaces; B: dislocation lines; C: dislocation bundles originating from impurity or inclusions; D: core and side core; E: growth striations

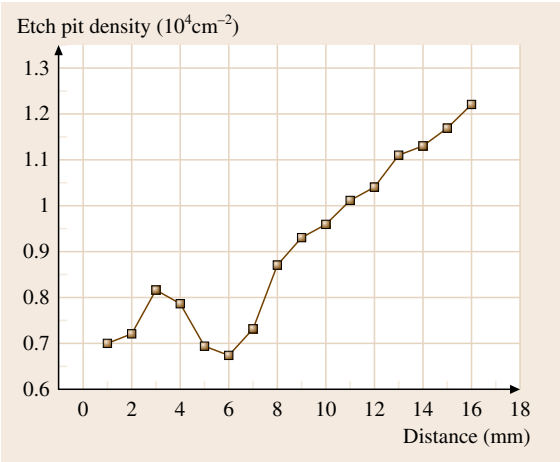


Fig. 15.28 Radial distribution of etch-pit density on (0001) face of Yb:FAP crystal

shapes: one is triangular, and the other is six-sided. The pit pattern on (211) is triangular with a tail and the pit pattern on (110) is a distorted rhombus. In Yb:FAP crystals, etch pits associated with dislocations emerging on the (0001) plane are hexagonal, while those on the $(10\bar{1}0)$ plane have an irregular shape. For Yb:YAP, the etch pits have rhombus shape on the (010) face, haricot-beam shape on the (100) face, and elliptic form on the (101) face. The typical etching patterns are shown in Fig. 15.26.

For Yb:YAG (111) slices, more etch pits can be observed in the initial growth period, which implies that the crystal is imperfect, and with an increase of distance from the seed the number of pits decreases gradually and they are mainly centered at the periphery of the sections. In the middle parts of Yb:YAG crystal, there are few etch pits, which implies that the crystal is perfect. Figure 15.27 shows the transmission synchrotron topography of a (110) slice of Yb:YAG crystal with (121) reflection, displaying typical growth defects in Yb:YAG. This shows that dislocation bundles and dislocation lines distribute towards the crystal periphery in the upper parts of the Yb:YAG crystal. However, in the middle parts of Yb:YAG crystal, they vanish, as shown in Fig. 15.27d. These experimental results are in good agreement with those obtained by chemical etching. Such a rule can also be demonstrated by the radial distribution of etch-pit density along the diameter of Yb:FAP crystal [15.130], as shown in Fig. 15.28.

According to the observations in Fig. 15.27a–c, the growth dislocations may originate from the following sources: (1) dislocations already existing in the seed; (2) dislocations produced by nucleation at the seed–crystal interface, where some defects such as mechanical damage of the seed end, aggregation of impurity particles and inclusions, and thermal shock stress exist, as shown in Fig. 15.27a,b. These dislocations are the main types of source in the as-grown Yb:YAG crystals; (iii) dislocations emerging from impurity particles and inclusions trapped within the crystal during crystal growth. Comparing Fig. 15.27a–c, it can be seen that the propagation direction of the dislocations is perpendicular to the solid–liquid interface and as a result the dislocations are mainly found at the periphery of the upper parts. This rule can be explained by the minimum-energy principle, since the dislocations take the shortest path and locate in the lowest-energy state only when they take this route. *Schmidt* [15.131] found a similar rule in GGG crystal and calculated the propagating path of dislocations with Klapper theory [15.132]. Therefore, in order to obtain high-quality Yb:YAG crystal, it is necessary to choose high-quality seeds free from dislocations and grow the initial part of the crystal with a highly convex solid–liquid interface to eliminate dislocations. Usually, the neck technique is applied to eliminate dislocations originating from the seed or introduced by thermal shock during dipping of a seed crystal into the melt.

15.2.4 Other Activator-Doped Laser Crystals

While flashlamp-pumped ruby lasers are now primarily an artifact of the past, many of the common transition-metal lasers still appear to be a useful system for some specialized applications. Alexandrite, Cr:$LiCaAlF_6$ (Cr:LiCAF), and Cr:$LiSrAlF_6$ (Cr:LiSAF) lasers operate on the vibronic sideband of Cr, and consequently have a much lower threshold than ruby, which renders them much more useful. Cr:LiCAF was found to lase very efficiently. Forsterite (Mg_2SiO_4:Cr^{4+}) was found to be an exciting new tunable laser material, and MgF_2:Co^{2+} proved not to require cryogenic cooling if it is pumped on a timescale short compared with the excited-state storage time of 40 µs. Otherwise, several researchers have carefully assessed whether the Mn^{3+} ion might prove to be a useful laser ion [15.63].

While all of the rare-earth ions have been lased, systems based on Er, Tm, and Ho, besides Yb and Nd, have thus far proved to be the most useful. The Cr,Tm:YAG laser material is characterized by a particularly low gain cross section and, as a result, is most efficiently operated in a quasi- or true-CW type of mode. The Cr,Tm,Ho:YAG crystal has been found to be a very

efficient flashlamp-pumped system that operates near 2.09 μm, since Cr^{3+} and Tm^{3+} can act as sensitizers of Ho^{3+} to enhance the absorption of flashlamp light. Later, it was noted that the Tm,Ho:YLF crystal is similar to the YAG system. Finally, the Er:YAG crystal has turned out to be useful as a long-wavelength system. The 2.3 μm lasers are particularly useful for novel medical procedures and for applications requiring eye-safe laser output.

During the growth of these crystals, the defects that should be specially mentioned are absorptions at the laser wavelength induced by impurities and the thermal stresses formed in the crystals.

Absorption at Laser Wavelength

As discussed above in Sect. 15.2.1, the presence of absorptive loss at the laser wavelength can strongly degrade the performance of melt-grown crystals. An example similar to the presence of Ti^{4+} in Ti^{3+}:sapphire is the unintended incorporation of Cr^{4+} into tetrahedral Ga-sites of the $Gd_3Sc_2Ga_3O_{12}$ (GSGG) garnet when the crystal is co-doped with Nd^{3+} and Cr^{3+} [15.133]. This problem is complicated by the interplay of numerous growth conditions, such as volatilization of Ga_2O_3 from the melt, oxidation of the crucible, requirement for calcium additives to stabilize growth, and scattering centers under certain conditions. This problem has been particularly vexing because the absorption strength of the tetrahedral Cr^{4+} is orders of magnitude greater than that of the normal Cr^{3+} (on the octahedral Sc^{3+} site), thereby requiring that much less than 1% of the Cr ions be incorporated in the tetravalent state. It is worthwhile to note that, ironically, the Cr^{4+} ion was later recognized to be useful as a saturable absorber in Q-switching applications and then as a laser ion in the forsterite crystal (Mg_2SiO_4). Other examples of the presence of interfering oxidation states of chromium include Cr^{2+} in Cr^{3+}-doped LiCAF and LiSAF [15.134], while Cr^{3+} is found to absorb pump radiation in Cr^{4+}-doped forsterite [15.135].

The growth atmosphere can have a profound effect on the oxidation state of dopants and impurities and hence on the quality of the crystal via the phase diagram. For example, Nd:YLF is generally grown in an HF atmosphere to maintain low concentration of YOF forming from oxide impurities [15.136]. Cr^{4+}:forsterite is grown under oxidizing conditions [15.135], while Ti^{3+}:sapphire is grown under moderately reducing conditions [15.137]. For the gallium-containing garnets, i. e., GGG and GSGG, the formation of a reduced Gd – Ga compound that is insoluble in the molten garnet can be prevented by the addition of 2–3 vol. % oxygen to the growth atmosphere (N_2) [15.98]. In addition to preventing the formation of a second phase, the addition of oxygen to the growth atmosphere reduces the evaporation of Ga_2O_3 from the liquid surface. In general, for most oxide material systems, the addition of small (≈ 500 ppm) to moderate (approximately 2.5% by volume) amounts of oxygen to the growth atmosphere will prevent the partial reduction of the oxide constituents.

Furthermore, during the growth of oxide-based laser materials, the lasing action is dependent upon the dopant ion being in a particular oxidation state, e.g., Cr^{4+} in forsterite [15.138, 139]. Maintaining the correct oxidation state of Cr^{4+} can require a growth atmosphere that is more oxidizing than that required to prevent partial decomposition of the constituent oxides. Postgrowth annealing of the crystal has also been used to convert the dopant ion to the desired valence state. However, the impact of this process is highly dependent upon either cation or anion valencies in the lattice. Therefore, the preferred approach is to produce these crystals by adjusting the initial growth conditions and starting materials to directly yield the desired dopant oxidation state.

The converse can also be true. For Cr,Nd:GSGG and Cr,Nd:GGG, the presence of Cr^{4+} introduces a broad absorption band in the 1 μm region. In this case, it was found that low-level divalent impurities such as Ca^{2+} in the starting materials were charge-compensated in the lattice by the conversion of Cr^{3+} to Cr^{4+}. The elimination of Cr^{4+} in the crystal was achieved by the addition of another tetravalent ion such as Ti^{4+} into the starting composition, thereby providing the growing crystal with a readily available source of another tetravalent ion [15.140, 141].

Thermal Stresses

Thermal stresses result from nonlinear temperature fields in growing crystals, scale linearly with the second derivative of temperature (assuming no external traction forces), and often scale quadratically with the length scale over which they occur [15.142]. The details are actually much more complicated, particularly in noncubic crystals. However, increasing the size of a crystal increases the imposed thermal stress, subject to the degree to which it can be controlled. In CZ growth, radial temperature gradients are required to maintain control over the growth process. Curvature along the growth direction is generally nonlinear, but in principle could be linearized through suitable furnace design to minimize thermal stresses. In TGT, VBT or HEM growth, radial

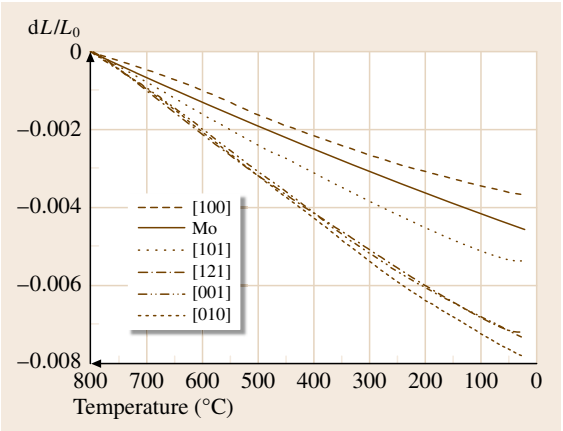


Fig. 15.29 Thermal contraction curves along several typical directions of YAP crystal

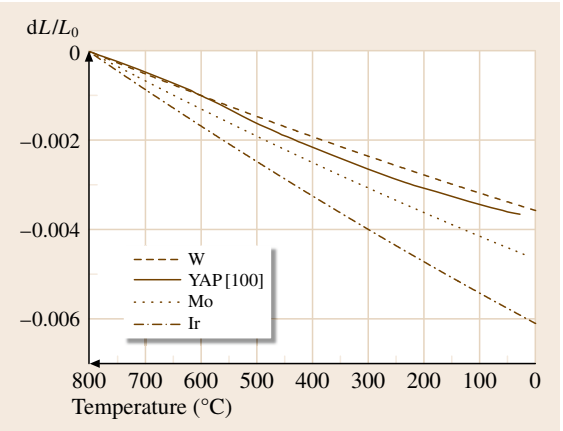


Fig. 15.30 Thermal contraction curves of several common crucible materials in comparison with that along the [100] direction of YAP

(lateral) temperature gradients can be minimized since the crystal takes the shape of the ampoule. However, the ampoule itself can also act as a source of stress in the crystal usually during cool-down.

For robust oxide crystals such as Nd:YAG and Ti:sapphire, scaling up the growth process may ultimately be successful for obtaining larger crystals suitable for large slabs. For fluorides, which have much lower fracture toughness, the thermal stresses present in the CZ process may ultimately limit the sizes that can be grown. The TGT and Bridgman process does not require lateral thermal gradients for stability, and the furnace can be designed to minimize these gradients. As was noted above, however, use of the TGT and Bridgman process can lead to other stress problems due to the different thermal contraction coefficients of the crystal and crucible. A typical example is the cracking and twining defects occurred in TGT-grown YAP crystals using a Mo crucible. YAP possesses a deformed perovskite-like structure, and is highly anisotropic in its coefficient of thermal expansion (CTE), with approximate values of $4.2\times10^{-6}\,\mathrm{K}^{-1}$, $11.7\times10^{-6}\,\mathrm{K}^{-1}$, and $5.1\times10^{-6}\,\mathrm{K}^{-1}$ along the *a*-, *b*-, and *c*-axes, respectively. As shown in Fig. 15.29, since the CTE of the Mo crucible is higher than that along the *a*-axis in YAP, the crystal is compressed along its *a*-axis by the crucible as it cools, hence leading to cracking and twining. Such defects can be reduced or even eliminated by growing YAP crystal using an *a*-oriented seed or tungsten crucible since the tungsten has a lower CTE, as shown in Fig. 15.30.

Cr:LiCAF is also anisotropic in its CTE. Along the *a*-axis the CTE is approximately $2.2\times10^{-6}\,\mathrm{K}^{-1}$, while along the *c*-axis the CTE is only $3.6\times10^{-6}\,\mathrm{K}^{-1}$. Since the graphite ampoule has a CTE of $8\times10^{-6}\,\mathrm{K}^{-1}$, the crystal is compressed along its *c*-axis by the ampoule as it cools. For slab growth, this places the two broad faces of the slab under compression. Materials generally do not fail under compression, and this is probably not a problem for Cr:LiCAF. However, by pinning the crystal (either partially or completely) along the *c*-axis, the slab is put under tension in the orthogonal directions since the CTE is larger than that of graphite. Evidence of failure in tension in the form of long, linear fractures that run the length of slab has been seen by *Atherton* et al. [15.63]. They tried to compensate for this fracture mode by using compressible graphite foam inserts in the ampoule to take up the imposed stress along the *c*-axis. While this clearly helped, it did not eliminate the fracture problem entirely. In addition, there also exist small, nonlinear temperature gradients in the crystal as it cools down, thus creating another type of stress field. Calculations have indicated that these stresses are at least an order of magnitude smaller than the traction-induced stresses, but they may still be important, especially given the experience with the foam inserts.

Should the need for large slabs of Cr:LiCAF (or Cr:LiSAF and other analogues) arise in the future, further modification of the ampoule in the form of lower-CTE graphite, a softer foam insert or an ampoule design that opens as it cools could be utilized to address the traction-induced stress problem. The furnace itself can be modified to further linearize the temperature field imposed on the crystal as it cools to minimize thermal stresses.

15.3 Crystal Growth Techniques Characterization

15.3.1 Czochralski (CZ) Process

The CZ process is by far the most commonly used process for the growth of laser materials. The main CZ characteristics are as follows.

Advantages of CZ

An appropriate thermal field is easy to establish for various crystals with a wider span of materials and melting points than any other melt-growth method. Not only by varying the ceramic insulation and its dimensions but by changing the rotation rate of the crystal, the adjustment of radial and vertical thermal gradients in the melt can be easily accomplished. Moreover, the convenience of the observation of the growing crystal makes it possible to adjust the growth parameter promptly, which is essential for realizing real-time control of the growth process.

Where CZ is used, crystals grow from the free surface of the melt without contacting with crucible. Therefore, defects induced by contact stress and parasitic nucleation can be eliminated, and the selection of crucible material is no longer limited by the mismatch of CTE between crystal and crucible.

In CZ, a neck process can be easily employed to eliminate dislocations originating from the seed and thermal shock. Compared with other methods, CZ can provide a higher growth rate to obtain a relatively large crystal with good perfection.

Disadvantages of CZ

The CZ furnace is usually constructed of either Al_2O_3 or stabilized ZrO_2 ceramics, which contact directly with the crucible. This configuration leads to a weakly oxidizing atmosphere in the furnace. Such conditions may result in the oxidation of crucible and introduce pollutants into the melt.

In CZ growth, appreciable temperature gradients are usually needed to control the diameter of the growing crystal. Otherwise, the space above the crucible is commonly opening due to the presence of the lift mechanism. Such a configuration increases the loss of heat. In addition, the growing crystal can act as a light-conduction tunnel for radiative heat loss. So CZ often has higher temperature gradients, which will introduce thermal stress into the crystal.

15.3.2 Temperature Gradient (TGT)

The TGT method has the following advantages and disadvantages with respect to the CZ technique.

Advantages of TGT

Since the crystal shape is dictated by the crucible, there is no need for sophisticated diameter control based on weight gain or various optical techniques. This aspect is especially significant when growing relatively large sample.

For application where large crystal plates are required, the TGT process can be effectively utilized. This is especially valuable for crystals in which significant scale-up is required.

In TGT growth with the melt above the crystal, the vertical temperature gradient is stabilizing with respect to natural convection (hot above cold), as opposed to the CZ configurations, which is destabilizing, as discussed in Sect. 15.2.2. In addition, the furnace, crucible, and crystal are fixed in space, so this configuration is mechanically simple, which enhances the temperature stability.

In TGT growth, the temperature gradient can be as small as practically required, depending on thermodynamic considerations. This can be important for controlling thermal stresses or selective evaporation from multicomponent systems. In CZ, appreciable temperature gradients are required to control the crystal diameter.

Disadvantages of TGT

Because the crystal is growing in contact with the crucible, two problems can arise. One is spurious nucleation on the crucible wall that gives rise to large-angle grain boundaries. This problem is magnified when insufficient temperature gradients are utilized. The second problem stems from stress imposed on the crystal during cool-down for the cases where the crucible has a large coefficient of thermal expansion for contraction, or where adhesion due to wetting of the crucible wall occurs. The magnitude of this problem is determined by the strength of the crystal and of the adhesion.

Poor mixing in TGT growth stems from the lack of convection in the melt due to the stabilizing temperature gradient discussed above. This aspect is only a disadvantage for growth of multicomponent systems

that either grow noncongruently or show selective evaporation of one or more of the components. In this case, convection is absolutely required to homogenize the melt continually.

Blind seeding is a commonly cited disadvantage of the TGT, VBT, and HEM techniques. A combination of diagnostics (usually strategically placed thermocouples) and experience can overcome this disadvantage, even for growth in very low temperature gradients.

15.3.3 Heat-Exchanger Method (HEM)

The HEM process shares most of the advantages and disadvantages of TGT method. The most important differences are noted below.

Advantages of HEM

One of the unique features of HEM is that there are no significant temperature gradients built into the heat zone. The temperature gradients required for crystal growth are controlled by the furnace and heat-exchanger temperatures. For a given material, the furnace temperature determines the temperature gradients in the liquid, and the heat-exchanger temperature determines the temperature gradients in the solid. These temperatures are sensed and controlled externally and, therefore, the temperature gradients can be varied during the growth cycle. This unique feature allows independent control of temperature gradients in the liquid and solid during most of the growth cycle. Once the growth cycle is established, the furnace and heat exchanger temperatures can be readily automated using microprocessors.

Disadvantages of HEM

The HEM process usually uses helium gas as the heat-exchanger medium, which is very expensive. Furthermore, the common growth cycle is very long, so the consumption of helium gas is high.

15.3.4 Vertical Bridgman Technique (VBT)

One of the most distinguishing characters of VBT is the translation of the crucible vertically through a hot zone with a temperature gradient designed to crystallize the materials. This feature leads to both advantages and disadvantages of the growth process relative to TGT.

Advantages of VBT

In VBT growth, only sufficient temperature gradients are needed near the solid–liquid interface, whilst elsewhere a small one is enough. However in TGT growth, a linear temperature gradient is required all along the crucible from the bottom to the top. Apparently, this will increase the difficulty of establishing the thermal field, especially for high-melting-temperature crystals.

For complicated thermodynamic systems, the Bridgman process can be utilized by adding a third zone to the furnace (Fig. 15.9b). If large crystals, especially slabs, are required, this may be the only practical route to growing these crystals.

Disadvantages of VBT

The employment of the lift mechanism will give rise to flow vibration on the solid–liquid interface, and enhance the risk of striation formation, which can degrade crystal performance.

15.3.5 Horizontal Bridgman Technique (HBT)

In the HBT, the crucible is translated horizontally through the hot zone, in contrast with VBT, which leads to some advantages and disadvantages, as noted below.

Advantages of HBT

By using either a boat or a sealed crucible that is not completely filled with starting material, the problem of a crucible imposing stresses on the crystal during cool-down can be overcome. This assumes that either the crystal has a larger coefficient of thermal expansion than the crucible in one or more directions, or that it does not adhere to the crucible during cool-down.

As in this method the melt height is much smaller than the dimension of its surface, this condition is good for effective withdrawal of the impurities at the expense of evaporation. For multicomponent systems, as discussed above, the lack of a stabilizing temperature field can be an advantage. This produces more intense convection that may be crucial for multicomponent systems. Besides, the open surface of the melt provides the opportunity to insert the activating impurity at any stage of crystallization.

HBT possesses the advantage that crystallization is carried out under conditions facilitating the evaporation of extraneous impurities. As a result the chemical purity of the crystal is enhanced on average by one order of magnitude compared with the raw material.

Disadvantages of HBT

The more intense flows generated by the horizontal Bridgman configuration can produce a highly concave

interface shape. This can be counteracted by suitable modification of the externally imposed furnace temperature profile, but the process is interactive and definitely not straightforward.

Melt flows in the horizontal configuration can be vigorous, and in addition to complicating control of interface shape, they can also produce striations. This problem can only be overcome by modifying the temperature gradients or the ampoule geometry.

15.3.6 Laser-Heated Pedestal Growth (LHPG)

LHPG and the related float zone growth technique are microvariants of the CZ growth method. Several advantages of LHPG have become apparent, not only in the growth of fibers for applications but, more importantly, as a general way to explore material synthesis and the properties of crystal growth. Other practical advantages of the LHPG method have also become apparent, as follows.

The LHPG relies on surface tension to maintain the integrity of the melt and hence it does not require crucibles, nor does the enclosure containing the fiber growth region possess walls heated to high temperatures as is the case in crystal growth furnaces. Both crucible and furnace surfaces are generally understood to be the primary sources of contamination in normal crystal growth, hence it follows that the absence of these surfaces allows the growth of very pure crystal materials. The impurity levels found in LHPG fibers are solely determined by the purity of the starting materials of the source rod. Furthermore, it is also generally accepted that thermal gradients within the melt container are responsible for introducing stresses and other defects in bulk crystals. Because of this, LHPG pulled fibers can be made practically stress free.

The source rod length as well as the melt volume in LHPG is typically small, of the order of 10 mm and 1 mm^3, respectively. The cost of the chemical compounds required for the growth of single-crystal fibers is, as a consequence, relatively small. Because of this, it is possible to grow fiber crystals of materials which would be prohibitively expensive to grow by traditional methods, especially on a basis. The small volume of the growth area also facilitates the introduction of external perturbations during synthesis of the crystal. The application of an external field to the melt may influence the growing process by encouraging the inclusion of domains or the formation of other stoichiometric combinations.

One of the most attractive features of the LHPG methods is the rapidity with which fibers can be grown by this method. The information feedback made possible by this allows for rapid readjustment of stock compositions and growth conditions for optimized materials.

15.3.7 Flux Technique (FT)

The FT is interesting from the point of view of the peculiarities of crystallization, especially at relatively low temperature. For those crystals that cannot be easily grown from melt, FT may be the most useful method to obtain them. The relatively low growth rate is an obvious disadvantage of this technique.

References

15.1 T.H. Maiman: Stimulated optical radiation in ruby masers, Nature **187**, 493–494 (1960)

15.2 H.G. Danielmeyer, F.W. Ostermayer: Diode-pump-modulated Nd:YAG laser, J. Appl. Phys. **43**, 2911–2913 (1972)

15.3 P.F. Moulton: Spectroscopic and laser characteristics of Ti:Al_2O_3, J. Opt. Soc. Am. B **3**, 125–133 (1986)

15.4 L. De Shazer: Vanadate crystals exploit diode-pump technology, Laser Focus World **30**, 88 (1994)

15.5 P. Lacovara, H.K. Choi, C.A. Wang, R.L. Aggarwal, T.Y. Fan: Room-temperature diode-pumped Yb:YAG laser, Opt. Lett. **16**, 1089–1091 (1991)

15.6 R. Scheps, J.F. Myers, S.A. Payne: End-pumped Yb-doped fluorapatite laser, IEEE Photon. Technol. Lett. **5**, 1285–1288 (1993)

15.7 Y. Jeong, J.K. Sahu, D.N. Payne, J. Nilsson: Ytterbium-doped large-core fiber laser with 1.36 kW continuous-wave output power, Opt. Exp. **12**, 6088–6092 (2004)

15.8 A. Ikesue, T. Kinoshita, K. Kamata, K. Yoshida: Fabrication and optical properties of high-performance polycrystalline Nd:YAG ceramics for solid-state lasers, J. Am. Ceram. Soc. **78**, 1033–1040 (1995)

15.9 J. Czochralski: A new method for the measurement of crystallization rate of metals, Z. Ver. Deutsch. Ing. **61**, 245–351 (1917)

15.10 G.K. Teal, J.B. Little: Growth of germanium crystals, Phys. Rev. **78**, 647 (1950)

15.11 A.E. Paladino, B.D. Roiter: Czochralski growth of sapphire, J. Am. Ceram. Soc. **47**, 465–468 (1964)

15.12 B. Cockayne, M. Chesswas, D.B. Gasson: Single-crystal growth of sapphire, J. Mater. Sci. **2**, 7–11 (1967)

15.13 M. Katsurayama, Y. Anzai, A. Sugiyama, M. Koike, Y. Kato: Growth of neodymium doped $Y_3Al_5O_{12}$ single crystals by double crucible method, J. Cryst. Growth **229**, 193–198 (2001)

15.14 K.J. Gärtner, K.F. Rittinghaus, A. Seeger, W. Uelhoff: An electronic device including a TV-system for controlling the crystal diameter during Czochralski growth, J. Cryst. Growth **13/14**, 619 (1972)

15.15 T.R. Kyle, G. Zydzik: Automated crystal puller, Mater. Res. Bull. **8**, 442–450 (1973)

15.16 R.C. Reinert, M.A. Yatsko: Crystal weighing mechanism for growth monitoring of Czochralski grown crystals, J. Cryst. Growth **21**, 283–286 (1974)

15.17 D.T.J. Hurle: Control of diameter in Czochralski and related crystal growth techniques, J. Cryst. Growth **42**, 473–482 (1977)

15.18 E. Kanchanavaleerat, D. Cochet-Muchy, M. Kokta, J. Stone-Sundberg, P. Sarkies, J. Sarkies, J. Sarkies: Crystal growth of high doped Nd:YAG, Opt. Mater. **26**, 337–341 (2004)

15.19 G. Boulon: Yb^{3+}-doped oxide crystals for diode-pumped solid state lasers: crystal growth, optical spectroscopy, new criteria of evaluation and combinatorial approach, Opt. Mater. **22**, 85–87 (2003)

15.20 L. Fornasiero, E. Mix, V. Peters, K. Petermann, G. Huber: Czochralski growth and laser parameters of RE^{3+}-doped Y_2O_3 and Sc_2O_3, Ceram. Int. **26**, 589–592 (2000)

15.21 K. Shimamura, H. Sato, A. Bensalah, V. Sudesh, H. Machida, N. Sarukura, T. Fukuda: Crystal growth of fluorides for optical applications, Cryst. Res. Technol. **36**, 801–813 (2001)

15.22 S.L. Baldochi, K. Shimamura, K. Nakano, N. Mujilatu, T. Fukuda: Growth and optical characteristics of Ce-doped and Ce:Na-codoped $BaLiF_3$ single crystals, J. Cryst. Growth **200**, 521–526 (1999)

15.23 S. Licia Baldochi, K. Shimamura, K. Nakano, N. Mujilatu, T. Fukuda: Ce-doped $LiYF_4$ growth under CF_4 atmosphere, J. Cryst. Growth **205**, 537–542 (1999)

15.24 F. Cui, Y. Zhou, J. Qiao: Growth of high quality monocrystal sapphire by seed-induced temperature gradient technique (STGT), J. Chin. Ceram. Soc. **8**, 109–113 (1980)

15.25 Y. Zhou: A temperature gradient furnace for growing high-melting crystals, Chin. Patent 85100534.9 (1985)

15.26 Y. Zhou, H. Xia, Z. Huang, M. Lu, P. Deng, J. Qiao, Q. Zhang, B. Hu: Growth of large-size $Ti:Al_2O_3$ tunable laser crystal, SPIE **1627**, 230–233 (1992)

15.27 Y. Zhou: Growth of high quality large Nd:YAG crystals by temperature gradient technique (TGT), J. Cryst. Growth **78**, 31–35 (1986)

15.28 G. Zhao, H. Li, J. Zhu, M. Jie, X. He, J. Xu: The temperature gradient technique (TGT) growth and optical properties of Yb-doped $YAlO_3$ single crystal, J. Cryst. Growth **280**, 483–489 (2005)

15.29 L. Su, J. Xu, H. Li, L. Wen, W. Yang, Z. Zhao, J. Si, Y. Dong, G. Zhou: Crystal growth and spectroscopic characterization of Yb-doped and Yb,Na-codoped CaF_2 laser crystals by TGT, J. Cryst. Growth **277**, 264–268 (2005)

15.30 D.C. Harris: A peek into the history of sapphire crystal growth, Proc. SPIE **5078**, 1–11 (2003)

15.31 J. Dong, P. Deng: Ti:sapphire crystal used in ultrafast lasers and amplifiers, J. Cryst. Growth **261**, 514–519 (2004)

15.32 J. Xu, Y. Zhou, H. Li, P. Deng: Growth of high-doped Nd:YAG laser crystals, Proc. SPIE **3889**, 420–421 (2000)

15.33 F. Schmid, D. Viechnicki: Growth of sapphire disks from the melt by a gradient furnace technique, J. Am. Ceram. Soc. **53**, 528 (1970)

15.34 C.P. Khattak, A.N. Scoville: Growth of laser crystals by heat exchanger method (HEM), SPIE **681**, 58–61 (1986)

15.35 V. Peters, A. Bolz, K. Petermann, G. Huber: Growth of high-melting sesquioxides by the heat exchanger method, J. Cryst. Growth **237–239**, 839–883 (2002)

15.36 C.P. Khattak, P.J. Guggenheim, F. Schmid: Growth of 15-inch diameter sapphire boules, Proc. SPIE **5078**, 47–53 (2003)

15.37 C.P. Khattak, F. Schmid: Growth of large-diameter crystals by HEM for optical and laser application, SPIE **505**, 4–8 (1984)

15.38 J.L. Caslavsky, D. Viechnicki: Melt growth of $Nd:Y_3Al_5O_{12}$ (Nd:YAG) using the heat exchange method (HEM), J. Cryst. Growth **46**, 601–606 (1979)

15.39 C.P. Khattak, F. Schmid, K.F. Wall, R.L. Aggarwal: Growth and characterization of $Ti:YAlO_3$ for turnable solid state laser applications, Proc. SPIE **1104**, 95–99 (1989)

15.40 P.W. Bridgman: Certain physical properties of single crystals of tungsten, antimony, bismuth, tellurium, cadmium, zinc, and tin, Proc. Am. Acad. Arts Sci. **60**, 305–383 (1925)

15.41 D.C. Stockbarger: The Production of large single crystals of lithium fluoride, Rev. Sci. Instrum. **7**, 133–136 (1936)

15.42 D.C. Stockbarger: The production of large artificial fluorite crystals, Disc. Faraday Soc. **5**, 294–299 (1949)

15.43 H.E. Buckley: *Crystal Growth* (Wiley, New York 1951) pp. 71–99

15.44 A.G. Petrosyan: Crystal growth of laser oxides in the vertical Bridgman configuration, J. Cryst. Growth **139**, 372–392 (1994)

15.45 J. Xu, M. Shi, B. Lu, X. Li, A. Wu: Bridgman growth and characterization of calcium fluoride crystals, J. Cryst. Growth **292**, 391–394 (2006)

15.46 K.S. Bagdasarov: http://www.bagdasarovcrystals.com/v1/ (2007)

15.47 G. Boulon, M. Ito, C. Goutaudier, Y. Guyot: Advances in growth of fiber crystal by the LHPG technique. Application to the optimization of Yb^{3+}-doped CaF_2 laser crystals, J. Cryst. Growth **292**, 230–235 (2006)

15.48 R.P. Poplawsky: Ferrite crystals using an arc image furnace, J. Appl. Phys. **33**, 1616 (1962)

15.49 R.S. Feigelson: Pulling optical fibers, J. Cryst. Growth **79**, 669–680 (1986)

15.50 W.M. Yen: Synthesis, characterization, and applications of shaped single crystals, Phys. Solid State **41**, 693–696 (1999)

15.51 L. Laversenne, C. Goutaudier, Y. Guyot, M.T. Cohen-Adad, G. Boulon: Growth of rare earth (RE) doped concentration gradient crystal fibers and analysis of dynamical processes of laser resonant transitions in RE-doped Y_2O_3 ($RE = Yb^{3+}$, Er^{3+}, Ho^{3+}), J. Alloys Compd. **341**, 214–219 (2002)

15.52 R.A. Lefever, J.W. Torpy, A.B. Chase: Growth of single crystals of yttrium aluminum garnet from lead oxide–lead fluoride melts, J. Appl. Phys. **32**, 962–963 (1961)

15.53 R.C. Linares: Substitution of aluminum and gallium in single-crystal yttrium iron garnets, J. Am. Ceram. Soc. **48**, 68–70 (1965)

15.54 L.G. van Uitert, W.H. Grodkiewicz, E.F. Dearborn: Growth of large optical-quality yttrium and rare-earth aluminum garnets, J. Am. Ceram. Soc. **48**, 105–108 (1965)

15.55 J.W. Nielsen: Garnet gemstones, US Patent 3091540 (1963)

15.56 G. Garton, B.M. Wanklyn: The rare earth aluminates, J. Cryst. Growth **1**, 164–166 (1967)

15.57 S. Erdei, B.M. Jin, F.W. Ainger, B. Keszei, J. Vandlik, A. Suveges: Possible trends for the growth of low scattering Nd:YVO_4 laser crystals; phase relations-growth techniques, J. Cryst. Growth **172**, 466–472 (1997)

15.58 X. Han, G. Wang, T. Tsuboi: Growth and spectral properties of Er^{3+}/Yb^{3+}-codoped $KY(WO_4)_2$ crystal, J. Cryst. Growth **242**, 412–420 (2002)

15.59 C. Pujol, M. Aguil, F. Diaz, C. Zaldo: Growth and characterisation of monoclinic $KGd_{1-x}RE_x(WO_4)_2$ single crystals, Opt. Mater. **13**, 33–40 (1999)

15.60 N.I. Leonyuk, E.V. Koporulina, V.V. Maltsev, O.V. Pilipenko, M.D. Melekhova, A.V. Mokhov: Crystal growth and characterization of $YAl_3(BO_3)_4$ doped with Sc, Ga, Pr, Ho, Tm, Yb, Opt. Mater. **26**, 443–447 (2004)

15.61 E. Fahey, A.J. Strauss, A. Sanchez, R.L. Aggarwal: Growth of Ti:Al_2O_3 crystals by a gradient-freeze technique. In: *Tunable Solid State Lasers II*, Springer Series in Optical Sciences, Vol. 52, ed. by A.B. Budgor, L. Esterowitz, L.G. DeShazer (Springer, New York 1987) pp. 82–88

15.62 R. Uecker, D. Klimm, S. Ganschow, P. Reiche, R. Bertram, M. Robberg, R. Fornari: Czochralski growth of Ti:sapphire laser crystals, Proc. SPIE **5990**, 599006-1–5990006-9 (2005)

15.63 L.J. Atherton, S.A. Payne, C.D. Brandle: Oxide and fluoride laser crystals, Annu. Rev. Mater. Sci. **23**, 453–502 (1993)

15.64 P.F. Moulton: Spectroscopic and laser characteristics of Ti:Al_2O_3, J. Opt. Soc. Am. E **3**, 125–133 (1986)

15.65 P. Albers, E. Stark, G. Hube: Continuous-wave laser operation and quantum efficiency of titanium-doped sapphire, J. Opt. Soc. Am. B **3**, 134–139 (1986)

15.66 G.F. Albrecht, J.M. Eggleston, J.J. Ewing: Measurements of Ti^{3+}:Al_2O_3 as a lasing material, Opt. Commun. **52**, 401–404 (1985)

15.67 R.C. Powell, J.K. Caslavsky, Z. AlShaieb, J.M. Bowen: Growth, characterization, and optical spectroscopy of Al_2O_3:Ti^{3+}, J. Appl. Phys. **58**, 2331–2336 (1985)

15.68 R.L. Aggarwal, A. Sanchez, M.M. Stuppi, R.E. Fahey, A.J. Strauss, W.R. Rapoport, C.P. Khattak: Residual infrared absorption in As grown and annealed crystals of Ti:Al_2O_3, IEEE J. Quantum Electron. **24**, 1003–1008 (1988)

15.69 G.A. Keig: Influence of the valence state of added impurity ions on the observed color in doped aluminum oxide single crystals, J. Cryst. Growth **2**, 356–360 (1968)

15.70 T.P. Jones, R.L. Coble, C.J. Mogab: Defect diffusion in single crystal aluminum oxide, J. Am. Ceram. Soc. **52**, 331–334 (1969)

15.71 K.S. Mohapatra, F.A. Kroger: Defect structure of α-Al_2O_3 doped with titanium, J. Am. Ceram. Soc. **60**, 381–387 (1977)

15.72 M.R. Kokta: Processes for enhancing Ti:Al_2O_3 tunable laser crystal fluorescence by annealing, US Patent 4587035 (1986)

15.73 M.R. Kokta: Processes for enhancing fluorescence of tunable titanium-doped oxide laser crystals, US Patent 4988402 (1991)

15.74 K.S. Bagdasarov, E.R. Dobrovinskaya, V.V. Pishchik, M.M. Chernick, Y.Y. Kovalev, A.S. Gershum, I.F. Zvyagintseva: Low dislocation density single crystals of corundum, Soy. Phys. Crystallogr. **18**, 242–245 (1973)

15.75 C.T. Bodur, J. Chang, A.S. Argon: Molecular dynamics simulations of basal and pyramidal system edge dislocations in sapphire, J. Europ. Ceram. Soc. **25**, 1431–1439 (2005)

15.76 A. Nakamura, T. Yamamoto, Y. Ikuhara: Direct observation of basal dislocation in sapphire by HRTEM, Acta Mater. **50**, 101–108 (2002)

15.77 C.P. Khattak, A.N. Scoville, F. Schmid: Recent developments in sapphire growth by heat exchanger method (HEM), SPIE **683**, 32–35 (1986)

15.78 J. Xu, Y. Zhou, G. Zhou, J. Xu, P. Deng: Producing large ⟨0001⟩-oriented sapphire for optical applications, SPIE **3557**, 11–14 (1998)

15.79 J. Xu, Y. Zhou, G. Zhou, K. Xu, P. Deng, J. Xu: Growth of large-sized sapphire boules by temperature gra-

dient technique (TGT), J. Cryst. Growth **193**, 123–126 (1998)
15.80 J.R. Carruthers: Origins of convective temperature oscillations in crystal growth melts, J. Cryst. Growth **32**, 13–26 (1976)
15.81 T. Surek: Theory of shape stability in crystal growth from the melt, J. Appl. Phys. **47**, 4384–4393 (1976)
15.82 J. Basterfield, M.J. Prescott, B. Cockayne: An X-ray topographic study of single crystals of melt-grown yttrium aluminium garnet, J. Mater. Sci. **3**, 33–40 (1968)
15.83 N. Ming, Y. Yang: Facet and vicinical growth of YAG by Czochralski, Acta Phys. Sin. **28**, 285–295 (1979)
15.84 B. Cockayne, M. Chesswas, D.B. Gasson: The growth of strain-free $Y_3Al_5O_{12}$ single crystals, J. Mater. Sci. **3**, 224–225 (1968)
15.85 G. Zydzik: Interface transitions in Czochralski growth of garnets, Mater. Res. Bull. **10**, 701–707 (1975)
15.86 B. Cockayne, B. Lent: A complexity in the solidification behaviour of molten $Y_3Al_5O_{12}$, J. Cryst. Growth **46**, 371–378 (1979)
15.87 E.W. O'Dell, D.J. Nelson, D. Narasimhan, R.C. Morris, J.E. Marion: Development of a large scale Nd:YAG growth process, SPIE **1223**, 94–102 (1990)
15.88 B. Cockayne, M. Chesswas, D.B. Gasson: Facetting and optical perfection in Czochralski grown garnets and rubies, J. Mater. Sci. **4**, 450–456 (1969)
15.89 Y. Miyazawa, M. Mori, S. Honma: Interface shape transitions in the Czochralski growth of $Dy_3Al_5O_{12}$, J. Cryst. Growth **43**, 541–542 (1978)
15.90 A.G. Petrosyan: Crystal growth of laser oxides in the vertical Bridgman configuration, J. Cryst. Growth **139**, 372–392 (1994)
15.91 P. Deng, J. Qiao, B. Hu, Y. Zhou, M. Zhang: Perfection and laser performances of Nd:YAG crystals grown by temperature gradient technique (TGT), J. Cryst. Growth **92**, 276–286 (1988)
15.92 R.C. Pastor: Effect of RAP purification on materials characterization, J. Cryst. Growth **75**, 54–60 (1986)
15.93 M. Robinson: Processing and purification techniques of heavy metal fluoride glass (HMFG), J Cryst. Growth **75**, 184–194 (1986)
15.94 C.D. Brandle, A.J. Valentino, G.W. Berkstresser: Czochralski growth of rare-earth orthosilicates (Ln_2SiO_5), J. Cryst. Growth **79**, 308–315 (1986)
15.95 D. Mateika, J. Herrnring, R. Rath, C. Rusche: Growth and investigation of $\{Gd_{3-x}Ca_x\}[Ga_{2-y-z}Zr_yGd_z](Ga_3)O_{12}$ garnets, J. Cryst. Growth **30**, 311–316 (1975)
15.96 D. Mateika, C. Rusche: Coupled substitution of gallium by magnesium and zirconium in single crystals of gadolinium gallium garnet, J. Cryst. Growth **42**, 440–444 (1977)
15.97 D.C. Miller: Defects in garnet substrates and epitaxial magnetic garnet films revealed by phosphoric acid etching, J. Electrochem. Soc. **120**, 678–685 (1973)
15.98 C.D. Brandle, D.C. Miller, J.W. Nielsen: The elimination of defects in Czochralski grown rare-earth gallium garnets, J. Cryst. Growth **12**, 195–200 (1972)
15.99 G. Boulon, A. Brenier, L. Laversenne, Y. Guyot, C. Goutaudier, M.T. Cohen-Adad, G. Metrat, N. Muhlstein: Search of optimized trivalent ytterbium doped-inorganic crystals for laser applications, J. Alloys Compd. **341**, 2–7 (2002)
15.100 D. De Loach, S.A. Payne, L.L. Chase, L.K. Smith, W.L. Kway, W.F. Krupke: Evaluation of absorption and emission properties of Yb^{3+} doped crystals for laser applications, IEEE J. Quantum Electron. **29**, 1179–1191 (1993)
15.101 X. Xu, Z. Zhao, J. Xu, P. Deng: Distribution of ytterbium in Yb:YAG crystals and lattice parameters of the crystals, J. Cryst. Growth **255**, 338–341 (2003)
15.102 P. Lacovara, H.K. Choi, C.A. Wang, R.L. Aggarwal, T.Y. Fan: Room-temperature diode-pumped Yb:YAG laser, Opt. Lett. **16**, 1089–1090 (1991)
15.103 F. Lu, M. Gonga, H. Xueb, Q. Liu, W. Gong: Analysis on the temperature distribution and thermal effects in corner-pumped slab lasers, Opt. Lasers Eng. **45**, 43–48 (2007)
15.104 X. Xu, Z. Zhao, J. Xu, P. Deng: Thermal diffusivity, conductivity and expansion of $Yb_{3x}Y_{3(1-x)}Al_5O_{12}$ (x=0.05, 0.1 and 0.25) single crystals, Solid State Commun. **130**, 529–532 (2004)
15.105 S.A. Payne, R.J. Beach, C. Bibeau, C.A. Ebbers, M.A. Emanuel, E.C. Honea, C.D. Marshall, R.H. Page, K.I. Schaffers, J.A. Skidmore, S.B. Sutton, W.F. Krupke: Diode arrays, crystals, and thermal management for solid-state lasers, IEEE J. Quantum Electron. **3**, 71–81 (1997)
15.106 D.J. Ripin, J.R. Ochoa, R.L. Aggarwal, T.Y. Fan: 300-W cryogenically cooled Yb:YAG laser, IEEE J. Quantum Electron. **41**, 1274–1277 (2005)
15.107 S. Chenais, F. Druon, F. Balembois, P. Georges, A. Brenier, G. Boulon: Diode-pumped Yb:GGG laser: comparison with Yb:YAG, Opt. Mater. **22**, 99–106 (2003)
15.108 J.B. Willis, M. Dixon: Assessment and control of imperfections in crystals for laser devices, J. Cryst. Growth **3-4**, 236–240 (1968)
15.109 V.A. Antonov, P.A. Arsenev, I.G. Linda, V.L. Farshtendiker: Studies of some point defects in $YAlO_3$ and $GdAlO_3$ single crystals, Phys. Status Solidi (a) **5**, K63–K68 (1973)
15.110 B. Cockayne, B. Lent, J.S. Abell, I.R. Harris: Cracking in yttrium orthoaluminate single crystals, J. Mater. Sci. **8**, 871–875 (1973)
15.111 P. Yang, P. Deng, J. Xu, Z. Yin: Growth of high-quality single crystal of 30 at. % Yb:YAG and its laser performance, J. Cryst. Growth **216**, 348–351 (2000)
15.112 H. Qiu, P. Yang, J. Dong, P. Deng, J. Xu, W. Chen: The influence of Yb concentration on laser crystal Yb:YAG, Mater. Lett. **55**, 1–4 (1998)

15.113 X. Xu, Z. Zhao, G. Zhao, P. Song, J. Xu, P. Deng: Comparison of Yb:YAG crystals grown by CZ and TGT method, J. Cryst. Growth **257**, 297–300 (2003)

15.114 C.Y. Chen, G.J. Pogatshnik, Y. Chen, M.R. Kokta: Optical and electron paramagnetic resonance studies of Fe impurities in yttrium aluminum garnet crystals, Phys. Rev. B **38**, 8555–8561 (1988)

15.115 K. Mori: Transient colour centres caused by UV light irradiation in yttrium aluminium garnet crystals, Phys. Status Solidi (a) **42**, 375–384 (1977)

15.116 T.I. Butaeva, K.L. Ovanesyan, A.G. Petrosyan: Growth and spectral investigations of oxide laser crystals with Pr^{3+} ions, Cryst. Res. Technol. **23**, 849–854 (1988)

15.117 R.F. Belt, J.R. Latore, R. Uhrin, J. Paxton: EPR and optical study of Fe in Nd:$YAlO_3$ laser crystals, Appl. Phys. Lett. **25**, 218–220 (1974)

15.118 J. Kvapil, J. Kvapil, J. Kubelka, R. Autrata: The role of iron ions in YAG and YAP, Cryst. Res. Technol. **18**, 127–131 (1983)

15.119 J. Kvapil, B. Perner, M. Košelja, J. Kvapil: Aborption background and laser properties of YAP:Nd, Czech. J. Phys. **40**, 99–108 (1990)

15.120 Y. Dong, G. Zhou, J. Xu, G. Zhao, F. Su, L. Su, H. Li, J. Si, X. Qian, X. Li, J. Shen: Color centers and charge state recharge in γ-irradiated Yb:YAP, Opt. Mater. **28**, 1377–1380 (2006)

15.121 A. Matkovski, A. Durygin, A. Suchocki, D. Sugak, G. Neuroth, F. Wallrafen, V. Grabovski, I. Solski: Photo and gamma induced color centers in the $YAlO_3$ and $YAlO_3$:Nd single crystals, Opt. Mater. **12**, 75–81 (1999)

15.122 D. Sugak, A. Matkovski, D. Savitski, A. Durygin, A. Suchocki, Y. Zhydachevskii, I. Solskii, I. Stefaniuk, F. Wallrafen: Growth and induced color centers in $YAlO_3$–Nd single crystals, Phys. Status Solidi (a) **184**, 239–250 (2001)

15.123 S.M. Kaczmarek: Role of the type of impurity in radiation influence on oxide compounds, Cryst. Res. Technol. **34**, 737–743 (1999)

15.124 V.G. Baryshevsky, M.V. Korzhik, B.I. Minkov, S.A. Smirnova, A.A. Fyodorov, P. Dorenbos, C.W.E. van Eijk: Spectroscopy and scintillation properties of cerium doped $YAlO_3$ single crystals, J. Phys. Condens. Matter **5**, 7893–7902 (1993)

15.125 J. Dong, M. Bass, Y. Mao, P. Deng, F. Gan: Dependence of the Yb^{3+} emission cross section and lifetime on temperature and concentration in yttrium aluminum garnet, J. Opt. Soc. Am. B **20**, 1975–1979 (2003)

15.126 T.Y. Fan, R.L. Byer: Diode laser pumped solid-state laser, IEEE J. Quantum Electron. **24**, 895–912 (1988)

15.127 F.D. Patel, E.C. Honea, J. Speth, S.A. Payne, R. Hutcheson, R. Equall: Laser demonstration of $Yb_3Al_5O_{12}$ (YbAG) and materials properties of highly doped Yb:YAG, IEEE J. Quantum Electron. **37**, 135–144 (2001)

15.128 R. Sang: *Etching of Crystal Theory, Experiment and Application* (North-Holland, Amsterdam 1987) p. 303

15.129 P. Yang, P. Deng, Z. Yin, Y. Tian: The growth defects in Czochralski-grown Yb:YAG crystal, J. Cryst. Growth **218**, 87–92 (2000)

15.130 P. Song, Z. Zhao, X. Xu, P. Deng, J. Xu: Defect analysis in Czochralski-grown Yb:FAP crystal, J. Cryst. Growth **286**, 498–501 (2006)

15.131 W. Schmidt, R. Weiss: Dislocation propagation in Czochralski grown gadolinium gallium garnet (GGG), J. Cryst. Growth **43**, 515–525 (1978)

15.132 H. Klapper, H. Kuppers: Directions of dislocation lines in crystals of ammonium hydrogen oxalate hemihydrate grown from solution, Acta Cryst. A **29**, 495–503 (1973)

15.133 W.F. Krupke, M.D. Shinn, J.E. Marion, J.A. Caird, S.E. Stokowski: Spectroscopic, optical, and thermomechanical properties of neodymium- and chromium-doped gadolinium scandium gallium garnet, J. Opt. Soc. Am. B **3**, 102–114 (1986)

15.134 S.A. Payne, L.L. Chase, L.J. Atherton, J.A. Caird, W.L. Kway, M.D. Shinn, R.S. Hughes, L.K. Smith: Properties and performance of the $LiCaAlF_6$:Cr^{3+} laser material, Proc. SPIE **1223**, 84 (1990)

15.135 P. Pan, H. Zhu, S. Yan, Y. Chai, S. Wang, Y. Hou: Distribution and valence of chromium in forsterite crystals grown by the Czochralski technique, J. Cryst. Growth **121**, 141–147 (1992)

15.136 R. Uhrin, R.F. Belt, V. Rosati: Preparation and crystal growth of lithium yttrium fluoride for laser applications, J. Cryst. Growth **38**, 38–44 (1977)

15.137 M.R. Kokta: Process for enhancing Ti:Al_2O_3 tunable laser crystal fluorescence by controlling crystal growth atmosphere, US Pat 4711696 (1987)

15.138 C.B. Finch, G.W. Clark: Czochralski growth of single-crystal Mg_2SiO_4 (forsterite), J. Cryst. Growth **8**, 307–308 (1971)

15.139 H. Takei, T. Kobayashi: Growth and properties of Mg_2SiO_4 single crystals, J. Cryst. Growth **23**, 121–124 (1974)

15.140 C.D. Brandle, V.J. Fratello, A.J. Valentino, S.E. Stokowski: Effects of impurities and atmosphere on the growth of Cr-doped gadolinium scandium gallium garnet. I, J. Cryst. Growth **85**, 223–228 (1987)

15.141 V.J. Fratello, C.D. Brandle, A.J. Valentino, S.E. Stokowski: Effects of impurities and atmosphere on the growth of Cr-doped gadolinium scandium gallium garnet. II, J. Cryst. Growth **85**, 229–233 (1987)

15.142 B.A. Bolev, J.H. Weiner: *Theory of Thermal Stresses* (Wiley, New York 1960) p. 586

16. Shaped Crystal Growth

Vitali A. Tatartchenko

Crystals of specified shape and size (shaped crystals) with controlled defect and impurity structure have to be grown for the successful development of modern engineering. Since the 1950s many hundreds of papers and patents concerned with shaped growth have been published. In this chapter, we do not try to enumerate the successful applications of shaped growth to different materials but rather to carry out a fundamental physical and mathematical analysis of shaping as well as the peculiarities of shaped crystal structures. Four main techniques, based on which the lateral surface can be shaped without contact with the container walls, are analyzed: the Czochralski technique (CZT), the Verneuil technique (VT), the floating zone technique (FZT), and technique of pulling from shaper (TPS). Modifications of these techniques are analyzed as well. In all these techniques the shape of the melt meniscus is controlled by surface tension forces, i.e., capillary forces, and here they are classified as capillary shaping techniques (CST). We look for conditions under which the crystal growth process in each CST is dynamically stable. Only in this case are all perturbations attenuated and a crystal of constant cross section grown *without any special regulation*. The dynamic stability theory of the crystal growth process for all CST is developed on the basis of Lyapunov's dynamic stability theory. Lyapunov's equations for the crystal growth processes follow from fundamental laws. The results of the theory allow the choice of stable regimes for crystal growth by all CST as well as special designs of shapers in TPS. SCG experiments by CZT, VT, and FZT are discussed but the main consideration is given to TPS. Shapers not only allow crystal of very complicated cross section to be grown but provide a special distribution of impurities. A history of TPS is provided later in the chapter, because it can only be described after explanation of the fundamental principles of shaping. Some shaped crystals, especially sapphire and silicon, have specified structures. The crystal growth of these materials, and some metals, including crystal growth in space, is discussed.

16.1 **Definitions and Scope of Discussion: SCG by CST** 510

16.2 **DSC – Basis of SCG by CST** 512
16.2.1 Lyapunov Set of Equations 513
16.2.2 Capillary Problem – Common Approach 514
16.2.3 The Equation of Crystal Dimension Change Rate 515
16.2.4 The Equation of the Crystallization Front Displacement Rate 516
16.2.5 SA in a System with Two Degrees of Freedom 516

16.3 **SA and SCG by CZT** 517
16.3.1 Capillary Problem 517
16.3.2 Temperature Distribution in the Crystal–Melt System 517
16.3.3 SA and Crystal Growth 519

16.4 **SA and SCG by VT** 519
16.4.1 Practical Results of the Theoretic Analysis 519
16.4.2 SA-Based Automation of VT 521

16.5 **SA and SCG by FZT** 522

16.6 **TPS Capillary Shaping** 522
16.6.1 Capillary Boundary Problem 522
16.6.2 Stability Analysis 529
16.6.3 Experimental Tests of the Capillary Shaping Statements 530
16.6.4 Impurity Distribution 534
16.6.5 TPS Definition 537
16.6.6 TPS Brief History 537

16.7 TPS Sapphire Growth 539
16.7.1 Modifications of TPS 540
16.7.2 Crystal Defects 541
16.7.3 Applications 545
16.8 TPS Silicon Growth 546
16.8.1 Shaped Silicon Structure 546
16.8.2 Local Electronic Properties of Shaped Silicon 549
16.8.3 TPS Silicon Growth 551
16.9 TPS Metals Growth 551
16.10 TPS Peculiarities 552
References 552

16.1 Definitions and Scope of Discussion: SCG by CST

Modern engineering usually uses device details fabricated from crystals in the shape of plates, rods or tubes. Sometimes the shapes can be more complicated. Traditional ways of the detail fabrication (a growth of a bulk crystal and its machining) bring a loss of expensive material (often up to 90%) as well as an appearance of structure defects. Therefore, crystals of specified shape and size with controlled defect and impurity structure have to be grown. It allows using the crystals as final products with minimal additional machining as well as without one.

The problem of shaped crystal growth seems to be simply solved by profiled container crystallization just as in the case of casting. Indeed, it is possible to find a realization of this idea by the vertical or horizontal Bridgman techniques for growth of silicon, fluoride, sapphire or YAG crystals with different cross section of the crucible used [16.1–3]. But in these cases the crucible material should satisfy a whole set of requirements: it should neither react with the melt nor be wetted by it. Even if all these requirements are satisfied, perfect-crystal growth is not secured: the crucible serves as a source of noncontrolled nucleation as well as internal residual stresses. In addition, if a crucible material is wetted by the melt, the crucible usually has been made from a thin foil and used only once [16.2, 3].

Therefore, the techniques of crystal lateral surface shaping without contact with container walls have to be considered as the candidates for a shaped crystal growth. Since early sixties, both theoretical and practical aspects of the shaped crystal growth by these techniques have been developed. The main information

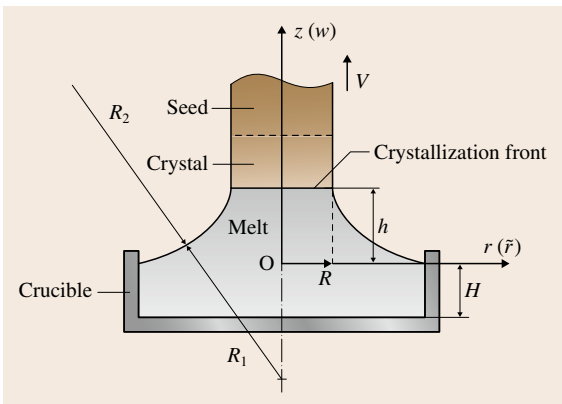
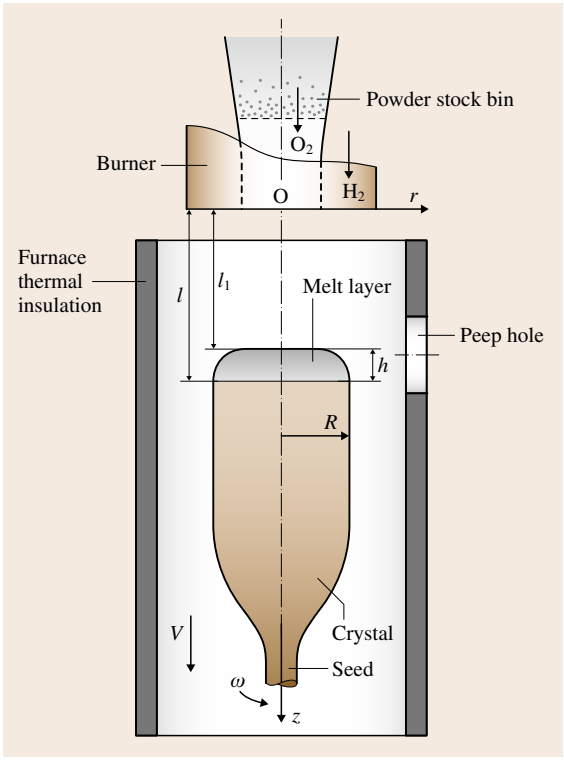


Fig. 16.1 Cylindrical crystal growth by CZT: R – crystal radius; h – crystallization front height; V – crystal pulling rate; H – melt level in crucible; $w\mathrm{O}\tilde{r}$ or $z\mathrm{O}r$ – coordinate systems; R_1 and R_2 – main radii of liquid surface curvature

Fig. 16.2 Cylindrical crystal growth by VT: H_2 – hydrogen flow; O_2 – mixed oxygen and powder flow; R – crystal radius; l_1 – melt surface position relative to the burner; l – crystallization front position relative to the burner; $h = l - l_1$ is the melt meniscus height; V – crystal displacement rate; ω – crystal rotation rate ▶

Fig. 16.4a–j Melt growth of crystalline rod by TPS **(a–j)**: pulling up **(a–e,h,i)** or lowering down **(f,g,j)** with rate V; shaping on the shaper surfaces **(a,c,g–i)**; shaping on the shaper edges **(b,d–f,j)**; positive melt pressure d **(b,f,g,j)**; negative melt pressure d **(d,e)**; C, G are counters of contact meniscus with shaper; $\boldsymbol{n}$ – normal vector to the shaper walls; d_0 – shaper depth; R – crystal radius; r_0 – edge counter radius; h – crystallization front height; Θ – wetting angle; ψ_0 – growth angle; α_d – meniscus inclination angle with respect to positive r-direction at the point of the contact with the shaper; $\alpha_1 = \pi - \alpha_d$; β – angle of cone shaper wall inclination; r_1 – cone radius on the melt free surface level ▶



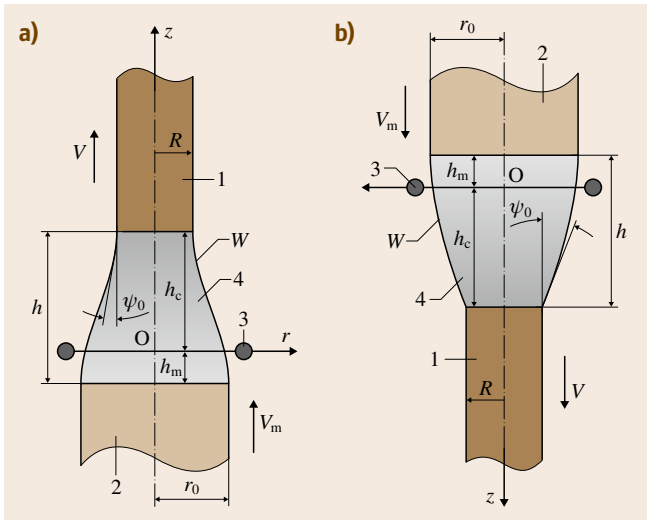
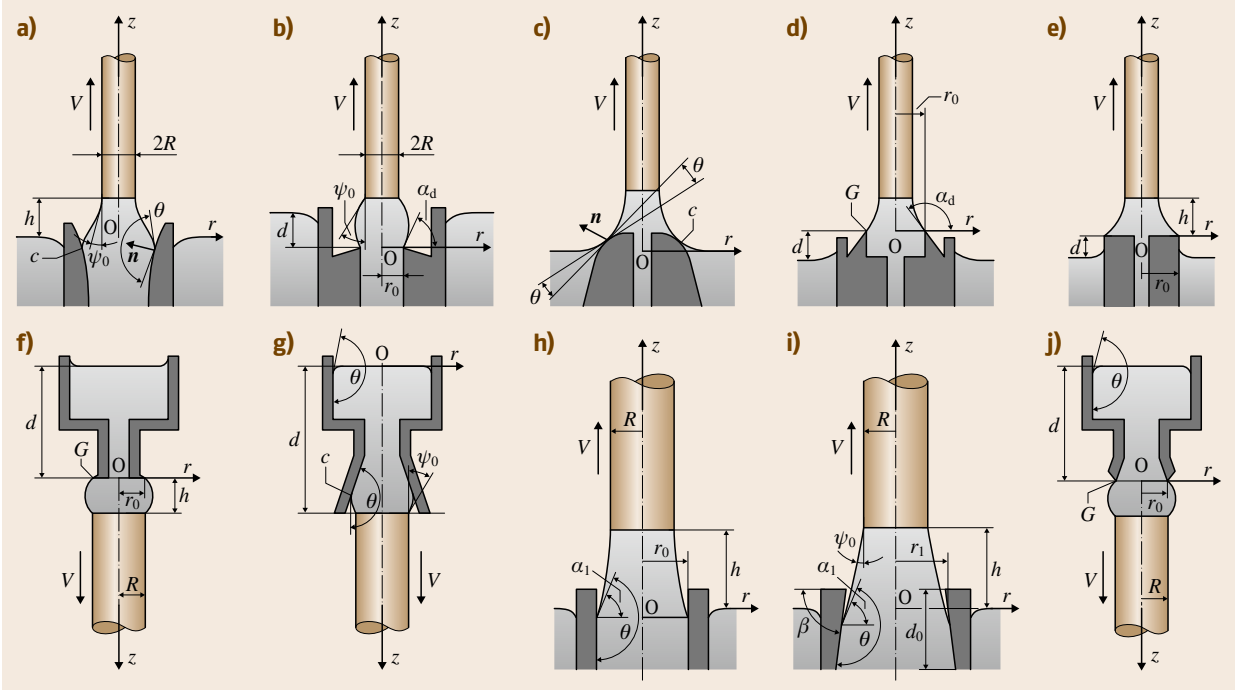


Fig. 16.3a,b Cylindrical crystal growth by FZT. **(a)** Pulling up, **(b)** lowering down: (1) growing crystal with radius R; (2) feeding rod with radius r_0; (3) heater; (4) melted zone; h_c, h_m – positions of crystallization front and melting front relative to the heater, respectively; $h = h_c + h_m$ is the length of the melted zone; W – volume of the melted zone; ψ_0 – growth angle; V – rate of growing crystal displacement relative to the induction heater; V_m – the same for the melting rod



concerned with all of them was published in some books and reviews [16.4–10], in the proceedings of three international conferences [16.11–13] and in hundreds of papers.

The few *classical* techniques of this type are well known: the Czochralski technique (CZT, Fig. 16.1), the Verneuil technique (VT, Fig. 16.2), the floating zone technique (FZT, Fig. 16.3). For all these techniques the shapes and the dimensions of the crystals grown are controlled by the shapes and the dimensions of meniscus of melt existing at the vicinity of interface crystal–melt. A shape of meniscus is controlled by the surface tension forces of the melt – capillary forces. Let the above-mentioned techniques (some *no classical* ones will be added below) be classified as capillary shaping techniques (CST). As a rule, all these techniques are used to grow crystals of nonregular cylindrical shape. On the other hand, all of them have been used for shaped crystal growth as well. For shaped crystal growth it is necessary to guarantee a special shape for the melt meniscus and a dynamical stability of the crystal growth process. But in any case, all above mentioned techniques allow obtaining only simple shaped crystals (cylinders, plates or tubes) and they have to be modified for the growth of more complicated ones. It has to be mentioned that *classical* Kyropoulos technique also belongs to CST but, in fact, it has never been used for the shaped growth because of specific thermal growth conditions [16.8].

Some possible schemes of the modification of *classical* CST are shown on the Fig. 16.4a–j. The schemes Fig. 16.4a–e,h,i differ from CZT by the presence of a shaper at the melt. The schemes Fig. 16.4f,g,j may be classified as FZT modified with lowering down where the melting rod is replaced by a shaper with a melt inside.

16.2 DSC – Basis of SCG by CST

As the crystal is not restricted by crucible walls its cross section depends upon the growth regimes. Any deviations of pulling or lowering (for a down growth) rate, as well as temperature conditions result in changes of the crystal cross section (pinches formation). A lot of defects (an increased amount of inclusions, nonuniform impurity distributions, subgrain formation) are observed at the pinch locations. It is not the pinches themselves, that seem to cause defect formation, but some deviation of the growth conditions (mainly, the crystallization rate) from the optimal ones indicated by a change in the crystal dimensions. Therefore, the stabilization of the crystal cross section as well as the crystallization front position has to be achieved. Why is it very important the stabilization of the crystallization front position? We can see from the schemes of CST (Figs. 16.1–16.4) that, if the crystallization front position is unmoved, a crystal growth speed is exactly equal to the one of pulling or lowering of a seed. A displacement of the crystallization front position changes the real crystal growth, see (16.10). As a result, in spite of the pulling or lowing rate stabilization, there is defect formation.

The modern systems of regulation using weight or crystal diameter detectors allow obtaining the cylindrical crystals by CST. These systems effect with a change of a power or pulling rate. Sometimes, the regulation is not stable and there is a permanent perturbation of the crystallization front position. The solution is to analyze theoretically the dynamic stability of concrete schemes of crystal growth and to select on the basis of this analysis the stable ones. In the dynamically stable system, the perturbations of parameters attenuate because of internal processes and, without any additional active regulation, it is possible to provide crystals of specified shape and of controlled cross section. If the active regulator is included in the system under investigation, this dynamically stable system can improve the shape and the quality of crystals.

For the first time, a comparative theoretical analysis of a dynamic stability of crystallization process for CZT and TPS had been carried out by the author of this chapter in 1971. The very impressive result was published in 1973 [16.14]. It was explained why it is difficult to pull crystals of constant cross section by CZT and easy by TPS: the use of a shaper allows obtaining a dynamic capillary stability of the crystal growth process. In the same year, the first paper concerning the investigation of VT dynamic stability was published [16.15]. In 1974 the investigation of CZT, TPS, VT and FZT stability was presented at the 4th International Conference of Crystal Growth in Japan [16.16]. The analysis of capillary and heat stability in detail using Lyapunovs approach was published in 1976 [16.17]. In 1976 *Surek* published only capillary stability analysis [16.18] repeating our main results for CZT and TPS from [16.14].

16.2.1 Lyapunov Set of Equations

The main results of stability analysis for all CST [16.4–10] were obtained by applying of the Lyapunovs approach [16.19]. With respect to Lyapunov, the crystallization techniques under consideration have to be characterized by a finite number n of the variables (degrees of freedom) X_i which can arbitrarily vary in the process of crystallization. Each CST has to include, as a minimum, crystal dimension R and crystallization front position h as degrees of freedom, i. e. a minimal degree of freedom quantity min n have to be two. Sometimes, it is sufficient for the dynamic stability analysis (CZT, Fig. 16.1; TPS, Fig. 16.4). But for VT, min $n = 3$ (Fig. 16.2): R, l, h; for the FZT, min $n = 4$ (Fig. 16.3): R, W, h_c, h_m. It has to be mentioned that the min n depends also on the cross section of the crystal to be grown. For instance, for a tube crystal, the internal diameter, as well as the external one, are the degrees of freedom. Therefore, min $n = 3$ for CZT and for TPS.

If n exceeds min n, the analysis is more fruitful. Sometimes we can use several iterations. The first iteration can include the stability investigating for min n. After that, one or more variables can be added. For instance, in [16.6, pp. 71–145], the stability of TPS as a system with min n was investigated. As a second step [16.6, pp. 155–159], the melt pressure was added as a third degree of freedom and a complimentary information concerning the influence of pressure perturbation on the stability of growth was obtained. So, we can confirm that min $n \geq 2$ but we can not propose any simple choosing of min n as well as optimal n. For us, in every case, it has been a result of very special investigation.

To realize a mathematical analysis of stability, a set of equations (16.1) for derivation of each degree of freedom X_i with respect to time t as a function of all n degrees of freedom $X_1, \ldots, X_n$, their other (except i) $n-1$ derivatives, time t, and parameters of process C (a temperature of melt, a velocity of pulling, a regime of cooling, etc.) has to be obtained

$$\frac{\mathrm{d}X_i}{\mathrm{d}t} = f_i\left(X_1, X_2, \ldots, X_n, \frac{\mathrm{d}X_1}{\mathrm{d}t}, \frac{\mathrm{d}X_2}{\mathrm{d}t}, \ldots, \frac{\mathrm{d}X_{n-1}}{\mathrm{d}t}, t, C\right), \quad i = 1, 2, \ldots, n . \tag{16.1}$$

To find the explicit function f_i, a set of fundamental laws have to be used. The set should include:

1. The Navier–Stokes equation for a melt with the boundary conditions on the meniscus free surface (the Laplace capillary equation)
2. The continuity equation (the law of crystallizing substance mass conservation)
3. The heat transfer equations for the liquid and the solid phases with the equations of heat balance at the crystallization front and at the melting front as the boundary conditions (the law of energy conservation)
4. The diffusion equation (impurity mass conservation)
5. The growth angle certainty condition
6. Some others.

The set of these equations is general for all the crystallization techniques under consideration (but it does not mean that each time we use all of them) while the specific features of each of crystallization schemes are characterized by the set of boundary conditions and concrete values of the parameters included in the equations.

Equation 16.1 with zero left side corresponds to the system under conditions of equilibrium ($X_i = X_i^0$): the growth of crystals of constant cross section X_1^0 with stationary crystallization front position X_2^0 etc.

$$f_i\left(X_1^0, X_2^0, \ldots, X_n^0, t, C\right) = 0 . \tag{16.2}$$

We are looking for the stable solutions of (16.1). According to Lyapunov [16.19], the solutions of (16.1) are stable if they are stable for the linearized set of equations

$$\frac{\mathrm{d}X_i}{\mathrm{d}t} = \sum_{k=1}^{n} \frac{\partial f_i}{\partial X_k}\delta X_k = \sum_{k=1}^{n} A_{ik}\delta X_k . \tag{16.3}$$

Here, $\delta X_k = X_k - X_k^0$, $\partial f_i / \partial X_k = A_{ik}$, all partial derivatives are taken with $X_k = X_k^0$. The stability of (16.3), in turn, is observed when all the roots S in the characteristic equation (16.4)

$$\det\left(\frac{\partial f_i}{\partial X_k} - S\delta_{ik}\right) = 0 \tag{16.4}$$

have negative real components (δ_{ik} is the Kronecker delta [16.19]). This equilibrium will be unstable if (16.4) has at least one root with a positive real component. If an imaginary number can be found among the roots, additional study including an allowance for the nonlinear terms in (16.3) is required.

Calculation of the time-dependent non stationary functions f_i is usually rather difficult. These difficulties can be avoided using a quasi-stationary approach.

We successfully have been used it in the most of our dynamic stability investigations and can show other examples of the same approach. For instance, *Mullins* and *Sekerka* [16.20] applied it to the temperature and impurity distribution problem while studying the morphological stability of the crystallization-front shape. However, in each particular case, the quasi-stationary approach has to be justified.

A number of constrains imposed on the systems and perturbations occurring in the course of Lyapunov stability study should be noted. Stability is examined over an infinitely long period of time. In this case, the perturbations are considered to be small and are imposed on the initial conditions only, i. e. after the perturbations, the same forces and energy sources affect the system as before the perturbations.

16.2.2 Capillary Problem – Common Approach

Melt Meniscus Shaping Conditions

For the capillary shaping techniques, the crystal cross section is determined by the melt meniscus section formed by the crystallization surface. The melt meniscus shape can be calculated on the basis of the Navier–Stocks equation, the Laplace capillary equation being the free-surface boundary condition.

The full-scale solution of this problem offers considerable mathematical difficulties. Therefore, to simplify the problem formulation, the contributions of various factors of meniscus shaping should be estimated: the inertial forces associated with the melt flow, the capillary forces, the gravity forces, viscous and the thermocapillary forces [16.6, 21]. The relative effect of the first three factors can be estimated by means of dimensionless numbers: the Weber number $\mathrm{We} = \rho V^2 L/\gamma$, characterizing comparative action of the inertial and capillary forces, the Froude number $\mathrm{Fr} = V/(gL)^{1/2}$ characterizing comparative action of the inertial and gravity forces; the Bond number $\mathrm{Bo} = \rho g L^2/\gamma$, characterizing comparative action of the gravity and capillary forces. Here ρ denotes the liquid density, L the liquid meniscus characteristic dimensions, γ the liquid surface tension coefficient, V is the liquid flow rate, and g relates to the gravity acceleration. When the Weber and Froude numbers are small, the melt flow can be neglected. The Bond number defines the region of capillary or gravity force predominance (Fig. 16.5). The effect of the inertial force as compared with the gravity and capillary ones proves to be negligible, if liquid flow rate is considered to

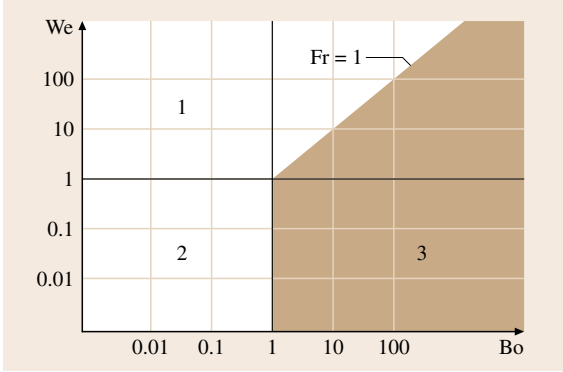


Fig. 16.5 Inertial (1), capillary (2), and gravitational force effects (3) on the melt column shaping (We, Bo, and Fr are characteristic Weber, Bond and Froude numbers, respectively)

be equal to the crystallization rate. Indeed, if we assume that the linear dimensions of the meniscus lie within the range of 10^{-3}–10^{-2} m, $\rho \approx 10^{-3}\,\mathrm{kg\,m^{-3}}$, $\gamma \approx 1\,\mathrm{N\,m^{-1}}$ the liquid meniscus shaping can be examined in the hydrostatic approximation up to the fluid speed of 0.1–$1.0\,\mathrm{m\,s^{-1}}$.

Convective flows, whose rates can substantially exceed the crystallization rate, can occur in a liquid column in addition to the flow associated with crystallization. These flow effects on meniscus shaping and on liquid-phase heat-transfer as well as the influence of the two latter factors can be found in [16.6].

The Meniscus Surface Equation

In the hydrostatic approximation, the equilibrium shape of the liquid surface is described by the Laplace capillary equation [16.22]

$$\frac{\gamma}{R_1} + \frac{\gamma}{R_2} + \rho g w = \text{const}\,. \tag{16.5}$$

Here, R_1 and R_2 denote the main radii of liquid surface curvature. They have to be located in two perpendicular planes. As a rule one of the planes coincides with the diagram plane (R_2, Fig. 16.1) and second one is perpendicular to it (R_1, Fig. 16.1). The w-axis is directed vertically upwards. The value of const. depends upon w-coordinate origin selection and is equal to the pressure p on the liquid in the plane $w = 0$. In particular, if the w-coordinate origin coincides with the plane of the liquid surface, const. $= 0$ (Fig. 16.1).

In this chapter our study will be restricted to considering meniscus possessing axial symmetry (Figs. 16.1–16.4). Such meniscus is obtained during melt

pulling of straight circular cylinder, tube-shaped crystals as well as a flat part of ribbon. We will find the equation of such meniscus surface, by introducing the cylindrical coordinates $w, \tilde{r}$. The problem of liquid meniscus shape calculation for an axially symmetric meniscus is reduced to finding the shape of a profile curve $w = f(\tilde{r})$, the liquid surface meniscus being obtained by rotating this curve around the w-axis. Let us introduce the capillary constant a, and pass to the dimensionless coordinates and parameters

$$\left(\frac{2\gamma}{\rho g}\right)^{1/2} = a\,, \quad \frac{w}{a} = z\,,$$
$$\frac{\tilde{r}}{a} = r\,, \quad \frac{pa}{2\gamma} = d\,.$$

This transition means that the capillary constant serves as a linear dimension unit, and the weight of a liquid column of one capillary constant high corresponds to the pressure equal to one unit. The approach allows application of the calculated results to any substance and magnitude of gravity, with the scale changing alone. Then (16.5) takes the form

$$z''r + z'\left(1 + z'^2\right) \pm 2(d - z)\left(1 + z'^2\right)^{3/2} r = 0\,. \tag{16.6}$$

For large Bond numbers (Bo $\gg 1$, Fig. 16.5) gravity prevails (this condition corresponds to growing big diameter crystals with $R \geq 5a$) and (16.6) can be simplified

$$z''r \pm 2(d - z)\left(1 + z'^2\right)^{3/2} r = 0\,. \tag{16.7}$$

For small Bond numbers (Bo $\ll 1$, Fig. 16.5) capillarity prevails (this condition corresponds to growing small diameter crystals $R < a$ as well as it was easily satisfied in our TPS experiments on the board of space stations [16.6] when the capillary constant is high) and (16.6) can also be simplified to give

$$z''r + z'\left(1 + z'^2\right) \pm 2d\left(1 + z'^2\right)^{3/2} r = 0\,. \tag{16.8}$$

Static Stability of the Melt Meniscus as well as the dynamic stability of crystal growth process has to be provided. A presence of static stability means that the melt meniscus exists for all values of crystallization parameters. An analysis of the stability can be realized on the basis of Jacobis equation investigation. For the TPS, this analysis was realized in [16.23, 24].

Growth Angle Certainty – Common Boundary Condition for CST

As the Laplace capillary equation is a second order differential one, formulation of a boundary problem for melt meniscus shape calculation requires assignment of two boundary conditions. The first of them is determined by the structural features of each specific CST and will be analyzed in details below. But second of the boundary conditions (the crystal–melt interface condition) is mutual for all CST. This condition follows from the growth angle certainty.

Let the angle ψ_0 (Figs. 16.3, 16.4a,b), made by the line tangent to the meniscus and the lateral surface of the growing crystal, be called the growth angle. The growth angle should not be confused with the wetting angle. The wetting angle characterizes particular equilibrium relative to the liquid movement along a solid body and is not directly associated with crystallization [16.6]. In the first studies of the CZT and TPS, a crystal of constant cross section was considered to grow in case $\psi_0 = 0$. Judging by a purely geometric diagram of liquid–solid phase conjugation, such assumption is quite natural. However, experimental and theoretical investigations of the crystal growth process showed that the geometrical condition $\psi_0 = 0$ is not satisfied while growing crystals of constant cross sections and ψ_0 is a physical characteristic of the crystals. Particular case $\psi_0 = 0$ is available only for some metals. Experimental determinations of the ψ_0 have included direct measurements as well as indirect calculations. Indirect techniques, as a rule, are more precise [16.6]. In our experiments [16.6, 25], we studied shapes of crystallized drops obtained on the bottom of silicon, germanium and indium antimonide crystals detached from the melts in the process of pulling by the CZT. The values of $\psi_0 = 25 \pm 1°$ for indium antimonide, $\psi_0 = 11 \pm 1°$ for silicon, and $\psi_0 = 12 \pm 1°$ for germanium were obtained. Theoretical investigations have shown that ψ_0 is an anisotropic value as well as it depends on the crystallization speed. In [16.6], a reader can find a discussion of the problem in detail. In this chapter, for the dynamic stability analysis, we will use ψ_0 as a constant value for the crystal to be grown.

16.2.3 The Equation of Crystal Dimension Change Rate

Proceeding from the condition of growth angle certainty, we can obtain an equation for the crystal characteristic dimension change rate $\mathrm{d}R/\mathrm{d}t$ that is common for all CST. On the diagram (Fig. 16.6) a vector

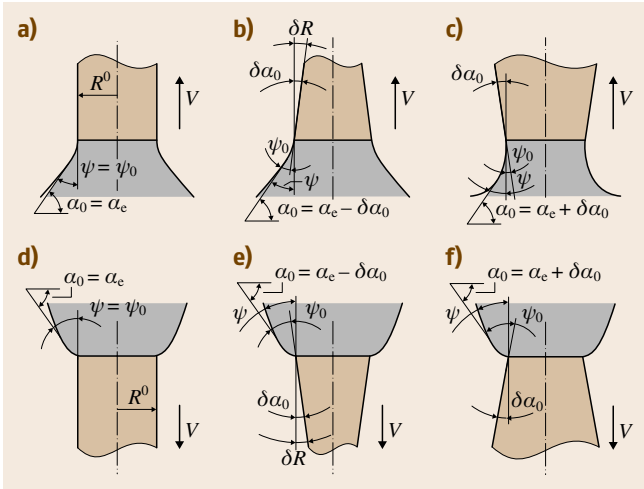


Fig. 16.6a–f Crystal growth by CST: pulling up **(a–c)**; lowering down **(d–f)**; $\alpha_0 = \alpha_e$: growth of constant cross section crystal **(a,d)**; $\alpha_0 < \alpha_e$: growth of widening cross section crystal **(b,e)**; $\alpha_0 > \alpha_e$: growth of narrowing cross section crystals **(c,f)**; V is the crystal displacement rate; other symbols given in the text

R is located within the diagram plane and represents the radius for a straight circular cylinder-shaped crystal. For a plate it is its half-thickness. Now we introduce the angles made by the line tangent to the meniscus on the three-phase line with the horizontal α_0 and with the vertical ψ (the crystal grows in the vertical direction). When the angles α_0 and ψ add up to $\frac{\pi}{2}$, a crystal of constant cross section R^0 grows. In this case, the angle ψ is equal to the growth angle ψ_0 and the value of the angle α_0 is denoted α_e. If $\psi \neq \psi_0$ the crystal lateral surface declines from the vertical on the angle $\psi - \psi_0 = \alpha_0 - \alpha_e = \delta\alpha_0$ the crystal changes its dimension $\delta R = R - R^0$ in accordance with (Fig. 16.6)

$$\frac{\mathrm{d}R}{\mathrm{d}t} = V_c \tan(\delta\alpha_0) = V_c \tan(\alpha_0 - \alpha_e) . \tag{16.9}$$

The angle $\delta\alpha_0$ is the angle of crystal tapering at any moment, the crystallization rate V_c is equal to the difference in rates between pulling and front displacement

$$V_c = V - \frac{\mathrm{d}h}{\mathrm{d}t} . \tag{16.10}$$

Near the stationary state that we need for (16.3), deviations $\mathrm{d}h/\mathrm{d}t$ as well as $\delta\alpha_0$ have to be negligible. Hence, the crystallization rate V_c can be replaced by the rate of the pulling V and $\tan(\delta\alpha_0) \approx \delta\alpha_0$. The angle α_0 together with the meniscus shape as a function of R, h and other parameters can be determined by solving the capillary boundary problem whose equation was discussed above. Assuming that the capillary problem is solved, i. e., the function $\alpha_0(X_1^0, X_2^0, \ldots, X_n^0, t, C) = 0$ is found, (16.9) can be represented by

$$\frac{\mathrm{d}R}{\mathrm{d}t} = \sum_{k=1}^{n} \frac{\partial\alpha_0}{\partial X_k}\delta X_k = \sum_{k=1}^{n} A_{ik}\delta X_k . \tag{16.11}$$

16.2.4 The Equation of the Crystallization Front Displacement Rate

The equation of the crystallization front displacement rate belongs to the set (16.3) and as well as (16.11) is common for all CST. It follows from the heat-balance condition on the crystallization front

$$-\lambda_S G_S(h) + \lambda_L G_L(h) = \zeta V_c . \tag{16.12}$$

Here λ_S and λ_L denote thermal conductivities of the solid and liquid phases respectively, $G_S(h)$ and $G_L(h)$ are the temperature gradients in the solid and liquid phases at the crystallization front, h is a crystallization front position, ζ denotes the latent melting heat of a material unit volume, V_c is the crystallization rate. In accordance with (16.10), we obtain a (16.1)-type equation for $\mathrm{d}h/\mathrm{d}t$

$$\frac{\mathrm{d}h}{\mathrm{d}t} = V - \zeta^{-1}\left[\lambda_L G_L(h) - \lambda_S G_S(h)\right] . \tag{16.13}$$

The equation of (16.3)-type is

$$\frac{\mathrm{d}h}{\mathrm{d}t} = \zeta^{-1}\sum_{k=1}^{n}\left[\lambda_S\left(\frac{\partial G_S}{\partial X_k}\right) - \lambda_L\left(\frac{\partial G_L}{\partial X_k}\right)\right]\delta X_k . \tag{16.14}$$

Now the functions $G_L(h)$ and $G_S(h)$ have to be found, which can be done by solving the Stefans problem – a nonstationary thermal conductivity problem with interface boundary as a heat source.

16.2.5 SA in a System with Two Degrees of Freedom

If only the crystal radius R and the crystallization front position h are regarded as variable parameters, (16.11) and (16.14) look like

$$\frac{\mathrm{d}R}{\mathrm{d}t} = A_{RR}\delta R + A_{Rh}\delta h , \tag{16.15}$$

$$\frac{\mathrm{d}h}{\mathrm{d}t} = A_{hR}\delta R + A_{hh}\delta h , \tag{16.16}$$

where the notations $A_{RR} = -V(\partial\alpha_0/\partial R)$; $A_{Rh} = -V(\partial\alpha_0/\partial h)$; $A_{hR} = \zeta^{-1}[\lambda_S(\partial G_S/\partial R) - \lambda_L(\partial G_L/\partial R)]$;

$A_{hh} = \zeta^{-1}[\lambda_S(\partial G_S/\partial h) - \lambda_L(\partial G_L/\partial h)]$ have been used. The solutions of the set (16.15), (16.16) are

$$\delta R = C_1 \exp(S_1 t) + C_2 \exp(S_2 t)\,, \tag{16.17}$$

$$\delta h = C_3 \exp(S_1 t) + C_4 \exp(S_2 t)\,. \tag{16.18}$$

Here S_1 and S_2 are the roots of the characteristic equation (16.4) that, for our case, reads

$$S^2 - (A_{RR} + A_{hh})\,S + (A_{RR}A_{hh} - A_{Rh}A_{hR}) = 0\,. \tag{16.19}$$

To estimate the stability of the set of equations (16.15) and (16.16) there is no need to solve the equations themselves but the Routh–Gurvitz conditions [16.6] can be used. For the set (16.15) and (16.16) to be stable, it is necessary and sufficient that the coefficients satisfy the inequalities

$$A_{RR} + A_{hh} < 0\,, \tag{16.20}$$

$$A_{RR}A_{hh} - A_{Rh}A_{hR} > 0\,. \tag{16.21}$$

The stability types mentioned are *rough* in the sense that the system stability remains unchanged within a wide range of values of the coefficients $A_{ik}(i, k = R, h)$. If at least one of the inequalities (16.20), (16.21) is replaced by the equality, the roots of the characteristic equation (16.19) are either imaginary or zero. In this case we can not judge the system's stability by its linear approximation, and the nonlinear model should be analyzed.

The coefficients A_{RR} and A_{hh} indicate direct correlation between $\mathrm{d}R/\mathrm{d}t$ and δR, as well as $\mathrm{d}h/\mathrm{d}t$ and δh, i. e., self-stability of the parameters. The coefficients A_{Rh} and A_{hR} represent the effect of the change in one value on the rate of change of the other value, i. e., inter-stability of the parameters. It can be concluded from the analysis of (16.20) and (16.21) that the crystal growth system is stable if

$$A_{RR} < 0\,,\quad A_{hh} < 0\,,\quad A_{Rh}A_{hR} < 0\,, \tag{16.22}$$

$$A_{RR} < 0\,,\quad A_{hh} < 0\,,\quad A_{Rh}A_{hR} > 0\,,$$
$$|A_{RR}A_{hh}| > |A_{Rh}A_{hR}|\,, \tag{16.23}$$

$$A_{RR} < 0\,,\quad A_{hh} > 0\,,\quad |A_{RR}| > |A_{hh}|,$$
$$A_{Rh}A_{hR} < 0\,,\quad |A_{RR}A_{hh}| < |A_{Rh}A_{hR}|\,, \tag{16.24}$$

$$A_{RR} > 0\,,\quad A_{hh} < 0\,,\quad |A_{RR}| < |A_{hh}|\,,$$
$$A_{Rh}A_{hR} < 0\,,\quad |A_{RR}A_{hh}| < |A_{Rh}A_{hR}|\,. \tag{16.25}$$

We can see, that negative values of A_{RR} and A_{hh} coefficients to be, is a very important condition for the crystal growth system stability. Below, we will use the following terminology. There is a capillary stability in the system if $A_{RR} < 0$ and there is a heat stability if $A_{hh} < 0$.

16.3 SA and SCG by CZT

16.3.1 Capillary Problem

A solution of the boundary capillary problem allows finding coefficients A_{RR} and A_{Rh}. In [16.6], the reader can find the investigation of the problem in detail. Here are the brief results. The problem includes (16.6) with $d = 0$ and the two boundary conditions

$$\left.\frac{\mathrm{d}z}{\mathrm{d}r}\right|_{r=R} = -\tan\alpha_0\,, \tag{16.26}$$

$$z|_{r\to\infty} = 0\,. \tag{16.27}$$

The boundary problems numerical solution is presented on the Fig. 16.7 and

$$A_{RR} > 0\,;\quad A_{RR}|_{r\to\infty} \to 0\,, \tag{16.28}$$

$$A_{hR} < 0\,;\quad A_{hR}|_{r\to\infty} \to \approx 4V\,. \tag{16.29}$$

For the numerical calculation the dimensionality of A_{ik} is s^{-1}; all angles have to be measured in radians, the units of length is the capillary constant a and speed of pulling is a/s.

16.3.2 Temperature Distribution in the Crystal–Melt System

A solution of the boundary heat problem allows finding A_{hh} and A_{hR} coefficients. There exists a great number of works dealing with calculation of the temperature fields in the crystal–melt system. They form a group of the Stefan problems in which a crystal–melt boundary is a heat source. However, owing to the variety of growth schemes and presence of a great number of factors that are to be taken into account for the thermal conductivity problems, for instance, complex temperature dependence of the thermophysical characteristics of various matters as well as convective flows in melts, a complete mathematical description of heat patterns during crystal growth is very difficult. Obtaining the solution in its analytical form is usually achieved by significant simplifications. With this end in view, the following equation from [16.26] allowing simple analytical solutions will be used to analyze the heat conditions in the

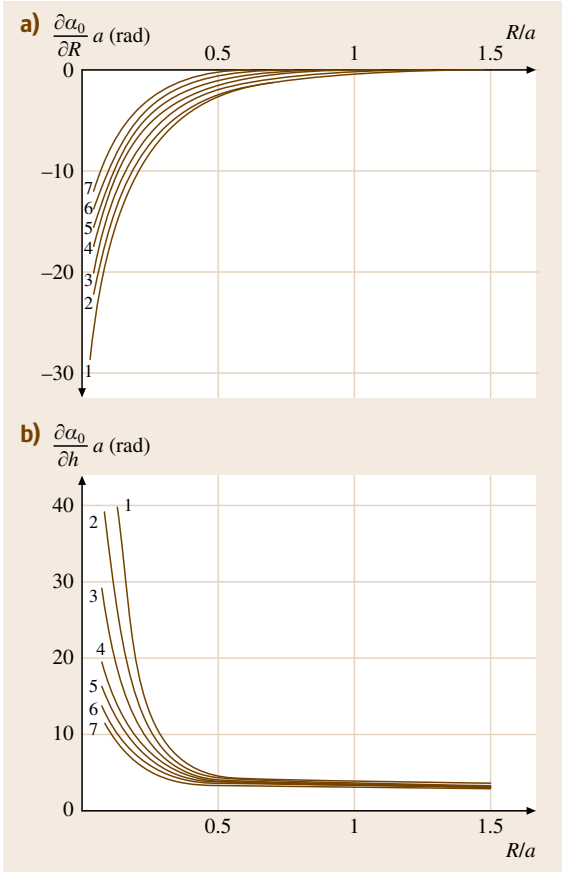


Fig. 16.7a,b For CZT **(a)** $\partial\alpha_0/\partial R$ and **(b)** $\partial\alpha_0/\partial h$ versus crystal radius for various values of the growth angle ψ_0: (1) 15°; (2) 5°; (3) 0°; (4) 10°; (5) 20°; (6) 30°; (7) 40°. Capillary constant a is used as a unit of all dimensions

crystallization process

$$k_i^{-1}\frac{\partial T_i}{\partial t} = \frac{\mathrm{d}^2 T_i}{\mathrm{d}z^2} - Vk_i^{-1}\frac{\mathrm{d}T_i}{\mathrm{d}z} - \mu_i\lambda_i^{-1}F\,(T_i - T_\mathrm{e})\ . \tag{16.30}$$

Here $i = \mathrm{L}, \mathrm{S}$ ($i = \mathrm{L}$ for a liquid, $i = \mathrm{S}$ for a solid body), T_i denotes the temperature, k_i is the thermal diffusivity coefficient, z is the vertical coordinate, μ_i denotes the coefficient of heat-exchange with the environment, F denotes the crystal (meniscus) cross section perimeter-to-its area ratio, T_e is the environment temperature, λ_i is the thermal conductivity coefficient.

There are few peculiarities for the use of (16.30):

1. It describes the temperature distribution of the crystal–melt system in a one-dimensional approximation that means that the temperature in the crystal (meniscus) cross section is averaged and isotherms are flat.
2. The heat exchange with the environment is allowed for not in the form of the boundary condition but by introducing heat run-offs on the lateral surface in the form of an additional term in the equation.
3. It gives a good description of real temperature distribution for small Biot numbers ($\mathrm{Bi} = \mu_i R\lambda_i^{-1} \ll 1$) – this can be observed during growth of small diameter or thickness wall crystals, for low coefficients of convective heat transfer from the crystal (melt) surface, and high thermal conductivities.
4. Heat exchange is allowed for by the Newton law that means the convective heat exchange is much higher than the heat losses caused by radiation (the heat losses caused by free convection are comparable with the heat losses caused by radiation at the surface temperatures of $\approx 1000\,^\circ\mathrm{C}$ and even higher in case specimen surface blowing is provided).
5. The equation is not available for vacuum pulled refractory materials and this for the radiation heat-exchange, the Stefan–Boltzmann law should be necessarily allowed for which leads to considerable nonlinearity of the problem; in this case a linearization of the crystal–surface radiation law described in [16.6] can be applied that allows (16.30) to be used up to temperatures of 2000 °C.

In Sect. 16.2.1 we discussed a possibility to use a quasi stationary approximation, according to which temperature distribution in the crystal–melt system at any moment of time satisfies the stationary thermal conductivity equation with instantaneous values of all the process parameters. For this approximation to be applied, the time of crystallization front relaxation to the stationary state should be significantly longer than the characteristic time of temperature relaxation. As a rule, this condition is satisfied [16.6]. So, we can use (16.30) with left part set to zero for the calculation of G_S and G_L.

As an example of A_hh and A_hR calculation, we consider a growth of a long crystal (the limiting case is a continuous pulling), with good thermal screening of the melt column provided. So, we use (16.30) with zero left part for crystal as well as for the melt meniscus with $\mu_\mathrm{L} = 0$. Boundary conditions of the problem are the following:

1. The melt temperature at the bottom of the liquid column at the level of the melt free surface is fixed: $T_\mathrm{L}|_{z=0} = T_\mathrm{m}$.

2. The crystallization-front temperature is equal to the melting temperature T_0: $T_L|_{z=h} = T_S|_{z=h} = T_0$.
3. The temperature of the crystal end is equal to the environment temperature: $T_S|_{z\to\infty} = T_e$.

The solution of (16.30) with these boundary conditions [16.6] allows obtaining A_{hh} and A_{hR}

$$A_{hh} = -\zeta^{-1}\lambda_L h^{-2}\,(T_m - T_0)\ , \tag{16.31}$$

$$A_{hR} = \zeta^{-1}\mu_s R^{-2}\varsigma_S^{-1}\,(T_0 - T_e)\ ; \tag{16.32}$$

where

$$\varsigma_s = \left(\tfrac{1}{4}V^2 k_S^{-2} + 2\mu_s\lambda_S^{-1}R^{-1}\right)^{1/2}\ .$$

So, on the basis of the capillary and heat boundary problems solution, the signs and the values of CZT growth stability coefficients are found. The signs are $A_{RR} > 0$; $A_{Rh} < 0$; $A_{hR} > 0$; $A_{hh} < 0$, if the melt is superheated ($T_m > T_0$).

16.3.3 SA and Crystal Growth

It can be concluded that:

1. The capillary stability is absent for all diameters of crystal.
2. Heat stability can be realized.
3. It is a chance to satisfy conditions (16.25) and to have the crystal growth stable if the following two inequalities can be fulfilled.

$$\left|\frac{\partial\alpha_0}{\partial R}\right| < \lambda_L V^{-1}\zeta^{-1}h^{-2}\,(T_m - T_0)\ , \tag{16.33}$$

$$\left|\frac{\partial\alpha_0}{\partial R}\right| < \left|\frac{\partial\alpha_0}{\partial h}\right| h^2\mu_s R^{-2}\lambda_L^{-1}\varsigma_S^{-1} \times (T_0 - T_e)\,(T_m - T_0)^{-1}\ . \tag{16.34}$$

Practically it means that a constant cross section crystal can be grown if the diameter of crystal is bigger than a melt capillary constant and the melt is superheated. If a crystal has a smaller diameter, superheating has to be high as well as a special combination of a process crystal growth parameters given the inequalities (16.33) and (16.34) has to be realized. Our experience of CZT crystal growth without a special diameter regulation as well as the growth of cylindrical crystals of silver [16.27] and of big diameter silicon tubes [16.28] confirms the conclusions of this paragraph. It has to be mentioned a necessity of very good stabilization of the pulling speed: it was shown [16.29] even a stable system can not compensate a sudden speed change and as a result there is a pinch formation.

16.4 SA and SCG by VT

At the beginning of seventies, our attention in some experiments was turned to the fact that growth of corundum crystals of small diameters ≈ 5 mm (they are grown especially as seed crystals) was easy. Practically the growth regime required no correction by an operator. The crystals had smooth surfaces and cylindrical shapes. This stimulated our works on the VT dynamic stability investigation. As was mentioned above, the analysis had been carried out with 3 degrees of freedom for cylindrical crystals (Fig. 16.2) and with 4 ones for tubular ones. The limited volume of the chapter does not allow us to give further details about the theoretical model. The reader can find them in [16.6, 15, 30–32]. Let us notice some peculiarities of the problem formulation for VT and the main conclusions. *First of all*, the mass balance condition in a system including a charge feeder, a melt layer, and a crystal has been used as a third equation for the set (16.2). *Second peculiarity* concerned with a heat problem formulation. As a rule, when formulating the heat problem for crystal growth from melts, the melt temperature has been specified as the boundary condition (Sect. 16.3.2). This boundary condition for the VT does not correspond to the real situation. Crystal displacement in the furnace muffle results in melt-temperature change on its surface. This is a reason why the heat conditions of the technique under consideration will be allowed for by specifying the density Q of the heat flow fed from the burner onto the surface of the melted layer. With the gas flow specified, the density of the heat flow Q depends on the distance between the burner and the level of the melt surface $Q(l)$. The function $Q(l)$ is determined by the burner design and the gas debit.

16.4.1 Practical Results of the Theoretic Analysis

Round Cylindrical Crystals

For the process to be stable the following three conditions have to be fulfilled:

1. The diameter of crystal $2R$ has to be small ($R < a$). We can see that the situation is the opposite one to the CZT.
2. Change in the heat flow density $Q(l)$ along the furnace muffle in the vicinity of the growth zone at the distance of an order of R should not exceed the crystallization heat.
3. The heat flow density value $Q(l)$ in the vicinity of growth zone has to be decreased if the distance between the melt surface and the burner l_1 is increased.

The result of the theoretical investigation explains why growth of corundum crystals of small diameters (≈ 5 mm) is easy. They grow in the dynamically stable regime; it means that there are internal mechanisms for dissipation of perturbations. With respect to our terminology, the capillary stability exists for $R < a$ (for the sapphire melt $a = 6$ mm).

In spite of the capillary stable growth is impossible for the cylindrical round sapphire crystals with the diameters more than 12 mm, the theoretical model allows a minimizing of the crystallization process perturbations while growing big diameter crystals. For this, the previous two conditions have to be fulfilled (evidently, without the crystal dimension limitation) and also:

- The temperature of a muffle wall has to be increased.
- The irregularity of the density distribution of the charge flow falling on the melted layer has to be decreased.

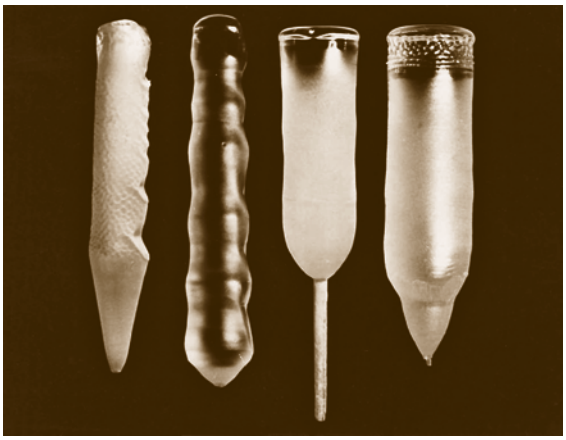


Fig. 16.8 Corundum cylindrical crystals grown by VT in optimized (*two right ones*) and nonoptimized (*two left ones*) regimes

These requirements of the crystallization conditions (we classify them as optimized) are in good agreement with our experimental results [16.15, 30–32]. In the experiments such hydrogen- and oxygen-flow debits in a three-channel burner had set that a crystal grown closer to the burner had a larger diameter. This condition corresponds to the heat-flow density increase when approaching the burner. Preheating the gas before feeding it into the burner and increasing the furnace muffle temperature were also used. As a rule, no parameter control to maintain constant cross section of the crystal was required. Crystals, grown under these conditions, exhibited a smoother surface and improved optical and structural characteristics. In the Fig. 16.8, corundum crystals of 40 mm diameter, grown in 1972 without any automatic control by the author of this chapter with collaborators from the Leningrad State Optical Institute, are presented.

Tube Shaped Crystals

The theoretical analysis states: Crystallization of tubes of arbitrary outer diameters is stable if the tube wall thickness is smaller than some critical thickness. This thickness is smaller than the capillary constant a and depends both on the heat conditions of the process and on the outer diameter of the tube. It increases with the outer diameter increase. In our experiments [16.6, 32] tubes with an outer diameter of 16–25 mm with walls 3–4 mm thick were grown (Fig. 16.9). A crystallization apparatus fitted with a four-channel burner providing charge supply via the central and periphery channels was used. It was experimentally stated the optimal gas distribution in the burner channels: oxygen-hydrogen-oxygen-hydrogen. Crystal growth was initiated from



Fig. 16.9 Six corundum single crystals (five tubes and one cylindrical crystal) grown by VT in the same regime

a seed 3–4 mm in diameter. Firstly, a seed cone was grown. The cone was widened by feeding the charge through the central channel, the periphery oxygen flow rate being increased. As soon as the crystal diameter reached the specified value 20–22 mm the charge was fed through the periphery channel. A little later (10–15 min) charge supply from the central tank was cut off and within 30–60 min the rate of the central oxygen flow was reduced. This growth regime has provided smooth transition from a solid crystal to a tube. The sink rate was smoothly increased. After that the process of stationary growth went on. Tubes up to 120 mm in length were grown. Usually no parameter control to maintain constant cross section of the tube was required, i. e., stable growth conditions the existence of which had been theoretically predicted could be attained. Figure 16.9 shows some of the tubes grown in 1981 by the authors of this chapter with collaborators from the Solid State Institute of the Russian Academy of Science. Three of the tubes are cut (one of them along the axe, and two ones obliquely) to show the tube walls. For the comparison, a cylindrical crystal of the same diameter, grown in the same furnace, is shown on the figure. The irregular crystal shape indicates that for it this regime is not optimal from the point of view of stability that is not at variance with our theoretical prediction.

Plate Shaped Crystals

The theoretical results are applicable for the growth of plate shaped crystals: The crystal plates of less than two capillary constants thick (12 mm for sapphire) have to grow stably. Information of corundum crystal plate growth by VT can be found in our review [16.8].

16.4.2 SA-Based Automation of VT

As was shown above, when passing to crystals with diameters exceeding the two capillary constants crystallization stability is lost. Practically it means that the crystallization front position and crystal dimensions are changed during the crystal growth process. In this case, an operator controls the parameters by changing the gas debit, charge feed and crystal sinking rate using his experience and intuition. Automatic system of control provides better result. When developing systems of growing crystal automatic diameters control, a problem of the laws of automatic control of the process parameters under some changes in crystal dimensions arises. Up to publication of our paper [16.33] the required laws of parameters control were defined from the results of empirical search. In [16.33] it was shown that the laws can be performed on the basis of the crystal growth stability analysis. In this instance the controllable parameters side by side with the crystal diameter, the liquid–gas interface position and the melt meniscus height can be required as the degrees-of-freedom of the crystal growth process. For VT the density of the heat flow from the burner Q, (it is regulated by the changing of the gases debit P), the rate of crystal sinking V and the powder charge flow rate Ω can be used as controllable parameters. Usually, P as well as Ω is used as controllable parameters on the stage of crystal widening. But after the crystal has already widened from the seed dimension up to the desired diameter, the control is provided by Ω regulation. In our approach Ω has to be regarded as an additional 4th degree-of-freedom for the cylindrical crystal. But coefficients of the linear equation for W are unknown. They have to be found from the necessary and sufficient conditions of the set of 4 equations stability of (16.3)-type. The problem can have several solutions. Each of them can be used as the regulation law in the control system. In this case our system of crystal growth including the regulator has to be stable. In [16.33] three different Ω change laws, allowed stable growth, were found. Fig. 16.10 illustrates corundum crystals grown with one of the stable laws of Ω regulation and the proportional one. The crystals were grown in 1979 by the author of this chapter with collaborators from the Institutes of Crystallogra-

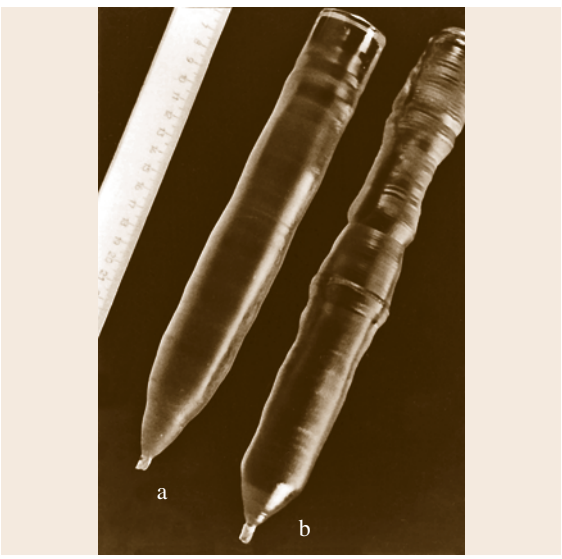


Fig. 16.10 Corundum crystals grown by VT using stable (a) and unstable (b) laws of powder charge control

phy and Solid State Physics of the Russian Academy of Science. A standard industrial Verneuil furnace was used for the experiments. A comparison of crystals from Figs. 16.8 and 16.10 shows that a design of the furnace corresponding optimized, from the point of view of stability, growth conditions can provide the same (or even better) crystal quality as using of automatic system control.

16.5 SA and SCG by FZT

The FZT has been widely used for different materials crystal growth, especially: semiconductors (RF heating), high-melting metals and dielectrics (electron beam, plasma or laser heating). There are a lot of publications concerning a FZT theoretical study but only two aspects have been the investigation topics: a static meniscus stability, melt flows included, and impurity segregation. Only few papers have been devoted the dynamic stability analysis. Reference [16.18] has been the first of them. However, this analysis has not been completed as a heat conditions of crystallization have not been taken into account and a capillary part of the problem has been violently simplified. As a result, in [16.18] a capillary stability proved to exist in all versions of FZT. Our analysis based on the Lyapunovs theory [16.34, 35] is more common and includes the following main points:

1. Min $n = 4$ were chosen (Fig. 16.3).
2. The crystal up pulling as well as down lowering with different diameters ratio of the growing crystal and the rod to be melted were analyzed.
3. Equation (16.11) for $\partial R/\partial t$ was obtained as a result of the capillary boundary problem with the boundary condition of the angle growth certainty on the crystallization front.
4. It has been shown the boundary condition of the angle certainty is not available for the melting front [16.6, 36].
5. The equation for $\mathrm{d}W/\mathrm{d}t$ was obtained from the mass balance of melted and crystallized substances.
6. Equation (16.14) for $\mathrm{d}h_\mathrm{c}/\mathrm{d}t$ was obtained as a result of the solution of (16.30) near the crystallization front as well as for $\mathrm{d}h_\mathrm{m}/\mathrm{d}t$ near the melting front.

The analysis of the result is rather complicated because four Routh–Gurvitz inequalities have to be simultaneously satisfied. Here are the main conclusions:

1. The capillary stability exists ($A_{RR} < 0$) for big growing crystal and melted rod diameters ($R > a$, $r_0 > a$) with all ratios of them (R/r_0).
2. For small ($R < a$, $r_0 < a$) crystal and rod diameters, $A_{RR} < 0$ if $R > R_{min} \approx \frac{1}{2} r_0$.
3. The biggest negative value of A_{RR} coefficient corresponds to $R = r_0$.
4. The capillary stability exists for both direction of growth (up or down) but down lowering is the preferable one.

As for practical using of FZT for shaped crystal growth, besides widely spreaded round shape rode, the ribbon-to-ribbon (RTR) technique [16.37] has to be mentioned. A ribbon was used for a feeding as well as a ribbon crystal was grown. RTR achieved silicon ribbons for a solar cells application of a width 75 mm, a thickness 0.1 mm, and a 3–9 cm/min growth rate with laser heating being used.

16.6 TPS Capillary Shaping

While analyzing stability of TPS as a system with two degrees of freedom, the equations (16.15)–(16.25) have to be used. Therefore, we can proceed to the analysis of the melt-column shaping conditions in TPS.

16.6.1 Capillary Boundary Problem

For axisymmetrical case, the Laplace capillary equations (16.6)–(16.8) will be used in our analysis. As was mentioned above, each equation is a second order differential one and a boundary problem for a melt meniscus shape calculation strictly requires assignment of two boundary conditions. The first of them is (16.26), common for all CST but the second one is determined by the structural features of each specific TPS. A shaper is used for melt-column shaping in TPS (Fig. 16.4). The functions of the shaper in TPS are wide and we will discuss all of them later. At the moment, we characterize the shaper as a device to control the melt-column shape only. This problem is a fundamental one for

a shaped crystal growth by TPS and we will discuss it in detail. In a mathematical description of the problem, a shaper function is to determine the meniscus shape by means of fixation of a capillary problem second boundary condition. For the first time, the characterization of shapers from this point of view was accomplished by us in 1967 [16.38, 39]. In the most cases, the shaper (Fig. 16.4) is characterized by its wall or free edge curvature radius r_0 in the horizontal plane, the angle β made by its wall with the horizontal. The wetting angle Θ formed by the melt and the shaper surface, is a very important shaper characteristic. If this angle exceeds 90°, the shaper material is not wetted by the melt (Fig. 16.4a,b,g–j); if it is smaller, the melt wets the shaper material (Fig. 16.4c–f). Shaping is accomplished either on the surfaces (Fig. 16.4a,c,g–i) or on the sharp edges (Fig. 16.4b,d–f,j) of the shaper. It corresponds to the following boundary conditions of the capillary boundary problem:

Catching Boundary Condition

In case the shaper material is wetted by the melt, the melt is easily caught by its sharp edge. This boundary condition will be termed the *catching condition*. There is a possibility of providing the catching conditions at nonwettable shaper free-edges which will be discussed below. The catching condition means that a counter line on the meniscus surface is fixed by the edge of the shaper, i. e., it coincides with the edge counter of the shaper. It does not matter if the edge counter is internal (Fig. 16.4d,j) or external (Fig. 16.4e,f), if the pulling up (Fig. 16.4d,e) or down lowering (Fig. 16.4f,j) is used for the shape crystal growth. The catching condition has the following mathematical form in the cylindrical coordinate system

$$z|_G = d(r, \phi) \,. \tag{16.35}$$

Here G is the counter of the shaper edge, d is the distance from the shaper edge to the coordinate plane. In case the shaper is flat and is positioned parallel to the melt plane, $d = \text{const}$. For axisymmetric flat shaper edges the condition (16.35) has the following form

$$z|_{r=r_0} = \text{const.} = d \,, \tag{16.36}$$

where r_0 is a shaper edge counter radius. If the coordinate plane coincides with the free level of the melt, d represents the pressure of feeding the melt to the shaper. In this case, the pressure is included in the boundary condition and in the Laplace capillary equation, const. = 0. If the coordinate plane coincides with the shaper edge plane (Fig. 16.4b,d–f,j) the right part of (16.36) is equal zero and the pressure d is included in the Laplace capillary equation (16.5–16.8) as a parameter (const. = d). The pressure being positive, the shaper edges are positioned below the melt free-surface level and vice versa.

Angle Fixation Boundary Condition (the Wetting Condition)

If the melt has a contact with the shaper surface, it makes the wetting angle, Θ with the shaper surfaces (Fig. 16.4a,c,g–i). This boundary condition will be termed the *angle fixation condition or wetting condition*. It can be realized for nonwettable shaper material (Fig. 16.4a,g–i) as well as for wettable one (Fig. 16.4c), for pulling up (Fig. 16.4a,c,h,i) as well as for lowering down (Fig. 16.4g) shaped crystal growth. The condition means that shaper walls fix the meniscus angle on a counter C belonging to the shaper surface by forming the angle of wetting. The condition has the following forms:

In common case, where $\boldsymbol{n}$ denotes the direction of the normal towards the shaper wall, C is a counter of the contact of the meniscus with the shaper walls

$$\left[1 + \left(\frac{\partial z}{\partial x}\right)^2 + \left(\frac{\partial z}{\partial y}\right)^2\right]^{-1/2} \left.\frac{\partial z}{\partial \boldsymbol{n}}\right|_C = -\cos\Theta \,. \tag{16.37}$$

The shapers of complicated surfaces (Fig. 16.4a,c) can illustrate this condition although in the figure they represent a particular case of the cylindrical symmetry system (z, r coordinates) whereas, for the common case, the use of x, y, z coordinate system is necessary.

For an axisymmetrical problem (a rod, a tube) on the vertical shaper walls (Fig. 16.4h)

$$\left.\frac{\mathrm{d}z}{\mathrm{d}r}\right|_{r=r_0} = \tan\left(\Theta - \tfrac{\pi}{2}\right) = -\tan\alpha_1 \,. \tag{16.38}$$

For circular cone shaper walls formed the angle β with the horizontal (Fig. 16.4i)

$$\left.\frac{\mathrm{d}z}{\mathrm{d}r}\right|_{r=r_1 - z\cot\beta} = \tan\left(\Theta + \beta - \frac{\pi}{2}\right) = -\tan\alpha_1 \,. \tag{16.39}$$

Wetting-to-Catching Condition Transition

With the melt pressure increasing, the catching boundary condition at the nonwettable shaper free-edges can be obtained. Figure 16.11a illustrates this transition with the pressure to be increased by gradual shaper immersing into the melt. The diagram is based on [16.40]

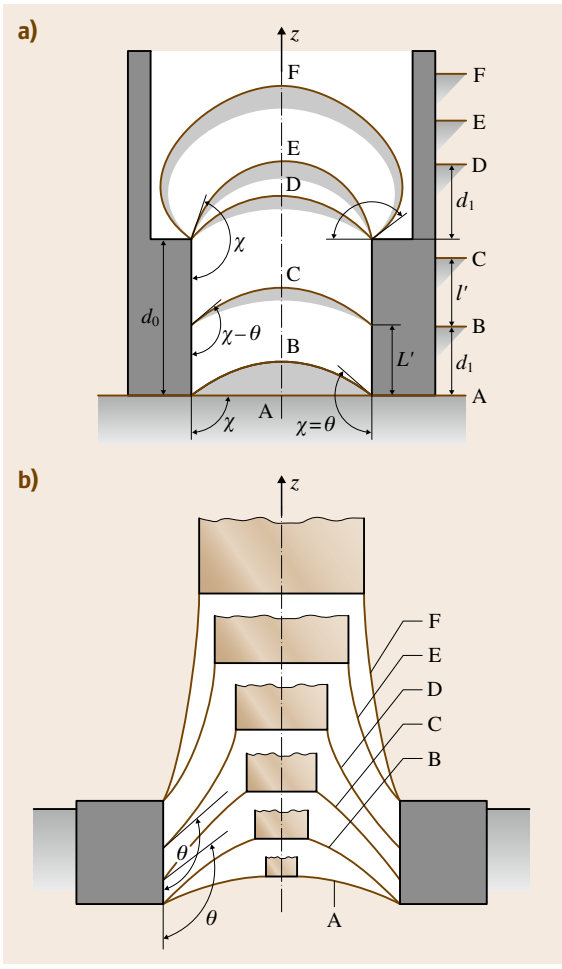


Fig. 16.11a,b Transition of the shaper lower free-edge catching boundary condition (meniscus A) to the wetting condition (menisci B, C, D) and further to the shaper upper free-edge catching condition (menisci E, F); **(a)** pressure changes (the *horizontal lines* denote successive positions of the liquid free surface); **(b)** the seed–shaper dimension ratio changes; χ is the angle between the line tangent to the melt surface and the shaper wall, θ is the wetting angle

describing the particle buoyancy conditions for the flotation processes. A nonwettable shaper, with a hole of d_0 depth, possessing vertical walls is considered. The angle χ between the line tangent to the liquid surface and the shaper wall is introduced. Let us analyze a number of shaper successive positions. *Position* A: The shaper touches the melt with its lower plane. The lower-plane immersion depth is equal to zero. The line tangent to the liquid surface coincides with the liquid surface. Angle χ is $\frac{\pi}{2}$. The catching condition holds at the lower free edge of the shaper. With the shaper being immersed into the liquid, the angle χ increases, and when the shaper lower plane reaches some depth d_1, (*position* B) the angle χ will be equal to the wetting angle Θ, (within the immersion depth range from 0 to d_1 the catching condition holds at the lower free edge). With further shaper immersing into the liquid, χ remains equal to the wetting angle Θ. The liquid–shaper wall contact line goes up by the value of L', the shaper immersion depth, the distance between this line and the free surface level remaining equal to d_1 (*position* C). As soon as the immersion depth is equal to $d_0 + d_1$, the liquid–shaper contact line coincides with the shaper sharp edge (*position* D), and with further pressure increase, the catching condition at the shaper upper free edge holds (*position* E). In this case the angle χ will increase until the wetting angle Θ is formed by the liquid and the shaper surface [16.40]. For the horizontal shaper surface $\chi = \frac{\pi}{2} + \Theta$ (*position* F). Further increase in pressure is impossible as it will lead to liquid spreading over the shaper surface and the shaper will not operate properly. But if shaper's free edges are sharp, pressure increase is possible (Fig. 16.4b) up to the loss of the meniscus' static stability.

The presence of a seed or a profile being pulled considerable changes into the conditions of the transition described. It means that the condition at the upper boundary (along the crystal–melt contact line) can affect the character of the condition at the lower boundary (along the melt–shaper contact line). The diagram, that will be proved when solving the boundary problem, is given in Fig. 16.11b. By changing the seed-to-shaper hole dimension ratio alone, the catching boundary condition at the lower free edge (menisci A, B), the wetting condition on the shaper walls (menisci C, D), the catching boundary condition at the upper free edge (menisci E, F) can be achieved. The very important conclusion is the following: the wetting boundary condition means the angle χ is fixed but the counter of the meniscus with the shaper contact is movable. Its position on the shaper walls depends on the melt pressure and the crystal–shaper dimensions ratio.

Certainly, we could change a melt pressure by any other way as well as a growth direction doesnot matter. For instance, by changing a melt pressure or the crystal–shaper edge dimensions ratio, it is possible to realize the scheme of either Fig. 16.4g or j.

A comparison of Fig. 16.11a and b diagrams shows that there are two very different situations: before seed-

ing and after seeding (during pulling). In the second case, even for non wettable shaper walls, the meniscus, changing its curvature with forming a negative pressure inside, raises the melt above the shaper edge, up to the crystallization front (the same situation exists in CZT).

Hereafter it will be shown that the catching boundary condition usually leads to more capillary stability of the process, therefore, the ways of achieving the catching condition at the shaper free edges in TPS should be specified: *Firstly*, a melt-wettable material should be used for the shaper, and the latter should be designed in such a way that the melt could raise up to the shaper free-edges due to capillary forces (Fig. 16.4d–f). *Secondly*, for melt-nonwettable materials, the melt column should be embraced from outside, providing additional pressure on the liquid to make the melt–shaper contact point touch the shaper sharp edge (Fig. 16.4b,j). *Thirdly*, for poorly wettable shaper materials, the crystal–shaper dimensions ratio should be used in order that it could ensure melt column contact with the shaper sharp edges, compare Fig. 16.4g and j.

Influence of the Wetting-Angle Hysteresis on Capillary Boundary Conditions

While analyzing all the capillary effects, the existence of wetting-angle hysteresis should be taken into consideration. The wetting angle hysteresis reveals itself in the fact [16.40] that the wetting angle of liquid run on a solid body is larger than that of liquid run off a solid body. This means that the stationary wetting angle depends upon the process of meniscus formation (on-run or off-run). This results, for example, in the fact that a higher pressure is to be applied to create the catching condition at the shaper free edge than that required to keep it unchanged. In case the catching condition is created by the seed, this condition can remain unchanged in the process of growth, with the clearance between the shaper free edge and the growing crystal changing.

A Comparison of the Catching Boundary Condition and the Angle Fixation One

The comparison can be done on the basis of the previous description of transition one to another. It exhibits a big difference of these two boundary conditions: The catching one fixes a coordinate of the meniscus end counter but an angle of the inclination of the meniscus is not fixed. The wetting one fixes an angle of inclination of the meniscus end counter but not a coordinate. In this case the meniscus is movable (Fig. 16.11b). Its position on the shaper wall depends on the second boundary condition (a seed or growing crystal presence as well as a growing crystal dimension and a growth angle) and can be found as a result of the capillary boundary problem solution. So, for capillary shaping by walls, a shaper has to be designed taking account for this phenomena as well as the angle-wetting hysteresis. We carefully explain this difference because there is a big misunderstanding of this key problem for capillary shaping. Let us analyze some of wrong approaches. For the boundary capillary problem solution, *Stepanov* et al. [16.41] use the idea of *Tsivinskii* from [16.42], where, for the axisymmetrical meniscus described the Laplace equation (16.5), it was suggested to replace $1/R_2$ (Fig. 16.1) by a linear function of the vertical co-

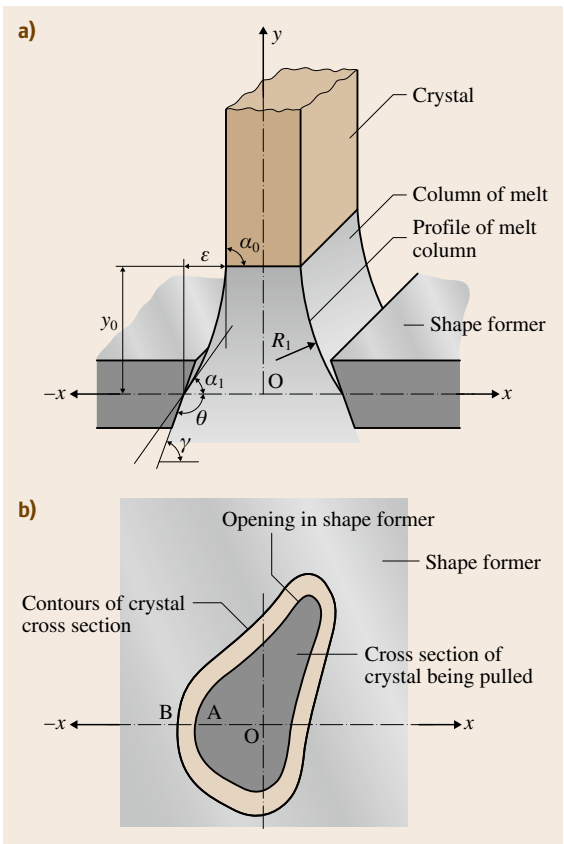


Fig. 16.12a,b Arrangement for producing a crystal with cross section of arbitrary form. Melt column parameters: y_0 represents the melt column height, α is the inclination of the profile curve tangent to the x axis (α_0 at $y = 0$ and α_{01} at $y = y_0$), and R_1 is the radius of curvature of the melt column surface, lying in a plane perpendicular to the tangent (R^0 at $y = 0$ and R^{01} at $y = y_0$) (after [16.41])

ordinate. There are, as minimum, four mistakes in this approach (Fig. 16.12):

1. The axisymmetrical meniscus is applied for the growth of arbitrary cross section crystals
2. A priori, we need to know if the meniscus is concave, convex or concave–convex
3. A priori, for concave–convex meniscus, we need to know the coordinates of the inflection point
4. We need to know y_0, α_0, and α_{01}.

The fourth mistake is the worst. Indeed, the fixation of these parameters means that we need to use three boundary conditions for the second order differential equation: a fixation of the angle growth on the crystal–melt boundary and the catching as well as the wetting boundary conditions on the shaper. But it is nonsense. Authors of this approach had published a lot of papers including cumbersome formulas that never have been used or verified. The main argument of the authors: this approach is applied for CZT – there are a lot of experimental evidences of it. But it is clear, why the approach works for CZT. The second boundary condition for CZT (16.27) confirms the vertical coordinate strives for the zero on the infinity. Automatically it means that the first derivative also strives for the zero on the infinity. So, this is the well known in mathematics peculiarity of the boundary condition on the infinity and, as a result, we have three boundary conditions. For the first time we had explained nonapplicability of this approach to the TPS in [16.43] (1969) and later in our reviews [16.5, 6, 9]. But many journals have continued publishing including *Pet'kov* and *Red'kin* paper [16.44] concerned with the investigation of the shaped growth dynamic stability. In our paper [16.45] we once more explained nonapplicability of this approach.

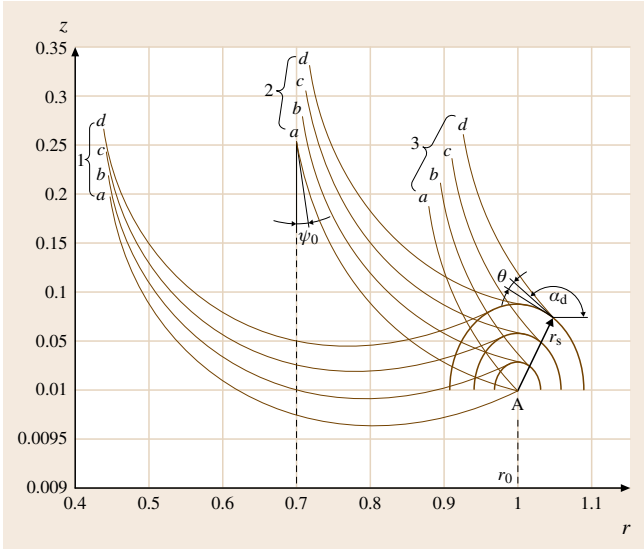


Fig. 16.13 Mid-range Bo. Profile curves $z(r)$, starting from surfaces of toruses (b–d) of different radius r_S and from a sharp edge of the shaper (a) (after [16.23])

More Precise Definition of the Catching Boundary Condition

Nevertheless, we understood that there is a weak point in our approach: From the formal point of view we are right – mathematical formulation of the problem requires two boundary conditions. But from the physical point of view a melt has to form a wetting angle with a shaper surface. This discrepancy was explained in [16.23]. The paper contents well-grounded mathematical proof but here we only illustrate the main idea. Figure 16.13 presents one specific case: the growth of round cylindrical crystal with respect to scheme Fig. 16.4d. The shaper edges are replaced by circular coaxial tours of four different curvature radiuses r_S (the last $r_S \to 0$). The example corresponds to middle-range bond numbers Bo ≈ 1. The shaper radius $r_0 = 1$. The unit of lengths measurement is the capillary constant a which is equal for silicon 7.6 mm, for sapphire 6 mm, for germanium 4.8 mm, for indium antimonide 3.7 mm [16.6]. It means that for silicon the diameter of the shaper edges circle is 15.2 mm, for sapphire 12 mm. The origin of the z-coordinate is located on the melt free surface. The negative melt pressure $d = -1$, e.g. the melt free surface is located on the distance a lower than the shaper edge (Fig. 16.4). Three set of profile curves (a profile curve is a section of the meniscus by the figure plane) are presented on the Fig. 16.13. Each set consists of four profile curves and is characterized by the same value of the angle α_d-meniscus inclination angle with respect to positive r-direction at the point of the contact with the shaper. The lower end of each profile curve is located on the surface of a torus and forms the wetting angle $\Theta = 10°$ with the surface of the torus. The each torus corresponds to the shaper edge of a different radius of curvature r_S: $r_S = 0.09$ (0.68 mm for Si) for the all three profile curves of set d, $r_S = 0.06$ (0.46 mm for Si) for the curves c, $r_S = 0.03$ (0.23 mm for Si) for curves b, $r_S \to 0$ for curves a. The upper end of each profile curve forms the angle 10° with the vertical. It corresponds to crystal growth of the respective dimension with the growth angle $\psi_0 = 10°$: $R \approx 0.45$ (the crystal of 7 mm diameter for Si) for set 1, $R \approx 0.7$ (the crystal of 10.6 mm diameter for Si) for set 2, $R \approx 0.9$

(the crystal of 16 mm diameter for Si) for set 3. The crystallization front is located on the height (from the plane of the shaper edges) 0.20 (1.5 mm for Si) for sets 1 and 3, 0.30 (2.2 mm for Si) for set 2.

So, on the microlevel, the melt forms the wetting angle with the torus surfaces and we have a normal physical wetting condition. If the crystal changes its dimension the contact point also changes its position on the torus surface but, in any case, its position will be in the vicinity (torus radius r_S) of the point A. With the r_S decreasing, a location of the lower end of the profile curve is more definite near the point A with the coordinates ($r_0 = 1$, $z = 1$). If the torus radius is infinitely small we have, in macroscopic sense, the catching of the meniscus on the sharp shaper edge (in point A). So, the catching condition is just a useful mathematical approach to satisfy a capillary boundary problem. From the physical point of view it defines a wetting boundary condition on the sharp edges of the shaper. It seems, everything is clear. But in spite of the publication of our papers [16.23, 45], the history of application of the approach from [16.42] to TPS has not been finished [16.46].

Capillary Boundary Problem Solution

The solution of the problem we are dividing on three parts with respect to the Bond numbers Bo: large, middle-range and small ones. For large and small Bo, the Laplace equation has the forms (16.7) and (16.8), respectively. A solution of the boundary problems for both of them can be obtained in analytical form (sometimes with the using of special functions). For a middle-range Bo a numerical solution is needed. A comparison of the analytical and numerical solutions shows that, with a sufficient accuracy for practice, we can use:

1. The large Bo approximation for the growth of cylindrical round rods or tubes of $10a$ minimal diameter (remind that for the silicon it corresponds 76 mm, for the sapphire 60 mm)
2. The small Bo approximation for the growth of cylindrical round rods or tubes of a maximal diameter (remind that for the silicon it corresponds 7.6 mm, for the sapphire 6 mm) on the Earth surface as well as for the very big diameters crystals growth under microgravity conditions

A solution of a boundary capillary problem allows to obtaining very interesting information concerning a capillary shaping as a function of a shaper design, melt pressure, wetting angle. The information can include:

1. A shape of meniscus-conditions of existence of concave, convex and convexo–concave ones
2. A range of parameters for existence of catching and wetting boundary conditions
3. Design of a shaper and a range of parameters for existence of a meniscus with the definite growth angle ψ_0
4. The same with the fixed crystallization front position
5. Signs and values A_{RR} and A_{Rh} coefficients [16.6, 23, 24, 47].

Here are few examples of this kind.

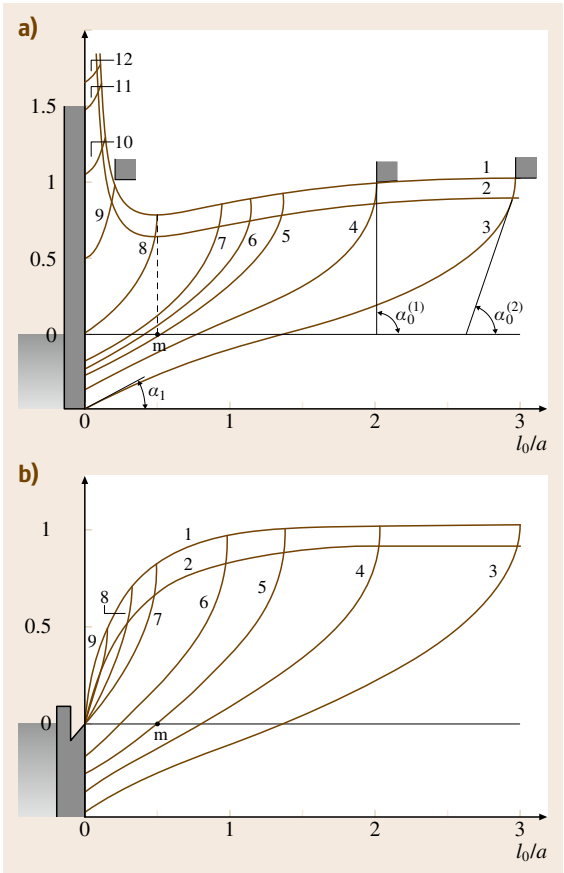


Fig. 16.14a,b Large Bo: **(a)** Wetting boundary condition ($\theta = 135°$); convex–concave (3–7) and concave (8–12) profile curves $z(r)$; boundary 1 ($\psi_0 = 0$) and 2 ($\psi_0 = 15°$) curves $h(R)$; **(b)** transition from the wetting boundary condition (3–6) to the catching condition (7–9) by changing the shaper design

Large Bo: Let us formulate the following crystal growth conditions (Fig. 16.14) which corresponds to the scheme Fig. 16.4h [16.6,47]: To the right, where $r = r_0$, the non wetted shaper wall is located. The line tangent to the melt surface in the melt–shaper contact point makes the wetting angle Θ with the shaper wall. Let us introduce the angle $\alpha_1 = \Theta - \frac{\pi}{2}$. To the left, where $r = R$, the edge of a melt-growing flat crystalline tape or that of a circular cylindrical crystal of a large diameter is situated. Let the angle α_0 (Fig. 16.6a), made by the line tangent to the melt surface at the melt–crystal growing contact point and the negative direction of the r-axis, be specified (while growing crystals of constant cross sections, the angle $\alpha_0 = 1/2\pi - \psi_0$ is the complement of the growth angle ψ_0). Let l_0 denotes the clearance between the crystal edge and the shaper: $l_0 = r_0 - R$. Let us consider what process parameter data can be obtained with such problem formulation. According to our terminology, we have the angle-fixation boundary conditions (or wetting conditions) on both the ends of the r-variation interval: the equation (16.7), boundary conditions (16.26) and (16.38). The analytical solution of the problem was obtained in the Legendre elliptical functions (e.g. [16.6]) and is presented on the Fig. 16.14a for the following parameter values: $\Theta = 135°$ ($\alpha_1 = 45°$), $\psi_0 = 15°$ ($\alpha_0 = 75°$) and $\psi_0 = 0$ ($\alpha_0 = 90°$). The origin of the z-coordinate coincides with the free melt surface. The profile curves 3–12 are the sections of the melt meniscus by the diagram plane. Each profile curve corresponds to the definite distance l_0 between the growing crystal and the shaper wall. The edges of the crystals are located on the one of two boundary curves $h(R)$ corresponding two different growth angles: (1) for $\psi_0 = 0$ and (2) for $\psi_0 = 15°$. Based on this boundary problem solution, the following conformities can be established:

1. With the angle fixation boundary condition satisfied at both the ends of the l_0-variation interval, the vertical coordinates of the liquid–solid phase contact points with respect to the melt free surface are not fixed but depend on the relation between the angles at both the ends of the interval and on the value of the clearance between the shaper and the crystal being pulled. It is a confirmation the scheme Fig. 16.11b.
2. There exists some minimum value m of the clearance between the shaper and the crystal being pulled (for our parameter values it is equal approximately to one capillary constant a) when the meniscus lies both above and below the melt free surface. When this gap is smaller than m, the point of the meniscus contact with the shaper wall is located higher of the melt free surface.
3. The meniscus part, located below the melt surface is convex, the meniscus part, located above the melt surface is concave.
4. A higher crystallization front position corresponds to a smaller growth angle.
5. For the crystal–shaper gap being more than capillary constant a the crystallization front height doesnot exceed capillary constant. For smaller gaps, the crystallization front height can be infinitely tall.
6. Any change in the melt level during pulling will produce the following effect on the crystal dimensions: with the level decreasing, the tape thickness (or the rod diameter) can be kept unchanged only in case the crystallization front is lowered by the same value. With the crystallization front position kept unchanged, the tape thickness or the crystal diameter will decrease with the melt lowering and vice versa. It means that the melt level can be qualified as one of degrees of freedom. We investigated these phenomena (e.g. [16.6]).
7. $|\partial\alpha_0/\partial h| > 0$; $|\partial\alpha_0/\partial R| > 0$ for $l_0 < m$; $|\partial\alpha_0/\partial R| < 0$ for $l_0 > m$. It means that there is a capillary stability ($A_{RR} < 0$) only if the gap between the shaper wall and the pulling crystal is more than capillary constant ($l_0 > m \approx a$).

Now, let us modify the shaper design: let us locate a sharp shaper edge on the melt free surface level. The solution of the new boundary problem is presented on Fig. 16.4b. Let us discuss new results:

1. For $l_0 > m \approx a$, the situation is the same as in previous case.
2. But for $l_0 < m \approx a$, the situation is dramatically changed: the catching boundary condition is realized (this is a second confirmation of the scheme of Fig. 16.11b) and, as a result, either for $l_0 < m \approx a$, $|\partial\alpha_0/\partial R| > 0$, i. e., the capillary stability exists for all range of l_0 variations.
3. On the other hand, a crystallization front $h(R)$ has to be located much lower than in the previous case. In particular, $h(R)|_{R\to r_0} \to 0$.

Middle-ranged Bo: For a middle-ranged Bo (Bo ≈ 1), three profile curves a of the sets 1–3 on the Fig. 16.13 present an example of the numerical solution of the capillary boundary problem with the catching boundary condition that corresponds to Fig. 16.4d Therefore, we use (16.6) and the boundary conditions

(16.26) and (16.36). The results were discussed above but the two peculiarities have to be mentioned here:

1. A middle part of the meniscus, corresponding to the crystal radius $R \approx 0.5$, is located lower than the shaper edge.
2. The highest crystallization front position corresponds to the crystal radius $R \approx 0.7$.

Small Bo: As an example of the capillary boundary problem solution for a small Bo (Bo $\ll 1$), studied in detail in the analytical form with using of the Legendre elliptical functions in [16.6, 47], we show (Fig. 16.15) a melt pressure influence on the shape of profile curves $z(r)$, with the boundary condition of catching in the point r_0 (the shaper radius $r_0 = 0.05$), as well as on the boundary curves $h(R)$ (1–4), corresponding to the growth angle $\psi_0 = 0$. Hence, we use the equation (16.8) and the boundary conditions (16.26) and (16.36). It is very important to mention that in the capillary problem with small Bo it is neglected by the influence of gravity. This is a reason, why these results are applicable for the growth of different size crystals in microgravity conditions. As for the growth in the condition of normal gravity, the results are applicable for filaments growth (for sapphire, for instance, the case under consideration corresponds to growth of a filament of 0.6 mm diameter)

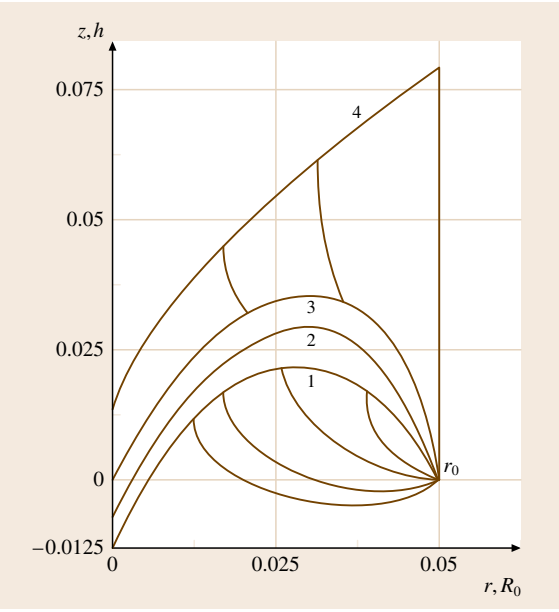


Fig. 16.15 Small Bo: Boundary curves $h(R)$ 1–4 and some profile curves $z(r)$ for shaper with $r_0 = 0.05$, under various pressures d: −10 (1), −5 (2), 0 (3), 10 (4)

with pulling up as well as lowering down. Consequently, the schemes Fig. 16.4b,d–f,j are described in the frame of this model. Here are some peculiarities of the results presented on the Fig. 16.15:

1. The order of magnitude of the crystallization front position is the same as the shaper radius for all values pressures under investigation. In our example, $r_0 = 0.05$. It means that for sapphire, for instance, the crystallization front is located on the distance 0.5–0.6 mm from the plane of sharp shaper edges.
2. For all boundary curves, except 4, $h(R)|_{R \to r_0} \to 0$).
3. The boundary curve 4 is the particular one. From the theoretical study [16.6], it follows that if d corresponds to the value from the formula $2dr_0 = 1$, the boundary curves for all r_0 values (but only from the range of small Bo values) has to have the shape similar to the curve 4. The main particularity of this curve is the following one: $h(R)|_{R=r_0} = 0.5\pi r_0$. Hence, for this particular pressure, if the diameter of pulling crystal is equal to the shaper edge diameter, the very special meniscus in the shape of the right circular cylinder exists.
4. All boundary curves, except 4, have a maximum. The maximum position corresponds to $R = R_m \approx 0.7r_0$ and it divides all range of the crystal dimensions on two parts for which: $\partial\alpha_0/\partial R > 0$ if $R > R_m$ and $\partial\alpha_0/\partial R < 0$ if $R < R_m$. It means that for d values characterized the formula $2dr_0 < 1$, there is a capillary stability ($A_{RR} < 0$) only if the gap between the shaper edge and the pulling crystal is less than $0.3r_0$.

16.6.2 Stability Analysis

Signs of capillary coefficients A_{RR} and A_{Rh} are presented on Fig. 16.16. For the stability estimation, heat coefficients (16.31) and (16.32) can be used: $A_{hh} < 0$, $A_{hR} > 0$. With respect to Fig. 16.16, we can choose a shaper design to have a capillary stability: $A_{RR} < 0$, $A_{Rh} < 0$. Therefore, with respect to (16.22) inequalities fulfilled, a dynamic stability of a shaped crystal growth will be provided.

Here we formulated a common problem of stability for growth of arbitrary cross section crystals by TPS. But only the simplest case (a growth of a round cylindrical crystal in the thermal condition described by the one dimensional thermoconductivity equation) was analyzed. Complimentary information on the topic can be found in our reviews [16.6, 9] and papers [16.23, 24]. It includes:

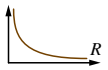
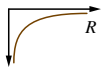
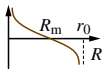
Conditions of crystallization				A_{RR}	A_{Rh}
Method	Bond number	Boundary condition	Parameter values		
CZT					
TPS	Small	Catching	$\sin\alpha_0 < 2r_0 d$	< 0	< 0
			$\sin\alpha_0 > 2r_0 d$		< 0
		Catching	$\alpha_0 < \alpha_1$	< 0	< 0
			$\alpha_0 > \alpha_1$	> 0	< 0
	Large	Catching	Single- and double-valued meniscus	< 0	< 0
			Double-valued meniscus $R \approx r_0$	< 0	> 0
		Angle fixing	$\alpha_0 < \alpha_1$	< 0	< 0
			$\alpha_0 > \alpha_1, r - R > m$	< 0	< 0
			$\alpha_0 > \alpha_1, r - R > m$	> 0	< 0

Fig. 16.16 CZT and TPS capillary coefficients for different Bo values and different capillary boundary conditions

1. Investigation of the meniscus static stability.
2. Investigation of tubes growth dynamic stability – three degrees of freedom stability problem where internal tube diameter is a third degree of freedom.
3. Investigation of a melt pressure influence on the dynamic stability – three degrees of freedom stability problem where melt pressure is a third degree of freedom.
4. Crystal cross section shape stability. So, some problems are solved but for theory up to now, there have been a lot of problems to be solved. The main of them is the stability of complicated shape crystal growth and an influence of crystallographic anisotropy.

Now, for preliminary analysis of the capillary shaping conditions before the experiments, we use rough estimations. For instance, for ribbon growth, an approximation including three steps, we proposed [16.6]:

1. A solution of the capillary problem with large Bo for the ribbon flat part
2. A solution of the capillary problem with small Bo for the ribbon edge
3. A joining of two solutions on the boundary near ribbon edge with the condition of the same growth angle for two parts.

16.6.3 Experimental Tests of the Capillary Shaping Statements

Growth Angle Certainty

A growth angle certainty is one of the main capillary shaping theory statements. This is a reason, why we carried out special experiments to examine it [16.6, 48]. A growth of thin sapphire crystal from a shaper with 0.8 mm diameter was carried out (Fig. 16.16). By changing the slope between the crystallization front and the surface of the skew shaper by means of a different heating, various boundary conditions were created for left and right sections of the same crystal. In Fig. 16.16a the rod of a constant cross section grows: the angles ψ_1 between the crystallization front and the growth direction are different on the left and on the right crystal sides; constancy of the diameter is provided by maintaining the angle $\alpha_0 = \alpha_e(\alpha_e = \pi/2 - \psi_0)$ all over the perimeter. In Fig. 16.17b on the left $\alpha_0 = \alpha_e$, on the right $\alpha_0 < \alpha_e$, the right side of the crystal widens. In Fig. 16.17c deviation α_0 from the equilibrium value α_e on the right side has led to crystal contraction. In the transient region, the crystal surface is convex on the Fig. 16.17b and concave on the Fig. 16.17c, which corresponds to the capillary stability presence.

Integration of the equation (16.9) in the range of the crystal radius R change from R_0 to the final value R_{01}

gives the following formula

$$\ln D = -\left(\frac{\mathrm{d}\alpha_0}{\mathrm{d}R}\right) z \,, \qquad (16.40)$$

where

$$D = \frac{R - R_{01}}{R_0 - R_{01}} \,.$$

Linear dependence $\ln D$ versus z has to be a proof of the (16.9) correctness. Figure 16.18 presents the date processing from Fig. 16.17b,c.

The Space Experiments. We carried out some model experiments in the microgravity conditions (small Bo) to test some capillary shaping theory statements [16.6, 49–54].

Simulation Experiments. Crystal growth experiments under microgravity conditions in the Space were preceded by simulating the liquid column shape with using immiscible liquids of equal densities [16.6, 49–51]. A meniscus of the alcohol/water solution was formed between two glass tubes, surrounded by the equal-in-density mineral oil (Fig. 16.19). Pressure d in meniscus was equal to the weight of column of the alcohol solution in the upper tube. The lower tube (3) of $2r_0 = 13.12$ mm diameter imitated the shaper, and the upper one (1) of $2R$ in diameter – the crystal. For a right circular cylindrical meniscus (2) existence, a pressure 16.8 dyn/cm^2 was determined experimentally (Fig. 16.19a). A convex meniscus (2) (Fig. 16.19b) was formed under pressure 27.14 dyn/cm^2. The sphere menisci (4) on the ends of the lower tubes (3) were used for the pressure estimation as well as, with a certain pressure, for a surface tension value on the two liquids boundary. The same types of the experiments were carried out by us on the board of a flight laboratory with the 20 s microgravity time.

Crystallization of Copper Under Short-Time Microgravity Conditions. The simulation experiments with liquids were only the first step to estimate the crystal growth real conditions. Moreover, a doubt appeared that a shaped crystal growth under microgravity could be realized because, sometimes, in simulation experiments, the liquid flew on the crystal surface [16.6, 49]. Therefore, we crystallized the copper under the capillary shaping, on a high-altitude rocket, with 20 min time of microgravity [16.6, 50, 51]. The metal has a relatively low melting point (1083 °C), resistance to overloading (it is important for rocket launching as well as for a capsule landing), and its physical-chemical properties are well known.

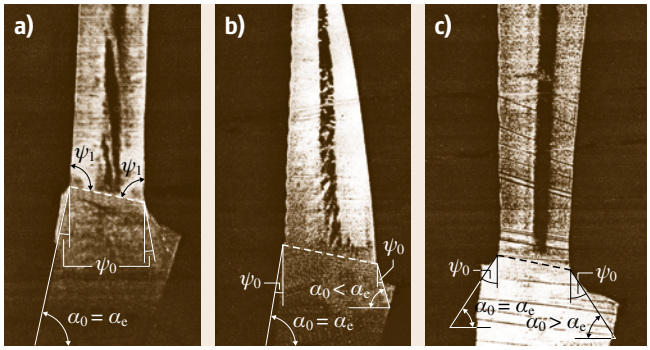


Fig. 16.17a–c TPS growth of a thin sapphire filament, the shaper being skew: **(a)** constant cross section, **(b)** widening from the right, **(c)** constriction from the right

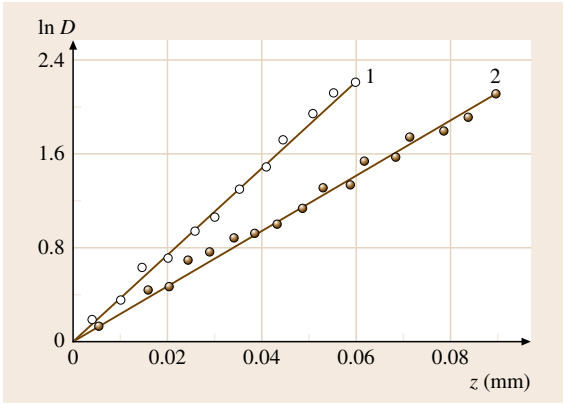


Fig. 16.18 Sapphire filament constriction (1) and widening (2) in the transient range

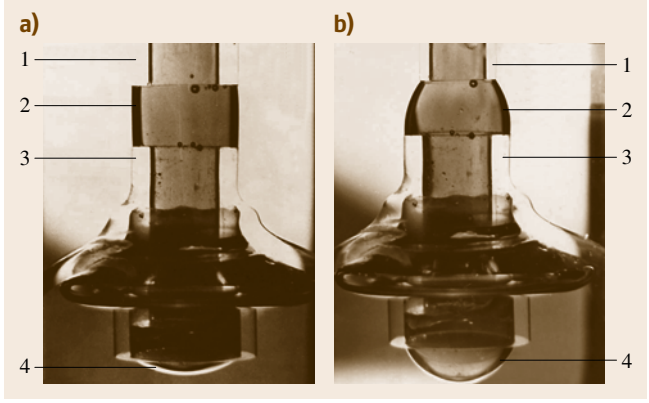


Fig. 16.19a,b Meniscus model of pulling a circular rod under zero-g conditions: **(a)** right circular cylinder, **(b)** convex

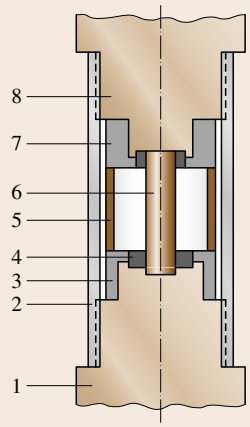


Fig. 16.20 Design of the capsule used to investigate the crystallization process from a melt under microgravity conditions (notations given in the text)

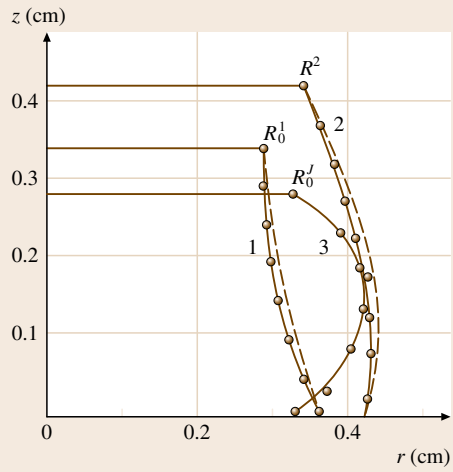


Fig. 16.21 Calculated profile curves of the melted copper columns (*dotted line*) and crystallized specimens (*continuous line*) for different (1, 2, 3) internal meniscus pressures; experimental data for the crystallized specimen shape are indicated by *bullets*

The technique of capillary shaping was preliminary used to produce a rod specimen in an evacuated enclosure. This enables us to reduce the amount of gas in the metal. Specimen (6) in the form of a cylinder, 5–8 mm in diameter, and about 5–6 mm long (Fig. 16.20) was placed between two molybdenum shapers (1) and (8) into which copper (4) was fused preliminary. This guaranteed complete wetting of the shaper during the space experiment. Two graphite guard rings (3) and (7) were introduced to prevent the escape of the melt beyond the sharp lip of the shaper. These rings were supported by the graphite spacer (5), which also acted as a thermal shield. Both shapers were pushed into the coupling tube (2). The above design ensured rigidity, simplicity of assembly, and constant separation between the shapers. Tungsten-rhenium thermocouples were mounted near the ends of the specimens to estimate the temperature distribution along its length. The capsule was inserted into a heating device using the energy of the exothermic chemical reaction. The device did not contain any movable parts. The experiment was carried out by the following way. When a microgravity conditions had achieved, the specimen was completely melted. After that during the microgravity existence, a directional crystallization of the melt column was realized by the heat removing from the upper shaper. On the high-altitude rockets, we had no photographic facilities for recording the crystallization process. Therefore, the shapes of the crystallized specimens had examined experimentally and was compared with the calculated for $\psi_0 = 0$ ones. Figure 16.21 confirms:

1. Our model of capillary shaping is applicable for a crystal growth in the conditions of microgravity.
2. Under recorded by the thermocouples crystallization speed 5–7 mm/min, $\psi_0 = 0$ for Cu crystallization.
3. The melt did not flow on the crystal surface during the crystallization; therefore, the crucible-free zone melting and capillary shaping crystal growth could be realized in the space.

A little later, these crystallization processes were realized in the *shape* and *ribbon* experiments.

Shape Experiment. The main idea of the experiment was to realize a crystal growth by using the right cylindrical melt column which can not exist in the terrestrial condition (except a filament growth). Under microgravity (Figs. 16.15 and 16.19a), such a column of melt is formed if $R = r_0$; $\alpha_0 = \frac{\pi}{2}$ under pressure d, satisfying equality $2dr_0 = 1$, but, reaching the altitude $h \approx \pi r_0$, it loses static stability and transforms first to a meniscus, its profile curve having an ambiguous projection onto the abscissa axis, and then with increasing h, it falls into two independent meniscus. At $h < \pi r_0$ and $d = 0$, a meniscus is a catenoid; with increasing pressure its curvature in the axial cross section decreases, reaching infinity at $2dr_0 = 1$. When pressure increases above this value the meniscus becomes convex (Fig. 16.19b).

A cylindrical meniscus can be used for a crystal growth only at $\psi_0 = 0$, which means that a metal should be chosen for the material grown experimentally (for metals the angle of growth is usually close to zero). In 1984, under microgravity, at *Salyut* orbital space probe, crystallization of indium was carried out by big group of Russian scientists governed by the author of this chapter [16.6, 50, 52]. The advantage of indium is its low melting temperature (156 °C). It is very important for the simplicity of the space furnace and the limited energy power on the space craft board. Here are some other In physical characteristics: a comparatively high density in a solid state (7.28 g/cm^3) which only slightly differs from that of the melt (7.03 g/cm^3), the surface tension of the melt $\gamma = 592$ erg/cm^2, and capillary constant under terrestrial conditions $a = 0.41$ cm.

Figure 16.22 depicts a scheme of the growth device. A plastic case (1) with a lid (2) has a graphite container (3) filled with indium preliminary. A resistive heater (4), separated by a foam-polyurethane layer (5), is used. The heat is delivered to the container through a copper capsule (6), which also serves for holding a copper cap (7) (shaper itself) and supplied with a hole for leveling the inert gas pressure inside and outside the container (3). The meniscus of melt (8) is formed first between the initial copper rod (9), fastened to a rod (10), and the edge of the shaper (7). The meniscus shape is fixed by a photo camera with an illumination system of windows (11). The most important part of this setup was the system of maintaining a pressure inside of meniscus by means of a melt meniscus formed near the crucible bottom. The pressure depends on the radius R of the graphite container and a wetting angle. The idea had been suggested by the author of this chapter and was used either for the *ribbon* experiments. Figure 16.23 depicts the shape of a drop (a), formed at the edge of the shaper, and of the meniscus of melt (b). Pressure, which had been found from the shape of the drop (Fig. 16.23a), exceeded approximately by 40% that required for formation of a cylindrical column. A reason of non accuracy is evident – there are a lot of factors (a hysteresis included) governed by the wetting angle. Some of them could be found only under real space conditions and could not be taking into account before. Unfortunately, we did not have any possibility to repeat the same experiment with the correction. But the main aim of the experiment was achieved: the typical shape of a meniscus has the ratio $h/r_0 \approx 3.6$ (10 mm) that one order exceeds terrestrial TPS growth conditions. After the seed rod was wetted with the melt, it was pulled at the speed $V \approx 3$ mm/min. The pulling

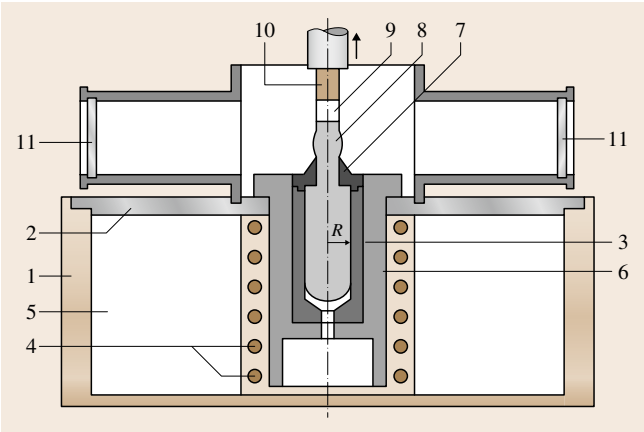


Fig. 16.22 Experimental setup for space crystal growth (notations given in the text) in the *shape* experiment

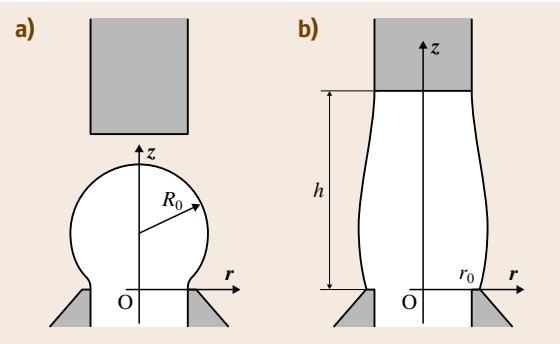


Fig. 16.23a,b Melt drop at the edge of the shaper **(a)** and the meniscus formed thereupon **(b)** in the *shape* space experiment

speed of the test indium specimen, grown with the analogous device in terrestrial conditions, could not be elevated above 0.2 mm/min. The flight specimen diameter was ≈ 5.6 mm, whereas it was 2.9–3.2 mm of the test one. No special regulation systems were used, but it is evident that both pulling processes were stable. The both samples were mainly single crystals in structure.

Ribbon Experiment. The crystallization of ribbons from the melt of Ge and GaAs in the orbital station *Mir* is the next example of TPS realization at microgravity conditions [16.6]. The melt is placed in a fixed gap between two non wettable flat plates (Fig. 16.24). The right part of the melt is a free surface of the $1/r$ curvature which depends on the wetting angle and the distance $2r_0$ between the plates. It was the same idea,

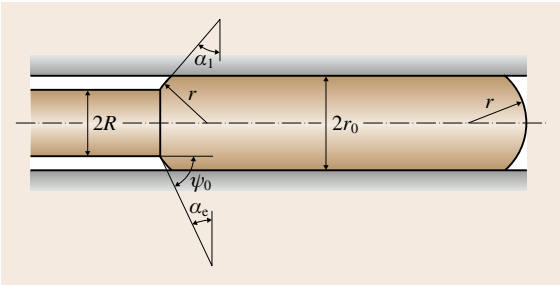


Fig. 16.24 Schematic drawing of tape growth in the *ribbon* space experiment

which before had been realized in the *shape* experiment, to maintain a definite pressure inside the growth meniscus by the curvature of the melt free surface. The growth meniscus projection in the gaps between the walls and the growing crystal are the circular arcs of the same radius r. It is the realization of TPS with the wetting boundary conditions on the walls of the shaper. The employment of unwetted walls has to be successful, if the following inequality is fulfilled

$$\alpha_1 = \Theta - \tfrac{\pi}{2} > \alpha_0 = \tfrac{\pi}{2} - \psi_0 \,, \tag{16.41}$$

that is

$$\Theta > \pi - \psi_0 \,.$$

Here Θ is the wetting angle and ψ_0 is the growth angle.

The ribbon thickness $2R$, the capillary coefficients A_{RR} and A_{Rh} are the following ones

$$2R = \frac{2r_0 \sin\alpha_0}{\sin\alpha_1} \,, \tag{16.42}$$

$$A_{\mathrm{RR}} = \frac{-V \sin\alpha_1}{r_0 \cos\alpha_0} \,, \tag{16.43}$$

$$A_{\mathrm{Rh}} = \frac{-V \sin\alpha_1}{r_0 \sin\alpha_0} \,. \tag{16.44}$$

The both capillary coefficients are negative and there is a capillary stability. For the common dynamic stability estimation, the heat coefficients (16.31) and (16.32) can be used: $A_{\mathrm{hh}} < 0$, $A_{\mathrm{hR}} > 0$. Therefore, with respect to (16.22) inequalities fulfilled, the dynamic stability of the scheme under investigation is provided.

At the flight experiments, Ge and GaAs ribbons were grown between pyrocarbon plates. Unfortunately, a heating regime was not optimal, the seeds were melted and the ribbon structures were polycrystalline [16.6]. But smooth surfaces and constant thicknesses of the ribbons, grown without any special regulation, is an evidence of the process stability.

16.6.4 Impurity Distribution

Impurity distribution in crystals grown by the Bridgman, CZT and FZT is studied ratter thoroughly, however extension of the mechanisms known to thin-profile growth using TPS can lead to wrong conclusions. Application of the Burton–Prim–Slichter equation [16.55] to calculation of the impurity distribution effective coefficient K requires specification of the boundary diffusion layer thickness. In case this thickness is assumed to be equal to the total height of the meniscus and the shaper capillary channel, $K = 1$ for any impurity [16.56] that does not correspond to reality. The present section gives a model of impurity transfer for the TPS under consideration that allows relating K-values to the parameters of capillary shaping and feeding [16.6, 57]. Figure 16.25a illustrates the case of a thin tape growth.

Stationary process is considerated; it is assumed that the melt in the zone of the meniscus and the capillary channel is not stirred and the conditions of complete stirring are maintained in the crucible. Under the assumptions made, an impurity transfer in the meniscus is described by

$$D\left(\frac{\mathrm{d}^2C}{\mathrm{d}r^2} + r^{-1}\frac{\mathrm{d}C}{\mathrm{d}r}\right) = -V\frac{\mathrm{d}C}{\mathrm{d}r} \,, \tag{16.45}$$

with the following boundary condition at the crystallization front

$$-D\frac{\mathrm{d}C}{\mathrm{d}r}\bigg|_{r=r_0} = V_0\,(1-K_0)\,C(r_0) \,. \tag{16.46}$$

Here C denotes impurity concentration in the melt, D is the diffusion coefficient, K_0 is the impurity distribution equilibrium coefficient, others notations are given in Fig. 16.25a.

The polar coordinate system chosen allows easy specification of the melt-flow rate distribution in the meniscus $V(r) = V_0 r_0/r$. Then (16.45) is rearranged into the following form

$$\frac{\mathrm{d}^2C}{\mathrm{d}r^2} + r^{-1}\left(1 + \frac{V_0 r_0}{D}\right)\frac{\mathrm{d}C}{\mathrm{d}r} = 0 \,. \tag{16.47}$$

Impurity transfer in the capillary channel is described by the equation

$$D\frac{\mathrm{d}^2C}{\mathrm{d}z^2} = -V_{\mathrm{c}}\frac{\mathrm{d}C}{\mathrm{d}z} \,, \tag{16.48}$$

with the following boundary condition

$$C|_{z\to\infty} \to C_\infty \,. \tag{16.49}$$

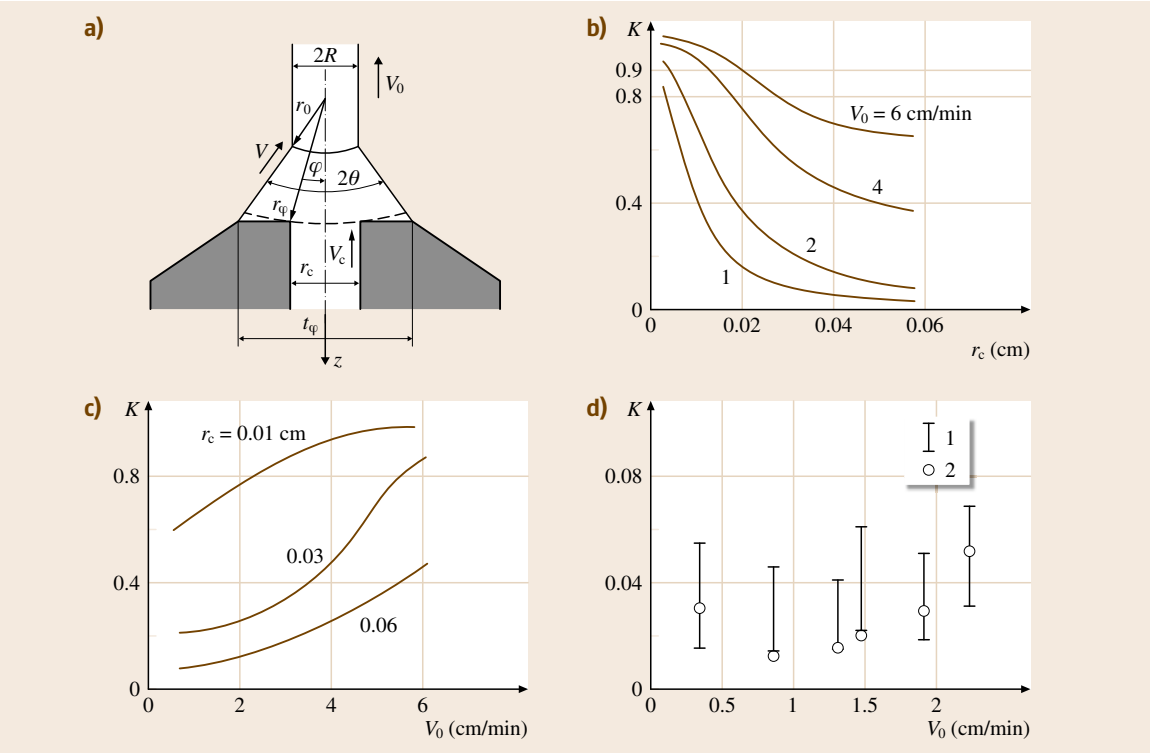


Fig. 16.25a–d Calculating the impurity distribution effective coefficient K **(a)** diagram; **(b)** $K = f(r_c)$ – calculated; **(c)** $K = f(V_0)$ – calculated; **(d)** comparison of experimental (1) and calculated (2) K-values from (16.50) for the In distribution in thin-walled shaped Si crystal

It is assumed that the impurity concentration in the bulk of the melt C_∞ is constant in the process of tape growth. The solution of the problem relates the value of the impurity distribution effective coefficient K to the parameters of the crystallization conditions (V_0 and $2R$), with the conditions of capillary shaping (t_ϕ, r_c, Θ) and the impurity characteristics (D and K_0)

$$K = K_0 \Big/ \left\{ K_0 \left[1 + \left(\frac{\Theta r_c}{\varphi t_\varphi} - 1 \right) \cos\varphi \right] + (1 - K_0)(1 - \cos\varphi) \left(\frac{2R}{t_\varphi} \right) \right\}^{V_0 R / D \sin\Theta} . \tag{16.50}$$

If the width of the capillary channel r_c reaches its maximum value t_φ, equation (16.50) is reduced to

$$K = K_0 \Big/ \left[K_0 (1 + (1 - K_0) \times (1 - \cos\varphi) \left(\frac{2R}{t_\varphi} \right) \right]^{V_0 R / D \sin\Theta} . \tag{16.51}$$

Figure 16.25b shows $K = f(r_c)$ calculated for aluminum impurities in silicon. The following values are used: $K_0 = 0.002$, $D = 0.53 \times 10^{-3}\,\mathrm{cm^2\,s^{-1}}$, $2R = 0.03\,\mathrm{cm}$, $t_\varphi = 0.06\,\mathrm{cm}$. Figure 16.25c presents $K = f(V_0)$ calculated from (16.51) for various r_c values. It is obvious that K increases with V_0 (and as a result V_c) increasing. Under actual conditions of growing thin-walled profiled silicon crystals $K_{Al} < 1$. Processing of the data of [16.58] gives the value of $K_{Al} = 0.039$ in silicon, which agrees very well with the value of $K_{Al} = 0.3$–0.4 calculated from (16.50) in accordance with the initial data of [16.58].

Figure 16.26 gives data on sulfur distribution along the axis of a TPS silicon tape obtained by laser emission microanalysis (LEM). The ratio of the sulfur spectral line strength J_S to that of silicon J_{Si} (the ratio is proportional to the concentration of the element analyzed in the silicon matrix) is plotted on the ordinate. The rate of tape pulling was equal to 12 mm/min. Increase of sulfur concentration in the silicon tape in the process of its pulling shows that $K_S < 1$ (it is assumed that

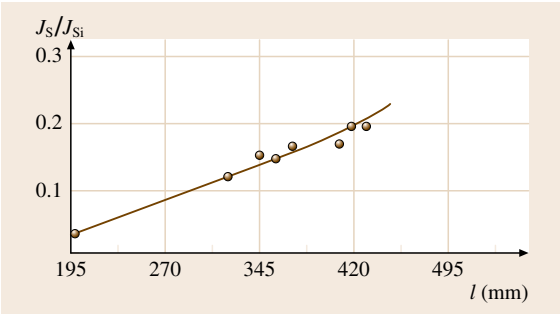


Fig. 16.26 Sulfur distribution along the length of a silicon tape (LEM data)

for sulfur impurity in silicon $K_0 = 0.001 \times 10^{-3}$). While analyzing other impurities, no explicit regularities were observed.

To verify the main equation (16.50) a series of 0.01 mass indium-doped silicon tapes was grown. The mass of each tape-shaped crystal did not exceed 7% of that of silicon charged into the crucible. The tape thickness $2R$, the shaper transverse dimension t_φ, the capillary slot dimension r_c, the growth rate V_0 were measured. Then photometrical spectral lines of indium in the crystals grown and in the crucible residue were drawn. The measurement accuracy of the indium distribution effective coefficient was equal to (40–50%). The results obtained are depicted in Fig. 16.25d. Vertical arrows indicate experimental results, circles show the values calculated from (16.50) in accordance with the above mentioned parameters. The values of $D = 0.52 \times 10^{-3}\,\mathrm{cm^2\,s^{-1}}$, $K_0 = 0.4 \times 10^{-3}$ are assumed for indium impurity in silicon. The results shown in Fig. 16.25d do not allow plotting K versus the growth rate V_0 since the thickness of a silicon tape, $2R$, decreases with V_0 increasing (the value of $2RV_0$ practically was constant in the experiments), and they can only demonstrate satisfactory agreement between calculated and experimental values. The values of K calculated from the Burton–Prim–Slichter equation are equal to 0.8–0.9, i. e., they are some orders of magnitude greater than the experimental values.

Impurity distribution along the widths profiled crystals is to a great extent determined by the technique used to feed the melt to the growth meniscus. In Fig. 16.27a,b resistivity ρ distributions across of silicon tapes, grown under the conditions of the two versions of meniscus melt replenishment, are compared. The shaper shown in Fig. 16.27d possesses one long capillary slot, while the shaper given in Fig. 16.27e has two short slots at its end faces. The same feeding system was used for the sapphire ribbon growth. A diffusion reflection of light (Fig. 16.27c) indicates a bubbles concentration at the center of ribbon. The following explanation of nonuniformity of impurity distribution across the crystal (Fig. 16.27a–c) observed can be offered. In the case of horizontal melt flow in the meniscus from the shaper edges towards its center, impurities with $K < 1$ driven off by the growing crystal accumulate in the central part of the meniscus. Hence, corresponding distribution of

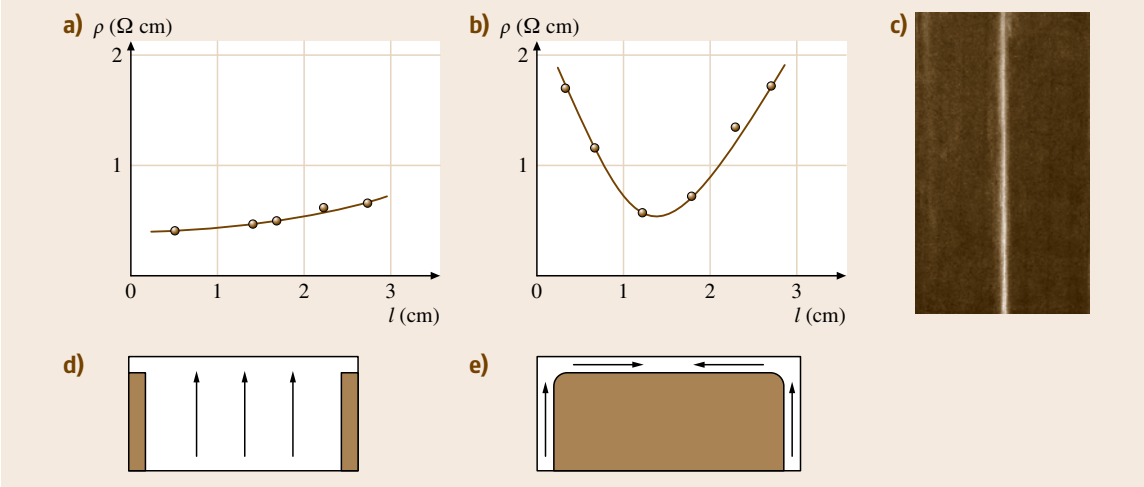


Fig. 16.27a–e Impurity distribution across ribbons using two different versions of melt replenishment of the meniscus: **(a)** silicon ribbon and **(d)** corresponding feeding scheme; **(b)** silicon and **(c)** sapphire ribbon and **(e)** corresponding feeding scheme

capillary channels in the shaper allows controlling impurity distribution at the cross section of crystals being grown.

16.6.5 TPS Definition

On the basis of the theoretical analysis, accomplished above, we can define TPS:

> *TPS is the shape crystal growth technique which uses a solid body (shaper) to define a melt meniscus shape by means of either catching (on edges of the shaper) or wetting (on surfaces of the shaper) capillary boundary condition to obtain the crystal of predominant cross section and impurity distribution as a result of pulling it in a dynamically stable regime.*

This definition follows from our analysis of capillary catching and wetting boundary conditions, completed in 1967 and published for the first time in 1968 [16.38], as well as from our dynamical stability analysis with a capillary shaping, completed in 1970 and published for the first time in 1973 [16.14]. Now, on the basis of this definition, we can analyze a TPS development history.

16.6.6 TPS Brief History

A development of shaped crystal growth for industrial application was begun from the set of papers [16.59–63] published in 1958–1959. The papers [16.59, 60] informed that during 1938–1941, Russian scientist A.V. Stepanov had carried out experiments concerning pulling of shaped polycrystalline and single-crystalline specimens (sheets, tubes and so on) from melts of some metals, especially aluminum and its alloys. The Second World War interrupted these experiments and they have been continued since 1950s in the Physical and Technical Institute of the USSR Academy of Sciences. During 1950–1958 few Stepanovs collaborators, especially postgraduated students *Shakch-Budagov* and *Goltsman*, continued these experiments with low-melting metals and alkaline halides. The papers [16.61–63] described the main results of these experiments. The author of this chapter has been a participant of the below described events because in 1959 he began a scientific activity as the undergraduated student in the Stepanov's laboratory.

In 1963 *Stepanov* formulated his global idea [16.64]:

> *it is necessary to find a way to pull all types of industrial profiles from melts of aluminum, steel and other alloys. It could save energy, and eliminate extruding, rolling, cutting and many other types of mechanical treatments.*

It was a basis of large investigations in the field carried out in the Stepanov's laboratory. Two main directions were being developed:

1. Polycrystalline metals and alloys
2. Semiconductors single crystals.

The author of this chapter was nominated as the head of the first direction. First of all, *Stepanov* and *Tatartchenko* decided to demonstrate the possibilities of the technique as widly as possible. For this, *Tatartchenko* designed an installation for the continuous production of aluminum tubes. During development of the installation, a lot of technical problems were solved [16.65]. The installation was completed in 1963. It contained two connected crucibles: the first for feeding and a second for the pulling of 6 mm diameter tube, automatically wound on a coil. During testing of the installation, specimens of tubes with a length up to 4000 m and a speed of pulling up to 15 m/h were obtained. The installation was made very compact to demonstrate its operation at different exhibitions. In 1964, the installation was shown in Italy. There was a full success: many articles described a new metallurgical technique. After that, a second variant of the installation was developed for the production of the aluminum profiles of different complicated cross sections with lengths up to 3 m [16.10]. The operation of it was demonstrated at exhibitions in Hungary (twice in 1967), in Italy (1968), in Czechoslovakia (1971). Examples of aluminum profiles obtained with this installation are presented in Fig. 16.28. A possibility to use the technique for steel profiles and combined aluminum-steel profiles pulling was either demonstrated by the author of this chapter [16.66] (Fig. 16.29).

In the application of the technique for single crystals pulling, the laboratory intensively was working with the huge industrial germanium project. Some industrial laboratories and plants were included in the project and, at the end of the 60s, in the former Soviet Union, about 85% of the germanium was produced as shaped crystals. For instance, for electronic applications, instead of one crystal by the CZT, 26 round cylindrical crystals with the diameter of 10.0 ± 0.1 mm we pulled, from the same crucible, without any special control [16.10]. The author of this chapter participated in the project by developing the theory described above as well as the application of the theory for the technology (e.g. [16.67]).



Fig. 16.28 Aluminum heat exchangers and other profiles grown by TPS in Stepanov's laboratory by the author of this chapter with collaborators

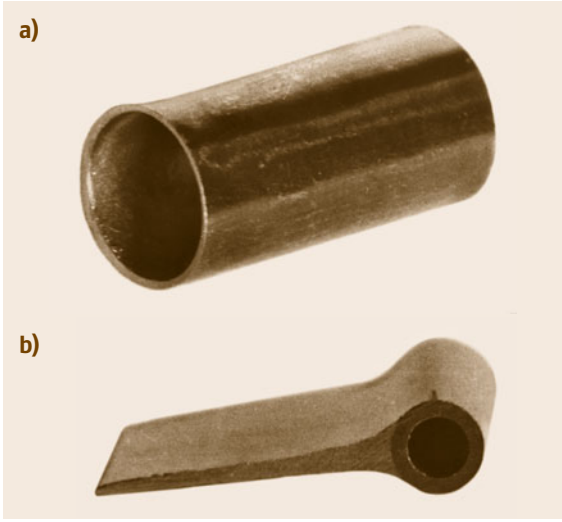


Fig. 16.29a,b Steel tube (a) and steel tube with Al rib (b) grown by TPS in Stepanov's laboratory by the author of this chapter

Up to 1967 shaped crystal growth was developing only in the former Soviet Union. The publication of the information concerning shaped filaments growth [16.68, 69] and especially edge defined film fed growth (EFG) [16.70] changed the situation drastically: Shaped crystal growth appeared in the USA. It was a beginning of shaped crystal growth spreading in many scientific groups, especially for the sapphire and silicon growth. As for former Soviet Union, the shaped crystal growth direction has continued the development. Since 1968 every year, Russian National Conferences has been organised with publication of the special Proceedings (e.g. [16.38]) as well as special issues of Bulletin of the Academy of Sciences of the USSR, Physical Series (e.g. [16.39]). All variants of pulling techniques from the shaper were named Stepanov's technique. In 1972, A.V. Stepanov died. His laboratory has continued to work. The author of this chapter was invited as the head of the Crystal Growth department in the Solid State Physics Institute of the Academy of Sciences of the USSR. In the frame of the department, the shaped crystal growth laboratory was organized with the stuff of 40 persons. Many theoretical and experimental aspects of shaped growth, Space growth included, were developed there. The main competitor during long time was being the Tyco laboratory where EFG growth was developing for sapphire and silicon. In 1978, the author of this chapter visited the Tyco laboratory and had very interesting discussion with La Belle, the author of EFG patent. That time, it was impossible to imagine that he would work in this laboratory (later Saphikon, and Saint-Gobain Crystals) as the chief scientist twenty four years later.

Now, shaped crystal growth is widely spreaded but there are a lot of titles used, especially EFG and Stepanov's technique. We are sure the situation must be clarified. As for us, since 1980s, we have preferred not to use the title Stepanov's technique neither EFG. We insist to combine all these techniques by the title *technique of pulling from shaper* (TPS). Here are the reasons of that.

A priority in applying of a shaper (holes in plates placed onto the melt surface for shaping melt-pulled crystals) belongs to Gomperz [16.71]. In 1922, he used mica plates floating on melt surfaces to pull Pb, Zn, Sn, Al, Cd, Bi thin filaments through holes in the plates. Sometimes the filaments had a single crystalline structure. In 1923, the same technique was used either for filaments pulling [16.72]. In 1929, for Zn single crystalline filaments growth, for the first time, a single crystalline seed was used [16.73]. In 1929, the technique was titled Czochralski–Gomperz technique [16.74, 75]. In 1928, P. Kapitza, later the Nobel Prize rewarded, used this technique for Bi rods growth [16.76]. So, during 1922–1931, six papers concerned with a shaper using were published. Moreover, the technique was titled as a CZT modification Czochralski–Gomperz technique. Hence, Stepanov

does not have a priority. Never in his publications, have we found any of these six references. What about the explanation of the shaper functions? He is one of our coauthors of [16.38, 39] papers, explaining catching and wetting boundary conditions. On the other hand, at the same time his name as a coauthor we can see in the [16.41] publication, the no applicability of which to shaped growth we explained in some our papers, among them with Stepanovs participation [16.43]. This absurd situation does not need any comments [16.7]. In [16.64] Stepanov pretended to have invented:

> *the principle of shape formation from a melt, using capillary forces or some other actions (except of crucible walls) on the melt, of the cross section or an element of a cross section of solid profile its following crystallisation.*

This is a typical *umbrella* formulation which covers CZT, VT, FZT techniques as well as electromagnetic, ultrasonic, inertial and other possibilities of shaping. It can not be discussed seriously. At the same manuscript we read:

> *A shaper should be distinguished from a die. A die is the embodiment of a brute force. A shaper is a more spiritual system. Its aim, first of all, is to provide a delicate effect on the curvature and shape of the mobile column of the liquid melt stretching itself behind the crystal by creating new boundary conditions along its contour.*

We agree that there is a big difference between a die and shaper, but in spite of Stepanovs big role in the TPS spreading [16.7], *new boundary conditions* never have been specified in Stepanov's papers. We think there is sufficient quantity of arguments not to use the title Stepanov's technique. On the contrary, our capillary shaping analysis of TPS, that has been done in 1968 [16.38] is completed: It is impossible to suggest something new, beside catching or wetting if using a shaper. From this point of view EFG technique is simply TPS with catching boundary condition. Probably, this is because of a low level of patent experts that the independent EFG patent exists. Edge defined condition for meniscus was published in our paper [16.39] as catching boundary conditions before the EFG patent appearance. We only agree that capillary feeding was described in the EFG patent for the first time. Certainly, many shaped growth schemes of TPS have peculiarities and we will discuss some of them below.

Now we will describe shaped crystal growth of few materials. The most impressive results of TPS industrial application were obtained for sapphire and silicon. Furthermore structures of shaped sapphire and silicon have a lot of peculiarities.

16.7 TPS Sapphire Growth

Sapphire belongs to the family of corundum crystals. The term corundum designates α-aluminum oxide. Pure corundum crystals are colourless and are named *leucosapphire* ones. But now the name *sapphire* crystals is very often used, although historically the title *sapphire* crystals has been applied to the blue corundum ones. Different colours of corundum can be obtained by the addition of different metallic oxides to aluminum one. Natural and synthetic red ruby contains 1–7% chromium oxides. Synthetic alexandrite is produced by the addition of vanadium oxide. 1% titanium and 2% iron oxides give a blue colour. Nickel oxide gives a yellow colour. An addition of vanadium and cobalt oxides imparts a green colour. Green crystals are also produced if the chromium content exceeds 8%.

The application of TPS for sapphire is an example of the most successful one because of coexistence of few factors [16.8]: First of all, it is a demand for advance techniques of a material with unique physical and chemical properties: high melting point, exceptional hardness, transmission over a wide band of wavelengths, radiation and chemical resistance. Secondly, exceptional hardness of sapphire hinders its machining if it could be grown by other techniques. Thirdly, it has been impossible to growth very big crystals (for instance, optical windows 320 x 500 mm^2 for aircrafts and spacecrafts) by using other crystal growth techniques. Fourthly, chemically resistant and wettable materials (W, Mo, Ir) have been found for shapers.

La Belle and *Mlavsky* were the first who grew shaped sapphire crystals. In [16.68] there was information concerning shaped filament growth without any detail. In [16.69, 70, 77] edge defined film fed growth, EFG, technique was described. EFG corresponds to the scheme Fig. 16.4e, i. e., TPS with a catching boundary

condition. A peculiarity of EFG is a capillary feeding. The capillary together with wettable shaper facilitates a seeding. It is important to repeat once more that the capillary from Fig. 16.4e serves only for feeding and does not participate in the capillary shaping: the meniscus, catched on the edge of a shaper, changes its curvature with forming a negative pressure inside, and raises the melt above the shaper edge, up to the crystallization front.

16.7.1 Modifications of TPS

The presence of the shaper in TPS allows many manipulations during growth. The variable shaping technique VST described for the first time in [16.79], gives a possibility to change a cross section of crystal (periodically if it is necessary) during of pulling. Monocrystalline sapphire profiles, grown by TPS and VST by the authors with collaborators in the Solid State Physics Institute of Academy of Sciences of Russia, are presented on the Fig. 16.30. VST is based on controlling the melt mass flow towards the crystallization interface when passing to a new specific cross section shape. One of VST variants described in [16.78] is shown on the Fig. 16.31. The scheme allows not only changing the shape of the crystal but also its composition. It works by the following way: At the beginning both channels 5 and 6 plunged in the melts but, only through capillary channel 5, melt reaches the shaper edge. As a result, during a first stage, a tube (cross section A) grows. Because of a vacuum, formed inside of the growing tube, the other melt through non capillary channel 6 reaches the shaper edges and, during a second stage, the rod of two different compositions grows (section B). During the thirds stage shown on the diagram, the feeding through the channel 5 is eliminated by the crucible lowering (section C). By the similar way, changing of shaper plunging in the melt, different edges or walls of the shaper can operate by turns. As a result, we obtain a variety of shaped crystals, examples of which are presented on the Fig. 16.30. There is very interesting modification of TPS used especially for a dome growth [16.80]. There the seed is rotated around horizontal axes.



Fig. 16.30 Monocrystalline sapphire profiles grown by TPS and VST

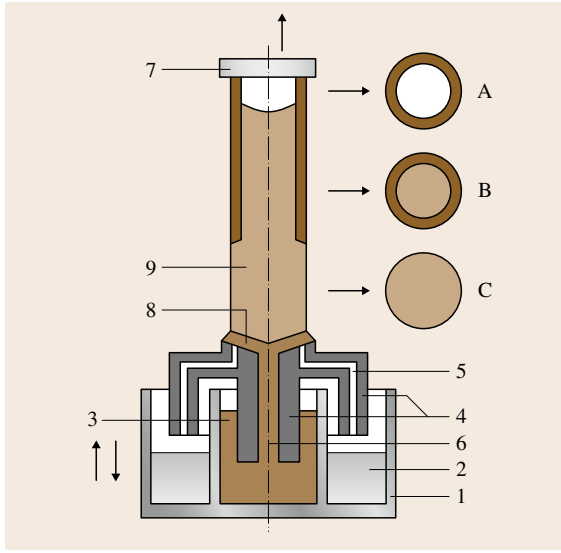


Fig. 16.31 The scheme from [16.78] for growth at various cross sections and various compositions crystals: 1 – crucible; 2 – undoped melt; 3 – doped melt; 4 – shaper; 5 – capillary feeding channel; 6 – noncapillary feeding channel; 7 – seed; 8 – meniscus; 9 – growing crystal; A, B, C – cross sections of the different parts of the growing crystal

The local shaping technique, LST [16.81], shapes only an element of the crystal that we need to grow. During growth, the horizontal displacement of the seed and shaper with respect to each other in combination with rotation and pulling of the seed allows obtaining a variety of shape crystals. Figure 16.32 presents a tube growth: A shaper of a diameter q shapes an element of the tube of thickness $p = r_2 - r_1$. The seed is rotated with the angle speed ω and is moved up with the speed V. A middle tube radius R is equal to a distance between the shaper center and the axe of the seed rotation. Practically any complicated body of revolution, for instance, a dome with the thin wall, can be obtained by this technique. A dynamic stability investigation of LST was carried out in [16.81]. It has to be mentioned that

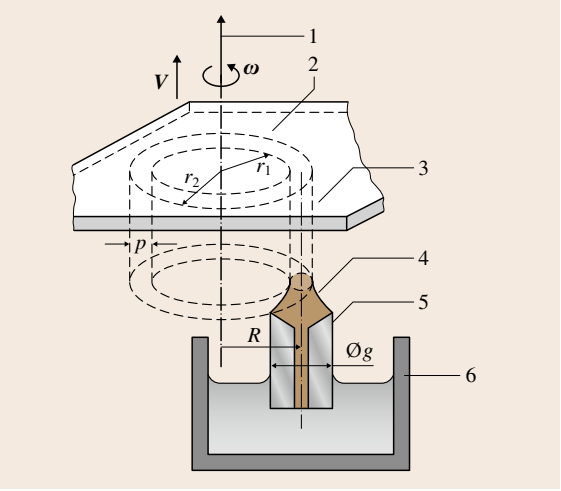


Fig. 16.32 Local shaping technique scheme: 1 – rotation axis, 2 – seed crystal, 3 – growing tube, 4 – melt meniscus, 5 – shaper, 6 – crucible

40 years ago LST was being used in our experiments with aluminum growth as well as a vacuum inside of a tube grown for a seeding. Some specimens are shown on the Fig. 16.28.

16.7.2 Crystal Defects

In compared with other crystal growth techniques, the peculiarities of TPS crystal defect structures are mainly determined by two factors:

1. High growth speed which, as a rule, one or two orders more
2. Small thickness.

Bubbles are the major defects in shaped corundum crystals (e.g. Fig. 16.27c). There are two aspects of the problem concerned with its appearance in the crystal. The first of them is an enrichment of the melt by gas and the bubble formation in the melt. The second one is a capture of the bubbles by grown crystal.

A vacuum treatment of the melt before the crystal growth reduces the bubble contents in the crystals. This is a proof that a dilution of gases in the melt is one of the sources of its gas enrichment. But there is a more important gas source for the corundum melt. In spite of the aluminum oxide is stable under normal conditions; its heating is accompanied with thermal dissociation, evaporation of some reaction products and coagulation of others. Mass spectroscopic analysis shows [16.82] that the products of dissociation of aluminum oxide are O^+, O_2^+, Al^+, AlO^+, Al_2O^+, AlO_2^+, $Al_2O_2^+$. The intensity of thermal dissociation depends greatly on the temperature and environment. It is the most intensive if the hydrogen is presented, less intensive in the vacuum and the least intensive in the inert atmosphere (argon, nitrogen). The VT improves this thesis. One of the first bubble formation versions in VT corundum crystals was concerned with the gas adsorption on the surface of feeding powder particles. But the hypothesis is at variance with the following experimental fact. The γ-Al_2O_3 powder is more friable than α-Al_2O_3 and, therefore, adsorbs more gas on the surface. But corundum crystals grown from γ-Al_2O_3 charge have less bubble inclusions. So, the charge dissociation has to be the main reason of bubble formation because of the hydrogen presence, and α-Al_2O_3 powder is worse because of sticking of α-Al_2O_3 powder particles.

The crucible and shaper presence complicates the situation. Although the problem is not completely understood at this time, the thermal dissociation of the melt because the chemical interaction of the melt with the crucible material seems to be very important cause of the gas appearance in the melt. Here is the list of chemical activity of the main container materials for sapphire crystal growth (from the best to the worst): Ir, W, Mo, Nb, Ta, Zr. As rule, only three first materials are used for the containers. The reaction of Al_2O_3 with refractory metals is generally believed to involve two stages. For example with Mo: $Al_2O_3 \rightarrow Al_2O + O_2$; $Mo + O_2 \rightarrow MoO_2$. In reality, the presence above mentioned aluminum oxide dissociation products does the situation much more complicated. Mass spectroscopic measurements point to the presence of MoO, MoO_2, MoO_3 ions.

The diluted gases and the gas products of the above mentioned reactions are impurities in the melt and assist a gas inclusions formation in the crystals. Here are two possibilities:

1. As rule, dilution of gases is decreased with the temperature. The liberated gases form the bubbles. The crystal catches the bubble existed in the melt.
2. A nuclear bubble forms on the interface, grows and catches by the crystal.

The surface energies estimation [16.83] deduced that the interface is not an effective heterogeneous site for bubble formation. We agree that this deduction is correct for a flat interface but cavities on the interface can be effective bubble nucleation spots. In any case, the melt layer near the interface has to be preferable for the bubble formation because of enrichment of the diluted

gas rejected by the growing crystal. Direct experiments of the melted zone quenching [16.84] improved this mechanism of the bubble formation.

As other impurities, bubbles can form striations, parallel to the interface. The striations are concerned with the variations of growth rate and captures of the bubbles situated in the melt layer near the crystallization front. Sometimes it is a result of constitutional super cooling. Sometimes long tube similar bubble can be found in the corundum crystals. A mechanism of this type bubble formation suggested in [16.85, 86].

In each case, the caverns on the interface, formed as a result of morphological stability loss, provokes the bubbles capture, especially for the big growth rate. In our experiments [16.5, 6, 87] with ribbons and tubes grown by TPS in the ***C***-direction the following results were obtained. At the crystallization rate of order of 0.2 mm/min the bubble practically were absent. In [16.88] the critical growth rate (0.5 mm/min for sapphire) has been calculated below which a foreign particle is not trapped by the grown crystal. The interface is plane below this rate. At crystallization rates 0.75–1.5 mm/min the bubble distribution is in the shape of a treelike pile-up with a branch diameter of up to 1 mm (Fig. 16.33). The ends of ribbon are bubbles free, probably, because of gas diffusion to the melt surface and leaving of the melt. The same result was obtained in [16.83] where small diameter crystals were bubbles free.

The distribution of bubbles over a specimen section normal to the growth direction is shown in Fig. 16.34a,b. The following explanation is proposed for the bubble distribution observed. The plane interface becomes morphologically unstable. Macroscopic concavities, with a diameter to 1 mm, arise on the crystallization front; these concavities are characterized by an enhanced trapping of bubbles. We suppose that the change of position of the concavities on the crystallization front with time depends on the pattern of the convective flows in the melt that leads to the bubble distribution shown in Figs. 16.33 and 16.34a. This process is in accordance with the *Mullins* and *Sekerka* [16.20] theory for the lowest frequencies. When growing shaped sapphire crystals at rates of 1–3 mm/min the interface has, as a rule, a convex central part and concave peripheral sections that traps the bubbles (Fig. 16.34b).

As the growth rate is increased further, the entire solid–liquid interface becomes unstable. The crystallization front becomes faceted, with the new interface shape becoming stabilized by the faceting. Figure 16.35

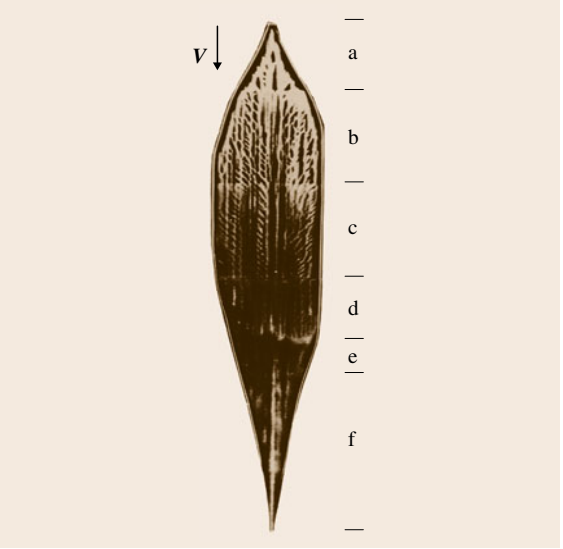


Fig. 16.33 Bubbles in a sapphire ribbon pulled with step changes in the rate ***V***: the *arrow* indicates the growth direction, ***V*** mm/min = 0.75 (a); 1.0 (b); 1.25 (c); 1.5 (d); 1.75 (e); 2.0 (f)

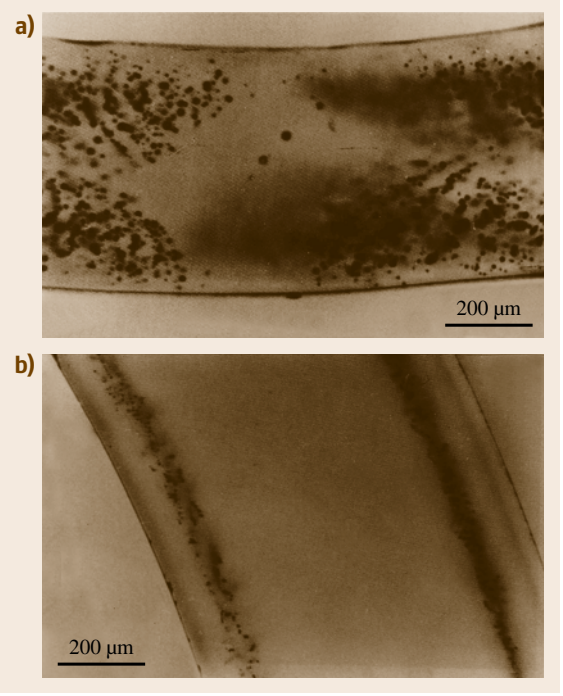


Fig. 16.34a,b Cross section of sapphire ribbon pulled with rate of ***V*** (mm/min) = 0.75 **(a)**; 2.0 **(b)**

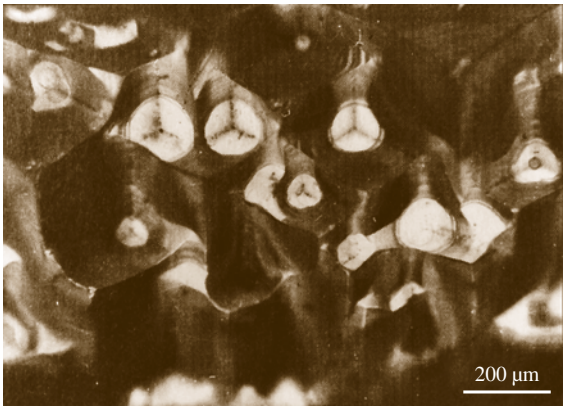


Fig. 16.35 Interface of decanted sapphire ribbon grown with $V = 3$ mm/min

shows the decanted crystallization front of a tube faceted by rhombohedral planes. The bubbles distribution in the crystal is a hexagonal pattern and corresponds to the positions of grooves on the interface. Always the bubble agglomerations correspond to cavity positions. The decanted crystallization front of a tube faceted by the $\{11\bar{2}0\}$ and $\{10\bar{1}1\}$ planes is shown in Fig. 16.36a. From geometrical considerations

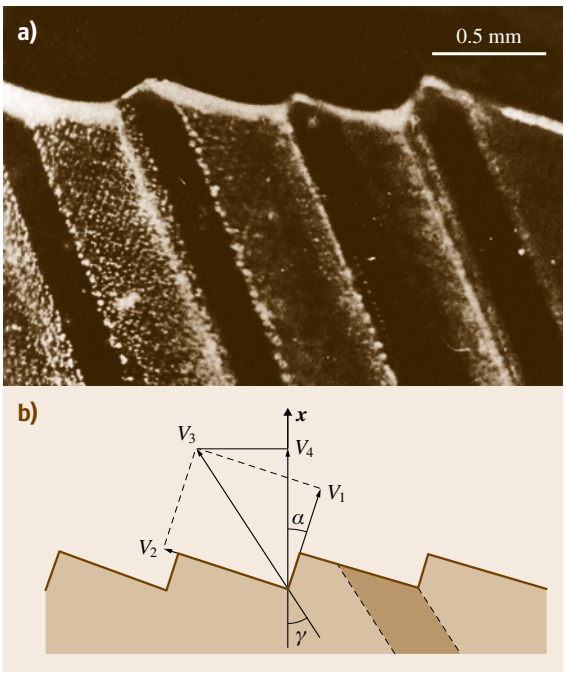


Fig. 16.36 **(a)** View and **(b)** schematic of the decanted crystallization front of a tube pulled at $V > 5$ mm/min

(Fig. 16.36b), it is apparent that the angle γ between the crystal pulling direction and the direction of the band of void pile-up depends on the ratio of two mentioned faces growth rates.

Solid inclusions are the second type of inclusions. Container material gives metal particle inclusions, sometimes as a result of complicated chain of chemical reactions mentioned above – volatile oxides formation, gas transport in the melt and decomposition of oxides with metal inclusion formation. Experiments show that the small particle of container metal (Ir, Mo), as rule, presents at the crystal. Innumerable experimental data demonstrate that the density of small dimensions (about 10 μm) inclusions (bubbles and metal particles) is a few orders of magnitude greater than of large dimensions (about 1000 μm) ones. The low growth speed and low gradients favor to crystal growth with minimum inclusions. Here is an example (American 80/50 standard) of bubbles and solid inclusions requirement for window-grade corundum: maximal allowable size is 500 μm, and maximal allowable sum of diameters within any 20 mm – diameter circle is 1000 μm. As rule, modern technology of TPS sapphire meets this requirement.

Dislocations, Low Angle Grain Boundaries, Internal Stresses

Four possible mechanisms of dislocation appearance in the corundum crystals can be postulated:

1. Intergrowth from seed
2. Formation on rough defects (inclusions, grain boundaries, twins) during growth
3. Condensation of vacancies during growth and cooling
4. Plastic deformation during growth and annealing.

Theoretically all dislocations can be identified. The dislocation identification of the first and the second types is evident. The third type dislocations, as rule, have a circle shape because they are a result of collapse of flat round discs obtained by a condensation of nonequilibrium vacancies. The geometry of the last type dislocations depends on two plastic deformation glissile systems $\{0001\}\ \langle 11\bar{2}0\rangle$ and $\{11\bar{2}0\}\ \langle 10\bar{1}0\rangle$ in the corundum crystals. The first source can be eliminated by necks formation. The second one – by crystal growth without rough defects. The third mechanism concerned with a fundamental physical phenomena, but their density are not significant for the corundum crystals. As to the plastic deformation, it is a main source of dislocations in the corundum crystals.

The defect structure of TPS crystals is formed as a result of complex interactions of growth, in situ annealing and cooling. A systematic investigation of the defect structure of TPS grown sapphire crystals was carried out both by the optical polarization method and by the technique of widely diverging x-ray beams [16.5, 6, 87]. The tube samples with diameters of 4–40 mm and wall thickness in the range 0.5–3 mm were investigated.

It has been established that, in the absence of low-angle grain boundaries propagating from the seed, the initial part of the crystal does not contain subgrain (or low-angle grain) boundaries. Then, as the crystal grows the dislocation density increases and subgrain boundaries are formed. The disorientation of adjacent subgrains increases with distance from the seed, reaches a certain limit, and then decreases slightly with further growth. The decrease is probably associated with a rearrangement of the subgrain structure; i. e. subgrains with large disorientations branch into a series of subgrain boundaries with smaller disorientations. In addition, there is a decrease in the density of subgrain boundaries which are at large angles to the growth direction. The subgrain boundaries which remain are approximately parallel to the growth direction; the density of these boundaries (with disorientation as high as 5−10° stays constant.

It should be noted that, at high crystallization rates, crystals which are free of low-angle grain boundaries can sometimes be grown. This is probably explained by the fact that the time spent by the growing crystal in the plastic zone is not long enough for polygonization processes to occur. The presence of bubbles is a source of additional stresses which gives rise to dislocation generation and boundary formation. Sub grain boundaries are frequently observed to form along planes of bubbles pile-up. So, we can conclude that the quality of crystals at the beginning, at lower temperature gradient, was better.

Our experience of sapphire crystals growth by different techniques, TPS included, allows a statement that only temperature gradient less than 2 K/mm gives the possibility to grow the crystals without low angle boundaries and the dislocation density on the level $\leq 10^3\ \mathrm{cm}^{-2}$. Certainly, the dislocation density is a relative characteristic of crystal because the crystal quality can be characterized only taking into account, as minimum, six dependent parameters:

1. The dislocation density
2. The density of low angle boundaries
3. The degree of subgrain disorientation
4. Residual stresses value
5. Twins
6. Impurity inhomogeneities.

Twins

In the temperature lower than 800 °C single crystal sapphire is essentially brittle and is not deformed by usual dislocation mechanism. A twinning is only mode of deformation. The following two main rhombohedral twin systems in sapphire were identified: $\{01\bar{1}2\}\ \langle 0\bar{1}11\rangle$, $\{0\bar{1}14\}\ \langle 02\bar{2}1\rangle$.

Twinning process consists of two distinct stages: the twin nucleation and the twin growth. The nucleation stress is higher than growth stress. In [16.89] the nucleation stress for 600 °C was determined experimentally. It is high and strictly depends on surface treatment. It was found as 13–18 $\mathrm{kg/mm}^2$ for polished specimens and 36–41 $\mathrm{kg/mm}^2$ for polished and heat treated ones. During growth the stress of twin formation has to be average. It corresponds to the residual stress $\approx 20\ \mathrm{kg/mm}^2$, where the twins can be more often found.

Faceting, Inhomogeneities of Impurity

Faceted growth is a normal mode of some growth techniques. The singular faces appearance on the interface in CZT is not very important for sapphire growth but assists nonhomogeneity in ruby growth because the coefficient of chrome distribution is different for faceted and nonfaceted interface. But for TPS faceting may be serious defects.

The geometrical form of TPS tubes can differ slightly from ideal for reasons of a crystallographic nature. According to the Curie theorem, in the process of growth, there is an interaction between the crystal symmetry and that of the medium (i. e. the thermal environment in which the crystal grows). In the grown crystal, only those elements of symmetry are exhibited which are common both for the crystal and for the medium. That is the reason why grown crystals are faceted depending on the orientation. If a sapphire tube is pulled in the directions $\langle 10\bar{1}0\rangle$, $\langle 11\bar{2}0\rangle$ or intermediate ones with $\rho = 90°$ (ρ is the angle between the $\boldsymbol{C}$-axis and the pulling direction), the close-packed basal plane (0001) becomes parallel to the growth direction and facets the tube [16.5, 6, 87]. If ρ differs slightly from 90°, a steplike faceting by the basal plane appears on the lateral surface of the tube. Tubes grown in the [0001] direction are faceted on the outside by $\{11\bar{2}0\}$ planes and on the inside by $\{10\bar{1}0\}$ prismatic planes. Faceting is reduced if the temperature gradient at the

interface increases. The faceting can be explained because of supercooling that singular face needs to grow with the same speed as an isothermal part of interface.

Impurity inhomogeneities are important for ruby crystals. There are macroscopic and microscopic periodic inhomogeneities (striations) along axes of growth. Macroscopic ones concerned with the impurity concentration changing during the growth because of the coefficient of distribution that is not equal of one. TPS allows growing of crystals with macroscopically homogeneous distribution of impurity. Microscopic inhomogeneity concerned with the periodic changing of growth parameters or constitutional supercooling.

Growth Direction

The corundum crystal growth in the direction of ***C***-axis is very difficult for all techniques of the melt growth, except TPS. TPS allows growing of all profile crystals in ***C***-direction without any problems. And what is more, if we grow corundum filaments without seeds, the spontaneous orientation of the filament coincides with ***C***-axis. What is the reason? For many melt growth techniques the growth in the ***C***-direction requires an appearance of the singular ***C***-plane on the interface. ***C***-plane has the lowest growth speed. TPS crystals, the filaments especially, grow with high speed. The interface loses morphologic stability and is faceted by the rhombohedral faces, as it is shown on Fig. 16.35. So, ***C***-plane does not participate in the growth. As for filament orientation, the orientation of ***C***-axes is the most preferable orientation for its growth with respect to Curie principle. On the other hand, the filament interface also is faceted by the rhombohedral faces.

16.7.3 Applications

Special Windows

Application for modern airborne optical reconnaissance systems is one of the most impressive fields of TPS sapphire using [16.8]. Practically TPS does not have any competitors here. Below are the evidences that TPS sapphire meets all requirements for this application:

1. The maximal dimensions achieved are $315 \times 480\,\mathrm{mm}^2$ [16.90]. It is necessary up to 750 mm diameter.
2. It has *high optical transmission* in the 3–5 μm wavelength atmospheric transmission window.
3. Sapphire has *a hardness 9 on the Moose scale* (the hardness of diamond is 10). It is the most durable commercially available infrared window material. It has the best resistance to erosion by rain and sand of any available window materials.
4. It also has *excellent thermal shock resistance*. But its thermal shock resistance is limited by loss of mechanical strength at high temperature from $70\,\mathrm{kg/mm}^2$ at room temperature to $20\,\mathrm{kg/mm}^2$ at 600 °C. Doping or ion implantation with Mg, Ti can double the compressive strength at 600 °C. Heat treatment at 1450 °C in an air atmosphere enriched with oxygen increases compressive strength by 1.5 times. Neutron irradiation with 1×10^{22} neutrons increases the ***C***-axes compressive strength by a factor of 3 at 600 °C.
5. It is available routinely with *minimal optical scatter*.
6. *High refractive index uniformity* is achieved because of simple oxide composition. For stringent optical applications, ***C***-axes optics is preferred as this is zero birefringence orientation.

Domes

The requirements for rocket nose cones correspond mentioned above ones. The traditional technique of dome production is a mechanical treatment of big sapphire crystals. The effort of production concerned with minimization of treatment by a growth of crystals having a shape close to dome. TPS has suggested some successful examples of this kind [16.80, 81, 91].

Substrates

An application of sapphire in electronics as substrate for silicon on sapphire devices was rather large at 1970s. In that case the face $\{1\bar{1}02\}$ was used. The requirements were not very rigid. But since 1990s, sapphire has been becoming the main substrate material for blue and white laser diodes. The face {0001} is used for the epitaxy. The requirements to the wafers concerning a crystal structure and orientation as well as polishing quality are very high. Sometimes special misorientation of wafer is used to get better deposited layer. It is evident, that this TPS application is very promising. But practically there are no publications concerning this topic, except rare ones [16.92], probably because of technological secrets.

Construction Material

Sapphire is increasingly becoming the material of choice for engineers faced with the design challenges of extreme conditions, such as those found in high-temperature, high-pressure or aggressive chemical environment. There are a lot of examples of this TPS sapphire product using in the former Saphikon (now

Saint-Gobain Crystals) catalog. The industrial technique of welding of sapphire pieces is developed there. Sapphire tubes, plates and more complicated assemblies are used a superior alternative to quartz, alumina, and silicon carbide: in semiconductor processing application (plasma containment tubes, process gas injectors, thermocouple protectors); in spectroscopy and chemical and biological analysis; lamps and lamp envelopes (high intensity lamps, flash-lamps, ultraviolet sterilizations); GaAs backer/carriers; mail sorting optical windows.

16.8 TPS Silicon Growth

Silicon is the second example of the TPS successful industrial application. But this case is not similar to the sapphires one. All numerous attempts to grow shaped Si crystals of electronic grade quality have not been successful because shaped silicon is characterized by the presence of a defect structure influencing its electronic properties. At the same time, a quality of big surface thin sheets obtained is acceptable for no expensive solar cells industrial production. We carried out a complex investigation of shaped ribbons and tubes defect structures [16.93, 94]. The aims of these investigations were to understand why it is difficult to obtain a single crystal structure as well as what is an electric activity of different defects. Its influence on the lifetime of secondary charge carriers is of particular importance, since the efficiency of solar elements is determined primarily by the lifetime of the secondary carriers. It is well known that inhomogeneity of the properties results from the inhomogeneous distribution of electrically active defects. The processes occurring at the solid–liquid (S–L) interface essentially affect formation of defects and their electronic properties as well. The simultaneous study of electric and photoelectric properties of sheet and tube crystals, its defect structure and the S–L interface was carried out. The graphite and the quartz were used as materials for crucibles and the graphite – for shapers.

16.8.1 Shaped Silicon Structure

Shaped silicon crystals possess characteristic defects of their crystalline structures including flat boundaries (most often those of the twinning type), dislocations and pileups thereof as well as SiC particles and particle-aggregations. As a result of twinning along intersecting planes, which can be observed at the initial stage of growth, a stable and quasi-equilibrium structure characterized by existence of defect areas (flat boundaries) perpendicular to the tape plane and parallel to the pulling direction. In this case the silicon tape surface orientation is {110} and the crystallographic axis ⟨211⟩ coincides with the direction of pulling. Such orientation is formed and maintained irrespective of the seed orientation and can be attained directly at the seed–crystal contact boundary in case the seed orientation is {110} ⟨211⟩ or a stable-structure section of the previously grown silicon tape is used as a seed. Figure 16.37 gives a photograph of the surface of a silicon tape of a stable defect structure: SiC inclusion surrounded with dislocation pileups can be observed on the tape surface.

As a result of x-ray structure analysis it was established that the orientation of silicon-tape surfaces can deflect within the range of 15° from {110}. Considerable dimensional fragments of defect structures identical to those of tapes are observed in silicon tubes (Fig. 16.38a). The tube-surface orientation in the vicinity of such a fragment deflects from {110} due to surface curvature. This change in orientation does not cause additional structure defects up to the values equal to 15° and as soon as that value reaches 15° surface orientation abruptly changes because there appears *a severely defect spot* that provides an indispensable turn of the crystal orientation in such a way so that the system of twin-boundary planes should be again approximately perpendicular to the tube surface. Either grain boundaries of a general type or dislocation pileups can act as such defect areas (Fig. 16.38b)

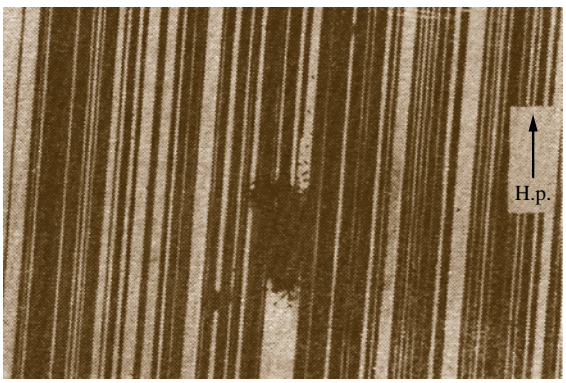


Fig. 16.37 Defect structure of a silicon tape: selective chemical etching pattern, 120×; an SiC inclusion is located in the *center*; the label "H.p." indicates the direction of crystal growth

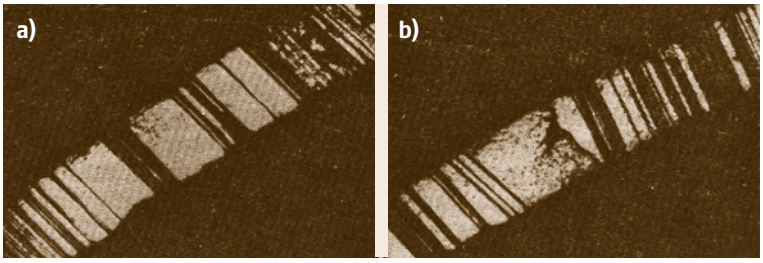


Fig. 16.38a,b Defect structures of silicon tubes (cross-sectional fragments): selective chemical etching pattern, 200×: **(a)** typical structure; **(b)** defect area providing rotation of the system of twin-boundary planes

Apparently, the number of *severely defect spots* and correspondingly the number of fragments of steady structures is determined by the necessity of closing the system of fragments into a cylinder. Since the angular magnitude of an arc of 30° corresponds to the variation of the tube surface orientation of 15° from {110}, the overall number of defect spots is equal to at least twelve, which is experimentally proved. It should also be noted that this linear length of *severely defect spots* along the perimeter of a tube depends little on its diameter, therefore the relation of the volume of *severely defect spots* to crystal volume should quickly decrease with the tube diameter increasing.

Defect structures of silicon tapes were studied by the TEM. With a ≈ 200 magnification, the defect structure pattern proved to be similar to that of selective etching (Fig. 16.37). It was observed that the width of defective areas is equal to ≈ 5 μm and the width of monocrystalline regions between them varies from 10–500 μm. Interpretation of fine structures of defect areas, that look like dark lines parallel to the direction of pulling in the pattern of selective chemical etching (Fig. 16.37) revealed that each area represents a set of microtwins 40–200 Å wide (Fig. 16.39). Small-angle disorientation of monocrystalline sections adjacent to the defect area is caused by such set of microtwins. Disorientation measured by the Kikuchi-line technique varied from 40 to 4°. Besides defect areas of twinning nature, other types of defects were observed in 2% of cases. Those included multilayer lattice defects, small-angle dislocation boundaries as well as separate dislocations and inclusions.

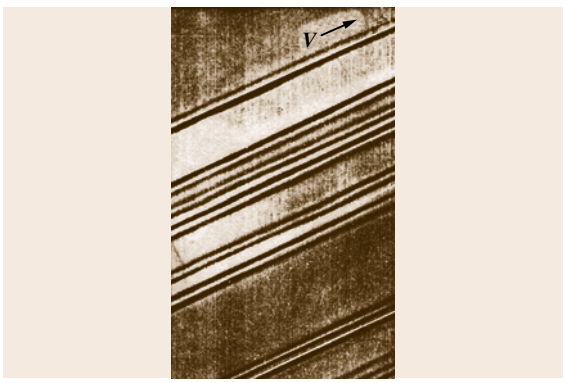


Fig. 16.39 TEM image of a silicon tape: flat defect area structure in the form of a system of microtwins; magnification 160 000; ***V*** denotes the direction of crystal growth

To interpret the defect structure and macroscopic pattern of profiled silicon crystal growth, a model, according to which the crystallization front tends to be shaped by the most slowly growing crystal faces {111} while high rates are provided by availability of inlet angles with their vertexes coinciding with twin boundaries, was postulated (Fig. 16.40a). To check the model offered, experiments on investigation of the crystallization front shape visualized by impulse changes in the crystal-pulling rate were carried out. In this case local changes in crystal thickness follow the changes in crystallization front shape, so does the horizontal hatching observed on the surface of profiled silicon crystals (Fig. 16.40d).

Crystallization front shaping by faces {111} proved to be observed only in the vicinity of high-energy boundaries of a general type and at twin boundaries of higher orders, e.g., {111}–{115}. Crystallization front deflection from the flat one does not exceed 2 μm in the coherent-twin region. The overall crystallization front area made by faces {111} is not large; the major part of the crystallization front follows the crystallization isotherm and corresponds to the face close to {112} and in separate cases to {110} (Fig. 16.40b,c) each of which can grow according to the normal mechanism, i. e., both layer-by-layer and normal mechanisms of growth take place when shaped crystals grow.

The specific features of the crystallization front reviled might be associated with the impurity influence on the face free energy or on the growth kinetics. Therefore it can be assumed that front shaping and perhaps inlet angle formation at twin boundaries are not necessary for high rates of profiled silicon crystal growth to be put

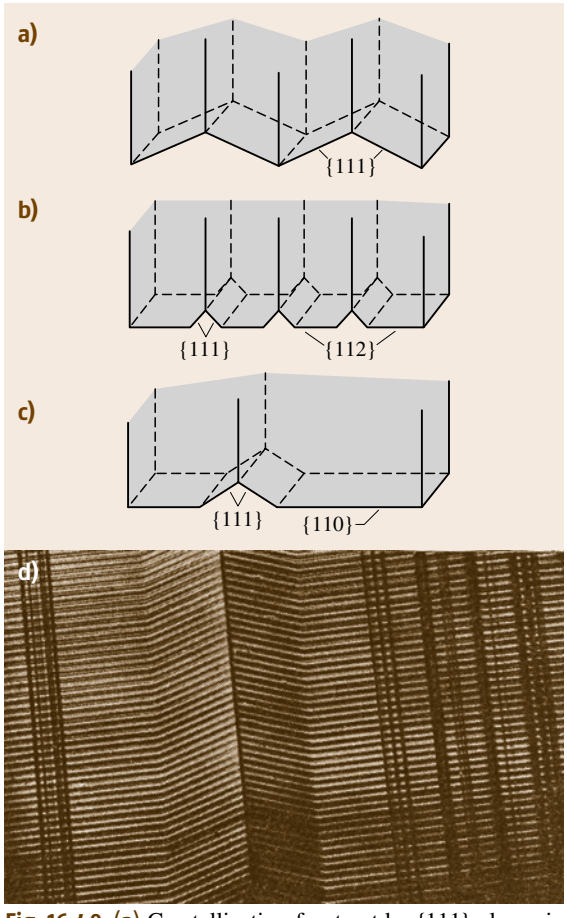


Fig. 16.40 (a) Crystallization front cut by {111} planes in accordance with the postulated model; (b,c) experimentally observed crystallization front shape; (d) correspondence between the crystallization front shape and the horizontal hatching on the surface of profiled crystals

into practice. It can be confirmed by the fact that in separate cases silicon tapes with wide (up to 10–15 mm) monocrystalline areas can be grown.

It was noticed that in the process of silicon tube growth the melt meniscus height strongly influences the character of defect formation in crystals. With the crystallization front in a tube sinking, the number of boundaries of a general type increases, i. e., profile defect structure depends on the interaction efficiency in the crystallization front–shaper system. The shaper influence is mainly determined by the distortions (thermal and capillary) introduced by the silicon carbide layer formed on the operating free edges of a graphite shaper when it interacts with the silicon melt.

Besides such indirect influence on the structure of profiles, silicon carbide entering the crystal subsurface layer in the form of SiC particles greatly affects the quality of the material produced. SiC microcrystals measuring 25–30 μm, produced in the melt meniscus, form a carbide layer growing on the shaper free edges. When bulges appear on the layer the meniscus becomes distorted and on the crystal surface there appear distinctive furrows and in separate cases bulges along the direction of pulling that break when SiC particles and aggregations thereof results from random fluctuations of the crystallization front when particles reaching the size of the meniscus escape the carbide layer. The number and the size of simultaneously entrapped particles depend on the amplitude of front fluctuations and on the mean height of the meniscus. The mechanism of carbide inclusion entrapment offered is confirmed by the results of silicon tube growth when the number of SiC particles entrapped sharply decreases for a high meniscus since the number of particles whose dimensions reach the meniscus height decreases.

The number of carbide inclusions in shaped silicon crystals can be decreases in several ways: by using crucibles made of graphite of high density; by replacing the

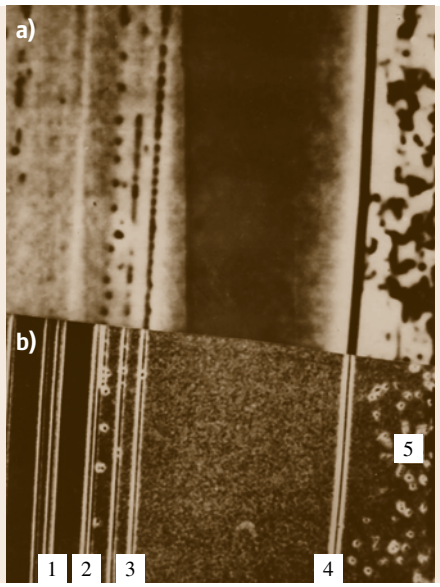


Fig. 16.41a,b The patterns (a) of spatial distribution of the secondary carrier current (EBIC, *dark regions* correspond to increased recombination) and (b) selective chemical etching; recombination boundaries: (1) inactive, (2) intermittent active, (3) low active, (4) high active, and (5) active dislocations

graphite container for crucibles with a protective layer-coated container; by maintaining a high melt meniscus (easy to secure when growing closed profiles). Besides, experiments on alloying shaped silicon with rare-earth elements showed that no SiC inclusions can be found on profile surfaces for any meniscus height in case at least 0.05 mass % of gadolinium dopant is introduced into silicon melt.

16.8.2 Local Electronic Properties of Shaped Silicon

The electric and photoelectric properties of crystals have been studied by local methods at $T = 300\,\mathrm{K}$: electron-beam induced current (EBIC), spreading resistance (SR), light-beam induced voltage (LBIV) and light-beam induced current (LBIC). EBIC–method is the widely used one. In the case of the SR method, the local conductivity of the sample was detected by an acicular probe displaced on the crystal surface with 8 μm step. In this case the spatial resolution of the method was 30 μm. The LBIV method was used for measuring the potential difference at the edges of a sample locally illuminated by a scanning light beam of 5 μm in diameter. This method made it possible to reveal the built-in electric fields caused by the defects of the crystal structure. In order to apply the LBIC method, a p-n junction was prepared or tin and indium oxide film was grown on the silicon surface, and then the current of minority carriers generated by a method analogous to the LBIV

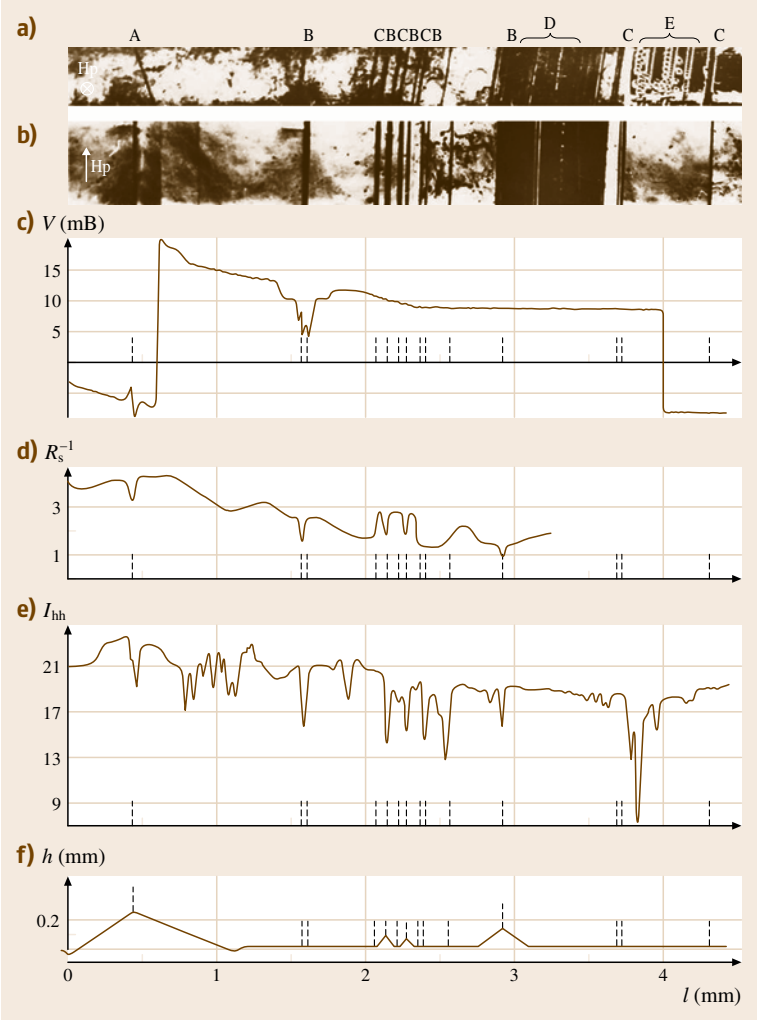


Fig. 16.42 Local study of the defect structure **(a,b)**, electric properties **(c–e)**, and S–L interface shape **(f)** of a silicon ribbon: **(a)** defect structure of the transverse cross section of an etched silicon ribbon, A–E indicate different types of defects, the label "Hp" indicates the growth direction; **(b)** structural defects on the surface of an etched ribbon, the label "Hp" indicates the growth direction; **(c)** distribution of photo-EMF obtained by the LBIV method across the ribbon; **(d)** spatial distribution of crystal conductivity, obtained by the spreading resistance method (arbitrary unit); **(e)** spatial distribution of minority carriers across the ribbon obtained by the LBIC method (arbitrary unit); **(f)** shape of the S–L interface crystal is shown above the curve, and the melt is below; at $l \geq 2\,\mathrm{mm}$ the height h of the S–L interface distortion is expanded by a factor of 10. The *dashed lines* in **(c–f)** show the locations of some twin boundaries in **(b)**

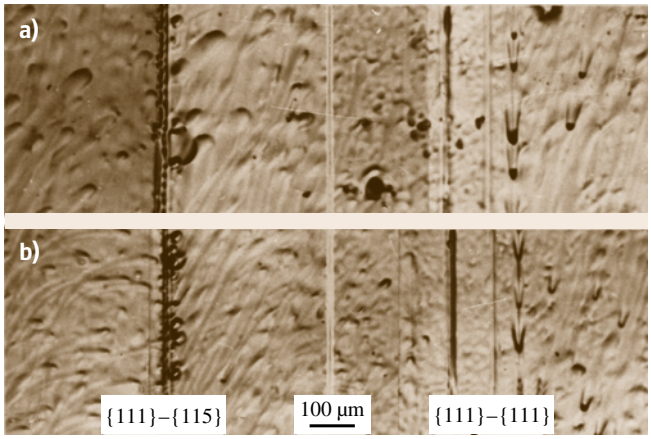


Fig. 16.43a,b Morphology of the melting crystal surface in the region of twin boundaries {111}–{115} at $l = 0.43$ mm, and {111}–{111} at $l = 2.2$ mm. The distances from the melting front are **(a)** 5 mm and **(b)** 3 mm

method was recorded. Effective centers of recombination were revealed by the LBIC method.

The spatial distribution of crystal defects was analyzed by the method of selective chemical etching. In addition, the structure of boundaries was examined with a scanning electron microscope. The morphology of the S–L interface was investigated as it is written above (Fig. 16.40d). Preliminary EBIC investigations of shaped crystals show that the electrical activity of twin boundaries as centers of increased recombination of nonequilibrium charge carriers differs (Fig. 16.41): there are electrically inactive boundaries, which are evidently coherent, boundaries with discontinuous activity, and boundaries of moderate and high activity. In the latter case, the boundaries are evidently incoherent. The combined results are presented on the Fig. 16.42 analyzed in detail in [16.94]. Here are brief results. The most important are defects whose electrical activity, as recombination centers of nonequilibrium carriers, is constant all along the silicon ribbon. It can be seen from comparing the LBIC spectra (Fig. 16.42e) with the pattern of selective chemical etching (Fig. 16.42b), that there are three types of such defects, at least. They are narrow bands of submicrons defects, accumulations or agglomerations of point defects with the coordinate $l = 0.8–1.2$ mm extended along the crystal growth direction. Dislocation etch pits are not visible here. The rows of dislocations denoted by index E in Fig. 16.42a and some twin boundaries are highly electrically active. Twin boundaries are the main defects. Its electric activity, as shown by the analysis in detail, depends on structural properties as well as enriching by impurities.

We have assumed that the decreased melting temperature of boundaries enriched with impurities may affect the S–L interface structure. Therefore, experiments were performed on melting shaped silicon crystals. It has turned out that melting starts on the surface and melt drops are formed in the vicinity of impurity inclusions. Fig. 16.43 shows that their concentration at the boundary with the coordinate $l = 0.43$ mm (Fig. 16.42) is of order of 400 cm^{-1}, which is in accordance with a density of inclusions equal to 10^5 cm^{-2} found along this boundary after crystal cleavage. At the distance 5 mm from the melting front of reference single crystalline regions, separate drops coalesce and make up a uniform melt band of 10 µm in width. The process of melting thus proceeds mainly along the boundary, and a crystal can be divided into two parts by melting.

So, the main defects of the shaped silicon are the following ones: SiC inclusions, block boundaries, acute-angle boundaries, monocrystalline sections with

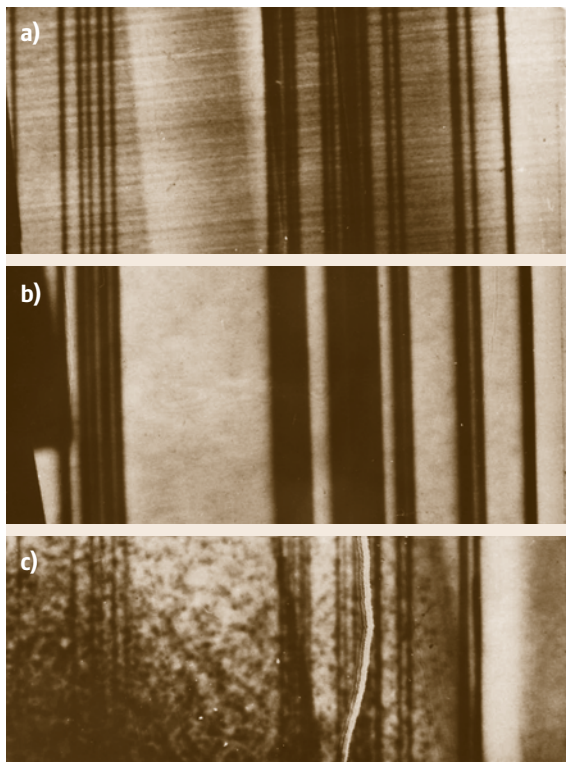


Fig. 16.44a–c Influence of annealing on the EBIC contrast of a silicon strip: **(a)** initial sample; **(b)** annealed at 450 °C for 50 h; **(c)** annealed at 1000 °C for 50 h (130 ×)

reduced lifetime, incoherent twin boundaries, dislocations, and coherent twin boundaries. The electrical activity of the structural defects falls in the order listed: in the region of the SiC inclusion, the lifetime of secondary carriers $\tau \leq 10^{-8}$ s, increasing to a magnitude of the order of 10^{-6} s in monocrystalline regions of Si crystals with a resistivity of the order of 1 Ω cm.

The concentration of electrically active defects may possibly be reduced at the stage of crystal growth by improving the procedure. Decreasing of electrical activity of crystal defects in postgrowth treatment is a promising method of increasing the efficiency of solar elements. It has been established that annealing crystals at temperature of the order of 500 °C is a largely ineffective. In the EBIC spectra shown in Fig. 16.44, the regions of increased recombination of nonequilibrium carriers in the vicinity of the boundaries are seen to be only slightly broaden. However, annealing at 1000 °C leads to an increase in lifetime of the secondary carriers as a result of the decrease in electrical activity of the boundaries.

16.8.3 TPS Silicon Growth

The first experiments in the field of shaped silicon growth, especially for solar cells, were carried out more than thirty years ago. More than twenty different techniques have been tested. Information concerning this activity with numerous bibliographies can be found in [16.11–13]. The recent situation was analyzed in [16.95] review where four shaped silicon growth techniques are estimated as promising. There are TPS-EFG production of octagon profiles of 5 m length with 8 faces of 12.5 cm width and 0.3 mm thickness: RWE Schott Solar produces more than 200 000 kg/year with solar cell efficiency 14%. There is no any sawing loss because a laser cutting is used. In the frame of R&D project, a growth of tubes with the diameter of 0.5 m was realized [16.96].

Three other techniques are the following ones:

1. Evergreen Solar uses the string ribbon technique – a vertical growth from free melt surface between two metal strings
2. AstroPower uses the Silicon Film technique – a horizontal growth on a substrate with separation of the ribbon from the substrate
3. ECN uses RGS – the horizontal growth on a substrate when the substrate is used as a part of the solar cell.

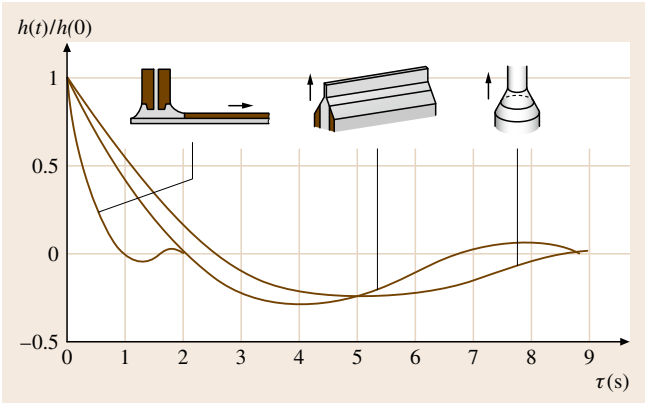


Fig. 16.45 Calculated curves of attenuation of crystallization front perturbation for a silicon tape

We suggested this variant of shaped silicon growth 22 years ago with the name two shaping elements technique, TSET [16.97]. The scheme of the technique can be seen on the Fig. 16.45. When a graphite cloth is used as the substrate we title the technique the silicon on cloth, SOC.

At the conclusion of the silicon shaped growth discussion, let us show how the stability theory can be used for a crystal growth process characterization. On the Fig. 16.45 the curves of attenuations of crystallization front perturbation are presented. The special experiments were carried out for TSET. The relocation time was calculated as a function of the growth speed. It was found that it is decreased with the speed increasing up to the growth speed 6 cm/min and is not changed with the farter speed increasing. Two speeds (1.5 and 6 cm/min) were used in the experiments. The surface quality of the ribbons grown with the speed 6 cm/min was much better. The amplitude of the roughness was five times less.

16.9 TPS Metals Growth

What are the results of TPS application for metals and alloys? On the basis of our big experience in the field, we can conclude: when we find a material for the shaper (both wetted or nonwetted, but chemically inert) we can pull profiles from pure metals and eutectic alloys. The profiles have good quality surfaces (sometimes like a mirror). It is easy to grow low-melting metal single crystals by this technique. But there is no any technical

application. As for refractory metal single crystals, for instance Mo that is used for foil production, it is very difficult to find a material for shaper.

Polycrystalline profiles could be used for many applications, for instance heat exchangers from alloys of aluminum (Fig. 16.28). But when we need alloys of high mechanical properties, the composition of alloys is complicated. There is a big gap between the temperatures of liquidus and solidus. Dendrite crystals appear in the meniscus and the problem of profile pulling is rather difficult both from point of view of surface quality and internal structure. So, TPS is difficult to compete with extrusion. On the other hand, the structure and mechanical properties of profiles are better than ones of cast profiles. We think the history is not finished yet. The problem of industrial application is not easy and a lot of efforts will need from numerous researchers. First of all alloys of special compositions have to be developed. Our success in the TPS application for the special steel [16.66] (Fig. 16.29a) and never published before stainless steel with aluminum rib (Fig. 16.29b) were promising but unfortunately have not been continued.

16.10 TPS Peculiarities

1. The crystals have the shape that we need for the most rational practical using.
2. The technique can be applied for any matters if a material for the shaper (both wetted or nonwetted, but chemically inert) is found.
3. The range of crystal dimensions is large: filaments of 0.02 mm diameter; tubes of 0.5 m diameter; plates $480 \times 320 \times 10\,\mathrm{mm}^3$.
4. A growth speed, as rule, is much higher than in other crystal growth techniques.
5. Crystal, as rule, has a special structure concerned with the interface faceting.
6. Shaper influences on the interface shape.
7. The separation of growth zone from the melt in the crucible allows realization of continuous feeding by the raw material during growth process. As a result, we can have a short time of the melt presence before the growth, if it is necessary. Periodical change of the doping also is possible.
8. A distribution of impurities along the axis of crystal is more uniform. Indeed, if a coefficient of distribution of impurities is not equal to one during crystal growth a quantity of impurities changes along an axis of crystals in the most of crystal growth techniques. A solution of this problem can be found by localization of the melt at the zone of growth without stirring it with other melt volume. This situation we have, for instance, in using of additional crucible of small volume for CZT. The more effective result gives the capillary feeding at the TPS.
9. The using of special systems of capillaries for feeding allows controlling a distribution of impurities at the cross section of crystal.
10. A combination of doped and undoped parts is achieved in the same crystal.
11. The dynamic stability theory, developed for TPS, was successfully used for other CST as well as for analysis of cylindrical pores (negative crystals) growth and the radial instability of vapor whisker growth [16.5, 6].

References

16.1 A. Horowitz, S. Biderman, D. Gazit, Y. Einav, G. Ben-Amaz, M. Weiss: The growth of dome-shaped sapphire crystals by the gradient solidification method (GSM), J. Cryst. Growth **128**, 824–828 (1993)

16.2 D. Petrova, O. Pavloff, P. Marinov: Optical quality and laser characteristics of YAG:Nd crystals grown by the Bridgman–Stockbarger method, J. Cryst. Growth **99**, 841–844 (1990)

16.3 C.S. Bagdasarov: Problems of synthesis of refractory optic crystals. In: *Rost Kristallov*, Vol. 11, ed. by E.I. Givargizov (Transl. Growth of Crystals, Consultants Bureau, New York 1978) pp. 169–195, in Russian

16.4 V.A. Tatartchenko: Growth of shaped crystals from the melt. In: *Encyclopedia of Materials: Science and Technology*, ed. by K.H.J. Buschow, R.W. Cahn, M.C. Flemings, B. Ilschner, E.J. Kramer, S. Mahajan, P. Veyssière (Elsevier Science, Amsterdam 2001) pp. 3697–3703

16.5 V.A. Tatartchenko: Shaped crystal growth. In: *Handbook of Crystal Growth*, Vol. 2b, ed. by

D.T.J. Hurle (North-Holland, Amsterdam 1994) pp. 1011–1110
16.6 V.A. Tatartchenko: *Shaped Crystal Growth* (Kluwer Academic, London 1993)
16.7 V.A. Tatartchenko: The life of Alexander Stepanov and a brief history of shaped crystal growth, J. Jpn. Assoc. Cryst. Growth, **28**, 55–59 (2001)
16.8 V.A. Tatartchenko: Sapphire crystal growth and applications. In: *Bulk Crystal Growth of Electronic, Optical and Optoelectronic Materials*, ed. by P. Capper (Wiley, London 2005) pp. 299–338
16.9 V.A. Tatartchenko: *Stable Crystal Growth* (Nauka–Science, Moscow 1988), in Russian
16.10 P.I. Antonov, L.M. Zatulovskiy, A.S. Kostigov, D.I. Levinzon, S.P. Nikanorov, V.V. Peller, V.A. Tatartchenko, V.S. Juferev: *Preparation of Shaped Single Crystals and Products by Stepanov's Technique* (Nauka–Science, Moscow 1981), in Russian
16.11 G.W. Cullen, T. Surek, P.I. Antonov (Eds.): Shaped crystal growth, J. Cryst. Growth **50**(1), 1–396 (1980)
16.12 J.P. Kalejs, T. Surek, V.A. Tatartchenko (Eds.): Shaped crystal growth, J. Cryst. Growth **82**(1/2), 1–268 (1987)
16.13 J.P. Kalejs, T. Surek (Eds.): Shaped crystal growth, J. Cryst. Growth **104**(1), 1–199 (1990)
16.14 V.A. Tatartchenko: Influence of capillary phenomena on the stability of the crystallization process during the pulling of shaped specimens from the melt, Phys. Chem. Mater. Treat. **6**, 47–53 (1973), in Russian
16.15 V.A. Tatartchenko, G.I. Romanova: Stability of crystallization by Verneuile technique, Sov. Single Cryst. Tech. **2**, 48–53 (1973), in Russian
16.16 V.A. Tatartchenko: Stability of profiled pattern crystallization from the melt, 4th Int. Conf. Cryst. Growth Abstr. (Tokyo 1974) pp. 521–522
16.17 V.A. Tatartchenko, E.A. Brener: Stability of crystallization from a melt with a capillary shaper, Izv. Akad. Nauk SSSR, Ser. Fiz. **40**, 1456–1467 (1976), in Russian – Translation in Bull. Acad. Sci. USSR Phys. Ser. **40**, **7**, 106–115 (1976)
16.18 T. Surek: Theory of shape stability in crystal growth from the melt, J. Appl. Phys. **47**, 4384–4393 (1976)
16.19 G.A. Korn, T.M. Korn: *Mathematical Handbook for Scientists and Engineers* (McGraw-Hill, New York 1961) pp. 282–284
16.20 V.W. Mullins, F.R. Sekerka: Stability of the flat interface during crystallization of dilute binary alloys, J. Appl. Phys. **35**, 444–455 (1964)
16.21 V.A. Tatartchenko: Survey of quantitative analyses of the effects of capillary shaping on crystal growth, J. Cryst. Growth **82**, 74–80 (1987)
16.22 L.D. Landau, E.M. Lifchits: *Mecanique des Fluids* (Mir, Moscow 1971) p. 289
16.23 V.A. Tatartchenko, V.S. Uspenski, E.V. Tatartchenko, J.P. Nabot, T. Duffar, B. Roux: Theoretical Model of Crystal Growth Shaping Process, J. Cryst. Growth **180**, 615–626 (1997)
16.24 V.A. Tatartchenko, V.S. Uspenski, E.V. Tatartchenko, B. Roux: Theoretical investigation of crystal growth shaping process with the wetting boundary condition, J. Cryst. Growth **220**, 301–307 (2000)
16.25 G.A. Satunkin, V.A. Tatartchenko, V.I. Shaitanov: Determination of the growth angle from the shape of a crystal lateral face and solidified separation drops, J. Cryst. Growth **50**, 133–139 (1980)
16.26 H.S. Carslaw, J.C. Jaeger: *Conduction of Heat in Solids* (Clarendon, Oxford 1959) p. 148
16.27 K.J. Bachmann, H.J. Kirsch, K.J. Vetter: Programmed Czochralski growth of metals, J. Cryst. Growth **7**, 290–295 (1970)
16.28 A.A. Alioshin, N.I. Bletscan, S.I. Bogatyriov, V.N. Fedorenko: Silicon furnace components for microelectronic applications fabricated from shaped silicon tubes, J. Cryst. Growth **104**, 130–135 (1990)
16.29 V.A. Tatartchenko, A.I. Saet: Thermal regime of profile pulling from melt, J. Eng. Phys. **13**(2), 255–258 (1967), in Russian – Translation in J. Eng. Phys. USA
16.30 G.I. Romanova, V.A. Tatartchenko, N.P. Tichonova: Stability of crystallization at the crystal growth by the gas flame technique, Trudi Goi **54**(188), 10–13 (1976), in Russian – Sov. Proc. State Opt. Inst., Leningrad
16.31 V.A. Borodin, E.A. Brener, V.A. Tatartchenko: Investigation of the crystallization process in the Verneuile technique, Cryst. Res. Technol. **16**, 1187–1197 (1982)
16.32 V.A. Borodin, E.A. Brener, T.A. Steriopolo, V.A. Tatartchenko, L.I. Chernishova: Growing single crystal corundum tubes by Verneuile technique in stable conditions, Cryst. Res. Technol. **16**, 1199–1207 (1982)
16.33 V.A. Borodin, E.A. Brener, V.A. Tatartchenko, V.I. Gusev, I.N. Tsigler: Automation of the Verneuile technique on the basis of stability analysis, J. Cryst. Growth **52**, 505–508 (1981)
16.34 E.A. Brener, G.A. Satunkin, V.A. Tatartchenko: Some aspects of the macroscopic theory of oriented crystallization from the melt. IV. The floating zone techniques, Acta Phys. Acad. Sci. Hung. **47**, 159–165 (1979)
16.35 E.A. Brener, G.A. Satunkin, V.A. Tatartchenko: Macroscopic theory of crystallization from a melt with capillary shaping. The floating-zone method. In: *Growth of Crystals*, Vol. 14, ed. by E.I. Givargizov (Nauka Science, Moscow 1983) pp. 153–158, in Russian – Translation in *Growth of Crystals*, Vol. 14 (Consultants Bureau, New York 1987), 181–186

16.36 E.A. Brener, V.A. Tatartchenko, V.E. Fradkov: Differences between the mass transfer processes at a crystal surface near a three-phase line during crystallization and melting, Kristallografiya **27**, 205–206 (1982), in Russian – Translation in Sov. Phys. Crystallogr. **27** 127–128 (1982)
16.37 I.A. Lesk, A. Baghdadi, R.W. Gurtler, R.J. Ellis, J.A. Wiese, M.G. Coleman: Ribbon-to-ribbon crystal growth, Proc. 12th IEEE Photovolta. Spec. Conf. (IEEE, New York 1976) pp. 163–167
16.38 V.A. Tatartchenko, A.I. Saet, A.V. Stepanov: The shape of liquid column on producing of specified shape product by crystallization of melt, Proc. 1st Conf. Stepanov's Growth Semiconduct. Single Cryst. (Ioffe Phys.-Techn. Inst., Leningrad 1968) pp. 83–97, in Russian
16.39 V.A. Tatartchenko, A.I. Saet, A.V. Stepanov: Boundary conditions of capillary shaping at crystallization from melts, Izv. Akad. Nauk SSSR, Ser. Fiz. **33**, 1954–1959 (1969), in Russian – Translation in Bull. Acad. Sci. USSR, Phys. Ser. USA
16.40 N.K. Adam: *The physics and Chemistry of surfaces* (Clarendon, Cambridge 1930)
16.41 S.V. Tsivinskii, P.I. Antonov, A.V. Stepanov: Melt column form in crystal pulling process, Sov. Phys. Tech. Phys. **15**, 274–277 (1970), American translation of Sov. Zh. Tek. Fiz.
16.42 S.V. Tsivinskii: Application of capillary phenomena theory to manufacturing articles of predominant shape directly from the melt by Stepanov's method, J. Eng. Phys. **5**(9), 59–63 (1962), in Russian – Translation in J. Eng. Phys. USA
16.43 V.A. Tatartchenko, A.V. Stepanov: Calculation of the height of liquid column in crystal growth from melts, Izv. Akad. Nauk SSSR Ser. Fiz. **33**, 1960–1962 (1969), in Russian – Translation in Bull. Acad. Sci. USSR, Phys. Ser. USA
16.44 I.S. Pet'kov, B.S. Red'kin: Stability analysis of movable menisci, J. Cryst. Growth **104**, 20–22 (1990)
16.45 V.A. Tatartchenko, J.P. Nabot, T. Duffar, E.V. Tatarchenko, B. Roux: Some problems of stability of movable meniscus, J. Cryst. Growth **148**, 415–420 (1995)
16.46 L.L. Kuandykov, P.I. Antonov: Shaped melt column optimal choice on the basis of an equilibrium growth angle value, J. Cryst. Growth **222**, 852–861 (2001)
16.47 V.A. Tatartchenko: Capillary shaping in crystal growth from melts, I. Theory, J. Cryst. Growth **37**, 272–284 (1977)
16.48 V.A. Tatartchenko, G.A. Satunkin: Capillary shaping in crystal growth from melts, II. Experimental results for sapphire, J. Cryst. Growth **37**, 285–288 (1977)
16.49 V.A. Tatartchenko, S.K. Brantov: A model for a capillary shaper under conditions of weightlessness, Izv. Akad. Nauk SSSR, Ser. Fiz. **40**, 1468–1484 (1976), in Russian – Translation in Bull. Acad. Sci. USSR Phys. Ser. USA **40**7, 116–129 (1976)
16.50 Y.A. Osipian, V.A. Tatartchenko: Crystal growth from melt by capillary shaping technique, Adv. Space Res. **8**(12), 16–34 (1988)
16.51 M.S. Agafonov, G.A. Gavrilov, L.I. Gubina, V.A. Kislov, L.V. Leskov, Y.B. Levin, V.V. Savichev, V.A. Tatartchenko, N.I. Timofeeva: Crystallization from the melt by the Stepanov method under zero-gravity conditions, Izv. Akad. Nauk SSSR, Ser. Fiz. **43**, 1935–1939 (1979), in Russian – Translation in Bull. Acad. Sci. USSR, Phys. Ser. **43**(9), 124–128 (1979)
16.52 V.A. Tatartchenko, S.K. Brantov, L.V. Leskov, V.L. Levtov, M.S. Agafonov: Experimental results of the crystallization of indium by the Stepanov method in conditions of micro-gravitation, Izv. Akad. Nauk SSSR, Ser. Fiz. **49**, 708–710 (1985), in Russian – Translation in Bull. Acad. Sci. USSR, Phys. Ser. **49**(4), 77–79 (1985)
16.53 V.A. Tatartchenko: Stability of melt crystal growth under microgravity condition, Adv. Space Res. **11**(7), 307–321 (1991)
16.54 L.A. Slobozhanin, M.A. Svechkareva, V.A. Tatartchenko: Stability of melt meniscus during growth of crystals by the technique of pulling from shaper under zero-gravity conditions, J. Cryst. Growth **133**, 273–280 (1993)
16.55 J.A. Burton, P.C. Prim, W.P. Slichter: The distribution of solute in crystals grown from the melt. Part I. Theoretical, J. Chem. Phys. **21**, 1987–1991 (1953)
16.56 J.C. Swartz, T. Surek, B. Chalmers: EFG (edge-defined, film-fed growth) process applied to the growth of silicon ribbons, J. Electron. Mater. **4**, 255–264 (1975)
16.57 S.K. Brantov, V.A. Tatartchenko: On effective coefficient of impurity distribution at the Stepanov thin-walled crystal growth (EFG), Cryst. Res. Technol. **18**, K59–K64 (1983)
16.58 J.P. Kalejes: Impurity redistribution in EFG, J. Cryst. Growth **44**, 329–334 (1978)
16.59 A.V. Stepanov: A new technique of production of sheets, of tubes, of rods with different cross sections from a melt, J. Tech. Phys. **29**, 382–393 (1959), in Russian – Translation in Sov. Phys. Tech. Phys. USA
16.60 A.V. Stepanov: A new technique of products fabrication from a melt, Mech. Eng. Bull. **11**, 47–50 (1959), in Russian
16.61 A.L. Shakch-Budagov, A.V. Stepanov: A new technique of production of sheets, of tubes, of rods with different cross sections from a melt, J. Tech. Phys. **29**, 394–405 (1959), in Russian – Translation in Sov. Phys. Tech. Phys. USA
16.62 B.M. Goltsman, A.V. Stepanov: A technique of production of sheets and tubes directly from a melt of aluminum and its alloys, Bull. Acad. Sci.

USSR, Metall. Fuel Ser. **5**, 49–53 (1959), in Russian
16.63 B.M. Goltsman: A pulling of crystalline sheets and tubes from a melt, Opt. Mech. Ind. **11**, 45–46 (1958), in Russian
16.64 A.V. Stepanov: *The Future of Metals Machining* (Lenizdat, Leningrad 1963), in Russian
16.65 V.A. Tatartchenko, A.V. Stepanov: The installation for investigation of crystallization parameters influence on the structure properties of crystallized specimens. In: *Machines and Devices for Testing of Materials*, ed. by G.V. Kurdiumov (Metallurgy, Moscow 1971), in Russian
16.66 V.A. Tatartchenko, V.V. Vakhrushev, A.S. Kostygov, A.V. Stepanov: Profile shaping in iron alloys of high carbon content, Izv. Akad. Nauk SSSR, Ser. Fiz. **35**, 511–513 (1971), in Russian – Translation in Bull. Acad. Sci. USSR, Phys. Ser. USA
16.67 G.V. Sachkov, V.A. Tatartchenko, D.I. Levinzon: Control of the capillary shaping process for single crystals grown from a melt, Izv. Akad. Nauk SSSR, Ser. Fiz. **37**, 2288–2291 (1997), in Russan – Translation in Bull. Acad. Sci. USSR, Phys. Ser.
16.68 H.E. La Belle, A.I. Mlavsky: Growth of sapphire filaments from the melt, Nature **216**, 574–575 (1967)
16.69 H.E. La Belle, A.I. Mlavsky: Growth of controlled profile crystals from the melt. Part 1. Sapphire filaments, Mater. Res. Bull. **6**, 571–580 (1971)
16.70 H.E. La Belle, A.I. Mlavsky: Growth of controlled profile crystals from the melt. Part 2. Edge-defined film fed growth (EFG), Mater. Res. Bull. **6**, 581–590 (1971)
16.71 E.V. Gomperz: Untersuchungen an Einkristalldrähten, Z. Phys. **8**, 184–190 (1922), in German
16.72 H. Mark, M. Polanyi, E. Schmid: Vorgänge bei der Dehnung von Zinkkristallen, Z. Phys. **12**, 58–77 (1923), in German
16.73 E. Grüneisen, E. Goens: Untersuchungen an Metallkristallen, Z. Phys. **26**(4/5), 235–273 (1924), in German
16.74 A.G. Hoyem, E.P.T. Tyndall: An experimental study of the growth of zinc crystals by the Czochralski–Gomperz method, Phys. Rev. **33**, 81–89 (1929)
16.75 A.G. Hoyem: Some electrical properties of spectroscopically pure zinc crystals, Phys. Rev. **38**, 1357–1371 (1931)
16.76 P. Kapitza: The study of the specific resistance of bismuth crystals and its change in strong magnetic field and some allied problems, Proc. R. Soc. Lond. Ser. A, **119**(782), 358–443 (1928)
16.77 H.E. LaBelle: EFG, the invention and application to sapphire growth, J. Cryst. Growth **50**, 8–16 (1980)
16.78 V.N. Kurlov, S.V. Belenko: The growth of sapphire shaped crystals with continuously modulated dopants, J. Cryst. Growth **191**, 779–782 (1998)
16.79 V.A. Borodin, V.V. Sidorov, T.A. Steriopolo, V.A. Tatartchenko: Variable shaping growth of refractory oxide shaped crystals, J. Cryst. Growth **82**, 89–94 (1986)
16.80 J.W. Locher, H.E. Bennet, P.C. Archibald, C.T. Newmyer: Large diameter sapphire dome: Fabrication and characterization, Proc. SPIE **1326**, 2–10 (1990)
16.81 V.A. Borodin, V.V. Sidorov, S.N. Rassolenko, T.A. Steriopolo, V.A. Tatartchenko, T.N. Yalovets: Local shaping technique and new growth apparatus for complex sapphire products, J. Cryst. Growth **104**, 69–76 (1990)
16.82 K.S. Bagdasarov: Synthesis of large single crystals of corundum. In: *Ruby and Sapphire*, ed. by L.M. Belyaev (National Bureau of Standards, Washington, DC 1980) pp. 15–38, Translation from Russian
16.83 M. Saito: Gas-bubble formation of ruby single crystals by floating zone melt growth with an infrared radiation convergence type heater, J. Cryst. Growth **71**, 664–672 (1985)
16.84 M. Saito: Growth process of gas-bubble in ruby single crystals by floating zone method, J. Cryst. Growth **74**, 385–390 (1986)
16.85 A.V. Zhdanov, G.A. Satunkin, V.A. Tatartchenko, N.N. Talyanskaya: Cylindrical pores in a growing crystal, J. Cryst. Growth **49**, 659–660 (1980)
16.86 V.A. Tatartchenko: Cylindrical pores in a growing crystal, J. Cryst. Growth **143**, 294–300 (1994)
16.87 V.A. Tatartchenko, T.N. Yalovets, G.A. Satunkin, L.M. Zatulovsky, L.P. Egorov, D.Y. Kravetsky: Defects in shaped sapphire crystals, J. Cryst. Growth **50**, 335–340 (1980)
16.88 A.A. Chernov, D.T. Temkin, A.M. Melnikova: Theory of inclusion capture at the melt crystal growth, Kristallographia (Sov. Crystallography) **21**(4), 652–660 (1976)
16.89 E. Savrun, C. Toy, W.D. Scott, D.C. Harris: Is sapphire inherently weak in compression at high temperature?, Proc. SPIE **3705**, 12–16 (1999)
16.90 J.W. Locher, S. Zanella, H. Bates, V.A. Tatartchenko: Production of large sapphire crystals by EFG, Abstracts 14th Int. Conf. Cryst. Growth (Grenoble 2004) p. 560
16.91 V.N. Kurlov, B.M. Epelbaum: Fabrication of near-net-shaped sapphire domes by noncapillary shaping method, J. Cryst. Growth **167**, 165–180 (1997)
16.92 V.S. Yuferev, V.M. Krymov, L.L. Kuandykov, S.I. Bakholdin, Y.G. Nosov, I.L. Shulpina, P.I. Antonov: The growth of sapphire ribbons with basal facet surface, J. Cryst. Growth **275**, 785–790 (2005)
16.93 J. Shi, G. Geitos, N.V. Abrosimov, S.K. Brantov, S.A. Erofeeva, V.A. Tatartchenko: Some structural and electrophysical properties of silicon ribbons produced by Stepanov's method, Izv. Akad. Nauk SSSR, Ser. Fiz. **43**, 1992–1994 (1979), in Russian – Translation in Bull. Acad. Sci. USSR, Phys. Ser. USA **43**, 164–165 (1979)

16.94 N.V. Abrosimov, A.V. Bazhenov, V.A. Tatartchenko: Growth features and local electronic properties of shaped silicon, J. Cryst. Growth **82**, 203–208 (1987)
16.95 J.P. Kalejs: An overview of new developments in crystalline silicon ribbon material technology for solar cells, Proc. 3rd World Conf. Photovolta. Energy Convers. (Osaka 2003)
16.96 D. Garcia, M. Ouellette, B. Mackintosh, J.P. Kalejs: Shaped crystal growth of 50 cm diameter silicon thin-walled cylinders by EFG, J. Cryst. Growth **225**, 566–571 (2001)
16.97 S.K. Brantov, B.M. Epelbaum, V.A. Tatartchenko: Unidirectional growth of silicon layers on a graphitized fabric substrate, Mater. Lett. **2**, 274–277 (1984)

Part C Solution

Part C Solution Growth of Crystals

17 Bulk Single Crystals Grown from Solution on Earth and in Microgravity
Mohan D. Aggarwal, Normal, USA
Ashok K. Batra, Normal, USA
Ravindra B. Lal, Normal, USA
Benjamin G. Penn, Huntsville, USA
Donald O. Frazier, Huntsville, USA

18 Hydrothermal Growth of Polyscale Crystals
Kullaiah Byrappa, Mysore, India

19 Hydrothermal and Ammonothermal Growth of ZnO and GaN
Michael J. Callahan, Hanson, USA
Qi-Sheng Chen, Beijing, China

20 Stoichiometry and Domain Structure of KTP-Type Nonlinear Optical Crystals
Michael Roth, Jerusalem, Israel

21 High-Temperature Solution Growth: Application to Laser and Nonlinear Optical Crystals
Joan J. Carvajal, Tarragona, Spain
Maria Cinta Pujol, Tarragona, Spain
Francesc Díaz, Tarragona, Spain

22 Growth and Characterization of KDP and Its Analogs
Sheng-Lai Wang, Jinan, Shandong, China
Xun Sun, Jinan, China
Xu-Tang Tao, Jinan, China

17. Bulk Single Crystals Grown from Solution on Earth and in Microgravity

Mohan D. Aggarwal, Ashok K. Batra, Ravindra B. Lal, Benjamin G. Penn, Donald O. Frazier

The growth of crystals has been of interest to physicists and engineers for a long time because of their unique properties. Single crystals are utilized in such diverse applications as pharmaceuticals, computers, infrared detectors, frequency measurements, piezoelectric devices, a variety of high-technology devices, and sensors. Solution crystal growth is one of the important techniques for the growth of a variety of crystals when the material decomposes at the melting point and a suitable solvent is available to make a saturated solution at a desired temperature. In this chapter an attempt is made to provide some fundamentals of growing crystals from solution, including improved designs of various crystallizers.

Since the same solution crystal growth techniques could not be used in microgravity, authors had proposed a new cooled sting technique to grow crystals in space. Authors' experiences of conducting two Space Shuttle experiments relating to solution crystal growth are also detailed in this work. The complexity of these solution growth experiments to grow crystals in space are discussed. These were some of the earliest experiments performed in space, and various lessons learnt are described.

A brief discussion of protein crystal growth, which also shares the basic principles of the solution growth technique, is given along with some flight hardware information for such growth in microgravity.

17.1 **Crystallization: Nucleation and Growth Kinetics** 561
17.1.1 Expression for Supersaturation 561
17.1.2 Effects of Convection in Solution Growth 563
17.1.3 Effect of Impurities 564

17.2 **Low-Temperature Solution Growth** 566
17.2.1 Solution Growth Methods 566

17.3 **Solution Growth by Temperature Lowering** 567
17.3.1 Solvent Selection and Solubility 567
17.3.2 Design of a Crystallizer 569
17.3.3 Solution Preparation and Starting a Growth Run 573

17.4 **Triglycine Sulfate Crystal Growth: A Case Study** 574
17.4.1 Growth of Single Crystals of Triglycine Sulfate 574
17.4.2 Growth Kinetics and Habit Modification 576

17.5 **Solution Growth of Triglycine Sulfate Crystals in Microgravity** 582
17.5.1 Rationale for Solution Crystal Growth in Space 583
17.5.2 Solution Crystal Growth Method in Space 583
17.5.3 Results and Discussion 588

17.6 **Protein Crystal Growth** 592
17.6.1 Protein Crystal Growth Methods 592
17.6.2 Protein Crystal Growth Mechanisms 593
17.6.3 Protein Crystal Growth in Microgravity 593

17.7 **Concluding Remarks** 594

References 594

The growth of crystals with tailored physical and chemical properties, the characterization of crystals with advanced instrumentation, and their eventual conversion into devices play vital roles in science and technology. Crystal growth is an important field of materials science, involving controlled phase transformation. Growth of crystals from solution at low temperature is one of the important techniques in the fields of pharmaceutical, agriculture, and materials science. Crystal growth acts as a bridge between science and technology for practical applications. In the past few decades, there has been growing interest in the crystal growth process, particularly in view of the increasing demand for materials for technological applications. The strong influence of single crystals in present-day technology is evident from recent advances in the fields of semiconductors, transducers, infrared detectors, ultrasonic amplifiers, ferrites, magnetic garnets, solid-state lasers, nonlinear optics, piezoelectrics, acousto-optics, photosensitive materials, and crystalline thin films for microelectronics and computer applications. All these developments could only be achieved due to the availability of single crystals such as silicon, germanium, and gallium arsenide, and also through the discovery of nonlinear optical properties in some inorganic, semiorganic, and organic crystals. Researchers have always sought new materials for growth of single crystals for new applications and the modification of present crystals for various applications. Any crystal growth process is complex; it depends on many parameters, which can interact. A complete description of a process may well be impossible, since this would require the specification of too many variables. This is why crystal growth is sometimes called an art as well as a science, but like other crafts, it can provide great satisfaction after successful crystal growth of a desired material.

Solid-state materials can be classified into single crystals, polycrystalline, and amorphous materials depending upon the arrangement of their constituent molecules, atoms or ions. An ideal crystal is one in which the surroundings of any atom would be exactly the same as the surroundings of every similar atom in three dimensions. However, real crystals are finite and contain defects. The consistency of the characteristics of devices fabricated from a crystal depends on the homogeneity and defect contents of the crystal. Hence, the process of producing single crystals, which offer homogeneous media at the atomic level with directional properties, attracts more attention than any other process. The methods of growing crystals are mainly dictated by the characteristics of the material and the desired size of the crystal. The method of growing crystals at low and high temperature can be broadly divided into the following six categories:

1. Growth from aqueous solution (low-temperature growth)
2. Growth by gel method (low-temperature growth)
3. Growth from flux or top-seeded solution growth method (high-temperature growth)
4. Hydrothermal growth (high-temperature growth)
5. High-pressure growth (high-temperature growth)
6. Growth by electrodeposition.

Growth of bulk crystals from aqueous solution is technically very important. Besides bulk crystal growth, this method is also used for purification of materials and separation of impurities. Growth of large single crystals from aqueous solution is of interest for essentially two reasons. First, there is a growing need for solution-grown crystals in the area of high-power laser technology, such as potassium dihydrogen phosphate (KDP)-type crystals. Second, research in this area of crystal growth and the corresponding in-depth examination of several key parameters provides fundamental case studies generating theory and technology that are applicable to all solution crystal growth processes, including new aqueous growth systems and high-temperature solution growth.

In this chapter, the fundamental aspects of solution growth and the various methods of bulk crystal growth from solution are described, along with solution crystal growth in the microgravity environment of space. Based on extensive experience of the authors in growing inorganic and organic crystals on Earth and in space, the authors have tried to provide a lucid explanation of the fundamentals of solution crystal growth and crystal growth systems. However, enough details are given on fabrication of crystallizers, associated instruments, and techniques that new researchers may be able to design and set up his/her own solution crystal growth system after review of this chapter. Furthermore, growth and perfection of a technologically important crystal from aqueous solution based on the case study of triglycine sulfate is presented. The effects of various parameters such as the design of the seed holder, seed morphology, the characteristics of the solution such as pH, the growth temperature, dopants, impurities, and microgravity on the physical properties are presented in detail.

17.1 Crystallization: Nucleation and Growth Kinetics

The study and investigation of crystal growth implies the determination of growth laws and growth mechanisms, and the explanation of the final result, i. e., the crystal habit. These aspects are interconnected. Since the growth rate of a face depends on its growth mechanisms and contributes to define the crystal habit, detailed knowledge of these aspects is essential for production of crystals of specific physical or morphological properties. Crystal growth is due to deposition of solute particles on crystal faces, which can grow layer by layer at different rates. The growth rate of a face, i. e., the advancement of its surface in the normal direction per unit time, depends upon both internal and external factors. Internal factors include the surface structure of faces, which in turn are related to the bulk crystal structure, and their degree of perfection. Defects usually occur in the crystals and can emerge at the surface, affecting the growth kinetics. The external factors include the supersaturation, the solute concentration, which is related to solubility, the temperature of the solution, the composition of the solution, mechanical conditions such as the use of stirring, and the presence of impurities or a magnetic or gravitational field. The crystal growth of a face is a succession of complex processes that take place at the interface between the liquid and solid phase. This therefore implies transport of matter and energy across the interface, which is the site of major importance in crystal growth.

In the following section, the fundamentals of nucleation and crystal growth in low-temperature solution are described.

17.1.1 Expression for Supersaturation

The supersaturation of a system can be expressed in a number of ways. A basic unit of concentration as well as temperature must be specified. The concentration driving force (ΔC), the supersaturation ratio (S), and the relative supersaturation (σ) are related to each other as follows.

The concentration driving force is

$$\Delta C = C - C^* \,, \tag{17.1}$$

where C is the actual concentration of the solution and C^* is the equilibrium concentration at a given temperature.

The supersaturation ratio is

$$S = \frac{C}{C^*} \,. \tag{17.2}$$

The relative supersaturation is

$$\sigma = \frac{C - C^*}{C^*} \quad \text{or} \quad \sigma = S - 1 \,. \tag{17.3}$$

If the concentration of a solution can be measured at a given temperature and the corresponding equilibrium saturation concentration is known, then the supersaturation can be estimated.

The required supersaturation can be achieved either by cooling/evaporation or by the addition of a precipitant. *Meirs* and *Isaac* reported a detailed investigation on the relationship between supersaturation and spontaneous crystallization [17.1]. The results of their analysis are shown in Fig. 17.1, which shows three zones, termed regions I, II, and III. The lower continuous line indicates the normal solubility of the salt concerned. The temperature and concentration at which spontaneous crystallization occurs are represented by the upper broken curve, generally referred to as the supersolubility curve. This curve is not well defined, as the solubility curve and its position in the diagram depend on the degree of agitation of the solution. The three zones are defined as:

I. The stable (undersaturated) zone, where crystallization is not possible.
II. The metastable zone, where spontaneous crystallization is improbable. However, if a seed crystal is placed in such a metastable solution, growth will occur.

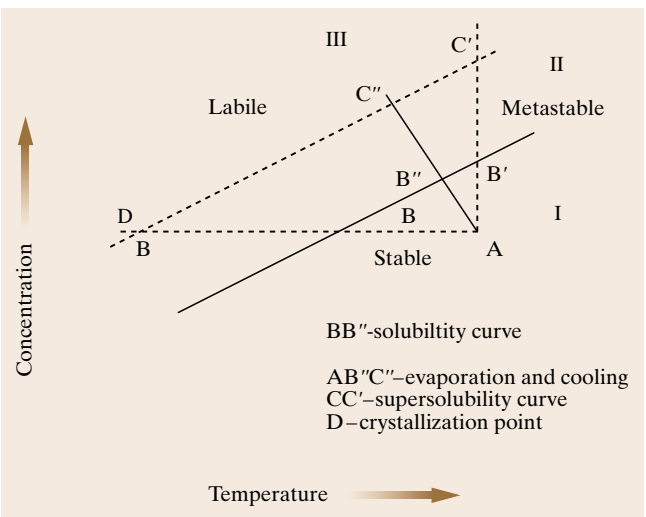


Fig. 17.1 Meirs and Issac solubility curve

III. The unstable or labile (supersaturation) zone, where spontaneous crystallization is more probable.

The achievement of supersaturation is not sufficient to initiate crystallization. The formation of embryos or nuclei with a number of minute solid particles present in the solution, often termed centers of crystallization, is a prerequisite. Nucleation may occur spontaneously or can be induced artificially. Broadly speaking, nucleation can be classified into primary and secondary. All types of nucleation, whether homogeneous or heterogeneous, in systems that do not contain crystalline matter are described as primary. On the other hand, nucleation generated in the vicinity of crystals present in a supersaturated system is termed secondary nucleation.

The formation of stable nuclei occurs only by the addition of a molecule (A_1) until a critical cluster is formed

$$A_{n-1} + A_1 \rightarrow A_n \quad \text{(critical cluster)} \,. \tag{17.4}$$

Subsequent additions to the critical cluster result in nucleation followed by growth. The growth units (ions or molecules) in a solution can interact with one another, resulting in a short-lived cluster. Short chains or flat monolayers may be formed initially, and eventually the lattice structure is built up. This process occurs very rapidly and continues in regions of very high supersaturation. Many nuclei fail to achieve maturity and simply dissolve due to their unstable nature. If the nuclei grow beyond a certain critical size, they become stable under the average conditions of supersaturation in the bulk of the solution.

The formation of a solid particle within a homogeneous solution results from the expenditure of a certain quantity of energy. The total quantity of work W required for the formation of a stable nucleus is equal to the sum of the work required to form the surface W_S (a positive quantity) and the work required to form the bulk of the particle W_V (a negative quantity).

$$W = W_S + W_V \,. \tag{17.5}$$

The change in Gibbs free energy (ΔG) between the crystalline phase and the surrounding mother liquor results in a driving force, which stimulates crystallization. This ΔG is the sum of the surface free energy and the volume free energy

$$\Delta G = \Delta G_S + \Delta G_V \,. \tag{17.6}$$

For a spherical nucleus

$$\Delta G = 4\pi r^2 \gamma + \frac{4}{3}\pi r^2 \Delta G_V \,, \tag{17.7}$$

where r is the radius of the nucleus, γ is the interfacial tension, and ΔG_V is the free energy change per unit volume.

For rapid crystallization, $\Delta G < 0$; the first term in the above equation expresses the formation of new surface, and the second term expresses the difference in chemical potential between the crystalline phase (μ) and the surrounding mother liquor (μ_0). At the critical condition, the free energy formation obeys the condition $\mathrm{d}\Delta G/\mathrm{d}r = 0$. Hence the radius of the critical nucleus is expressed as

$$r^* = \frac{2\gamma}{\Delta G_V} \,. \tag{17.8}$$

The critical free energy barrier is

$$\Delta G^* = \frac{16\pi\gamma^3 v^2}{3\,(\Delta\mu)^2} \,. \tag{17.9}$$

The number of molecules in the critical nucleus is

$$I^* = \frac{4}{3}\pi\gamma(r^*)^3 \,. \tag{17.10}$$

The crucial parameter between a growing crystal and the surrounding mother liquor is the interfacial tension γ. This complex parameter can be determined by conducting nucleation experiments.

Growth of crystals from the vapor, melt or solution occurs only when the medium is supersaturated. The process involves at least two stages [17.2]:

1. Formation of stable three-dimensional (3-D) nuclei
2. Development of the stable 3-D nuclei into crystals with well-developed faces.

The formation of 3-D nuclei is usually discussed in terms of reduction in the Gibbs free energy of the system. At a given supersaturation and temperature, there is a critical value of the free energy at which 3-D nuclei of a critical radius are formed. Only those nuclei which are greater than the critically sized nucleus are capable of growing into crystals of visible size by the attachment of growth species (i. e., molecules, atoms or ions) at energetically favorable growth sites such as kinks (K) in the ledges (L) of a surface. The surfaces of growing crystals may be flat (F), stepped (S) or kinked (K). However, crystals of visible size are usually bounded by slowly growing F-faces which grow by the attachment of growth units at energetically favorable sites. Figure 17.2 shows different positions for the attachment of growth units at a flat crystal–medium interface of a simple cubic lattice. A growth unit attached at a surface terrace (T), smooth ledge (L) or kink (K)

site has one, two or three out of the six potential nearest neighbors, respectively. Therefore, a growth unit arriving at a surface terrace, ledge or kink simply loses one, two or three degrees of freedom. If ϕ is the binding energy per pair, the corresponding binding energy of a growth unit attached at these sites is ϕ, 2ϕ, and 3ϕ, respectively. Since the probability of capture of a growth unit at a given site depends on the term $\exp(n\phi/k_B T)$ (where n is the number of bonds formed, k_B is the Boltzmann constant, and T is the temperature in Kelvin), the growth unit has a much higher probability of becoming a part of the crystal at a kink site than at a ledge or surface terrace. Consequently, in contrast to ledges, the contribution of kinks is overwhelmingly high in the rate v of displacement of a step along the surface and in the rate R of displacement of the surface normal to it. Similarly, the contribution to the face growth rate R by the direct attachment of growth units at the terrace is negligible.

From the above discussion, it may be concluded that the kinetics of crystal growth may, in general, be considered to occur in the following stages:

1. Transport of growth units to the growing surface by bulk diffusion and their capture onto the surface terrace
2. Migration of growth units adsorbed onto the terrace to the step by surface diffusion and their capture at the step
3. Migration of growth units adsorbed onto the step to the kink site and their integration into the kink
4. Transport of the released heat of the reaction and solvent molecules from the solvated atoms/molecules.

One or more of the above stages may control the growth rate but the slowest one is always rate limiting. However, it should be noted that growth kinetics, characterized by the rates v' and R, depends on the crystal structure, the structure of the crystal–medium interface (i. e., rough or smooth), the presence of dislocations emerging on the growing face, the supersaturation of the growth medium, the growth temperature, stirring, and impurities present in the growth medium. It is also these factors that ultimately determine the surface morphology of the crystal.

To explain the crystal growth processes, various theories, models, and role of impurities have been proposed in the past. Some of these are listed below. For details, one can refer to various excellent references, and references therein [17.2–36]. The important growth models are: (i) the two-dimensional nucleation model, (ii) the spiral growth model, (iii) the bulk diffusion model, and (iv) growth by a group of cooperating screw dislocations.

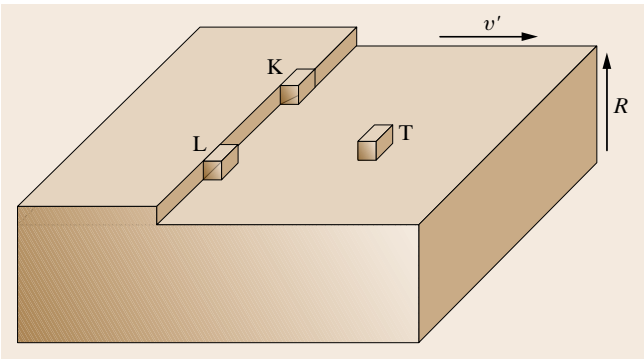


Fig. 17.2 Different positions for the attachment of growth units at a flat crystal–medium interface of a simple cubic lattice

17.1.2 Effects of Convection in Solution Growth

Convection is comprised of two mechanisms: energy transfer due to random molecular motion (diffusion) and energy transferred by bulk or macroscopic motion of the fluid. This fluid motion is associated with the fact that, at any instant, large numbers of molecules are moving collectively or as aggregates. Such motion, in the presence of a temperature gradient, contributes to heat transfer. Because the molecules in the aggregate retain their random motion, the total heat transfer is then due to a superposition of energy transport by the random motion of the molecules and by the bulk motion of the fluid. It is customary to use the term *convection* when referring to this cumulative transport and the term *advection* when referring to transport due to bulk fluid motion.

Natural Convection

Convectional heat flow can be classified as natural (or free) convection or forced convection according to the nature of the fluid flow. Natural convection is due to the density difference of a solution near a crystal and far from it. This density difference is due primarily to the change in concentration of a solution during growth or the dissolution of a crystal; and, secondly, due to the absorption or evolution of heat in the fluid. In natural convection, fluid motion is due to buoyancy forces within the fluid. Buoyancy is due to the combined presence of a fluid density gradient and a body force that

is proportional to density. In practice, the body force is usually the gravitational force. Free convection flows may occur in the form of a plume. The well-known convective flow pattern for solution growth is associated with fluid rising from the bottom of the crystal. During the growth of a crystal, solution rises because the solution near a crystal is less dense as a result of a reduction in its concentration, and the temperature is higher because of the evolution of the heat of crystallization. With this depletion of the heavier solute, the solution around the crystal becomes lighter and, thus, rises. When a crystal is dissolved, the direction of motion is opposite (downward). Under these conditions, the diffusion of molecules is supplemented by the more energetic convective transport of matter.

Diffusion is the distribution of a substance by random motion of individual particles. It is due to the presence of a gradient of the chemical potential in the system. A gradient is defined as the increment of a function in an infinitely short distance, along the direction of the most rapid variation of the function. Diffusion always reduces this gradient. Molecular diffusion is observed in viscous media and at low supersaturations, as well as in the growth of crystals, in thin films of liquids, and in capillaries. In molecular diffusion the transport of matter to a crystal is slower than under other diffusion conditions. The thickness of the boundary layer increases with time and the concentration gradient gradually decreases. Therefore, the rate of growth decreases with time. The time interval during the formation of a boundary diffusion layer represents the non-steady-state condition. During this initial period, the rate of growth varies considerably. The thickness of the boundary layer depends on the difference between the densities of different parts of the solution (i. e., on the rate of growth of a crystal), the viscosity of the solution, and the dimensions of the crystal. The presence of the boundary near the crystal and the orientation of the crystal itself affect the nature of the convection currents and the thickness of the boundary layer at different crystal faces.

Forced Convection

Forced convection is produced by the action of external forces such as the forced motion of a crystal in the solution. There is no basic difference between forced and natural convection. When the velocity of motion of a solution with respect to a crystal is increased, the thickness of the boundary layer increases and the supply of matter to a face of the crystal increases. Therefore, by increasing the rate of motion of a solution, we can increase the growth rate of the crystal faces. However, we cannot continue this process indefinitely. A temperature gradient constitutes the driving potential for heat transfer. Similarly, a concentration gradient of a species in a mixture (or solution) provides the driving potential for mass transfer. Both conduction heat transfer and mass diffusion are transport processes that originate from molecular activities. Crystal growers are actually concerned with two aspects of nutrient-to-crystal transport:

1. The mass flux across an interface, which we will call the interfacial flux and which determines the crystal growth rate
2. The concentration profile of growth species in the nutrient adjacent to the crystal, which is an essential parameter in morphological stability discussions.

Let us now introduce the dimensionless numbers that govern forced and free convection. The Grashof number Gr is

$$\mathrm{Gr} = \frac{g\beta\Delta T L^3}{v^2} , \tag{17.11}$$

where g is gravitational acceleration ($\mathrm{m/s^2}$), $\beta = 1/\rho(\delta\rho/\delta T)$ is the thermal expansion coefficient (where ρ is density), ΔT is the temperature difference between the horizontal surfaces that are separated by L, and v is kinematic viscosity ($\mathrm{m^2/s}$). The Grashof number Gr plays the same role in free convection that the Reynolds number plays in forced convection. The Reynolds number Re is

$$\mathrm{Re} = \frac{VL}{v} = \frac{\rho VL}{\mu} , \tag{17.12}$$

where V is velocity (m/s), L is the characteristic length (m), v is kinematic viscosity ($\mathrm{m^2/s}$), ρ is density, and μ is viscosity ($\mathrm{kg/(s\,m)}$). The Reynolds number Re provides a measure of the ratio of the inertial to viscous forces acting on a fluid element. In contrast, the Grashof number Gr, indicates the ratio of the buoyancy force to the viscous force acting on the fluid.

17.1.3 Effect of Impurities

We will now define impurities, which are inherently present, and additives or dopants, which are deliberately added. The former are naturally present in the growth environment and are unwanted; the latter are deliberately added in order to control nucleation, improve crystal quality, increase the size, and change the crystal habit or other physical properties. This topic

has received great attention since it is of relevant theoretical and practical interest in the growth of crystals of industrial importance. The ability of impurities to change the growth behavior has been studied by many authors [17.23–36]. It is well known that the influence of impurities on the crystal form and the growth rate is based on the adsorption of ions, atoms or molecules of foreign species at kinks, ledges, and terraces of a growing crystal. The change of the crystal form is based on a difference in adsorption energies on different faces. Impurity molecules will be preferentially adsorbed on surfaces where the free adsorption energy is maximum. It has been possible to predict this preferred surface using computational approaches [17.37]. Recently the mechanisms and models of adsorption of impurities during the growth of bulk crystals have been surveyed by *Sangwal*, including kinetic effects of impurities on the growth of single crystals from solution [17.36].

The solvent itself is an impurity. High temperatures and high supersaturations increase growth rate, but in the presence of a solvent the effect of temperature is stronger, since it promotes water desorption and growth kinetics much more than supersaturation, as found for sucrose [17.38, 39]. Anomalies found by *Chernov* and *Sipyagin* [17.40] at 10 and 40 °C in growth rates disappeared when ethanol, which is known to disrupt the bulk structure of water, was added to the solution. Indeed, water adsorbed on crystal surfaces has properties differing from those of free water. This is attributed to the different structures of the adsorbed layer which undergo phase-like transformations at these temperatures.

Impurity adsorption can be studied indirectly through the adsorption isotherm, i. e., the fraction θ of adsorbed sites which are occupied as the impurity concentrations C_i increase. The simplest model of localized adsorption, i. e., situated at lattice sites, is the Langmuir isotherm

$$K_a C_i = \frac{\theta}{1+\theta} , \tag{17.13}$$

where K_a is the temperature-dependent adsorption constant, which is different for each crystal face. Other models, which take into account the interactions between adsorbed impurities or the occupation probability, have been proposed.

Impurities can act in different ways. When they interact with the solute or solvent, they can have strong influences on the solubility and consequently on the supersaturation and kinetic processes. When impurities are adsorbed on crystals, they can have thermodynamic and kinetic effects. The dominant effect is on the rates of exchange in which the adsorbed molecule or ions and growth units are involved. If the former are exchanged more rapidly than the latter, adsorption mainly affects surface and edge free energy. For a face, a decrease of γ_i (interfacial energy of face i) results in, according to the Gibbs equation,

$$\Delta\gamma_i = k_B T \ln(1-\theta)/S , \tag{17.14}$$

where S is the area of the adsorption site. Similarly, the edge free energy is decreased. These effects should cause an increase in the nucleation and growth rate. If the exchange rate of the adsorbed molecules is slower, impurities can strongly decrease the kinetic coefficients ($R_F = K\sigma^2$ at low supersaturation and $R_F = K'\sigma$ at high supersaturation, where K and K' are kinetic coefficients that depend on the temperature and growth mechanisms, R_F is the growth rate of face F, and σ is the relative supersaturation). So that as a final result the kinetic effects dominate the thermodynamic ones and a decrease in growth rate and impingement flux occur. The interpretation of impurity effects can be done on a structural and kinetic basis:

1. Low concentrations of impurity can form an adsorbed monolayer on the surface even in undersaturated solutions, due to the structural relationship between the two-dimensional (2-D) crystal face and the adsorbed layer (as in the case of NaCl grown in the presence of $CdCl_2$, where a monolayer of $Na_2CdCl_2 \cdot 3H_2O$ is formed). The main influence is on the crystal habit.
2. The kinetic interpretation considers the possibility of adsorption on the different surface sites. If impurities are adsorbed at the kinks, the advancement rate of the edge is hindered even at very low impurity concentrations and the growth rate is strongly decreased and even blocked. Adsorption can also occur on the surface with so strong bonds that impurity molecules cannot move and form a barrier through which the steps have to filter. The spreading of steps beyond this barrier demands supersaturation higher than a critical value for each impurity concentration. In this case impurities are incorporated. Such additives are tailor-made to modify the crystal habit for industrial needs. The molecules of these impurities are similar to those of crystals, but contain some structural differences, so that when they are incorporated into the crystal they disrupt some bonds and change the growth rate of the faces.

17.2 Low-Temperature Solution Growth

Among the various methods of growing single crystals [17.41–43], solution growth at low temperature occupies a prominent place owing to its versatility and simplicity. Growth from solution occurs close to equilibrium conditions and hence crystals of high perfection can be grown.

Solution growth is the most widely used method for the growth of crystals when the starting materials are unstable or decompose at high temperatures. This method demands that the materials must crystallize from solution with prismatic morphology. In general, this method involves seeded growth from a saturated solution. The driving force, i. e., the supersaturation, is achieved either by lowering the temperature or solvent evaporation. This method is widely used to grow bulk crystals that have high solubility and solubility variation with temperature. After many modifications and refinements, the process of solution growth now yields good-quality crystals for a variety of applications. Growth of crystals from solution at room temperature has many advantages over other growth methods, though the rate of crystallization is slow. Since growth is carried out close to room temperature, the density of structural imperfections in solution-grown crystals is relatively low.

17.2.1 Solution Growth Methods

Low-temperature solution growth can be subdivided into the following categories: (i) the slow cooling method, (ii) the slow evaporation method, (iii) the temperature gradient method, and (iv) the chemical/gel method.

Slow Cooling Method

Slow cooling is the best way to grow crystals by solution technique. The main disadvantage of the slow cooling method is the need to use a narrow temperature range. The possible range of temperature is usually narrow and hence much of the solute remains in the solution at the end of the growth run. To compensate for this effect, a large volume of solution is required. A wide range of temperature may not be desirable because the properties of the grown crystal may vary with temperature. Even though this method has the technical difficulty of requiring a programmable temperature control, it is widely used with great success. In this method, growth occurs without any secondary nucleation in the solution, if the supersaturation is fixed within the metastable zone limit. A large cooling rate changes the solubility beyond the metastable zone width and multinucleation occurs at the expense of the seed crystal. A balance between temperature lowering and the growth rate has to be maintained. Growth at low supersaturation prevents strain and dislocation formation at the interface. Supersaturation can be increased after initial growth to achieve a reasonable growth rate.

Slow Evaporation Method

This method is similar to the slow cooling method in terms of the apparatus requirements. The tem-

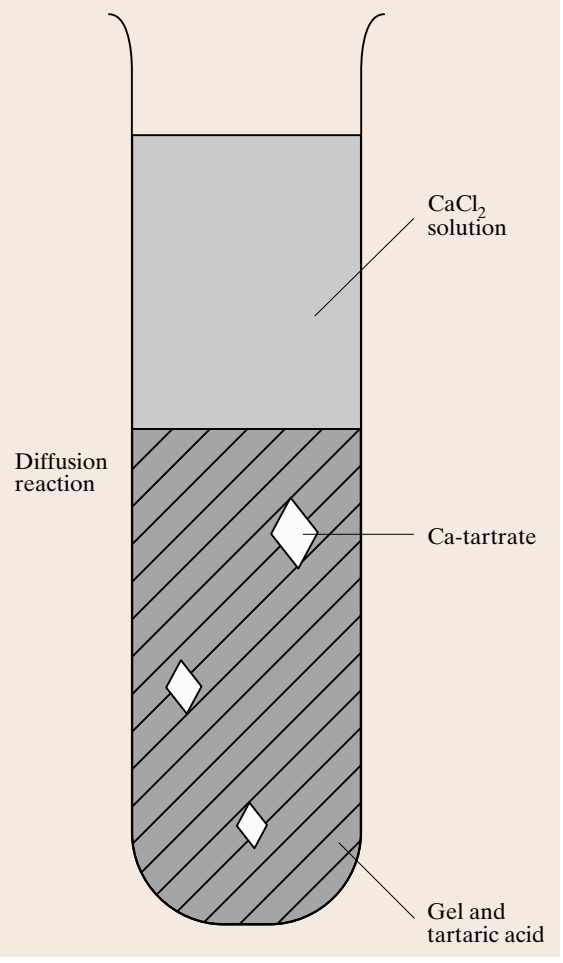


Fig. 17.3 Schematic diagram of the gel crystal growth process

perature is fixed and provision is made for evaporation. With nontoxic solvents such as water, it is permissible to allow evaporation into the atmosphere. Typical growth conditions involve a temperature stabilization of about $\pm 0.05\,^{\circ}\mathrm{C}$ and rates of evaporation of a few mm^3/h. The evaporation technique has the advantage that the crystals grow at fixed temperature, but inadequacies of the temperature control system still have a major effect on the growth rate. This method can be used effectively for materials with very low temperature coefficient of solubility.

Temperature Gradient Method

This method involves the transport of materials from a hot region containing the solute material to be grown in a cooler region, where the solution is supersaturated and the crystal grows. The main advantages of this method are

1. Crystal growth at fixed temperature
2. Insensitivity to changes in temperature, provided that both the source and growing crystal undergo the same change
3. Economy of solvent and solute.

On the other hand, a small temperature difference between the source and the crystal zones has a large effect on the growth rate.

Chemical/Gel Method

The gel method is exceedingly simple. One procedure is to prepare a gel using commercial waterglass, adjusted to a specific gravity of $1.06\,\mathrm{g/cm}^3$. Gel is then mixed with 1 M tartaric acid and allowed to gel in a test tube. Once the gel is formed, some other solution can be placed on top (1 M $CaCl_2$ solution), as shown in Fig. 17.3. In the course of time, crystals of calcium tartrate tetrahydrate are formed in the gel. In a nutshell, one solution diffuses through the gel and reacts with the other solution to form crystals of appropriate chemicals [17.44].

17.3 Solution Growth by Temperature Lowering

The growth of crystals from low-temperature solutions occupies a prominent place, especially when materials are not stable at elevated temperatures. A number of concepts for solution crystal growth systems can be found in the literature. One of the best concepts for growth of both inorganic and organic crystals from solution is by temperature lowering of a solution, provided that the material has a positive temperature coefficient of solubility. In this method, a saturated solution of the material to be grown is prepared at a chosen temperature and kept at this temperature for 24 h. Then a seed holding rod is inserted into the growth chamber and its rotation is initiated. The growth process is initiated by lowering the temperature slowly. The temperature of the solution is lowered at a preprogrammed rate, typically $0.05–2.0\,^{\circ}\mathrm{C/day}$, depending on the solubility of the chosen material. The complete crystallization process may take from one to several weeks. To terminate the growth process the grown crystals are taken out of the solution without thermal shock.

Solution crystal growth is a highly complex process and depends on various growth parameters such as the quality of the seed, the growth temperature, the temperature lowering rate, the character of the solution, the seed rotation speed, and stirring of the solution, besides other conditions. To grow good-quality crystals, these parameters have to be optimized for each crystal.

17.3.1 Solvent Selection and Solubility

A solution is a homogeneous mixture of a solute in a solvent. Generally, the solute is the component present in a smaller quantity. For a given solute, there may be different solvents. Apart from high-purity starting materials, solution growth requires a good solvent. The solvent must be chosen by taking into account the factors:

1. High solubility for the given solute
2. Good solubility gradient
3. Low viscosity
4. Low volatility
5. Low corrosion.

If the solubility is too high, it is difficult to grow bulk single crystals and, if it is too small, solubility restricts the size and growth rate of the crystals. Solubility data at various temperatures is essential to determine the level of supersaturation. Hence, the solubility of the solute in the chosen solvent must be determined before starting the growth process. If the solubility gradient is very

Table 17.1 Solubility parameters δ of water and some organic solvents at 25 °C

Solvent	δ (MPa$^{1/2}$)	Solvent	δ (MPa$^{1/2}$)
Water	47.9	Acetic acid	20.7
Methanol	29.6	1,4-Dioxane	20.5
Ethanol	26.0	Carbondisulfide	20.4
Formamide	39.3	Cyclohexanone	20.3
N-Methyl-formamide	32.9	Acetone	20.2
1,2-Ethanediol	29.9	1,2-Dichloroethane	20.0
Tetrahydrothiophene-1,1-dioxide	27.4	Chlorobenzene	19.4
N,*N*-Dimethylformamide	24.8	Chloroform	19.0
Dimethylsulfoxide	24.5	Benzene	18.8
Acetonitrile	24.3	Ethylacetate	18.6
1-Butanol	23.3	Tetrahydrofuran	18.6
Cyclohexanol	23.3	Tetrachloromethane	17.6
Pyridine	21.9	Cyclohexane	16.8
tert-Butanol	21.7	*n*-Hexane	14.9
Aniline	21.1	Perfluoro-*n*-heptane	11.9

small, slow evaporation of the solvent is the other option for crystal growth to maintain supersaturation in the solution. Growth of crystal from solution is mainly a diffusion-controlled process; the medium must be less viscous to enable faster transference of the growth units from the bulk solution to the growth site by diffusion. Hence a solvent with lower viscosity is preferable. Most important single crystals, such as potassium dihydrogen phosphate (KH_2PO_4) and L-arginine phosphate monohydrate (LAP), are grown in aqueous solutions or in solvents that are mixtures of water and miscible organic solvents. Of all known substances, water was the first to be considered for use as a solvent because it is nontoxic, most abundant, and low cost. A proper choice of solvent based on a knowledge of its chemical reactivity helps one to avoid undesired reactions between solute and solvent. Except that, in general, the solubility of the growth materials in solvents is required to be sufficiently large, the solubility parameter δ can often be used in estimating the solubility of nonelectrolytes in organic solvents

$$\delta = \left(\frac{\Delta U}{V_m}\right)^{1/2} = \left(\frac{\Delta H - RT}{V_m}\right)^{1/2}, \qquad (17.15)$$

where V_m is the molar volume of the solvent, ΔU is the molar energy, and ΔH is the molar enthalpy; δ is a solvent property that measures the work necessary to separate the solvent molecules. Often a mixture of two solvents, one having a δ value higher than that of a solute and the other lower, is a better solvent than either of the two solvents separately [17.45]. A selection of δ-values is given in Table 17.1.

Another property, that is, the dipole moments between the solute and solvent, may also be considered for selecting solvent for crystal growth. Most typical organic solvents have a dipole moment less than about 3 debye. Therefore, in the case of a solute having a similar value of dipole moment, a much wider choice of solvents is possible.

Solubility Determination

Solubility is an important parameter for crystal growth from solution at low temperature. Before any solution growth technique can be applied, determination of congruent or incongruent solubility and the establishment of absence of compound formation with pure or mixed solvents must be achieved. In the latter cases, a special compositional and thermal regime will be necessary to crystallize the desired phase. A simple apparatus for solubility studies is shown in Fig. 17.4. Visual inspection allows the determination of the solubility. Upon cooling, crystallized material is obtained for solid-phase analysis. This apparatus is easily fabricated and is very convenient for measuring solubility. The following is a description of how this has been achieved. The solute and solvent are weighed into a glass ampoule. The ampoule is seated and rotated in a bath controlled by a thermostat, the temperature of which is increased in steps of 0.5 °C every 1–2 h. The final disappearance of the solute yields the saturation temperature. The accuracy of this measurement is within ±0.5 °C.

However, the time needed to reach equilibrium for most covalent organic materials is usually shorter than that of sparingly soluble salts, although the settling times before analyses may be longer. In many soluble salts, such as potassium dihydrogen phosphate, KH_2PO_4 (KDP), triglycine sulfate $(NH_2CH_2COOH)_3H_2SO_4$ (TGS), and ethylene dithiotetrathiafulvalene $(CH_2NH_2)_2C_2H_4O_6$ (EDT), the solubility is strongly temperature dependent. On the other hand, for some soluble salts, such as $LiIO_3$ and $Li_2SO_4 \cdot H_2O$, the solubility is not dependent on temperature and even has a negative slope.

Various techniques for measuring solubility, such as methods based on the vortex flow caused by concentration and optical effects, can be found in the literature. However, accurate measurement of supersaturation is usually difficult. Some new methods such as holographic phase-contrast interferometric microphotography and trace fluorescent probe have been developed. Using these techniques, the concentration distributions and thickness of the boundary layers under different convection conditions can be measured with greater accuracy. Although these methods still need more development and refinement to become more generally applicable, they are promising alternatives for the determination of supersaturation of easily soluble compounds. Of course, if the solubility is known, supersaturation can be calculated by measuring the temperature of the solution and its equilibrium temperature. The problem is that equilibrium temperature measurements are not always easy.

17.3.2 Design of a Crystallizer

When designing a crystallizer for growing crystals from solution by the temperature lowering method, the following conditions should be met [17.43, 46, 47]:

1. A range of operating temperature from room temperature to 80 °C, depending on the solvent
2. The choice of hydrodynamic conditions in the solution
3. Measurements of growth parameters such a growth rate
4. Arrangement for taking grown crystals out of the crystallizer without any thermal shock
5. Arrangement for changing the saturation/temperature decrease rate
6. The possibility of interchanging different kinds of seed holders
7. Long-term operating reliability.

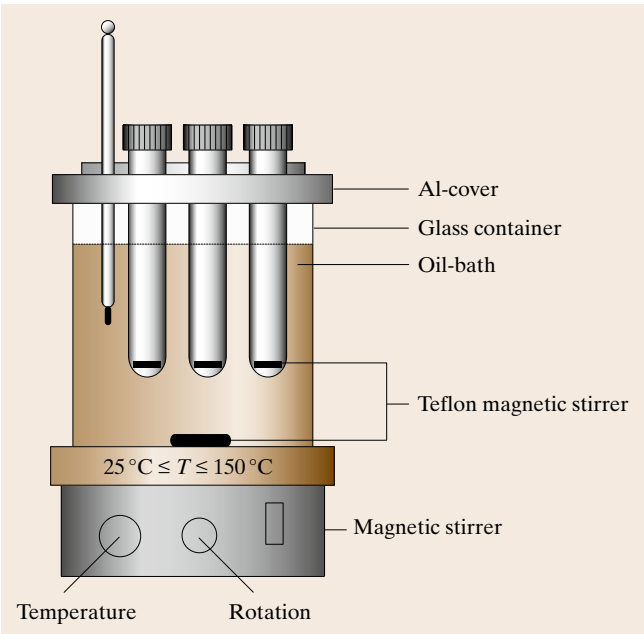


Fig. 17.4 Apparatus for solubility studies as well as equilibration of feed material and growth solution

Since these types of solution crystallizers are not available on the market, one has to design and fabricate one's own system based on one's requirements. A description of a modified crystallizer for growing large crystals from solutions along with the design of a versatile electronic reciprocating control system to change and reciprocate the motor speed containing the seed holding rod for solution growth crystallizer is given below.

In this system, the rotation rate and number of revolutions in the clockwise and counterclockwise direction can be adjusted as desired. This electronic system alleviates the problem of jerky motion of the seed holder [17.48] during reciprocation as in earlier electromechanical systems designed by the authors. Good-quality crystals of important nonlinear optical materials such as 2-methyl-4-nitroaniline:methyl -(2,4-dinitrophenyl)-aminopropanoate (MNA:MAP), L-arginine phosphate (LAP), L-histidine tetrafluoroborate (LHFB), L-arginine tetrafluoroborate (LAFB), and others such as triglycine sulfate and potassium dihydrogen sulfate have been successfully grown in authors' laboratory using this system [17.47, 49–54]. The complete crystallization apparatus along with the electronic circuit can be easily fabricated in the laboratory with readily available components.

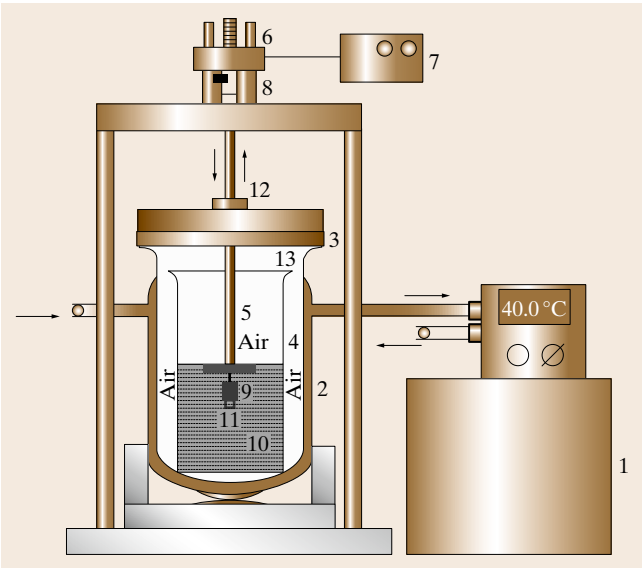


Fig. 17.5 Schematic diagram of a new type of crystallizer for growing organic crystals. (1) Circulating bath, (2) jacked reaction kettle, (3) RTV/Teflon seal, (4) crystallizer jar, (5) Teflon seed holder, (6) reversible motor, (7) circuit for reciprocating and controlling the stirring rate of seed holder, (8) arrangement for pulling the crystal during growth, (9) Teflon tape cover, (10) solution, (11) seed crystal, (12) Teflon seal, and (13) glass lid

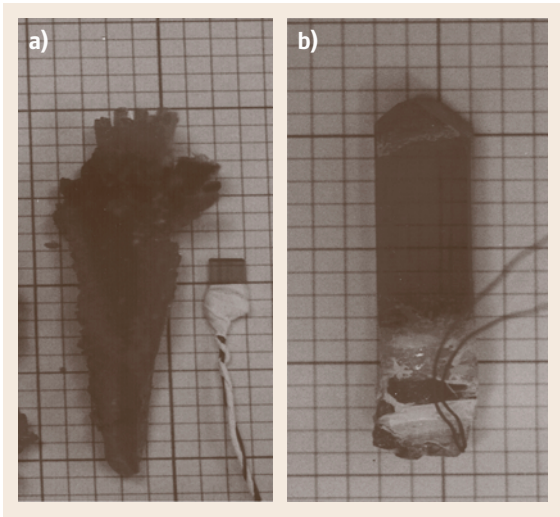


Fig. 17.6a,b MNA:MAP seed: **(a)** with aloe-vera-tree-type growth and **(b)** without aloe-vera-tree-type growth

A Typical Solution Crystal Growth Crystallizer

A schematic diagram of a modified solution crystal growth system that the authors designed and fabricated after designing a number of crystallizers [17.48, 55–57] in our laboratory is shown in Fig. 17.5. It consists of a 250 ml crystallizer jar (4), which holds the growth solution that is placed inside a 2.5 l glass-jacketed kettle (2). The linear and reciprocating motion of the Teflon seed holder (5) is controlled by a rack–pinion arrangement (8) and electronic circuit (7), respectively. A reversible motor (6) is used for rotating the seed holder. The temperature of the growth solution is controlled and programmed by circulating water using a NesLab bath (1). To prevent evaporation of the solvent, a specially designed oil–Teflon seal (3) and/or room temperature vulcanizing silicone RTV/Teflon seal (3) are used. The main advantages of our crystal growth system are: (i) better temperature stability even with sudden fluctuations in room temperature, (ii) better control over evaporation of organic solvents, (iii) a mechanical screw-type arrangement for pulling the seed crystal at a controlled rate, (iv) the possibility of varying the seed orientation and type, and (v) a versatile electronic reciprocating control system to change and reciprocate the motor speed containing the seed holding rod. Better temperature stability was accomplished by loading the growth solution into a beaker kept inside the jacketed vessel.

An air gap provides extra insulation. Moreover, spontaneous nucleation at the bottom of the growth vessel, which hampers growth and impacts on the crystal yield, is completely eliminated. By providing an extra lid on the inside beaker and a Teflon seal over the jacketed vessel, the evaporation of the solvent was dramatically reduced. The inner beaker is filled halfway with solution rather than three-quarters as is usually done, and the growing crystal is pulled in a controlled fashion. Since filling of the inner beaker to three-quarters is not required, not only is the crystal annealed in situ but also spurious aloe-vera-tree-like growth near the seed in some crystals such as MNA:MAP is greatly reduced or completely eliminated.

Figure 17.6a shows the seed crystal along with a MNA:MAP crystal grown using the usual technique, i. e., without pulling the growing crystal. Figure 17.6b shows the same crystal grown with pulling where aloe-vera-tree-type growth is avoided. Furthermore, large crystals can be grown from a smaller amount of expensive mother liquor when the crystal is pulled while growing.

Another modified solution growth crystallizer was also designed in our laboratory, whose three-dimensional cutout view with reciprocating seed ar-

rangement and other components is illustrated in Fig. 17.7. It uses a magnetic stirrer to keep the temperature of the water bath uniform at a particular temperature. A layer of silicon oil on the surface of water was found to reduce the evaporation of water to a minimum, which is a big improvement over earlier designs.

Besides temperature control, the uniform rotation of seeds is required so that stagnant regions or recirculating flows are not produced, otherwise inclusions in the crystals will be formed. To study and achieve uniform and optimum transport of solute to the growing crystals, various seed rotation mechanisms have been used in the past. Unidirectional rotation of the seed leads to the formation of cavities in central regions of a crystal face because of lesser solute transport to this region than to edges and corner of the growing crystal. Furthermore, nonuniform solute supply favors the formation of thick layers which subsequently lead to the trapping of inclusions and the generation of dislocations. Periodic rotation of the growing crystal in opposite directions suppresses edge formation but does not eliminate the formation of the central cavity. To avoid these defects and stagnant regions in the solution, eccentric or clockwise and counterclockwise motion of the seed holder is used when growing crystals from solutions. Several mechanisms [17.48, 55, 58] have been used in the past to generate reciprocating motion of the seed holder, such as electromechanical [17.55] and rack–pinion methods [17.48]. In the electromechanical system, a connection of the motor polarity is reversed mechanically by using a microswitch. In this mechanical system, there is a jerky motion on reversal, which sometimes causes seeds to fall down. The jerky motion also creates a turbulent flow in the fluid and hence nonuniform transfer of solute to the growing faces, which may lead to the formation of defective crystals. Also, the microswitch has to be changed frequently due to mechanical failure. Furthermore, the effect of seed rotation rates on the growth rate and the quality of the crystals cannot be systematically studied because the rotation rate cannot be varied. In the rack–pinion arrangement, there is no jerking motion but one has to change gears to change rotation and reversal rate, which is quite an involved process.

To address these drawbacks, in our Crystal Growth Laboratory at Alabama A&M University, a versatile solid-state electronic circuit for reciprocating the direction of the seed holder was designed along with added features in such a way as to vary the rotation rate and stopping time on reversal, and control the timing for

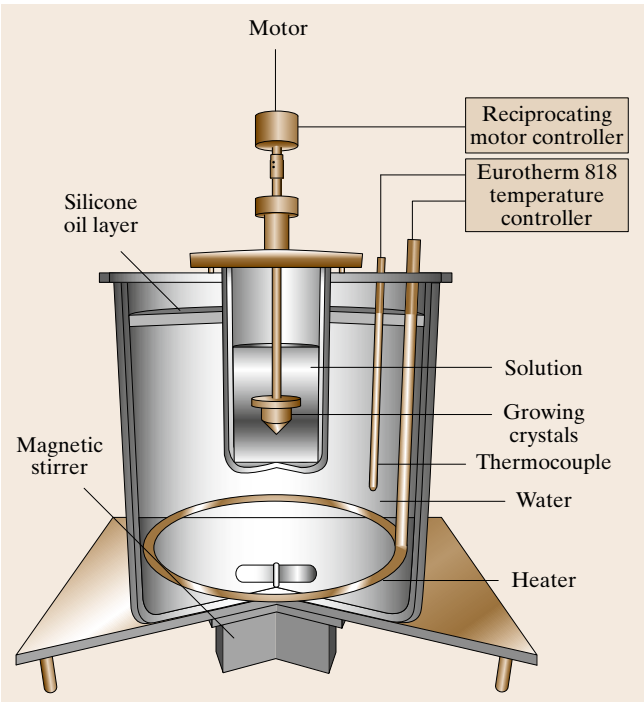


Fig. 17.7 A modified crystallizer with arrangement to stop water evaporation

clockwise and counterclockwise motion of the crystal/seed holder [17.56]. These design features will allow crystal growers to study more clearly the effect of seed rotation rate on the growth and quality of the grown crystals, thereby optimizing this important parameter for growing better-quality crystals.

A schematic diagram of the basic electronic circuit for reciprocating motion control is shown in Fig. 17.8. In Fig. 17.8, the timer (chip LM 555, U3) produces a square-wave timing pulse. It may be set to a particular frequency (POT1) and duty cycle (POT2) in combination with a timing capacitor (C3) and reset if necessary by a switch (S2). The timing waveform is divided by the J–K flip-flop chip 74LS112 (U1) to one-half of the timer frequency. Parasitic oscillations are suppressed by three capacitors (C1, C2, and C4). The two waveforms are combined by a NAND gates chip SN7400 (U2) to turn on two transistors (Q1 and Q2) alternately to control the solid-state relays (1 and 2) which connect alternate sides of the motor capacitor to the 110 V_{AC} return line. Similarly, the transistors (Q3 or Q4) alternately turn on the indicator lamps (LED1 and LED2). Current limiting and bias is provided by resistors (R1 through R8). Motor rotation speed is controlled by a potentiome-

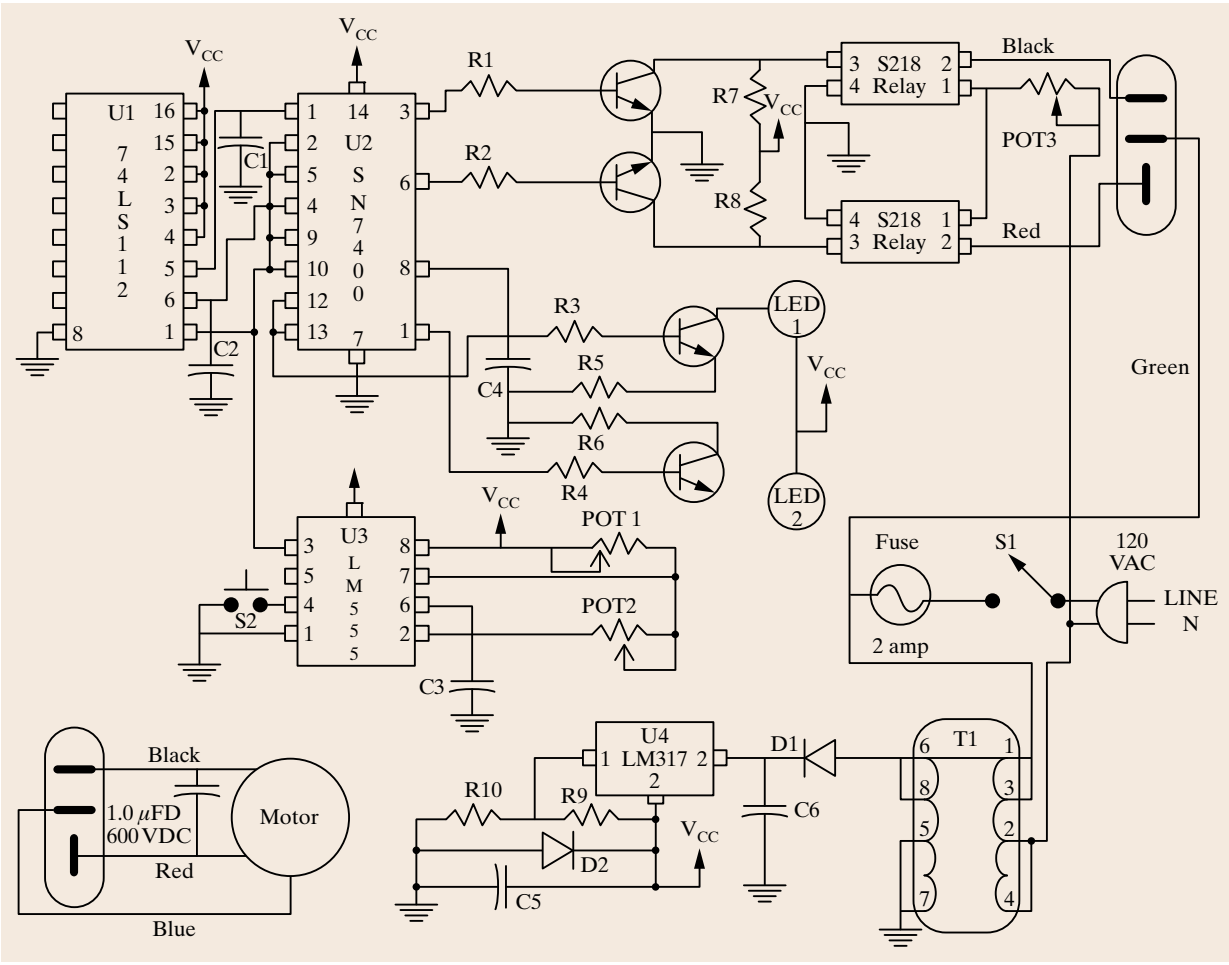


Fig. 17.8 Diagram of electronic circuit for control of the reciprocating motion of the seed holder for solution crystallizer

ter (POT3). A power supply consisting of a step-down transformer (T1), a voltage regulator (U4), and an associated filtering circuit (D1, D2, C5, and C5), and voltage setting divider (R9 and R10) provides 5 V_{DC} to the circuit. The operation of the circuit causes the following sequence of states in the system: during first interval, the seed holder motor runs counterclockwise; during the second interval, the motor comes to a stop; during the third interval, the motor runs clockwise; and during the fourth interval, the motor again comes to stop. Then the entire cycle of operation in repeated, and the intervals can be varied as needed for a particular crystal growth experiment.

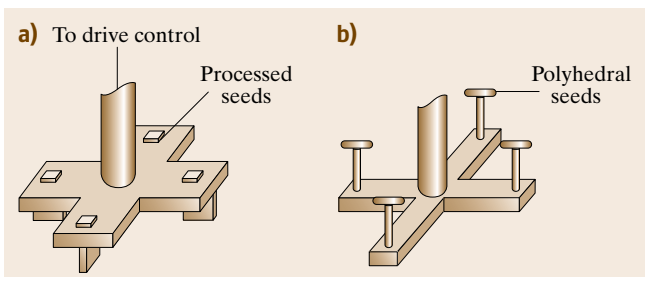


Fig. 17.9a,b Plexiglas seed holders for solution-growth crystallizers: **(a)** with processed seeds and **(b)** with polyhedral seeds

Crystal Seed Holder

In order to ensure the best growth conditions, it is necessary to use a special crystal holder because the success of an experiment may depend upon its suitability. The selection of the crystal holder and the method for attach-

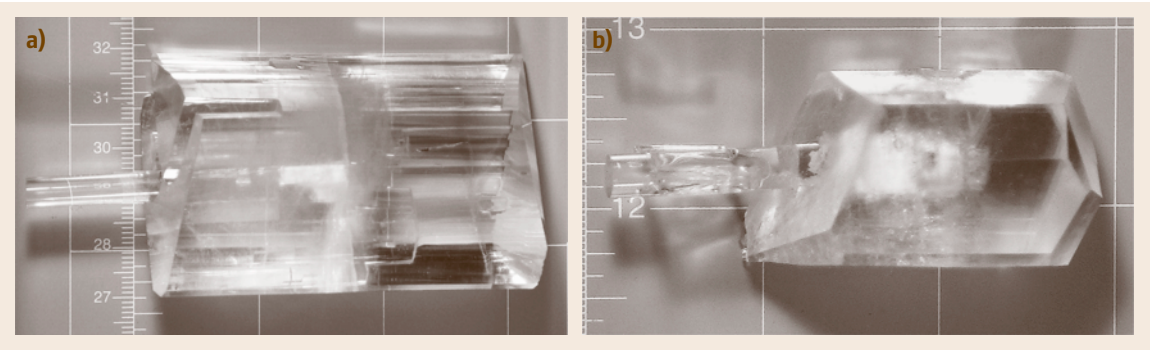


Fig. 17.10a,b Photographs of crystals grown at Alabama A&M University: **(a)** L-histidine tetrafluoroborate and **(b)** L-pyroglutamic acid crystals

ing a seed to it are no less important than the selection of the growth method. A crystal holder should ensure that a seed is held securely in a desired orientation and that the seed and therefore the growing crystal can be moved in any required manner. Also, the crystal holder should not become deformed at the selected speed and direction of the motion or by the weight of the final crystal grown on it. The crystal holder material should be chemically inert in the solution of the substance being crystallized.

A schematic diagram of two plexiglas seed holders that were specially designed, fabricated, and successfully used by the authors for aqueous solution crystal growth are shown in Fig. 17.9.

Preparation of the Seed Crystal and Mounting

A seed is a small fragment of a crystal or a whole crystal which is used to start the growth of a larger crystal in a solution. This seed must meet the following requirements:

1. It should be a single crystal free of cracks or boundaries.
2. It should be free of inclusions.
3. Its surface should be free of any sharp cleaved edges.
4. It must be grown under the same conditions as those to be used in growing the desired single crystals.

Following the above requirements in preparing the seed crystals will result in the growth of high-quality crystals, if other criteria such as solution preparation are performed carefully as well. Prior to crystal growth, seed crystals are mounted on plexiglas rods using 100% silicon rubber Dow Corning Silastic 732 RTV adhesive.

17.3.3 Solution Preparation and Starting a Growth Run

For solution preparation it is essential to have the solubility data of the growth material at different temperatures. Sintered glass filters of different pore sizes are used for solution filtration. The clear solution, saturated at the desired temperature, is poured into the growth vessel. For growth by slow cooling, the vessel is sealed to prevent solvent evaporation. Before starting the crystal growth process, a small crystal suspended in the solution is used to test the saturation. By varying the temperature, a situation is obtained where neither growth nor dissolution occurs. The test seed is then replaced with a good-quality seed. All unwanted nuclei and the surface damage on the seed are removed by dissolving at a temperature slightly above the saturation point. Growth is initiated after lowering the temperature to the equilibrium saturation. Controlled solvent evaporation can also be used in initiating the growth. The quality of the grown crystal depends on (a) the nature of the seed, (b) the cooling rate employed, and (c) the agitation of the solution.

Various new nonlinear optical crystals which hold promise for use in optical processing devices such as L-arginine phosphate, L-histidine tetrafluoroborate, L-arginine tetrafluoroborate, 2-methyl-4-nitroaniline:methyl-(2,4-dinitrophenyl)-aminopropanoate (MNA:MAP) and L-pyroglutamic acid have been successfully grown using the above-mentioned reciprocating system in combination with the temperature lowering technique, as described by the authors [17.47, 49–51]. Some of these crystals are shown in Fig. 17.10. In the investigators' observation and experience, there is significant improvement in the quality of grown crystals and success rates of the growth runs, as evident from the

transparency and lower scattering observed using laser illumination. This electronic system for reciprocal motion control of solution growth crystallizers has been in use in our laboratory for several years, and continues to work satisfactorily.

It is worth mentioning that this simple and versatile crystallization apparatus can be fabricated in any college, university or scientific laboratory from readily available components. Besides its use in physics or chemistry laboratory experiments, it can also be used for doing extensive research on the effect of important parameters such as seed rotation rate, stopping time of reversal, and number of rotations in the clockwise or counterclockwise direction on the quality and growth rate of technologically important crystals.

17.4 Triglycine Sulfate Crystal Growth: A Case Study

Triglycine sulfate (TGS) is one of the most important ferroelectric materials. The ferroelectric nature of triglycine sulfate, $(NH_2CH_2COOH)_3 \cdot H_2SO_4$, usually abbreviated as TGS, was discovered by Matthias et al. and discussed by *Jona* and *Shirane* [17.59]. The crystal structure of TGS was reported by Hoshino, Okaya, and Pepinsky and discussed in the above reference. In the ferroelectric phase below the Curie temperature ($T_C \approx 49\,^\circ C$), the symmetry is monoclinic with space group $P2_1$. Above the Curie temperature, the structure gains an additional set of mirror planes in the space group $P2_{1/m}$. It has been reported that the lattice parameters are $a = 9.42\,\text{Å}$, $b = 12.64\,\text{Å}$, $c = 5.73\,\text{Å}$, and $\beta = 110°23'$ and that the structure contains three independent glycine molecules. One of the structures, designated as glycine II, has a zwitterion configuration $(NH_3)^+CH_2OO^-$, and the other two, $(NH_3)^+CH_2COOH$. TGS may be called glycine-diglycinium sulfate with chemical formula $((NH_3)^+CH_2COO^-) \cdot ((NH_3^+)CH_2COOH)_2 \cdot SO_4^{2-}$. The projection of the structure along the c-direction is illustrated in Fig. 17.11. Glycine I deviates only slightly from the plane m' at $y = \frac{1}{4}$ on which the $[SO_4]^{2-}$ tetrahedra also lie, whereas glycine II and III are approximately related by inversion through $(\frac{1}{2}, \frac{1}{2}, \frac{1}{2})$ [17.60].

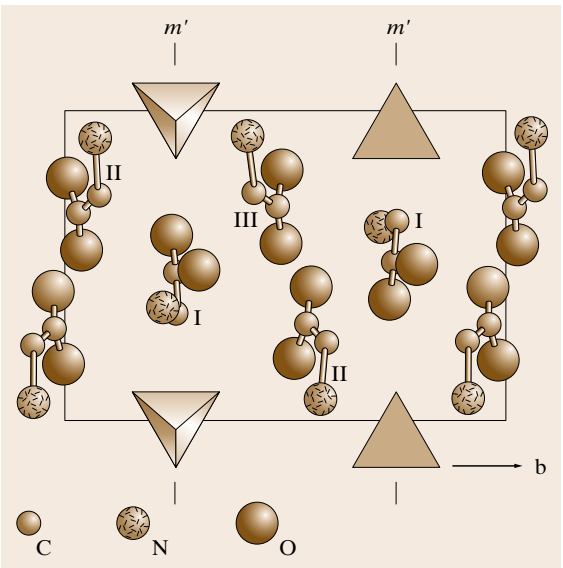
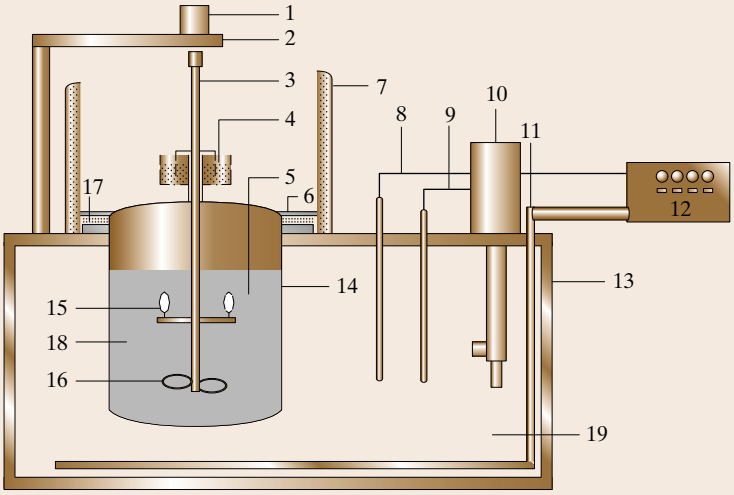


Fig. 17.11 Projection of the structure of TGS crystal along the c-direction: m' represents the set of pseudomirror planes in which glycine I molecules are inverted on ferroelectric switching

17.4.1 Growth of Single Crystals of Triglycine Sulfate

Single crystals of TGS have usually been grown from aqueous solution by the temperature lowering or solvent evaporation method. The authors have successfully grown TGS crystals using the crystallizer whose schematic diagram is shown in Fig. 17.12 [17.57]. The outside water bath, with a capacity of about 12 l, and the inside smaller cubical growth cell with 1 l capacity were made out of Plexiglas. Temperature control of the crystallizer was achieved using 250 W immersion heaters controlled by YSI 72 proportional temperature controllers to an accuracy of $\pm 0.1\,^\circ C$. Uniformity of the temperature throughout the bath was achieved with the help of a fluid circulation pump. The bath temperature is monitored at two points during the crystal growth using NIST (National Institute of Standards and Technology) calibrated thermometers. The crystals were grown by slow cooling of the solution at any desired rate.

TGS crystals are doped with L-alanine to enhance its performance and check depoling for their use in infrared sensor element. A rotating disc technique [17.61] has been applied to grow uniformly L-alanine-doped TGS crystals using a large-area seed crystal having large



1. Reciprocating motor
2. Motor mounting stand
3. Seed mounting stand
4. Seal to limit evaporation
5. Glass thermometer
6. Air tight glass cover
7. Post growth anealing heater
8. Control thermister
9. Recording thermister
10. Fluid circulation pump
11. Water heater
12. Temperature controller/programmer
13. Plexiglass water bath
14. Pyrex crystal growig cell
15. Seed/crystal
16. Stirrer blades
17. Teflon gasket
18. Solution
19. Water

Fig. 17.12 Schematic diagram of reciprocating motion crystallizer

(010) face. A conventional crystallizer was modified to allow growth under suitable hydrodynamic conditions in order to stabilize growth on the (010) face. Such a crystallizer is shown in Fig. 17.13. In this crystallizer, a seed crystal in the form of a disc was held in a circular holder with the (010) face exposed to the solution. The disc was attached to the end of a spindle that was rotated at 340 rpm. This creates a uniform boundary layer of solution over the crystal's exposed face. The container with 30 l capacity was heated by a hot plate spaced from its bottom surface and regulated to hold the temperature within $\pm 0.01\,^{\circ}\mathrm{C}$. The solution rises from the bottom of the vessel but hotter liquid is prevented from reaching the crystal directly by a plexiglas baffle. A growth rate of 1 mm/day was maintained by lowering the temperature uniformity at $0.05\,^{\circ}\mathrm{C}$/day. The resulting crystals were found to be visibly of good quality, without defects propagating from the seed. In addition to uniform doping and growth of high-quality crystal, the method has several other useful features such as short growth time, with decreased cost and reuse of seeds, and that growth occurs within a narrow temperature range. *Brezina* et al. [17.62] designed a crystallizer for growing L-alanine-doped deuterated triglycine sulfate (DTGS) crystals by isothermal evaporation of D_2O. *Satapathy* et al. [17.63] have described a novel technique for mounting the TGS seeds and a crystallizer. *Banan* [17.64] has also described a crystallizer and a seed holder for growing pure and doped TGS crystals.

TGS crystals weighing more than 100 g have been grown from solution with ethyl alcohol additions [17.65]. When alcohol is mixed in an aqueous solution of TGS, part of the water in the solution associates with alcohol, which concentrates the solution. Thus, the supersaturation can be controlled to a certain degree, making it easier to grow TGS crystals.

To achieve success in growing crystals from aqueous solutions, it is important to prepare a solution with a well-determined saturation temperature, solubility profile, and absence of any foreign particles. For our investigation, TGS solution was prepared using high-purity crystalline triglycine sulfate from BDH, UK. The solubility of TGS at various temperature were determined and compared with information available from various sources. TGS solution was prepared at $40\,^{\circ}\mathrm{C}$ saturation temperature. To prepare saturated solution,

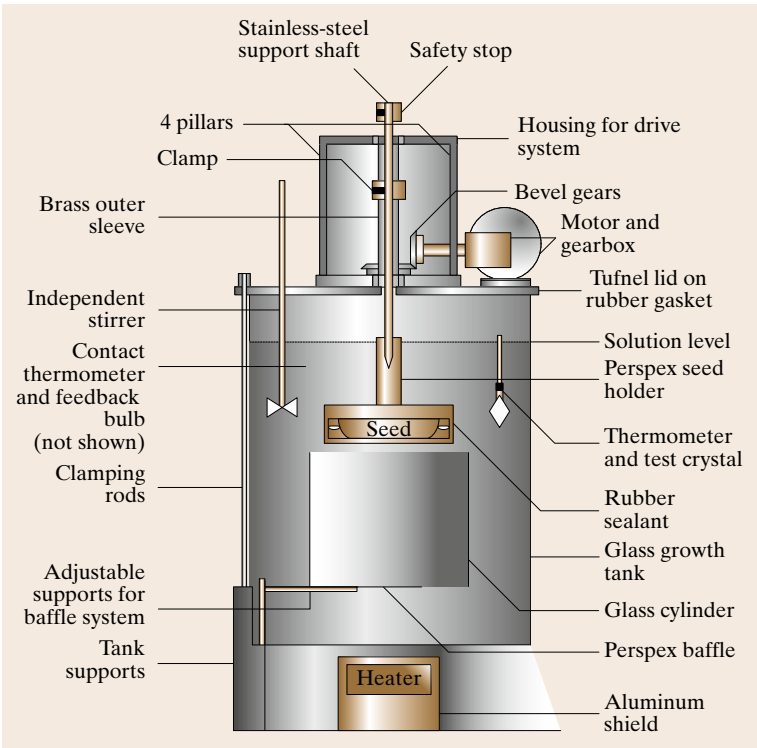


Fig. 17.13 Apparatus for spinning disc growth

464 g TGS was weighed and dissolved in 1000 cm^3 distilled water. The mixture was heated to 50 °C and mixed thoroughly using a Teflon-coated magnetic stirrer. The solution was then filtered through a 5 μm filter funnel using a vacuum unit. After filtration, this solution was transferred to the growth chamber. To start the growth run, the bath temperature was kept at 45 °C. The solution was poured into the growth cell. Then the temperature was reduced to 41.5 °C, 1.5 °C above the saturation temperature and allowed to stabilize over night. The saturation temperature was again checked by the technique of crystal insertion into the solution as well as refractive index measurements. For each saturation point the refractive index was measured at different temperatures beforehand using an Abbe refractometer. The starting growth temperature was adjusted based on the result of this procedure. After this the seed crystal holder was placed in an oven and heated to 45 °C. Prior to transfer to the growth cell, all precautions were taken to keep the seeds as well as the holder surface free of dust and foreign particles. The preheated seed crystals holder were then inserted into the growth cell and holder attached to the reciprocating apparatus. The seed crystals were slightly dissolved and the growth run started. The bath temperature was reduced by 0.1 °C/day initially and at the final stage of growth by 0.2 °C/day. The removal of the grown crystals from the mother liquor requires some care. Mishandling may induce defects, thus destroying the scientific value of the crystal or even fracturing it altogether. To avoid cracking the crystals due to thermal shock, the crystals were wrapped in a lint-free paper towel maintained at final growth temperature. The crystals were then transferred to an oven kept at an appropriate temperature. The temperature of the oven was slowly lowered to room temperature. Grown crystals can be easily removed from the seed holder by slight finger force, as RTV 732 adhesive was used for mounting the seed crystal.

17.4.2 Growth Kinetics and Habit Modification

Triglycine sulfate crystal normally grows with the habit shown schematically in Fig. 17.14a. A photograph of the TGS crystal grown at authors' laboratory is shown in Fig. 17.14b. It is observed that the $V_{(010)}$ growth rate is much faster than $V_{(001)}$. So the (010) face, as seen in Fig. 17.14, is very small or not present. Both

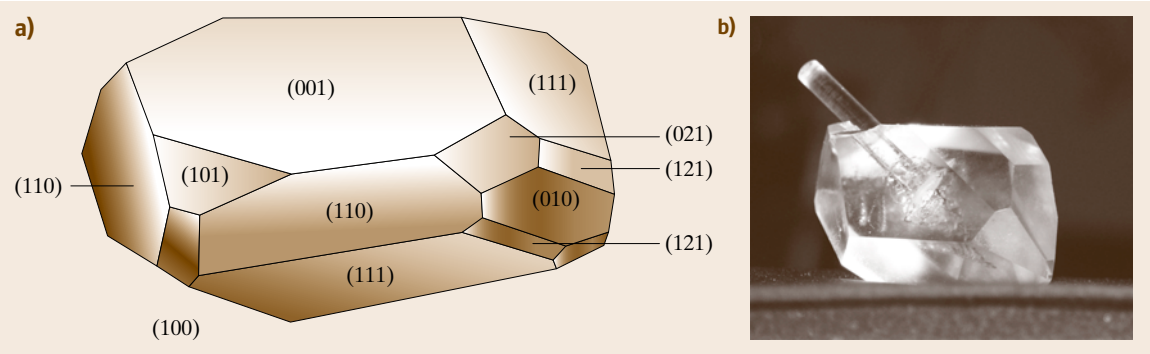


Fig. 17.14a,b Normal growth habit of TGS crystal. **(a)** Normal growth habit of TGS crystal, **(b)** photograph of as grown crystal of TGS at Alabama A&M University

growth kinetics and habit modifications of TGS have been extensively studied over the past few decades. The work published so far has resulted in a description sufficient for reliable growth of this crystal as described above. A number of studies of the growth kinetics of TGS grown from aqueous solution have been reported in the literature [17.66–71]. *Novotny* et al. [17.69] studied the growth of the (110) face of TGS crystals grown isothermally above the phase transition, at higher supersaturation ($\sigma > 10^{-3}$), and under constant hydrodynamically controlled conditions. The researchers observed that the ratio of growth rates along the individual axes is $V_a : V_b : V_c = 0.67 : 1 : 0.25$. On the basis of the measured dependence of the linear growth rate on the supersaturation (σ), it was found that the growth of the (110) face is probably controlled by volume diffusion of TGS molecules towards the surface of the growing crystal. Increasing the supersaturation caused a reduction of the number of faces in the prismatic zone of the crystal and an increase of the dislocation density in the (110) faces. Measurements of the growth rates [17.69] of (110) and (001) faces as a function of supersaturation of the solution were also analyzed on the basis of the surface diffusion model of *Burton*, *Cabrera*, and *Frank* (BCF) [17.67]. It was shown that surface diffusion is responsible for the low growth rates of (001) faces; in the case of (110) faces, the mechanism is less important at higher values of supersaturation than volume diffusion. *Rashkovich* [17.68] investigated the growth of (001) faces below the transition temperature. The results were qualitatively consistent with the dislocation model of crystal growth, but the growth at low supersaturation did not agree with the BCF model [17.67]. *Reiss* et al. [17.71] studied the growth of crystals at 33.55 °C at relative supersaturations of 0.004 and 0.045. In their study, the BCF law is fitted to the growth rate data. They also found that qualitative aspects of the growth are consistent with the BCF model.

The role of pH, impurities, degree of supersaturation, growth temperature and technical parameters, including seed preparation and attachment etc. on growth kinetics has also been quantitatively investigated by various investigators [17.72–90]. The results are described below.

Effect of Seed Crystal

It has been observed that morphology does not change much for seed crystals obtained at different temperatures [17.80]. However, at higher temperatures (35–45 °C) seeds tend to be elongated in the (001) direction, while seeds grown at lower temperatures are nearly isometric. Morphological study of the crystals grown using the above-cited seeds showed dependency of the crystal habit on the characteristics of the seed. The grown crystals tended to be elongated when elongated seeds were used. Crystals with large (010) faces grew when cleaved platelets were used for seeding. Crystals with high transparency and lower dislocation densities were obtained when the crystal growth tem-

Table 17.2 Crystal growth data for TGS crystals grown on poled and unpoled seeds [17.72]

TGS crystals	Crystal yield weight (g/(day °C))	Growth velocity $V_{(010)}$ (mm/(day °C))
(010) poled seed	0.618	1.05
(010) unpoled seed	0.621	1.16
$(0\bar{1}0)$ poled seed	0.624	1.20
$(0\bar{1}0)$ unpoled seed	0.637	1.25

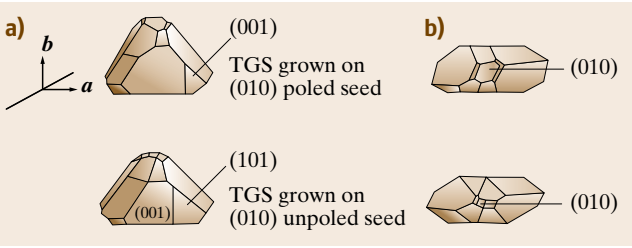


Fig. 17.15a,b Growth habits of TGS crystals grown on **(a)** poled and **(b)** unpoled seeds

perature was kept the same as that used to grow the seed. Crystal growth was seriously impaired when cleaved platelets were used as seeds, because of unwanted nucleation that started growing during the growth process. *Banan* et al. [17.82] studied the effect of using poled seed on the morphology and growth rate of TGS crystals. Table 17.2 summarizes the normalized growth data for two crystal growth runs using poled and unpoled seeds, and Fig. 17.15 gives the morphology of resulting TGS crystals. A number of interesting effects on the growth rate and morphology of these crystals were observed. Generally, the growth rate along the ($-b$-axis) (010) was faster than along the ($0\bar{1}0$) ($+b$-axis). The well-developed (010)/($0\bar{1}0$) faces, which are generally not present or less developed in pure TGS crystals, were prominent and large in crystals grown on poled seed. In this way, the identification of the ferroelectric axis in the TGS crystal becomes easier, and cleaving normal to the ferroelectric axis for preparation of pyroelectric infrared (IR) element can be economically accomplished. It can be inferred from Table 17.2 that growth velocity along the [010] axis of TGS crystal is affected by using a poled seed crystal. The decrease in growth rate along the [010] direction in the case of poled seed helps in the emergence of larger (010) face.

Effect of Growth Temperature and Supersaturation

The effect of crystal morphology and quality on growth temperature using the seed also grown at the same

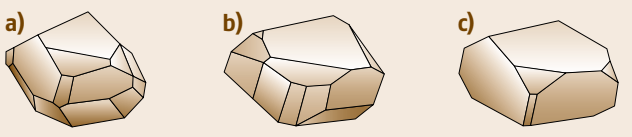


Fig. 17.16a–c Change of growth habits of TGS with growth temperature and supersaturation: **(a)** 32 °C, 0.7×10^{-3} **(b)** 32 °C, 3.0×10^{-3}, and **(c)** 52 °C, 3.0×10^{-3}

Table 17.3 Growth rates of various faces of TGS versus solution pH [17.76]

pH	$V_{(001)}$ (10^{-3} mm/h)	$V_{(010)}$ (10^{-3} mm/h)	$V_{(100)}$ (10^{-3} mm/h)
2.70	71.6	291.5	260.9
2.14	49.6	118.2	117.6
1.25	207.0	262.0	109.0
1.00	144.6	156.2	43.9
0.30	109.9	120.9	40.5

growth temperature, and from the same solution, has also been studied [17.80]. The change in morphology was not substantial, but the rate of growth in different directions changed with temperature, and relative change in the size of the faces was observed. Extra nuclei hindered growth at higher temperature (40 °C), and the crystals were of poor quality with low transparency. The change in habit of TGS crystals [17.76] as a function of temperature and supersaturation is shown in Fig. 17.16.

Effect of Solution pH

The influence of solution pH on the growth, morphology, and quality of TGS crystals has been studied by a number of workers. It was observed that crystal quality is not greatly affected by pH variation [17.80]. The influence of growth solution pH on growth rates of various faces: {(001), (010), (100)} and habit of TGS was studied by *Tsedrik* et al. [17.76].

At pH < 1, diglycine sulfate (DGS) was formed. Table 17.3 gives average values of the growth rate V of (001), (010), and (100) faces of TGS crystals versus pH of the solution as well as DGS grown at pH 0.3. Values of $V_{(100)}$ decreased monotonously with lowering pH, and $V_{(001)}$ and $V_{(100)}$ had a local minima near the pH value corresponding to the stoichiometric (pH = 2.14) value and a local maxima around pH = 1.25. The crystal habit is defined by the growth rates of the faces. Figure 17.17 shows the dependence of crystal habit on pH [17.76]. The most isometric crystals were obtained at pH = 1.55, when $V_{(100/001)} \approx 1$ (Fig. 17.17c). Almost all crystals at low pH had gaps on the (111) and ($11\bar{1}$) faces (Fig. 17.17d,e). The above observed changes in morphology of TGS single crystals with the pH of the solution were apparently affected by different capture of incidental impurities, which are always present in the solutions. Chemical (structural) impurities captured by the crystal faces reduced the growth rates of the corresponding faces, and mechanical impurities (defects) increased these rates. At low pH values,

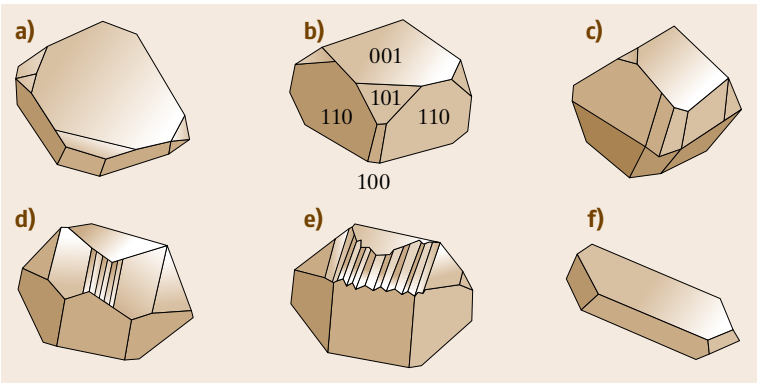


Fig. 17.17a–f Change of habit of TGS crystals with solution pH: **(a)** 2.75, **(b)** 2.1, **(c)** 1.55, **(d)** 1.23, **(e)** 1.0, and **(f)** 0.3 (DTGS)

chemical impurities played the predominant role. Their entry into the growing crystal was increased with reducing pH. Table 17.3 clearly shows that the growth rate of all faces decreased with reducing pH, starting with pH = 1.25. The gaps on the (111) and (11$\bar{1}$) faces were connected with strong hindering of the growth layers by the adsorbed impurities (Fig. 17.17d,e). At high pH (> 2) another kind of impurity (mechanical defects) has a predominant influence on crystal morphology. Their entry increased with rising pH, so the growth rates of all faces increased (Table 17.3). At pH = 1.55 the action of impurities of both kinds was comparable, and mostly isometric crystals were formed (Fig. 17.17c). Recently, it has been shown [17.91] that the growth rate of (010) face of TGS and L-alanine doped triglycine sulfo-phosphate (ATGSP) crystals varies with the pH of the solution.

With the same supersaturation, the growth rate of TGS crystals was slowest in the neutral solution (pH = 2.25). It grew faster in both acidic (pH = 1.73–2.25) and alkaline solution (pH = 2.25–2.52). In alkaline solution, the growth rate of TGS varied faster with changing pH value. However, if the pH was too high, then the (010) face capped quickly. The variation of growth rate of L-alanine-doped triglycine sulfophosphate (ATGSP) with pH was not similar to that of TGS. The growth rate of ATGSP crystals in a neutral solution (pH = 2.5) was the fastest, and it was slower in both acidic (pH = 2.20–2.50) and alkaline (pH = 2.5–2.85) solutions. The above results demonstrate that, on the basis of the pH of a solution, one can grow crystals at higher growth rates.

Effect of Impurities on TGS Crystal Growth

The presence of impurities in the process of crystal growth results in modification of the crystal shape and growth rates. Various workers have studied the effects of inorganic and organic impurities on the kinetics of growth of doping TGS crystals. It was observed that Ni-doped crystals were very similar in habit to pure TGS crystals, while in the case of Cu- and Fe-doped crystals, the numbers of developed faces were strongly reduced [17.70]. In the presence of Ni, Co, and Cu ions, the rate of crystallization decreased [17.81]. An odd behavior was found while growing Cr-doped crystals. The addition of Cr with a concentration of 1% changed the regime of crystallization owing to the high chemical activity of these ions. At a concentration of about 3%, the rate of crystallization became very fast even without lowering the temperature [17.81]. In Pd-doped crystals, the ratios of the growth rate along the *c*-axis to the growth rate along the *a*- and *b*-axes slightly decreased as the crystal grew larger [17.85]. For medium-sized crystals ($\approx$ 30 g), the average relative growth rate along the *c*-axis was larger by more than an order of magnitude in Pd-doped crystals than in pure TGS. Pd-doped crystals also developed other faces which have not been observed before. *Banan* et al. [17.82] studied the effect of Ce-, Cs-, L-alanine, and L-alanine + Cs on the growth and morphology of TGS crystals. Table 17.4 shows the crystal growth data, and Fig. 17.17 shows their habit. The well-developed (010)/(0$\bar{1}$0) faces, which were generally not present or less developed in pure TGS crystals are obtained with L-alanine- or Cs-doped crystals. Moreover, (101) faces obtained in crystals doped with L-alanine and in crystals doped with Cs and L-alanine were more dominant than pure TGS crystals. Also, the axial velocities, $V_{(001)}$ and $V_{(100)}$, were affected by doping (Table 17.4). Lower growth rates were especially obvious in Cs-doped crystals. The crystals became plate-like for $V_{(010)}/V_{(001)} \approx 28.0$; and the habits was strongly disturbed (Fig. 17.18). L-Alanine-doped crystals developed a habit which was asymmetric about the (010) plane. The growth rate in

Table 17.4 Growth data of doped TGS crystals [17.82]

	Crystal yield (g/(day °C))	$V_{(010)}$ (mm/(day °C))	$V_{(001)}$ (mm/(day °C))	$V_{(010)}$ (mm/(day °C))
TGS	0.171	0.88	0.34	2.58
TGS + Ce	0.021	0.079	0.047	1.68
TGS + Cs	0.009	0.198	0.007	28.20
TGS + L-alanine	0.192	0.89	0.44	2.02
TGS + L-alanine + Cs	0.132	0.65	0.063	10.30

the positive *b*-direction was higher than in the negative *b*-direction [17.29]. In D-alanine and L-alanine-doped TGS crystals, (101) faces developed more prominently than (001) faces, so the deuterated L-alanine-doped triglycine sulfate (DLATGS) crystals seemed to be thinner than pure TGS crystals. The (010) faces were more developed in aniline-doped crystals [17.84]. Recently, *Seif* et al. [17.92] studied the dependence of growth rate of the faces of TGS and KDP crystals on concentration of Cr(III) [17.92]. They proposed the following hypothesis to explain the effect of impurities on TGS and KDP crystals. It has long been known that, when a solute crystallizes from its supersaturated solution, the presence of impurities can often have a spectacular effect on the crystal growth kinetics and the habit of the crystalline phase. The impurities exhibit a marked specificity in their action as they are absorbed onto growing crystal surfaces. Adsorption of impurities onto crystal faces changes the relative surface free energies of the face and may block sites essential to the incorporation of new solute molecules into the crystal lattice and hence slow down the growth. The habit is thus determined by slow-growing faces. Furthermore, in the TGS:Cr(III) system dope with metal ions, metal–glycine complexes are formed in solution and enter the crystal lattice in the process of growth. The structure and type of metal ion complexes formed in the TGS lattice will determine the growth rate and hence the crystal habit.

It is also worthwhile to describe the effect of the same impurity on different types of crystals. The growth kinetic data of TGS and KDP crystals grown in the

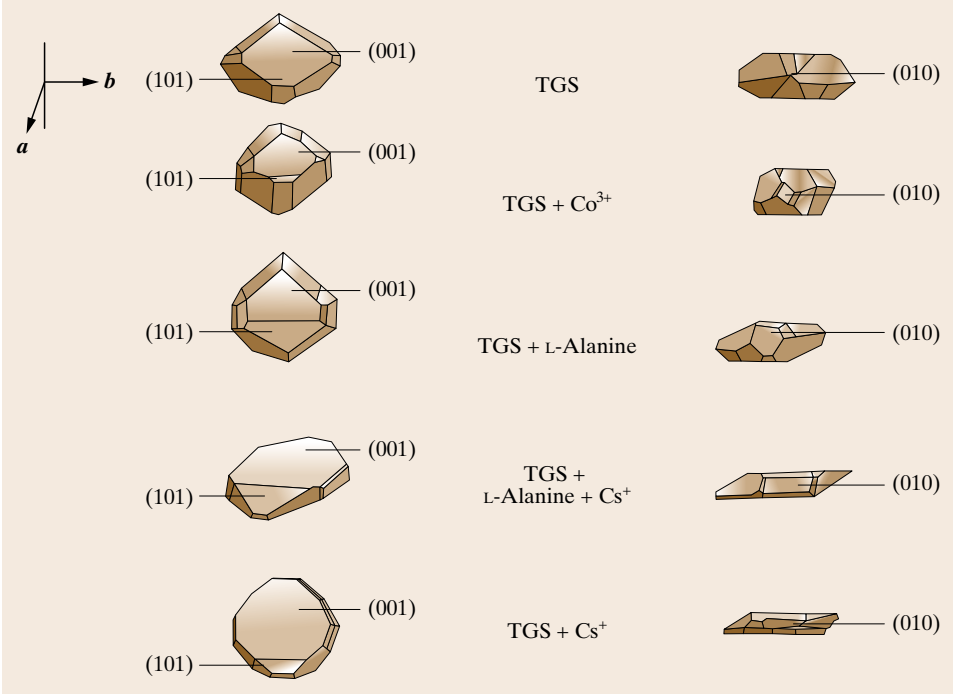


Fig. 17.18 Growth habits of doped TGS crystals

presence of Cr(III) ions are presented in Figs. 17.19 and 17.20. This data show the effect of impurity concentration on the growth rate of different faces of TGS and KDP crystals grown under constant, low supersaturation. In the case of KDP crystal, the mean growth rate along the [001] direction increases while along the [100] direction it remains almost constant with an increase in the concentration of Cr(III) in the solution/crystal with a slight fall below 7000 ppm. A similar type of effect of Fe(III) on growth rate of KDP crystal has been reported by *Owxzarek* and *Sangwal* [17.25]. $Cr_2(SO_4)_3$ molecules are considered to dissolve as an active complex such as $[Cr(H_2O)_2(OH)]^{2+}$, $[Cr(H_2O)_4(OH)_2]^{+}$ or $[Cr_2(SO_4)_2(H_2O)_7(OH)]^{+}$ and are assumed to become adsorbed on the crystal faces, thereby suppressing the growth rate. The impurities adsorbed on the surface of growing crystal at low supersaturation impede movements of steps by different mechanisms depending on the site of adsorption. Models of different types which describe the adsorption process and growth reduction have been reported in the literature [17.26, 27, 36, 93]. The models assume that the impurity species (ions, molecules or atoms) are adsorbed on the crystal surface into kinks, ledges, and terraces of growing surfaces. As soon as kinks and steps are occupied by impurity particles, there is a reduction in growth rates due to coverage of the crystal faces. This decrease in the growth rate can be explained on the basis of a model proposed by *Sangwal* and *Mielniczek-Brzoska* [17.32] based on their recent studies involving the Cu(II)–ammonium oxalate monohydrate crystal system. As shown in Fig. 17.19, the decrease in growth rate of (100) face of KDP crystals should be a kinetic effect involving a reduction in the value of the kinetic coefficient ($\beta = a\nu \exp^{(-W/k_B T)}$), where a is the dimension of growth units perpendicular to the step, ν is the frequency of vibration of molecules/atoms on the surface (s^{-1}), W is the activation energy for growth, k_B is the Boltzmann constant, and T is temperature (in Kelvin) for motion of steps on the surface. Above a certain critical concentration of impurity, there is no kinetic effect of impurity on growth kinetics. This may be due to the fact that all the active centers for crystallization are blocked, thus reducing the growth rate to zero. In our study, no growth of the {100} face was observed with more than 8000 ppm Cr(III) im-

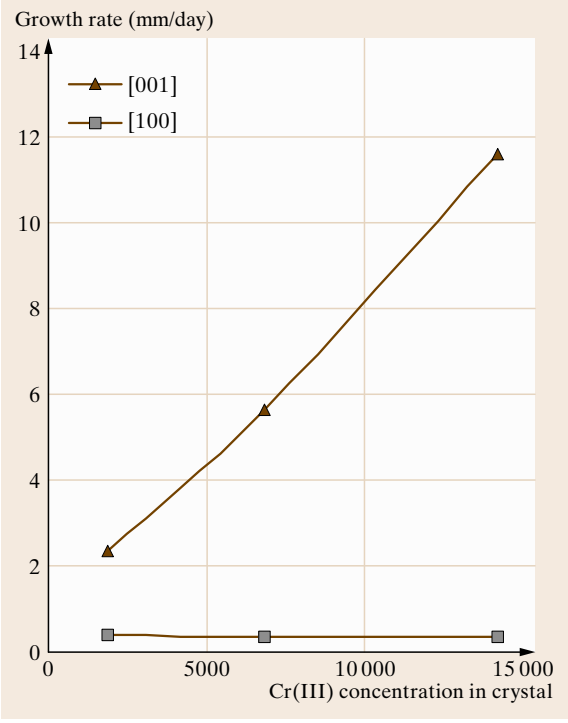


Fig. 17.19 Dependence of growth rate of the faces of KDP crystals on concentration of Cr(III)

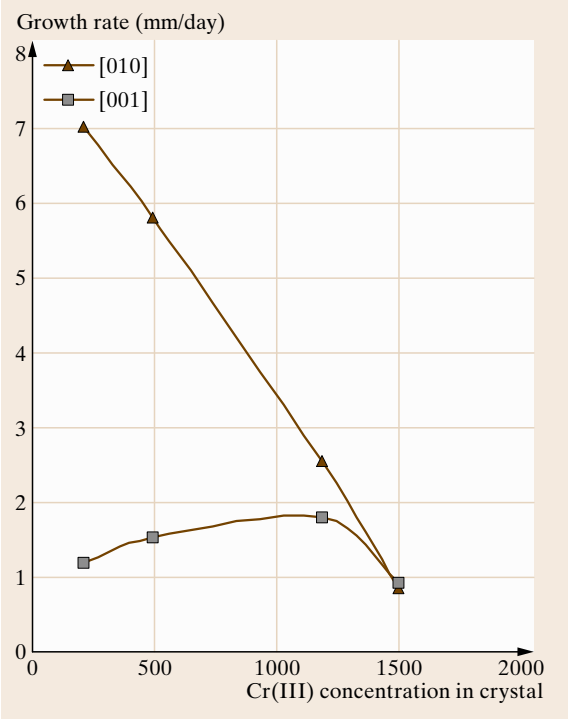


Fig. 17.20 Dependence of growth rate of the faces of TGS crystals on concentration of Cr(III)

purity in the KDP solution. An increase in growth rate along the [001] direction of KDP crystals may be caused by a decrease in the free energy of the face (thermodynamic effect); the surface energy decreases with an increase in impurity concentration, and hence increase in the growth rate. The above discussion suggests that the kinetic or thermodynamic effect depends on the structure of the crystal face, i. e., atomic arrangement, besides other factors.

Figure 17.20 shows that in the case of TGS crystals, the growth rate along the [010] direction decreases with an increase in the concentration of Cr(III) in the growth solution. This decrease in growth rate is due to the kinetic effect as explained above for the KDP crystal system. However, there is a slight increase in the growth rate along the [001] direction, with maxima around 1300 ppm Cr(III), and then there is a decrease. According to layer growth models, the consequence of a decrease in the edge free energy is an increase in the growth rate. Additionally, a decrease in the edge free energy may cause the growth mechanism to change. This effect of an initial increase followed by a subsequent decrease in growth rate with increasing concentration of impurity has been suggested by *Davey* [17.94], to opposite effects of thermodynamic and kinetic parameters. Furthermore, that ability of additives to form complexes with adventitious impurities present in a growth medium cannot be ruled out, as it can alter the atomic arrangement in crystal faces. To explain the effect of impurities on growth in more detail, one needs to collect more experimental data, including studies of the micromorphology of crystal surfaces as well as growth kinetics.

Effects of various organic dopants such as L-asparagine, L-tyrosine, L-cystine, guanidine, L-valine, and other dopants on morphology, growth, mechanical, and some physical properties of TGS have also been reported in the recent past [17.91, 95–99]. However, no explanation is given for change in the morphology of crystals by the authors of these publications.

17.5 Solution Growth of Triglycine Sulfate Crystals in Microgravity

The US National Aeronautics and Space Administration (NASA) has carried out about 115 Space Transportation Systems (STS) space flight missions (STS-1 to STS-127) from 1980 to the present day [17.100].

The authors were associated with two NASA missions called Spacelab-3 and the International Microgravity Laboratory (IML-1) on which single crystals of triglycine sulfate were grown from solution in microgravity for a period of 7 days aboard a Space Shuttle.

The general goal of the programs within NASA's Microgravity Research Division was to conduct basic and applied research under microgravity conditions (10^{-6} g) that would increase our understanding of fundamental physical, chemical, and biological processes specifically biotechnology, combustion science, fluid physics, fundamental physics, and materials science.

The microgravity environment of space provides a unique opportunity to further our understanding of various materials phenomena involving the molten, fluidic, and gaseous states by reducing or eliminating buoyancy-driven effects. Microgravity experiments in space are affected by residual microaccelerations on the spacecraft deriving from atmospheric drag, reaction control systems, momentum wheels, gravity gradients, crew involvement, and other disturbances. Mostly there is no actual suggestion by the scientific community as to the microgravity level required for their experiments. The general opinion is that microgravity will reduce the influence of convection, buoyancy, and sedimentation. Hardly any quantitative estimates have been made.

The anticipated results of microgravity materials science research range from establishing baselines for fundamental materials processes to generating results with more direct commercial significance. NASA's objectives for the microgravity materials science program include:

- Advancing our knowledge base for all classes of materials
- Designing and facilitating the execution of microgravity experiments that will help achieve this goal
- Determining road maps for future microgravity studies
- Contributing to NASA's Human Exploration and Development of Space enterprise
- Contributing to the national economy by developing enabling technologies valuable to the US private sector.

To accomplish these goals, the materials science program has tried to expand both its scientific scope and

research community's involvement in microgravity research. Based on their requirements for experimental facilities most of the current materials science microgravity experiments can be divided into four general categories. The first category involves melt growth experiments, such as those used for processing multicomponent alloys from the liquid. The experiments in this category frequently require high temperatures and closed containers or crucibles to prevent elemental losses. The second group includes aqueous or solution growth experiments for materials such as triglycine sulfate and zeolite. These experiments usually require moderate to low temperatures. Hydrothermal processing of inorganic compounds and sol–gel processing also fit in this category. The third category of experiments involves vapor or gaseous environments, such as those used for growing mercury iodide or plasma processing. Unlike the first three categories that use containers for the parent materials and products, the fourth category involves processes and experiments that require containerless processing environments. Examples of these experiments include the formation of metallic and nonmetallic glasses during levitation melting and solidification, float-zone growth of crystals, and measurement of thermophysical properties such as diffusion coefficients and surface tension.

17.5.1 Rationale for Solution Crystal Growth in Space

In the microgravity environment of space, several physical phenomena taken for granted on Earth change dramatically. Convection in solution due to density differences is greatly reduced. Crystallization and solidification are two processes that can benefit from microgravity environment. As a part of the US National Aeronautics and Space Administration (NASA) microgravity and applications program, a study of TGS crystals growth from solution was carried out on Spacelab-3 (SL-3) and first International Microgravity Laboratory (IML-1) missions in 1985 and 1992, respectively. Crystals from solution are usually grown in a closed container of limited volume. Thus, any convection that is generated tends to lead to a circular to steady laminar convection, due to buoyancy. The density differences in the fluid can arise from both temperature and concentration variations. On Earth buoyancy-driven convection may cause microscopic gas/solution inclusions and fluctuating dopants incorporation and other defects in the crystals. Besides degrading pyroelectric device performance, the growth yield of useful crystals is also severely impacted due to incorporation of these types of defects. In a low-gravity environment, convection is greatly suppressed and diffusion becomes the predominant mechanism for thermal and mass transport. Thus, growth in microgravity can eliminate these problems and enhance our knowledge about the science of crystal growth.

17.5.2 Solution Crystal Growth Method in Space

Since the ground solution technique could not be used in the microgravity environment of space, the authors developed a new method known as the cooled sting technique to grow crystals in space from solution, as described below.

Cooled Sting Technique

As the conventional techniques of solution crystal growth cannot be used for growing crystals in space, a new technique was proposed and developed [17.100–102]. On Earth, in the absence of stirring, conventional techniques of solution crystal growth cause a lowering of concentration of the solution in the vicinity of the growing crystal, resulting in an upward flow of solution. At constant temperature this reduction in concentration would cause the growth rate to decrease rapidly. In a $1g$ environment, most solution growth techniques are directed towards increased convection mass transport by applying forced convection with very slow programmed cooling of a saturated solution. However, in the absence of convection, a change of temperature must move inward toward the crystal by conduction. The characteristic time for this to occur is $T = L^2\rho C_\mathrm{p}/k$, where L is the distance over which the heat must be conducted, ρ is the density, C_p is the heat capacity, and k is the thermal conductivity of solution. For water, it takes 48 min for a temperature change of 1 °C to be felt at a distance of 2 cm. This is too slow to keep a constant growth rate. So a unique technique was developed by the authors, which uses programmed cooling of the seed crystal itself. This is accomplished by using a cold finger (*sting*) in direct contact with the seed crystal, which allows temperature lowering in accordance with a predetermined polynomial [17.103, 104] for maintaining a supersaturated TGS solution near the surface of the crystal. Because of the L^2 dependence of T, it takes less time for a change of sting temperature to be transmitted through the growing crystal and to be felt at the surface. The construction of the ground-based cooled sting and solution growth apparatus [17.103, 104] are

illustrated in Figs. 17.21 and 17.22, respectively. In this case, crystals are grown by lowering the sting/seed and solution temperature, thereby creating a desired supersaturation.

Flight Hardware

The experiment in space utilizes the fluid experiments system (FES) and crystals are grown by a new technique developed by the authors called the *cooled sting technique* as described earlier [17.101–103]. This technique utilizes heat extraction from the seed crystal through a copper rod (sting), thereby creating the desired supersaturation near the growing crystal. The sting temperature profile follows a predetermined polynomial so as to obtain uniform growth. Figure 17.23 shows a detailed diagram of the flight cell with sting incorporated in the experimental module. The FES is an apparatus with the crystal growth cell as an integral part. It was developed by NASA and fabricated by TRW, CA.

The cell is designed to allow a variety of holographic diagnostics and real-time schlieren viewing of the crystal and the surrounding fluid. Schlieren images are transmitted down a link as black-and-white video to reveal flow patterns and variation in fluid density. Holograms that are recorded in space give 3-D information that leads to quantitative determination of concentration fields surrounding the crystal and motion of particles, if present, to determine g-jitters. The modified FES incorporates holographic tomography which enables the taking of optical data through the cell at multiple angles. During the SL-3 mission, two TGS crystals (named FES-2 and FES-3) were grown using (001)-oriented seed-type disc (as shown in Fig. 17.24). The objectives

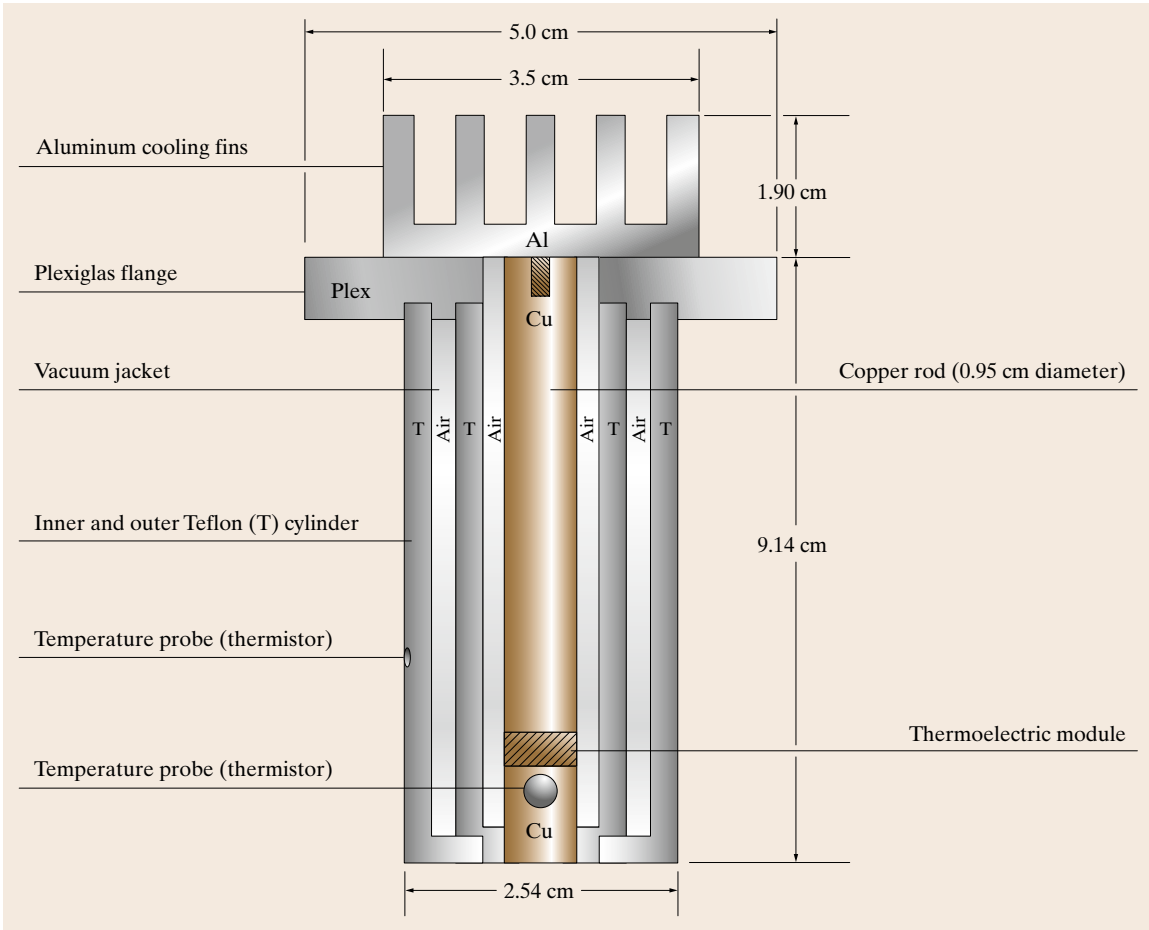


Fig. 17.21 Laboratory version of cooled sting assembly for the proposed crystal growth technique for microgravity

of the IML-1 flight experiments were: (a) to grow TGS crystals, (b) to perform holographic tomography of fluid field in the test cell in three dimensions, (c) to study fluid motion due to g-jitter by multiple-exposure holography of tracer particles (200, 400, and 600 μm), and (d) to study the influence of g-jitter on crystal quality and growth rate. One of the authors (R. B. Lal) was the principal investigator of the Spacelab-3 and IML-1 experiments. The coinvestigators were A. K. Batra, J. Trolinger, and W. R. Wilcox. During the IML-1 flight, due to serious hardware problems, only one TGS crystal was grown on a (010)-oriented seed crystal. The growth surface of seed crystal was a natural (010) face (unlike experiments performed in SL-3, in which processed seeds were used) cut from a polyhedral TGS crystal, with a thickness of about 3.5 mm. In TGS, the crystal growth rate is fast (maximum) in the [010] direction. On the ground, good-quality crystals are grown on (001)-oriented seed because growth on (010) face is nonuniform and multifaceted. Thus, it was important to investigate the growth on an (010)-oriented seed in the absence of buoyancy-driven convection,

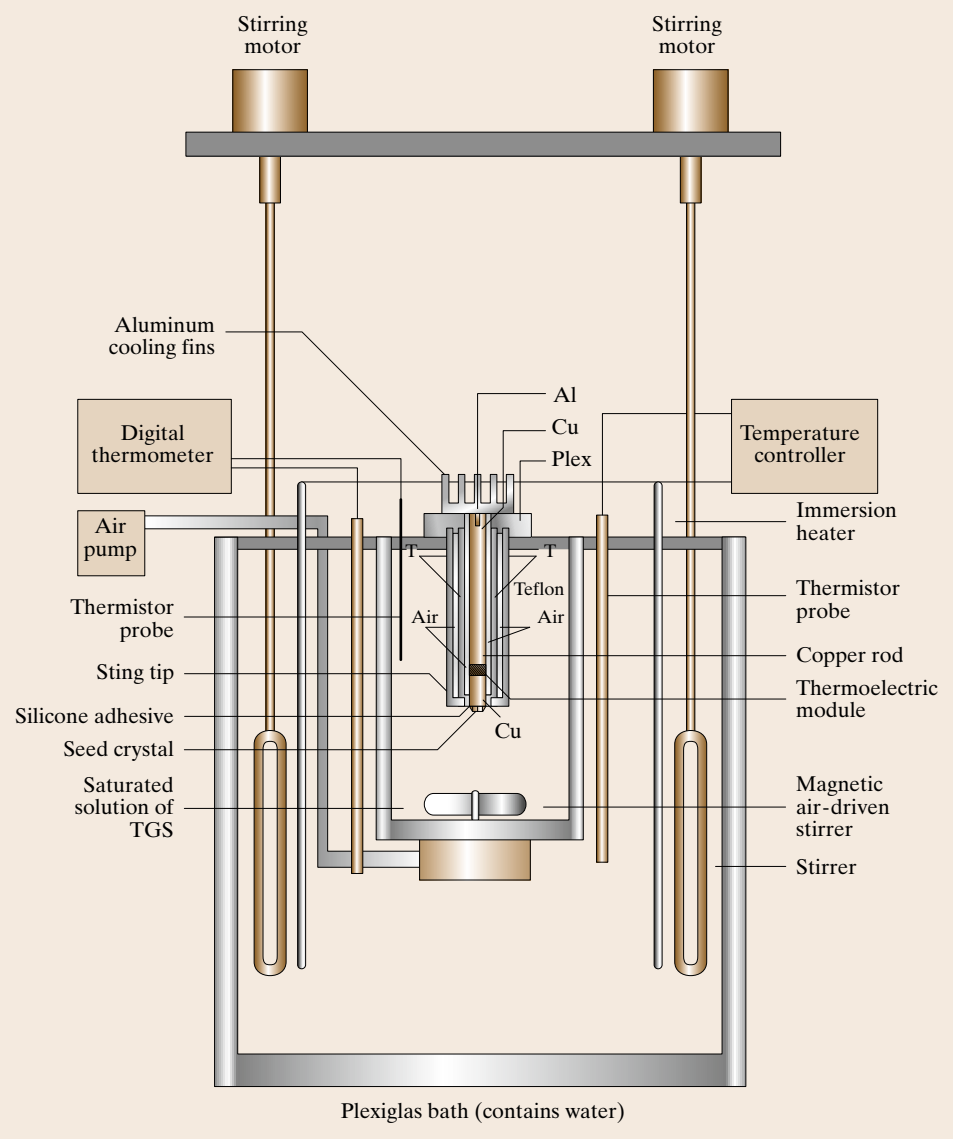


Fig. 17.22 Schematic diagram of the ground-based cooled sting solution growth apparatus

where growth is expected to be mainly diffusion controlled. This crystal was grown with undercooling of 4 °C for about 4 h. The growth rate was estimated to be about 1.6 mm/day and the quality of the grown crystal was substantially good. This can be attributed to a smooth transition from dissolution to growth in space experiment.

Flight Optical System

The fluids experiment system (FES) is a fully instrumented space flight chamber that can characterize the growth process through diagnostics of the crystal environment. Figure 17.25 shows the layout of optical system. Optical diagnostic instruments include two holographic cameras and a schlieren system, the output of which can be viewed in real time by television (TV) downlink. The optical and electronic instruments provide measures of solution concentration, temperature, convection, growth rate, and crystal properties during growth.

By recording light passing through the cell as well as light scattered from the crystal, holography provided diagnostics of the fluid through holographic interferometry, and particle diagnostics through three-dimensional particle imaging velocimetry. Figure 17.26 shows the layout of the optical system in which a 4 inch diameter, collimated He-Ne (Spectra Physics 107) laser beam passes through a double window into the crystal growth chamber, through the TGS solution, and across the surface of the crystal, finally emerging from a second set of windows. The beam then continues to the hologram plane, which is approximately 20 cm away, where it is mixed with a collimated reference wave on 70 mm-format roll film. The film is drawn flat on the platen by a vacuum in a unique film implementation of hologram recording for interferometry. In addition to the use of vacuum platens for recording and reconstruction, a special reconstruction process, necessary for holographic interferometry with film, described below, was developed to account for the imperfect optical quality of the film. A second holocamera views the crystal face directly from a lateral window [17.105]. Four types of holograms were produced, including singly exposed and multiply exposed holograms. The backlighting of the crystal was accomplished in two different ways, each with advantages and limitations; one method employs the direct laser beam and a second employs a diffuse beam, produced by inserting a diffuser into the object beam path before the beam enters the first cell window. The diffuse beam illuminates the field with

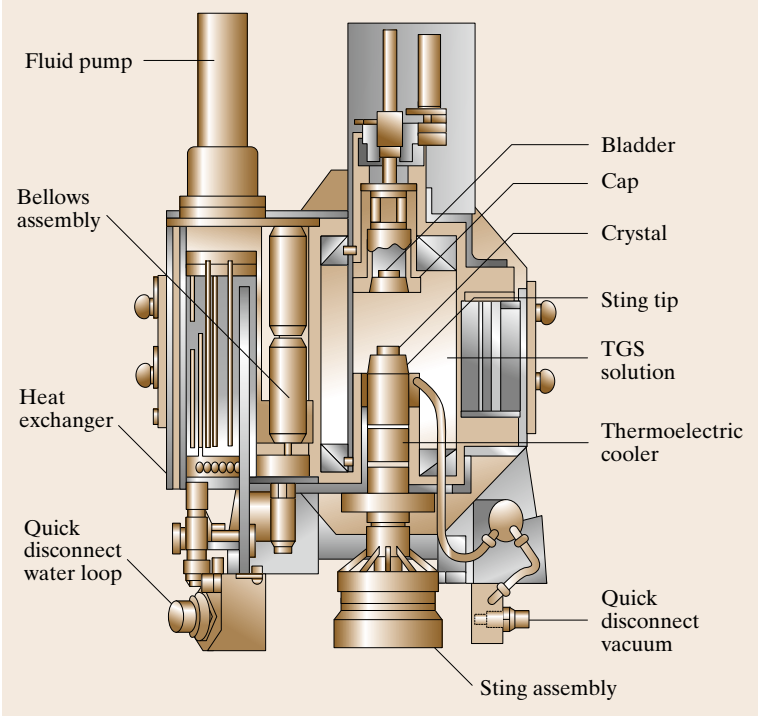


Fig. 17.23 Flight crystal growth cell designed and developed by NASA

many directions and is convenient for some types of viewing. However, such illumination is not useful for interferometry or schlieren in this system. Direct illumination is also used for interferometry and schlieren. With conventional optics, the direct illumination beam would provide a single illumination and viewing angle through the field.

Our previous experience in Spacelab-3 had taught us that more than one viewing angle is desirable. We achieved multiple viewing angles in IML-1 through the use of windows equipped with holographic optical elements (HOEs). The input window contains HOEs that convert the single input beam into three beams that pass over the crystal at angles of 0 and ±23.5°. The opposite window contains HOEs that redirect these beams to the recording film plane so that they can all be recorded and separated again during reconstruction. Consequently, each recording comprises three superimposed, but independently viewable, holograms. The schlieren system is viewed by TV, allowing real-time viewing both by the crew and by the TV downlink. A primary use of the schlieren system is to view and judge the transition of the crystal from a dissolution phase to a growth phase since control of this transition is considered to be critical in producing a high-quality crystal. The knife-edge in the schlieren system was set so that, when the crystal was dissolving, light rays entering the resulting higher-refractive-index region above the crystal would be refracted in the direction of the crystal and be removed by the knife-edge, appearing dark in the image. When the transition from dissolution to growth occurred, the region immediately above the crystal would be depleted of solute, thus reducing the refractive index and causing the refracted rays to pass

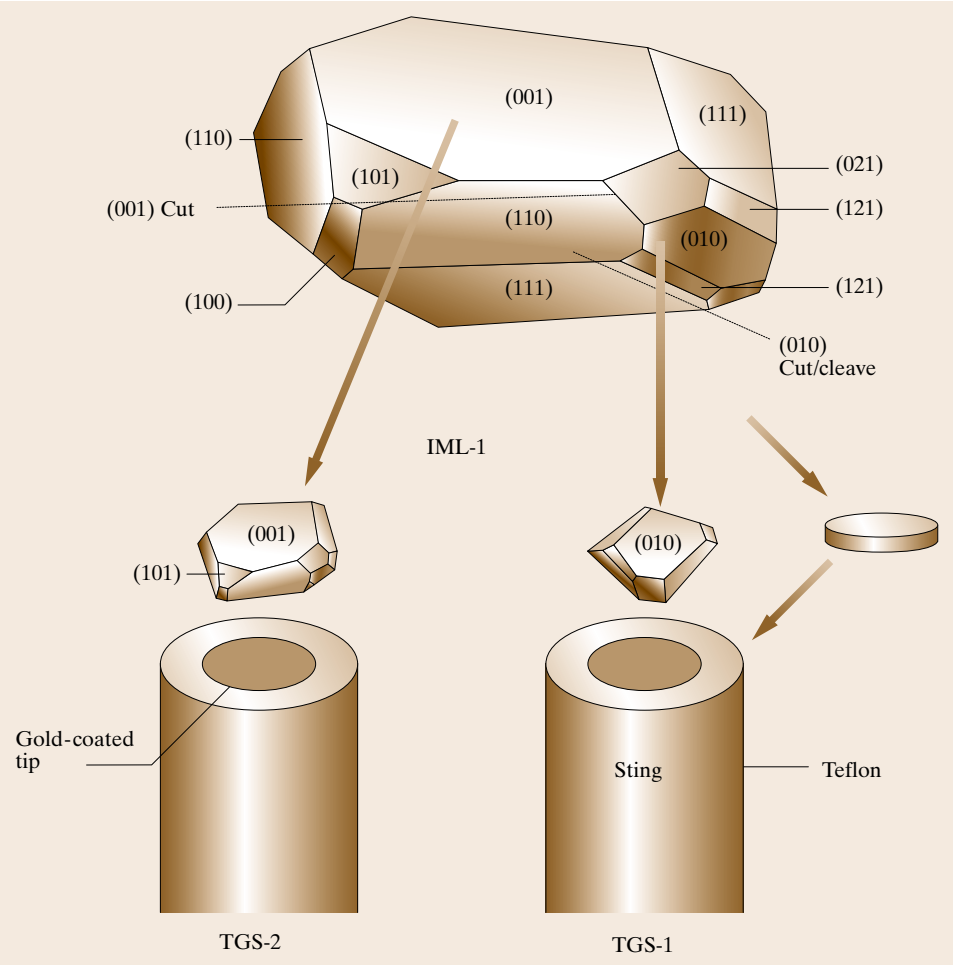


Fig. 17.24 TGS seed crystals used for growth runs on NASA's first International Microgravity Laboratory-1 (IML-1) mission

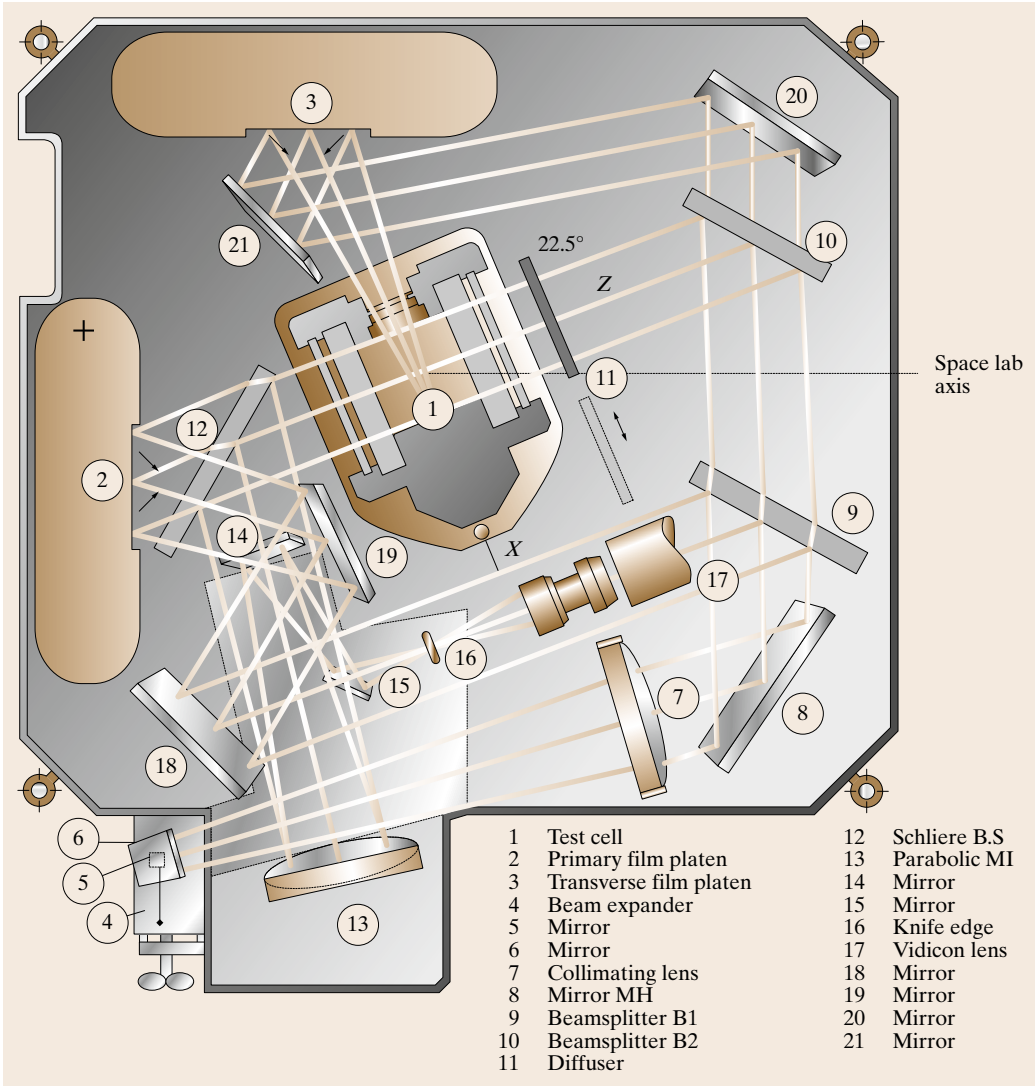


Fig. 17.25 Modified fluid experiment system (FES) optical system with various components

above the knife edge, causing a bright region to appear above the crystal within the larger, dark region of higher concentration. The method proved to be an extremely sensitive way to identify the transition from dissolution to growth.

17.5.3 Results and Discussion

The flight TGS crystals were examined with a high-resolution monochromatic synchrotron x-radiation diffraction technique, both before and after slicing for the fabrication of infrared detectors to check the lattice regularity, identify inclusions and dislocations, draw inferences about growth mode and stability, and locate the interface between the seed and the new growth. The experiments were performed at the National Synchrotron Light Source at Brookhaven National Laboratory in collaboration with B. Steiner of the US National Institute of Standards and Technology (NIST). The performance of materials is determined by their structure; in this performance, irregularity typically plays a leading role. The growth of crystals in low-g has long been of interest because of the anticipation that reduction in gravitational forces would strongly affect crystal growth and

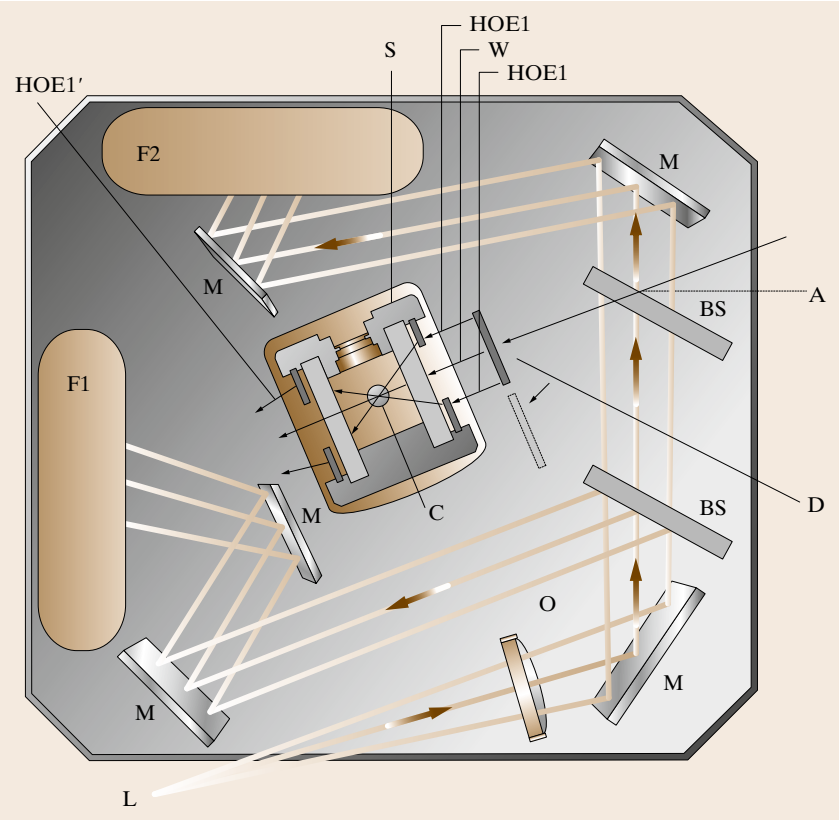


Fig. 17.26 Detailed optical layout for the fluid experiment system (FES) designed and developed by TRW. HOE 1′: note that ray emerges at an angle to simplify separation. A – Angle between optical axis and space shuttle axis, M – mirror, BS – beamsplitter, C – crystal, O – lens, D – removable diffusor, F1 – hologram 1, F2 – hologram 2, L – He-Ne laser underneath, S – side window, W – window

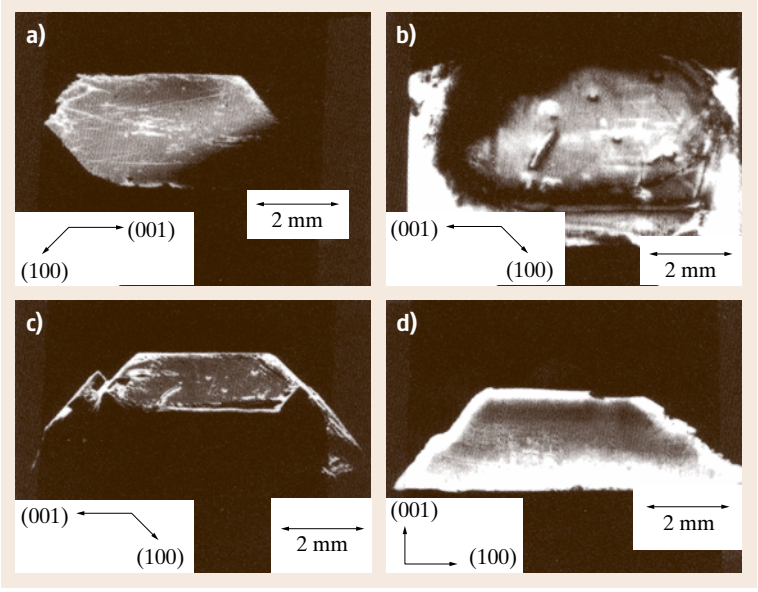


Fig. 17.27a–d High-resolution synchrotron x-ray radiation diffraction imaging of 1*g*- and microgravity-grown TGS crystals. **(a)** Uncut flight seed crystal, **(b)** high-resolution ($\bar{1}10$) diffraction image of the interior of the IML-1 crystal, **(c)** space-grown crystal with polystyrene particles, **(d)** cut edge of the IML-1 crystal

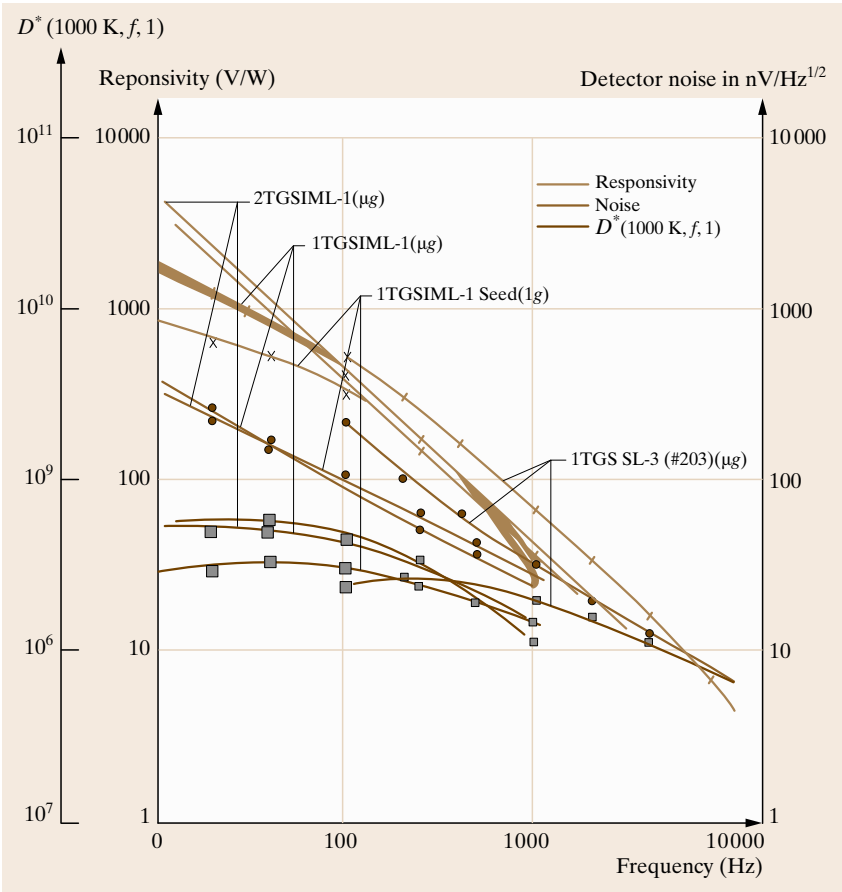


Fig. 17.28 Relevant parameters of infrared detectors fabricated from 1g- and microgravity-grown TGS crystals

thereby the nature of resulting irregularities. Many factors affect crystal growth, and because these can interact strongly with one another, the understanding of the structural variation necessary for its effective exploitation has not been fully achieved. Gaining knowledge of irregularities in space- and Earth-grown crystals, developed in conjunction with an understanding of their genesis and detailed effects on properties, is an important challenge. Such knowledge is also expected to contribute to dramatically improving single-crystal production, both in space and on the Earth. The local acceptance angle for diffraction from the uncut flight TGS-1 crystal of 1–2 arcsec (Fig. 17.27) indicates extraordinary crystal quality [17.106]. Polystyrene particles that had been included in the space-grown material in IML-1 experiment are observed as small imperfections in Fig. 17.27b. Also, clearly distinguishable in Fig. 17.27b is the faceted growth mode. Two sets of edge dislocations in the seed, one [101] oriented and the other [001] oriented, were noted as well in images taken in Laue geometry, but they appear not to have affected the space growth. Observation of the cut edge of the crystal (Fig. 17.27d) shows continuity between the seed at the top and space grown part. The demarcation between the seed and the space-grown material is indistinct. High-resolution imaging of terrestrial crystals has shown that the surface treatment of the seed crystal is critical to growth perfection. The ground control TGS crystals were of extremely high perfection. Slice next to many possible flight seeds were examined by high-resolution diffraction imaging. The selection of the flight seed was based on the perfection of the slice next to the seed crystal.

Infrared detectors from the flight and ground control crystals were fabricated at EDO/Barnes Engineering Division, Shelton, CT. The detectivity (D^*) and other parameters for these infrared detectors are shown in

Table 17.5 Detector characteristics of space-grown TGS crystals

Crystal (TGS)	Noise ($nV/Hz^{1/2}$)	Responsivity (V/W)	Detectivity (1000 K, f, 1) $\times 10^{-8}$	f (Hz)	Remarks
SL-3/FES2-TGS (μg grown)	320	510	0.99	100	Area = $0.3 \times 3\,mm^2$, blackened
IML-1TGS seed ($1g$ grown)	418	320	2	100	Area = $1 \times 1\,mm^2$, no window
IML-1TGS (μg grown)	90	400	4.2	100	Area = $1 \times 1\,mm^2$
IML-1TGS ($1g$ grown)	98	420	4.5	100	Area = $1 \times 1\,mm^2$
IML-1TGS (μg grown)	100	340	3	100	Area = $1 \times 1\,mm^2$

Fig. 17.28. The detector characteristics are given in Table 17.5. The detectivity (D^*) for IR detectors fabricated from the IML-1 crystal shows an improvement over the ground-grown crystals and crystals grown on Spacelab-3.

The motion of three different-sized particles were mapped using techniques described elsewhere [17.105, 107]. The combined effects of fluid convection, particle interaction, residual gravity, Space Shuttle maneuvers, and g-jitters have been observed. However, the interferograms show several noteworthy features. When the crystal enters a growth phase, the solution in the region near the crystal is depleted of solute, thus reducing its refractive index below that of the surrounding fluid, creating a hemispherical cap of fringes over the crystal, as shown in Fig. 17.29. The stability of this cloud in the interferograms confirmed that the crystal was growing in a diffusion-controlled process. The cloud did show, however, that the process was not completely axisymmetric, due to equipment-related problems that were encountered during the mission.

To sum up, in spite of problems with the operation of the FES, two important objectives were attained in the IML-1 experiment: (a) a high-quality TGS crystal was grown, (b) the particle dynamics experiment was successful.

In spite of limited time and fast growth, the growth on the (010) face was substantially uniform over a period of 18 h. The growth on the (010) face on ground is mostly nonuniform. Polystyrene particles of three sizes that had been occluded by the growing TGS were observed as small imperfections in the grown crystal. The observations of the cut edge of the flight crystal (TGS-1) show continuity between the seed at the bottom and the space growth at the top, indicating a high degree of epitaxy of the space-grown material. The demarcation between the seed and the space-grown material is indistinct, indicating a smooth transition from dissolution to growth so that solvent inclusions are not formed between the seed and the grown layer. Experiments on Earth have shown that such inclusions tend to result in dislocations that propagate through subsequently grown material and degrade properties. The infrared detectors fabricated from the TGS-1 flight crystal show improved detectivity (D^*) compared with ground samples and even with detectors fabricated from crystals grown on Spacelab-3. The dielectric loss in the IML-1 crystal is lower than in ground crystals and in crystals grown in Spacelab-3.

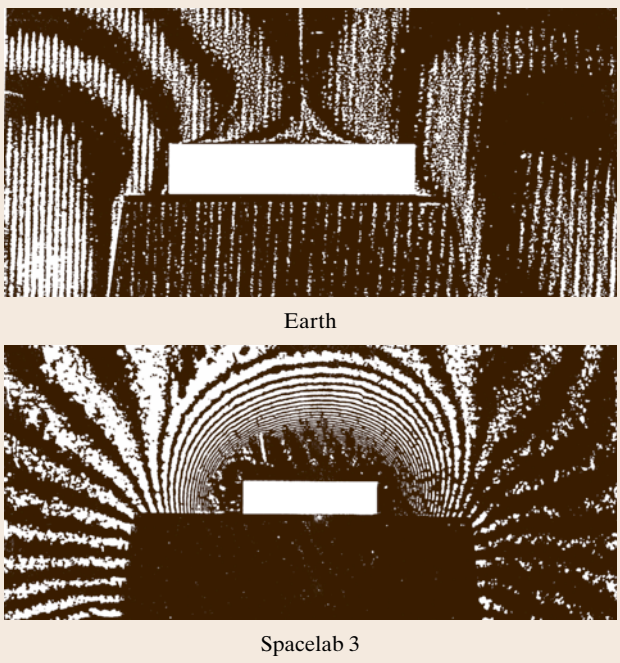


Fig. 17.29 Interferograms of concentration field in TGS solution on Earth and in microgravity onboard Spacelab-3

17.6 Protein Crystal Growth

The human body contains thousands of different proteins, which play essential roles in maintaining life. A protein's structure determines the specific role that it plays in the human body; however, researchers lack detailed knowledge about the structures of many proteins. The crystallization of proteins has three major applications: (1) structural biology and drug design, (2) bioseparations, and (3) controlled drug delivery. In the first application, protein crystals are used with the techniques of crystallography to ascertain the three-dimensional structure of the molecule. This structure is indispensable for correctly determining the often complex biological functions of these macromolecules. The design of drugs is related to this, and involves designing a molecule that can exactly fit into a binding site of a macromolecule and block its function in a disease pathway. Producing better-quality crystals will result in more accurate 3-D protein structure, which in turn means that the protein's biological function can be known more precisely, also resulting in improved drug design. The second application, bioseparations, refer to the downstream processing of the products of fermentation. Typically, the desired product of the fermentation process is a protein (e.g., insulin), which then needs to be separated from biomass. Crystallization is one of the commonly employed techniques for separation of protein. It has the advantage of being a benign separation process, that is, it does not cause the protein to unfold and lose its activity. The other application of protein, controlled drug delivery, is also very important. Most drugs are cleared by the body rapidly following administration, making it difficult to achieve a constant desired level over a period of time. When the drug is a protein such as insulin or α-interferon, administrating the drug in the crystalline form shows promise of achieving such controlled delivery. The challenge is to produce crystals of relatively uniform size so that dosage can be correctly prescribed.

17.6.1 Protein Crystal Growth Methods

Protein crystallization is inherently difficult because of the fragile nature of protein crystals. Proteins have irregularly shaped surfaces, which result in the formation of large channels within any protein crystal. Therefore, the noncovalent bonds that hold the lattice together must often be formed through several layers of solvent molecules. In addition, to overcoming the inherent fragility of protein crystals, successful production of x-ray-worthy crystals is dependent upon a number of environmental factors because so much variation exists among proteins, with each one requiring unique conditions for successful crystallization. Therefore, attempting to crystallize a protein without a proven protocol can be very tedious. Some factors that require consideration are protein purity, pH, concentration of protein, temperature, and the precipitants. In order to initiate crystallization the protein solution has to be brought to a thermodynamically unstable state of supersaturation. The solution can be brought back to the stable equilibrium state through precipitation of the protein, which is the most frequent process, or through crystallization. The supersaturation state can be achieved by several techniques: evaporation of solvent molecules, change of ionic strength, change of pH, change of temperature or change of some other parameter.

Two of the most commonly used methods for protein crystallization fall under the category of vapor diffusion [17.108–110]:

1. Hanging drop method
2. Sitting drop method.

Both of these methods entail the use of a droplet containing purified protein, buffer, and precipitants in higher concentration. Initially, the droplet of protein solution contains an insufficient concentration of precipitant for crystallization, but as water vaporizes from the drop and transfers to the reservoir, the precipitant concentration increases to a level optimal for crystallization. Since the system is in equilibrium, these optimum conditions are maintained until the crystallization is complete. Figures 17.30 and 17.31 depict

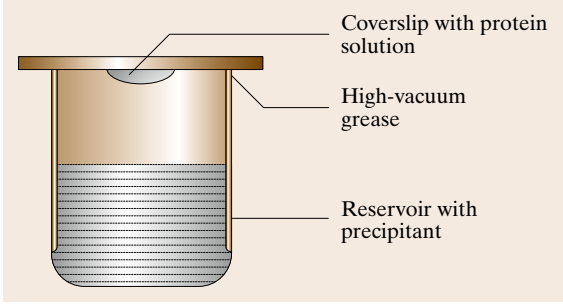


Fig. 17.30 Schematic diagram of the hanging drop method

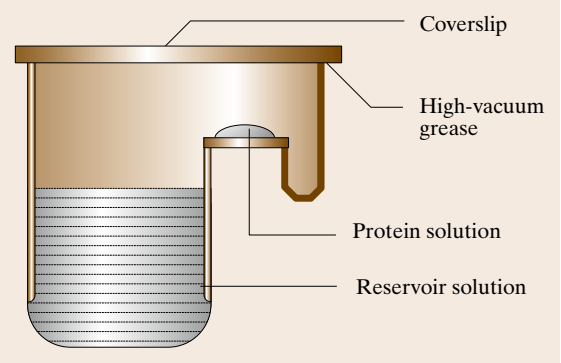


Fig. 17.31 Schematic diagram of the sitting drop method

the hanging drop and sitting drop systems, respectively. The hanging drop method differs from the sitting drop method in the vertical orientation of the protein solution drop within the system. It is important to mention that both methods require a closed system, that is, the system must be sealed off from outside using an airtight container. It is worth mentioning that the reservoir solution usually contains buffer and precipitant. The protein solution contains the same compounds, but in lower concentrations. The protein solution may also contain trace metals or ions necessary for precipitation; for instance, insulin is known to require trace amounts of zinc for crystallization.

17.6.2 Protein Crystal Growth Mechanisms

From the presence of well-defined facets on most protein crystals one can unambiguously conclude that growth occurs via the spreading of layers from growth step sources such as dislocations and 2-D nuclei. This has been confirmed on a molecular level. Ex situ electron microscopy observations have resolved individual growth steps on (010) and (110) faces of tetragonal lysozyme [17.111] that, contrary to recent claims [17.112, 113], are of monomolecular height. In situ atomic force microscopy of lysozyme has produced particularly instructive images of growth step generation at screw dislocations outcrops and of 2-D nucleation-induced islands.

Most recent atomic force microscopy observations on a larger number of other proteins and viruses [17.114] have reproduced the whole body of growth morphology and kinetics scenarios known for inorganic solution growth. These include layer spreading from dislocations and 2-D nuclei, interaction between growth steps from sources of different activities, and impediment of step propagation by foreign particles. Particle engulfment was observed to often result in dislocation formation. Crystallites that impinged on the interface became either epitaxially aligned with main crystal, or remained misaligned and caused various defects during further growth. There even appears to be some indication of kinetic roughening on certain facets of some proteins [17.115].

17.6.3 Protein Crystal Growth in Microgravity

The microgravity environment aboard spacecraft in low Earth orbit provides a convection- and sedimentation-free environment for the study and applications of fluid-based systems. With the advent of the US Space Shuttle, scientists had regular access to such environments and many experiments were initiated, including those in protein crystallization. After many trials it became clear that, for several proteins, crystallization in microgravity environment resulted in bigger and better crystals. In some instances, crystals that could not be crystallized at all on the ground were found to crystallize in space. Conversely, for numerous proteins the space environment was found to be no better or was worse than ground-based conditions. As a result of these observations, NASA has become one of the leading federal agencies in prompting and funding protein crystallization research. Efforts are directed at both utilizing the space environment to improve the crystallization of novel proteins and at fundamental studies of the causes (if any) of the improvement in protein crystals produced in microgravity. The results from flying more, and studying in more detail, have significantly altered attitudes towards space-based protein crystal growth. Persuasive explanations have emerged, and a strong theoretical model has emerged to explain why space-based growth is better.

Since the inception of protein crystal growth in microgravity research by *Littke* and *John* [17.116], several research groups have developed microgravity hardware and experiments [17.116–121]. Some of those are listed below:

1. Handheld protein crystallization apparatus for microgravity (HH-PCAM) [17.122]
2. Diffusion-controlled crystallization apparatus for microgravity (DCAM) [17.123]
3. High-density protein crystal growth system (HDPCG) [17.124]
4. Protein crystal growth facility (PCF) [17.125]

5. A multiuser facility-based protein crystallization apparatus for microgravity (PCAM) [17.122]
6. Advanced protein crystallization facility (APCF) [17.123].

Several thousand individual protein crystal growth experiments have been flown using the PCAM facility hardware aboard the US Space Shuttle. According to the developer of this facility, this hardware represents a pioneering development in design and deployment of space flight hardware based on disposable interface elements [17.122]. Furthermore, it has resulted in an ultrahigh-resolution structure and first example of neutron diffraction achieved as a result of protein crystal growth in microgravity [17.125–127]. Additionally, using this facility, fundamental differences in protein partitioning in microgravity have been documented, which represent the first direct experimental observation of the factors contributing to quality improvements in the growth of protein crystals in microgravity [17.128]. The other important hardware, referred to as the diffusion-controlled crystallization apparatus for microgravity (DCAM), utilizes the dialysis method and allows the equilibration rate of each individual experiment to be passively controlled from several days to several months. It is worth mentioning that precision control rate of supersaturation has routinely produced macrocrystals of size 5 mm to 1.25 cm for a variety of protein in this hardware. Analysis of serum albumin, ferritin, lysozyme, bacteriorhodopsin, and nucleosome core particles exhibit superior diffraction properties as compared with ground-based controls [17.123]. Further improvements of the hardware is ongoing for the International Space Station, where x-ray analysis can be done aboard the Space Station [17.124].

17.7 Concluding Remarks

Bulk high-quality single crystals are required for use in fabricating devices for various technological applications. Since crystal growth is a complicated process that depends on many parameters that can interact, the complete process is not well understood. This is one of the reasons to grow crystals in microgravity of space, to separate omnipresent convection on Earth and have only diffusion-controlled growth. The authors have attempted to give a comprehensive overview of the various problems encountered in the solution growth of single crystals on Earth and in space experiment based on their experience over almost three decades. The solutions of the various problems encountered during growth on ground and in spaceflight experiments are described. This chapter will serve as a foundation for those who desire to initiate a research program in the growth of bulk single crystals of technological importance that can be grown from low-temperature solution technique. A brief review of crystal growth fundamentals is presented, including key techniques for solution crystal growth such as solubility determination and the design of various crystal growth systems including mechanical and electronic crystal motor reciprocating arrangements. Three generations of modifications to solution crystallizers designed and fabricated in the laboratory and a crystallizer for space growth based on the cooled sting technique advanced by the authors are described. A number of solution-grown crystals grown at Alabama A&M University are shown. A detailed description of the crystal growth experiments on an important infrared material, triglycine sulfate, and the difficulties encountered in the space crystal growth experiment aboard the Space Shuttle in the NASA Spacelab-3 and first International Microgravity Laboratory (IML-1) missions are given. Since basic principles of solution growth technique are shared by protein crystal growth, basic techniques of protein crystal growth are briefly mentioned and efforts towards protein crystal growth in microgravity are also discussed.

References

17.1 H.A. Meirs, F. Isaac: The spontaneous crystallization, Proc. R. Soc. Lond. A **79**, 322–325 (1987)

17.2 K. Sangwal: Growth kinetics and surface morphology of crystals grown from solutions: recent observations and their interpretations, Prog. Cryst. Growth Charact. Mater. **36**(3), 163–248 (1998)

17.3 I.F. Nicolau: Growth kinetics of potassium-dihydrogen phosphate crystals in solution, Krist. Tech. **9**(11), 1255–1263 (1974)

17.4 R. Janssen-Van Rosmalen, P. Bennema, J. Garside: The influence of volume diffusion on crystal growth, J. Cryst. Growth **29**, 342–352 (1975)

17.5 A. Chianese: Growth and dissolution of sodium perborate in aqueous solutions by using RDC technique, J. Cryst. Growth **91**, 39–49 (1988)

17.6 K. Sangwal: On the mechanism of crystal growth from solutions, J. Cryst. Growth **192**, 200–214 (1998)

17.7 Y. Wang, X.L. Yu, D.I. Sun, S.T. Yin: Mass transport and growth kinetics related to the interface supersaturation oh lithium formate monohydrate, Cryst. Res. Technol. **36**(4/5), 441–448 (2001)

17.8 N. Zaitseva, L. Carman: Rapid growth of KDP-type crystals, Prog. Cryst. Growth Charact. Mater. **43**, 1–118 (2001)

17.9 I.V. Melikhov, L.B. Berliner: Crystallization of salts from supersaturated solutions; diffusion kinetics, J. Cryst. Growth **46**, 79–84 (1979)

17.10 P. Bennema: Sprial growth and surface roughening: development since Burton, Cabrera and Frank, J. Cryst. Growth **69**, 182–197 (1984)

17.11 X.Y. Liu, K. Malwa, K. Tsukamoto: Heterogeneous two dimension nucleation and growth kinetics, J. Chem. Phys. **106**(5), 1870–1879 (1997)

17.12 A.F. Izmailov, A.S. Myerson: Momentum and mass transfer in supersaturation solutions crystal growth from solution, J. Cryst. Growth **174**, 263–368 (1997)

17.13 M. Rak, K. Izdebski, A. Brozi: Kinetic Monte Carlo study of crystal growth from solution, Comput. Phys. Commun. **138**, 250–263 (2001)

17.14 F. Rosenberger, B. Mutaftschiev (Eds.): *Interfacial Aspects of Phase Transformation* (Reidel, Dordrecht 1982)

17.15 A.A. Chernov: Present day understanding of crystal growth from aqueous solutions, Prog. Cryst. Growth Charact. **26**, 121–151 (1993)

17.16 R. Mohan, A.S. Myerson: Growth kinetics: A thermodynamic approach, Chem. Eng. Sci. **57**, 4277–4285 (2002)

17.17 C.M. Pina, A. Putnis, J.M. Astilleros: The growth mechanisms of solid solutions crystallization from aqueous solutions, Chem. Geol. **204**, 145–161 (2004)

17.18 I. Sunagawa, K. Tsukamoto, K. Maiwa, K. Onuma: Growth and perfection of crystals from aqueous solution: Case studies on Barium nitrate and K-Alum, Prog. Cryst. Charact. **30**, 153–190 (1995)

17.19 W.R. Wilcox: Influence of convection on the growth of crystals from solution, J. Cryst. Growth **65**, 133–142 (1983)

17.20 I.V. Markov: *Crystal Growth for Beginners* (World Scientific, Hobohen 2004)

17.21 I. Sunagawa: *Crystals Growth, Morphology and Perfection* (Cambridge Univ. Press, Cambridge 2005)

17.22 T. Ogawa: A phenomenological analysis of crystal growth from solutions as an irreversible process, Jpn. J. Appl. Phys. **16**(5), 689–695 (1977)

17.23 S. Veintemillas-Verdaguer: Chemical aspects of the effect of impurities in crystal growth, Prog. Cryst. Growth Charact. **32**, 76–109 (1996)

17.24 K. Sangwal: Kinetics effects of impurities on the growth of single crystals from solutions, J. Cryst. Growth **203**, 197–212 (1999)

17.25 I. Owczarek, K. Sangwal: Effect of impurities on the growth of KDP crystals: Mechanism of adsorption on (101) faces, J. Cryst. Growth **102**, 574–580 (1990)

17.26 K. Sangwal: Effects of impurities on the crystal growth processes, Prog. Cryst. Charact. **32**, 3–43 (1996)

17.27 E. Kirkova, M. Djarova, B. Donkova: Inclusions of isomorphism impurities during crystallization from solutions, Prog. Cryst. Growth Charact. **32**, 111–134 (1996)

17.28 M. Rauls, K. Bartosch, M. Kind, S. Kuch, R. Lacmann, A. Mersmann: The influence of impurities on crystallization kinetics – A case study on ammonium sulfate, J. Cryst. Growth **312**, 116–128 (2000)

17.29 E. Mielniczek-Brzoska, K. Gielzak-Kocwin, K. Sangwal: Effects of Cu(II) ions on the growth of ammonium oxalate monohydrate crystals from aqueous solutions: Growth kinetics, segregation coefficient and characterization of incorporation sites, J. Cryst. Growth **212**, 532–542 (2000)

17.30 K. Sangwal, E. Mielniczek-Brzoska, J. Bore: Effect of Mn(II) ions on the growth of ammonium oxalate monohydrate crystals from aqueous solutions: Growth habit and surface morphology, Cryst. Res. Technol. **38**(2), 103–112 (2003)

17.31 N. Kubota, M. Yokota, J.W. Mullin: Supersaturation dependence of crystal growth in solutions in the presence of impurity, J. Cryst. Growth **182**, 86–94 (1997)

17.32 K. Sangwal, E. Mielniczek-Brzoska: On the effect of Cu(II) impurities on the growth kinetics of ammonium oxalate monohydrate crystals from aqueous solutions, Cryst. Res. Technol. **36**(8-10), 837–849 (2001)

17.33 K. Sangwal, E. Mielniczek-Brzoska, J. Bore: Study of segregation coefficient of cationic impurities in ammonium oxalate monohydrate crystals during growth from aqueous solutions, J. Cryst. Growth **244**, 183–193 (2002)

17.34 K. Sangwal, T. Palcznska: On the supersaturation and impurity concentration dependence of segregation coefficient in crystals grown from solutions, J. Cryst. Growth **212**, 522–531 (2002)

17.35 P.S. Delineshev: Growth of crystals in the presence of impurities, a hypotheses based on a kinetic approach, Cryst. Res. Technol. **33**(6), 891–897 (1998)

17.36 K. Sangwal: Kinetic effects of impurities on the growth of single crystals from solutions, J. Cryst. Growth **203**, 197–212 (1999)

17.37 A.S. Myerson, S.M. Jang: A comparison of binding energy an metastable zone width for adipic acid

with various additives, J. Cryst. Growth **156**, 459–466 (1995)
17.38 D. Aquilano, M. Rubbo, G. Mantovani, G. Sgualdino, G. Vaccari: Equilibrium and growth forms of sucrose crystals in the {*h*0*l*} zone, J. Cryst. Growth **74**, 10–20 (1986)
17.39 D. Aquilano, M. Rubbo, G. Mantovani, G. Sgualdino, G. Vaccari: Equilibrium and growth forms of sucrose crystals in the {*h*0*l*} zone, J. Cryst. Growth **83**, 77–83 (1987)
17.40 A.A. Chernov, V.V. Sipyagin: Peculiarities in crystal growth aqueous solutions connected with their structure. In: *Current Topics in Materials Science*, Vol. 5, ed. by E. Kaldis (North-Holland, Amsterdam 1980) pp. 279–333
17.41 K. Byrappa, H. Klapper, T. Ohachi, R. Fornari (Eds.): *Crystal Growth of Technologically Important Electronic Materials* (Allied, New Delhi 2003)
17.42 M.D. Aggarwal, T. Gebre, A.K. Batra, M.E. Edwards, R.B. Lal, B.G. Penn, D.O. Frazier: Growth of nonlinear optical materials at Alabama University, Proc. SPIE **4813**, 52–65 (2002)
17.43 M.D. Aggarwal, W.S. Wang, K. Bhat, B.G. Penn, D.O. Frazier: Photonic crystals: crystal growth processing and physical properties. In: *Handbook of Advanced Electronic and Photonic Materials and Devices*, Vol. 9, ed. by H.S. Nalwa (Academic, New York 2001) pp. 193–228
17.44 H.K. Henisch: *Crystal Growth in Gels* (Dover, New York 1970)
17.45 A.F. Barton: *Handbook of Solubility Parameters and Other Cohesion Parameters* (CRC, Boca Raton 1983)
17.46 J. Novotny: A crystallizer for the investigation of conditions of growth of single crystals from solutions, Krist. Tech. **6**(3), 343–352 (1971)
17.47 M.D. Aggarwal, J. Choi, W.S. Wang, K. Bhat, R.B. Lal, A.D. Shields, B.G. Penn, D.O. Frazier: Solution growth of a novel nonlinear optical material: L-histidine tetrafluoroborate, J. Cryst. Growth **204**, 179–182 (1999)
17.48 A.K. Batra, S.C. Mathur: Reciprocating arrangement for solution crystal growth, Res. Ind. **29**, 20–22 (1984)
17.49 W.S. Wang, M.D. Aggarwal, J. Choi, K. Bhat, T. Gebre, A.D. Shields, B.G. Penn, D.O. Frazier: Solvent effects and polymorphic transformation of organic nonlinear optical crystal L-pyroglutamic acid in solution growth processes. I. Solvent effects and growth morphology, J. Cryst. Growth **198/199**, 578–582 (1999)
17.50 C. Owens, K. Bhat, W.S. Wang, A. Tan, M.D. Aggarwal, B.G. Penn, D.O. Frazier: Bulk growth of high quality nonolinear optical crystals of L-arginine tetrafluoroborate (L-AFB), J. Cryst. Growth **225**, 465–469 (2001)
17.51 R.B. Lal, H.W. Zhang, W.S. Wang, M.D. Aggarwal, H.W.H. Lee, B.G. Penn: Crystal growth and optical properties of 4-aminobenzophenone crystals for NLO applications, J. Cryst. Growth **174**, 393–397 (1997)
17.52 H.W. Zhang, A.K. Batra, R.B. Lal: Growth of large methyl-(2,4-dinitrophenyl)-aminopropanoate: 2-methyl-4-nitroaniline crystals for nonlinear applications, J. Cryst. Growth **137**, 141–144 (1994)
17.53 M.R. Simmons: An investigation of crystals matrices of single crystals doped with rare earth ions. M.Sc. Thesis (Alabama Univ., Alabama 2002)
17.54 J.-M. Chang, A.K. Batra, R.B. Lal: Growth and characterization of doped TGS crystals for infrared devices, Cryst. Growth Des. **2**(5), 431–435 (2002)
17.55 M.D. Aggarwal, R.B. Lal: Simple low-cost reciprocating crystallizer for solution crystal growth, Rev. Sci. Instrum. **54**, 772–773 (1983)
17.56 A.K. Batra, C.R. Carmichael-Owens, M. Simmons, M.D. Aggarwal, R.B. Lal: Design of a solution crystal growth crystallizer with versatile electronic reciprocal motion control for a crystal holder, Cryst. Res. Technol. **40**(8), 757–760 (2005)
17.57 A.K. Batra, M.D. Aggarwal, R.B. Lal: Growth and characterization of doped DTGS crystals for infrared sensing devices, Mat. Lett. **57**, 39–43 (2003)
17.58 R.B. Lal, M.D. Aggarwal: Reciprocating crystallizer: Automatic crystallizer grows crystals from aqueous solutions, NASA Tech. Briefs **8**, 419 (1984)
17.59 F. Jona, S. Shirane: *Ferroelectric Crystals* (Dover, New York 1993)
17.60 R.B. Lal, A.K. Batra: Growth and properties of triglycine (TGS) sulfate crystals: Review, Ferroelectrics **142**, 51–82 (1993)
17.61 E.A.D. White, J.D.C. Wood, V.M. Wood: The growth of large area, uniformly doped TGS crystals, J. Cryst. Growth **32**, 149–156 (1976)
17.62 B. Brezina, M. Havrankova, M. Vasa: Enhanced growth of non-polar {001} growth sectors of deuterated triglycine sulfate doped with L-alanine (LADTGS), Cryst. Res. Technol. **27**(1), 13–20 (1992)
17.63 S. Satapathy, S.K. Sharma, A.K. Karnal, V.K. Wadhawan: Effects of seed orientation on the growth of TGS crystals with large (010) facets needed for detector applications, J. Cryst. Growth **240**, 196–202 (2002)
17.64 M. Banan: Growth of pure and doped triglycine sulfate crystals for pyroelectric infrared detector applications. M.Sc. Thesis (Alabama A&M Univ., Alabama 1986)
17.65 D. Zhao-De: A new method of growth of ferroelectric crystal, Ferroelectrics **39**, 1237–1240 (1981)
17.66 F. Moravec, J. Novotny: Study on the growth of triglycine sulphate single crystals, Krist. Techn. **7**, 891–902 (1972)
17.67 W.K. Burton, N. Cabrera, F.C. Frank: The growth of crystals and the equilibrium structure of their surfaces, Philos. Trans. R. Soc. Lond. **243**, 299–358 (1951)

17.68 L.N. Rashkovich: Interferometric investigation of growth rate of {001} faces of triglycine sulfate at various supersaturation and temperature, Sov. Phys. Crystallogr. **28**, 454–458 (1983)

17.69 J. Novotny, F. Moravec, Z. Solc: The role of surface and volume diffusion in the growth of TGS single crystals, Czech. J. Phys. B **23**, 261–266 (1973)

17.70 J. Novotny, F. Moravec: Growth of TGS from slightly supersaturated solutions, J. Cryst. Growth **11**, 329–335 (1971)

17.71 D.A. Reiss, R.L. Kroes, E.E. Anderson: Growth kinetics of the (001) face of TGS below the ferroelectric transition temperature, J. Cryst. Growth **84**, 7–10 (1987)

17.72 M. Banan, R.B. Lal, A.K. Batra, M.D. Aggarwal: Effect of poling on the morphology and growth rate of TGS crystals, Cryst. Res. Technol. **24**(3), K53–K55 (1989)

17.73 F. Moravec, J. Novotny: A contribution to the study of the influence of impurities on the growth and some physical properties of TGS single crystals, Krist. Techn. **6**(3), 335–342 (1971)

17.74 R.V. Whipps, R.S. Cosier, L.K. Bye: Orthorhombic diglycine sulphate, J. Mater. Sci. **7**(12), 1476–1477 (1972)

17.75 E. Dominquez, R. Jimenez, J. Mendiola, E.J. Vivas: Diglycine sulphate – An interesting new dielectric crystal species, J. Mater. Sci. **70**(3), 363–364 (1972)

17.76 M.S. Tsedrik, V.N. Ulasen, G.A. Zaborovski: Growing TGS and TGSe single crystals at various pH of solution, Krist. Techn. **10**(1), 49–54 (1975)

17.77 E.J. Weidmann, E.A.D. White, V.M. Wood: Induced growth anisotropy in TGS crystals, J. Mater. Sci. Lett. **7**, 719–720 (1972)

17.78 L. Szczepanska: Growth investigations of single crystal sulphates containing molecular glycine groups, Krist. Techn. **11**, 265–271 (1976)

17.79 L. Prokopova, J. Novotny, Z. Micka, V. Malina: Growth of triglycine sulphate crystals doped by cadmium phosphate, Cryst. Res. Technol. **36**, 1189–1195 (2001)

17.80 G.R. Pandya, D.D. Vyas: On growth and morphological studies of TGS single crystals, Cryst. Res. Technol. **16**, 1353–1358 (1981)

17.81 R.B. Lal, S. Etminan, A.K. Batra: Effect of simultaneous organic and inorganic dopants on the characteristics of triglycine sulfate crystals, Proc. 9th IEEE Int. Symp. Appl. Ferroelectr. (1994) pp. 695–697

17.82 M. Banan, A.K. Batra, R.B. Lal: Growth and morphology of triglycine sulphate (TGS) crystals, J. Mater. Sci. Lett. **8**, 1348–1349 (1989)

17.83 N. Nakatani: Ferroelectric domain structure and internal bias field in DL-α-alanine-doped triglycine sulfate, Jpn. J. Appl. Phys. **30**(12A), 3445–3449 (1991)

17.84 J. Eisner: The physical properties of TGS single crystals, grown from aqueous TGS solutions containing aniline, Phys. Status Solidi **43**, K1–K4 (1977)

17.85 F. Moravec, J. Novotny, J. Strajblova: Single crystals of triglycine sulphate containing palladium, Czech J. Phys. **23**, 855–862 (1977)

17.86 A.S. Sidorkin, A.M. Kostsov: Exoelectron emission from a ferroelectric crystal of triglycine sulfate with defects, Sov. Phys. Solid State **33**(8), 1383–1384 (1991)

17.87 L. Yang, A.K. Batra, R.B. Lal: Growth and characterization of TGS crystals grown by cooled sting technique, Ferroelectrics **118**(1-4), 85–89 (1991)

17.88 N. Nakatani: Ferroelectric domain structure and internal bias field in DL-α-alanine doped triglycine sulfate, Jpn. J. Appl. Phys. **30**, 3445–3449 (1991)

17.89 B. Brezina, M. Havrankova: Orientation of structure and crystals of TGS and TGS doped with D, al or L, al, Cryst. Res. Technol. **20**, 781–786 (1985)

17.90 G.M. Loiacono, J.P. Dougherty: *Final Technical Report* (Night Vision and Electro-optics Laboratories, Fort Belvoir 1978), Contract No. DAAK70-77-C-0098

17.91 G. Arunmozhi, E. De Matos Gomes, J. Ribeiro: Dielectric properties of L-asparagine doped TGS (Asp-TGS) crystals, Ferroelectrics **295**, 87–95 (2003)

17.92 S. Seif, K. Bhat, A.K. Batra, M.D. Aggarwal, R. B.Lal: Effect of Cr(III) impurity on the growth kinetics of potassium dihydrogen phosphate and triglycine sulfate grown from aqueous solutions, Mater. Lett. **58**, 991–994 (2004)

17.93 V.A. Kuznetov, T.M. Okhrimenko, M. Rak: Growth promoting effect of organic impurities on growth kinetics of KAP and KDP crystals, J. Cryst. Growth **193**, 164–173 (1998)

17.94 R.J. Davey: *Industrial Crystallization*, Vol. 78, ed. by E.J. de Jong, S.J. Jancic (North-Holand, Amsterdam 1979) pp. 169–198

17.95 O.W. Wang, C.S. Fang: Investigation of the solution status of TGS and ATGSP crystals, Cryst. Res. Technol. **27**, 245–251 (1992)

17.96 K. Meera, R. Muralindharan, A.K. Tripathi, P. Ramasamy: Growth and characterization of l-threonine, dl-threonine, l-methionine admixtured TGS crystals, J. Cryst. Growth **263**, 524–531 (2004)

17.97 G. Su, Y. He, H. Yao, Z. Shi, Q. Wu: A new pyroelectric crystal L-lysine-doped THS (LLTGS), J. Cryst. Growth **209**, 220–222 (2000)

17.98 J. Novotny, J. Zelinkay, F. Moravec: Broadband infrared detectors on the basis of PATGS/Pt(IV) single crystals, Sens. Actuators A **119**, 300–304 (2005)

17.99 S. Kalainathan, M.B. Margaret, T. Trusan: Morphological changes of L-asparagine doped TGS crystal, Cryst. Eng. **5**, 71–78 (2002)

17.100 http://www.nasa.gov/missions/index.html (last accessed August 9, 2009)

17.101 R.B. Lal, R.L. Kroes: Solution growth of crystal on Spacelab-3, Proc. 24th AIAA Sci. Meet. (Reno 1985)

17.102 R.B. Lal, M.D. Aggarwal, R.L. Kroes, W.R. Wilcox: A new technique of solution crystal growth, Phys. Status Solidi (a) **80**, 547–551 (1983)

17.103 A.K. Batra, R.B. Lal, M.D. Aggarwal: Electrical properties of TGS crystals grown by new technique, J. Mater. Sci. Lett. **4**, 1425–1427 (1985)

17.104 R.B. Lal, M.D. Aggarwal, A.K. Batra, R.L. Kroes: Solution growth of crystals in zero-gravity, final technical report (NASA, Washington 1987), NASA contract number NAS8–32945

17.105 R.B. Lal: Solution growth of crystals in low-gravity, final technical report (1995), NASA contract number NAS8–36634

17.106 B. Steiner, R. Dobbyn, D. Black, H. Burdette, M. Kuriyama, R. Spal, L. van den Berg, A. Fripp, R. Simchick, R.B. Lal, A.K. Batra, D. Mathiesen, B. Ditchek: High resolution diffracting imaging of crystals grown, Microgravity and closely related terrestrial crystals (NIST, Gaithersburg 1991), Technical Note 1287

17.107 R.B. Lal, A.K. Batra, J.D. Trolinger, W.R. Wilcox: TGS crystal growth experiment on the first international microgravity laboratory (IML-1), Microgravity Q. **4**(3), 186–198 (1994)

17.108 D.E. McRee: *Practical Protein Crystallography* (Academic Press, San Diego 1993) pp. 1–23

17.109 G. Rhodes: *Crystallography Made Crystal Clear* (Academic, San Diego 1993) pp. 8–10

17.110 G. Rhodes: *Crystallography Made Crystal Clear* (Academic, San Diego 1993) pp. 29–38

17.111 S.D. Durbin, G. Feher: Studies of crystal growth mechanisms of proteins by electron microscopy, J. Mol. Biol. **212**, 763–774 (1990)

17.112 E. Forsythe, M.L. Pusey: The effects of temperature and NaCl concentration on tetragonal lysozyme face growth rates, J. Cryst. Growth **139**, 89–94 (1994)

17.113 A. Nadaraja, E.L. Forsythe, M.L. Pusey: The averaged face growth rates of lysozyme crystals: The effect of temperature, J. Cryst. Growth **151**, 163–172 (1995)

17.114 W. Littke, C. John: Protein single crystal growth under microgravity, Science **225**, 203–204 (1984)

17.115 F. Rosenberger: Protein crystallization, J. Cryst. Growth **166**, 40–54 (1996)

17.116 W. Littke, C. John: Protein single crystal growth under microgravity, J. Cryst. Growth **76**, 663–672 (1986)

17.117 L.J. DeLucas, F.L. Suddath, R.S. Snyder, R. Naumann, M.B. Broom, M.L. Pusey, V. Yost, B. Herren, D.C. Carter, B. Nelson, E.J. Meehan, A. McPherson, C.E. Bugg: Preliminary investigations of protein crystal growth using the space shuttle, J. Cryst. Growth **76**, 681–693 (1986)

17.118 L.J. DeLucas, C.D. Smith, H.W. Smith, V.K. Senadhi, S.E. Senadhi, S.E. Ealick, D.C. Carter, R.S. Snyder, P.C. Weber, F.R. Salemme, D.H. Ohlendorf, H.M. Einspahr, L.L. Clancy, M.A. Navia, B.M. Mc-Keever, T.L. Nagabhushan, G. Nelson, A. McPherson, S. Koszelak, G. Taylor, D. Stammers, K. Powell, G. Darby, C.E. Bugg: Protein crystal growth in microgravity, Science **246**, 651–653 (1989)

17.119 S. Simic-Stefani, M. Kawaji, H.U. Hu: G-jitter induced motion of a protein crystal under microgravity, J. Cryst. Growth **294**, 373–384 (2006)

17.120 A. McPherson: Virus and protein crystal growth on earth and in microgravity, J. Phys. D **26**, B104–B112 (1993)

17.121 D.C. Carter, T.E. Dowling: Protein crystal growth apparatus for microgravity, US Patent 5643540 (1997)

17.122 D.C. Carter, B. Wright, T. Miller, J. Chapman, P. Twigg, K. Keeling, K. Moody, M. White, J. Click, J.R. Ruble, J.X. Ho, L. Adcock-Downey, T. Dowling, C.-H. Chang, P. Ala, J. Rose, B.C. Wang, J.-P. Declercq, C. Evrard, J. Rosenberg, J.-P. Wery, D. Clawson, M. Wardell, W. Stallings, A. Stevens: PCAM: A multi-user facility-based protein crystallization apparatus for microgravity, J. Cryst. Growth **196**, 610–622 (1999)

17.123 D.C. Carter, B. Wright, T. Miller, J. Chapman, P. Twigg, K. Keeling, K. Moody, M. White, J. Click, J.R. Ruble, J.X. Ho, L. Adcock-Downey, G. Bunick, J. Harp: Diffusion-controlled crystallization apparatus for microgravity (DCAM): Flight and ground-based applications, J. Cryst. Growth **196**, 602–609 (1999)

17.124 L.J. DeLucas, K.M. Moore, M.M. Long, R. Rouleau, T. Bray, W. Crysel, L. Weise: Protein crystal growth in space, past and future, J. Cryst. Growth **237–239**, 1646–1650 (2002)

17.125 J.P. Declercq, C. Evrard, D.C. Carter, B.S. Wright, G. Etienne, J. Parello: A crystal of a typical EF-hand protein grown under microgravity diffracts x-rays beyond 0.9 resolution, J. Cryst. Growth **196**, 595–601 (1999)

17.126 S. Gorti, E.L. Forsythe, M.L. Pusey: Measurable characteristics of lysozyme crystal growth, Acta Cryst. D **61**, 837–843 (2005)

17.127 http://science.nasa.gov/ssl/msad/pcg/ (last accessed August 9, 2009)

17.128 D.C. Carter, K. Lim, J.X. Ho, B.S. Wright, P.D. Twigg, T.Y. Miller, J. Chapman, K. Keeling, J. Ruble, P.G. Vekilov, B.R. Thomas, F. Rosenberger, A.A. Chernov: Lower dimmer impurity incorporation may result in higher perfection of HEWL crystals grown in microgravity: a case study, J. Cryst. Growth **196**, 623–637 (1999)

18. Hydrothermal Growth of Polyscale Crystals

Kullaiah Byrappa

In this chapter, the importance of the hydrothermal technique for growth of polyscale crystals is discussed with reference to its efficiency in synthesizing high-quality crystals of various sizes for modern technological applications. The historical development of the hydrothermal technique is briefly discussed, to show its evolution over time. Also some of the important types of apparatus used in routine hydrothermal research, including the continuous production of nanosize crystals, are discussed. The latest trends in the hydrothermal growth of crystals, such as thermodynamic modeling and understanding of the solution chemistry, are elucidated with appropriate examples. The growth of some selected bulk, fine, and nanosized crystals of current technological significance, such as quartz, aluminum and gallium berlinites, calcite, gemstones, rare-earth vanadates, electroceramic titanates, and carbon polymorphs, is discussed in detail. Future trends in the hydrothermal technique, required to meet the challenges of fast-growing demand for materials in various technological fields, are described. At the end of this chapter, an Appendix 18.A containing a more or less complete list of the characteristic families of crystals synthesized by the hydrothermal technique is given with the solvent and pressure–temperature (PT) conditions used in their synthesis.

Crystals are the unacknowledged pillars of modern technology owing to their ever-increasing applications in various technologies such as electronics, microelectronics, magnetics, optics, nonlinear optics, photonics, optoelectronics, magnetoelectronics, biomedicine, biophotonics, biotechnology, nanotechnology, etc. Accordingly the size and quality of crystals control their application potential, as the properties also vary greatly with size, i. e., from bulk crystals to nanocrystals, due to the quantization effect. Hence, a new terminology (*polyscale crystals*) has become more appropriate in recent years for contributions like this devoted to the hydrothermal growth of crystals of different compositions and sizes. When the hydrothermal technique was initiated in the mid 19th century, the focus was essentially on mineral synthesis, also in the form of bulk single crystals. During World War II the importance of the hydrothermal technique was realized with the tremendous success in the growth of larger-size quartz crystals, and the focus shifted to the design of different types of autoclaves which could hold fluids under high-pressure and high-temperature conditions over a longer period. A greater variety of crystals hitherto unknown or without natural counterparts was synthesized during the 1960s and 1970s. Although there was a slight decline in the popularity of the hydrothermal technique during the 1980s, it has now picked up as one of the best methods to grow not only bulk crystals, but also fine and nanocrystals with desired shape, size, and properties. Hence, there has been a sudden surge in activities related to hydrothermal research in the last decade, because of the high-quality crystals of different sizes that can be grown well under hydrothermal conditions. This is further supported by the overwhelming success in the field of thermodynamic modeling and solution chemistry under hydrothermal conditions, which have drastically reduced the PT conditions required for crystal growth.

18.1 **History of Hydrothermal Growth of Crystals** 603

18.2 **Thermodynamic Basis of the Hydrothermal Growth of Crystals** .. 606

18.2.1 Hydrodynamic Principles of the Hydrothermal Growth of Crystals 606

18.2.2 Thermodynamic Modeling of the Hydrothermal Growth of Crystals 608
18.2.3 Solutions, Solubility, and Kinetics of Crystallization under Hydrothermal Conditions 610
18.3 **Apparatus Used in the Hydrothermal Growth of Crystals** .. 615
18.3.1 Morey Autoclave..... 617
18.3.2 Tuttle–Roy Cold-Cone Seal Autoclaves..... 617
18.3.3 General-Purpose Autoclaves and Others 618
18.4 **Hydrothermal Growth of Some Selected Crystals** 620
18.4.1 Quartz..... 620
18.4.2 Aluminum and Gallium Berlinites . 625
18.4.3 Calcite 628
18.4.4 Gemstones 629
18.4.5 Rare-Earth Vanadates..... 633
18.5 **Hydrothermal Growth of Fine Crystals** 634
18.6 **Hydrothermal Growth of Nanocrystals** 637
18.7 **Concluding Remarks** 640
18.A **Appendix**..... 641
References 646

The term *hydrothermal* is purely of geological origin. It was first used by the British geologist *Sir Roderick Murchison* (1792–1871) to describe the action of water at elevated temperature and pressure, in bringing about changes in the Earth's crust leading to the formation of various rocks and minerals. It is well known that the largest single crystal formed in nature (a beryl crystal of > 1000 kg) and some of the largest quantities of single crystals created by man in one experimental run (quartz crystals of several 1000 kg) are both of hydrothermal origin [18.4]. The technique is very important for its technological efficiency in developing high-quality crystals of different sizes. The term *polyscale* is relatively new and refers to different sizes of crystals, covering bulk single crystals, small crystals, and micrometer to nanosize crystals [18.5]. This concept becomes more relevant with the progress achieved in nanotechnology, wherein the quantization size effect explains the changes in the physical properties of the crystalline materials with size. The hydrothermal technique is becoming one of the most important tools for advanced materials processing, particularly owing to its advantages in the processing of nanostructural materials for a wide variety of technological applications such as electronics, optoelectronics, catalysis, ceramics, magnetic data storage, biomedicine, biophotonics, etc. The hydrothermal technique greatly helps in processing monodispersed and highly homogeneous nanocrystals [18.6]. The hydrothermal technique refers to any

Table 18.1 Different terminologies used in the hydrothermal technique

Conventional hydrothermal	Solvothermal	Supercritical hydrothermal	Related terminologies	Multi-energy hydrothermal
Aqueous solvent; Refers to conditions above atmospheric temperature and pressure; Suitable for high quality; Bulk, fine nanocrystals [18.1]	Nonaqueous solvents; Low to high temperature conditions; Suitable for good quality; Bulk, fine nanocrystals [18.1, 2]	Critical to supercritical conditions; Both aqueous and nonaqueous solvents; Suitable for fine and nanocrystals; Rapid [18.3]	Ammonothermal, glycothermal, lyothermal, alcothermal, carbonothermal, etc. depending upon the specific solvent used; Spray pyrolysis; Suitable for fine to nanocrystals and thin films [18.1, 2]	Hydrothermal in combination with extra energy likesuch as microwave, electrochemical, sonar, mechanochemical, biomolecular, sol–gel, etc. Extremely efficient for thin films, fine to nanocrystals; Epitaxy, etc. Very fast processing [18.2]

homogeneous (nanocrystals) or heterogeneous (bulk single crystals) reaction in the presence of aqueous solvents or mineralizers under high-pressure and high-temperature conditions to dissolve and recrystallize (recover) materials that are relatively insoluble under ordinary conditions. *Byrappa* and *Yoshimura* define *hydrothermal* as any homogeneous or heterogeneous chemical reaction in the presence of a solvent "(whether aqueous or nonaqueous) above the room temperature and at pressure greater than 1 atm in a closed system" [18.1, 2]. However, chemists prefer to use the term *solvothermal*, meaning "any chemical reaction in the presence of a nonaqueous solvent or solvent in supercritical or near-supercritical conditions". Table 18.1 gives different terminologies used by different specialists for hydrothermal technology.

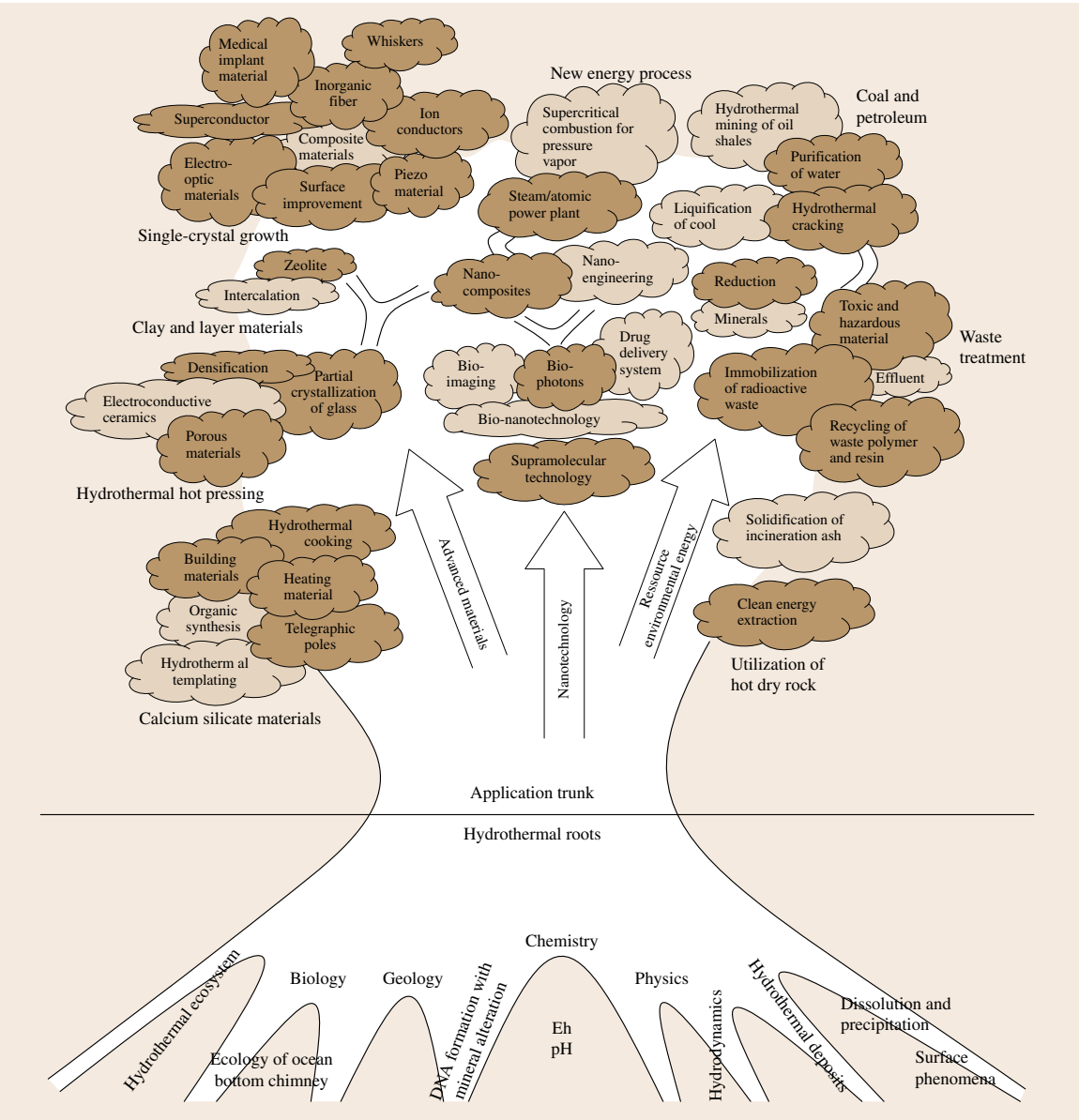


Fig. 18.1 Hydrothermal tree showing different branches of science and technology (after [18.6])

In recent years, the addition of energy into the hydrothermal process, such as in hydrothermal-electrochemical, hydrothermal-mechanochemical, hydrothermal-microwave, hydrothermal-sonar, hydrothermal-sol–gel, hydrothermal-biomolecular, etc., methods has made the process extremely effective and fast. It also leads us to a new concept of chemistry at the speed of light [18.2, 6]. However, this new process is only suitable for the preparation of fine to nanosize crystals, and thin films with high crystallinity and desired properties. In recent years, capping agents, organic molecules, surfactants, etc., have become popular for use in crystal growth in order to achieve growth in the desired crystallographic direction and stunt growth in the undesired crystallographic directions under hydrothermal conditions. Such developments have made the hydrothermal technique unique in terms of its ability to fabricate functional products with in situ control over their growth. All these recent developments in the last 10 years have completely changed the concept of hydrothermal growth of crystals. Earlier, researchers had always considered hydrothermal growth of crystals to be a high-temperature and high-pressure technique that was very expensive and slow in terms of growth rate. However, a new generation of hydrothermal researchers now consider it to be a simple technique that requires mild to low temperature/pressure, which is not expensive, and which is fast with a maximum product yield. Thus hydrothermal technique is being popularly employed by physicists, chemists, ceramists, hydrometallurgists, material scientists, biologists, engineers, geologists, technologists, and so on. Figure 18.1 shows the various branches of science either emerging from the hydrothermal technique or closely linked with it. One could firmly say that this family tree will keep expanding its branches and roots in the years to come.

Here, the author uses the term *hydrothermal* only in a broad sense covering a set of all the above-mentioned variations given in Table 18.1 to describe chemical reactions taking place in the presence of a solvent – aqueous or nonaqueous – under subcritical or supercritical conditions in a closed system. Similarly, the hydrothermal method has been widely accepted since the 1960s and practically all inorganic species, from native elements to the most complex silicates, germinates, phosphates, and others, have been obtained by this method. The technique is being employed on an industrial scale to prepare bulk to nanosize crystals for piezoelectric, optoelectronic, magnetic, ceramic, photonic, etc., applications. It offers several advantages over the conventional techniques of crystal growth in terms of purity, homogeneity, crystal symmetry, metastable-phase formation, reproducibility, lower crystallization temperature, single-step processing, simple equipment, lower energy requirements, fast reaction times, desired polymorphic modifications, growth of ultralow-solubility materials, etc.. For example, it is the only method that has been successfully employed to produce large-size single crystals of α-quartz on an industrial scale. Similarly compounds with elements in oxidation states that are difficult to obtain (especially transitional-metal compounds) by other ordinary methods can be synthesized well under hydrothermal conditions, for example, ferromagnetic chromium(IV) oxide. The synthesis of metastable phases such as subiodides of tellurium (Te_2I) can be carried out more easily under hydrothermal conditions [18.7]. The scope of the present chapter has been limited to the hydrothermal growth of crystals – bulk single crystals to selected nanocrystals – instead of describing the application of the entire hydrothermal technology that deals with the hydrothermal reactions, hydrothermal treatment of various organic and inorganic materials including recycling, frequently employed on a large scale. Also it is impossible to discuss the growth of each and every crystalline compound available in the literature, as they exceeds several hundred; the focus is limited to selected crystals of current interest and also some exceptionally major works of the past. The following aspects have been covered in the present chapter:

1. The history of hydrothermal growth of crystals
2. The thermodynamic basis of the hydrothermal growth of crystals
3. Hydrothermal apparatus and safety measures to be adopted
4. Hydrothermal growth of selected crystals:
   a) Bulk crystals
   b) Small crystals
   c) Nanocrystals
5. Future trends in the hydrothermal growth of crystals.

The theory of hydrothermal growth of crystals dealing with the growth mechanism is a recent subject; hence more emphasis is placed on the experimental aspects of crystal growth under hydrothermal conditions. However, the growth mechanism is briefly discussed for those compounds where this is available in the literature.

18.1 History of Hydrothermal Growth of Crystals

The history of hydrothermal growth of crystals has been elaborated in several works by *Byrappa* and co-workers [18.1, 2, 6, 7]. Here, the history of the hydrothermal growth of crystals is discussed briefly. The hydrothermal technique was initiated by Earth scientists during the middle of the 19th century to understand the genesis of rocks and minerals by simulating the natural conditions existing under the Earth's crust and crystallizing them in the laboratory. The first hydrothermal experiment was carried out by *Schafthaul* in 1845 to synthesize quartz crystals upon transformation of freshly precipitated silicic acid in Papin's digester [18.8]. Followed by this there were quite a few works by French and German mineralogists on the hydrothermal synthesis of minerals [18.9–12]. However, the size of the crystals obtained in general did not exceed thousands or hundreds of a millimeter. Thus, it was well known that the majority of the early hydrothermal experiments carried out during the 1840s to the early 1900s mainly dealt with fine to nanocrystalline products, which were discarded as failures due to the lack of sophisticated electron microscopic techniques available during that time to observe such small-sized products. Many times, when the bulk crystals or single crystals of several millimeter sizes were not obtained in the products, the experiments were considered as failures and the materials were washed away. Perhaps the greatest contribution during the 19th century in the field of hydrothermal synthesis of crystals was by De Senarmount, the founder of hydrothermal synthesis in geoscience. He synthesized mineral carbonates, sulfates, sulfides, and fluorides using glass liners in autoclaves [18.11]. *Bunsen* first used thick-walled glass tubes to contain high-temperature high-pressure liquids and prepare strontium and barium carbonates [18.9]. Although *Saint-Claire Deville* attempted to transform bauxite into corundum under hydrothermal conditions using NaOH as a mineralizer, the experimental results were not definite; perhaps he was the first to use a mineralizer other than water [18.13]. *Von Chrustschoff* first proposed the noble-metal lining of autoclaves to prevent corrosion [18.14]. Before this the glass tubes that were used were frequently attacked under hydrothermal conditions, and earlier researchers do not mention anything about the precautions taken in this regard. With the introduction of steel autoclaves and noble-metal linings, the tendency to reach higher-pressure/temperature conditions began. However, the majority of works up to 1880 continue to pertain to quartz, feldspar, and related silicates. *Hannay* claimed to have synthesized artificial diamond by the hydrothermal technique [18.15]. Similarly, *Moissan* also claimed to have synthesized diamond as large as 0.5 mm artificially from charcoal [18.16]. Though, the success of these experiments was treated as dubious, they certainly provided a further stimulus for hydrothermal research, particularly the development of high-pressure techniques. Perhaps the first large crystals obtained using this technique in the 19th century were by *Friedel* and *Sarasin* (1881), who synthesized hydrated potassium silicate, 2–3 mm long [18.17]. Then, in 1891 *Friedel* obtained corundum crystals by heating a solution of NaOH with excess Al_2O_3 at a high temperature for that time: 530–535 °C [18.18].

Towards the end of the 19th century, Spezia from the Torino Academy of Science began his classical work on the seeded growth of quartz. His contribution to the field of hydrothermal growth of crystals is remembered even today. *Spezia* (1896) found that plates of quartz kept at 27 °C for several months with water under a pressure of 1750–1850 atm did not lose their weight and also showed no etch figures; thus, he concluded that pressure alone has no influence on the solubility of quartz [18.19]. *Spezia* studied the solubility of quartz in such great detail that the growth of bulk single crystals of quartz became possible [18.20]. So before the end of the 19th century, a large number of minerals had been synthesized, and experiments had been carried out on a wide variety of geological phenomenon ranging from the origin of ore deposits to the origin of meteorites. According to *Morey* and *Niggli*, around 150 mineral species including diamond had been synthesized by 1900 [18.21]. *Morey* quotes a horrible experience of one of the earliest hydrothermal experiments in which, after reacting a mixture of colloidal silicon, colloidal ferric hydroxide, colloidal ferrous oxide, lime water, magnesium hydroxide, and potassium hydroxide in glass for 3 months at 550 °C, some fine crystals of hornblende were obtained, which had no bearing on the petrogenesis or the phase equilibria of the mineral system [18.22]. This was definitely due to lack of knowledge in areas of solvent chemistry, thermodynamics, kinetics, and compound solubility.

The entire activity on the hydrothermal research was concentrated in Europe, and there was no activity in North America or Asia, including Japan, China, India, and Taiwan, which are included today in the top ten countries actively engaged in hydrothermal research.

Perhaps the first published work from North American on hydrothermal research was by *Barus*, who essentially worked on the impregnation of glass with water to such an extent that it melted below 200 °C by using steel autoclaves [18.23]. Following this, Allen published his classic work on the growth of quartz crystals 2 mm long using steel autoclaves with copper sealing. The first commercialization of the hydrothermal technique took place in the early 20th century to leach bauxite, an aluminum ore, by Bayer's process. However, this is not related to crystal growth. The establishment of the Geophysical Laboratory at the Carnegie Institute of Washington in 1907 probably marked the most important milestone in the history of hydrothermal research. The credit goes to pioneers such as Bridgman, Cohen, Morey, Niggli, Fenner, and Bowen in the early 20th century, who changed the scenario of hydrothermal research. They carried out an impressive amount of basic research, along with their European counterparts. However, the total research effort was small and the study passed into a period of dormancy except for phase equilibria studies in some systems relevant to natural systems. This was connected with the need for materials with a combination of high strength and corrosion resistance at high temperatures. Although, a great deal of research was carried out during the 20th century, the facilities for large-scale hydrothermal research before the end of World War II were virtually nonexistent, with the exception of at the University of Chicago and Harvard University. This situation changed dramatically with the development of test-tube-type pressure vessels by Tuttle, later modified by Roy. These test-tube-type pressure vessels are some of the most versatile autoclaves used worldwide today; also popularly known as batch reactors, that could hold temperatures up to 1150 °C at lower pressures and pressure up to 10 kbar at lower temperatures (the modified titanium zirconium molybdenum (TZM) autoclaves).

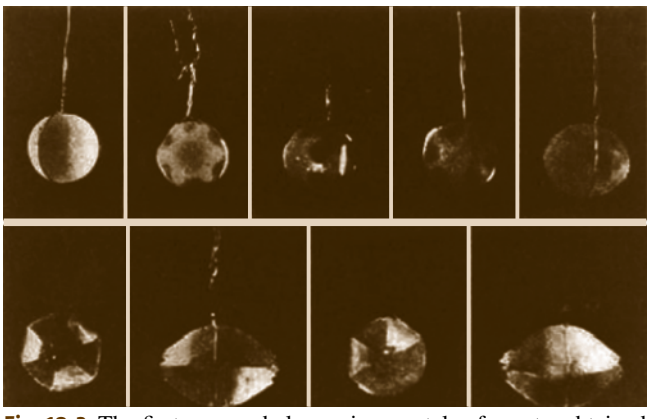


Fig. 18.2 The first manmade large-size crystals of quartz, obtained by *Nacken* [18.24]

The actual impetus for hydrothermal growth of crystals began during World War II with the growth of quartz. Here, in contrast to the very slow growth rate achieved by earlier workers such as *De Senarmount* and *Spezia*, captured German reports show that *Nacken*, using natural α-quartz as seed crystals and vitreous silica as the nutrient, had grown quartz crystals in an isothermal system and succeeded in obtaining a large quartz crystal from a small seed [18.25, 26]. *Nacken* (1884–1971) worked on the synthesis of various crystals from 1916 onwards, but left this field. In 1927 or 1928, he started working only on the hydrothermal growth of quartz crystals. On Nacken's work, Sawyer writes (cited by Bertaut and Pauthenet, 1957) that, "... Nacken made quartz crystals of 1″ diameter by using hydrothermal method and the conditions are given as ..." followed by some biographical data. Similarly, Nacken's emphasis on quartz growth has also been documented by Sawyer. Almost at the same time, Nacken made emerald single crystals by the hydrothermal method and also beryl or corundum crystals for watch bearings. He prepared a large number of synthetic emeralds by using a trace of chromium to produce color and could obtain hexagonal prisms of emerald weighing about 0.2 mg in a few days [18.27]. Figure 18.2 shows the first large-size manmade quartz crystals obtained by *Nacken* [18.24]. At almost this time, Russian researchers were producing bulk quartz crystals using old discarded cannon barrels as autoclaves. Unfortunately, these works were not published. However, the author of this chapter had an opportunity to interact on several occasions with the late *Prof. Shternberg*, from the Institute of Crystallography, Academy of Sciences (erstwhile USSR), who was mainly responsible for such great and unpublished Russian work [18.28].

With the publication of Nacken's work in 1950, several laboratories around the world began working on large-scale production of quartz crystals. During the 1960s, interest in the hydrothermal method was boosted in connection with the industrial growth of good-quality quartz single crystals and the successful growth of most complex inorganic compounds. Perhaps this is the beginning of the growth of crystals which did not have natural analogues. During the 1970s, there was a question about the search for and growth of hitherto unknown compounds of photosemiconductors, ferromagnets, lasers, and piezo- and ferroelectrics,

and the hydrothermal method attracted great attention. Several established laboratories in the world began to study systematically various aspects of the hydrothermal growth of crystals such as the physicochemical principles, kinetics, designing new apparatus, growing new compounds, and so on. Specific aspects of the hydrothermal method as a modeling tool to understand the natural processes of mineral formation changed dramatically into an important method characteristic for inorganic chemistry. During the 1980s, a new sealing method for large-size autoclaves was designed, viz. Grey-Loc sealing, which facilitates the construction of very large-size autoclaves with a volume of 5000 l [18.29]. Toyo Electric Co., Japan, houses the world's largest autoclave for the growth of quartz crystals.

Towards the end of the 1970s, on the whole, the hydrothermal field experienced a declining trend for two reasons: there was no major scope for further work on the growth of large-size single crystals of quartz on the one hand, and on the other hand, large-scale attempts to grow larger crystals of other compounds investigated during the 1960s and 1970s failed miserably. It was unanimously decided that the hydrothermal technique was not suitable for the growth of large crystals other than quartz. The focus at this time was on Czochralski, molecular chemical vapor deposition (MOCVD), and molecular-beam epitaxy (MBE). This is mainly connected to the general approach of the hydrothermal researchers to grow large single crystals without looking into the hydrothermal solvent chemistry and the kinetics of the crystallization process. However, the Nobel Symposium organized by the Swedish Academy of Sciences, during September 17–21, 1979, on *The Chemistry and Geochemistry of Solutions at High Temperatures and Pressures* is remembered as an eye-opener. The presence of pioneers in the field of hydrothermal physical chemistry such as *Franck*, *Seeward*, *Helgeson*, *Pitzer*, and so on, drew the attention of hydrothermal crystal growers and a new trend was set to look into the hydrothermal solvent chemistry and the physical chemistry of the hydrothermal systems [18.30–33]. Following this, *Prof. Somiya*, Japan, organized the first ever International Symposium on Hydrothermal Reactions, in 1982, which was attended largely by specialists from different branches of science such as physical chemistry, inorganic chemistry, solid-state physics, material scientists, organic chemists, hydrometallurgists, hydrothermal engineers, etc. [18.34]. This was the dawn of modern hydrothermal research, and since then new avenues in the field of hydrothermal research are being explored. As evident from the recent literature data, the hydrothermal technique is one of the most efficient techniques for the growth of high-quality crystals of GaN, ZnO, $GaPO_4$, etc. as well as traditional quartz crystals. Obviously there is a surge in the activities related to hydrothermal growth of crystals. This is greatly supported by developments in thermodynamic modeling and also understanding of the fluid dynamics in autoclaves through simulation.

There is a great difference between the hydrothermal research carried out during the previous century and the early 21st century. During the mid-20th century the hydrothermal technique was at its peak and the focus was mainly on the high-temperature and high-pressure regime of crystal growth, because of lack of knowledge on the solubility of several compounds and also on the selection of an appropriate solvent. The First International Hydrothermal Symposium (1982) held at the Tokyo Institute of Technology, Japan, brought together specialists from the interdisciplinary branches of science [18.34]. Since then knowledge on the physical chemistry and the PVT relationship in hydrothermal systems has greatly improved, which helped in drastically reducing the temperature and pressure conditions required for crystal growth. Similarly solvothermal and supercritical processing have been developed, which use a variety of other solvents such as organic and organometallic complexes in the synthesis, thereby moving this technique towards "green" chemistry. Table 18.2 presents trends in the hydrothermal growth of crystals, taking the hydrothermal

Table 18.2 Current trends in hydrothermal technology [18.5]

Crystal	Earlier works	Present Author
$Li_2B_4O_7$	$T = 500–700\,°C$ $p = 500–1500$ bar	$T = 240\,°C$ $p \leq 100$ bar
$Li_3B_5O_8(OH)_2$	$T = 450\,°C$ $p = 1000$ bar	$T = 240\,°C$ $p = 80$ bar
$NaR(WO_4)_2$ R = La, Ce, Nd	$T = 700–900\,°C$ $p = 2000–3000$ bar	$T = 200\,°C$ $p \leq 100$ bar
$R:MVO_4$ R = Nd, Eu, Tm; M = Y,Gd	Melting point $> 1800\,°C$	$T = 100\,°C$ $p \leq 30$ bar
$LaPO_4$	Synthesized at $> 1200\,°C$	$T < 120\,°C$ $p < 40$ bar
Zoisite	$T = 500\,°C$ $p = 5$ kbar	$T = 250\,°C$ $p \leq 100$ bar

technique towards green technology for sustained human development, since it consumes less energy, no or little solid/liquid waste, no recovery treatment, no hazardous processing materials, high selectivity, a closed processing system, etc. [18.5]. Hydrothermal chemistry has to be understood precisely in order to grow crystals under soft and environmentally benign conditions.

18.2 Thermodynamic Basis of the Hydrothermal Growth of Crystals

The thermodynamic basis of the hydrothermal growth of crystals is perhaps the least explored aspect in the literature. As such, there is no major review or book dealing with this aspect, although some significant developments have occurred in this area since the Nobel Symposium organized by the Royal Swedish Academy of Sciences in 1978, followed by the First International Symposium on Hydrothermal Reactions, organized by the Tokyo Institute of Technology in 1982, helped in setting a new trend in hydrothermal technology by attracting physical chemists in large numbers. Hydrothermal physical chemistry today has enriched our knowledge greatly through a proper understanding of hydrothermal solution chemistry. The behavior of the solvent under hydrothermal conditions dealing with aspects such as structure at critical, supercritical, and subcritical conditions, dielectric constant, pH variation, viscosity, coefficient of expansion, density, etc., are to be understood with respect to pressure and temperature. Similarly, thermodynamic studies have yielded rich information on the behavior of solutions at various pressure–temperature conditions. Since most hydrothermal crystal growth experiments are carried out under conditions with temperature gradients in standard autoclaves, growth occurs due to the recrystallization of the solid substance, including dissolution in the liquid phase and convective mass transfer of the dissolved part of the substance to the growth zone or seed, and also through the dissolution of the mixture of the nutrient components with the help of their convective mass transport into the growth zone and interaction of the dissolved components on the seed surface. However, there are several macro- and microprocesses occurring at the interface boundary of the solution and the crystal/seed. Therefore, the composition and concentration of the solution, and the temperature, pressure, and hydrodynamic conditions and surface contact of the phases are some of the basic physical and chemical parameters that determine the regime and rate of dissolution of the nutrient, the mass transport, and the possibility of the formation of new phases.

18.2.1 Hydrodynamic Principles of the Hydrothermal Growth of Crystals

The hydrodynamic principles of growth of crystals under hydrothermal conditions have been studied by several groups since the 1990s using numerical modeling to understand the fluid flow in an autoclave. There are quite a few publications on this aspect. In order to grow good-quality crystals with minimum possible defects, one has to understand the flow dynamics. *Laudise* and *Nielsen* were perhaps the first to draw the attention of hydrothermal crystal growers to the thermal conditions during growth, which lead to strong buoyancy-driven flow carrying nutrient from the lower dissolution chamber to the upper growth chamber [18.35]. Then *Klipov* and *Shmakov* studied the shape and morphology of the surfaces, the growth rate, the macroscopic defects, and the inclusion density of hydrothermally grown quartz crystals, and found a strong correlation with the fluid flow around the crystals [18.36]. *Ezersky* et al. have studied the hydrodynamics under hydrothermal conditions using a shadowgraph technique [18.37, 38]. This helped the authors to understand the spatiotemporal structure of hydrothermal waves in Marangoni convection. *Roux* et al. have developed both two-dimensional (2-D) axisymmetric and three-dimensional (3-D) models for hydrothermal crystal growth, by focusing on the bulk flow pattern in an autoclave [18.39]. Their 2-D axisymmetric model gave an unrealistic nonaxisymmetric flow pattern, while their 3-D model considers a square cross-section for the container instead of a circular or cylindrical one actually used in hydrothermal experiments. However, the results obtained were based on very low Rayleigh numbers (up to 6×10^4), corresponding to very small autoclaves, which cannot be applied to the larger autoclaves used for bulk or commercial crystal growth. *Chen* et al. [18.40, 41] have studied the flow dynamics by using a numerical model with a higher Rayleigh numbers and developed a comprehensive 3-D model for the hydrothermal growth of crystals. The

significant aspect of their work is the introduction of a fluid-superposed porous raw material bed in the lower dissolution chamber of the autoclave. This model predicts a strong 3-D flow in the autoclave and a strong temperature fluctuation. However, the best works to date on the numerical modeling of flow pattern dynamics comes from *Evans* and group [18.42–45]. Their 3-D modeling is based on industrial-scale hydrothermal autoclaves with various aspect ratios with nonuniform heating conditions. The nonuniform heating is introduced on the surface of the lower dissolving chamber and the upper growing chamber of an autoclave with or without a baffle at the middle height. It was found that the circumferentially nonuniform surface temperature has dramatic effects on the fluid flow and therefore the temperature distribution in the bulk fluid. With a temperature deviation, the flow is three dimensional. When only the dissolving chamber is subjected to circumferentially nonuniform heating, a baffle is essential to create a uniform growth environment in the growth chamber. It is evident from their work that, in order to obtain high-quality single crystals, wall-temperature control on the growth chamber wall is more important than on the dissolving chamber wall. Figure 18.3 shows the velocity distributions and temperature contours for an autoclave without a baffle and with a 15% baffle, respectively. The velocity field is much stronger in the case without a baffle than that with a baffle. The numerical study of the effects of various baffles (with 2–25% opening) on the fluid flow and temperature fields have been investigated by these authors. Accordingly a smaller opening leads to a weaker flow field and a more uniform temperature profile. A multihole baffle establishes a more uniform temperature in the upper chamber than does a single-hole baffle of the same area opening. The number of holes in the multihole baffle has significant effects, while the hole arrangements affect the thermal condition only near the baffle.

The flow pattern, with a high flow velocity in the upper growing chamber, could have a significant negative effect on solute transport from the solution to the seed crystals and therefore on the crystal growth rate and quality. The strong flow also leads to strong distortion of the temperature field. A nonuniform temperature field in the growth region is not desirable for growing uniform high-quality crystals. A significant development in the field of numerical modeling of heat transfer processes and flow fields under hydrothermal conditions is the work related to the crystal growth of beryl, $AlPO_4$, and $GaPO_4$ [18.46, 47]. These studies have yielded some insight into the flow pattern under hydrothermal conditions. For example, the influence of a rotating solid crystal or a seed crystal inside the autoclave has also been considered in such numerical modeling.

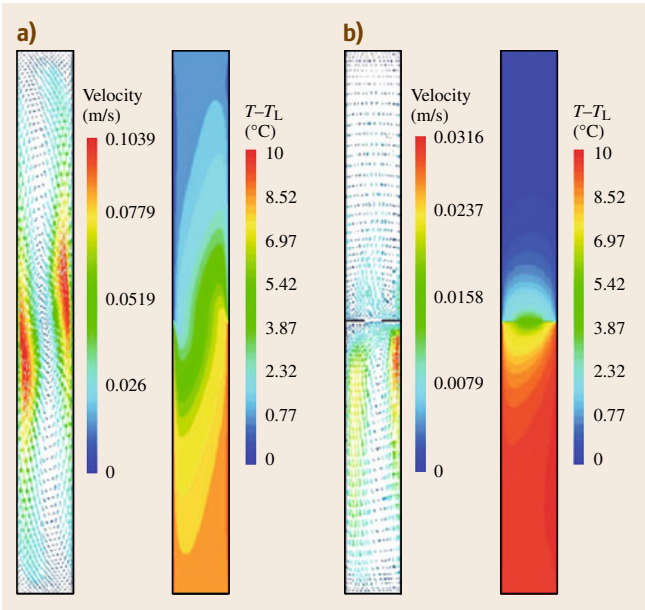


Fig. 18.3a,b Velocity pattern and isotherms in the symmetry plane. $\Delta T = 10\,°C$. On the lower chamber $\Delta T = 0.1\,°C$ only. **(a)** Without baffle; and **(b)** with a 15% area baffle opening at the median plane

However, most of these models on numerical flow patterns are based on several assumptions and are applied mainly to simple or single-phase systems. Also, the nature of the fluid is important and the flow dynamics will vary with the type of fluid; and 3-D simulation models of the flow in the autoclave show that the turbulent flow is not in fact 3-D. The effect of the simultaneous existence of the crystals and the raw materials has not been considered in most of these models. Thus there is an incomplete picture on the whole with respect to the flow dynamics. A lot more experimental and theoretical investigations are needed to clarify and complete the description of the hydrothermal flow dynamics.

During the late 1980s to early 1990s a good number of publications appeared on the physicochemical foundation of crystal growth under hydrothermal conditions. Balitsky and Bublikova carried out detailed physicochemical investigations on malachite bulk crystal growth. Similarly Kuznetsov has reviewed the physical chemistry of hydrothermal crystal growth of II–VI compounds. Further, Popolitov has reviewed the physical chemistry of the hydrothermal growth of tellurium dioxide crystals. The reader can get more valuable

information in the book *Hydrothermal Growth of Crystals* [18.4]. However, all these studies are again based on several assumptions and indirect approaches with less bearing on the thermodynamic modeling principles.

18.2.2 Thermodynamic Modeling of the Hydrothermal Growth of Crystals

A key limitation to the conventional hydrothermal method has been the need for time-consuming empirical trial-and-error methods as a means of process development. Currently, research is being focused on the development of an overall rational-engineering-based approach that will speed up process development. The rational approach involves four steps:

1. Computation of thermodynamic equilibria as a function of chemical processing variables
2. Generation of equilibrium diagrams to map the process variable space for the phases of interest
3. Design of hydrothermal experiments to test and validate the computed diagrams
4. Utilization of the processing variables to explore opportunities for controlling reactions and crystallization kinetics.

Hydrothermal crystallization is only one of the areas where our fundamental understanding of hydrothermal kinetics is lacking due to the absence of data related to the intermediate phases forming in solution. Thus our fundamental understanding of hydrothermal crystallization kinetics is in the early stage, although the importance of studies of the kinetics of crystallization was realized with the commercialization of the synthesis of zeolites during the 1950s and 1960s. In the absence of predictive models, we must empirically define the fundamental role of temperature, pressure, precursor, and time on the crystallization kinetics of various compounds. Insight into this would enable us to understand how to control the formation of solution species, solid phases, and the rate of their formation. In recent years, thermochemical modeling of chemical reactions under hydrothermal conditions has become very popular. The resulting thermochemical computation data helps in the intelligent engineering of the hydrothermal processing of advanced materials. The modeling can be successfully applied to very complex aqueous electrolyte and nonaqueous systems over wide ranges of temperature and concentration and is widely used in both industry and academy. For example, OLI Systems Inc., USA, provides software for such thermochemical modeling, and using such a package, aqueous systems can be studied within the temperature range −50–300 °C, pressure ranging from 0 to 1500 bar, and concentration 0–30 M in molal ionic strength; for nonaqueous systems the temperature range covered is 0–1200 °C and pressure from 0 to 1500 bar, with species concentration from 0 to 1.0 mol fraction.

Such a rational approach has been used quite successfully to predict the optimal synthesis conditions for controlling phase purity, particle size, size distribution, and particle morphology of lead zirconium titanates (PZT), hydroxyapatite (HA), and other related systems [18.48–50]. The software algorithm considers the standard state properties of all system species as well as a comprehensive activity coefficient model for the solute species. Table 18.3 gives an example of thermodynamic calculations and the yield of solid and liquid species outflows at $T = 298$ K, $p = 1$ atm, $I = 0.049$ M, and pH = 12.4.

Using such a modeling approach, theoretical stability field diagrams (also popularly known as yield diagrams) are constructed to obtain 100% yield. Assuming that the product is phase-pure, the yield Y can be expressed as

$$Y_i = 100\frac{m_i^{\mathrm{ip}} - m_i^{\mathrm{eq}}}{m_i^{\mathrm{ip}}}\% \,, \tag{18.1}$$

where m^{ip} and m^{eq} are the input and equilibrium molal concentrations, respectively, and the subscript i indicates the designated atom. Figures 18.4 and 18.5 show stability field diagrams for the PZT and HA systems.

From Fig. 18.4 it is observed that the region shaded represents 99% yield of PZT, although the PZT forms within a wide range of KOH and Ti concentrations. The figure clearly illustrates the region where all the solute species transform towards 100% product yield. Simi-

Table 18.3 Thermodynamic calculations for the HAp system

Species name	Inflows (mol)	Outflows Liquid/mol	Outflows Solid/mol
H_2O	55.51	55.51	8.1×10^{-2}
$Ca(OH)_2$	0.1	7.2×10^{-6}	
CaO			
Ca^{2+}		1.5×10^{-2}	
$Ca(OH)^+$		4×10^{-3}	
H^+		4.45×10^{-13}	
OH^-		3.41×10^{-2}	
Total	55.61	55.56	8.1×10^{-2}

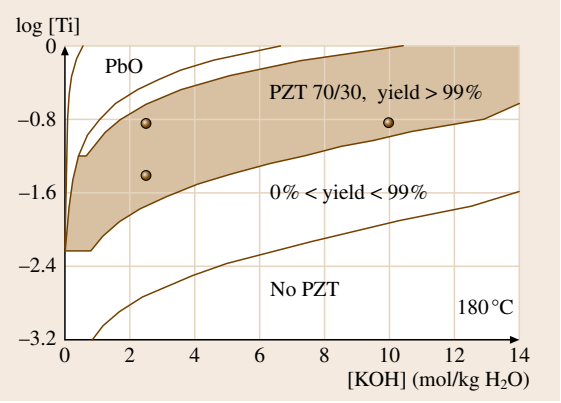


Fig. 18.4 Calculated stability field diagram for the PZT system at 180 °C with KOH as the mineralizer (after [18.48])

larly, from Fig. 18.5, it is observed that all the Ca species participate in the reaction to form HA, thus leading to 100% yield of HA in the region denoted by a black square. Thick dotted lines indicate the boundary above which 99% Ca precipitates as HA. The other regions mark mixed-phase precipitation such as hydroxyapatite, monatite, and other calcium phosphate phases.

Such thermodynamic studies help to intelligently engineer the hydrothermal process and also to obtain a maximum yield for a given system. This area of research has great potential for application in crystal growth, including of nanocrystals. However, in the majority of cases, the conventional and nonconventional (composition diagrams) phase diagrams are still constructed based on phase equilibria studies carried out under hydrothermal conditions for systems of interest. Nonconventional phase diagrams (composition diagrams) plotted for equilibrium conditions are popular, especially among Russian workers, and are known as NC diagrams or TC diagrams, where N stands for the nutrient composition, T stands for experimental temperature, and C stands for solvent concentration. There are hundreds of such diagrams in the literature. Figure 18.6 represents an NC diagram for the system Na_2O–RE_2O_3–SiO_20–H_2O, showing the distribution of silicon–oxygen radical groups in the rare-earth silicates under hydrothermal conditions with fixed pressure and temperature conditions [18.51]. The solid lines indicate the regions of monophase crystallization, and dashed lines indicate the beginning of crystallization of the excess component. Similarly there is one more type of composition diagrams used routinely in crystal growth to select the conditions of crystallization of

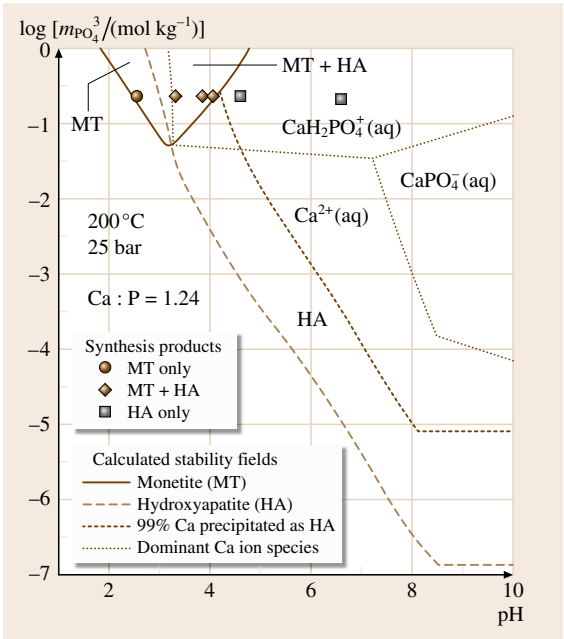


Fig. 18.5 Calculated stability field diagram for the HAp system at 200 °C and 25 bar with Ca : P ratio of 1.24 (after [18.50])

various phases in a given system. Figure 18.7 represents the concentration versus temperature diagram for the system K_2O–La_2O_3–P_2O_5–H_2O [18.52]. This dia-

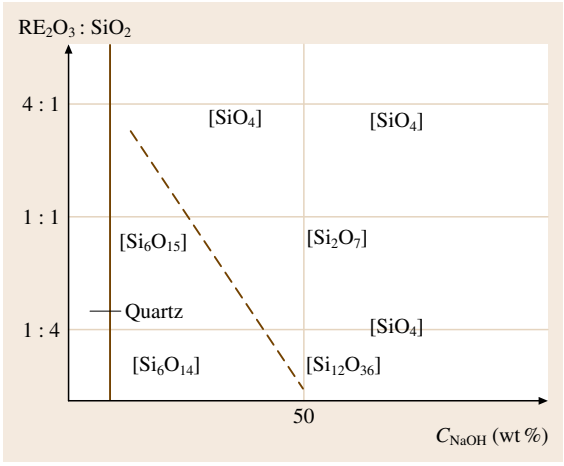


Fig. 18.6 NC diagram for the system Na_2O–RE_2O_3–SiO_2–H_2O giving the distribution of silicon–oxygen radical groups in the rare-earth silicates under hydrothermal conditions with fixed pressure and temperature conditions (after [18.51])

gram helps in selecting the experimental temperature for the growth of rare-earth orthophosphate crystals. These nonconventional phase diagrams are relatively easy to obtain and are highly useful for the growth of single crystals as they clearly depict the growth conditions.

In addition to such unconventional phase diagrams, researchers frequently use standard phase diagrams such that shown in Fig. 18.8 for the potassium titanyl phosphate (KTP) system [18.53]. This type of phase diagram occurs in the thousands for various compounds, and is commonly used in crystal growth. Such phase diagrams give in general the phase boundaries and the phase formation within a given system under fixed PT conditions, and help to select the conditions for crystal growth.

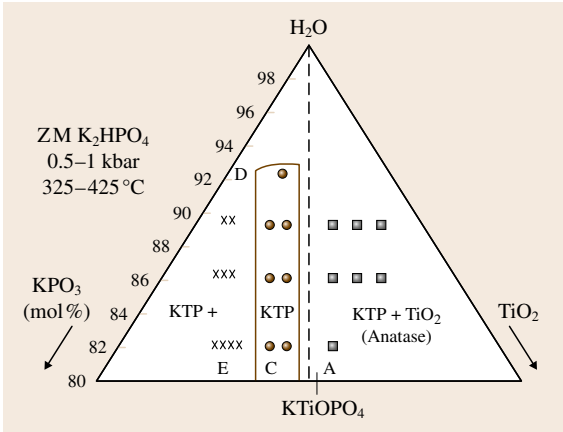


Fig. 18.8 Phase diagram for the KTP system (after [18.53])

18.2.3 Solutions, Solubility, and Kinetics of Crystallization under Hydrothermal Conditions

This is one of the most important aspects of the hydrothermal growth of crystals. Initial failures in the hydrothermal growth of a specific compound are usually the result of lack of proper data on the type of solvents, the solubility, and the solvent–solute interaction. A hydrothermal solution is generally considered as a thermodynamically ideal one, yet in the case of strong and specific interaction between the solute and the solvent, or among the components of the soluble substance in them, significant deviations from Raoult's law occur. Consequently, real hydrothermal solutions differ from ideal solutions and their understanding requires knowledge of the influence of the solvent in the process of dissolution and crystallization of various compounds. Obviously, as shown in most of the experiments, the type of solvent and its concentration determine a specific hydrothermal process and its important characteristics such as the solubility of the starting materials, the quantity of the phases, their composition, and the output of the phases, kinetics, and growth mechanism of single crystals.

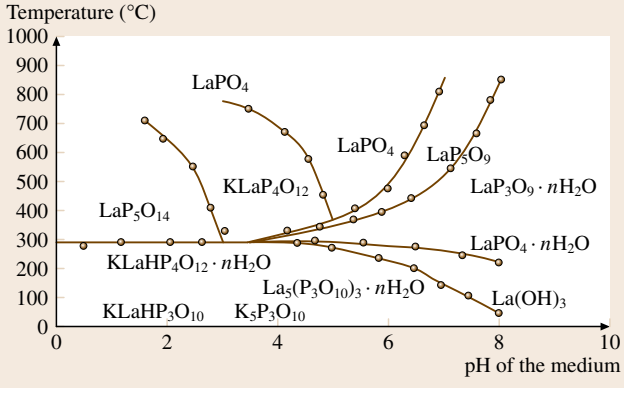


Fig. 18.7 Concentration versus temperature diagram for the system K_2O–La_2O_3–P_2O_5–H_2O (after [18.52])

At the moment there is no theory which can explain and estimate solubility in real solutions. However many of the problems connected with solubility can be explained on the basis of overall physicochemical principles or laws.

In some cases, it is always better to use the empirical rule that solubility becomes high in solvents with higher dielectric constant (ε) and for types of chemical bond which are close to those of the solute substance. Deviation from this takes place when specific interactions between the solid substance and solvent occur.

The synthesis and recrystallization of a specific compound and the growth of single crystals on the seed are all carried out using different solvents on the basis of physicochemical considerations.

The following conditions are adopted in selecting the most suitable mineralizers:

1. Congruence of the dissolution of the test compounds
2. A fairly sharp change in the solubility of the compounds with changing temperature or pressure
3. A specific quantitative value of the absolute solubility of the compound being crystallized
4. The formation of readily soluble mobile complexes in the solution

5. A specific redox potential of the medium, ensuring the existence of ions of the required valence.

Additionally the solvent should have the desired viscosity, insignificant toxicity, and very weak corrosion activity with respect to the apparatus. These factors fulfill the requirements of the hydrothermal mineralizer (solvent) in addition to determining the values of solubility of the compound under investigation. Some of the basic properties of the hydrothermal medium, such as viscosity, dielectric constant, compressibility, and coefficient of expansion, are discussed here briefly in the context of crystal growth. Since diffusion is inversely proportional to solvent viscosity, one can expect very rapid diffusion in hydrothermal growth. This leads to the growth of perfect single crystals with well-developed morphology. We can expect higher growth rates, a narrower diffusion zone close to the growing interface, and less likelihood of constitutional supercooling and dendritic growth. It is thus no wonder that quartz growth rates as high as 2.5 mm/day without faults or dendritic growth have been observed [18.54].

Let us consider briefly the role of water as a solvent in the hydrothermal growth of crystals. Water is always the major component of hydrothermal solutions, with various chemical compositions in the laboratory and nature. All solutions used in hydrothermal experiments vary from one another in their properties, their ability to dissolve and crystallize, and the nature of the linking between water and electrolyte. Moreover, the properties of each solution depend upon physicochemical aspects and the structure of the pure water. The formation of associates and complexes in the aqueous solutions of electrolytes is possible because of the presence of structural water, i. e., water molecules with directional hydrogen bonding. Several chemical changes arise from changes in ionic dissociation of the solution. Therefore, it is better to understand the characteristics of the pure water under hydrothermal conditions. The hydrogen ions show an influence on the solubility of various compounds under hydrothermal conditions. Figure 18.9 shows the viscosity of water as a function of density and temperature [18.55]. It has been demonstrated that the mineralizer solutions (typically 1 M NaOH, Na_2CO_3, NH_4F, K_2HPO_4, etc.) have properties quite close to those of water. For 1 M NaOH at room temperature, $\eta_{solution}/\eta_{water} = 1.25$ [18.56] and one can expect that the viscosity of hydrothermal solutions can be as much as two orders of magnitude lower than *ordinary* solutions. The mobility of molecules and ions in the supercritical range is much higher than under normal conditions. Also electrolytes which are completely dissociated under normal conditions tend to associate with rising temperature [18.57].

Hasted et al. (1948) observed that the dielectric constant of electrolyte solutions (ε) can be regarded as a linear function of molarity up to 1–2 M, depending on the electrolyte [18.58]. *Franck* [18.55] discussed ionization under hydrothermal conditions and made careful and complete conductivity studies, showing that the conductance of hydrothermal solutions remains high despite the decrease in ε, because this effect is more than compensated for by an increase in the ion mobility brought about by the decreased viscosity under hydrothermal conditions. Figure 18.10 shows the dielectric constant of water [18.59]. Thermodynamic and transport properties of supercritical water are remarkably different from those of ambient water. Supercritical water is unique as a medium for chemical processes. The solubility of nonpolar species increases, whereas that of ionic and polar compounds decreases as a result of the drop of the solvent polarity, and the molecular mobility increases due to a decrease in the solvent viscosity (η). Drastic changes of ionic hydration are brought about by the decrease in the dielectric constant (ε) and density (ρ). Largely as a consequence of the dramatic decrease in the dielectric constant of water with increasing temperature at constant pressure and/or de-

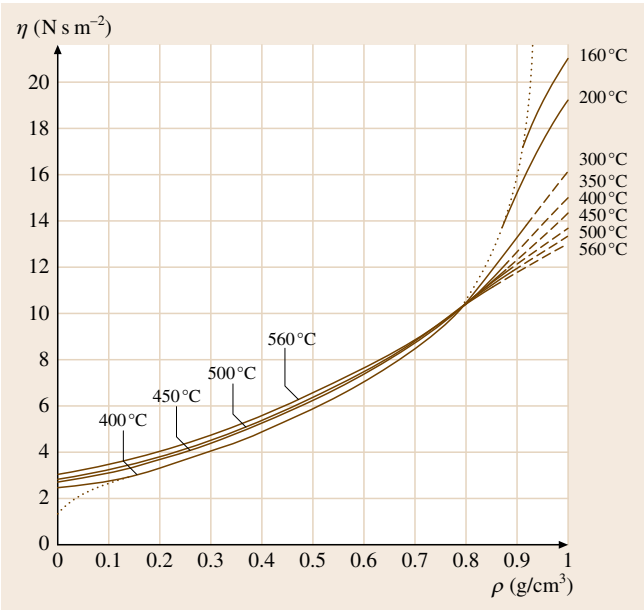


Fig. 18.9 Viscosity of water as a function of density and temperature (after [18.55])

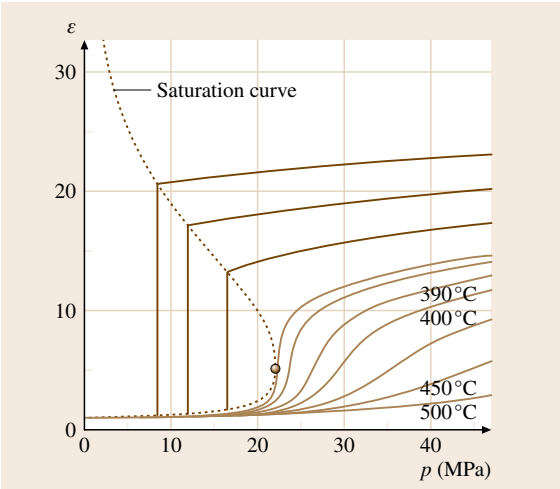


Fig. 18.10 Dielectric constant of water around the critical point (after [18.59])

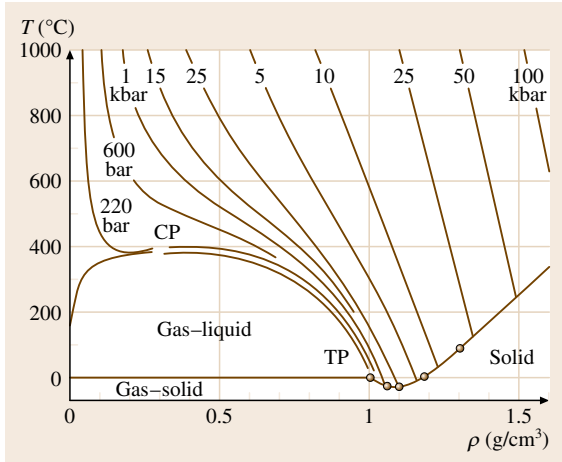


Fig. 18.11 Temperature–density diagram of water with pressure as a parameter (after [18.60])

creasing pressure at constant temperature, *completely* dissociated electrolytes at low temperatures and pressures may become highly associated in the supercritical region.

Water is an environmentally safe material and cheaper than other solvents, and it can act as a catalyst for the transformation of desired materials by tuning temperature and pressure. Studies of the structure dynamics and reactivity of supercritical water have led to a better understanding of how complicated compounds are adaptively evolved from simple ones in hydrothermal reactions. It is important to elucidate how the structure and dynamics of supercritical water are controlled by intermolecular interactions (ρ) as well as kinetic energies (T). This is a new frontier of solution chemistry. The PVT data for water up to 1000 °C and 10 kbar is known accurately enough (to within 1% error) [18.60, 62, 63]. At very high-PT conditions (1000 °C and 100 kbar), water is completely dissociated into H_3O^+ and OH^-, behaving like a molten salt, and has a higher density of the order of 1.7–1.9 g/cm^3. Figure 18.11 shows the temperature–density diagram of water, with pressure as a parameter [18.60].

In hydrothermal crystal growth, the PVT diagram of water proposed by *Kennedy* is very important even today for reasons of simplicity (Fig. 18.12), although there are several recent diagrams available with greater accuracy [18.61]. Usually, in most routine hydrothermal experiments, the pressure prevailing under the working conditions is determined by the degree of filling and the temperature. When concentrated solutions are used, the critical temperature can be several hundred degrees above that of pure water. The critical temperatures are not known for the, usually complex, solutions at hand; hence one cannot distinguish between sub- and supercritical systems for reactions below 800 °C. Although the temperature in the growth zone and the actual vapor pressure are not known to 100% accuracy, the PVT diagram of Kennedy is routinely used by most hydrothermal crystal growers. The PVT relations for several other systems, such as $AlPO_4$ and SiO_2, have been reviewed in [18.52, 64, 65].

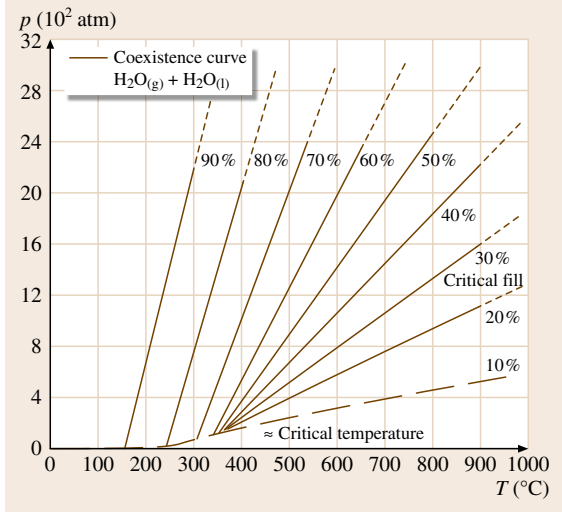


Fig. 18.12 PVT diagram of water (after [18.61])

Solubility

Solubility is one of the most important aspects of hydrothermal crystal growth. The early failures in the growth of bulk crystals using the hydrothermal technique were mainly due to the lack of solubility data on those compounds. This topic was almost neglected until the works of Spezia, who studied the solubility of quartz in detail and gave a new direction to hydrothermal growth of crystals. During the 1960s, new methods of investigating the solubility and the new experimental setup for the determination of solubility under hydrothermal conditions were proposed [18.66, 67]. There are two basic methods of determining the solubility under hydrothermal conditions: (a) the sampling technique, and (b) the weight loss method [18.68, 69]. Both methods have their merits and demerits. In many cases the solubility obeys the van't Hoff equation and is linearly dependent on solution density [18.70]. The ratio of solubility to mineralizer concentration often gives clues to the species present [18.71]. Some dedicated equipment have been designed and fabricated for solubility studies under hydrothermal conditions [18.72]. Herein we describe the different types of solubility under hydrothermal conditions by selecting appropriate examples such as quartz, berlinite, gallium orthophosphate, and potassium titanyl phosphate, because of their contrasting solubilities. As mentioned earlier (Sect. 18.1) the earliest hydrothermal researchers used only water as the solvent. Today we use a great variety of mineralizers, both aqueous and nonaqueous solvents, and also mixed solvents in many cases. However, *Hannay* and *Hogarth* used alcohol as the solvent [18.73], although that work did not draw the attention of scientists until recently. Although water can be a good solvent under very high-pressure and high-temperature conditions, the use of acids, salts, bases, and mixtures of them considerably reduces the PT conditions required for crystallization. The commonly used nonaqueous solvents are NH_3, HF, HCl, HBr, Br_2, S_2Cl_2, S_2Br_2, $SeBr_2$, $H_2S + N(C_2H_5)_3$, NH_4Cl, C_2H_5OH, CS_2, CCl_4, C_6H_6, CH_3NH_2, etc. In the last 15 years, the growth conditions for a variety of crystals have been further reduced with the use of some high-molar acid solvents such as HCl, H_2SO_4, H_3PO_4, HNO_3, HCOOH, etc. which has reduced the growth temperature to below 300 °C. This reduction in the growth temperature considerably reduces the working pressure, which in turn helps in the use of simple apparatus. Even silica autoclaves can be used, which facilitates direct visibility of the growth medium just as in any other low-temperature solution growth. This has greatly attracted the attention of crystal growers in the last decade, and a great variety of compounds which hitherto were produced only at high temperature and pressure have been today obtained at lower-PT conditions. Hence the mineralizer plays an important role in the hydrothermal growth of crystals and has given a new perspective to the method.

Solubility of Quartz. The first systematic study of the solubility of quartz was carried out by *Spezia*, which opened up the trend for the growth of bulk crystals on the whole using the hydrothermal method [18.20]. The solubility of quartz in pure water was found to be too low for crystal growth (0.1–0.3 wt %), but the solubility could be markedly increased by the addition of OH^-, Cl^-, F^-, Br^-, I^-, and acid media, which act as mineralizers. For example, the reactions

$$SiO_2 + 2OH^- \rightarrow SiO_3^{2-} + H_2O\,,$$
$$2OH^- + 3SiO_2 \rightarrow Si_3O_7^{2-} + H_2O\,,$$

show the formation of various complexes or species during the hydrothermal crystallization of quartz. *Hosaka* and *Taki* have used Raman spectra to identify and quantify such species [18.74].

In pure aqueous solutions (even at 400 °C and 25 000 psi), the solubility of quartz is too low to allow growth to take place in any reasonable time. Alkaline additions, such as NaOH, Na_2CO_3, KOH, and K_2CO_3, are all effective as mineralizers in this pressure and temperature range. However, higher molarity of the alkaline solutions introduce other alkali silicates along with quartz. Therefore, a moderate molarity and especially mixed mineralizers are more effective to achieve higher growth rate. *Laudise* and *Ballman* have measured the solubility of quartz in 0.5 M NaOH as a function of temperature [18.75] and even today the classical work carried out by Laudise and group remains the standard one as far as quartz growth under hydrothermal conditions is considered. Figure 18.13 shows the solubility curve for quartz in 0.5 M NaOH as a function of temperature and percentage fill [18.75]. An important result of solubility determinations is the delineation of the pressure, temperature, and composition regions where the temperature coefficient of solubility is negative. These regions are to be avoided in the growth of quartz, since it requires a different setup to avoid the loss of seed crystals. In recent years, for quartz crystal growth, mixed solvents are used in most cases.

Solubility of Berlinite. The solubility of berlinite was first determined by *John* and *Kordes* in orthophosphoric

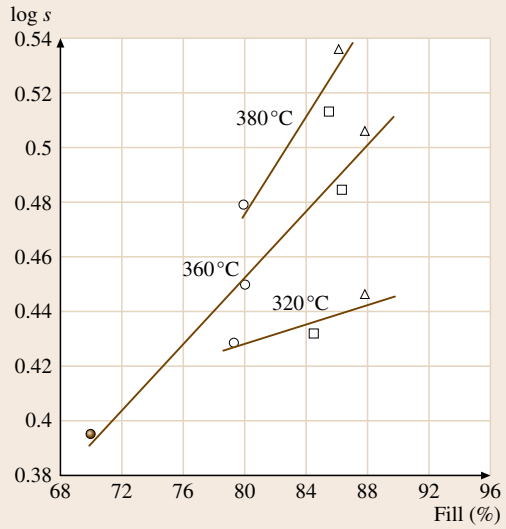


Fig. 18.13 Quartz solubility dependence on percentage fill (after [18.75])

acid above 300 °C and was found to be positive [18.76]. Subsequently *Stanley* reported a negative solubility for berlinite in 6.1 M H_3PO_4 [18.77]. The solubility of $AlPO_4$ varies widely with the type of solvent used. Some authors claim that solubility of $AlPO_4$ in HCl is similar to that in H_3PO_4. The most important difference is the higher solubility at comparable mineralizer concentration. The authors of [18.78] have studied the solubility of $AlPO_4$ in some new solvents such as HCOOH, NH_4Cl, Na_2CO_3, $NH_4H_2PO_4$, NaF, KF, and LiF. The solubility of $AlPO_4$ (in wt %) as a function of temperature and at a pressure of 2 kpsi, in 2 M HCOOH solution is shown in Fig. 18.14.

Solubility of Gallium Orthophosphate. Gallium orthophosphate has been studied extensively for the past 12 years owing to its excellent piezoelectric properties, which are much better than those of conventional α-quartz. The solubility of gallium orthophosphate is quite interesting, although it is isostructural and isoelectronic with α-quartz and berlinite. Several studies exist on the solubility of $GaPO_4$ [18.79–82]. $GaPO_4$ shows a negative coefficient of solubility, like berlinite, with some significant differences between the two. Figure 18.15 shows a more precise solubility curve for $GaPO_4$ crystals [18.82]. The solubility of another very important crystal, ZnO, has been discussed in detail by M. J. Callahan et al. in this Handbook.

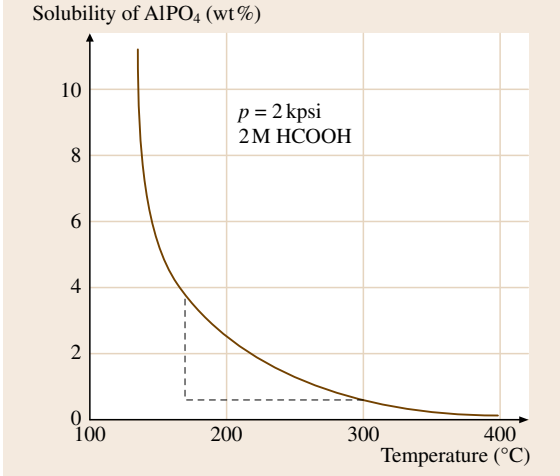


Fig. 18.14 Solubility of $AlPO_4$ (in wt %) as a function of temperature at a pressure of 2 kpsi, in 2 M HCOOH solution (after [18.78])

Kinetics of Crystallization under Hydrothermal Conditions

Studies related to the kinetics of crystallization under hydrothermal conditions began during the 1950s and 1960s with the commercialization of the synthesis of zeolites, and the large-scale growth of bulk crystals of quartz. Subsequently, several other crystals, such as $GaPO_4$, $AlPO_4$, malachite, ZnO, calcite, and ruby, were studied in detail. The anisotropy in the rate of growth of different faces during growth on the seed, if understood

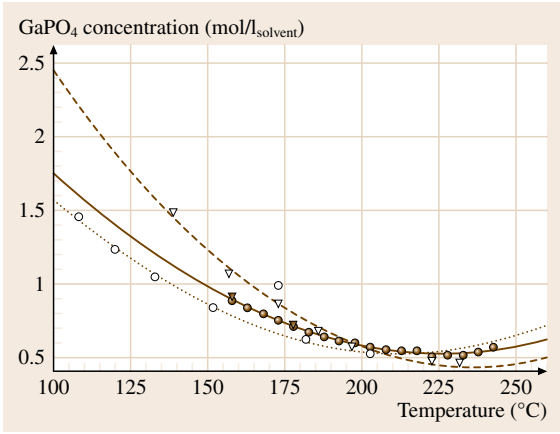


Fig. 18.15 Solubility curve of $GaPO_4$ under hydrothermal conditions in 15 M phosphoric acid: △ and ▽ correspond to the crystallization data; ○ and ● correspond to the dissolution data (△, ○ after [18.79]; ▽, ● after [18.80])

clearly, can allow the orientation of the seeds in such a way that the fastest growth can be achieved within a short time without compromising crystal quality. The crystallization kinetics of ZnO crystals under hydrothermal conditions have been discussed in this Handbook by the other authors (*Callahan* et al., Chap. 19). However, the crystallization kinetics are discussed in general for one or two selected compounds in this section. Various general laws characterizing the relationship between the anisotropy of the rates of growth of the faces and the chemical nature of the solvent have been studied by several workers.

The high activation energies of the growth of the faces, combined with other factors – the anisotropy of the rates of growth of the faces, the marked dependence of the rate of crystallization on the composition of the solution, etc. – provide strong evidence in support of the suggestion that, in hydrothermal crystallization under conditions of excess mass transfer, a primary role is played by surface processes taking place directly at the crystal–solution interface. It should be remembered that the activation energy of diffusion in solutions usually does not exceed 4–5 kcal/mol [18.83], while the activation energies of dissolution rarely exceed ≈ 10 kcal/mol. These values are much lower than the activation energies of growth, indicating that diffusion in the solution and dissolution of the charge do not limit the rate of crystallization with increase in the concentration of the solution. The rate of crystallization can increase in two ways. For crystals which do not contain components of the solvent, the rate increases sharply at low concentrations and remains practically unchanged at high concentrations. Similarly, in some cases, an increase in the rate of growth of the faces with increase in pressure has been observed. Pressure apparently does not have any significant direct effect on the rate of growth crystals, but it may have an influence through other parameters: mass transfer and solubility.

Kuznetsov reported the effects of temperature, seed orientation, filling, and temperature gradient (ΔT) on the growth kinetics of corundum crystals [18.84]. The activation energies calculated were 32 kcal/mol for the (1011) face and 17.5 kcal/mol for the (1120) face. *Kaneko* and *Imoto* have investigated the effects of pressure, temperature, time, and Ba:Ti ratio on the kinetics of a hydrothermal reaction between barium hydroxide and titania gels to produce barium titanate powders [18.85]. *Ovramenko* et al. conducted kinetics studies to compute the activation energy (E_a) of 21 kJ/mol [18.86]. In contrast, *Hertl* calculated an activation energy of 105.5 kJ/mol [18.87]. *Riman* and group have investigated the crystallization kinetics of various perovskite-type oxides using the computation modeling under hydrothermal conditions, and were able to construct speciation and yield diagrams [18.88, 89].

Thermodynamic modeling, solubility studies, and kinetics of crystallization under hydrothermal conditions is still an attractive field of research in the hydrothermal growth of crystals. During the 1980s and 1990s, external energy such as microwave, sonar, mechanochemical, and electrochemical, was employed to enhance the crystallization kinetics under hydrothermal conditions, especially in the preparation of fine crystals; and now in the last half-decade, the processes have been better understood to prepare crystalline particles with desired shape and size [18.90, 91].

18.3 Apparatus Used in the Hydrothermal Growth of Crystals

Designing an ideal hydrothermal apparatus, popularly known as an autoclave, is the most difficult task and perhaps impossible to define, because each project has different objectives and tolerances. Obviously several autoclave designs exist to meet requirements for a specific objective such as the study of phase equilibria, solubility, growth of bulk or small crystals, continuous production of nanocrystals, etc. However, an ideal hydrothermal autoclave should have the following characteristics irrespective of the goal:

1. Inertness to acids, bases, and oxidizing agents
2. Ease of assembly and disassembly
3. Sufficient length to obtain a desired temperature gradient
4. Leakproof, with unlimited resistance to the required temperature and pressure
5. Rugged enough to bear high-pressure and high-temperature experiments for long duration, so that no machining or treatment is needed after each experimental run.

The most commonly used autoclaves in hydrothermal research are listed in Table 18.4. The last four types listed are useful for the preparation of nanocrystals and powders under extreme conditions. When selecting

a suitable autoclave, the first and foremost parameter is the experimental temperature and pressure conditions and its corrosion resistance in that pressure temperature range for a given solvent or hydrothermal fluid. If the reaction is taking place directly in the vessel, the corrosion resistance is of course a prime factor in the choice of autoclave material. The most successful materials are corrosion-resistant high-strength alloys, such as 300-series (austenitic) stainless steel, iron, nickel, cobalt-based superalloys, and titanium and its alloys. However, the hydrothermal experimenter should pay special attention to systems containing hydrogen, nickel, etc., which can be dangerous under high-PT conditions in the presence of some solvents. Therefore, selection of autoclaves, PT conditions, and the chemical media under hydrothermal conditions are extremely important to know before running actual experiments. Glass autoclaves were used in the 19th century for lower-PT conditions. In recent days in some laboratories thick quartz tubes are used for lower-temperature experiments [18.92]. Autoclaves are usually provided with liners made of various materials depending upon the type and purpose of the crystals to be grown. For example, quartz growth can be carried out in regular stainless-steel autoclaves without any lining or liners. If high-quality and high-purity quartz crystals are desired then platinum or gold liners should be used. Even glass, copper, silver, Teflon, etc., tubes can be used, depending upon the PT conditions and the hydrothermal media. Autoclave lining is not new and in fact began

Table 18.4 Autoclaves

Type	Characteristic data
Pyrex tube 5 mm i.d., 2 mm wall thickness	6 bar at 250 °C
Quartz tube 5 mm i.d., 2 mm wall thickness	6 bar at 300 °C
Flat plate seal, Morey type	400 bar at 400 °C
Welded Walker-Buehler closure 2600 bar at 350 °C	2000 bar at 480 °C
Delta ring, unsupported area	2300 bar at 400 °C
Modified Bridgman, unsupported area	3700 bar at 500 °C
Full Bridgman, unsupported area	3700 bar at 750 °C
Cold-cone seal, Tuttle–Roy type	5000 bar at 750 °C
Piston cylinder	40 kbar, 1000 °C
Belt apparatus	100 kbar, > 1500 °C
Opposed anvil	200 kbar, > 1500 °C
Opposed diamond anvil	Up to 500 kbar > 2000 °C

Table 18.5 Materials used as reactor linings

Material	T (°C)	Solutions	Remarks
Titanium	550	Chlorides Hydroxides Sulfates Sulfides	Corrosion in >25% NaOH solution in >10% NH_4Cl solution (at 400 °C)
Armco iron	450	Hydroxides	Gradual oxidation producing magnetite
Silver	600	Hydroxides	Gradual recrystallization and partial dissolution
Platinum	700	Hydroxides Chlorides Sulfates	Blackening in chlorides in the presence of sulfur ions Partial dissolution in hydroxides
Teflon	300	Chlorides Hydroxides	Poor thermal conduction
Tantalum	500	Chlorides	Begins to corrode in 78% NH_4Cl solution
Pyrex	300	Chlorides	
Copper	450	Hydroxides	Corrosion reduced in the presence of fluoride ions and organic compounds
Graphite	450	Sulfates	Pyrolytic graphite most suitable for linings
Nickel	300	Hydroxides	
Quartz	300	Chlorides	
Gold	700	Hydroxides Sulfates	Partial dissolution in hydroxides

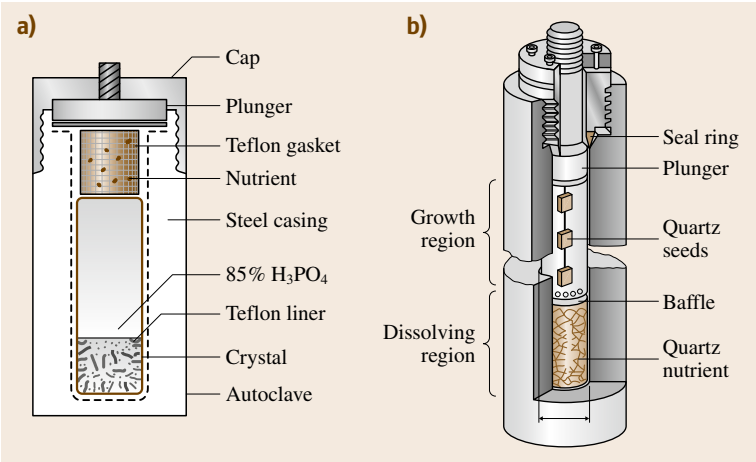


Fig. 18.16a,b The internal liner assembly. **(a)** Berlinite with negative temperature coefficient of solubility has the seed crystals (growth zone) at the bottom and nutrient (dissolution zone) at the top [18.78]. **(b)** Quartz with positive temperature coefficient of solubility has the nutrient (dissolution zone) at the bottom and the seed crystals (growth zone) in the top (courtesy of *Laudise* [18.94])

during the 19th century. Table 18.5 gives a list of the materials used as linings [18.93].

The internal assembly of the liners in hydrothermal experiments varies with the type of compounds to be grown and their solubility. For example, quartz and berlinite have contrasting solubility, and accordingly their crystal growth insists upon a completely different experimental setup, as shown in Fig. 18.16.

Here, only the standard designs used in hydrothermal research related to phase equilibria studies, solubility, kinetics, and crystal growth will be discussed, since the number of autoclave designs available in the literature exceeds more than 100.

18.3.1 Morey Autoclave

This autoclave was designed in 1913 by *Morey* with a simple sealing gasket; its volume is generally 25–100 ml [18.21]. It is widely used in hydrothermal research and a cross-section of a typical Morey autoclave is shown in Fig. 18.17. The usual dimensions of are 10–20 cm length and 2.5 cm inner diameter. The closure is made by a Bridgman unsupported area seal gasket made of copper, silver or teflon. Therefore it is also called a flat plate closure autoclave. The autoclave generates an autogeneous pressure depending on the degree of filling, the fluid, and the temperature. The autoclave is limited to $\approx 450\,^{\circ}\mathrm{C}$ and 2 kbar in routine use. In later versions, the pressure can be directly measured and adjusted during an experiment by providing an axial hole through the closure nut, but this sometimes causes compositional changes as the material is transported to the cooler region. A thermocouple is inserted in the well close to the sample and the vessel is placed inside a suitable furnace so that the entire Morey autoclave and closure lie within the element of the furnace. At the end of the run the vessel is quenched in a jet of air followed by dipping in water and the closure seal is broken.

18.3.2 Tuttle–Roy Cold-Cone Seal Autoclaves

This consists of a longer vessel in which the open end and seal are outside the furnace, hence the term *cold-cone seal* (although in fact the seal is far from being cold). Pressure is transmitted to the sample, which is contained in a sealed capsule, through a hole in the clo-

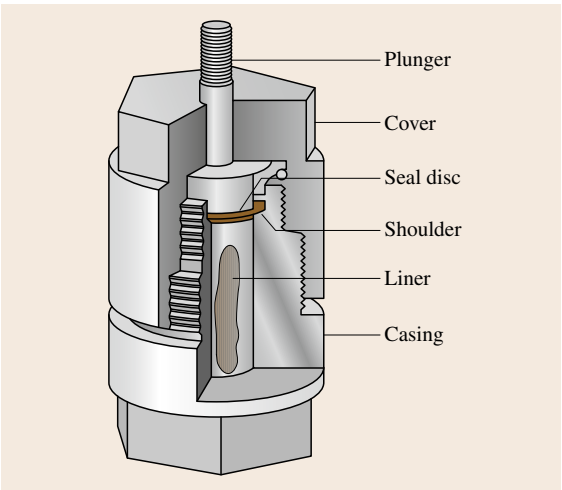


Fig. 18.17 Cross-section of a typical Morey autoclave [18.21]

sure. The capsules are normally made of noble metals (platinum, gold or silver). These vessels may be operated closure up, closure down, or horizontally. The ratio of the vessel diameter to the wall diameter determines the strength of the vessel. In most standard Tuttle vessels this ratio is 4%. Using steallite 25, experiments can be carried out at 900 °C and 1 kbar or 750 °C and 3 kbar for long-term use (from hours to weeks). Roy and Tuttle made many hydrothermal experimental runs for several months in the late 1950s. Moreover, the reaction could be *quenched* by lowering the furnace quickly and surrounding the bomb with a container of water [18.95]. Figure 18.18 shows the cross section of a Tuttle–Roy autoclave [18.95].

Around 1950, *Roy* and *Osborn* [18.96] also designed a simple universal pressure intensifier for compressing (virtually) all gases (H_2, N_2, CO_2, and NH_3) or liquids such as H_2O from the compressed gas tank pressures of about 100–200 bar to 5 kbar. From 1950 onwards *test-tube racks* of hydrothermal vessels including such compressors were used worldwide for hydrothermal research, mainly in the geochemical community. Figure 18.19 shows the advertisement of Leco Company, Tem-Press Research (Bellefonte, USA), which was set up by Tuttle, Roy, and Licastro to make these key tools for hydrothermal research available worldwide. This continues to the present day, mainly due to the overriding convenience and simplicity of the design.

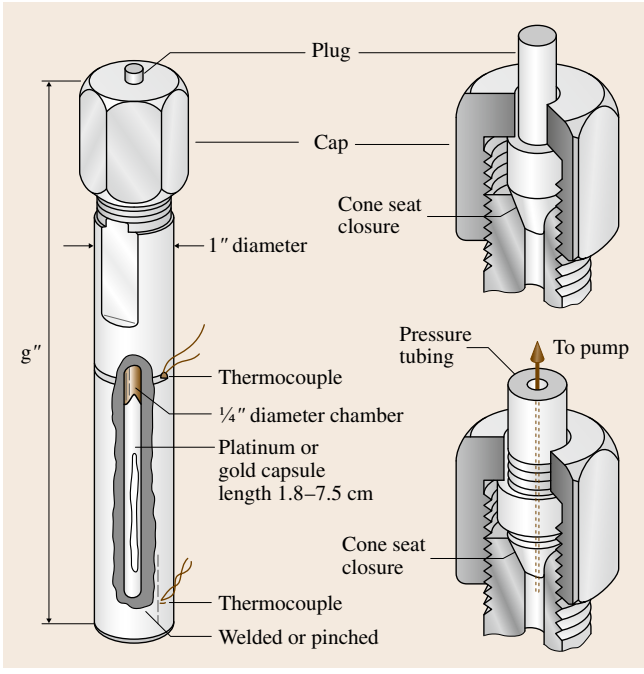


Fig. 18.18 Cross-section of the Tuttle–Roy autoclaves [18.95]

These autoclaves are highly useful for hydrothermal researchers to carry out phase equilibria studies, solubility, high-temperature/pressure synthesis, nanocrystals synthesis, etc. Today they are also called batch reactors by several researchers and are popularly used for nanomaterials synthesis. The advent of new materials, particulary molybdenum-based alloys, has extended the temperature capabilities of cold-seal vessels to about 1150 °C at pressure above 4 kbar (so-called TZM vessels). The prospects of new refractory alloys extending up to this range are encouraging. These cold-seal vessels are safe, inexpensive, simple, and operationally routine. Unlike the Morey type of autoclaves, in the Tuttle cold-seal vessel the pressure is built up by an external pump and the pressure medium is usually distilled water with a little glycol added to inhibit corrosion. For higher fluid pressure, a hydraulic intensifier or air-driven pump is used with argon or nitrogen as the pressure medium. Normally, several vessels run from a single pump, where each vessel is connected to a high-pressure line by a valve and T-junction. The (two-way) valve isolates the vessels from the line. Each vessel is connected to a separate Bourdon gauge with a safety glass dial and blowout block. An autocontroller is normally used. The types of pressure tubing, valves, and fittings used depend on the operating pressures. Normally stainless-steel alloy is used up to 13 kbar, and size is recommended to be 1.4 inch outer diameter and 1/16 inch inner diameter. Although there has been rather little evolution in the basic design of cold-seal pressure vessels, marked changes have occurred in the controllers and pumps.

18.3.3 General-Purpose Autoclaves and Others

Other autoclaves, such as welded closures and modified Bridgman autoclaves, were used as the workhorses during the 1950s to 1980s; now their usage has reduced significantly because handling of them is quite cumbersome. However, these autoclaves contributed enormously to the development of both the hydrothermal technique itself and the growth of bulk crystals.

For the synthesis of crystals under hydrothermal conditions, these days very simple general-purpose autoclaves are used. Such autoclaves are commercially

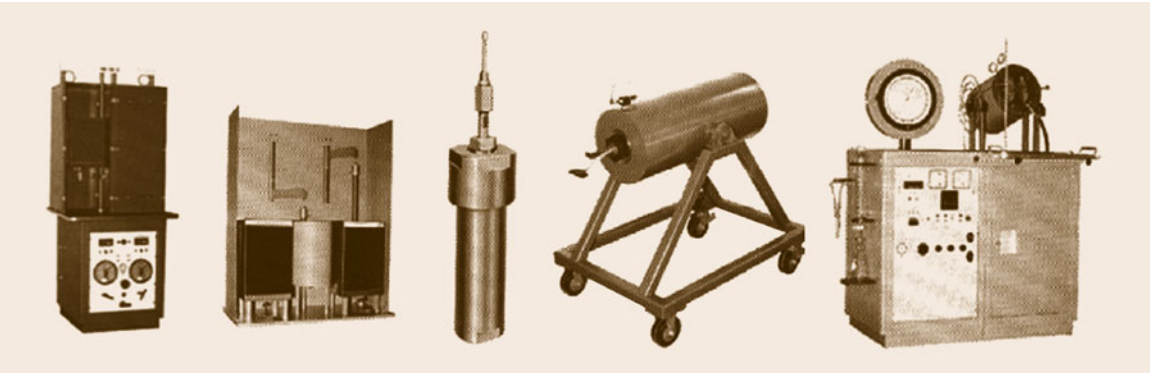


Fig. 18.19 Various test-tube-type cold-cone closure autoclaves (after [18.95])

available from many sources. Also several laboratories fabricate such autoclaves in their laboratories. Figure 18.20 shows the general-purpose autoclave used at the author's laboratory.

Many other designs are available today to meet the specific requirements, such as stirred autoclaves (Fig. 18.21), which are very useful to stir the mixture during the hydrothermal synthesis, to extract the contents from inside the reactor during the experiments, and also to pump in the desired gas into the reactor at any given time. The internal pressure can be read directly. The products can be quenched readily by the circulation of chilled water through the cooling coils running inside the autoclave. These additional advantages have helped greatly to understand the hydrothermal crystallization mechanism, kinetics, and the metastable phases more precisely.

In the last two decades the use of continuous-flow reactors has become very popular to synthesize small, micrometer-sized crystals to nanocrystals with a high degree of control over the shape and size of the crystals.



Fig. 18.20 General-purpose autoclaves popularly used for hydrothermal synthesis

These reactors operate at or above the supercritical conditions of the solvents – both aqueous and nonaqueous in nature. The method is also popularly known as the supercritical fluid (SCF) technology. With the invention of *green chemistry* in the early 1990s, there was a surge in the popularity of SCF technology. Today SCF technology has replaced organic solvents for the fabrication of a number of nanocrystals. Also it is emerging as an alternate to most existing techniques for designing and crystallizing new drug molecules.

Several designs and variations are available today for continuous-flow reactors to generate small to nanocrystals within the shortest possible time. The solubility of the materials has no major role to play in these flow systems. The use of capping agents and surfactants helps to control the size and shape of the nanocrystals and also to modify the surface characteristics of the crystals produced. By this method a great variety of crystals starting from metal oxides to silicates, vanadates, phosphates, germanates, titanates, etc., are produced for a wide range of modern technological applications within a few seconds. Hence, this technique is highly suitable for the commercial production of nanocrystals. The technique has been reviewed extensively and the reader can find additional information in several works [18.97–99]. Figure 18.22 shows a continuous-flow semi-pilot-scale reactor used in the crystallization of nanocrystals.

There are many more reactor designs for special purposes, such as rocking autoclaves, PVT apparatus, multichamber autoclaves, fluid sampling autoclaves, micro-autoclaves, autoclaves for visual examination, hydrothermal hot-pressing, vertical autoclaves, continuous-flow reactors, hydrothermal-electrochemical autoclaves, autoclaves for solubility measurements, autoclaves for kinetic study, pendulum autoclave, hor-



Fig. 18.21 Commercially available stirred autoclaves [18.100]

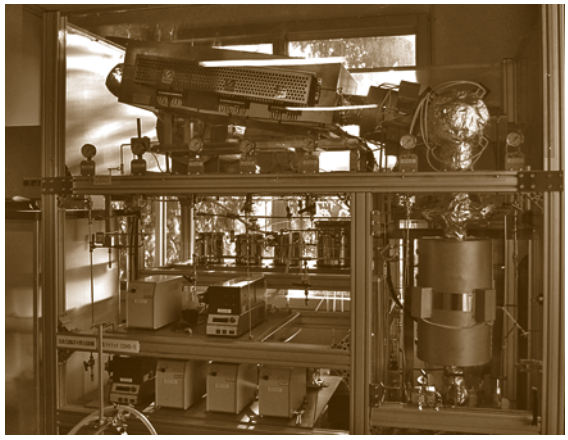


Fig. 18.22 The semi-pilot plant scale continuous-flow reactor used in the crystallization of nanocrystals [18.6]

izontal autoclaves for controlled diffusion study, and so on. The reader can find details of the construction and working mechanism of these autoclaves from the source [18.1].

Safety and maintenance of autoclaves is the prime factor one has to bear in mind while carrying out experiments under hydrothermal conditions. It is estimated that for a 100 cm^3 vessel at 20 000 psi, the stored energy is about 15 000 lbf/in^2. Figure 18.23 shows the autoclaves ruptured because of pressure surges.

Hydrothermal solutions – either acidic or alkaline – at high temperatures are hazardous to human beings if the autoclave explodes. Therefore, the vessels should have rupture discs calibrated to burst above a given pressure. Such rupture discs are commercially available for various ranges of bursting pressure. The most important arrangement is that provision should be made for venting the live volatiles in the event of rupture. Proper shielding of the autoclave should be given to divert the corrosive volatiles away from personnel. In the case of a large autoclave, the vessels are to be placed with proper shielding in a pit.

18.4 Hydrothermal Growth of Some Selected Crystals

As mentioned earlier, in this chapter only the growth of some selected crystals of current technological significance will be discussed. However, a more or less complete list of the compounds obtained under hydrothermal conditions is given in the form of a table at the end of this chapter, as Appendix 18.A.

18.4.1 Quartz

Advances in the hydrothermal method of growing crystals have been linked very closely with the progress achieved in the field of quartz growth ever since the technique was discovered. Quartz (SiO_2) exists in both crystalline and amorphous forms in nature. The crystalline form has over 22 polymorphic modifications. Among them, α-quartz is the most important one, which transforms into β-quartz above 573 °C. In order to grow this low-temperature modification of quartz, only the hydrothermal technique is suitable. α-quartz, as a piezoelectric crystal, has the ability to convert electric waves into mechanical waves and vice versa. Because of this property α-quartz is widely used in the electronics industries. In recent years, quartz for *tuning forks* has become essential for timing functions in electronic watches and in timing circuits for computers and telecommunications.

The principal source of electronics-grade natural quartz is Brazil. Today, the electronics industries are largely inclined to use synthetic quartz, because natural quartz crystals are generally irregular in shape, automatic cutting is cumbersome, and the yield is low. Many countries in the world, such as the USA, Japan, the UK, Germany, Russia, Poland, China, Belgium, and Taiwan, have entered the world market. Over 3000 t of quartz is produced annually for a variety of applications. The production of high-quality defect-free quartz has a large potential market among all electronic materials. Japan alone produces more than 50% of the

world's production, followed by the USA and China. More recently several other Japanese companies such as Kyocera, Shin-Etsu, Asahi Glass Co., etc. have started producing quartz for highly specialized applications. Perhaps Toyo is the largest single company in the world producing quartz. About 50% of the quartz produced goes into devices in the automotive industries, 30% of production goes into frequency control-devices, and the remaining 20% goes into optical devices. The total cost involved in the production of quartz is:

End users: ≈ US$ 1 000 000 000 000
Equipment: ≈ US$ 5 000 000 000
Components: ≈ US$ 100 000 000.

Thus, quartz takes the first place in value and quantity of single-crystal piezoelectric materials produced. Much of the research related to quartz today is confined to industry, while only scant publications emerge from research laboratories on new applications of quartz and the preparation of nanoscale silica particles. Otherwise, it is mainly research and development (R&D)-based industries that carry out research on the production of high-quality quartz and its applications, and these results are not published.

After the successful growth of quartz (Fig. 18.2) by Nacken in the 1940s, *Walker* synthesized large-size crystals of quartz (Fig. 18.24), much bigger than the size of the crystals produced by Nacken [18.101]. Subsequently major research activity was initiated at AT&T Bell Labs, and the most important contributions to the quartz growth came from the workers such as Ballman, Laudise, Kolb, and Shtenberg during the 1970s. Figure 18.25 shows the quartz crystals obtained at AT&T Bell Labs during the 1970s, the biggest crystals of that period. Each autoclave could produce around 70 kg of quartz crystals during the 1970s. In contrast, today in Japan, in one experimental run, about 4000–4500 kg of quartz is produced using the world's largest autoclave with a volume of 5000 l. Figure 18.26 shows the growth of quartz crystals in the world's largest autoclave at Toyo Communications Ltd., Japan. The early success in producing commercial quartz crystals in Japan during the post-war period paved the way for the entry of several others into the field. Some of the prominent contributors were Professor Noda, Doimon, Kiyoora, Dr. Itoh, and Dr. Taki. Today Japan is the world's largest producer of synthetic quartz for a variety of applications, followed by China.

In recent years mixed solvents are being used in the growth of quartz. High-quality quartz crystals have been obtained in NaCl and KCl solutions, NaOH, and

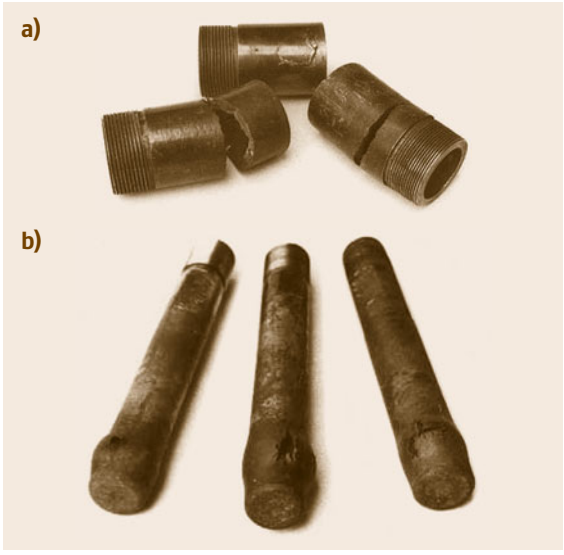


Fig. 18.23a,b Ruptured autoclaves. **(a)** General-purpose autoclaves, **(b)** Tuttle–Roy autoclaves

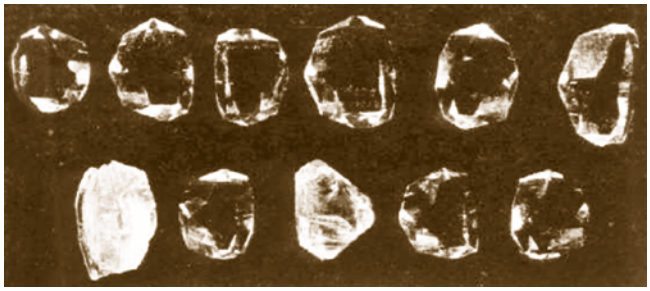


Fig. 18.24 Quartz crystals obtained by *Walker* [18.101]

Na_2CO_3 solutions (10%) [18.102, 103]. It has been observed that the high-frequency applications of α-quartz require sheets with small thickness, of the same order of size as the defects (such as inclusions, etch pits, and dislocations). Thus the pressure can promote new solvents viable for hydrothermal growth, especially by reducing their concentrations. The recent experimental results have shown the following enthalpy values calculated for α-quartz

$$\Delta H_T = 2395 \pm 5\,\text{cal/mol}\,, \quad \text{for NaOH (1 M)}\,,$$
$$200\,\text{MPa} \le p \le 350\,\text{MPa}\,;$$
$$\Delta H_T = 4001 \pm 2\,\text{cal/mol}\,, \quad \text{for } Na_2CO_3\ (1\,\text{M})\,,$$
$$150\,\text{MPa} \le p \le 350\,\text{MPa}\,.$$

In the growth of α-quartz, available nutrient material, such as small-particle-size α-quartz, silica glass, high-

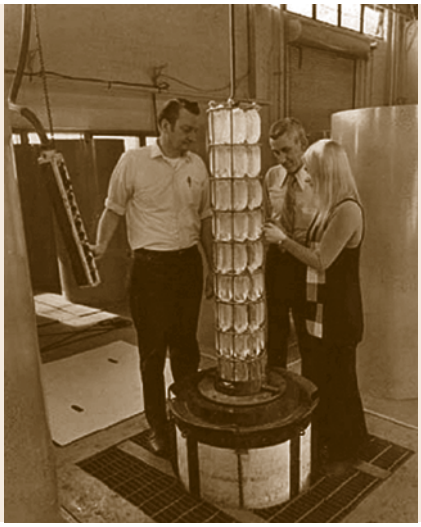


Fig. 18.25 Quartz crystals obtained at AT&T Bell Labs during the 1970s [18.102]

quality silica sand or silica gel, is placed in a liner made of iron or silver with a suitable baffle and a frame holding the seed plates. A mineralizer solution with a definite molarity is poured into the liner to achieve the required percentage fill. The increased solubility in the presence of mineralizer increases the supersaturation without spontaneous nucleation and consequently allows more rapid growth rates on the seeds. Figure 18.16b shows a cross-section of a modified Bridgman autoclave used in the growth of quartz crystals.

The commercial autoclaves used have 10 inch inner diameter, and are 10 ft long unlined. These autoclaves can work at conditions up to 30 000 psi and 400 °C. Most of these experiments are carried out for 25–90 days to obtain full-size crystals of 4 cm in the z-direction and 12.5–15 cm in the y-direction. The temperature gradient is varied according to the nutrient used. About 1 N NaOH or Na_2CO_3 is the most commonly used mineralizer. The solubility change with temperature is smaller in NaOH and slightly larger in Na_2CO_3. The temperature of the autoclave at the nutrient zone is usually kept at 355–369 °C and, in the growth zone, kept at 350 °C. The addition of lithium improves the growth rate, and small amounts of Li salts are routinely added to the solution [18.104].

The solubility is also, to some extent, a function of increasing pressure. The pressure is controlled by the percentage fill of the autoclave and is usually about 80% for hydroxyl mineralizer (20 000 psi internal pressure). In most experiments the percentage opening of the baffle is 20%, although lower values are used by several workers. However, the actual percentage opening of the baffle area and its geometry are not disclosed, especially by commercial growers.

The optimum growth conditions for synthesis of quartz based on the work in Bell Laboratories are [18.105, 106]:

Dissolution temperature:	425 °C
Growth temperature:	375 °C
Pressure:	15 000–25 000 psi.
Mineralizer concentration:	0.5–1.0 M NaOH
Temperature gradient (ΔT):	50 °C
% fill:	78–85%
Growth rate in (0001):	1.0–1.25 mm/day.

The quality of the grown crystals is also a function of the seed orientation and its quality. Strained seeds generally produce strained growth regions [18.107]. The seeds are polished to a very fine finish before use. Most high-quality crystals are grown using seeds with the surface perpendicular to the z-direction, since this region has the lowest aluminum concentration. Though most quartz production consists of *y bar* crystals, that is, small crystals ($z = 20$–25 mm, 64 mm seed) capable of several y bar per crystal, *pure* z bars are also produced, representing 10–20% of production. However, for medium- and high-quality grades we notice a rise in demand for crystals of very large dimensions and upper–medium quality, especially in the USA, for manufacturing wafers used in surface wave applications [18.108]. Earlier, most seeds used were natural quartz cut in a definite orientation, but in recent years this practice is only used when a high-quality crystal is desired.

The growth of quartz crystals has been understood precisely with reference to the growth temperature, temperature gradient, percentage fill, solubility, percentage of baffle opening, orientation and nature of seed, and type of nutrient. Also many kinetic studies have been carried out [18.35, 109]. Figure 18.27 shows the growth rate of quartz as a function of seed orientation [18.109]. The solubility of quartz has been studied as a function of temperature, and the growth rate as a function of seed orientation and percentage fill. Figure 18.28 shows hydrothermally grown quartz crystals.

The type of crystal to be grown depends on the application, as different properties are required in each case. For optical use, high uniformity, low strain, and low inclusion counts are needed, since all of these can affect transparency. For surface acoustic wave de-



Fig. 18.26 Growth of quartz crystals in the world's largest autoclave at Toyo Communications Ltd., Japan (courtesy of S. Taki). Dissolution temperature: 425 °C; growth temperature: 375 °C; pressure: 15 000–25 000 psi; mineralizer concentration: 0.5–1.0 M NaOH; temperature gradient (ΔT): 50 °C; percentage fill: 78–85%; growth rate of (0001): 1.0–1.25 mm/day

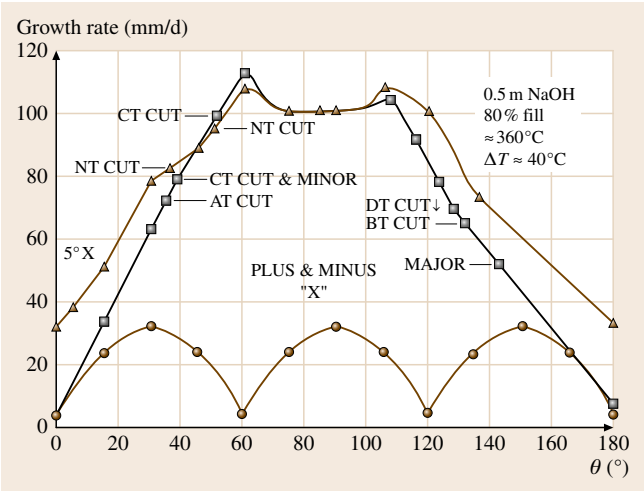


Fig. 18.27 Growth rate of quartz as a function of seed orientation [18.109]

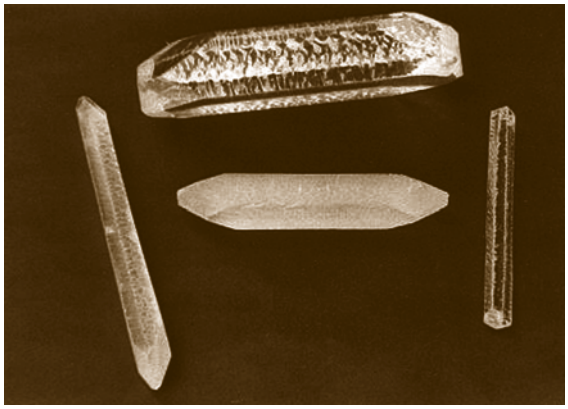


Fig. 18.28 Hydrothermally grown quartz crystals

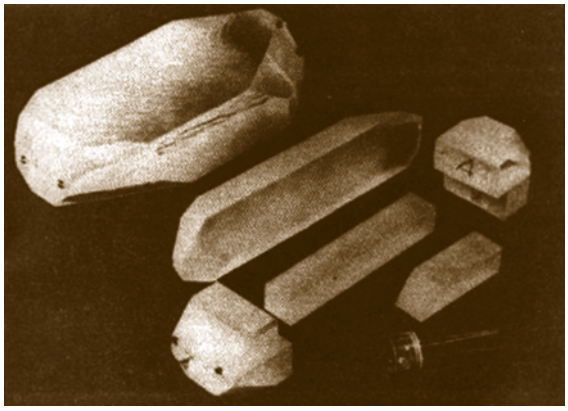


Fig. 18.29 Fabrication of resonators from a single crystal

vices, large pieces that can take a very high-quality surface finish are needed. The quality of the material required for resonators used in time and frequency devices varies with the application. The more precise the need, the more stringent the requirements. For most applications, a truly high-quality material is not needed. For high-precision uses, such as in navigational devices and satellites, a very high-quality material must be used. Most recent research on quartz growth is for improved resonator performance, which requires the growth of high-quality low-dislocation quartz. Figure 18.29 shows the fabrication of resonators from a single crystal.

Several criteria are used to evaluate the quality of quartz crystals. The most commonly used criterion is the Q value or quality factor, which is a measure of the acoustic loss of the material. It is important for a resonator to have high electrical Q value and superior frequency–temperature characteristics. In a piezoelectric resonator, electrical energy and mechanical energy are interconvertible. In such a case, Q is expressed as

$$Q = \frac{[X]}{R}\,, \tag{18.2}$$

where X is the inductive or capacitive reactance at resonance and R is the resistance.

The acoustic Q for natural α-quartz crystal varies in the range 1 to 3×10^6, while for synthetic quartz crystals the value drops to 2×10^5 to 1×10^6. Thus in the last two decades, the main objective among quartz crystal growers has been to improve Q, which in turn leads to a low concentration of physicochemical and structural defects.

The growth rate is determined by the ratio of increase in thickness of the seed and the duration of the run. The growth rate along the main crystallographic axes R_c is determined by dividing the thickness of the layer grown on the seed, $(h_1 - h_0)/2$, by the run duration t, and is expressed in millimeters per day. It has also been known for quite some time that, qualitatively, acoustic Q is inversely proportional to growth rate and directly related to chemical impurities. The internal friction (the inverse of the mechanical Q) is dependent on the growth rate of synthetic quartz crystals. *Martin* and *Armington* have studied the effect of growth rate on the aluminum content at low growth rates [18.110]. Al^{3+} and H^+ are the most deleterious impurities in quartz used for frequency and timing applications, and they also influence the growth rates. Similarly the percentage fill and pressure strongly influence the growth rate of quartz.

For any crystal growth, seed crystals play a vital role in controlling the quality, growth rate, and morphology of the grown crystals. Usually, in the case of quartz for higher-frequency applications, a smaller x-axis dimension is needed. z-Growth material is desired for resonators, as it has been shown that this material has about an order of magnitude lower aluminum concentration. In the majority of crystal growth experiments, in general the thickness of the seed crystal is usually 1–2 mm. Until recently, it was necessary to use natural seeds for the preparation of low-dislocation crystals. However, most crystals grown from synthetic seeds contain large numbers of dislocations, of the order of several hundred per square centimeters. These results in the formation of etch channels in the resonator, which weaken it mechanically and can be a problem when electronic devices are deposited on the surface. When a seed perpendicular to the z-axis (but from the x-growth region) is used, the dislocation density can be reduced to below ten and sometimes to zero dislocations per square centimeter [18.111]. The purity of the crystals produced using seeds cut from the x-region is as good as that from crystals produced from the usual z-seed.

In the growth of quartz crystals, the nutrient has a profound effect on the quality of the grown crystal. It is well known that most of the impurities and in turn the defects in the grown crystals come from the nutrient and only to some extent from the autoclave walls. Nutrient selection is one of the attractive research topics in crystal growth on the whole. Even in the 19th century, researchers tried the use of several varieties of nutrient to obtain quartz under hydrothermal conditions. There are several reasons for using varieties of nutrients, including: to obtain high-purity crystal, to obtain higher solubility in the desired PT conditions for a given solvent, to achieve higher growth rate, to obtain higher yield, and to lower the PT conditions for growth. In the case of quartz, to obtain high-quality crystals, even α-cristobalite has been used as a nutrient [18.112].

Tables 18.6 and 18.7 show the distribution of impurities in different sectors of synthetic quartz. Hence, attention has to be paid to the solvent, nutrient, seed orientation, and seed quality in order to obtain high-quality crystals, as well as the experimental PT conditions.

In the growth of α-quartz for high-frequency device applications (24–100 MHz or more), the existence of defects, either physicochemical or structural, in synthetic quartz crystals leads to critical modifications of devices. Low-defect, high-purity synthetic quartz should have the characteristics given in Table 18.8 [18.113]. Sweeping is one of the most popularly used techniques in recent years to enhance the performance of quartz resonators. Sweeping, or solid-state electrolysis or electrodiffusion, is generally performed under vacuum, air, hydrogen or a desired atmosphere. During sweeping, the crystal is placed in an electric field and heated. Then, migration of the impurities and some modifications are induced within the

Table 18.6 Impurities in different sectors in synthetic quartz

Sector	Al	Na	Li
Z	5	1	0.5
$+X$	31	9	5
$-X$	122	40	5
S	85	26	16

Table 18.7 Dislocation density in different seeds

Seed	Mineralizer	Etch channel density
Z	Hydroxide	253
Z	Carbonate	247
$X+$	Hydroxide	1
$X+$ (reused)	Hydroxide	14

Table 18.8 Desirable and achieved parameters in synthetic quartz [18.113]

Parameter	Desirable	So far achieved
Etch channel density	$< 10/cm^2$	< 86
Inclusion density	< 10/bar	
Impurity concentration (ppb)		
Al	< 200	700
Li	< 300	300
Na	< 500	1640
K	< 40	300
Fe	< 100	1800
Q ($3500/3800\,cm^{-1}$)	$< 2.5\times10^6$	$< 2.5\times10^6$
Strain	None	Variable
Fringe distorion	< 0.05 RMS	Variable

crystal. Sweeping reduces the formation of etch tunnels. The effect of sweeping is to remove lithium and sodium deposited interstitially in the lattice during the growth. These ions are usually trapped along an angstrom-wide tunnel, which is parallel to the z-axis in the quartz crystal lattice. These ions, in an interstitial position, interact with substitutional aluminum impurities in the lattice to form Al-Li centers, which have been shown to be weakly bonded and are the cause of low radiation tolerance in a resonator. In the sweeping process, these are replaced by Al–OH or Al–hole centers, which have a much higher radiation tolerance. The sweeping is carried out at 500–550 °C usually for a period of 7 days or even more to remove alkalies. However, it should be remembered that sweeping cannot become a routine process even if the same experimental conditions are always applied.

There are several other techniques employed for the fabrication of piezoelectric high- to ultrahigh-frequency devices based on quartz resonators. The important ones are: chemical polishing, ion beam etching (IBE). The reverse thermodynamic relations are employed for the refinement of chemical polishing. Several solvents such as HF and NH_4HF_2, NaOH, $KOH\cdot xH_2O$, and $NaOH\cdot xH_2O$ are employed [18.114].

Similarly, the industrial chemical etching process is specially dedicated for large thickness removals without damaging the blank surface texture. This is most useful for frequency applications of quartz, because the mechanical grinding and lapping introduce surface stresses. Fluoride media is the most popular for this type of chemical polishing [18.115]. Recently, *Cambon* et al. tried industrial chemical etching successfully in the temperature range 150–180 °C using concentrated NaOH solvents [18.116]. During the chemical etching process, several factors influence the process: kinetics, etching temperature, etching time, plate orientation, SiO_2 concentration, solvent concentration, wafer carrier geometry, and so on. By using this process about 3200 quartz plates can be processed in a single run. The resonators manufactured by this process have demonstrated a high level of performance, even higher than that of plates obtained by mechanical means.

In recent years there has been growing interest in morphological variations, growth-rate monitoring using various seed orientations, and computer simulation for the precise calculation of growth rates of various faces [18.117–119]. These studies greatly help in understanding the growth technology for commercial production of defect-free and economic quartz crystals.

The growth of bulk single crystals of quartz is still an attractive field of research, especially the growth of defect-free quartz crystals for space-grade applications. Understanding of solubility and the growth mechanism is still incomplete, although laser Raman spectroscopy and other advanced techniques such as computer simulation are yielding rich information about how to intelligently engineer the growth processes, thereby minimizing growth defects.

The preparation of quartz for other applications, such as photomask substrates for lithography, poly-Si thin-film transistor liquid-crystal displays (TFT-LCDs), and high-purity and high-precision polishing devices, is a new trend in science. For example, Shin-Etsu Chemical (Japan), Asahi Glass Co. (Japan), NDK America (USA), and APC International Ltd. (USA) are engaged in such research and development, whereas companies such as Sawyer Research Inc., General Electric (GE), Philips, and Toyo Communication are engaged in production of bulk crystals of quartz for oscillators, frequency devices, etc.

18.4.2 Aluminum and Gallium Berlinites

Berlinite ($AlPO_4$) and gallium berlinite ($GaPO_4$) are the two most important crystals that are isoelectronic and isostructural with α-quartz. These compounds are used to replace quartz in electronic devices because of their larger mechanical coupling factors than α-quartz, and because their resonant frequency is nearly independent of temperature for certain orientations [18.120–122]. Table 18.9 gives a comparison of some piezoelectric characteristics of these materials [18.123]. The growth of berlinite and gallium berlinite does not differ much

between the two materials because they both have a negative temperature coefficient of solubility, and hence a similar experimental arrangement is used for both. During the 1980s the growth of berlinite was studied extensively, and it was considered at one time as a replacement for α-quartz [18.124]. However, results were not encouraging for bulk crystal growth of berlinite on a par with that of α-quartz. Although the growth of gallium berlinite began sometime during the late 1980s, momentum picked up during 1995. It is important to discuss the growth of these crystals from a scientific point of view in order to learn about the hydrothermal technique in general, as these crystals – although isoelectronic and isostructural with α-quartz – have a completely contrasting experimental setup for their crystal growth.

John and *Kordes* were the first to grow berlinite crystals successfully, followed by *Stanley* using completely different conditions [18.76, 77]. The greatest disadvantage in the growth of these berlinites is their negative temperature coefficient of solubility, which demands a special experimental setup. Although much progress has been achieved in the growth of these berlinite crystals, our knowledge on the growth of $AlPO_4$ and $GaPO_4$ is still comparable to that of quartz some 50 years ago, particularly with reference to size, crystal perfection, reproducibility, etc. The highly corrosive nature of the solvent is the major hindrance in the growth of bulk crystals of these berlinites.

The solubility of these berlinites has been discussed earlier. Although several reports have appeared on solubility measurements as a function of various parameters, there is still no unanimity in these results.

Berlinites could be best grown using the hydrothermal technique. α-Berlinite is stable up to 584 °C, and below 150 °C the hydrates and $AlPO_4 \cdot H_2O$ are stable. Therefore, the growth temperatures should be greater than 150 °C but less than 584 °C. However, solubility and PVT studies have clearly shown that crystal growth must be carried out at less than 300 °C because of the reverse solubility. Several versions of the hydrothermal growth of berlinite single crystals have been tried to suit the solubility. In contrast to aluminum berlinite, gallium berlinite has no phase transitions, and therefore some researchers have even synthesized this crystal using the flux growth method [18.125]. However, the quality of these flux-grown gallium berlinite crystals is far inferior to that of hydrothermally grown crystals. In the hydrothermal growth of these berlinites, usually acid mineralizers are used at various concentrations. Mixed acid mineralizers such as HCl, H_3PO_4, H_2SO_4, HCOOH, etc. are much more widely used in practice. However, other mineralizers such as NaOH, Na_3PO_4, Na_2HPO_4, $NaHCO_3$, NaF, KF, LiF, NH_4HF_2, NaCl, Na_2CO_3, etc. have also been tried. More details can be found in [18.126].

Small crystals of both aluminum berlinite and gallium berlinite can be obtained through hydrothermal reactions of H_3PO4 with various chemicals containing Al and Ga [18.94, 126, 127]

$$M_2O_3 + 2H_3PO_4 \rightarrow 2MPO_4 + 3H_2O\,.$$

These fine crystals of berlinite can in turn be used as the nutrient to grow bigger bulk single crystals. Since the solubility of these compounds is negative, the seed is placed in the hotter zone in the bottom, while nutrient is placed in the upper cooler region. The most important modifications suggested from time to time in the growth of berlinite crystals are:

1. Crystal growth by slow heating method
2. Crystal growth by composite gradient method
3. Crystal growth by temperature gradient
4. Growth on seeds.

The crystal growth by slow heating method was mainly used for improving the quality of seeds and to enhance the size of the crystal, with conditions similar to those used for nucleation. A major drawback of this method is the impossibility of obtaining crystals of sufficient size in one operation due to the limited quantity of metal phosphate available in the solution. Usually Morey autoclaves are used to carry out crystal growth by the slow heating method ($T \leq 250$ °C; $p = 100–1000$ atm). The size of the crystals obtained through spontaneous nucleation is usually 0.1–4 mm, depending upon the experimental conditions.

The crystal growth by composite gradient method gives more flexibility in adjusting the growth rates and avoids the preliminary work of crystal growth or nutrient preparation.

Table 18.9 Comparison of some piezoelectric characteristics (* AT cut)

Parameter	Quartz	Berlinite	Gallium berlinite
Coupling coefficient K (%)*	8.5	11.0	> 16.0
Surtension coefficient Q*	3×10^6	10^6	$> 5\times10^4$
α–β phase transition (°C)	573	584	No

The crystal growth with reverse temperature gradient method is much more versatile for these compounds in general. In this approach, the nutrient (either crystalline powder or fine grains of $AlPO_4$ usually obtained from the slow heating method) is kept in a gasket at the upper portion of the autoclave, which is cooler than the bottom of the liner that is kept at slightly higher temperature, forming the crystallization zone (Fig. 18.16a).

The crystal growth on seeds method uses spontaneously nucleated seeds and oriented seeds cut from grown crystals, usually mounted on a platinum frame placed in the bottom (hotter) region of an autoclave, and the nutrient (≈ 60 mesh particle size prepared by other methods) is placed above in a platinum gasket in the upper region (or in a Teflon gasket). Thus, the seeds are in the warmer, supersaturated region at the bottom of the autoclave and the temperature gradient achieved by cooling the top allows proper convection.

Figure 18.30 shows aluminum berlinite crystals grown by the hydrothermal method. The orientation of the seed is important, as in the case of quartz, because the growth rate and crystal quality depend upon the seed orientation. The following growth rates are shown for seeds whose faces are indicated below:

(0001) (basal plane):	0.25–0.50 mm/day
$(10\bar{2}1)$ (x-cut):	0.23–0.30 mm/day
$(10\bar{1}0)$ (y-cut):	0.12–0.15 mm/day
$(01\bar{1}1)$ (minor rhombohedral face):	0.12 mm/day
$(10\bar{1}1)$ (major rhombohedral face):	0.15 mm/day.

The relative growth rates are in general agreement with the morphology of the equilibrium form, as judged from observing spontaneously nucleated crystals which are bounded by small prism faces and terminated by minor and major rhombohedral faces. The dissolution rate of aluminophosphate glass charge is three times greater than that of the crystalline charge [18.128].

The morphology of spontaneously crystallized aluminum berlinite crystals varies greatly, depending upon the type of solvent, its concentration, and the experimental temperature. The most commonly observed morphologies are hexagonal, rhombohedral, rods, needles, and equidimensional crystals. Impurities also play a prominent role in controlling the crystal morphology. In the growth of aluminum berlinite the typical experimental conditions used are:

Growth temperature:	240 °C
Pressure:	15–35 MPa
Solvents:	Mixed acid mineralizers
Nutrient:	Powdered nutrient, preferably aluminum phosphate glass
Filling:	80%
ΔT:	$5\,°C < T < 30\,°C$
Growth rate:	0.35 to 0.50 mm/day in H_3PO_4 0.35 to 0.45 mm/day in HCl 0.25 to 0.35 mm/day in HNO_3 0.2 to 0.3 mm/day in H_2SO_4.

It is interesting to note that the berlinite crystals show internal structural defects on x-ray Lang topography. No fundamental differences were found by x-ray topography between the horizontal gradient, vertical gradient, and slow heating methods. The two principal imperfections readily observable in berlinite are crevice flawing and cracks. Although crystals appear quite transparent from the outside, they contain many internal defects. A combination of optimum growth conditions, reducing the water content, and using heat treatment to control the water distribution could be of great interest for improving the piezoelectric device potential of aluminum berlinite.

During the 1980s and early 1990s work on aluminum berlinite was at its peak, and then activity suddenly dropped, because of several difficulties associated with its growth as bulk crystal. However, crystal growth of gallium berlinite, which began during the late 1980s, is still an attractive field, and several research groups are actively engaged in bulk crystal growth of gallium berlinite. The solubility and crystal growth kinetics of gallium phosphate have been extensively studied by various groups [18.129–131] and basically resemble those of aluminum berlinite. The necessary conditions for crystal growth are:

1. Solubility of $GaPO_4$ nutrient is sufficient for crystal growth.
2. Convection of saturated fluids is intensive and not varying during the crystal growth cycle.
3. No formation of spontaneous crystallites.
4. Saturation of an initial solvent slowly appears, simultaneously. with the end of seed etching (very soft restart conditions).

The typical growth conditions are:

Experimental temperature:	280 °C
Experimental pressure:	8 MPa
Mineralizer:	$H_3PO_4 + H_2SO_4$ ($pH = 3 - 4$ under ambient conditions).

The biggest disadvantage is that, in the case of seeded growth under retrograde solubility, it is often accompanied by precipitation of spontaneous crystals or degradation of growth surfaces because of the irreversible character of the mass transportation (high or low relation of ΔS to growth kinetic parameters).

Figure 18.31 shows gallium berlinite crystals obtained under hydrothermal conditions. The commonly appearing faces are $(10\bar{1}1)$, $(01\bar{1}1)$, $(10\bar{1}0)$, and $(10\bar{1}2)$. The growth rates along various crystallographic directions decrease in the sequence

$$\gamma(0001) \gg \gamma(01\bar{1}2) > \gamma(10\bar{1}0) > \gamma(01\bar{1}1) > \gamma(10\bar{1}2) > \gamma(10\bar{1}1) .$$

The common twins observed in $GaPO_4$ obey the Dauphiné, Brazil, and Laydolt's twinning laws.

The crystallization process, dissolution process, rate of crystallization (i. e., the amount of $GaPO_4$ crystal formed per unit time), action of solvent, its concentration and temperature regime, etc. have been studied in detail for $GaPO_4$ crystal growth by several workers [18.127, 132, 133]. Also characterization of defects has been carried out in detail [18.134–136].

Although the first stage of $GaPO_4$ crystal growth began with epitaxy of $GaPO_4$ on $AlPO_4$ seeds, the subject still remains popular. Several substrates including quartz have been used to grow $GaPO_4$ crystal.

If the size of the $GaPO_4$ crystals grown by the hydrothermal technique is increased sufficiently, it would become the best piezoelectric material replacing quartz.

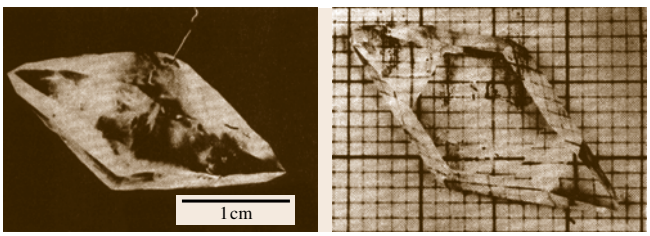


Fig. 18.30 Hydrothermally grown aluminum berlinite crystals (courtesy of Dr. Y. Toudic)

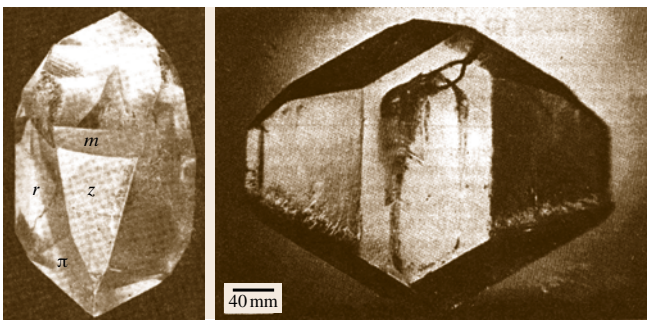


Fig. 18.31 Characteristic photographs of $GaPO_4$ crystals obtained by the hydrothermal method (courtesy of Prof. L. N. Demianets)

18.4.3 Calcite

Calcite (Ca_2CO_3) is an important carbonate mineral. Pure and optically clear calcite is called Iceland spar. Calcite single crystals form an important optical material owing to its large birefringence and transparency over a wide range of wavelengths. These properties make it a significant material for polarized devices such as optical isolators and Q-switches. It also exhibits antiferromagnetic properties. Although there are many deposits of calcite in the world, the optically clear quality calcite, Iceland spar, has been depleted in recent years, leading to its shortage in nature. However, the demand for optically clear calcite single crystals is increasing greatly with the development of laser devices such as the optical isolator [18.137, 138]. Many researchers have tried to grow calcite single crystals at relatively low temperatures, since calcite crystals dissociate to form CaO and CO_2 above 900 °C under atmospheric pressure. Various solvents have been used for hydrothermal growth of calcite, but none of them has been found to be the best to grow large single crystals.

The solubility of calcite is very interesting. The solubility is positive for increasing CO_2 pressure and negative for increasing temperature. This behavior of calcite has posed a real problem in the search for a suitable solvent to optimize the growth rate. Despite a large number of reports concerning calcite growth, hydrothermal reactions of calcite in chloride and other chloride solutions have appeared, because natural calcite crystals are formed in both chloride and carbonate hydrothermal solutions and these chloride solutions are almost analogous to natural carbonate thermal springs. *Ikornikova* has done extensive work on aspects of solubility, designing an apparatus to grow calcite crystals with changing CO_2 concentration as the pressure is reduced at constant temperature, crystal growth kinetics, and mechanism [18.139]. The following groups have carried out extensive studies on the solubility of calcite:

1. Ikornikova, Russia, during the 1960s and 1970s, using chloride solutions
2. Belt, USA, during the 1970s using carbonate solutions

3. Hirano, Japan, during the 1980s and early 1990s using nitrate solutions
4. Kodaira, Japan, during the 1990s using H_2O/CO_2
5. Yamasaki, Japan, during the 1990s using ammonium acetate and other organic solvents.

Each of the last three groups claims superiority of their solvents over the others. Figure 18.32 shows solubility curves for calcite in different solvents. *Yanagisawa* et al. have studied the effect of pH of CH_3COONH_4 on the growth of calcite [18.142]. When as-cleaved seeds are used, the calcite crystals obtained are usually opaque or not transparent and the surfaces show a greater degree of defects such as growth hillocks, a lot of small secondary grown crystals, and strains. In contrast, crystals grown on etched seed crystals are usually transparent and their surfaces are very smooth. Figure 18.33 shows a characteristic photograph of calcite single crystal grown in NH_4NO_3 solution using as-cleaved and etched seeds. Earlier experiments on calcite single-crystal growth were carried out under higher-PT conditions. For example, *Kinloch* et al. carried out calcite crystal growth at temperature greater than 435 °C with 1.72 kbar pressure using platinum liners and achieved about 50 μm/day growth rate for the {1011} face [18.137]. However, in recent years crystal growth has been carried out using lower-PT conditions using Teflon liners (below 250 °C), and a growth rate of > 120 μm/day has been achieved. Also several types of nutrients such as natural limestone, natural Iceland spar, reagent-grade carbonates, etc., have been attempted in recent years to obtain high-quality calcite single crystals [18.143].

There are several works in the literature on the growth of other carbonates such as $MnCO_3$ (rhodochrosite), $FeCO_3$ (siderite), $CdCO_3$ (otavit), $NiCO_3$, etc., using alkali chloride and carbonate solutions in the temperature range 300–500 °C and pressure up to 1 kbar with a temperature gradient [18.139].



Fig. 18.33 Characteristic photographs of calcite single crystal grown in NH_4NO_3 solution

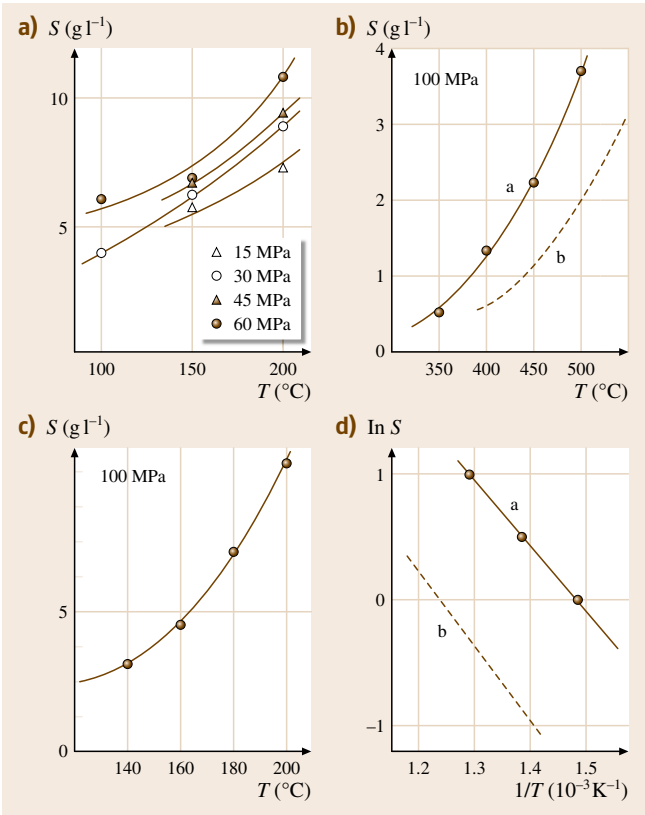


Fig. 18.32a–d Solubility curves for calcite in different solvents: **(a)** in 1 M NH_4NO3; **(b)** in 1.5 M $Ca(NO_3)_2$ (*a*), 3 M NaCl (*b*); **(c)** in 3 M NH_4NO_3; **(d)** in 1.5 M $Ca(NO_3)_2$ (*a*), 3 M NaCl (*b*) (after [18.140, 141])

18.4.4 Gemstones

The hydrothermal method has been popularly used from the third quarter of the 19th century for the growth of gemstones such as corundum, ruby, emerald, and garnet [18.15, 16, 18]. During the 1960s and 1970s work on hydrothermal growth of gemstones reached its peak, when successful and high-quality crystals of emerald, colored quartz, amethyst, ruby, corundum, malachite, silicon nitride, garnet, etc. were obtained. However, today, like quartz, much of the research on the hydrothermal growth of gemstones is commercial and hence few publications appear from research laboratories. However, some publications appear periodically on the growth of new gemstones, for example, zeosite. As the sources of natural colored gemstones continue to shrink and the population of the world continues to grow, one could expect increased demand for mater-

ials such as synthetic emerald (tempered, however, by occasional reverses in the world economy). Here, in order to understand the hydrothermal growth of crystals in general, knowledge on the growth of gemstones is also essential. Therefore, a few selected gemstones grown using this hydrothermal technique will be discussed below.

Corundum

Corundum (Al_2O_3) is stable under hydrothermal conditions at $T > 400\,^{\circ}C$ [18.146, 147] and is soluble in alkali and carbonate solutions. The hydrothermal growth of corundum is achieved using a metastable-phase technique because of its very low solubility. Gibbsite ($Al(OH)_3$) is used as a nutrient, α-Al_2O_3 as a seed, and an alkaline solution as a solvent. A higher growth rate is obtained in KOH or K_2CO_3 solution than in NaOH or Na_2CO_3 solution. The solubility is lower in KOH or K_2CO_3, but the interaction between the impurity absorbed beforehand onto the crystal surface and K^+ ions existing in the solution acts as a factor to augment the growth rate. As the pH of solution is lowered, thickness of the growth layer increases along the *c*-axis. The growth of corundum is extremely low in 6 N HCl. Kashkurov et al. have studied the growth of large corundum crystals at pressures of up to 2000 atm and temperatures of up to 550 °C in alkali solutions of various concentrations. Crystals weighing up to 1 kg were prepared by the hydrothermal technique, and the imperfect state of these crystals was apparently associated with internal stresses and the mosaic structure of seed crystals, which were prepared by Varneuil technique [18.148]. Figure 18.34 shows the solubility of corundum in potassium carbonate aqueous solutions.

The ideal experimental conditions for the growth of good-quality corundum crystals are:

Temperature: 480 °C
Pressure: 1.33 kbar
Mineralizer: 4 M K_2CO_3
Fill: 85%
ΔT: 30 °C.

Using these experimental conditions colorless and transparent crystals with (211), (311), and (111) faces were obtained. Increasing the temperature yields a higher growth rate in the temperature interval 400–500 °C.

Ruby and Sapphire

Ruby and sapphire crystals are grown using the hydrothermal method, with appropriate dopants added to experimental conditions similar to those described for corundum crystal growth. Sapphire was probably the second material after quartz to be grown in any size by the hydrothermal method. Similarly large ruby crystals could be grown using carbonate solutions. The solubilities of sapphire and ruby are the same as that of corundum and increase with temperature. Oxides of chromium and iron taken in the nutrient along with Na_2CO_3 solution strongly influence the crystallization of these two varieties of crystals than K_2CO_3 solution. However, when the concentration of these components in the nutrient is > 1.6% in 10% Na_2CO_3 solution, crystals barely grow. Figure 18.35 shows the growth rate of the (1011) face versus Cr_2O_3 concentration in the initial charge (10% Na_2CO_3 solution, 550 °C, autoclave 60% filled). In carbonate and bicarbonate solutions, chromic oxide and aluminum oxide have substantially different solubilities and rates of dissolution.

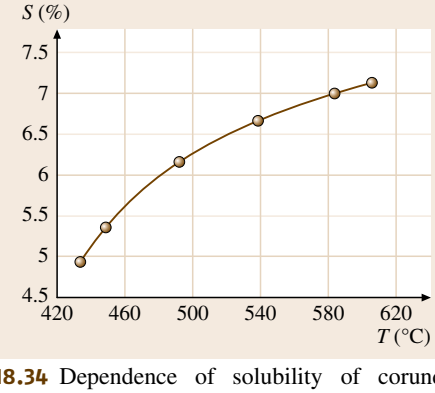


Fig. 18.34 Dependence of solubility of corundum in K_2CO_3 aqueous solutions (after [18.144])

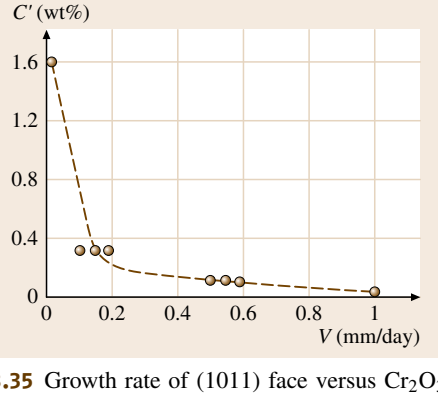


Fig. 18.35 Growth rate of (1011) face versus Cr_2O_3 concentration in the initial charge (after [18.145])

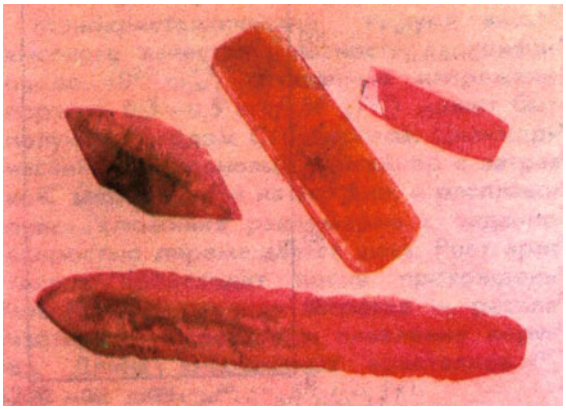


Fig. 18.36 Hydrothermally grown ruby crystals (courtesy of Prof. V. S. Balitskii)

Monchamp et al. have carried out very large-scale growth of sapphire and ruby with considerable success [18.149, 150]. Figure 18.36 shows hydrothermally grown ruby crystal [18.151]. Green crystals containing iron have been grown by carrying out the crystallization in welded liners directly, and essentially pure colorless crystals have been prepared by the use of silver tubes [18.150]. The overall features are similar to those for the growth of corundum crystals.

Emerald

Among the other gemstones grown popularly under hydrothermal conditions, emerald is one of the most important ones. It is also used as an effective tunable laser medium. The presence of Cr^{+3} in beryl ($Be_3Al_2(SiO_3)_6$) gives a green-colored emerald. The bluish-green variety is known as aquamarine. Gems that are greenish/yellow to iron-yellow and honey-yellow are called golden beryl. The rose-colored variety is called morganite or vorobyevite. Alkali elements such as Na^+, Li^+, and Cs^+ are sometimes present, replacing the beryllium at 0.25–5%. Artificial growth of beryl crystals began in the previous century itself. *Hautefeuille* and *Perrey* were the first to synthesize beryl crystals artificially [18.152]. Probably the earliest best work on hydrothermal growth of emerald was by Nacken. He made larger numbers of synthetic emeralds, using a trace of chromium to produce the color. Hexagonal prisms weighing about 0.2 g were grown in a few days. Several workers have reviewed the hydrothermal growth of emerald [18.153, 154]. Lechleitner of Innsbruck, Austria, released the first and not completely satisfactory product into the market during the 1960s and 1970s [18.155–157]. He used faceted beryl gemstones as the seed and grew a thin layer of hydrothermal emerald on the surface, which was subsequently given a light polish (not necessarily on all faces). Such stones were marketed for a short time under the names *Emerita* and *Symerald*. The first completely synthetic hydrothermal emerald was put on the market by the Linde Division of the Union Carbide Corporation in 1965. The first patent on beryl revealed that it could be grown in a neutral to alkali medium (pH of 7–12.5) using mineralizers such as alkali or ammonium halides (e.g., NH_4F + NH_4OH or KF), and that Fe, Ni, or Nd could be used as dopants [18.158]. The second patent dealt with the analogous growth of beryl in an acid medium (pH 0.2–4.5), using similar halide mineralizers but with an acid reaction (e.g., 8 N NH_4Cl) or with extra acid added [18.159]. Typical emerald growth conditions included a pressure of 10 000–20 000 psi at temperatures of 500–600 °C resulting from a 62% fill. A small temperature gradient of 10–25 °C was employed. The Al was supplied from gibbsite $Al(OH)_3$, Be from $Be(OH)_2$, Si from crushed crystals of quartz, and Cr from $CrCl_3 \cdot 6H_2O$. Growth rates as high as 0.33 mm/day could be attained. The pressure vessel was lined with gold.

Biron Mineral (Pvt.) Ltd., Australia, produces commercially popular Biron synthetic emerald, but the growth conditions remain unknown. However, chlorine, chromium, vanadium, some water, and also tiny gold crystals have been detected in these crystals [18.160, 161]. Today Russia produces the largest quantities of synthetic emerald in the world. Also there are several recent publications from Russian laboratories on synthetic emerald. This activity began in 1965 and the growth conditions used are:

Growth temperature:	590–620 °C
Temperature gradient:	45 °C 20–100 °C 70–130 °C
Pressure:	790–1481 atm
Solvent:	Acidic solution or flourine bearing solutions of complex components
Nutrient:	Natural beryl or oxides of Be, Al, and Si
Vessel:	Stainless steel (200–800 ml)
Seed:	Plate cut parallel to (5510).

Cr^{3+}, Fe^{2+}, Fe^{3+}, Ni^{3+}, and Cu^{2+} have been detected through chemical analysis as color-associated transition elements. Fe^{2+} and Cu^{2+} ions were assigned to the tetrahedral sites, and Ni^{3+}, Cr^{3+}, and Fe^{3+} ions to the octahedral sites [18.162]. Evolution of ions

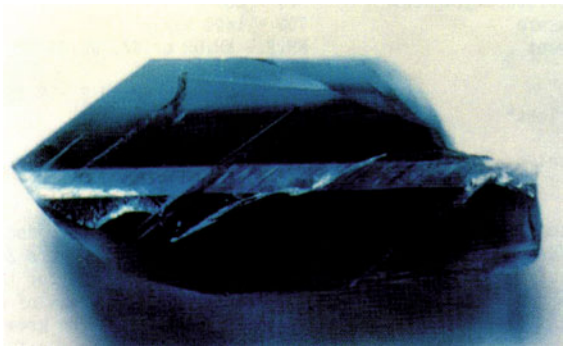


Fig. 18.37 As-grown crystals of regency emerald

from the inner wall of the autoclave is possible. It is, therefore, unknown which ions were added during the process of growth. The length of the crystal is 6.1 cm, width 1 cm, and thickness 0.7 cm. The solubility of emerald has been restudied recently using H_2SO_4 aqueous solution [18.163]. Also there are several works related to defect formation and zoning in emerald crystals obtained under hydrothermal conditions [18.164]. Figure 18.37 shows hydrothermally prepared regency emerald.

Colored Quartz

Throughout history, quartz has been the common chameleon of gemstones, standing in for more expensive gemstones ranging from diamond to jade. However, the incredible variety of quartz is now beginning to be appreciated for its own sake. Purple to violet amethyst and yellow to orange citrine are jewelry staples that continue to increase in popularity.

Ametrine combines the appeal of both amethyst and citrine as well as both the purple and yellow in one bicolored gemstone. Other major colors include the brownish smoky quartz, pink rose quartz, and colorless rock crystal quartz. Different colors and types of chalcedony, including agate, bloodstone, chrysoprase, and black onyx, have grown in popularity with growing appreciation for carved gemstones and art cutting and carving. Unusual quartz specialties such as drossy quartz, with its surface covered by tiny sparkling crystals, and rutilated quartz, which has a landscape of shining gold needles inside, are adding variety and nature's artistry to unusual one-of-a-kind jewelry. The hydrothermal growth of colored quartz is a major activity today owing to its commercial value. No colored synthetic quartz producing company has ever published the exact recipe of the growth of colored quartz.

The synthesis of amethyst was first described by *Tsinobar* and *Chentsova* [18.165]. After the growth of quartz on positive (r) and negative (z) seeds in an iron-containing alkaline solution, an amethystine color is produced by irradiation. The color intensity is high from the (z) to the (r) directions. This is due to the difference of growth rates between the positive and negative rhombohedra. This phenomenon has been exploited by a large group of researchers in growing a wide range of bicolored, color-zoned quartz crystals, which are very attractive as gemstones, for example, ametrine (amethyst-citrine) [18.166]. In alkaline solutions the growth rate of the positive rhombohedron is lower than that of the negative rhombohedron. So, the content of entrapped iron is higher in the positive than in the negative rhombohedron. This color inhomogeneity with the amount of entrapped iron is distinctly discerned at areas where Dauphiné twin quartz exists. A brown or green color is emitted from the basal surface of crystals, which is caused by nontrapping of structural iron in the basal surface and also a cut surface close to the basal surface [18.167]. The credit for hydrothermal growth of gem-quality colored quartz goes to pioneers such as Tsinobar, Nassau, and Balitsky. At present Balitsky is still very active in this area of research.

Purple-colored quartz has been synthesized under the following conditions [18.168]:

Growth temperature:	400–450 °C
ΔT:	25–50 °C
Pressure:	774–1260 atm
Solvent:	10 wt % NaCl; 10 wt % KCl,
Dopant:	Fe in the form of a metal;
	α-Fe_2O_3 in the form of a powder
Vessel:	Platinum-lined (16.5 ml)
Irradiation:	$2-15\times10^6$ R (Röntgen) (^{60}Co)

When the amount of impurities exceeds a certain level the growth is inhibited and pits or crevice flaws are induced in the crystal. Also, the type of dopant and its concentration controls the degree of growth inhibition. Faint-pink-colored quartz can be obtained in the presence of iron and titanium ions. The type and concentration of impurity ions used by the industries producing these colored quartz crystals commercially are not exactly known. However, these synthetic colored quartz crystals are even called poor man's diamond, emerald, ruby, etc., because of their beauty and closeness to those expensive natural gemstones. Readers can find more extensive information on this subject in [18.151, 169].

Zoisite

The commercial name for zoisite is tanzanite, a calcium aluminum silicate hydroxide ($Ca_2Al_3Si_3O_{12}(OH)$) having a very high commercial value that poses a real challenge to crystal growers to grow it as bulk single crystals. There are several groups throughout the world working on this, but the PT conditions involved are extreme. The special chatoyancy phenomena with vitreous luster observed in this crystal has made it a highly valuable gemstone. There are several imitations on the market as well.

Byrappa et al. have reported the synthesis of zoisite using mild hydrothermal conditions with sillimanite (Al_2SiO_5), calcium carbonate ($CaCO_3$), and quartz (SiO_2) in the ratio 3 : 4 : 3 [18.170]. Sillimanite gel was prepared using commercially available corundum (Al_2O_3) and quartz (SiO_2) gels. The advantages of gels as starting material is that numerous and complex phases can be intimately mixed. The experiments were carried out in general-purpose autoclaves using Teflon liners in the temperature range 10–250 °C with pressure of 60–80 bar in a desired solvent. The experimental temperature was raised slowly at the rate of 20 °C/h. Several mineralizers such as HCl, CH_3COOH, C_2H_5OH, glycol, methanol, NaOH, etc. have been tried, but only HCOOH and *n*-butanol were found to be the most suitable mineralizers to synthesize zoisite crystal. The probable reaction for zoisite synthesis when HCOOH is used as a mineralizer is as follows:

$$3Al_2SiO_5 + 4CaCO_3 + 3SiO_2 + HCOOH \rightarrow 2Ca_2Al_3Si_3O_{12}(OH) + 5CO_2 \,.$$

The usual pH conditions to obtain zoisite is between 1.6 and 1.8. The crystals were obtained through spontaneous nucleation in the size range 0.5–2 mm.

18.4.5 Rare-Earth Vanadates

R:MVO_4 (where R = Nd, Er, Eu; M = Y, Gd) form an important group of highly efficient laser-diode pumped microlasers, efficient phosphors, polarizer materials, and low-threshold laser hosts [18.171–174]. These crystals offer many advantages over the conventional Nd:YAG crystal, with larger absorption coefficient and gain cross section. Rare-earth vanadates are known as high-melting materials (> 1800 °C) with low solubility, and obviously their synthesis by any technique usually requires higher-temperature conditions. In spite of its excellent physical properties, high-tech applications have not been realized due to crystal growth difficulties. One of the major problems encountered in the growth of RVO_4 crystals is the presence of oxygen imperfections (color centers and inclusions), which are introduced during the crystal growth processes. Although YVO_4 melts congruently [18.175], vanadium oxides vaporize incongruently, causing changes in Y/V ratio and oxygen stoichiometry in the melt. These undesired effects could generate additional phases and oxygen defects in the YVO_4 crystals grown, especially from the melt [18.176]. Efforts to eliminate these defects did not yield significant success with the flux and melt techniques. The instability of pentavalent vanadium at higher temperatures and the loss of oxygen through surface encrustation by the reaction of the melt with the crucible material further complicate the growth processes. In order to overcome most of the difficulties encountered in the melt and high-temperature solution techniques, the hydrothermal technique has been proposed as a solution [18.177–181]. Since the experiments are carried out in a closed system, the loss of oxygen can be readily prevented. The experiments are usually carried out in the temperature range of 240–400 °C at pressure of 40 bar to 1 kbar. The starting materials (oxides of rare earths and V_2O_5 with a desired solvent in a particular concentration) are held in Teflon or platinum liners depending upon the PT conditions of the experiments, and the Morey or Tuttle type of autoclaves are used. The solubility of rare-earth vanadates is shown in Fig. 18.38 and is found to be negative. It increases with the concentration of the solvent. Both acid and basic mineralizers are used in the growth of these vanadates. However, acid mineralizers are more effective, especially the mixed acid mineralizers ($HCl + HNO_3$ in a particular molar ratio).

The morphology of these crystals can be tuned to a desired shape using appropriate starting materials and

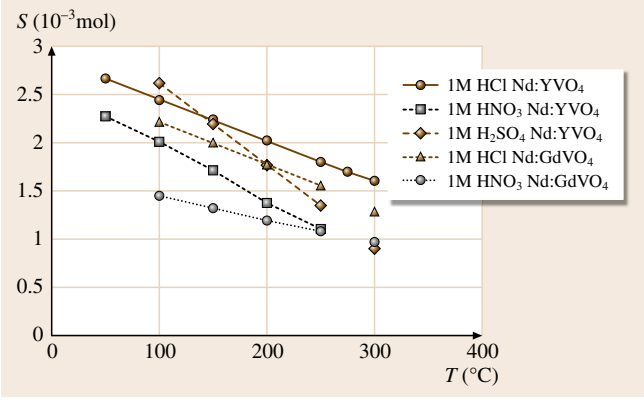


Fig. 18.38 Solubility of Nd:MVO_4 in different solvents

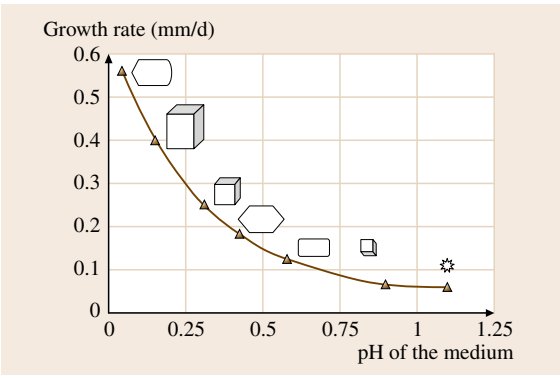


Fig. 18.39 Morphology variation with pH for Nd:YVO_4 crystals obtained from presintered nutrient in 1.5 M HCl + 3 M HNO_3 mineralizer (courtesy of K. Byrappa)

experimental conditions. Figure 18.39 shows the morphology of rare-earth vanadates and growth rate with pH of the medium. Both the chemical-reagent-grade nutrient and the presintered Nd:YVO_4 nutrient are used in the growth of rare-earth vanadates. In fact, the presintered nutrient gives better results. The most interesting part of this work is the need of an oxidizing agent such as hydrogen peroxide in the system, otherwise the crystals appear dark and opaque (Fig. 18.40). Often the crystals show twinning, depending upon the growth conditions. Some attempts at in situ morphology control of these vanadates have been made. The readers can refer to the works of the present author [18.174, 177, 178].

On the whole there is a slow decline in activity on bulk growth of other materials such as potassium titanyl phosphate, potassium titanyl arsenate, mixed-framework rare-earth silicates, germinates, rare-earth tungstates, borates, phosphates, oxides of various metal like tellurium, zirconium, hafnium, and a variety of sulfides of lead, copper, mercury, silver, cadmium, etc. The growth of these crystals was extremely popular from the 1960s to the 1980s. Readers can obtain more information on the growth of these crystals in earlier publications [18.1, 2, 4, 7]. The trend in hydrothermal research shifted towards the growth of fine crystals of various compounds, especially a large family of piezoelectric ceramic crystals such as lead zirconium titanates (PZT), ferrites, hydroxyapatites, etc., during the 1990s and towards the turn of the 20th century focus shifted to the growth of nanocrystals. Hence, the growth of selected fine and nanocrystals is now discussed. Accordingly the chapter refers to polyscale crystals, because it covers bulk crystals to nanocrystals. It should be noted that bulk growth of other important current technological materials such as ZnO, GaN, etc. has been discussed separately by Callaghan et al. in Chap. 19 of this handbook.

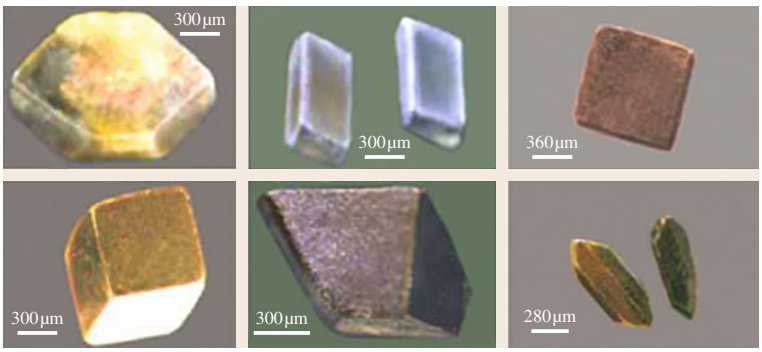


Fig. 18.40 Characteristic photographs of Nd:YVO_4 crystals (courtesy of K. Byrappa)

18.5 Hydrothermal Growth of Fine Crystals

The growth of fine crystals under hydrothermal conditions has been known since hydrothermal technology was born. The majority of early hydrothermal experiments carried out during the 1840s to early 1900s mainly dealt with fine to nanocrystalline products, which were discarded as failures due to the lack of sophisticated tools to examine the fine products except some chemical techniques [18.6]. During this period many experiments were carried out on the synthesis of fine crystals of zeolites, clays, some silicates, hydroxides, etc. [18.22]. When Barrer reported the hydrothermal synthesis of fine particles of zeolites during

the 1940s, it opened a new branch of science, viz. molecular sieve technology. During the late 1960s and 1970s, attempts were made to synthesize fine crystals of metal oxides using the hydrothermal method. This was a very popular field of research at that time [18.4, 182, 183]. Hydrothermal research during the 1990s marked the beginning of work on processing of fine to ultrafine crystals with controlled size and morphology. Today, it has evolved to be one of the most efficient methods of soft chemistry for the preparation of advanced materials such as fine to nanocrystals with controlled size and shape. Currently, the annual market value of electronic ceramics is over US$ 1 billion, and the market for nanocrystals processing (US$ 120 billion in 2002) is increasing at 15% annually, to reach US$ 370 billion by 2010, and will jump to become a trillion-dollar industry by 2015, according to National Science Foundation (NSF) predictions.

Of all the ceramics, the PZT family has been studied most extensively using the hydrothermal technique. Since the early 1980s several thousands of reports have appeared on the preparation of these ceramics. Thermodynamic calculation and kinetics of these systems have been studied extensively (Figs. 18.4 and 18.5) [18.48, 50]. Several new variants/approaches to the processing of these electronic ceramic crystals have been reported to enhance the kinetics, shorten the processing time, control the size and shape, maintain the homogeneity of the phases, and achieve reproducibility. A great variety of precursors and solvents have been attempted in the processing of these fine crystals. Similarly fine film formation of these on an appropriate substrate has been accomplished by several workers [18.184, 185]. Here only some selected crystals such as PZT and HAP will be discussed.

The important step in the synthesis of fine crystals of advanced materials is the use of surfactants and chelates to control the nucleation of a desired phase, such that the desired phase homogeneity, size, shape, and dispersibility can be achieved during the crystallization of these fine crystals. This marked the beginning of the study of precursor preparation for different systems, surface interactions with capping agents or surfactants, and polymerized complexes. The surfaces of the crystals can be altered to become hydrophobic or hydrophilic, depending upon the applications [18.186, 187]. Today this approach is playing a key role in preparing highly dispersed, oriented, and self-assembled fine to nanocrystals. Figure 18.41 shows the new chemical approach for preparation of precursors. Using such an approach a wide range of advanced materials such as the PZT family of ceramics, ferrites, phosphates, sulfides, oxides, hydroxyapatites, etc., as well as composites have been prepared as fine crystals for technological ap-

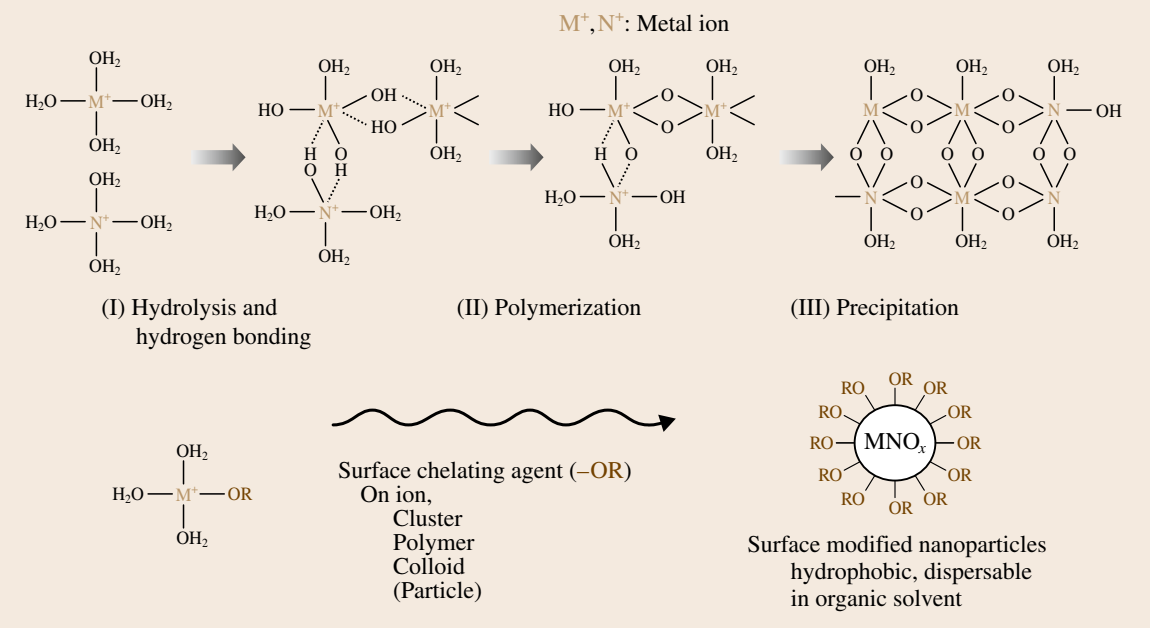


Fig. 18.41 A new preparative chemical approach for precursor preparation (courtesy of Prof. M. Yoshimura)

plications with preferred morphology such as whiskers, rods, needles, plates, spheres, etc., depending upon their application. This precursor-based chemical approach to hydrothermal synthesis has made tremendous progress in recent years and has also drastically reduced the temperature and pressure conditions required for crystal growth.

Riman and group have done extensive work on intelligent engineering of fine crystals of the PZT family and HA based on the thermodynamic modeling approach, and also calculated their crystallization kinetics in detail. Such studies not only helped in the hydrothermal synthesis of these fine crystals, but also in controlling their precise shape and size as per application requirements. Figures 18.42 and 18.43 show designer fine crystals of PZT, $LiMn_2O_4$, HA, etc., prepared under hydrothermal conditions.

The majority of the PZT systems incorporate intolerable amounts of alkaline metals, which are introduced in the form of mineralizers. In recent years organic mineralizers have become popular with a large number of workers. For example, *Riman* and group have found that tetramethylammonium hydroxide $[N(CH_3)_4OH]$ is a favorable substitute for alkaline metal hydroxide mineralizer in producing phase-pure PZT [18.89]. Phase-pure $MeTiO_3$ (Me = Ca, Sr, Ba) can be obtained at input molalities of Ba, Sr, and Ca greater than 7×10^{-5}, 10^{-6}, and 5×10^{-5} M respectively. Otherwise, the relative location of the 99.995% yield regions for the three titanates will be similar to the pattern noted in the stability diagrams. In concentrated solutions, the consumption of OH^- ions is caused by the predominant

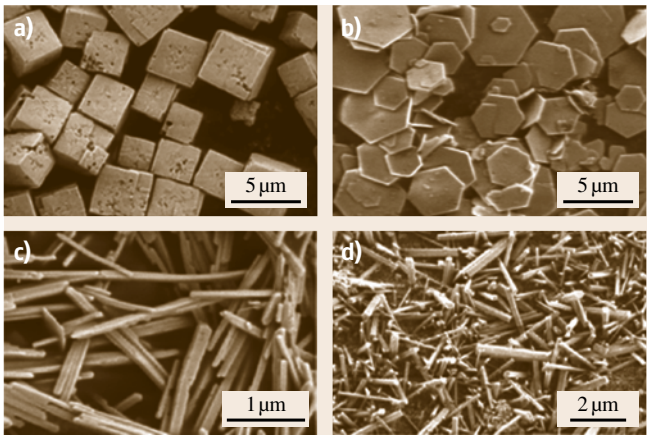


Fig. 18.42a–d Hydrothermally synthesized fine crystals: **(a)** PZT; **(b)** $LiMn_2O_4$; **(c)** $PbTiO_3$; **(d)** $BaTiO_3$ (courtesy of Prof. Richard E. Riman)



Fig. 18.43 SEM photograph of HAp crystals (courtesy of Dr. W. Suchanek)

reaction

$$Me^{2+} + TiO_2 + 2OH^- \rightarrow MeTiO_3 + H_2O\,.$$

Such an approach to understand the crystallization mechanism of the PZT family of crystals has been made by several workers and there are many commercial producers of these ceramic crystals, especially in the USA, Japan, and Europe.

Gersten has extensively reviewed the processing parameters for the synthesis of fine ferroelectric perovskite crystals by the hydrothermal method [18.49]. Accordingly, the first step in the growth of these fine particles is thermodynamic verification of the correct processing conditions for the reaction of the desired product. The chemical purity of the precursors should be high, and the pH adjusters or other additives should be decomposable at the calcination temperature. The supersaturation is influenced by the initial reagent concentration, pH, experimental temperature, stirring rate, type of mineralizer, and time. An increase in the supersaturation will result in a decrease in crystal size.

In recent years interest in fine HA crystals with desired size and shape has resulted in a rapid increase in the number of publications on HAp. Starting chemicals such as H_3PO_4, $Ca(OH)_2$, and lactic acid or other solvents are taken in a Teflon beaker, inserted into an autoclave, and hydrothermally treated in the temperature range 150–200 °C for a few hours under autogenous pressure. The molar ratios of solvent/Ca and Ca/P are adjusted appropriately to get the desired phase of calcium phosphate. The morphology of the resultant HA can be controlled through the initial precursors and their ratios, besides the experimental temperature and duration. Even stirring influences the morphology of the crystals. For example, the diameter of the grains increases with increasing Ca/P molar ratio in the starting solution and is generally larger for high lactic acid/Ca molar ratios. The aspect ratio of HAp crystals is in the

range of 5–20. It decreases with increasing Ca/P ratio and is lower in the case of high lactic acid/Ca ratios. When the lactic acid/Ca and Ca/P starting ratios are low, crystals have the shape of whiskers, whereas in other cases large, elongated grains form [18.188].

There is a steady flow of publications relating to the growth of fine crystals of oxides, silicates, vanadates, phosphates, tungstates, titanates, etc., for various applications. The interesting aspect of their growth is the adaptability of the hydrothermal technique for all these compounds, which can be synthesized through spontaneous nucleation without many complications as in the case of bulk crystal growth. The reaction mixtures can be stirred at different rates and the crystals can also be produced continuously with the use of a flow reactor. There are many publications related to the use of flow reactors for continuous production of such fine crystals [18.97, 98].

18.6 Hydrothermal Growth of Nanocrystals

The hydrothermal technique is becoming one of the most important tools to synthesize nanocrystals for a wide variety of technological applications such as electronics, optoelectronics, catalysis, ceramics, magnetic data storage, biomedicine, biophotonics, etc. On the whole 21st century hydrothermal technology is more inclined towards nanotechnology owing to its advantages in obtaining high-quality, monodispersed, homogeneous nanocrystals with controlled size and shape, as well as the lower-PT conditions of the synthesis, simple apparatus, shorter duration, and lower cost of production. The most important advantage is that nanocrystals with desired physicochemical characteristics can be prepared, and desired surface charge can be introduced onto the nanocrystals in situ with the help of surface modifiers, capping agents, etc.

Hundreds of types of nanocrystals have been synthesized using hydrothermal technique, with over 10 000 publications in the last 8 years. The number of publications is increasing year by year and covers all groups of advanced materials such as metals, metal oxides, semiconductors including II–VI and III–V compounds, silicates, sulfides, hydroxides, tungstates, titanates, carbon, zeolites, etc. It is not possible to discuss the synthesis of all these nanocrystals using hydrothermal technology. Instead, the synthesis of some representative and technologically important nanocrystals will be discussed.

In recent years noble-metal particles (such as Au, Ag, Pt, etc.), magnetic metals (such as Co, Ni, and Fe), metal alloys (such as FePt, CoPt), multilayers (such as Cu/Co, Co/Pt), etc. have attracted the attention of researchers owing to their new interesting fundamental properties and potential applications as advanced materials with electronic, magnetic, optical, thermal, and catalytic properties [18.189–192]. The intrinsic properties of noble-metal nanoparticles strongly depend upon their morphology and structure. The synthesis and study of these metals have implications for the fundamental study of the crystal growth process and shape control. The majority of the nanostructures of these metal alloys and multilayers form under conditions far from equilibrium [18.193]. Among these metals, alloys, and multilayers, shape anisotropy exhibits interesting properties. Both the hydrothermal and hydrothermal supercritical water techniques have been extensively used in the preparation of these nanoparticles.

The synthesis of metal oxide nanocrystals under hydrothermal conditions is important because of its advantages in the preparation of highly monodispersed nanocrystals with control over size and morphology. There are thousands of reports in the literature, which also include a vast number of publications on supercritical water (SCW) technology for the preparation of metal oxides. The most popular among these metal oxides are TiO_2, ZnO, CeO_2, ZrO_2, CuO, Al_2O_3, Dy_2O_3, In_2O_3, Co_3O_4, NiO, etc. Metal oxide nanocrystals are of practical interest in a variety of applications, including high-density information storage, magnetic resonance imaging, targeted drug delivery, bio-imaging, cancer therapy, hyperthermia, neutron capture therapy, photocatalytic, luminescent, electronic, catalytic, optical, etc. The majority of these applications require nanocrystals of predetermined size and narrow size distribution with high dispersibility. Hence, a great variety of modifications are used in the hydrothermal technique.

Al'myasheva et al. and *Jiao* et al. have reviewed the hydrothermal synthesis of corundum nanocrystals under hydrothermal conditions [18.194, 195]. A high specific surface area corundum has been synthesized through the conversion of diaspore to corundum under hydrothermal conditions. This nanosized alumina has great application potential. The authors were able

to develop a new transitional alumina reaction sequence that gave rise to an intermediate alpha structure, α'-Al_2O_3, with a very high surface area. Also they have investigated the thermodynamic basis and equilibrium relationships for the nanocrystalline phases. *Qian* and his group has studied extensively low temperature hydrothermal synthesis of a large variety of metal oxides under hydrothermal and solvothermal conditions [18.196]. Among the nanocrystals of the metal oxides, TiO_2 and ZnO occupy a unique place. Since the preparation of ZnO has been discussed in Chap. 19, only the synthesis of TiO_2 nanocrystals is discussed here. The synthesis of TiO_2 is usually carried out in small autoclaves of Morey type, provided with Teflon liners. The conditions selected for the synthesis of TiO_2 particles are: $T \leq 200\,^{\circ}\mathrm{C}$, $p < 100$ bar. Such pressure/temperature conditions facilitate the use of autoclaves of simple design provided with Teflon liners. The use of Teflon liners helps to obtain pure and homogeneous TiO_2 particles. Though the experimental temperature is low ($\approx 150\,^{\circ}\mathrm{C}$), TiO_2 particles with a high degree of crystallinity and desired size and shape could be achieved through a systematic understanding of the hydrothermal chemistry of the media [18.197]. A variety of surfactants are used to produce nanocrystals of the desired shape and size. Figure 18.44 shows TiO_2 nanocrystals obtained under supercritical hydrothermal conditions (400 °C and pressure 30 MPa) in the presence of hexaldehyde.

Adschiri and co-workers [18.198, 199] have worked out in detail a continuous synthesis of fine metal oxide particles using supercritical water as the reaction medium. They have shown that fine metal oxide particles are formed when a variety of metal nitrates are contacted with supercritical water in a flow system. They postulated that the fine particles were produced because supercritical water causes the metal hydroxides to rapidly dehydrate before significant growth takes place. The two overall reactions that lead from metal salts to metal oxides are hydrolysis and dehydration

$$\mathrm{M(NO_3)_2} + x\mathrm{H_2O} \rightarrow \mathrm{M(OH)}_x + x\mathrm{HNO_3}\,,$$
$$\mathrm{M(OH)}_x \rightarrow \mathrm{MO}_{x/2} + \tfrac{1}{2}x\mathrm{H_2O}\,.$$

Processing in SCW increases the rate of dehydration such that this step occurs while the particle size is small and the reaction rate is less affected by diffusion through the particle. Furthermore, the gas-like viscosity and diffusivity of water in the critical region lead to a negligible mass-transfer limitation. The net effect is that the overall synthesis rate is very large. The high temperature also contributes to the high reaction rate. Several metal oxides, including α-Fe_2O_3, Fe_3O_4, Co_3O_4, NiO, ZrO_2, CeO_2, $LiCoO_2$, α-$NiFe_2O_4$, $Ce_{1-x}Zr_xO_2$, etc., have been prepared by this technique.

Hydrothermal synthesis of sulfides of various divalent, trivalent, and pentavalent metals constitutes an important group of materials for a variety of technological applications. They popularly form II–VI, III–VI, and V–VI group semiconductors, which are being studied extensively with respect to their different morphologies and particle size, which in turn greatly influence their properties. There are several hundred reports on these sulfides, such as CdS, PbS, ZnS, CuS, NiS, NiS_2, NiS_7, Bi_2S_3, $AgIn_5S_8$, MoS, FeS_2, InS, and Ag_2S, prepared through hydrothermal or solvothermal routes with or without capping agents/surfactants/additives to alter their morphologies and sizes as desired.

Among II–VI group semiconductor nanocrystals, AX (A = Cd, Pb, Zn, X = S, Se, Te), CdS is an important one. These AX nanocrystals have important applications in solar cells, light-emitting diodes, nonlinear optical materials, optoelectronic and electronic devices, biological labeling, thermoelectric coolers, thermoelectronic and optical recording materials, etc. Furthermore, these compounds can exhibit varying structures such as zincblende, wurtzite, halite, etc. Several papers have been published recently reporting the synthesis of chalcogenides by the hydrothermal method [18.200–203]. On the whole, for crystallization of sulfides, nonaqueous solvents are found to be more favorable, also in terms of decreasing the PT conditions

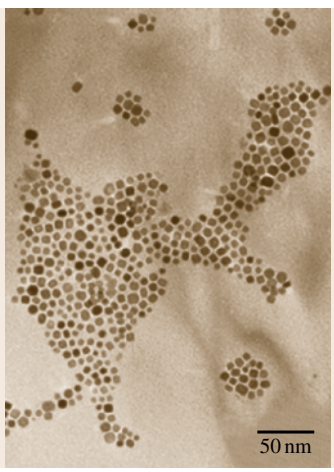


Fig. 18.44 TiO_2 nanocrystals prepared at 400 °C and 30 MPa pressure using hexaldehyde as the surface modifier (courtesy of Prof. T. Adschiri)

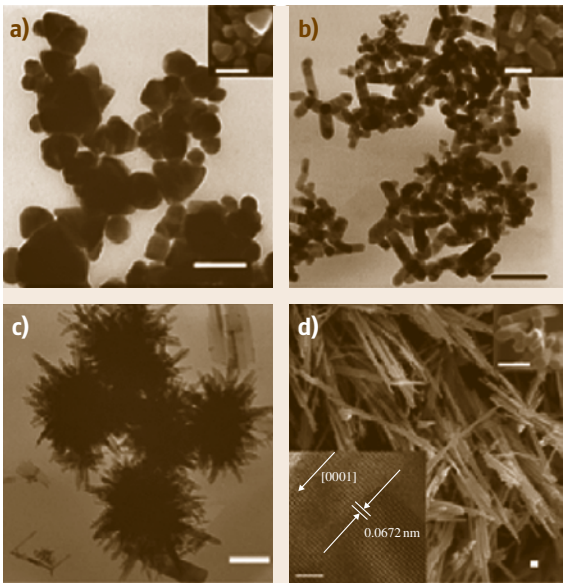


Fig. 18.45a–d TEM and SEM images of CdS products obtained at 180 °C for 5 h in mixed solvents with different volume ratios: **(a)** 5% ethylene, TEM image with SEM image as *inset*; **(b)** 15%, TEM image with SEM image as *inset*; **(c)** 65%, TEM image; **(d)** 100%, SEM image with the *upper right inset* showing a magnified picture of the hexagonal ends of the long rods, and the *lower left inset* showing the high-resolution TEM (HRTEM) image of a nanorod. The *scale bars* in the TEM and SEM images all represent 100 nm. The *scale bar* in the HRTEM image is 5 nm (courtesy of Prof. Yan Li)

required for crystallization. *Qian*'s group has reported the hydrothermal synthesis (using nonaqueous solvents) of nanocrystalline CdS in some coordinating solvents such as ethylenediamine and pyridine [18.204–206]. *Li* et al. have used thioacetamide as the sulfide source, as it easily releases sulfide ions, a process which is beneficial for lowering the reaction temperature and shortening the reaction period [18.207]. The hydrothermal route is more popular than all the other methods reported in the literature because of the lower temperature, shorter duration, and control over the size and morphology. The experiments are usually carried out in the temperature range 150–200 °C. Figure 18.45 shows transmission electron microscopy (TEM) and scanning electron microscopy (SEM) images of CdS nanocrystals.

The synthesis of various carbon polymorphs such as graphite, diamond or diamond-like carbon, fullerenes, etc., has attracted considerable interest for a long time because of their importance in science and technology. There are uncertainties about the phase stabilities of these polymorphs, as some of them do not find a place in the carbon pressure–temperature (PT) diagram and are also known for their contrasting physical properties. The exact physicochemical phenomena responsible for their formation are yet to be understood. Attempts to synthesize these forms under various conditions and with various techniques, sometimes even violating thermodynamic principles, have met with a fair amount of success. The stabilities of graphite and diamond in nature were mainly controlled by p–T–f_{O_2} in the C–O–H system [18.208–211]. The role of C–O–H fluids [18.212, 213], as well as the hydrothermal and organic origin of these polymorphs, especially with reference to diamond genesis, prompted material scientists to explore the possibility of synthesizing them at fairly low-pressure/temperature conditions. The hydrothermal technique is highly promising for reactions involving volatiles, as they attain the supercritical fluid state, and supercritical fluids are known for their greater ability to dissolve nonvolatile solids [18.214]. Silicon carbide powder has been used for the synthesis of carbon polymorphs [18.215, 216], and *Gogotsi* et al. [18.217] have reported decomposition of silicon carbide in supercritical water and discussed the formation of various carbon polymorphs. *Basavalingu* et al. have explored the possibilities of producing carbon polymorphs under hydrothermal conditions through decomposition of silicon carbide in the presence of organic compounds instead of pure water [18.218]. The organic compounds decompose into various C–O–H fluids; the main components are CO, OH, CO_2, and C_1H_x radicals. It is very well known that these fluids play a significant role in creating a highly reducing environment in the system and also assist in the dissociation of silicon carbide and precipitation of the carbon phase. The study of solid and gaseous inclusions in diamond also indicated the C–O–H fluids as the source for nucleation and growth of diamonds in nature [18.211].

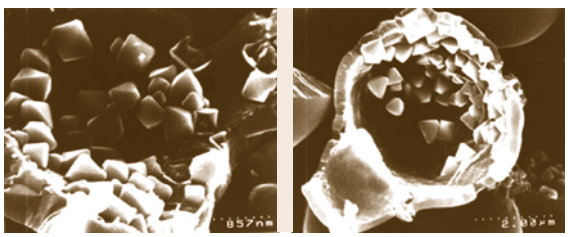


Fig. 18.46 SEM images of diamond nanocrystals with well-developed octahedral facets adhered to the inner walls of the broken spherical particles (courtesy of K. Byrappa)

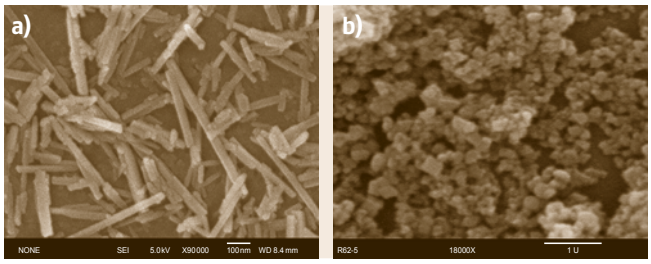


Fig. 18.47a,b SEM images of $LaPO_4$ and Nd:$LaPO_4$. **(a)** $LaPO_4$ synthesized at 120 °C for about 16 h; **(b)** $LaPO_4$ synthesized at 120 °C for 30 h

The experiments were carried out in the pressure temperature range of 200–300 MPa and 600–800 °C using externally heated Roy–Tuttle test-tube-type autoclaves. Figure 18.46 shows SEM images of diamond nanocrystals with well-developed octahedral facets adhered to the inner walls of the broken spherical particles.

Very recently, great efforts have been made to develop new phosphor systems for white-LED, FED, and programmed data processor (PDP) applications based on rare-earth phosphate systems. Several authors have reported the synthesis of rare-earth phosphate compounds via different methods. However, the hydrothermal method has distinct advantages over the other methods for the preparation of these rare-earth orthophosphates as good-quality nanocrystals. The present author's laboratory has prepared $LaPO_4$ and Nd^{3+}-doped $LaPO_4$ under hydrothermal conditions. The effect of experimental temperature, solvents, the ratio of the starting materials, stirring, and experimental duration has been studied in great detail with respect to crystal size, morphology, and the crystallinity of the resultant products in order to find the optimum experimental conditions for preparation of biophotonic materials. The experiments were carried out using Teflon-lined Morey autoclaves, Tuttle–Roy autoclaves, and stirred autoclaves. In a typical preparation, La_2O_3 and H_3PO_4 were taken in 1 : 1.2 molar ratio in a beaker containing water (14 ml) to prepare $LaPO_4$, and Nd_2O_3 (1–6 mol %) was added for the preparation of Nd^{3+}:$LaPO_4$. The pH of the solution was adjusted to 1.4–2 using ethanol. Usually the experimental duration was from 12 to 16 h. Figure 18.47 shows nanocrystals of rare-earth orthophosphates prepared under hydrothermal conditions.

There are hundreds of reports on the hydrothermal preparation of nanocrystals for various applications: to mention a few, the preparation of $AlPO_4$, ferrites, phosphors such as Eu:$Y_2Sn_2O_7$, Nd:$YAlO_3$, GaN, GaP, Ga_3P, vanadates, fluorides, carbonates, garnets, C_3N_4, hydroxides, etc. using both hydrothermal and solvothermal routes [18.219–225]. On the whole, solvothermal routes or the use of nonaqueous solutions is becoming more popular even for ultra-high-melting compounds such as GaN and diamond. Furthermore, the solvothermal route can minimize the entry of undesired carbonate or hydroxyl molecules into the final compounds. Similarly, the stoichiometry of the starting materials, and in some cases the change in valency of the metals, can be well controlled when using both the hydrothermal and solvothermal routes. However, the experimenter has to bear in mind that, though nonaqueous solvents show very high reactivity, one has to understand the exothermic and endothermic reactions taking place inside the autoclave, the pressure surge, and the release or formation of highly dangerous components with high volatility. If these things are checked in advance then the method can be well suited to advanced nanomaterial synthesis.

18.7 Concluding Remarks

The hydrothermal technique has evolved into one of the most efficient methods to grow crystals of different size with desired properties. The importance of the hydrothermal technique for the preparation of highly strategic materials such as GaN and ZnO has been realized in recent years. Numerical modeling has contributed greatly to understand the hydrodynamic conditions, which in turn assists in improving the quality of the crystals without any macro- or microdefects even for an industrial-scale autoclave. The recent progress in the thermodynamic modeling and also the solution chemistry of the hydrothermal media has greatly contributed to the drastic reduction in the PT conditions of the growth of crystals, even with ultralow solubility and high melting temperature. The generation of yield diagrams or stability field diagrams helps in the intelligent engineering of the crystal growth process, so that the yield is almost 100%, i. e., all the solute is converted into the product without any loss of the nutrient. The study of solubility in the success-

ful growth of crystals under hydrothermal conditions is essential, as is the kinetics of crystallization, which helps greatly in enhancing the growth rate. The application of additional energy such as microwave, sonar, mechanochemical, electrochemistry, biomolecules, etc. takes us into a different field of chemistry at the speed of light, because of the increased growth kinetics. The stirring of the precursor during the crystal growth under hydrothermal conditions also contributes to the size and shape of the crystals, especially in the case of fine crystal growth. In recent years, organic molecules, capping agents, and surfactants have been extensively used to introduce a desired surface charge to the crystal surface, and also the properties of the crystal surface can be altered to either hydrophobic or hydrophilic. Similarly the crystal size and shape can be altered with the help of such organic agents. This area of in situ crystal growth process is fast growing and making the hydrothermal technique into one of the most efficient methods in crystal growth. However, our knowledge today on the growth of crystals such as diamond, gallium nitride, gallium berlinite, etc., is comparable to that of quartz some 60 years ago. Therefore, a collective multidisciplinary approach is essential to understand the hydrothermal technique in order to grow crystals of desired shape, size, and properties. Knowledge on the hydrothermal phase equilibrium is also essential and has to be supported by thermodynamic modeling and computation techniques. Although much of the recent work on the hydrothermal growth of bulk crystals such as quartz, gemstones, gallium nitride, etc., is treated as classified, there is still enormous scope for the application of this technique to grow crystals of technological significance. The number of publications on this important tool of materials processing is also increasing year by year.

18.A Appendix

Table 18.10 List of the polycrystals prepared under hydrothermal conditions. Auts. = autogenous pressure

Compound	Mineralizer(s)	Temperature (°C)	Pressure (kbar)	References
Native elements				
Au, Ag, Pt, Co, Ni, Te, As, Bi, C	NaOH, KOH, HCl, HI, HBR	400–600	> 0.60	[18.189–192] [18.218, 226]
Se	NaOH, KOH	–	–	[18.227]
Cd	NaOH, KOH	–	–	[18.228]
Pb, Cu	NaOH, KOH	450–550	> 0.05	[18.229]
Oxides				
CuO, Cu_2O	NaOH, KOH	350–450	0.65–0.8	[18.230]
BeO	NaOH, KOH	450–550	0.8	[18.231]
ZnO	NaOH, KOH, NH_4Cl	350–600	0.78–1.0	[18.232]
CdO	NaOH, Na_2CO_3, $(NH_4)_2SO_4$	250–500	0.3–2.0	[18.233]
NiO	NH_4Cl	300	0.3	[18.234]
HgO	NaOH	200–300	0.1	[18.235]
PbO	LiOH	450	0.6	[18.236]
Al_2O_3, emerald	NaOH, KOH, Na_2CO_3, K_2CO_3	300–620	0.5–0.7	[18.27, 194, 195]
RE_2O_3	H_2O	> 500	0.2–0.9	[18.237]
In_2O_3	NaOH, NH_4Cl	350–600	0.4–3.0	[18.238]
V_2O_3	NaOH	550–700	1.3	[18.239]
Sb_2O_3	KF, Na_2CO_3	460–600	1.0–1.5	[18.240]
Bi_2O_3	NaOH, KOH	360–600	0.4–1.2	[18.241]
Au_2O_3	Na_2CO_3	300	3.0	[18.242]

Table 18.10 (continued)

Compound	Mineralizer(s)	Temperature (°C)	Pressure (kbar)	References
Fe_3O_4	NaOH	350–405	0.75–0.8	[18.243]
MnO_2	NaOH	450	0.75–0.8	[18.244]
TiO_2	KF, NaF, NH_4F, NaOH, KOH	100–700	0.5–3.0	[18.197]
ZrO_2, HfO_2	NaF, KF, NH_4F	520–690	1.0	[18.2, 34]
SnO_2	NaOH, KOH	450–600	0.7	[18.245]
TeO_2	HCl, HF, HI, HBr, HNO_3	250–385	0.05–0.8	[18.246]
PbO_2	NH_4OH	230–290	0.5	[18.247]
CrO_2	$HCLO_4$, HIO_4, NH_4ClO_4	350–400	2.0	[18.248]
SiO_2, quartz	$NaOH + Na_2CO_3$, $NaCl + KCl$	350–370	1.5	[18.35]
Amethyst	NH_4F	210–450	–	[18.167]
GeO_2	NaOH, KOH	350	1.0	[18.249]
$K_2Te_4O_9 \cdot 3H_2O$	$K_3PO_4 + H_2O$	380	–	[18.250]
$Y_3Fe_5O_{12}$	KOH	420	2.0	[18.251]
$Y_3Al_5O_{12}$	K_2CO_3, Na_2CO_3, NaOH	350	2.0	[18.252]
$ABi_{12}O_{20}$ (A = Ti, Si, Ge)	NaOH	500–570	1.5–2.0	[18.253]
$NiFe_2O_3$	NH_4Cl	475	–	[18.109]
Hydroxide				
$M(OH)_2$ (M = Be, Mg, Ca, Cd, Mn, Ni, Co	NaOH, H_2O)	100–550	0.6–4.0	[18.254]
$RE(OH)_3$ (RE = La – Gd, Dy, Er, Yb)	NaOH	350–450	0.6	[18.254]
$M(OH)_3$ (M = Cr, In)	NaOH	300–450	0.4–1.5	[18.254]
$Al(OH)_3$	H_2O	< 150	0.04	[18.255]
MOOH, MOOD, $In(OD)_3$ M = In, Cr, Gd, Sn	H_2O, D_2O	180–600	0.02–1.4	[18.256]
α-ScOOH, β-ScOOH	H_2O	162–350	0.006–0.17	[18.257]
$Sr_3Cr_2(OH)_{12}$	H_2O	150–200	–	[18.258]
Malachite, azurite	–	–	–	[18.259]
Garnets				
$A_3B_2Si_3O_{12}$ (A = Mn, Ca, Fe, Cd; B = Al, Fe, In, V, Cr)	$CaCl_2$, $CdCl_2$, NH_4Cl	400–900	0.4–30.0	[18.260, 261]
Silicates				
Li_2SiO_3	LiOH	450	0.15	[18.262]
$KHSiO_2O_5$	KOH	300	–	[18.263]
Al_2SiO_5	H_2O	900	20.0	[18.264]
$CaBSiO_4(OOH)$	$CaCl_2 + HCl$	300–400	0.3–0.35	[18.264]
Zn_2SiO_4	HCl	400–500	0.4	[18.265]
$Zn_2SiO_4:Mn^{2+}$	Ethanol	220	Auts.	[18.266]
$R_2Si_2O_7$ (R = La – Lu, Sc, Y, Cd)	H_2O	700	2.5	[18.267]
$Na_2Fe_5TiSiO_{20}$	H_2O	500–700	0.5	[18.268]
$Na_2R_6Si_6O_{24}(OH)_2$ (R = La, Y)	H_2O	500–700	2.0	[18.269]

Table 18.10 (continued)

Compound	Mineralizer(s)	Temperature (°C)	Pressure (kbar)	References
$M_4R_6Si_6O_{24}(OH)_2$ (M = Ba, Ca, Sr, Pb, Mn; R = La, Nd, Sm, Gd, Dy, Y)	H_2O	500–700	2.0	[18.269]
$MPbSiO_4$ (M = Mn, Fe, Co, Ni, Zn, Mg, Cd, Be)	H_2O	300–500	2.0	[18.270]
$MBe_2Si_2O_7$ (M = Ba, Sr, Pb)	H_2O	450–750	1.5–3.0	[18.271]
$Na_2Be_2Si_6O_{14}$	NaOH	400–600	1.5–3.0	[18.272]
$Na_2BeSi_2O_6$	NaOH, H_2O	400–600	–	[18.272]
$Ca_2MgSi_2O_7$	H_2O	798	4.06	[18.273]
$Na_2TiZnSiO_7$	NaOH	350–550	> 3.0	[18.274]
$Ba_2TiSi_2O_8$	$Ba(OH)_2$	200–500	> 2.0	[18.275]
$Li_4Sn_2Si_{12}O_{30}$	LaOH	500–600	> 2.0	[18.276]
$K_2SnSi_3O_9$	KOH	400–650	> 1.5	[18.277]
$RbFeSi_3O_8$	RbOH	480	1.6	[18.278]
$K_2CeSi_6O_{15}$	KOH	450	2.0	[18.279]
$K_3NdSi_6O_{15}$	$KOH + K_2CO_3$	400–600	2.0	[18.280]
$K(Mn,Fe)_2(Zn,Mn)_3Si_{12}O_{30}$	KOH + KCl	580–600	0.8	[18.281]
$K_2Mn_2Zn_2Si_4O_{15}$	$KOH + KCl + MnCl_2$	580–600	0.8	[18.282]
$FeMgAl_4Si_2O_{10}(OH)_4$	H_2O	650	9.2	[18.283]
$Na_2MnZn(SiO_3OH)_2(OH)_2$	NaOH	450	> 0.5	[18.284]
$Na_4Fe_{10}Ti_2Si_{12}O_{40}$	H_2O	700	1.0	[18.285]
$Na_3CaMg_2Si_8O_{22}(OH)_2$	Na_2CO_3	400–970	0.1–0.8	[18.286]
$LiAlSi_2O_6 \cdot H_2O$	H_2O	300–350	2.0	[18.287]
$Na_8SnSi_6O_{18}$	NaOH	600	1.0	[18.288]
$K_2ZrSi_2O_7$	KOH	310	0.5–1.0	[18.289]
RERE′SiO_5 (RE = La, Ce, Pr, Sm)	NaOH + HCl	135–700	1.0	[18.290]
$K_2ZrSi_3O_8$	KOH	350–450	0.5	[18.291]
$(Na_2Ca)ZrSi_3O_9 \cdot H_2O$	Na_2CO_3	350–530	–	[18.292]
$PbCa_2Si_3O_9$	H_2O	350	2.0	[18.293]
$KLi_2AlSi_4O_{10}F_2$	H_2O	400–670	2.0–5.0	[18.294]
$K_3Li_3Al_3Si_6O_{20}(F,OH)_4$	H_2O	400–670	2.0–5.0	[18.295]
Sodalite				
Mica	KOH, K_2CO_3, $KHCO_3$	–	–	
$Na_8Al_6Si_6O_{24}(OH)_2 \cdot nH_2O$	NaOH	200–450	0.5	[18.296]
Na_2MgSiO_4	NaOH	700	3.0	[18.297]
$Na_4Zr_2Si_3O_{12}$	NaOH	600	3.0	[18.298]
$NaAlSiO_4$, $Na_2Zn_2Si_2O_7$, $Na_2ZnSi_3O_8$, Na_2ZnSiO_4, $Na_2Mn_2Si_2O_7$	NaOH, $NaOH + Na_2CO_3$	375–450	1.0–2.0	[18.299]
Germanates				
$MGeO_4$ (M = Zr, Hf, U)	H_2O	150–300	1.0	[18.300]
Al_2GeO_5	H_2O	400–700	0.5	[18.301]
Pb_3GeO_5	KOH	450–500	0.6–1.2	[18.302]
$Sb_2Ge_2O_7$	KF	400–550	0.6–1.2	[18.303]
$Sb_4Ge_3O_{12}$	K_2CO_3	450–550	0.6–1.2	[18.304]

Table 18.10 (continued)

Compound	Mineralizer(s)	Temperature (°C)	Pressure (kbar)	References
$Bi_4Ge_3O_{12}$	NaOH	350–450	0.6–0.8	[18.305]
$CaGeO_3$	H_2O	150–450	0.8–1.8	[18.306]
$SrGeO_3$	NaOH	300–600	> 1.0	[18.307]
$Mg_5GeO_6(OH)_2$	H_2O	470–570	> 0.3	[18.308]
$Y_2GeO_6(OH,F)_4$	KF	450	1.5	[18.309]
$Yb_4Ge_3O_9(OH,F)_4$	KF	450	1.0	[18.310]
$Er_4Ge_3O_9(OH,F)_4$	CsF	450	0.6	[18.311]
$M_6Ge_4O_{10}(OH)_4$ (M = Na, Li, Rb, K, Cs)	H_2O	180–500	0.1	[18.312]
$Na_2LaGe_4(OH)$	NaOH	450	1.0	[18.313]
Na_2TiGeO_5, $Na_2Zn_2TiGeO_7$	NaOH	400–550		[18.314]
$Na_3ZrHGe_2O_8$	NaOH	500	1.2–2.0	[18.315]
Na_2ZrGeO_5, $Na_2ZrGe_2O_7$, $Na_4Zr_2Ge_3O_{12}$, Na_2BeSiO_2	NaOH	450–500	1.0	[18.316]
$KAlGe_2O_6$, $NaFeGe_2O_6$	KOH, NaOH	450	1.0	[18.317]
$NaAlGe_3O_9$	H_2O	800	10.0	[18.318]
$AgAlGe_3O_8$	$H_2O + O_2$	600	1.5	[18.319]
$TiAlGe_3O_8$	H_2O	1000	2.5	[18.319]
$MAlGe_3O_8$ (M = Li, Na, K, Rb, Cs)	H_2O	800–900	13.0–25.0	[18.319]
$Na_6Sn_4Ge_5O_{20}(OH)_2$		450	1.0	[18.320]
$Na_2SnGe_2O_6(OH)_2$		450	0.5	[18.321]
$Na_3REGe_2O_7$ (RE = La, Nd, Eu)		800	1.5	[18.322]
$Y_7Ge_2O_{12}(F,OH)_5$, $Sm_4Ge_3O_9(OH)_6$, $Y_4GeO_6(OH,F)_4$, Nd_4GeO_8, $Yb_2Ge_2O_7$, $RE_3GeO_5(OH)_3$ (RE = Gd, Sm, Dy, Er)	KF, CsOH, RbOH, NaOH	450–500	1.5–2.0	[18.323]
Phosphates				
$AlPO_4$	H_3PO_4, H_2SO_4, HCl, HCOOH	150–300	0.03–0.2	[18.324]
ABO_4 (A = Fe, Bi, Mn, Cr, Al, B; B = P, V, As)	NaOH, H_3PO_4	200–900	0.03–50.0	[18.325,326]
$Ce(HPO_4)_2 \cdot 33H_2O$	H_3PO_4	160	–	[18.327]
$CuTi_2(PO_4)_3$	H_3PO_4	500	3.0	[18.328]
$RbNbOPO_4$	H_3PO_4	600	1.8	[18.329]
$Cu_3(PO_4)_2 \cdot H_2O$	$H_3PO_4 + H_2O$	220	–	[18.330]
$NH_4Zr_2(PO_4)_3$	NH_4Cl	250–300	0.1	[18.331]
$(H_3O)Zr_2(PO_4)_3$	H_2O	200	< 0.1	[18.332]
$KMnO_2 \cdot O(PO_4)(H_3PO_4)$	H_2O	400	3.0	[18.333]
NdP_5O_{14}, TmP_5O_{14}	H_3PO_4, $HCl + H_3PO_4$	240–300	0.05–0.1	[18.334]
$MREP_4O_{12}$ (M = Le, Na, K, Rb, Cs; RE = La–Nd)	H_3PO_4	300–500	0.1–0.5	[18.335]
$(Na_{2/3}Zr_{1/3})_2P_2O_7$	$H_3PO_4 + HCl$	250	< 0.01	[18.336]
$Na_2H_3Al(P_2O_7)_2$	H_3PO_4	200–250	0.01	[18.337]

Table 18.10 (continued)

Compound	Mineralizer(s)	Temperature (°C)	Pressure (kbar)	References
$NaHMP_2O_7$ (M = Ni, Co)	H_3PO_4	200–250	0.01	[18.338]
KH_2MoPO_7	H_3PO_4	180	< 0.01	[18.339]
$NaH_2(MoO)_2(PO_4)_3 \cdot \frac{1}{2}H_2O$	H_3PO_4	600	1.8	[18.340]
KTP	$K_2HPO_4 + KPO_3$	425–600	10 kpsi	[18.53]
Vanadates				
$TMAV_3O_7$, $TMAV_4O_{10}$	TMAOH, LiOH	200	Auts.	[18.174, 341–343]
$TMAV_8O_{10}$		–	–	
$Li_xV_{2-\delta}O_{4-\delta}$		–	–	
R:MVO_4 (R = Nd, Er, Eu; M = Y, Gd)		–	–	
γ-LiV_2O_5		–	–	
Borates				
$Zn_4B_6O_{12}$	NaOH	500	2.4	[18.344]
$Li_2B_4O_7$	HCl	250	0.12	[18.345]
$Li_3B_5O_8(OH)_2$	–	–	–	[18.346]
$REBO_3$ (RE = Sm, Er, Gd, Eu, Tm, Yb)	1.4 Butanediol	315	Auts.	[18.347]
$LiBO_2$, $LiZnBO_3$	NaOH, KOH	> 300	1.0	[18.344]
$LiH_2B_5O_9$	HCOOH	> 240	0.01	[18.348]
Carbonates				
MCO_3 (M = Ca, Mg, Sr, Ba)	NH_4Cl, LiCl, H_2CO_3, HNO_3	200–450	0.6–0.8	[18.139]
Chalcogenides				
Cu_9S_5, Ag_2S		180–343	0.01–0.15	[18.349]
Cu_2S		312	0.01	[18.350]
α-MnS	Thiourea, benzene	100–200	–	[18.351]
PbS	Toluene	220	Auts.	[18.352]
MoS_2	$C_2H_4NS + NH_3$	160–195	Auts.	[18.353]
Ag_2Se		180–343	0.01–0.5	[18.354]
MSe (M = Zn, Cd, Hg, Co, Pb)		180–500	0.01–1.5	[18.355]
MTe (M = Zn, Cd, Pb, Hg, Co)		180–400	0.05–2.0	[18.356]
MS (M = Cu, Zn, Hg, Pb, Fe, Cd, Mn, Co, Ni)		190–640	0.05–2.0	[18.357]
Bi_2Se, Sb_2Se		180–343	0.01–1.4	[18.355]
Sb_2Si_3, In_2Si_3, Bi_2S_3		180–343	0.01–0.15	[18.358]
$Bi_2Fe_3Sb_2Te_3$		180–343	0.01–0.15	[18.359]
$AgMS_2$ (M = Bi, Ga, In, Sb, Be)		180–343	0.01–0.15	[18.358]
$CuMS_2$ (M = Ga, In, Fe)		–	–	
Cu_8MS_6, M = Ge, Sb		312	0.1	[18.350]
$CuInTe_2$		265–343	0.05–0.15	[18.360]
$Cu_6ZnAs_2S_7$, $Cu_6FeAs_2S_7$		180–343	0.01–0.05	[18.361]
AX (A = Cd, Pb, Zn, In; X = S, Se, Te)	Ethylenediamine	150–200	Auts.	[18.204–206]
Titanates				
$PbTiO_3$, $PbTi_3O_7$, $PbZrO_3$	KF	450–700	0.8–3.0	[18.362]
$MTiO_3$ (M = Ca, Co, Mn, Ba, Sr)	NaOH, KOH, KF	200–700	0.3–2.0	

Table 18.10 (continued)

Compound	Mineralizer(s)	Temperature (°C)	Pressure (kbar)	References
$Na_2Ti_2O_5$, $Na_2Ti_6O_{13}$, $Na_2Ti_3O_7$, $Na_2Ti_3O_7 \cdot H_2O$	NaOH, HCl, HCOOH	200–500	0.08–3.0	[18.363, 364]
Molybdates				
$MMoO_4$ (M = Cd, Sr, Pb, Ba)	NH_4Cl, NaOH, KOH	350–500	–	[18.365]
$KLn(MoO_4)_2$ (Ln = La – Yb)	K_2MoO_4	525–600	–	[18.366]
$K_5Ln(MoO_4)$ (Ln = La – Yb)		–	–	
Ln_2MoO_6 (Ln = Pr – Er)		–	–	
Tunstates				
MWO_4 (M = Ba, Sr, Cd)	NH_4Cl	450	–	[18.365]
$Li_2Fe(WO_4)_2$	$LiCl + Na_2WO_4$	575–600	1.0–1.5	[18.367]
$MLn(WO_4)_2$	LiCl, KCl, NH_4Cl	400–720	1.2–1.7	[18.368, 369]
$LnWO_4 \cdot OH$ (M = Li, Na, K, NH_4; Ln = Ce, Pr, Nd)	$LiCl + NH_4Cl$	–	–	[18.366]
Niobates, tantalates, arsenates, gallates, etc.				
ABO_4 (A = Al, Fe, Ga, B, Bi; B = P, V, As)	NaOH, NaF, KF, HBr, HI	> 500	2.0	[18.370]
$LiNbO_3$	LiOH	650	2.0	[18.371]
$LiGaO_2$	NaOH	360–420	–	[18.372]
$Gd_3Ga_5O_{12}$	NaOH, Na_2CO_3, K_2CO_3	350–605	1.5	[18.252]
Potassium titanyl arsenate (KTA)	KOH	590	1.8	[18.373]
Chlorides, bromides, fluorides				
$Fe_6O_{11}Cl_2$, $TeOCl_2$, CuBr, PbBr,	HCl, HBr, HI	100–200	0.1	[18.370]
$AREF_4$, $AREF_6$, A_2REF_5 (A = Li, Na, K, Rb, Cs; RE = Nd, Sm, Eu, Gd, Tb, Yb, Ho, Y)	KF, H_2O	450–500	Auts.	[18.374]
Nitrides				
AlN, GaN, InN	Toluene, THF, trioctylamine	265–290	Auts.	
	$NH_3 + NH_4Cl$, $NH_3 + NH_4Br$, $NH_3 + NH_4I$, (or admixture of all)	360–550	1.4	[18.375, 376]
Miscellaneous				
α-ZrP	H_3PO_4, H_2O	120–280	Auts.	[18.377]
β-TiP	H_3PO_4	300	Auts.	[18.378]

References

18.1 K. Byrappa, M. Yoshimura: *Handbook of Hydrothermal Technology* (Noyes, New York 2001)

18.2 M. Yoshimura, K. Byrappa: J. Mater. Sci. **43**, 2085–2103 (2007)

18.3 K. Byrappa, S. Ohara, T. Adschiri: Adv. Drug Del. Rev. **60**, 299–327 (2007)

18.4 K. Byrappa (Ed.): Hydrothermal growth of crystals, Prog. Cryst. Growth Charact. Mater. **21**, 1–365 (1990)

18.5 K. Byrappa: Hydrothermal processing of advanced materials. In: *Kirk-Othmer Encyclopedia of Chemical Technology* (Wiley, London 2005)
18.6 K. Byrappa, T. Adschiri: Prog. Cryst. Growth. Charact. Mater. **53**, 117–166 (2007)
18.7 K. Byrappa: Hydrothermal growth of crystals. In: *Handbook of Crystal Growth*, Vol. 2, ed. by D.T.J. Hurle (Elsevier, Amsterdam 1994) p. 465
18.8 K.F.E. Schafthaul: Gelehrte Anz. Bayer. Akad. **20**, 557 (1845)
18.9 R. Bunsen: Bemerkungen zu einigen Einwürfen gegen mehrere Ansichten über die chemisch-geologischen Erscheinungen in Island, Annalen **65**, 70 (1848)
18.10 F. Wöhler: Annalen **65**, 80 (1848), cited by R. Bunsen
18.11 H. De Senarmount: Ann. Chim. Phys. **32**, 142 (1851)
18.12 M. Daurree: Ann. Mines **12**, 289 (1857)
18.13 H.E. Saint-Claire Deville: Ann. Chim. Phys. **61**, 309–314 (1857)
18.14 K. von Chrustschoff: Am. Chem. **3**, 281 (1873)
18.15 J.B. Hannay: Proc. R. Soc. Lond. **30**, 178–189 (1880)
18.16 R. Moissan: *Experimental Petrology, Basic Principles and Techniques* (Clarendon, Oxford 1973) p. 5, cited by A.D. Edgar
18.17 C. Friedel, E. Sarasin: C. R. **92**, 1374–1378 (1881)
18.18 C. Friedel: Bull. Soc. Min. **14**, 7–10 (1891)
18.19 G. Spezia: Atti. Accad. Sci. Torino **35**, 95–107 (1900)
18.20 G. Spezia: Atti. Accad. Sci. Torino **40**, 254–262 (1905)
18.21 G.W. Morey, P. Niggli: J. Am. Chem. Soc. **35**, 1086–1130 (1913)
18.22 G.W. Morey: J. Am. Ceram. Soc. **36**, 279–285 (1953)
18.23 C. Barus: Am. J. Sci. **6**, 270 (1898)
18.24 R. Nacken: Chem. Z. **74**, 745–749 (1950)
18.25 R. Nacken: Captured German Reports RDRC/13/18 (1946)
18.26 R. Nacken: US Office of Technical Services Reports PB-6948 (1946)
18.27 K. Nassau: J. Cryst. Growth **35**, 211–222 (1976)
18.28 A.A. Shternberg: private communication (Moscow 1981, 1982)
18.29 J. Asahara, K. Nagai, S. Harada: Synthetic crystals by large autoclaves – The reality and characterization, Proc. 1st Int. Symp. Hydrotherm. React., ed. by S. Somiya (Gakujutsu Bunken Fukyu-Kai 1982) pp. 430–441
18.30 E.U. Franck: Survey of selected non-thermodynamic properties and chemical phenomena of fluids and fluids mixtures. In: *Chemistry and Geochemistry of Solutions at High Temperatures and Pressure*, Proc. Nobel Symp., Vol. 13/14, ed. by D.T. Rickard, F.E. Wickman (Pergamon, New York 1979) pp. 65–88
18.31 T.M. Seward: Metal complex formation in aqueous solutions at elevated temperatures and pressures. In: *Chemistry and Geochemistry of Solutions at High Temperatures and Pressure*, Proc. Nobel Symp., Vol. 13/14, ed. by D.T. Rickard, F.E. Wickman (Pergamon, New York 1979) pp. 113–132
18.32 H.C. Helgeson: Prediction of the thermodynamic properties of electrolytes at high pressures and temperatures. In: *Chemistry and Geochemistry of Solutions at High Temperatures and Pressure*, Proc. Nobel Symp., Vol. 13/14, ed. by D.T. Rickard, F.E. Wickman (Pergamon, New York 1979), pp.133–178
18.33 K.S. Pitzer: Characteristics of very concentrated aqueous solutions. In: *Chemistry and Geochemistry of Solutions at High Temperatures and Pressure*, Proc. Nobel Symp., Vol. 13/14, ed. by D.T. Rickard, F.E. Wickman (Pergamon, New York 1979) pp. 249–272
18.34 S. Somiya (Ed.): Hydrothermal reactions, Proc. 1st Int. Symp. Hydrotherm. React. (Gakujutsu Bunken Fukyu-Kai, 1982) pp. 430–441
18.35 R.A. Laudise, J.W. Nielsen: Solid State Phys. **12**, 149 (1961)
18.36 V.A. Klipov, N.N. Shmakov: Influence of convective flow on the growth of quartz crystals, Proc. 45th Annu. Symp. Freq. Control, IEEE (New York 1991) p. 29
18.37 A.B. Ezersky, A. Garcimartin, J. Burguete, H.L. Mancini, C. Pérez-García: Phys. Rev. E. **47**, 1126–1131 (1993)
18.38 A.B. Ezersky, A. Garcimartin, H.L. Mancini, C. Pérez-García: Phys. Rev. E. **48**, 4414–4422 (1993)
18.39 B. Roux, O. Louchart, O. Terhmina: J. Phys. (France) **4**(C), 2–3 (1994)
18.40 Q.S. Chen, V. Prasad, A. Chatterjee: Modelling of fluid flow and heat transfer in a hydrothermal crystal growth system, Proc. Am. Soc. Mech. Eng. Heat Transf. Div. (1998) p. 119, HTD 361-4
18.41 Q.S. Chen, V. Prasad, A. Chatterjee, J. Larkin: J. Cryst. Growth **198/199**, 710 (1999)
18.42 E.A. Evans, H. Li, G.-X. Wang: Bulk flow of solution in an autoclave for crystal growth, Proc. CD IMECE 2001 (New York 2001), Paper No. HTD 24342
18.43 H. Li, E.A. Evans, G.-X. Wang: J. Cryst. Growth **256**, 146–155 (2003)
18.44 H. Li, G.-X. Wang, E.A. Evans: J. Cryst. Growth **271**, 257–267 (2004)
18.45 H. Li, E.A. Evans, G.-X. Wang: J. Cryst. Growth **275**, 561–571 (2005)
18.46 R.-U. Barz, M. Grassl: J. Cryst. Growth **249**, 345–353 (2003)
18.47 V.N. Popov, Y.S. Tsivinskaya, T.B. Bekker, K.A. Kokh, A.E. Kokh: J. Cryst. Growth **289**, 652–658 (2006)
18.48 M.M. Lencka, R.E. Riman: Thermodynamics of multicomponent perovskite synthesis in hydrothermal solution. In: *Handbook of Crystal Growth Technology*, ed. by K. Byrappa, T. Ohashi (Springer, Berlin Heidelberg 2003) p. 271
18.49 B. Gersten: Growth of multicomponent perovskite oxide crystals: Synthesis conditions of the hydrothermal growth of ferroelectric powders. In:

Handbook of Crystal Growth Technology, ed. by K. Byrappa, T. Ohashi (Springer, Berlin Heidelberg 2003) p. 299
18.50 R.E. Riman, W.L. Suchanek, K. Byrappa, C.W. Chen, P. Shuk, C.S. Oakes: Solid State Ion. **151**, 393 (2002)
18.51 O.V. Dimitrova: Investigations of the phase formations in the system Na_2O-RE_2O_3-SiO_2-H_2O under hydrothermal conditions. Ph.D. Thesis (Moscow State University, Moscow 1975)
18.52 K. Byrappa, J.R. Paramesha: Mater. Sci. Forum **315–317**, 514–518 (1999)
18.53 R.A. Laudise, W.A. Sunder, R.F. Belt, G. Gashurov: J. Cryst. Growth **102**, 427–433 (1990)
18.54 R.A. Laudise, A.A. Ballman, J.C. King: J. Phys. Chem. Solids **26**, 1305 (1965)
18.55 E.U. Franck: Pure Appl. Chem. **24**, 13–30 (1970)
18.56 R.C. Weast (Ed.): *Handbook of Physics and Chemistry*, 64th edn. (CRC, Boca Raton 1983)
18.57 H.C. Helgeson: Phys. Chem. Earth **13/14**, 133 (1981)
18.58 J.B. Hasted, D.M. Ritson, C.H. Collie: J. Chem. Phys. **16**, 1 (1948)
18.59 M. Uematsu: Phase equilibria and static properties. In: *Supercritical Fluids – Molecular Interaction, Physical Properties, and New Applications*, Springer Series in Materials Processing, ed. by Y. Arai, T. Sako, Y. Takebayaschi (Springer, Berlin Heidelberg 2002) p. 71
18.60 E.U. Franck: Int. Corros. Conf. Ser., 109 (1973)
18.61 G.C. Kennedy: Am. J. Sci. **248**, 540–543 (1950)
18.62 S.D. Haman: Phys. Chem. Earth **13/14**, 89 (1981)
18.63 K. Todheide: Ber. Bunsenges. Phys. Chem. **86**, 1005 (1982)
18.64 E.D. Kolb, P.L. Key, R.A. Laudise, E.E. Simpson: Bell Syst. Tech. J. **61**, 639 (1983)
18.65 W.L. Marshall, E.V. Jones, J. Jones: Inorg. Nucl. Chem. **36**, 2313 (1974)
18.66 A.A. Shternberg: Controlling the growth of crystals in autoclaves. In: *Crystallization Processes Under Hydrothermal Conditions*, ed. by A.N. Lobachev (Consultants Bureau, New York 1973) pp. 225–240
18.67 L.N. Demianets, E.N. Emelyanova, O.K. Melnikov: Solubility of sodalite in aqueous solutions of NaOH under hydrothermal conditions. In: *Crystallization Processes Under Hydrothermal Conditions*, ed. by A.N. Lobachev (Consultants Bureau, New York 1973) pp. 125–150
18.68 G.W. Morey, J.M. Hesselgesser: Am. J. Sci., 367 (1952)
18.69 R.A. Laudise: J. Am. Chem. Soc. **81**, 562 (1959)
18.70 R.A. Laudise: Hydrothermal growth of crystals. In: *Progress in Inorganic Chemistry*, Vol. 3, ed. by F.A. Cotton (Wiley, New York 1962)
18.71 D.J. Marshall, R.A. Laudise: Crystal growth by hydrothermal technique. In: *Crystal Growth*, ed. by H.S. Peiser (Pergamon, New York 1966) p. 557
18.72 N.Y. Ikornikova, A.N. Lobachev, A.R. Vasenin, V.M. Egrov, A.V. Autoshin: Apparatus for precision research in hydrothermal experiments. In: *Crystallization Processes Under Hydrothermal Conditions*, ed. by A.N. Lobachev (Consultants Bureau, New York 1973) p. 241
18.73 J.B. Hannay, J. Hogarth: Proc. R. Soc. Lond. **30**, 178 (1880)
18.74 M. Hosaka, S. Taki: J. Cryst. Growth **100**, 343 (1990)
18.75 R.A. Laudise, A.A. Ballman: J. Phys. Chem. **65**, 1396–1400 (1961)
18.76 V.M. John, S. Kordes: Chem. Earth **70**, 75–89 (1953)
18.77 J.M. Stanley: Ind. Eng. Chem. **468**, 1684–1689 (1954)
18.78 K. Byrappa, V. Venkatachalapathy, B. Puttaraju: J. Mater. Sci. **19**, 2855–2862 (1984)
18.79 M. Cochez, A. Ibanez, A. Goiffon, E. Philippot: Eur. J. Solid State Ionorg. Chem. **30**(55), 509–519 (1993)
18.80 O.V. Zvereva, M.Y. Mininzon, L.N. Demianets: J. Phys. (France) **4**(C2), 19–24 (1994)
18.81 P. Yot, O. Cambon, D. Balitsky, A. Goiffon, E. Philippot, B. Capelle, J. Detaint: J. Cryst. Growth **224**, 294–302 (2001)
18.82 R.-U. Barz, M. Grassl, P. Gille: J. Cryst. Growth **245**, 273–277 (2002)
18.83 O.Y. Samoilov: *The Structure of Aqueous Solutions and the Hydration of Ions* (Akademy Nauk, Moscow 1957)
18.84 V.A. Kuznetsov: Sov. Phys. Crystallogr. **12**, 608–611 (1968)
18.85 S. Kaneko, F. Imoto: Nippon Kagaku Kaishi **6**, 985–990 (1975)
18.86 N.A. Ovramenko, L.I. Shvets, F.D. Ovcharenko, B.Y. Kornilovich: Izv. Akad. Nauk USSR, Inorg. Mater. **15**, 1982–1985 (1979)
18.87 W. Hertl: J. Am. Ceram. Soc. **71**, 879–883 (1988)
18.88 M.M. Lencka, R.E. Riman: Chem. Mater. **53**, 31–41 (1981), .
18.89 J.O. Eckert Jr., C.C. Hung-Houston, B.L. Gersten, M.M. Lencka, R.E. Riman: J. Am. Ceram. Soc. **79**, 2929–2939 (1996)
18.90 S. Komarneni: Enhanced reaction kinetics under microwave-hydrothermal conditions, Proc. 2nd Int. Conf. Solvotherm. React. (Takamatsu 1996) pp. 97–100
18.91 S.H. Zhung, J.H. Lee, P.M. Forster, G. Ferey, A.K. Cheetham, J.S. Chang: Chem. Eur. J. **12**, 7899–7905 (2006)
18.92 V.I. Popolitov: Hydrotherm. Growth Crystals Prog. Cryst. Growth Charact. Mater. **21**, 255–297 (1990)
18.93 B.N. Litvin, D.A. Tules: Apparatus for hydrothermal synthesis and growth of monocrystals. In: *Crystallization Process under Hydrothermal Conditions*, Studies in Soviet Science, ed. by A.N. Lobachev (Consultant Bureau, New York 1973), p.139
18.94 R.A. Laudise, E. Kaldis (Ed.): *Crystal Growth of Electronic Materials* (Elsevier, Amsterdam 1985) p. 159
18.95 Leco Catalogue, Tem-Press Research Division, (Bellefonte, Pennsylvania 2005)
18.96 R. Roy, E.F. Osborn: Econ. Geol. **47**, 717–721 (1952)
18.97 T. Adschiri, K. Arai: Hydrothermal synthesis of metal oxide nanoparticles under supercritical con-

ditions. In: *Supercritical Fluid Technology in Materials Science and Engineering*, ed. by Y.-P. Sun (Marcel Dekker, New York 2002) pp. 311–325
18.98 E. Reverchon, R. Adam: J. Supercrit. Fluids **37**, 1–22 (2006)
18.99 M. Goto (Ed.): Proc. 8th Int. Symp. Supercrit. Fluids (Kyoto 2006)
18.100 Catalogue of M/s Berghof, Germany; M/s Nittokoatsu, Japan
18.101 A.C. Walker: Ind. Eng. Chem. **36**, 250–256 (1953)
18.102 M. Hosaka, S. Taki: J Cryst. Growth **52**, 837 (1981)
18.103 F. Lafon, G. Demazean: J. Phys. (France) **4**(C2), 177–182 (1994)
18.104 R.A. Laudise, A.A. Ballman, J.C. King: J. Phys. Chem. Solids. **26**, 1305–1308 (1965)
18.105 R.A. Laudise: Hydrothermal crystal growth – some recent results. In: *Advanced Crystal Growth*, ed. by P.M. Dryburgh, B. Cockayne, K.G. Barraclough (Prentice Hall, NewYork 1987) pp. 267–288
18.106 R.A. Laudise, R.A. Sullivan: Chem. Eng. Prog. **55**, 55–59 (1959)
18.107 R.L. Barns, E.D. Kolb, R.A. Laudise, E.E. Simpson, K.M. Kroupa: J. Cryst. Growth **34**, 189–197 (1976)
18.108 X. Buisson, R. Arnaud: J. Phys.(France) **4**(C2), 25–32 (1994)
18.109 A.A. Ballman, R.A. Laudise: Solution growth. In: *Art and Science of Growing Crystals*, ed. by J.J. Gilman (Wiley, New York 1963) p. 231
18.110 J.J. Martin, A.F. Armington: J. Cryst. Growth **62**, 203–206 (1983)
18.111 A.F. Armington, J.J. Larkin: J. Cryst. Growth **71**, 799 (1985)
18.112 M. Hosaka, T. Miyata: Mater. Res. Bull. **28**, 1201–1208 (1993)
18.113 G.R. Johnson, R.A. Irvine, J.W. Foise: A parametric study of the variables involved in quartz growth, IEEE Proc. 44th Annu. Symp. Freq. Control (1990) pp. 216–221
18.114 M. Deleuze, O. Cambon, A. Goiffon, A. Ibanez, E. Philippot: J. Phys. (France) **4**(C2), 79–84 (1994)
18.115 K. Bräuer, E. Müller: Cryst. Res. Technol. **19**, 101–109 (1984)
18.116 O. Cambon, M. Deleuze, J.P. Michel, J.P. Aubry, A. Goiffon, E. Philippot: J. Phys. (France) **4**(C2), 85–91 (1994)
18.117 H. Iwasaki, F. Iwasaki, E.A. Marina, L.V. Balitskaya: Process for producing unsintered cristobalite silica, US Patent 4853198 (1989)
18.118 H. Iwasaki, F. Iwasaki, V.S. Balitsky, L.V. Balitskaya: J. Cryst. Growth **187**, 481 (1998)
18.119 H. Iwasaki, F. Iwasaki, M. Kurashige, K. Oba: J. Cryst. Growth **234**, 711 (2002)
18.120 Z.P. Chang, G.R. Barsch: IEEE Trans. Sonics Ultrasonics **23**, 127 (1976)
18.121 R.M. O'Connell, P.H. Corr: Temperature compensated cuts of berlinite and β-eucryptite: for saw devices, Proc. 31st Annal. Freq. Control Symp. (1977) pp. 182–186
18.122 E.D. Kolb, A.M. Glass, R.L. Rosenberg, J.C. Grenier, R.A. Laudise: Frequency dependence in quartz seed orientation, Proc. 35th Ultrasonic Symp. (New York 1981)
18.123 E. Philippot, D. Palmier, M. Pintard, A.A. Goiffon: J. Solid State Chem. **123**, 1–13 (1996)
18.124 K. Byrappa, S. Srikantaswamy: Prog. Cryst. Growth. Charact. Mater. **21**, 199 (1990)
18.125 M. Beaurain, P. Armand, P. Papet: J. Cryst. Growth **294**, 396–400 (2006)
18.126 B.H.T. Chai, M.L. Shand, I. Bucher, M.A. Gillee: Berlinite synthesis and SAW characteristics, Proc. IEEE Ultrasonic Symp. (1979) p. 557
18.127 V.I. Popolitov, I.M. Yaroslavskii: Izv. Akad. Nauk USSR, Neorg. Mater. **26**, 892 (1990)
18.128 I.M. Yaroshavskii, V.I. Popolitov: Neorg. Mater. Izv. Akad. Nank SSSR **26**, 1055–1059 (1990)
18.129 N. Prud'homme, D. Cachau-Herreillat, P. Papet, O. Cambon: J. Cryst. Growth **286**, 102–107 (2006)
18.130 D.V. Balitsky, E. Philippot, P. Papet, V.S. Balitsky, F. Pey: J. Cryst. Growth **275**, 887–894 (2005)
18.131 M. Haouas, F. Taulelle, N. Prud'homme, O. Cambon: J. Cryst. Growth **296**, 197–206 (2006)
18.132 W. Wallnofer, P.W. Krempl, F. Krispel, V. Willfurth: J. Cryst. Growth **198/199**, 487 (1999)
18.133 R.-U. Barz, M. Grassl, P. Gille: J. Cryst. Growth **237–239**, 843–847 (2002)
18.134 P. Hofmann, U. Juda, K. Jacobs: J. Cryst. Growth **275**, 1883–1888 (2005)
18.135 M. Grassl, R.-U. Barz, P. Gille: Cryst. Res. Technol. **37**, 531–539 (2002)
18.136 K. Jacobs, P. Hofmann, D. Klimm: J. Cryst. Growth **237–239**, 837–842 (2002)
18.137 D.R. Kinloch, R.F. Belt, R.C. Puttbach: J. Cryst. Growth **24/25**, 610–613 (1974)
18.138 S. Hirano, K. Kikuta: J. Cryst. Growth **79**, 223–226 (1986)
18.139 N.Y. Ikornikova: *Hydrothermal Synthesis of Crystals in Chloride Systems* (Nauka, Moscow 1975) pp. 1–222, in Russian
18.140 S. Hirano, K. Kikuta: J. Cryst. Growth **94**, 351–356 (1989)
18.141 S. Hirano, T. Yogo, K. Kikuta, Y. Yoneta: J. Ceram. Soc. Jpn. **101**, 113–117 (1993)
18.142 K. Yanagisawa, Q. Feng, K. Ioku, N. Yamasaki: J. Cryst. Growth **163**, 285–294 (1996)
18.143 K. Yanagisawa, K. Kageyama, Q. Feng, I. Matsushita: J. Cryst. Growth **229**, 440–444 (2001)
18.144 V.N. Rumyantsev, I.G. Ganeev, I.S. Rez: Solubility of SiO_2 in alkali and carbonate solutions. In: *Crystal Growth*, Vol. 9 (Nauka, Moscow 1972) pp. 51–54
18.145 V.A. Kuznetsov, A.A. Shternberg: Sov. Phys. Crystallogr. **12**, 280–285 (1967)
18.146 R.L. Barus, R.A. Laudise, R.M. Shields: J. Phys. Chem. **67**, 835–840 (1963)
18.147 G. Yamaguchi, H. Yanagida, S. Sojma: Bull. Soc. Chem. Jpn. **35**, 1789–1791 (1962)

18.148 K.F. Kashkurov, P.I. Nikitichev, V.V. Osipov, L.D. Sizova, A.V. Simonov: Sov. Phys. Crystallogr. **12**, 837–839 (1968)
18.149 R.R. Monchamp, R.C. Puttbach, J.W. Nielson: J. Cryst. Growth **2**, 178 (1968)
18.150 R.A. Laudise, A.A. Ballman: J. Am. Chem. Soc. **80**, 2655–2657 (1958)
18.151 V.S. Balitsky, E.E. Lisinstina: *Synthetic Analogues and Imitation of Natural Gemstones* (Nedra, Moscow 1981)
18.152 P. Hautefeuille, A. Perrey: C. R. Acad. Sci. **106**, 1800–1810 (1888)
18.153 R. Webster: *Gems*, 3rd edn. (Newnes–Butterworths, London 1975)
18.154 M. Hosak: Hydrothermal Growth of Crystals, Prog. Crystal Growth Charact. **21**, 71–96 (1990)
18.155 B.W. Anderson: *Gem Testing*, 8th edn. (Butterworths, London 1971)
18.156 R.T. Liddicoat Jr.: *Handbook of Gem Identification*, 10th edn. (Gemmological Institute of America, Los Angeles 1975)
18.157 P.J. Yancey: Hydrothermal process for growing crystals having the structure of beryl in highly acid chloride medium, US Patent 3723337 (1973)
18.158 E.M. Flanigen: Hydrothermal process for growing crystals having the structure of beryl in an alkaline halide medium, US Patent 3567642 (1971)
18.159 E.M. Flanigen, N.R. Mumbach: Hydrothermal process for growing crystals having the structure of beryl in an acid halide medium, US Patent 3567643 (1971)
18.160 R.E. Kane, R.T. Liddicoat Jr.: Gems Gemol. **21**(3), 156 (1985)
18.161 K. Scarratt: J. Gemmol. **21**(5), 294 (1989)
18.162 K. Schmetzer: J. Gemmol. **21**(3), 145 (1988)
18.163 Z. Chen, G. Zhang, H. Shen, C. Huang: J. Cryst. Growth **244**, 339–341 (2002)
18.164 V.G. Thomas, S.P. Demin, D.A. Foursenko, T.B. Bekker: J. Cryst. Growth **206**, 203–214 (1999)
18.165 L.I. Tsinobar, I.G. Chentsova: Kristallografiya **4**, 633 (1959)
18.166 V.S. Balitsky, I.B. Machina, A.A. Marin, J.E. Shigley, G.R. Rossman, T. Lu: J. Cryst. Growth **212**, 255–260 (2000)
18.167 V.S. Balitsky: J. Cryst. Growth **41**, 100 (1977)
18.168 M. Hosaka, S. Taki: J. Cryst. Growth **64**, 572 (1983)
18.169 K. Nassau: *Gemstone Enhancement*, 2nd edn. (Butterworths, Boston 1994)
18.170 K. Byrappa, M.K. Devaraju, P. Madhusudan, A.S. Dayananda, B.V. Suresh Kumar, H.N. Girish, S. Ananda, K.M.L. Rai, P. Javeri: J. Mater. Sci. **41**, 1395 (2006)
18.171 B.C. Chakoumakos, M.M. Abraham, L.A. Batner: J. Solid State Chem. **109**, 197 (1994)
18.172 M. Prasad, A.K. Pandit, T.H. Ansari, R.A. Singh, B.M. Wanklyn: Phys. Lett. A **138**, 61 (1989)
18.173 B.H.T. Chai, G. Loutts, X.X. Chang, P. Hong, M. Bass, I.A. Shcherbakov, A.I. Zagumennyi: *Advanced Solid State Lasers, Technical Digest*, Vol. 20 (Optical Society of America, Washington 1994) p. 41
18.174 K. Byrappa, K.M.L. Rai, B. Nirmala, M. Yoshimura: Mater. Sci. Forum **506**, 315 (1999)
18.175 F.M. Levin: J. Am. Ceram. Soc. **50**, 381 (1967)
18.176 L.G. Vanuitret, R.C. Linares, R.R. Soden, A.A. Ballman: J. Chem. Phys. **36**, 702 (1962)
18.177 K. Byrappa, C. Ramaningaiah, K. Chandrashekar, K.M.L. Rai, B. Basavalingu: J. Mater. Sci. **506**, 315 (1999)
18.178 K. Byrappa, B. Nirmala, K.M. Lokanatha Rai, M. Yoshimura: Crystal growth, size, and morphology control of Nd:RVO_4 under hydrothermal conditions. In: *Crystal Growth Technology*, ed. by K. Byrappa, T. Ohachi (Springer, Berlin, Heidelberg 2003) p. 335
18.179 H. Wu, H. Xu, Q. Su, T. Chen, M. Wu: J. Mater. Chem. **13**, 1223 (2003)
18.180 S. Erdei, B.M. Jin, F.W. Ainger: J. Cryst. Growth **174**, 328 (1997)
18.181 S. Erdei, M. Kilmkiewicz, F.W. Ainger, B. Keszei, J. Vandlik, A. Suveges: Mater. Lett. **24**, 301 (1995)
18.182 T. Mitsuda: Ceram. Jpn. **15**, 184 (1980)
18.183 S. Somiya: J. Mater. Sci. **41**, 1307 (2006)
18.184 K. Kajiyoshi, K. Tomono, Y. Hamaji, T. Kasanami, M. Yoshimura: J. Am. Ceram. Soc. **78**, 1521 (1995)
18.185 W.S. Cho, M. Yashima, M. Kakihana, A. Kudo, T. Sakata, M. Yoshimura: J. Am. Ceram. Soc. **80**, 765 (1997)
18.186 S. Ohara, T. Mousavand, T. Sasaki, M. Umetsu, T. Naka, T. Adschiri: J. Mater. Sci. **41**, 1445 (2006)
18.187 T. Mousavand: Synthesis of organic–inorganic hybrid nanoparticles by in-situ surface modification under supercritical hydrothermal conditions. Ph.D. Thesis (Tohoku University, Sendai 2007)
18.188 M. Yoshimura, H. Suda, K. Okamoto, K. Ioku: J. Mater. Sci. **29**, 3399–3402 (1994)
18.189 S. Forster, M. Antonietti: Adv. Mater. **10**, 195 (1998)
18.190 Y. Zhu, H. Zheng, Y. Li, L. Gao, Z. Yang, Y.T. Qian: Mater. Res. Bull. **38**, 1829 (2003)
18.191 V.F. Puntes, K.M. Drishnan, A.P. Alivisatos: Science **291**, 2115 (2001)
18.192 Q. Xie, Z. Dai, W. Huang, J. Liang, C. Jiang, Y.T. Qian: Nanotechnology **16**, 2958 (2005)
18.193 Z. Tian, J. Liu, J.A. Voigt, H. Xu, M.J. Mcdermott: Nano Lett. **3**, 89 (2003)
18.194 O.V. Al'myasheva, E.N. Korytkova, A.V. Maslov, V.V. Gusarov: Inorg. Mater. **41**, 460 (2005)
18.195 X. Jiao, D. Chen, L. Xiao: J. Cryst. Growth **258**, 158 (2003)
18.196 M. Wu, Y. Xiong, Y. Jia, J. Ye, K. Zhang, Q. Chen: Appl. Phys. A **81**, 1355 (2005)
18.197 K. Byrappa, K.M.L. Rai, M. Yoshimura: Environ. Technol. **21**, 1085 (2000)
18.198 T. Adschiri, K. Kanaszawa, K. Arai: J. Am. Ceram. Soc. **75**, 1019 (1992)
18.199 T. Adschiri, Y. Hakuta, K. Arai: Ind. Eng. Chem. Res. **39**, 4901 (2000)

18.200 M. Schur, H. Rijnberk, C. Nather: Polyhedron **18**, 101 (1998)
18.201 C.L. Cahill, B. Gugliotta, J.B. Parise: Chem Commun. **16**, 1715 (1998)
18.202 G.C. Guo, R.M.W. Kwok, T.C.W. Mak: Inorg. Chem. **36**, 2475 (1997)
18.203 W. Wang, Y. Geng, P. Yan, F. Liu, Y. Xie, Y. Qian: J. Am. Chem. Soc. **121**, 4062 (1999)
18.204 Y. Li, H. Liao, Y. Fan, Y. Zhang, Y. Qian: Inorg. Chem. **38**, 1382 (1999)
18.205 S. Yu, J. Yang, Z. Han, Y. Zhou, R. Yang, Y. Qian, Y. Zhang: J. Mater. Chem. **9**, 1283 (1999)
18.206 Y. Li, H. Liao, Y. Fan, L. Li, Y. Qian: Mater. Chem. Phys. **58**, 87 (1999)
18.207 Y. Li, F. Huang, Q. Zhang, Z. Gu: J. Mater. Sci. **35**, 5933 (2000)
18.208 C.E. Melto, A.A. Giardini: Am. Mineral. **59**, 775 (1974)
18.209 M. Schrauder, O. Navon: Nature **365**, 42 (1999)
18.210 O. Navon: Nature **353**, 746 (1991)
18.211 G.D.J. Guthrie, D.R. Veblen, O. Navon, G.R. Rossman: Earth Planet Sci. Lett. **105**, 1 (1991)
18.212 R.C. De Vries: Synthesis of diamond under metastable conditions, Ann. Rev. Mater. Sci. **17**, 161–187 (1987)
18.213 R.C. DeVries, R. Roy, S. Somiya, S. Yamada: Trans. Mater. Res. Soc. Jpn. B **14**, 641 (1994)
18.214 C.A. Eckert, B.L. Knutsan, P.G. Debenedetti: Nature **383**, 313 (1996)
18.215 Y.G. Gogotsi, K.G. Nickel, P.J. Kofstad: Mater. Chem. **5**, 2313 (1995)
18.216 R. Roy, D. Ravichandran, P. Ravindranathan, A. Badzian: J. Mater. Res. **11**, 1164 (1996)
18.217 Y.G. Gogotsi, P. Kofstad, M. Yoshmura, K.G. Nickel: Diam. Rel. Mater. **5**, 151 (1996)
18.218 B. Basavalingu, J.M. Calderon Moreno, K. Byrappa, Y.G. Gogotsi: Carbon **39**, 1763 (2001)
18.219 X. Zhang, H. Liu, W. He, J. Wang, X. Zi, R.I. Boughton: J. Cryst. Growth **275**, 1913 (2005)
18.220 S. Krupanidhi, C.N.R. Rao: Adv. Mater. **16**, 425 (2004)
18.221 B. Huang, J.M. Hong, X.T. Chen, Z. Yu, X.Z. You: Mater. Lett. **59**, 430 (2005)
18.222 Y. Zhang, H. Guan: Mater. Res. Bull. **40**, 1536 (2005)
18.223 U.K. Gautam, K. Sardar, F.L. Deepak, C.N.R. Rao: Pramana **65**, 549 (2005)
18.224 H. Xu, W. He, H. Wang, H. Yan: J. Cryst. Growth **260**, 447 (2004)
18.225 M. Cao, X. He, X. Wu, C. Hu: Nanotechnology **16**, 2129 (2005)
18.226 A. Rabenau, H. Rau: Naturwissenschaften **55**, 336 (1968)
18.227 J.F. Balasico, R.B. White, R. Roy: Mater. Res. Bull. **2**, 913 (1967)
18.228 L.N. Demianets: *Hydrothermal Synthesis of Crystals* (Nauka, Moscow 1968), in Russian
18.229 L.N. Demianets, L.S. Garashina, B.N. Litvin: Kristallografiya **8**, 800 (1963)
18.230 I.P. Kuzmina: Geol. Ore Depos. **6**, 101 (1963)
18.231 P. Hartman: Phys. Status Solidi **2**, 585 (1962)
18.232 D. Ehrentraut, H. Sato, Y. Kagamitani, H. Sato, A. Yoshikawa, T. Fukuda: Prog. Cryst. Growth Charact. Mater. **52**, 280 (2006)
18.233 J. Bauer, P. Kaczerovsky: Vysok. Skola Chem.–Tech. Praze G. **12**, 153 (1970)
18.234 E. Prochazkova, D. Rykl, V. Seidl: Czechoslovakian Patent 170391 (1973), No. 5939–73
18.235 I.P. Kuzmina, B.N. Litvin: Crystal Growth **4**, 160 (1964)
18.236 C.J.M. Rooymans, W.F. Langenhoff: J. Cryst. Growth **3–4**, 411 (1968)
18.237 V.B. Glushkova: *Polymorphism of Rare Earth Oxides* (Nauka, Leningrad 1967), in Russian
18.238 I.P. Kuzmina, N.M. Khaidukov: *Crystal Growth from High Temperature Aqueous Solutions* (Nauka, Moscow 1977), in Russian
18.239 H. Guggenheim: Solid State Phys. **12**, 780 (1961)
18.240 V.I. Popolitov, A.N. Lobachev, V.F. Perkin: Kristallografiya **17**, 436 (1972)
18.241 B.N. Litvin, V.I. Popolitov: *Hydrothermal Synthesis of Inorganic Compounds* (Nauka, Moscow 1984), in Russian
18.242 E.D. Kolb, A.J. Caporaso, R.A. Laudise: J. Cryst. Growth **19**, 242 (1973)
18.243 K. Byrappa, S. Srikantaswamy, G.S. Gopalakrishna, V. Venkatachalapathy: J. Mater. Sci. **21**, 2202 (1986)
18.244 S.P. Fedoseeva: J. Cryst. Growth **8**, 59 (1972)
18.245 I.P. Kuzmina, B.N. Litvin: Kristallografiya **7**, 478 (1963)
18.246 V.I. Popolitov, A.N. Lobachev: Izv. Akad. Nauk USSR: Inorg. Mater. **8**, 960 (1972)
18.247 T. Eiiti, K. Iodji, K. Kendzi, S. Tatsuro: Patent 5248959 (1975), Japan No. 50-102484
18.248 G. Demazeau, P. Maestro: Hydrothermal growth of Cr_2O_3, Proc. 7th Int. AIRAPT Conf. (Le Creusot), Vol. 1 (1979) p. 572
18.249 I.P. Kuzmina: *Author's Abstract IKAN* (SSSR, Moscow 1968), in Russian
18.250 B.N. Litvin, V.I. Popolitov: *Hydrothermal Synthesis of Inorganic Compounds* (Nauka, Moscow 1984) p. 165, in Russian
18.251 R.A. Laudise, E.E. Kolb: J. Am. Ceram. Soc. **45**, 51 (1962)
18.252 G.I. Distler, S.A. Kobzareva, A.N. Lobachev, O.K. Melnikov, N.S. Triodina: Krist. Tech. **13**, 1025 (1978)
18.253 S.C. Abraham, P.B. Jameson, J.L. Bernstein: J. Chem. Phys. **47**, 4034 (1967)
18.254 B.N. Litvin, V.I. Popolitov: *Hydrothermal Synthesis of Inorganic Compounds* (Nauka, Moscow 1984) p. 216, in Russian
18.255 G. Ervin, E.F. Osborn: J. Geol. **59**, 381 (1951)
18.256 A.N. Christensen: Acta Chem. Scand. **20**, 896 (1966)
18.257 A.N. Christensen: Acta Chem. Scand. **30**, 133 (1976)
18.258 H. Schwarz: Z. Naturforsch. **226**, 554 (1967)
18.259 V.S. Balitsky, T. Bublikova: Prog. Cryst. Growth. Charact. Mater. **21**, 139 (1990)

18.260 B.V. Mill: Dokl. Akad. Nauk SSSR **156**, 814 (1964)
18.261 J. Ito, C. Frondel: Am. Mineral. **53**, 1276 (1968)
18.262 B.A. Maksimov, Y.A. Kharitonov, V.V. Ilyukhin, N.V. Belov: Dokl. Akad. Nauk SSSR **178**, 980 (1968)
18.263 M. Bihan, T.A. Katt, R. Wey: Bull. Soc. France Mineral. Crystallogr. **941**, 15 (1971)
18.264 D.E. Appleman, J.R. Clark: Am. Mineral. **50**, 679 (1965)
18.265 K. Kodaira, S. Ito, T. Matsushita: J. Cryst. Growth **29**, 123 (1975)
18.266 J. Wan, Z. Wang, X. Chen, L. Mu, W. Yu, Y. Qian: J. Lumin. **121**, 32 (2006)
18.267 Z. Ito, I. Harold: Am. Mineral. **53**, 778 (1968)
18.268 D.H. Lindsley: *Carnegie Inst. Annu. Rep.* (Direct. Geophys. Lab., Washington 1971) p. 188
18.269 J. Ito: Am. Mineral. **53**, 782 (1968)
18.270 J. Ito, C. Frondel: Am. Mineral. **52**, 1077 (1967)
18.271 J. Ito, C. Frondel: Arkiv. Min. Geol. **58**, 391 (1968)
18.272 G.V. Bukin: Mineralogical Museum, Akad. Nauk SSSR **19**, 131 (1969)
18.273 R.J. Harker, O.G. Tuttle: Am. J. Sci. **254**, 468 (1956)
18.274 P.A. Sandomirskii, M.A. Smirnov, A.V. Arakcheeva, N.V. Belov: Dokl. Akad. Nauk SSSR **227**, 856 (1976)
18.275 B.Y. Kornilovich, N.A. Ovramenko, F.D. Ovcharenko: Dokl. Akad. Nauk SSSR **261**, 245 (1981)
18.276 I.Y. Nekrasov, T.P. Dadze: J. Mineral. **3**, 287 (1980)
18.277 I.Y. Nekrasov, T.P. Dadze, N.V. Zayakina: Dokl. Akad. Nauk SSSR **261**, 479 (1981)
18.278 G.D. Brunton, L.A. Harris, O.C. Kopp: Am. Mineral. **57**, 1720 (1972)
18.279 E.E. Strelkova, O.G. Karpov, B.N. Litvin: Kristallografiya **22**, 174 (1977)
18.280 D.Y. Pushcharovskii, O.G. Karpov, E.A. Pobedimskaya, N.V. Belov: Dokl. Akad. Nauk SSSR **234**, 1323 (1977)
18.281 D.Y. Pushcharovskii, T. Baatarin, E.A. Pobedimskaya, N.V. Belov: Kristallografiya **16**, 899 (1971)
18.282 D.Y. Pushcharovskii, E.A. Pobedimskaya, N.V. Belov: Dokl. Akad.Nauk SSSR **185**, 395 (1969)
18.283 L.B. Halferdahl: J. Petrol. **2**, 49 (1961)
18.284 D.Y. Pushcharovskii, E.A. Pobedimskaya, B.N. Litvin, N.V. Belov: Dokl. Akad. Nauk SSSR **214**, 91 (1974)
18.285 R.N. Thomson, J.E. Chisholm: Mineral. Mag. **37**, 253 (1969)
18.286 C.F. Warren: Am. Mineral. **56**, 997 (1971)
18.287 D.J. Drysdale: Am. Mineral. **56**, 187 (1971)
18.288 A.N. Safronov, N.N. Nevskii, V.I. Ilyukhin, N.V. Belov: Dokl. Akad. Nauk SSSR **255**, 278 (1980)
18.289 R. Caruba, A. Baumer, G. Turco: C. R. Acad. Sci. Paris **270**, 1 (1970)
18.290 V.G. Chykhlanstev, K.V. Alyamovskaya: Izv. Akad. Nauk SSSR: Inorg. Mater. **6**, 1639 (1970)
18.291 N.G. Shymyaskaya, V.A. Blinov, A.A. Voronkov: Dokl. Akad. Nauk SSSR **208**, 1876 (1973)
18.292 M.C. Michel-Levy: Bull. Soc. France Mineral. Crystallogr. **84**, 2989 (1967)
18.293 J. Ito: Am. Mineral. **53**, 998 (1968)
18.294 J.L. Munoz: Am. Mineral. **53**, 1490 (1968)
18.295 A. Baronnet, M. Amouric, B. Chabot, F. Corny: J. Cryst. Growth **43**, 255 (1978)
18.296 L.N. Demianets, E.N. Emelyanova, O.K. Melnikov: Solubility of sodalite under hydrothermal conditions. In: *Crystallization Process Under Hydrothermal Conditions*, ed. by A.N. Lobachev (Consultant Bureau, New York 1973) p. 151
18.297 R.D. Shannon: Phys. Chem. Mineral. **4**, 139 (1979)
18.298 D. Tranqui, J.J. Capponi, J.C. Joubert, R.D. Shannon: J. Solid State Chem. **73**, 325 (1988)
18.299 J.W. Cobble: Rapp. Tech. Cent. Belge Etude Corros. **142**, 119 (1982)
18.300 R. Caruba, A. Baumer, G. Turco: Geochim. Cosmochim. Acta **39**, 11 (1975)
18.301 A. Baumer, G. Turco: C.R. Acad. Sci. D **270**, 1197 (1970)
18.302 A.A. Bush, S.A. Ivanov, S.Y. Stefanovich: Izv. Akad. Nauk SSSR: Inorg. Mater. **13**, 1656 (1977)
18.303 M.N. Tseitlin, G.F. Plakhov, A.N. Lobachev: Kristallografiya **18**, 836 (1973)
18.304 V.I. Popolitov, G.F. Plakhov, S.Y. Stefanovich: Izv. Akad. Nauk SSSR: Inorg. Mater. **17**, 1841 (1981)
18.305 B.N. Litvin: Hydrothermal chemistry of silicates and germinates. Ph.D. Thesis (Academy of Sciences Russia, Moscow 1978)
18.306 A.N. Lazarev, A.K. Shirivinskaya: Izv. Akad. Nauk SSSR: Inorg. Mater. **12**, 771 (1976)
18.307 T.N. Nadezhdina, E.A. Pobedimskaya, V.V. Ilyukhin, N.V. Belov: Dokl. Akad. Nauk SSSR **223**, 1086 (1977)
18.308 S.R. Lyon, E.S. Ehlers: Am. Mineral. **56**, 118 (1970)
18.309 B.A. Maksimov, Y.V. Nikolskii, Y.A. Kharitonov: Dokl. Akad. Nauk SSSR **239**, 87 (1978)
18.310 A.M. Dago, D.Y. Pushcharovskii, E.A. Pobedimskaya, N.V. Belov: Dokl. Akad. Nauk SSSR **250**, 857 (1980)
18.311 D.Y. Pushcharovskii, A.M. Dago, E.A. Pobedimskaya, N.V. Belov: Dokl. Akad. Nauk SSSR **251**, 354 (1980)
18.312 D.M. Roy, R. Roy: Am. Mineral. **39**, 957 (1954)
18.313 D.Y. Pushcharovskii, E.A. Pobedimskaya, O.V. Kudryasteva, B. Hettash: Kristallografiya **1**, 1126 (1976)
18.314 I.P. Kuzmina, O.K. Melnikov, B.N. Litvin: *Hydrothermal Synthesis of Crystals* (Nauka, Moscow 1968) p. 41
18.315 N.A. Nosirev: Investigations of germanate system in hydrothermal condition. Ph.D. Thesis (Institute of Crystallography, Moscow 1975)
18.316 Y.K. Egorov-Tismenko, M.A. Simonov, N.V. Belov: Dokl. Akad. Nauk SSSR **227**, 2 (1976)
18.317 I.I. Soloveva, V.V. Bakanin: Kristallografiya **12**, 591 (1967)
18.318 S. Kume, S. Ueda, M. Koizumi: J. Geophys. Res. **74**, 2145 (1969)
18.319 N. Kinomura: J. Am. Ceram. Soc. **56**, 344 (1973)
18.320 N.V. Belov: Dokl. Akad. Nauk SSSR **268**, 360 (1983)
18.321 A.N. Christensen: Acta Chem. Scand. **24**, 1287 (1970)
18.322 O. Jarchow, K.H. Kalska, H. Schenk: Naturwissenschaften **68**, 475 (1981)

18.323 L.N. Demianets, A.N. Lobachev, G.A. Emelchenko: *Rare Earth Germanates* (Nauka, Moscow 1980)
18.324 E.D. Kolb, R.A. Laudise: J. Cryst. Growth **43**, 313 (1978)
18.325 F. Dachille, R. Roy: Z. Kristallogr. **111**, 451 (1959)
18.326 S. Srikantaswamy: Phases and crystallization in the system aluminum orthophosphate. Ph.D. Thesis (University of Mysore, India 1988)
18.327 R.G. Hermann: Ph.D. Thesis (Ohio University, Ohio 1972)
18.328 E.M. McCarron, J.L. Calabrene, M.A. Subramanian: Mater. Res. Bull. **22**, 1421 (1987)
18.329 J.M. Congo, P. Kierkegaard: Acta Chem. Scand. **20**, 72 (1966)
18.330 H. Effenberger: J. Solid State Chem. **57**, 1240 (1985)
18.331 A. Clearfield, B.D. Roberts, A. Clearfield: Mater. Res. Bull. **19**, 219 (1984)
18.332 M.A. Subramanian, B.D. Roberts, A. Clearfield: Mater. Res. Bull. **19**, 1417 (1984)
18.333 P. Lightfoot, A.K. Cheetam, A.W. Sleight: J. Solid State Chem. **73**, 325 (1988)
18.334 K. Byrappa, S. Srikantaswamy, S. Gali: J. Mater. Sci. Lett. **9**, 235 (1990)
18.335 K. Byrappa, B.N. Litvin: J. Mater. Sci. **18**, 703 (1983)
18.336 S. Gali, K. Byrappa: Acta Crystallogr. C **46**, 2011 (1990)
18.337 S. Gali, A. Cardenas, K. Byrappa, G.S. Gopalakrishna: Acta Cryst. C **48**, 1650 (1992)
18.338 K. Byrappa, B.V. Umesh Dutt, D. Poojary, A. Clearfield: J. Mater. Res. **9**, 1519 (1994)
18.339 A. Clearfield: Prog. Cryst. Growth. Charact. Mater. **21**, 1 (1990)
18.340 R. Peascoe: Ph.D. Thesis (Texas University, Austin 1989)
18.341 T. Chirayil, P.Y. Zavalij, M.S. Whittingham: Chem. Mater. **10**, 2629 (1998)
18.342 K. Byrappa, C.K. Chandrashekar, B. Basavalingu, K.M.L. Rai, S. Ananda, M. Yoshimura: J. Cryst. Growth **306**, 94 (2007)
18.343 Y.W. Wang, H.Y. Xu, H. Wang, Y.C. Zhang, Z.Q. Song, H. Yan, C.R. Wan: Solid State Ion. **167**, 419 (2004)
18.344 L.N. Demianets: Prog. Cryst. Growth. Charact. Mater. **21**, 299 (1990)
18.345 K. Byrappa, K.V.K. Shekar: J. Mater. Chem. **2**, 13 (1992)
18.346 K. Byrappa, K.V.K. Shekar, S. Gali: Cryst. Res. Technol. **6**, 768 (1992)
18.347 S. Hosokawa, Y. Tanaka, S. Iwamoto, M. Inoue: J. Mater. Sci. **43**, 3079 (2008)
18.348 A. Cardenas, J. Solans, K. Byrappa, K.V.K. Shekar: Acta Cryst. C **49**, 645 (1992)
18.349 M. Elli, L. Cambi: Atti. Accad. Naz. Lincei, Rend. C1. Sci. Fis. Mat. Nat. **39**, 87 (1965)
18.350 L. Cambi, M. Elli: Chim. Ind. Ital. **47**, 136 (1968)
18.351 S. Biswas, S. Kar, S. Chaudhuri: J. Cryst. Growth **284**, 129 (2005)
18.352 U.K. Gautam, R. Seshadri: Mater. Res. Bull. **39**, 669 (2004)
18.353 J.R. Ota, S.K. Srivastava: J. Nanosci. Nanotechnol. **6**, 168 (2006)
18.354 L. Cambi, M. Elli: Chim. Ind. Ital. **51**, 3 (1969)
18.355 L. Cambi, M. Elli: Atti. Accad. Naz. Lincei. Rend. Cl. Sci. Fis. Mat. Nat. **40**, 553 (1966)
18.356 E.D. Kolb, A.J. Caporaso, R.A. Laudise: J. Cryst. Growth **3/4**, 422 (1968)
18.357 N.K. Abrikosov, V.F. Bankina, L.V. Porestkaya: J. Cryst. Growth **7**, 176 (1967)
18.358 L. Cambi, M. Elli: Chim. Ind. Ital. **48**, 944 (1966)
18.359 L. Cambi, M. Elli: Atti. Accad. Naz. Lincei. Rend. Cl. Sci. Fis. Mat. Nat. **41**, 241 (1966)
18.360 L. Cambi, M. Elli: Chim. Ind. Ital. **50**, 94 (1968)
18.361 V.S. Balitsky, V.V. Komova, N.A. Ozerova: Izv. Akad. Nauk SSSR Ser. Geol. **12**, 93 (1971)
18.362 V.A. Kuznetsov, A.N. Lobachev (Ed.): *Crystal Processes Under Hydrothermal Conditions* (Consultant Bureau, New York 1973)
18.363 I. Keeman: Z. Anorg. Allg. Chem. **346**, 30 (1966)
18.364 K. Byrappa, B.V. Umesh Dutt, R.R. Clemente, S. Gali, A.B. Kulkarni: In: *Current Trends in Crystal Growth and Characterization*, ed. by K. Byrappa (MIT, Bangalore 1991) p. 272
18.365 L.N. Demianets: *Hydrothermal Synthesis of Crystals* (Nauka, Moscow 1968) p. 93, in Russian
18.366 L.Y. Kharchenko, V.I. Protasova, P.V. Klevstov: J. Inorg. Chem. **22**, 986 (1977)
18.367 P.V. Klevstov, N.A. Novgorodsteva, L.Y. Kharchenko: Dokl. Akad. Nauk SSSR **183**, 1313 (1968)
18.368 K. Byrappa, A. Jain: J. Mater. Res. **11**, 2869 (1996)
18.369 R.F. Klevstova, L.Y. Kharchenko, S.V. Borisov, V.A. Efremov, P.V. Klevstov: Kristallografiya **24**, 446 (1979)
18.370 V.I. Popolitov, B.N. Litvin: *Growth of Crystals Under Hydrothermal Conditions* (Nauka, Moscow 1986) p. 38
18.371 V.G. Hill, K. Zimmerman: J. Electrochem. Soc. Solid State **115**, 978 (1968)
18.372 E.D. Kolb, A.J. Caporoso, R.A. Laudise: J. Cryst. Growth **8**, 354 (1971)
18.373 R.F. Belt, J.B. Ings: J. Cryst. Growth **128**, 956 (1993)
18.374 A.V. Novoselova: Izv. Akad. Nauk SSSR, Inorg. Mater. **20**, 967 (1984)
18.375 J. Choi, E.G. Gillan: J. Mater. Chem. **16**, 3774 (2006)
18.376 D. Ehrentraut, N. Hoshino, Y. Kagamitani, A. Yoshikawa, T. Fukuda, H. Itoh, S. Kawabata: J. Mater. Chem. **17**, 886 (2007)
18.377 A. Clearfield, G.D. Smith: Inorg. Chem. **7**, 431 (1969)
18.378 S. Alluli, C. Ferraggiva, A. Laginestra, M.A. Massucci, N. Tomassini: J. Inorg. Nucl. Chem. **399**, 1043 (1977)

19. Hydrothermal and Ammonothermal Growth of ZnO and GaN

Michael J. Callahan, Qi-Sheng Chen

Zinc oxide (ZnO) and gallium nitride (GaN) are wide-bandgap semiconductors with a wide array of applications in optoelectronic and electronics. The lack of low-cost, low-defect ZnO and GaN substrates has slowed development and hampered performance of devices based on these two materials. Their anisotropic crystal structure allows the polar solvents, water and ammonia, to dissolve and crystallize ZnO and GaN at high pressure. Applying the techniques used for hydrothermal production of industrial single-crystal quartz to ZnO and GaN opens a pathway for the inexpensive growth of relatively larger crystals that can be processed into semiconductor wafers. This chapter will focus on the specifics of the hydrothermal growth of ZnO and the ammonothermal growth of GaN, emphasizing requirements for industrial scale growth of large crystals. Phase stability and solubility of hydrothermal ZnO and ammonothermal GaN is covered. Modeling of thermal and fluid flow gradients is discussed and simulations of thermal and temperature profiles in research-grade pressure systems are shown. Growth kinetics for ZnO and GaN respectively are reviewed with special interest in the effects of crystalline anisotropy on thermodynamics and kinetics. Finally, the incorporation of dopants and impurities in ZnO and GaN and how their incorporation modifies electrical and optical properties are discussed.

19.1 **Overview of Hydrothermal and Ammonothermal Growth of Large Crystals** 657
19.1.1 Comparison of Ammonia and Water as Solvents 657
19.1.2 Growth of Large Crystals by the Transport Growth Model 659

19.2 **Requirements for Growth of Large, Low-Defect Crystals** 661
19.2.1 Thermodynamics: Solubility and Phase Stability 661
19.2.2 Environmental Effects on Growth Kinetics and Structure Perfection (Extended and Point Defects) 664
19.2.3 Doping and Alloying 665

19.3 **Physical and Mathematical Models** 666
19.3.1 Flow and Heat Transfer 666
19.3.2 Porous-Media-Based Transport Model 666
19.3.3 Numerical Scheme 667

19.4 **Process Simulations** 669
19.4.1 Typical Flow Pattern and Growth Mechanism 669
19.4.2 Effect of Permeability on the Porous Bed 670
19.4.3 Baffle Design Effect on Flow and Temperature Patterns 670
19.4.4 Effect of Porous Bed Height on the Flow Pattern 672
19.4.5 Simulation of Reverse-Grade Soluble Systems 672

19.5 **Hydrothermal Growth of ZnO Crystals** 674
19.5.1 Growth Kinetics and Morphology . 674
19.5.2 Structural Perfection – Extended Imperfections (Dislocations, Voids, etc.) 676
19.5.3 Impurities, Doping, and Electrical Properties 678
19.5.4 Optical Properties 679

19.6 **Ammonothermal GaN** 681
19.6.1 Alkaline Seeded Growth 681
19.6.2 Acidic Seeded Growth 683
19.6.3 Doping, Alloying, and Challenges . 684

19.7 **Conclusion** 685

References 685

Gallium nitride (GaN) and zinc oxide (ZnO) are emerging semiconductor materials that will have an enormous impact in electronics and optoelectronics. GaN and ZnO both have the anisotropic wurtzite crystal structure (space group $P6_3mc$) as their thermodynamically stable phase. This anisotropy, along with a large ionic component in their chemical bonds, accounts for the high spontaneous and piezoelectric polarization found in both GaN and ZnO [19.1]. GaN and ZnO also have large saturation velocities, high mobilities, large radiation resistance, nonlinear optical properties, and are chemically and thermally robust. They both have direct bandgaps in the ultraviolet (UV) region (GaN, $E_g = 3.42\,\text{eV}$ at 300 K; ZnO, $E_g = 3.37\,\text{eV}$ at 300 K) and have the ability to form direct-bandgap alloys for the fabrication of quantum wells (AlN and InN with GaN and MgO and CdO with ZnO) [19.2–5].

Devices based on the GaN [19.2, 3] and ZnO [19.4, 5] material systems are currently or will be produced in the future for a myriad of applications including solid-state lighting, power electronics, high-power radio-frequency (RF) monolithic microwave integrated circuit (MMIC) arrays, terahertz detection, high-density optical storage, and UV–infrared (IR) detection. GaN-devices have seen rapid development in the last 10 years due to the overcoming of major technological hurdles in the early 1990s [19.6]. A multibillion-dollar market now exists for GaN green–violet light-emitting diodes (LEDs) and the overall GaN-device market is forecasted to increase by the tens of billions of dollars in the next several decades. GaN-based blue and violet laser diodes are in high demand for high-definition digital versatile disk (DVD) drives. ZnO-based devices have not seen penetration into the semiconductor marketplace because of its own set of technical hurdles yet to be overcome (P-doping, contacts, low-defect active layers, etc.) [19.7], but an intense research and development effort for commercial ZnO-based devices is currently progressing.

Semiconductor devices have typically been manufactured on *native* substrates that have nearly identical crystalline structure to the active device layers manufactured on them. Semiconductor substrates are normally cut from large single boules that have been grown by melt techniques, with variations of the Czochralski and Bridgman growth methods being the most common [19.8]. The melt techniques are generally preferred over vapor or solution methods for the growth of large single crystals, owing to the higher growth rates, which allow for lower costs and rapid scaling of boule diameters.

There is an important class of semiconductor materials where growth of large single crystals is problematic. These materials have different and in many cases superior electrical, optical, and structural properties compared with traditional semiconductors such as Si. ZnO and the group III nitrides: AlN, GaN, and InN are in this class of semiconductors, which also include SiC and diamond. The reactivity of molten ZnO and the relatively high oxygen overpressure ($\approx 50\,\text{atm}$) required to melt ZnO makes the melt growth of large single-crystal ZnO boules difficult [19.9]. GaN also cannot be grown by traditional melt techniques due to the extreme pressures and temperatures required to prevent the dissociation of GaN to form molten GaN [19.10]. In fact, all of the group III nitrides decompose into their corresponding group III metal and N_2 well before their melting points when heated at atmospheric pressure.

Techniques for growing nitride thin films on Si, sapphire (Al_2O_3), and silicon carbide (SiC) substrates were developed in the 1980s and 1990s due to the lack of GaN substrates [19.6]. GaN thin-film growth on nonnative substrates such as sapphire produces a large number of threading dislocations and other defects caused by the large lattice and thermal expansion mismatch between GaN and the nonnative substrate. These defects are deleterious to device reliability and performance. Low-cost commercial GaN substrates would enable enhanced performance, increased yields, and allow rapid market penetration of nitride-based devices. Therefore, there has been a considerable amount of research in producing GaN wafers grown by nonmolten techniques. The most widely developed is the hydride vapor-phase epitaxy (HVPE) technique. Several research institutes have demonstrated GaN-based devices, processed on HVPE GaN wafers with improved device metrics compared with nitride devices fabricated on SiC and sapphire wafers. Although an improvement over heteroepitaxy, GaN HVPE wafers are inferior in structural quality compared with Si or GaAs wafers. GaN-based laser diodes manufactured on HVPE GaN substrates have extremely low yields and reduced performance compared with the red diodes grown on low-defect GaAs substrates. HVPE GaN substrates are available only in limited quantities and are extremely expensive. Several other techniques such as high-pressure Ga flux and alkali fluxes have been investigated for the growth of large GaN crystals but have not produced the scale and quality that is required for high-volume low-cost GaN semiconductor wafers.

Large zinc oxide single crystals were first produced in the 1960s due to the interest in using single-crystal

ZnO for piezoelectric transducers and surface acoustical wave (SAW) devices. Renewed interest arose because of ZnO's potential as an isostructural, nearly lattice-matched substrate for group III nitride semiconductor device structures. Advances in fabricating ZnO and ZnMgO quantum wells on sapphire that exhibit strong optically stimulated UV emissions have further driven demand for development of ZnO substrates [19.11]. Zinc oxide boules up to 2 inch in diameter and 1 cm thick have been grown by vapor-phase transport [19.12], and melt-grown wafers of 2 in diameter are now also available [19.9]. Both processes typically yield wafers with dislocation densities of 10^4–10^5 cm^{-2}. Recently, the most promising method for the growth of inexpensive, large, low-defect ZnO boules is the hydrothermal method [19.13].

The similarity of water and ammonia as polar solvents allows GaN crystals to be grown in ammonia solvents (ammonothermal growth) similar to the hydrothermal growth of oxides crystals in high-pressure water solutions. Large quantities of low-cost ZnO and GaN wafers could theoretically be manufactured by applying the same scaling techniques used for quartz growth to the hydrothermal growth of ZnO and ammonothermal growth of GaN.

This chapter will focus on the specifics of hydrothermal growth of large single crystals of zinc oxide (ZnO) and ammonothermal growth of gallium nitride (GaN). Ammonia and water will be compared as solvents and a brief overview of the temperature gradient method, which is the predominant technique employed for large-scale hydrothermal growth of single crystals, will be presented. Phase stability, adequate solubility, and optimization of thermal and fluid flow gradients in hydrothermal systems through modeling and simulation will be reviewed. Finally, growth kinetics for hydrothermal ZnO and ammonothermal GaN and how the incorporation of dopants and impurities influence the electrical and optical properties on these two important semiconductor materials will be discussed.

19.1 Overview of Hydrothermal and Ammonothermal Growth of Large Crystals

19.1.1 Comparison of Ammonia and Water as Solvents

Water's abundance, low toxicity, high purity, liquid phase at room temperature and atmospheric pressure, high dielectric constant, and its amphoteric properties make it the most widely used solvent. Several large crystals have been grown in water at ambient conditions such as aluminum potassium sulfate (ALUM) and potassium dihydrogen phosphate (KDP), but many compounds need higher temperatures to obtain the high solubility and kinetics for the growth of large crystals. Hundreds of different crystalline compounds have been grown by the hydrothermal technique, but only quartz crystals have been produced in the size and quantities that are required for semiconductor substrates. Ammonia is the most common anhydrous solvent because of the many similarities with water, as shown in Table 19.1. Ammonia is readily available, with 109 000 metric tons produced worldwide in 2004 [19.14]. Costs for ultrahigh-purity anhydrous ammonia have been driven down due to its use in the synthesis of Si_2N_3 during complementary metal–oxide–semiconductor (CMOS) processing, and in the production of GaN LEDs.

Like water, ammonia is a polar molecule. Polar molecules have a nonuniform or anisotropic structure that causes positive and negative charges to form in opposite parts of the molecule. The old alchemist's

Table 19.1 Physical properties of ammonia and water

Property	Ammonia	Water
Boiling point (°C)	−33.4	100
Freezing point (°C)	−77.7	0
Critical temperature (°C)	132.5	374.2
Critical pressure (bar)	113	221
Density ($g\,cm^{-3}$)	0.68 (−33 °C)	0.96 (100 °C)
Ionic product	$\approx 10^{-29}$	10^{-14}
Heat of vaporization (kcal/mol)	5.58	9.72
Heat of fusion (kcal/mol)	1.35	2.0
Viscosity of liquid at 25 °C (cP)	0.135	0.891
Dielectric constant	22 (−33 °C)	80 (0 °C)
Dipole moment (D)	1.46	1.84
Polarizability (cm^3) ($\times 10^{24}$)	2.25	1.49
Specific conductance ($\Omega^{-1}cm^{-1}$)	4×10^{-10} (−15 °C)	4×10^{-8}

adage: *similia similibus solvuntur* (i.e., like dissolves like), a basic rule of solution growth, holds for polar solvents, which tend to dissolve ionic and polar solids. Ammonia has a lower, but still relatively high, dielectric constant and lower dipole moment than water (the dielectric constant and dipole moment are measures of the degree of polarization of a molecule), and therefore has less ability to dissolve highly ionic compounds than water, but a greater ability to dissolve organic molecules. Thus, ammonia-based solutions have been used predominately for chemical synthesis of fertilizers, pharmaceutical products, and plastics. Water and ammonia are also both protic solvents, which means they can donate a hydrogen bond to a solvated compound. Ammonia has a slightly higher proton affinity than that of water, and thus is a more basic solvent than water and enhances the acidity of many compounds. Table 19.1 lists some of the physical properties of ammonia and water.

Byrappa and *Yoshimura* define hydrothermal growth as [19.15]

> *any heterogeneous chemical reaction in the presence of a solvent (whether aqueous or nonaqueous) above room temperature at a pressure greater than* 1 atm *in a closed system.*

The term *solvothermal growth* has also been used generically when discussing both aqueous and nonaqueous solvents at above ambient conditions, but recently has been used more specifically when discussing the use of organic solvents at above ambient temperatures and pressures. The term *hydrothermal* is more commonly used when discussing aqueous (water-based) solvents, and the term *ammonothermal* has been recently adopted for discussing ammoniated (ammonia-based) solvents. Here we will define hydrothermal and ammonothermal as subclasses of the generic term of solvothermal growth as shown in Fig. 19.1 to avoid confusion while discussing differences and similarities of aqueous and ammoniated solvents.

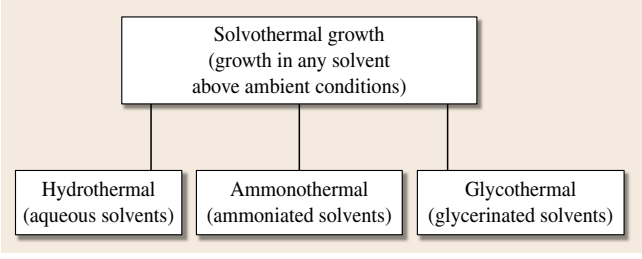


Fig. 19.1 Several subclasses of solvothermal growth

Solvothermal crystal growth offers several advantages over better known methods such as melt growth. Solvothermal growth is a low-temperature process, which often makes possible the growth of materials that are difficult or impossible to melt, or materials which, on solidifying from a melt and cooling down, would undergo phase changes (because of such changes, α-quartz cannot be grown from the melt). Low-temperature solvothermal growth can also minimize or eliminate the incidence of temperature-induced point defects, as illustrated by the hydrothermal growth of $Bi_{12}SiO_{20}$ [19.16], and can produce large amounts of material by simultaneous growth on multiple seeds (over 4000 kg of single-crystal quartz has been produced in a single run [19.15]). Only a small amount of user intervention and monitoring is required during growth because of the extremely uniform temperature gradients that can be maintained and the absence of moving parts. Some disadvantages of solvothermal growth are the low growth rates and initial capital equipment costs, but these are offset by the ability to grow multiple crystals in a single run and the extended lifetimes of the autoclaves.

The autoclaves are made out of high-strength steels or special alloys. The vessel must be corrosion resistant and able to withstand the temperature and pressure requirements for long periods of time. Corrosive solutions employing concentrated acids and bases are sometimes required to increase the solubility to obtain acceptable growth rates. Therefore, to protect the autoclave, a noble-metal liner (e.g., silver, gold, platinum or Teflon depending upon the pressure and temperature (PT) conditions and the solvent medium) is used in this case. Superstrong high-content-nickel alloy autoclaves are used for ammonothermal growth of GaN due to the higher temperatures and pressures required for the growth of large crystals of GaN. These autoclaves currently have small volumes, but should be easily scalable to larger sizes, albeit at greater expense than current industrial-scale autoclaves. Four centimeter-diameter autoclaves have recently been used to grow GaN crystals [19.17].

Additional tasks must be preformed when ammonia is being used as a high-pressure solvent. Ammonia, which is a vapor at ambient temperatures and pressures, can be condensed at room temperature and atmospheric pressure into an autoclave immersed in a chilled alcohol bath, pumped into an autoclave using high-pressure pumps, or chilled and poured into an autoclave. Precautions have to be taken, such as the use of glove boxes and vacuum apparatus, for any reactants or products that are air or moisture sensitive, e.g., alkali metals and their amides and azides used as mineralizers. Ammonia is

also toxic, so autoclaves with internal volumes greater than 50 cm^3 should be run inside chemical exhaust cabinets in case of a seal leak or rupture. There are several publications that cover specific details of the apparatus and autoclaves used in both hydrothermal [19.15, 18] and ammonothermal reactions [19.19, 20].

19.1.2 Growth of Large Crystals by the Transport Growth Model

Solvothermal growth is typically performed for two reasons:

1. The desired material is not thermodynamically favorable at ambient conditions;
2. The kinetics is such that the growth rate of the desired material is extremely slow at ambient conditions.

The *transport growth* model (also called the *temperature-differential* or *dissolution–crystallization* model) is predominately used for solvothermal growth of large single crystals, due to the low growth rate of quartz and many other technologically important materials grown in high-pressure solvents. Table 19.2 shows the dissolution–crystallization mechanism which is kinetically enhanced by the addition of *mineralizers*. Ammonia, like water, is amphoteric and can be made either acidic or alkaline depending on which compounds or *complexing agents* are combined with it. These complexing agents, or *mineralizers*, ionize in the solvent; it is these cations (acidic ions) or anions (alkaline ions) that promote the high solubility of many solid-phase compounds at low temperature. Source material is dissolved to form an intermediate species (left to right flow in the reversible chemical reactions in Table 19.2). Subsequently, the intermediate species becomes supersaturated by an external force and crystallizes out as single-crystal deposits (right to left flow in reactions in Table 19.2).

The *transport growth model* and all solvothermal growth mechanisms are based on supersaturation. Figure 19.2 shows a schematic of the model. A temperature zone is established where the lower half of the autoclave, called the dissolution zone (T_2 in Fig. 19.2), is at a higher temperature than the upper half of the autoclave, called the crystallization zone (T_1 in Fig. 19.2). A baffle is placed between the two zones to help establish near-isothermal conditions in each zone. The solvent at the bottom of the vessel dissolves the nutrient until it reaches saturation. The solvated species is transported by the lower density fluid in the warmer dissolution zone, through natural fluid convection, to the cooler crystallization zone. Because of the lower temperature at the seed the solvated species becomes supersaturated, comes out of solution, and deposits on the seed (normal saturation conditions). Fluid convection returns the higher-density depleted solution to the lower-density fluid in the dissolution zone, where additional nutrient is dissolved. The cycle repeats as long as there is nutrient in the lower zone. Quartz [19.15], zinc oxide [19.21–27], GaN [19.20], and many other inorganic crystals have

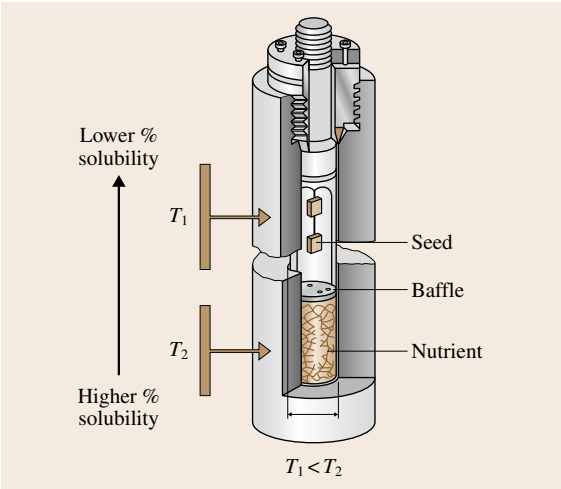


Fig. 19.2 Schematic of solvothermal crystal growth by the transport growth model (after [19.18])

Table 19.2 Comparison of dissolution–crystallization cycle of the hydrothermal and ammonothermal techniques

Hydrothermal: oxides	Ammonothermal: nitrides
Water: $2H_2O \rightarrow H_3O^+ + OH^-$	Ammonia: $2NH_3 \rightarrow NH_4^+ + NH_2^-$
ZnO in alkali water solution	GaN in ammonobasic solution
$ZnO + 2H_2O + 4OH^- \leftrightarrow Zn(H_2O)_2(OH)_4^-$	$GaN + (x-3)NH_2^- + 2NH_3 \leftrightarrow Ga(NH_2)_x^{3-x}$
Mineralizers	Mineralizers
Acids: HNO_3, HCl, HI	Acids: NH_4Cl, NH_4I, HI
Bases: KOH, NaOH, LiOH	Bases: KNH_2, $NaNH_2$, $LiNH_2$

Table 19.3 Status of technology, ca. 2006, for solvothermal growth of SiO_2, ZnO, and GaN crystals (after [19.28])

Parameter	SiO_2	ZnO	GaN
Autoclave inner diameter	0.65 m	$\leq$ 0.2 m	$\leq$ 0.03 m
Autoclave inner length	14 m	$\leq$ 3 m	0.2–0.7 m
Volume	4.6 m^3	$\leq$ 0.2 m^3	$\leq 5\times10^{-4}$ m^3
Seed size	$70\times45\times230$ mm^3	$\approx$ 50 mm diameter	$\leq$ 25 mm diameter
Seeds per batch	1400	112	1–4
Weight of crystal	1700 g	320 g; 20 mm thick	Few gram
Total yield per batch	2300 kg	36 kg	Few gram
Growth rate (*c*-axis)	25 µm/h	10 µm/h	$\leq$ 2 µm/h
3-Run-per-year yield	6900 kg	108 kg	0.12 kg

been grown solvothermally by the transport growth model.

A recent publication by *Fukuda* and *Ehrentraut* [19.28] gives an outlook of industrial growth of hydrothermal ZnO crystals and ammonothermal GaN by projecting their current and future development path with that of quartz growth. Table 19.3 shows the current status of hydrothermal quartz, hydrothermal zinc oxide, and ammonothermal gallium nitride. Even with the slow growth rates of zinc oxide and gallium nitride (20–40% and 5–20% of the growth rate of quartz, respectively) under current solvothermal conditions it is theoretically possible to grow hundreds of kilograms of zinc oxide or gallium nitride in a single autoclave.

Hydrothermal zinc oxide crystals of several hundred grams have been grown with batch sizes in the tens of kilograms in small production autoclaves as shown in Table 19.3. An industrial-scale 500 l autoclave was recently used to grow 200 ZnO crystals at a growth temperature of 330 °C. The run lasted for 100 days and the weight of the crystals varied in the range 100–250 g [19.29]. If there is a large demand for ZnO wafers, economies of scale will allow for price reductions (200–400 US$ /cm^2 in 2006), as there is no reason ZnO crystals could not be grown in large industrial-scale autoclaves currently used to grown single-crystal quartz. Figure 19.3a shows 2 inch-diameter ZnO crystals grown in an autoclave with the equivalent dimensions as the *ZnO autoclave* listed in Table 19.3 [19.13]. Figures 19.3b and 19.3c show the largest current ZnO crystal and corresponding 3 inch-diameter wafer cut from the crystal.

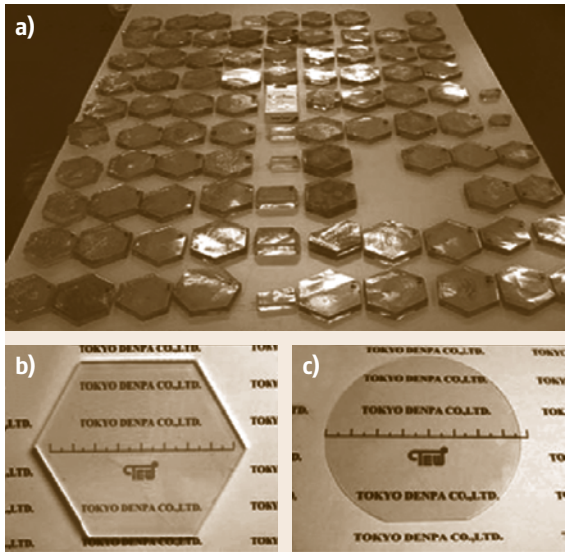


Fig. 19.3 **(a)** Two inch-size ZnO crystals produced during single growth run; **(b)** 3 inch ZnO crystal viewed down *c*-axis; **(c)** 3 inch (0001) ZnO wafer (after [19.13])

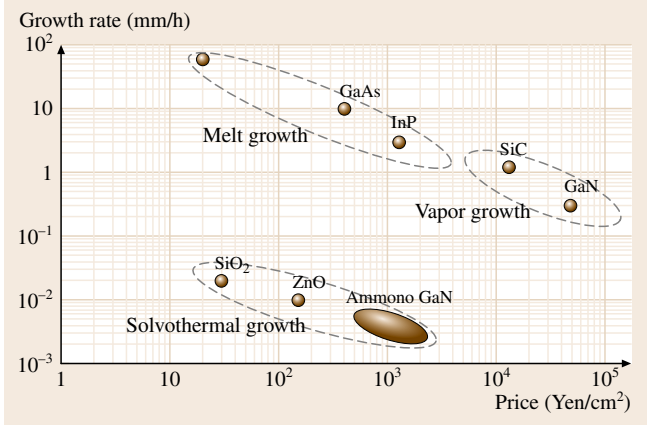


Fig. 19.4 Growth rates and cost of large-area single crystals (projected cost for ZnO and GaN) (after [19.28])

Fukuda and Ehrentraut go on to apply SiO_2 quartz development to future ZnO and GaN development in order to project the cost of ZnO and GaN wafers when

their development cycle fully matures. The authors claim that hydrothermal ZnO and ammonothermal GaN wafers will be cost-competitive with tradition compound semiconductor wafers such as GaAs and InP in the future. This comparison is shown in Fig. 19.4, which shows the potential of applying solvothermal growth techniques for industrial production of semiconductor wafers.

19.2 Requirements for Growth of Large, Low-Defect Crystals

19.2.1 Thermodynamics: Solubility and Phase Stability

In solvothermal growth of large crystals a *nutrient*, often the compound one intends to crystallize out as a single crystal, is dissolved in the solvent. The dissolved compound may form intermediate complexes or species in solution. In solvothermal growth, convective circulation and/or diffusion of these species throughout the solvent provides the primary mechanism for synthesizing crystalline compounds. A solvothermal growth system is designed to bring the soluble species into a region of the solvent medium where a change in conditions – e.g., in temperature, solvent composition, pH, or pressure – promotes crystal growth. Ideally, this change of conditions puts the soluble species in supersaturation, so the species must come out of solution – hopefully as the desired compound (e.g., ZnO, GaN) – until an equilibrium state (saturation) is achieved.

Thus, there are four fundamental thermodynamic requirements for the growth of high numbers of low-defect crystals by the hydrothermal/solvothermal method:

1. The desired material must have an adequate solubility at a given set of conditions (solvent, dissolution temperature, and pressure);
2. The solubility of the desired material must have adequate temperature dependence between the dissolution zone and crystallization zone;
3. The desired material must be the thermodynamically preferred material in the crystallization zone for a given set of conditions (solvent, crystallization temperature, and pressure);
4. The solvent must be thermodynamically stable at the temperatures and pressure needed to fulfill requirements 1–3 over long periods of time.

Low solubility will result in low growth rates; excessively high solubility will result in polycrystalline growth or spontaneous nucleation, which may be desirable for solvothermal powder synthesis, but prohibits growth of low-defect-density single crystals. Typically, the nutrient should be 1–10 wt.% soluble in the solvent. Solubility can be increased by adding a proper complexing agent (mineralizer). Most mineralizers used in solvothermal growth change the pH of the solvent, making the solvent either acidic or alkaline, i. e., increasing the number of cations (H_3O^+ in water, NH_4^+ in ammonia) or anions (OH^- in water, NH^- or NH_2^{2-} in ammonia) that attack the nutrient material in ionic solutions. For zinc oxide and gallium nitride, a solubility of approximately 5% by weight in alkaline solution yields high-quality single crystals at reasonable growth rates.

Because temperature is used to create supersaturation for large crystals, solubility of the compound must have temperature dependence. Natural convection allows solute to transport to the seed interface, where varying the temperature gradient between the nutrient and seed controls crystal growth kinetics.

The third requirement above can be difficult to achieve because of the multicomponent nature of solvothermal growth. If an oxide such as zinc oxide is desired, the hydride, hydroxide or hydrate should not be thermodynamically favored for the specific mineralizer, temperature, and pressure conditions employed. Also, chemical elements that are components in the mineralizer must not contribute to the formation of undesirable solid compounds at the growth interface.

The final requirement is not readily apparent in hydrothermal growth. Water is stable as a liquid or supercritical fluid to temperatures above the maximum operating conditions of even small super-high-pressure research autoclaves. Ammonia however starts decomposing well below 500 °C at atmospheric pressure, and even under 3–4 kbar of pressure a significant percentage of ammonia will decompose above 500 °C [19.19]. This has two deleterious effects, first the change in solvent composition by ammonia decomposition over long periods of time will change the kinetic and possibly the thermodynamics of the growing GaN crystals, and secondly, hydrogen could have adverse effects on the autoclave vessels through hydrogen embrit-

tlement. The decomposition of ammonia is therefore one of the main issues that must be addressed for the growth of large crystals by the ammonothermal method.

The solubility and phase stability of ZnO in hydrothermal solvents and GaN in ammonothermal solvents are presented here.

Solubility of Hydrothermal ZnO

The solubility of hydrothermal zinc oxide in an OH^- alkaline medium is shown in Fig. 19.5 [19.23]. Note that solubility increases with temperature. This is called *normal or forward-grade solubility*.

Zinc oxide is an amphoteric oxide, meaning it acts as an acid in alkaline solutions and as a base in acidic solutions. It is possible to grow hydrothermal zinc oxide in acidic solutions as well as the alkaline solutions shown in Fig. 19.6. *McCandlish* and *Uhrin* recently studied the solubility of ZnO in an acidic medium and grew ZnO at 100–250 °C, with growth rates up to 0.25 mm/day [19.30]. Figure 19.6 illustrates the solubility in acidic regimes. The squares signify 2 molal aqueous nitric acid and the circles signify a proprietary acidic solution. Note that the nitric acid solution exhibits normal solubility, whereas the proprietary solution exhibits decreasing solubility with increasing temperature (*retrograde or reverse-grade solubility*). To grow ZnO crystals under conditions of normal solubility the seed is placed in a colder region than the source material (Fig. 19.2); to grow under conditions of retrograde solubility, the seed is placed in the hotter region.

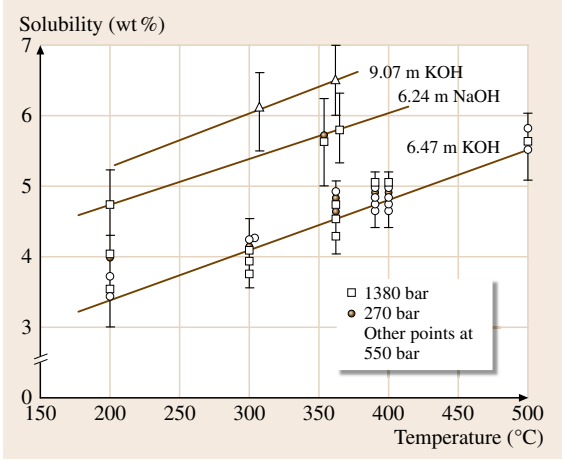


Fig. 19.5 Solubility of ZnO versus T in aqueous NaOH and KOH solutions (after [19.23])

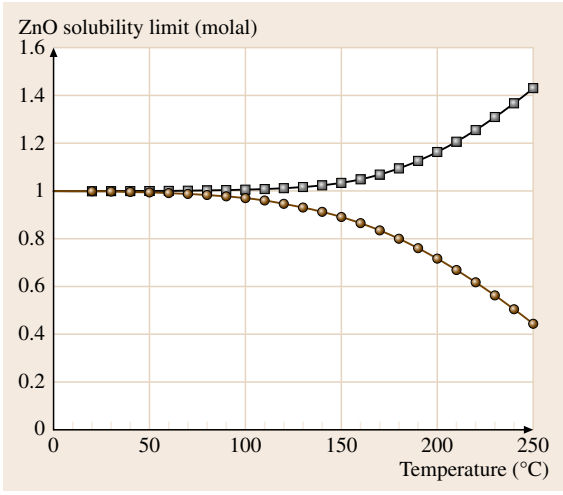


Fig. 19.6 Normal solubility of ZnO in 2 molal nitric acid (*squares*), and retrograde solubility of ZnO in a proprietary acid solution (*circles*) (after [19.30])

Phase Equilibrium of ZnO in Hydrothermal Solvents

Hüttig and *Möldner* studied the phase equilibrium of the ZnO–H_2O system to 40 °C and found zinc oxide to be the stable solid phase at pressures above 50 torr and temperatures above 35 °C [19.31]. *Lu* and *Yeh* experimentally showed that zinc oxide is the stable product up to pH = 12.5 in an aqueous ammonia solution at 100 °C [19.32]. *Laudise* and *Ballman* grew large zinc oxide crystals in alkaline media and found zinc oxide to be the stable product at 200–400 °C in 1.0 M NaOH [19.33]; subsequently it was found that zinc oxide can be grown in hydroxide solutions up to 10 M at temperatures exceeding 300 °C [19.27].

Recent advances in thermodynamic modeling of aqueous solution chemistry can aid in choosing conditions that achieve crystal growth of zinc oxide and other materials. A thermodynamic model of aqueous-based chemistry has been developed that computes the stability of zinc oxide in different aqueous regimes. The model uses commercial software (OLI Systems Inc., Morris Plains) and is detailed in several publications [19.34–36]. McCandlish and Uhrin initially modeled zinc oxide in the hydroxide system to validate the model against experimental data. Subsequently, a thermodynamic model was created for the growth of zinc oxide in acidic environments. Figure 19.7 shows the computed stability of ZnO at 150 °C as a function of pH with HNO_3 as the mineralizer [19.30].

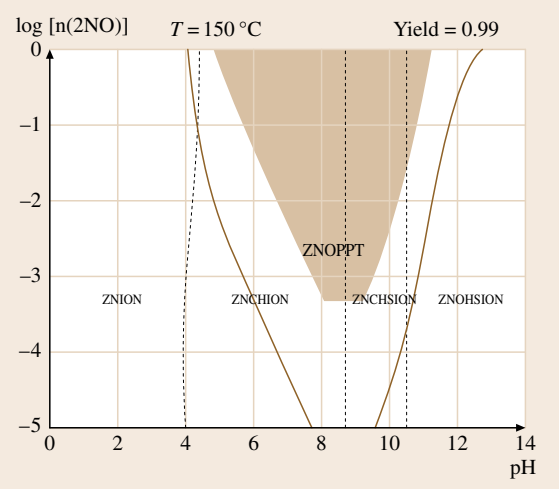


Fig. 19.7 Yield diagram for the precipitation of ZnO in 2 molal nitric acid at 150 °C as a function of pH; log [n(2NO)] signifies the log of the molar concentration of nitric acid in solution; ZNION, ZNCHION, ZNCHSION and ZNOHSION signifies the basic atomic chemical composition of the ionic compounds in solution for a given pH: Zn ion, ZnCH ion, ZnCHS ion, ZnOHS ion; ZnOPPT signifies ZnO crystallites that participated out of solution for a given pH (after [19.30])

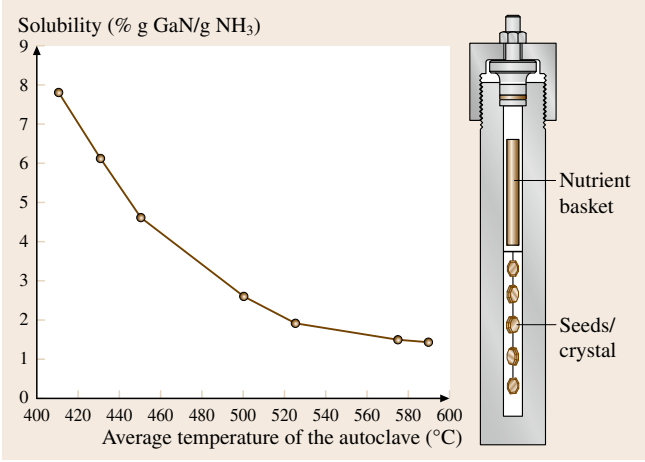


Fig. 19.8 Solubility of GaN polycrystalline in KNH_2-NH_3 system, 3.5 ± 0.5 M KNH_2 concentration (after [19.42])

Solubility of Ammonothermal GaN

Ammonothermal growth of GaN has retrograde solubility in alkaline solutions and normal solubility in acidic solutions. Figure 19.8 shows the solubility of polycrystalline GaN after a series of runs in the KNH_2–NH_3 system (±10% variability in filling and molarity) [19.42]. The KNH_2 concentration is about 3.5 ± 0.5 M, the temperature gradient is around 10 °C/cm, and the pressure is 1.3–2.4 kbar. The solubility of GaN in solutions of greater than 1 molal NaN_3-NH_3, KN_3–NH_3, KNH_2–NH_3, and $NaNH_2$–NH_3 has similar tendencies: a negative solubility coefficient and rather high solubility, in the range of 1–10% between 400 °C and 600 °C.

Using acidic mineralizers such as 0.4 M NH_4Cl, GaN has a normal solubility in ammonia [19.43]. The acidic conditions required the use of a Pt inner liner to protect the autoclave from corrosion. A growth rate of 0.02–0.03 mm/day can be achieved at a temperature of 550 °C and a pressure of less than 1.5 kbar. Normal solubility has also been claimed using other ammonium halide mineralizers [19.41, 43].

Phase Equilibrium of GaN in Ammonothermal Solvents

The early work on ammonothermal synthesis of nitride powders was performed by *Jacobs* and *Schmidt* [19.19]. They synthesized several novel nitrogen-based compounds and designed apparatus specifically for ammonothermal powder synthesis. Later *Peters* [19.44]

Table 19.4 Growth conditions of ammonothermal synthesis of GaN microcrystals

Investigators	Mineralizers	Temperature (°C)	Pressure (kbar)	Growth rate and habit
Dwilinski et al. [19.37]	KNH_2	550	1–5	Hexagonal microcrystals
Purdy [19.38]	NH_4Cl, NH_4Br or NH_4I	250–500	0.7	Mixed cubic and hexagonal microcrystals
Ketchum and *Kolis* [19.39]	KNH_2/KI	400	2.4	Hexagonal submillimeter-size plates
Yoshikawa et al. [19.40]	NH_4Cl	500	1.2	Hexagonal needle shape 0.02–0.03 mm/day
Lan et al. [19.41]	NH_4F, NH_4Cl, NH_4Br or NH_4I	450–600	1–2	Hexagonal microcrystals

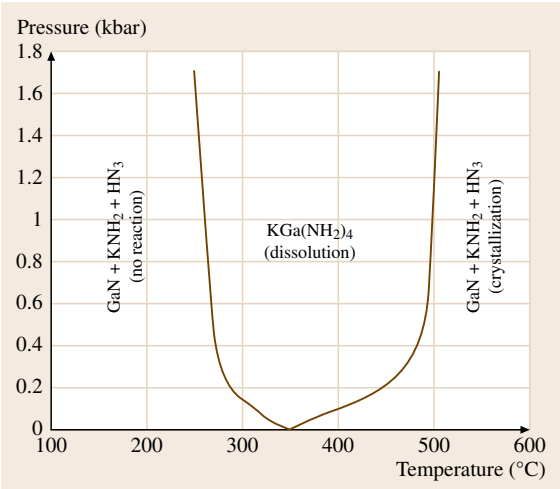


Fig. 19.9 Phase diagram of GaN in the GaN−KNH_2−NH_3 system (after [19.45]) (*curves* based on experiments between 0.3–2.4 kbar (5–35 kpsi); below 0.3 kbar the tendency is estimated).

and *Dwilinski* et al. [19.37] were the first to synthesize AlN and GaN microcrystals ammonothermally. The work on ammonothermal microcrystalline synthesis is summarized in Table 19.4.

Dwilinski et al. [19.37] obtained microcrystals of BN, AlN, and GaN by the ammonothermal method using lithium or potassium amide as mineralizer at pressures in the range 1–5 kbar and temperatures up to 550 °C. *Ketchum* and *Kolis* [19.39] grew ammonothermal single crystals of gallium nitride in supercritical ammonia at 400 °C and 2.4 kbar by using potassium amide (KNH_2) and potassium iodide (KI) as mineralizers. Hexagonal GaN crystals of $0.5 \times 0.2 \times 0.1\,mm^3$ were obtained. They also used potassium azide (KN_3) or sodium azide (NaN_3) to increase the solubility of GaN in ammonia [19.48].

The phase diagram of GaN in the GaN–KNH_2–NH_3 system is shown in Fig. 19.9 [19.45]. Unlike hydrothermal ZnO, high temperatures are needed to precipitate GaN out of an ammonothermal solution. The reaction $KGa(NH_2)_4 \leftrightarrow KNH_2 + GaN + 2NH_3$ did not produce GaN at temperatures below 400 °C. Pressure variations had little effect on the thermodynamics of GaN formation.

GaN has a metastable cubic phase that has been formed ammonothermally. *Purdy* et al. synthesized both cubic and hexagonal GaN by ammonothermal reactions of gallium metal or GaI_3 under acidic (NH_4Cl, NH_4Br or NH_4I) conditions [19.38, 49]. The reaction temperatures were 250–500 °C and pressures were up to 10 000 psi (0.6895 kbar).

Figure 19.10a shows well-defined cubic crystals grown in ammonia with the addition of lithium chloride to an acidic solution [19.46]. *Hashimoto* et al. [19.50] have shown that the ammonium halides (acidic mineralizer) and the alkali halide (neutral mineralizer) can form mixed cubic and hexagonal phases of GaN. *Ehrentraut* et al. [19.47] showed that pure hexagonal phases can be obtained in acidic ammonia solutions. Figure 19.10b shows that hexagonal formation is favored at lower temperatures in solutions for successively smaller halide cations. Pure phase hexagonal GaN was obtained at ≥ 470 °C for NH_4Cl mineralizer, ≥ 500 °C for NH_4Br mineralizer, and ≥ 550 °C for NH_4I mineralizer. If one takes into account the metastable nature of cubic GaN (*Purdy* [19.51] showed a correlation between cubic GaN formation and short-duration experiments), a phase conversion of the metastable cubic GaN to the stable hexagonal GaN could be possible in long-duration experiments as performed by *Ehrentraut* et al. [19.47].

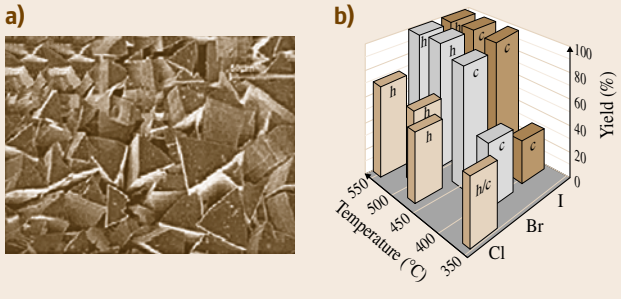


Fig. 19.10 (**a**) Ammonothermal cubic GaN formed under acidic conditions with the addition of lithium (after [19.46]); (**b**) temperature and mineralizer effect on phase stability of gallium nitride synthesized under acidic ammonothermal conditions (after [19.47]) (h – hexagonal, c – cubic)

19.2.2 Environmental Effects on Growth Kinetics and Structure Perfection (Extended and Point Defects)

The stable phase of ZnO and GaN has the wurtzite crystal structure, which is hexagonal with a space group of $P6_3mc$. The noncentrosymmetric structure of the wurtzite structure produces an anisotropy in which the opposite sides of a basal plane wafer have different atomic arrangements at their surfaces. This anisotropy in hexagonal GaN and ZnO also causes a nonsymmet-

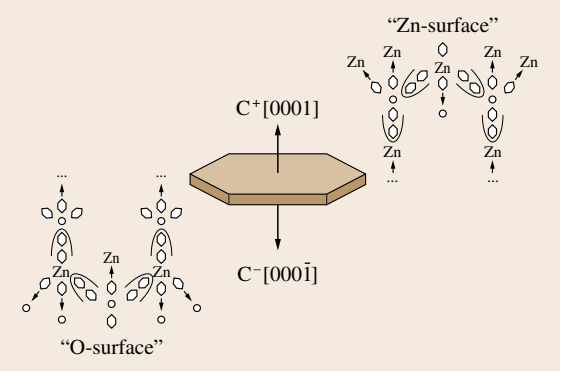


Fig. 19.11 Electronic charge distribution of zinc oxide basal faces *(*GaN *has the same crystal structure as* ZnO*)* (after [19.21, 52])

rical charge state due to its anisotropic crystal structure. The C^+ side of the basal plane is comprised of a Zn-rich layer for ZnO or a Ga-rich layer for GaN, and the C^- is comprised of an O-rich layer for ZnO or a N-rich layer for GaN, as illustrated in Fig. 19.11 (a zinc oxide crystal is shown; gallium nitride has the exact same configuration).

The C^+ plane has a net positive surface charge because of the greater number of positive dangling bonds (Zn or Ga) on its surface, in contrast to the C^- plane, which has a net negative surface charge due to the greater number of negative dangling bonds (O or N). The resulting distribution of electric charge causes disparities, among the various growth planes, in growth rates, as well as in impurity incorporation, chemical etching, and optical and electrical properties.

Many anisotropic or polar crystals including inorganic and organic materials have been grown from solutions. When growing polar crystals from solutions, especially a highly polarized solution such as water or ammonia, investigations into the surface chemistry of the crystals and the composition of the growth medium need to be taken into consideration. Typically the solvent, the intermediate species in solution, and the crystal itself all have surface charge states. The intermediate species can be broken down into fundamental growth units that react with the crystal's growth facets. The structure of these growth units determines growth kinetics on the various polar faces of the crystal due in large part to the charge state of these faces in relation to the charge states of the fundamental growth units.

Impurities in solutions cause changes in molecular diffusion and atomic absorption on advancing crystal surfaces, which in turn, influences the growth kinetics of the crystal. Because ZnO and GaN have anisotropic crystal structures, impurities, even at small levels, can effect a change in growth rates along specific crystallographic axes which induce point and line defects. In addition, the concentrations of impurities incorporated in the various growth sectors of a polar crystal can vary. ZnO and GaN grown on their positive polar surfaces have different impurity concentrations, growth rates, and morphologies than material grown on the negative polar surfaces. In short, the growth characteristics (growth morphology, impurities distribution, and crystal quality) are influenced by the anisotropic nature of polar crystals. The influence of impurities on hydrothermal ZnO and ammonothermal GaN will be discussed in Sects. 19.4 and 19.5, respectively.

19.2.3 Doping and Alloying

Semiconductor wafers ideally should be conducting or insulating. The previous section discusses how impurities can dramatically influence the growth kinetics. Therefore, great care must be taken while applying doping in a solvothermal medium. The majority of dopants slow down growth rates because they block the diffusion and/or absorption of the matrix atoms to the lattice sites of the various surfaces of the crystal. Dopants can have different segregation coefficients in solution growth, similar to impurities in molten solidification. It is difficult to control growth morphology in anisotropic crystals grown from solution with high levels of impurities or dopants. As in any semiconductor crystal growth process, impurities must be reduced to the lowest possible levels. This will allow for the smallest levels of dopants introduced for the synthesis of semiconductor boules with the desired conductivity levels. Finally solvothermal has several advantages over molten techniques for the growth of alloy wafers, such as solid sources and low temperature gradients. Preliminary experiments of hydrothermal ZnMgO [19.53] and solvothermal AlGaN [19.54] have been conducted.

Fluid flow and optimization of temperature zones are extremely important for the formation of low-defect crystals. The next two sections will discuss how to model fluid velocity and temperature gradient in a solvothermal system.

19.3 Physical and Mathematical Models

19.3.1 Flow and Heat Transfer

The hydrothermal and ammonothermal growth processes employ aqueous and ammoniated solvents under high temperatures and high pressures to dissolve and recrystallize materials that are relatively insoluble under ordinary conditions. After the system is pressurized, the solvent occupies most of the volume. The convection system for hydrothermal/ammonothermal growth consists of a porous bed whose height changes with the growth, a fluid layer overlying this porous bed, a metal baffle with holes (which lies above the porous bed), and solid seed plates whose size increase with the growth. Figure 19.12 shows the schematic of growth system that has been used experimentally to synthesize GaN [19.39]. The autoclave has an internal diameter of 0.932 cm, external diameter of 3.5 cm, internal height of 18.4 cm, and external height of 20.3 cm (Tem-Press MRA 138R with a volume of 12.5 ml). The thicknesses of the sidewall and bottom of the autoclave are 1.28 cm. The charge height is 1 cm, and the gap between the baffle and charge bed is 2 cm. A baffle made from 0.28 mm Ag foil is used to divide the autoclave into two parts: the upper and lower portions.

Hence the upper portion can be considered as a fluid layer with the assumption of incompressible flow and the Boussinesq approximation [19.56, 57], and the Navier–Stokes equations can be used in the fluid layer. Suppose that the density has a linear temperature dependence of the form

$$\rho = \rho_0[1 - \beta(T - T_0)] \,, \tag{19.1}$$

where ρ, β, and T are density, isobaric coefficient of expansion, and temperature, and ρ_0 and T_0 are constant reference values for the density and temperature, respectively.

In the solid region which comprises the autoclave walls, the baffle, and the seeds, only conductive heat transfer is considered. In the fluid region, convective heat transfer is considered.

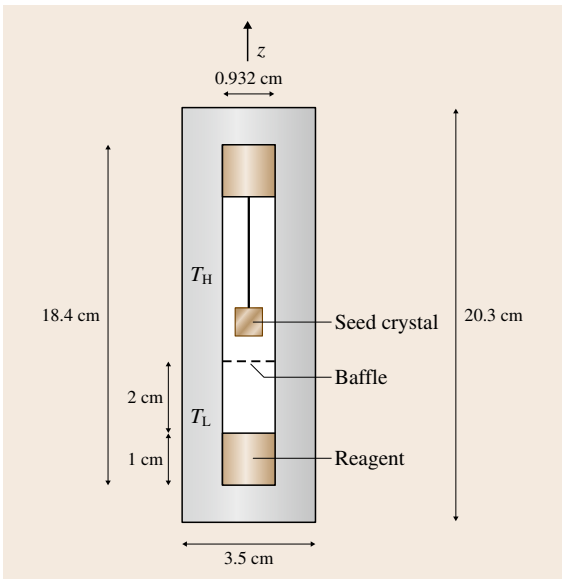


Fig. 19.12 Schematic of an ammonothermal growth system (after [19.55])

19.3.2 Porous-Media-Based Transport Model

The nutrient particles (e.g., ZnO or GaN) in the bottom of the autoclave can be considered as a porous medium. In this case, the Darcy–Brinkman–Forchheimer model can be employed in the porous layer [19.58, 59]. The dimensionless parameters of the system are listed as follows

$$A = H/R, \quad \mathrm{Gr} = g\beta R^3 \Delta T/\nu^2, \quad \mathrm{Pr} = \nu/\alpha,$$
$$\mathrm{Da} = K/R^2, \quad \mathrm{Fs} = b/R \,,$$

where A, Gr, Pr, Da, and Fs denote the aspect ratio, Grashof number, Prandtl number, Darcy number, and Forchheimer number, respectively. H is the internal height of the autoclave, R is the internal radius of the autoclave, g is acceleration due to gravity, ΔT is the maximum temperature difference on the sidewall of the autoclave, ν is kinematic viscosity, α is thermal diffusivity, the permeability of porous matrix $K = d_\mathrm{p}^2\varepsilon^3/[150(1-\varepsilon)^2]$ with d_p as the average diameter of the nutrient particles, and the Forchheimer coefficient $b = 1.75K^{0.5}/(\sqrt{150}\varepsilon^{1.5})$.

The governing equations in the porous and fluid layers can be combined by defining a binary parameter B as: $B = 0$ in the fluid layer and $B = 1$ in the porous layer, respectively. The porosity is $\varepsilon = 0$ in solid, $0 < \varepsilon < 1$ in porous layer, and $\varepsilon = 1$ in fluid layer, respectively. The combined governing equations in a cylindrical coordinate system are

$$\frac{\partial(\varepsilon\rho_\mathrm{f})}{\partial t} + \nabla\cdot(\rho_\mathrm{f}\boldsymbol{u}) = 0 \,, \tag{19.2a}$$

$$\frac{\rho_f}{\varepsilon}\frac{\partial \boldsymbol{u}}{\partial t}+\frac{\rho_f}{\varepsilon}(\boldsymbol{u}\cdot\nabla)\frac{\boldsymbol{u}}{\varepsilon}$$
$$=-\nabla p-\rho_f\beta(T-T_0)\boldsymbol{g}$$
$$+\nabla\cdot(\mu_e\nabla\boldsymbol{u})-B\left[\left(\frac{\mu_f}{K}+\frac{\rho_f b}{K}|\boldsymbol{u}|\right)\boldsymbol{u}\right], \quad (19.2b)$$
$$(\rho c_p)_e\frac{\partial T}{\partial t}+(\rho c_p)_f[(\boldsymbol{u}\cdot\nabla)T]=\nabla\cdot(k_e\nabla T), \quad (19.2c)$$

where μ, k, and c_p denote dynamic viscosity, thermal conductivity, and specific heat, respectively, and $\boldsymbol{g}$ is the gravity vector. Subscripts f and e denote fluid and effective, respectively.

The following scales are used to nondimensionalize the governing equations: length, R; velocity, $u_0=\nu/R$; time, $t_0=R^2/\nu$; pressure, $\rho\nu^2/R^2$; temperature, T_H-T_L. T_H and T_L are the high and low temperature applied on the sidewall of the autoclave, respectively. The resulting nondimensionalized equations are

$$\frac{\partial\varepsilon\bar{\rho}}{\partial t}+\frac{1}{r}\frac{\partial}{\partial r}(r\bar{\rho}u)+\frac{\partial}{\partial z}(\bar{\rho}w)=0, \quad (19.3a)$$
$$\frac{\partial}{\partial t}\left(\frac{1}{\varepsilon}\bar{\rho}u\right)+\frac{1}{r}\frac{\partial}{\partial r}\left(\frac{1}{\varepsilon^2}r\bar{\rho}uu\right)+\frac{\partial}{\partial z}\left(\frac{1}{\varepsilon^2}\bar{\rho}wu\right)$$
$$=\bar{\mu}\left[\frac{1}{r}\frac{\partial}{\partial r}\left(r\frac{\partial u}{\partial r}\right)+\frac{\partial^2 u}{\partial z^2}-\frac{u}{r^2}\right]-\frac{\partial p}{\partial r}$$
$$-B\left(\frac{1}{\mathrm{ReDa}}+\frac{\mathrm{Fs}}{\mathrm{Da}}|\boldsymbol{u}|\right)u, \quad (19.3b)$$
$$\frac{\partial}{\partial t}\left(\frac{1}{\varepsilon}\bar{\rho}w\right)+\frac{1}{r}\frac{\partial}{\partial r}\left(\frac{1}{\varepsilon^2}r\bar{\rho}uw\right)+\frac{\partial}{\partial z}\left(\frac{1}{\varepsilon^2}\bar{\rho}ww\right)$$
$$=\bar{\mu}\left[\frac{1}{r}\frac{\partial}{\partial r}\left(r\frac{\partial w}{\partial r}\right)+\frac{\partial^2 w}{\partial z^2}\right]-\frac{\partial p}{\partial z}+\mathrm{Gr}\Theta$$
$$-B\left(\frac{1}{\mathrm{ReDa}}+\frac{\mathrm{Fs}}{\mathrm{Da}}|\boldsymbol{u}|\right)w, \quad (19.3c)$$
$$\bar{\rho}\bar{c}_p\frac{\partial\Theta}{\partial t}+\frac{1}{r}\frac{\partial}{\partial r}(r\bar{\rho}u\Theta)+\frac{\partial}{\partial z}(\bar{\rho}w\Theta)$$
$$=\frac{1}{\mathrm{Pr}}\bar{k}\left[\frac{1}{r}\frac{\partial}{\partial r}\left(r\frac{\partial\Theta}{\partial r}\right)+\frac{\partial}{\partial z}\left(\frac{\partial\Theta}{\partial z}\right)\right], \quad (19.3d)$$

where $\bar{\rho}=\frac{\rho_e}{\rho_f}$, $\bar{\mu}=\frac{\mu_e}{\mu_f}$, $\bar{c}_p=\frac{c_{pe}}{c_{pf}}$, $\bar{k}=\frac{k_e}{k_f}$.

19.3.3 Numerical Scheme

The momentum equations (19.3b,c) and energy equation (19.3d) are solved using an in-house-developed finite-volume algorithm [19.60, 61]. The above conservation equations (19.3b–d) can be written in the following general form

$$\frac{\partial}{\partial t}(rc\bar{\rho}\phi)+\frac{1}{r}\frac{\partial}{\partial r}(dr\bar{\rho}u\phi)+\frac{\partial}{\partial z}(d\bar{\rho}w\phi)$$
$$=\frac{\partial}{\partial r}\left(r\Gamma\frac{\partial\phi}{\partial r}\right)+\frac{\partial}{\partial z}\left(r\Gamma\frac{\partial\phi}{\partial z}\right)+r(S_C+S_p\phi), \quad (19.4)$$

where ϕ is the generalized variable, Γ is the diffusion coefficient, and S_C is the volumetric source. The coefficients are defined as

$$c=\frac{1}{\varepsilon},\quad d=\frac{1}{\varepsilon^2},\quad \Gamma=\bar{\mu},\quad S_C=-\frac{\partial p}{\partial r},$$

and

$$S_p=-B\left(\frac{1}{\mathrm{ReDa}}+\frac{\mathrm{Fs}}{\mathrm{Da}}|\boldsymbol{u}|\right)-\frac{1}{r^2}\ \text{for (19.3b)}$$
$$(\phi=u);$$
$$c=\frac{1}{\varepsilon},\quad d=\frac{1}{\varepsilon^2},\quad \Gamma=\bar{\mu},\quad S_C=-\frac{\partial p}{\partial z}+\mathrm{Gr}\Theta,$$

and

$$S_p=-B\left(\frac{1}{\mathrm{ReDa}}+\frac{\mathrm{Fs}}{\mathrm{Da}}|\boldsymbol{u}|\right)\ \text{for (19.3c)}\ (\phi=w);$$
$$c=\bar{\rho}\bar{c}_p,\quad d=1,\quad \Gamma=\frac{\bar{k}}{\mathrm{Pr}},\quad S_C=0,$$

and

$$S_p=0\ \text{for (19.3d)}\ (\phi=\Theta).$$

The grid used for this task is a structured trapezoidal mesh. For a typical primary point, the discretized form of the continuity (19.3a) in a generalized coordinate system (ξ,η) is then written as

$$\frac{\varepsilon\bar{\rho}-\varepsilon^0\bar{\rho}^0}{\Delta t}rJa\Delta\xi\Delta\eta$$
$$+\left[(r\bar{\rho}\alpha_\xi u_\xi)_e-(r\bar{\rho}\alpha_\xi u_\xi)_w\right]\Delta\eta$$
$$+\left[(r\bar{\rho}\alpha_\eta u_\eta)_n-(r\bar{\rho}\alpha_\eta u_\eta)_s\right]\Delta\xi$$
$$=S_{NO}\Delta\xi\Delta\eta, \quad (19.5)$$

where Δt is the time step, the curvature source term arising from the nonorthogonal grid $S_{NO}=[(r\bar{\rho}\beta_\xi u_\eta)_e-(r\bar{\rho}\beta_\xi u_\eta)_w]\times\Delta\eta+[(r\bar{\rho}\beta_\eta u_\xi)_n-(r\bar{\rho}\beta_\eta u_\xi)_s]\Delta\xi$, α_ξ and β_ξ are the primary area and the secondary area over the control-volume face, which is represented by $\xi=$ const, e.g., $\boldsymbol{u}\cdot\boldsymbol{e}^\xi h_\eta=\alpha_\xi u_\xi-\beta_\xi u_\eta$, where $\boldsymbol{e}^\xi$ is the contravariant base vector, and h_η is the scale factor. So, $\alpha_\xi=h_\xi h_\eta^2/(Ja)$ and $\beta_\xi=h_\xi h_\eta^2(\boldsymbol{e}_\xi\cdot\boldsymbol{e}_\eta)/(Ja)$ [19.60,61].

The momentum equations (19.3b,c) can be written as

$$\begin{aligned}&\frac{(rc\bar{\rho}\phi Ja - rc\bar{\rho}^0\phi^0 Ja^0)_P\Delta\xi\Delta\eta}{\Delta t}\\&+[(r\alpha_\xi J_\xi)_e-(r\alpha_\xi J_\xi)_w]\Delta\eta\\&+[(r\alpha_\eta J_\eta)_n-(r\alpha_\eta J_\eta)_s]\Delta\xi\\&=[r(S_C+S_p\phi)Ja+S_\phi]\Delta\xi\Delta\eta\,,\end{aligned}\tag{19.6}$$

where the curvature source term S_ϕ arises from the nonorthogonal grid, and is given by $S_\phi=[(r\beta_\xi J_\eta)_e-(r\beta_\xi J_\eta)_w]\Delta\eta+[(r\beta_\eta J_\xi)_n-(r\beta_\eta J_\xi)_s]\Delta\xi$. The flux components in the ξ and η directions are $J_\xi=d\bar{\rho}u_\xi\phi-\frac{1}{h_\xi}\Gamma\frac{\partial\phi}{\partial\xi}$ and $J_\eta=d\bar{\rho}u_\eta\phi-\frac{1}{h_\eta}\Gamma\frac{\partial\phi}{\partial\eta}$, respectively.

Multiplying (19.5) by $d\phi$, subtracting it from (19.6), and multiplying the resulting equation by $(1+i)$ yields the discretized equation for u and v in the control volume [19.55, 61]

$$\begin{aligned}a_P\phi_P=&\,a_E\phi_E+a_W\phi_W+a_N\phi_N+a_S\phi_S\\&-(a_E+a_W+a_N+a_S)_{conv}\phi_P+S_\phi\\&-dS_{NO}\phi+b\,,\end{aligned}\tag{19.7}$$

where

$$\begin{aligned}a_p=&\,(1+i)rc\bar{\rho}Ja\frac{1}{\Delta t}-(1+i)rJaS_p\\&+(a_E+a_W+a_N+a_S)_{cond}\,,\\b=&\,(1+i)rc\bar{\rho}^0Ja^0\frac{1}{\Delta t}\phi_p^0+(1+i)rJaSc+iS_{conv}\,,\end{aligned}$$

and

$$\begin{aligned}S_{conv}=&\,a_E\phi_E^0+a_W\phi_W^0+a_N\phi_N^0+a_S\phi_S^0\\&-(a_E+a_W+a_N+a_S)\phi_P^0+S_\phi^0-dS_{NO}\phi^0\,.\end{aligned}$$

The subscripts *conv* and *cond* indicate convective and conductive terms, respectively. The discretization in time is first order when $i=0$ and second order when $i=1$.

The momentum equations can be written as

$$A_Pu_P=(H_u)_P-(1+i)\frac{\partial p}{\partial r}\,,\tag{19.8a}$$

$$A_Pw_P=(H_w)_P-(1+i)\frac{\partial p}{\partial z}\,,\tag{19.8b}$$

where the subscript P represents the central point of a finite volume

$$\begin{aligned}A=&\,(1+i)c\bar{\rho}\frac{1}{\Delta t}-(1+i)S_p\\&+\left[(a_E+a_w+a_N+a_S)_{cond}\right]/(rJa)\,,\\(H_u)_P=&\left[a_Eu_E+a_Wu_W+a_Nu_N+a_Su_S\right.\\&-(a_E+a_W+a_N+a_S)_{conv}\phi_P+S_\phi\\&\left.-dS_{NO}\phi+b'\right]/(rJa)\,,\end{aligned}$$

and b' represents b without the pressure term. The velocity component and pressure gradient in ξ direction are, respectively,

$$u_\xi=\frac{r'_\xi u+z'_\xi w}{h_\xi}\,,\tag{19.9a}$$

$$\frac{\partial p}{\partial\xi}=\frac{\partial p}{\partial r}r'_\xi+\frac{\partial p}{\partial z}z'_\xi\,,\tag{19.9b}$$

where the prime denotes the differential. By setting $(1+i)p$ as p, combining (19.8a,b), and using the procedures for pressure treatment as in [19.55, 62], we obtain

$$\begin{aligned}(u_\xi)_P=&\frac{(H_u-A_Pu_P)r'_\xi+(H_w-A_Pw_P)z'_\xi-\left(\frac{\partial p}{\partial\xi}\right)_P}{h_\xi A_P}\\&+(u_\xi)_P^0\,,\end{aligned}\tag{19.10}$$

and

$$\begin{aligned}(\bar{\rho}u_\xi\alpha_\xi)_P=&\left[(H_u-A_Pu_P)r'_\xi+(H_w-A_Pw_P)z'_\xi\right.\\&\left.-\left(\frac{\partial p}{\partial\xi}\right)_P\right]\bar{\rho}\alpha_\xi/(h_\xi A_P)+(\bar{\rho}u_\xi\alpha_\xi)_P^0\,.\end{aligned}\tag{19.11}$$

Substituting the above into the continuity equation, we obtain the pressure equation as

$$a_Pp_P=a_Ep_E+a_Wp_W+a_Np_N+a_Sp_S+b\,,\tag{19.12}$$

where

$$\begin{aligned}a_E=&\,D_e\Delta\eta\,,\\a_P=&\,a_E+a_W+a_N+a_S\,,\\D_e=&\,[\bar{\rho}\alpha_\xi/(h_\xi A)]_e\,,\\b=&-\{[(H_\xi-Au_\xi)h_\xi]_eD_e+(\rho u_\xi\alpha_\xi)_e^0\}\Delta\eta\\&+\{[(H_\xi-Au_\xi)h_\xi]_wD_w+(\rho u_\xi\alpha_\xi)_w^0\}\Delta\eta\\&-\{[(H_\eta-Au_\eta)h_\eta]_nD_n+(\rho u_\eta\alpha_\eta)_n^0\}\Delta\xi\\&+\{[(H_\eta-Au_\eta)h_\eta]_sD_s+(\rho u_\eta\alpha_\eta)_s^0\}\Delta\xi\\&+S_{NO}\,,\end{aligned}$$

and

$$H_\xi=\frac{H_ur'_\xi+H_wz'_\xi}{h_\xi}\,.$$

For the temperature equation, profiled temperature boundary conditions are applied on the outer surfaces of the autoclave. The temperature profile set on the sidewall of the autoclave is $T=T_H$, $z<H_B-0.5\delta_T$; $T=T_H-(T_H-T_L)(z-H_B+0.5\delta_T)/\delta_T$; $H_B-0.5\delta_T\le$

$z < H_B + 0.5\delta_T$; $T = T_L$, $z > H_B + 0.5\delta_T$, where H_B is the height of the baffle and δ_T is the length of the portion of the wall where the temperature changes from T_H to T_L. The top and bottom of the autoclave are considered adiabatic. The temperature distribution is considered axisymmetric, $\partial T/\partial r = 0$, at $r = 0$.

For solving the momentum equations and the pressure equation inside the autoclave, the fluid boundaries were searched inside the autoclave in the r and z directions, respectively [19.55]. For example, when solving the equations using the tridiagonal matrix algorithm (TDMA) method, the fluid boundaries were searched in the r or z direction separately, and the equations were solved in different intervals of fluid space in this direction. In this way, the fluid field was obtained inside the autoclave that contains different shapes of baffles and seeds. A mesh size of 302×77 was used in the simulation, and the nondimensional time step was $\Delta t = 10^{-6}$.

19.4 Process Simulations

19.4.1 Typical Flow Pattern and Growth Mechanism

For the solubility curve with a positive coefficient of temperature, the growth zone is maintained at a lower temperature than that in the dissolving zone, thus the nutrient becomes supersaturated in the growth zone. The critical properties of ammonia are $T_c = 405.5\,\mathrm{K}$ and $P_c = 112.8\,\mathrm{bar}$. The reduced pressure and reduced temperature at 2 kbar and 250 °C for the growth condition in [19.39] are $P_r = 2000/112.8 = 17.7$ and $T_r = 523/405.5 = 1.3$. For $P_r = 10$ and $T_r = 1.3$, the viscosity and conductivity of ammonia are $\mu/\mu_1 = 4.3$ and $k/k_1 = 5.0$, where μ_1 and k_1 are the dynamic viscosity and the thermal conductivity at 250 °C and atmospheric pressure [19.63].

Solubility data of GaN for mineralizers of KN_3, KNH_2/KI were obtained in [19.39,55]. The solubility of GaN for mineralizer of 1.6 M KN_3 is high in the temperature range of 300–450 °C. It seems that, by using azide as mineralizer, a high solubility of GaN can be obtained at low growth temperatures. For 0.8 M KNH_2/KI, the solubility is low in the range of 350–550 °C. Mineralizer of 2–6 M KNH_2 or $NaNH_2$ was used to increase the solubility of GaN [19.55].

For charge particle size of 0.6 mm, $T_H - T_L$ applied on the sidewall of 50 K, and $\delta_T = 1\,\mathrm{cm}$, the aspect ratio, Grashof number, Prandtl number, Darcy number, and Forchheimer number for the system in [19.39] are $A = 40$, $\mathrm{Gr} = 4.46 \times 10^6$, $\mathrm{Pr} = 0.73$, $\mathrm{Da} = 2.2 \times 10^{-5}$, and $\mathrm{Fs} = 2.6 \times 10^{-3}$, respectively. The baffle has an opening of 30% in the cross-sectional area, including the central opening of 20% and a gap between the baffle and autoclave of 10% in the cross-sectional area. The reference velocity and time scale are $u_0 = 3.5 \times 10^{-5}\,\mathrm{m/s}$ and $t_0 = 131\,\mathrm{s}$, respectively.

The flow pattern is shown in Fig. 19.13a. There are two flow cells rotating in different directions under the baffle. The flow goes up along the sidewall driven by the buoyancy, which is caused by the high temperature applied on the lower part of the sidewall. Some flow penetrates through the gap between the baffle and the sidewall of the autoclave, and some flow goes inward along the baffle and then downward near the central opening of the baffle. The flow in the porous layer is much weaker than that in the fluid layer. The modified Grashof number can be used to measure the flow strength in the porous charge, $\mathrm{Gr}^* = \mathrm{Gr} \cdot \mathrm{Da}$. In this case, the modified Grashof number is $\mathrm{Gr}^* = 98.2$. The fluid flow cannot penetrate the porous layer, and heat and mass transfer in the porous layer are mainly by conduction and diffusion, respectively.

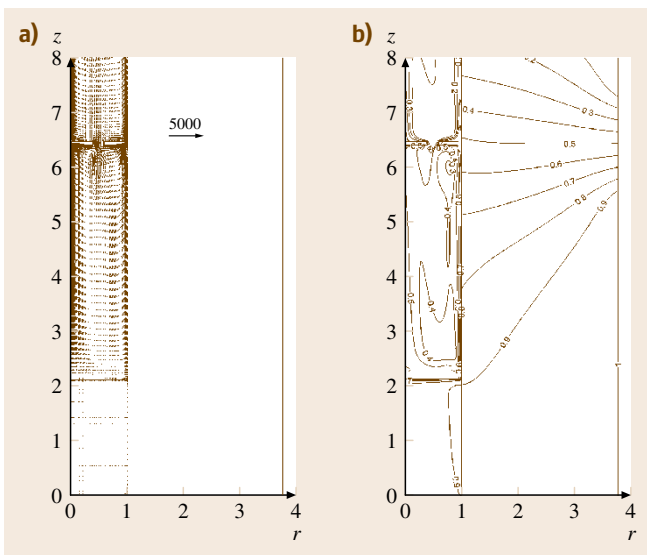


Fig. 19.13 (**a**) Fluid flow and (**b**) temperature distribution in an autoclave with internal diameter of 0.932 cm, internal height of 18.4 cm, particle size of 0.6 mm, and $\Delta T = 50\,\mathrm{K}$ (after [19.55])

The temperature distribution is shown in Fig. 19.13b. The temperatures in the porous charge are almost the same as the high temperature T_H applied on the lower part of the sidewall of the autoclave. A large temperature gradient occurs near the fluid–charge interface. The aspect ratio in this case is 40 and the temperatures at $z > 20$ within the autoclave are almost the same as the low temperature T_L applied on the upper part of the sidewall of the autoclave.

19.4.2 Effect of Permeability on the Porous Bed

The optimum precursor sizes found in the ZnO growth experiments have been confirmed by numerical simulations [19.55]. When the charge particle size is increased from 0.6 mm to 3 mm, the Darcy number in the charge increases by 25 times and the modified Grashof number is $Gr^* = 2455$. Figures 19.14a and 19.14b show the flow pattern and temperature distribution in the autoclave, respectively. Significant convective effects are seen occurring in the charge (Fig. 19.14a), and the velocity is large in the porous layer. There are again two flow cells below the baffle. The flow moves upward through the gap between the baffle and the sidewall, and fluid flow is oscillating in the central hole. The flow structure above the baffle is complex and oscillating.

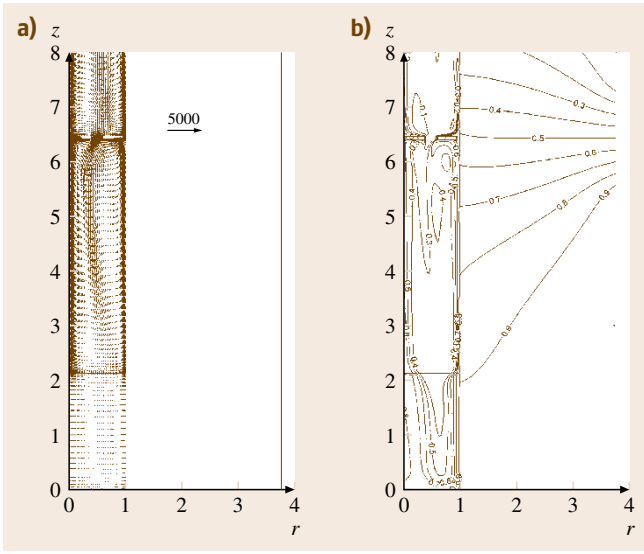


Fig. 19.14 (a) Fluid flow and (b) temperature distribution in a growth system with particle size of 3 mm and $\Delta T = 50$ K. The autoclave has an internal diameter of 0.932 cm and internal height of 18.4 cm (after [19.55])

As can be seen from Fig. 19.14b, the temperature distribution in the charge is in the convection mode, and large temperature gradients appear near the interface between the charge and the sidewall of the autoclave. It is obvious that the particle size is an important factor to consider for successful growth of GaN by the ammonothermal method.

The constraints for ammonothermal growth include dissolving of the charge, nucleation on the sidewall, transfer of nutrient from charge to seed, and growth kinetics. Mass transfer between the charge and the fluid layer is important for successful growth. The flow strength in the fluid layer depends on the Grashof number, which is proportional to the temperature difference on the sidewall and the cube of the internal radius of the autoclave. Flow in the charge layer depends on the product of the Grashof and Darcy numbers, which is proportional to the square of the average diameter of particles. The flow strength in the porous layer is increased by increasing the size of the particles, or by putting particles in bundles as in the hydrothermal growth.

19.4.3 Baffle Design Effect on Flow and Temperature Patterns

The optimization of the baffle design has been performed numerically in [19.62] for the growth system used in [19.64] which has an internal diameter of 0.875 inch (2.22 cm), external diameter of 3 inch (7.62 cm), internal height of 14 inch (35.56 cm), and external height of 15 inch (38.10 cm) (Tem-Press MRA 378R with a volume of 134 ml) [19.64]. The thickness of the sidewall of the autoclave is 1 inch (2.54 cm). The baffle is located at a distance of 6 inch (15.24 cm) from the bottom of the autoclave. The charge particle size is 0.6 mm. $\Delta T = 50$ K is applied on the sidewall and the baffle thickness is 0.28 mm. The aspect ratio, Grashof number, Prandtl number, Darcy number, and Forchheimer number are, $A = 16$, $Gr = 6.0 \times 10^7$, $Pr = 0.73$, $Da = 3.8 \times 10^{-6}$, and $Fs = 1.1 \times 10^{-3}$, respectively. The reference velocity and time scale are $u_0 = 1.4 \times 10^{-5}$ m/s and $t_0 = 748$ s, respectively.

Figure 19.15a shows the flow pattern for a system with a baffle opening of 15% in the cross-sectional area, e.g., 10% in the central hole and 5% in the ring opening between the baffle and the sidewall of the autoclave. The flow is very weak in the porous layer, and the flow in the fluid layer is much stronger. The modified Grashof number, which is used to measure the flow strength in the porous charge, is $Gr^* = 228$. Thus, heat

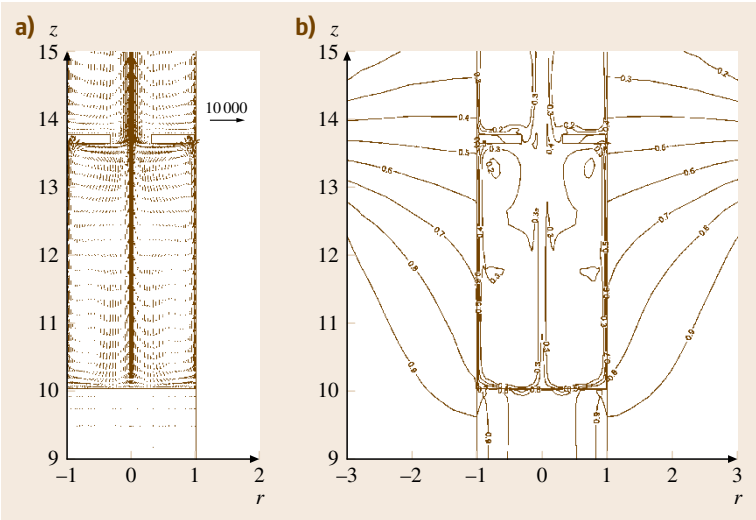


Fig. 19.15 **(a)** Fluid flow and **(b)** temperature field in a system with a baffle opening of 15% in the cross-sectional area (central opening of 10% and ring opening of 5%) (after [19.62])

and mass transfer in the porous layer is mainly by conduction and diffusion. This will constrain the nutrient transport between the charge and fluid layer, and cause nutrient deposition on the sidewall of the autoclave near the fluid–charge interface, as observed in experiments.

The temperature distribution is shown in Fig. 19.15b. The charge has a temperature of T_H as applied on the lower part of the autoclave. A large temperature gradient exists at the fluid–charge interface and the fluid–autoclave interface. Supersaturation in the fluid is related to the temperature difference between the charge and the fluid layer. A large temperature gradient at the fluid–charge interface may cause a large supersaturation, and subsequently nucleation near the fluid–charge interface.

The mixing of flow across the baffle has been investigated. Figure 19.16 shows the changes of the vertical velocity at the center of the central hole opening in certain time period. The patterns of oscillations of velocity are repeatable for a longer time period than that

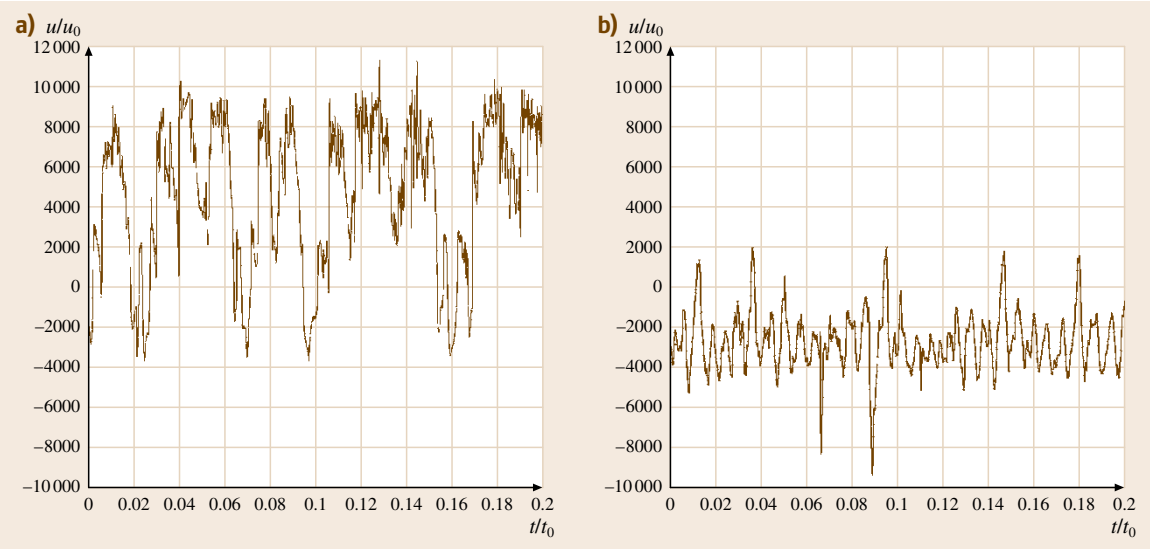


Fig. 19.16a,b Changes of the vertical velocity with time at the center of the central hole opening for baffle with **(a)** opening of 15% in the cross-sectional area, and **(b)** opening of 20% (after [19.62])

shown in Fig. 19.16. The heating on the bottom and cooling on the top promote Bénard-type convection in the fluid layer, which interacts with the vertical temperature boundary layer near the sidewall of the autoclave, causing the unsteady and oscillatory flow. For a long time period, it is observed that the amplitude of velocity oscillation in the center of the central hole is larger in the case of the 15% opening (Fig. 19.16a) than in the case of the 20% opening (Fig. 19.16b). The vertical velocity in the center of the central hole changes direction over time in the case of the 15% opening, while it is negative most of the time in the case of the 20% opening. In the case of the 20% opening, the fluid can go up through the ring opening of 10% in the cross-sectional area and return back through the central opening of the same size as the ring opening, so the flow is mixed more thoroughly across the baffle. Oscillation of the vertical velocity in the central hole can be decreased by reducing the difference between the sizes of the central opening and ring opening.

19.4.4 Effect of Porous Bed Height on the Flow Pattern

The influence of the height of the porous bed on transport phenomena in a hydrothermal system was investigated in [19.59]. Since the hydrothermal growth is a very slow process, it can be considered as quasisteady, and the flow and temperature fields for given porous bed height under steady-state condition were obtained in [19.59]. Note that the height of the porous bed decreases as the polycrystalline charge dissolves and the solute moves up for deposition on the seed. Evidently the flow and temperature patterns will change with the porous bed height. *Chen* et al. [19.59] examined the effect of decreasing height in a case with $A = 3$, $\eta = 0.4$, $\mathrm{Pr} = 1$, $\mathrm{Da} = 10^{-4}$, and $\mathrm{Gr} = 10^5$, where η denotes the ratio of the porous bed height and the overall height.

As shown in Fig. 19.17a, a small portion of the hot surface lies in the fluid region, which promotes a local recirculation on top of the porous layer because of the increased buoyancy effect in this region. The small cell now acts as a buffer restricting the fluid moving from the porous region to the fluid region. It gains fluid from both of the stronger cells and feeds back to them. When the Grashof number is low, the flow may show an axisymmetric pattern with two strong convective rolls and one weak cell. However, the axisymmetric nature of the flow field is completely destroyed at higher Grashof number. A convective roll may then appear in the central region directly above the porous bed and, depending on its location, the large convective rolls in the fluid region may shift. As can be expected, this does not influence the flow and temperature fields in the porous region in any appreciable manner as long as the Darcy number or permeability is low. From growth considerations, a change in flow pattern in the porous bed has no special meaning. However, a major shift in flow characteristics in the fluid region can significantly change the growth dynamics and quality of the crystal. The isotherm pattern is shown in Fig. 19.17b, which is distorted accordingly even though in the central region of the system.

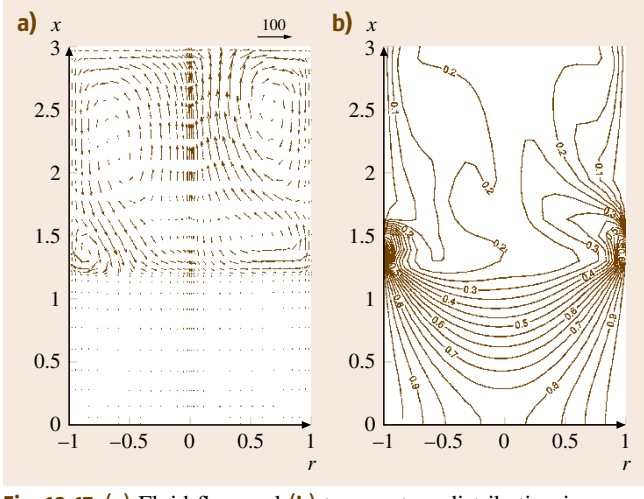


Fig. 19.17 (a) Fluid flow and (b) temperature distribution in a vertical cross-section of the autoclave; $A = 3$, $\eta = 0.4$, $\mathrm{Pr} = 1$, $\mathrm{Da} = 10^{-4}$, and $\mathrm{Gr} = 10^5$ ($\mathrm{Gr}^* = 10$) (after [19.59])

19.4.5 Simulation of Reverse-Grade Soluble Systems

For the ammonothermal growth of GaN with a retrograde solubility, the predetermined amount of GaN particles is loaded above the baffle inside an autoclave (Fig. 19.18). GaN seeds are hung on a wire below the baffle. In this case, the solubility of GaN has a negative coefficient with respect to temperature, so that the growth zone in the lower part is maintained at a higher temperature than that in the upper part. The baffle opening is used to control the mixing of nutrients in two

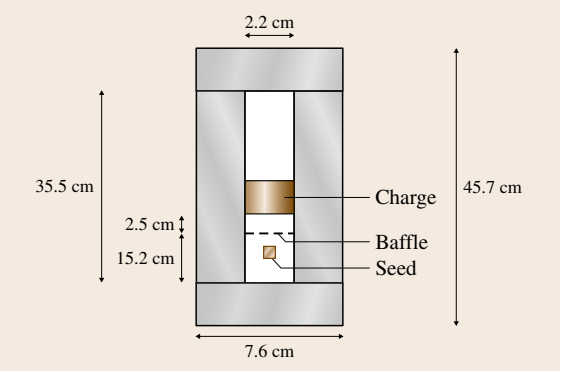


Fig. 19.18 Schematic of an ammonothermal growth system with retrograde solubility (after [19.65])

zones, and cause the transfer of nutrient from the upper part to the lower part.

By using a mineralizer of 2–3 M KNH_2, GaN has a retrograde solubility in ammonia as in [19.64]. The solubility of GaN in ammonia changes from 10% by weight to 2% if temperature increases from 350 °C to 600 °C. With a fill of 60–85% and temperature of 600 °C, pressure is in the range of 25–45 kpsi. A typical run takes 14–21 days and deposition can be observed both on the seeds and on walls of the autoclave.

Numerical studies were performed for an autoclave used in [19.64]. The baffle is located at a distance of 6 inch (15.24 cm) from the bottom of the autoclave. The charge of 4 inch in height is put 1 inch above the baffle, and the charge particle size is 0.6 mm. $\Delta T = 50$ K is applied on the sidewall and the baffle thickness is 0.28 mm.

Figure 19.19a shows the flow pattern for the growth system with retrograde solubility. The baffle openings are 15% of the cross-sectional area, including 10% in the central hole and 5% in the ring opening between the baffle and the sidewall of the autoclave. Since the GaN charge is put above the baffle, the flow is much stronger below the baffle, as shown in Fig. 19.19a. Highly oscillatory flow is observed across the central hole in the baffle. The flow in the central hole first moves downwards, sending nutrient to the growth zone at the bottom of the autoclave, then the flow moves upwards, sending exhausted fluid back to the dissolving zone in the porous layer. This process repeats with time. The opening of 15% causes very large flow oscillation across the baffle in this case.

The temperature distribution in the case of the retrograde solubility is shown in Fig. 19.19b. The temperature difference between the dissolving zone and growth zone is smaller than the temperature difference applied on the sidewall of the autoclave. A larger baffle opening means more fluid mixing across the baffle and less temperature difference between the two zones. In this case, the temperature across the baffle oscillates with time, and the magnitude of the oscillation of temperature is very large for baffle opening of 15%.

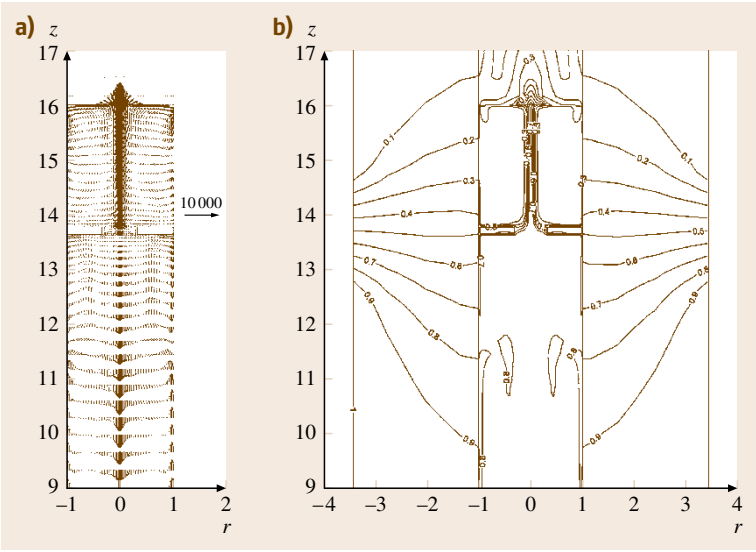


Fig. 19.19 (a) Fluid flow and (b) temperature distribution in an ammonothermal system with a retrograde solubility. Baffle opening is chosen as 15% in cross-sectional area (central opening of 10% and ring opening of 5%) (after [19.65])

19.5 Hydrothermal Growth of ZnO Crystals

19.5.1 Growth Kinetics and Morphology

Figure 19.20 shows the growth planes for hydrothermal zinc oxide crystals. Hydrothermal crystals are highly faceted due to the slow growth rates and lack of confinement during growth. Because each facet has an associated free energy, crystal growth rates can differ for different facets. Hydrothermal ZnO in an alkaline medium grows with the following facets: (0001) and $(000\bar{1})$ monohedra (C^+ and C^- planes, respectively) and the six $(10\bar{1}0)$ prismatic faces (M planes). The six $(10\bar{1}1)$ pyramid faces (P planes) also can form under certain conditions, which will be describe in Sect. 19.5.2. *Laudise* and *Ballman* first observed the anisotropic growth rate on both spontaneous crystallites and crystals grown on seeds in 1 M NaOH [19.33]. ZnO crystals grown on a C-plane seed and a M-plane seed are shown in Fig. 19.20.

Growth on the C^+ face is always faster than on the C^- face in hydroxide solutions above 1 M. Typical growth rates for 6 M KOH and 1 M LiOH are

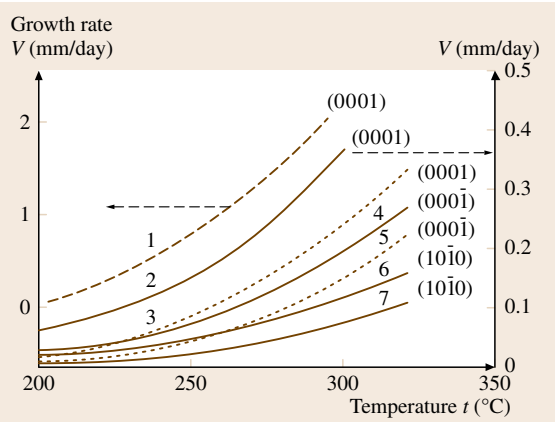


Fig. 19.21 Growth rates of the faces of the monohedra and the $\{10\bar{1}0\}$ prism of ZnO single crystals in alkaline solutions as a function of temperature: (1) 5 M KOH and (2–7) 5.15 M KOH + 1.2 M LiOH as functions of temperature. *Solid lines* correspond to $\Delta t = 75\,^{\circ}\mathrm{C}$; *dashed lines* to $\Delta t = 50\,^{\circ}\mathrm{C}$ (after [19.67])

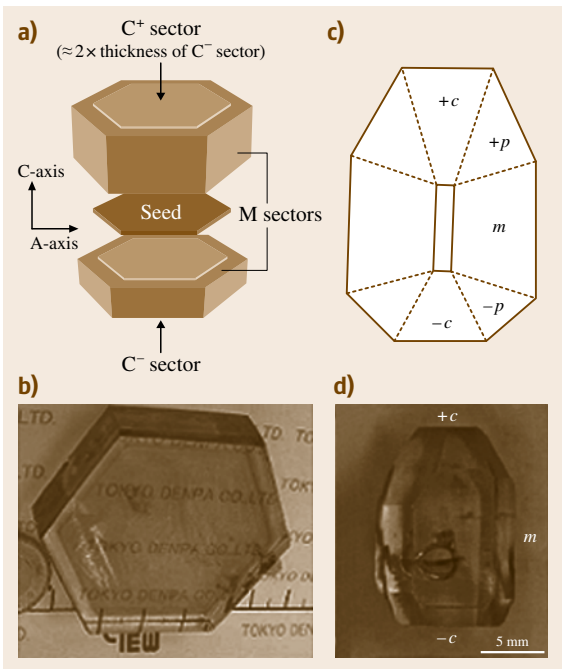


Fig. 19.20a–d Hydrothermal ZnO: **(a)** schematic and **(b)** crystal formed by growth on C-plane seed (after [19.13]), **(c)** schematic and **(d)** crystal formed by growth on M-plane seed (after [19.66])

0.45 mm/day in the C^+ direction, and 0.22 mm/day in the C^- direction for growth on C-plane seeds [19.24]. Growth rates on M-plane seeds average 0.2 mm/day in the direction normal to the M-plane [19.33]. *Demianets* et al. measured the growth kinetics on the different crystallographic faces by varying the type and concentration mineralizer, growth temperature, and temperature difference between the dissolution and crystallization zones [19.67]. Figure 19.21 shows more detailed kinetics of ZnO growth as a function of temperature. Note the effect that the addition of lithium, which improves the perfection of the ZnO crystal, has in decreasing the growth rate.

The authors went on to determine the elementary surface layers for the possible growth facets of ZnO. The elementary surface layers were then used to determine the relative theoretical growth velocities under ideal conditions (*the absence of any additional components in the crystallization medium*) for the different crystallographic faces of ZnO. The relationships of the velocities are

$$V(10\bar{1}0) < V(000\bar{1}) \sim V(0001) < V(10\bar{1}1) < V(10\bar{1}2) < V(1\bar{1}20)\,.$$

The sequence would be reversed to characterize the prevalence of the faces in the formed crystal. The ideal

velocities above would form simple shapes such as monohedra and prisms but water, a polar solvent, adds a great deal of complexity to the kinetics of crystal growth.

The anisotropy of the growth rates for the various crystal facets is related to the charge distribution on the facets and the charge of the ions in solution. Several researchers have studied the solubility and thermodynamic parameters of aqueous Zn species for natural hydrothermal systems. *Khodakovsky* and *Yelkin* concluded that $Zn(OH)_4^{2-}$ is the dominant species in alkaline solution at the high temperatures and high pH values at which bulk crystals are grown [19.70]. *Bénézeth* et al. investigated solubility of zinc oxide in 0.03–1.0 M sodium trifluoromethanesulfonate solutions to determine thermodynamic properties of the transport species in dilute acidic and alkaline solutions solutions [19.60, 71]. The Gibbs free energy of formation, entropy, and enthalpy at 25 °C and 1 atm were determined for Zn^{2+}, $Zn(OH^+)$, $Zn(OH)_2^0$, and $Zn(OH)_3^-$ by employing a hydrogen electrode concentration cell and periodic sampling of cell potentials. Solubility data at temperatures up to 200 °C for $Zn(OH^+)$, $Zn(OH)_2^0$, and $Zn(OH)_3^-$, and at temperatures up to 290 °C for Zn^{2+}, were also obtained. The authors concluded that $Zn(OH)_4^{2-}$ was the predominant species in OH^- solutions above 0.1 M NaOH. *Wang* and *Li* et al. performed systematic studies of the morphology and growth rates of zinc oxide powder in alkaline solutions [19.68, 69, 72]. Starting with $Zn(OH)_2$ colloids as nutrient, they investigated morphological changes as a function of pH (Fig. 19.22).

The studies assumed that $Zn(OH)_4^{2-}$ growth units were the predominant species in solution when hydroxide colloids were dissolved. These growth units have a tetrahedral form and charge distribution similar to those of ZnO, which itself is a series of tetrahedra (Fig. 19.23). The corner (point) of a zinc oxide tetrahedron can bind with three hydroxide growth units, the edge with two growth units, and the face of the tetrahedron with only one growth unit. The viscosity of the hydrothermal growth solution is low, so the crystal interface structure plays a large role in kinetics. Thus analysis of Fig. 19.23 would predict the following relative growth rates under ideal conditions

$$V\langle 0001\rangle > V\langle 01\bar{1}\bar{1}\rangle > V\langle 0\bar{1}10\rangle > V\langle 01\bar{1}1\rangle > V\langle 000\bar{1}\rangle \,.$$

The hydroxide growth units cluster together by dehydration. In strong alkali solution these clusters are shielded by ions such as Na•O^-, shielding the growth units and slowing down growth. Wang et al. contend that these mechanisms account for the growth rates and shape of bulk zinc oxide crystals in strong alkali solutions. *Demianets* and *Kostomarov* proposed a similar mechanism, but argued that $Zn(OH)_4^{2-}$ dissociates into $ZnO_2^{2-} + 2H^+$, and that the ZnO_2^{2-} concentration increases with increasing pH [19.26]. Reaction of one ZnO_2^{2-} with the zinc surface of the crystal allows two ZnO units to form, whereas reaction on the oxygen

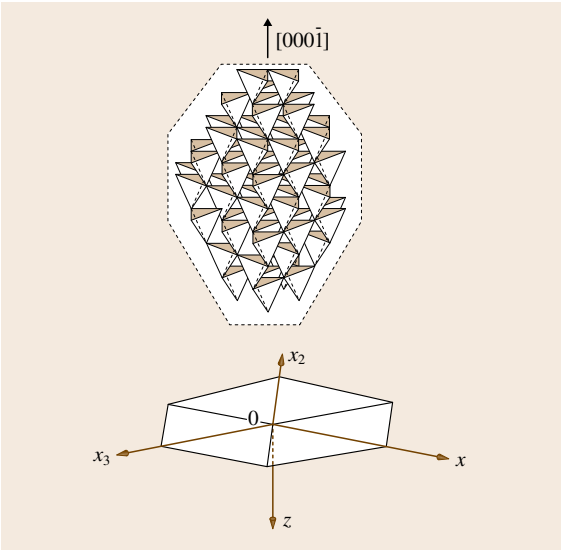


Fig. 19.23 ZnO crystal structure image represented in the form of the coordination tetrahedron along the x-direction (C^- surface made up of flat faces at top) (after [19.69])

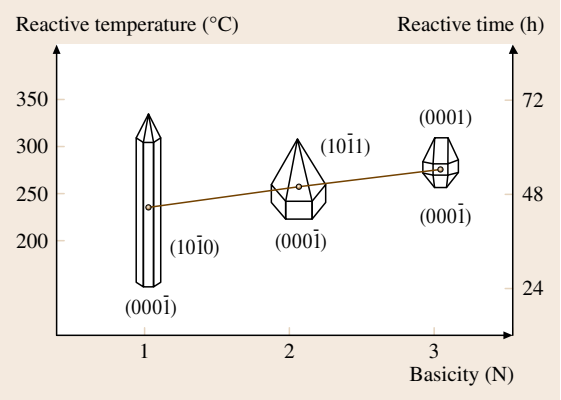


Fig. 19.22 Morphological changes of ZnO crystallites with increasing pH of the growth solution (after [19.68])

surface allows only one ZnO unit because of charge compensation.

Addition of lithium to the solution, as hydroxide or carbonate, improves the quality of the bulk zinc oxide crystals but also reduces the growth rate in the (0001) facet while increasing the rate on the $(10\bar{1}0)$ facets [19.67, 73]. This may be due to the shielding mechanism mentioned above. *Kuz'mina* et al. grew ZnO crystals grown in KOH solutions that had higher structural quality but more highly faceted than those grown in NaOH solutions [19.27]. *Suscavage* et al. used a 3 M NaOH:1 N KOH:0.1–0.5 N Li_2CO_3 solution which produced ZnO crystals with low defect densities and less P-plane faceting than KOH-grown crystals [19.21]. The mixed NaOH–KOH solvent had the added benefit of being less corrosive than KOH solutions. The crystal shown on the left-hand side in Fig. 19.20 [19.13] has negligible P-plane faceting and fits the kinetic models of Wang and Demainets discussed before. The low impurity levels in these crystals, high levels of lithium, and growth on fully faceted C-plane seeds may have suppressed formation of the P-plane in these crystals.

Sakagami found that hydrothermal zinc oxide crystals have tens of ppm excess zinc [19.25]. He therefore added H_2O_2 as an oxidizer; excess zinc was reduced to 1–2 ppm. The addition of an oxidizer such as hydrogen peroxide slows the growth rate on all faces, especially the C^- facet [19.27]. Manganese and nickel had no effect on the kinetics but did color the crystals red and green, respectively. No effect of these dopants on the electrical resistance could be discerned [19.27]. Addition of NH_4^+ increased the growth rate on the $(10\bar{1}0)$ facets, but crystal quality was degraded [19.27]. *Demianets* et al. published a more detailed paper on the effect of Li^+ and several of the divalent and trivalent metals (Co^{2+}, Fe^{2+}, Mn^{2+}, Fe^{3+}, Mn^{3+}, Sc^{3+}, In^{3+}) on growth kinetics and morphology of hydrothermal ZnO [19.67]. Figure 19.20 shows that, as metallic impurities are increased in the ZnO growth medium, P-plane facets are formed and C-axis growth rates decreases. The decrease in growth rates can be explained by the shielding effects impurities can have on the matrix compound (i. e. ZnO) as discussed in Sect. 19.2.

19.5.2 Structural Perfection – Extended Imperfections (Dislocations, Voids, etc.)

Because hydrothermal zinc oxide and quartz are both amphoteric single-component oxides, many insights into zinc oxide hydrothermal can be obtained from studies on hydrothermal quartz growth, which has been intensely investigated during the last 50 years. *Laudise* and *Barnes* [19.74] and *Armington* [19.75] have published excellent reviews on the growth of high-perfection quartz and on dislocation mechanisms. Extended imperfections that can be formed in both zinc oxide and quartz include the following:

- Seed veils and etch channels – small holes or channels filled with voids, water vapor or liquid, caused by etch tracks that form on seeds during initial growth

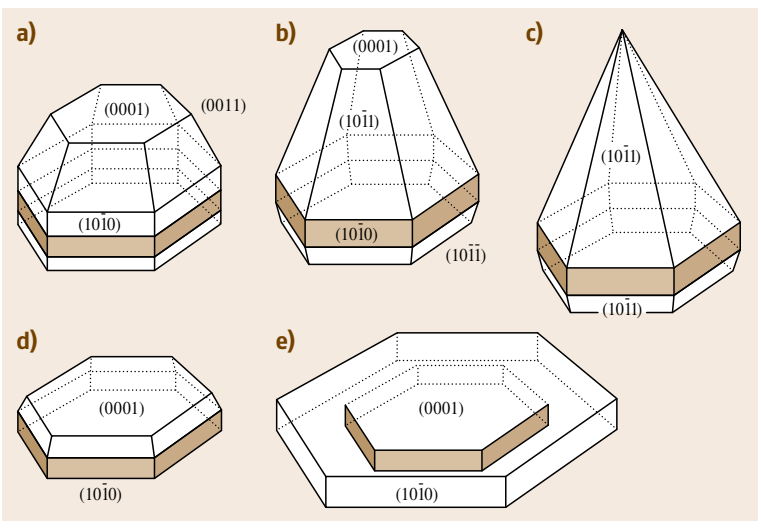


Fig. 19.24a–e Impurity effects on morphology of hydrothermal ZnO crystals **(a)** Li^+, **(b,c)** Fe^+, **(d)** Mn^{2+}, **(e)** In^{3+} (after [19.67])

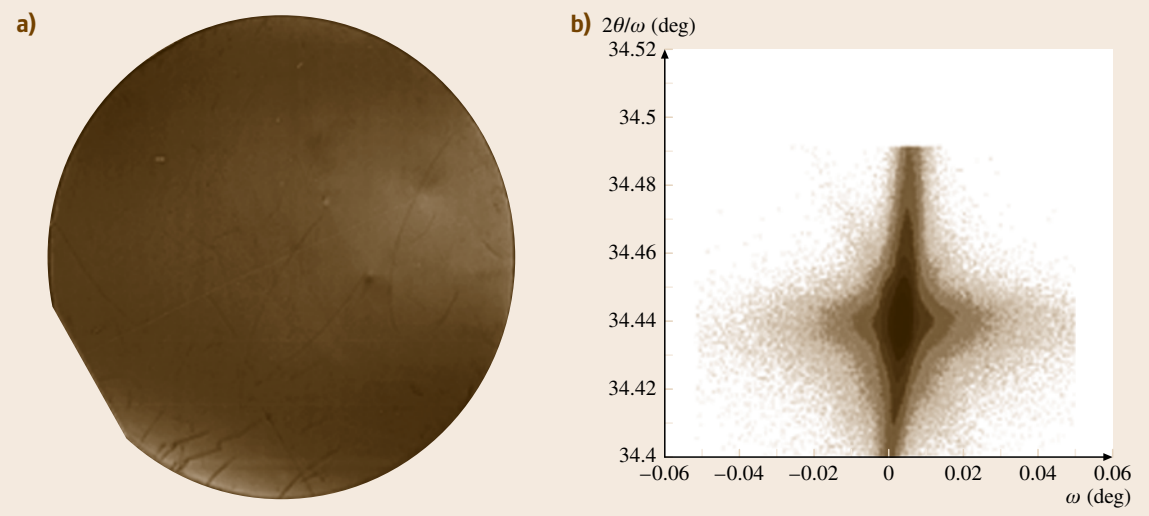


Fig. 19.25 **(a)** Reflection x-ray topograph of 2 inch ZnO wafer in C-axis projection. **(b)** (002) reciprocal-space map of corresponding wafer (after [19.13])

- Voids – small holes filled with air, water vapor or liquid; can occur whenever growth conditions change abruptly at the growth surface (impurity clusters, cracks, or crystalline particles from nutrient brought to growth interface by fluid flow)
- Crevice flaws – equivalent to dendritic growth in metals. Uneven or rough growth caused by a change of surface kinetics on growth faces. In extreme cases can cause gaps, cracks, and large numbers of dislocations
- Dislocations – equivalent to those in melt-grown bulk crystals. Strain-induced, because of impurity incorporation or intersection of growth planes, dislocations often propagate from seed into crystal
- Vertical etch channels – equivalent to micropipes that form in vapor-grown crystals. Dislocations decorated with impurities causing cylindrical voids that can reach from the seed to the surface of the crystal

All these imperfections have been observed in hydrothermal zinc oxide bulk crystals. *Laudise* and *Barnes* [19.74] stated that very small nutrient particle size resulted in low growth rates and flawed growth, and an optimal particle of several millimeters was determined, which was confirmed by *Chen* et al. [19.55] by numerical simulation. Addition of lithium, use of low dislocation-density seeds, and use of high purity nutrient also reduces the concentrations of most imperfections. Lithium may reduce imperfections by decreasing the surface free energy when lithium ions incorporate at the growth interface. Lithium may also limit the incorporation of H_2O and OH^- into the crystal lattice at the growth interface [19.76–78].

Figure 19.25 shows a reflection x-ray topograph and the (002) reflection reciprocal-space map for a low-defect commercial 2 inch-diameter (0001) ZnO wafer. Both measurements demonstrate very low defect concentrations in the wafer analyzed [19.13]. Commercial hydrothermal ZnO wafers have measured etch pit densities in the range of $100\,cm^{-2}$ and the full-width half-maximum (FWHM) of the rocking curve below 20 arcsec, another indication of the high crystallinity of hydrothermal ZnO wafers.

Synchrotron white-beam x-ray topography (SWBXT) in Laue configuration was performed on a series of crystals grown at AFRL-Hanscom [19.79]. To trace the growth history of the crystal, $(10\bar{1}0)$ crystal plates containing both the seed crystal and the bulk region were imaged. One set of topographs showed the usual propagation of edge dislocations from the seeds (Fig. 19.26). The growth sector (GS) boundary can also clearly be seen, marking a change of growth morphology.

On several other crystals the topographs revealed a capping phenomenon similar to that observed in KDP [19.80]. Figure 19.26b shows that the dislocation density is very high near the seed–crystal interface, revealing strain associated with growth initiation rather than dislocations propagating from the seed into the bulk. A growth band, possibly because of a fluctuation

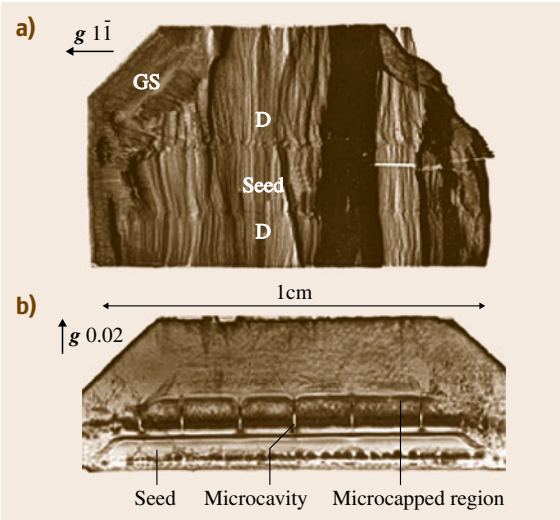


Fig. 19.26a,b Synchrotron white-beam x-ray topographs of ZnO seed–crystal interfaces (after [19.79]): **(a)** normal seed interface (D – dislocations, GS – growth sector boundary); **(b)** ZnO microcapped region, exhibiting microcavities and low dislocation generation above microcapped region in the C^+ direction

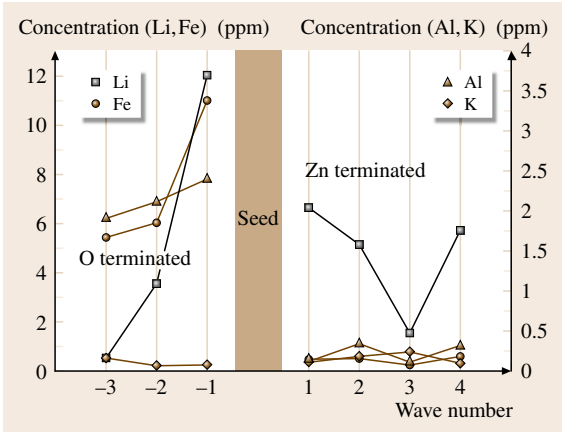


Fig. 19.27 Discharge mass spectroscopy (DMS) data for ZnO wafers sliced along the C^- and C^+ growth directions of a commercial 2 inch-diameter boule (after [19.13])

in the growth conditions, stops many of these dislocations. In some cases microcavities originating at the seed–crystal interface were observed; the cavities heal during subsequent growth, nucleating dislocations.

The cause of microcapping has not been established. One possible mechanism is seed etch-back during initial growth, due to fluctuations in the temperature gradient coupled with seed misalignment from C-plane orientation.

Surface studies on hydrothermal crystals showed the C^+ surface to be smooth and specular, with spiral hexagonal growth pyramids [19.27]. The C^- surface is more three-dimensional, with layer-like growth. The M-planes also have layered growth; the P-planes have a series of terraces. No in-depth study has addressed the mechanisms responsible for these various morphologies on the growth surfaces.

19.5.3 Impurities, Doping, and Electrical Properties

Generally the impurity concentrations in hydrothermal ZnO depend not only upon the purity of starting materials, but also upon the growth conditions (solution chemistry, growth temperature, etc.). Fe, Ag, Si, Na, Li, K, and Al are the primary impurities found in hydrothermal ZnO crystals. *Sekiguchi* et al. reported impurity concentration variations among crystals that were grown under various conditions of temperature and pressure but that otherwise were nominally identical [19.66]. Nonetheless, low-ppm impurity and sub-$10^{16}\,cm^{-3}$ donor/acceptor concentrations have been achieved [19.13, 21], demonstrating that hydrothermal ZnO crystals can have purities that rival or exceed the purities of bulk ZnO grown by other methods – purities, in fact, that rival or exceed those of III–V semiconductors such as InP and GaN. Figure 19.27 shows glow discharge mass spectroscopy (GDMS) data for ZnO wafers sliced along the C^- and C^+ growth directions of a commercial 2 inch-diameter boule [19.13]. High levels of lithium were incorporated in the crystal for growth in both the C^- and C^+ directions. The divalent and trivalent metals levels are two orders of magnitude lower in the wafers grown in the C^+ (Zn-terminated) growth direction.

The resistivity over a 2 inch hydrothermal wafer cut from the C^+ sector (Zn-terminated growth) was measured to be $380\,\Omega\,cm \pm 15\%$ [19.13].

Lithium is often added to hydrothermal solutions as hydroxide or carbonate because it improves crystallinity and morphology, as stated in the previous section. Li can therefore occur in concentrations of >10 ppm in hydrothermal ZnO [19.13, 21, 25, 66]; it has been employed to achieve resistivities as high as $10^{10}\,\Omega cm$ by compensating native donors [19.18]. Lithium is anathema to most electronic and optical device fabricators, who fear that Li – typically a fast diffuser – will incorporate into devices and thereby *poison* them. This may

not be an insurmountable obstacle for device applications, as Li apparently can be removed from ZnO by annealing in a zinc atmosphere [19.77]. Also, using appropriate mineralizer solutions, it is possible to obtain high-quality as-grown hydrothermal ZnO crystals that have sub-ppm Li concentrations [19.21].

In, Ga, and Al are shallow donors in ZnO [19.82, 83]. As mentioned above, Li occupying the Zn site is believed to be an acceptor (interstitial Li is believed to be a donor [19.77]); addition of Li or Cu increases the resistivity of ZnO after annealing in air or Zn [19.22,24,76,77], probably by compensating donors. The donor/acceptor properties of Fe^{2+} and Fe^{3+} in ZnO are not known. The role of hydrogen in ZnO is controversial: recent theoretical calculations predict it should be a shallow donor [19.84], in overall agreement with experimental measurements performed in the 1950s that associated increases in electrical conductivity with hydrogen incorporation (reviewed in [19.85]); however, in recent work on MOCVD-grown ZnO films, the conductivity increase was attributed to passivation of acceptors [19.86]. Hydrothermal growth of ZnO in an effective overpressure of H_2 was achieved by adding Zn powder to the growth solution; unfortunately only the carrier concentrations after annealing in vacuum or air ($2–5\times10^{15}\,cm^{-3}$), not carrier concentrations in as-grown ZnO, were reported [19.77].

Native defects such as oxygen vacancies or zinc interstitials have long been regarded as donor centers in ZnO (see, e.g., [19.84, 87] and references therein). In many cases, they may constitute the most numerous donor sites. *Sakagami*'s observation that the ZnO electrical resistance increased when an oxidizing agent was added to the hydrothermal growth solution (equivalent to growth in an oxygen overpressure) [19.25] is indirect evidence that many donor defects result from imperfect zinc–oxygen stoichiometry.

Semi-insulating behavior in hydrothermal ZnO has, as already noted, been achieved through lithium doping [19.83] and growth in an effective oxygen overpressure [19.25]. Semi-insulating behavior, with a net room-temperature free electron concentration of $\approx 2\times10^{12}\,cm^{-3}$, and electron mobility of $\approx 175\,cm^2/V\,s$, was observed [19.21]. The cause of this behavior was found to be a donor center located 340 meV below the conduction band; the microscopic nature of this donor is not understood.

The presence of large growth facets on hydrothermal ZnO crystals facilitates study of electronic properties as a function of crystallographic orientation and surface polarity. *Urbieta* et al. employed scanning tunneling microscopy and found clear differences in surface electronic structure that distinguished the C^+ (zinc-surface), C^- (oxygen-surface), and m (nonpolar surfaces) [19.88]. *Sakagami* et al. measured *I–V* and *C–V* characteristics on the crystallographic C^+, C^-, and m faces [19.89]. Along all crystallographic axes studied, they observed nearly ohmic behavior when surfaces were zinc-rich and rectifying behavior when surfaces were oxygen rich. The authors' judgment that *m*-sectors are more suitable than c^+ and c^- sectors for making electrical contacts, if confirmed, has potential significance for device fabrication that could stimulate interest in ZnO crystal growth on nonbasal plane.

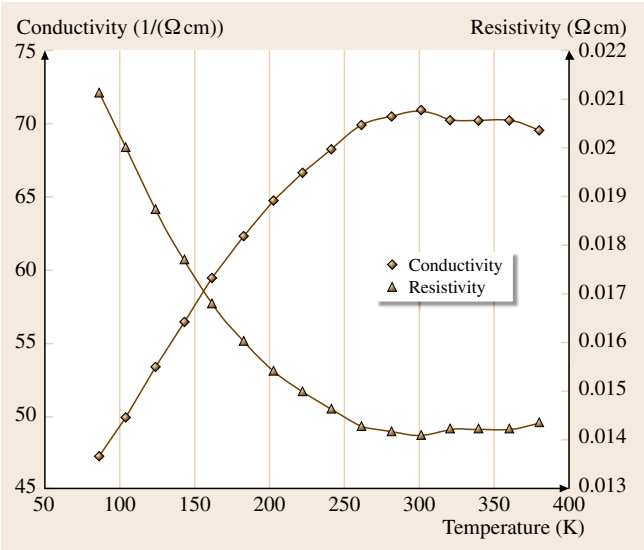


Fig. 19.28 Hall-effect data for indium-doped ZnO wafer (after [19.81])

Hydrothermal conducting indium-doped ZnO was grown using sintered zinc oxide powder that was mixed with a small percentage indium oxide [19.81]. As previously stated, growth rates were dramatically reduced in the C-axis (Fig. 19.23c). Conductivity measurements for a $5\times5\,mm^2$ In:ZnO sample is shown in Fig. 19.28. The conductivity achieved is adequate for most semiconductor device applications that would benefit from conducting substrates.

19.5.4 Optical Properties

The most sensitive indications of crystal quality often come from optical measurements at near-liquid-helium temperatures, where excitonic and other bands indicate the underlying quality (or lack thereof) of the material.

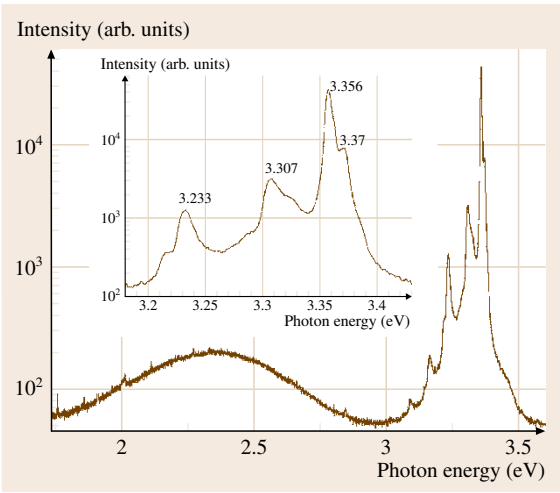


Fig. 19.29 Low-temperature broadband photoluminescence spectrum (after [19.13])

Broadband spectra at both high and low temperatures can provide useful information about impurities and native defects.

The broadband low-temperature photoluminescence (PL) spectrum of a 2 inch ZnO wafer is shown in Fig. 19.29. In addition to the UV band (excitonic and donor–acceptor bands at energies above 3 eV), there is a broad band centered at ≈ 2.3 eV. Similar broad extrinsic *orange* and *green* bands have been reported in several PL [19.90] and cathodoluminescence (CL) [19.91, 92] measurements of hydrothermal grown ZnO. Several authors have shown that the intensity of the UV band compared with the intensity of the broadband can provide qualitative information on the crystal quality of hydrothermal ZnO [19.92, 93].

Conflicting mechanisms have been advanced for the origin of the green band. *Reynolds* et al. compared the ZnO green band to the *yellow band* in GaN (a wurtzitic crystal having a bandgap similar to that of ZnO), whose origin remains a matter of debate, and concluded that both bands arise from a transition between a shallow donor and a deep level [19.94]. However, *Garces* et al. concluded, from electron paramagnetic resonance (EPR) and PL spectra of unannealed and annealed vapor-phase-grown ZnO, that ZnO green bands are caused by emission from Cu^{+} and Cu^{2+} ions, respectively [19.82].

Orange and green CL has been observed in the *m*, *c*, and *p* sectors of hydrothermal ZnO crystals. Strong green emission (in addition to near-band-edge emission, which is ignore for the purposes of this discussion) was observed from C^{+} (Zn-terminated) surfaces, and weak orange emission from C^{-} (oxygen-terminated) surfaces; green emission was observed from P^{-} surfaces (Zn-terminated) and orange emission from P^{+} (oxygen terminated) surfaces; and there was weak orange emission from the (nonpolar) M face [19.66]. Combining these and related observations with the growth kinetic models, *Sekiguchi* et al. [19.66] and *Urbieta* et al. [19.95, 96] associated the occurrence of ZnO green and orange CL bands with impurity incorporation efficiencies (during crystal growth) that the growth model attributes to the polarization state of ZnO sectors (c^{+}, c^{-}, *m*, etc.); similarly, UV and broadband luminescence efficiencies were associated with presumed incorporation rates of nonradiative recombination centers. In this vein, *Sekiguchi* et al. noted that orange emission was strongest in their sample that had the highest Li concentration and lower in a flux-grown crystal that contained virtually no Li; they also noted that use of H_2O_2 in the hydrothermal growth solution, which presumably lowered the concentration of oxygen vacancies, significantly reduced the orange emission [19.66]. An overview of visible luminescence in ZnO has more comprehensive information of the possible mechanisms

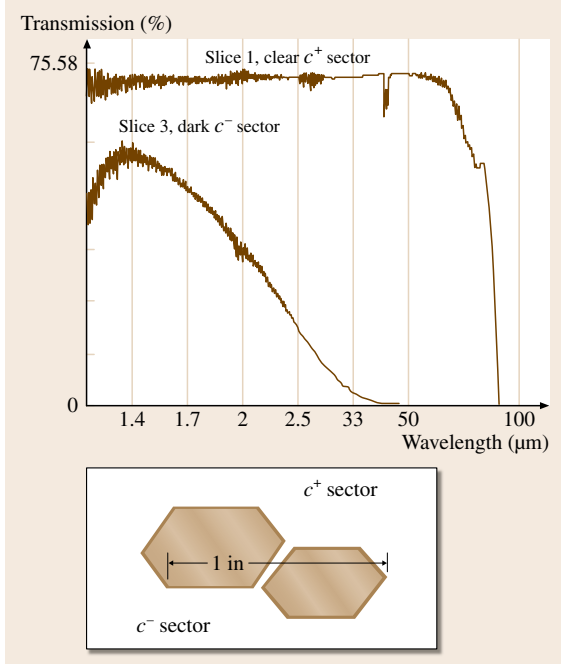


Fig. 19.30 IR transmission spectra of ZnO slices cut from c^{+} and c^{-} growth sectors of a ZnO crystal (after [19.21])

of broadband emission in ZnO bulk crystals and thin films [19.97].

We complete our summary of the optical properties of hydrothermal ZnO by considering transmission spectra (Fig. 19.30) [19.98]. Insulating ZnO is transparent from the near-ultraviolet almost to 10 μm (the spectrum in Fig. 19.30 labeled *clear* c^+ *sector*). Electrically conducting samples (e.g., the spectrum labeled *dark* c^- *sector*) exhibit a long-wavelength free-carrier absorption tail. The optical transparency shown in Fig. 19.30, together with the high laser breakdown strength of ZnO [19.98], have made ZnO the leading candidate for transparent conducting electrodes for high-power near-IR laser beam steering devices [19.99].

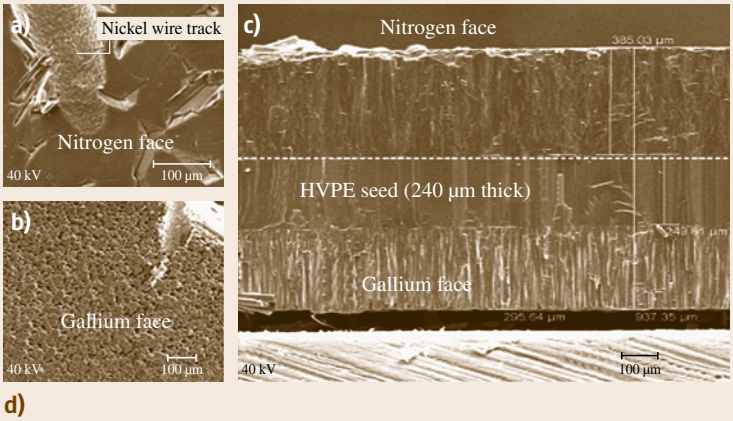
19.6 Ammonothermal GaN

19.6.1 Alkaline Seeded Growth

Callahan et al. [19.64] synthesized and grew GaN crystals in a retrograde configuration (Fig. 19.8) with 2–3 M KNH_2 concentration. Seeded growth experiments employed autoclaves with 2.2 cm internal diameter and 140 ml volume. Both sets of autoclaves are capable of sustained operation at 600 °C and pressures up to 4 kbar.

Polycrystalline GaN, synthesized by an in-house vapor process [19.100], was suspended in a scaffold near the bottom of the autoclave to obtain solubility data. Single-crystal *free-standing* gallium nitride up to 200 μm thick with a surface area of 1 cm^2 grown by hydride vapor-phase epitaxy (HVPE) was used as seeds and suspended by a wire scaffold near the bottom (warmer portion) of the autoclave. Seeded growth experiments were carried out for 5–30 days. Transported material nucleates on the walls of the autoclave, the wire scaffold, and on the GaN HVPE seeds. The mass of heterogeneously nucleated materials recovered from the lower walls (crystallization zone) is often eight to ten times the weight gain of the seeds.

Single-crystal growth on the seeds occurred at a rate of up to 40 μm per day. Growth approaching 1 mm in thickness was achieved on multiple seeds. Etching studies were conducted to determine the polarity of the crystalline surfaces. Previous work [19.101] indicates that the C^+ face (gallium face) when exposed to phosphoric acid etchants shows little erosion of the bulk material. The nitrogen polar face (Fig. 19.31a) has flatter surface than the gallium polar face (Fig. 19.31b). A cleaved cross-section of as-grown gallium nitride is shown in Fig. 19.31c. Growth in the C^+ and C^- directions (gallium face and nitrogen face, respectively) exhibits a columnar-type growth, with much more pronounced grain boundaries seen in the growth on the gallium face. Under different experimental conditions growth rates of the C^+ and C^- planes differ, but are approximately equal. Substantial growth in the a-direction has also been observed.



d)

Bulk concentrations (atoms/cm^3) in GaN								
Sample ID	**C**	**O**	**Si**	**K**	**Co**	**Fe**	**Ni**	**Pt**
Ga face	1.2E+17	5.6E+20	3.5E+18	1E+20	<8E+15	2E+17	<8E+15	5E+15
N face	2.5E+16	2.5E+20	7.9E+17	3E+16	2E+16	4E+16	<8E+15	<5E+16

Fig. 19.31a–d Thick ammonothermal GaN growth (after [19.64]) **(a)** SEM image of nitrogen polar face. **(b)** SEM image of gallium polar face. **(c)** SEM image of a cleaved cross-section of gallium nitride grown on HVPE seed. **(d)** Impurity concentrations of Ga and nitrogen faces measured by secondary ion mass spectrometry (SIMS)

Secondary ion mass spectrometry (SIMS) were performed on as-grown ammonothermal gallium nitride crystal samples. The results from a characteristic sample are shown in Fig. 19.31d. Impurities do not incorporate into the bulk crystal homogeneously. Concentrations of impurities were different between the gallium and nitrogen surfaces of the bulk crystal. In general metallic impurities incorporated less on the nitrogen face than the gallium face. Figure 19.31d shows that the impurity levels for oxygen and hydrogen are above 10^{19} atoms per cm^3 for both faces. Potassium impurities for the mineralizer were 10^{19} cm^3 atoms per cm^3 on the gallium face and mid 10^{18} cm^3 atoms per cm^3 on the nitrogen face.

The reciprocal-space maps and reflection topographs are shown in Fig. 19.32 for an ammonothermal crystal grown under similar conditions as those in Fig. 19.31 [19.102].

It is evident that the ammonothermal growth has higher defects levels than the HVPE seed. When a thinner film of $\approx 50\,\mu$ was grown [19.103] there was less columnar growth. The levels of impurities in the crystals and the nonuniform crystallinity of the HVPE seeds make quantitative analysis difficult.

The ammonothermal growth of 1 inch-size (0001) GaN crystal in a cylindrical high-pressure autoclave having an internal diameter of 40 mm was reported by *Hashimoto* et al. [19.17, 104]. About 15 µm-thick GaN films were uniformly grown on each side of the GaN seed, which has an oval shape of $3\times4\,cm^2$. The applied temperature and pressure were 625–675 °C and about 2.14 kbar. Basic mineralizers were used, resulting in retrograde solubility of GaN in supercritical ammonobasic solutions. The nutrient was placed in the colder region (upper region) and free-standing C-plane HVPE GaN seed crystals were placed in the hotter region (lower

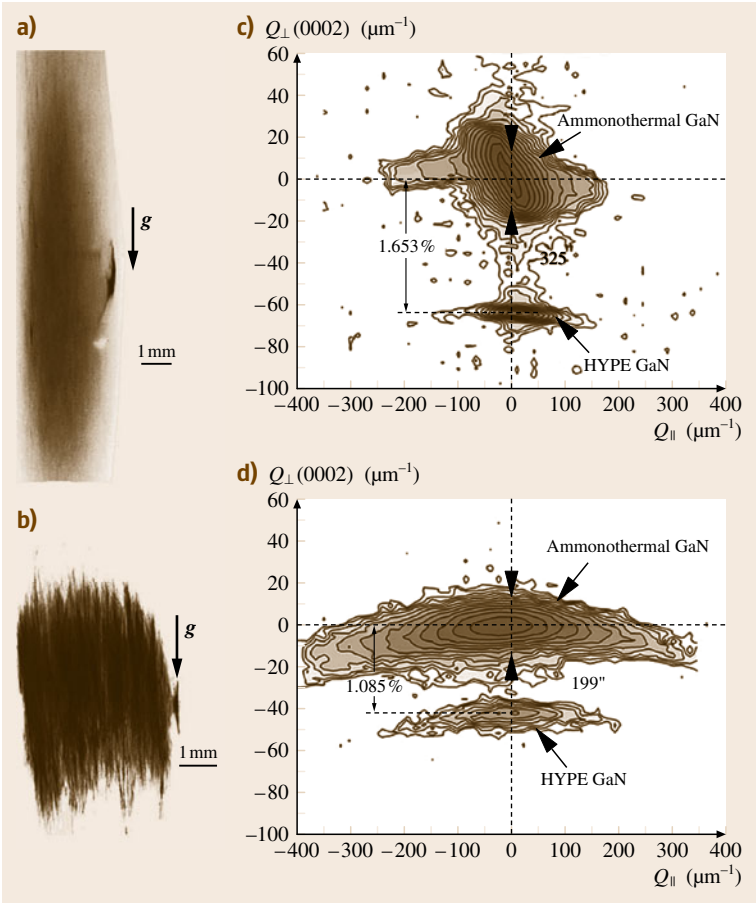


Fig. 19.32a–d Reciprocal-space maps and reflection topographs for ammonothermal GaN and HVPE seed grown with KNH_2 mineralizer (after [19.102])

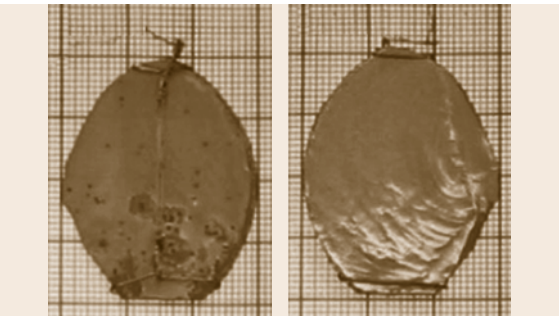


Fig. 19.33 Ammonothermal growth on $40 \times 30\,mm^2$ HVPE seed (after [19.17, 104])

region). A baffle divides the reactor into an upper region and a lower region to set a temperature difference between the dissolving region and the crystallization region. Uniform growth of GaN films on an over-1 inch oval-shaped seed crystal was achieved through fluid transport of Ga nutrient. Ga nutrient was transformed to GaN on the crucible wall, resulting in abrupt drop of the growth rate in about a day. The crystal is shown in Fig. 19.33.

Polycrystalline GaN nutrient and higher mineralizer concentration was used for longer growth runs. Due to thick wall of the autoclave, the temperature difference between the upper and lower regions of the fluid is estimated to be less than 50 °C. The resulting ammonia pressure was about 1.8–1.9 kbar. The growth rates along C^+ (Ga face), C^- (N face) and *M* direction were 0.8, 3.6, and 6 μm/day. The authors showed a defective growth interface with numerous voids and defects; as growth progressed the structure improved [19.106].

Dwilinski et al. recently reported on GaN crystals grown in alkaline ammonia with a dislocation density on the order of $5 \times 10^3\,cm^{-2}$ [19.107], which is several orders of magnitude lower than what has previously been reported. An x-ray rocking curve FWHM of 17 arcsec was measured on a 1 inch substrate cut from one of the GaN crystals and subsequently polished. There was no evidence of mosaicity or low-angle grain boundaries. X-ray rocking curves under 20 arcsec and radius of curvature on the order of 10^2–10^3 meters were measured on various crystals from separate growth runs. The authors did not disclose how the superior crystallinity of the GaN crystals was obtained.

Figure 19.34 is unpublished data [19.105] that shows photoluminescence (PL) of an alkaline ammonia sample, rack, and wall nucleation. The PL is improved over previous experiments. The broadband emission is reduced over previous runs [19.103] and there is no evidence of a PL signature at 3.4 eV that was identified as stacking-fault-related emission [19.108]. The wall nucleation has a greater number of broadband emissions. This might be evidence of impurities leaching from the autoclave.

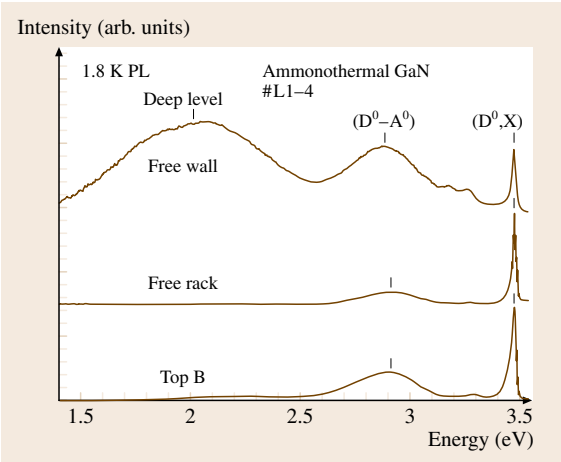


Fig. 19.34 Photoluminescence spectra of ammonothermal GaN (note the difference in broadband emission) (after [19.105])

19.6.2 Acidic Seeded Growth

Due to the corrosive nature of acidic solvents a platinum or silver liner must be used to contain the experiment. Figure 19.35 shows a scanning electron microscopy (SEM) image of acidic ammonothermal growth at a relatively low pressure of ≤ 170 MPa and temperature in the range 500–550 °C. The film was grown in standard configuration (forward-grade solubility). The authors increase the temperature and obtained columnar growth.

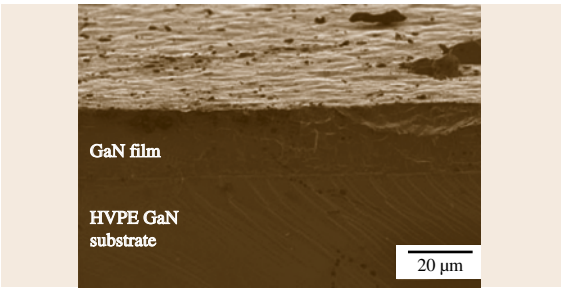


Fig. 19.35 Cross-sectional SEM image of 21 μm of ammonothermal growth on a HVPE seed using NH_4Cl as a mineralizer (after [19.43])

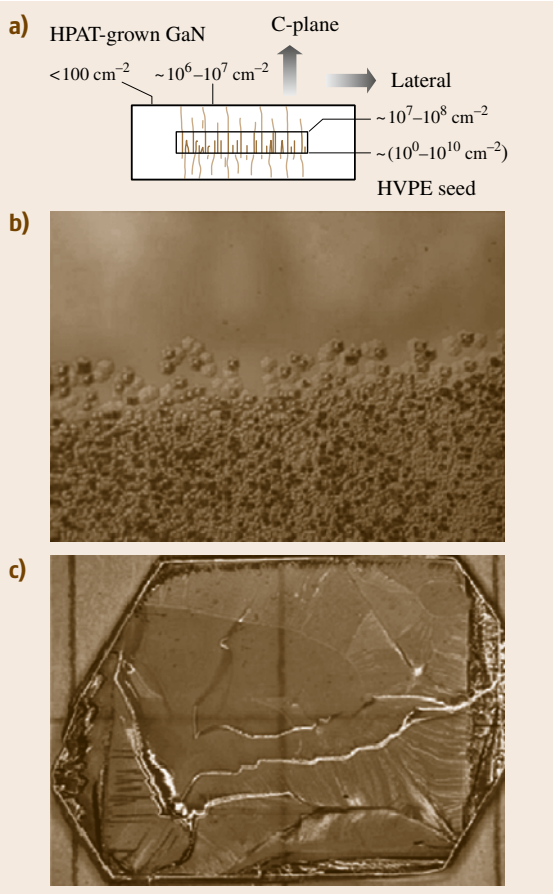


Fig. 19.36a–c GaN grown in high-pressure anvil cell at 700 °C; **(a)** schematic of growth; **(b)** SEM of low-defect/high-defect seed interface in the m-plane direction; **(c)** picture of large HVPE seed with ammonothermal growth showing smooth morphology (after [19.109])

Figure 19.36 shows a GaN crystal grown in a sealed capsule that is placed in a high-pressure cell with a solid pressure medium [19.109]. The cell is similar to the type used for piston-press and belt-press synthesis of diamond. The cell was heated between 600–1000 °C with a pressure in the range 5–20 kbar. The authors show a standard forward-grade solubility configuration for growth. The higher pressure and temperatures that this system can withstand allow for much higher growth rates than those that can be obtained in autoclaves. Figure 19.36a shows a schematic of the dislocation density of a crystal grown by the high-pressure ammonothermal technique (HPAT). Growth in the direction perpendicular to the HVPE seed was almost free of dislocations and other defects. This shows the advantage of using the ammonothermal technique to obtain very low-defect material. The impurities in the crystals grown were reduced by two orders of magnitude (10^{20}–10^{18}) from a previous publication. The authors fabricated a functional laser diode on one of the HPAT substrates.

19.6.3 Doping, Alloying, and Challenges

There has been synthesis of InGaN nanocrystals [19.110], polycrystalline AlN [19.111], and GaN microcrystals doped with transition-metal ions (Mn, Fe, and Cr) for dilute magnetic semiconductor applications [19.112]. Transition metals could also be used to increase resistance in GaN wafers. Finally, AlGaN microcrystalline balls were synthesized ammonothermally [19.54]. The Al metal nutrient was depleted before the end of the run. The result was two different compositions of AlGaN in the inner and outer portions of the ball, as seen in Fig. 19.37. It is surmised that an AlGaN alloy liquid droplets formed during the heating process and the AlGaN crystallized around the droplets.

Several challenges need to be overcome with ammonothermal technology in order to bring GaN-based crystal growth from research into full production. High-quality seeds, nutrient, equipment, and a complete understanding of the chemistry are required. Ammonothermal growth will leverage other growth technologies such as flux growth and HVPE growth for sources of seeds and nutrient. Electrical and optical characterization will proceed as large-area ammonothermal GaN crystals become available. *Denis* et al. published an excellent review of GaN bulk growth [19.113]. This technology is still in its infancy and there are many unique avenues to be explored.

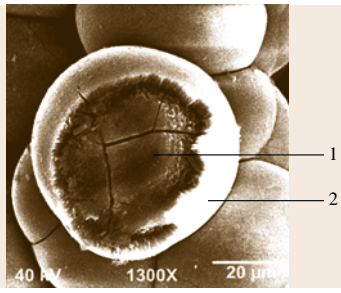


Fig. 19.37 Ammonothermal AlGaN balls (after [19.54]): 1 – $Al_{0.5}Ga_{0.5}N$; 2 – $Al_{0.25}Ga_{0.75}N$; nutrient – molar ratio of Al : Ga = 3 : 7 (Al nutrient was depleted during course of experiment)

19.7 Conclusion

Hydrothermal growth has produced very high-quality zinc oxide crystals. Nearly dislocation-free growth can be produced in zinc-terminated growth sectors and on nonpolar prism faces. Semi-insulating and conducting crystals have been grown, as well as crystals exhibiting superior low-temperature PL characteristics.

The various crystallographic faces of hydrothermal ZnO exhibit pronounced differences not only in the growth rates, but also in structural, electrical, and optical properties. The growth mechanisms, the incorporation of impurities, and the generation of native defects are (at least in part) connected to the polarity of the growth surfaces; however, the precise mechanisms – and especially the properties of impurities and native defects – have not been fully elucidated. Exploiting the faceted morphology of hydrothermal crystals may facilitate studies of these phenomena, many of which surely have counterparts in ZnO thin-film growth and ZnO bulk growth by other methods. Hydrothermal ZnO technology has progressed rapidly in the last 5 years with the capability to produce hundreds of wafers in a single run. Therefore economical growth of large, low-defect-density ZnO crystals is waiting for innovative strategies in ZnO device design and fabrication to spur demand for large-scale commercialization of ZnO-based devices and therefore ZnO substrates.

Significant progress has been made in acidic and alkaline ammonothermal growth of GaN. Forward solubility in ammonia has been determined when using acidic mineralizers such as NH_4Cl, in contrast with alkaline mineralizers such as KNH_2, where a retrograde solubility was discovered. Several groups have demonstrated that low-defect-density GaN can be produced using the ammonothermal technique, and growth on 1–2 inch-diameter GaN HVPE templates has been shown.

Process modeling and simulation based on physics are necessary in the scale-up of solvothermal systems. Forward solubility has been simulated for an autoclave with an internal diameter of 0.932 cm and internal height of 18.4 cm. The optimum precursor sizes found in the GaN growth experiments have been confirmed by numerical simulations. The fluid field can be significantly increased by an increase of the particle size from 0.6 mm to 3 mm. The optimization of the baffle design has been performed numerically and needs to be carefully selected to achieve a predefined temperature difference across the baffle, to achieve the necessary supersaturations required for the crystallization of single crystals at elevated growth rates.

Ammonothermal technology is a fertile ground for the production of many nitrogenated compounds that are difficult to synthesize by other techniques. The production of gallium nitride by the ammonothermal method requires a large amount of further investigation just as the production of quartz did in the early 20th century. In-depth phase, solubility, growth kinetics, and fluid dynamics studies need to be completed for a multiplicity of mineralizers, and high-strength vessels must be designed for the increased pressure requirements of supercritical ammonia. The cost advantages afforded by growing on multiple seeds simultaneously make this technique an attractive means for meeting the demand for high-quality gallium nitride substrates.

References

19.1 F. Bernardini, V. Fiorentini, D. Vanderbilt: Spontaneous polarization and piezoelectric contants of III-V nitrides, Phys. Rev. B **56**(R10), 24–27 (1997)

19.2 S.J. Pearton, C.R. Abernathy, F. Ren: *Gallium Nitride Processing for Electronics, Sensors and Spintronics* (Springer, Berlin Heidelberg 2006)

19.3 B. Gil: *Low-Dimensional Nitride Semiconductors* (Oxford Univ. Press, Oxford 2002)

19.4 C. Jagadish, S.J. Pearton: *Zinc Oxide, Thin Films and Nanostructions: Processing, Properties, and Applications* (Elsevier Science, Amsterdam 2006)

19.5 Ü. Özgür, Y.I. Alivov, C. Liu, A. Teke, M.A. Reshchikov, S. Doğan, V. Avruntin, S.-J. Cho, H. Morkoç: A comprehensive review of ZnO material and devices, Appl. Phys. Rev. **98**(041301), 1–103 (2005)

19.6 I. Akasaki: Key inventions in the history of nitride-base blue LED and LD, J. Cryst. Growth **300**, 2–10 (2007)

19.7 C. Klingshirn, R. Hauschild, H. Priller, M. Decker, J. Zeller, H. Kalt: ZnO rediscovered – once again!?, Superlattice Microstruct. **38**, 209–222 (2005)

19.8 H.J. Scheel: Historical aspects of crystal growth technology, J. Cryst. Growth Technol. **211**, 1–12 (2000)

19.9 J. Nause, B. Nemeth: Pressurized melt growth of ZnO boules, Semicond. Sci. Technol. **20**, S45–S48 (2005)

19.10 J. Karpiński, J. Jun, S. Porowski: High pressure thermodynamics of GaN, J. Cryst. Growth **66**, 1–10 (1984)

19.11 H.D. Sun, Y. Segawa, M. Kawasaki, A. Ohtomo, K. Tamura, H. Koinuma: Phonon replicas in ZnO/ZnMgO multiquantum wells, J. Appl. Phys. Lett. **91**(10), 6450–6457 (2002)

19.12 D.C. Look, D.C. Reynolds, J.R. Sizelove, R.L. Jones, C.W. Litton, G. Cantwell, W.C. Harsch: Electrical properties of bulk ZnO, Solid-State Commun. **105**, 399–401 (1998)

19.13 D. Ehrentraut, H. Sato, Y. Kagamitani, H. Sato, A. Yoshikawa, T. Fukuda: Solvothermal growth of ZnO, Prog. Cryst. Growth Charact. Mater. **52**, 280–335 (2006)

19.14 D.A. Kramer: Nitrogen (fixed) Ammonia. In: *US Geological Survey*, ed. by US Department of the Interior (United States Government Printing Office, Washington 2005) pp. 116–117

19.15 K. Byrappa, M. Yoshimura: *Handbook of Hydrothermal Technology* (William Andrew, New York 2001)

19.16 M.T. Harris, J.J. Larkin, J.J. Martin: Low-defect colorless $Bi_{12}SiO_{20}$ grown by hydrothermal techniques, Appl. Phys. Lett. **60**, 2162–2163 (1992)

19.17 T. Hashimoto, K. Fujito, M. Saito, J.S. Speck, S. Nakamura: Ammonothermal growth of GaN on an over-1-inch seed crystal, Jpn. J. Appl. Phys. **44**, L1570–1572 (2005)

19.18 R.A. Laudise: *Hydrothermal Growth in The Growth of Single Crystals* (Prentice-Hall, New Jersey 1970) pp. 275–293

19.19 H. Jacobs, D. Schmidt: High-pressure ammonolosis in solid-state chemistry. In: *Current Topics in Materials Science*, Vol. 8, ed. by E. Kaldis (North Holland, Amsterdam 1982) pp. 381–427

19.20 B. Wang, M.J. Callahan: Ammonothermal synthesis of III-nitride crystals, Cryst. Growth Des. **6**(6), 1227–1246 (2006)

19.21 M. Suscavage, M. Harris, D. Bliss, P. Yip, S.Q. Wang, D. Schwall, L. Bouthillette, J. Bailey, M. Callahan, D.C. Look, D.C. Reynolds, R.L. Jones, C.W. Litton: High quality ZnO crystal, Mater. Res. Soc. Symp. Proc. **537**, 294–299 (1999)

19.22 R. R. Monchamp, R. C. Puttbach, J. W. Nielson: Hydrothermal growth of ZnO crystals (Airtron Division of Litton Industries, Morris Plains, technical report AFML-TR-67-144 1967)

19.23 R.A. Laudise, E.D. Kolb: The solubity of zincite in basic hydrothermal solvents, Am. Mineral. **48**(3), 642–648 (1963)

19.24 D.F. Croxall, R.C.C. Ward, C.A. Wallace, R.C. Kell: Hydrothermal growth and investigation of Li-doped zinc oxide crystals of high purity and perfection, J. Cryst. Growth **22**, 117 (1974)

19.25 N. Sakagami: Hydrothermal growth and characterization of ZnO single crystals of high purity, J. Cryst. Growth **99**, 905–909 (1990)

19.26 L. Demianets, D. Kostomaro: Mechanism of zinc oxide single crystal growth under hydrothermal conditions, Ann. Chim. Sci. Mater. **26**(1), 193–198 (2001)

19.27 I.P. Kuz'mina, A.N. Lobachev, N.S. Triodina: *Synthesis of Zincite by the Hydrothermal Method in Crystallization Process Under Hydrothermal Conditions* (Nauka, Moscow 1973) pp. 27–41

19.28 T. Fukuda, D. Ehrentraut: Prospects for the ammonothermal growth of large GaN crystals, J. Cryst. Growth **305**, 304–310 (2007)

19.29 E.V. Kortunova, P.P. Chvanski, N.G. Nikolaeva: The first attempts of industrial manufacture of ZnO single crystals, J. Phys. IV France **126**, 39–42 (2005)

19.30 L.E. McCandlish, R. Urhin: Mild conditions for hydrothermal growth of ZnO with potential for p-type semiconductor behavior, Poster Presentation at 5th Int. Conf. Solvotherm. React. Conf (East Brunswick, 2002), image supplied directly by L.E. McCandlish

19.31 G.F. Hüttig, H. Möldner: The specific heat of crystallized zinc hydroxide and calculation of the affinities between zinc oxide and water, Z. Anorg. Chem. **211**, 368–378 (1933)

19.32 C.H. Lu, C.H. Yeh: Influence of hydrothermal conditions on the morphology and particle size of zinc oxide powder, Ceram. Int. **26**, 351–357 (2000)

19.33 R.A. Laudise, A.A. Ballman: Hydrothermal synthesis of zinc oxide and zinc sulfide, J. Phys. Chem. **64**(5), 688–691 (1960)

19.34 M.M. Lencka, R.E. Riman: Synthesis of lead titanate: thermodynamic modeling and experimental verification, J. Am. Ceram. Soc. **76**, 2649–2659 (1993)

19.35 M.M. Lencka, A. Anderko, R.E. Riman: Hydrothermal precipitation of lead zirconate titanate solid solutions: thermodynamic modeling and experimental synthesis, J. Am. Ceram. Soc. **78**, 2609–2618 (1995)

19.36 M.M. Lencka, R.E. Riman: Themodynamic modeling of hydrothermal synthesis of ceramic powders, Chem. Mater. **5**, 61–70 (1993)

19.37 R. Dwilinski, R. Doradzinski, J. Garczynski, L. Sierzputowski, J.M. Baranowski, M. Kaminska: AMMONO method of GaN and AlN production, Diam. Relat. Mater. **7**, 1348–1350 (1998)

19.38 A.P. Purdy: Ammonothermal sythesis of cubic gallium nitride, Chem. Mater. **11**, 1648–1651 (1999)

19.39 D.R. Ketchum, J.W. Kolis: Crystal growth of gallium nitride in supercritical ammonia, J. Cryst. Growth **222**, 431–434 (2001)

19.40 A. Yoshikawa, E. Ohshima, T. Fukuda, H. Tsuji, K. Oshima: Crystal growth of GaN by ammonothermal method, J. Cryst. Growth **260**, 67–72 (2004)

19.41 Y.C. Lan, X.L. Chen, M.A. Crimp, Y.G. Cao, Y.P. Xu, T. Xu, K.Q. Lu: Single crystal growth of gallium nitride in supercritical ammonia, Phys. Status Solidi (c) **2**(7), 2066–2069 (2005)

19.42 B. Wang, M.J. Callahan, K. Rakes, D.F. Bliss, L.O. Bouthillette, S.-Q. Wang, J.W. Kolis: Am-

monothermal growth of GaN crystals in alkaline solutions, J. Cryst. Growth **287**, 376–380 (2006)
19.43 Y. Kagamitani, D. Ehrentraut, A. Yoshikawa, N. Hoshino, T. Fukuda, S. Kawabata, K. Inaba: Ammonothermal epitaxy of thick GaN film using NH_4Cl mineralizer, Jpn. J. Appl. Phys. **45**(5A), 4018–4020 (2006)
19.44 D. Peters: Ammonothermal synthesis of aluminium nitride, J. Cryst. Growth **104**, 411–418 (1990)
19.45 B. Wang, M.J. Callahan: Transport growth of GaN crystals by the ammonothermal technique using various nutrients, J. Cryst. Growth **291**, 455–460 (2006)
19.46 A.P. Purdy, R.J. Jouet, F.G. Clifford: Ammonothermal recrystallization of gallium nitride with acidic mineralizers, Cryst. Growth Des. **2**(2), 141–145 (2002)
19.47 D. Ehrentraut, N. Hoshino, Y. Kagamitani, A. Yoshikawa, T. Fukuda, H. Itoh, S. Kawabata: Temperature effect of ammonium halogenides as mineralizers on the phase stability of gallium nitride synthesized under acidic ammonothermal conditions, J. Mater. Chem. **17**, 886–893 (2007)
19.48 B. Raghothamachar, W.M. Vetter, M. Dudley, R. Dalmau, R. Schlesser, Z. Sitar, E. Michael, J.W. Kolis: Synchrontron white beam topography charctrization of physical vapor transport grown AlN and ammonothermal GaN, J. Cryst. Growth **246**, 271–280 (2002)
19.49 A.P. Purdy, S. Case, N. Murastore: Synthesis of GaN by high-pressure ammonolysis of gallium triiodide, J. Cryst. Growth **252**, 136–143 (2003)
19.50 T. Hashimoto, K. Fujito, R. Sharma, E.R. Letts, P.T. Fini, J.S. Speck, S. Nakamura: Phase selection of microcrystalline GaN synthesized in supercritical ammonia, J. Cryst. Growth **291**, 100–106 (2006)
19.51 A. Purdy: Growth of cubic GaN crystals from hexagonal GaN feedstock, J. Cryst. Growth **281**, 355–363 (2005)
19.52 A.N. Mariano, R.E. Hanneman: Crystallographic polarity of ZnO crystals, J. Appl. Phys. **34**, 384–389 (1963)
19.53 B. Wang, M.J. Callahan, L.O. Bouthillette: Hydrothermal growth and photoluminescence of $Zn_{1-x}Mg_xO$ alloy crystals, Cryst. Growth Des. **6**, 1256–1260 (2006)
19.54 M. J. Callahan, B. Wang, unpublished results
19.55 Q.-S. Chen, V. Prasad, W.R. Hu: Modeling of ammonothermal growth of nitrides, J. Cryst. Growth **258**, 181–187 (2003)
19.56 M. Carr: Penetrative convection in a superposed porous-medium-fluid layer via internal heating, J. Fluid Mech. **509**, 305–329 (2004)
19.57 V. Prasad: Convective flow interaction and heat transfer between fluid and porous layers. In: *Convective Heat and Mass Transfer in Porous Media*, ed. by S. Kakaç, B. Kilkiş, F.A. Kulacki, F. Arinç (Kluwer, Netherlands 1991) pp. 563–615
19.58 Q.-S. Chen, V. Prasad, A. Chatterjee, J. Larkin: A porous media-based transport model for hydrothermal growth, J. Cryst. Growth **198/199**, 710–715 (1999)
19.59 Q.-S. Chen, V. Prasad, A. Chatterjee: Modeling of fluid flow and heat transfer in a hydrothermal crystal growth system: use of fluid-superposed porous layer theory, J. Heat Transf. **121**, 1049–1058 (1999)
19.60 H. Zhang, V. Prasad, M.K. Moallemi: Numerical algorithm using multizone adaptive grid generation for multiphase transport processes with moving and free boundaries, Num. Heat Transf. **29**(B), 399–421 (1996)
19.61 H. Zhang, V. Prasad: An advanced numerical scheme for materials process modeling, Comput. Model. Simul. Eng. **2**, 322–343 (1997)
19.62 Q.-S. Chen, S. Pendurti, V. Prasad: Effects of baffle design on fluid flow and heat transfer in ammonothermal growth of nitrides, J. Cryst. Growth **266**, 271–277 (2004)
19.63 A.J. Chapman: *Heat Transfer* (Macmillan, New York 1984)
19.64 M. Callahan, B.-G. Wang, K. Rakes, D. Bliss, L. Bouthillette, M. Suscavage, S.-Q. Wang: GaN single crystals grown on HVPE seeds in alkaline supercritical ammonia, J. Mater. Sci. **41**, 1399–1407 (2006)
19.65 Q.-S. Chen, S. Pendurti, V. Prasad: Modeling of ammonothermal growth of gallium nitride single crystals, J. Mater. Sci. **41**, 1409–1414 (2006)
19.66 T. Sekiguchi, S. Miyashita, K. Obara, T. Shishido, N. Sakagami: Hydrothermal growth of ZnO single crystals and their optical characterization, J. Cryst. Growth **214/215**, 72–76 (2000)
19.67 L.N. Demianets, D.V. Kostomarov, I.P. Kuz'mina, S.V. Pushko: Mechanism of growth of ZnO single crystals from hydrothermal alkali solutions, Cryst. Rep. **47**, S86–S98 (2002), Supp 1
19.68 B.G. Wang: Understanding and controlling the morphology of ZnO crystallites under hydrothermal conditions, Cryst. Res. Technol. **32**, 659–667 (1997)
19.69 W.J. Li, E.W. Shi, W.Z. Zhong, Z.W. Yin: Growth mechanism and growth habit of oxide crystals, J. Cryst. Growth **203**, 186–196 (1999)
19.70 I.L. Khodakovskiy, A.Y. Yelkin: Measurement of the solubility of zincite in aqueous NaOH at 100, 150, and 200 °C, Geokhimiya **10**, 1490–1498 (1975)
19.71 P. Bénézeth, D. Palmer, D. Wesolowski: The solubility of zinc oxide in 0.03 m NaTr as a function of temperature with in-situ pH measurement, Geochim. Cosmochi. Acta **63**, 1571–1586 (1999)
19.72 B.G. Wang, E.W. Shi, W.Z. Zhong: Twinning morphologies and mechanisms of ZnO crystallites under hydrothermal conditions, Cryst. Res. Technol. **33**, 937–941 (1998)

19.73 M.M. Lukina, M.V. Lelekova, V.E. Khadzhi: Effect of lithium on the growth rate of zincite and quartz under hydrothermal conditions, Sov. Phys. Crystallogr. **15**, 530–531 (1970)

19.74 R.A. Laudise, R.L. Barnes: Perfection of quartz and its connection to crystal growth, IEEE Trans. Ultrasonics Ferroelectr. Freq. Control. **35**, 277–287 (1998)

19.75 A.F. Armington: Recent advances in the growth of high quality quartz, Prog. Cryst. Growth Charact. **21**, 97–111 (1990)

19.76 E.D. Kolb, R.A. Laudise: Hydrothermally grown ZnO crystals of low and intermediate resistivity, J. Am. Ceram. Soc. **49**, 302–305 (1966)

19.77 E.D. Kolb, S. Coriell, R.A. Laudise, A.R. Hutson: The hydrothermal growth of low carrier concentration ZnO at high water and hydrogen pressures, Mater. Res. Bull **2**, 1099–1106 (1967)

19.78 I.P. Kuz'mina: Crystallization kinetics of zincite under hydrothermal conditions, Sov. Phys. Crystallogr. **13**(5), 803–805 (1969), translated from Kristallogr., Vol. 13, No.5

19.79 G. Dhanaraj, M. Dudley, D. Bliss, M. Callahan, M. Harris: Growth and process induced dislocation in zinc oxide crystals, J. Cryst. Growth **297**, 74–79 (2006)

19.80 H. Youping, Z. Jinbo, W. Dexang, S. Genbo, Y. Mingshan: New technology of KDP crystal growth, J. Cryst. Growth **169**, 196–198 (1996)

19.81 B. Wang, M.J. Callahan, C. Xu, L.O. Bouthillette, N.C. Giles, D.F. Bliss: Hydrothermal growth and characterization of indium-doped-conducting ZnO crystals, J. Cryst. Growth **304**, 73–79 (2007)

19.82 N.Y. Garces, L. Wang, L. Bai, N.C. Giles, L.E. Halliburton, G. Cantwell: Role of copper in the green luminescence from ZnO crystals, Appl. Phys. Lett. **81**, 622–624 (2002)

19.83 E.D. Kolb, R.A. Laudise: Hydrothermally grown ZnO crystals of low and intermediate resistivity, J. Am. Ceram. Soc. **49**, 302–305 (1966)

19.84 C.G. Van de Walle: Hydrogen as a cause of doping in zinc oxide, Phys. Rev. Lett. **85**(5), 1012–1015 (2000)

19.85 R. Littbarski: Carrier concentration and mobility. In: *Current Topics in Materials Science*, Vol. 7, ed. by E. Kaldis (North-Holland, Amsterdam 1981) pp. 212–225

19.86 B. Theys, V. Sallet, F. Jomard, A. Lusson, J. Rommeluère, Z. Teukam: Effects of intentionally introduced hydrogen on the electric properties of ZnO layers grown by metalorganic chemical vapor deposition, J. Appl. Phys. **91**, 3922–3924 (2002)

19.87 D.C. Look, J.W. Hemsky, J.R. Sizelove: Residual native shallow donor in ZnO, Phys. Rev. Lett. **82**, 2552–2555 (1999)

19.88 A. Urbieta, P. Fernández, J. Piqueras, T. Sekiguchi: Scanning tunneling spectroscopy characterization of ZnO single crystals, Semicond. Sci. Technol. **16**, 589–593 (2001)

19.89 N. Sakagami, M. Yamashita, T. Sekiguchi, S. Miyashita, K. Obara, T. Shishido: Variation of electrical properties on growth sectors of ZnO single crystals, J. Cryst. Growth **229**, 98–103 (2001)

19.90 M. Yoneta, K. Yoshino, M. Ohishi, H. Saito: Photoluminescense studies of high-quality ZnO single crystals by hydrothermal method, Phys. B **376–377**, 745–748 (2006)

19.91 J. Mass, M. Avella, J. Jiménez, M. Callahan, E. Grant, K. Rakes, D. Bliss, B. Wang: Cathodoluminescence characterization of hydrothermal ZnO crystals, Superlattice Microstruct. **38**, 223–230 (2005)

19.92 L.N. Dem'yanets, V.I. Lyutin: Status of hydrothermal growth of bulk ZnO: latest issues and advantages, J. Cryst. Growth **310**, 993–999 (2008)

19.93 J. Mass, M. Avella, J. Jiménez, A. Rodriquez, T. Rodriquez, M. Callahan, D. Bliss, B. Wang: Cathodoluminescence study of ZnO wafer cut from hydrothermal crystals, J. Cryst. Growth **310**, 1000–1005 (2008)

19.94 D.C. Reynolds, D.C. Look, B. Jogai, H. Morkoç: Simililarities in the bandedge and deep-centre photoluminescence mechanisms of ZnO and GaN, Solid State Commun. **101**, 643–646 (1997)

19.95 A. Urbieta, P. Fernández, J. Piqueras, C. Hardalov, T. Sekiguchi: Cathodoluminescence microscopy of hydrothermal and flux grown ZnO single crystals, J. Phys. D Appl. Phys. **34**, 2945–2949 (2001)

19.96 A. Urbieta, P. Fernández, C. Hardalov, J. Piqueras, T. Sekiguchi: Cathodoluminescense and scanning tunneling spectroscopy, Mater. Sci. Eng. **B91–92**, 345–348 (2002)

19.97 J. Mass, M. Avella, J. Jiménez, M. Callahan, E. Grant, K. Rakes, D. Bliss, B. Wang: Visable luminescence in ZnO. In: *New Materials and Procecesses for Incoming Semiconductor Technologies*, ed. by S. Dueñas, H. Castán (Transworld Research Network, Kerala 2006)

19.98 D. Bliss: Zinc oxide. In: *Encyclopedia of Advanced Materials*, ed. by D. Bloor, M.C. Flemings, R.J. Brook, S. Mahajan, R.W. Cahn (Pergamon, Oxford 1994) pp. 9888–9891

19.99 C. Woods, A.J. Drehman: Presentation, Natl. Space Missile Mater. Symp. (Monterey, 2001)

19.100 B. Wang, M. Callahan, J. Bailey: Synthesis of dense polycrystalline GaN of high purity by the chemical vapor reaction process, J. Cryst. Growth **286**, 50–54 (2005)

19.101 K. Lee, K. Auh: Dislocation density of GaN grown by hydride vapor phase epitaxy, MRS Int. J. Nitride Semicond. Res. **6**, 9 (2001)

19.102 B. Raghothamacher, J. Bai, M. Dudley, R. Dalmau, D. Zhuang, Z. Herro, R. Schlesser, Z. Sitar, B. Wang, M. Callahan, K. Rakes, P. Konkapaka, M. Spencer: Characterization of bulk-grown GaN and AlN single-crystals materials, J. Cryst. Growth **287**, 349–353 (2006)

19.103 M.J. Callahan, B. Wang, L. Bouthillette, S.-Q. Wang, J.W. Kolis, D. Bliss: Growth of GaN crystals under ammonothermal conditions, MRS Fall Meet. Symp. Proc. **798**, Y2.10 (2004)
19.104 T. Hashimoto, M. Saito, K. Fujito, F. Wu, J.S. Speck, S. Nakamura: Seeded growth of GaN by the basic ammonothermal method, J. Cryst. Growth **305**, 311–316 (2007)
19.105 Images provided by Prof. Brian Skromme's group, Arizona St. Univ.
19.106 T. Hashimoto, K. Fujito, F. Wu, B.A. Haskell, P.T. Fini, J.S. Speck, S. Nakamura: Structural characterization of thick GaN films grown on free-standing GaN seeds by the ammonothermal method using basic ammonia, Jpn. J. Appl. Phys. **44**(25), L797–L799 (2005)
19.107 R. Dwilinski, R. Doradzinski, J. Garzynski, L.P. Sierzputowski, A. Puchalski, Y. Kanaba, K. Yagi, H. Minakuchi, H. Hayashi: Excellent crystallinity of truly bulk ammonothermal GaN, J. Cryst. Growth **310**, 3911–3916 (2008)
19.108 J. Bai, M. Dudley, B. Raghothamachar, P. Gouma, B.J. Skrome, L. Chen, P.J. Hartlieb, E. Michaels, J. Kolis: Correlated structural and optical characterization of ammonothermally grown bulk GaN, Appl. Phys. Lett. **84**(17), 3289–3291 (2004)
19.109 M.P. D'Evelyn, H.C. Hong, D.-S. Park, H. Lu, E. Kaminsky, R.R. Melkote, P. Perlin, M. Lesczynski, S. Porowski, R.J. Molnar: Bulk GaN crystal growth by th high-pressure ammonothermal method, J. Cryst. Growth **300**, 11–16 (2007)
19.110 S.V. Bhat, K. Biswas, C.N.R. Rao: Synthesis and optical properties of In-doped GaN nanocrystals, Solid State Commun. **141**, 325–328 (2007)
19.111 B.T. Adekore, K. Rakes, B. Wang, M.J. Callahan, S. Pendurti, Z. Sitar: Ammonothermal synthesis of aluminum nitride crystals on group III-nitride templates, J. Electron. Mater. **35**, 1104–1111 (2006)
19.112 M. Zajac, J. Gosk, E. Grzanka, S. Stelmakh, M. Palczewska, A. Wysmołek, K. Korona, M. Kamińska, A. Twardowski: Ammomonothermal sythesis of GaN doped with transition metal ions (Mn, Fe, Cr), J. Alloys Compd. **456**, 324–338 (2008)
19.113 A. Denis, G. Goglio, G. Demazeau: Gallium nitride bulk crystal growth processes: a review, Mater. Sci. Eng. R **50**, 167–194 (2006)

20. Stoichiometry and Domain Structure of KTP-Type Nonlinear Optical Crystals

Michael Roth

In recent years the growth technologies of only a few inorganic oxide crystals, such as BBO (BaB_2O_4), LBO (LiB_3O_5), and the KTP ($KTiOPO_4$) group of isomorphic compounds, have matured to a degree allowing their extensive integration into commercial laser systems in the form of nonlinear optical (NLO) and electrooptic (EO) devices. The KTP-type crystals are ferroelectrics at room temperature. They are also well known for their large birefringence, high NLO and EO coefficients, wide acceptance angles, thermally stable phase-matching properties, and relatively high damage threshold. These properties make them especially useful for high-power wavelength-conversion applications, such as the second-harmonic generation (SHG) and optical parametric oscillations (OPO), as well as for electrooptic phase modulation and Q-switching. Lately, a great deal of effort has been put into the development of periodically poled KTP (PPKTP) devices based on quasi-phase-matched (QPM) wavelength conversion. However, both birefringent and QPM properties of KTP crystals depend on their structural characteristics, such as morphology, chemical composition, point defect distribution (stoichiometric and impurities), and particularly the ferroelectric domain structure, which are closely related to the specific crystal growth parameters. Current research includes studies of nonstoichiometry and distribution of point defects, e.g., vacancies and impurities, as well as the basic mechanisms underlying ferroelectric domain formation during KTP crystal growth and cool-down. By controlling the stoichiometry and achieving single-domain growth of bulk crystals it is also possible to create as-grown periodic domain structures useful for nonlinear QPM applications.

20.1 **Background** 691
20.1.1 KTP Crystal Structure 692
20.1.2 Crystal Growth 694
20.2 **Stoichiometry and Ferroelectric Phase Transitions** 697
20.2.1 $KTiOPO_4$ Crystals 697
20.2.2 $RbTiOPO_4$ Crystals 700
20.2.3 Other KTP Isomorphs 702
20.3 **Growth-Induced Ferroelectric Domains** 703
20.3.1 Domains in Top-Seeded Solution-Grown KTP 704
20.3.2 Domain Boundaries 705
20.3.3 Summary of Ferroelectric Domain Structures 707
20.3.4 Single-Domain Growth 707
20.4 **Artificial Domain Structures** 708
20.4.1 Electric Field Poling 708
20.4.2 As-Grown Periodic Domain Structure 711
20.5 **Nonlinear Optical Crystals** 713
20.5.1 Optical Nonuniformity 713
20.5.2 Gray Tracks 715
References 716

20.1 Background

Potassium titanyl phosphate (KTP) belongs to the family of isomorphic compounds with generic composition of $MTiOXO_4$, where X = {P or As} and M = {K, Rb, Tl, NH_4 or Cs (for X = As only)} [20.1]. All crystals of this family, including their solid solutions, are orthorhombic and belong to the noncentrosymmetric point group *mm*2

Table 20.1 Selected physical properties of KTP-family crystals

Crystal	KTP	RTP	KTA	RTA	CTA	References
Optical transparency (μm)	0.35–4.3	0.35–4.3	0.35–5.3	0.35–5.3	0.35–5.3	[20.2–4]
Birefringence, $n_z - n_x$ at 1.064 μm	0.0921	0.0884	0.0863	0.0782	0.0700	[20.4–8]
NLO susceptibilities (pm/V) at 1.064 μm						
d_{33}	16.9	17.1	16.2	15.8	18.1	[20.9, 10]
d_{32}	4.4	4.1	4.2	3.8	3.4	
d_{31}	2.5	3.3	2.8	2.3	2.1	
d_{24}	3.6	–	3.2	–	–	
d_{15}	1.9	–	2.3	–	–	
d_{eff} for type-II SHG	3.35	2.51	–	–	–	[20.4, 11]
SHG cutoff (μm) along						
x-direction	1.082	1.147	1.134	1.243	1.548	[20.11]
y-direction	0.994	1.038	1.074	1.138	1.280	
EO coefficients (pm/V) at 0.633 μm						
r_{33}	36.3	39.6	37.5	40.5	38.0	[20.10, 12]
r_{23}	15.7	17.1	15.4	17.5	18.5	
r_{13}	9.5	12.5	11.5	13.5	14.2	

at room temperature. The unique ferroelectric, EO, and NLO properties of the KTP-family crystals are stipulated by this specific structure. Table 20.1 gives a partial list of the important physical properties exhibited by the five more extensively studied KTP group members: $KTiOPO_4$ (KTP), $RbTiOPO_4$ (RTP), $KTiOAsO_4$ (KTA), $RbTiOAsO_4$ (RTA), and $CsTiOAsO_4$ (CTA).

All these crystals exhibit a broad optical transparency range allowing for NLO [20.13] and EO [20.14] interactions from the visible to the near- and mid-infrared. The larger birefringence and suitable dispersion of the orthophosphates, KTP and RTP, brings their phase-matching directions into the x–y plane for efficient second-harmonic generation (SHG) of the principal Nd:YAG laser radiation at 1.064 μm. Although not suitable for frequency doubling into the green, CTA includes the 1.32 μm line of the Nd:YAG laser in its phase-matchable wavelength interval within the x–y plane [20.9] allowing doubling into the red. In general, the transparency range of the orthoarsenates extends by 1 μm further into the mid-infrared (Table 20.1) and contains no orthophosphate overtone absorption at wavelengths shorter than 3.5 μm, which makes them particularly attractive for noncritically phase-matched (NCPM) eye-safe OPO (signal at ≈ 1.5 μm) with negligible absorption of the idler radiation at ≈ 3.3 μm [20.15]. It is noteworthy that a more detailed insight into the idler absorption problem in KTP, namely its reduced value for z-polarization, demonstrates that orthophosphates may also generate high-average-power eye-safe OPO [20.16]. All KTP-family crystals also feature large EO coefficients necessary for electrooptic modulation and switching [20.14], but mainly KTP, and especially RTP, are widely used for these applications [20.17, 18]. This may be associated with the fact that the orthoarsenates are apt to ferroelectric multidomain formation [20.19, 20], and their crystal growth is a costly process [20.21]. Therefore, the more technologically important KTP and RTP materials will be primarily discussed in terms of their defect structure and the structure–properties relationships versus the main processing parameters.

20.1.1 KTP Crystal Structure

The five KTP-family members identified above have identical crystal structures at room temperature. The orthorhombic structure ($a \neq b \neq c$, $\alpha = \beta = \gamma = 90°$) of KTP belongs to the space group $Pna2_1$, as initially determined by *Tordjman* et al. in 1974 [20.22]. There are 64 atoms in a unit cell in the KTP-type lattice. This 64-atom group separates into four subgroups of 16 atoms each, and within each such subgroup there are two inequivalent K (Rb) sites, two inequivalent titanium sites, two inequivalent P (As) sites, and ten inequivalent oxygen sites. Two of the latter oxygen sites represent bridging ions located between titanium ions, while the other eight are contained in PO_4 (AsO_4) groups where they link one Ti and one P (As) ion.

Table 20.2 Crystal lattice parameters of KTP-family crystals

Lattice constants ()	KTP [20.23]	RTP [20.24]	KTA [20.25]	RTA [20.26]	CTA [20.27]
a	12.819	12.952	13.125	13.264	13.486
b	6.399	6.4925	6.5716	6.682	6.682
c	10.584	10.555	10.786	10.7697	10.688

Lattice Parameters and Site Occupation

The room-temperature lattice constants of KTP-family crystals are given in Table 20.2. They change relatively little in going from KTP even to CTA. The values for KTP and RTP are very close, thus verifying that the PO_4 tetrahedra have much more influence on the lattice constants than the monovalent cations K and Rb. In KTA, the *a* and *b* lattice constants are approximately 1.2% larger than in KTP and the *c* lattice constant is about 2.1% larger than in KTP, thus reflecting the slightly larger size of the AsO_4 tetrahedron compared with PO_4. One 16-atom subgroup can be transformed into one of the other three subgroups by simple transformations within the unit cell. The [001] projection of the KTP structure is shown in Fig. 20.1.

The physical structure of the KTP-type crystal contains helical chains of distorted TiO_6 octahedra running parallel to the ⟨011⟩ crystallographic directions and forming a two-dimensional network in the *b*–*c* plane. The TiO_6 octahedra are linked at two corners by alternately changing long and short Ti(1)−O bonds which are commonly assumed as primarily responsible for the optical nonlinearity [20.28]. Other sources of optical nonlinearities have been invoked as well. Bond-polarizability calculations of KTP [20.29] show that the nonlinearity derives from the various K−O bonds and $P(2)O_4$ groups rather than from the TiO_6 groups. Nuclear magnetic resonance (NMR) studies of KTP [20.30] suggest that the large electric field gradients at the Ti sites and associated charge-transfer mechanisms are important factors establishing the necessary conditions for high nonlinear response. However, very recent stimulated Raman measurements show that, in KTP, the strongest vibrations occur in the direction collinear with the distortion of TiO_6 octahedra [20.31]. The other four oxygen ions around a titanium ion are parts of the PO_4 (or AsO_4) tetrahedra. These tetrahedra bond the −Ti−O−Ti−O− networks into a three-dimensional covalent ($TiOPO_4$) framework. The crystal structure is completed by potassium (or rubidium) ions occupying cavities, or cages, within this framework. These monovalent ions are either 8- or 9-coordinated with respect to oxygen, and they are denoted as K(1) and K(2), respectively, in Fig. 20.1 representing the KTP structure. Each K atom is asymmetrically coordinated by O atoms in the two inequivalent sites, and at a short distance along the *b*-direction from each K atom there is a void similar in size and coordination to the K site. The voids are termed *hole sites*, h(1) and h(2) [20.32], and they are pseudosymmetrically related to the K(2) and K(1) sites respectively, as is apparent from Fig. 20.1. At high temperatures, above the transition to the ferroelectric ($Pna2_1$) to paraelectric (centrosymmetric) *Pnan* phase, the K(1) and h(1) as well as K(2) and h(2) sites merge along the *b*-direction into positions halfway between the room-temperature K sites and their associated holes sites. More refined studies of the crystallographically unique K(1) and K(2) sites reveal additional subsplittings of their positions [20.33, 34]. Also, the K(1) cage has a volume 25% smaller than the K(2) cage [20.35]. This may explain why the larger Rb atoms substituting for K atoms in mixed $K_xRb_{1-x}TiOPO_4$ crystals occupy preferentially the larger K(2) sites, independently of the Rb incorporation mechanism, by crystal growth or ion exchange [20.36].

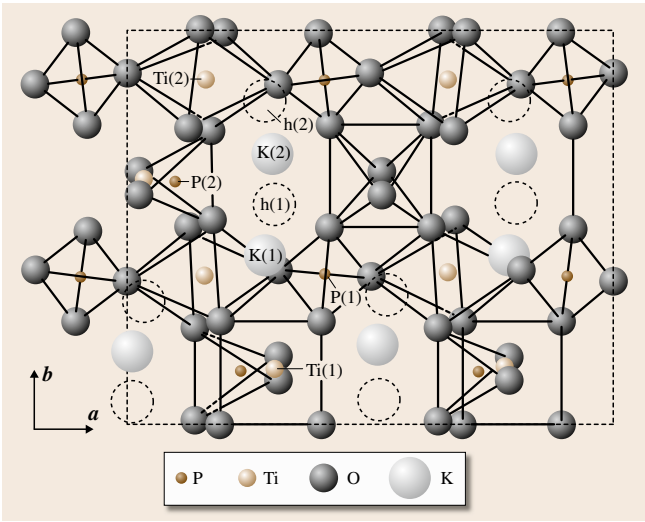


Fig. 20.1 A view of the KTP crystal structure along the *c*-axis direction

Ionic Conductivity

Finally, we refer again to Fig. 20.1 and conclude that there are additional consequences to the quite different environments for the K(1) and K(2) atoms. The $K(2)O_9$ cage forms a channel, parallel to the *c*-axis, which runs through the entire crystal structure and along which the K(2) atoms are expected to move relatively freely. On the other hand, the K(1) atom is constrained from a similar motion by the confinement of the $P(1)O_4-Ti(2)O_6$ chain which restricts its movement along the *c*-axis. Although the $K(1)O_8$ cage forms a channel along the *a*-axis, the K(1) atom does not show any significant movement along this axis even at high pressures [20.35]. Therefore, when KTP is described as a quasi-one-dimensional superionic conductor [20.37], with the conductivity σ_{33} being about three orders of magnitude higher than σ_{11} and σ_{22} [20.38], mainly K(2) ions can diffuse through cavities combined into channels along the *c*-axis direction via a vacancy mechanism [20.39]. Similar ionic conductivity anisotropy is valid also for KTA [20.2]. In RTP and RTA, σ_{33} is relatively smaller, since the activation energy for hopping of larger ions is higher [20.40,41]. The concentration of potassium/rubidium vacancies, or the degree of deviation from stoichiometry, depends on the crystal growth method and on specific growth parameters that will be discussed throughout the chapter.

20.1.2 Crystal Growth

KTP-family crystals decompose before melting (e.g., KTP decomposes at 1172 and 1158 °C in air and argon atmospheres, respectively [20.42]) and may be thus grown only from solutions. Relatively small but high-quality crystals can be grown from aqueous solutions by the hydrothermal process. Larger crystals, yet requiring meticulous quality control, can be grown from high-temperature tungstate and molybdate fluxes or self-fluxes. All these methods are being used for commercial production of KTP-family crystal in their seeded versions, although unseeded small crystals are occasionally processed for research purposes. The typical morphology of a KTP crystal [20.43, 44] grown on a seed fully immersed into the solution (by either of the methods mentioned above) is shown in Fig. 20.2.

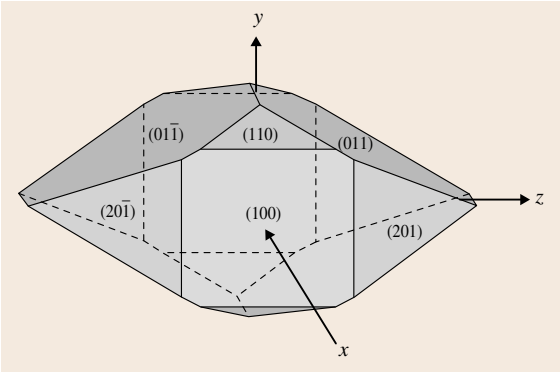


Fig. 20.2 Typical habit of an immersion-seeded KTP crystal

The crystal exhibits 14 facets belonging to four families of crystallographic planes, namely: {100}, {110}, {011} and {201}. Accordingly, 14 growth sectors develop simultaneously on the submerged seed. The morphology can be altered depending also on the seed shape and the solution composition [20.45, 46].

Hydrothermal Growth

A detailed description of the first attempts to grow a few millimeter-sized optical-quality KTP-family crystals hydrothermally was given by *Bierlein* and *Gier* in the patent literature [20.47, 48]. Typically, the hydrothermal process involved growing the crystal in an autoclave having a growth region and a nutrient region, and an aqueous mineralizer solution was employed. For example, *Laudise* et al. [20.49] used a Pt-lined low-carbon steel autoclave (75% filled) at a constant pressure of about 1360 atm with baffle-separated flux-grown KTP crystals as a nutrient (at 435 °C) and a ($2\,M\,K_2HPO_4 + 0.5\,M\,KPO_3$) mineralizer and TiO_2 to grow KTP crystals at around 400 °C. Better quality crystals were obtained by growing on (201)- and (010)-oriented seeds at $\approx 0.07-0.14$ mm/day rates. A typical commercial production of KTP crystals uses a potassium phosphate mineralizer at temperatures in the range of about 520–560 °C and pressures in the range of about 1700–2000 atm [20.50]. The relatively high temperatures and pressures employed in this process makes scale-up difficult and expensive, yet the use of more moderate conditions can lead to a problem of anatase (TiO_2) coprecipitation [20.51], making the process less useful. In principle, it has been shown that growth temperatures (< 500 °C) and pressure (< 1000 atm) can be reduced while using potassium-rich mineralizer solutions, but the growth rate becomes limited (< 0.13 mm/day) due to the relatively low solubility of $KTiOPO_4$ in the mineralizer [20.52].

Other types of mineralizers adopted for the hydrothermal growth of KTP involve the use of KF solutions, as suggested by *Jia* et al. [20.53, 54]. By utilizing KF as a mineralizer, relatively lower temperature

and pressure (≈ 1000 atm) can be employed for a hydrothermal KTP crystal growth process. In addition, the use of pure KF mineralizer provides a solubility of about 2% under the stated growth conditions, but like the process described by *Laudise* et al. [20.49], the higher solubility occurs near the phase-stability boundary (with respect to temperature, pressure, and mineralizer concentration), so the possibility of coprecipitation of an undesirable non-KTP phase exists. To avoid this disadvantage, *Cheng* [20.55] suggested complex aqueous solutions as mineralizers comprising both KF and potassium (rubidium) phosphates (arsenates) for hydrothermal production of KTP-family crystals, in amounts effective to assure solubility of the KTP-type crystals of at least about 1% by weight. Although grown under higher temperatures and pressures, optical-quality KTP and KTA crystals of at least 1 mm^3 volume could be recovered after a few hours rather than days and weeks. In the most recent report on hydrothermal KTP growth a process utilizing a (2 M K_2HPO_4 + 0.1 M KH_2PO_4 + 1 wt % H_2O_2) solution as a mineralizer and crushed flux-grown KTP crystals as a nutrient was described [20.56]. Crystals with dimensions up to $14.5 \times 28 \times 17\,mm^3$ have been grown on (011) and spherical seeds at a rate of 0.15 mm/day in the 400–540 °C temperature range and 1200–1500 atm pressure range. They exhibited an exceptionally high (for KTP) optical damage threshold of 9.5 GW/cm^2.

Growth from Low-Viscosity Melts

In the early days of optical-grade KTP development, the only commercial process reported was the hydrothermal crystal growth technique requiring cumbersome high-pressure vessels with noble-metal liners and yielding relatively small crystals. Initial attempts to grow KTP crystals from phosphate fluxes at atmospheric pressure conditions [20.42] seemed to encounter the problem of high melt viscosity. *Ballman* et al. [20.57] were the first to report on the growth of up to 1 cm^3 KTP single crystals from a low-melting low-viscosity water-soluble tungstate flux. Tungstic anhydride was added to the potassium phosphate-titanium oxide melt, and KTP as a single stable phase formed according to the following reaction

$$4K_2HPO_4 + 2TiO_2 + 3WO_3 \xrightarrow{1000\,^\circ C} 2KTiOPO_4 + 3K_2WO_4 \cdot P_2O_5 + 2H_2O\,. \quad (20.1)$$

Iliev et al. [20.58] found that with a $K_2O : P_2O_5$ ratio of 0.9 : 0.1 and 40 mol % WO_3 in the melt, the flux viscosity was as low as 10–15 cP in the 1050–850 °C temperature range. High-optical-quality KTP crystals up to $30 \times 20 \times 20\,mm^3$ in size could be grown from the K_2O-P_2O_5-TiO_2-WO_3 system in the 930–700 °C temperature range at a rate of 0.9 mm/day [20.59]. Not only KTP, but also RTP, KTA, and RTA crystals were subsequently grown from both tungstate and molybdate fluxes [20.44]. However, optical inhomogeneities associated with tungsten-containing (0.5–1.0 wt %) striations parallel to the {011} faces were identified [20.60, 61]. Indeed, electron paramagnetic resonance (EPR) measurements show that tungsten enters KTP as an impurity occupying both the Ti(1) and Ti(2) sites as W^{5+} and, partly, the Ti(2) site as W^{4+} [20.62]. The tungsten impurity is found to cause detrimental multiplication of growth sectors in the case of ⟨011⟩-seeded (and less ⟨010⟩-seeded) KTP crystal growth from $3K_2WO_4 \cdot P_2O_5$ fluxes [20.63].

When small amounts of MoO_3 are added to the phosphate flux ($K_6P_4O_{13}$) in the case of spontaneous nucleation growth, only trace amounts of Mo are detected in the KTP crystal, but they prevent spurious nucleation and increase the crystal hardness necessary for improved polishing [20.64]. In a different attempt to reduce the melt viscosity, potassium halides were added to the phosphate flux to grow KTP [20.65] or RbI to grow RTP [20.66] crystals.

Growth from Self-Fluxes

The main crystal growth problems pointed out above were that the hydrothermal process yielded high-quality but small single crystals, and the use of tungstate fluxes resulted in incorporation of W impurities into the crystals, increasing the optical loss [20.60] and lowering their laser damage resistance [20.67]. Therefore, the development of most of the practical NLO devices unfolded in parallel with constant advancement of the seeded growth of large and ever-improving quality KTP-family crystals from self-fluxes, namely high-temperature solutions in alkali phosphates. In the early work [20.42, 68, 69], KTP crystals up to 1 cm^3 in size were grown from flux compositions within the KPO_3-$K_4P_2O_7$ system. The end components obtained by thermal decomposition of K_2HPO_4 and KH_2PO_4 together with TiO_2 were used for flux preparation, e.g., according to the following high-temperature reactions

$$KH_2PO_4 + TiO_2 \rightarrow KTiOPO_4 + H_2O\uparrow\,,$$
$$2KH_2PO_4 + 2K_2HPO_4 \rightarrow K_6P_4O_{13} + 3H_2O\uparrow\,. \quad (20.2)$$

More chemical routes for preparing self-fluxes of KTP and its isomorphs are given by *Iliev* et al. [20.70] and *Cheng* et al. [20.10]. $K_6P_4O_{13}$ (denoted as K6 in the literature), with the K-to-P ratio $R = 1.5$, is the most popular solvent for KTP growth due to the moderate viscosity [20.71] and volatility [20.70] of the KTP/K6 flux and relatively high solubility of KTP. Other solvents, such as $K_4P_2O_7$ (K4), $K_5P_3O_{10}$ (K5), $K_8P_6O_{19}$ (K8), $K_{10}P_8O_{25}$ (K10), $K_{15}P_{13}O_{40}$ (K15), and $K_{18}P_{16}O_{49}$, have been also studied, mainly in terms of KTP solubility [20.46, 72] in the 900–1100 °C temperature range. The solubility decreases down this sequence due to the relative decrease of the concentration of $(P_2O_7)^{-4}$ anions in the flux, since all the above solvents can be viewed as composed of $(xKPO_3 + yK_4P_2O_7)$ [20.72]. In the case of KTP isomorphs, their solubility in similar self-fluxes (RTP/R6 [20.73, 74], KTA/K6, RTA/R5, and CTA/C5 [20.10], KTA/K5 [20.75], and RTP/R4 [20.76]) has been also reported.

Reproducible and controllable seeded growth of large-size KTP crystals from the KTP/K6 flux has been repeatedly reviewed [20.77–79]. In view of the small undercooling required for KTP nucleation, close to nongradient conditions in the growth furnace are appropriate. However, it is necessary to provide for a high degree of spatial temperature uniformity in order to avoid spurious nucleation. *Bordui* et al. [20.80] used a heat-pipe-based furnace for this purpose with submerged seeding. Others used three-zone [20.81] or five-zone [20.82] furnaces to produce large (200–300 g) and almost inclusion-free KTP crystals by the top-seeded solution growth (TSSG) method. *Angert* et al. [20.83] suggested a way to improve the yield of KTP crystal growth by combining the TSSG technique with seed pulling. Figure 20.3 shows the growth schemes typical for the submerged seed, top-seeded, and top-seeded with pulling configurations.

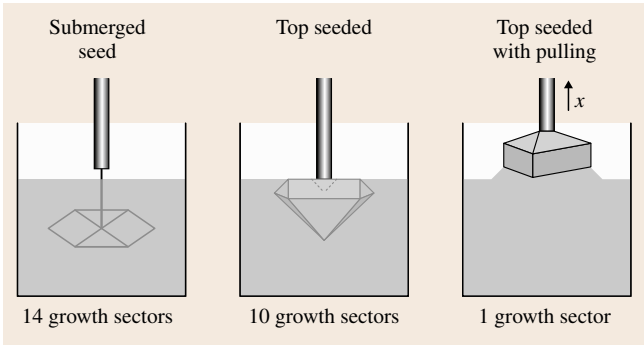


Fig. 20.3 Three configurations for seeded high-temperature solution growth of KTP-family crystals

The convection-dominated mass transfer in submerged seed growth of KTP (left image in Fig. 20.3) was studied theoretically by *Vartak* and *Derby* [20.84], and some modeling problems were pointed out. An interesting approach to the submerged growth was put forward earlier by *Bordui* and *Motakef* [20.85] (modeling and experiment), who suggested an asymmetric 90° seed orientation and rotation at 50 rpm with periodic reversal in order to reduce the amount of inclusions. Their model was initially supported by numerical analyses performed by *Vartak* et al. [20.86], but a more recent boundary-layer analysis for flow and mass transfer [20.87] showed that the straightforward computational approach, such as the use of a spinning disk approximation, could provide satisfactory results only under experimental conditions not matching the realistic setups employed in the field. It is noteworthy that surface kinetics must be also considered in the growth of KTP crystals [20.46, 88].

Although the submerged seed method is still being used for commercial production by a few vendors, clearly the development of up to 14 growth sectors (Fig. 20.2) limits the use of such KTP crystals to fab-

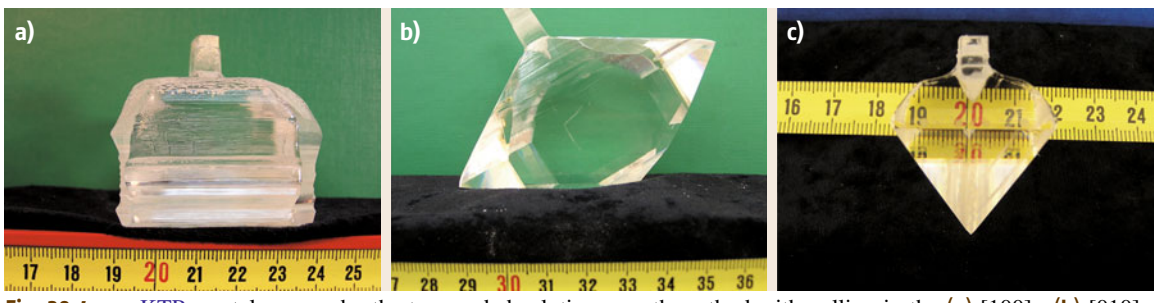


Fig. 20.4a–c KTP crystals grown by the top-seeded solution growth method with pulling in the **(a)** [100]-, **(b)** [010]-, and **(c)** [001]-directions

ricating only small optical elements, since elements cut from a single sector are required for high-quality performance [20.89]. Multiplication of growth sectors results in nonuniform growth rates [20.46, 63] and incorporation of trace impurities at the sector boundaries and may affect the ferroelectric domain structure to be discussed below. The same is true for the conventional top-seeding method, shown in the middle sketch of Fig. 20.3. In contrast, TSSG with pulling reduces the number of growth sectors formed. *Bolt* et al. [20.81] suggest the use of a [001]-oriented seed, since maximal linear growth rate can be achieved in this direction. (Note that the low growth rate in the [100] direction can be overcome by using seeds elongated in this direction [20.45] to grow larger crystals.) However, in the case of [001] seeding, four growth sectors form, and the crystal is bound by the {201} and {011} facets. The use of [100]-oriented seeds is, therefore, favorable [20.83], since growth of a single growth sector crystal can be achieved. The corresponding configuration is shown on the right side of Fig. 20.3. With the largest (100) facet (Fig. 20.2) parallel to the growth front, as is typical for growth from the KTP/K6 flux, a planar solid–liquid interface bounds the crystal, assuring the best possible transverse uniformity of its physical properties. Photographs of three KTP crystals grown by the TSSG method with pulling on [100]-, [010]-, and [001]-directed seeds are shown in Fig. 20.4 to illustrate their distinct morphologies.

20.2 Stoichiometry and Ferroelectric Phase Transitions

Regardless of the growth method of KTP-family crystals from self-fluxes, say of $MTiOXO_4$ (M = {K, Rb} and X = {P, As}) from $MTiOXO_4/M_6X_4O_{13}$, the M-to-X ionic ratio increases as the crystal grows out, leaving behind a solution that becomes gradually enriched in M cations. Obviously, the M-metal content in the growing crystal increases accordingly, presumably improving the associated stoichiometry; for example, in the initially solidifying portion of the KTP crystal grown from the KTP/K6 flux, large concentrations of potassium vacancies (500–800 ppm) have been detected [20.90]. These vacancies can be charge-compensated by holes trapped at bridging oxygen ions between two titanium ions [20.91] and by positively charged oxygen vacancies [20.92]. This is reflected in the high-temperature defect formation reaction [20.93]

$$KTiOPO_4 \rightarrow K_{1-x}TiOPO_{4(1-x/8)} + \tfrac{x}{2}K_2O\,, \quad (20.3)$$

where x is the concentration of potassium vacancies.

Most of the KTP-family crystals are high-temperature ferroelectrics [20.9] which undergo a second-order phase transition changing its point group symmetry from *mmm* in the high-temperature paraelectric phase to the *mm*2 polar symmetry class in the low-temperature ferroelectric phase [20.94]. The ferroelectric phase transition (Curie) temperature, T_C, is very sensitive to the crystal stoichiometry and ionic substitution, which is manifested in the large spread of published Curie temperatures for all KTP-family crystals [20.95]. In this section we will discuss the correlation between the Curie temperatures and the defect structure, mainly stoichiometry, in KTP and RTP and present the limited results available also on other related crystals.

20.2.1 $KTiOPO_4$ Crystals

In KTP, addition of dopants, such as Ga, Al, and Ba, in the 400–2000 ppm concentration range is known to reduce the Curie temperature by several tens of degrees and modifies the Curie constant in the Curie–Weiss law [20.96, 97]. Isomorphic substitution of K and P ions by Rb, Cs or Tl and As reduces the Curie temperature by hundreds of degrees [20.97, 98]. Partial substitution of Na for K has been shown to initially increase the T_C from 944 °C for pure KTP to 956 °C and then decrease it to 914 °C for [Na] = 4 and 47 mol %, respectively [20.99]. A large diversity of Curie temperatures was reported for pure KTP crystals. The highest T_C values, 955–959 °C [20.97, 99, 100], were measured on hydrothermally grown crystals. A variety of lower T_C values was given for flux-grown KTP crystals: 952 °C [20.95] (second-harmonic generation (SHG) measurements), 947–951 °C [20.100], 946 °C [20.97], 944 °C [20.99], 934 °C [20.101], 910 °C [20.102] (dielectric measurements), and 892 °C [20.103] (birefringence measurements). Such scatter of data is beyond any imaginable experimental error and can be explained only in terms of variable stoichiometry of the KTP crystals grown from different solutions under variable growth conditions. *Angert* et al. [20.72] have studied the dependency of T_C on the composition of self-fluxes in great detail, and the main results will be presented below. The influence of high-temperature annealing on T_C has been addressed as well.

Curie Temperature Versus Composition

Curie temperatures of numerous crystals grown from different self-fluxes with varying initial concentrations were measured by a standard dielectric technique [20.72]. The results are reproduced in Fig. 20.5, where the measured T_C values are given as a function of weight concentration of KTP in each of the seven fluxes used, namely corresponding to KTP dissolved in the K4, K5, K6, K8, K10, K15, and K18 solvents with [K]/[P] ratios (R) varying from 2 to 1.125. The lowest T_C value found was 898 °C and the highest was 960 °C, but these limits could be stretched even further upon broadening the KTP concentration and solvent composition ranges. Within the part of the crystallization field studied (of the K_2O-TiO_2-P_2O_5 ternary system) the T_C dependencies can be approximated by straight lines for all fluxes employed. This provides the possibility of a quantitative representation of the T_C dependences on two parameters: R and the KTP concentration in the flux (C), which can be fitted by the equation

$$T_C(C, R) = 980 + (C + 0.24) \times (98R^3 - 555.6R^2 + 1074R - 733) , \quad (20.4)$$

for $1 < R \leq 2$. Equation (20.4) allows to forecast or to choose any desirable initial T_C for the crystal, since it holds for any arbitrary self-flux composition. In principle, the higher the T_C value, the more perfect the crystal in terms of stoichiometry or content of impurities, which may be important for many physical applications of this type of crystals.

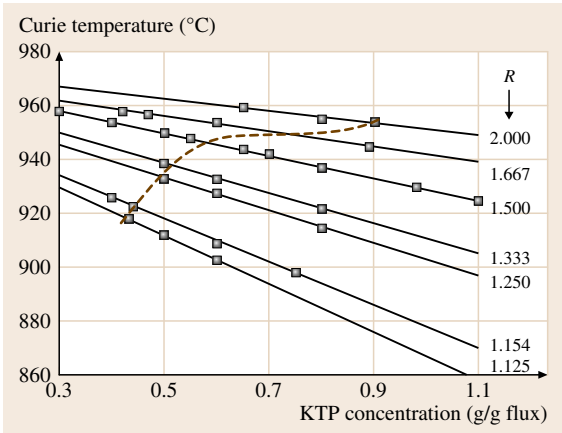


Fig. 20.5 Curie temperatures as a function of KTP concentration in the flux for seven different solvents ($K_4P_2O_7$, $K_5P_3O_{10}$, $K_6P_4O_{13}$, $K_8P_6O_{19}$, $K_{10}P_8O_{25}$, $K_{15}P_{13}O_{40}$, and $K_{18}P_{16}O_{49}$) corresponding to different potassium-to-phosphorus ratios (R). The *dotted line* crosses the slopes at compositions of equal Curie and crystallization temperatures (deduced from the measured solubilities of each flux)

It is apparent from Fig. 20.5 that, the lower the KTP concentration in any particular self-flux, the higher the Curie temperature of the solid. Also, for any given concentration, the Curie temperatures are higher for self-fluxes exhibiting higher values of R. These two observations can be combined into one conclusion, namely that higher overall concentrations of K in the solution result in higher Curie temperatures of KTP crystals. Moreover, this implies a gradual increase in T_C during growth of a large KTP crystal, since for any given self-flux the solution becomes richer in K while the crystal grows out. T_C increase of up to 20 °C along the growth direction in some large KTP crystals grown from the $K_6P_4O_{13}$ solvent are reported [20.72]. Such spatial variation of T_C in the crystal is obviously associated with compositional (mainly stoichiometry) gradients resulting in nonuniformity of the crystal physical properties. Indeed, *Miyamoto* et al. [20.104] have observed appreciable gradients in the refractive indices, $\Delta n_x/\Delta x = 1.2\times10^{-5}\,\mathrm{mm}^{-1}$ and $\Delta n_z/\Delta z = -2.0\times10^{-5}\,\mathrm{mm}^{-1}$, in a large TSSG KTP crystal.

Another a priori observation from Fig. 20.5 is that growth above the dotted line is supposed to yield single-ferroelectric-domain crystals, while growth below this line is apt to result in multidomain crystals, which is occasionally claimed [20.105]. However, in reality, multidomain KTP crystals are frequently obtained for growth below T_C, and single-domain crystals may form when growth is initiated above T_C [20.106]. This may be understood after a more detailed insight into the nature of compositional gradients arising from the variable potassium stoichiometry. Even a relatively large concentration of potassium vacancies of up to 800 ppm [20.90] is small in comparison with the overall amount of potassium ions. Therefore, the gradients of the latter are small in absolute terms. The diffusion coefficient of the K^+ ions at typical growth temperatures is small as well, e.g., $8\times10^{-10}\,\mathrm{cm}^2/\mathrm{s}$ at 965 °C [20.107]. This explains why the growth-induced potassium concentration gradients essentially *freeze in* along the crystal. The associated gradients of ionized oxygen vacancies are, in contrast, relatively high, and they are responsible for the production of a built-in electric field according to the model proposed earlier by *Kugel* et al. [20.92]. This built-in field may be signifi-

cantly larger than the coercive field [20.92] depending on the magnitude of the existing concentration gradients of charged species. The resulting *memory* effects may have an impact on the ferroelectric domain formation.

Effect of Thermal Treatment

Direct proof for the existence of a close relationship between potassium nonstoichiometry and the Curie temperatures of KTP crystals has been found while monitoring the T_C variation in samples exposed to high-temperature annealing in air. A typical example of the results is shown in Fig. 20.6. A set of 1.35–1.5 mm thick z-cut samples exhibiting an initial T_C value of 950 °C has been maintained at 1000 °C in air for variable long periods of time. Exposure to high temperatures causes partial decomposition of the crystal surface, which manifests itself in the appearance of a translucent outer layer, a few tens of micrometer thick. This layer has been removed upon cooling to room temperature, leaving behind a transparent, colorless crystal. Figure 20.6 shows that the Curie temperature can be reduced by prolonged high-temperature annealing in air down to 883 °C, i. e., even beyond the lowest T_C values obtained in as-grown KTP crystals. This effect can be explained in terms of gradual potassium escape, or increasing potassium deficiency in the crystal, upon heat treatment [20.92, 107, 108]. A moderate increase in the Curie temperature following 400 h of heat treatment is not an artifact and has been repeatedly observed with a number of samples. This may result from as-yet unknown kinetics of stoichiometry variation in high-temperature-annealed KTP crystals associated with the surface layer decomposition [20.108].

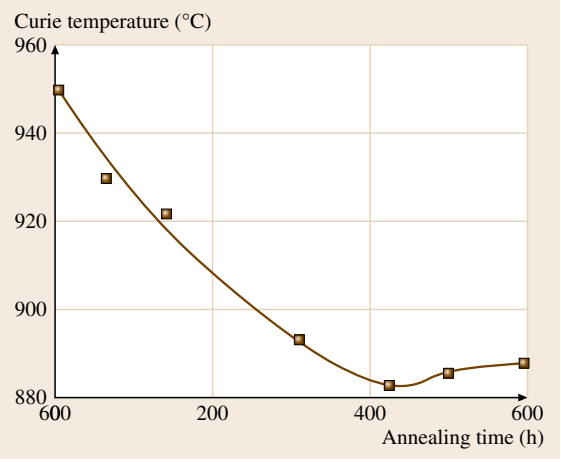


Fig. 20.6 Dependence of Curie temperature on time for long-term high-temperature annealing (at 1000 °C) of 1.35–1.5 mm thick KTP crystals grown from a 0.5 (g/g) KTP/$K_6P_4O_{13}$ flux (after [20.72])

The existence of potassium nonstoichiometry in KTP crystals was realized a long time ago [20.109], but there was disagreement about the limits of its range. According to some reports, this range is narrow, less than 0.1 mol % [20.90], while others claim that it may exceed 10 mol % [20.108]. Our preliminary electron microprobe measurements indicate that the potassium deficiency may be of the order of a few mol. % and that phosphorus nonstoichiometry may exist as well [20.110]. An attempt to evaluate the KTP composition based on T_C measurements has been made only using ceramic KTP compounds synthesized at 800 and 900 °C [20.89], since the single crystal decomposes before melting. It is common to think that stoichiometry of as-grown KTP depends on the crystallization temperature alone [20.90]. However, this is true only for a single kind of self-flux (Fig. 20.5), when the saturable KTP concentration (solubility) is a direct function of temperature. A generally more correct statement is that KTP stoichiometry, and thus the Curie temperature, depend on the self-flux composition; for example, two crystals grown from 1.1 g/g $K_6P_4O_{13}$ and 0.4 g/g $K_{15}P_{13}O_{40}$ fluxes have an identical T_C value of 925 °C, yet their crystallization temperatures (1080 and 926 °C, respectively) are completely different.

Effect of Impurities

We have referred above to the gradients of potassium and oxygen vacancies V_K and V_O, respectively. However, the latter can be superimposed by the gradients of residual impurities on the various KTP cation and anion sites. Some impurities may create a charge-compensating effect and alter the magnitude of the built-in electric field. Depending on the valence and the nature of a substitutional site captured, impurity ions may enhance or diminish the concentration of oxygen vacancies that are normally charge-compensating the potassium vacancies. Table 20.3 gives a chart of the influence of various impurities located at different sites, assuming that the effective distribution coefficients (k_{eff}) of all impurities are less than one. The parallel arrows indicate enhancement of the V_O concentration gradients, while antiparallel arrows indicate their compensation with a consequent reduction in the value of the built-in electric field in the z-direction.

It should be noted that miscellaneous dopants are frequently introduced into the KTP crystals for a variety of reasons, such as alteration of their resistivity [20.90]

Table 20.3 Concentration gradients of oxygen vacancies in KTP crystals grown from self-fluxes and solutions with charge-compensating dopants ($k_{eff} < 1$)

Case	Type of doping	Direction of V_O concentration gradient induced by		
		V_K in self-flux	Doping	Result
1	Self-flux	⇓	None	⇓
2	A^{3+}/Ti^{4+}	⇓	⇓	⇓ ⇓
3	A^{5+}/Ti^{4+}	⇓	⇑	⇓ or ⇑
4	A^{6+}/T^{4+}	⇓	⇑	⇓ or ⇑
5	B^{2+}/K^{+}	⇓	⇑	⇓ or ⇑
6	Si^{4+}/P^{5+}	⇓	⇓	⇓ ⇓
7	F^{-}/O^{2-}	⇓	⇑	⇓ or ⇑

⇓ Direction from the seed to a growing facet, ⇑ direction from a growing facet to the seed,
$A^{3+} = Sc^{3+}, Ga^{3+}, Al^{3+}, In^{3+}, Cr^{3+}$; $A^{5+} = Nb^{5+}, Ta^{5+}$; $A^{6+} = W^{6+}, Mo^{6+}$; $B^{2+} = Pb^{2+}, Ca^{2+}, Mg^{2+}$

or nonlinear optical properties [20.111, 112]. Lead oxide is deliberately added to the K6 self-flux [20.106] in order to enhance the crystal growth rate and to reduce the probability of spurious nucleation at the crucible wall. As a result, several hundred ppm of Pb^{2+} ions have been introduced into the crystal [20.113]. They cause a beneficial effect of significantly reducing the concentration of color centers responsible for the detrimental *gray-tracking* phenomenon [20.67] in frequency-doubling the 1.06 μm Nd:YAG laser. Most stable *gray-track* defects are attributed to the presence of oxygen-vacancy-associated Ti^{3+} centers in the KTP crystal. Addition of small amounts of Pb^{2+} ions substituting for K^{+} ions provides charge compensation for potassium vacancies, and oxygen vacancies are no longer needed. (Gray-tracking will be discussed in more detail at the end of this chapter.) Reduction in the concentration of oxygen vacancies and their gradients has the effect of diminishing the built-in electric field and is, therefore, influencing the ferroelectric domain formation in KTP crystals during growth and cooling through the Curie temperature.

20.2.2 $RbTiOPO_4$ Crystals

Presently, RTP is viewed as a particularly useful member of the KTP family of crystals for electrooptic applications, such as high-frequency Q-switching and light modulation, due to its large electrooptic coefficients, high damage threshold, and the absence of piezoelectric ringing [20.14, 114]. The low-ionic-conductivity RTP crystals are required for low-leakage-current operation of the devices. Although the Rb^{+} ion is larger than the K^{+} ion, RTP is also a classical ionic conductor [20.39], and vacancy-assisted one-dimensional ionic conductivity is expected. It is thus important to monitor the concentration of Rb vacancies, or the degree of Rb stoichiometry, which may and usually does depend on the crystal growth conditions. The fundamental ideas about such dependence for growing RTP crystals from self-fluxes can be based on the knowledge accumulated with KTP crystals as described above. In the present section, we will review the recent results on the variable stoichiometry of RTP crystals as assessed using the Curie temperature measurements by *Roth* et al. [20.76]. Some peculiar results distinct from those observed with KTP were revealed.

Differentiation of Growth Sectors

In similarity with KTP, an RTP crystal growing out from a particular flux, e.g., $Rb_6P_4O_{13}$ (R6), and becoming enriched in rubidium in course of the process is expected to be gradually more stoichiometric in terms of Rb^{+} ions. To verify this, a 300 g RTP crystal (of Fig. 20.4a type) was grown from an R6 solvent by pulling on a [100]-oriented seed, and the Curie temperatures of the top and bottom parts of the boule were measured using the dielectric (capacitance) anomaly technique. The top part exhibited $T_C = 782\,°C$, and the bottom part showed a higher T_C value by 5 °C. This result was in accord with the expected improvement of rubidium stoichiometry. The absolute T_C values depend, of course, on the specific solute content and solvent composition in the flux, to be discussed below.

Before engaging in the analysis of Curie temperature dependencies on the flux chemical composition, we will address the peculiar effect revealed in the course of taking the capacitance versus temperature characteristics in some RTP samples. These characteristics frequently feature two peaks, pointing to the fact that

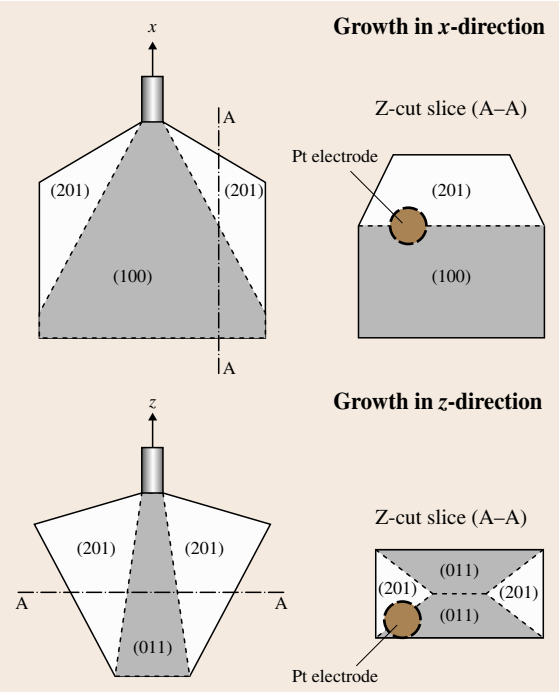


Fig. 20.7 Schematic representation of growth sectors developed in RTP crystals grown on x- and z-oriented seeds; z-cut slices may contain two growth sectors, which can be partially included in the area below the Pt electrode

two different Curie temperatures exist in the same sample. A close examination of such samples revealed that they were cut from crystal areas comprising two different growth sectors, and that the Pt electrodes covered areas containing both sectors. We recall that RTP crystals (like other KTP-family crystals) contain 14 growth sectors, displayed through four types of well-developed facets: 2 × {100}, 4 × {110}, 4 × {011}, and 4 × {201}, in its typical morphological habit (Fig. 20.2). The number of growth sectors and the volume and geometry of each particular sector depend on the growth direction and type (submerged, TSSG, with or without pulling). Figure 20.7 shows schematically the structure of main growth sectors in two RTP crystals grown by the TSSG method from R6 fluxes, one with pulling on an x-oriented [100] seed and the other without pulling and grown on a z-oriented [001] seed. Samples for T_C measurements were machined from z-cut slices along the A–A lines shown in the figure for both cases. Apparently, Pt electrodes could cover either a single growth sector or two sectors, and a double-peaked $C = C(T)$ characteristic was obtained in the latter case.

Curie Temperature Versus Composition

The intriguing result described above implies that the variation of the Curie temperature, or of the stoichiometry of RTP crystals, as a function of the flux chemical composition must be studied for each growth sector separately. In Fig. 20.8, the results for three differen-

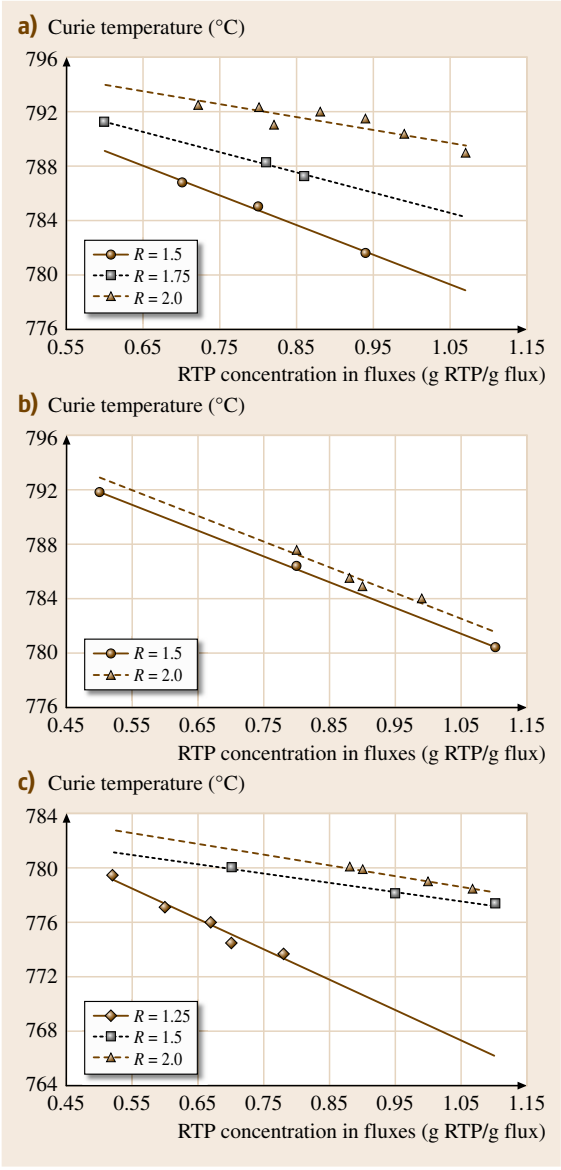


Fig. 20.8a–c Curie temperatures as a function of RTP concentration in the solution for various self-fluxes, measured separately for three growth sectors: **(a)** {100}, **(b)** {011}, and **(c)** {201}

tial growth sectors, of the {100}, {011}, and {201} types, are presented. For each sector, T_C as a function of RTP concentration (in weight units) is given for self-fluxes with different R ([Rb]/[P]) values. The nearly linear dependencies obtained are in complete similarity with the KTP case: (1) the lower the RTP concentration, in any self-flux, the higher the T_C value of the crystal, and (2) for any given RTP concentration, T_C is higher for self-fluxes with higher values of R. The combined result is that a higher Curie temperature corresponds to a higher overall concentration of the Rb ions in the solution, and therefore to higher rubidium content in the crystal. Naturally, the solution becomes gradually enriched in rubidium in the course of RTP crystal growth. The important practical consequence of this behavior is that a rubidium concentration gradient builds up in the as-grown crystal. This gradient is not averaged out during the cool-down stage, since the diffusion coefficient of the larger Rb^+ ions is presumably even smaller than that of K^+ ions.

The observed span of T_C values in RTP, from 770 to 800 °C, is much narrower than the corresponding range of Curie temperatures in KTP (880–960 °C). In addition, the slopes of the linear dependencies are shallower. We presume, therefore, that the overall extent of change of the Rb stoichiometry in RTP crystals is essentially smaller than the corresponding variation of K stoichiometry in KTP crystals. Another distinctive feature of RTP crystals is that they exhibit abrupt *jumps* in the Curie temperature over boundaries between any pair of simultaneously solidifying growth sectors of different types, as can be deduced from Fig. 20.8. It is noteworthy that a sign of a double peak in the $C(T)$ curve has been reported for the isomorphic CTA crystal [20.20], but has never been observed in nominally pure (undoped) KTP crystals. Only deliberately doped KTP may show double peaks due to the different distribution coefficients of dopants at various growth faces along the crystal–melt interfaces [20.76].

Extensive studies of nominally pure and deliberately doped RTP crystals exhibiting double peaks in their $C(T)$ curves, with a separation of over 10 °C between the T_C values on a single sample, cannot be explained by the presence of trace impurities. A different explanation must be invoked. It starts with the recognition that the RTP growth temperatures are typically 100–200 °C higher than the T_C values, and the crystals solidify in the pseudosymmetric *mmm* phase [20.116], in which the R(1) and R(2) sites are symmetrically identical [20.24]. However, the likely diverse formation mechanisms of native defects within the various growth facets at high temperatures may cause a variation in the statistical distribution of the Rb ions between the Rb(1) and Rb(2) sites during cooling through the ferroelectric phase transition. The defects may be associated not only with the rubidium and charge-compensating oxygen vacancies, but also with other stoichiometric components, namely titanium and phosphorus ions. However, initial attempts to identify any deviation from the stoichiometric composition of these components using the electron-microprobe technique did not contribute positive results.

20.2.3 Other KTP Isomorphs

Only a limited attempt has been made to study the crystal stoichiometry versus flux composition dependencies in KTP isomorphs other than RTP. This is regrettable, since the arsenates, especially KTA, are very useful for OPO applications in the near-infrared [20.15], and optically uniform long x-cut elements are required. The same applies to RTA crystals used for periodically poled waveguide frequency-doubling devices [20.117]. In this section, some preliminary results on the arsenate isomorphs are given.

Curie Temperature Variation

In a recent work [20.118], a series of relatively small ($< 1\,cm^3$) KTP, RTP, KTA, and RTA crystals were grown by the TSSG method from high-temperature K6 and R6 self-fluxes containing different starting concentrations of the (KTP, KTA) and (RTP, RTA) solutes, respectively. Figure 20.9 shows the Curie tempera-

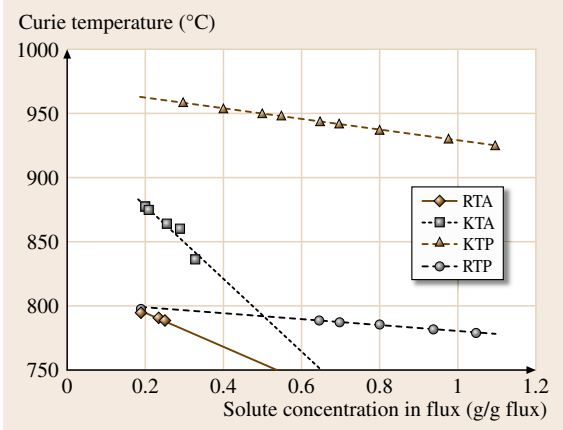


Fig. 20.9 Curie temperature dependence on solute (KTP, RTP, KTA, and RTA) concentration in the respective K6 or R6 flux for four KTP isomorphs (after [20.115])

ture dependencies of all the corresponding crystals on the solute concentration in the flux for comparison. The trend lines expanded for the two arsenate crystals do not represent accurate slopes, since only a few growth experiments have been carried out, at small solute concentrations. There is a difficulty in obtaining such crystals with reliably changing compositions from highly concentrated solutions, namely at higher growth temperatures, due to arsenic evaporation. However, the common rule for all isomorphs is quite apparent, namely, the more dilute the solution, the higher the Curie temperature, and the more stoichiometric the crystal. This reflects the fact that, at smaller solute concentrations, the crystal solidifies from solutions richer in (primarily) potassium or rubidium ions with respect to titanium.

In the preceding discussion, we have referred only to the potassium or rubidium stoichiometry. The reasons for such approach are that (1) titanium (oxide) alone is left behind during prolonged high-temperature annealing of KTP, while the potassium and phosphorus compounds evaporate [20.93], and (2) there is a general belief that PO_4 tetrahedra are the basic building blocks of the KTP structure [20.115], making phosphorus non-stoichiometry less likely. On the contrary, the existence of potassium [20.90] and rubidium [20.119] vacancies in KTP and RTP, respectively, has been demonstrated.

Concluding Remarks

To summarize this section, large crystals of KTP and its isomorphs, such as RTP, KTA, and RTA, are found to exhibit gradual compositional changes in their stoichiometric components (primarily potassium or rubidium ions) during TSSG from self-fluxes. This has been verified by measuring the ferroelectric transition (Curie) temperatures of the various crystals grown from fluxes of different initial solute concentrations. Higher Curie temperatures of crystals solidified from dilute solutions indicate their improved stoichiometry, which translates into better performance in optical devices; for example, more stoichiometric KTP becomes highly resistant to the detrimental gray-tracking in SHG [20.89]. Better stoichiometry implies also lower coercive fields necessary for efficient processing of KTP-based periodically poled nonlinear optical devices (see Sect. 20.4.1 for more detail) and orders of magnitude higher electrical resistivity, which is particularly important for the use of RTP crystals in electrooptic devices [20.14].

20.3 Growth-Induced Ferroelectric Domains

Single-domain KTP-family crystals can be readily grown from high-temperature solutions well below the Curie temperature. However, high-temperature growth is of more practical interest due to the lower viscosity or significantly larger growth rates involved [20.83]. When the high-temperature growth results in multidomain crystals, the latter can be converted into single-domain structures by complex thermal annealing [20.105, 107]. The presence of multiple domains degrades the optical uniformity and, thus, the device performance of the crystals. Numerous questions associated with the domain structure and their formation during crystal growth, cooling through the Curie temperature, and thermal annealing are still not understood to a full extent. Historically, *Zumsteg* et al. [20.116] were the first to predict the existence of a ferroelectric domain structure in KTP-family crystals. *Bierlein* and *Ahmed* [20.120] used piezoelectric, electrooptic, and pyroelectric techniques to reveal the domain structure in hydrothermally grown KTP crystals. They found domains oriented parallel to the (100) crystallographic plane and zigzag domain walls characteristic of a head-to-head domain configuration. A more complex domain structure was observed by *Loiacono* and *Stolzenberger* [20.121] in flux-grown KTP crystals. This structure, termed *dark line defects*, could not be ascribed any definite crystallographic orientation. Moreover, the domain pattern could not be altered by thermal cycling to above the Curie temperature and, thus, the domains were identified as possible nonferroelectric Dauphiné twins. *Shi* et al. [20.122] reported on the existence of a ferroelectric domain twin boundary in KTP parallel to the crystallographic (001) plane. They concluded, based on X-ray double-crystal diffraction measurements, that the (100) facet of KTP was formed by two symmetric vicinal planes with the interface between the vicinal planes being the 180° twin boundary. However, other authors [20.10, 83] pointed out that the (100) vicinal plane boundary and the corresponding 180° twinned domain wall might not coincide with the (001) plane but rather exhibit a considerably more complicated structure.

20.3.1 Domains in Top-Seeded Solution-Grown KTP

KTP crystals grown from highly concentrated solutions usually crystallize in the paraelectric phase above the Curie temperature (Fig. 20.5). The ferroelectric domain structure is formed upon postgrowth cooling, at a rate of $\approx 25-40\,^{\circ}\mathrm{C}$ in a 2–5 K/cm temperature gradient. In order to visualize the domain structure, diverse techniques are employed, such as etching and piezoelectric measurements [20.107] or pyroelectric toning [20.123]. Below, visualization of the various KTP ferroelectric domain structures will be presented as obtained by simple etching in a 2 : 1 (molar ratio) KOH : KNO_3 solution at 220 °C. The main parameters governing the kinetics of the diverse domain shape formation are elucidated in this section as well.

Bidomain Structure

TSSG of KTP crystals from the K6 self-flux by pulling on x-oriented seeds and initiated above the T_C (Fig. 20.4a) frequently results in a bidomain structure, namely the boule contains two large ferroelectric domains of opposite sign in a head-to-head configuration. Figure 20.10a shows the details of this structure through a crystal cross-section cut perpendicularly to the growth direction. Two central domains with vectors of spontaneous polarization $\boldsymbol{P}_S$ pointing towards the domain boundary, or inwards, usually exist. The domain boundary coincides with the z-plane or has an orientation very close to it (since this is not always a coherent boundary [20.107]) and crosses vertically the entire crystal. Additionally, the boule is enveloped by a thin domain layer, 0.5–2 mm thick, and a fragment of such envelope is shown in Fig. 20.10b. Its polarization is always opposite in sign to the neighboring main domain and positive towards the outer surface. The surface appears to be the Ti (or K) positive face of the crystal. The envelope domain is clearly formed during the slow crystal cooling above the melt. As a result, the outer crystal surface is charged positively, however can be reversed by an appropriate thermal treatment [20.83].

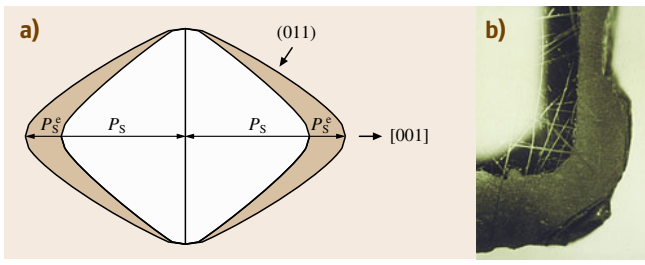


Fig. 20.10a,b Typical bidomain structure scheme in a (100) cross-section of an as-grown (above Curie temperature) KTP crystal **(a)** and a photograph (×30) of an envelope domain fragment **(b)**

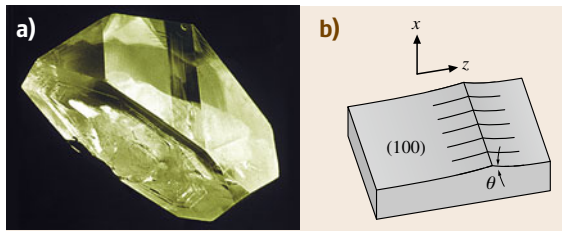


Fig. 20.11a,b Photograph of a hillock **(a)** on the flat (100) facet of a TSSG KTP and sketch of the associated edge-like perturbation **(b)**

The origin of the bulk bidomain structure is of particular importance and interest. We recall that in the course of pulling KTP crystals on x-oriented seeds the growth interface is formed entirely by the large flat (100) facet. However, *Bolt* and *Enckevort* [20.124] have reported on the existence of one or several hillocks on the (100) facet, or the formation of growth surfaces vicinal to the (100) crystallographic plane at an angle of about 30′. In fact, they have observed such hillocks on top of all facets parallel to the z-direction. Our experimental observations are consistent with their reports as well. A sample photograph of a hillock on the (100) facet of a top-seeded KTP crystal is shown in Fig. 20.11a. These linear hillocks are essentially edge-like perturbations on flat facets, described by *Chernov* [20.125] over three decades ago, and they are due to temperature fluctuations at the growth interface. A sketch of the edge-like perturbation is given in Fig. 20.11b.

Kinetics of Domain Formation

As discussed above, potassium concentration gradients are developed in the growing KTP crystal perpendicularly to the growth interface. With the existence of vicinal surfaces inclined at small angles to the z-direction, small components of the concentration gradients in this direction inevitably emerge. If the associated built-in electric field is larger than the coercive field, the direction of the concentration gradient's z-component defines the domain direction when the crystal undergoes the ferroelectric transition upon cooling. A bidomain structure is thus formed, as shown in Fig. 20.12a. Subsequent temperature fluctuations may cause additional edge-like perturbations resulting in formation of new domains by a similar mechanism. Local

variations in the magnitude of the built-in field may cause an opposite effect, namely healing of the main domain (also shown in Fig. 20.12a) leaving behind domain islands of opposite sign. Examples of such islands are shown in Fig. 20.12b, and their existence has been reported elsewhere [20.126] as well. Incorporation of residual impurities may play a role in this process, as follows from Table 20.3. Each half of the bidomain crystal can be monodomainized using high-temperature thermal treatment [20.83].

If seeded growth above the Curie temperature is enforced in such a way that the crystal is always submerged in the solution, no envelope domain is formed, but the bidomain structure can be also readily obtained. Figure 20.13a shows a y-cut cross-section of such a crystal, which generally acquires the typical morphology sketched in Fig. 20.2. The (100)- and (201)-type growth sectors are defined by dotted lines in the drawing. Clearly, the (201)-type facet forms a large angle (about 31°) with the z-direction, which results in a large z-component of the concentration gradient and a large built-in electric field. Relatively small temperature fluctuations cannot reverse the domain sign in this case, and single-domain (201)-type sectors always grow. The same applies to the (011)-type growth sectors not shown in the picture. The bidomain formation within the (100)-type growth sector is also reflected in Fig. 20.13a; similar structure occurs in the (110)-type growth sectors, since the (110) crystallographic plane is also parallel to the z-axis. Figure 20.13b demonstrates that, when the growth is initiated below the Curie temperature, the compositional gradient may be so strong across the {201} and {011} facets that a double-domain structure rather than a single-domain occasionally occurs, with a configuration as shown.

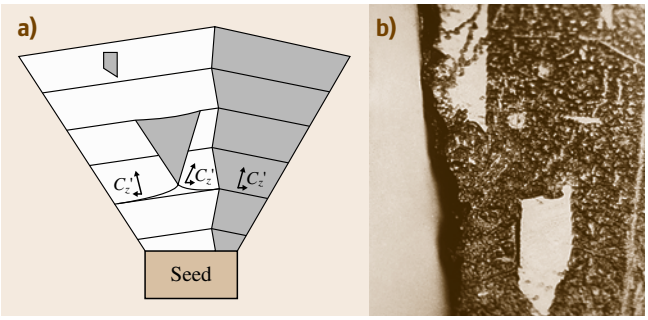


Fig. 20.12a,b Formation of ferroelectric domains in the (100) growth sector of KTP due to edge-like perturbations: **(a)** schematic drawing, **(b)** image of etched surface parallel to the [100]-direction

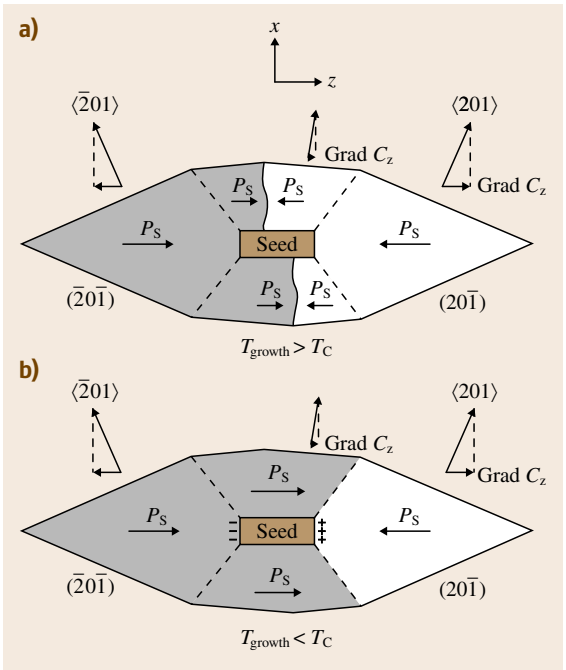


Fig. 20.13a,b Ferroelectric domain structure in immersion-seeded KTP crystals (central cuts in the y-plane) grown above **(a)** and below **(b)** the Curie temperature

20.3.2 Domain Boundaries

We have already demonstrated elsewhere [20.107] that the domain boundary within the (100) growth sector is diffuse rather than a sharp 180° twin boundary [20.10]. Similar diffuse boundaries exist within the (110) growth sector. Of special interest are the domain boundaries at the borders of growth sectors, which are formed at the edges of two meeting facets during growth. In the following, the various types and subtypes of ferroelectric domain boundaries will be described in more detail.

Classification of Boundaries

It should be pointed out that not only the intrasector boundaries, but also the edge boundaries between (100)- and (110)-type sectors are diffuse, while those between (011)- and (01$\bar{1}$)-type sectors (Fig. 20.2) are always sharp. A boundary between (110)- and (011)-type growth sectors may not exist at all or appear in its special form shown in Fig. 20.14a. Such apex-like perturbations of the edge between the corresponding growth facets may arise [20.125] due to temperature fluctuations, and a z-component of the potassium con-

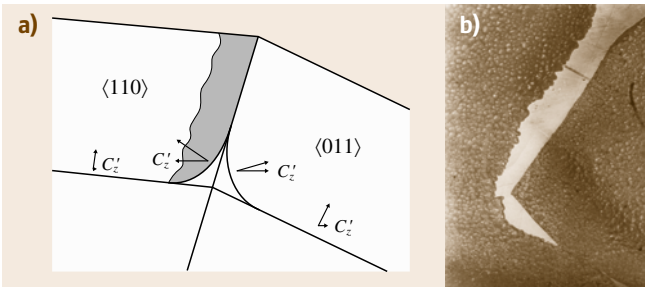


Fig. 20.14a,b Complex ferroelectric domain boundary between (110) and (011) growth sectors: **(a)** schematic drawing, **(b)** metallographic image (×40)

centration gradient is created on the (110) facet. The associated built-in electric field may be large enough to reverse the domain sign near the boundary, but only within the (110) growth sector. This results in a special type of edge domain boundary, which is sharp on the (011) sector side and diffuse on the (110) sector side. Such complex boundaries are frequently observed experimentally, as shown in Fig. 20.14b.

The variety of domain boundaries and their extent depend directly on the number of growth sectors formed and on the kinetics of growth of each sector, which in turn depend on the growth method employed and on the chemical composition of the flux. According to *Loiacono* et al. [20.46], in the case of K6 flux, complex ions of $(PO_4)^{3-}$, $(P_2O_5)^{4-}$, and $(P_3O_{10})^{5-}$ are present in the solution in a ratio 3 : 8 : 1, leading to the ratio of 1 : 2 : 3 for growth rates in the x, y, and z crystallographic directions, respectively. They report on a relatively close to the former growth rate ratio of 1 : 1 : 3 for K8 and K15 fluxes, but a quite distinct ratio of 1 : 18 : 17 (extremely slow growth of the x facet) for the K4 flux. The differences in growth rates are reflected in the variation of morphological shapes of KTP crystals [20.43]. Certain facets may be overdeveloped or underdeveloped or not exit at all. A good example is the (001) facet that is expected to exist

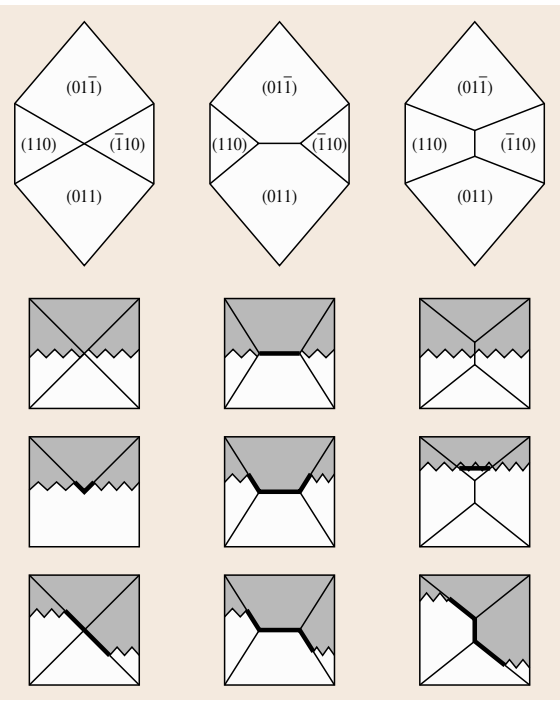


Fig. 20.15 Ferroelectric domain structure and types of domain boundaries in TSSG KTP crystals terminating with edges or sharp spikes in the z-direction

Table 20.4 Classification of ferroelectric domain boundaries in KTP-type crystals*

Type of domain boundary		Details and comments
Edge boundary		Traces of intersection of growing planes; they are always sharp boundaries
	– Full-size edge	{011}/{011}; {201} types never intersect
	– Partial edge	{110}/{110}, {110}/{201}, {110}/{100}
Intrasector boundary		
	– Central	Inside {100} and {110} growth sectors (diffuse boundaries)
	– Streak	Adjacent to {011}/{110} edge (sharp on the {011} side, diffuse inside the {110} sector)
	– Dispersed	Contours of small domains inside the {100} and {110} growth sectors (irregular shape)
	– Envelope	External crystal surface (for TSSG – on top of the crystal, for SSSG – the entire surface)

* {201}/{100} and {201}/{011} boundaries *do not* exist

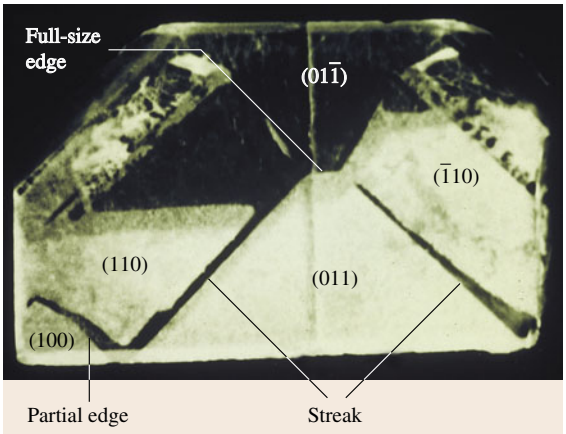


Fig. 20.16 Metallographic image of a full (011)-cut slice of a TSSG KTP crystal showing a real structure of ferroelectric domains and domain boundaries

theoretically [20.43], but which is rarely observed experimentally. Usually, only edges parallel to the *x*- (as in Fig. 20.2) or *y*-directions or just sharp spikes develop instead of this facet. These three cases are presented schematically in Fig. 20.15, where the central cut (perpendicularly to the *y*-axis) reveals the specific domain structure and the various domain boundaries of TSSG KTP crystals.

Similar types of diffuse and sharp domain boundaries can be found in crystals cut also along other crystallographic planes, but the *y*-cut slice reveals this variety sufficiently, allowing to suggest their presumably complete classification, which is summarized in Table 20.4. In this classification, the main distinction is made between domain boundaries forming at the borders of different growth sectors and within the growth sectors. Boundaries associated with the envelope domains discussed above and the irregular shape domains within the {100} growth sectors are added as a special case of intrasector boundaries. Figure 20.16 shows a real domain structure as revealed on the etched surface of a (011)-cut slice of a TSSG KTP crystal as well as part of the domain boundaries shown in Fig. 20.15 (for a *y*-cut surface) and listed in Table 20.4.

20.3.3 Summary of Ferroelectric Domain Structures

The foregoing analysis of the domain structure and boundaries applies to all KTP-type crystals grown by the TSSG method, both above and below the corresponding Curie temperatures. The main features observed are as follows:

- The ferroelectric domain structure of high-temperature solution grown KTP crystals is defined by the nature of growth sector development.
- Domain formation within the (100)- and (110)-type growth sectors (containing central and streak boundaries) is governed by the elementary crystal growth mechanisms.
- (100)- and (110)-type growth sectors exhibit predominantly bidomain and rarely multidomain structures; (011)- and (201)-type growth sectors are single domain.
- The bidomain, or 180° twin domain, is not a twin in the crystallographic sense.
- The diverse domain boundaries can be classified into edge type (partial and full size) forming at intersections of growth sectors and intrasector type (central, streak, dispersed, envelope).
- Domain orientation is defined by the direction of the built-in electric field originating from the concentration gradients of stoichiometric components (mainly potassium in KTP) and cation impurities.

20.3.4 Single-Domain Growth

The kinetics of ferroelectric domain formation during growth of KTP crystals described above allows to suggest a number of avenues for growing single-domain crystals. A few examples are given below:

- Meniscus growth with pulling on (201)- or (011)-oriented seeds yields single-domain growth immediately, which becomes clear from the observation of Fig. 20.13. Large compositional gradients formed upon crystallization on {201} and {011} facets imply high built-in electrical fields, preventing domain inversion and keeping the body of the crystal enclosed within these facets' single domain. The drawback of this method is that *boot-like* growth occurs due to the lack of symmetry in these directions, and the crystals may hit the crucible wall before a large chunk of crystal is grown.
- TSSG with pulling on a *z*-oriented seed generally starts with a multidomain structure, but eventually converts into a single domain when the main body of the crystal is formed solely by the (201)- and (011)-type growth sectors as well.
- Bidomain growth is frequently also acceptable for practical applications, when the crystals are large

enough. Such growth has already been discussed above for the case of TSSG with pulling on x-oriented seeds. Naturally, the same applies to growth on ⟨110⟩-oriented seeds. Hereby, there is always a danger of multidomain formation, which can be prevented by minimizing temperature fluctuations at the growth interface.

- TSSG with pulling in the y-direction behaves as follows: the (110)-type facets grow out fast, and the growth is governed by two (011)-type sectors, resulting in a bidomain growth with a sharp $(011)/(01\bar{1})$ domain boundary.

We reiterate that growth of KTP or KTA below the Curie temperature, even by several tens of degrees, may result in similar domain formation features due to the large potassium concentration gradients, or large built-in electric fields involved. The rubidium isomorphs follow these rules very closely as well.

20.4 Artificial Domain Structures

Single-domain KTP-family crystals are indispensable for most nonlinear optical and electrooptic applications; for example, their excellent birefringent phase-matching properties, such as appreciable effective nonlinear coefficients, broad temperature tolerance, and large angular bandwidth, make them highly suitable for frequency doubling of near-infrared lasers. Unfortunately, in the useful type II phase-matching scheme, the optical birefringence is too small to allow for frequency doubling into the green by KTA or into the blue by KTP [20.127]. In the latter case, it is possible to obtain the important blue coherent radiation with KTP using sum-frequency generation [20.128] or broadening its birefringence range by doping [20.129] or with the thermally unstable $KNbO_3$ crystal [20.130]. However, all these methods are not attractive due to their technological complexity. An appropriate alternative is the use of quasi-phase-matching (QPM) based on periodic domain structures (PDS). The QPM technique, first suggested by *Armstrong* et al. [20.131], corrects the relative phase of the fundamental and secondary waves at regular intervals by means of structural periodicity built into the nonlinear medium. Phase-matching is thus achieved by periodic spatial modulation of the nonlinear coefficient along the direction of propagation. The most efficient implementation of QPM occurs when the sign of the nonlinear coefficient is periodically reversed, which can be achieved by periodic domain inversion in a ferroelectric material. This has been initially performed by means of fabricating several-micrometer-deep KTP waveguides by the ion-exchange method [20.132–134], in which Rb^+ and Ba^{2+} ions replace K^+ ions. Attempts to obtain deeper periodic domain structures involve scanned electron beams [20.135] in KTP and, more recently, atomic force microscopy (AFM) cantilever tips [20.136] in RTP. Well-controlled domain inversion in more than 1 mm thick KTP-type crystals with down to a few μm small period structures has been obtained reproducibly using electrical field poling, and we will review this technique and structures in more detail below. As-grown periodic domain structures allowing for larger apertures and, thus, for higher-average-power laser applications will be discussed as well.

20.4.1 Electric Field Poling

Fabrication of QPM PDS by external electrical field poling has been initially implemented in $LiNbO_3$ [20.137, 138], where the coercive field is $\approx 21\,\mathrm{kV/mm}$ (congruent crystals) and the wafer thickness is limited to 0.5 mm due to the high field (24 kV/mm) needed to produce domain inversion. The coercive field of KTP and its isomorphs is about an order of magnitude lower and, unlike $LiNbO_3$, they do not suffer from photorefractive damage. The main problem of KTP-type crystals is the relatively high ionic conductivity, which may complicate the periodic poling. Among the techniques employed to overcome this problem are ion exchange in the surface layer and low-temperature poling. Alternatively, more stoichiometric (in potassium or rubidium) crystals exhibiting lower ionic conductivities can be used. These approaches will be discussed in more detail below.

Periodically Poled KTP

KTP is the most readily available material within the family, and the main bulk of published work in the field of QPM structures describes periodically poled KTP (PPKTP). The conventional process of periodic domain structure fabrication [20.137–139] is based on the application of an electric field to a photolithographically patterned electrode on the z-cut crystal surface, com-

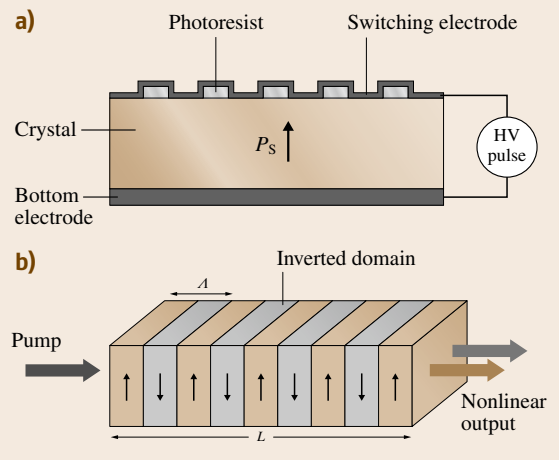


Fig. 20.17 **(a)** Conventional experimental setup for fabrication of domain gratings; **(b)** basic structure of electrically poled crystal for frequency conversion. The SHG efficiency, $\eta \propto d_{\text{eff}}^2 L$ [20.140], with L the crystal length, and the effective nonlinear coefficient for SHG of an order of m is given by [20.141] $d_{\text{eff}} = (2/\pi m)\sin(\pi m D) d_{33}$, where D is the duty cycle (ratio between inverted and uninverted domain widths). With $m = 1$ for the first-order interaction and $D = 0.5$, the optimal $d_{\text{eff}} = 2d_{33}/\pi$. Most importantly, the z-direction of light propagation with the highest nonlinear coefficient d_{33} can be chosen

prising a periodic array of metal and insulating stripes, as shown in Fig. 20.17a, or forming a grating. For SHG, the grating period (Λ) shown in Fig. 20.17b is related to the refractive indices of the fundamental (pump) and second-harmonic waves, $n_{2\omega}$ and n_{ω}, respectively, by

$$\Lambda = \frac{\lambda_{\omega}}{2(n_{2\omega} - n_{\omega})} , \tag{20.5}$$

where λ_{ω} is the pump wavelength. For $\lambda_{\omega} = 0.84\,\mu\text{m}$, frequency doubling into the blue requires PPKTP with $\Lambda = 4\,\mu\text{m}$ [20.139], while for $\lambda_{\omega} = 1.06\,\mu\text{m}$ (Nd:YAG laser) doubling into the green $\Lambda \approx 9\,\mu\text{m}$ [20.142]. Much larger periods are sufficient for OPO, where they are deduced from the first-order ($m = 1$) phase-matching condition [20.138]

$$\frac{1}{\Lambda} = \frac{n_{\text{p}}}{\lambda_{\text{p}}} - \frac{n_{\text{s}}}{\lambda_{\text{s}}} - \frac{n_{\text{i}}}{\lambda_{\text{i}}} , \tag{20.6}$$

where n_{p}, n_{s}, and n_{i} are the pump, signal, and idler refractive indices, respectively. The signal and idler outputs are shown by arrows in Fig. 20.17b. For example, for an OPO interaction with $\lambda_{\text{p}} = 1.06\,\mu\text{m}$, the period required is $\Lambda = 37.8\,\mu\text{m}$ in PPKTP [20.143].

As shown in Fig. 20.17, the pulsed switching voltage is applied to the polar z-faces of the crystal through metal electrodes. The required periodic domain inversion is obtained if spontaneous polarization switching occurs only under the micrometer-wide metal stripes (top electrode) that are in intimate contact with the crystal and does not occur below the dielectric photoresist layers of the same width. If polarization switching below the insulating stripes is not prevented, domain broadening takes place below them [20.144], which degrades the duty cycle of the device (Fig. 20.17b). The resulting inverted domain narrowing is due to high tangential fields arising immediately below the dielectric barrier layer and causing depolarization by internal charge carriers [20.144]. The kinetics of depolarization thus depends strongly on the crystal electrical conductivity. In insulating ferroelectric crystals, e.g., $LiNbO_3$, the polarization relaxes very slowly ($\tau \approx 10^5$ s), while in KTP and its isomorphs exhibiting high ionic conductivity the relaxation process is very fast ($\tau \approx 0.2\,\mu\text{s}$) [20.144]. One way of decreasing the relaxation time, or screening of depolarization, is the reduction of electrical conductivity by ion exchange.

A detailed experimental account of ion-exchange-assisted poling of KTP crystals was given by *Karlsson* and *Laurell* [20.145]. They made use of the fact that the larger Rb^+ ions had a lower mobility than K^+ ions in the KTP lattice and indiffused Rb^+ ions, by immersing flux-grown KTP crystals in a $RbNO_3$ melt, to obtain low conductivity ($\sim$ three orders of magnitude lower than the bulk) thin (2–5 μm) layers of $Rb_xK_{1-x}TiOPO_4$ at the two z-faces, where x varies gradually from 100% at the surface to 0% in the bulk. When voltage is applied to such crystal, the field in the exchanged layer is significantly higher than in the bulk, due to the difference in conductivity. At a certain voltage the coercive field is exceeded in the exchanged layer and an inverted domain nucleates. It continues growing towards the opposite side of the crystal under the influence of the remaining field in the bulk. The periodicity of the field near the surface is well defined, and the domains formed there can grow in a low field (lower than the coercive field) without significant broadening. Up to 1 mm thick PPKTP wafers could be fabricated using this method, and efficient first and higher-order green SH signals were obtained with 9.01 and 31 μm domain gratings [20.145] and blue SH with 6.09 μm gratings [20.146].

Another method of poling under reduced KTP ionic conductivity and requiring no chemical treatment of the crystal is the low-temperature polarization

switching suggested by *Rosenman* et al. [20.147]. They used 0.5 mm thick KTP wafers with a room-temperature conductivity of $10^{-7}\,\Omega^{-1}\mathrm{cm}^{-1}$. The latter reduced to about $10^{-12}\,\Omega^{-1}\mathrm{cm}^{-1}$ at $T = 170\,\mathrm{K}$ due to the freeze-in of K^+-ion migration. This increased the relaxation time τ by five orders of magnitude as well, and polarization switching under the dielectric layer stipes (Fig. 20.17) was prevented. One negative feature of the low-temperature poling method is that it causes a strong increase in the coercive field, but even at $T = 170\,\mathrm{K}$ it is still twice as low as in $LiNbO_3$ [20.147]. High-quality PPKTP elements with 9 μm domain grating period were fabricated using this method for efficient frequency doubling into the green [20.142] and OPO [20.148], while no optical damage due to gray tracking (green-induced infrared absorption) was observed up to continuous pump power of $4.5\,\mathrm{kW/cm}^2$.

In spite of the tangible technological progress in PPKTP processing, many aspects of the field-induced ferroelectric domain formation still remain unclear, and additional research efforts have to be made for their understanding. Clearly, the domain propagation speed along the polar z-axis is orders of magnitude larger than that in the x–y plane [20.149] in consonance with the anisotropy of ionic conductivity. In addition, anisotropy in the domain wall propagation velocity between the x- and y-directions exists as well, being 6–30 times larger in favor of the latter [20.149, 150]. Room-temperature polarization reversal in conventional KTP superionic conductor results in spontaneous nucleation of domains in the crystal bulk, since the mobile potassium ions can screen the depolarization field of the nucleating domain [20.151]. Additional observations related to room-temperature poling include the widely known features, such as domain nucleation at the electrode edges, domain broadening due to charge deposition underneath the dielectric layer and overpoling by multiple pulses, lateral domain growth and merging before reaching the opposite electrode, and also nonuniformity of the domain growth kinetics across the wafer. The latter is attributed to the variable stoichiometry of the KTP crystal [20.152]. Some attempts to return to the doping schemes for increasing the KTP resistivity for poling have been made lately as well [20.153].

High-Potassium KTP

Improvement of the morphology of PPKTP domain structures by ion exchange or low-temperature poling discussed above incorporates also certain disadvantages. Ion exchange is a two-step method involving chemical treatment of the crystal and resulting in variable success. Low-temperature poling requires application of external electric fields above the coercive field, which is as high as 12 kV/mm [20.147]. Therefore, a better alternative is to use more stoichiometric (in potassium) KTP crystals, exhibiting lower ionic conductivities and allowing poling at higher temperatures and lower voltages. Such an attempt has been made by *Rosenman* et al. [20.154], who have studied polarization reversal in three different KTP crystals denoted as HK, IK, and LK for high, intermediate, and low potassium content, since it is quite difficult to determine the exact potassium stoichiometry. The conductivities of the samples varied from 10^{-12} to $10^{-8}\,\Omega^{-1}\mathrm{cm}^{-1}$ at room temperature. Both HK and IK samples exhibited a relatively long polarization switching relaxation time, $\tau \approx 0.18\,\mathrm{s}$, which is sufficient for preventing domain broadening. Their measured room-temperature coercive field was less than 3 kV/mm, namely four times lower than that of LK at 170 K. The crystallographically more perfect 0.5 mm thick IK sample was used for actual poling at 248 K under a 4.6 kV/mm electric field. The duty cycle obtained was 50%, which indicated a complete lack of domain broadening. The element with a grating period of 24.7 μm was subsequently used for successful doubling of 1.55 μm radiation from a 18 mW diode laser into the deep red.

In a follow-up paper, *Jiang* et al. [20.155] grew HK-grade KTP crystals from a highly potassium-containing K4 flux for electric poling application. Their results confirmed that crystals with better potassium stoichiometry exhibited significantly lower ionic conductivities and lower coercive fields, allowing successful room-temperature poling. Application of a less than 3 kV/mm electric field to a 1 mm thick HK-grade KTP crystal resulted in polarization reversal throughout the sample thickness, and PPKTP elements with grating periods of 60 μm could be obtained. A surprising detail pointed out by the authors was that periodic poling for the grating vectors along [100]- and [010]-directions gave similar results, which was presumably sample dependent, since it was never observed with the usual smaller 9 μm gratings.

KTP Isomorphs

Very few attempts have been made to produce PPKTA crystals, since in addition to the difficulties of arsenate growth the dielectric and ferroelectric properties of KTA are hardly better than those of KTP crystals. In fact, the arsenate crystallographic framework is even more open [20.25, 26], facilitating the enhanced chi-

ral mobility of the K^+ ions in KTA. Consequently, the superionic-to-insulating transition occurs at even lower temperature than in KTP, and the crystal temperature must be reduced to 150 K for low-temperature poling [20.156]. The reported coercive field is as high as 90 kV/cm at $T = 150$ K, and 0.5 mm thick KTA wafers have been poled at this temperature under 5 kV switching bias to obtain PPKTA elements with grating periods of 37.4 and 39 μm. It was suggested that domain inversion hereby occurred by twinning across the (100) domain walls with As(1) acting as linking atoms [20.157]. KTA has better transparency in the infrared than KTP [20.15] and is preferred for OPO applications, hence the large grating periods prepared [20.156].

Periodically poled rubidium isomorphs, namely 1 mm thick PPRTP [20.158, 159] and 3 mm thick PPRTA [20.143, 160, 161], have been prepared as well. Unlike KTP and KTA, commercially available RTP and RTA crystals have low electrical conductivities in the 10^{-12}–$10^{-8}\,\Omega^{-1}\mathrm{cm}^{-1}$ range [20.14, 143]. This is due to the larger size of Rb^+ ions in comparison with K^+ ions and thus their lower mobility along the polar axis. The much narrower span of the Curie temperatures in RTP crystals (Fig. 20.8) than in KTP (Fig. 20.5) also indicates a smaller deviation from stoichiometry, which is likely in the case of RTA as well. As a result, PDS in RTP and RTA can be obtained by electrical poling at room temperature. The reported room-temperature coercive fields of RTP vary from 2.65 to 6 kV/mm, obviously depending on the specific resistivity of the crystals used [20.40, 149]. Typically, ≈ 4 kV voltages are used for creating PPRTP homogeneous structures over more than 80% of the 1 mm depth [20.158]. Both HK KTP and RTP crystals can be successfully poled at room temperature for a variety of applications. Unfortunately, the commercial production of PPKTP devices existing to date is based mostly on the low-temperature poling technology. Voltage pulses as low as 5.3 kV are sufficient for obtaining 3 mm thick PPRTA elements, also at room temperature [20.143]. PPRTA, like PPKTA, is used mainly in OPO applications [20.143, 162–164] due to the lower absorption in the mid-infrared. The detailed study of the thermal dependences of refractive indices performed for RTP and RTA shows that PPRTP is more appropriate for applications that require immunity to thermal lensing, whereas PPRTA is suitable for realizing temperature-tuned nonlinear devices [20.165]. Of great current interest are PPRTP-based submicrometer-size ($\Lambda = 1.18$ μm) domain structures produced in a 200 μm thick RTP crystal by applying a voltage of 650 V from a high-voltage atomic force microscope [20.136]. Such PPRTP nanodomain gratings are used, for example, in backward-propagating quasi-phase-matched converters [20.136] and noncollinear SHG [20.166]. It is noteworthy that, concurrently, 0.5 mm thick flux-grown KTP crystals have been poled by the ion-exchange-aided method with application four 1 ms long 1 kV pulses to produce submicrometer PPKTP gratings with a period as small as 800 nm [20.167]. The latter have been used for demonstrating electrically adjustable Bragg reflectivity.

20.4.2 As-Grown Periodic Domain Structure

Domain miniaturization in electrically poled PDS, discussed at the end of the previous paragraph, is of great interest for the development of novel photonic devices. However, the ability to produce large-aperture PDS for high-power QPM nonlinear optical devices is of equal technological importance. The straightforward way of generating periodic domains in the bulk of large ferroelectric crystals is to introduce appropriate temperature oscillations during their growth to induce striations associated with impurities. This has been attempted with other ferroelectric crystals, such as rare-earth-doped $LiNbO_3$ [20.168, 169] and Li-doped $KTa_xNb_{1-x}O_3$ [20.170]. In the case of KTP, the influence of the various impurities on the direction of impurity-related concentration gradients and, therefore, domain formation has been discussed in Sect. 20.2.1. An additional advantage of KTP over $LiNbO_3$ is that the latter grows (by Czochralski pulling from the melt) with a curved interface, whereas KTP exhibits a flat facet morphology. Until now, only a single attempt to grow a large KTP crystal with a periodic domain structure has been made [20.106], and it will be described comprehensively below.

Kinetics of Impurity Incorporation

It has been pointed out in Sect. 20.3.4 that TSSG growth of KTP crystals by pulling on z-oriented seeds eventually results in stable single-domain growth due to large potassium concentration gradients, or their vacancies, in the ⟨201⟩ and ⟨011⟩ growth directions. However, the presence of charge-compensating impurities, such as divalent ions (Mg^{2+} or Pb^{2+}) on K^+-sites, may minimize or eliminate these gradients and the associated built-in electric fields. In this case, periodic variation in the domain sign during crystal cooling through the Curie temperature can be achieved by imprinting a periodic variation in the impurity effective distribution coeffi-

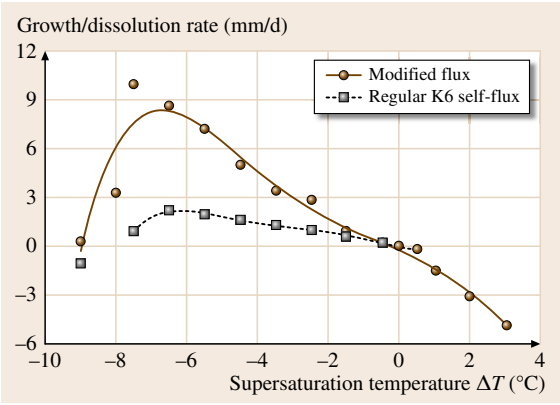


Fig. 20.18 Growth and dissolution rate of KTP in z-direction

cient [20.171]

$$k_{\mathrm{eff}} = \frac{k^*}{k^* + (1-k^*)\exp(-f^*\delta_{\mathrm{D}}/D_{\mathrm{L}})}\,, \qquad (20.7)$$

where k^* is the interface distribution coefficient, f^* is the interfacial linear growth rate, δ_{D} is the diffusion boundary layer, and D_{L} is the diffusion coefficient. Since $\delta_{\mathrm{D}} \sim \sqrt{\nu/\omega}$, where ν and ω are the kinematic viscosity and crystal rotation rate, respectively, one way of altering k_{eff} is to introduce a variable rotation rate. This is complex, since the hydrodynamic flow may be altered and is then difficult to control. The second approach is to vary the growth rate by controlling the interface temperature.

The average linear growth rate can be expressed by [20.172]

$$\langle f \rangle = \frac{V}{A\rho}\left(\frac{\mathrm{d}C_{\mathrm{e}}}{\mathrm{d}T}\right)\frac{\Delta T}{\Delta t}\,, \qquad (20.8)$$

where V is the volume of the solution, A is the growing crystal area, ρ its density, C_{e} is the equilibrium concentration of the solute, $\mathrm{d}C_{\mathrm{e}}/\mathrm{d}T$ is the change of solubility per degree (known from the solubility curve), ΔT is the undercooling, and $\Delta T/\Delta t$ is the cooling rate. The magnitude of undercooling is defined by the width of the metastable zone, which has been studied experimentally for the regular K6 and modified K6 (addition of PbO) fluxes [20.106]. The results are reproduced in Fig. 20.18, showing the growth or dissolution rate as a function of undercooling.

Temperature Oscillations and Crystal Growth

It is apparent from Fig. 20.18 that the width of the metastable zone almost does not depend on the type of flux, and its average value is 6.6 K. This is remarkably close to the theoretically estimated value of 6.67 K [20.173] for the K6 self-flux. The average undercooling, $\langle \Delta T \rangle$, must be of the order of half of the width of the metastable zone, or about 3.3 K, for normal KTP growth. If an additional periodic, e.g., sinusoidal, temperature oscillation is superimposed on the average undercooling, the actual undercooling can be expressed by

$$\Delta T = \langle \Delta T \rangle + B\sin(2\pi t/\tau)\,, \qquad (20.9)$$

where τ is the time period of temperature oscillation and the constant B must be chosen so that the undercooling does not exceed the limits of the metastable zone. As a result, growth rate oscillations will occur followed by variable (positive and negative) concentration gradients of the solute and production of a periodic domain structure. The domain metric period, Λ, depends on the

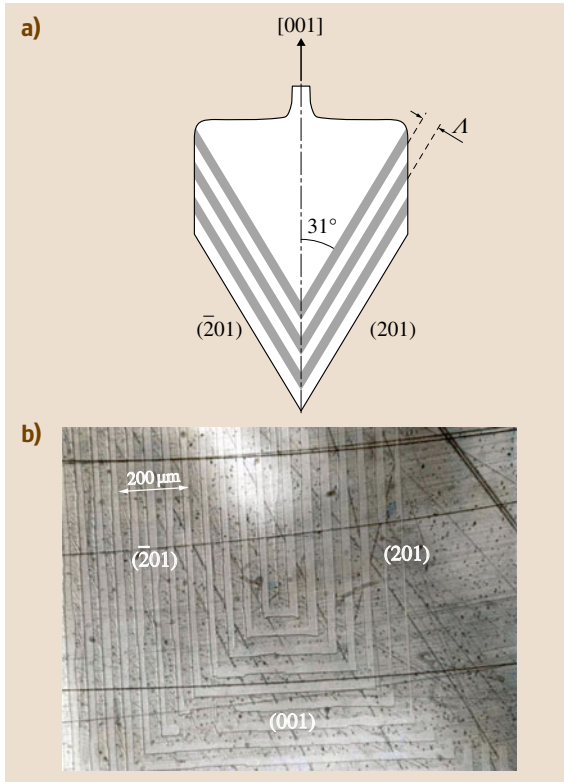


Fig. 20.19a,b Periodic ferroelectric domain structure in as-grown KTP crystal pulled in the z-direction: **(a)** schematic drawing of domain formation; **(b)** etched z-cut slice showing the rectangular periodic domain pattern within {201} and {011} growth sectors

average growth rate and the time period of temperature oscillations through the straightforward relation

$$\langle f \rangle \tau = \Lambda \,. \tag{20.10}$$

Growth experiments involving an undercooling oscillatory regime by multistep programming of the growth system's temperature controller yield large KTP crystals with a well-defined periodic domain structure. The geometry of such structure for TSSG with pulling in z-direction is presented schematically in Fig. 20.19a. When the {201} and {011} facets are fully developed, temperature oscillation is turned on, and the periodic domain structure is formed with period Λ. This is not the true period for nonlinear interactions; the latter is $\Lambda/\cos(31°)$, since wafers are cut perpendicularly to the [001] axis in order to utilize the largest d_{33} nonlinear coefficient.

Figure 20.19b shows an etched surface of a fraction of a real z-cut slice, where clearly defined domain structures are visible within the {201} and {011} growth sectors. The domain contours are straight since both the {201} and {011} are perfectly flat. The grating period in this picture is 50 μm, but structures with Λ of 25–40 μm have been easily obtained. They can be effectively used for a variety of OPO applications. Frequency doubling requires smaller periods, such as 9 μm, for SHG of the 1.06 μm radiation of the Nd:YAG laser, and there is no principal limitation in creating the narrower domain as-grown structures. The quality of the PDS is determined by the value of the duty cycle, $D = a/\Lambda$, where a is the actual inverted domain width. The optimal effective NLO coefficient and, thus, frequency conversion efficiency is obtained at $D = 0.5$ [20.142]. The D values in Fig. 20.19b are in the 0.2–0.5 range along 10 mm of the wafer in the [100] direction (within a single growth sector), which are still useful for practical implementation of the as-grown PDS. It is noteworthy that in $LiNbO_3$ reasonable quality PDS can be obtained only along 1 mm due to the curved Czochralski growth interface where the inverted domains are obtained.

20.5 Nonlinear Optical Crystals

The combined knowledge of KTP-type crystal morphology development, compositional variations, and ferroelectric domain formation kinetics during growth allows one to adapt the crystal growth method to the requirements of particular applications. It has been pointed out in the previous section that TSSG of KTP crystals with pulling in the [001]-direction is most suitable for creating as-grown PDS. Crystals grown by top-seeding with pulling from K6-forming fluxes in the [100]-direction are the best choice for extracting x-oriented (for highest electrooptic coefficients) Q-switching elements, since the large flat (100) facet (Fig. 20.2) assures excellent transverse optical homogeneity needed for maximum extinction ratio [20.118]. This approach is specifically implemented in producing RTP Q-switching devices [20.14, 114]. Fortunately, TSSG with pulling in both [001]- and [100]-directions allows to obtain large volumes of single-domain crystals, as summarized in Sect. 20.3.4. In addition, establishment of compositional gradients during growth and poor potassium stoichiometry in general can not only influence the domain formation mechanisms (Sect. 20.3.1) but also affect the optical properties of KTP crystals. In the following, we will analyze the nonuniformity in the distribution of refractive indices associated with compositional gradients [20.118] and generation of detrimental point defects related to potassium vacancies [20.89].

20.5.1 Optical Nonuniformity

Every application of nonlinear optical and electrooptic crystals requires variable degrees of optical uniformity. However, one has to make a distinction between the relative importance of transverse and longitudinal uniformity with respect to the direction of propagation of the laser beam. While x-oriented crystal pairs of electrooptic Q-switches are not too sensitive to longitudinal distribution of refractive indices [20.14], their inhomogeneity along the OPO interaction path may lead to phase mismatch and, consequently, to degradation of the OPO interaction efficiency. In this section, we will mainly focus on this latter example.

Distribution of Refractive Indices

The variation of refractive indices in large solution-grown KTP crystals, from the seed to the crystal periphery, has been studied experimentally by transmission interferometry and reported in a series of works by *Sasaki* et al. [20.60, 82, 104]. They have discovered the

existence of constant gradients of the refractive indices in different crystallographic directions of TSSG-grown KTP crystals, which are ascribed to compositional variation in the solute, in agreement with the Curie temperature variation described in Sect. 20.2.1. Particularly useful are the results of [20.82], where growth and characterization details of a large TSSG-grown crystal are given including the initial flux composition and saturation temperature, final crystal weight, and the end values of the refractive indices measured at 633 nm. With the knowledge of KTP solubility in K6 [20.10], their data allow to calculate the average variation of the refractive indices per degree for growing out crystal volumes upon the solution temperature reduction. The values obtained are [20.118]

$$\frac{\Delta n_{x,y}}{\Delta T} \approx 10^{-7}\,\mathrm{K}^{-1} \quad \text{at } 633\,\mathrm{nm}\,,$$
$$\frac{\Delta n_z}{\Delta T} \approx 2\times 10^{-6}\,\mathrm{K}^{-1} \quad \text{at } 633\,\mathrm{nm}\,. \qquad (20.11)$$

Assuming, as a simplifying approximation, that Δn varies linearly with the increase of the solidified mass and depends weakly on wavelength, (20.11) are a universal result, independent of the specific method of solution growth (Fig. 20.3). In particular, this result can be applied to crystals obtained by TSSG with pulling, and their optical uniformity in specific crystallographic directions can be assessed if certain growth parameters are known.

Figure 20.20 shows a photograph of an almost ideal TSSG (meniscus-pulled in the [100]-direction) KTP crystal of ≈ 850 g weight. A nearly constant growth interface area has been maintained after developing the shoulders of the crystal by careful monitoring the temperature reduction program and the pulling rate. The height of the nearly rectangular part of the crystal l is about 50 mm, and the temperature drop during its growth was 75 K. Using these parameters and the data of (20.11), the following average gradients of the refractive indices along the crystal length can be calculated

$$\frac{\Delta n_z}{\Delta l} = 3\times 10^{-5}\,\mathrm{cm}^{-1}\,,$$
$$\frac{\Delta n_{x,y}}{\Delta l} = 1.5\times 10^{-6}\,\mathrm{cm}^{-1}\,. \qquad (20.12)$$

OPO Interaction in KTP

[100]-Cut KTA and KTP crystals are widely used in frequency conversion of Nd-doped solid-state lasers to longer wavelengths by OPO, primarily for eye-safe lidar systems operating in the 1550 nm spectral region [20.15,16]. One of the major advantages of KTP-family crystals is the ability to operate with noncritical phase matching (NCPM), allowing large acceptance angles of the incident beam. The basic configuration of the type II process in a KTP-type crystal pumped in the x-direction is shown in Fig. 20.21. In this interaction, a y-polarized pump (p) generates a y-polarized signal (s) and z-polarized idler (i) beams, and the corresponding frequencies are bound by the following equations:

$$n_y^{\mathrm{p}}\omega^{\mathrm{p}} = n_y^{\mathrm{s}}\omega^{\mathrm{s}} + n_z^{\mathrm{i}}\omega^{\mathrm{i}}\,,$$
$$\omega^{\mathrm{p}} = \omega^{\mathrm{s}} + \omega^{\mathrm{i}}\,, \qquad (20.13)$$

which are the perfect NCPM phase-matching conditions, namely the momentum and energy conservation laws, respectively. (The frequencies can be recalculated from the known wavelengths, which for the Nd:YAG-

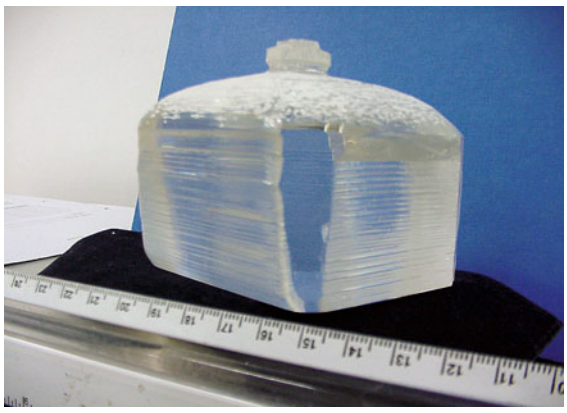


Fig. 20.20 TSSG KTP crystal meniscus pulled on a [100]-oriented seed

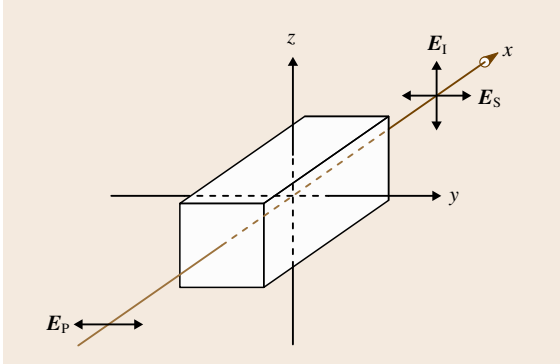


Fig. 20.21 Noncritical phase-matching scheme for type II OPO in the x–z plane of a KTP crystal ($\boldsymbol{E}_{\mathrm{p}}$, $\boldsymbol{E}_{\mathrm{s}}$, and $\boldsymbol{E}_{\mathrm{i}}$ are the appropriate electric field polarization vectors)

induced NCPM OPO in KTP are $\lambda^p = 1064.2\,\text{nm}$, $\lambda^s = 1576\,\text{nm}$, and $\lambda^i = 3277\,\text{nm}$ [20.16].)

It is well known that the inherently present variation of the refractive indices due to gradual compositional changes inevitably causes a phase mismatch during the interaction. This mismatch can be evaluated by deriving the associated bandwidth of the generated signal wave $\Delta\omega^s$. If we disregard the negligible change in n_y [20.104] and assume that only $\Delta n_z \neq 0$, the signal bandwidth is given by

$$\Delta\omega^s = \frac{\Delta n_z^i}{n_z^i - n_y^s}\omega^i \,. \tag{20.14}$$

Keeping in mind that Δn_z does not vary dramatically with wavelength, the value of $\Delta n_z^i = 3\times10^{-5}$ for a 1 cm long crystal, from the first of (20.12), can be used as a rough approximation. The relevant refractive indices can be calculated from the Sellmeier equations for KTP [20.10] as $n_z^i = 1.7717$ and $n_y^s = 1.7362$. Final calculation using these parameters gives $\Delta\omega^s = 2.6\,\text{cm}^{-1}$, which is well within the KTP/OPO acceptance bandwidth of $9.02\,\text{cm}^{-1}$ for a 1 cm interaction length [20.174]. This explains the high NCPM OPO conversion efficiency achieved even by pumping 20 mm long KTP crystals with a multimode laser [20.16].

It is also important to remember that, with a proper choice of the growth method, KTP-type crystals of sufficient optical uniformity can be obtained for both nonlinear optical and electrooptic applications. We recall that the main cause of inhomogeneity in the distribution of refractive indices along the growing crystal is the composition gradient, mainly of potassium ions, building up in the course of growth from self-fluxes. Such gradients are considerably smaller in the case of one-dimensional meniscus growth with pulling in the x-direction than in the case of three-dimensional submerged-seeded growth (Fig. 20.3).

20.5.2 Gray Tracks

In some applications where KTP is used to generate the second harmonic of the 1064 nm Nd:YAG laser radiation [20.175–179] or OPO pumped at 532 nm [20.180], detrimental optical absorption often builds up in the crystal bulk following intense high-repetition pulse or continuous-wave (CW) pumping. This phenomenon is termed gray-tracking, since darkening is observed along the laser beam path, which is attributed to formation of color centers absorbing in most of the visible 400–700 nm range [20.67] and emitting in the 700–1200 nm range under green laser excitation [20.181]. The induced absorption diminishes the nonlinear output power and causes significant local heating, leading to severe beam distortion. It is imperative, therefore, to understand the nature of color centers involved and to find the means of their suppression.

Origin of Gray Track Centers

Gray tracks have been unambiguously related to the presence of Ti^{3+} ions [20.67, 178, 182], which are electron color centers induced photochemically via electron trapping by the constitutional Ti^{4+} ions. The latter can be reduced to Ti^{3+} also by high-temperature annealing in vacuum or by charge transfer (e.g., $Fe^{2+} \rightarrow Ti^{4+}$) from adjacent transition-metal impurities [20.108]. Yet, in thermally untreated and nominally pure KTP crystals, EPR and electron-nuclear double resonance (ENDOR) measurements have revealed four distinct types of Ti^{3+} centers as well [20.183, 184]. Two of them, appearing only in hydrothermal KTP, have a Ti^{3+} ion occupying the inequivalent Ti(1) and Ti(2) sites with a proton (in the form of an OH^- ion) bonded to an adjacent oxygen ion as a stabilizing entity for the electron trapping. The remaining two types of centers are present only in flux-grown crystals. One of them represents a self-trapped electron at the Ti(1) site stabilized by a neighboring divalent cation impurity, according to a tentative suggestion [20.184], but it is unstable above 140 K. The other is a Ti^{3+} ion located at the Ti(2) site adjacent to an oxygen vacancy and is stable at room temperature for days or weeks.

It is now well established that the reason for the existence of electron-trap-stabilizing OH^- ions (in hydrothermal crystals) and oxygen vacancies (in flux-grown crystals) is charge compensation of K^+ vacancies present to variable degrees in all KTP crystals [20.185], as also discussed in Sect. 20.2. In an attempt to reduce the concentration of oxygen vacancies, PbO was added to the KTP growth flux to form the modified flux referred to in Sect. 20.4.2. A Pb^{2+} ion, with its $6s^2$ closed shell configuration, has an ionic radius approximately 0.2 Å smaller than a K^+ ion, and thus easily substitutes for the K^+ ion to provide charge compensation for one potassium vacancy. Oxygen vacancies are no longer needed to stabilize the Ti^{3+} color center if a sufficient amount of the Pb^{2+} dopant is present. Instead, [Ti^{3+}-Pb^{2+}] centers may form under intense laser irradiation. Four types of these centers have been revealed by EPR and ENDOR measurements [20.113], but they are all unstable above 250 K and thus short-lived at room temperature. Of course, operation under the extreme conditions of high-

power, high-repetition-rate or CW pumping will cause the transient formation of large concentrations of Ti^{3+} centers with the detrimental optical absorption in the visible. Therefore, doping with lead is only a partial remedy. A better way to eliminate gray-tracking is the reduction of potassium vacancies, or improvement of potassium stoichiometry, in as-grown KTP crystals by using K-rich solvents and/or more dilute solutions as discussed in Sect. 20.2.

Kinetics of Gray Track Formation

Figure 20.5 shows explicitly that KTP crystals grown at lower temperatures, especially from self-fluxes with higher [K]/[P] ratios, are more stoichiometric, exhibiting higher Curie temperatures. In order to test the influence of potassium stoichiometry, a comparative study of the kinetics of gray track formation in high- and low-T_C KTP crystals has been conducted [20.89]. This has been done using the green-radiation-induced infrared absorption (GRIIRA) method which has been initially developed for periodically poled $LiNbO_3$ [20.186]. In the quoted experiment [20.89], a $10\,kW/cm^2$ CW green (532 or 514 nm) excitation beam was used to induce the gray track damage, while the resulting infrared (1064 nm) absorption was monitored. At the initial stage of gray track formation, usually lasting from several seconds to several minutes, an increase in the infrared absorption can be observed. This increase (after the onset of green irradiation) is clearly seen in Fig. 20.22.

During the studied initial stage (80 s) the gray track is located within the green beam region and disappears fast when the green light is turned off. However, the first minute of the test is sufficient to determine the quality of the sample. The results of Fig. 20.22 clearly show that the infrared absorption of the HK KTP crystals with a higher potassium content (high-T_C) saturates deep below the level of $10^{-4}\,cm^{-1}$ while the similar absorption of a low-T_C crystal (LK) continues to rise linearly. Obviously, crystals with an improved potassium stoichiometry reveal a higher resistance to gray track formation. Such crystals may compete successfully with hydrothermal KTP (where the concentration of gray track centers is higher, but

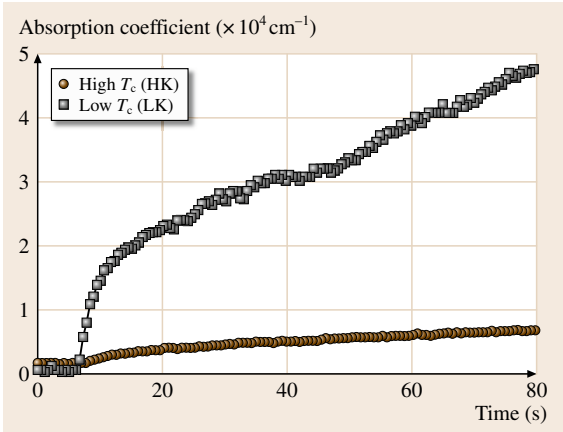


Fig. 20.22 Initial stages of gray-track formation in potassium-deficient (LK, low-T_C) and potassium-rich (HK, high-T_C) grown from self-fluxes

they are less stable [20.183, 184]) in high-power frequency doubling. Crystals grown from pure self-fluxes have an advantage also with respect to low-power applications, since their initial absorption never exceeds $10^{-5}\,cm^{-1}$ (Fig. 20.22). The known initial absorption of most hydrothermal KTP crystals is typically higher than $10^{-4}\,cm^{-1}$, presumably due to the presence of impurities associated with the hydrothermal growth.

RTP crystals are seldom used for frequency doubling into the green [20.4] and, therefore, their susceptibility to gray track formation has not been investigated directly. However, very recent EPR and ENDOR studies have shown that room-temperature-stable Ti^{3+} centers stabilized by oxygen vacancies can be created also in this crystal [20.187]. The narrow range of Curie temperature variation in RTP (Fig. 20.8) and the usually observed high electrical resistivity of these crystals [20.14] imply that their concentration of stable Ti^{3+} electron trap centers is generally low. Nevertheless, current attempts to develop Yb and Nb co-doped RTP crystals as new self-doubling laser media [20.188] necessitates an examination of RTP crystals using the GRIIRA test, similarly to the one described above for KTP.

References

20.1 J.D. Bierlein, H. Vaherzeele: Potassium titanyl phosphate: Properties and new applications, J. Opt. Soc. Am. B **6**, 622–633 (1989)

20.2 G.M. Loiacono, D.N. Loiacono, J.J. Zola, R.A. Stolzenberger, T. McGee, R.G. Norwood: Optical properties and ionic conductivity of $KTiOAsO_4$

crystals, Appl. Phys. Lett. **61**, 895–897 (1992)
20.3 D.E. Spence, C.L. Tang: Characterization and applications of high repetition rate, broadly tunable, femtosecond optical parametric oscillators, IEEE J. Sel. Top. Quantum Electron. **1**, 31–43 (1995)
20.4 Y.S. Oseledchik, A.I. Pisarevsky, A.L. Prosvirin, V.V. Starshenko, N.V. Svitanko: Nonlinear optical properties of the flux grown $RbTiOPO_4$ crystal, Opt. Mater. **3**, 237–242 (1994)
20.5 T.Y. Fan, C.E. Huang, B.Q. Hu, R.C. Eckardt, R.L. Byer, R.S. Feigelson: Second harmonic generation and accurate index of refraction measurements in flux-grown $KTiOPO_4$, Appl. Opt. **26**, 2390–2394 (1987), .
20.6 C.-S. Tu, R.S. Katiyar, V.H. Schmidt, R.-M. Chien, R. Guo, A.S. Bhalla: Hypersonic anomalies and optical properties of $RbTiOAsO_4$ and $KTiOPO_4$ single crystals, Phys. Rev. B **59**, 251–256 (1999)
20.7 L.T. Cheng, L.K. Cheng, J.D. Bierlein, F.C. Zumsteg: Properties of doped and undoped single domain $KTiOAsO_4$, Appl. Phys. Lett. **62**, 346–348 (1993)
20.8 L.T. Cheng, L.K. Cheng, J.D. Bierlein, F.C. Zumsteg: Nonlinear optical and electro-optical properties of single crystal $CsTiOAsO_4$, Appl. Phys. Lett. **63**, 2618–2620 (1993)
20.9 L.K. Cheng, J.D. Bierlein: KTP and isomorphs – Recent progress in device and material development, Ferroelectrics **142**, 209–228 (1993)
20.10 L.K. Cheng, L.T. Cheng, J. Galperin, P.A. Morris Hotsenpiller, J.D. Bierlein: Crystal growth and characterization of $KTiOPO_4$ isomorphs from the self-fluxes, J. Cryst. Growth **137**, 107–115 (1994)
20.11 L.K. Cheng, L.T. Cheng, J.D. Bierlein: Phase-matching property optimization using birefringence tuning in solid solutions of $KTiOPO_4$ isomorphs, Appl. Phys. Lett. **64**, 1321–1323 (1994)
20.12 M. Roth, N. Angert, M. Tseitlin, G. Wang, T.P.J. Han, H.G. Gallagher, N.I. Leonyuk, E.V. Koporulina, S.N. Barilo, L.A. Kurnevich: Recent developments in crystal growth and characterization of nonlinear optical borate and phosphate materials, Proc. 3rd Int. Conf. Single Crystal Growth, Strength Probl. Heat Mass Transf., Vol. 2, ed. by V.P. Ginkin (Uch.-Izd., Obninsk 2000) pp. 416–426
20.13 D.N. Nikogosyan: *Nonlinear Optical Crystals: A Complete Survey* (Springer, New York 2005)
20.14 M. Roth, M. Tseitlin, N. Angert: Oxide crystals for electro-optic Q-switching of lasers, Glass Phys. Chem. **31**, 86–95 (2005)
20.15 M.S. Webb, P.F. Moulton, J.J. Kasinski, R.I. Burnham, G. Loiacono, R. Stolzenberger: High-average-power $KTiOAsO_4$ optical parametric oscillator, Opt. Lett. **23**, 1161–1163 (1998)
20.16 L.S. Lingvay, N. Angert, M. Roth: High-average-power KTP ring OPO, Proc. SPIE **3928**, 52–56 (2000)
20.17 X.D. Wang, P. Basseras, R.J.D. Miller, H. Vanherzeele: Investigation of $KTiOPO_4$ as an electro-optic amplitude modulator, Appl. Phys. Lett. **59**, 519–521 (1991)
20.18 S. Pearce, C.L.M. Ireland: Performance of a CW pump Nd:YVO_4 amplifier with kHz pulses, Opt. Laser Technol. **35**, 375–379 (2003)
20.19 M.G. Jani, J.T. Murray, R.R. Petrin, R.C. Powell: Pump wavelength tuning of optical parametric oscillations and frequency mixing in $KTiOAsO_4$, Appl. Phys. Lett. **60**, 2327–2329 (1992)
20.20 G.M. Loiacono, D.N. Loiacono, R.A. Stolzenberger: Crystal growth and characterization of ferroelectric $CsTiOAsO_4$, J. Cryst. Growth **131**, 323–330 (1993)
20.21 J. Nordborg, G. Svensson, R.J. Bolt, J. Albertsson: Top seeded solution growth of [Rb,Cs]$TiOAsO_4$, J. Cryst. Growth **224**, 256–268 (2001)
20.22 I. Tordjman, R. Masse, J.C. Guitel: Crystalline-structure of monophosphate $KTiPO_5$, Z. Krist. **139**, 103–115 (1974)
20.23 P.A. Thomas, A.M. Glazer, B.E. Watts: Crystal structure and nonlinear optical properties of $KSnOPO_4$ and their comparison with $KTiOPO_4$, Acta Crystallogr. B **46**, 333–343 (1990)
20.24 P. Delarue, C. Lecomte, M. Jannin, G. Marnier, B. Menaert: Evolution towards centrosymmetry of the nonlinear-optical material $RbTiOPO_4$ in the temperature range 293 – 973 K: Alkaline displacements and titanyl deformations, Phys. Rev. B **58**, 5287–5295 (1998)
20.25 S.C. Mayo, P.A. Thomas, S.J. Teat, G.M. Loiacono, D.N. Loiacono: Structure and nonlinear-optical properties of $KTiOAsO_4$, Acta Crystallogr. B **50**, 655–662 (1994)
20.26 P.A. Thomas, S.C. Mayo, B.E. Watts: Crystal structures of $RbTiOAsO_4$, $KTiO(P_{0.58}As_{0.42})O_4$, $RbTiOPO_4$ and $(Rb_{0.465}K_{0.535})TiOPO_4$ and analysis of pseudosymmetry in crystals of the $KTiOPO_4$ family, Acta Crystallogr. B **48**, 401–407 (1992)
20.27 J. Protas, G. Marnier, B. Boulanger, B. Menaert: Crystal structure of $CsTiOAsO_4$, Acta Crystallogr. C **45**, 1123–1125 (1989)
20.28 M. Munowitz, R.H. Jarman, J.F. Harrison: Theoretical study of the nonlinear optical properties of $KTiOPO_4$: Effects of Ti–O–Ti bond angles and oxygen electronegativity, Chem. Mater. **5**, 1257–1267 (1993)
20.29 D. Xue, S. Zhang: The origin of nonlinearity in $KTiOPO_4$, Appl. Phys. Lett. **70**, 943–945 (1997)
20.30 P.A. Thomas, A. Baldwin, R. Dupree, P. Blaha, K. Schwartz, A. Samoson, Z.H. Gan: Structure-property relationships in the nonlinear optical crystal $KTiOPO_4$ investigated using NMR and ab initio DFT calculations, J. Phys. Chem. B **108**, 4324–4331 (2004)
20.31 V. Pasiskevicius, C. Canalias, F. Laurell: Highly efficient stimulated Raman scattering of picosecond pulses in $KTiOPO_4$, Appl. Phys. Lett. **88**, 041110 (2006)
20.32 P.A. Thomas, A.M. Glazer: Potassium titanyl phosphate, $KTiOPO_4$. II. Structural interpretation of

twinning, ion exchange and domain inversion, J. Appl. Cryst. B **24**, 968–971 (1991)
20.33 P. Delarue, C. Lecomte, M. Jannin, G. Marnier, B. Menaert: Behavior of the non-linear optical material $KTiOPO_4$ in the temperature range 293 – 973 K studied by x-ray diffractometry at high resolution: Alkaline displacements, J. Phys. Condens. Matter **11**, 4123–4134 (1999)
20.34 S.T. Norberg, N. Ishizawa: K-site splitting in $KTiOPO_4$ at room temperature, Acta Crystallogr. C **61**, i99–i102 (2006)
20.35 D.R. Allan, J.S. Loveday, R.J. Nelmes, P.A. Thomas: A high-pressure structural study of potassium titanyl phosphate (KTP) up to 5 GPa, J. Phys. Condens. Matter **4**, 2747–2760 (1992)
20.36 P.A. Thomas, R. Duhlev, S.J. Teat: A comparative structural study of a flux-grown crystal of $K_{0.86}Rb_{0.14}TiOPO_4$ and an ion-excganged crystal of $K_{0.84}Rb_{0.16}TiOPO_4$, Acta Cryst. B **50**, 538–543 (1994)
20.37 S. Furusawa, H. Hayasi, Y. Ishibashi, A. Miyamoto, T. Sasaki: Ionic conductivity of quasi-one-dimensional superionic conductor $KTiOPO_4$ (KTP) single crystal, J. Phys. Soc. Jpn. **62**, 183–195 (1993)
20.38 J.D. Bierlein, C.B. Arweiler: Electro-optic and dielectric properties of $KTiOPO_4$, Appl. Phys. Lett. **49**, 917–919 (1986)
20.39 B. Mohamadou, G.E. Kugel, F. Brehat, B. Wyncke, G. Marnier, P. Simon: High-temperature vibrational spectra, relaxation and ionic conductivity effects in $KTiOPO_4$, J. Phys. Condens. Matter **3**, 9489–9501 (1991)
20.40 Q. Jiang, A. Lovejoy, P.A. Thomas, K.B. Hutton, R.C.C. Ward: Ferroelectricity, conductivity, domain structure and poling conditions of rubidium titanyl phosphate, J. Phys. D Appl. Phys. **33**, 2831–2836 (2000)
20.41 P. Urenski, N. Gorbatov, G. Rosenman: Dielectric relaxation in flux grown $KTiOPO_4$ and isomorphic crystals, J. Appl. Phys. **89**, 1850–1855 (2001)
20.42 J.C. Jacco, G.M. Loiacono, M. Jaso, G. Mizell, B. Greenberg: Flux growth and properties of $KTiOPO_4$, J. Cryst. Growth **70**, 484–488 (1984)
20.43 R.J. Bolt, P. Bennema: Potassium titanyl phosphate $KTiOPO_4$ (KTP): Relation between crystal structure and morphology, J. Cryst. Growth **102**, 329–340 (1990)
20.44 L.K. Cheng, J.D. Bierlein, A.A. Ballman: Crystal growth of $KTiOPO_4$ isomorphs from tungstate and molybdate fluxes, J. Cryst. Growth **110**, 697–703 (1991)
20.45 X. Wang, X. Yuan, W. Li, J. Qi, S. Wang, D. Shen: Flux growth of large potassium titanyl phophate crystals and their electro-optical applications, J. Cryst. Growth **237–239**, 672–676 (2002)
20.46 G.M. Loiacono, T.F. McGee, G. Kostecky: Solubility and crystal growth of $KTiOPO_4$ in polyphosphate solvents, J. Cryst. Growth **104**, 389–391 (1990)
20.47 J.D. Bierlein, T.E. Gier: Crystals of $(K,Rb,Tl,NH_4)TiO(P,As)O_4$ and their use in electrooptic devices, US Patent 3949323 (1976)
20.48 T.E. Gier: Hydrithermal process for growing a single crystal with an aqueous mineralizer, US Patent 4305778 (1981)
20.49 R.A. Laudise, R.J. Cava, A.J. Caporaso: Phase relations, solubility and growth of potassium titanyl phosphate, KTP, J. Cryst. Growth **74**, 275–280 (1986)
20.50 R.F. Belt, G. Gashurov, R.A. Laudise: Low temperature hydrothermal growth of $KTiOPO_4$ (KTP), Proc. SPIE **968**, 100–106 (1988)
20.51 R.A. Laudise, W.A. Sunder, R.F. Belt, G. Gashurov: Solubility and P-V-T relations and the growth of potassium titanyl phosphate, J. Cryst. Growth **102**, 427–433 (1990)
20.52 A. Ferretti, T.E. Gier: Hydrothermal process for growing optical-quality crystals, US Patent 5066356 (1991)
20.53 S.Q. Jia, P.Z. Jiang, H.D. Niu, D.Z. Li, X.H. Fan: The solubility of $KTiOPO_4$ (KTP) in KF aqueous solution under high temperature and high pressure, J. Cryst. Growth **79**, 970–973 (1986)
20.54 S.Q. Jia, H.D. Niu, J.G. Tan, Y.P. Xu, Y. Tao: Hydrothermal growth of KTP crystals in the medium range of temperature and pressure, J. Cryst. Growth **99**, 900–904 (1990)
20.55 L.K. Cheng: Hydrothermal aqueous mineralizer for growing optical-quality single crystals, US Patent 5500145 (1996)
20.56 C. Zhang, L. Huang, W. Zhou, G. Zhang, H. Hou, Q. Ruan, W. Lei, S. Qin, F. Lu, Y. Zuo, H. Shen, G. Wang: Growth of KTP crystals with high damage threshold by hydrothermal method, J. Cryst. Growth **292**, 364–367 (2006)
20.57 A.A. Ballman, H. Brown, D.H. Olson, C.E. Rice: Growth of potassium titanyl phosphate (KTP) from molten tungsten melts, J. Cryst. Growth **75**, 390–394 (1986)
20.58 K. Iliev, P. Peshev, V. Nikolov, I. Koseva: Physicochemical properties of high-temperature solutions of the K_2O-P_2O_5-TiO_2-WO_3 system, suitable for the growth of $KTiOPO_4$ (KTP) single crystals, J. Cryst. Growth **100**, 225–232 (1990)
20.59 C.G. Chao, Z.Q. Qiang, T.G. Kui, S.W. Bao, T.H. Gao: Top seeded growth of $KTiOPO_4$ from molten tungsten solution, J. Cryst. Growth **112**, 294–297 (1991)
20.60 A. Yokotani, A. Miyamoto, T. Sasaki, S. Nakai: Observation of optical inhomogeneities in flux grown KTP crystals, J. Cryst. Growth **110**, 963–967 (1991)
20.61 D.P. Shumov, M.P. Tarassov, V.S. Nikolov: Investigation of optical inhomogeneities in $KTiOPO_4$ (KTP) single crystals grown from high-temperature tungsten-containing solutions, J. Cryst. Growth **129**, 635–639 (1993)
20.62 D. Bravo, X. Ruiz, F. Díaz, F.J. López: EPR of tungsten impurities in $KTiOPO_4$ single crystals grown from

molten tungstate solutions, Phys. Rev. B **52**, 3159–3169 (1995)
20.63 J.H. Kim, J.K. Kang, S.J. Chung: Effects of seed orientation on the top-seeded solution growth of $KTiOPO_4$ single crystals, J. Cryst. Growth **147**, 343–349 (1995)
20.64 F.J. Kumar, S.G. Moorthy, C. Subramanian, G. Bocelli: Growth and characterization of $KTiOPO_4$ single crystals, Mater. Sci. Eng. B **49**, 31–35 (1997)
20.65 G. Marnier: Process for the flux synthesis of crystals of the $KTiOPO_4$ potassium titanyl monophosphate type, US Patent 4746396 (1988)
20.66 Y. Guillien, B. Ménart, J.P. Fève, P. Segonds, J. Douady, B. Boulanger, O. Pacaud: Crystal growth and refined Sellmeier equations over the complete transparency range of $RbTiOPO_4$, Opt. Mater. **22**, 155–162 (2003)
20.67 G.M. Loiacono, D.N. Loiacono, T. McGee, M. Babb: Laser damage formation in $KTiOPO_4$ and $KTiOAsO_4$ crystals: Grey tracks, J. Appl. Phys. **72**, 2705–2712 (1992)
20.68 T.E. Gier: Method for flux growth of $KTiOPO_4$ and its analogues, US Patent 4231838 (1980)
20.69 D. Shen, C. Huang: A new nonlinear optical crystal KTP, Prog. Cryst. Growth Charact. **11**, 269–274 (1985)
20.70 K. Iliev, P. Peshev, V. Nikolov, I. Koseva: Physicochemical properties of high-temperature solutions of the K_2O–P_2O_5–TiO_2 system suitable for the growth of $KTiOPO_4$ (KTP) single crystals, J. Cryst. Growth **100**, 219–224 (1990)
20.71 P.F. Bordui, J.C. Jacco: Viscosity and density of solutions used in high-temperature growth of $KTiOPO_4$ (KTP), J. Cryst. Growth **82**, 351–355 (1987)
20.72 N. Angert, M. Tseitlin, E. Yashchin, M. Roth: Ferroelectric phase transition temperatures of $KTiOPO_4$ crystals grown from self-fluxes, Appl. Phys. Lett. **67**, 1941–1943 (1995)
20.73 Y.S. Oseledchik, S.P. Belokrys, V.V. Osadchuk, A.L. Prosvirin, A.F. Selevich, V.V. Starshenko, K.V. Kuzemchenko: Growth of $RbTiOPO_4$ single crystals from phosphate systems, J. Cryst. Growth **125**, 639–643 (1992)
20.74 C.V. Kannan, S. Ganesa Murthy, V. Kannan, C. Subramanian, P. Ramasamy: TSSG of $RbTiOPO_4$ single crystals from phosphate flux and their characterization, J. Cryst. Growth **245**, 289–296 (2002)
20.75 L.I. Isaenko, A.A. Merkulov, V.I. Tyurikov, V.V. Atuchin, L.V. Sokolov, E.M. Trukhanov: Growth and real structure of $KTiOAsO_4$ crystals from self-fluxes, J. Cryst. Growth **171**, 146–153 (1997)
20.76 M. Roth, N. Angert, M. Tseitlin, G. Schwarzman, A. Zharov: Ferroelectric phase transition temperatures of self-flux-grown $RbTiOPO_4$ crystals, Opt. Mater. **26**, 465–470 (2004)
20.77 M.E. Hagerman, K.R. Poeppelmeier: Review of the structure and processing-defect-property relationships of potassium titanyl phosphate: A strategy for novel thin-film photonic devices, Chem. Mater. **7**, 602–621 (1995)
20.78 M.N. Satyanarayan, A. Deepthy, H.L. Bhat: Potassium titanyl phosphate and its isomorphs: growth, properties and applications, Crit. Rev. Solid State **24**, 103–189 (1999)
20.79 J. Wang, J. Wei, Y. Liu, X. Yin, X. Hu, Z. Shao, M. Jiang: A survey of research on KTP and its analogue crystals, Prog. Cryst. Growth Charact. **40**, 3–15 (2000)
20.80 P.F. Bordui, J.C. Jacco, G.M. Loiacono, R.A. Stolzenberger, J.J. Zola: Growth of large single crystals of $KTiOPO_4$ (KTP) from high-temperature solution using heat pipe based furnace system, J. Cryst. Growth **84**, 403–408 (1987)
20.81 R.J. Bolt, M.H. van der Mooren, H. de Haas: Growth of $KTiOPO_4$ (KTP) single crystals by means of phosphate and phosphate/sulfate fluxes out of a three-zone furnace, J. Cryst. Growth **114**, 141–152 (1991)
20.82 T. Sasaki, A. Miyamoto, A. Yokotani, S. Nakai: Growth and optical characterization of large potassium titanyl phosphate crystals, J. Cryst. Growth **128**, 950–955 (1993)
20.83 N. Angert, L. Kaplun, M. Tseitlin, E. Yashchin, M. Roth: Growth and domain structure of potassium titanyl phosphate crystals pulled from high-temperature solutions, J. Cryst. Growth **137**, 116–122 (1994)
20.84 B. Vartak, J.J. Derby: On stable algorithms and accurate solutions for convection-dominated mass transfer in crystal growth modeling, J. Cryst. Growth **230**, 202–209 (2001)
20.85 P.F. Bordui, S. Motakef: Hydrodynamic control of solution inclusion during crystal growth of $KTiOPO_4$ (KTP) from high-temperature solution, J. Cryst. Growth **96**, 405–412 (1989)
20.86 B. Vartak, Y. Kwon, A. Yeckel, J.J. Derby: An analysis of flow and mass transfer during the solution growth of potassium titanyl phosphate, J. Cryst. Growth **210**, 704–718 (2000)
20.87 B. Vartak, A. Yeckel, J.J. Derby: On the validity of boundary layer analysis for flow and mass transfer caused by rotation during the solution growth of large single crystals, J. Cryst. Growth **283**, 479–489 (2005)
20.88 E.G. Tsvetkov, V.N. Semenenko, G.G. Khranenko, V.I. Tyurikov: Growth peculiarities and polar structures formation in potassium titanyl phosphate crystals, J. Surf. Invest. X-Ray Synchrotron Neutron Tech. **5**, 65–70 (2002), in Russian
20.89 M. Roth, N. Angert, M. Tseitlin, A. Alexandrovski: On the optical quality of KTP crystals for nonlinear optical and electro-optic applications, Opt. Mater. **16**, 131–136 (2001)
20.90 P.A. Morris, A. Ferretti, J.D. Bierlein, G.M. Loiacono: Reduction of the ionic conductivity of flux grown $KTiOPO_4$ crystals, J. Cryst. Growth **109**, 367–375 (1991)

20.91 M.G. Roelofs: Identification of Ti^{3+} in potassium titanyl phosphate and its possible role in laser damage, J. Appl. Phys. **65**, 4976–4982 (1989)

20.92 V.D. Kugel, G. Rosenman, N. Angert, E. Yaschin, M. Roth: Domain inversion in $KTiOPQ_4$ crystal near the Curie point, J. Appl. Phys. **76**, 4823–4826 (1994)

20.93 M.E. Hagerman, V.L. Kozhevnikov, K.R. Poeppelmeier: High-temperature decomposition of $KTiOPO_4$, Chem. Mater. **5**, 1211–1215 (1993)

20.94 D.K.T. Chu, H. Hsiung: Ferroelectric phase transition study in $KTiOPO_4$ – An optical 2nd harmonic generation study, Appl. Phys. Lett. **61**, 1766–1768 (1992)

20.95 K. Zhang, X. Wang: Structure sensitive properties of KTP-type crystals, Chin. Sci. Bull. **46**, 2028–2036 (2001)

20.96 T.F. McGee, G.M. Blom, G. Kostecky: Growth and characterization of doped KTP crystals, J. Cryst. Growth **109**, 361–366 (1991)

20.97 D.K.T. Chu, H. Hsiung, L.K. Cheng, J.D. Bierlein: Curie temperatures and dielectric-properties of doped and undoped $KTiOPO_4$ and isomorphs, IEEE Trans. Ultrason. Ferroelectr. Fraq. Control **40**, 819–824 (1993)

20.98 R.V. Pisarev, R. Farhi, P. Moch, V.I. Voronkova: Temperature-dependence of Raman-scattering and soft modes in $TlTiOPO_4$, J. Phys. Condens. Matter **2**, 1555–1568 (1990)

20.99 G.M. Loiacono, R.A. Stolzenberger, D.N. Loiacono: Modified $KTiOPO_4$ crystals for noncritical phase matching applications, Appl. Phys. Lett. **64**, 16–18 (1994)

20.100 P.F. Bordui, R.G. Norwood, M.M. Fejer: Curie-temperature measurements on $KTiOPO_4$ single-crystals grown by flux and hydrothermal techniques, Ferroelectrics **115**, 7–12 (1991)

20.101 V.K. Yanovskii, V.I. Voronkova, A.P. Leonov, S.Y. Stefanovich: Ferroelectric properties of $KTiOPO_4$ type crystals, Sov. Phys. Solid State **27**, 1506–1516 (1985)

20.102 B.C. Choi, J.B. Kim, B.M. Jin, S.I. Yun, J.N. Kim: Dielectric properties of flux-grown $KTiOPO_4$ single crystals, J. Korean Phys. Soc. **25**, 327–331 (1992)

20.103 Y.V. Shaldin, R. Poprawski: Spontaneous birefringence and pyroelectricity in $KTiOPO_4$ crystals, Ferroelectrics **106**, 399–404 (1990)

20.104 A. Miyamoto, Y. Mori, Y. Okada, T. Sasaki, S. Nakai: Refractive index and lattice constant variation in flux grown KTP crystals, J. Cryst. Growth **156**, 303–306 (1995)

20.105 M.N. Satyanarayan, H.L. Bhat: Influence of growth below and above T_C on the morphology and domain structure in flux-grown KTP crystals, J. Cryst. Growth **181**, 281–289 (1997)

20.106 M. Roth, N. Angert, M. Tseitlin: Growth-dependent properties of KTP crystals and PPKTP structures, J. Mater. Sci. Mater. Electron. **12**, 429–436 (2001)

20.107 N. Angert, M. Tseitlin, L. Kaplun, E. Yashchin, M. Roth: Ferroelectric domain reversal in KTP crystals by high-temperature treatment, Ferroelectrics **157**, 117–122 (1994)

20.108 M.J. Martín, D. Bravo, R. Solé, F. Díaz, F.J. López, C. Zaldo: Thermal reduction of $KTiOPO_4$ crystals, J. Appl. Phys. **76**, 7510–7518 (1994)

20.109 P.A. Morris: Impurities in nonlinear optical oxide crystals, J. Cryst. Growth **106**, 76–88 (1990)

20.110 M. Roth, N. Angert, L. Weizman, A. Gachechiladze, M. Shachman, D. Remennikov, M. Tseitlin, A. Zharov: Development of KTP crystals for laser applications, Ann. Isr. Phys. Soc. **14**, 89–92 (2000)

20.111 L.T. Cheng, L.K. Cheng, R.L. Harlow, J.D. Bierlein: Blue light generation using bulk single crystals of niobium-doped $KTiOPO_4$, Appl. Phys. Lett. **64**, 155–157 (1994)

20.112 V.I. Chani, K. Shimamura, S. Endo, T. Fukuda: Growth of mixed crystals of the $KTiOPO_4$ (KTP) family, J. Cryst. Growth **171**, 472–476 (1997)

20.113 K.T. Stevens, L.E. Halliburton, M. Roth, N. Angert, M. Tseitlin: Identification of Pb-related Ti^{3+} center in flux-grown $KTiOPO_4$, J. Appl. Phys. **88**, 6239–6244 (2000)

20.114 E. Lebiush, R. Lavi, Y. Tsuk, N. Angert, A. Gachechiladze, M. Tseitlin, A. Zharov, M. Roth: RTP as a Q-switch for high repetition rate applications, Proc. Adv. Solid State Lasers, TOPS **34**, 63–65 (2000)

20.115 Y. Stefanovich, L.A. Ivanova, A.V. Astafyev: *Ionic and Superionic Conductivity in Ferroelectrics* (Nitekhim, Moscow 1989) p. 37, in Russian

20.116 F.C. Zumsteg, J.D. Bierlein, T.E. Gier: $K_xRb_{1-x}TiOPO_4$: A new nonlinear optical material, J. Appl. Phys. **47**, 4980–4985 (1976)

20.117 W.P. Risk, G.M. Loiacono: Periodic poling and wavegude frequency doubling in $RbTiOAsO_4$, Appl. Phys. Lett. **69**, 311–313 (1996)

20.118 M. Roth, M. Tseitlin, N. Angert: Composition-dependent electro-optic and nonlinear optical properties of KTP-family crystals, Opt. Mater. **28**, 71–76 (2006)

20.119 Y. Jiang, L.E. Halliburton, M. Roth, M. Tseitlin, N. Angert: Hyperfine structure associated with the dominant radiation-induced trapped hole center in $RbTiOPO_4$ crystals, Phys. Status Solidi (b) **242**, 2489–2496 (2005)

20.120 J.D. Bierlein, F. Ahmed: Observation and poling of ferroelectric domains in $KTiOPO_4$, Appl. Phys. Lett. **51**, 1328–1330 (1987)

20.121 G.M. Loiacono, R.A. Stolzenberger: Observation of complex domain walls in $KTiOPO_4$, Appl. Phys. Lett. **53**, 1498–1500 (1988)

20.122 L.P. Shi, J. Chrosch, J.Y. Wang, Y.G. Liu: Twinning in $KTiOPO_4$ crystals, Cryst. Res. Technol. **27**, K76–K78 (1992)

20.123 F. Laurell, M.G. Roelofs, W. Bindloss, H. Hsiung, A. Suna, J.D. Bierlein: Detection of ferroelectric

domain reversal in $KTiOPO_4$ wave-guides, J. Appl. Phys. **71**, 4664–4670 (1992)
20.124 R.J. Bolt, W.J.P. Enckevort: Observation of growth steps and growth hillocks on the {100}, {210}, {011} and {101} faces of flux-grown $KTiOPO_4$ (KTP), J. Cryst. Growth **119**, 329–338 (1992)
20.125 A.A. Chernov: Stability of faceted shapes, J. Cryst. Growth **24/25**, 11–31 (1974)
20.126 N.R. Ivanov, N.A. Tikhomirova, A.V. Ginzberg, S.P. Chumakova, E.I. Eknadiosyants, V.Z. Borodin, A.N. Pinskaya, V.A. Babanskikh, V.A. D'yakov: Domain structure of $KTiOPO_4$ crystals, Crystallogr. Rep. **39**, 593–599 (1994)
20.127 W.P. Risk, R.N. Payne, W. Lenth, C. Harder, H. Meier: Noncritically phase-matched frequency doubling using 994 nm dye and diode laser radiation in $KTiOPO_4$, J. Appl. Phys. **55**, 1179–1181 (1989)
20.128 W.P. Risk, W.J. Kozlovsky: Efficient generation of blue-light by doubly resonant sum-frequency mixing in a monolithic KTP resonator, Opt. Lett. **17**, 707–709 (1992)
20.129 L.T. Cheng, L.K. Cheng, R.L. Harlow, J.D. Bierlein: Blue light generation using bulk single crystals of niobium-doped $KTiOPO_4$, Appl. Phys. Lett. **64**, 155–157 (1994)
20.130 H. Mabuchi, E.S. Polzik, H.J. Kimble: Blue-light-induced infrared-absorption in $KNbO_3$, J. Opt. Soc. Am. B **11**, 2023–2029 (1994)
20.131 J.A. Armstrong, N. Bloembergen, J. Ducuing, P.S. Pershan: Interaction between light waves in a nonlinear dielectric, Phys. Rev. **127**, 1918–1939 (1962)
20.132 J.D. Bierlein, D.B. Laubacher, J.B. Brown: Balanced phase matching in segmented $KTiOPO_4$ waveguides, Appl. Phys. Lett. **56**, 1725–1727 (1990)
20.133 C.J. van der Poel, J.D. Bierlein, J.B. Brown: Efficient type I blue second harmonic generation in periodically segmented $KTiOPO_4$ waveguides, Appl. Phys. Lett. **57**, 2074–2076 (1990)
20.134 M.G. Roelofs, P.A. Morris, J.D. Bierlein: Ion exchange of Rb, Ba, and Sr in $KTiOPO_4$, J. Appl. Phys. **70**, 720–728 (1991)
20.135 M.C. Gupta, W.P. Risk, A.C.G. Nutt, S.D. Lau: Domain inversion in $KTiOPO_4$ using electron beam scanning, Appl. Phys. Lett. **63**, 1167–1169 (1993)
20.136 G. Rosenman, P. Urenski, A. Agronin, A. Arie, Y. Rosenwaks: Nanodomain engineering in $RbTiOPO_4$ ferroelectric crystals, Appl. Phys. Lett. **82**, 3934–3936 (2003)
20.137 M. Yamada, N. Nada, M. Saitoh, K. Watanabe: First-order quasi-phase matched $LiNbO_3$ waveguide periodically poled by applying an external field for efficient blue second harmonic generation, Appl. Phys. Lett. **62**, 435–437 (1993)
20.138 L.E. Myers, R.C. Eckardt, M.M. Fejer, R.L. Byer, W.R. Bosenberg, J.W. Pierce: Quasi-phase-matched optical parametric oscillators in bulk periodically poled $LiNbO_3$, J. Opt. Soc. Am. B **12**, 2102–2116 (1995)
20.139 Q. Chen, W.P. Risk: Periodic poling of $KTiOPO_4$ using an applied electric field, Electron. Lett. **30**, 1516–1517 (1994)
20.140 G.D. Boyd, D.A. Kleinman: Parametric interaction of focused Gaussian light beams, J. Appl. Phys. **39**, 3597–3639 (1968)
20.141 M.M. Fejer, G.A. Magel, D.H. Jundt, R.L. Byer: Quasi-phase-matched second harmonic generation: tuning and tolerances, J. Quantum Electron. **QE-28**, 2631–2654 (1992)
20.142 A. Arie, G. Rosenman, V. Mahal, A. Skliar, M. Oron, M. Katz, D. Eger: Green and ultraviolet quasi-phase-matched second harmonic generation in bulk periodically-poled $KTiOPO_4$, Opt. Commun. **142**, 265–268 (1997)
20.143 M. Peltz, U. Bäder, A. Borsutzky, R. Wallerstein, J. Hellström, H. Karlsson, V. Pasiskevicius, F. Laurell: Optical parametric oscillators for high pulse energy and high average power operation based on large aperture periodically poled KTP and RTA, Appl. Phys. B **73**, 663–670 (2001)
20.144 G. Rosenman, K. Garb, A. Skliar, D. Eger, M. Oron, M. Katz: Domain broadening in quasi-phase-matched nonlinear optical devices, Appl. Phys. Lett. **73**, 865–867 (1998)
20.145 H. Karlsson, F. Laurell: Electric field poling of flux grown $KTiOPO_4$, Appl. Phys. Lett. **71**, 3474–3476 (1997)
20.146 M. Pierrou, F. Laurell, H. Karlsson, T. Kellner, C. Czeranowsky, G. Huber: Generation of 740 mW of blue light by intracavity frequency doubling with a first-order quasi-phase-matched $KTiOPO_4$ crystal, Opt. Lett. **24**, 205–207 (1999)
20.147 G. Rosenman, A. Skliar, D. Eger, M. Oron, M. Katz: Low temperature periodic poling of flux-grown $KTiOPO_4$ and isomorphic crystals, Appl. Phys. Lett. **73**, 3650–3652 (1998)
20.148 A. Garashi, A. Arie, A. Skliar, G. Rosenman: Continuous-wave optical parametric oscillator based on periodically poled $KTiOPO_4$, Opt. Lett. **23**, 1739–1741 (1998)
20.149 C. Canalias, J. Hirohashi, V. Pasiskevicius, F. Laurell: Polarization-switching characteristics of flux-grown $KTiOPO_4$ and $RbTiOPO_4$ at room temperature, J. Appl. Phys. **97**, 124105 (2005)
20.150 P. Urenski, M. Lesnykh, Y. Rosenwaks, G. Rosenman: Anisotropic domain structure of $KTiOPO_4$ crystals, J. Appl. Phys. **90**, 1950–1954 (2001)
20.151 P. Urenski, M. Molotski, G. Rosenman: Bulk ferroelectric domain nucleation in $KTiOPO_4$ crystals, Appl. Phys. Lett. **79**, 2964–2966 (2001)
20.152 C. Canalias, S. Wang, V. Pasiskevicius, F. Laurell: Nucleation and growth of periodic domains during electric field poling in flux-grown $KTiOPO_4$ observed by atomic force microscopy, Appl. Phys. Lett. **88**, 032905 (2006)

20.153 J. Zhang, J. Wang, B. Ge, Y. Liu, X. Hu, G. Zhao, S. Zhu, R.I. Boughton: Growth, conductivity and periodic poled structure of doped $KTiOPO_4$ and its analogue crystals, Opt. Mater. **28**, 355–359 (2006)

20.154 G. Rosenman, P. Urenski, A. Arie, M. Roth, N. Angert, A. Skliar, M. Tseitlin: Polarization reversal and domain grating in flux-grown $KTiOPO_4$ crystals with variable potassium stoichiometry, Appl. Phys. Lett. **76**, 3798–3800 (2000)

20.155 Q. Jiang, P.A. Thomas, D. Walker, K.B. Hutton, R.C.C. Ward, P. Pernot, J. Baruchel: High potassium $KTiOPO_4$ crystals for the fabrication of quasi-phase matched devices, J. Phys. D: Appl. Phys. **36**, 1236–1241 (2003)

20.156 G. Rosenman, A. Skliar, Y. Findling, P. Urenski, A. Englander, P.A. Thomas, Z.W. Hu: Periodically poled $KTiOAsO_4$ crystals for optical parametric oscillation, J. Phys. D: Appl. Phys. **32**, L49–L52 (1999)

20.157 P. Pernot-Rejmánková, P.A. Thomas, P. Cloenets, F. Lorut, J. Baruchel, Z.W. Hu, P. Urenski, G. Rosenman: Periodically poled KTA crystal investigated using coherent X-ray beams, J. Appl. Cryst. **33**, 1149–1153 (2000)

20.158 H. Karlsson, F. Laurell, L.K. Cheng: Periodic poling of $RbTiOPO_4$ for quasi-phase matched blue light generation, Appl. Phys. Lett. **74**, 1519–1521 (1999)

20.159 A. Fragemann, V. Pasiskevicius, J. Nordborg, J. Hellström, H. Karlsson, F. Laurell: Frequency converters from visible to mid-infrared with periodically poled $RbTiOPO_4$, Appl. Phys. Lett. **83**, 3090–3092 (2003)

20.160 H. Karlsson, F. Laurell, P. Hendriksson, G. Arvidsson: Frequency doubling in periodically poled $RbTiOAsO_4$, Electron. Lett. **32**, 556–557 (1996)

20.161 H. Karlsson, M. Olson, G. Arvidsson, F. Laurell, U. Bäder, A. Borsutzky, R. Wallenstein, S. Wikström, M. Gustafsson: Nanosecond optical parametric oscillator based on large-aperture periodically poled $RbTiOAsO_4$, Opt. Lett. **24**, 330–332 (1999)

20.162 G.T. Kennedy, D.T. Reid, A. Miller, A. Ebrahimzadeh, H. Karlsson, G. Arvidsson, F. Laurell: Near- to mid-infrared picosecond optical parametric oscillator based on periodically poled $RbTiOAsO_4$, Opt. Lett. **23**, 503–505 (1998)

20.163 P. Loza-Alvarez, D.T. Reid, M. Ebrahimzadeh, W. Sibbett, H. Karlsson, P. Hendriksson, G. Arvidsson, F. Laurell: Periodically poled $RbTiOAsO_4$ femtosecond optical parametric oscillator tunable from 1.38 to 1.58 µm, Appl. Phys. B **68**, 177–180 (1999)

20.164 W. Chen, G. Mouret, D. Boucher, F.K. Tittel: Mid-infrared trace gas detection using continuous-wave difference frequency generation in periodically poled $RbTiOAsO_4$, Appl. Phys. B **72**, 873–876 (2001)

20.165 I. Yutsis, B. Kirshner, A. Arie: Temperature-dependent dispersion relations for $RbTiOPO_4$ and $RbTiOAsO_4$, Appl. Phys. B **79**, 77–81 (2004)

20.166 S. Moscovich, A. Arie, R. Urenski, A. Agronin, G. Rosenman, Y. Rosenwaks: Noncollinear second-harmonic generation in sub-micrometer-poled $RbTiOPO_4$, Opt. Exp. **12**, 2242 (2004)

20.167 C. Canalias, V. Pasiskevicius, R. Clemens, F. Laurell: Submicrion periodically poled flux-grown $KTiOPO_4$, Appl. Phys. Lett. **82**, 4233–4235 (2003)

20.168 D. Feng, N. Ming, J. Hong, Y. Yang, J. Zhu, Z. Yang, Y. Wang: Enhancement of send-harmonic generation in $LiNbO_3$ crystals with periodic laminar ferroelectric domains, Appl. Phys. Lett. **37**, 607–609 (1980)

20.169 V. Bermudez, E. Callejo, E. Dieguez: Effect of temperature annealing on periodically poled rare-earth doped lithium niobate crystal, J. Optoelectron. Adv. Mater. **5**, 55–59 (2003)

20.170 C.E.M. de Oliveira, G. Orr, N. Axelrod, A.J. Agranat: Controlled composition modulation in potassium lithium tantalate niobate crystals grown by off-centered TSSG method, J. Cryst. Growth **273**, 203–206 (2004)

20.171 J.A. Burton, R.C. Prim, W.P. Slichter: The distribution of solute in crystals grown from the melt. Part I. Theoretical, J. Chem. Phys. **21**, 1987–1991 (1953)

20.172 D. Elwell, H.J. Scheel: *Crystal Growth from High-temperature Solutions* (Academic, New York 1975) p. 294

20.173 F.J. Kumar, D. Jayaraman, C. Subramanian, P. Ramasamy: Nucleation kinetic study of $KTiOPO_4$ crystallizing from high temperature solution, J. Cryst. Growth **137**, 535–537 (1994)

20.174 A.V. Smith: *SNLO nonlinear optics code*, available from: www.sandia.gov./imrl/x1118/xxtab.htm

20.175 J.C. Jacco, D.R. Rockafello, E.A. Teppo: Bulk-darkening threshold of flux-grown $KTiOPO_4$, Opt. Lett. **16**, 1307–1309 (1991)

20.176 R. Blachman, P.F. Bordui, M.M. Fejer: Laser-induced photochromic damage in potassium titanyl phosphate, Appl. Phys. Lett. **64**, 1318–1320 (1994)

20.177 B. Boulanger, M.M. Fejer, R. Blachman, P.F. Bordui: Study of $KTiOPO_4$ gray-tracking at 1064, 532 and 355 nm, Appl. Phys. Lett. **65**, 2401–2403 (1994)

20.178 M.P. Scripsick, D.N. Loiacono, J. Rottenberg, S.H. Goellner, L.E. Halliburton, F.K. Hopkins: Defects responsible for gray tracks in flux-grown $KTiOPO_4$, Appl. Phys. Lett. **66**, 3428–3430 (1995)

20.179 J.P. Feve, B. Boulanger, G. Marnier, H. Albrecht: Repetition rate dependence of gray-tracking in $KTiOPO_4$ during second-harmonic generation at 532 nm, Appl. Phys. Lett. **70**, 1–3 (1997)

20.180 W.R. Bosenberg, D.R. Guyer: Single-frequency optical parametric oscillator, Appl. Phys. Lett. **61**, 387–389 (1992)

20.181 A. Deepthy, M.N. Saryanarayan, K.S.R.K. Rao, H.L. Bhat: Photoluminescence studies on gray tracked $KTiOPO_4$ single crystals, J. Appl. Phys. **85**, 8332–8336 (1999)

20.182 B.V. Andreev, V.A. Maslov, A.A. Mikhailov, S.K. Pak, O.P. Shaunin, I.A. Sherbakov: Exprtimental study of the laser-induced absorption effect and the nature of color centers in potassium titanyl phosphate crystals, Proc. SPIE **1839**, 280–289 (1991)

20.183 M.P. Scripsick, G.J. Edwards, L.E. Halliburton, R.F. Belt, G.M. Loiacono: Effect of crystal growth on Ti^{3+} centers in $KTiOPO_4$, J. Appl. Phys. **76**, 773–776 (1994)

20.184 S.D. Setzler, K.T. Stevens, N.C. Fernelius, M.P. Scripsick, G.J. Edwards, L.E. Halliburton: Electron paramagnetic resonance and electron-nuclear double-resonance study of Ti^{3+} centres in $KTiOPO_4$, J. Phys. Condens. Matter **15**, 3969–3984 (2003)

20.185 P.A. Morris, M.K. Crawford, M.G. Roelofs, J.D. Bierlein, P.K. Gallagher, G. Gashurov, G. Loiacano: Proton effects in $KTiPO_5$, MRS Proc. Opt. Fiber Mater. Process. **172**, 283–289 (1990)

20.186 R.G. Batchko, G.D. Miller, A. Alexandrovski, M.M. Fejer, R.L. Byer: *Limitations of High-Power Visible Wavelength Periodically Poled Lithium Niobate Devices due to Green-Induced Infrared Absorption and Thermal Lensing*, OSA Technical Digest, Vol. 6 (OSA, Washington 1998) pp. 75–76

20.187 Y. Jiang, L.E. Halliburton, M. Roth, M. Tseitlin, N. Angert: EPR and ENDOR study of an oxygen-vacancy-associated Ti^{3+} center in $RbTiOPO_4$ crystals, Physica B **400**, 190–197 (2007)

20.188 J.J. Carvajal, R. Solé, J. Gavaldà, J. Massons, P. Segonds, B. Boulanger, A. Brenier, G. Boulon, J. Zaccaro, M. Aguiló, F. Díaz: Spectroscopic and second harmonic generation properties of a new crystal: Yb-doped $RbTiOPO_4$, Opt. Mater. **26**, 313–317 (2004)

21. High-Temperature Solution Growth: Application to Laser and Nonlinear Optical Crystals

Joan J. Carvajal, Maria Cinta Pujol, Francesc Díaz

Growth methods based on high-temperature solutions, traditionally also known as flux growth methods, and especially the top-seeded solution growth (TSSG) and liquid-phase epitaxy (LPE) methods, are some of the most popular methods by which to grow single crystals. These methods have to be used when the grown materials melt incongruently, melt at very high temperatures, or suffer from polymorphic transitions below the crystallization temperature. In this chapter we review the main advances produced in these crystal growth techniques during recent years, both in bulk and epitaxial films, and for two families of oxide materials, specifically those commonly used for solid-state lasers and nonlinear optical crystals. We intend to focus on the application to the real problems related to crystal growth in solutions with different viscosities, while revisiting some of the main strategies developed to overcome these problems to enable growth of bulk single crystals and single-crystalline films with good optical quality.

21.1 **Basics** 726
21.1.1 Historical Background and Overview 726
21.1.2 Most Important Families of Laser and Nonlinear Optical Materials 727

21.2 **High-Temperature Solution Growth** 731
21.2.1 Top-Seeded Solution Growth (TSSG) 732
21.2.2 Liquid-Phase Epitaxy (LPE) 734

21.3 **Growth of Bulk Laser and NLO Single Crystals by the TSSG Method** 736
21.3.1 Crystal Growth from Low-Viscosity Solutions: Fluorides, Tungstates, and Vanadates..... 736
21.3.2 Crystal Growth from High-Viscosity Solutions: Phosphates and Borates. 739

21.4 **Liquid-Phase Epitaxy: Growth of Epitaxial Films of Laser and NLO Materials** 746
21.4.1 Epitaxial Films of Laser Materials: Lanthanide-Doped KLuW on KLuW Substrates 746
21.4.2 Epitaxies Within the Structural Field of KTP ... 748

References 752

Interest in crystal growth technology started at the beginning of the 20th century, initially in the jewelery and watch industry, and later on in microelectronics (semiconductors), solid-state devices, and laser technology.

During the period 1900–1939, before World War II, the basis of high-temperature solution growth technology was developed, but industrial applications were limited almost only to the ruby single crystal, so the new crystal growth method, and the crystals grown from it, were limited to the academic level. The widespread technological application of single crystals began with the military application of piezoelectric single crystals for transducers in sonar and radar devices. In 1948, after World War II, the discovery of the transistor effect substantially increased the demand for single crystals. The deficient performance of the first generation of transistors based on germanium, principally related to the existence of micro- and macrodefects in germanium single crystals, induced and impelled the study and improvement of high-temperature solution crystal growth methods.

After 1990, the expansion to large-scale industrial production of transistors and the progress in the field of electronics definitively motivated crystal growth as a new scientific field in the material science area. Semiconductors such as Si, GaAs, InAs, etc., and crystalline materials such as $BaTiO_3$, ferrites, yttrium iron garnet YIG, and yttrium aluminum garnet (YAG), among oth-

ers, have been obtained with a high enough level of perfection, and have been incorporated as core materials for different solid-state devices.

Now, technology uses thousands of single-crystal materials, especially in microelectronics, optoelectronics, optics, and laser technologies. Research is oriented to develop methods and technologies to control the crystallinity, purity, and homogeneity of the grown crystals. The most extended crystal growth methods, based on producing controlled solidification of a melt of the stoichiometric composition of the material, are related to the production of semiconductor materials such as silicon and GaAs. However, several crystalline materials cannot be obtained from melt methods and have to be grown from a solution with a convenient solvent. In this chapter we discuss the high-temperature solution growth methodologies as some of the most suitable ways to obtain several optical materials, specifically in the fields of the laser and nonlinear optical technologies.

21.1 Basics

21.1.1 Historical Background and Overview

Crystal growth is a central step in the processing of solid-state laser and nonlinear optical (NLO) materials. Crystal size, optical losses, and optical uniformity, as well as ultimate crystal cost, tend to be dominated by the crystal growth process. A variety of techniques are practiced, but for most materials, there emerges a preferred crystal growth technique. The process-dependent properties and limitations of a crystal tend to reflect the inherent nature of that growth technique.

In general, crystal growth from the melt is preferable whenever possible. However, other crystal growth methods have to be used when materials melt incongruently, when they suffer from polymorphic transitions below crystallization temperature, or when they melt at very high temperatures. In these cases high-temperature solution methods must be used, in processes analogous to crystal growth from aqueous solutions, but in which the solvent solidifies before reaching room temperature. The main advantage of these methodologies is that crystals are grown below their melting temperature, or in a fluid with lower viscosity than the melt. In high-temperature solution growth, thermal strain is minimized due to the relatively low growth temperature, the much smaller thermal gradients used in these methods compared with classical methods based on growth from melts, and the free growth into a liquid. These factors make crystal growth proceed in physical conditions near thermodynamic equilibrium, allowing crystals to grow in a way that minimizes the superficial energy, developing facets. However, these low growth rates, in general hundreds of times smaller than the growth rates that can be achieved in melt-based growth methods, constitute the main disadvantage of the high-temperature solution growth methods. This, together with the differences in linear growth rates among the different faces of

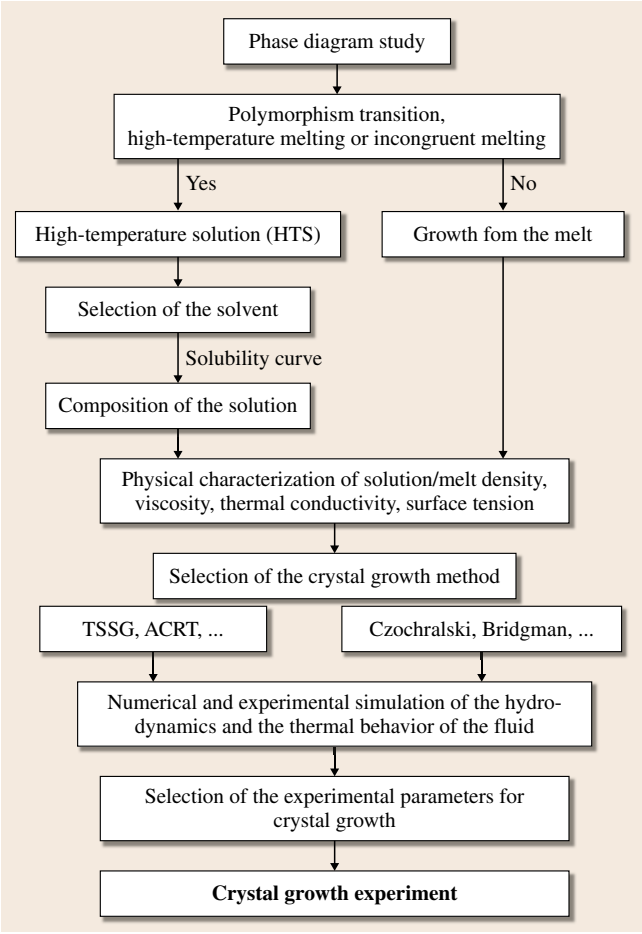


Fig. 21.1 Flow chart with the criteria used to determine the crystal growth method of a material from the melt or from high-temperature solutions ◀

Table 21.1 Structural, thermal, and optical properties of the most important families of inorganic SSL single crystal

	Space group of symmetry	Optical class	Moh's hardness	Thermal conductivity (W/m K)	Transparency range (nm)	Growth method	References
YAG	*Ia3d*	Isotropic	8.2–8.5	14	200–6000	Czochralski Floating zone μ-Pulling	[21.1, 2]
$REVO_4$[a]	$I4_1/amd$	Uniaxial	5	$c_{\parallel} = 5.23$ $c_{\perp} = 5.10$	400–5000	Czochralski HTS EDFF TSSG	[21.3–5]
YAP	*Pbnm*	Biaxial	≈ YAG	11	300–10 000	Czochralski	[21.6]
KREW[b]	*C2/c*	Biaxial	4.5–5	2.2–3.5	300–5000	TSSG INFC TNFC	[21.7–10]
RELF[c]	$I4_1/a$	Uniaxial	4–5	6	120–7500	Bridgman Czochralski VGF	[21.11, 12]
BaREF[d]	*C2/m*	Biaxial	3–3.5	6	125–12 000	Czochralski	[21.13, 14]
LiSAF	$P\bar{3}1c$	Uniaxial		3.3–3.6		Czochralski Bridgman TSSG	[21.15, 16]

[a] Data for YVO_4; [b] Data for $KGd(WO_4)_2$; [c] Data for YLF; [d] Data for $BaYF_8$

the crystal, which lead to chemical and structural inhomogeneities in the crystal, has hampered the industrial production of crystals grown from high-temperature solution methods.

Figure 21.1 summarizes the criteria used to determine the possibility of use of growth methods based on melt, or when not possible, the use of growth methods based on high-temperature solutions.

21.1.2 Most Important Families of Laser and Nonlinear Optical Materials

Laser Materials

Kaminskii [21.17] mentioned that currently there are over 575 single crystals for solid-state laser (SSL) applications, among them, different structure fluorides, oxides, chlorides, bromides, and compounds with mixed anion pairs such as chlorine–oxygen, fluorine–oxygen, and sulfur–oxygen, which can produce continuous wave (CW) or pulsed stimulated emission (SE) generation over a very wide spectral range from ≈ 0.172 to ≈ 7.24 μm.

The desirable properties of a good laser material are: feasibility of growth; high capacity to incorporate the active ions without affecting the structure; transparency in the suitable range; favorable spectroscopic properties for the active ions; high thermal conductivity; low and similar thermal expansion coefficients; inertness; low cost; and hardness, which favors polishing. They especially have to favor large absorption and emission cross sections, and have: a high gain coefficient; an optimum distance between the active ions (i. e., if laser transition is based on a scheme where cross-relaxation phenomena favors the population of the emitting level, the distance must be short to increase this populating level; on the other hand, if the laser emitting level could be depopulated by a cross-relaxation or energy transfer among active ions, then the distance must be longer); long lifetime to allow population inversion; and low phonon energy modes of the structure to avoid nonradiative transitions.

Table 21.1 lists the most important families of inorganic SSL single crystals, summarizing some of their main structural, thermal, and optical properties.

Oxides

$Y_3Al_5O_{12}$, Yttrium Aluminum Garnet (YAG). YAG crystallizes in the cubic system. The active ions substitute Y^{3+} in the structure in a D_2 position. It is a very stable compound with high robustness and high thermal conductivity. Optically YAG is isotropic. YAG is one of the most widely produced gain laser hosts. The Nd:YAG laser is by far the most commonly used solid-state laser since its first reported lasing at Bell Telephone Laboratories and RCA Laboratories in 1964. Tm-, Ho-, and Er-doped YAG lasers are also widely studied and used in the 2 μm region.

$REVO_4$, Rare-Earth Vanadate. Rare-earth vanadates crystallize in the tetragonal system. The trivalent active ions substitute the optically inert trivalent cations RE^{3+} at lattice sites with $\bar{4}2m$ symmetry. Optically they are positive uniaxial crystals, with $n_o = n_a = n_b$ and $n_e = n_c$. YVO_4 is a strongly birefringent material ($\Delta n = 0.2225$ at 633 nm at room temperature). Their advantages when compared with YAG are the high absorption and emission cross sections, broad bandwidths, and natural polarization of these materials.

$YAlO_3$, Yttrium Aluminum Perovskite (YAP). Several possible crystalline structures can be found in the literature for $YAlO_3$ [21.6]. The active lanthanide ions substitute the Y^{3+} in the lattice sites in C_{1h}. The physical properties of YAP, such as hardness, thermal conductivity, etc., are quite similar to those of YAG [21.18]. From the optical point of view, YAP is a biaxial, birefringent material (Δn, at 1.06 μm, $n_a = 1.929$, $n_b = 1.943$, and $n_c = 1.952$). The transparency region is from around 300 nm to 10 μm. The advantage of this material is related to its anisotropy, which allows the possibility of short tuning of the wavelength with the variation of the wavevector direction in the crystal, and the generation of linearly polarized output beams.

$KRE(WO_4)_2$, Potassium Double Tungstates (KREW). The monoclinic KREW is another well-known family of laser host compounds. The active lanthanide ions substitute the RE^{3+} cation in the structure at the local symmetry lattice site C_2. The physical properties of KREW materials are governed by their huge anisotropy. Their thermal conductivity is anisotropic, and depends also on the RE^{3+} cation. Optically, monoclinic KREW are biaxial crystals. The N_p orthogonal principal crystallooptic axis is parallel to the twofold symmetry axes. The other two principal axes are in the a–c plane. The principal axis N_g is located at $\kappa = 18.5$–$21.5°$ (angle value depending on the RE^{3+} of the host) clockwise to the $\boldsymbol{c}$-crystallographic axis when the positive $\boldsymbol{b}$-axis is pointing towards the observer. N_m is rotated at $\beta + \kappa - 90°$ with respect to the $\boldsymbol{a}$ crystallographic axis in the clockwise direction. Their anisotropy is responsible for the large absorption and emission cross sections of the active ions. Furthermore, these crystals are also very interesting for their stimulated Raman scattering (SRS) properties, and recently for their high efficiency as laser optical cooling materials [21.19].

Fluorides

$RELiF_4$, Rare-Earth Lithium Fluoride (RELF). This material crystallizes in the tetragonal system. The active ions substitute the RE^{3+} in the S_4 positions of the structure. It is an anisotropic uniaxial crystal, with the optical axis along the $\boldsymbol{c}$ crystallographic direction. Its birefringence at 633 nm is $n_o = 1.443$ and $n_e = 1.464$, and at 1064 nm is $n_o = 1.448$ and $n_e = 1.470$. Fluoride crystals are useful for coherent optical sources in the ultraviolet (UV) wavelength region. It can host a high percentage of doping elements, and possesses a low thermal lensing effect, when compared with YAG.

$BaREF_8$, Barium Rare-Earth Fluoride (BaREF). These materials crystallize in the monoclinic system. The rare-earth dopant substitutionally enters the RE^{3+} sites, whose symmetry is S_4. The BaYF refractive index n is 1.5. Optically, $BaREF_8$ is a biaxial crystal. Their monoclinic structure compensates the thermal lens effect under strong pumping better than cubic crystals such as YAG. Additionally, these materials have low-energy phonons: the maximum phonon energy is 400 cm^{-1}.

$LiSrAlF_6$, Lithium Strontium Aluminum Fluoride (LiSAF). LiSAF crystals belong to the colquiriite fluoride family of crystals LiMAF (where M = Sr, Ga, Ca). These materials crystallize in the trigonal system. Optically, these materials are uniaxial. Among them, $LiCaAlF_6$:Cr (LiCAF:Cr) is more robust and has more advantageous thermo-optical properties. It exhibits higher scattering and smaller absorption and emission cross sections when compared with LiSAF. Cr^{3+}-doped single crystals of this family have been described as efficient broadly tunable laser materials [21.20, 21].

Nonlinear Optical Materials

Since its first demonstration in 1961 [21.22], nonlinear frequency conversion has been a field limited by

the available materials, with practical advances largely controlled by progress in making improved NLO materials. To date, the most important class of materials used in nonlinear optics has been inorganic single crystals. Organic materials, although promising, have yet to be produced with good enough chemical and mechanical properties to find broad practical application. Relatively few materials find application in nonlinear optics. The physics of the frequency conversion process places severe demands on potential NLO crystals. Beyond the NLO physics are the additional practical requirements of mechanical and chemical stability and the possibility for production in the form of adequately sized and uniform single crystals.

Table 21.2 lists the main inorganic NLO crystals together with their main structural, thermal, and optical properties.

Niobates. $LiNbO_3$ (LN) crystallizes in the trigonal system. Its NLO coefficients are relatively high, and the birefringence is of a magnitude, enabling phase matching for noncritical type I second-harmonic generation (SHG) of a 1064 nm fundamental at room temperature. Its thermal conductivity is very high. LN can suffer from photorefractive damage when illuminated with visible radiation. Certain Mg-doped LN crystals have been measured to have a photorefractive damage threshold more than 10^5 times greater than that of typical

Table 21.2 Structural, thermal, and optical properties of the main inorganic NLO single crystals [21.23]

	Space group of symmetry	Optical class	Thermal conductivity (W/m K)	Transparency range (nm)	NLO coefficients (pm/V)	Growth method
LN	$R3c$	Uniaxial	0.0015	350–5000	$d_{21} = d_{16} = -2.1$ $d_{22} = 2.1$ $d_{14} = d_{25} = d_{36} = 0$ $d_{31} = d_{15} = -4.3$ $d_{32} = d_{24} = -4.3$ $d_{33} = -27$	Czochralski VTE TSSG DC-Czochralski
KN	$Amm2$	Biaxial		400–5500	$d_{21} = d_{16} = 0$ $d_{22} = 0$ $d_{14} = d_{25} = d_{36} = 0$ $d_{31} = d_{15} = -11.3$ $d_{32} = d_{24} = -12.8$ $d_{33} = -19.5$	HTS
KTP	$Pna2_1$	Biaxial	2–3.3	350–4500	$d_{21} = d_{16} = 0$ $d_{22} = 0$ $d_{14} = d_{25} = d_{36} = 0$ $d_{31} = d_{15} = 2.0$ $d_{32} = d_{24} = 3.6$ $d_{33} = 8.3$	HTS Hydrothermal
KDP	$I\bar{4}2d$	Uniaxial	1.86–2.09	180–1800	$d_{21} = d_{16} = 0$ $d_{22} = 0$ $d_{14} = d_{25} = d_{36} = 0.37$ $d_{31} = d_{15} = 2.0$ $d_{32} = d_{24} = 3.6$ $d_{33} = 8.3$	Aqueous solution
β-BBO	$R3c$	Uniaxial	0.001–0.002	198–2600	$d_{21} = d_{16} = -2.3$ $d_{22} = 2.3$ $d_{14} = d_{25} = d_{36} = 0$ $d_{31} = d_{15} = 0.1$ $d_{32} = d_{24} = 0.1$ $d_{33} = 0$	HTS Metastable growth Czochralski

Table 21.2 (cont.)

	Space group of symmetry	Optical class	Thermal conductivity (W/m K)	Transparency range (nm)	NLO coefficients (pm/V)	Growth method
LBO	$Pna2_1$	Biaxial		160–2300	$d_{21} = d_{16} = 0$ $d_{22} = 0$ $d_{14} = d_{25} = d_{36} = 0$ $d_{31} = d_{15} = -0.67$ $d_{32} = d_{24} = 0.85$ $d_{33} = 0.04$	HTS
BIBO	$C2$	Biaxial		286–2500	$d_{222} = 2.53(4)$ $d_{211} = 2.3(2)$ $d_{233} = 1.3(1)$ $d_{231} = 2.3(2)$ $d_{112} = 2.8(2)$ $d_{332} = 0.9(1)$ $d_{312} = 2.4(3)$ $d_{132} = 2.4(3)$	Czochralski
$AgGaS_2$	$I\bar{4}2d$	Uniaxial	0.01	500–13 000	$d_{21} = d_{16} = 0$ $d_{22} = 0$ $d_{14} = d_{25} = d_{36} = 17.5$ $d_{31} = d_{15} = 0$ $d_{32} = d_{24} = 0$ $d_{33} = 0$	Bridgman
$LiIO_3$	$P6_3$	Uniaxial	8×10^{-4}	310–5000	$d_{21} = d_{16} = 0$ $d_{22} = 0$ $d_{14} = d_{25} = d_{36} = 0$ $d_{31} = d_{15} = 4.4$ $d_{32} = d_{24} = 4.4$ $d_{33} = 4.5$	Aqueous solution

undoped LN. Mg doping appears to have little effect on the NLO coefficients.

$KNbO_3$ (KN) is notable for its very large NLO coefficients and birefringence. The transmission range is similar to that of LN, although residual losses are generally higher and much less consistent from crystal to crystal. It suffers from significant processing limitations, due to the material's low Curie temperature and its pyroelectric and ferroelastic character.

Phosphates. $KTiOPO_4$ (KTP) belongs to family of compounds with the general formula $ABOXO_4$ where A = K, Rb, Na, Cs, Tl, NH_4; B = Ti, Sn, Sb, Zr, Ge, Al, Cr, Fe, V, Nb, Ta, and X = P, As, Si, crystallizing in the orthorhombic system [21.24]. KTP single crystals are chemically inert. Optically they are biaxial crystals. The KTP transmission range, NLO coefficients, and birefringence are similar to those of LN, although KTP's residual absorption is notably higher. Perhaps most important for KTP are its very large thermal and angular phase-matching bandwidths for SHG of fundamental wavelengths near 1064 nm.

KH_2PO_4 (KDP) and its homologs are among the most widely used commercial NLO materials. Although members of the family have relatively low NLO coefficients, they feature good UV transmission, high birefringence, and relatively high resistance to laser damage. KDP is widely used to generate second, third, fourth, and fifth harmonics of 1.06 μm radiation.

Borates. Single crystals of the low-temperature phase of barium metaborate, β-BaB_2O_4 (β-BBO) and $LiBO_3$ (LBO) have found important applications for NLO devices. β-BBO has a wide transparent spectral range, and good mechanical properties. In general, borates

combine UV transparency, high-laser damage thresholds, and adequate birefringence for phase-matching a broad range of visible and UV interactions. β-BBO has larger nonlinear susceptibilities than LBO, and can be phase-matched more readily in the UV, but suffers from smaller angular acceptance and lower damage threshold, and is more hygroscopic.

BiB_3O_6 (BIBO) is another outstanding NLO crystal. It belongs to the monoclinic system. BIBO is an appropriate material for phase-matching condition for near-infrared (NIR) wavelengths. It possesses a large effective nonlinear coefficient and high damage threshold, and is nonhygroscopic. Its nonlinear coefficient is 3.5–4 times higher than that of LBO, and 1.5–2 times higher than that of β-BBO [21.25].

Chalcopyrites. The most important of these compounds are $AgGaS_2$, $AgGaSe_2$, and $ZnGeP_2$. These materials exhibit broad transparency far into the infrared, sufficient birefringence to enable phase-matching over a major portion of the transparency range, and relatively high nonlinear coefficients. Laser damage resistance tends to be very low. The greatest limitation to application of the chalcopyrites has been optical loss.

$LiIO_3$. Because of its large birefringence, lithium iodate, $LiIO_3$ is broadly phase-matchable, but suffers from large walk-off effects that limit conversion efficiencies despite its larger nonlinear susceptibility. Applications taking advantage of the broad tuning range are the most common.

21.2 High-Temperature Solution Growth

When compared with growth from the melt, crystal growth from solution produces remarkable improvements in the quality of the grown crystals, principally due to a much lower crystallization temperature. Using lower temperatures during the growth process means a lower density of structural defects and less contamination in the liquid phase from the crucible or the ambient. Furthermore, the low growth rate developed at lower temperatures enables better control of all the parameters involved in a stable growth process. Finally, careful choice of a suitable solvent can help reduce the viscosity of the solution, minimizing problems related to deficient mass transport that can generate solvent inclusions in the crystals. However, crystal growth by high-temperature solution (HTS) presents some disadvantages when compared with crystal growth techniques from the melt. Substitution, or generation of interstitial defects when the solvent contains ions alien to the grown material, and the relatively low crystal growth rates inherent to HTS techniques constitute the main disadvantages of these techniques, especially when scaling up these processes to industrial production.

Nevertheless, there is no doubt that HTS growth methods have a huge field of application and they constitute the basis of several of the current solid-state technologies, mainly in microelectronics and optoelectronic devices. Theoretically, this method presents no limits – it is always possible to find a suitable solvent and the most convenient crystallization conditions to obtain any material. In practice, however, it is not this easy. Despite this, the list of materials that have been obtained by HTS methods is very long, covering materials from diamond or oxide compounds to metals. Hundreds of single-crystalline materials are grown by HTS-based methods, among them the magnetic ferrites developed in the 1970s, the superconductor materials such as $YBa_2Cu_3O_{7-x}$ (YBCO) developed during the 1980s and 1990s, many ferroelectric materials such as KTP, etc. Crystal growth from HTS is also one of the most popular growth methods as it does not require sophisticated equipment. At present, several research laboratories around the world are not only growing new and different crystalline materials, but are also studying and modeling the fundamentals of the transport processes involved in crystal growth using these HTS techniques.

The principle of crystal growth by HTS lies in choosing a suitable solvent S for the components A and B of a given α_{AB} phase, all solids at room temperature, with a lower solubility for the α_{AB} phase at a given temperature than for the initial components.

By heating the reagents it will be possible to induce HTS growth

$$A_S + B_S + S_S \rightarrow A_L + B_L + S_L \rightarrow \alpha_{AB} + S_L \,. \tag{21.1}$$

The driving force for HTS growth is supersaturation of the $\alpha_{AB} + S_L$ solution. This supersaturation can be created by slow cooling of the solution, by evaporation of the solvent or by increasing the solute concentration at constant temperature.

To control spurious nucleation and improve the quality of the grown crystals, modifications to HTS methods have been applied through the years. Methods based on homogeneous nucleation used in the 1960s have been displaced by methods based on induced growth (secondary nucleation), which involve techniques such as rotation and pulling of the growing crystals that enhance mass transport conditions in the solution, avoid supersaturation gradients, and allow growth of larger crystals. Top-seeded solution growth and liquid-phase epitaxy are the most popular methods based on HTS growth technologies. In the next sections the main features of these two methods will be described.

21.2.1 Top-Seeded Solution Growth (TSSG)

To grow a crystal the first step, after having selected a suitable candidate solvent, is the study of the phase diagram of the different compounds that will be mixed to create the growth solution to determine the composition and temperature range in which the desired crystalline phase (solute into the solution) can be grown. As an example the phase diagram of $K(Gd_{0.5}Nd_{0.5})(PO_3)_4$ in the ternary system $(Nd_2O_3+Gd_2O_3)$–K_2O–P_2O_5 is shown in Fig. 21.2a. Parameters such as the existence of other neighboring crystalline phases, the crystallization temperature, the solute-to-solvent ratio, etc. will influence the selection of the most suitable point of the phase diagram at which to perform the crystal growth experiments. The solubility curve of the crystallizing phase in the chosen solvent must then be determined. Figure 21.2b shows the solubility curve of the KREW–$K_2W_2O_7$ system. When the solubility curve has been determined, the crystallization experiment can be performed by choosing the most suitable solute–solvent composition while accounting for the slope of the solubility curve. If the growth experiment is performed in a solution with a solute–solvent composition in region I of Fig. 21.2b, where the solubility curve shows a pronounced slope, a temperature fluctuation ΔT produces a small change in the concentration of solute Δc_1. However, if the experiment is performed in a solution with a composition in region II, where the solubility curve has a flat slope, the same temperature fluctuation ΔT will produce a larger change in the concentration of solute Δc_2 that can lead to fluctuations in the supersaturation levels created in the solution. In order to obtain crystals with a lower density of defects it is important to avoid fluctuations in the supersaturation levels in the growth solution. Thus, region I is the most suitable region to grow crystals in these solutions, as it provides better control of the solutal fluctuations by small changes in the temperature.

The TSSG method represents an improvement of crystal growth from HTS methodologies as it restricts and forces crystal growth only at a point of the free surface of the solution, i. e., on a crystal seed in contact with the surface of the solution that can be rotated and pulled. Figure 21.3a shows the experimental con-

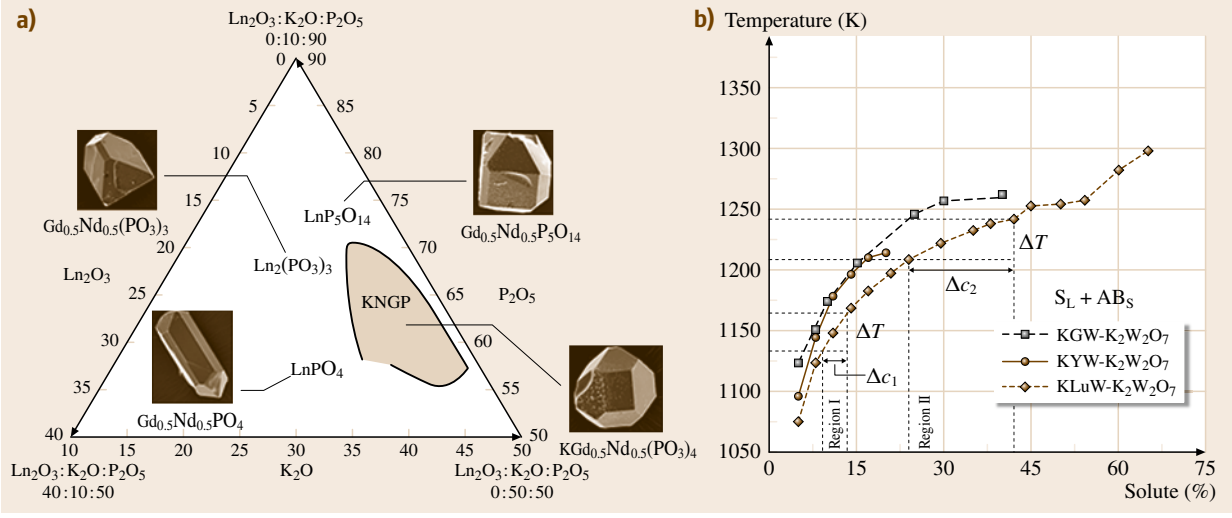


Fig. 21.2 **(a)** Crystallization region of $KGd_{0.5}Nd_{0.5}(PO_3)_4$ with solution isotherms in the Ln_2O_3–K_2O-P_2O_5 system. SEM images of $K(Gd, Nd)(PO_3)_4$ crystals and neighboring phases. **(b)** Solubility curve of KREW (RE = Gd, Y, and Lu) in $K_2W_2O_7$ solvent

figuration of the TSSG method. Before configuring the values of the TSSG parameters it is necessary to know the physicochemical properties of the solution such as density, viscosity, thermal conductivity, and surface tension [21.26]. This knowledge enables numerical and experimental simulation to determine the best solute–solvent composition and to know the hydrodynamics of the solution needed for a successful crystal growth experiment [21.27]. These experimental simulation studies will provide the most suitable values for parameters such as the aspect ratio (diameter/height) of the crucible that will contain the solution, axial and radial thermal gradients in the solution, rotation rate of the crystal seed, extent of the crucible's rotation, ratio between the size of the growing crystal and the crucible radius, etc. Figure 21.3b shows a nonaxisymmetric horizontal flow pattern of the solution obtained by visualization techniques in an experimental simulation of a growth experiment. The best conditions for real growth should avoid nonaxisymmetric flow patterns. Figure 21.3c shows an axial cross section of a growth solution by visualizing the flow established by a crystal/crucible counter-rotation configuration. These experimental simulations have been obtained from liquid simulation under similar thermal and hydrodynamics conditions to

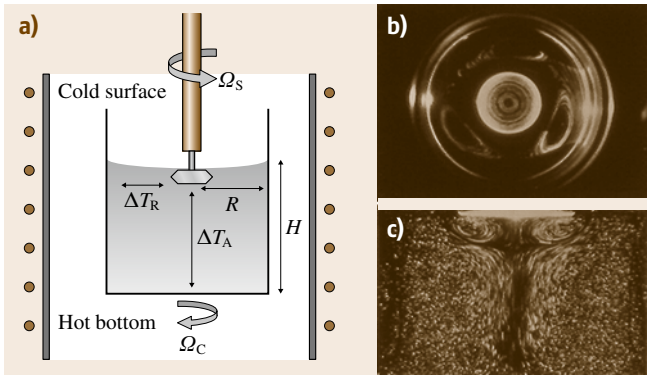


Fig. 21.3a–c TSSG method. **(a)** Scheme of the experimental configuration. **(b)** Nonaxisymmetric horizontal flow pattern obtained by visualization techniques of the solution. **(c)** Axial cross section of a solution of growth, visualizing the flow established by a crystal/crucible counter-rotation configuration

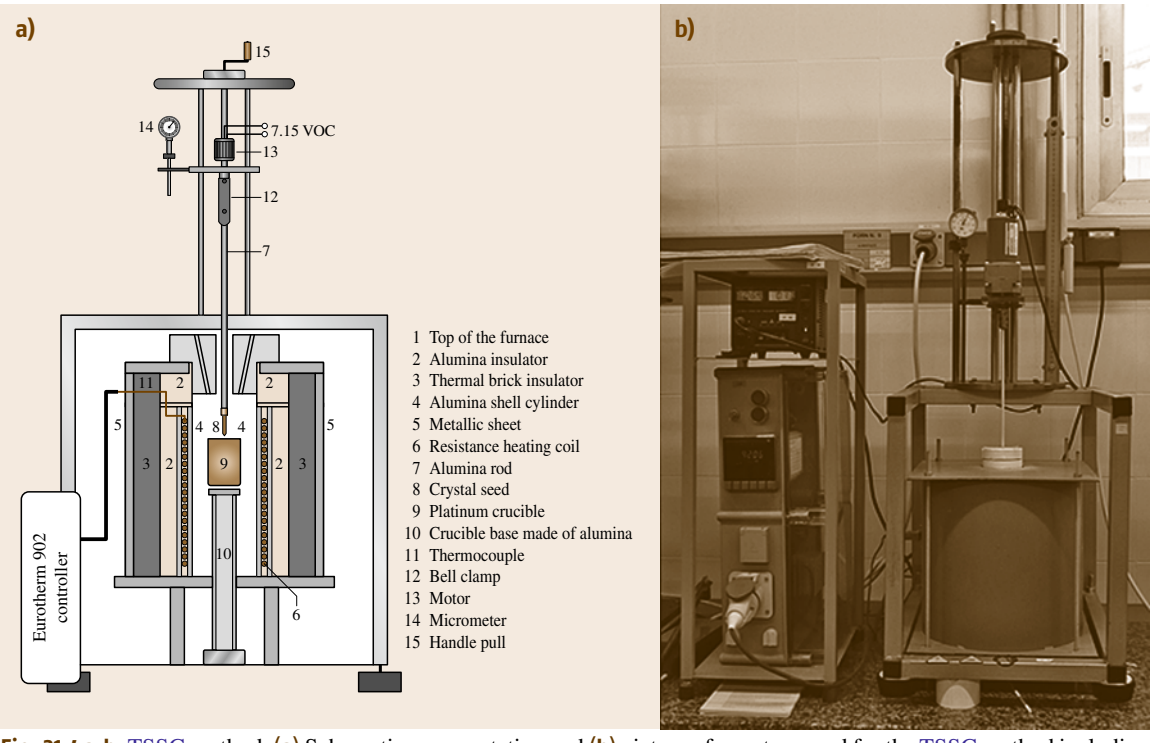


Fig. 21.4a,b TSSG method. **(a)** Schematic representation and **(b)** picture of a system used for the TSSG method including a single-thermal-zone vertical tubular furnace, the crystal seed attach, rotation, and pulling system, the crucible and its support, and temperature controller/programmer

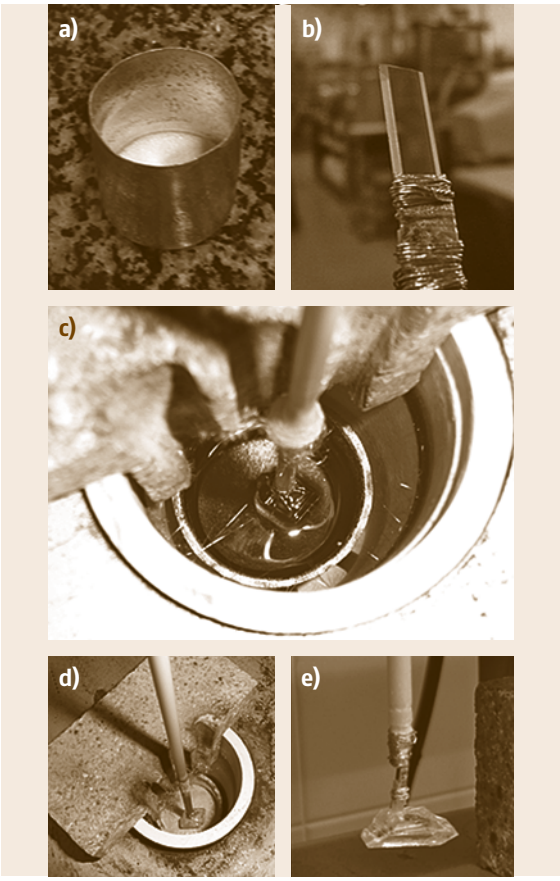


Fig. 21.5a–e Process of growth of a double tungstate single crystal by the TSSG method. **(a)** Platinum crucible containing the flux or solution at room temperature. **(b)** Crystal seed ready to be used for the crystal growth experiment. **(c)** Single crystal growing inside the solution. **(d)** Single crystal after being removed from the solution while cooling the furnace to room temperature. **(e)** Single crystal attached to the crystal seed at the end of the experiment

those of a real growth solution (equal Reynolds and Prandtl numbers). In high-viscosity solutions the use of angular acceleration of the crystal or the crucible, or both, with periodic changes in their direction of rotation, has also been used to improve the homogeneity of the solution. For very-high-viscosity systems a HTS alternative technology such as the accelerated crucible rotation technique (ACRT) must be used [21.28].

Figure 21.4 shows a schematic representation and a picture of the system used for the TSSG method. It includes a single-thermal-zone vertical tubular furnace, the crystal seed attach, rotation, and pulling system, the crucible and its support, and the temperature controller/programmer. The furnace is heated by an electrical resistance, and the thermal insulation and the alumina shell cylinder can also be seen in the cross section of the furnace provided in the schematic representation. The seed attach, rotation, and pulling system consist of a series of high-precision mechanisms attached to two different stepper motors that allow simultaneous rotation and pulling of the crystal seed. Both the speed of rotation and the speed of pulling can be modified according to the voltage provided by the power source. The attach system can be moved up and down to locate the crystal seed precisely in contact with the surface of the solution. This movement can be monitored with a micrometric comparer for better precision. The support of the crucible allows it to be located at the correct height along the axis of the furnace to obtain the desired thermal gradient inside the solution. Finally, the heating or cooling rate and the temperature of the furnace are precisely controlled by the controller/programmer systems, connected to a thyristor.

Figure 21.5 shows a sequence of pictures representing the process of growth of a double tungstate single crystal using the TSSG method. Figure 21.5a shows a platinum crucible containing the flux or solution, which is a solid at room temperature. Figure 21.5b shows a crystal seed attached to an alumina rod and a platinum support ready for the crystal growth experiment. In Fig. 21.5c, the single crystal growing inside the solution while attached to the crystal seed can be seen. Figure 21.5d shows the single crystal after being removed from the solution and standing near the surface of the solution while the furnace is being cooled slowly to room temperature to avoid thermal cracking of the crystal. Finally, Fig. 21.5e shows the single crystal at the end of the crystal growth experiment still attached to the crystal seed.

21.2.2 Liquid-Phase Epitaxy (LPE)

The term epitaxy can be defined as the deposition of a single-crystal layer on a single-crystal substrate such that the crystalline structure of the substrate is continued into the layer. For a given substrate, the lattice parameter mismatch between the layer and the substrate is limited by a critical value, above which continuity of the crystalline construction across the substrate–layer interface is impossible. LPE is the growth of epitaxial layers, hereafter epilayers, from solutions at high temperatures.

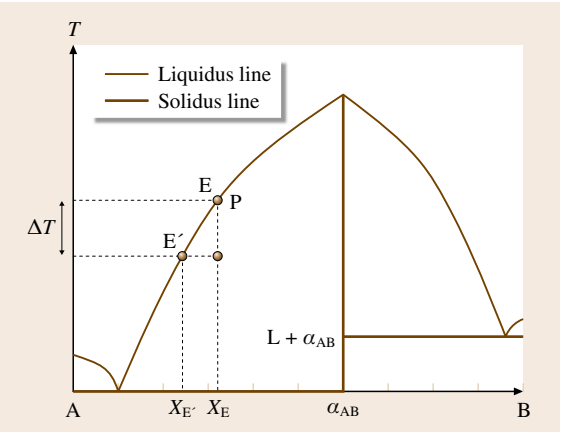


Fig. 21.6 Cooling effect in a binary diagram

The process of LPE growth involves three main steps:

1. Creation of supersaturation
2. Mass transport from solution to solid–liquid interface
3. Nucleation and surface attachment [21.29, 30]

1. *Creation of supersaturation*. Figure 21.6 introduces the fundamentals of LPE as a crystal growth method. A substrate is introduced into a solution, which is cooled by a discrete amount ΔT and the equilibrium liquid-phase composition is shifted from X_E to $X_{E'}$, which has a lower α_{AB} (solute) concentration. The decrease in solubility creates a supersaturated solution and yields deposition of α_{AB} solid phase onto the substrate.
   The supersaturation created in the solution
   $$\sigma = \frac{X_E(T) - X_{E'}(T)}{X_{E'}(T)} \qquad (21.2)$$
   is related to the change of free energy when crystallization occurs $\Delta G \approx RT\sigma$ and to the gradient of chemical potential $\Delta G \approx \Delta\mu$. The chemical potential at point P in Fig. 21.6 of the supersaturated solution is higher than its equilibrium value at the same temperature, point E′ in Fig. 21.6. This constitutes the driving force of LPE growth, and induces heterogeneous nucleation, which exhibits a lower activation energy than homogeneous nucleation because the surface of the substrate catalyzes the crystal growth process.
2. *Mass transport from the solution to the solid–liquid interface*. When the epilayer starts to grow, and because of the limitations of mass transport near the substrate surface, a solutal boundary layer is established, as can be seen in Fig. 21.7.

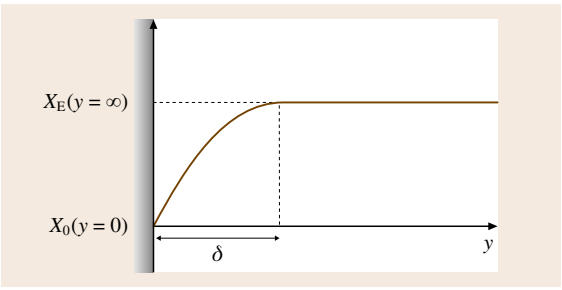


Fig. 21.7 Solutal boundary layer adjacent to substrate surface

   The velocity of mass transport from the solution to the solid–liquid interface in stationary conditions is given by Fick's equation
   $$R = \frac{D_v}{\rho}\frac{X_{E'} - X_0}{\delta} = \frac{1}{\rho}\frac{D_v}{\delta}(X_{E'} - X_0) = \frac{1}{\rho}\frac{1}{\delta/D_v}(X_{E'} - X_0)\,, \qquad (21.3)$$
   where D_v is the volumetric diffusivity of the solute in the solution, ρ is the density, and δ is the thickness of the solutal boundary layer. The quotient δ/D_v is called the diffusional resistivity of mass transport.
   In a situation of natural thermal convection under low Rayleigh number (low thermal gradients) and also in growth experiments with forced convection but with low Reynolds number (low rotational velocity of the substrate), the boundary thickness is given by
   $$\delta \propto D_v^{1/3}\nu^{1/6}\omega^{-1/2}\,, \qquad (21.4)$$
   where ν is the kinematic viscosity and ω is the revolution rate of the substrate.
3. *Heterogeneous nucleation and surface attachment*. The capture of the atoms onto the surface of the

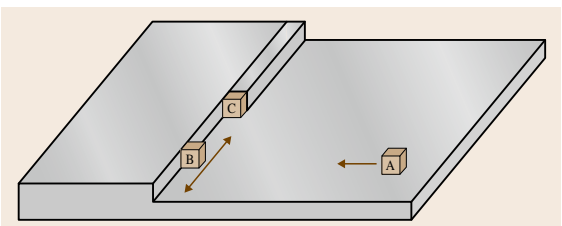


Fig. 21.8 Heterogeneous nucleation and surface attachment process on the substrate surface

substrate takes place in a number of successive steps:

a) The nucleation, or the formation of stable clusters of atoms on the surface of the substrate at sites such as A (Fig. 21.8)
b) The migration of atoms on the surface to the growth step by surface diffusion and their adsorption at sites such as B
c) Migration of the adsorbed atoms in B positions to energetically favorable sites such as C
d) Removing the released heat from the global reaction and transport of the solvent from the lost solute–solvent solvation

The contributions of all surface processes on the kinetics of the crystal growth process can be evaluated by adding a new resistivity $1/\kappa$ to the crystal growth rate formula

$$R = \frac{1}{\rho}\left(\frac{1}{\kappa} + \frac{\delta}{D_v}\right)^{-1}(X_{E'} - X_0)\,. \qquad (21.5)$$

21.3 Growth of Bulk Laser and NLO Single Crystals by the TSSG Method

A favourable viscosity of the growth solution can be defined in the range 1–100 cP, while the maximum practical viscosity that allows development of a crystal growth process would be about 10 P. An ideal solvent was defined by *Elwell* and *Scheel* [21.29] as a solvent with a viscosity in the range 1–10 cP. However, it is not trivial to find compounds that can be used as solvents in high-temperature solutions with such viscosities. In this chapter we define low-viscosity solutions as those with viscosity below 40–50 cP, typical of fluorides, vanadates, and tungstates. Solutions containing phosphates and borates present a much higher viscosity, with values that can reach up to 10 P. Crystal growth using high-temperature solutions with low or high viscosities present different difficulties that we will try to summarize here, together with the strategies proposed to overcome these problems.

21.3.1 Crystal Growth from Low-Viscosity Solutions: Fluorides, Tungstates, and Vanadates

Double Tungstates MREW (M = Na, K, Rb; RE = Y and Lanthanides)

The crystallization temperature of the required phase, the presence of other phases crystallizing at higher temperature, the nature of possible polymorphic phase transformations, and the melting character of the compound are the factors that determine the most suitable growth method to obtain single crystals of a particular $MRE(WO_4)_2$ compound. The Czochralski method is the most used method to obtain double tungstate compounds that melt congruently and do not show polymorphic transformations, such as Na-based double tungstates compounds with RE ions with large

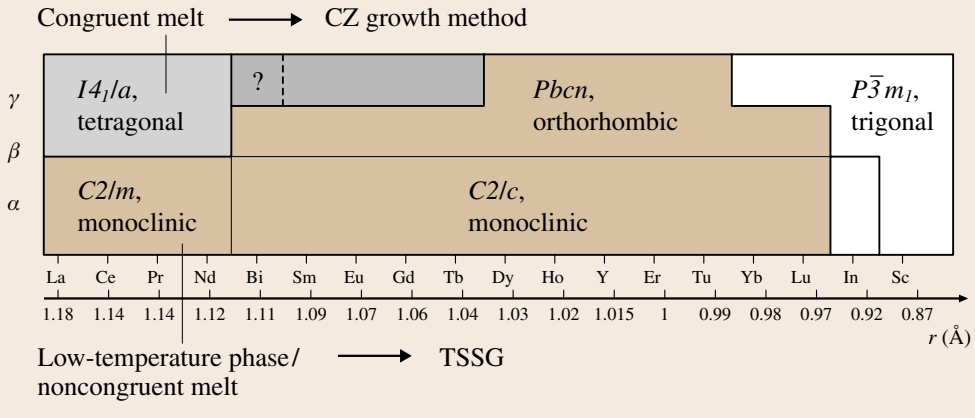


Fig. 21.9 Polymorphism of KREW compounds at room temperature, and recommended methods to grow the different crystal of this family of materials

Table 21.3 Concentration of precursor oxides to form a growth solution of KGdW using $K_2W_2O_7$ as a solvent, with a composition 85 mol % solvent–15 mol % solute

Molar ratio of oxides in the composition of growth: 30.85% K_2O – 2.5% Gd_2O_3 – 66.67% WO_3
Molar ratio of oxides in the solvent: 33.3% K_2O – 66.67% WO_3
Molar ratio of oxides in the solute: 16.6% K_2O – 16.6% Gd_2O_3 – 66.67% WO_3
Solvent: $(K_2O + 2WO_3) \times 0.85$
Solute: $(0.5K_2O + 0.5Gd_2O_3 + 2WO_3) \times 0.15$
Total: $0.925K_2O + 0.075Gd_2O_3 + 2WO_3 = 30.85\%\ K_2O - 2.5\%\ Gd_2O_3 - 66.67\%\ WO_3$

ionic radii, such as $NaGd(WO_4)_2$. However, melting is not congruent when the ionic radius of the lanthanide decreases [21.31]. On the other hand, KREW monoclinic single crystals are usually grown by the TSSG slow-cooling (SC) method, as they present a phase transformation at a lower temperature than the congruent melting temperature. Figure 21.9 summarizes the polymorphism of KREW compounds together with the recommended methods that can be used to grow these crystals.

The appropriate solvent for growing KREW crystals has been chosen among the stable compounds of the K_2O–WO_3 binary system [21.32,33] to avoid introduction of foreign ions in the solution that can contaminate the crystals. The most used solvents are K_2WO_4 and $K_2W_2O_7$. $K_2W_2O_7$ has a lower melting point when compared with the other stable compounds in the K_2O–WO_3 system, and due to a higher tungsten content, it exhibits a low viscosity during the growth process. K_2WO_4 was used as well [21.34], as a solvent for the growth of KREW, but it did not yield good homogenization of the solution and was more prone to evaporation. The solubility curves of the monoclinic KREW (RE = Gd, Y, and Lu) in $K_2W_2O_7$ are shown in Fig. 21.2b.

The limits of the solubility curve are given by the properties of this binary system. At around 45 mol % solute, the phase that crystallizes first when decreasing the temperature does not belong to the monoclinic system [21.35]. The lower limit at around 5 mol % solute is related to the economical profitability of the growth procedure. Although the monoclinic phase of KREW can be grown in the range 5–42 mol % solute, it is better to use a solution with < 15 mol % solute, where small variations of the temperature lead to small changes in supersaturation. The growth temperatures when using these solutions are around 1090–1230 K and guarantee a low economical cost for the growth procedure.

The thermal gradients in the solutions are usually low, in the range of 1.5 and 11.5 K/cm for axial and radial gradients, respectively, with the bottom and the crucible wall as the hottest spots. Growth of double tungstates is very sensitive to thermal gradients [21.36, 37]. Large thermal gradients may crack the growing crystal due to the high anisotropy of the linear thermal expansion coefficients of monoclinic double tungstates. The solution was prepared by melting the mixed oxide precursors, weighed in stoichiometric ratio. Table 21.3 shows the molar ratio of the precursor oxides for the growth of $K_2W_2O_7$/KGdW with composition 85 mol % solvent–15 mol % solute.

The solution was homogenized by keeping it at ≈ 50 K above the saturation temperature for several hours (up to 24 h in some cases). Then, the saturation temperature was determined by observing the growth/dissolution of an oriented prism crystal of KREW acting as a seed in contact with the surface of the solution.

For KGdW the saturation temperature was in the range 1173–1203 K, for KYbW it was in the range 1170–1195 K, and for KLuW it was in the range 1146–1162 K. The fact that to reach the same solubility value we have to increase the temperature in the sequence $T(\text{sol})_{\text{KGdW}} < T(\text{sol})_{\text{KYbW}} < T(\text{sol})_{\text{KLuW}}$, as observed in Fig. 21.2b, is translated to a lower temperature of crystal growth when decreasing the ionic radius of the lanthanide ion $T_{\text{S,KGdW}} > T_{\text{S,KYbW}} > T_{\text{S,KLuW}}$ for a fixed solute-to-solvent ratio.

Growth experiments could be made using the same growth conditions but not the same crystal seed orientation. Crystal seeds were cut with a parallelepipedal shape and oriented along the ***b***-, ***c***-, and $\boldsymbol{a}^*$-directions. The use of ***b***-oriented seeds allows us to apply a slightly faster cooling rate and consequently to obtain a higher growth rate than when using crystal seeds oriented along other orientations [21.7,38], still obtaining defect-free single crystals. Seeding along $[\bar{1}11]$ direction has also been reported [21.39]. The seed was rotated at a broad range of rotation velocities from 4.5 to 90 rpm. Once the saturation temperature was determined, the crystal seed was placed in contact with the surface of the solution and slow cooling was applied to cre-

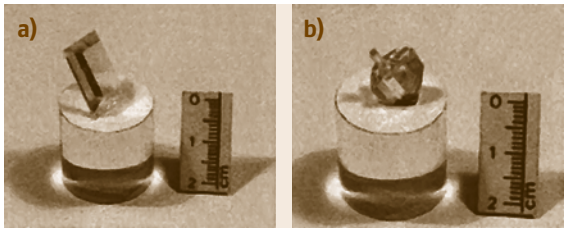


Fig. 21.10a,b Monoclinic undoped $KGd(WO_4)_2$. **(a)** Crystal grown on a ***b***-oriented seed. **(b)** Crystal grown on a ***c***-oriented seed

ate supersaturation. The temperature of the solution was usually decreased for ≈ 10 K at a cooling rate of 0.03–0.05 K/h. After that, the crystals were removed slowly from the solution and cooled to room temperature at 15 K/h to avoid thermal shocks. The results obtained clearly showed that the crystal quality depended strongly on the cooling rate. The slower the applied cooling rate, the better the quality of the crystals.

In the growth of KHoW single crystals, *Borowiec* et al. [21.40] used programmed changes of the cooling rate to grow crystals with larger dimensions.

Pulling at rates of 2–5 mm/day has also been used to grow these crystals [21.40, 41]. In this way, crystals grow as cylinders bounded by {110} and {011} prisms and by {100}, {010}, and {001} pinacoids [21.40].

Figure 21.10 shows some examples of KREW crystals grown by the TSSG method.

As the main application of these crystals is to be used as hosts for other active laser lanthanides ions, it is worth mentioning the effects of lanthanide doping on the growth procedure. First, it is important to highlight the feasibility of growing highly doped lanthanide monoclinic tungstates, up to 100% stoichiometric KREW, with RE as the active ion, such as KErW and KYbW [21.42]. The difference of ionic radii between the RE constituting element of the KREW host and the doping Ln^{3+} cation governs the difficulty of the crystal growth process and the attainable limit of substitution. For example, when growing praseodymium-doped KGdW crystals, it was necessary to reduce the cooling rate to 0.02 K/h to obtain high-quality single crystals. The degree of substitution can be evaluated by the distribution coefficient $K_{Ln^{3+}}$, which provides the ratio between the lanthanide concentration in solution and the lanthanide concentration in the crystal. This measures how easy it is to dope the crystal with a particular ion. The distribution coefficient can be calculated by the following expression

$$K_{Ln^{3+}} = \frac{\{[Ln^{3+}]/([Ln^{3+}]+[RE^{3+}])\}_{crystal}}{\{[Ln^{3+}]/([Ln^{3+}]+[RE^{3+}])\}_{solution}} . \quad (21.6)$$

Distribution coefficients close to 1 favor homogeneity of doping element inside the crystal. Figure 21.11 shows the distribution coefficient for lanthanide doping in KGdW. Figure 21.11a shows the dependence of the distribution coefficient on the ionic radii of the lanthanide doping ion: the larger the ion, the more difficult it is for it to enter the structure. Figure 21.11b shows that, the smaller the ionic radii difference between the rare-earth host and the lanthanide ion, the larger the distribution coefficient.

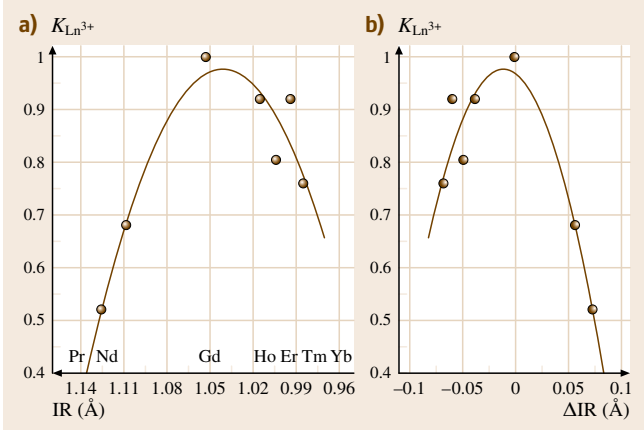


Fig. 21.11a,b Lanthanide doping distribution coefficient in KGdW crystal with RE = Gd, Y, Yb, and Lu. **(a)** Ionic radii (IR). **(b)** Difference between RE host and lanthanide ion

Fluorides

$LiYF_4$ (YLF) has been grown by the TSSG method [21.43] based on the phase diagram of the binary system LiF–YF_3, which presents a peritectic point at 49 mol % YF_3 and 1090 K, and a eutectic point at 19 mol % YF_3 and 970 K. Crystals were grown by pulling in a melt containing YF_3 and a slight excess of LiF over the stoichiometric amount in a purified helium atmosphere.

KYF_4 (KYF) and $KLiYF_5$ (KLYF) have also been grown by the TSSG method [21.44]. Crystals were grown by slow cooling of ***b***-oriented crystal seeds, controlling their dimensions by pulling of the crystal from the solution and using weight control feedback. However, the existence of cleavage planes perpendicular to the ***b***-axis limits growth to some extent.

Other fluorides such as $LiCaAlF_6$ and $LiSrAlF_6$ can also be grown by TSSG using inert or reactive gas atmospheres to avoid traces of H_2O and O_2 that can degrade

their optical quality. Wet chemical methods, ammonium salt methods, or hot hydrofluorination processes have to be used to obtain the high-purity halides to be used in these growth processes, as they are not commercially available [21.45]. The control of the diameter by a weight-sensing feedback system, and pulling of the growing crystal from the solution, have been used to grow these crystals.

Vanadates

$REVO_4$ single crystals are usually grown by the Czochralski method, but these compounds melt congruently at very high temperatures [21.46]. So, the TSSG method has also been reported as a suitable technique to grow these crystals. This technique allows one to avoid the formation of nonpentavalent vanadium oxides. Various fluxes have been used to grow these crystals: $NaVO_3$ [21.47], V_2O_5 [21.48], $Pb_2V_2O_7$ [21.4, 47], $PbO + PbF_2$ [21.49], and $LiVO_3$ [21.5]. However, $PbO + PbF_2$ is not very appropriate because of its toxicity, and $Pb_2V_2O_7$ has a high viscosity and a low solubility for these solutes. Large axial thermal gradients in the growth solution were used to grow crystals with this solvent on ***c***-oriented crystal seeds rotated at 100 rpm [21.50]. $LiVO_3$ has a suitable solubility for YVO_4, low viscosity, low evaporation in the working temperature range, and no toxicity [21.51]. $LiVO_3$ is a very hydroscopic soluble in water, which facilitates crystal and crucible cleaning after the growth procedure. Crystals were grown by slow cooling of the solution. Rotation and pulling of nonoriented YVO_4 seeds have been used.

21.3.2 Crystal Growth from High-Viscosity Solutions: Phosphates and Borates

Crystal growth in highly viscous solutions is very difficult because the high viscosity limits the hydrodynamics and mass transport in the melted solution. It also creates a thick growth boundary layer and makes both heat extraction and impurity expulsion difficult. All these factors interfere with the growth process, resulting in many crystal macrodefects, such as inclusions. This, coupled with the tendency of the melt to supercool, makes this type of growth especially challenging.

Phosphates

KTP was first synthesized in 1890 by Ouvrard, and was crystallized in a polycrystalline form from a flux by *Masse* and *Grenier* [21.52]. KTP melts incongruently at 1172 °C when heated in air [21.24, 53], and therefore it cannot be grown directly from its melt. Various solvents have been used to grow KTP crystals from high-temperature solutions. Table 21.4 summarizes the chemical reactions used to synthesize KTP and its solvents. The crystallization region of KTP in the K_2O–P_2O_5–TiO_2 system was first studied by *Voronkova* and *Yanovskii* [21.54], and later in detail by *Iliev* et al. [21.55]. The solubility of KTP in this system has been shown to increase as the concentration of the anion $(P_2O_7)^{4-}$ increases [21.56–58]. The viscosity of these solutions range from 50 to 80 cP, increasing as the TiO_2 content increases, due to the formation of $[Ti(PO_4)_3]^{5-}$ complexes that polymerize upon addition of TiO_2 [21.55, 59].

KTP single crystals on crystal seeds were first grown from the phosphate system and patented by *Gier* [21.60]. *Alexandrovskii* et al. [21.61] used fused KPO_3 with excess K_2O for the same purpose. *Loiacono* et al. [21.58] reported that crystals of KTP grown in $K_4P_2O_7$ solvent resulted in a platy morphology. The growth process has been developed with slow cooling of the saturated solutions [21.54], and with gradient transport at constant ΔT [21.56]. However, the viscosity of phosphate solutions increases to unacceptable levels when decreasing the temperature. This leads to supersaturation gradients in the solution and results in spurious nucleation and solvent inclusion in the crystals. These inclusions can be a source of strain that cracks the crystals on cooling to room temperature. By imposing motion of the growing crystal, inclusion-free single crystals can be obtained, as this rotation improves the mass transport in the solution [21.62, 63]. Crystals can be rotated about the center of the surface of the solution or eccentrically, although the latter method does not use the crucible space as efficiently as the former one [21.57, 64]. The accelerated crucible rotation technique, by which the accelerating motion of the solution relative to the growing crystal surface prevents the adverse effects of constitutional supercooling, has also been used to improve the mass transport in the solution [21.56]. Strictly controlled cooling rates and a specially designed monitoring of crystal weight changes were employed to crystallize the largest KTP inclusion-free crystal reported [21.64]. Figure 21.12 shows some single crystals of the KTP family obtained by the TSSG method.

Dhanaraj et al. [21.65, 66] realized that using cooling rates that are too fast (1 K/h) in these viscous solutions resulted in coarse dendritic structures on the crystal surfaces and flux inclusion in the bulk of the crystal, due to a rapid increase in supersaturation, es-

Table 21.4 Chemical reaction of formation of KTP and several fluxes used for its growth from TSSG method

Formation of KTP
$KH_2PO_4 + TiO_2 \rightarrow KTiOPO_4 + H_2O$
$K_2CO_3 + 2TiO_2 + P_2O_5 \rightarrow 2KTiOPO_4 + CO_2$
$K_2CO_3 + 2TiO_2 + 2NH_4H_2PO_4 \rightarrow 2KTiOPO_4 + CO_2 + 2NH_3 + 3H_2O$
$K_2TiO(C_2O_4)_2 \cdot 2H_2O + KH_2PO_4 \rightarrow KTiOPO_4 + H_2C_2O_4 + K_2C_2O_4 + 2H_2O$
Formation of phosphate solvents
$3K_2CO_3 + 3P_2O_5 \rightarrow 2K_3P_3O_9 + 3CO_2$
$2K_2HPO_4 \rightarrow K_4P_2O_7 + H_2O$
$2K_2CO_3 + P_2O_5 \rightarrow K_4P_2O_7 + 2CO_2$
$KH_2PO_4 + 2K_2HPO_4 \rightarrow K_5P_3O_{10} + 2H_2O$
$3K_4P_2O_7 + K_3P_3O_9 \rightarrow 3K_5P_3O_{10}$
$2K_2HPO_4 + 2KH_2PO_4 \rightarrow K_6P_4O_{13} + 3H_2O$
$2KH_2PO_4 + 2K_2HPO_4 \rightarrow K_6P_4O_{13}$ (or $2KPO_3 \cdot K_4P_2O_7$)$+3H_2O$
$4KH_2PO_4 + K_2CO_3 \rightarrow K_6P_4O_{13} + 4H_2O + CO_2$
$3K_4P_2O_7 + 2K_3P_3O_9 \rightarrow 3K_6P_4O_{13}$
$4KH_2PO_4 + 2K_2HPO_4 \rightarrow K_8P_6O_{19} + 5H_2O$
$11KH_2PO_4 + 2K_2HPO_4 \rightarrow K_{15}P_{13}O_{40} + 12H_2O$
Formation of tungstate solvents
$6K_2HPO_4 + 6WO_3 \rightarrow 6K_2WO_4 + 3P_2O_5 + 3H_2O$
Formation of other solvent
$NaF + KH_2PO_4 \rightarrow KNaPO_3F + H_2O$
$5KH_2PO_4 + 2BaCO_3 \rightarrow KBa_2(PO_3)_5 \cdot 2K_2O + 2CO_2 + 5H_2O$

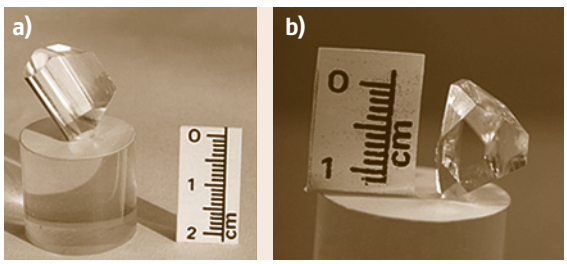


Fig. 21.12a,b Single crystal of **(a)** $KTiOPO_4$ and **(b)** $RbTiOPO_4$ obtained by the TSSG method in phosphate and tungstate fluxes

pecially during the final stages of growth. When growth is performed on ***c***- and ***b***-oriented seeds, since the {001} and {010} faces are fast-growing faces which do not occur on KTP naturally, a capping process takes place at the initial stages of growth, until the {201} and {011} faces, or the {110} and {011} faces, have appeared, respectively [21.67]. Crystals grown on [100]-oriented seeds showed inclusions parallel to {011} faces, although this seeding may yield large single-sector KTP crystals [21.68]. [201]-Oriented seeding produced a tilt of the growing crystal to respect the rotation axis that improves the hydrodynamics of the solution, helping in melt mixing and allowing optimal utilization of the available melt volume by placing the long ***c***-direction of the crystal along the body diagonal of the crucible [21.69]. KTP crystals have also been grown from phosphate fluxes by the TSSG method with pulling [21.67,70] to avoid their multifaceted shape that leads to inefficient cutting of optical elements from KTP crystals [21.67]. As crystal growth proceeds on natural faces, they show relatively low dislocation densities, allowing one to obtain single crystals without inclusions or growth striations [21.70].

Carvajal et al. [21.71] developed a crystal growth system comprising a Pt stirrer immersed in the growth solution and two crystal seeds in contact with the solution surface, symmetrically distributed at about 1.5 cm from the rotation axis and 2 cm up the platinum turbine, as can be seen in Fig. 21.13. This system improved the mass transport conditions in the solution, thus minimizing problems associated with nonhomogeneous supersaturation in these viscous solutions. Stirring the solution decreases the frequency of spontaneous nucle-

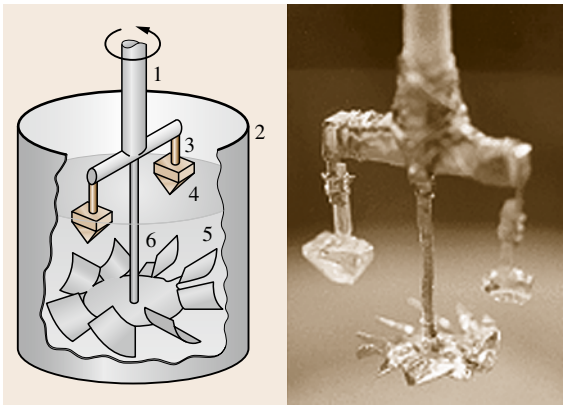


Fig. 21.13 Schematic and picture of the crystal growth system used in TSSG experiments to grow $RbTiOPO_4$ crystal and isostructurals that included a Pt turbine rotating together with the crystal seeds: (1) alumina rod, (2) platinum crucible, (3) crystal seeds, (4) growing crystals, (5) solution, and (6) platinum turbine

ation during the growth process and yields a higher quantity of high-quality inclusion-free single crystals of the KTP family.

Other KTP isostructurals, such as $RbTiOPO_4$ (RTP), which shows almost the same NLO properties of KTP, have been grown from these phosphate solutions. *Oseledchik* et al. [21.72] determined the crystallization region of RTP in the phosphate system and obtained crystals containing some inclusions, indicating the presence of unstable temperature control, high cooling rates, unsatisfactory temperature profile, and unsatisfactory dynamics of the melt flowing around the crystal.

An alternative to the improvement of the mass transport is the reduction of the viscosity of the solution by adding a modifier. *Ballman* et al. [21.73] proposed the low-viscosity, very fluid, non-glass-forming, water-soluble tungstate melts as a solvent, which greatly improves circulation and mixing during the crystallization process and results in a higher yield of inclusion-free material. *Iliev* et al. determined the phase diagram of KTP in the K_2O–P_2O_5–TiO_2–WO_3 system, as well as the viscosity of these solutions [21.74]. An increase in concentration of WO_3 results in a decrease of the solubility of KTP; however, the shallower slope of the solubility curves indicates a low degree of supersaturation for a given temperature drop and allows for a more controllable growth process. The addition of lithium to these solutions further enhances the fluidity of the melt and helps in the crystal growth process [21.69]. However, the use of tungstate fluxes leads to incorporation of tungsten ions in KTP crystals and reduces their optical transparency [21.75]. Striations and growth sectors were observed for all the existing faces on the crystals, which was attributed to changes in tungsten concentration in the crystal caused by variations in growth rates, temperature fluctuations in the furnace, or convective motion of the solution in the crucible [21.75, 76]. *Carvajal* et al. [21.71] determined the variation of the crystallization region of RTP when introducing WO_3 in the solution. The crystallization regions became narrower, and were displaced towards Rb_2O-rich regions when the concentration of WO_3 increased, as can be seen in Fig. 21.14. In these solutions the time of homogenization was shorter, the interval cooling of temperatures could be wider, and the cooling process to obtain high-quality crystals could be made faster than in phosphate fluxes.

Marnier proposed the use of alkaline halide (KF, KCl, and KBr) fluxes as an alternative to tungstate fluxes [21.77]. Alkaline halides also reduce the viscosity of the solution and enable a satisfactory growth rate at low temperature while enhancing the solubility of KTP and isostructurals. Sulfate-containing fluxes also reduce the viscosity of the solution due to the presence of SO_4^{2-} ions in the flux that breaks the titanate chains of the flux. However, a certain amount of incorporation of sulfur into the crystals takes place [21.67]. More recently, *Suma* et al. [21.78, 79] carried out rapid growth of KTP single crystals by using $KBa_2(PO_3)\cdot 2K_2O$ and $KNaPO_3F$ as fluxes. The steepness of the solubility

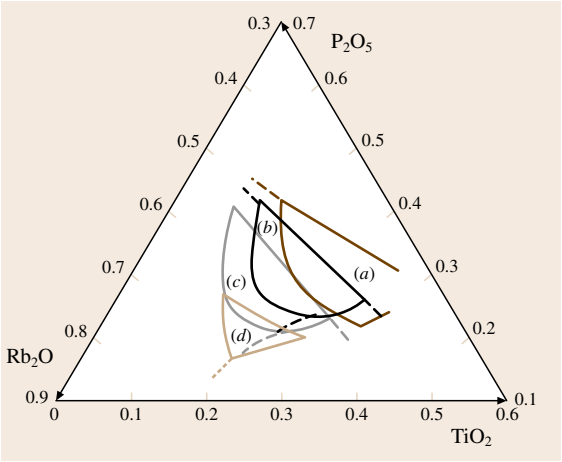


Fig. 21.14 Crystallization region of $RbTiOPO_4$ in the system Rb_2O–P_2O_5–TiO_2–WO_3 for *(a)* 0 mol % WO_3 *(b)* 10 mol % WO_3 *(c)* 20 mol % WO_3, and *(d)* 30 mol % WO_3 in solution

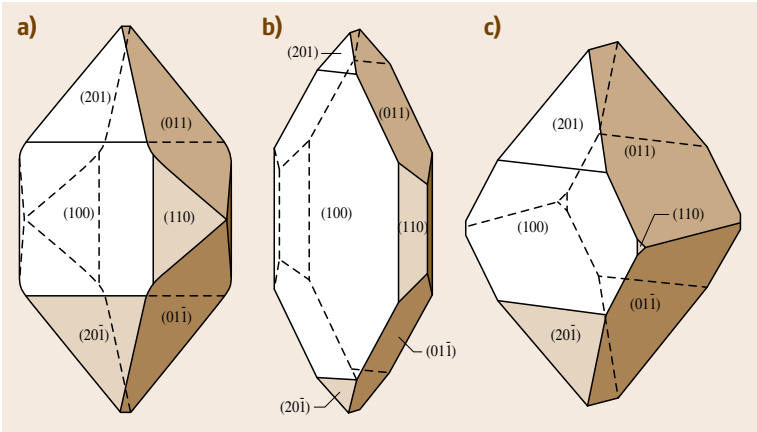


Fig. 21.15a–c Morphology of **(a)** RTP crystal, **(b)** RTP crystal doped with Nb grown on a thin crystal seed in the ***a***-direction, and **(c)** RTP crystal doped with Nb grown on a thin crystal seed in the ***a***-direction. The morphology of these crystals improved, where the {110} form tends to disappear, and the {011} and the {01$\bar{1}$} forms become larger, which provide a larger useful area of crystal in the *a*–*b* plane with benefits for applications in SHG

curve of KTP in these systems enables rapid cooling of the solution and fast growth of KTP.

In the last decade, much effort has been devoted to doping of KTP and isostructurals with various ions to change some of their physical properties, such as the crystal's optical transmission [21.80, 81], Curie temperature [21.82], ionic conductivity [21.83, 84], refractive indexes [21.85], and NLO properties [21.86, 87]. For this purpose, Nb is one of the most used ions with which KTP and isostructural crystals have been doped. However, this ion increases the difficulty of crystal growth: the growth solution is more viscous, the homogenization time increases, the saturation temperature increases, the solution is more prone to spurious nucleation, the efficiency of the crystal growth process decreases, crystals tend to crack, and they show more solution inclusions. Furthermore, these tendencies increase with increasing Nb concentration in the crystal. The crystal morphology is flat, long, and narrow, and especially small in size in the ***a***-axis direction, suggesting that crystals may grow by a two-dimensional nucleation mechanism. When crystals were grown on ***a***-oriented seeds, they showed poor transparency with many inclusions and twin-crystal flaws along the (100)-plane. In spite of this, this seeding orientation has a good effect on controlling spurious nucleation. When crystals were grown on ***c***-oriented crystal seeds, they had a larger transparent area and fewer inclusions with no twin-crystal flaws. If the crystal seed was rotated, reversing the rotation direction periodically during the growth process, crystals showed even larger transparent areas. Using crystal seeds with the same composition as the crystal to be grown further reduced the number of cracks observed in the crystals [21.88]. By forcing crystal growth in the ***a***-direction using crystal seeds with a larger dimension in this direction than in any other crystallographic direction, crystals with typical dimensions of $5 \times 5 \times 5\,\mathrm{mm}^3$ in the three crystallographic directions could be obtained [21.87]. Figure 21.15 summarizes these changes in morphology caused by Nb in RTP crystals.

$KNd(PO_3)_4$ (KNP) and $KGd(PO_3)_4$ (KGdP) single crystals have been grown by the TSSG technique [21.89, 90]. The crystallization regions of KNP, KGdP, and the intermediate $KGd_{0.5}Nd_{0.5}(PO_3)_4$ compound in the system Ln_2O_3–K_2O–P_2O_5 (where Ln = Nd or Gd) have been studied [21.89–91]. Figure 21.2a shows a comparison of these crystallization regions. Although the viscosity of the solution is very high throughout the crystallization region, when the Ln_2O_3/K_2O molar ratio (Ln = Nd or Gd) is above $\frac{3}{97}$, it is so high that it hinders crystallization.

TSSG experiments were carried out with axial temperature gradients in the solution of 0.75–0.92 K/mm for KNP, and 1.2 K/mm for KGdP. Crystals were grown with constant rotation at 75 rpm using KNP or KGdP parallelepipedal oriented seeds located at the center of the solution surface, by slow cooling at 0.1 K/h for an interval of 15–20 K. To improve the mass transport in the solution, a platinum turbine similar to that described for KTP and isostructural crystals was used, resulting in better quality crystals. Seeding along the $\boldsymbol{a}^*$-direction in the crystallographic reciprocal space and the $\boldsymbol{c}^*$-crystallographic direction in the reciprocal space was suitable for growing KNP and KGdP single crystals. Seeding along the ***b***-direction in the direct space was unsuitable because crystals tended to crack perpendicularly to this direction when they were too heavy. When solutions contained 65 mol % P_2O_5 or higher, small crystals with poor quality were obtained,

due to the high viscosity of the solution. KGdP:Nd crystals showed some inclusions, especially when the Nd content increased, which could be avoided when the cooling rate was decreased to 0.05 K/h.

Borates

LBO has been known since 1926; in 1958 the Li_2O–B_2O_5 phase diagram was studied [21.93], and in 1978 small LBO single crystals were grown. LBO is a peritectic compound that cannot be grown by congruent melting and solidification. It can be synthesized by the peritectic reaction, a process that is too slow and difficult to carry to completion. Thus, the sole method of obtaining LBO single crystals is the flux growth method [21.94]. However, fluxed melt systems for growing LBO make controlling the temperature gradients difficult, as the main heat transport occurs by means of radiation energy. This leads to the appearance of growth defects, such as inclusions, inhomogeneous distribution of uncontrolled impurities, and nonstoichiometry of composition [21.95].

LBO crystals have been grown in different solution compositions of the Li_2O–B_2O_3 system. Solutions containing B_2O_3 are, in general, too viscous. In this system, the most suitable region of LBO concentrations to grow LBO crystals is 72–82 wt % LBO as the viscosity has a relatively low value and changes slightly with concentration. If the concentration is lower than 72 wt %, the mass transport is rather difficult because of the high viscosity. At concentrations higher than 82 wt %, the initial values of the supersaturation are high and drive the crystallization process too fast and hard for operating [21.96]. Additionally, the steep temperature versus composition slope places tight constraints on the seeding temperature: too high a temperature resulted in melting the seed, whereas too low a temperature resulted in polycrystal forming. The melt also showed a strong tendency to supercool. Furthermore, as LBO is sensitive to thermal shocking it has to be cooled after growth at very low cooling rates (≈ 3 K/h) [21.97]. Use of small thermal gradients in the furnace favors the growth of good-quality crystals [21.94]. Properly thermally insulating the upper part of the growth chamber, reducing temperature gradients above the melt during growth, and lowering the melt from the crystal when growth was terminated instead of lifting the crystal away from the melt helped to reduce cracking in the crystals. This leaves the crystal in the heated position of the chamber, allowing better control of cooling and resulting in smaller thermal gradients in the crystal. However, growth in solution with insufficiently high thermal gradients resulted in the appearance of large inclusions of fluxed melt and oxygen nonstoichiometry in the crystals. This is due to the presence of concentrations of inhomogeneities in the fluxed melt, which cannot be readily removed via the usual diffusion process during the period of their movement across the surface of the growing crystal because of the high viscosity of the fluxed melt. As the axial and radial thermal gradients increase near the crystallization front, the fluxed melts become more homogeneous and the quality of LBO crystals improves.

The surfaces of LBO crystals gradually decompose due to moisture present in the ambient atmosphere, forming a millimeter-thick, optically opaque, white, polycrystalline skin, replicating the original surface of the growing crystal. Upon cooling, severe cracking occurs on the crystal surfaces adjacent to this layer. The formation of this layer, and the subsequent cracking, can be avoided by growing crystals under dry nitrogen atmospheres [21.98].

Increasing rotation rates and the use of accelerated crucible rotation yields larger crystals due to the enhancement of forced convection. Seeding in the direction normal to widely developed faces is thought to enlarge the diameter of the crystal, as happens in LBO when using a seed normal to the (011) face compared with seeding in the [001] direction, while the thickness and the quality of crystal were almost the same, keeping the remaining growth conditions constant. In general, the forced convection in the solution caused by rotation is affected by the ratio of the crystal to crucible diameters. As the diameter of the growing crystal increases, the forced convection in the solution increases, which increases the crystal yield by increasing the mixing and the mass transfer in the solution. Figure 21.16 shows this effect in two LBO single crys-

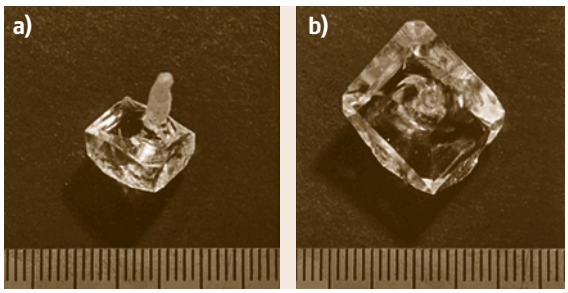


Fig. 21.16a,b LBO crystals grown by seeding in different directions while maintaining the rest of the conditions of growth [21.92]: **(a)** seeding along [001] and **(b)** seeding along [011]. Each scale is 1 mm

tals grown under the same conditions except for the seeding direction.

As the viscosity of the LBO–B_2O_3 system cannot be decreased by increasing the growth temperature because of the low decomposition temperature of LBO, it is very important to find new solvents which can reduce the viscosity while having sufficient solubility for LBO. B_2O_3 solutions form three-dimensional networks, mainly consisting of randomly oriented boroxol rings interconnected by B–O–B bridges, the structure of which may be altered by the addition of alkali oxides, reducing the viscosity of the solutions as a function of the O-to-B ratio. However, the phase region for the growth of LBO crystals is located near the maximum of the temperature-dependent viscosity curve, so the addition of small amounts of alkali oxides has little effect on the overall viscosity of the solution [21.99]. The addition of halide ions such as Cl^- and F^- can weaken the network in alkali borate melts. Cl^- anions do not take part in the boron–oxygen network, but lie in the space between the network as free ions. Therefore, the large size of the Cl^- anions and the electrical repulsion between the Cl^- ions and the $[BO_4]^{5-}$ ions is effective in reducing the viscosity of the melt. F^- ions terminate the network by forming B–F nonbridging bonds, thereby reducing the viscosity of the solution. In the $Li_2B_4O_7$–B_2O_3–NaCl system, the viscosity of the solution and the seeding temperature were found to decrease as the amount of NaCl in the solution increased, while the metastable zone for crystallization of LBO became wider. This made it possible to increase the growth rate by up to 2–3 times for solutions containing 4 mol % NaCl with no obvious effect on crystal quality. The addition of MoO_3 also reduced the viscosity of the system. However, phases of enriched MoO_3, which can be incorporated into the growing crystal, appear [21.100].

Although BBO melts congruently at 1369 K, the structural reordering that occurs during the phase transition at 1198 K causes cracking of grown crystals during cooling. Of all the growth techniques used to grow β-BBO, only in the TSSG method can large-sized crystals of β-BBO be grown [21.101–105]. However, even when using this technique, the real success in growing β-BBO came with the discovery of a suitable solvent for this material [21.106]. Up to now, B_2O_3, BaF_2, $BaCl_2$, Li_2O, Na_2O and $Na_2B_4O_7$ [21.107], NaF [21.101], NaCl [21.108], Na_2O–NaF [21.109], Na_2O–BO_3 [21.110], $Na_2B_2O_4$ [21.101], Na_2SO_4, and CaF_2 [21.111] have been used as fluxes to grow β-BBO crystals. Using B_2O_3, Li_2O, $Na_2B_2O_4$, and $Na_2B_4O_7$ as fluxes limits the growth of β-BBO crystals due to the high viscosity of the solutions or narrow crystallizing range. Growth of β-BBO using NaCl, Na_2SO_4, $BaCl_2$, BaF_2, and CaF_2 as fluxes is difficult because of the high volatility of the solutions, and in some cases, because of the high-temperature hydrolysis that releases HCl vapor during growth. Na_2O is the flux which produced the best results, in terms of crystal size and defect density, when using the TSSG method with pulling to grow β-BBO crystals [21.104].

In the BBO–Na_2O pseudobinary diagram [21.101], there is a large temperature range from 1198 to 1028 K to grow β-BBO crystals. Normally, after cooling the melts for 70–85 K, an onset of growth interface instability was observed, which could be readily detected since, before its occurrence, melt flow patterns could be clearly seen through the growing crystals, whereas after it happened, the melt convection was obscured. Above a certain diameter of the growing crystal, the free convection flow in the solution around the crystal in the direction from the crystal edge to its center is opposed by a counterflow of forced convection due to the rotation of the crystal. The interaction between these two flows below the crystal leads to a temperature instability, and hence to disturbance of the growth stability [21.110]. Moderate and steeper radial and axial temperature gradients have been used to grow β-BBO crystals with this solvent. A suitable value for the vertical thermal gradient has been estimated to be ≈ 20 K/cm. Nevertheless, large single crystal with optical quality could be grown 3–4 times faster in high thermal gradient furnaces, as it was possible to cool farther before encountering interface instabilities.

Pulling at a rate commensurate with the growth rate has also been applied to the growth of these crystals, which allows the growth of thicker crystals at higher growth rates in smaller crucibles, which prevents seed failure that occurs when crystals touch the crucible wall. However, during pulling, if a steep thermal gradient is used, the quality of the crystals grown will be poor, but if a moderate thermal gradient is used, it is difficult to control the diameter of the crystal. However, if the pulling method is not used, the crystals assumed a shallow lens shape typical of BBO crystals.

Normally, during the growth period, the seed was rotated. However, large rotation rates make the forced convection gradually overcome natural convection, eventually reversing the direction of radial fluid flow along the growth interface, resulting in lower supersaturation at the center of the growth interface and a change in the interface shape from convex to concave. As the highest-quality crystals are usually grown with a flat

or slightly convex interface, rotation rates have to be limited to avoid concave interfaces.

A major limitation of using ***c***-axis oriented crystal seeds was the tendency toward interface breakdown after 15 mm of growth, and that crystals tended to show a higher defect density in the core region, corresponding to the center of the star-shaped convective flow pattern, where there is stagnation and little mixing due to crystal rotation. Boule cross sections were more elliptical, and faceting on the top surface of the boule was less pronounced, when using ***a***- and ***b***-oriented crystal seeds, growing in a nearly cylindrical shape when pulled. However, crystals tended to fracture along the (0001) cleavage planes during cooling due to anisotropy in the thermal expansion.

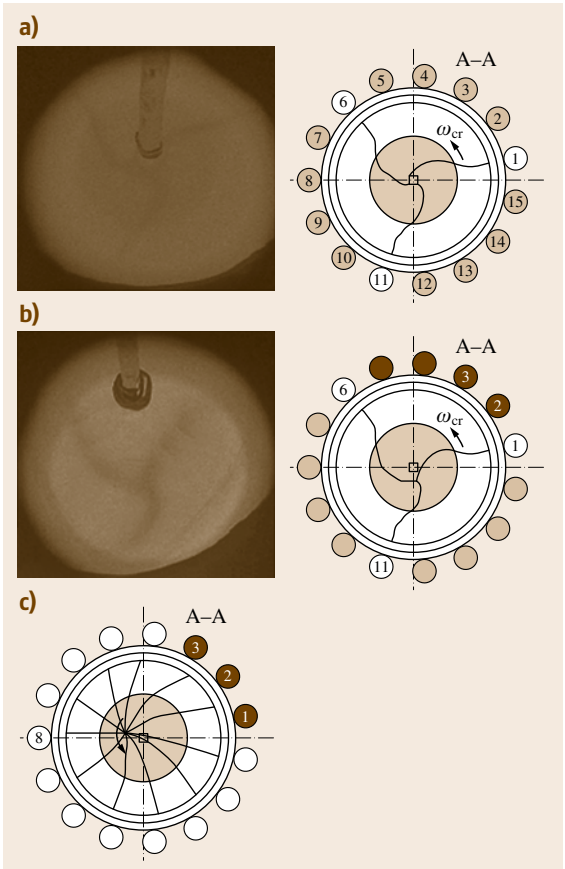


Fig. 21.17a–c Schematic of the setup for growing BBO crystal with the change of the symmetry and rotation of the thermal field and convective patterns observed on the free surface and through a growing BBO crystal [21.112]: (1–15) heating elements (*dark color* indicates switched-on elements, and *white color* indicates switches-off elements), **(a)** and **(b)** creation of thermal fields with a threefold and a quasi-threefold symmetry; **(c)** rotating thermal fields

Inclusions are generally linked to unstable growth conditions, and a standard method of improving the growth stability is by mechanical stirring of the solution. However, none of the conventional stirring techniques, including convective stirring, uniform crucible rotation, accelerated crucible rotation, and uniform boule rotations have produced any substantial change in the quality of β-BBO crystals. The change of the symmetry and the rotation of the thermal field that create inhomogeneous stationary and cyclically varying external thermal fields to control the convective heat and mass transfer, and the application of a vibrational temperature mode in the growth zone, has been proved to be very successful in the growth of β-BBO crystals. An appropriate commutation of the heating elements around the crucible creates a rotating thermal field that considerably intensifies the stirring both in the flux bulk and in the vicinity of the crystallization front, as can be seen in Fig. 21.17. Thus, the thickness of the diffuse layer at the crystallization front decreases and the concentration supercooling is delayed, making it possible to grow large β-BBO single crystals with circular cross section and high structural quality [21.112].

Another method used to improve the quality of the β-BBO crystals grown in BBO–Na_2O solution is continuous feeding during growth by adding pure BBO. This provides the possibility of isothermal growth at a suitable temperature. Gradual depletion of the solution during growth was constantly compensated by manual addition of pure BBO through an alumina tube that transferred the feed material to a small platinum crucible partially immersed in the melt whose bottom was punched, allowing for slow dissolution of the feed [21.103]. The main drawback of using this solvent is that β-BBO crystals contained up to 200 ppm of Na, which affects the optical transmission of the crystals, especially in the UV region [21.113].

Adding Nd_2O_3 to the BBO–Na_2O system with the aim of obtaining a new self-frequency-doubling material resulted in a strong stabilization effect of the β-BBO phase (Fig. 21.18). However, as the Nd_2O_3 concentration and the saturation temperature in the system become higher, the creeping of the solution along the crucible wall was stronger, which meant that relatively good β-BBO single crystals, doped with up to 2 mol % of Nd^{3+}, were only obtained from solutions with low Nd_2O_3 concentration (12 mol %) [21.114].

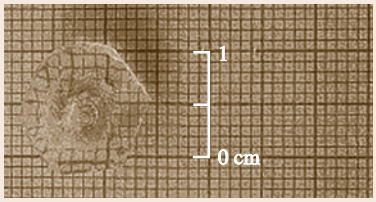


Fig. 21.18 Crystal of β-BaB_2O_4 growth in a solution of BBO–Na_2O

Roth and *Perlov* [21.104] determined the BBO–NaF pseudobinary diagram. Compared with the BBO–Na_2O system, in the BBO–NaF system the slope of the liquid curve is smoother and the maximal range of the BBO composition change wider, which allows higher yields of β-BBO crystals. The BBO–NaF pseudobinary phase diagram has a single eutectic point at a composition of 61 mol % NaF and a temperature of 1027 K. The solution viscosities are lower by about 15% on average over the entire temperature range of interest when compared with BBO–Na_2O solutions. Although the volatility of BBO–NaF solutions is almost an order of magnitude higher than that of BBO–Na_2O, the average escape of 6 mg of solution per hour (mainly NaF) does not affect the crystal growth process considerably and can be corrected by adjusting the cooling rate during the growth process. A breakdown of the solid–liquid interface into a cellular structure also occurs at a certain stage of growth. However, the crystal yield before breakdown is larger than in the case of Na_2O-containing solutions. Crystals grown from NaF solutions had smaller diameters and larger thickness than those grown from Na_2O solution, which could be attributed to the low viscosity of the solution, which would make natural convection dominant over forced convection, and which resulted in vertical growth dominating radial growth [21.115]. Adding Na_2O to the BBO–NaF system reduces the volatility of the solutions to less than 1% during the entire growth process [21.107].

21.4 Liquid-Phase Epitaxy: Growth of Epitaxial Films of Laser and NLO Materials

The thin-disk laser approach was introduced by *Giesen* et al. in 1994 [21.116] to ameliorate the quality of the beam and the thermal loading using efficient longitudinal cooling; moreover the thermal lensing effect is also minimized, especially in the high-power regime [21.117]. The thickness of the active layer minimizes reabsorption phenomena in quasi-three-level systems such as ytterbium or 2 µm thulium emissions. Some examples of thin-disk lasers have been realized [21.118, 119], including those which employ monoclinic KREW active layers [21.120, 121]. KREW materials are good hosts for thin-disk lasers due to the high absorption and emission cross sections of lanthanide-doped KREW. This has propelled, in recent years, the growth of single-crystalline thin films of these materials by LPE techniques.

Growth of thin films of NLO materials, specifically phosphate materials of the structural field of $KTiOPO_4$ (KTP), attracts attention as a means to fabricate optical waveguides. The confinement of light in a micrometer-sized waveguide and its propagation without appreciable diffraction greatly increases the optical fields, and the efficiencies of NLO processes [21.122]. Waveguides of KTP and related materials could be used to control or convert high-intensity optical beams with input wavelengths extending from the visible to the infrared (IR) with thermal and mechanical stability [21.123].

21.4.1 Epitaxial Films of Laser Materials: Lanthanide-Doped KLuW on KLuW Substrates

For the thin-disk approach, as well as for waveguide lasers, homoepitaxial growth of lanthanide-doped KREW (RE = Y, Gd, Lu) by LPE has been recently reported for Yb:KYW films grown on KYW substrates [21.124, 125] and for Yb:KLuW films grown on KLuW substrates [21.126].

Successful growth of these epitaxial layers was demonstrated in a special vertical furnace with a wide zone of uniform temperature to achieve a zero temperature gradient in the solution. The most common solvent for this epitaxial growth is $K_2W_2O_7$ in a solution with a 5 mol % solute and 85 mol % solvent composition. Taking into account the solubility curves of KREW in $K_2W_2O_7$ (Fig. 21.2b), the average degree of supersaturation at 5 mol % solute is 0.16×10^{-2} g/K (g of solution). This low level of supersaturation allows the growth to occur near equilibrium. Also Yb:KYW

Table 21.5 Mismatch for Ln^{3+}:KLuW/KLuW (Ln = Yb and Tm) on different faces

Epitaxial layer	$f(010)$	$f(110)$	$f(310)$	$f(\bar{1}11)$
$KLu_{0.88}Yb_{0.12}W$/KLuW	−0.074	−0.081	−0.085	−0.089
$KLu_{0.78}Yb_{0.22}W$/KLuW	−0.107	−0130	−0.142	−0.135
$KLu_{0.48}Yb_{0.52}W$/KLuW	−0.143	−0.220	−0.259	−0.211
KYbW/KLuW	−0.215	−0.354	−0.425	−0.324
$KLu_{0.97}Tm_{0.03}W$/KLuW*	−0.069	−0.064	−0.062	−0.073
$KLu_{0.95}Tm_{0.05}W$/KLuW*	−0.086	−0.087	−0.087	−0.090
$KLu_{0.925}Tm_{0.075}W$/KLuW*	−0.085	−0.099	−0.106	−0.103
$KLu_{0.90}Tm_{0.10}W$/KLuW*	−0.116	−0.136	−0.147	−0.140
$KLu_{0.80}Tm_{0.20}W$/KLuW*	−0.198	−0.261	−0.293	−0.248

* The epitaxial layer stoichiometry is expressed by the initial solution composition (not corrected by distribution coefficient)

thin films on KYW substrates have been grown using a NaCl–KCl–CsCl solvent. Although this leads to precipitation of yttrium and tungsten oxides on the bottom of the crucible, this problem can be solved by following the methodology of *Kawaguchi* et al. [21.126] using LPE from a solid–liquid coexisting solution.

The step of homogenization of the flux is to increase the temperature 50 K above the expected saturation temperature for 24 h.

Before being placed in the furnace, the substrates must be carefully cleaned in $HNO_3 : H_2O$ (1 : 1 in volume), distilled water, acetone, and ethanol in 5 min steps each. They are then slowly introduced into the furnace to prevent thermal stress and kept at a constant temperature for about 1 h above the surface of the solution. The temperature of the solution is then reduced to 1 K above the saturation temperature and the substrate is introduced into the solution and kept at this temperature for 5 min, so that the outer layer of the substrate dissolves, without introducing defects into the subsequent epitaxial growth.

The growth of the epilayers is achieved by creating a ≈ 5 mol % supersaturation with a decrease of the saturation temperature by 2–6 K. The substrate is rotated at 15–60 rpm. In some experiments, a cooling rate of 0.67 K/h is used.

Wiping off the solution is not difficult due to its low viscosity. When the substrate is removed from the solution, it is still rotating while the whole system cools to room temperature.

Aznar et al. mentioned that on the (010) faces the epitaxial growth mainly exhibits a flat surface, which indicates a layer-by-layer growth mechanism. However *Romanuyk* et al. reported a three-dimensional (3-D) nucleation, also known as the Volmer–Weber growth mode [21.127].

The substrates were oriented perpendicular to the ***b***-crystallographic direction, as preliminary studies of thin-film growth had demonstrated that epitaxial growth on the (010) face resulted in high-quality films at the fastest growth rate. Generally, higher density of growth steps is observed on epilayers grown on (310) and $(\bar{1}11)$. A possible reason is the higher growth rate of this faces when compared with their neighboring faces. The layer–substrate mismatches on the $(\bar{1}11)$ and (010) faces are rather similar. The lattice mismatch for Yb-doped KLuW thin films grown on KLuW substrates and Yb-doped KYW thin films grown on KYW substrates are listed in Table 21.5. No thermal mismatch data are available for these epitaxial layers.

Growth hillocks have been observed on Yb:KLuW films grown on KLuW substrates, which is a typically observed micromorphology that develops during the growth process.

Figure 21.19 shows the comparison of the thickness on different faces.

The chemical composition of the layer is usually measured by x-ray spectrometry or electron probe microanalysis to quantify the concentration and to calculate the distribution coefficient of the doping element in the epilayer, and also to determine if diffusion of the doping element into the substrate occurs. The distribution coefficient of the different lanthanide doping ions in the epilayers is near unity. No diffusion into the substrate has been observed. Higher doping levels of the epitaxial film will lead to an increase of the lattice mismatch and, consequently, difficulties in the growth of the epitaxial layers. When doping KYW with Yb the doping level obtained in the epitaxial films with high crystalline quality was 10 at. % in the growth solution. In the case of KLuW, it is possible to increase the dop-

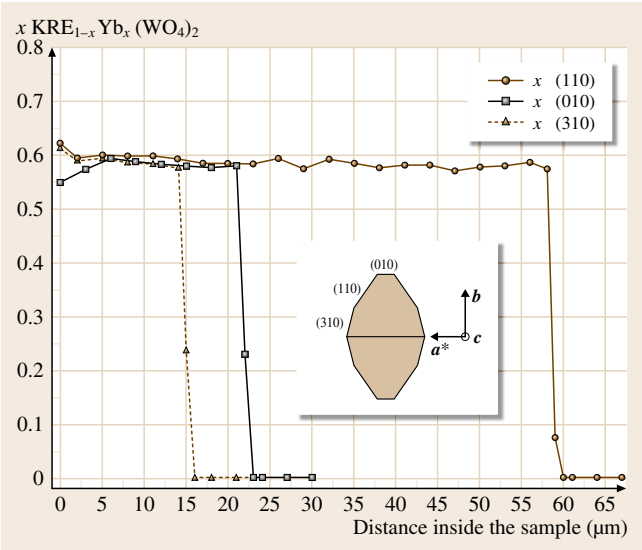


Fig. 21.19 Ytterbium concentration profile for the $KLu_{0.48}Yb_{0.052}W$ layer on KluW substrates on three different faces: (310), (110), and (010) (after [21.128])

ing concentration to 50 at. % while maintaining high quality of the epitaxial layer.

Recently, the growth of thulium-doped epitaxial layers on KYW and KLuW substrates has been reported. For the KLuW host the doping level can reach 7.5 at. % substitution of lutetium by thulium while maintaining high film quality.

21.4.2 Epitaxies Within the Structural Field of KTP

Optical waveguides in KTP have been produced by ion exchange of K^+ by Rb^+, Cs^+ or Tl^+ on the surface of a KTP substrate immersed in molten salts of Rb, Cs, and Tl [21.129]. A metal mask (e.g., Al, Au, Ti) has been used to fabricate channel waveguides by this procedure. These waveguides appear to be optically uniform over the width of the channel and show no evidence of lateral ion diffusion [21.130], which enables fabrication of high-density waveguide arrays and modulated index waveguides, while at the same time optimizing the electric-field overlap for modulators, switches, and nonlinear waveguide devices [21.123]. When $Ba(NO_3)_2$ is added to the molten $RbNO_3$, the ion-exchange process changes not only the optical indices of the crystal but also its polarity, enabling the fabrication of not only Rb-exchanged quasi-phase-matched waveguides of KTP [21.131].

However, ion-exchange processes have their drawbacks. Due to the inherently diffusive and strongly anisotropic nature of the process, it is the difficult to control the waveguide depth, producing guides with a broad, poorly defined index profile along the ***c***-axis [21.24, 131]. This index profile, although satisfactory for many applications, is less effective for confinement of optical fields, especially in waveguiding second-harmonic generation [21.132] where variations of ionic conductivity due to crystal growth methods and with impurities make the device fabrication process difficult and results in poor yields.

Optical waveguides in KTP have been produced by proton or ammonium exchange [21.122], yielding a more step-like index profile by sol–gel chemistry [21.133] producing continuous KTP polycrystalline films with a grain size of 0.3 μm, and by pulsed excimer laser ablation [21.134], allowing growth of KTP films on foreign substrates such as sapphire, silicon [21.135], and quartz.

Unlike other techniques used to fabricate waveguides, the LPE technique enables growth of a homogeneous single-crystal film and allows control of the thickness by adjusting the supersaturation of the solution and the growth time. Films with well-defined step-like refractive-index profile can be grown directly by LPE [21.131]. Good-quality single-crystal epitaxial layers of KTP suitable for producing optical waveguides can be obtained by LPE on substrates of the same family. This can be done by controlling the mismatch between the cell parameters of the substrate and those of the film using the solid solutions offered by this family of crystals. Thin films of $KTiOP_xAs_{1-x}O_4$ were grown by *Cheng* et al. on KTP substrates using both tungstate and the pure phosphate–arsenate self-fluxes [21.132]. The KTA–KTP system was chosen, since the substitution of arsenic for phosphorus provides the desired refractive-index difference without compromising the nonlinearity of the material. $KTiOP_xAs_{1-x}O_4$ films with a thickness of 5–50 μm were grown on polished KTP substrates. These substrates were polished with diamond-based polishing powder and finished with a 30 s chemical–mechanical polish in colloidal silica prior to epitaxial growth. A small (≈ 0.75 mm) hole, drilled at one corner of the substrate, allows it to be tied vertically onto a crystal rotation–pulling head with a thin platinum wire to assist flux drainage after dipping. Slight etching of the substrate in warm dilute hydrochloric acid prior to the dipping improved the quality of the epitaxial layer. {100}, {011}, {110}, and {201} oriented plates cut from a single crystal grown

by the flux method were chosen as substrates. Although {001} films would be preferred in device applications, since the largest nonlinear optical coefficients of KTP lie in this plane, growth of high-quality {001} films has not been successful due to the fast growth and *c*-capping habit of KTP. The same problem was observed when growing thin epitaxial layers of KTP on {010} substrates. It should be noted that the use of substrates cut from hydrothermally grown crystals leads to optical degradation with the formation of fine white filaments in the substrate due to the precipitation of fine water-based inclusions [21.131].

The dipping setup [21.131] consisted of a 250 ml crucible placed at the bottom of a short-zone top-loading crucible furnace. The melt ($\approx$ 200 ml) was homogenized overnight at $\approx$ 50 K above its liquidus temperature, which was determined accurately by repeated seeding. The substrate was introduced into the growth furnace slowly ($\approx$ 5–25 mm/min) to avoid cracks due to thermal stress, and the flux was cooled to $\approx$ 1.5–3 K below the saturation point and allowed to equilibrate for 30 min prior to dipping the substrate into the melt. The substrate was spun unidirectionally at 10 rpm. The dipping time varied depending on the desired film thickness, the degree of supersaturation used, the choice of flux, and the growth temperature. Experimentally it was found that back-etching of the substrate in the same LPE solution prior to growth resulted in significantly better quality films. This was accomplished by taking advantage of the thermal inertia of the system and submerging the substrate before the melt reached the growth temperature. Upon completion of the dipping, the substrate–epitaxy was removed from the flux and washed with warm diluted hydrochloric acid.

Optical-quality films could be readily obtained using a 3–4 K supersaturation and a growth temperature of $\approx$ 1173 K. The observed growth rate was found to be weakly dependent on the orientation of the substrates. An abrupt increase in the arsenic concentration at the film–substrate interface was revealed, and resulted in an abrupt, step-like refractive index profile. It was concluded that the maximum lattice mismatch between the film and the substrate that still yields high-quality films was $\approx$ 1%, which corresponds to a $\approx$ 35% increase in arsenic content in the $KTiOAs_xP_{1-x}O_4$ film. Film cracking was observed for films grown on substrates with larger lattice mismatch.

Significantly different growth properties were observed for tungstate and $K_6P_4O_{13}$ fluxes. First, a longer soak time was needed when using the $K_6P_4O_{13}$ flux. Second, under the same growth conditions (temperature and supercooling), the growth rate normal to the natural face used as the substrate was substantially lower in the $K_6P_4O_{13}$ flux, necessitating supercooling roughly twice that used in tungstate flux to achieve a comparable growth rate. Third, films grown from $K_6P_4O_{13}$ flux tend to show film–substrate interfaces of poorer quality due to the slow dissolution kinetics of this flux, which makes the implementation of pregrowth etching difficult.

Appropriate replacement of the titanyl group via solid solution formation (e.g., Sn or Ge) or impurity doping could also generate epitaxial films with well-defined refractive index boundaries [21.24]. However, the growth of $KTi_{1-x}Sn_xOPO_4$ films proved to be difficult due to the anomalously slow dissolution properties of $KSnOPO_4$. As an alternative, growth of $KTi_{1-x}Ge_xOPO_4$ thin films on KTP substrates using a 20% Ge solution has been tested [21.131]. Films (10 μm thick) of $KTi_{0.96}Ge_{0.04}OPO_4$ on {011} KTP substrates were grown. Discouragingly, even with a low 4.3% Ge incorporation, numerous cracks perpendicular to the ***c***-crystallographic direction were observed in thicker (30 μm) films because the $KTi_{0.96}Ge_{0.04}OPO_4$ films grew under tensile stress.

Cheng et al. [21.131] suggested that this situation can be improved by reversing the film–substrate configuration, such as growing KTP films on $KTi_{1-x}Ge_xOPO_4$ substrates. In this way, *Solé* et al. [21.85, 136] produced KTP thin films grown on $KTi_{1-x}Ge_xOPO_4$ substrates also using both tungstate and pure phosphate self-fluxes. These LPE experiments were performed in a special vertical furnace built to provide a wide enough region in which there was practically no axial gradient so that the epitaxial film thickness did not depend on the solution depth. Platinum cylindrical crucibles, 30 mm in diameter and 40 mm high, filled with about 50 g of solution with composition of $K_2O : P_2O_5 : TiO_2 = 49.8 : 33.2 : 17$ (mol %) in self-flux and $K_2O : P_2O_5 : TiO_2 : WO_3 = 42 : 14 : 14 : 30$ in tungstate flux were used. After homogenization of the solution, special attention was paid to determining the saturation temperature of the solution using a ***c***-oriented seed rotating at 16 rpm. A new approach was used to study the quality of the films simultaneously on different substrates with different orientation. The epitaxial growth was made directly on the natural faces of as-grown single crystals of $KTi_{1-x}Ge_xOPO_4$. Thus, the growth conditions were forced to be the same for all the different orientations of the crystal faces used as substrates. The substrates were fixed using their own growth crystal seeds at the end of an alumina rod and cleaned for 5 min in $HNO_3 : H_2O = 1 : 1$ by volume,

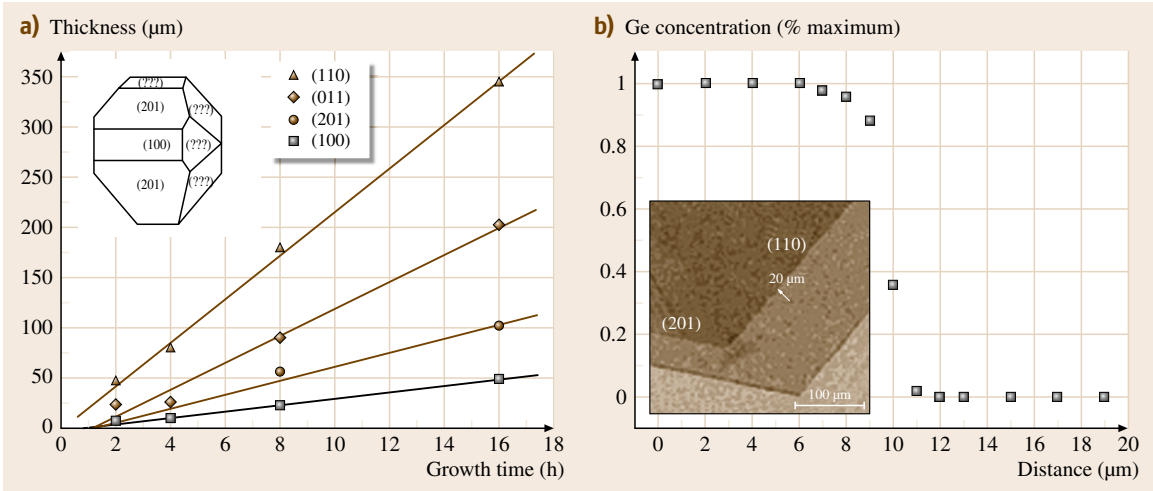


Fig. 21.20 (a) Epitaxial film thickness on different faces of a $KTi_{0.988}Ge_{0.012}OPO_4$ crystal as a function of the time of growth. The thin films were grown at 2 K below the saturation temperature of the solution. A morphology sketch with the difference faces of the $KTi_{0.988}Ge_{0.012}OPO_4$ crystal is included. (b) Normalized germanium concentration around the substrate–film interface determined by electron probe microanalysis. A scanning electron microscopy image of a cross section of the substrate–film interface taken with a secondary-electron detector is included. The difference in contrast indicates where the substrate–film interface is located, suggesting also a sharp interface (after [21.85])

for 5 min in distilled water, and for 5 min in ethanol. The whole cleaning process was carried out with crystal rotation. The crystal was then introduced into the furnace slowly to avoid cracks caused by thermal stress and heated for 30 min above the solution surface. The substrate was then dipped into the solution at a temperature 3–5 K above the saturation temperature for 1 h to dissolve the substrate surface before the beginning of growth. In tungsten solutions, the dissolution of the substrate was performed at 1 K above the saturation temperature for 10 min since this solution is significantly less viscous than the solution without WO_3, and all these processes are much quicker. The temperature of the solution was maintained at 2 K below the saturation temperature for several hours to induce epitaxial growth when self-flux was used, or for several minutes when tungstate flux was used. The growth was performed at 1 K below the saturation temperature only when the growth time was long (16 h) and the degree of substitution was high. In all cases, the crystal rotation was maintained at 16 rpm. After the epitaxial growth, the crystal was removed from the flux and extracted from the furnace slowly to avoid thermal stresses in the crystal.

In general, the surface morphology and quality of the epitaxial films obtained depends on the crystal face on which they grew. Other parameters such as Ge content in the substrate and time of growth have significantly less influence. The films on (201) and (100) faces were found to be of high quality and smooth. Films grown on (100) faces tended to show small macrosteps that could be a reproduction of the steps already existing on the substrates. The films on (011) and (110) faces tended to show small hillocks when the time of growth and the Ge in the substrate increased and a tendency for films grown on (011) face to be of best quality compared with those grown on (110) face. This difference in quality could be related to the faster velocity of film growth on these faces. The worst quality films grew on (101) face. This face, although it exists in $KTi_{1-x}Ge_xOPO_4$ crystals, is not a usual face in pure KTP. The defects in films grown on the (101) face are due to the faster growth velocity in pure KTP relative to the growth velocity on the other faces. In general, films grown on $KTi_{0.918}Ge_{0.082}OPO_4$ substrates showed some cracks. The quality of epitaxial growth in tungstate flux on (100), (201), and (011) faces was found to be good up to the highest concentration of Ge studied and the longest time studied. The epitaxy on (011) face, however, seemed to show a greater tendency to have macrosteps and growth hillocks than the other two faces. Similarly, when the Ge substitution for Ti in the substrate, and/or the growth time increased, the epitaxial film on (110) face showed a slight tendency to exhibit more defects.

A linear correlation between the epitaxial thickness and the time of growth was observed for all films grown on the faces of $KTi_{0.988}Ge_{0.012}OPO_4$. Figure 21.20a shows the epitaxial film thickness on the different faces as a function of the growth time for films grown at 2 K below the saturation temperature of the solution. The epitaxy on the (100) face showed the lowest rate of growth, followed by the film grown on the (201) face. The quality of these epitaxial films remained good even for long growth times and high concentrations of Ge in the substrate. The epitaxial films on (011) and (110) faces showed a faster rate of growth. Thus, when the time of growth increased, the density of defects also increased. Because of the poor quality of the epitaxial film on (101) face it was difficult to measure the epitaxial thickness accurately. For the case of growth in tungstate solutions, the epitaxy on (100) face showed the lowest rate of growth, followed by the films grown on (201), (011), and (110) faces, which showed similar rates of film growth. A sharp change in the germanium concentration at the substrate–film interface was observed. Figure 21.20b shows the normalized germanium concentration around the substrate–film interface.

The mismatch between the substrate and the film, defined as $f_{s(hkl)} = (S_{s(hkl)} - S_{0(hkl)})/S_{0(hkl)}$, where $S_{s(hkl)}$ and $S_{0(hkl)}$ are the areas obtained from the periodicity vectors of the substrate and the film, respectively, is listed for each face in Table 21.6. For {100} and {201} faces, these mismatches were positive, meaning the substrate was larger than the film. For {110} and {011} faces the mismatches were always negative, which is believed to produce films of lower quality. The different quality of the epitaxial films grown on the different crystal faces could also be explained by considering the position of titanium in the KTP structure with respect to the different planes that constitute the external morphology of the crystals used as the substrate on which the epitaxial films are grown. The Ti planes parallel to (100), (201), and (011) faces are regularly located in the structure and equidistant, while planes parallel to the (110) and (101) faces are not equidistant. Thus, the structural distortion produced by the Ge substitution in these planes was not distributed as homogeneously as in the case of the (100), (201), and (011) faces. This could lead to a larger tendency to generate defects in the film.

Epitaxial $Rb_xK_{1-x}TiOPO_4$ films were grown from a 20% Rb solution on a KTP substrate [21.133]. Although the grown layer was measured to be 50 μm, the diffusion of Rb into the substrate at the growth temperature (≈ 1125 K) significantly broadened the waveguiding layer up to ≈ 125 μm. It is therefore more appropriate to view the liquid-phase epitaxy of $Rb_xK_{1-x}TiOPO_4$ on KTP as an ion-exchange waveguide fabrication process using molten tungstate instead of nitrate.

Liquid-phase epitaxy was also used as a tool to test the morphological stability of the $(00\bar{1})$ face, which is a natural face in $KTiOAsO_4$ crystals and on KTP crystals. For this purpose, a *c*-cut KTP plate was submerged into a slightly supercooled (≈ 4 K) $K_6P_4O_{13}$ solution of KTP at 920 °C for ≈ 35 min. Smooth planar growth steps at the center of the KTP plate suggest that the $(00\bar{1})$ face is indeed singular in KTA. Stable $\{01\bar{1}\}$ and $\{20\bar{1}\}$ lamellae extend rapidly along the $\langle 00\bar{1}\rangle$ and $\langle 20\bar{1}\rangle$ directions to form overhangs which eventually enclose the (001) and $(00\bar{1})$ faces and thus eliminate them from the final growth form [21.137].

A completely new combination of both top-down and bottom-up approaches has been reported recently to grow two-dimensional (2-D) photonic crystals of KTP involving liquid-phase epitaxial techniques [21.138]. KTP rods grew inside the air holes of an ordered silicon matrix closely bound to a ***c***-oriented KTP substrate and following the orientation of the substrate. The 2-D KTP patterning implemented can be summarized in a four-step procedure, shown in Fig. 21.21a, that involves preparation of a high-quality ordered macroporous silicon template, epitaxial growth of the KTP rods into the silicon template, polishing of the top or bottom surface of the KTP columns, and finally partial selective etching of the silicon matrix. A platinum wire was used to bind the silicon template to a KTP substrate. The template–substrate was dipped for 5 min into a high-temperature solution with a mol % composition $K_2O : P_2O_5 : TiO_2 : WO_3 = 42 : 14 : 14 : 30$ without any additional thermal gradient. We initiated the epitaxial growth of the KTP 2-D photonic structure

Table 21.6 Mismatches between $KTi_{1-x}Ge_xOPO_4$ substrates and KTP films

Epitaxial layer	*f*(100)	*f*(201)	*f*(101)	*f*(110)	*f*(011)
$KTi_{0.988}Ge_{0.012}OPO_4$/KTP	−0.003	0.006	0.018	−0.017	−0.007
$KTi_{0.955}Ge_{0.045}OPO_4$/KTP	0.009	0.032	0.060	−0.035	−0.009
$KTi_{0.918}Ge_{0.082}OPO_4$/KTP	−0.071	−0.029	0.023	−0.156	−0.107

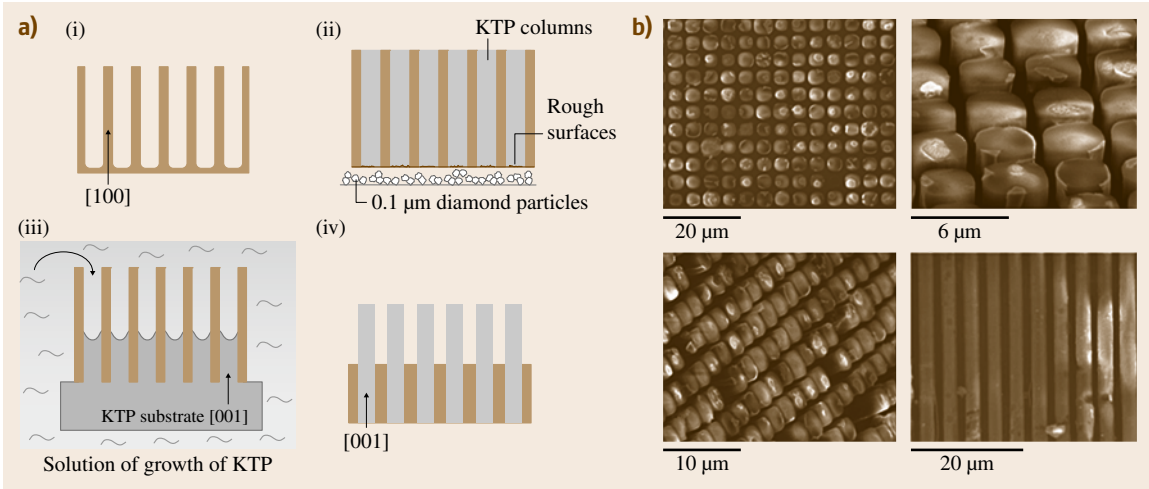


Fig. 21.21 **(a)** Schematic view of the four stages of growth of KTP 2-D photonic crystals: (i) preparation of the oriented 2-D macroporous silicon membrane, (ii) the silicon template is attached to an oriented KTP substrate and then immersed in the growth solution of KTP. The direction of growth of the KTP rods is the same as oriented of the KTP substrate, [001]. (iii) After growth, the top of the rods is polished with diamond particles in order to obtain an optical-quality surface. (iv) Silicon is partially removed by selective chemical etching. **(b)** Scanning electron microscopy images of (i) the top of a 2-D KTO phonic crystal after polishing and partially etching of the macroporous silicon template, (ii) side view of the KTP rods after removing the silicon template, (iii) a detailed view of a 2-D KTP phonic crystal with a period of 4.5 μm, and (iv) side view of a plane of rods of a 2-D KTP photonic crystal lattice

2 K below the saturation temperature, which provided a supersaturation in the solution of about 2%. The template–substrate–epitaxy composite was then removed from the solution, but kept inside the furnace above the surface of the solution while the furnace was cooled to room temperature at a rate of 15 K/h to avoid thermal stress that could result in cracks either in the 2-D photonic structures or in the substrate. The final 2-D photonic structures are formed from independent rods of KTP with square cross section, perfectly aligned with the orientation of the KTP substrate. Figure 21.21b shows several scanning electron microscopy (SEM) images of these photonic structures.

References

21.1 M.M. Kuklja: Defects in yttrium aluminium perovskite and garnet crystals: atomistic study, J. Phys. Condens. Matter **12**, 2953–2967 (2000)

21.2 V. Lupei: RE^{3+} emission in garnets: multisites, energy transfer and quantum efficiency, Opt. Mater. **19**, 95–107 (2002)

21.3 J. Petit, B. Viana, P. Goldner, D. Vivien, P. Louiseau, B. Ferrand: Laser oscillation with low quantum defect in Yb:$GdVO_4$, a crystal with high thermal conductivity, Opt. Lett. **29**, 833–835 (2004)

21.4 S.H. Smith, G. Garton, B.K. Tanner: Top-seeded flux growth of rare-earth vanadates, J. Cryst. Growth **23**, 335–340 (1974)

21.5 S. Erdei: Growth of oxygen deficiency-free YVO_4 single crystal by top-seeded solution growth technique, J. Cryst. Growth **134**, 1–13 (1993)

21.6 D.I. Savytskii, L.O. Vasylechko, A.O. Matkovskii, I.M. Solskii, A. Suchocki, D.Y. Sugak, F. Wallrafen: Growth and properties of $YAlO_3$:Nd single crystals, J. Cryst. Growth **209**, 874–882 (2000)

21.7 R. Solé, V. Nikolov, X. Ruíz, J. Gavaldà, X. Solans, M. Aguiló, F. Díaz: Growth of β-$KGd_{1-x}Nd_x(WO_4)_2$ single crystals in $K_2W_2O_7$ solvents, J. Cryst. Growth **169**, 600–603 (1996)

21.8 M.C. Pujol, M. Aguiló, F. Díaz, C. Zaldo: Growth and characterisation of monoclinic $KGd_{1-x}RE_x(WO_4)_2$ single crystals, Opt. Mater. **13**, 33–40 (1999)

21.9 G. Métrat, N. Muhlstein, A. Brenier, G. Boulon: Growth by the induced nucleated floating crystal (INFC) method and spectroscopic properties of $KY_{1-x}Nd_x(WO_4)_2$ laser materials, Opt. Mater. **8**, 75–82 (1997)

21.10 A. Brenier, F. Bourgeois, G. Métrat, N. Muhlstein, M. Boudelle, G. Boulon: Spectroscopic characterization of Nd^{3+}-doped $KY(WO_4)_2$ single crystal, J. Lumin. **81**, 135–141 (1999)

21.11 D. Gabbe, A.L. Harmer: Scheelite structure fluorides: The growth of pure and rare earth doped $LiYF_4$, J. Cryst. Growth **3**, 544 (1968)

21.12 K. Shimamura, H. Sato, A. Bensalah, V. Sudesh, H. Machida, N. Sarukura, T. Fukuda: Crystal growth of fluorides for optical applications, Cryst. Res. Technol. **36**, 801–813 (2001)

21.13 A. Agnesi, G. Carraro, A. Guandalini, G. Reali, E. Sani, A. Toncelli, M. Tonelli: 1-mJ Q-switched diode-pumped Nd:BaY_2F_8 laser, Opt. Exp. **12**, 3766–3769 (2004)

21.14 S. Bigotta, D. Parisi, L. Bonelli, A. Toncelli, M. Tonelli, A. Di Lieto: Spectroscopic and laser cooling results on Yb^{3+}-doped BaY_2F_8 single crystal, J. Appl. Phys. **100**, 013109 (2006)

21.15 R.F. Belt, R. Uhrin: Top seeded solution growth of Cr^{3+}:$LiCaAlF_6$ in HF atmosphere, J. Cryst. Growth **109**, 340–344 (1991)

21.16 D. Klimm, P. Reiche: Ternary colquiriite type fluorides as laser hosts, Cryst. Res. Technol. **34**, 145–152 (1999)

21.17 A.A. Kaminskii: Modern developments in the physics of crystalline laser materials, Phys. Status Solidi (a) **200**, 215–296 (2003)

21.18 A.A. Kaminskii: *Laser Crystals. Their Physics and Properties* (Springer, Berlin 1981)

21.19 C.E. Mungan, S.R. Bowman, T.R. Gosnell: Solid-state laser cooling of ytterbium-doped tungstate crystals, Proc. Lasers 2000 (2001) pp. 819–826

21.20 A.N. Medina, A.C. Bento, M.L. Baesso, F.G. Gandra, T. Catunda, A. Cassanho: Temperature dependence of the Cr^{3+} site axial distortion in $LiSrAlF_6$ and $LiSrGaF_6$ single crystals, J. Phys. Condens. Matter **13**, 8435–8443 (2001)

21.21 S.A. Payne, L.L. Chase, H.W. Newkirk, L.K. Smith, W.F. Krupke: $LiCaAlF_6$:Cr^{3+}: A promising new solid-state laser material, IEEE J. Quantum Electron. **QE-24**, 2243–2252 (1988)

21.22 J.A. Armstrong, N. Bloembergen, J. Ducuing, P.S. Pershan: Interactions between light waves in a nonlinear dielectric, Phys. Rev. **127**, 1918–1939 (1962)

21.23 P.F. Bordui, M.M. Fejer: Inorganic crystals for nonlinear optical frequency conversion, Annu. Rev. Mater. Sci. **23**, 321–379 (1993)

21.24 M.E. Hagerman, K.R. Pöppelmeier: Review of the structure and processing defect property relationships of potassium titanyl phosphate: A strategy for novel thin film photonic devices, Chem. Mater. **7**, 602–621 (1995)

21.25 H. Hellwig, J. Liebertz, L. Bohaty: Exceptional large nonlinear optical coefficients in the monoclinic bismuth borate BiB_3O_6 (BIBO), Solid State Commun. **190**, 249–251 (1998)

21.26 R. Solé, X. Ruíz, R. Cabré, M. Aguiló, F. Díaz, V. Nikolov, P. Peshev: High temperature solutions of the $(0.4Na_2O-0.6\ B_2O_3)-BaO-((6-x)+xCoSnO_3)$ system. Physical properties, Mater. Res. Bull. **30**, 779–788 (1995)

21.27 X. Ruíz, M. Aguiló, J. Massons, F. Díaz: Numerical and experimental study of the forced convection inside a rotating disk-cylinder configuration, Exp. Fluids **14**, 333–340 (1993)

21.28 H.J. Scheel, E.O. Schulz-Dubois: Flux growth of large crystals by accelerated crucible-rotation technique, J. Cryst. Growth **8**, 304–306 (1971)

21.29 D. Elwell, H.J. Scheel: *Crystal Growth from High-Temperature Solutions* (Academic, London 1975)

21.30 M.G. Astles: *Liquid-Phase Epitaxial Growth of III–V Compound Semiconductor Materials and Their Device Applications* (Adam Hilger, New York 1990)

21.31 A.A. Maier, M.V. Provotorov, V.A. Balashov: Double molybdates and tungstates of the rare earth and alcali metals, Russ. Chem. Rev. **42**, 822–833 (1973)

21.32 E. Gallucci, C. Goutadier, G. Boulon, M.T. Cohen-Adad: Growth of $KY(WO_4)_2$ single crystal: Investigation of the rich WO_3 region in the $K_2O-Y_2O_3-WO_3$ ternary system. 1. The K_2O-WO_3 binary system, Eur. J. Solid State Inorg. Chem. **34**, 1107–1117 (1997)

21.33 R. Guérin, P. Caillet: Sur les phases du système $K_2WO_4-WO_3$ et leur reduction par la vapeur de potassium, C. R. Acad. Sci. Ser. C **271**, 815–817 (1970), in French

21.34 G. Wang, Z.D. Luo: Crystal growth of $KY(WO_4)_2$: Er^{3+},Yb^{3+}, J. Cryst. Growth **116**, 505–506 (1992)

21.35 P.V. Kletsov, L.P. Kozeeva, L.Y. Kharchenko: Study on the crystallization and polymorphism of double potassium and trivalent metal tungstates, $KR(WO_4)_2$, Sov. Phys. Crystallogr. **20**, 732–735 (1976)

21.36 A. Majchrowski: *Supermaterials* (Kluwer, Dordrecht 2000)

21.37 A. Majchrowski, M.T. Borowiec, E. Michalski: Top seeded solution growth of $KHo(WO_4)_2$ single crystals, J. Cryst. Growth **264**, 201–207 (2003)

21.38 M.C. Pujol, R. Solé, J. Gavaldà, J. Massons, M. Aguiló, F. Díaz: Growth and ultraviolet optical properties of $KGd_{1-x}RE_x(WO_4)_2$ single crystals, J. Mater. Res. **14**, 3739–3745 (1999)

21.39 K. Wang, J. Zhang, J. Wang, W. Yu, H. Zhang, Z. Wang, X. Wang, M. Ba: Predicted and real habits of flux grown potassium lutetium tungstate single crystals, Cryst. Growth Des. **5**, 1555–1558 (2006)

21.40 M.T. Borowiec, A. Majchrowski, V. Domuchowski, V.P. Dyakonov, E. Michalski, T. Zayarniuk, J. Żmija, H. Szymczak: Crystal growth and x-ray structure investigation of the $KHo(WO_4)_2$, Proc. SPIE **5136**, 20–25 (2003)

21.41 A.A. Kaminskii, J.B. Gruber, S.N. Bagaev, K. Ueda, U. Hömmerich, J.T. Seo, D. Temple, B. Zandi, A.A. Kornienko, E.B. Dunina, A.A. Pavlyuk, R.F. Klevtsova, F.A. Kuznetsov: Optical spectroscopy and visible stimulated emission of Dy^{3+} ions in monoclinic α-$KY(WO_4)_2$ and α-$KGd(WO_4)_2$ crystals, Phys. Rev. B **65**, 125108 (2002)

21.42 M.C. Pujol, M. Bursukova, F. Güell, X. Mateos, R. Solé, J. Gavaldà, M. Aguiló, J. Massons, F. Díaz, P. Klopp, U. Griebner, V. Petrov: Growth, optical characterization, and laser operation of the stoichiometric crystal $KYb(WO_4)_2$, Phys. Rev. B **65**, 165121 (2002)

21.43 H.P. Jenseen, A. Linz: Analysis of the optical spectrum of Tm^{3+} in $LiYF_4$, Phys. Rev. B **11**, 92–101 (1975)

21.44 B. Chai, J. Lefaucheur, A. Pham, G. Lutts, J. Nicholls: Growth of high-quality single crystals of KYF_4 by TSSG method, Proc. SPIE **1863**, 131–135 (1993)

21.45 P. Hagenmüller: *Inorganic Solid Fluorides* (Academic, New York 1985)

21.46 E.M. Levin: The system Y_2O_3-V_2O_5, J. Am. Ceram. Soc. **50**, 381–382 (1967)

21.47 L.G. Van Uitert, R.C. Linares, R.R. Soden, A.A. Ballman: Role of f-orbital electron wave function mixing in the concentration quenching of Eu^{3+}, J. Chem. Phys. **36**, 702–705 (1962)

21.48 W. Hintzmann, G. Müller-Vogt: Crystal growth and lattice parameters of rare-earth doped yttrium phosphate, arsenate and vanadate prepared by the oscillating temperature flux technique, J. Cryst. Growth **5**, 274–278 (1969)

21.49 S.H. Smith, B.M. Wanklyn: Flux growth of rare earth vanadates and phosphates, J. Cryst. Growth **21**, 23–28 (1974)

21.50 B.M. Wanklyn: Use of a crystalline seal in flux growth – Rare-earth borates, vanadates and garnets, $KNiF_3$ and $CsNiMF_6$ (M = Fe, Cr), J. Cryst. Growth **54**, 610–614 (1981)

21.51 V.A. Timofeeva: Physicochemical aspects of flux crystallization of the oxide materials. In: *Growth of Crystals* (Consultants Bureau, New York 1988)

21.52 R. Masse, J.C. Grenier: Étude des monophosphates du type $M'TiOPO_4$ avec $M' = K$, Rb et Tl, Bull. Soc. Fr. Mineral. Cristallogr. **94**, 437–439 (1971), in French

21.53 M.N. Satyanarayan, A. Deepthy, H.L. Bhat: Potassium titanyl phosphate and its isomorphs. Growth, properties, and applications, Crit. Rev. Solid State Mater. Sci. **24**, 103–191 (1999)

21.54 V.I. Voronkova, V.K. Yanovskii: Growth of $KTiOPO_4$-group crystals from a solution in a melt and their properties, Inorg. Mater. **24**, 273–277 (1988)

21.55 K. Iliev, P. Peshev, V. Nikolov, I. Koseva: Physicochemical properties of high-temperature solutions of the K_2O-P_2O_5-TiO_2 system suitable for the growth of $KTiOPO_4$ (KTP) single crystals, J. Cryst. Growth **100**, 219–224 (1990)

21.56 J.C. Jacco, G.M. Loiacono, M. Jaso, G. Mizell, B. Greenberg: Flux growth and properties of $KTiOPO_4$, J. Cryst. Growth **70**, 484–488 (1984)

21.57 P.F. Bordui, J.C. Jacco, G.M. Loiacono, R.A. Stolzenberger, J.J. Zola: Growth of large single crystals of $KTiOPO_4$ (KTP) from high-temperature solution using heat pipe based furnace system, J. Cryst. Growth **84**, 403–408 (1987)

21.58 G.M. Loiacono, T.F. McGee, G. Kostecky: Solubility and crystal growth of $KTiOPO_4$ in polyphosphate solvents, J. Cryst. Growth **104**, 389–391 (1990)

21.59 P.F. Bordui, J.C. Jacco: Viscosity and density of solutions used in high-temperature solution growth of $KTiOPO_4$, J. Cryst. Growth **82**, 351–355 (1987)

21.60 T.E. Gier: Method for flux growth of $KTiOPO_4$ and its analogues, US Patent 4231838 (1980)

21.61 A.L. Aleksandrovskii, S.A. Akhmanov, V.A. D'yakov, N.I. Zheludev, V.I. Pryalkin: Efficient nonlinear optical converters made of potassium titanyl phosphate crystals, Sov. J. Quantum Electron. **15**, 885–886 (1985)

21.62 P.F. Bordui, S. Motakef: Hydrodynamic control of solution inclusion during crystal growth of $KTiOPO_4$ (KTP) from high-temperature solution, J. Cryst. Growth **96**, 405–412 (1989)

21.63 B. Vartak, Y.I. Kwon, A. Yeckel, J.J. Derby: An analysis of flow and mass transfer during the solution growth of potassium titanyl phosphate, J. Cryst. Growth **210**, 704–718 (2000)

21.64 T. Sasaki, A. Miyamoto, A. Yokotani, S. Nakai: Growth and optical characterization of large potassium titanyl phosphate crystals, J. Cryst. Growth **128**, 950–955 (1993)

21.65 G. Dhanaraj, T. Shripathi, H.L. Bhat: Defect characterization of KTP single-crystals, Bull. Mater. Sci. **15**, 219–227 (1992)

21.66 G. Dhanaraj, H.L. Bhat: Dendritic structures on habit faces of potassium titanyl phosphate crystals grown from flux, Mater. Lett. **10**, 283–287 (1990)

21.67 R.J. Bolt, M.H. van der Mooren, H. de Haas: Growth of $KTiOPO_4$ (KTP) single crystals by means of phosphate and phosphate/sulphate fluxes out of a three-zone furnace, J. Cryst. Growth **114**, 141–152 (1991)

21.68 M. Roth, N. Angert, M. Tseitlin, A. Alexandrovski: On the quality of KTP crystals for nonlinear optical and electro-optic applications, Opt. Mater. **16**, 131–136 (2001)

21.69 L.K. Cheng, J.D. Bierlein, A.A. Ballman: Crystal growth of $KTiOPO_4$ isomorphs from tungstate and molybdate fluxes, J. Cryst. Growth **110**, 697–703 (1991)

21.70 N. Angert, L. Kaplun, M. Tseitlin, E. Yashchin, M. Roth: Growth and domain structure of potassium titanyl phosphate crystals pulled from high-temperature solutions, J. Cryst. Growth **137**, 116–122 (1994)

21.71 J.J. Carvajal, V. Nikolov, R. Solé, J. Gavaldà, J. Massons, M. Rico, C. Zaldo, M. Aguiló, F. Díaz: Enhancement of the erbium concentration in $RbTiOPO_4$ by co-doping with niobium, Chem. Mater. **12**, 3171–3180 (2000)

21.72 Y.S. Oseledchik, S.P. Belokrys, V.V. Osadchuk, A.L. Prosvirnin, A.F. Selevich, V.V. Starshenko, K.V. Kuzemchenko: Growth of $RbTiOPO_4$ single crystals from phosphate systems, J. Cryst. Growth **125**, 639–643 (1992)

21.73 A.A. Ballman, H. Brown, D.H. Olson, C.E. Rice: Growth of potassium titanyl phosphate (KTP) from molten tungstate melts, J. Cryst. Growth **75**, 390–394 (1986)

21.74 K. Iliev, P. Peshev, V. Nikolov, I. Koseva: Physicochemical properties of high-temperature solution of the K_2O–P_2O_5–TiO_2–WO_3 system, suitable for the growth of $KTiOPO_4$ (KTP) single crystals, J. Cryst. Growth **100**, 225–232 (1990)

21.75 D.P. Shumov, M.P. Tarassov, V.S. Nikolov: Investigation of optical inhomogeneities in $KTiOPO_4$ (KTP) single crystals grown from high-temperature tungsten-containing solutions, J. Cryst. Growth **129**, 635–639 (1993)

21.76 A. Yokotani, A. Miyamoto, T. Sasaki, S. Nakai: Observation of optical inhomogeneities in flux grown KTP crystals, J. Cryst. Growth **110**, 963–967 (1991)

21.77 G. Marnier: Process for the flux synthesis of crystals of the $KTiOPO_4$ potassium titanyl monophosphate type, US Patent 4746396 (1988)

21.78 S. Suma, N. Santha, M.T. Sebastián: Growth of KTP crystals from potassium sodium fluoride phosphate solution, Mater. Lett. **34**, 322–325 (1998)

21.79 S. Suma, N. Santha, M.T. Sebastián: A new flux for the fase growth of potassium titanyl phosphate (KTP) single crystals, J. Mater. Sci. Mater. Electron. **9**, 39–42 (1998)

21.80 A. Miyamoto, Y. Mori, T. Sasaki, S. Nakai: Improvement of optical transmission of $KTiOPO_4$ crystals by growth in nitrogent ambient, Appl. Phys. Lett. **69**, 1032–1034 (1996)

21.81 J. Zhang, J. Wang, B. Ge, Y. Liu, X. Hu, R.I. Boughton: Growth, conductivity and generation of blue coherent laser of cesium doped $KTiOPO_4$ crystals, J. Cryst. Growth **267**, 517–521 (2004)

21.82 N. Angert, M. Tseitlin, E. Yashchin, M. Roth: Ferroelectric phase transition temperatures of $KTiOPO_4$ crystals grown from self-fluxes, Appl. Phys. Lett. **67**, 1941–1943 (1995)

21.83 P.A. Morris, A. Ferretti, J.D. Bierlein, G.M. Loiacono: Reduction of the ionic conductivity of flux grown $KTiOPO_4$ crystals, J. Cryst. Growth **109**, 361–366 (1991)

21.84 J. Zhang, J. Wang, B. Ge, Y. Liu, X. Hu, G. Zhao, S. Zhu, R.I. Boughton: Growth, conductivity and periodic poled structure of doped $KTiOPO_4$ and its analogue crystals, Opt. Mater. **28**, 355–359 (2006)

21.85 R. Solé, V. Nikolov, A. Vilalta, J.J. Carvajal, J. Massons, J. Gavaldà, M. Aguiló, F. Díaz: Growth of $KTiOPO_4$ films on $KTi_{1-x}Ge_xOPO_4$ substrates by liquid-phase epitaxy, J. Mater. Res. **17**, 563–569 (2002)

21.86 J.Y. Wang, Y.G. Liu, J.Q. Wei, L.P. Shi, M. Wang: Crystal growth and properties of rubidium titanium oxide phosphate, $RbTiOPO_4$, Z. Kristallogr. **191**, 231–238 (1990)

21.87 S. Ganesa Moorthy, F.J. Kumar, C. Subramanian, G. Bocelli, P. Ramasamy: Structure refinement of nonlinear optical material $K_{0.97}Ti_{0.97}Nb_{0.03}OPO_4$, Mater. Lett. **36**, 266–270 (1998)

21.88 D.Y. Zhang, H.Y. Shen, W. Liu, W.Z. Chen, G.F. Zhang, G. Zhang, R.R. Zeng, C.H. Huang, W.X. Lin, J.K. Liang: Crystal growth, x-ray diffraction and nonlinear optical properties of Nb:$KTiOPO_4$ crystal, J. Cryst. Growth **218**, 98–102 (2000)

21.89 I. Parreu, R. Solé, J. Gavaldà, J. Massons, F. Díaz, M. Aguiló: Crystallization region, crystal growth, and phase transitions of $KNd(PO_3)_4$, Chem. Mater. **15**, 5059–5064 (2003)

21.90 I. Parreu, R. Solé, J. Gavaldà, J. Massons, F. Díaz, M. Aguiló: Crystal growth, structural characterization, and linear thermal evolution of $KGd(PO_3)_4$, Chem. Mater. **17**, 822–828 (2005)

21.91 I. Parreu, J.J. Carvajal, X. Solans, F. Díaz, M. Aguiló: Crystal structure and optical characterization of pure and Nd-substituted type III $KGd(PO_4)_3$: A new material for laser and nonlinear optical applications, Chem. Mater. **18**, 221–228 (2006)

21.92 H.G. Kim, J.K. Kang, S.H. Lee, S.J. Chung: Growth of lithium triborate crystals by the TSSG technique, J. Cryst. Growth **187**, 455–462 (1998)

21.93 B.S.R. Sastry, F.A. Hummel: Studies in lithium oxide systems: I, $Li_2OB_2O_3$–B_2O_3, J. Am. Ceram. Soc. **41**, 7–17 (1958)

21.94 Z. Shuqing, H. Chooen, Z. Hongwu: Growth of lithium triborate (LBO) single crystal fiber by the laser-heated pedestal growth method, J. Cryst. Growth **112**, 283–286 (1990)

21.95 S.A. Guretskii, A.P. Ges, D.I. Zhigunov, A.A. Ignatenko, N.A. Kalanda, L.A. Kurnevich, A.M. Luginets, A.S. Milanov, P.V. Molchan: Growth of lithium triborate single crystals from molten salt solution under various temperature gradients, J. Cryst. Growth **156**, 410–412 (1995)

21.96 D.P. Shumov, V.S. Nikolov, A.T. Nenov: Growth of LiB_3O_5 single crystals in the Li_2O–B_2O_3 system, J. Cryst. Growth **144**, 218–222 (1994)

21.97 T. Ukachi, R.J. Lane, W.R. Bosenberg, C.L. Tang: Phase-matched second-harmonic generation and growth of a LiB_3O_5 crystal, J. Opt. Soc. Am. B **9**, 1128–1133 (1992)

21.98 E. Bruck, R.J. Raymakers, R.K. Route, R.S. Feigelson: Surface stability of lithium triborate crystals grown

from excess B_2O_3 solutions, J. Cryst. Growth **128**, 933–937 (1993)
21.99 J.W. Kim, C.S. Yoon, H.G. Gallagher: The effect of NaCl melt-additive on the growth and morphology of LiB_3O_5 (LBO) crystals, J. Cryst. Growth **222**, 760–766 (2001)
21.100 C. Parfeniuk, I.V. Samarasekera, F. Weinberg: Growth of lithium triborate crystals. I. Mathematical model, J. Cryst. Growth **158**, 514–522 (1996)
21.101 W. Chen, A. Jiang, G. Wang: Growth of high-quality and large-sized β-BaB_2O_4 crystal, J. Cryst. Growth **256**, 383–386 (2003)
21.102 W.R. Bosenberg, R.J. Lane, C.L. Tang: Growth of large, high-quality beta-barium metaborate crystals, J. Cryst. Growth **108**, 394–398 (1991)
21.103 D. Perlov, M. Roth: Isothermal growth of β-barium metaborate single crystals by continuous feeding in the top-seeded solution growth configuration, J. Cryst. Growth **137**, 123–127 (1994)
21.104 M. Roth, D. Perlov: Growth of barium borate crystals from sodium fluoride solutions, J. Cryst. Growth **169**, 734–740 (1996)
21.105 A. Liang, F. Cheng, Q. Lin, Z. Cheng, Y. Zheng: Flux growth of large single crystals of low temperature phase barium metaborate, J. Cryst. Growth **79**, 963–969 (1986)
21.106 R.S. Feigelson, R.J. Raymakers, R.K. Route: Solution growth of barium metaborate crystals by top seeding, J. Cryst. Growth **97**, 352–366 (1989)
21.107 L.H. Brixner, K. Babcock: Inorganic single crystals from reactions in fused salts, Mater. Res. Bull. **3**, 817–824 (1968)
21.108 P.F. Bordui, G.D. Calvert, R. Blachman: Immersion-seeded growth of large barium borate crystals from sodium chloride, J. Cryst. Growth **129**, 371–374 (1993)
21.109 Y.S. Oseledchik, V.V. Osadchuk, A.L. Prosvirnin, A.F. Selevich: Growth of high-quality barium metaborate crystals from Na_2O-NaF solution, J. Cryst. Growth **131**, 199–203 (1993)
21.110 V. Nikolov, P. Peshev, K. Khubanov: On the growth of β-BaB_2O_4 (BBO) single crystals from high-temperature solutions: II. Physicochemical properties of barium borate solutions and estimation of the conditions of stable growth of BBO crystals from them, J. Solid State Chem. **97**, 36–40 (1992)
21.111 Q. Huang, Z. Liang: Studies on flux systems for the single crystal growth of β-BaB_2O_4, J. Cryst. Growth **97**, 720–724 (1989)
21.112 A.E. Kokh, N.G. Kononova, T.B. Bekker, V.A. Vlezko, P.V. Mokrushnikov, V.N. Popov: Change of symmetry and rotation of thermal field as a new method of control of heat and mass transfer in crystal growth (by example of β-BaB_2O_4), Crystallogr. Rep. **50**, 160–166 (2005)
21.113 S.C. Sabharwal, S.M. Goswami, S.K. Kulkarni, B.D. Padalia: Growth, optical transmission and x-ray photoemission studies of BaB_2O_4 single crystals, J. Mater. Sci. Mater. Electron. **11**, 325–329 (2000)
21.114 R. Solé, V. Nikolov, M.C. Pujol, J. Gavaldà, X. Ruíz, J. Massons, M. Aguiló, F. Díaz: Stabilization of β-BaB_{20_4} in the system BaB_2O_4-Na_2O-Nd_2O_3, J. Cryst. Growth **207**, 104–111 (1999)
21.115 H.G. Kim, J.K. Kang, S.J. Park, S.J. Chung: Growth of the nonlinear crystals of lithium triborate and beta barium borate, Opt. Mater. **9**, 356–360 (1998)
21.116 A. Giesen, H. Hügel, A. Voss, K. Wittig, U. Brauch, H. Opower: Scalable concept for diode-pumped high-power solid-state lasers, Appl. Phys. B **58**, 363–372 (1994)
21.117 S. Chénais, F. Balembois, F. Druon, G. Lucas-Leclin, P. Georges: Thermal lensing in diode-pumped ytterbium lasers – Part I: theoretical analysis and wavefront measurements, IEEE J. Quantum Electron. **QE-40**, 1217–1233 (2004)
21.118 C. Stewen, K. Contag, M. Larionov, A. Giesen, H. Hügel: A 1-kW CW thin disc laser, IEEE J. Sel. Top. Quantum Electron. **6**, 650–657 (2000)
21.119 R. Paschotta, J. Aus der Au, G.J. Spühler, S. Erhard, A. Giesen, U. Keller: Passive mode locking of thin-disk lasers: effects of spatial hole burning, Appl. Phys. B **72**, 267–278 (2001)
21.120 U. Griebner, J. Liu, S. Rivier, A. Aznar, R. Grunwald, R.M. Solé, M. Aguiló, F. Díaz, V. Petrov: Laser operation of epitaxially grown Yb:$KLu(WO_4)_2$-$KLu(WO_4)_2$ composites with monoclinic crystalline structure, IEEE J. Quantum Electron. **QE-41**, 408–414 (2005)
21.121 Y.E. Romanyuk, C.N. Borca, M. Pollnau, S. Rivier, V. Petrov, U. Griebner: Yb-doped $KY(WO_4)_2$ planar waveguide laser, Opt. Lett. **31**, 53–55 (2006)
21.122 M.G. Roelofs, A. Ferretti, J.D. Bierlein: Proton-exchanged and ammonium-exchanged waveguides in $KTiOPO_4$, J. Appl. Phys. **73**, 3608–3613 (1993)
21.123 J.D. Bierlein, H. Vanherzeele: Potassium titanyl phosphate-properties and new applications, J. Opt. Soc. Am. B. **6**, 622–633 (1989)
21.124 A. Aznar, R. Solé, M. Aguiló, F. Díaz, U. Griebner, R. Grunwald, V. Petrov: Growth, optical characterization, and laser operation of epitaxial Yb:$KY(WO_4)_2$/$KY(WO_4)_2$ composites with monoclinic structure, Appl. Phys. Lett. **85**, 4313–4315 (2004)
21.125 Y.E. Romanyuk, I. Utke, D. Ehrentraut, V. Apostolopoulos, M. Pollnau, S. Garcia-Revilla, R. Valiente: Low-temperature liquid-phase epitaxy and optical waveguiding of rare-earth-ion-doped $KY(WO_4)_2$ thin layers, J. Cryst. Growth **269**, 377–384 (2004)
21.126 T. Kawaguchi, D.H. Yoon, M. Minakata, Y. Okada, M. Imaeda, T. Fukuda: Growth of high crystalline quality $LiNbO_3$ thin films by a new liquid phase epitaxial technique from a solid-liquid coexisting melt, J. Cryst. Growth **152**, 87–93 (1995)

21.127 E. Bauer: Phänomenologische Theorie der Kristallabscheidung an Oberflächen II, Z. Kristallogr. **110**, 395–431 (1958), in German
21.128 A. Aznar, O. Silvestre, M.C. Pujol, R. Solé, M. Aguiló, F. Díaz: Liquid-phase epitaxy crystal growth of monoclinic $KLu_{1-x}Yb_x(WO_4)_2/KLu(WO_4)_2$ layers, Cryst. Growth Des. **6**, 1781–1787 (2006)
21.129 J.D. Bierlein, A. Ferretti, L.H. Brixner, W.Y. Hsu: Fabrication and characterization of optical waveguides in $KTiOPO_4$, Appl. Phys. Lett. **50**, 1216–1218 (1987)
21.130 A. Raizman, D. Eger, M. Oron: X-ray characterization of Rb exchanged KTP, J. Cryst. Growth **187**, 259–267 (1998)
21.131 L.K. Cheng, J.D. Bierlein, C.M. Foris, A.A. Ballman: Growth of epitaxial thin-films in the $KTiOPO_4$ family of crystals, J. Cryst. Growth **112**, 309–315 (1991)
21.132 L.K. Cheng, J.D. Bierlein, A.A. Ballman: $KTiOP_xAs_{1-x}O_4$ optical wave-guides grown by liquid-phase epitaxy, Appl. Phys. Lett. **58**, 1937–1939 (1991)
21.133 M.A. Harmer, M.G. Roelofs: Sol-gel synthesis of thin-films of potassium titanyl phosphate for nonlinear optical applications, J. Mater. Sci. Lett. **12**, 489–491 (1993)
21.134 F. Xiong, R.P.H. Chang, M.E. Hagerman, V.L. Kozhevnikov, K.R. Pöppelmeier, H. Zhou, G.K. Wong, J.R. Ketterson, C.W. White: Pulsed excimer-laser deposition of potassium titanyl phosphate films, Appl. Phys. Lett. **64**, 161–163 (1994)
21.135 P.M. Lundquist, H. Zhou, D.N. Hahn, J.B. Ketterson, G.K. Wong, M.E. Hagerman, K.R. Pöppelmeier, H.C. Ong, F. Xiong, R.P.H. Chang: Potassium titanyl phosphate thin-films on fused quartz for optical waveguide applications, Appl. Phys. Lett. **66**, 2469–2471 (1995)
21.136 R. Solé, V. Nikolov, A. Vilalta, J.J. Carvajal, J. Massons, J. Gavaldà, M. Aguiló, F. Díaz: Liquid phase epitaxy of $KTiOPO_4$ on $KTi_{1-x}Ge_xOPO_4$ substrates, J. Cryst. Growth **237–239**, 602–607 (2002)
21.137 L.K. Cheng, L.T. Cheng, J. Galperin, P. Morris-Hotsepiller, J.D. Bierlein: Crystal-growth and characterization of $KTiOPO_4$ isomorphs from the self-fluxes, J. Cryst. Growth **137**, 107–115 (1994)
21.138 A. Peña, S. Di Finizio, T. Trifonov, J.J. Carvajal, M. Aguiló, J. Pallares, A. Rodriguez, R. Alcubilla, L.F. Marsal, F. Díaz, J. Martorell: Two dimensional KTP photonic crystal grown using a macroporous silicon template, Adv. Mater. **18**, 2220–2225 (2006)

22. Growth and Characterization of KDP and Its Analogs

Sheng-Lai Wang, Xun Sun, Xu-Tang Tao

Crystals of potassium dihydrogen phosphate (KDP, KH_2PO_4) and its deuterated analogs (DKDP, $K(D_xH_{1-x})_2PO_4$) have been studied for their interesting electrical and optical properties, structural phase transitions, and ease of crystallization. They are the only nonlinear crystals currently applied in inertial confinement fusion (ICF), which has made them a hot topic of research for decades. To yield enough large crystals exceeding 50 cm in all three dimensions, the point-seed technique was recently developed. This method can grow crystals one order of magnitude faster than conventional methods. Recent developments in both the techniques and science of growth phenomena and defect formation under various conditions are described in this chapter, which also reviews significant advances in understanding of the fundamentals of KDP crystal growth, other growth methods to yield large high-quality crystals, growth defects and optical performance, and evaluations of crystal quality.

22.1 **Background** 759
22.2 **Mechanism and Kinetics of Crystallization** 761
22.2.1 Studies of KDP Crystal Surfaces 761
22.2.2 Nucleation Studies in Supersaturated Solution 763
22.2.3 Dislocation Mechanism 765
22.2.4 Growth on Two-Dimensional Nuclei 767
22.2.5 Growth from Crystal Edges 767
22.3 **Growth Techniques for Single Crystals** 769
22.3.1 Parameters Affecting Growth Rate .. 769
22.3.2 Stability of Solution 770
22.3.3 Conventional Methods 771
22.3.4 Rapid Growth from a Point Seed 773
22.4 **Effect of Growth Conditions on Defects of Crystals** 776
22.4.1 Impurity Effect 776
22.4.2 Supersaturation 779
22.4.3 Filtration 780
22.4.4 Hydrodynamic Effects 781
22.5 **Investigations on Crystal Quality** 783
22.5.1 Spectroscopic Studies 783
22.5.2 Homogeneity 784
22.5.3 Laser Damage Threshold 787
References 789

22.1 Background

Crystals of potassium dihydrogen phosphate (KDP) and its isomorphs have been the subject of a wide variety of investigations for over half a century owing to their interesting electrical and optical properties, structural phase transitions, and ease of crystallization [22.1–4]. Today, these crystals are widely used in both laboratory and industrial settings to control the parameters of laser light, such as pulse width, polarization, and frequency, through first- and second-order electrooptic effects [22.4, 5]. Their application in inertial confinement fusion (ICF) research [22.6] has made them a hot topic of research for decades.

The very high-energy Nd-glass lasers used for ICF research need large plates of nonlinear crystals for electrooptic switches and frequency converters (Fig. 22.1). The lasers under construction in the USA and France with about $40\times40\,cm^2$ aperture require single-crystal boules with linear dimensions in the 50–100 cm range. KDP (KH_2PO_4) and its deuterated analogs DKDP ($K(D_xH_{1-x})_2PO_4$) are the only nonlinear crystals currently used for these applications due to their unique physical properties, which include transparency over a wide region of the optical spectrum, resistance to damage by laser radiation, and relatively high nonlin-

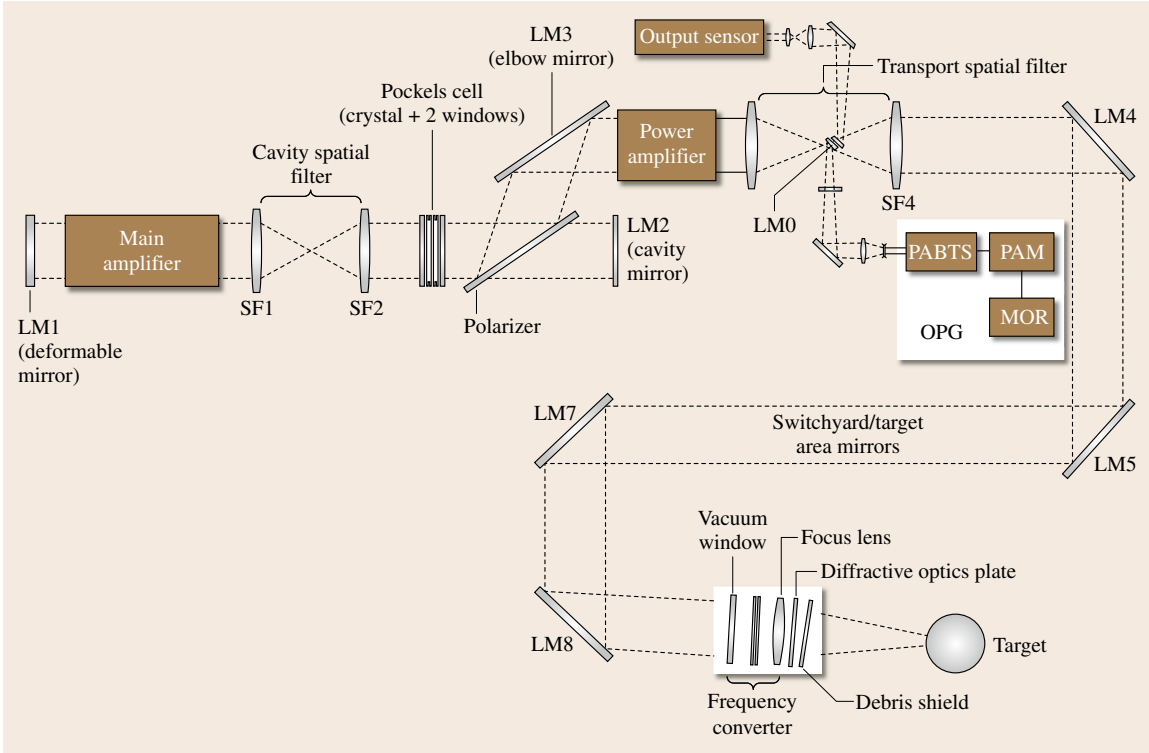


Fig. 22.1 Schematics of single NIF beamline showing positions of major optical components (after [22.7], with permission of ASM) (LM – laser mirror, SF – spatial filter, OPG – optical pulse generation)

ear efficiency, in combination with reproducible growth to large size and perfection.

The main limitation in growth of such large crystals by traditional techniques is the growth rates of only 0.5–1 mm/day typical for low-temperature solution growth, which leads to growth cycles exceeding 1–2 years. Work on rapid growth of KDP crystals started in the early 1980s when the world's biggest laser of that time, Nova, was being built at the Lawrence Livermore National Laboratory (LLNL). New rapid growth techniques [22.9–11] explored at that time involved radical modification of standard crystallization equipment. However, the complicated designs proposed could not solve the problems such as hydrodynamic conditions [22.9] and control of high supersaturation needed to avoid defect formation and spontaneous nucleation [22.10]. As a result, the $27 \times 27\,\mathrm{cm}^2$ plates of KDP crystals for the frequency-conversion arrays on Nova were grown by traditional techniques.

Also, a rapid crystal growth method called the point-seed technique, based on the traditional solution growth process, was initiated at Moscow State University [22.12]. This technique demonstrated that KDP and DKDP crystals could be grown in standard Holden-

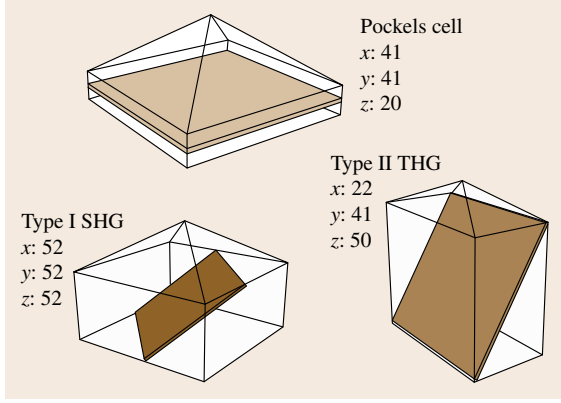


Fig. 22.2 The minimum size of KDP single-crystal boules (in cm) needed for obtaining Pockels cell and harmonic-generation plates of different types for the NIF project (after [22.8], with permission of Elsevier) (SHG – second harmonic-generation, THG – third harmonic-generation)

type rotary crystallizers without spontaneous nucleation and visible defects, one to two orders of magnitude faster than by conventional methods. Later this method was further developed and scaled for production of crystals for Nova's successor – the National Ignition Facility (NIF), under construction at LLNL [22.8]. To achieve economically useful yield, crystals grown for NIF should exceed 50 cm in all three dimensions (Fig. 22.2).

The development of new techniques required both technical solutions and scientific knowledge about growth phenomena, defect formation at varying degrees of supersaturation, and growth rate. The purpose of this chapter is to describe recent developments in growth and characterization of KDP and its analogs. The chapter also includes significant advances in understanding the fundamentals of KDP crystal growth, developing growth methods to yield large-dimension high-quality crystals, and the relation between growth defects and optical performance. To this end, the chapter is divided into four sections encompassing the mechanism and kinetics of crystallization, growth techniques for single crystals, the effect of growth conditions on crystal defects, and problems with crystal quality.

22.2 Mechanism and Kinetics of Crystallization

As we know, since the growth of crystals takes place at the crystal–solution interface, structural information on the immersed solid is essential for understanding crystal growth from solution or melt. This is also a very important topic for KDP-type crystals, which can help us to understand the relaxations and possible reconstructions of the top layers, the influence of impurities on morphology, and even the possible reason for change in optical properties of crystals.

22.2.1 Studies of KDP Crystal Surfaces

The crystallographic theory of Hartman and Perdok aims to predict the morphology of growing crystals dominated by the so-called F (flat) faces, referred to by the Miller indices (*hkl*) [22.14, 15]. However, the theory has its limitations. Often more than one surface termination is possible for a given orientation (*hkl*) and it is impossible to predict which of the alternatives will control the crystal growth.

The theory predicts that the pyramidal faces {101} and the prismatic faces {100} of KDP are flat in solution [22.16, 17], in agreement with the observed habit of these crystals (Fig. 22.3a). For the prismatic {100} faces exactly one surface termination is predicted (Fig. 22.4). For the pyramidal {101} faces, however, two alternative terminations are theoretically possible. One has the negative $H_2PO_4^-$ groups on the outside, and the other the positive K^+ ions (Fig. 22.3b). The difference in polarity of the layers and, especially, the differences in size and polarizability of the ions will result in a different surface free energy. From the surface morphology observed with interference-contrast reflection microscopy

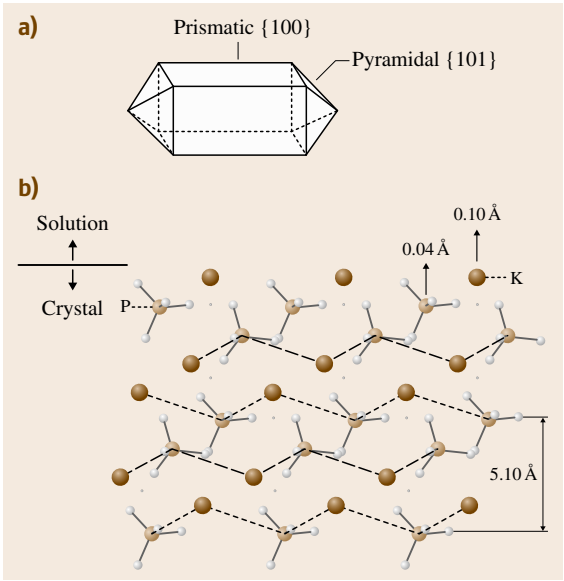


Fig. 22.3 (**a**) Growth habit of a KDP crystal with the prismatic and pyramidal faces indicated. (**b**) Schematic side view of the pyramidal face, KDP {101}, projected on the {111} plane. The *big circles* are the potassium atoms while the PO_4 groups are depicted as a *circle* for the phosphor atom connected by sticks to the four neighboring oxygen atoms, shown as *small white circles*. The *dots* give the positions of the hydrogen atoms between two oxygen atoms. The layers with the K^+ ions on top are schematically indicated by the *dashed lines* and the layers with the $H_2PO_4^-$ groups on top by the *discontinuous lines*. *Arrows* indicate the relaxations in the topmost layer as determined from fitting the experimental data (after [22.13])

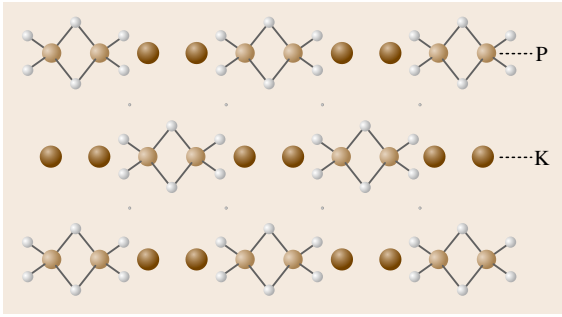


Fig. 22.4 The prismatic KD P{100} face projected on the {010} plane. Here only one termination is possible (after [22.13])

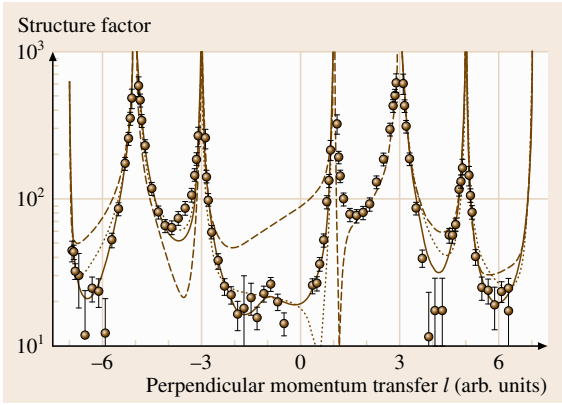


Fig. 22.5 Structure-factor amplitudes along the $(hk) = (10)$ crystal truncation rod for KDP {101} as a function of the diffraction index, which is expressed in reciprocal lattice units. The *dotted line* is a calculation for a bulk K^+-terminated surface, the *dashed curve* for a $H_2PO_4^-$-terminated one. The *solid line* is the best fit starting from a K^+-terminated surface and allowing the K^+ ions and the $H_2PO_4^-$ groups in the top layer to relax (after [22.13])

and considering the symmetry of the crystal [22.17, 18] it can be concluded that the surface is bounded by only one of the polar layers. This is confirmed by atomic force microscopy measurements where the height of the steps on the {101} face is always found to correspond to 0.5 nm, the thickness of double layers [22.19].

De Vries and coworkers used the technique of surface x-ray diffraction at a third-generation synchrotron radiation source to determine the structure of KDP crystal surfaces in air, vacuum, and solution [22.13, 20]. They measured the distribution of diffracted intensities along so-called crystal truncation rods (CTRs) [22.21], which is hardly influenced by the solution and mainly depends on the crystal surface atomic structure. All data show that the pyramidal {101} faces are terminated with K^+ atoms rather than with $H_2PO_4^-$ groups, while the prismatic {100} faces terminate in alternating rows of K^+ and $H_2PO_4^-$ ions (Fig. 22.5).

From the atomic structure of both faces, it is easy to be understood why small traces of trivalent metal ion impurities such as Fe^{3+} or Cr^{3+} block the growth of the prismatic faces, but affect the growth of the pyramidal faces to a much lesser extent [22.17, 22, 23]. With only K^+ ions on the surface of the crystal, metal impurities such as Fe^{3+} and Cr^{3+} ions will experience a large barrier to adsorption onto the positively charged face. The impurity content is limited by adsorption kinetics on the terraces rather than incorporation kinetics at the steps. On the prismatic faces, however, these ions can adsorb easily, and small amounts of Fe^{3+} or Cr^{3+} will already block the growth.

Furthermore, De Vries et al. present the results of experiments about the solid–liquid interface during growth, with and without the addition of Fe^{3+} impurities. The surface was roughened, as seen from the decrease in intensity in between the Bragg peaks. The overall shape of the CTR is unchanged, so no ordered layer of Fe^{3+} is formed on the surface. Apparently, the amounts of adsorbed Fe^{3+} are very small. These impurities locally pin the moving steps [22.24–26], which causes an increased meandering of the steps and thus leads to a rougher surface.

The molecular structure of interface boundary layers in the crystal growth of KDP and DKDP has been an interesting topic for a long period. The Raman spectra of saturated KDP solution show that only 40% of the phosphates exist as monomers and that anion–anion association via hydrogen bonds does cease at the dimer [22.27]. *Lu* et al. [22.28] studied the growth units of KDP crystal from the growth solution by using space group theoretical analyses and Raman spectra; the result proved that the growth unit is dimers of $[H_2PO_4^-]$ anions. *Yu* et al. [22.29] used holography to measure the thickness of boundary layers to be a few hundred micrometers during KDP crystal growth in free convection. Their real-time Raman microprobe experiments show that the smectic ordering structure of the anions–cations called the crystallization unit is formed within the boundary layer of KDP and DKDP growth solutions [22.30].

An in situ x-ray diffraction study of growth surface by *Reedijk* et al. [22.31] revealed interface-induced ordering in the first four layers of water molecules. The first two layers behave ice-like and are strongly bound

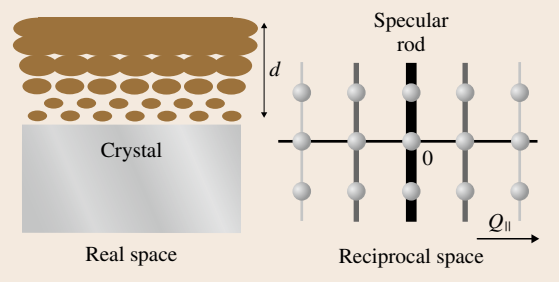


Fig. 22.6 Schematic drawing of a crystal covered with a partly ordered liquid layer of thickness d. The contribution of the (partially) ordered liquid to the substrate diffraction rods is strongest in the specular rod and diminishes at higher parallel momentum transfer ($Q_{\|}$) in reciprocal space (after [22.31])

to the surface. The next two layers are more diffuse and show only minor lateral and perpendicular ordering (Fig. 22.6). The highly ordered *liquid* at the interface is expected to slow down the incorporation and diffusion of the growth units.

Further research [22.33] on the solid–liquid interface structure of the {101} and {100} faces of KDP crystals in contact with growth solutions of different pH values showed in all cases several liquid layers with varying degrees of lateral and perpendicular order. The structural changes are large for the {101} face and small for the {100} face. The changes at the {101} face are likely due to the pH-dependent competition between K^+ and H_3O^+ bonding.

22.2.2 Nucleation Studies in Supersaturated Solution

Nucleation theory has developed since the early 18th century. *Mullin* [22.34] classified nucleation into two major group: primary nucleation and secondary nucleation, where nuclei are generated in the vicinity of crystals already present in a supersaturated system. Primary nucleation consists of homogeneous nucleation and heterogeneous nucleation. The study on the stability of solution by *Zaitseva* et al. [22.32] provided the basis to develop fast growth techniques for KDP and DKDP crystals.

Primary Nucleation

Cooling a solution with concentration C to a temperature T under its equilibrium temperature leads to a supersaturated solution. The supersaturation ΔC is $C - C_0$. In classic nucleation theory, the homogeneous nucleation rate of the supersaturated solutions, i.e., the frequency of formation of a particle with critical nucleus in a unit volume, is expressed as

$$J = B_1 \exp\left(-\frac{16\pi\alpha^3\omega^3}{3k_B^3T^3\left(\ln\frac{C}{C_0}\right)^2}\right) . \qquad (22.1)$$

The induction period is inversely proportional to the nucleation rate, which leads to the expression

$$\mathrm{int_i} = B + \frac{16\pi\alpha^3\omega^3}{3k_B^3T^3\left(\ln\frac{C}{C_0}\right)^2} . \qquad (22.2)$$

Equations (22.1) and (22.2) express the width of the metastable zone in terms of the supersaturation and induction time for homogeneous nucleation. However, the quantitative estimation of these parameters for real crystallization systems using these equations is practically impossible because of the many unknown parameters, such as α, the specific free energy of the interface, that form the constants. It is not of much help in practical work because a real growth system obviously does not deal with homogenous nucleation. The presence of crystallizer walls, parts of equipment, and extraneous particles in the supersaturated solution makes heterogeneous nucleation more probable. Some theoretical calculations and experiments in pure containerless systems show that homogeneous nucleation occurs at extremely high concentrations, exceeding the solubility limit by several factors [22.35–37].

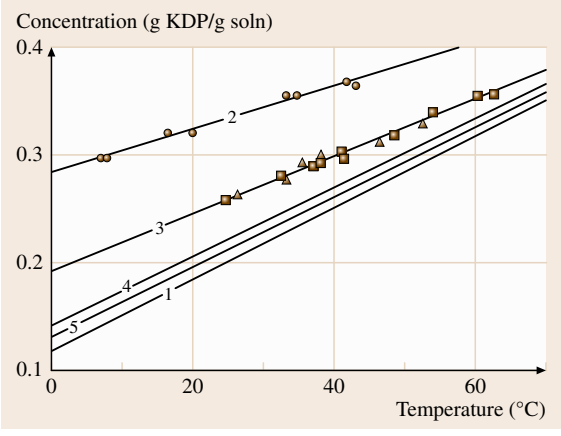


Fig. 22.7 Stability of supersaturated KDP solutions: (1) solubility curve; (2) and (3) metastable boundaries of solutions without (●) and with (■) a growing crystal, respectively; (▲) experiments with the empty platform; (4) and (5) traditional level of stability (after [22.32])

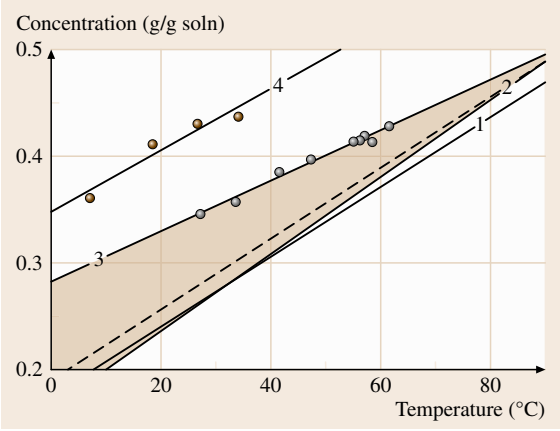


Fig. 22.8 Metastable zone of DKDP solutions ($X = 98\%$). (1) Monoclinic phase solubility. (2) Tetragonal phase solubility. (3) Metastable boundary in the presence of a growing crystal. The region of tetragonal crystals growth is shaded. For comparison the data of [22.38] are shown (*dashed line*). (4) Metastable boundary without crystals (after [22.32])

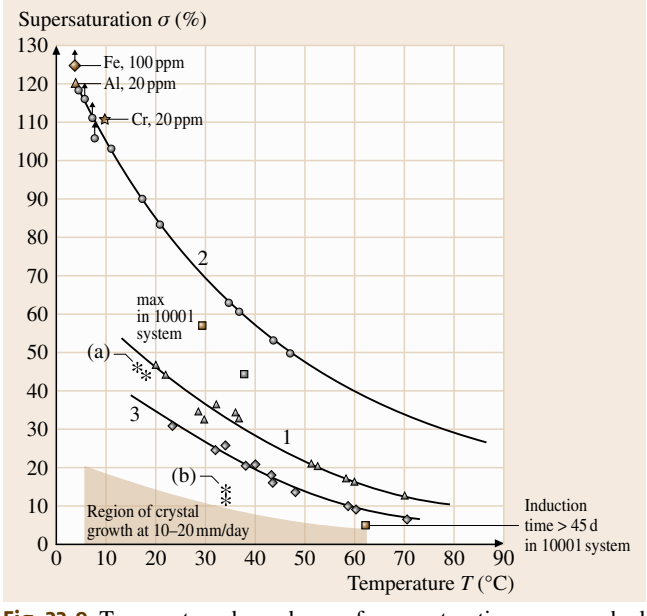


Fig. 22.9 Temperature dependence of supersaturation σ_{max} reached in KDP solutions without spontaneous nucleation: (○) filtered and (△) unfiltered solutions without crystals overheated at 80 °C; (◇) filtered solution in the presence of a crystal overheated at 80 °C; (∗) filtered (a) and unfiltered (b) solutions without crystals overheated at 54 °C (after [22.42])

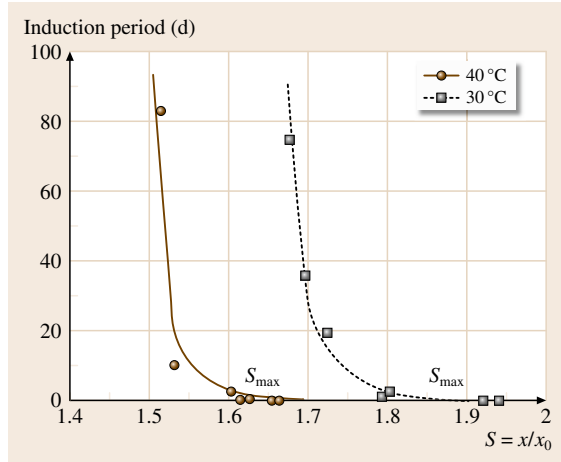


Fig. 22.10 Effect of supersaturation on induction period in KDP solutions (after [22.32])

In order to understand the nature of nucleation in a real crystallization system there was no other way but to perform experiments in the system. *Zaitseva* et al. measured the metastable zone of KDP solution by the polythermal method in standard Holden-type crystallizers with volumes of 5–201 and 10001 [22.32]. Figures 22.7–22.9 present the results, which show the maximum concentration and supersaturation reached without spontaneous nucleation in stirred KDP and DKDP solutions without growing crystals. The level of supersaturation that can be reached is much higher than that expected from previous studies [22.10, 38]. The experiments show a much narrower metastable zone when the solution is not filtered. The drop of stability is due to the effect of typical heterogeneous particles present in the salts generated during their commercial production. Insufficient overheating can cause a similar drop in stability as in the absence of filtration. Solution overheating of 80 °C can result in reproducible stability, independent of the saturation temperature. They found no correlation between spontaneous nucleation and the chemical purity of the solutions, which is different from other investigations [22.34, 39–41].

The induction period was also measured for various supersaturated solutions by the isothermal method in the same crystallizers [22.32]. The results (presented in Fig. 22.10) show a sharp increase of induction period at supersaturation of less than some certain values (35% for 40 °C, 50% for 30 °C). Experimentally this means that no precipitation was observed for 3 months with supercooling more than 30 °C below the saturation point.

Secondary Nucleation

Secondary nucleation is more difficult to explain in detail as there are at least three categories of secondary nucleation: apparent (small fragments washed from the surface of crystalline seeds), true (when the current level of supersaturation is higher than the supersaturation level or the solute particles present in solution), and contact nucleation (when a growing particle contacts the walls of the baffles, stirrer or other objects, thus leaving behind residual solute particles that have been broken off from primary crystals) [22.43].

Randolph and *Larsen* stated that, in either continuously stirred crystallizers or seeded batch crystallizers, the main source of secondary nuclei is the crystal suspension itself [22.44]. *Boistele* also agrees that a major source is the crystal surface; secondary nuclei form whenever the tiny embryos, or crystallites, that are removed from the surface and dispersed into a supersaturated solution exceed the critical size [22.45].

Secondary nucleation initiated by a well-faceted crystal is often treated as aggregates appearing and being held in a stagnant supersaturated (transitional boundary) layer under the influence of the force field of the crystal [22.46]. These aggregates are thought to be stripped off the crystal surface by fluid motion, providing secondary nuclei [22.46, 47]. However, there is still a certain contradiction, as supersaturation in the immediate vicinity of the growing crystal is lower than elsewhere in the solution.

Most empirical expressions based on the results obtained in real crystallization systems predict very narrow metastable regions with a width of a few degrees [22.38, 48–50]. However, the metastable zone reported by *Zaitseva* et al. is much larger than those listed above [22.32]. The experiments show that a defectless crystal does not produce any secondary nucleation and does not influence spontaneous nucleation from solution. The initial results shown in Figs. 22.7–22.9 show that the presence of a growing crystal reduces the solution stability, which was supposed to not be caused by secondary nucleation but rather by introduction of the platform into the otherwise closed system.

22.2.3 Dislocation Mechanism

The bulk of a faceted crystal is built up by deposition of surface layers parallel to the crystallographic faces. Recent experimental studies by means of optical interferometry [22.1] and atomic force microscopy (AFM) [22.25, 51] present clear evidence that the dislocation growth mechanism remains dominant during the growth of KDP-type crystals. Dislocation bunches which give rise to growth hillocks on crystal faces form during seed regeneration. During further growth, dislocations arise from mutual displacement of the layers overlapping a solution inclusion or an extraneous particle. Two or more growth sources of the same activity can exist on a face simultaneously. The growth sources initiated during regeneration can be replaced by new leading hillocks that become more active under the changing conditions. The change of the leading hillock is inevitably accompanied by the formation of growth bands due to the appearance of new growth steps of various orientations [22.52]. When very strong and dense dislocation bunches form, cracking may occur due to great internal stress in the crystal during the growth process [22.53].

Dislocation hillocks on the pyramidal {101} and prismatic {100} faces of KDP and DKDP crystals have the different shapes shown in Fig. 22.11. The shapes of the hillocks reflect the crystallography of the face such that each hillock is comprised of a set of sectors with unique slopes and step. Growth occurs on monomolecular steps, and the hillocks on the {101} faces are shaped as trihedral pyramids with three neighboring slopes (vicinal sectors) of different steepness. The hillocks on the {100} faces have an elliptical shape that changes from almost round to nearly a parallelogram with four vicinal sectors at increasing supersaturation [22.1]. The intersection of the vicinal sectors of the hillocks form the edges of a hillock, called vicinal-sectoral boundaries, which are typically straight lines on both sets of faces. Intervicinal boundaries are the geometrical

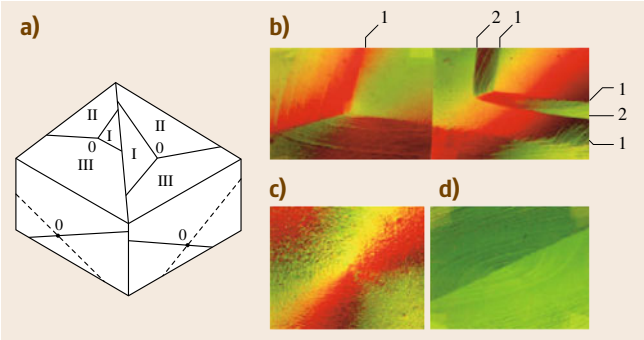


Fig. 22.11a–d Geometry and shape of the dislocation hillocks of KDP: **(a)** position on the adjacent faces; I, II, and III are vicinal sectors on {101} faces. **(b)** Micrograph of the hillocks on {101} face; 1 – vicinal boundaries; 2 – intervicinal boundary; as grown surface at $t = 30\,^{\circ}\mathrm{C}$ and $\sigma = 0.06$; **(c,d)** growth hillocks on {100} face of KDP at low and high supersaturation, respectively (after [22.42])

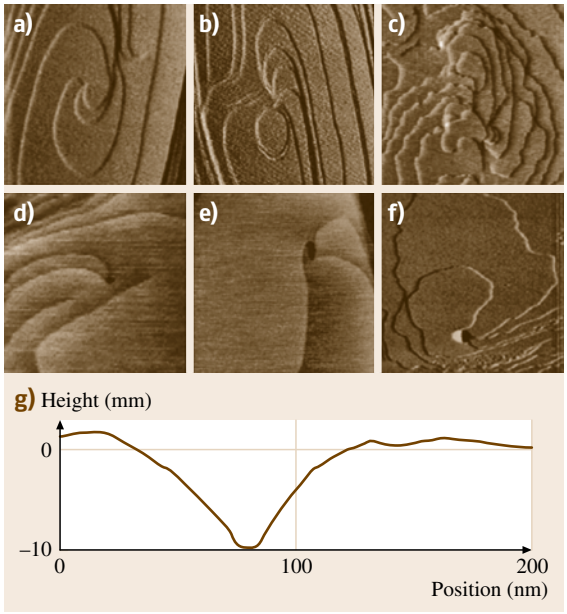


Fig. 22.12a–g AFM images of typical growth hillocks on {100} face of KDP showing complex structure of dislocation sources **(a–c)** and {101} face showing hollow cores at dislocation sources **(d–f)**: cross-section of typical hollow core is shown in **(g)** (after [22.7]). **(a)** $1\times1\,\mu m^2$; **(b)** $1.5\times1.5\,\mu m^2$; **(c)** $2\times2\,\mu m^2$; **(d)** $3\times3\,\mu m^2$; **(e)** $2.6\times2.6\,\mu m^2$; **(f)** $8.4\times8.4\,\mu m^2$

points where the steps from the neighboring vicinal hillocks meet [22.42]. The position of the vicinal-sectoral boundaries is determined by the location of the dislocation outcrop on a crystal face. Their orientation, strictly connected with the crystal symmetry, can vary only within several degrees, depending on growth conditions [22.1, 54].

The AFM studies revealed that, for Burgers vectors in excess of one unit step, even simple sources exhibit hollow cores at the dislocation source on {101} faces (Fig. 22.12) [22.7, 19]. The shape of the cores demonstrates that the step edge energy is isotropic. X-ray projection topograph of a {101} KDP plate shows that the adjacent vicinal sectors are each slightly disoriented relative to the others, and the average difference of the lattice parameters is of the order of 10^{-6} of the average lattice parameter value (Fig. 22.13) [22.18, 55]. As a rule, the lattice deformations are maximal at these boundaries that form the vicinal sector I on {101} faces, whereas the steps of the vicinal sectors II and III smoothly convert into each other without clearly discernible deformations. Different impurities selectively

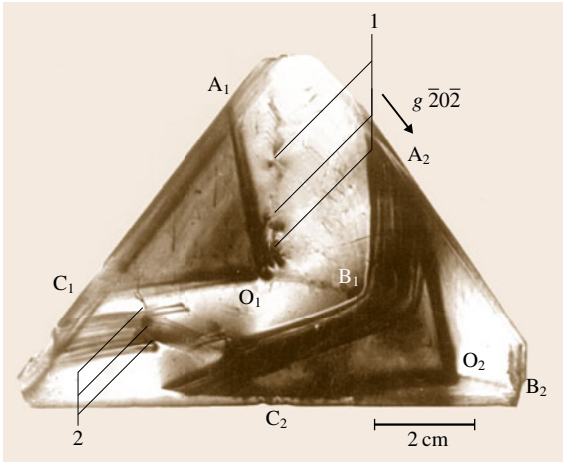


Fig. 22.13 Projection x-ray topograph of a plate cut parallel to the {101} dipyramid face of KDP crystal. O_1 and O_2, are tips of vicinal hillocks formed by dislocations, O_1A_1 , O_1B_1, O_1C_1 and O_2A_2, O_2B_2, O_2C_2, are vicinal-sectorial boundaries, $A_2B_1C_2$ is an intervicinal boundary; 1, 2 are dislocations which do not form vicinal hillocks (after [22.42])

incorporate into the different vicinal sectors depending on their nature [22.55]. For example, Fe^{3+} and other metal impurities preferentially incorporate into sector I [22.56]. In DKDP crystals this defect can be

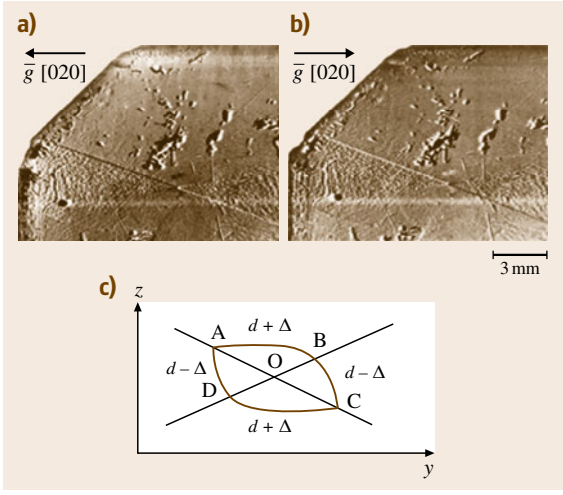


Fig. 22.14a–c X-ray topographic images of a vicinal hillock on the prismatic face of a KDP crystal **(a,b)** and diagram with notations for analyzing the contrast **(c)**. d – lattice parameter, Δ – the difference of the parameter in adjacent vicinal sectors (after [22.42])

more pronounced because of the different composition of deuterium and hydrogen in the three vicinal sectors [22.42].

On the {100} face, the dislocation sources are often complex (Fig. 22.14). Vicinal hillocks on the face are shown in Fig. 22.11. Growth steps change their orientation on the edge AC abruptly, while on the edge BD the orientation changes more smoothly. The x-ray topograph reveals that the lattice parameters are greater in vicinal sectors AOB and COD than in sectors BOC and AOD [22.42]. Formation of these vicinal sectors can be also explained by the different incorporation of impurities into the differently oriented steps.

22.2.4 Growth on Two-Dimensional Nuclei

The main mechanism of growth was clear because the dislocation growth sources could be easily seen on the growing faces. At the same time, the growth of KDP {101} surfaces occurs also on islands formed by two-dimensional (2-D) nucleation (Fig. 22.16) at moderate supersaturations (10%) [22.19]. Furthermore, on the terraces of the vicinal hillocks formed by 2-D nucleation, island growth competes with step flow when the interisland spacing is comparable to the terrace width. For example, 2-D nucleation [22.57, 58] was found to contribute to the rapid growth of crystal on the *negative* pyramidal faces $\{10\bar{1}\}$ just above the platform (Fig. 22.15). All the dislocations formed during regeneration very quickly vanish from these negative pyramidal faces because of their orientation at some angle to the platform surface. The dislocation-free growth rate measured in the range of 63–60 °C at $a = 0.06$ is about one order of magnitude (1–1.5 mm/day) slower than for the case of dislocation growth (about 15–17 mm/day under the same conditions).

De Yoreo et al. [22.19] estimated that, at supersaturation below 5%, layer growth on {101} faces is dominated by the dislocation mechanism, and that growth on 2-D nuclei begins to compete at 5–10% supersaturation. Results from *Alexandru* [22.59] showed that growth by the dislocation mechanism on {100} surface is severely retarded by the stopper action of impurities, particularly towards smaller supersaturation. At supersaturation less than 8–10% the dislocation mechanism of growth appears to compete with 2-D nucleation mechanism at lower impurity concentration. The two-dimensional nucleation mechanism of growth becomes dominant at higher supersaturation.

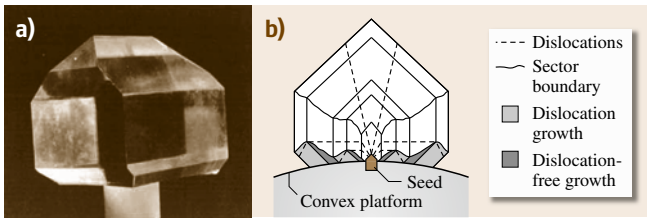


Fig. 22.15 **(a)** KDP crystal with clearly pronounced {101} low pyramids growing periodically by dislocation and dislocation-free mechanism; **(b)** schematic of dislocation geometry on convex-shaped platform (after [22.42])

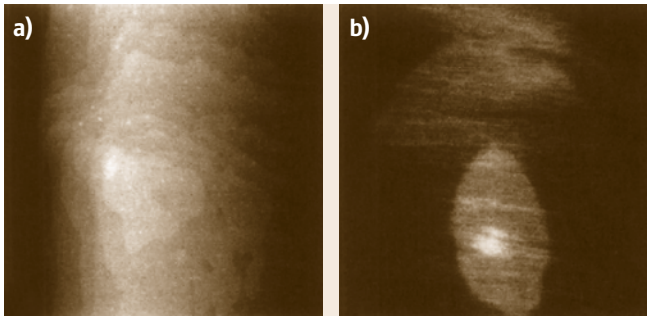


Fig. 22.16 **(a)** AFM image ($5.4 \times 5.4\,\mu m^2$) of typical hillock on KDP {101} at which no dislocations are observed. **(b)** Higher-resolution ($715 \times 715\,nm^2$) image of one such hillock showing the topmost island, for which the radius is 42 nm (after [22.19])

22.2.5 Growth from Crystal Edges

Existing models of dislocation growth typically do not take into account mutual effects of growing crystal faces and participation of the edges in the growth process. The edges of faceted crystals are often considered as passive places where the steps produced on adjacent faces meet, although evidence of growth-step generation from the edges has been reported in many experimental works [22.60, 61].

Zaitseva et al. proposed a possible mechanism of growth-step generation from the edges of faceted crystals obtained from experimental observations with KDP crystals [22.62]. It suggests that growth from the crystal edges is initiated by the deviation of the edges from their crystallographic orientation and formation of incomplete shapes of singular facets. An incomplete crystallographic shape of a singular face is determined by the existence of concave angles formed by the edges in the plane of this face. These concave angles are sources of growth steps in the surface layer. The surface layer generated from a concave angle on a singular

crystal face completes the crystallographic shape of the face. Growth of this surface layer does not require the existence of a preceding layer of the same orientation.

Formation of the layers on the crystal edges, such as the z-cut seed regeneration process, can be observed during growth of KDP crystals. The thin surface layers can grow from the edges in crystallographic planes without pre-existing layers under them. A typical explanation for this phenomenon is attributed to a supersaturation gradient and better hydrodynamic conditions on the edges [22.63].

Experiments [22.62] including regeneration of singular faces with incomplete crystallographic shape (Fig. 22.17) and formation of the thin surface layers during joining of two equally oriented crystals were performed to clarify what effect such deviations produce during growth and formation of the surface structure. These experiments suggested that the process of step generation from the edges was connected with the deviation of faces from crystallographic orientations and shape, resulting from vicinal hillocks on the crystal surface.

The growth velocity of these layers has the same order of magnitude as the tangential growth rate V of a dislocation step. Estimations give values for the velocity of the thin-film advancement of 1×10^{-4}–4×10^{-4} cm/s at temperature of 30 °C and supersaturation of about 0.09, while the value of V from [22.64] is 7×10^{-4} cm/s for about the same growth conditions. The measurements done at 60 °C gave higher values of about 1×10^{-3} cm/s at approximately the same supersaturation [22.62].

According to this mechanism, the crystal surface should be considered as an entire system. The structure of one separate face is connected with the phenomena that take place on the other faces through the crystal edges, which play an important role during crystal growth. During the growth of faceted crystals, this mechanism may work in combination with the dislo-

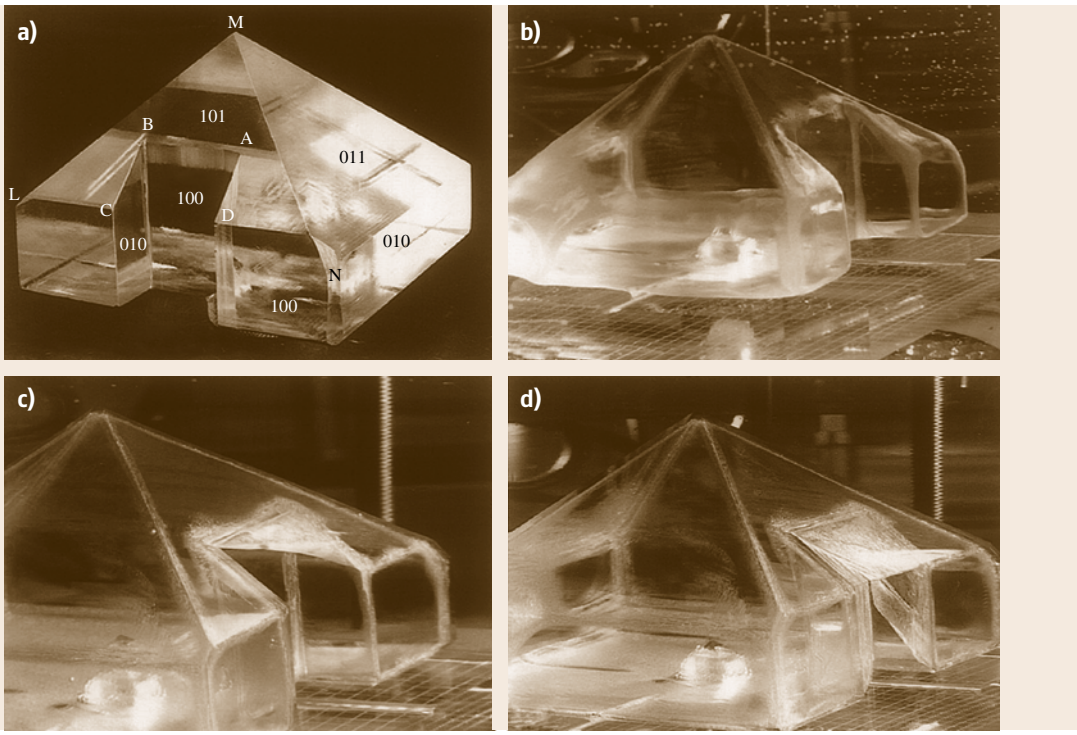


Fig. 22.17a–d Regeneration of KDP crystal surfaces of incomplete crystallographic shape: **(a)** initial crystal with a removed part; **(b)** first stage of the regeneration process; **(c)** formation of a thin surface layer from concave angles A and B on the edge of the {101} face; **(d)** formation of the {100} surface by thin layers; $t_0 = 65$ °C; $\sigma = 0.08$; crystal cross section about 10×10 cm^2 (after [22.62])

cation mechanism of growth. Dislocation sources of steps form vicinal slopes which lead to a deviation of the crystal faces and edges from their crystallographic orientation. The reconstruction of the complete crystallographic shape of adjacent faces occurs by the incorporation of building units into the crystal edges. This process results in the generation of growth steps to the deviated faces. The deviation from singularity caused by the presence of vicinal slopes of a crystal face is compensated for and corrected by growth steps generated from the edges.

However, the question that still exists is why these crystals grow not by close packing of the volume but by creating thin surface layers and hollow spaces under them. Formation of the thin layers creates at least double the surface area. In this regard, close packing should be more beneficial because of minimization of the surface energy.

22.3 Growth Techniques for Single Crystals

There have been more than 80 years of research on the growth of KDP/DKDP crystals. The need for large single-crystal plates for use as Q-switches and laser radiation converters [22.6] has stimulated the development of growth techniques for KDP crystals, but the key problems to be solved are centered on the rapidly growing large-aperture crystals and improving the optical quality of the crystal.

22.3.1 Parameters Affecting Growth Rate

The growth rate of KDP crystals depends on many parameters, such as growth temperature, supersaturation of growth solution, impurities, and hydrodynamic conditions, as described in detail by *Zaitseva* et al. [22.55] and other authors [22.7, 66–68]. KDP/DKDP crystals typically grow by the screw dislocation mechanism. The growth rate R of a crystal face in the direction normal to it is given by the geometrical relation

$$R = pV \,. \tag{22.3}$$

Here p is the slope of the dislocation hillock and V is the tangential speed of the elementary steps. As follows from (22.3), the hillock structure and the step velocity affect the growth rate. In the kinetic limit, the step speed V is linearly connected with the supersaturation σ through

$$V = b\beta\sigma \,, \tag{22.4}$$

$$\beta = \beta_0 \exp(-E_A/k_B T) \,, \tag{22.5}$$

where b and β_0 are constants, β is the kinetic coefficient, E_A is the activation barrier of the slowest stage of growth, T is the temperature, and k_B is the Boltzmann constant. According to (22.4) and (22.5), the step speed V can be increased by increasing either σ or T. Increasing supersaturation has always been known as an obvious way to accelerate crystal growth. The shift of the growth process to higher temperature can also increase the growth rate by increasing the value of the kinetic coefficient [22.65, 69]. In agreement with the above analysis, the growth rates empirically measured by *Zaitseva* et al. [22.42] show very close relationship with temperature T and supersaturation σ, as shown in Fig. 22.18.

The slope p in the expression (22.3) is determined by the structure of a dislocation hillock. It depends on the amount of dislocations in the growth source m; the distance between them, defined by the length $2L$; the el-

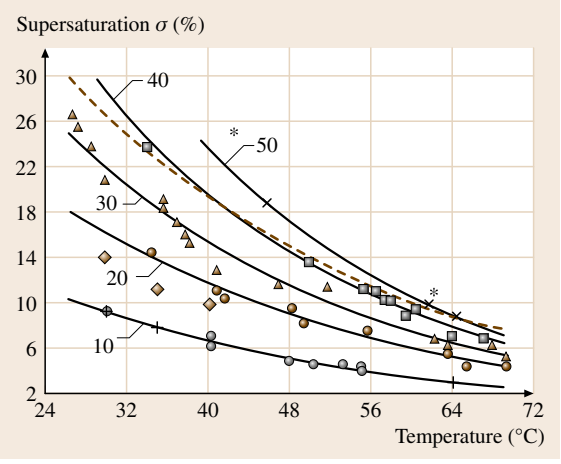


Fig. 22.18 Temperature dependence $\sigma(T)$ corresponding to approximately constant growth rates of KDP crystals Rz: 10 mm/day (○), 20 (●), 30 (▲), 40 (□), 50 (×), and 60 (∗); + and ◆ are data from [22.65] for 10 and 20 mm/day, respectively. The *dashed line* is the boundary of the metastable zone (after [22.42], with permission of Elsevier)

ementary step height h; and the critical radius r_c, given by

$$p = mh/(19r_c + 2L)\,, \tag{22.6}$$

$$r_c = \omega\alpha/k_B T\sigma\,, \tag{22.7}$$

where ω is the volume of a molecule of the crystallizing matter and α is the specific free energy of a step edge. Expression (22.7) is obtained from the Gibbs–Thomson formula. According to (22.6) and (22.7), p (and hence R) can be increased by increasing σ or changing the number of dislocations in the growth source. Direct control of the growth rate by changing the dislocation structure is difficult because of the complicated relationship between the structure of a dislocation source, σ, and T [22.71]. However, as recently shown [22.68], for $\sigma > 5\%$ the activity of a growth hillock is dominated by the presence of strain-induced dislocation cores and is nearly independent of σ.

There are two more important parameters affecting growth rate: impurities and mass transfer, or hydrodynamic conditions. The metallic cations, especially those with high valency, were considered to greatly affect the growth rate. It is well known that metallic cations (such as Sn^{4+}, Fe^{3+}, Cr^{3+}, and Al^{3+}) affect the growth rate of prismatic faces of KDP crystals much more than the pyramidal ones [22.72]. Fe^{3+} and Al^{3+} ions can decelerate the growth rate of {100} faces [22.66]. With increasing impurity concentration of Fe^{3+} or Cr^{3+} ions, the crystal growth rate of {101} faces first increases and then decreases [22.67]. Sn^{4+} ions can decrease the growth rate of both {100} and {101} faces [22.73].

Anions with strong H-bond affinity such as oligophosphate, are easily adsorbed on the pyramidal faces and inhibit their growth, resulting in extended prismatic faces [22.74–76]. Organic materials such as glycol and ethylene diamine tetraacetic acid (EDTA) show growth-promoting effects on both pyramidal and prismatic faces at very low concentration [22.77], but the growth rate decreases with continuous increase of additive concentration.

Thus, the growth rate can be increased by purification of the raw material, as well as by shifting the growth process into the kinetic regime by increasing the velocity of the solution flow relative to the surface of the growing crystal [22.1, 34]. Unfortunately, wide variations in impurity levels and hydrodynamic conditions are limited because of their undesirable influence on the optical quality of growing crystals. Greater acceleration of the growth rate can obviously be obtained by increasing the supersaturation.

22.3.2 Stability of Solution

Conventional methods could tolerate the presence of some spontaneous crystals during the growth process, but spontaneous nucleation means termination of the growth run for rapid crystal growth. *Zaitseva* et al. [22.32] performed experiments to show that KDP solution has a wide metastable zone, which provided the basis to develop fast growth techniques for KDP crystals.

A number of methods are reportedly used to improve the stability of the growth solution. These include superheating of the solution to dissolve microcrystals, filtration to remove insoluble particles, reduction of rough surfaces in the crystallizer, and prevention of cavitations by solution stirring. *Nakatsuka* et al. [22.70] found that the maximum supersaturation reached 120% with overheating above the saturation temperature (by 25 K) at pH 3.2. They also found that lower pH was effective to yield higher supersaturation. Strong acoustic energy can be used to achieve greater solution supersaturation, replacing overheating (Fig. 22.19). The applied acoustic energy may greatly accelerate cluster disconnection. *Zaitseva* found that a continuous filtration system (CFS) (Fig. 22.20) could improve the stability and minimize the potential for spontaneous nucleation. They designed a continuous filtration system for 10001 crystallizers to grow large KDP crystals [22.78]. Degassing the solution is also a useful means to prevent nucleation [22.79].

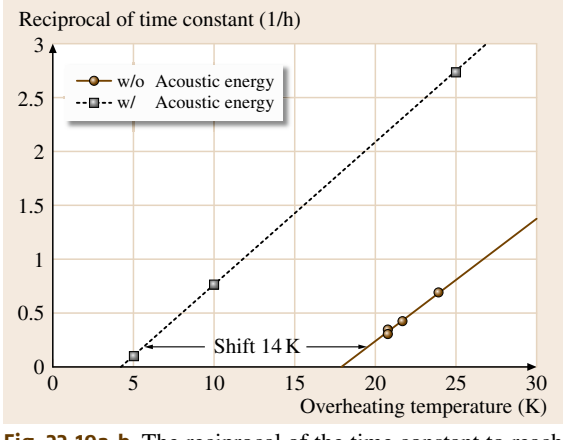


Fig. 22.19a,b The reciprocal of the time constant to reach a steady state of the supersaturation **(a)** without acoustic energy, and **(b)** with acoustic energy, as a function of overheating temperature (after [22.70], with permission of Elsevier)

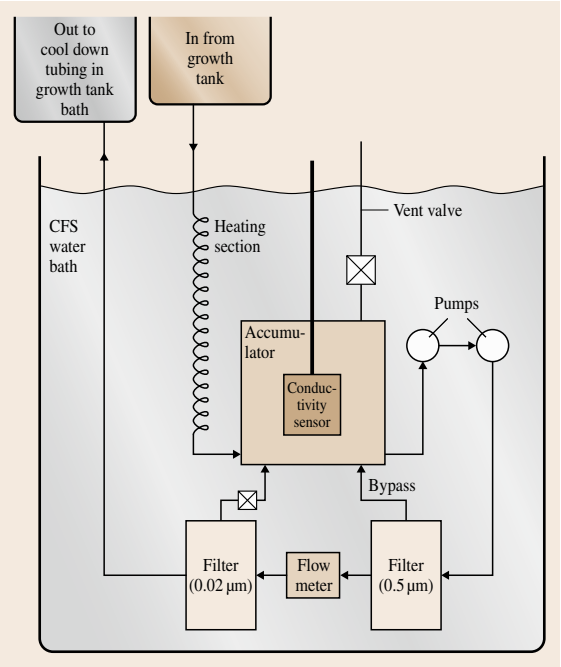


Fig. 22.20 Schematic of the continuous filtration system (CFS) (after [22.55], with permission of Elsevier)

There are some factors associated with crystallization systems that may cause spontaneous nucleation, which lowers the stability of solution during growth [22.42]. Insufficient sealing of the system leads to the possibility of nucleation on the liquid–vapor interface. Nucleation can occur from embryos retained in small cracks and cavities in the surface or joined parts of the equipment immersed in the solution. Nucleation can happen easily at spots of intensive evaporation or dry spots on the parts of the system with an interfacial boundary between solution and vapor that appear as a result of the absence of condensation of the solute on these parts. A classic example of such nucleation is crystallization on the walls of the crystallizer. Secondary nucleation occurs from the main crystal as a result of defect formation or friction between the crystal and supporting parts during the process of stirring.

The impurity composition of the raw material is typically considered an important factor affecting the stability of supersaturated solutions during growth. Some researchers have described the effect, both positive and negative, of different impurities on the stability of solutions [22.40, 73]. However, experiments performed by *Zaitseva* et al. [22.32] show no correlation between spontaneous nucleation and the chemical purity of the solutions. Solutions intentionally doped with Fe, Cr, and Al were measured to have the same stability as regular ones up to very high supersaturation (Fig. 22.9).

22.3.3 Conventional Methods

The temperature-reduction method (TRM) and solution circulating method were two major conventional techniques used to grow large KDP/DKDP crystals before the development of rapid growth from point seed; there are many other methods for KDP/DKDP crystals growth, such as the gel growth and electrodialysis growth methods [22.81].

KDP/DKDP crystals are grown from aqueous solutions by using TRM [22.82,83] in standard Holden-type crystallizers due to their positive temperature coefficient of solubility [22.32]. The growth equipment is simple, and supersaturation during growth is only controlled by the rate of temperature reduction (Fig. 22.21). Using this method it is difficult to maintain stabilization of supersaturation and the growth rate is generally slow, 1–2 mm/day. *Sasaki* [22.83] grew large KDP crystal of size, $400 \times 400 \times 600\,\mathrm{mm}^3$ in 10 months by this method (Fig. 22.22).

Polymorphism of DKDP crystal gives rise to difficulties in the growth of useful tetragonal crystal by TRM. Due to the isotope effect, DKDP crystal may exist in two polymorphs: the tetragonal form (point group *42m*) and monoclinic form (point group 2). The tetragonal–monoclinic phase transition temperature decreases with increasing deuterium concentration in the crystal, which depends on that of the solu-

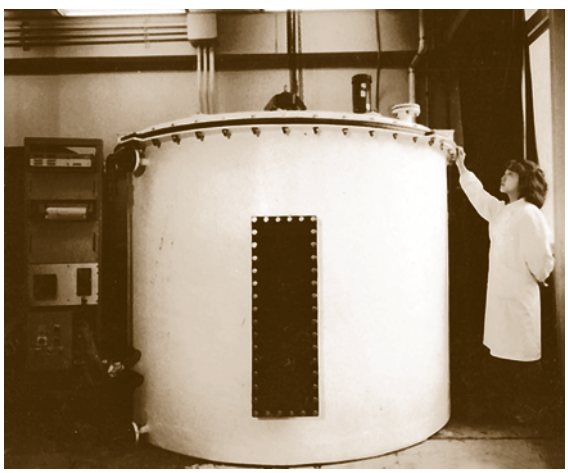


Fig. 22.21 A $1.5\,\mathrm{m}^3$ growth vessel for large KDP crystals (TRM) (after [22.80])

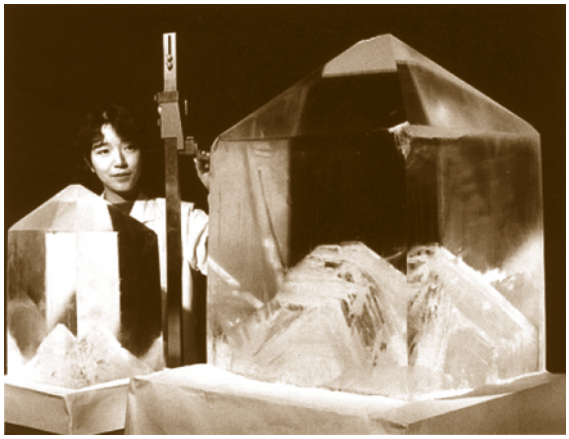


Fig. 22.22 KDP crystals grown at 2 mm/day on average by TRM (size $40 \times 40 \times 60\,cm^3$, growth period 10 months) (after [22.83], with permission of Elsevier)

tion in which the crystal grows. The phase equilibrium transition point of 99.6 mol % deuterated solution is $21 \pm 0.5\,°C$, whereas that of 90 mol % deuterated solution is $49 \pm 1\,°C$. The growth of tetragonal DKDP crystal is very difficult once the tetragonal–monoclinic phase transition takes place or monoclinic phase spurious crystals appear. Thus the degree of deuteration of DKDP imposes strict temperature limits on the growth process; for example, tetragonal DKDP is difficult to grow in a solution of 99.3% deuterium concentration from a starting temperature higher than 43 °C by TRM [22.38].

In the solution circulating method the supersaturation for crystal growth is maintained by circulating the supersaturated solution at constant temperature. Raw material can be added during growth. The system is usually composed of three tanks, namely, the saturation tank, buffer tank, and growth tank (Fig. 22.23) [22.83]. The supersaturation is provided by the difference in temperature between the saturation tank and growth tank. The three tanks are connected by tubes and the growth solution is circulated by using a pump, so crystal can be grown at constant temperature and supersaturation. This system is more complex and the tube is susceptible to blockage due to crystallization [22.82].

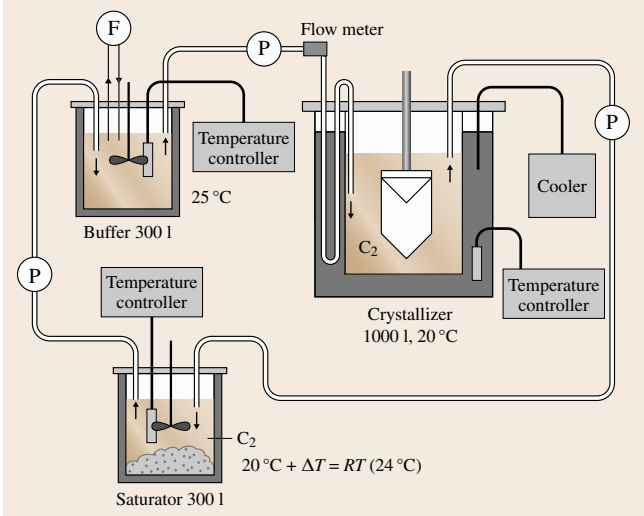


Fig. 22.23 Schematic diagram of the crystallizer with three-vessel solution circulating method (TVM) (after [22.83], with permission of Elsevier) (F – filter, P – pump)

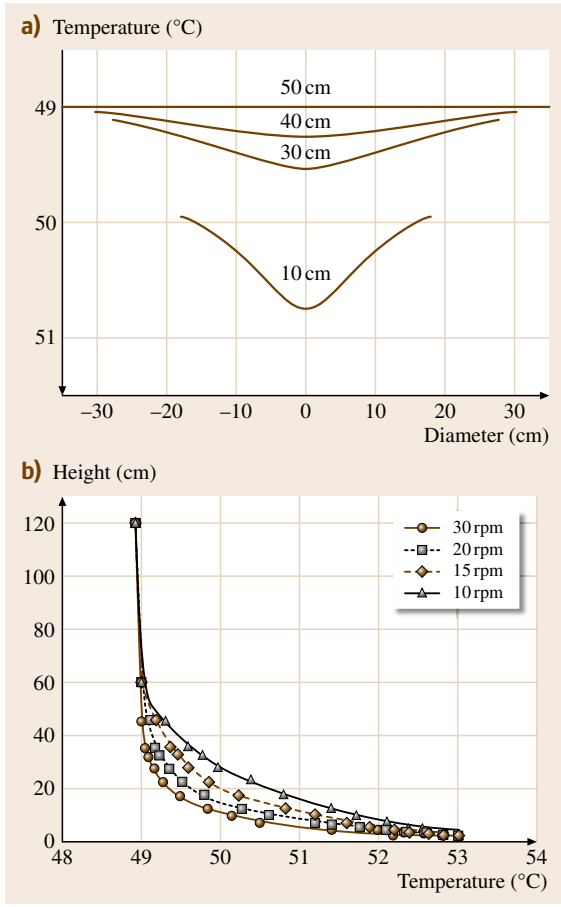


Fig. 22.24 **(a)** Radial temperature distribution at different height from the bottom of the crystallizer; **(b)** relation between crystal rotation rate and temperature distribution in axial direction (after [22.84])

In order to resolve the problem of blocking, *Sasaki* made the temperature of the growth tank lower than room temperature and the others higher [22.83]. *Lu* et al. [22.84] further modified the solution circulating system to resolve all of those problems. The stability of the growth solution and the growth temperature were improved by overheating the growth solution and adjusting the flux of solution and the temperature difference between the growth tank and saturation tank. Also, a suitable temperature gradient inside the growth tank was obtained along the radial and axial directions with respect to the crystal rotation rate (Fig. 22.24). The crystal growth rate was thereby increased 3–5 times over that of conventional TRM. Figure 22.25 shows the bulk KDP crystal grown by them.

Besides, *Vladimin* et al. [22.85] designed a method to grow KDP crystal at constant temperature and constant supersaturation. In this method, supersaturation was provided by adding solution. This method, which is very simple, has the advantage of solution circulating at constant temperature. It has only a tank without tubes, and can decrease the volume of the growth tank. Especially for growth of DKDP crystal, this method can effectively decrease the dosage of heavy water to reduce the cost of crystal growth.

22.3.4 Rapid Growth from a Point Seed

With the development of ICF, more and larger KDP/DKDP crystals with higher quality were needed.



Fig. 22.25 Bulk KDP crystal grown by solution circulating method (weight: 110 kg; size: $260\times250\times770\,\mathrm{mm}^3$)

However, the problem of low growth rate was particularly daunting. The main limitation on growth of large crystals by conventional techniques is the growth rates of only 1–2 mm/day for KDP and not faster than 1 mm/day in the case of DKDP crystal. In addition, the growth of each crystal required the production of seed material of equal cross-section, adding significantly to the production time. Difficulties in providing reliable equipment, high risk of failure, and defect formation during such long periods resulted in low yield and high cost of final crystals. These reasons stimulated the development of new techniques to accelerate the growth rate without the sacrificing optical quality of large crystals.

Work on rapid growth of KDP/DKDP crystals started in the early 1980s, aimed at conducting the growth process in the kinetic regime [22.9]. It improved the growth rate efficiently by increasing the velocity of the solution flow relative to the crystal surface. A high z-direction rate of 5–25 mm/day was achieved using a novel turbine to enhance mass transport [22.11]. Up to $150\times150\times80\,\mathrm{mm}^3$ KDP and DKDP crystals were grown at a rate of 0.5–1 mm/h by the technique of properly feeding the growing surfaces [22.86]. The quality of crystals was reported to remain the same as those grown by conventional technique, but the results proved that this was not the ultimate solution.

Zaitseva et al. [22.8, 32] realized that the primary factor controlling the growth rate was supersaturation, while a number of other researchers focused on increasing mass transport to the crystal surface. Results of nucleation and kinetic experiments made it possible to achieve stable growth rates that were one order of magnitude faster than conventional techniques. Rapid growth on both {100} and {101} faces of a point seed was carried out in Holden-type crystallizers (Fig. 22.26) at high supersaturation by using extensively purified raw material. The process is depicted in references [22.7, 42].

Growth solution was prepared by dissolving salt in water with saturation temperature depending on the required mass of the crystal. The solubility data in the temperature range $T = 10–80\,^{\circ}\mathrm{C}$ for KDP, and DKDP with 90% deuteration, are expressed as [22.42]

$$C_0 = 0.1165 + 3.0017\times10^{-3}T + 8.5768\times10^{-6}T^2\,, \tag{22.8}$$

$$C_0 = 0.1701 + 3.4817\times10^{-3}T + 2.8062\times10^{-6}T^2\,, \tag{22.9}$$

respectively.

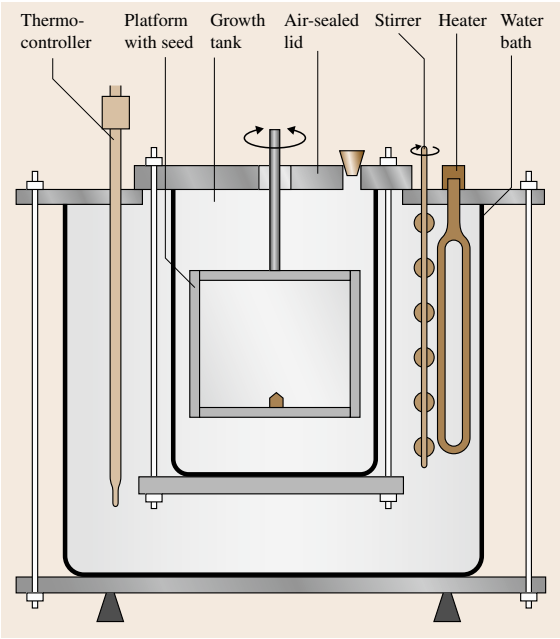


Fig. 22.26 Scheme of the crystallizer used for fast growth (after [22.32], with permission of Elsevier)

Solutions were filtered through submicrometer filters in two ways: prior to growth, or continuously during the whole growth process. After the filtration was stopped, all solutions were overheated for not less than 24 h. Both filtration and overheating were carried out in air-sealed crystallizers with continuous stirring at 80 °C.

Square seeds with T-shaped cross-section were cut from previously grown crystals without visible defects. A water-polished seed was glued into a square hole in the middle of the platform. After the glue had dried, the platform with the seed was assembled in an empty crystallizer and slowly heated to 80 °C. Growth solution that was overheated at the same temperature in a separate vessel was carefully introduced into the crystallizer without splashing. Alternatively, for small-scale growth, the platform with the seed was heated to 80 °C in hot water vapor in a separate crystallizer and then quickly introduced into the overheated solution.

After the seed had been introduction, the crystallizer was tightly sealed and the solution was maintained at 80 °C for 10–15 min. During this time, the seed was slightly dissolved to eliminate any surface crystallites. Additionally, all dry surfaces that could produce spontaneous nucleation were wetted by condensation of the hot solvent vapor. This overheating time was limited by seed dissolution. Typically, the solution was cooled to the saturation temperature before the upper part of the seed had dissolved to the edge of the hole.

Continuous cooling was stopped when the temperature corresponded to the supersaturation for regeneration. Under these conditions, the regeneration process was completed in 1–2 h. During regeneration, the solution was stirred by reversible rotation of the platform at 40–60 rpm with a period of about 30 s in one direction and a 2–3 s pause. This platform rotation was also used during the crystal growth procedure that followed.

After the regeneration process was completed, the temperature reduction continued according to a program that provided stable growth at the desired growth rate. The process could be done completely automatically by using concentration sensors [22.87, 88]. Crystals could be grown at nearly constant growth rate using this procedure. The growth rate could be monotonically decreased toward the end of growth to avoid increasing supersaturation at lower temperature. When the growth was completed, the solution was removed from the crystallizer. If the process finished below or above room temperature T_r, the system was slowly heated or cooled to T_r before the crystal was taken out.

To meet the demands of the National Ignition Facility (NIF) for a large number of 0.5 m high-quality KDP/DKDP crystals, many scientific developments and engineering design changes were incorporated into the rapid growth crystallizer system (Figs. 22.26 and 22.27). The crystal is rotated alternately in one direction and then in the other using a symmetrically programmed schedule with controlled acceleration, de-

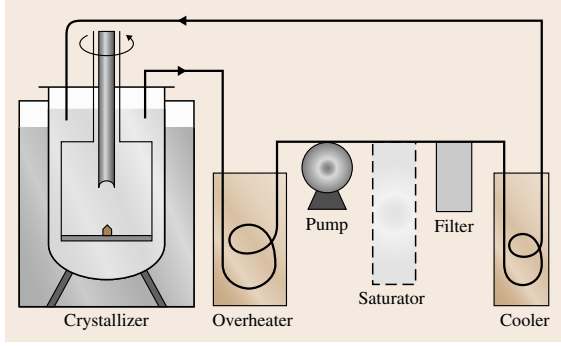


Fig. 22.27 Schematic diagram of the 1000 l crystallizer (after [22.7], with permission of ASM Int.)



Fig. 22.28 Photograph of the large 10001 crystallizer (after [22.7], with permission of ASM Int.)

celeration, and rotation rates. A special device, called a seed protector, is inserted within the platform shaft in order to cover the point seed during the filtration or overheating procedures [22.89]. The continuous filtration system shown in Fig. 22.20 contains three temperature-controlled sections: a superheater and filter (operating at 80 °C), and the third section where the filtered solution is cooled to the growth temperature [22.78]. The details of this classical loop are designed such that the solution can be continuously filtered during the entire growth process at supersaturations up to 20% without generating spontaneous nucleation. Other important changes include a rigid and streamlined platform compatible with hot KDP solution that could rotate at sufficiently high rates without flexing, oscillating or creating a large wave at the solution–air interface [22.7], and a semi-automated system for temperature reduction [22.87]. Successful incorporation of these design elements led to a reliable method. By using this method, a KDP crystal of 317.97 kg was grown in 52 days in LLNL (ICF Monthly Highlights, January 2000 UCRL-TB-128550-00-04) (Fig. 22.29).

The combination of the regeneration conditions with a convex-shaped platform and continuous filtration makes it possible to control the KDP crystal habit for production. The ratio of dimensions along the

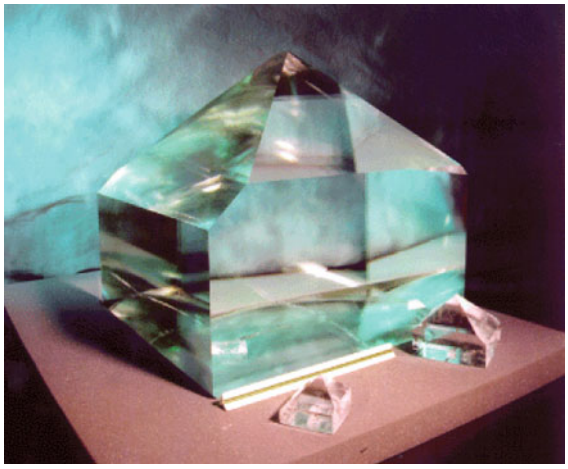


Fig. 22.29 First KDP crystal of the NIF SHG size ($53 \times 54 \times 55\,cm^3$) grown on the convex platform with continuous filtration (after [22.42], with permission of Elsevier)

crystallographic axes was controlled by two methods: (1) creation of special dislocation structures during the seed regeneration process and (2) change in the orientation of the seed [22.58]. These methods enable the growth of large crystals with specified habit without the deleterious effects of intentionally introduced chemical impurities. KDP and DKDP crystals of various habits were grown at rates of 10–20 mm/day to linear sizes near 90 cm (Fig. 22.30).

In addition, for DKDP crystal, growth by the point-seed rapid growth method not only decreases the growth period but also avoids the emergence of monoclinic DKDP crystal. This is very important for the growth of highly deuterated DKDP crystals [22.32, 53, 90].

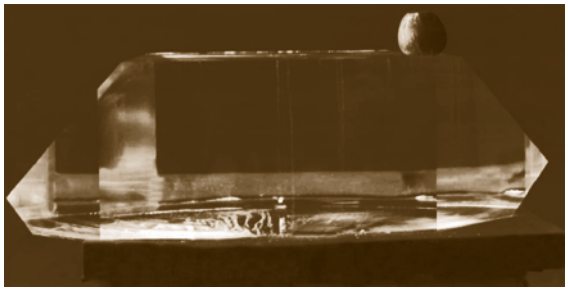


Fig. 22.30 DKDP crystal grown for THG on a horizontally oriented seed; $X : Y : Z = 1 : 2.2 : 3$; length $Z = 86$ cm; convex platform (after [22.58], with permission of Elsevier)

22.4 Effect of Growth Conditions on Defects of Crystals

Growth conditions as well as the after-growth treatment [22.91, 92] affect the optical quality of crystals. Discussion of the mechanisms of growth and their influence on the defect formation process showed that the major factors that determine the defect structure of KDP crystals are the impurities content and the dislocation structure of the crystals. Vicinal sectorality, striations, and strain are the main parameters affecting the optical quality of crystals. Solution inclusions and cracks, which make crystals completely inappropriate for optical applications, are also largely influenced by the same factors.

22.4.1 Impurity Effect

Impurities, which originate from the precursors and from dissolution of the crystal growth tank, can be divided into three main kinds: metal cations such as Al^{3+}, Fe^{3+}, Cr^{3+}, Ca^{2+}, Mg^{2+}, Na^{+}, etc., anions such as SO_4^{2-}, NO_3^{-}, Cl^{-}, etc., and organic impurities such as EDTA, organic dyes, etc. The impurities, as well as the crystal growth rate, affect the defect structure of KDP crystal, which in turn affects the optical quality of KDP crystals.

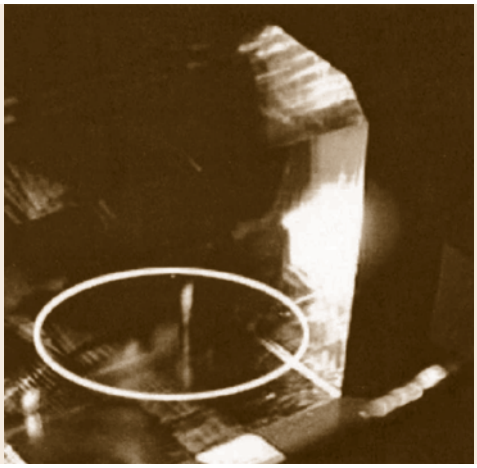


Fig. 22.31 Photograph of foggy inclusions along prism–prism boundary of NIF-size KDP boule grown in solution having high Al content during middle of growth run (after [22.7],with permission of ASM Int.)

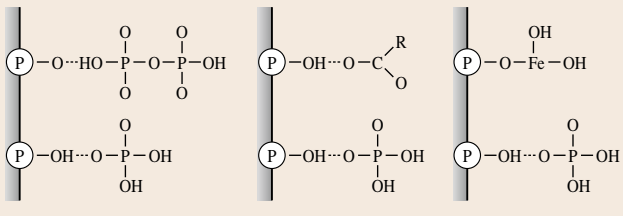


Fig. 22.32 Scheme of adsorption of anionic and cationic species (after [22.75], with permission of Elsevier)

The metallic cations, particularly those with high valency were considered to strongly affect the growth habit and optical properties of crystals. Trivalent metal cations such as Fe^{3+}, Cr^{3+}, and Al^{3+} have a deleterious effect on the growth of {100} faces of KDP [22.1]. Their introduction into the growth solution poisons the {100} faces, producing a region of no growth at low supersaturation commonly referred to as the *dead zone*. They also promote macrostep formation as the supersaturation is increased and growth begins. At impurity concentrations in the range 1–10 ppm, this phenomenon often results in the formation of solution inclusions [22.1, 93]. In addition, these impurities are strongly incorporated into the {100} face with effective segregation coefficient of the order of 10. In contrast, these impurities have little or no effect on the growth of the {101} faces and are strongly rejected with segregation coefficient of 1.0 [22.92]. This nearly hundredfold difference in impurity incorporation results in strong optical inhomogeneities which are manifested in the refractive indices, the linear and two-photon absorption coefficients, and the anomalous birefringence near the {100}/{101} boundaries of the crystal [22.94,95]. It was found that a correlation exists between *foggy* inclusions (Fig. 22.31) at the corners of the prismatic sectors and aluminum concentrations in the growth solution when a certain concentration is exceeded [22.96].

Table 22.1 presents the relationship between the concentration of the most common impurities in initial solutions and their distribution in pyramidal and prismatic sectors of KDP crystals. From these results one can see that most impurities, especially trivalent metal cations, go preferably into the prismatic growth sectors. However, some impurities, such as Rb, have approximately the same low concentration in both prismatic and pyramidal parts of the crystals. Some impurities (B, Na, Mg, and Ca) seem to be completely rejected by the crystals.

Anions were traditionally considered to have slight effect on the quality and growth of KDP crystals. However, recent research gives us new insights into this hypothesis [22.74–76, 97, 98]. Some anionic impuri-

Table 22.1 Distribution of impurity concentration C_i in raw material and pyramidal and prismatic sectors of KDP crystals

Impurity	MDL (ng/g KDP)	C_i raw material (ng/g KDP)	C_i pyramid (ng/g KDP)	C_i prism (ng/g KDP)
B	1000	14000	ND	ND
Na	300	86000	ND	ND
Mg	5	100	ND	D
Al	100	900	200	4400
Si	100	12000	D	390
Ca	100	3600	ND	ND
V	0.5	< 80	0.1	6.0
Cr	100	2000	490	11000
Fe	50	5300	110	12000
As	200	< 200	ND	D
Rb	10	10000	2600	2100
Sr	5	320	870	1800
Mo	10	790	66	1100
Sb	4	70	30	280
Ba	5	52	120	600

MDL – method detection limit, D – detected, ND – not detected

ties (sodium metaphosphate, potassium pyrophosphate, formic acid, acetic acid, oxalic acid, and tyrosine) were found to have an inhibiting effect on the growth of KDP crystals. Complete stoppage of pyramidal face growth was observed in the presence of high concentration of both $[H_{x-n}(PO_3)_x]^{n-}$ and $[H_2P_2O_7]^{2-}$. In these cases, the crystal habit was changed into a closed octahedron and the whole crystal stopped growing. The inhibition is assumed to be caused by the adsorption of these anions at the growing crystal surface, especially on pyramidal surface, through the formation of H-bonds between anions and H_2PO_4 groups (Fig. 22.32). When the doped metaphosphate concentration is high enough, mother-liquor macroinclusions occur along the sector boundaries and in pyramidal sectors (Fig. 22.33). In observations using laser tomography, the density of scatter increases with increasing concentration of doped metaphosphate. The scatters are suggested to be microsolution inclusions caused by the inhibition effect of metaphosphate on the growing faces. These anions have a harmful effect on the laser damage threshold due to possible incorporation (Table 22.2). Sulfate

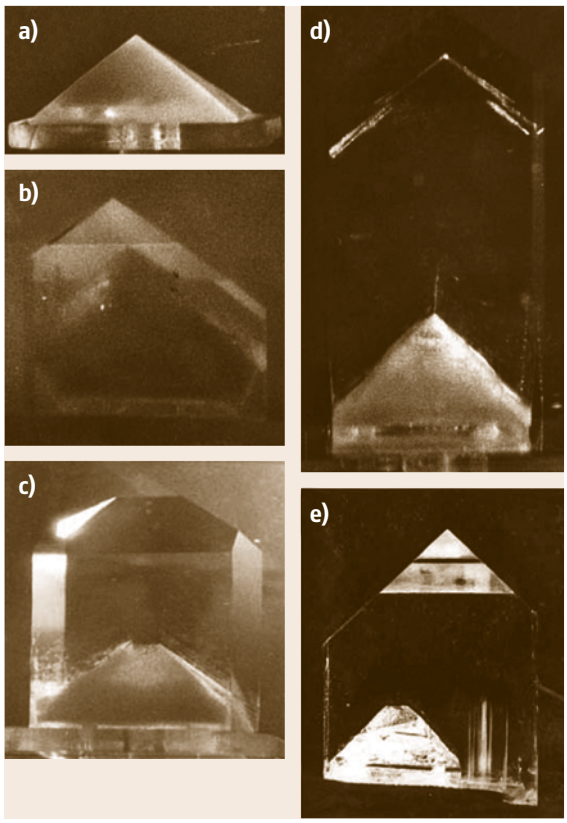


Fig. 22.33a–e Photographs of KDP crystals grown on *Z*-cut plate seed from metaphosphate-doped solutions with addition of **(a)** 50 ppm, **(b)** 30 ppm, **(c)** 15 ppm, **(d)** 10 ppm, and **(e)** 1 ppm (after [22.76], with permission of Elsevier) ►

Table 22.2 The effect of anionic species on the optical properties of KDP crystal

Dopants	Mass ratio (ppm)	A (%/cm)	F_{th} (J/cm^2)
Potassium pyrophosphate	100	5.1	34.3
EDTA	300	5.5	52.0
Tyrosine	20	4.7	40.4
Tyrosine	50	4.8	40.4
Tyrosine	300	4.9	35.1
Formic acid	300	6.1	42.7
Oxalic acid	300	4.5	45.8
Pure KDP material		5.2	52.0

A – absorption coefficient; F_{th} – laser damage threshold, 1-on-1, 1.06 μm, 10 ns

(SO_4^{2-}) anions, which can join into the KDP crystal lattices through H-bonding and electron attraction, have a great effect on the growth habit of KDP crystals at high dopant concentration. KDP crystals showed many defects such as mother liquor inclusions, parasite crystals, and cracks. Besides, SO_4^{2-} content also adversely affects crystal transparency. At high dopant concentration, KDP crystal transmittance decreases significantly in the ultraviolet region [22.98].

Organic additives such as glycerol, ethylene glycol, polyethylene glycol, and EDTA show growth-promoting effects on both pyramidal and prismatic faces at very low concentration [22.75–77, 99]. In KDP crystals grown in the presence of optimal amounts of organic additives, there is a decrease in the concentration of inorganic background impurities of the cations, an increase in the transparency in the (100) growth sector in a certain range, and an increase in optical uniformity and laser damage threshold.

The distribution of impurities in the KDP crystal is nonuniform, as is evident in crystals grown from solutions doped with impurities that can produce visible color. KH_2PO_4 shows a strong tendency to incorporate anionic dyes only on the {101} faces, presumably because these faces are terminated with K^+ ions [22.93]. However, impurities may inhomogeneously deposit not only between growth sectors, but also within a single growth sector depending on the crystal surface topography. Surfaces of crystals grown in the regime of lower supersaturation often propagate through dislocations that produce growth spirals or hillocks, and shallow-stepped pyramids with single or multiple dislocations at the apex [22.100, 101]. Polygonization of hillocks partitions faces into vicinal regions, each having slightly different inclinations. Impurity partitioning among vicinal slopes and intrasectoral zoning result from selective interactions of impurities with particular stepped hillock slopes.

Zaitseva and coworkers [22.1] perfected KH_2PO_4 crystal growth conditions as a prerequisite to the development of the National Ignition Facility. Amaranth, which displayed exclusive affinity for the {101} surfaces of KH_2PO_4 [22.93, 102], was both inter- and intrasectorally zoned [22.92]. This observation required introduction of the dye during late growth, thereby coloring only a thin surface layer so that patterns of color were not confounded by moving dislocation cores. Figure 22.34 highlights the {101} faces of KH_2PO_4/amaranth crystals. The heterogeneities resulted from amaranth having distinguished among the A, B, and C slopes of the polygonized hillocks prevalent on the pyramid faces. Incorporation followed the trend B > A > C. On the other hand, Chicago sky blue preferred C [22.103]. At low Chicago sky blue concentration, B remained colorless. The incorporation was associated with a critical temperature above which the dye was not captured. In situ interferometry [22.104] was used to show the influence of the dye on the surface morphology at different concentrations and KH_2PO_4 supersaturations.

The effect of impurities on the recovery of surfaces out of the dead zone was traditionally explained by the classic theory of Cabrera and Vermilyea in terms of pinning of elementary step motion by impurities [22.105]. In this model, impurities adsorbed on the terraces create a field of *impurity stoppers* that act to block the motion of elementary steps. When the average impurity spacing is less than a critical distance, whose magnitude is approximately given by the Gibbs–

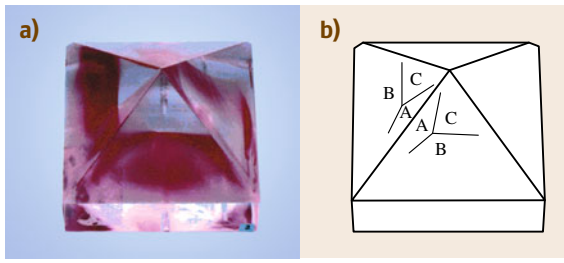


Fig. 22.34a,b Intrasectoral zoning in KH_2PO_4/amaranth. **(a)** Photograph of KH_2PO_4/amaranth crystal grown by *Zaitseva* et al. [22.55]. **(b)** Idealized representation of crystal in **(a)**, illustrating the hillocks observed on the surface

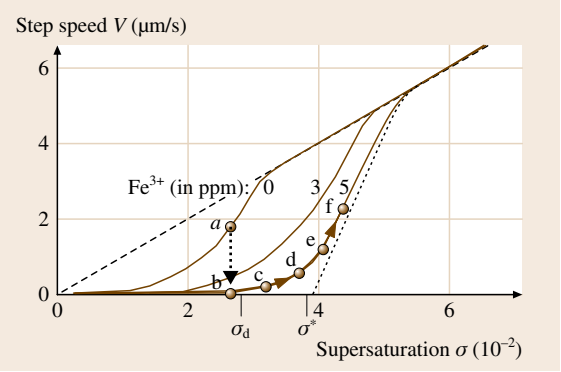


Fig. 22.35 Dependence of step velocity on supersaturation in the presence of Fe^{3+} (after [22.26], with permission of Macmillan)

Thomson critical diameter, the steps cannot advance. As the supersaturation is increased and the critical diameter becomes smaller, the steps begin to squeeze through the *fence* of impurities and the step speed rises rapidly. The dotted curve in Fig. 22.35 illustrates the prediction of such a model. No growth occurs below a percolation threshold given by σ^*, while for $\sigma > \sigma^*$, the step speed rises rapidly to its unimpeded value. While the model correctly predicts the rapid rise in step speed for $\sigma > \sigma^*$, no growth is predicted below σ^*, in contrast to what has been observed experimentally. *Land* et al. [22.106] considered that recovery of the KDP surface occurred through the movement of macrosteps (Fig. 22.36), which were mobile even when elementary steps remained pinned. This led to a slow increase in growth rate below σ^*, even for supersaturations in the region $\sigma_d < \sigma < \sigma^*$. At supersaturation near σ^*, elementary steps begin to straighten out and become mobile, but their speed is still considerably less than that of the macrosteps. Finally, at supersaturations in excess of σ^*, the surface once again consists of a combination of rapidly moving elementary steps and step bunches that resemble the step trains for the undoped solution. The elementary steps are now moving with a velocity that is close to that of the macrosteps.

De Yoreo et al. [22.54] point out that, although all the defects observed in KDP are also present in DKDP, there are some aspects of crystal quality which are peculiar to the deuterated crystals. DKDP crystals grown at rates of 1–15 mm/d have always been found to exhibit vicinal sectorality in their x-ray topograph. This inhomogeneity has a moderate effect on the optical uniformity.

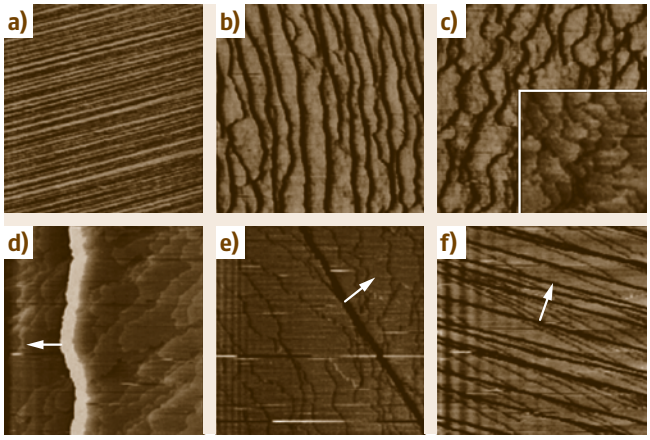


Fig. 22.36a–f Series of AFM images illustrating the process of impurity poisoning and recovery (after [22.7], with permission of ASM Int.): **(a–c)** $15 \times 15\ \mu m^2$ scans collected at $\sigma = 0.04$ along heavy *dashed line* trajectory from point a to point b in Fig. 22.35 showing poisoning of surface by introduction of 12 ppm Fe^{3+} (per mole of KDP); time at the start of each scan is **(a)** 0 s, **(b)** 64 s, and **(c)** 106.7 s, and Fe-doped solution was introduced at $t = 42.7$ s (steps in image **(c)** are immobile and *inset* shows $6 \times 6\ \mu m^2$ image of morphology of elementary steps on macrostep terraces); **(d)** $9 \times 9\ \mu m^2$ image collected at point c in Fig. 22.35 (elementary steps are immobile and macrosteps are distorted but moving slowly); **(e)** $13 \times 13\ \mu m^2$ image collected at point d in Fig. 22.35 (elementary steps are still immobile and macrosteps are straight and moving rapidly); **(f)** $12.5 \times 12.5\ \mu m^2$ image collected at point e in Fig. 22.35 (elementary steps are now moving but more slowly than macrosteps)

22.4.2 Supersaturation

According to the dependence of growth-step velocity of KDP prism faces on the supersaturation, three regions can be defined, corresponding to the dead zone, the transition region of high $dV/d\sigma$, and the linear part of $V(\sigma)$ with high supersaturation and growth rate.

When crystals grow in the dead zone, large variation occurs in steepness, resulting from different incorporation of impurities into separate vicinal slopes. This variation produces large misorientation between small crystals formed during regeneration on melted faces and the z-cut of the seed. This misorientation makes the process of joining difficult, which leads to the formation of cracks and subindividual crystals [22.107–110]. As a result, the crystallographic shape fails to regenerate. Even when regeneration occurred successfully, subindividual crystals and cracks often appeared if growth was performed within the dead zone.

The transition region of high $d\sigma/d\sigma$ is a region of surface instability that develops when elementary steps pass through the fence of impurity blockers with the accompanying macrostep bunching [22.1]. Solution inclusions form most likely in this region because of higher variations of supersaturation on the growing surface. Another reason for increasing instability is the formation of new hillocks, which are frequently observed during the transition. Besides, the change of leading hillock on the growing face in the region of low supersaturation and in the vicinity of the dead zone is inevitably accompanied by the formation of growth bands. This is due to the appearance of new growth steps of various orientations which lead to the formation of inhomogeneity.

When crystal grows at high supersaturation, corresponding to the linear part of $V(\sigma)$, no visible inclusions are formed on the vicinal slopes, despite the fact that microscopic investigation of the surface clearly shows the structure of bent macrosteps on both prismatic and pyramidal faces [22.111]. The formation of large, bent macrosteps is not a sufficient condition for inclusion formation. There is also no evidence that such bent macrosteps cause microsolution inclusions or dislocation since etching did not reveal any dislocation pits.

It can be concluded that, in order to minimize defect and inhomogeneity formation, crystals should be grown in the region of the dead zone (traditional growth) or in the region of the linear part of the dependencies $V(\sigma)$ (rapid growth).

22.4.3 Filtration

KDP crystals often contain hairlike inclusions that run roughly perpendicular to the growth direction (Fig. 22.37) [22.112]. They have the appearance of fine fibres a few centimeters in length, extending through the crystal in the direction of growth and deflecting away from the z-axis; they occur in both dipyramidal and prismatic growth sectors. Most of these inclusions, which lie at angles to the z-axis that vary between 20 and 90°, are not continuous but rather consist of long chains containing from dozens to hundreds of liquid inclusions.

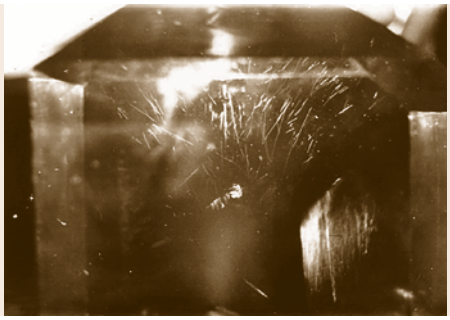


Fig. 22.37 Hairlike inclusions in rapidly grown KDP crystals (after [22.7], with permission of ASM Int.)

Many models of liquid inclusion formation have been proposed [22.113, 114]. A most likely source of hairlike inclusions is particle incorporation. During crystal growth, steps often close around particles, but do not cover them. Researchers at LLNL have observed this process in KDP during the passage of hundreds of layers. Figure 22.38 shows holes caused by this process in a number of crystals, including KDP. Apparently, once these holes are formed, they are difficult to fill in and result in the generation of hollow channels running at a high angle to the growth front. Given that the KDP crystals were grown by a temperature drop method, any channels which formed during growth would have contained solutions that became increasingly supersaturated as the temperature was decreased and thus might be expected to condense into chains of inclusions.

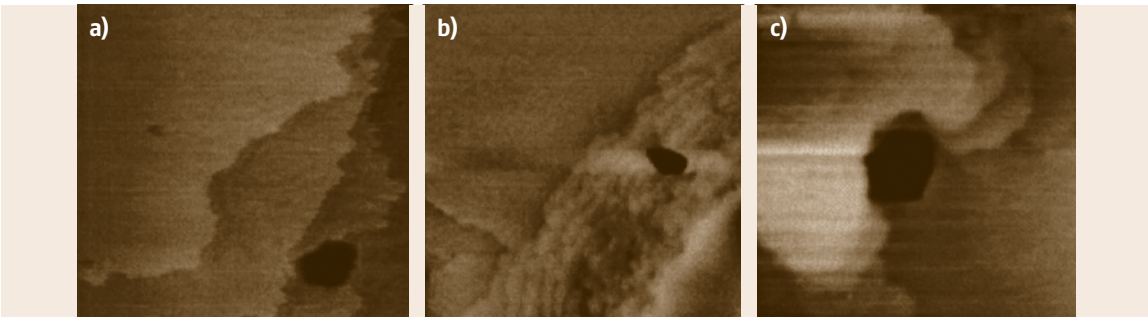


Fig. 22.38a–c Appearance of holes in crystals following inclusion of particle: **(a)** Canavalin, $6\times6\,\mu m^2$; **(b)** Satellite Tobacco Mosaic virus, $12\times12\,\mu m^2$; **(c)** KDP, $3\times3\,\mu m^2$ (after [22.7], with permission of ASM Int.)

Filtration of solution before crystallization to remove extraneous solid particles and thereby improve the crystal quality and laser damage threshold is a standard procedure for experimental or commercial crystal growth. However, no matter how well the solution is filtered before crystal growth, a large number of particles appear very soon after the filtration is stopped. This phenomenon is especially pronounced during the growth of large bulk crystals in equipment containing moving and rotating parts that generate particulate contamination and spoil previously purified growth solutions.

The requirement of high damage threshold in NIF crystals stimulated the design of a continuous filtration system. The system removes growth solution from the tank, heats it to prevent spontaneous nucleation, and filters the solution through 0.02 μm-pore filters. The solution is then cooled before its injection back into the growth tank. This system filters the solution not only before the growth (prefiltration) but also during the entire growth process in a continuous mode.

Comparison of crystals grown with and without continuous filtration showed substantial difference in structure and number of defects. When crystals grow from only prefiltered solutions, the pyramidal face of the crystal generally has a large number of dislocation pits uniformly distributed over the whole crystal (Fig. 22.39). This high density of dislocations, which shows that the distribution of growth sources on the face is not stable, is more or less typical for all KDP and DKDP crystals grown without continuous filtration.

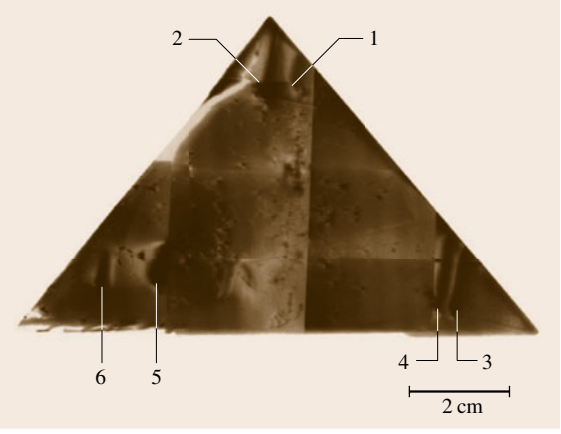


Fig. 22.39 X-ray synchrotron topographic image of dipyramid face of a KDP crystal grown without continuous filtration. *Black dots* are dislocation outcrops on the face. (1–6) Vicinal hillocks tips (after [22.78], with permission of Elsevier)

Initial dislocation hillocks formed after seed regeneration are located approximately in the center of each face, but the location of vicinal hillocks far from the central part of the face does not correspond to the distribution bunches created on the seed during regeneration. These dislocations were formed during the process of growth. When crystals grow with continuous filtration, positions of the leading hillocks do not change, and the crystal surface preserves its simple structure during the entire growth, with one growth hillock approximately in the middle of each face, corresponding to the locations formed during regeneration.

These results indicate that, under continuous filtration, the formation of new dislocations is significantly reduced. Large amounts of dislocations lead to the possibility of formation of vicinal hillocks that can compete in step generation under changing growth parameters, such as temperature, supersaturation or hydrodynamic conditions. The change of leading dislocation hillocks on the growing crystal face always results in the formation of structural defects. The shift of dislocation hillocks to the asymmetrical position close to the edges leads to a higher probability of formation of liquid inclusions and new dislocations on them. This is why crystals grown with continuous filtration have much higher optical homogeneity compared with crystals grown under usual conditions.

22.4.4 Hydrodynamic Effects

Obtaining the optimal hydrodynamic conditions in a crystallizer is a principal factor ensuring high quality of crystals.

The surface structure of each face of KDP crystal consists of growth hillocks, intervicinal valleys, and additional valleys produced by the *bending* of macrosteps originating from a single growth hillock (Fig. 22.40). By ex situ measurement on the surface topography of rapidly grown KDP crystals using a precision coordinate measuring machine (CMM) [22.106], these valleys are observed to be precursors of morphological instability and the formation of solution inclusions on the crystal surface. Results from numerical simulations of the hydrodynamics [22.115] and mass transfer [22.116] for the conditions used in the rapid growth process show that the surface supersaturation field generated on these crystals is inhomogeneous due to the spatially and temporally varying boundary layer thickness on the rotating crystal surface. These simulations clearly indicate that the process of step bending can produce the features which are observed in experiment. The simulations have

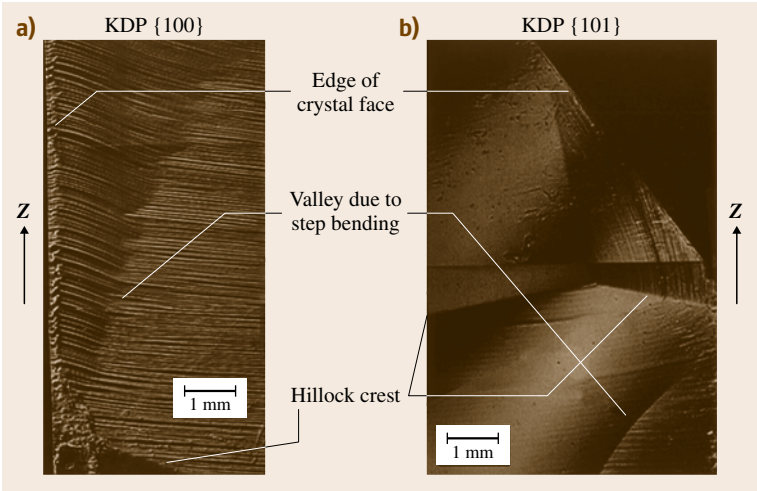


Fig. 22.40a,b Photographs of the typical surface structure resulting from step bending on the **(a)** {100} and **(b)** {101} face (after [22.106], with permission of Elsevier)

been used to explore the dependence of step bending on parameters such as crystal growth rate, rotation conditions, growth hillock location, and (for prismatic faces) impurity level [22.111]. It has been shown that the step bending and resulting valley formation is intensified by increasing crystal growth rate, by decreasing rotational speed, and (for the {100} face) by increasing the impurity level. It has also been shown that the resulting surface structure depends on the location and number of hillocks on the surface.

The crystallization process can be regarded as two stages: supply of crystallizing matter from solution to the crystallization surface through the diffusion boundary layer by molecular and convective diffusion, and the formation of a crystal. The former is rate-limiting if the supersaturation at the crystallization surface is lower compared with the bulk supersaturation, in which case the growth is said to proceed in the diffusion regime. The second stage is rate-limiting if the bulk supersaturation and crystal surface supersaturation are similar, in which case the growth regime is said to be kinetic. Crystals are generally considered to be in a mixed diffusion–kinetic regime. However, surface and bulk supersaturation should be made as close as possible to the kinetic regime so that the diffusion processes of supply of crystallizing matter do not limit the crystallization rate.

The traditional recommendation to approach the kinetic regime is to decrease the thickness of the diffusion layer by increasing the flow velocity or changing the flow geometry [22.36]. However, it can also be achieved by decreasing σ. Thus, to stay close to the kinetic regime, the growth rate should be lowered by increasing the rotation rate of platform. The dependence of the growth rate R_z on the rotation rate of the platform can be determined in a rapid growth crystallizer [22.37]. At very slow rotation of 0–25 rpm, inclusions always form on some crystal faces. Between 25 and 40 rpm, crystals grow with and without inclusions. With faster rotation, formation of solution inclusions is extremely rare and one can be considered to be close to the kinetic regime.

The hydrodynamic conditions most likely affect the solution inclusion process indirectly through changes of the dislocation structure. Low flow velocity at slow rotation results in a greater gradient of the thickness of the diffusion layer along the faces and of the supersaturation at the crystallization surface. The growth hillocks move to the positions of favorable hydrodynamic conditions, i.e., close to the crystal edges and apexes. Morphological instability develops on the large vicinal slope, which covers the whole face. Formation of macrosteps and increasing slope of the vicinals leads to large deviation of the face from its singular orientation and initiates step generation from edges. This phenomenon produces thin surface layers that cover the deviated vicinals with the formation of liquid inclusions. Shift of the hydrodynamic conditions towards the kinetic regime decreases the gradient of the supersaturation along the faces, which makes location of the growth sources close to the edges less probable. In practice, the approach to the kinetic regime is achieved in large crystallizers by increasing the rotation rate of the platforms, as well as by continuous filtration. The combination of these conditions almost completely eliminates solution inclusions without decreasing the growth rate.

22.5 Investigations on Crystal Quality

The optical parameters used to evaluate KDP-type crystals for the ICF project mainly include transparency, optical homogeneity, and resistance to damage by laser radiation.

22.5.1 Spectroscopic Studies

Transparent Spectrum

Transmission in the KDP crystal spectra is from 250 to 1700 nm. For DKDP crystals, the deuterated crystals have higher transmission efficiency (> 89%) at 1064 nm and lower optical absorption efficiency (< 3% cm^{-1}) than those of the undeuterated crystals (Fig. 22.41). The infrared (IR) absorption edges of the deuterated crystals are obviously red-shifted by 0.4–0.5 μm to about 2.0 μm in comparison with those of the undeuterated crystals (about 1.5 μm) so that DKDP crystals can be applied over a wider wavelength region. The infrared cutoff ratio of the hydrogen mode against the deuterium mode is 1/1.33, which nearly coincides with the ratio of the square root of the reduced mass of O−H against O−D, which is known to be 1/1.3743 [22.117].

Raman Spectra

The Raman spectra of KDP crystals exhibit a red-shift, similar to that observed in the transmission spectra [22.117]. The Raman peak 916 cm^{-1} of the $H_2PO_4^-$ group in KDP crystal is red-shifted by 35 cm^{-1} to the 881 cm^{-1} Raman peak of the $D_2PO_4^-$ group in DKDP crystal (Fig. 22.42). This red-shift is due to the isotope substitution effect. In the structure of the tetragonal phase, the PO_4 tetrahedra are coupled by potassium atoms, and four of these oxygen atoms are transformed to produce strong lines at 966 cm^{-1} in the DKDP crystal. These lines are not detected for the KDP crystal. This result confirms that the spectrum of Raman scattering in the deuterated crystal can be split into two parts related to internal and external vibrations.

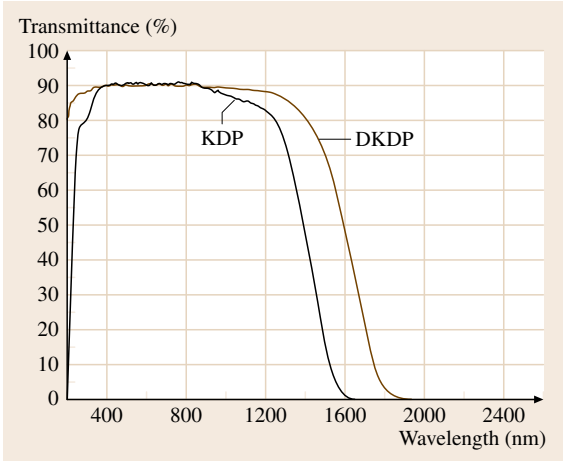


Fig. 22.41 Transmission spectra of *Z*-cut KDP/DKDP crystals (after [22.117], with permission of Elsevier)

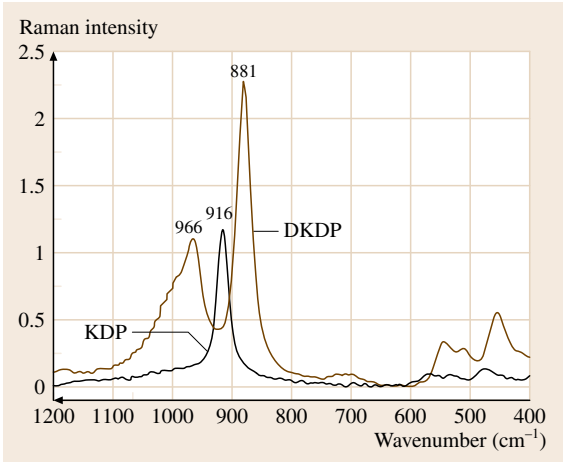


Fig. 22.42 Raman spectra of KDP/DKDP crystals (after [22.117], with permission of Elsevier)

Effect of Impurities on the Transmission Spectrum

Certain impurities have a discernible effect on the transmission of KDP crystals. For example, strong absorbtion in the wavelength region of 200–300 nm is a signature of metal impurities.

Many experiments have been done to investigate the dependence of near-ultraviolet (UV) absorption on the presence of impurities. *Garces* et al. [22.118] indicated that near-ultraviolet absorption is strongly related to the Fe^{3+} impurity in the growth solution. Near-ultraviolet optical absorption spectra taken from two KDP crystals are shown in Fig. 22.43. These data clearly indicate the presence of an intense 270 nm optical absorption band, along with additional absorption in the 200–230 nm region. They found a direct correlation between the Fe^{3+} content and the 270 nm band intensity. *Wang* et al. [22.73] also found that doping of Sn^{4+} lowers transmission near the ultraviolet region, as shown in Fig. 22.44.

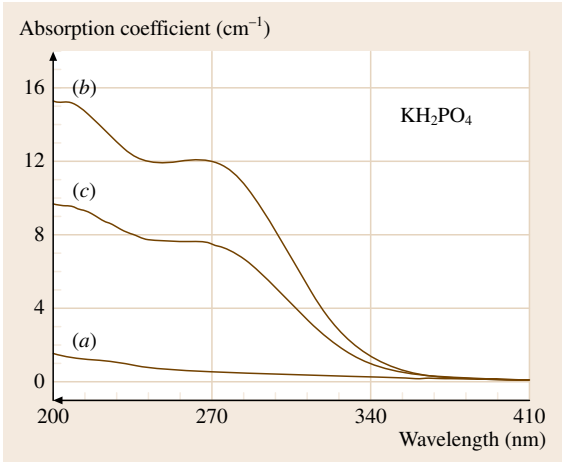


Fig. 22.43 Optical absorption of KDP crystals at room temperature (after [22.118], with permission of Elsevier)

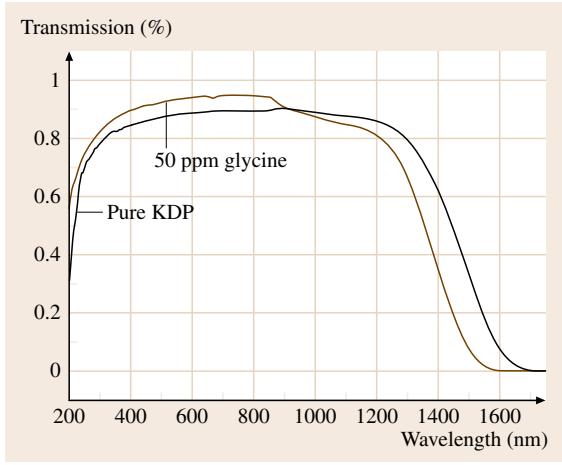


Fig. 22.45 Transmission curves of 50 ppm glycine doped KDP (after [22.119])

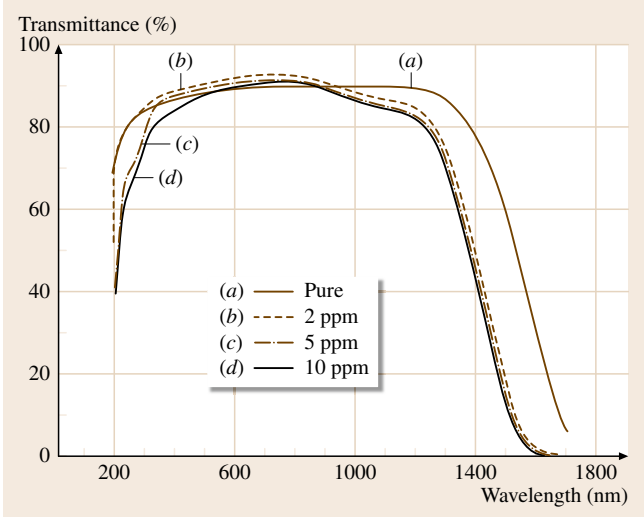


Fig. 22.44 Transmission spectra of KDP crystals grown from solution doped with different concentrations of Sn^{4+} ion by traditional temperature reduction method (after [22.73], with permission of Elsevier)

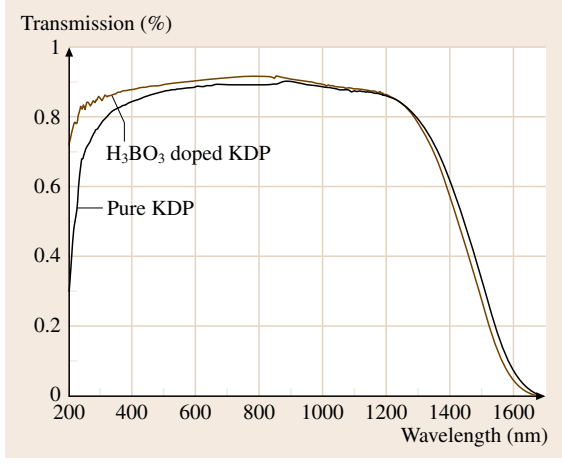


Fig. 22.46 Transmission curves of 10 ppm boric acid doped KDP (after [22.119])

The effects of some anion and amino-acid impurities have been studied and reported by *Sun* and others [22.98, 119], showing that pyrophosphoric acid shortens the transparency range while the addition of a certain concentration of EDTA can extend the range of transparency. As shown in Figs. 22.45 and 22.46, other impurities such as boric acid, glycine, and sulfate can affect the transmittance of KDP crystal.

Generally, metal impurities such as Fe^{3+} and Cr^{3+} are mainly responsible for the extra absorption in the near-ultraviolet band through an electron transition mechanism, while infrared and near-IR band shifts can be attributed to anion group and amino-acid impurities, as they can affect vibration in the IR band.

22.5.2 Homogeneity

Efficient operation of electrooptic devices such as Pockels cells and frequency converters requires crystals with a high degree of optical perfection. For a crystal to perform adequately when used in a laser system it must

maintain beam polarization, introduce minimal distortion of the spatial phase profile, and provide uniform phase matching for frequency conversion. All growth defects have the potential to degrade the performance of KDP and DKDP crystals either by altering the index of refraction or by generating inhomogeneities in the unit normal to the c-plane of the crystal. This latter phenomenon has been referred to as z-axis wander [22.94, 95].

Variations in the refractive index are caused by two primary effects: impurities and strain. Impurities, even when uniformly distributed, generate compositional variations which can alter the diagonal components in the projection onto the plane of polarization of the refractive index tensor. These control the velocity and therefore the phase front of a transmitted beam. However, unless the impurities are of sufficient concentration to alter the crystal symmetry, the induced anomalous birefringence would be insignificant.

In contrast, strain due to externally applied stresses, inhomogeneities in impurity concentrations, foreign inclusions or structural defects such as dislocations, twin boundaries or low-angle grain boundaries can both alter the diagonal components and introduce off-diagonal components, the latter being the source of anomalous birefringence. From the theoretical relationships between optic index and applied strain, measured spatial variations in transmitted phase and depolarization of an incident beam can be related to the internal strain field of a crystal.

The primary effect of z-axis wander is to generate spatial nonuniformities in the critical phase-matching angle for frequency conversion. The same sources which are responsible for anomalous birefringence can be expected to lead to z-axis wander.

Regarding the techniques employed, x-ray topography [22.94, 95], scatterometry [22.120], optical absorption [22.121], and secondary-ion mass spectrometry (SIMS) have been used to correlate optical distortions with defects in KDP crystals:

- X-ray topography and scatterometry reveal the presence of structural defects and inclusions.
- X-ray topography and optical absorption probe the large-scale impurity variations from growth bands, crystal sectorality, and vicinal sectorality.
- Secondary-ion mass spectrometry, and to some extent scatterometry, probes the small-scale distribution of impurity ions.

Effect of Dislocations

In conventionally grown crystals, high dislocation density near the seed cap results in a large degree of optical distortion. Because the majority of these dislocations emerge at high angles to the {101} faces, as the crystal grows along the z-direction they pass to the {100} faces. The resulting crystal has low dislocation density only far from the seed, as illustrated in Fig. 22.47a. Consequently, useful material can only be taken from areas that are remote from the seed cap.

In contrast, dislocations in rapidly grown crystals of both KDP and DKDP are a minor source of optical distortion. This is because regeneration of the point seed leads to discrete bunches of dislocations, as shown schematically in Fig. 22.47b.

The research of *Smolsky* et al. [22.122] indicates that a temperature change of 0.1 K is sufficiently high to form large secondary dislocation sources. The distribution of growth steps over the faces of a crystal during growth is not constant. They change not only because of the variations of the external growth conditions but also because of some internal factors. The steps generated

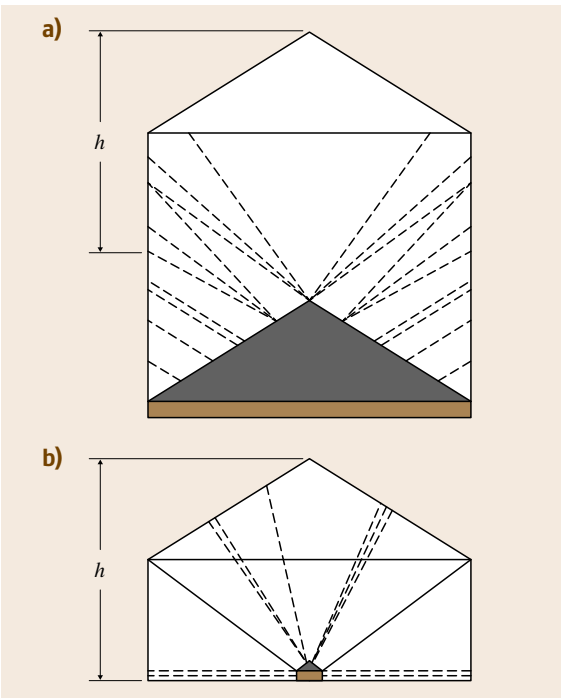


Fig. 22.47a,b Schematic of dislocation structure of (**a**) conventional and (**b**) rapidly grown KDP crystals (after [22.7], with permission of ASM Int.)

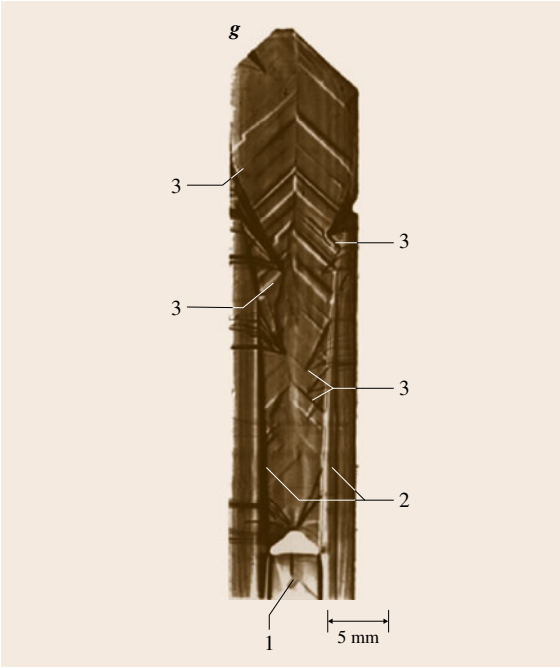


Fig. 22.48 Projection x-ray topograph of the *X*-cut of a KDP crystal. MoK_{α_1} radiation, reflection vector $\boldsymbol{g}$[020]: (1) seed; (2) sectorial boundaries between the prismatic and bipyramidal faces; (3) striation due to a lower activity of the leading growth hillocks at the face edge and the formation of new dislocation sources of steps (after [22.7], with permission of ASM Int.)

by new dislocations have new spreading directions on the face and density in accordance with the dislocation source position and activity. Therefore some stresses are formed between the old and new layers which, in turn, give rise to striation (Fig. 22.48).

De Yoreo's results [22.94] show a distinct dependence on position in the boule. Crystals from near the seed (grown first) show considerably more strain than those from near the end of the boule (grown last). This dependence may result from the distribution of dislocation as shown in Fig. 22.48.

Differences Across Sector Boundaries

There is evidence to show that the level of impurities changes sharply at {101}/{100} boundaries, but remains fairly uniform within each sector, when the crystal is grown at 5 mm/day. In contrast, depolarization data shows that the strain is concentrated near the boundary, where the impurity level changes sharply, supporting the expectation that impurities per se are not the source of strain but rather local variations in impurity levels [22.7].

Crystals grown at higher rates exhibit strong ultraviolet absorption in the {100} sectors, but the contrast between the two sectors is greatly reduced, as is the strain at the boundary. In fact, the level of optical distortion due to the presence of sector boundaries is now at the level of background distortion due to other factors. Even in crystals with rather uniform transmitted wavefront (TWF), significant inhomogeneities in phase-matching angle have been observed [22.123].

Perhaps the most troublesome aspect of crystal sectorality is the strong tendency of iron to incorporate into the {100} sectors, combined with its extremely high absorption coefficient in KDP at the third harmonic. In fact, of all the impurities that have been investigated in NIF development, iron appears to be the only impurity that generates significant optical absorption at 351 nm, which lies in the tail of an absorption band that peaks near 270 nm (Fig. 22.43).

Vicinal Sectorality

Within the {101} sectors of KDP crystals, the boundaries between the three sectors of each vicinal hillock as well as the boundaries between neighboring hillocks subdivide the crystal into regions of contrasting lattice parameters. This vicinal sectorality has a distinct dependence on growth rate. High growth rate cause high depolarization losses [22.7]. Impurities are the source of vicinal sectorality in KDP. The UV absorption and impurity content increase sharply at the boundary.

Deuterated KDP Crystals

De Yoreo et al. [22.7] point out that all the defects observed in KDP are also present in DKDP. Besides, there are some aspects of crystal quality which are peculiar to the deuterated crystals. These peculiarities arise from the fact that, in practice, all DKDP crystals contain significant levels of hydrogen, unless deuterated salt is utilized. Consequently, all deuterated crystals contain hydrogen as a substitutional impurity species at levels from $\approx 1\%$ to more than 10%. Indeed, in NIF development work, DKDP crystals grown at rates from less than 1 to 15 mm/day have always been found to exhibit vicinal sectorality in their x-ray topograph. This inhomogeneity has a moderate effect on optical uniformity. Figure 22.49a shows the TWF profile from a 92% DKDP crystal grown at 9 mm/day that exhibits strong vicinal sectorality.

The fact that such sectorality is due to variations in hydrogen content is demonstrated in Fig. 22.49b which

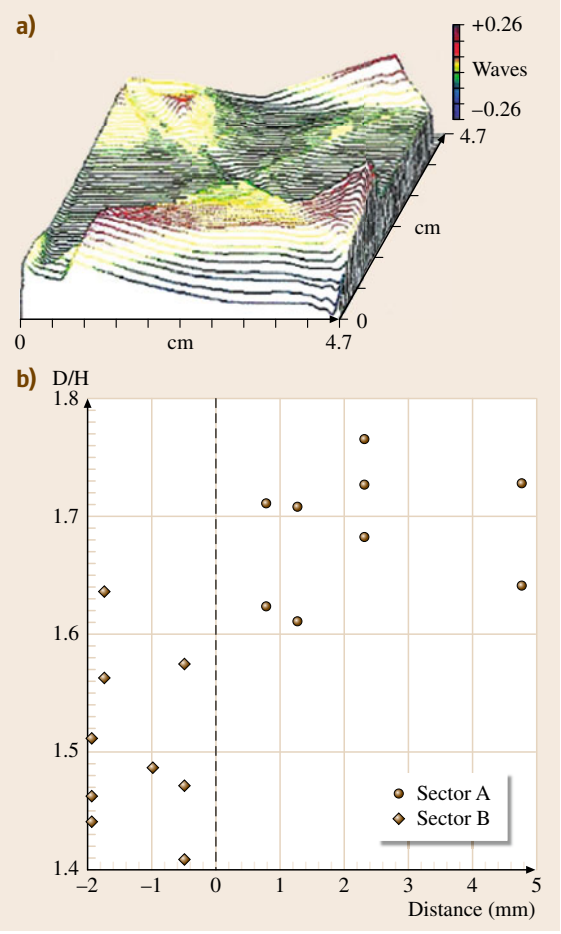


Fig. 22.49a,b Strong vicinal sectorality of 92% DKDP crystal grown at 9 mm/day **(a)** TWF profile; **(b)** profile of D/H ratio across vicinal sector boundary as determined from secondary-ion mass spectrometry (SIMS) (after [22.7], with permission of ASM Int.)

shows a SIMS profile of the D/H ratio collected across a vicinal sector boundary. Results demonstrate that the hydrogen content changes by 15% across the boundary. Other results have shown that the magnitude of this change depends inversely on growth temperature. The difference is optically undetectable for growth temperatures greater than about 60 °C.

A kind of inclusions also is found in the area of pyramidal–pyramidal sector boundary, the formation of which is related to the absorption of impurities. During the growth of pyramidal sector, the impurities are rejected from the sector and aggregate in the pyramidal–pyramidal sector boundary, causing lattice mismatch.

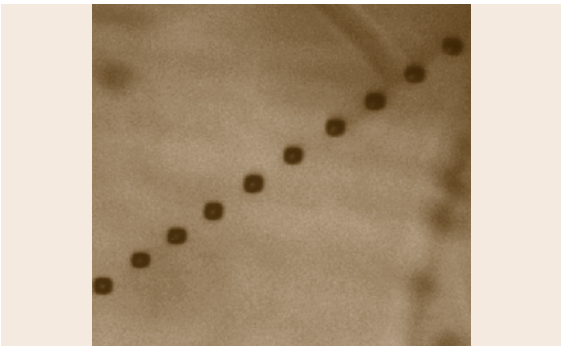


Fig. 22.50 Inclusions along Py–Pr sector (after [22.124])

This mismatch breaks the D-bond and creates a bunch of inclusions (Fig. 22.50) [22.124]. Similar results can be seen in the reports of *Joshi* and others [22.76, 105, 125].

In total, there are four possible sources of strain in crystals of $K(D_xH_{1-x})_2PO_4$. Each of them can act independently to produce strain in KDP–DKDP crystals [22.94]. First among these is dislocations, which produce strain fields that vary as $1/r$, where r is the distance from the dislocation. The second source is impurities, which gives rise to strain due to lattice mismatch. These first two factors are commonly found in the case of KDP crystals. The third one is the mixing of hydrogen and deuterium on the hydrogen sublattice, which generates strain due to the difference in structural parameters of KH_2PO_4 and KD_2PO_4. Both the cell parameters and orientation of the PO_4 tetrahedron are different for the two end members of this solid-solution series [22.126, 127], consequently the mixed crystals will be strained. The fourth source of strain is that the tetragonal–monoclinic phase transition in this solid-solution series occurs at increasingly lower temperature as the deuterium level increases.

22.5.3 Laser Damage Threshold

The mechanisms of laser-induced damage are still not well understood. Many papers are devoted to it and several models have been proposed, such as lattice defects, interstitial inclusions and vacancies, multiphoton ionization, and two-photon absorption, etc. [22.128, 129]. Impurities in the raw material and growth conditions have been proved to have a direct relation with the bulk laser-induced damage threshold (LDT) of the crystal, including inorganic impurities, such as Fe^{3+}, anion impurities, and some organic materials [22.7, 119].

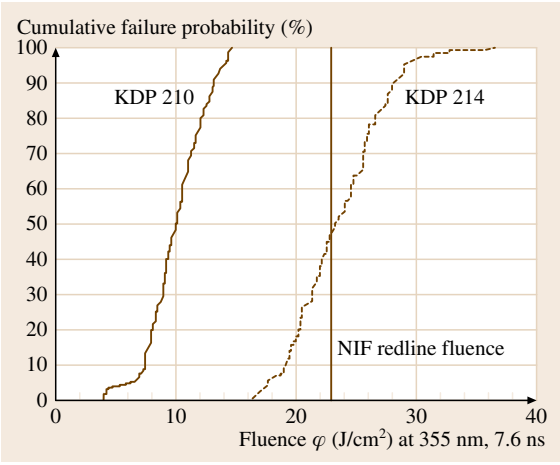


Fig. 22.51 Effect of continuous filtration of the 3ω damage performance of rapidly grown KDP. Samples were grown under nominally identical conditions with ultrahigh-purity salts. Sample 210 was prefiltered only, which resulted in high numbers of inclusions in the crystal, while sample 214 was continuously filtered during growth. Sample 214 represents the best damage performance of a rapid growth crystal to date (after [22.130])

Also, filtration before growth and continuous filtration during the growth process help to increase the LDT; investigations show that continuous filtration results in an increase in damage performance of $\approx 2\times$ over the entire cumulative failure distribution (CFD) range [22.130] (Fig. 22.51).

One should be aware that LDT is related to the laser conditions, such as wavelength, frequency, laser irradiation direction, and polarization, which makes it more complex [22.128, 133].

Effect of Postgrowth Treatment

Previous investigations of the effects of thermal annealing on KDP and KD*P damage performance [22.132–137] have indicated that it is possible to increase the 1ω damage threshold ($R/1$) by approximately 1.5× compared with the level without conditioning (Table 22.3). The 3ω thresholds, however, were not substantially affected by the annealing process.

LLNL testing showed that postgrowth thermal annealing of KDP crystals at 160 °C appears to increase the damage performance of rapidly grown samples by 2.7× at 1ω. The benefits of thermal annealing at 3ω are not as well defined as the dramatic increases seen at 1ω. On the other hand, thermal annealing appeared to suppress the low-fluence tail of the CFD at 3ω, thus leading to less expected damage at 1ω. When large-area beams were used to study the feasibility of online conditioning for NIF triplers, it was found that substantial conditioning was achievable in 8–12 shots of equal fluence interval. Analysis of scatter density versus fluence showed that the number of damage sites evolved exponentially. Furthermore, damage sites were stable against increases in fluence. *Fujioka* et al. [22.91] reported similar result. The full-width at half-maximum (FWHM) of x-ray diffraction of KDP crystals was detected to decrease obviously after conditioning at 165 °C, as shown

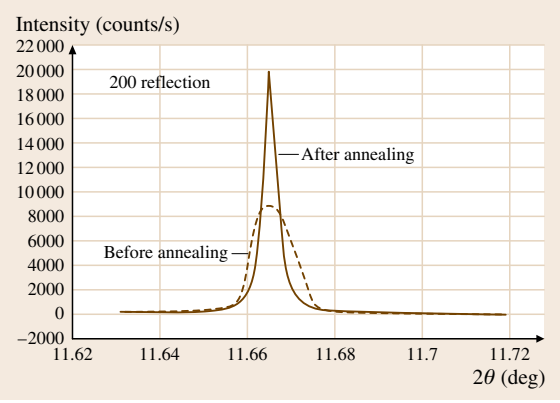


Fig. 22.52 Rocking curve of KDP crystal sample (200) double-crystal x-ray diffraction at same position before and after annealing at 165 °C (after [22.131])

Table 22.3 Compilation of thermal annealing on KDP damage performance [22.132]

Sample	Sector	Growth temperature (°C)	Growth (d)	Unannealed (J/cm²)	Annealed (J/cm²)	Annealed with SHG (J/cm²)
F6-1	Pyramid	48	40	32	33	26
F6-2	Pyramid	63	30	17	23	18
F6-3	Pyramid	72	14	17	23	23
F6-4	Prism	71	20	23	40	30
F6-5	Prism	60	33	21	37	36
F6-6	Prism	25	48	17	40	28

in Fig. 22.52, which suggested that internal stress was released partly and the structural perfection of crystal was improved [22.131]. The result that the perfection of rapidly grown crystal improved more than those grown using conventional methods is consistent with the improvement of optical property by annealing [22.91].

DKDP is not amenable to thermal conditioning, because the crystals tend to fog or fall apart as a result of either decomposition or phase transformation at the temperatures used to anneal KDP. Consequently, laser conditioning is the only option [22.139].

Simulation of the Mechanism of LID

Understanding the susceptibility of KDP crystals to laser-induced damage (LID) at high laser fluence an order of magnitude below the expected intrinsic breakdown limits is a long-standing issue [22.7]. Recently, *Carr* et al. [22.128] employed a novel experimental approach in order to understand the mechanisms of laser-induced damage of KDP crystal. Two notable sharp steps in the damage threshold centered at 2.55 eV (487 nm) and 3.90 eV (318 nm) are clearly demonstrated in their experimental results (Fig. 22.53). Recent simulation study of KDP crystal seems to be targeted at the wavelength dependence of laser-induced damage to support the defect-assisted multistep photon mechanism proposed by *Carr* et al. [22.128].

The effect of neutral and charged H-interstitial and H-vacancy on laser damage was investigated by *Liu* et al. [22.140]. They reported that the bandgap of the neutral H-interstitial and positively charged H-vacancy are greatly reduced to 2.6 and 2.5 eV, respectively. This result is well consistent with the first sharp step at 2.55 eV and suggests that these two types of defects may be responsible for lowering the damage threshold in KDP crystal [22.128]. *Wang* et al. [22.141] explained that −2 charged O-interstitials are responsible for laser-induced local collapse.

In *Liang*'s work [22.138], an ab initio study of $[SO_4]^{2-}$ in KDP is presented [22.142]. $[SO_4]^{2-}$ is such a common impurity ion in KDP raw materials that point defects of $[PO_4]^{3-}$ replaced by $[SO_4]^{2-}$ are easily created during crystal growth [22.143]. The same simulation model as that adopted by *Liu* et al. [22.140] and *Wang* et al. [22.141] was used, which made it possible to compare between different works. In the density of states (DOS) of KDP containing $[SO_4]^{2-}$ (Fig. 22.54), it is shown that the bandgap has reduced to 3.90 eV (318 nm), which can induce laser absorption at 318 nm [22.138]. The results of this study are consistent with the experimental work of *Carr* et al. [22.128]. So, it can be speculated that sulfate substitution accounts to some extent for the second sharp step.

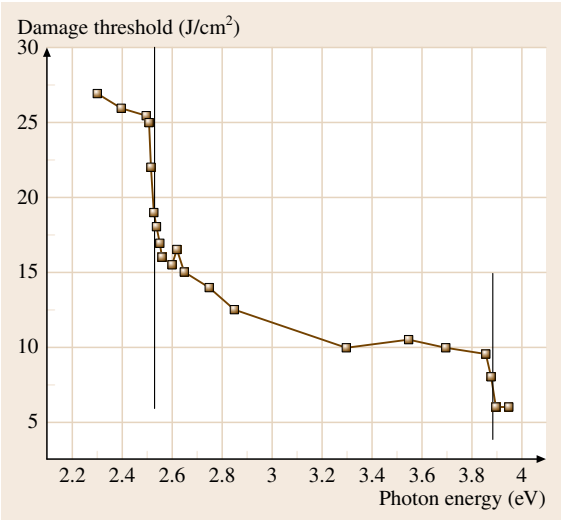


Fig. 22.53 Wavelength-dependent damage threshold (after 22.128)

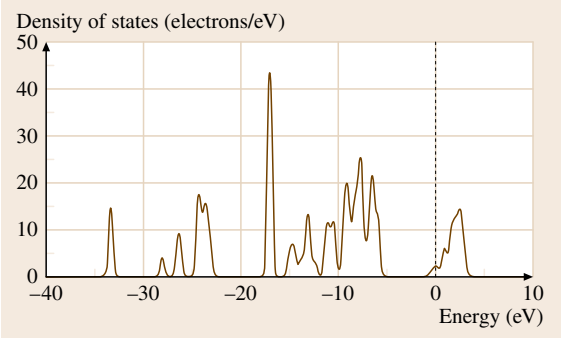


Fig. 22.54 Total density states of KDP ($[SO_4]^{2-}$) (after 22.138)

References

22.1 L.N. Rashkovich: *KDP Family Single Crystals* (Adam-Hilger, New York 1991)
22.2 Ferroelectrics **71** (1987)
22.3 Ferroelectrics **72** (1987)
22.4 J.F. Nye: *Physical Properties of Crystals* (Oxford Univ. Press, New York 1985), Chap. 13

22.5 D. Eimerl: Electro-optic, linear, and non-linear optical properties of KDP and its isomorphs, Ferroelectrics **72**, 95 (1987)

22.6 J.D. Lindl: Review of development of the indirect-drive approach to inertial confinement fusion and the target physics basis for ignition and gain, Phys. Plasmas **2**, 3933 (1995)

22.7 J.J. De Yoreo, A. Burnham, P.K. Whitman: Developing KDP and DKDP crystals for the world's most powerful laser, Int. Mater. Rev. **13**, 113–152 (2002)

22.8 N.P. Zaitseva, J.J. De Yoreo, M.R. Dehaven, R.L. Vital, K.E. Montgomery, M. Richardson, L.J. Atherton: Rapid growth of large-scale (40 – 55 cm) KH_2PO_4 crystals, J. Cryst. Growth **180**, 255–262 (1997)

22.9 V.I. Bespalov, V.I. Bredikhin, V.P. Ershov, V.I. Katsman, N.V. Kiseleva, S.P. Kuznetsov: Optical properties of KDP and DKDP crystals grown at high rates, Sov. J. Quantum Electron. **12**, 1527–1528 (1982)

22.10 G.M. Loiacono, J.J. Zola, G. Kostecky: Growth of KH_2PO_4 crystals at constant temperature and supersaturation, J. Cryst. Growth **62**, 545–556 (1983)

22.11 J.F. Cooper, M.F. Singlenton, J. Zandelevich: Rapid growth of potassium dihydrogen phosphate crystals, Proc. Int. Conf. Laser 1984 (1984) pp. 567–572

22.12 L.N. Rashkovich: High-speed growth of large crystals for nonlinear optics from solution, Vestn. Akad. Nauk SSSR **9**, 15–19 (1984)

22.13 S.A. de Vries, P. Goedtkindt, S.L. Bennett, W.J. Huisman, M.J. Zwanenburg, D.-M. Smilgies, J.J. De Yoreo, W.J.P. van Enckevort, P. Bennema, E. Vlieg: Surface atomic structure of KDP crystals in aqueous solution: An explanation of the growth shape, Phys. Rev. Lett. **80**, 2229 (1998)

22.14 P. Hartman: In: *Crystal Growth, An Introduction* (North-Holland, Amsterdam 1973) p. 367

22.15 P. Bennema: In: *Handbook of Crystal Growth*, Vol. 1a, ed. by T.J. Hurle (Elsevier Science Publishers, Amsterdam 1993) p. 477

22.16 P. Hartman: The morphology of zircon and potassium dihydrogen phosphate in relation to the crystal structure, Acta Crystallogr. **9**, 721–727 (1956)

22.17 B. Dam, P. Bennema, W.J.P. Van Enckevort: The mechanism of tapering on KDP-type crystals, J. Cryst. Growth **74**, 118–128 (1986)

22.18 W.J.P. Van Enckevort, R. Janssen-van Rosmalen, W.H. van der Linden: Evidence for spiral growth on the pyramidal faces of KDP and ADP single crystals, J. Cryst. Growth **49**, 502–514 (1980)

22.19 J.J. De Yoreo, T.A. Land, B. Dair: Growth morphology of vicinal hillocks on the {101} face of KDP: From step-flow to layer-by-layer growth, Phys. Rev. Lett. **73**, 838–841 (1994)

22.20 S.A. de Vries, P. Goedtkindt, W.J. Huisman, M.J. Zwanenburg, R. Feidenhans'l, S.L. Bennett, D.-M. Smilgies, A. Stierle, J.J. De Yoreo, W.J.P. van Enckevort: X-ray diffraction studies of potassium dihydrogen phosphate (KDP) crystal surfaces, J. Cryst. Growth **205**, 202–214 (1999)

22.21 I.K. Robinson: Crystal truncation rods and surface roughness, Phys. Rev. B **33**, 3830–3836 (1986)

22.22 B. Dam, W.J.P. van Enckevort: In situ observation of surface phenomena on {100} and {101} potassium dihydrogen phosphate crystals, J. Cryst. Growth **69**, 306–316 (1984)

22.23 B. Dam, E. Polman, W.J.P. van Enckevort: *Industrial Crystallization*, Vol. 84, ed. by S.J. Jancic, E.J. de Jong (Elsevier Science Publishers, Amsterdam 1984) p. 97

22.24 N. Cabrera, D.A. Vermilyea: The growth of crystals from solution. In: *Growth and Perfection of Crystals*, ed. by R.H. Doremus, B.W. Roberts, D. Turnbull (Wiley, New York 1958) pp. 393–410

22.25 T.A. Land, T.L. Martin, S. Potapenko, G.T. Palmore, J.J. De Yoreo: Recovery of surfaces from impurity poisoning during crystal growth, Nature **399**, 442–445 (1999)

22.26 W.J.P. van Enckevort, A.C.J.F. van den Berg: Impurity blocking of crystal growth: A Monte Carlo study, J. Cryst. Growth **183**, 441–455 (1998)

22.27 M.K. Cerreta, K.A. Berglund: The structure of aqueous solutions of some dihydrogen orthophosphates by laser Raman spectroscopy, J. Cryst. Growth **84**, 577–588 (1987)

22.28 L.G. Wu, X.H. Rui, G.J. Teng, Z.S. Qi, C. Yong, Z.Y. Qi: Lattice vibration modes and growth mechanism of KDP single crystals studied by Raman spectroscopy, Chin. J. Light Scatt. **01**, 28–34 (2002)

22.29 X. Yu, X. Yue, H. Gao, H. Chen: Quantitative studies of solute boundary layers around crystals by holographic phase-contrast interferometric microphotography, J. Cryst. Growth **106**, 690–694 (1990)

22.30 X. Yu, J. Yu, Y. Wang, Z. Cheng, B. Yu, S. Zhang, D. Sun, G. Jiang: Microprobe of structure of crystal/liquid interface boundary layers, Sci. China Ser. E **3**, 43–51 (2001)

22.31 M.F. Reedijk, J. Arsic, F.F.A. Hollander, S.A. de Vries, E. Vlieg: Liquid order at the interface of KDP crystals with water: Evidence for icelike layers, Phys. Rev. Lett. **90**, 66103 (2003)

22.32 N.P. Zaitseva, L.N. Rashkovich, S.V. Bogatyreva: Stability of KH_2PO_4 and $K(H,D)_2PO_4$ solutions at fast crystal growth rates, J. Cryst. Growth **148**, 276–282 (1995)

22.33 D. Kaminski, N. Radenovic, M.A. Deij, W.J.P. van Enckevort, E. Vlieg: pH-dependent liquid order at the solid-solution interface of KH_2PO_4 crystals, Phys. Rev. B **72**, 245404 (2005)

22.34 J.W. Mullin: *Crystallization* (Butterworths, London 1993)

22.35 D. Kashchiev, D. Verdoes, G.M. van Rosmalen: Induction time and metastability limit in new phase formation, J. Cryst. Growth **110**, 373–380 (1991)

22.36 A.S. Myerson, A.F. Izmailov, H.-S. Na: Thermodynamic studies of levitated microdroplets of highly supersaturated electrolyte solutions, J. Cryst. Growth **166**, 981–988 (1996)

22.37 M. Bohenek, A.S. Myerson, W.M. Sun: Thermodynamics, cluster formation and crystal growth in highly supersaturated solutions of KDP, ADP and TGS, J. Cryst. Growth **179**, 213–225 (1997)

22.38 M.H. Jiang, C.S. Fang, X.L. Yu, M. Wang, T.H. Zheng, Z.S. Gao: Polymorphism and metastable growth of DKDP, J. Cryst. Growth **53**, 283–291 (1981)

22.39 M. Shanmugham, F.D. Gnanam, P. Ramasamy: Non-steady state nucleation process in KDP solutions in the presence of XO_4 impurities, J. Mater. Sci. **19**, 2837–2844 (1984)

22.40 O. Shimomura, M. Suzuki: The increase of temperature range in the region of supersaturation of KDP solution by addition of impurity, J. Cryst. Growth **98**, 850–852 (1989)

22.41 S. Nagalingam, S. Vasudevan, R. Dhanasekaran, P. Ramasamy: Effect of impurities on the nucleation of ADP from aqueous solution, Cryst. Res. Technol. **16**, 647–650 (1981)

22.42 N.P. Zaitseva, L. Carman: Rapid growth of KDP-type crystals, Prog. Cryst. Growth Charact. Mater. **43**, 1–118 (2001)

22.43 A.B. Ahza: Kinetics of milk fat crystallization in a continous crystallizer, Ph.D. Thesis (University of Wisconsin-Madison 1995)

22.44 A.D. Randolph, M.A. Larson: *Thery of Particulate Processes. Analysis and Techniques of continuous crystallization*, 2nd edn. (Academic, San Diego 1988)

22.45 R. Boistele: Fundamentals of nucleation and crystal growth. In: *Crystallization and Polymorphism of Fats and Fatty Acids*, Surfactant, Vol. 31, ed. by N. Garti, K. Sato (Marcel Dekker, New York 1988) pp. 189–226

22.46 J. Nývlt, O. Söhnel, M. Matichová, M. Bruol: *The Kinetics of Industrial Crystallization* (Academia, Prague 1985)

22.47 E.G. Denk Jr., G.D. Botsaris: Fundamental studies in secondary nucleation from solution, J. Cryst. Growth **13/14**, 493–499 (1972)

22.48 J. Synowiec: A method calculation of the limiting supersaturation of inorganic salt solutions, Krist. Tech. **8**, 701–708 (1973)

22.49 O. Söhnel: Metastable regions of aqueous solutions of inorganic soluble salts, Krist. Tech. **11**, 141–148 (1976)

22.50 A. Mersmann, K. Bartosch: How to predict the metastable zone width, J. Cryst. Growth **183**, 240–250 (1998)

22.51 T.A. Land, J.J. De Yoreo, T.L. Martin, G.T. Palmore: A comparison of growth hillock structure and step dynamics on KDP {100} and {101} surfaces using force microscopy, Crystallogr. Rep. **44**, 704–716 (1999)

22.52 I.L. Smolsky, N.P. Zaitseva: *Growth of Crystals*, Vol. 19, ed. by E.I. Givargizov, S.A. Grinberg (Plenum Publ. Corp., New York 1995) p. 173

22.53 A.A. Chernov, N.P. Zaitseva, L.N. Rashkovich: Secondary nucleation induced by the cracking of a growing crystal: KH_2PO_4 (KDP) and $K(H,D)_2PO_4$ (DKDP), J. Cryst. Growth **102**, 793–800 (1990)

22.54 H. Hilscher: Microscopic investigations of morphological structures on the pyramidal faces of KDP and DKDP single crystals, Cryst. Res. Technol. **20**, 1351–1361 (1985)

22.55 N.P. Zaitseva, L. Carman, I.L. Smolsky, R. Torres, M. Yan: The effect of impurities and supersaturation on the rapid growth of KDP crystals, J. Cryst. Growth **204**, 512–524 (1999)

22.56 C. Belouet, M. Monnier, J.C. Verplanke: Autoradiography as a tool for studying iron segregation and related defects in KH_2PO_4 single crystals, J. Cryst. Growth **29**, 109–120 (1975)

22.57 A.I. Malkin, A.A. Chernov, I.V. Alexeev: Growth of dipyramidal face of dislocation-free ADP crystals; free energy of steps, J. Cryst. Growth **97**, 765–769 (1989)

22.58 N.P. Zaitseva, L. Carman, I.L. Smolsky: Habit control during rapid growth of KDP and DKDP crystals, J. Cryst. Growth **24**, 363–373 (2002)

22.59 H.V. Alexandru, S. Antohe: Prismatic faces of KDP crystal, kinetic and mechanism of growth from solutions, J. Cryst. Growth. **258**, 149–157 (2003)

22.60 A.A. Chernov: Stability of faceted shapes, J. Cryst. Growth **24/25**, 11–31 (1974)

22.61 H.J. Scheel, P. Niedermann: Growth mechanisms of $YBa_2Cu_3O_{7-x}$ platelet crystals from STM/SEM investigations, J. Cryst. Growth **94**, 281–284 (1989)

22.62 N.P. Zaitseva, I.L. Smolsky, L. Carman: Growth phenomena in the surface layer and step generation from the crystal edges, J. Cryst. Growth **222**, 249–262 (2001)

22.63 E.P. Lokshin: Growth and properties of KDP-group crystals, Crystallogr. Rep. **41**, 1061–1069 (1996)

22.64 L.N. Rashkovich, G.T. Moldazhanova: Growth kinetics and morphology of potassium dihydrogen phosphate crystal faces in solutions of varying acidity, J. Cryst. Growth **151**, 145–152 (1995)

22.65 J.W. Mullin, A. Amatavivadhana: Growth kinetics of ammonium and potassium dihydrogen phosphate crystals, J. Appl. Chem. **17**, 151–156 (1967)

22.66 L.N. Rashkovich, N.V. Kronsky: Influence of Fe^{3+} and Al^{3+} ions on the kinetics of steps on the {100} faces of KDP, J. Cryst. Growth **182**, 434–441 (1997)

22.67 T.A. Eremina, V.A. Kuznetsov, N.N. Eremin, T.M. Okhrimenko, N.G. Furmanova, E.P. Efremova, M. Rak: On the mechanism of impurity influence on growth kinetics and surface morphology of KDP crystals-II: Experimental study of influence of bivalent and trivalent impurity ions on growth kinetics and surface morphology of KDP crystals, J. Cryst. Growth **273**, 586–593 (2005)

22.68 J.J. De Yoreo, T.A. Land, L.N. Rashkovich, T.A. Onischenko, J.D. Lee, O.V. Monovskii, N.P. Zaitseva: The effect of dislocation cores on growth hillock vicinality and normal growth rates of KDP {101} surfaces, J. Cryst. Growth **182**, 442–460 (1997)

22.69 P.G. Vekilov, Y.G. Kuznetsov, A.A. Chernov: The effect of temperature on step motion; (101) ADP face, J. Cryst. Growth **121**, 44–52 (1992)

22.70 M. Nakatsuka, K. Fujioka, T. Kanabe, H. Fujita: Rapid growth over 50 mm/d of water-soluble KDP crystal, J. Cryst. Growth **171**, 531–537 (1997)

22.71 P.G. Vekilov, Y.G. Kuznetsov: Growth kinetics irregularities due to changed dislocation source activity; (101) ADP face, J. Cryst. Growth **119**, 248–260 (1992)

22.72 G.M. Loiacono, J.J. Zola, G. Kostecky: The taper effect in KH_2PO_4 type crystals, J. Cryst. Growth **58**, 495–499 (1982)

22.73 B. Wang, C.-S. Fang, S.-L. Wang, X. Sun, Q.-T. Gu, Y.-P. Li, X.-G. Xu, J.-Q. Zhang, B. Liu, X.-M. Mou: The effects of Sn^{4+} ion on the growth habit and optical properties of KDP crystal, J. Cryst. Growth **297**, 352–355 (2006)

22.74 Z.S. Gao, Y.P. Li, C. Wang, Z.K. Lu: Effect of metaphosphate on the growth in KDP crystal, J. Synth. Cryst. **23**(3/4), 52–55 (1994)

22.75 Y.-J. Fu, Z.-S. Gao, J.-M. Liu, Y.-P. Li, H. Zeng, M.-H. Jiang: The effects of anionic impurities on the growth habit and optical properties of KDP, J. Cryst. Growth **198/199**, 682–686 (1999)

22.76 S. Wang, Z.S. Gao, Y. Fu, X. Sun, J. Zhang, H. Zeng, Y. Li: Scattering centers caused by adding metaphosphate into KDP crystals, J. Cryst. Growth **223**, 415–419 (2001)

22.77 V.A. Kuznetsov, T.M. Okhrimenko, M. Rak: Growth promoting effect of organic impurities on growth kinetics of ADP and KDP crystals, J. Cryst. Growth **193**, 164–173 (1998)

22.78 N.P. Zaitseva, J. Atherton, R. Rozsa, L. Carman, I.L. Smolsky, M. Runkel, R. Ryon, L. James: Design and benefits of continuous filtration in rapid growth of large KDP and DKDP crystals, J. Cryst. Growth **197**, 911–920 (1999)

22.79 I. Owsczarek, B. Wojciechowski: Nucleation and growth behaviour of KDP from degassed and undegassed aqueous solutions, J. Cryst. Growth **84**, 329–331 (1987)

22.80 H.J. Scheel, T. Fukuda (Eds.): *Crystal Growth Technology* (Wiley, New York 2003) p. 446

22.81 I. Kolodyazhngl: *Abstracts of ICCG XI, P201A.21* (The Hague, 1995) pp. 18–23

22.82 M.S. Yan, D. Wu, J.B. Zeng, X. Zhang, Y. Guan, L. Wang: Growth of large cross section KDP-type crystals, J. Synth. Cryst. **115**, 1–4 (1986)

22.83 T. Sasaki, A. Yokotani: Growth of large KDP crystals for laser fusion experiments, J. Cryst. Growth **99**, 820–826 (1990)

22.84 Z.K. Lu, Z.S. Gao, Y.P. Li, C. Wang: Growth of large KDP crystals by solution circulating method, J. Synth. Cryst. **25**, 19–22 (1996)

22.85 V.M. Loginer: *Abstracts of ICCG XI, P203B.22* (The Hague, June 1995) pp. 18–25

22.86 V.I. Bespalov, V.I. Bredikhin, V.P. Ershov, V.I. Katsman, L.A. Lavrov: KDP and DKDP crystals for nonlinear optics grown at high rate, J. Cryst. Growth **82**, 776–778 (1987)

22.87 P.F. Bordui, G.M. Loiacono: In-line bulk supersaturation measurement by electrical conductometry in KDP crystal growth from aqueous solution, J. Cryst. Growth **67**, 168–172 (1984)

22.88 S.L. Wang, Y.J. Fu, W.C. Zhang, X. Sun, Z.S. Gao: In-line bulk concentration measurement by method of conductivity in industrial KDP crystal growth from aqueous solution, Cryst. Res. Technol. **35**, 1027–1034 (2000)

22.89 K. Montgomery, N.P. Zaitseva, J.J. De Yoreo, R. Vital: Device for isolation of seed crystals during processing of solutions, LLNL Docket No. IL-9643, DOE case No. S-82,943, US Patent 5904772

22.90 S.L. Wang, Z.S. Gao, Y.J. Fu, A.D. Duan, X. Sun, C.S. Fang, X.Q. Wang: Study on rapid growth of highly-deuterated DKDP crystals, Cryst. Res. Technol. **38**, 941–945 (2003)

22.91 K. Fujioka, S. Matsuo, T. Kanabe, H. Fujita, M. Nakatsuka: Optical properties of rapidly grown KDP crystal improved by thermal conditioning, J. Cryst. Growth **181**, 265–271 (1997)

22.92 M.J. Runkel, W.H. Williams, J.J. De Yoreo: Predicting bulk damage in NIF triple harmonic generators, Proc. SPIE **3578**, 322–335 (1998)

22.93 B. Kahr, S.-H. Jang, J.A. Subramony, M.P. Kelley, L. Bastin: Dyeing salt crystals for optical applications, Adv. Mater. **8**, 941–944 (1996)

22.94 J.J. De Yoreo, B.W. Woods: A study of residual stress and the stress-optic effect in mixed crystals of $K(D_xH_{1-x})_2PO_4$, J. Appl. Phys. **73**, 7780–7789 (1993)

22.95 J.J. De Yoreo, Z.U. Rek, N.P. Zaitseva, B.W. Woods: Sources of optical distortion in rapidly grown crystals of KH_2PO_4, J. Cryst. Growth **166**, 291–297 (1996)

22.96 R.A. Hawley-Fedder, H.F. Robey III, T.A. Biesiada, M.R. DeHaven, R. Floyd, A.K. Burnham: Rapid growth of very large KDP and KD*P crystals in support of the National Ignition Facility, Proc. SPIE **4102**, 152–161 (2001)

22.97 S. Wang, Z.S. Gao, Y. Fu, J. Zhang, X. Sun, Y. Li, H. Zeng, G. Huang, J. Yang, Y. Zhuang, Z. Xue: Effects of metaphosphate doping on growth and properties of KDP crystals, Acta Opt. Sin. **22**, 753–757 (2002)

22.98 J. Zhang, S. Wang, C. Fang, X. Sun, Q. Gu, Y. Li, B. Wang, B. Liu, X. Mu: Growth habit and transparency of sulphate doped KDP crystal, Mater. Lett. **61**, 2703–2706 (2007)

22.99 S. Hirota, H. Miki, K. Fukui, K. Maeda: Coloring and habit modification of dyed KDP crystals as functions

of supersaturation and dye concentration, J. Cryst. Growth **235**, 541–546 (2002)
22.100 W.J.P. van Enckevort: Surface microtopography of aqueous solution grown crystals, Prog. Cryst. Growth Charact. Mater. **9**, 1–50 (1984)
22.101 I. Sunagawa: In: *Materials Science of the Earth's Interior*, ed. by I. Sunagawa (Terra Scientific, Tokyo 1984) pp. 63–105
22.102 J.A. Subramony, S.-H. Jang, B. Kahr: Dyeing KDP, Ferroelectrics **191**, 293–300 (1997)
22.103 O.A. Gliko, N.P. Zaitseva, L.N. Rashkovich: Morphology and dynamics of crystal surfaces in complex molecular systems. In: *Materials Research Society Symposium Proceedings*, Vol. 620, ed. by J.J. De Yoreo, W. Casey, A. Malkin, E. Vlieg, M. Ward (Materials Research Society, Warrendale 2001)
22.104 L.N. Rashkovich, A.A. Mkrtchan, A.A. Chernov: Kristallografiya **30**, 380–387 (1985)
22.105 I.L. Smolsky, N.P. Zaitseva, E.B. Rudneva, S.V. Bogatyreva: Formation of "hair" inclusions in rapidly grown potassium dihydrogen phosphate crystals, J. Cryst. Growth **166**, 228–233 (1996)
22.106 H.F. Robey, S.Y. Potapenko, K.D. Summerhays: "Bending" of steps on rapidly grown KH_2PO_4 crystals due to an inhomogeneous surface supersaturation field, J. Cryst. Growth **213**, 340–354 (2000)
22.107 T.A. Land, J.J. De Yoreo: The evolution of growth modes and activity of growth sources on canavalin investigated by in situ atomic force microscopy, J. Cryst. Growth **208**, 623–637 (2000)
22.108 H.G. Van Bueren: *Imperfections in Crystals* (Interscience, New York 1960)
22.109 P. Feng, J.-K. Liang, G.-B. Su, Q.-L.. Zhao, Y.-P.. He, Y.-S. Hunag: Growth of KDP crystals by splicing parallel-seed in aqueous solution and its mechanism, Cryst. Res. Technol. **25**, 1385–1391 (1990)
22.110 P. Feng, J.-K. Liang, G.-B. Su, Y.-P. He, B.-R. Huang, Y.-S. Huang, Q.-L. Zhao: The growth of KDP crystals and its mechanism by splicing misoriented in aqueous solution, Cryst. Res. Technol. **26**, 289–295 (1991)
22.111 H.F. Robey, S.Y. Potapenko: Ex situ microscopic observation of the lateral instability of macrosteps on the surfaces of rapidly grown KH_2PO_4 crystals, J. Cryst. Growth **213**, 355–367 (2000)
22.112 I.L. Smolski, J.J. De Yoreo, N.P. Zaitseva, J.D. Lee, T.A. Land, E.B. Rudneva: Oriented liquid inclusions in KDP crystals, J. Cryst. Growth **169**, 741–746 (1996)
22.113 R. Brooks, A.T. Horton, J.L. Torgesen: Occlusion of mother liquor in solution-grown crystals, J. Cryst. Growth **2**, 279–283 (1968)
22.114 M.S. Joshi, B.K. Paul: Effect of supersaturation and fluid shear on the habit and homogeneity of potassium dihydrogen phosphate crystals, J. Cryst. Growth **22**, 321–327 (1974)
22.115 H.F. Robey, D. Maynes: Numerical simulation of the hydrodynamics and mass transfer in the large scale, rapid growth of KDP crystals. Part 1: Computation of the transient, three-dimensional flow field, J. Cryst. Growth **222**, 263–278 (2001)
22.116 H.F. Robey: Numerical simulation of the hydrodynamics and mass transfer in the large scale, rapid growth of KDP crystals. Part 2: Computation of the mass transfer, J. Cryst. Growth **259**, 388–403 (2003)
22.117 G. Li, L. Xue, G. Su, X. Zhuang, Z. Li, Y. He: Study on the growth and characterization of KDP-type crystals, J. Cryst. Growth **274**, 555–562 (2005)
22.118 N.Y. Garces, K.T. Stevens, L.E. Halliburton, M. Yan, N.P. Zaitseva, J.J. De Yoreo: Optical absorption and electron paramagnetic resonance of Fe ions in KDP crystals, J. Cryst. Growth **225**, 435–439 (2001)
22.119 X. Sun, X.-F. Cheng, Z.-P. Wang, Q. Gu, S. Wang, Y. Li, B. Wang, X. Xu, C. Fang: Effect of impurities on optical qualities of KDP crystal, Laser Part. Beams **16**, 830–834 (2004)
22.120 B. Woods, M. Runkel, M. Yan, M. Staggs, N.P. Zaitseva, M. Kozlowski, J.J. De Yoreo: Investigation of laser damage in KDP using light scattering techniques, Proc. SPIE **2966**, 20–31 (1997)
22.121 M. Yan: Chemistry and materials science, Progress Report UCID–20622–95 12–16 LLNL CA 1996
22.122 I.L. Smolsky, A.E. Voloshin, N.P. Zaitseva, E.B. Rudneva, H. Klapper: X-ray topography study of striation formation in layer growth of crystals from solutions, Philos. Trans. R. Soc. Lond. A **357**, 2631–2649 (1999)
22.123 J. Auerbach, P.J. Wegner: Modeling of frequency doubling and tripling with measured crystal spatial refractive-index nonuniformities, Appl. Opt. **40**, 1404–1411 (2001)
22.124 X. Sun, X. Xu, Z. Wang, Y. Fu, S. Wang, H. Zeng, Y. Li, X. Yu, Z. Gao: Inclusion in DKDP crystals, Chin. Sci. Bull. **46**(20), 1757–1760 (2001)
22.125 M.S. Joshi, A.V. Antony: Oriented inclusions in single crystals of potassium dihydrogen phosphate, Krist. Tech. **14**, 527–530 (1979)
22.126 R.J. Nelmes, Z. Tun, W.F. Kuhs: A compilation of accurate structural parameters for KDP and DKDP, Ferroelectrics **71**, 125–141 (1987)
22.127 Z. Tun, R.J. Nelmes, W.F. Kuhs, R.F.D. Stansfield: A high resolution neutron diffraction study of the effects of deuteration on the crystal structure of KH_2PO_4, J. Phys. C **21**, 245–258 (1988)
22.128 C.W. Carr, H.B. Radousky, S.G. Demos: Wavelength dependence of laser-induced damage: Determining the damage initiation mechanisms, Phys. Rev. Lett. **91**, 127402 (2003)
22.129 K. Wang, C. Fang, J. Zhang, X. Sun, S. Wang, Q. Gu, X. Zhao, B. Wang: Laser-induced damage mechanisms and improvement of optical qualities of bulk potassium dihydrogen phosphate crystals, J. Cryst. Growth **287**, 478–482 (2006)

22.130 M. Runkel, R. Jennings, J.J. De Yoreo, W. Sell, D. Milam, N. Zaitseva, L. Carmen, W. Williams: An overview of recent KDP damage experiments and implications for NIF tripler performance, Proc. SPIE **3492**, 374–385 (1999)
22.131 S. Wang, L. Li, X. Hu, Z. Gao, Y. Fu, X. Sun, Y. Li, H. Zeng: The effect of thermal conditioning on microstructure of KDP crystals, J. Funct. Mater. **34**, 331–333 (2003)
22.132 M. Runkel, M.S. Maricle, R.A. Torres, J. Auerbach, R. Floyd, R. Hawley-Fedder, A. Burnham: Effect of thermal annealing and second harmonic generation on bulk damage performance of rapid-growth KDP type-I doublers at 1064 nm, Proc. SPIE **4347**, 389–399 (2001)
22.133 H. Yoshida, T. Jitsuno, H. Fujita, M. Nakatsuka, M. Yoshimura, T. Sasaki, K. Yoshida: Investigation of bulk laser damage in KDP crystal as a function of laser irradiation direction, polarization, and wavelength, Appl. Phys. B **70**, 195–201 (2000)
22.134 F. Rainer, L.J. Atherton, J.J. De Yoreo: Laser damage to production- and research grade KDP crystals, Proc. SPIE **1848**, 46–58 (1992)
22.135 F. Rainer, F. De Marco, M. Staggs, M. Kozlowski, L. Atherton, L. Sheehan: A historical perspective on fifteen years of laser damage thresholds at LLNL, Proc. SPIE **2114**, 9–23 (1994)
22.136 J. Swain, S. Stokowski, D. Milam, F. Rainer: Improving the bulk laser damage resistance of potassium dihydrogen phosphate by pulsed laser irradiation, Appl. Phys. Lett. **40**(4), 350–352 (1982)
22.137 J. Swain, S. Stokowski, D. Milam, G. Kennedy: The effect of baking and pulsed laser irradiation on the bulk laser threshold of potassium dihydrogen phosphate crystals, Appl. Phys. Lett. **41**(1), 12–16 (1982)
22.138 L. Liang, Z. Xian, S. Xun, S. Xueqin: Sulfate may play an important role in the wavelength dependence of laser induced damage, Opt. Exp. **14**, 12196–12198 (2006)
22.139 L.J. Atherton, F. Rainer, J.J. De Yoreo, I. Thomas, N. Zaitseva, F. De Marco: Thermal and laser conditioning of production and rapid-growth KDP and DKDP crystals, Proc. SPIE **2114**, 36–45 (1994)
22.140 C.S. Liu, N. Kioussis, S.G. Demos, H.R. Radousky: Electron- and hole-assisted reactions of H defects in hydrogen-bonded KDP, Phys. Rev. Lett. **91**, 15505 (2003)
22.141 K. Wang, C. Fang, J. Zhang, C. Liu, R. Boughton, S. Wang, X. Zhao: First-principles study of interstitial oxygen in potassium dihydrogen phosphate crystals, Phys. Rev. B **72**, 184105 (2005)
22.142 M.C. Payne, M.P. Teter, D.C. Allen, T. Arias, J. Joannopoulos: Iterative minimization techniques for ab initio total-energy calculations: Molecular dynamics and conjugate gradients, Rev. Mod. Phys. **64**, 1045–1097 (1992)
22.143 J.-Q. Zhang, S.-L. Wang, C.-S. Fang, X. Sun, Q. Gu, Y. Li, K. Wang, B. Wang, Y. Li, B. Liu: Effects of sulphate doping on the growth habit of KDP crystal, J. Funct. Mater. **36**, 1505–1508 (2005)

Crystal Growth Part D

Part D Crystal Growth from Vapor

23 Growth and Characterization of Silicon Carbide Crystals
Govindhan Dhanaraj, Nashua, USA
Balaji Raghothamachar, Stony Brook, USA
Michael Dudley, Stony Brook, USA

24 AlN Bulk Crystal Growth by Physical Vapor Transport
Rafael Dalmau, Morrisville, USA
Zlatko Sitar, Raleigh, USA

25 Growth of Single-Crystal Organic Semiconductors
Christian Kloc, Singapore
Theo Siegrist, Tallahassee, USA
Jens Pflaum, Würzburg, Germany

26 Growth of III-Nitrides with Halide Vapor Phase Epitaxy (HVPE)
Carl Hemmingsson, Linköping, Sweden
Bo Monemar, Linköping, Sweden
Yoshinao Kumagai, Tokyo, Japan
Akinori Koukitu, Tokyo, Japan

27 Growth of Semiconductor Single Crystals from Vapor Phase
Ramasamy Dhanasekaran, Chennai, India

23. Growth and Characterization of Silicon Carbide Crystals

Govindhan Dhanaraj, Balaji Raghothamachar, Michael Dudley

Silicon carbide is a semiconductor that is highly suitable for various high-temperature and high-power electronic technologies due to its large energy bandgap, thermal conductivity, and breakdown voltage, among other outstanding properties. Large-area high-quality single-crystal wafers are the chief requirement to realize the potential of silicon carbide for these applications. Over the past 20 years, considerable advances have been made in silicon carbide single-crystal growth technology through understanding of growth mechanisms and defect nucleation. Wafer sizes have been greatly improved from wafer diameters of a few millimeters to 100 mm, with overall dislocation densities steadily reducing over the years. Device-killing micropipe defects have almost been eliminated, and the reduction in defect densities has facilitated enhanced understanding of various defect configurations in bulk and homoepitaxial layers. Silicon carbide electronics is expected to continue to grow and steadily replace silicon, particularly for applications under extreme conditions, as higher-quality, lower-priced large wafers become readily available.

23.1 **Silicon Carbide – Background and History** 797
23.1.1 Applications of SiC 798
23.1.2 Historical Development of SiC Crystal Growth 798
23.2 **Vapor Growth** 799
23.2.1 Acheson Method 799
23.2.2 Lely Method 799
23.2.3 Modified Lely Method 800
23.2.4 Sublimation Sandwich Method 800
23.2.5 Chemical Vapor Deposition 800
23.3 **High-Temperature Solution Growth** 801
23.3.1 Bulk Growth 801
23.3.2 Liquid-Phase Epitaxy 802
23.4 **Industrial Bulk Growth by Seed Sublimation** 802
23.4.1 Growth System 803
23.4.2 Seeding and Growth Process 804
23.5 **Structural Defects and Their Configurations** 805
23.5.1 Micropipes and Closed-Core Screw Dislocations 806
23.5.2 Basal Plane Dislocations in 4H-SiC 809
23.5.3 Threading Edge Dislocations (TEDs) in 4H-SiC 814
23.6 **Concluding Remarks** 816
References 817

23.1 Silicon Carbide – Background and History

Silicon carbide (SiC), one of the oldest known semiconductor materials, has received special attention in recent years because of its suitability for electronic and optoelectronic devices operating under high-temperature, high-power, high-frequency, and/or strong radiation conditions, where conventional semiconductor materials such as silicon, GaAs, and InP are considered to have reached their limits. SiC exists as a family of crystals with more than 200 polytypes and a bandgap range of 2.4–3.3 eV. As a wide-bandgap material, SiC possesses many superior properties, e.g., a larger operating temperature range, a high critical breakdown field (E_{cr}), high resistance to radiation, and the ability to construct visible-range light-emitting devices [23.1]. It also distinguishes itself by a combination of high thermal conductivity (higher than that of copper), hardness second only to diamond, high thermal stability, and chemical inertness.

23.1.1 Applications of SiC

High-Temperature Applications

Current and future applications of electronic components have placed much more critical environmental requirements on semiconductors [23.2]; for example, high-temperature electronic components and systems can play an important role in many areas, e.g., aircraft, spacecraft, automotive, defense equipment, power systems, etc. For reliable functioning of electronic devices under extreme conditions they need to withstand high temperatures. SiC appears to be a desirable candidate because of its high working temperature as well as Debye temperature. As reported by *Chelnokov* and *Syrkin* [23.2], 6H-SiC is superior to Si, GaAs, GaN, and AlN for high-temperature application. SiC can also find applications in sensors for high-temperature, high-pressure, and highly corrosive environments (e.g., combustion systems, gas turbines, and in the oil industry) [23.3]; for example, pressure sensors based on SiC thin layers deposited on an insulator structure have been successfully used to measure the pressure in a combustion engine up to 200 bar at temperatures up to 300 °C [23.4].

High-Power Devices

Power semiconductor devices are important for regulation and distribution of electricity. Since the efficient use of electricity depends on the performance of power rectifiers and switches, further improvements in efficiency, size, and weight of these devices are desirable. SiC has a high breakdown strength, and therefore it is possible to dope it at higher concentration while still having thinner layers for a given blocking voltage compared with corresponding Si devices [23.4]. Indeed, power losses can decrease dramatically with the use of SiC-based devices. Another desirable property of SiC for power application is its high thermal conductivity, which can facilitate quick dissipation of heat generated in the component. SiC power metal–oxide–semiconductor field-effect transistors (MOSFETs), diode rectifiers, and thyristors are expected to function over wider voltage and temperature ranges with superior switching characteristics.

High-Frequency Devices

Cellular phones, digital television (TV), telecommunication systems, and radars have made microwave technology an essential part of everyday life. Although some high-power microwave semiconductor components have existed for a long time, e.g., Gunn, impact ionization avalanche transit time (IMPATT), and trapped plasma avalanche transit time (TRAPATT) diodes, these devices can only operate in parametric amplifiers, which are much more difficult to manufacture and tune. SiC-based microwave transistors are predicted to produce more efficient microwave systems and further expand their existing applications [23.4]. Silicon carbide static induction transistors (SITs) and metal semiconductor field effect transistors (MESFETs) have already been developed for these applications.

Optoelectronic Applications

The special physical and optical properties of SiC have been further exploited to fabricate bright blue and green light-emitting diodes (LEDs) [23.5]. In terms of manufacturing, there are several advantages to using SiC as a substrate material, such as easier handling and cheaper processing. SiC is also being used as a substrate for the growth of GaN, an important material for LEDs. Compared with GaN growth on sapphire substrates, it is possible to obtain structurally more perfect epitaxial GaN layers on SiC due to the smaller lattice mismatch and closer match of thermal expansion coefficients.

The primary requirement for SiC-based devices is the production of high-quality thin films, which in turn requires high-quality substrates.

23.1.2 Historical Development of SiC Crystal Growth

SiC has been known in the materials world since 1824. It was recognized as a silicide of carbon in 1895 and could be synthesized successfully by the Acheson process [23.6] using sand and coke. SiC-based LEDs were made as early as 1907 using small SiC crystals obtained from the cavities formed in the Acheson system. In 1955, *Lely* demonstrated the growth of SiC on a porous SiC cylinder by vapor condensation [23.7]. This method was further refined by *Hamilton* [23.8] and *Novikov* and *Ionov* [23.9], and is commonly referred to as the Lely method. Based on this method SiC platelets were prepared in the laboratory for several different applications. *Halden* [23.10] grew single crystals of SiC using Si melt solutions, but this method was not continued because of the difficulty in obtaining larger crystals. *Kendal* [23.11] later proposed a method of cracking of gaseous compounds containing C and Si at high temperature to form SiC crystallites, which is probably the basis for today's SiC chemical vapor deposition (CVD) technology.

A real breakthrough occurred in 1978 when *Tairov* and *Tsvetkov* [23.12] demonstrated seeded growth of

SiC using the sublimation method. Since Tairov and Tsvetkov used Lely's concept of vapor condensation, their method is commonly known as the modified Lely method. Further research on bulk growth is only a refinement and improvement of this technology. Commercially SiC wafers were first made available by Cree Research, Inc., in 1991 [23.13]. The availability of SiC wafers in recent years has spurred extensive research on epitaxial growth. *Matsunami* group's [23.14] research in establishing step-controlled epitaxy is a notable development in optimizing SiC epitaxial growth morphology. Today, 100 mm SiC wafers are routinely available commercially, and overall defect densities show gradual improvement.

23.2 Vapor Growth

Unlike most semiconductor crystals, melt growth methods cannot be adopted for growth of silicon carbide since it is not possible to melt SiC under easily achievable process conditions. The calculated values show that stoichiometric SiC would melt only at above 10 000 atm and 3200 °C [23.15]. Because of these reasons, single crystals of silicon carbide are grown using techniques based on vapor growth, high-temperature solution growth, and their variants. Since SiC readily sublimes, physical vapor growth can be easily adapted and has become the primary method for growing large-size SiC boules. On the other hand, SiC can also dissolve in certain melts, e.g., silicon, which makes melt solution growth a possible technique. This method is predominantly used for growing single-crystal films.

23.2.1 Acheson Method

Commercial production of SiC was established as early as in 1892 [23.6] using the Acheson method. This process is primarily used for synthesis of low-purity polycrystalline material. The Acheson method also yields spontaneously nucleated SiC platelets of incomplete habit. In this process, a predetermined mixture of silica, carbon, sawdust, and common salt [23.16] (e.g., 50% silica, 40% coke, 7% sawdust, 3% salt) is heated by resistive heating of the core of graphite and coke placed at the center of the furnace. The furnace is heated to 2700 °C and maintained at that temperature for a certain amount of time, and then the temperature is gradually decreased. During the thermal cycle, different regions of the reactants are subjected to different temperatures. In between the outermost and innermost regions, the temperature reaches above 1800 °C and the mixture transforms to amorphous SiC. In the core region, SiC is formed first but as the temperature increases it decomposes into graphite and silicon. The decomposed graphite remains at the core and the silicon vapor reacts with the carbon in the adjacent cooler regions to form SiC. Crystalline SiC is therefore formed outside the graphite layers. The common salt reacts with metallic impurities and escapes in the form of chloride vapors, improving the overall purity of the charge. The reaction yields predominantly 6H-SiC polycrystalline materials. Platelet crystals up to 2–3 cm are formed in some hollow cavities. This method does not yield reproducible quality and dimensions of single crystals and hence is not suitable for commercial production, although one can obtain SiC platelets suitable for use as seeds in physical vapor growth.

23.2.2 Lely Method

In the Lely method, developed in 1955 [23.7], SiC lumps are filled between two concentric graphite tubes [23.8]. After proper packing, the inner tube is carefully withdrawn, leaving a porous SiC layer inside the outer graphite tube called the crucible. The crucible with the charge is closed with a graphite or SiC lid and is loaded vertically into a furnace. The furnace is then heated to ≈ 2500 °C in an argon environment at atmospheric pressure. The SiC powder near the crucible wall sublimes and decomposes because of a higher temperature in this region. Since the temperature at the inner surface of the charge is slightly lower, SiC crystals start nucleating at the inner surface of the porous SiC cylinder. These thin platelets subsequently grow larger in areas if the heating is prolonged at this temperature. Since crystals are nucleated on the lumps of SiC (at the inner surface) and it is difficult to impose higher supersaturation, there is no control over the nucleation process, leading to platelets of incomplete hexagonal habit. The original Lely method was later improved by *Hamilton* [23.8] and others [23.9], where SiC charge is packed in between the two annular graphite cylinders. The outer cylinder (crucible) is thick whereas the inner cylinder is thin and porous and acts as a diaphragm. The sublimed SiC vapor passes through the small holes in the diaphragm, and crystals are nucleated at the inner

surface. Thick layers of SiC are also deposited on the lids at both ends. This modification offers slightly better control over the number of nucleation sites and yield, and crystals up to $20 \times 20\,\mathrm{mm}^2$ have been grown using this method. Good-quality, larger crystals are obtained when the temperature variation in the cavity is small and the Ar pressure is maintained at about 1 atm [23.9]. Similar to the Acheson process, crystals of 6H polytype are predominantly produced by this method. The amount of crystals of other polytypes, such as 15R and 4H, depends on the growth temperature and dopant. Even though Lely platelets show good structural perfection, they have nonuniform physical and electrical characteristics. Also, since the yield is low ($\approx 3\%$), this method is not suitable for industrial production. The Lely method is, however, ideal for producing platelets of high structural perfection that can be used as seed crystals in bulk growth using other methods.

23.2.3 Modified Lely Method

In 1978, *Tairov* and *Tsvetkov* [23.12] developed the seeded sublimation growth technique, commonly known as the modified Lely method. They succeeded in suppressing the widespread spontaneous nucleation occurring on the (inner) graphite cylinder wall and achieved controlled growth on the seed (Fig. 23.1). This method also led to the control of polytypes to some extent. In the modified Lely method, growth occurs in argon environment at 10^{-4}–760 Torr in the temperature range of 1800–2600 °C and the vapor transport is facilitated by a temperature differential, $\Delta T = T_2 \approx T_1$, between the seed and the source material. The seed temperature T_1 is maintained slightly lower than the source temperature. The kinetics of the transport of Si- and C-containing species are primarily controlled by the diffusion process.

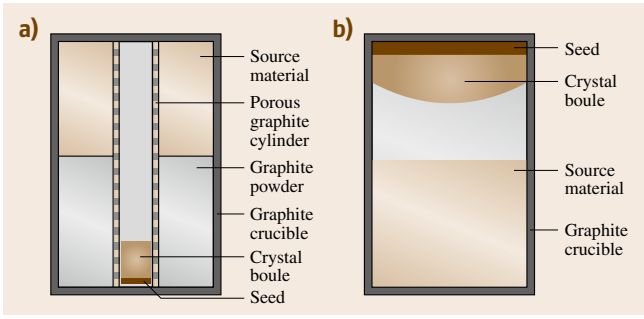


Fig. 23.1a,b Modified Lely method: **(a)** seed at the bottom, and **(b)** seed at the top

There are two different designs of the seeded sublimation growth system based on the locations of the charge and seed. In earlier work [23.17–19], the source SiC was placed in the upper half of the graphite crucible in a circular hollow cylindrical configuration between the crucible and a thin-walled porous cylinder (Fig. 23.1a). The seed platelet was held on a pedestal in the lower half of the crucible. Using this configuration, *Ziegler* et al. [23.17] grew 20 mm-diameter 24 mm-long crystals while *Barrett* et al. [23.18] succeeded in growing 6H-SiC of 33 mm diameter and 18 mm length. In the second configuration [23.15, 20–24] (Fig. 23.1b), which is commonly used today, the source material is held at the bottom of the crucible and the seed plate on the top. No graphite diaphragm is used in this configuration. This arrangement has a high yield (90%) [23.25] and has therefore become the industry standard for production of SiC boules.

23.2.4 Sublimation Sandwich Method

The sublimation sandwich method (SSM) is another variant of physical vapor transport (PVT) growth where the growth cell is partially open and the environment containing Si vapor may be used to control the gas-phase stoichiometry [23.26–30]. The source material consists of a SiC single-crystal or polycrystalline plate with small source-to-crystal distance (0.02–3 mm). There are several parameters, such as the source-to-substrate distance, small temperature gradient, and presence of Ta for gettering of excess carbon, that can be used to control the growth process. A high growth rate is achieved mainly due to the small source-to-seed distance and a large heat flux onto a small amount of source material with a low to slightly moderate temperature differential between the substrate and the source (0.5–10 °C). While growth of large boules is quite difficult, this method is quite promising for better-quality epitaxial films with uniform polytype structures.

23.2.5 Chemical Vapor Deposition

Chemical vapor deposition (CVD) is a popular method for growing thin crystalline layers directly from the gas phase [23.14, 31–33]. In this process a mixture of gases (source gases for Si and C, and carrier gas) is injected into the growth chamber with substrate temperatures above 1300 °C. Silane is the common Si source, and a hydrocarbon is used for C. Propane is quite popular, but methane is of interest because of its availability with very high purity, although it has lower carbon

cracking efficiency. The carrier gas is high-purity H_2, which also acts as a co-reactant. Conventional Si and C source molecules, called multiple-source precursors, have been used successfully, and reproducible CVD epitaxial films have been produced. However, the single-source CVD SiC precursor shows several advantages over the multiple-source precursors, including a lower growth temperature (less than 1100 °C).

The first successful large-area, heteroepitaxially grown 3C-SiC was obtained by *Nishinov* et al. [23.34] on a high-quality commercial Si wafer. With the availability of 6H-SiC wafers grown by the modified Lely method, homoepitaxial growth of 6H-SiC and heteroepitaxial growth of 3C-SiC have been achieved with good success [23.14]. SiC epitaxial growth is mainly performed on 4H and 6H substrates. Growth on the Si face is preferred because of the superior quality and well-understood doping behavior. In general, the quality of films obtained on the (0001) face is poor, but this problem can be overcome by using a wafer misoriented by 3–8° from the basal plane to control the morphology of the deposited epilayer [23.14], a process referred to as step-controlled epitaxy. Doping of the film is obtained in situ during the growth of each epilayer by flowing either a p-type or n-type source gas. The growth rates of CVD processes are low, a few tens of microns per hour, generally making it unsuitable for boule production. The rate can be increased by increasing the deposition temperature, but this makes control of the process much more difficult and also results in many other problems such as homogeneous nucleation in the gas phase. The high-temperature CVD (HTCVD) process [23.35, 36] is an improved version that can yield thicker films and higher growth rates. In HTCVD the substrate is placed at the top of a vertically held graphite susceptor, similar to the crucible used in the modified Lely method, with holes at the bottom and top. The gaseous reactants are passed from the bottom of the susceptor upwards through the hole at the bottom. To maintain the growth for a long time and obtain the maximum deposition on the substrate, the temperature of the susceptor wall is kept high and the substrate temperature is kept slightly lower. In principle, SiC growth by this method can be continued for longer periods, and bulk crystals can be obtained. The hot-wall CVD reported by *Kordina* et al. [23.37] is probably a good method to produce uniform epitaxial films on large-diameter wafers. In this approach, the CVD reactor is made of a single graphite block with a protective SiC layer. It has an elliptical outer cross-section with a rectangular tapered hole which runs through the entire length. The substrate wafers are placed appropriately on both sides of the rectangular slit. The mixture of gaseous precursors with carrier gas is passed through the reactor from the end containing the larger hole. The tapered hole compensates for severe depletion of Si and C content in the reactant. The flow rate of the gas can be sufficiently large. This design provides good temperature homogeneity, and epitaxial films of excellent thickness uniformity can be obtained. The surface morphology of the film can be controlled by choosing off-*c*-oriented substrate. Recent technological developments have allowed the growth of uniform epitaxial films on wafers as large as 100 mm in diameter [23.38–41].

23.3 High-Temperature Solution Growth

23.3.1 Bulk Growth

Carbon is soluble in a Si melt, which enables growth of SiC from high-temperature solution. The solubility ranges from 0.01% to 19% in the temperature interval 1412–2830 °C [23.20], although at high temperatures the evaporation of silicon makes the growth unstable. The solubility of carbon can be increased by adding certain transition metals to the Si melt [23.42]. In principle, this can enable growth of SiC from saturated solution by seeded solution growth. Unfortunately there is no crucible material that can remain stable at the required temperatures and with these melts, and also the evaporation of the Si melt poses a serious problem at higher temperatures. It is also speculated that the incorporation of the added metals into the growing crystal is too high to be acceptable for semiconductor applications [23.20]. These difficulties restrict the application of this method to bulk growth of SiC. *Halden* [23.10], however, has grown SiC platelets from Si melt at 1665 °C on a graphite tip in Czochralski configuration. *Epelbaum* et al. [23.43] have obtained SiC boules of 20–25 mm diameter and 20 mm length at pull rate of 5–15 mm/h in the temperature range of 1900–2400 °C at Ar pressure of 100–120 bar. Even though solution-grown crystals free of micropipes have been produced, they contain a number of flat silicon inclusions and show rather high rocking-curve width.

Because of the high temperature and high pressure involved in this process, the method is not considered economic for large-scale production.

23.3.2 Liquid-Phase Epitaxy

Even though the high-temperature solution method for SiC poses enormous difficulties and is not popular for bulk growth, it has been successfully adopted for growth of thin films by liquid-phase epitaxy (LPE). Indeed, LPE has been used for production of several SiC-based optoelectronic devices [23.17]. In LPE, semiconductor-grade silicon is used as a solvent in a graphite crucible. Carbon from the graphite crucible dissolves in the Si melt and is transported to the surface of the SiC substrate, which is placed at the bottom of the crucible at a relatively lower temperature. Bright LEDs have been fabricated using this process. However this method suffers from several setbacks such as cracking of the film due to differential thermal contraction while solidifying and the cumbersome process of extraction of the substrate containing the epitaxial film by etching off the solidified Si. These problems can be overcome using a dipping technique [23.44]. In this improved process a SiC substrate attached to a graphite holder is dipped into the molten Si heated by an induction furnace and is kept in the lower-temperature region of the crucible. The substrate is withdrawn from the melt after obtaining growth of the epitaxial film of a desired thickness. The growth is performed in an Ar environment at 1650–1800 °C, and the typical growth rate is 2–7 μm/h. Doping is obtained by adding Al to the Si melt for p-type layer, and Si_3N_4 powder to Si for n-type. It is also possible to obtain n-type film by passing N_2 gas along with Ar. Epitaxial films obtained on (0001) 6H-SiC substrate have shown degradation in LED performance. This problem can be resolved by using substrates misoriented with respect to the *c*-axis by a few degrees (3–10°), which leads to better polytype control and improved surface morphologies [23.14]. The method is known as step-controlled epitaxy and has led to improved quality of the film and thereby reliable device performance. A better epitaxial surface morphology is obtained by this process, which has been explained based on the nucleation concept [23.14].

It is possible to lower the growth temperature range by selecting an alternative melt which has a higher solubility than Si. *Tairov* et al. [23.45] have used Sn and Ga melts in the temperature range of 1100–1400 °C and have produced LPE layers by using a sliding boat technique. *Dmitriev* et al. [23.46] have grown p–n junctions in the temperature range of 1100–1200 °C. In addition they have demonstrated container-free epitaxial growth of 6H- and 3C-SiC films in which the melt is held by an electromagnetic field. This method has the advantage of mixing induced by the electromagnetic forces [23.47]. Recently, *Syvajarvi* et al. [23.48] used a special sandwich configuration in LPE and succeeded in obtaining growth rates as high as 300 μm/h. One of the main attractions of LPE of SiC is the potential for filling of micropipes. The substrate, after filling of micropipes, does not reveal the presence of micropipes by either optical microscopy or etching [23.35]. However, detailed analysis is needed to understand the defect configuration around the filled core of the micropipes.

23.4 Industrial Bulk Growth by Seed Sublimation

Seeded sublimation growth, commonly known as the modified Lely method, is the only method that has been implemented by industry. The method has spurred intense worldwide research activity in recent years and has become a standard method for growing SiC crystals [23.12, 17–24, 49–51]. The instrumentation and technology involved in bulk growth of SiC are complex, and hence the availability of large-size crystals is still limited. This is primarily due to the fact that the operating temperatures are extreme, and monitoring and control are difficult [23.20]. Even today, only a few companies are successful in producing SiC boules of reasonable quality and size. The main constraint is the difficulty in determining the optimum growth conditions for the modified Lely method, such as the right combination of pressure, temperature, temperature gradient, charge size, geometric configuration, etc. It is not feasible to determine the exact thermal conditions in the growth zone experimentally due to high operating temperatures and opacity of the graphite crucible. In spite of these limitations, great success has been achieved in the industrial production of SiC crystals in terms of crystal perfection and size [23.52–55]. Numerical modeling and simulation have been of great help in this endeavor [23.56].

23.4.1 Growth System

As described earlier, there are two main configurations for seeded sublimation growth (Fig. 23.1). The second configuration [23.20, 50, 54, 55], where the source material is held at the bottom of the crucible and the seed plate is fixed onto the crucible lid, is the system commonly used today (Fig. 23.1b). This arrangement yields a higher growth rate compared with the other approach, because of the smaller source-to-seed distance. Also, since the growing surface is facing downwards, there is no danger of incorporation of charge particles into the growing crystal as in the first case (Fig. 23.1a) where particulates can fall from the top. The main disadvantage of this configuration is that, in a system for growing larger-diameter boules, maintaining temperature uniformity in the source material becomes difficult. The first configuration is slightly less susceptible to temperature and pressure fluctuations. The operating temperature range of seeded sublimation growth is 1800–2600 °C [23.12], with the actual temperature for growth depending on many different process conditions. Induction furnaces operating at lower frequencies (4–300 kHz) [23.17, 58] are commonly used for the modified Lely method. The optimum operating frequency of the induction furnace is 10 kHz, which corresponds to a reasonably high skin depth for the graphite crucible. Recently, efficient solid-state induction furnaces have become readily available, and these low-frequency generators preferentially couple with the susceptor and crucible, with minimum induction on the graphite insulator. Additionally, in an induction furnace, it is possible to vary the temperature gradient at the initial stage as well as during the run. Another advantage of the induction furnace over the resistive furnace is the minimal thermal insulation required as the heat is generated directly on the susceptor and crucible. The dimensions and number of turns of the induction coil are selected based on geometric considerations, the temperature and temperature gradients desired, and heat losses.

The main chamber of the SiC growth system (Fig. 23.2) is a vertically mounted double-walled water-cooled assembly that consists of two concentric quartz tubes sealed with vacuum-tight end flanges using double O-ring seals on ground surfaces of the quartz tubes. Cooling water is circulated between the concentric quartz tubes from bottom to top, although *Yakimova* et al. [23.49] have shown that it is also possible to use an air-cooled quartz enclosure. The hot zone consists of a high-density graphite crucible

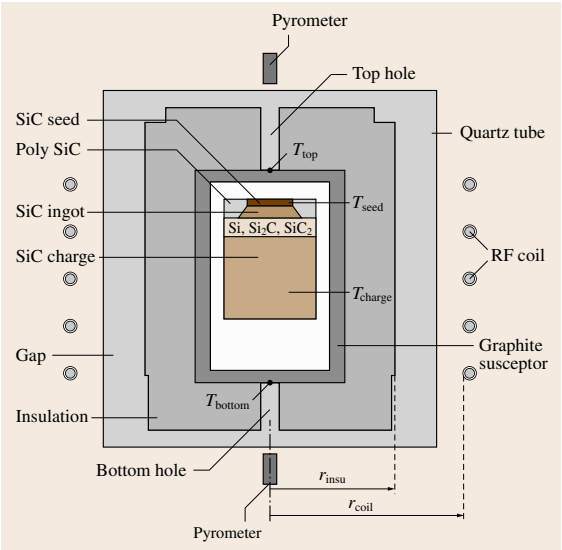


Fig. 23.2 Schematic of the SiC growth system (after [23.57])

and susceptor surrounded by rigid graphite insulation. Because of the higher resistivity of the rigid insulation compared with that of the graphite susceptor and crucible, heat is generated primarily on the susceptor by eddy currents induced by the low-frequency magnetic field. The graphite components of the growth chamber, particularly the crucible and susceptor, are treated at high temperatures in fluorine atmosphere to remove metallic impurities. The design of the hot zone is modified based on the requirements of the axial and radial gradient. This is accomplished with the help of computer modeling [23.56] and prediction of the temperature profile as a function of the growth front.

The normally practiced measurement procedure is to monitor temperatures of the top (T_1) and bottom (T_2) surfaces of the graphite crucible using two color pyrometers (Fig. 23.2). The temperatures are controlled by varying the output power of the induction furnace. Often, the induction coil is mounted on a motorized linear vertical translation stage, and the position of the coil is changed during the growth to vary the temperature gradient and the seed temperature. The vertical growth chamber is connected to a high-vacuum system to obtain initial degassing (at 10^{-7} Torr) as well as to maintain the required vacuum (e.g., 10–100 Torr) conditions during growth. Maintaining vacuum at a predetermined value, as closely as possible, is essential to control the growth rate.

23.4.2 Seeding and Growth Process

After repeated degassing and baking of the growth zone, the chamber is filled with Ar gas. The Ar partial pressure is maintained at about 600 Torr–1 atm while heating to the maximum required growth temperature (2200–2400 °C). The coil position is adjusted such that a desirable temperature gradient of 10–20 °C/cm is obtained. The seed temperature T_1 and the temperature differential ΔT can be varied by changing the coil position; however, T_1 and T_2 cannot be controlled independently. The Ar pressure is brought down to a lower value between 1 and 40 Torr at a predetermined pumping speed to initiate the growth smoothly. The axial temperature gradient influences the growth rate, whereas the radial temperature gradient changes the diameter of the crystal [23.56].

The main stages of the growth are:

1. Dissociative sublimation of SiC source
2. Mass transfer of gaseous species
3. Crystallization onto the seed

At a high temperature, the SiC source material decomposes into several Si- and C-containing species such as Si, C, SiC_2, and Si_2C. Since the crucible is made of graphite, vapor species will react with the graphite wall to form Si_2C and SiC_2, with the graphite crucible acting like a catalyst. Details of the reaction kinetics are described by *Chen* et al. [23.56]. The temperature difference between the seed and source ΔT works as a driving force and facilitates transport of vapor species, mainly Si, Si_2C, and SiC_2. The presence of the temperature gradient leads to supersaturation of vapor, and controlled growth occurs at the seed. Initially, a high-quality Lely plate is used as the seed crystal, and the diameter of the growing crystal is increased by properly adjusting the thermal conditions. To grow larger boules of approximately uniform diameter, wafers from previously grown boules are used as seed discs.

The seed crystal is attached to the graphite top using sugar melt [23.59], which decomposes into carbon and gets bonded to the graphite lid. Optimizing this bonding process is quite important, since the differential thermal expansion between the seed and the graphite lid can cause bending of the seed plate, leading to formation of domain-like structure, low-angle boundaries, and polygonization [23.60]. Micropipes can form at such low-angle boundaries. Any nonuniformity in seed attachment, such as a void between the seed and the lid, can cause variation in the temperature distribution, and the heat dissipation through the seed may be altered. This can result in uneven surfaces and depressions in the growth front corresponding to the void. Evaporation of the back surface of the seed crystal can create thermally decomposed voids which can propagate further into the bulk [23.59]. These voids can then become sources for the generation of micropipes. Protecting the back surface of the seed with a suitable coating eliminates these voids. Seed platelet attachment to the graphite lid is one of the important technical aspects of industrial growth.

If the growth process is not optimized, polycrystalline deposition due to uncontrolled nucleation may occur. In addition to optimizing the Ar pressure and temperature gradient to achieve controlled nucleation, removal of a thin layer of the seed surface by thermal etching, obtained by imposing a reverse temperature gradient [23.61], has been found to be helpful. Etching is also possible by oscillatory motion of the induction coil. The in situ thermal etching helps in cleaning the surface of the seed crystal before starting growth. In some cases, a small amount of excess silicon is added to the charge in order to maintain the Si vapor concentration and stabilize the growth of certain polytypes. The growth of boule is initiated at a very slow rate and is increased progressively by decreasing the pressure.

Depending on the design of the crucible and supersaturation ratio, simultaneous growth of polycrystalline SiC, predominantly 3C, occurs particularly on the graphite lid surrounding the seed crystal. If the growth conditions are not optimal, the polycrystalline SiC can get incorporated into the boule near the periphery, leading to cracking due to high stresses. If the growth rate of the boule is higher than the growth rate of polycrystalline SiC, smooth growth of the boule dominating over the polycrystalline mass is favored. Design of the crucible for increasing the diameter of the boule is normally accomplished through modeling [23.56].

Bahng et al. [23.62] have proposed a method of rapid enlargement of the boule using a cone-shaped platform, where enlargement depends on the taper angle of the cone. It has been reported that, in this technique, the broadening of the boule is not affected by the growth of polycrystalline SiC. After obtaining the required diameter of boule, seed discs of larger diameter are prepared from these boules for further growth in a specifically designed hot zone suitable for promoting predominantly axial growth. As growth of the boule progresses, the temperature of the growing surface changes, which can be compensated by moving the induction coil. It is evident that the process parameters must be optimized for a particular crucible design, system geometry, and boule dimension.

Among the numerous SiC polytypes, only 6H, 4H, 15R, and 3C have been studied for different applications. Polytypes 6H and 4H have been studied extensively in bulk crystal as well as epitaxial form, whereas 3C has been investigated predominantly in epitaxial form. Recently, work on bulk growth of 15R has been initiated for MOSFET applications [23.63]. Crystals of 4H polytype are grown in a narrow temperature range of 2350–2375 °C at 5 mbar using (0001)C face of 4H seed plates [23.35]. A lower growth rate (0.1 mm/h) is used in the beginning and then increased to 0.5 mm/h after growing a 1 mm-long boule. Above 2375 °C the 4H polytype transforms into 6H; below 2350 °C, crystal quality becomes a limiting factor. Among the SiC polytypes, 6H is the most extensively studied, and the reported growth temperature ranges vary widely, although this may be due to differences in growth cell configuration and temperature measurement convention. *Snyder* et al. [23.53] have reported the growth of 100 mm 6H boules at 2100–2200 °C and 5–30 Torr Ar pressure with 10–30 °C/cm temperature gradient. The clearly established result is that (0001)Si face should be used for growth of 6H, whereas (0001)C face is needed for growth of 4H. It seems that, for bulk growth of 15R, seed platelets of the same polytype are required. *Schulze* et al. [23.64] have demonstrated growth of 15R crystals on (0001)Si seed face at 2150–2180 °C with 5 °C/cm gradient. However, *Nishiguchi* et al. [23.58] have shown that 15R polytypes can grow stably on both C and Si of (0001) face at seed temperature not exceeding 2000 °C with growth rate controlled between 0.1 mm/h to 0.5 mm/h. In addition to temperature there are several other parameters that can be used to control polytype formation.

Growth of SiC boule depends on many parameters, such as growth temperature, temperature gradient, Ar pressure, crystal temperature, source-to-crystal distance, and the porosity of the source material [23.56]. Preparative conditions of the source material alter the vapor species concentrations and vary the growth conditions. Deviation from stoichiometry can lead to a lower growth rate. The growth rate increases as the seed crystal temperature increases. It also increases with the temperature differential ($T_2 \propto T_1$) and temperature gradient but decreases with the source-to-seed distance. The growth rate varies almost inversely with the Ar pressure, and the trend is consistent with $1/P$ dependence on the molecular diffusion coefficient [23.50]. There exists a saturation of growth rate at very low pressures, and one would tend to select this growth regime, but then control of the vapor composition becomes more difficult.

The growth rates have been measured by inducing growth bands by simultaneously introducing N_2 gas along with the Ar flow at different intervals and subsequent post mortem studies. In general, (0001) plate is used as a seed, and growth proceeds along the *c*-direction. Even though the crystal grows smoothly on (0001) plate, this is also the favorable orientation for nucleation of micropipes. There have been several attempts [23.65, 66] to grow crystals on non-(0001) orientation. Even though the micropipe density was reduced in the bulk, the generation of other types of defects such as stacking faults on the basal plane, which hinder electron transport in device applications, increased. Presently, seeding is restricted to (0001) orientation for industrial production of SiC boules.

Monitoring and controlling growth of SiC is very difficult because of the use of opaque graphite materials in the hot zone. Recently, radiography has been employed to study the growth interface during the growth process [23.67]. This imaging technique has also revealed the graphitization of the SiC source material, which could reduce the growth rate as well as affect the structural perfection of the growing boule. Attempts have also been made to study defect generation during the growth process using in situ x-ray topography [23.68].

23.5 Structural Defects and Their Configurations

Assessment of crystalline imperfections and growth inhomogeneities in grown crystals is necessary to understand how they are formed and for the development of engineering methods to eliminate them or minimize their effect in order to obtain high-quality crystals required for electronic applications. SiC crystals grown using different techniques can contain crystalline imperfections such as growth dislocations of screw character with closed or hollow cores (micropipes), deformation-induced basal plane dislocations, parasitic polytype inclusions, planar defects (stacking faults, microscopic twins, and small-angle boundaries), hexagonal voids, etc. that affect device performance. A review of SiC defect characterization efforts reveals that x-ray topog-

raphy, and in particularly synchrotron white-beam x-ray topography (SWBXT) [23.69–71], is superior to other techniques such as chemical etching, atomic force microscopy (AFM), scanning electron microscopy (SEM), transmission electron microscopy (TEM), and optical microscopy-based methods, although these other techniques can be used in a complementary manner. Defects imaged by x-ray topography are primarily discussed in this section.

23.5.1 Micropipes and Closed-Core Screw Dislocations

Origin of the Hollow Core and Frank's Theory

Among the various defects that exist in SiC crystals, screw dislocations lying along the [0001] axis are the most significant and are generally considered to be one of the major factors limiting the extent of the application of SiC. These screw dislocations (SDs) have been shown to have Burgers vectors equal to nc (where c is the lattice parameter along the [0001] direction in the hexagonal coordinate space and n is an integer), with hollow cores becoming evident with $n \geq 2$ for 6H-SiC and $n \geq 3$ for 4H-SiC [23.69]. These latter screw dislocations are generally referred to as micropipes (MPs), and their hollow cores can be understood from Frank's theory [23.73], which predicts that a screw dislocation whose Burgers vector exceeds a critical value in crystals with large shear modulus should have a hollow core with equilibrium diameter D related to the magnitude of the Burgers vector b by

$$D = \frac{\mu b^2}{4\pi^2 \gamma} , \qquad (23.1)$$

where μ is the shear modulus and γ is the specific surface energy. Experimentally, the diameter D can be measured directly using SEM or AFM, while the Burgers vector magnitude b can be obtained by determining the step height of the growth spiral on the as-grown surface using optical interferometry or AFM, or directly using x-ray topography. Detailed experimental results indicate a directly proportional relationship between D and b^2 for micropipes in both 6H- and 4H-SiC [23.69–71].

Growth Spirals and Screw Dislocations

Growth spirals observed on habit faces of as-grown SiC crystals [23.74, 75] are a clear manifestation of screw dislocations emerging on the growth surface. The emergence of screw dislocations on a habit face produces a ledge of height equal to the Burgers vector. The crystal grows by attachment of molecules to the edge of this ledge. The ledge is self-perpetuating and continues to be present on the surface as long as the dislocation line intersects the surface. The ledge winds itself into a circular or polygonal spiral with a dislocation line at the center and, as the growth proceeds, the spiral apparently revolves. The step height of these spirals is equal to an integer times c. Depending on the sign of the Burgers vector the spiral can revolve in a clockwise or anticlockwise direction [23.69]. These spirals have been studied using phase-contrast microscopy [23.76], scanning electron microscopy (SEM) [23.76], and recently by atomic force microscopy (AFM) [23.77]. When two screw dislocations of the same sign are present very close to each other, their spirals spin without intersecting each other, which are called cooperative spirals. Two dislocations of opposite sign can form a closed loop.

Back-Reflection Observation of Screw Dislocations

Screw dislocations in (0001)SiC wafers, of both closed and hollow core (micropipes), can be effectively characterized using back-reflection geometry in SWBXT [23.78]. Figure 23.3, a typical back-reflection topograph taken from a (0001)SiC wafer (grown by Cree Research, Inc.), clearly reveals the screw dislocations, both hollow and closed core, as white circular spots surrounded by black rings. The distribution of micropipes and screw dislocations as well as their detailed structures can be obtained from such images.

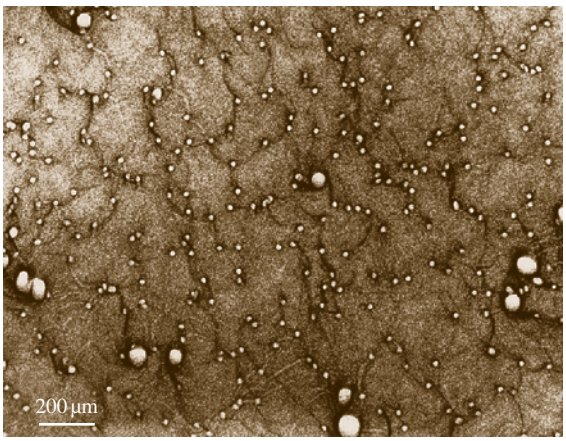


Fig. 23.3 SWBXT back-reflection images of closed-core (*smaller white spots*) and hollow-core (*large white spots*) screw dislocation in a (0001) 6H-SiC wafer. The *faint lines* connecting these screw dislocation images are basal plane dislocation images [23.72]

The circular white spots in Fig. 23.3 are not images of micropipes and closed-core screw dislocations but are actually related to diffraction effects associated with the long-range strain fields of the screw dislocations. Using a ray-tracing simulation based on the orientation contrast mechanism, a model for qualitative and quantitative interpretation of topographic observations in SiC has been developed [23.79–82]. It has been successfully used in back-reflection XRT to clarify the screw character of MPs and also to reveal the dislocation sense of threading screw dislocations (TSDs)/MPs, the Burgers vectors of threading edge dislocations (TEDs), the core structure of Shockley partial dislocations, and the sign of Frank partial dislocations [23.83–85]. Based on this ray-tracing principle, images of micropipes and screw dislocations can be rigorously simulated. Figure 23.4a shows a magnified image of an $8c$ micropipe in 6H-SiC, while Fig. 23.4b shows the simulated image of a screw dislocation with Burgers vector of $8c$ ($b \approx 12.1$ nm). It is apparent that the simulation is in excellent agreement with the recorded micropipe image. This proves that micropipes in SiC are indeed pure screw dislocations. The magnitude of the Burgers vector can be estimated from the diameter of the screw dislocation image, while the twist direction unambiguously indicates the dislocation sense, i. e., the direction of the Burgers vector [23.81]. Back-reflection section topographs of micropipes recorded with a 20 µm-wide slit-limited synchrotron beam can also reveal the sense of the screw dislocation (Fig. 23.5a–d).

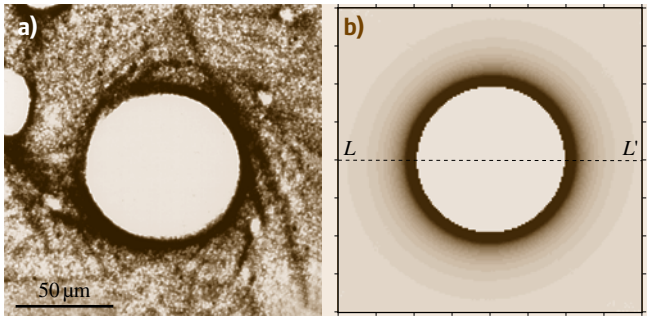


Fig. 23.4 **(a)** Back-reflection SWBXT image of an $8c$ micropipe taken from a (0001) surface of a 6H-SiC crystal, with sample-to-film distance of 20 cm. **(b)** Simulation of a screw dislocation with Burgers vector $|\boldsymbol{b}| = 8c$ [23.80]

Grazing-Incidence Imaging of Screw Dislocations

In the grazing-reflection geometry, the incident beam makes an extremely small angle (less than 1°) with respect to the (0001) plane, but there is no limitation for the exit angle of the diffracted beam. This is an especially useful geometry for characterizing micropipes and screw dislocations as well as threading edge dislocations in SiC epitaxial films, since one can control the penetration depth of x-rays at will by adjusting the incidence angle. Figure 23.6a shows a $11\bar{2}8$ topograph taken with the recording x-ray film parallel to the (0001) surface, in which the oval-shaped white spots are images of micropipes. The simulated images based on the ray-tracing principle are shown in Fig. 23.6b, c [23.84].

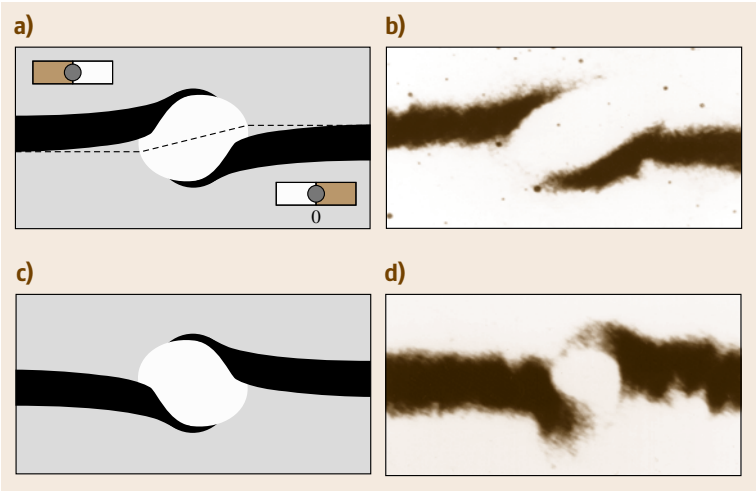


Fig. 23.5a–d Section topographs showing the senses of screw dislocations associated to micropipes. **(a)** and **(b)** are simulated and recorded images of a right-handed screw dislocation, respectively; **(c)** and **(d)** are simulated and recorded images of a left-handed screw dislocation [23.80]

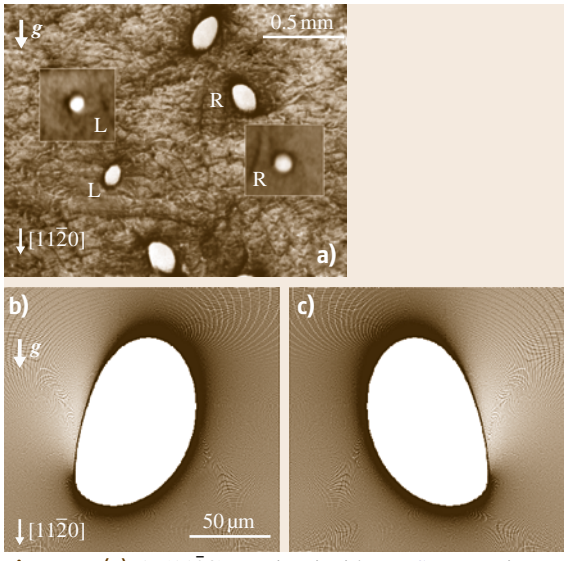


Fig. 23.6 **(a)** A (11$\bar{2}$8) grazing-incidence SWBXT image of 4H-SiC. MPs appear as roughly oval shaped with various orientations and dimensions. The MPs can be divided into two groups according to the orientation of the white elliptical contrast. Examples of each kind are shown (marked by "L" and "R"). Their images in back-reflection geometry appear as complete circular shapes (*insets*, on a different scale), indicating that they are isolated MPs (not MP pairs or groups). Simulated (11$\bar{2}$8) grazing-incidence x-ray topographic images of left-handed **(b)** and right-handed **(c)** 8*c* MPs at a specimen-to-film distance of 35 cm. Both images appear as roughly white ellipses canted clockwise **(a)** or counterclockwise **(b)** from vertical configuration [23.84]

The observed (Fig. 23.6a) and simulated (Fig. 23.6b,c) images correlate very well. Simulation shows that left-handed MPs appear as nearly elliptical features canted clockwise, while right-handed MPs are canted counterclockwise.

Model for the Origin of Screw Dislocations and Micropipes

Systematic observations of screw dislocation or micropipe formation processes using a variety of techniques [23.77, 86–89] suggest that a possible mechanism for nucleation of micropipes in SiC involves the incorporation of inclusions, which could be, for example, graphite particles, silicon droplets, or even voids, into the crystal lattice. Nucleation of screw dislocations at inclusions has been observed in several systems [23.90–92]. The formation of screw dislocation pairs from inclusions has been briefly proposed by *Chernov* [23.93] for crystals grown from solution. This approach has been extended to explain the observed nucleation of screw dislocations in SiC [23.94]. This model assumes that two macrosteps of different heights, approaching each other on the growth surface, trap a layer of foreign material (solvent, void or impurity) on the growth surface. As a result of the higher rate of feeding of the protruding edge than the re-entrant edge, an overhanging ledge can subsequently be produced as the crystal attempts to overgrow the inclusion and incorporate it into its lattice. This overhanging ledge is vulnerable to deformation and vibrations and, when the macrostep meets the approaching macrostep, horizontal atomic planes which were at the same original height may no longer meet along the line where the two steps meet. If the layer of foreign material constituted a void (or transport gases), downward depression of the overhanging ledge may be expected, whereas if it constituted an impurity, deformation of the opposite-sense dislocations might be expected. In order to accommodate this misalignment, screw dislocations of opposite sign are created with Burgers vector magnitudes equal to the magnitude of the misalignment. Since the degree of misalignment depends on the relative size of the two approaching steps and the lateral and vertical extent of the inclusion, the production of dislocations with a range of Burgers vectors becomes possible. In fact, micropipe-related screw dislocations in SiC can have Burgers vectors as large as several tens of times the basic lattice constant along the *c*-axis [23.95]. In addition, in cases of large inclusions or groups of inclusions, the deformation of the protruding ledge may be spread over the length of the line along which they meet, resulting in the creation of distributed groups of opposite-sign screw dislocations. These groups may not necessarily be distributed symmetrically, but in all cases, the sum of all the Burgers vectors of the dislocations created must equal zero.

In SiC the sources of the growth steps involved in the above-described model can be the vicinal nature of the growth surface (which tends to be slightly dome shaped), two-dimensional (2-D) nucleation, as well as spiral steps associated with intersections of screw dislocations with the surface. Differences in step height are certainly conceivable when a vicinal step meets a spiral step and can even occur when two spiral steps associated with screw dislocations of different Burgers vector magnitude meet or if step bunching occurs for a group of dislocations. Moreover, the merging of 2-D grown islands also plays an important role in the formation of growth steps as well as voids. These various sources in

conjunction with the formation of inclusions thus provide opportunities for micropipes as well as closed-core screw dislocations to be created during growth.

23.5.2 Basal Plane Dislocations in 4H-SiC

The primary slip plane for hexagonal 4H- and 6H-SiC is the basal plane. It is therefore not surprising that deformation-induced dislocations on the basal plane are observed in both structures [23.97, 98]. An example is shown in Fig. 23.7, which shows a transmission topograph recorded from a 4H-SiC basal plane wafer. Also shown in this figure is a grazing-incidence topograph recorded from the same region of the 4H-SiC crystal. Detailed Burgers vector analysis of these dislocations can be easily performed. Observation of the morphologies of the basal plane dislocation (BPD) loops clearly indicates that they are deformation induced and appear to have been nucleated both at the crystal edges and at the sites of micropipes/screw dislocations.

The Burgers vectors of the BPDs in SiC are $1/3\langle 11\bar{2}0\rangle$, and two extra $(11\bar{2}0)$ half-planes are associated with an edge-oriented BPD, as the magnitude of its Burgers vector is twice the d-spacing of $(11\bar{2}0)$ plane. The BPD is energetically favorable to be dissociated

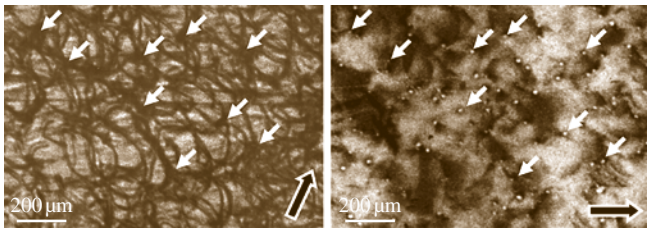


Fig. 23.7a,b Transmission x-ray topograph ((**a**), $g = [\bar{1}\bar{1}20]$) and grazing incidence ((**b**), $g = [11\bar{2}8]$) of 20 µm epilayer on 8° offcut 4H-SiC substrate. Circular basal plane dislocations (BPDs) anchored by SDs are seen. Some anchor points are marked by *arrows*

into two Shockley partial dislocations with a stacking fault (SF) area in between, and the equilibrium separation d of the two Shockley partial dislocations is given by $d = Gb^2/4\pi\gamma$, where G is the shear modulus, b is the magnitude of the Burgers vector of the Shockley partial dislocation, and γ is the energy of the SF. This equilibrium separation is ≈ 330 Å for 4H-SiC, assuming the SF energy to be 14.7 mJ/m^2 [23.99].

The dislocation character of a BPD is determined by the angle between its line direction and the Burgers vector. Figure 23.8 illustrates the various cases when

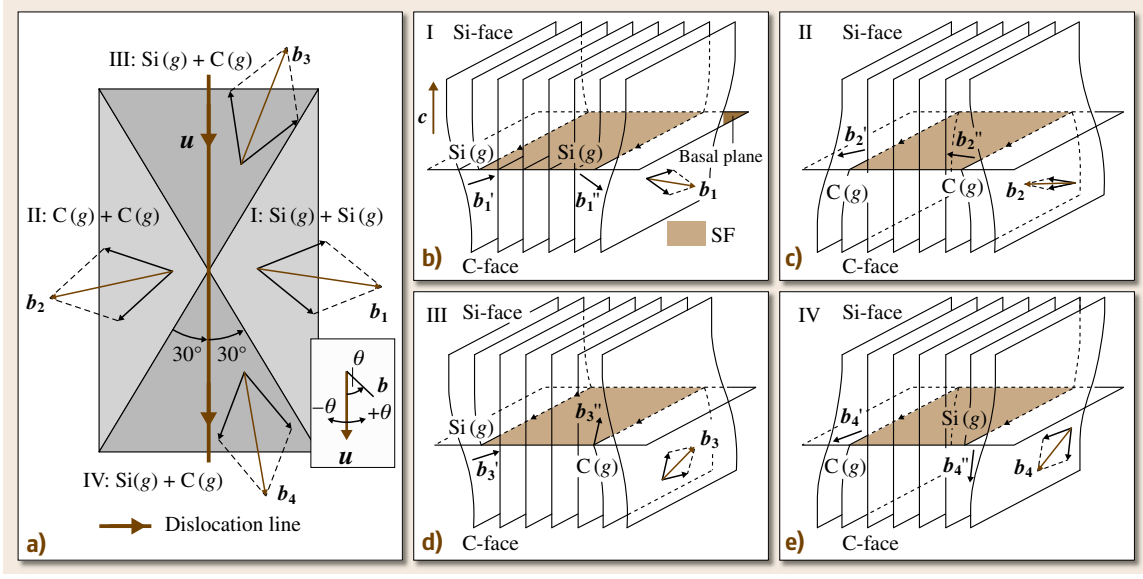


Fig. 23.8a–e Schematics showing Shockley partial dislocations of different core structures dissociated from a perfect BPD. (**a**) Four regions defined according to the direction of Burgers vector with respect to the line direction of the dislocation, assuming Si-face is facing up: (**b**) $30° < \theta < 150°$, the BPD is dissociated into two Si-core partials; (**c**) $210° < \theta < 330°$, the BPD is dissociated into two C-core partials; (**d**) $-30° < \theta < +30°$, one Si-core and one C-core; (**e**) $150° < \theta < 210°$, one Si-core and one C-core. θ is defined in the *inset* of (**a**) (after [23.96])

a perfect BPD is dissociated into Shockley partial dislocations [23.96]. The angle θ is the counterclockwise angle from the line direction to the Burgers vector direction (clockwise angles are negative); see the inset of Fig. 23.8a. In region I, in which $30° < \theta < 150°$, the extra half-plane(s) associated with the BPD extend toward the Si-face determined by the right-hand rule, $\boldsymbol{u}\times\boldsymbol{b}$. If $30° < \theta < 150°$, when the BPD with Burgers vector $\boldsymbol{b}_1$ is dissociated into two partial dislocations of Burgers vectors $\boldsymbol{b}_1'$ and $\boldsymbol{b}_1''$ (Fig. 23.8b), the angles between $\boldsymbol{b}_1'/\boldsymbol{b}_1''$ and their line directions (assuming the same line direction as the BPD) will be in the range (0°, 180°). The extra half-planes associated with the two partials can be subsequently determined again by right-hand rule: $\boldsymbol{u}\times\boldsymbol{b}_1'$ and $\boldsymbol{u}\times\boldsymbol{b}_1''$; both are extending toward the Si-face. Since the Shockley partials in SiC are glide set dislocations, both partials are Si-core. Under this circumstance, the SF will expand toward both directions, as both partials are mobile. Similar mechanism can be applied for regions II, III, and IV. In region II (Fig. 23.8c), both dissociated partials are C-core and neither of them advances, while for regions III (Fig. 23.8d) and IV (Fig. 23.8e), a Si-core and a C-core partial are formed and the SF expands as the Si-core partial advances. Notice that, if the Burgers vector of the BPD is at 30°/150°/210°/330° to its line direction, it is dissociated into a screw-oriented and a C-core or Si-core partial.

Susceptibility of Basal Plane Dislocations in 4H Silicon Carbide

Dissociation of basal plane dislocations (BPDs) into mobile silicon-core (Si-core) partial dislocations and subsequent advancement of these partial dislocations under forward bias pose a large challenge for the lifetime of SiC-based bipolar devices [23.100] since the expansion of Shockley stacking faults (SFs) associated with the advancement of Si-core partials causes the forward voltage to drop. Such expansion of basal SFs is activated by the electron–hole recombination-enhanced dislocation glide (REDG) process [23.101–103]. Through detailed x-ray topography analysis of a dislocation configuration formed after stacking fault expansion under forward bias, the susceptibility of basal plane dislocations to REDG has been determined. Figure 23.9 shows x-ray topographs (Fig. 23.9a–e) and the schematic configuration after advancement of the mobile partial. During the advancement of the partial, it interacted with a few threading screw dislocations (TSDs), and the final configuration obtained is shown in Fig. 23.9f. The Burgers vector $\boldsymbol{b}$ of the original BPD is determined to be $1/3(\bar{1}\bar{1}20)$, as indicated in Fig. 23.9f. Thus, the original BPD is screw oriented ($\theta = 0°$) and it is dissociated into a C-core and a Si-core partial. This corresponds to the case in region IV

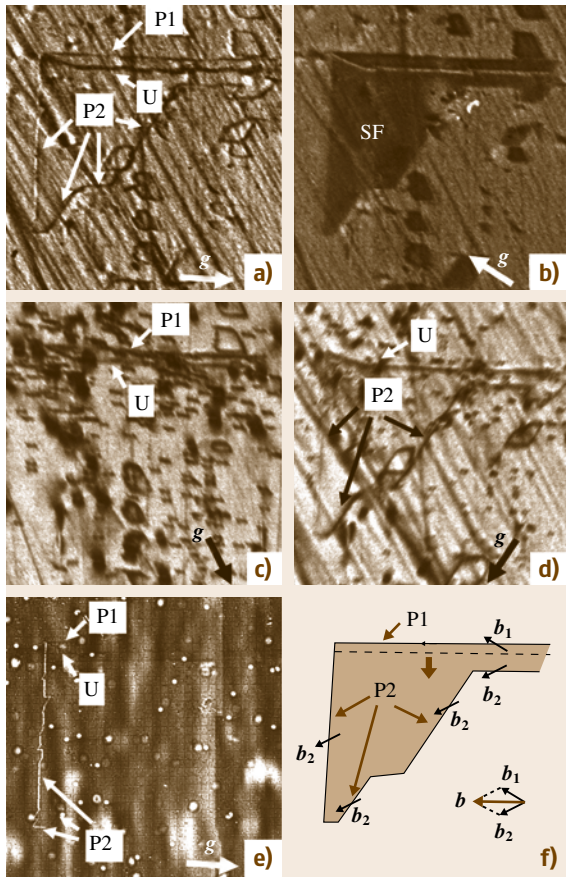


Fig. 23.9a–f REDG-activated SF after forward bias from a screw-oriented BPD. **(a)** $(11\bar{2}0)$ transmission topograph showing the partials (P1 and P2) bounding the SF. The SF area is out of contrast since $\boldsymbol{g}\cdot\boldsymbol{R}$ is equal to an integer; **(b)** $(\bar{1}010)$ transmission topograph showing the SF; **(c)** P2 is out of contrast in the $(2\bar{1}\bar{1}0)$ transmission topograph, indicating its Burgers vector of $1/3(0\bar{1}10)$; **(d)** P1 is out of contrast in the $(1\bar{2}10)$ transmission topograph, indicating its Burgers vector of $1/3(\bar{1}010)$; **(e)** (0008) back-reflection topograph. The sign of P1 and P2 can be determined; **(f)** schematics showing the SF configuration. The SF is obtained via expansion of Si-core partial toward the bottom edge of the view (*dashed line*) and interaction with TSDs. The Burgers vector of each partial segment is labeled; the Burgers vector $\boldsymbol{b}$ of the original BPD can be obtained and it is screw-oriented (after [23.96])

of Fig. 23.8, in which θ is between $-30°$ and $+30°$. Thus, the susceptibility of the basal plane dislocations to REDG process is determined by the counterclockwise angle θ from the line direction to its Burgers vector. Basal plane dislocations with $30° < \theta < 150°$ are most detrimental, as both partials will advance under forward bias. If $-30° < \theta < 30°$ or $150° < \theta < 210°$, only one partial advances. Both partials are immobile if $210° < \theta < 330°$ [23.96].

The Nucleation Mechanism in 4H-SiC Homoepitaxial Layers

BPDs in 4H-SiC homoepitaxial layers result largely from replication, during growth, of BPDs which intersect the surface of the offcut SiC substrates, a process which can be mitigated by the conversion of the BPDs into threading edge dislocations (TEDs) [23.105], which are not susceptible to REDG. While various schemes have been developed to increase the conversion rate to nearly 100% [23.106–109], BPDs which intersect the surface in screw orientation are observed to persist [23.110], and furthermore, they are observed to nucleate half-loop arrays. By recording the behavior of a half-loop array (HLA) from a Si-face epilayer using ultraviolet photoluminescence (UVPL) imaging, a model has been developed to explain the formation of HLAs. Figure 23.10a shows a screw-type BPD with Burgers vector $1/3[11\bar{2}0]$ intersecting the surface of the substrate, which is expected to be replicated during epitaxy, in contrast to those with significant edge components, which are likely to be converted into TEDs. As soon as the epilayer exceeds a critical thickness, as per

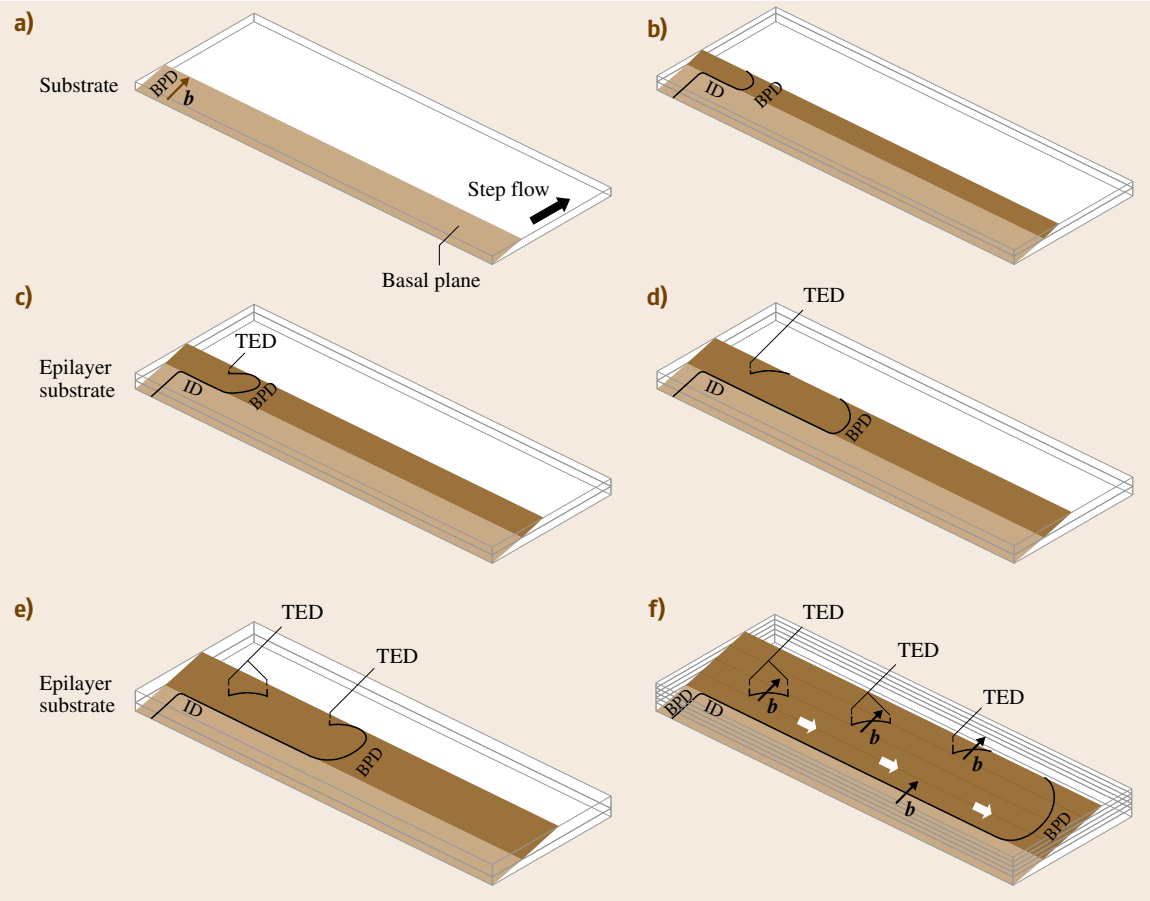


Fig. 23.10a–f Schematic showing the formation mechanism of a HLA. **(a–e)** Sequential stages in the process; **(f)** summary of process. The *lighter-shaded planes* in **(a–f)** indicate the basal plane on which the BPD lies in the substrate, while the *darker one* lies in the epilayer. See text for details of the mechanism (after [23.104])

the predictions of *Matthews* and *Blakeslee* [23.111], the threading segment of the screw-oriented BPD will be forced to glide sideways, leaving a trailing interfacial segment in its wake at or near the substrate–epilayer interface. During this glide process, the mobile threading segment adopts more edge character near the growth surface (Fig. 23.10b), rendering it susceptible to conversion to a TED during continued growth. Slip in SiC is confined to the basal plane, so that the sessile TED segment pins the surface intersection of the mobile BPD segment. During further growth, the TED segment is replicated while the mobile basal segment of dislocation pivots about the pinning point, as shown in Fig. 23.10c. At this juncture, part of the mobile BPD segment can escape through the epilayer surface (creating a surface step of magnitude equal to the Burgers vector), as shown in Fig. 23.10d, leaving two further BPD surface intersections which, since they are not in screw orientation, are susceptible to conversion to TEDs. Upon conversion, one of these TEDs is connected via a short BPD segment to the TED segment created in Fig. 23.10b, thus creating a half-loop comprising two TEDs and a connecting BPD. The other TED again acts as a pinning point for the still mobile segment of threading BPD, as shown in Fig. 23.10e, as the process repeats during continued growth as the TED segments further replicate and the threading BPD segment continues to glide. The net result of this process is an array of half-loops with short, large-edge-component BPD segments, all deposited on the exact same basal plane. The direction of the array is nearly perpendicular to the offcut direction, as summarized in Fig. 23.10f. The value of this angle depends on the competition between the growth rate and the rate of sideways glide of the threading BPD segment.

Dislocation Behavior in SiC Single Crystals

Recently, the availability of 76 and 100 mm-diameter 4H-SiC wafers with extremely low BPD densities ($3–4\times10^2\,\mathrm{cm}^{-2}$) has provided a unique opportunity to discern details of BPD behavior which were previously mostly unresolvable [23.113]. Figure 23.11a–d shows typical x-ray topographs from a section of such a 4H-SiC wafer (4° offcut towards $[11\bar{2}0]$). BPDs ($g = \bar{1}\bar{1}20$) belonging to the three $1/3\langle11\bar{2}0\rangle(0001)$ slip systems can be observed. For the dislocation inside the dashed frame pinned at points a–d, at point a, there is a TSD close to the surface intersection of the BPD which appears to be responsible for the pinning at that point, while no TSD is present at point d. Conversion of the BPD into a sessile TED at point d during growth creates an effective single-ended pinning point for the BPD. As the crystal grows, the BPD continues to glide, forming a spiral configuration around the TED pinning point, as shown schematically in Fig. 23.11e, thus operating as a single-ended Frank–Read source [23.112].

Figure 23.12a–d shows images of a $1/3[11\bar{2}0]$ basal plane dislocation exhibiting several loophole configurations that is pinned at five points a–e (Fig. 23.12a). The pinning at point a appears to have occurred close to the wafer surface at a TSD, while no TSDs are observed at any of the other pinning points. In this case, conversion of BPD segments into TEDs occurs during growth but also includes reconversion of the same TED into a BPD

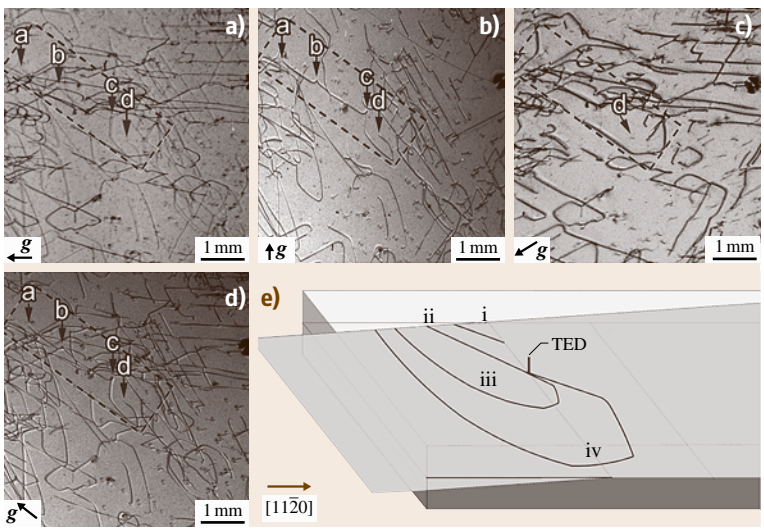


Fig. 23.11a–e SWBXT images showing BPD of interest inside dashed frame. Offcut direction is horizontal towards the right: **(a)** $g = \bar{1}\bar{1}20$; **(b)** $g = \bar{1}100$; **(c)** $g = 0\bar{1}10$; **(d)** $g = \bar{1}010$. **(e)** Schematic showing the originally screw-oriented BPD at position i being converted into a TED at its surface intersection at position ii and beginning to act as a single-ended Frank–Read source at positions iii and iv (after [23.112])

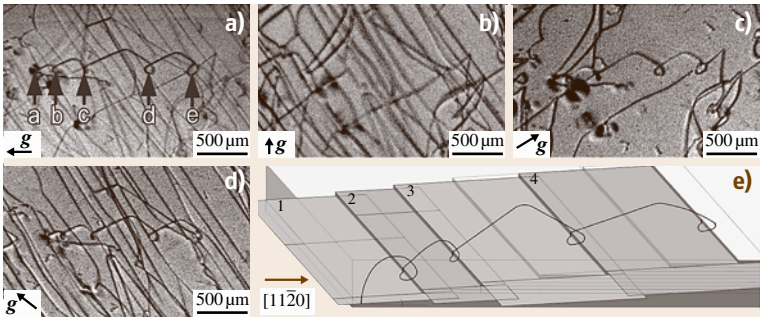


Fig. 23.12a–e SWBXT images showing dislocation loophole configurations. Offcut direction is horizontal towards the right: **(a)** $g = \bar{1}\bar{1}20$; **(b)** $g = \bar{1}100$; **(c)** $g = 01\bar{1}0$; **(d)** $g = \bar{1}010$. **(e)** Schematic showing the deflection of the BPD gliding on basal plane 1 into a TED, which then acts as a pinning point as the BPD continues to glide, followed by deflection of the TED onto basal plane 2 through overgrowth by a macrostep. The process repeats through basal planes 3 and 4 (after [23.112])

in a process that repeats throughout the growth process. This is shown schematically in Fig. 23.12e. The initial BPD segment may have had screw orientation, but continued glide may cause it to move away from screw orientation at its growth surface intersection, rendering it susceptible to conversion into a TED. During further growth, this short TED segment acts as a single-ended pinning point for the BPD which continues to glide under thermal stress. This TED can be redirected back into the basal plane as a screw-oriented BPD through overgrowth by a macrostep traveling from left to right. Once back in the basal plane, the screw-oriented BPD, being glissile, begins to glide in spiral configuration about its single-ended TED pinning point. Again, once the BPD moves away from screw orientation, it becomes more susceptible to conversion into a TED and the whole process repeats, as shown schematically in Fig. 23.12e, leading to the type of configuration observed in Fig. 23.12a,c,d [23.112].

In Fig. 23.13a, the transmission topograph from near the edge of a 75 mm wafer reveals several long, mostly straight dislocation images running approximately in the radial direction, e.g., at AB and CD. These dislocations are growth induced and may have been redirected from an originally threading orientation onto the basal plane, for example, due to overgrowth by a macrostep. These dislocations are associated with several overlapping stacking faults (Fig. 23.13b), the contrast from which arises from the phase shift experienced by the x-ray wave fields as they cross the fault plane [23.115]. Detailed analysis of the fault contrast on different reflections [23.114] indicates that there are three different types of faults present here. The first type is a pure Shockley fault, the second is a fault comprising the sum of a Frank fault ($c/4$) and a Shockley fault, and the third is a pure Frank fault ($c/4$). Figure 23.14a shows the surface intersection of the TED core, where the two extra $(1\bar{2}10)$ half-planes correspond to the $1/3[1\bar{2}10]$ Burgers vector. Note that, since the SiC structure comprises corner-sharing tetrahedra, overgrowth can only occur if the stacking position of the underside of the overgrowing step is able to maintain tetrahedral bonding with the top side of the terrace being overgrown, i. e., the stacking sequence rules, as, for example, described in [23.116], must be obeyed. As the macrostep advances over the surface outcrop, it is not able to admit the dislocation into itself so that the dislocation is necessarily deflected into the direction of step flow,

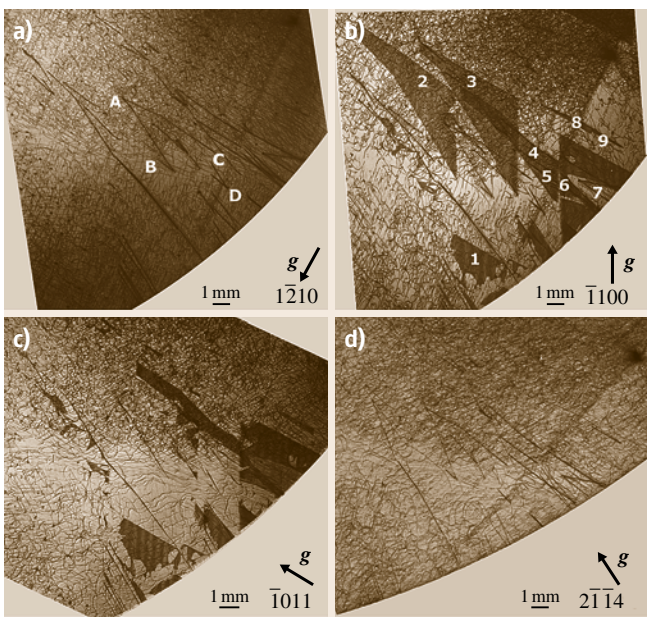


Fig. 23.13a–d SWBXT images recorded from a region near the edge of a 75 mm wafer cut with 4° offcut towards $[11\bar{2}0]$: **(a)** $1\bar{2}10$ reflection showing long straight dislocations, for example, at AB and CD; **(b)** $\bar{1}100$ reflection from the same area, showing stacking fault contrast. Faults of interest are numbered 1–9; **(c)** $\bar{1}011$ reflection from same area. Some of the fault images have disappeared on this image; **(d)** $2\bar{1}\bar{1}4$ reflection showing absence of all fault contrast [23.114]

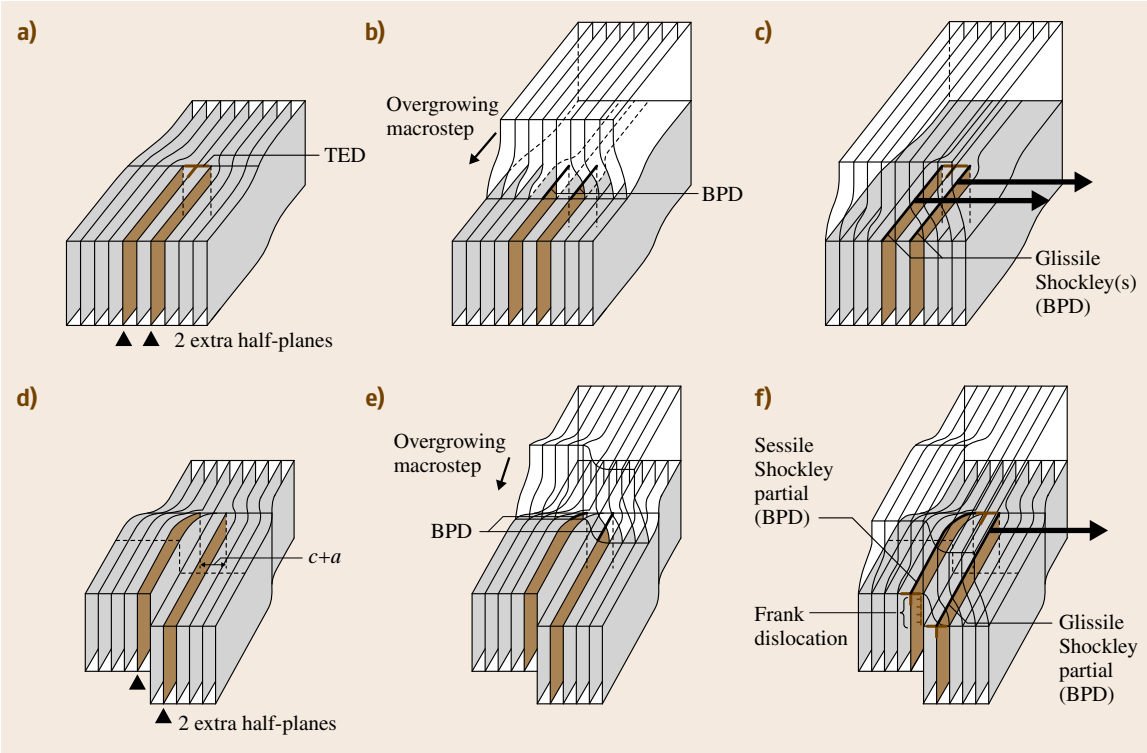


Fig. 23.14 (a–f) Overgrowth of the surface outcrop of a TED by a macrostep converting it to a BPD. Once on the basal plane, both Shockley partials are glissile and move in tandem; (b) overgrowth of a $c+a$ dislocation with a c-height step. After deflection, one Shockley is sessile and the other is glissile (after [23.114])

onto the basal plane. As this happens, the surface intersections of the two extra half-planes are frozen into the crystal and, in fact, define the line direction of the resulting BPD, as shown in Fig. 23.13b,c. If these surface intersections occur on an atomically flat terrace, the resulting BPD will comprise two extra half-planes on the exact same basal plane. Once on the basal plane, the BPD can become glissile (i. e., mobile) if sufficient basal plane shear stresses are available, and the glissile partials (comprising one extra half-plane each) will most likely separate to their equilibrium value of 20 nm and track each other as they move; i. e., the leading partial will fault the slip plane and the trailing partial will *unfault* the plane. If the surface intersections of the two extra half-planes occur on a region of surface such that they straddle the riser of a surface step which is parallel to them, it becomes possible for the overgrowth to result in two partials lying on slip planes separated by the height of the step, provided again that the overgrowth process does not breach the stacking rules [23.116].

Stacking faults are observed in the vicinity of what appear to be deflected threading dislocations. Detailed contrast analysis carried out on the faults is consistent with the Burgers vectors for the original threading dislocations of type $c+a$. The surface step (associated with the screw component) created at the surface intersection of the deflected dislocations creates a separation between the slip planes of the partials associated with the a component of the dislocations, causing one to be sessile and the other glissile. Glide of the glissile partial creates the stacking faults, which can be pure Shockley (if the original dislocation step is one unit cell high), Shockley plus $c/4$ (if the step is split into $c/4$ and $3c/4$ components), or $c/4$ if a second $c+a$ dislocation becomes involved [23.114].

23.5.3 Threading Edge Dislocations (TEDs) in 4H-SiC

In 4H-SiC, threading edge dislocations (TEDs) are dislocations with line directions roughly parallel to the

c-axis and Burgers vectors in the *c*-plane. TEDs have been observed to be one of the major components of the LAGBs, and they play critical roles in the defect structures in SiC, e.g., they act as a barrier for gliding BPDs if the spacing between adjacent TEDs is less than a critical value [23.117]. On {0001} wafer, TEDs have a $1/3\langle 11\bar{2}0\rangle$ Burgers vector. Thus six different directions of the TED Burgers vector, $[\bar{1}\bar{1}20]$, $[12\bar{1}0]$, $[2\bar{1}\bar{1}0]$, $[11\bar{2}0]$, $[1\bar{2}\bar{1}0]$, and $[2\bar{1}\bar{1}0]$, exist on the 4H-SiC epilayers, although all with the same Burgers vector magnitude. Figure 23.15a shows a $(11\bar{2}8)$ topograph recorded from a 4H-SiC wafer [23.118]. The large roughly white circles are images of TSDs, as marked in the figure. Other than the TSDs, smaller features are also seen, corresponding to the TEDs with various Burgers vectors. They appear as two dark arcs, either separated by a white spot or canted to one side or the other of the ***g*** vector. By carefully examining the images of the TEDs in more than 50 topographs recorded, six different configurations of TEDs were observed and their highly magnified images are shown in Fig. 23.15b–g. The topographic images of the expected six types of TEDs have been simulated by ray-tracing method and are shown in Fig. 23.16. The schematics of the six types of TEDs are illustrated at the top of the figure, according to the extra atomic half-

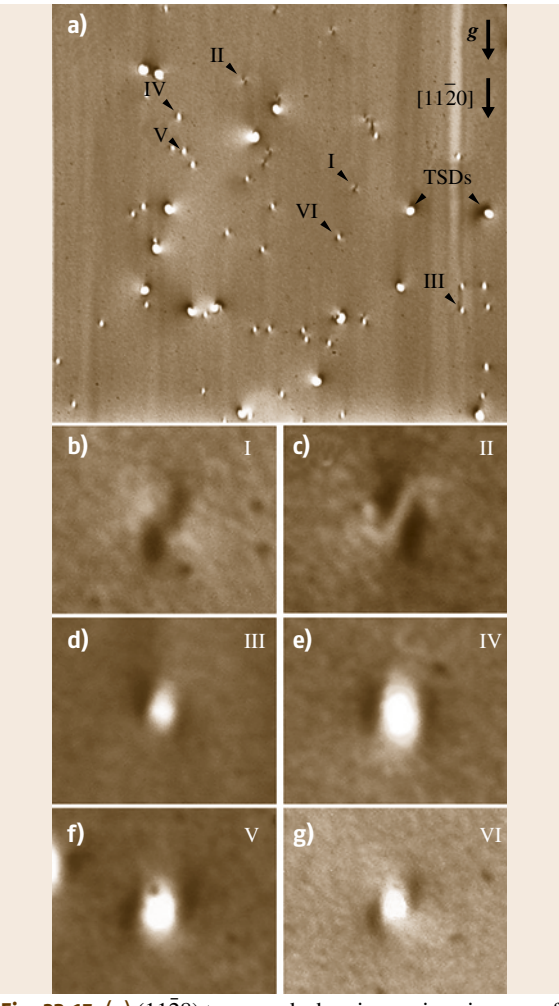


Fig. 23.15 **(a)** $(11\bar{2}8)$ topograph showing various images of TEDs. **(b–g)** Six different types of images of TEDs observed in the topographs, probably corresponding to the six types of TEDs

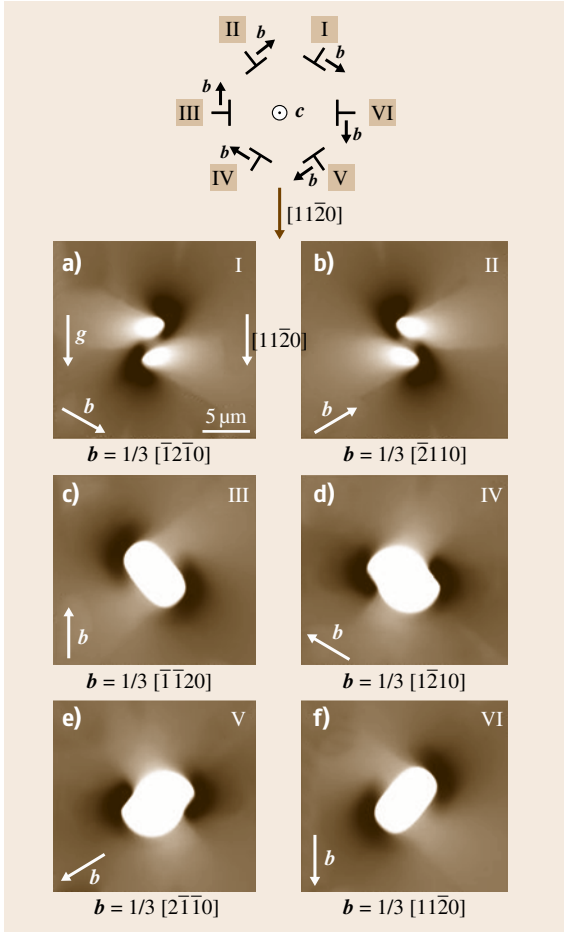


Fig. 23.16a–f Simulated $(11\bar{2}8)$ grazing-incidence XRT images of TEDs with six different Burgers vectors **(a–f)** *Top*: six types of TEDs are illustrated according to the position of the extra atomic half-planes associated with them

planes associated with them. They appear as two dark arcs canted to one side or the other of the $\boldsymbol{g}$-vector, and these two dark arcs are either shifted vertically (Fig. 23.15a, b) or separated by an area of white contrast (Fig. 23.15c–f). Their Burgers vectors are at 60°, 120°, 180°, 240°, 300°, and 0° counterclockwise from the $\boldsymbol{g}$-vector on the x-ray films for Fig. 23.15a–f, respectively. By comparing the simulated images in Fig. 23.15 and the observation in Fig. 23.16, one-to-one correspondence can be seen. Thus, the Burgers vectors of the TEDs can be revealed from a single-reflection $(11\bar{2}8)$ grazing-incidence x-ray topograph, based on their topographic contrast [23.118]. TED arrays in 4H-SiC prefer to be oriented along $\langle 1\bar{1}00\rangle$, and their Burgers vectors are perpendicular to the arrays. This is consistent with the fundamental dislocation theory that edge-oriented dislocations tend to align perpendicular to their Burgers vector to minimize the total strain energy.

23.6 Concluding Remarks

An extraordinary combination of physical and electronic properties makes silicon carbide a unique material for devices in high-power, high-frequency, high-temperature, and intense-radiation applications. Recent developments in SiC bulk growth and epitaxial film technology have greatly advanced SiC-based device technology. The modified Lely method has now become a standard process for industrial production of SiC boules. Wafers of 75 and 100 mm diameter are commercially available from numerous vendors. Dislocation densities have been reduced by optimizing the crystal growth technology in conjunction with modeling and computer simulation.

Defects, particularly micropipes, have nearly been eliminated by improving the growth technique, optimizing the process parameters, and developing better understanding of defect generation and propagation. Undesirable polytype inclusions have been understood reasonably well, and it is now possible to grow a single polytype using the modified Lely method. With the availability of 6H-SiC wafers, research on epitaxial growth has increased tremendously. High-quality films are being produced for different device applications using CVD techniques; in particular, HTCVD and hot-wall CVD have yielded films of good uniformity. Even though LPE of SiC is not as successful as CVD, recent developments such as container-free LPE growth show promise for better-quality films. In addition, the quality of the epitaxial film and thereby the functioning of the device have been greatly improved by using step-controlled epitaxy. High dopant incorporation can be achieved using the site-competition technique.

Defects present in SiC crystals have been characterized using x-ray topography and microscopy-based techniques such as chemical etching, AFM, SEM, TEM, and reflection and transmission optical microscopy. Even though many of these techniques are used in a complementary manner to obtain detailed information on defects present in the crystal, x-ray topography, particularly SWBXT, is quite superior to other methods in revealing defects present in SiC crystals. Indeed, SWBXT has provided complete quantitative characterization of both closed-core and hollow-core (micropipes) screw dislocations as well as basal plane dislocations and threading edge dislocations. It has also given insights into the formation mechanisms of these defects and various interesting configurations that can be formed. Since SWBXT is capable of imaging defects in a full-size wafer with devices fabricated on it, this technique can be successfully used to study the influence of various defects on device performance.

The challenges in SiC growth still remain quality, size, and cost. To enable widespread use of SiC as a semiconductor, it is important that further progress be made in all of these areas. While micropipe defects have been nearly eliminated, other defects such as basal plane dislocations and screw dislocations need to be substantially reduced. Another important area is polytype control and infringement of polycrystalline growth directly under the seed. Since different polytypes of SiC have different properties and also polytype inclusions can become potential sources for defect generation, it is critical that a single polytype is maintained throughout the growth of the boule.

Control of the growth process requires sensing, measurement, and control strategies. However, the process does not allow much measurement, in fact, nothing inside the growth zone. Measurement of temperatures at only two locations, far away from the growth surface and the bulk of the SiC charge, gives very little information on the actual growth temperature and temperature gradient, two critical growth parameters. Also, it is difficult to determine experimentally the rate of sublimation, the chemical composition of the vapor, the growth interface shape, etc., which makes control of the process very difficult.

References

23.1 A.A. Lebedev, V.E. Chelnokov: Wide-gap semiconductors for high-power electronics, Semiconductors **33**, 999–1001 (1999)

23.2 V.E. Chelnokov, A.L. Syrkin: High temperature electroics using SiC: Actual situation and unsolved problems, Mater. Sci. Eng. B **46**, 248–253 (1997)

23.3 A. Lloyd, P. Tobias, A. Baranzahi, P. Martensson, I. Lundström: Current status of silicon carbide based high-temperature gas sensors, IEEE Trans. Electron. Dev. **46**, 561–566 (1999)

23.4 C.I. Harris, A.O. Konstantinov: Recent developments in SiC device research, Phys. Scr. **79**, 27–31 (1999)

23.5 V. Harle, N. Hiller, S. Kugler, B. Hahn, N. Stath: Industrial aspects of GaN/SiC blue light emitting diodes in Europe, Mater. Sci. Eng. B **61–62**, 310–313 (1999)

23.6 A.G. Acheson: Br. Pat. **17**, 911 (1892)

23.7 A.J. Lely: Darstellung von Einkristallen von Siliziumcarbid und Beherrschung von Art und Menge der eingebauten Verunreinigungen, Ber. Dtsch. Keram. Ges. **32**, 229–231 (1955)

23.8 D.R. Hamilton: The growth of silicon carbide by sublimation. In: *Silicon Carbide. A High Temperature Semiconductor*, ed. by J.R. Connor, J. Smilestens (Pergamon, Oxford 1960) pp. 45–51

23.9 V.P. Novikov, V.I. Ionov: Production of monocrystals of alpha silicon carbide, Growth Cryst. **6**, 9–21 (1968)

23.10 F.A. Halden: The growth of silicon carbide from solution. In: *Silicon Carbide. A High Temperature Semiconductor*, ed. by J.R. Connor, J. Smilestens (Pergamon, Oxford 1960) pp. 115–123

23.11 J.T. Kendal: The growth of silicon carbide from gaseous cracking. In: *Silicon Carbide. A High Temperature Semiconductor*, ed. by J.R. Connor, J. Smilestens (Pergamon, Oxford 1960) pp. 67–72

23.12 Y.M. Tairov, V.F. Tsvetkov: Investigation of growth processes of ingots of silicon carbide single crystals, J. Cryst. Growth **43**, 209–212 (1978)

23.13 Cree Research, Inc., 2810 Meridian Parkway, Durham, NC 27713, USA

23.14 H. Matsunami, T. Kimoto: Step controlled epitaxial growth of SiC: High quality homoepitaxy, Mater. Sci. Eng. R **20**, 125–166 (1997)

23.15 R.C. Glass, D. Henshall, V.F. Tsvetkov, C.H. Carter Jr.: SiC-seeded crystal growth, MRS Bulletin **22**, 30–35 (1997)

23.16 W.F. Knippenberg: Growth phenomena in silicon carbide: Preparative procedures, Philips Res. Rep. **18**, 170–179 (1966)

23.17 G. Ziegler, P. Lanig, D. Theis, C. Weyrich: Single crystal growth of SiC substrate material for blue light emitting diodes, IEEE Trans. Electron. Dev. **30**, 277–281 (1983)

23.18 D.L. Barrett, R.G. Seidensticker, W. Gaida, R.H. Hopkins: SiC boule growth by sublimation vapor transport, J. Cryst. Growth **109**, 17–23 (1991)

23.19 R.A. Stein, P. Lanig, S. Leibenzeder: Influence of surface energy on the growth of 6H and 4H-SiC polytypes sublimation, Mater. Sci. Eng. B **11**, 69–71 (1992)

23.20 R.C. Glass, D. Henshall, V.F. Tsvetkov, C.H. Carter Jr.: SiC seeded crystal growth, Phys. Status Solidi (b) **202**, 149–162 (1997)

23.21 D.L. Barrett, J.P. Mchugh, H.M. Hobgood, R.H. Hopkins, P.G. McMullin, R.C. Clarke: Growth of large SiC single crystals, J. Cryst. Growth **128**, 358–362 (1993)

23.22 A.R. Powell, S. Wang, G. Fechko, G.R. Brandes: Sublimation growth of 50 mm diameter SiC wafers, Mater. Sci. Forum **264–268**, 13–16 (1998)

23.23 I. Garcon, A. Rouault, M. Anikin, C. Jaussaud, R. Madar: Study of SiC single-crystal sublimation growth conditions, Mater. Sci. Eng. B **29**, 90–93 (1995)

23.24 Y.M. Tairov, Y.V.F. Tsvetkov: General principles of growing large-size single crystals of various silicon carbide polytypes, J. Cryst. Growth **52**, 146–150 (1981)

23.25 Y.M. Tairov: Growth of bulk SiC, Mater. Sci. Eng. B **29**, 83–89 (1995)

23.26 S.Y. Karpov, Y.N. Makarov, E.N. Mokhov, M.G. Ramm, M.S. Ramm, A.D. Roenkov, R.A. Talalaev, Y.A. Vodakov: Analysis of silicon carbide growth by sublimation sandwich method, J. Cryst. Growth **173**, 408–416 (1997)

23.27 S.Y. Karpov, Y.N. Makarov, M.S. Ramm: Simulation of sublimation growth of SiC single crystals, Phys. Status Solidi (b) **202**, 201–220 (1997)

23.28 Y.A. Vodakov, A.D. Roenkov, M.G. Ramm, E.N. Mokhov, Y.N. Makarov: Use of Ta-container for sublimation growth and doping of SiC bulk crystals and epitaxial layers, Phys. Status Solidi (b) **202**, 177–200 (1997)

23.29 E.N. Mokhov, M.G. Ramm, A.D. Roenkov, Y.A. Vodakov: Growth of silicon carbide bulk crystals by the sublimation sandwich method, Mater. Sci. Eng. B **46**, 317–323 (1997)

23.30 S.Y. Karpov, Y.N. Makarov, M.S. Ramm, R.A. Talalaev: Control of SiC growth and graphitization in sublimation sandwich system, Mater. Sci. Eng. B **46**, 340–344 (1997)

23.31 A. Henry, I.G. Ivanov, T. Egilsson, C. Hallin, A. Ellison, O. Kordina, U. Lindefelt, E. Janzen: High quality 4H-SiC grown on various substrate orientations, Diam. Relat. Mater. **6**, 1289–1292 (1997)

23.32 D.J. Larkin: An overview of SiC epitaxial growth, MRS Bulletin **22**, 36–41 (1997)

23.33 H. Matsunami: Progress in epitaxial growth of SiC, Physica B **185**, 65–74 (1993)

23.34 S. Nishinov, J.A. Powell, H.A. Will: Production of large-are single-crystal wafers of cubic SiC for semiconductors, Appl. Phys. Lett. **42**, 460–462 (1983)

23.35 R. Yakimova, R.E. Janzen: Current status and advances in the growth of SiC, Diam. Relat. Mater. **9**, 432–438 (2000)

23.36 O. Kordina, C. Hallin, A. Ellison, A.S. Bakin, I.G. Ivanov, A. Henry, R. Yakimova, M. Touminen, A. Vehanen, E. Janzen: High temperature chemical vapor deposition of SiC, Appl. Phys. Lett. **69**, 14561458 (1996)

23.37 O. Kordina, C. Hallin, A. Henry, J.P. Bergman, I. Ivanov, A. Ellison, N.T. Son, E. Janzen: Growth of SiC by "hot-wall" CVD and HTCVD, Phys. Status Solidi (b) **202**, 321–334 (1997)

23.38 C.H. Carter, V.F. Tsvetkov, R.C. Glass, D. Henshall, M. Brady, S.G. Muller, O. Kordina, K. Irvine, J.A. Edmond, H.S. Kong, R. Singh, S.T. Allen, J.A. Palmour: Progress in SiC: From material growth to commericial device development, Mater. Sci. Eng. B **61–62**, 1–8 (1999)

23.39 E. Janzen, O. Kordina: SiC Material for high-power applications, Mater. Sci. Eng. B **46**, 203–209 (1997)

23.40 M. Nakabayashi, T. Fujimoto, M. Katsuno, N. Ohtani, H. Tsuge, H. Yashiro, T. Aigo, T. Hoshino, H. Hirano, K. Tatsumi: Growth of crack-free 100 mm diameter 4H-SiC crystals with low micropipe densities, Mater. Sci. Forum **600–603**, 3–6 (2009)

23.41 R.T. Leonard, Y. Khlebnikov, A.R. Powell, C. Basceri, M.F. Brady, I. Khlebnikov, J.R. Jenny, D.P. Malta, M.J. Paisley, V.F. Tsvetkov, R. Zilli, E. Deyneka, H. Hobgood, V. Balakrishna, C.H. Carter Jr.: 100 mm 4HN-SiC wafers with zero micropipe density, Mater. Sci. Forum **600–603**, 7–10 (2009)

23.42 M. Syväjärvi, R. Yakimova, I.G. Ivanov, E. Janzen: Growth of 4H SiC from liquid phase, Mater. Sci. Eng. B **46**, 329–332 (1997)

23.43 B.M. Epelbaum, D. Hofmann, M. Muller, A. Winnacker: Top-seeded soloution growth of bulk SiC: Search for the fast growth regimes, Mater. Sci. Forum **338–342**, 107–110 (2000)

23.44 A. Suzuki, M. Ikeda, N.T. Nagoa, H. Matsunami, T.J. Tanaka: Liquid phase epitaxial growth of 6H-SiC by the dipping technique for preparation of blue-light-emitting diodes, J. Appl. Phys. **47**, 4546–4550 (1976)

23.45 Y.M. Tairov, F.I. Raihel, V.F. Tsvetkov: Silicon solubility in tin and gallium, Neorg. Mater. **3**, 1390–1391 (1982)

23.46 V.A. Dmitriev, L.B. Elfimov, N.D. Il'inskaya, S.V. Rendakova: Liquid phase epitaxy of silicon carbide at temperatures of 1100–1200 °C, Springer Proc. Phys. **56**, 307–311 (1996)

23.47 V.A. Dmitriev, A. Cherenov: Growth of SiC and SiC-AlN solid solution by container by container free liquid phase epitaxy, J. Cryst. Growth **128**, 343–348 (1993)

23.48 M. Syväjärvi, R. Yakimova, H.H. Radamsom, N.T. Son, Q. Wahab, I.G. Ivanov, E. Janzen: Liquid phase epitaxial growth of SiC, J. Cryst. Growth **197**, 147–154 (1999)

23.49 R. Yakimova, M. Syväjärvi, M. Tuominen, T. Iakimov, R. Råback, A. Vehanen, E. Janz: Seeded sublimation growth of 6H and 4H-SiC crystals, Mater. Sci. Eng. B **61–62**, 54–57 (1999)

23.50 G. Augustine, H.M. Hobgood, V. Balakrishna, G. Dunne, R.H. Hopkins: Physical vapor transport growth and properties of SiC monocrystals of 4H polytype, Phys. Status Solidi (b) **202**, 137–148 (1997)

23.51 S.I. Nishizawa, Y. Kitou, W. Bahng, N. Oyanagi, M.N. Khan, K. Arai: Shape of SiC bulk single crystal grown by sublimation, Mater. Sci. Forum **338–342**, 99–102 (2000)

23.52 D. Hobgood, M. Brady, W. Brixius, G. Fechko, R. Glass, D. Henshall, J.R. Jenny, R. Leonard, D. Malta, S.G. Muller, V. Tsvetkov, C.H. Carter Jr.: Status of large diameter SiC crystal growth for electronic and optical applications, Mater. Sci. Forum **338–342**, 3–8 (2000)

23.53 D.W. Snyder, V.D. Heydemann, W.J. Everson, D.L. Barret: Large diameter PVT growth of bulk 6H SiC crystals, Mater. Sci. Forum **338–342**, 9–12 (2000)

23.54 R.R. Siergiej, R.C. Clarke, S. Sriram, A.K. Aggarwal, R.J. Bojko, A.W. Morse, V. Balakrishana, M.F. MacMillan, A.A. Burk, C.D. Brandt: Advances in SiC materials and devices: An industrial point of view, Mater. Sci. Eng. B **61–62**, 9–17 (1999)

23.55 S.G. Muller, R.C. Glass, H.M. Hobgood, V.F. Tsvetkov, M. Brady, D. Henshall, J.R. Jenny, D. Malta, C.H. Carter Jr.: The status of SiC bulk growth from an industrial point of view, J. Cryst. Growth **211**, 325–332 (2000)

23.56 Q.-S. Chen, V. Prasad, H. Zhang, M. Dudley: Silicon carbide crystals – Part II: Process physics and modeling. In: *Crystal Growth Technology*, ed. by K. Byrappa, T. Ohachi (Springer, Berlin, Heidelberg 2001) pp. 233–269

23.57 G. Dhanaraj, X.R. Huang, M. Dudley, V. Prasad, R.-H. Ma: Silicon carbide crystals – Part II: Process physics and modeling. In: *Crystal Growth Technology*, ed. by K. Byrappa, T. Ohachi (Springer, Berlin, Heidelberg 2001) pp. 181–232

23.58 T. Nishiguchi, S. Okada, M. Sasaki, H. Harima, S. Nishino: Crystal growth of 15R-SiC boules by sublimation method, Mater. Sci. Forum **338–342**, 115–118 (2000)

23.59 E.K. Sanchez, T. Kuhr, D. Heydemann, W. Snyder, S. Rohrer, M. Skowronski: Formation of thermal decomposition cavities in physical vapor transport of silicon carbide, J. Electron. Mater. **29**, 347–351 (2000)

23.60 M. Tuominen, R. Yakimova, R.C. Glass, T. Tuomi, E. Janzen: Crystalline imperfections in 4H SiC grown with a seeded Lely method, J. Cryst. Growth **144**, 267–276 (1994)

23.61 M. Anikin, R. Madar: Temperature gradient controlled SiC crystal growth, Mater. Sci. Eng. B **46**, 278–286 (1997)

23.62 W. Bahng, Y. Kitou, S. Nishizawa, H. Yamaguchi, M. Nasir Khan, N. Oyanagi, S. Nishino, K. Arai: Rapid enlargement of SiC single crystal using a cone-shaped platform, J. Cryst. Growth **209**, 767–772 (2000)

23.63 R. Schorner, P. Friedrichs, D. Peters, D. Stephani: Significantly improved performance of MOSFETs on silicon carbide using the 15R-SiC, IEEE Electron. Device Lett. **20**, 241–244 (1999)

23.64 N. Schulze, D. Barrett, M. Weidner, G. Pensl: Controlled growth of bulk 15R SiC single crystals by the modified Lely method, Mater. Sci. Forum **338–342**, 111–114 (2000)

23.65 J. Takahashi, M. Kanaya, Y. Fujiwara: Sublimation growth of SiC single crystalline ingots on faces perpendicular to the (0001) basal-plane, J. Cryst. Growth **135**, 61–70 (1994)

23.66 M. Touminen, R. Yakimova, E. Prieur, A. Ellison, T. Toumi, A. Vehanen, E. Janzen: Growth-related structural defects in seeded sublimation-grown SiC, Diam. Relat. Mater. **6**, 1272–1275 (1997)

23.67 N. Oyanagi, S.I. Nishizawa, T. Kato, H. Yamaguchi, K. Arai: SiC Single crystal growth rate by in-situ observation using the transmission x-ray technique, Mater. Sci. Forum **338–342**, 75–78 (2000)

23.68 T. Kato, N. Oyangi, H. Yamaguchi, Y. Takano, S. Nishizawa, K. Arai: In-situ observation of SiC bulk single crystal growth by x-ray topography, Mater. Sci. Forum **338–342**, 457–460 (2000)

23.69 W. Si, M. Dudley, R. Glass, V. Tsvetkov, C.H. Carter Jr.: Experimental studies of hollow-core screw dislocations in 6H-SiC and 4H-SiC single crystals, Mater. Sci. Forum **264–268**, 429–432 (1998)

23.70 W. Si, M. Dudley, R. Glass, V. Tsvetkov, C.H. Carter Jr.: Hollow-core screw dislocations in 6H-SiC single crystals. A test of Frank's theory, J. Electron. Mater. **26**, 128–133 (1997)

23.71 M. Dudley, W. Si, S. Wang, C.H. Carter Jr., R. Glass, V.F. Tsvetkov: Quantitative analysis of screw dislocations in 6H-SiC single crystals, Nuovo Cim. D **19**, 153–164 (1997)

23.72 M. Dudley, S. Wang, W. Huang, C.H. Carter Jr., V.F. Tsvetkov, C. Fazi: White beam synchrotron topographic studies of defects in 6H-SiC single crystals, J. Phys. D **28**, A63–A68 (1995)

23.73 F.C. Frank: Capillary equillibria of dislocated crystals, Acta Cryst. **4**, 497–501 (1951)

23.74 A.R. Verma: Spiral growth on carborundum crystal faces, Nature **167**, 939 (1951)

23.75 S. Amelinck: Spiral growth on carborundum crystal faces, Nature **167**, 939–940 (1951)

23.76 A.R. Verma: *Crystal Growth and Dislocations* (Butterworths Scientific, London 1953)

23.77 J. Giocondi, G.S. Rohrer, M. Skowronski, V. Balakrishna, G. Augustine, H.M. Hobgood, R.H. Hopkins: An AFM study of super-dislocation/micropipe complexes on the 6H-SiC(0001) growth surfaces, J. Cryst. Growth **181**, 351–362 (1997)

23.78 M. Dudley, W. Huang, S. Wang, J.A. Powell, P. Neudeck, C. Fazi: White beam synchrotron topographic analysis of multipolytype SiC device configurations, J. Phys. D **28**, A56–A62 (1995)

23.79 X.R. Huang, M. Dudley, W.M. Vetter, W. Huang, C.H. Carter Jr.: Contrast mechanism in superscrew dislocation images on synchrotron back-reflection topographs, Mater. Res. Soc. Symp. Proc. **524**, 71–76 (1998)

23.80 X.R. Huang, M. Dudley, W.M. Vetter, W. Huang, S. Wang, C.H. Carter Jr.: Direct evidence of micropipe-related pure superscrew dislocations in SiC, Appl. Phys. Lett. **74**, 353–356 (1999)

23.81 X.R. Huang, M. Dudley, W.M. Vetter, W. Huang, W. Si, C.H. Carter Jr.: Superscrew dislocation contrast on synchrotron white-beam topographs: An accurate description of the direct dislocation image, J. Appl. Crystallogr. **32**, 516–524 (1999)

23.82 M. Dudley, X.R. Huang, W. Huang: Assessment of orientation and extinction contrast contributions to the direct dislocation image, J. Phys. D **32**, A139–A144 (1999)

23.83 Y. Chen, M. Dudley: Direct determination of dislocation sense of closed-core threading screw dislocations using synchrotron white beam x-ray topography in 4H silicon carbide, Appl. Phys. Lett. **91**, 141918 (2007)

23.84 Y. Chen, G. Dhanaraj, M. Dudley, E.K. Sanchez, M.F. MacMillan: Sense determination of micropipes via grazing-incidence synchrotron white beam x-ray topography in 4H silicon carbide, Appl. Phys. Lett. **91**, 071917 (2007)

23.85 I. Kamata, M. Nagano, H. Tsuchida, Y. Chen, M. Dudley: Investigation of character and spatial distribution of threading edge dislocations in 4H-SiC epilayers by high-resolution topography, J. Cryst. Growth **311**, 1416–1422 (2009)

23.86 N. Schulze, D.L. Barret, G. Pensl: Near-equilibrium growth of micropipe free 6H-SiC single crystals by physical vapor transport, Appl. Phys. Lett. **72**, 1632–1634 (1998)

23.87 V. Tsvetkov, R. Glass, D. Henshall, D. Asbury, C.H. Carter Jr.: SiC seeded boule growth, Mater. Sci. Forum **264–268**, 3–8 (1998)

23.88 V.D. Heydemann, E.K. Sanchez, G.S. Rohrer, M. Skowronski: Structural evolution of Lely seeds during the initial stages of SiC sublimation growth, Mater. Res. Soc. Symp. Proc. **483**, 295–300 (1998)

23.89 V. Balakrishna, R.H. Hopkins, G. Augustine, G.T. Donne, R.N. Thomas: Characterization of 4H-SiC monocrystals grown by physical vapor transport, Inst. Phys. Conf. Ser. **160**, 321–331 (1998)

23.90 S. Gits-Leon, F. Lefaucheux, M.C. Robert: Effect of stirring on crystalline quality of solution grown

crystals – case of potash aluminum, J. Cryst. Growth **44**, 345–355 (1978)
23.91 H. Klapper, H. Kuppers: Directions of dislocation lines in crystals of ammonium hydrogen oxalate hemihydrate grown from solution, Acta Cryst. A **29**, 495–503 (1973)
23.92 G. Neuroth: Der Einfluß von Einschlußbildung und mechanischer Verletzung auf das Wachstum und die Perfektion von Kristallen. Ph.D. Thesis (University of Bonn, Bonn 1996)
23.93 A.A. Chernov: Formation of crystals in solutions, Contemp. Phys. **30**, 251–276 (1989)
23.94 M. Dudley, X.R. Huang, W. Huang, A. Powell, S. Wang, P. Neudeck, M. Skowronski: The mechanism of micropipe nucleation at inclusions in silicon carbide, Appl. Phys. Lett. **75**, 784–786 (1999)
23.95 P. Krishna, S.-S. Jiang, A.R. Lang: An optical and x-ray topographic study of giant screw dislocations in silicon-carbide, J. Cryst. Growth **71**, 41–56 (1985)
23.96 Y. Chen, M. Dudley, K.X. Liu, R.E. Stahlbush: Observations of the influence of threading dislocations on the recombination enhanced partial dislocation glide in 4H-silicon carbide epitaxial layers, Appl. Phys. Lett. **90**, 171930 (2007)
23.97 S. Wang: Characterization of growth defects in silicon carbide single crystals by synchrotron x-ray topography. Ph.D. Thesis (State University of New York at Stony Brook, Stony Brook 1995)
23.98 W.M. Vetter: Characterization of dislocation structures in silicon carbide crystals. Ph.D. Thesis (State University of New York at Stony Brook, Stony Brook 1999)
23.99 M.H. Hong, A.V. Samant, P. Pirouz: Stacking fault energy of 6H-SiC and 4H-SiC single crystals, Philos. Mag. A **80**, 919–935 (2000)
23.100 H. Lendenmann, F. Dahlquist, N. Johansson, R. Soderholm, P.A. Nilsson, J.P. Bergman, P. Skytt: Long term operation of 4.5 kV PiN and 2.5 kV JBS diodes, Mater. Sci. Forum **353–356**, 727 (2001)
23.101 A. Galeckas, J. Linnros, P. Pirouz: Recombination-enhanced extension of stacking faults in 4H-SiC p-i-n diodes under forward bias, Appl. Phys. Lett. **81**, 883 (2002)
23.102 J.D. Weeks, J.C. Tully, L.C. Kimerling: Theory of recombination-enhanced defect reactions in semiconductors, Phys. Rev. B **12**, 3286–3292 (1975)
23.103 H. Sumi: Dynamic defect reactions induced by multiphonon nonradiative recombination of injected carriers at deep levels in semiconductors, Phys. Rev. B **29**, 4616–4630 (1984)
23.104 N. Zhang, Y. Chen, Y. Zhang, M. Dudley, R.E. Stahlbush: Nucleation mechanism of dislocation half-loop arrays in 4H-silicon carbide homoepitaxial layers, Appl. Phys. Lett. **94**, 122108 (2009)
23.105 S. Ha, P. Mieszkowski, M. Skowronski, L.B. Rowland: Dislocation conversion in 4H silicon carbide epitaxy, J. Cryst. Growth **244**, 257–266 (2002)
23.106 Z. Zhang, T.S. Sudarshan: Basal plane dislocation-free epitaxy of silicon carbide, Appl. Phys. Lett. **87**, 151913 (2005)
23.107 J.J. Sumakeris, J.P. Bergman, M.K. Das, C. Hallin, B.A. Hull, E. Janzen, H. Lendenmann, M.J. O'Loughlin, M.J. Paisley, S. Ha, M. Skowronski, J.W. Palmour, C.H. Carter Jr.: Techniques for minimizing the basal plane dislocation density in SiC epilayers to reduce V_f drift in SiC bipolar power devices, Mater. Sci. Forum **527–529**, 141 (2006)
23.108 E.R. Stahlbush, B.L. VanMil, R.L. Myers-Ward, K.-K. Lew, D.K. Gaskill, C.R. Eddy Jr.: Basal plane dislocation reduction in 4H-SiC epitaxy by growth interruptions, Appl. Phys. Lett. **94**, 041916 (2009)
23.109 R.E. Stahlbush, B.L. VanMil, K.X. Liu, K.K. Lew, R.L. Myers-Ward, D.K. Gaskill, C.R. Eddy Jr., X. Zhang, M. Skowronski: Evolution of basal plane dislocations during 4H-SiC epitaxial growth, Mater. Sci. Forum **600–603**, 317–320 (2009)
23.110 H. Tsuchida, I. Kamata, M. Nagano: Investigation of defect formation in 4H-SiC(0001) and (000$\bar{1}$) epitaxy, Mater. Sci. Forum **600–603**, 267–272 (2009)
23.111 J.W. Matthews, A.E. Blakeslee: Defects in epitaxial multilayers: I. Misfit dislocations, J. Cryst. Growth **27**, 118–125 (1974)
23.112 M. Dudley, N. Zhang, Y. Zhang, B. Raghothamachar, S. Byrappa, G. Choi, E.K. Sanchez, D. Hansen, R. Drachev, M.J. Loboda: Characterization of 100 mm diameter 4H-Silicon carbide crystals with extremely low basal plane dislocation density, Mater. Sci. Forum **645–648**, 291 (2010)
23.113 M. Selder, L. Kadinski, F. Durst, T.L. Straubinder, P.L. Wellmann, D. Hofmann: Numerical simulation of thermal stress formation during PVT-growth of SiC bulk crystals, Mater. Sci. Forum **353–356**, 65 (2001)
23.114 M. Dudley, S. Byrappa, H. Wang, F. Wu, Y. Zhang, B. Raghothamachar, G. Choi, E.K. Sanchez, D. Hansen, R. Drachev, M.J. Loboda: Analysis of dislocation behavior in low dislocation density, PVT-grown, four-inch silicon carbide single crystals, Mater. Res. Soc. Symp. Proc. **1246**, (2010) in press
23.115 A. Authier, Y. Epelboin: Variation of stacking fault contrast with the value of the phase shift in x-ray topography, Phys. Status Solidi (a) **41**, K9–K12 (1977)
23.116 P. Pirouz, J.W. Yang: Polytypic transformations in SiC: The role of TEM, Ultramicroscopy **51**, 189–214 (1993)
23.117 Y. Chen, H. Chen, N. Zhang, M. Dudley, R. Ma: Investigation and properties of grain boundaries in silicon carbide, Mater. Res. Soc. Symp. Proc. E **955**, 0955I0750 (2007)
23.118 I. Kamata, M. Nagano, H. Tsuchida, Y. Chen, M. Dudley: Investigation of character and spatial distribution of threading edge dislocations in 4H-SiC epilayers by high-resolution topography, J. Cryst. Growth **311**, 1416–1422 (2009)

24. AlN Bulk Crystal Growth by Physical Vapor Transport

Rafael Dalmau, Zlatko Sitar

Despite considerable research in thin-film growth of wide-bandgap group III nitride semiconductors, substrate technology remains a critical issue for the improvement of nitride devices. With applications ranging from high-power electronics to optoelectronics, an increasing number of nitride semiconductor devices are becoming commercially available. Currently, many of these devices are being grown heteroepitaxially on nonnative substrates, leading to a high defect density in the active layers, which limits device performance and lifetime. Aluminum nitride (AlN) is considered a highly desirable candidate as a native substrate material for III-nitride epitaxy, especially for AlGaN devices with high Al concentrations. AlN crystals have been grown by a variety of methods. High-temperature growth of AlN bulk crystals by physical vapor transport (PVT) has emerged as the most promising growth technique to date for production of large, high-quality single crystals. This chapter reviews recent growth and characterization results of AlN bulk crystals grown by PVT and discusses several issues that remain to be addressed for continued development of this technology.

24.1 PVT Crystal Growth 822
24.2 High-Temperature Materials Compatibility 825
24.3 Self-Seeded Growth of AlN Bulk Crystals . 827
24.4 Seeded Growth of AlN Bulk Crystals 829
24.4.1 Growth on SiC Seeds 829
24.4.2 Growth on AlN Seeds 831
24.5 Characterization of High-Quality Bulk Crystals 832
24.5.1 Structural Properties 832
24.5.2 Fundamental Optical Properties of AlN 835
24.5.3 Impurities 838
24.6 Conclusions and Outlook 839
References 839

Wide-bandgap nitride semiconductors, AlN, GaN, and InN, have been identified as promising materials for a broad range of applications in electronics and optoelectronics [24.1]. Currently, epitaxial heterostructures involving these semiconductors are being grown by various techniques on a number of substrates [24.2–6]. The two most commonly used substrates, sapphire and SiC, are not closely lattice-matched to the III-nitride overlayers, leading to a high defect density in overgrown active layers, which limits device performance and lifetime. Additional limitations of the currently available substrates include cracking of the device layers due to the large thermal mismatch, and poor thermal conductivity. Thus, the performance of III-nitride semiconductor devices would be greatly improved by the availability of native substrates. High-quality, single-crystalline AlN substrates with low dislocation densities are expected to decrease defect density in the overgrown device structures by several orders of magnitude and, thereby, greatly improve the performance and lifetime of III-nitride devices. AlN has a number of excellent properties that make it a highly desirable candidate as a substrate for III-nitride epitaxy. Its crystalline structure is the same as that of GaN, with a lattice mismatch in the *c*-plane of approximately 2.5%. Since AlN makes a continuous range of solid solutions with GaN, it plays an important role in GaN-based devices and is highly suited as a substrate for AlGaN devices with high Al concentrations or structures with graded layers. Its high thermal conductivity

makes it desirable for high-temperature electronic and high-power microwave devices where heat dissipation is critical. The direct, large optical bandgap of 6.1 eV [24.7] makes it suitable for ultraviolet applications down to wavelengths as short as 200 nm. This chapter reviews recent growth and characterization results of AlN bulk crystals grown by physical vapor transport (PVT).

24.1 PVT Crystal Growth

The vast majority of commercially grown semiconductor bulk crystals are grown from the melt using one of several methods, such as the Czochralski, Bridgman, and vertical gradient freeze methods. However, bulk crystal growth by physical vapor transport is an alternative when melt growth is not possible, such as when the melting point is too high, the material decomposes before it melts or the melt reacts with the crucible. Because of the high melting temperature and large dissociation pressure at the melting point of the III-nitrides [24.8], bulk crystal growth from the melt is precluded unless very high pressure is applied. Although the first AlN was synthesized in 1862 by *Briegleb* and *Geuther* [24.9] by the reaction between molten aluminum and nitrogen, it took more than a century before any sizeable single crystals of AlN were grown [24.10]. Past efforts to grow AlN bulk crystals have explored sublimation of AlN, vaporization of Al, and solution routes, with sublimation yielding the most voluminous AlN crystals to date. Crystal growth by other methods, such as hydride vapor-phase epitaxy [24.11], ammonothermal growth [24.12], or solution growth [24.13, 14], has been reported, but only crystals of either inferior quality or size have been produced thus far. In recent years, several research groups [24.15–18] independently developed processes and models for growth of AlN crystals which all converge to the same basic growth principle and process parameter space. All these efforts clearly demonstrate that AlN bulk crystals of very high quality and of sizes appropriate for use as III-nitride substrates can be produced by PVT.

In a typical PVT process an AlN powder source is sublimed within a closed or semi-open crucible, and the vapors are subsequently transported in nitrogen (N_2) atmosphere through a temperature gradient to a region held at a lower temperature than the source, where they recrystallize. The region where recrystallization takes place can consist of the crucible walls, in which case we speak of self-seeded growth, or it may consist of an intentionally selected seed crystal, in which case we have seeded growth. AlN growth can be achieved at temperatures as low as 1800 °C; however, temperatures in excess of 2200 °C are required to achieve commercially viable growth rates. This high growth temperature, in combination with the highly reactive Al vapor, creates a challenge for the identification of appropriate crucible materials and has been a major obstacle in growth of high-purity, large-size AlN crystals.

Early kinetic theory formulation for the sublimation growth of AlN indicated that the useful growth temperature range was 2000–2400 °C, yielding growth rates ranging from 0.3 to 15 mm/h [24.19]. A two-dimensional model of mass transport in the gas phase was analyzed by *Liu* and *Edgar* [24.20], who determined that the activation energy for AlN growth was 681 kJ/mol, which is close to the heat of sublimation of AlN, 630 kJ/mol. To better describe growth at pressures below 100 Torr, a refined model [24.21] included the influence of surface kinetics (N_2 sticking coefficient), which is not a limiting factor at higher pressures. *Karpov* et al. [24.22] and *Segal* et al. [24.23] identified two mechanisms of vapor transport in AlN sublimation: at high pressure (760 Torr), vapor transport was controlled by diffusion in the gas phase, while at low pressure (10^{-4} Torr), it was dominated by drift of the reactive species, Al and N_2. Growth at low pressure required 350–400 °C lower temperature to achieve the same growth rate.

A one-dimensional model was developed for the high-temperature growth by *Noveski* et al. [24.24]. Gas-phase mass transfer of Al species was assumed to limit the overall growth rate. Thus an equation describing the temperature (T) and pressure (p) dependence of the growth rate (v_G) was derived by considering the transport of Al species through the N_2 gas,

$$v_G = k \frac{\exp\left(\Delta S - \frac{\Delta H}{T}\right)}{RT^{1.2} p^{1.5}} \frac{\Delta T}{\delta} , \qquad (24.1)$$

where the pre-exponential term k contains the diffusion coefficient of Al; ΔS and ΔH are the entropy and enthalpy of sublimation, respectively; R is the universal gas constant; and $\Delta T/\delta$ is the temperature gradient in the crucible. An apparent activation energy of

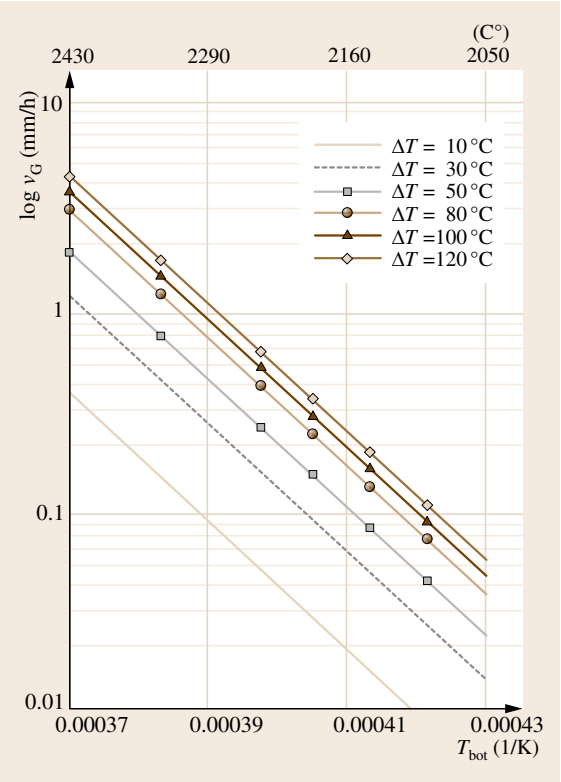


Fig. 24.1 Predicted growth rate as a function of temperature at the bottom of the crucible (T_{bot}) for different temperature differences (ΔT) along the crucible, 600 Torr pressure, and 10 mm source-to-seed distance (after [24.24], with permission)

638.1 kJ/mol was predicted. The theoretical model was experimentally validated by selecting growth parameters for which the model predicted a growth rate of 1 mm/h (Fig. 24.1). Sustained growth rates on the order of 1 mm/h were demonstrated, clearly showing that the growth rate is Al transport limited at total N_2 pressures in the range of 400–800 Torr.

The dependence of growth rate on temperature and pressure was also studied by *Epelbaum* et al. [24.25], who found that PVT transport of AlN was possible starting at 1850 °C, but temperatures exceeding 2100 °C were necessary to obtain stable growth of well-faceted crystals. The vapor pressure of Al as a function of temperature was calculated for different total system pressures (Fig. 24.2) and used to determine the corresponding AlN growth rates, under the assumption that reaction of adsorbed Al and N_2 species to form AlN is the rate-limiting growth step. According

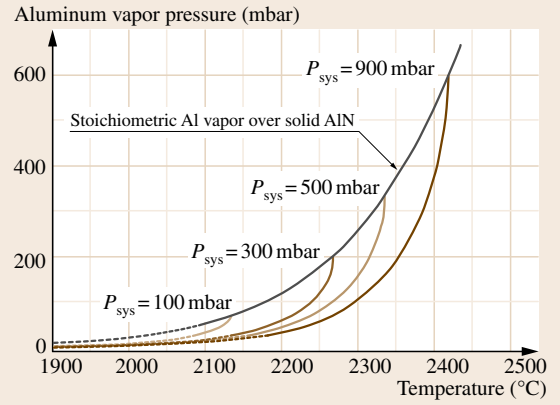


Fig. 24.2 Dependence of aluminum vapor pressure on temperature and system pressure (after [24.25], with permission of Trans Tech)

to the calculations, growth temperatures in excess of 2100 °C are required to obtain growth rates in excess of 1 mm/h for typical PVT process conditions (e.g., total pressure, thermal gradient). Experimentally observed growth rates in the range of 0.3–3 mm/h were achieved during growth of polycrystalline AlN boules up to 51 mm in diameter and 15 mm in length [24.25].

Two-dimensional simulations [24.26] demonstrated that at a given temperature both the powder source and the seed sublime below a critical pressure when the sum of the Al and N_2 partial pressures at the seed and source are greater than the ambient pressure. Under growth conditions below this critical pressure, the simulations showed that the gas phase is transported out of the growth cell and the sublimation growth fails. The simulations were used to explain the experimentally observed effect of growth temperature (T_g), source-to-seed temperature difference (ΔT), and ambient N_2 pressure on the growth rate [24.27]: For high ΔT, the source sublimation and crystal growth rates increased exponentially with temperature; as ΔT decreased, the sublimation rate continued to exhibit an exponential dependence with temperature, but the growth rate became a decreasing function of temperature, dropping sharply at temperatures greater than 2130 °C; finally, as the ambient nitrogen pressure was decreased, the growth rate initially increased, but then sharply dropped at a critical pressure. This critical pressure was found to increase from ≈ 50 Torr at 2100 °C to ≈ 120 Torr at 2200 °C. The simulation results are presented in Fig. 24.3, where the N_2 molar fraction distributions and the velocity vector fields in the crucible are shown for two differ-

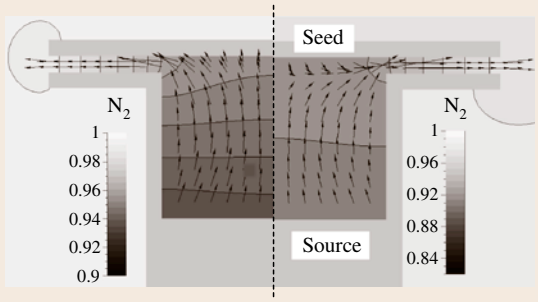


Fig. 24.3 Nitrogen molar fraction distributions and velocity vector fields in the crucible under different thermal conditions: (*left*) $\Delta T \approx 35\,\mathrm{K}$, $T_g \approx 2150\,^\circ\mathrm{C}$; (*right*) $\Delta T \approx 10\,\mathrm{K}$, $T_g \approx 2215\,^\circ\mathrm{C}$ (after [24.27], with permission of Trans Tech)

ent growth regimes. In the first regime, T_g is 2150 °C and ΔT is about 35 °C. The Al/N_2 gas mixture evaporated from the source is divided into two flows, one of which deposits on the growing crystal, while the other is transported out of the crucible. In the second regime, T_g is higher, 2215 °C, and ΔT is lower, about 10 °C. Now, the gas flows evaporated from the source and seed are both transported out of the crucible, and the growth fails. When AlN crystal growth experiments were performed using the optimized conditions determined from the simulations, a distinct dependence of the growth morphology on system pressure was observed. Crystals grown at close to atmospheric N_2 pressure had a hexagonal facet shape, with a nominally *c*-plane growth surface. At much lower pressures, the presence of many competing growth centers resulted in a rough, porous surface with a rounded shape. Under optimal growth conditions, growth proceeded from a single growth center and the surface exhibited distinct macroscopic steps, suggesting a layer growth mechanism.

The role of oxygen in the sublimation growth was also analyzed [24.28]. Closed-box thermodynamics calculations indicated that at elevated temperature Al_2O and AlO are the only major Al–O gaseous compounds, and that at temperatures less than ≈ 2350 °C the only condensed phase, solid AlN, is thermodynamically stable. Model calculations were performed for growth conditions where the growth rate is determined by the transport of Al-containing species from the source to the seed. After solving for the fluxes and partial pressures of all reactive species as a function of the source temperature (T_s), ΔT, total pressure (p_{tot}), and oxygen atomic fraction in the vapor averaged over the gas volume (X_O), the AlN growth rate was determined by the total aluminum flux from five Al-containing gaseous species: Al, Al_2, AlN, Al_2O, and AlO. The AlN growth rate as a function of temperature computed for pure and oxygen-contaminated N_2 atmospheres is shown in Fig. 24.4 for various oxygen atomic fractions and total

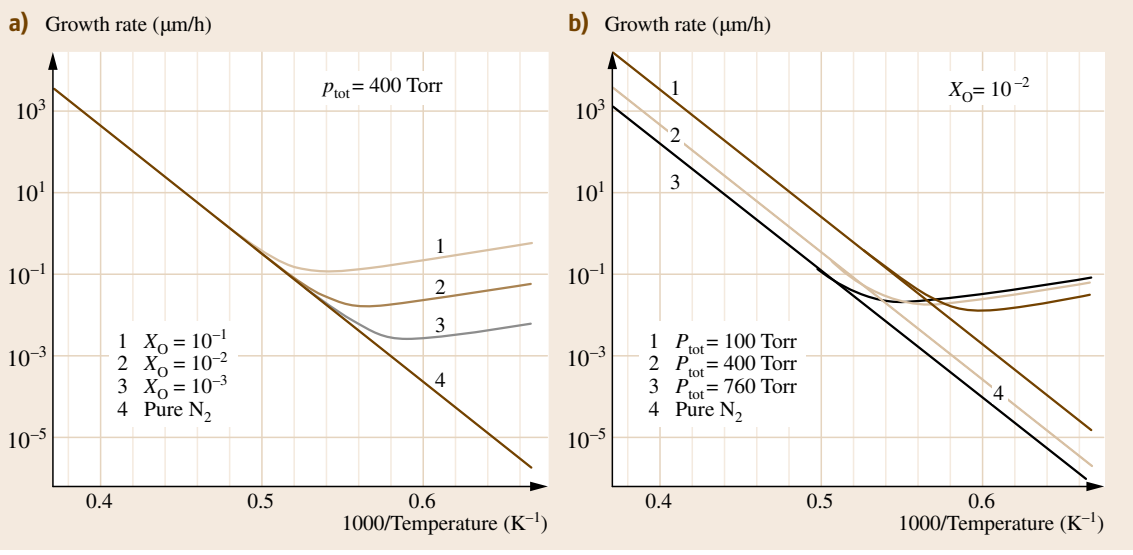


Fig. 24.4a,b The temperature variation of AlN growth rate computed for pure and oxygen-contaminated N_2 atmospheres, $\Delta T = 30\,\mathrm{K}$, and various X_O **(a)** or P_{tot} **(b)** (after [24.28], with permission of Wiley-VCH)

pressures. It is seen that the effect of oxygen on the growth rate is appreciable only for low growth temperatures and becomes negligible in the temperature range $1850\,°C < T < 2350\,°C$ typical for sublimation growth. In addition, the critical oxygen fraction in the vapor corresponding to Al_2O_3 inclusion generation on the AlN surface was determined [24.28]. It was found that, for typical growth temperatures, sufficient purification of AlN source powder is required to produce less than a 10^{-3} oxygen fraction in the vapor in order to avoid inclusion formation. High growth temperatures are also favorable for obtaining crystals free of inclusions.

The above analyses tend to assume, especially at high temperature, that the only gas-phase species of any significance are Al and N_2. First-principles gas-phase composition calculations have indicated that Al_nN $(n = 2, 3, 4)$ species, though present in much smaller mole fractions than Al and N_2, are supersaturated with respect to the AlN crystal (Fig. 24.5) and may contribute to the growth [24.29]. Additional analysis of the model was used to show how these trace precursors contribute to mass transport and the growth rate [24.30]. The model predicts the existence of a small mass transport barrier whose height is dependent primarily on the amount of Al_3N in the vapor, and is sensitive to changes in the source temperature and total pressure. Results were used to predict the effective range of ΔT as a function of T_s and p_{tot}, yielding good agreement with published experimental data. However, little is known about the kinetics of these trace species. Their existence and the effect they have on AlN bulk crystal growth have yet to be determined experimentally.

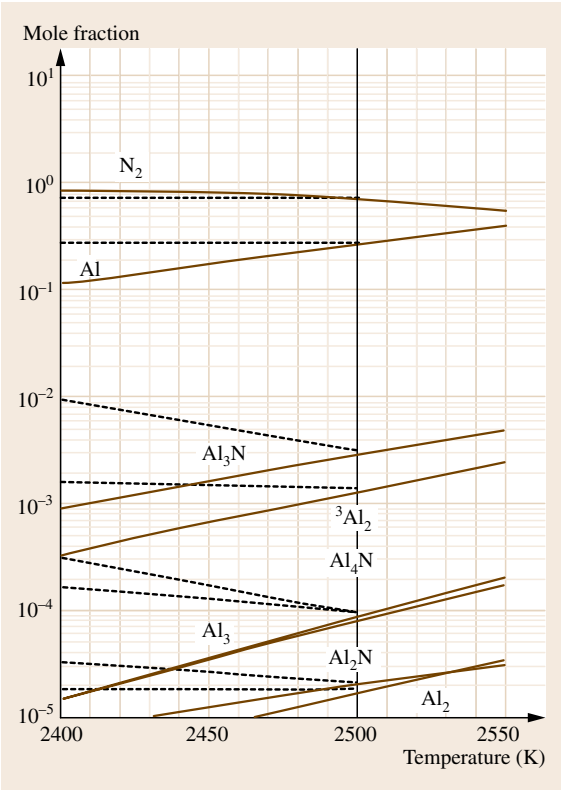


Fig. 24.5 Calculated equilibrium mole fractions of precursors for AlN sublimation growth at a nitrogen pressure of 400 Torr: boundary layer of an Al surface (*solid lines*); and boundary layer of the bulk gas (*dashed lines*) sublimed at $T = 2500\,K$ (*vertical line*) (after [24.29], with permission of APS)

24.2 High-Temperature Materials Compatibility

By necessity, commercially viable growth rates are achieved at very high process temperatures (typically $> 2200\,°C$), making furnace design and materials selection critical to the success of the overall process, both for achieving durability of growth hardware and keeping crystal impurity levels low. In particular, crucible materials must be refractory and compatible with elevated growth temperatures, inert to chemically aggressive Al vapor, a negligible source of contamination to the growth process, reusable for multiple growth runs, relatively inexpensive, and manufacturable in various shapes and dimensions [24.31].

In his early work, *Slack* [24.10] demonstrated successful growth using W crucibles; however, crucible lifetime was limited and ≈ 50 ppm of W incorporation was reported. Some efforts have employed graphite or coated (SiC, NbC, TaC) graphite crucibles. Several independent studies show that pure graphite crucibles should be avoided due to incompatibility with Al, high levels of carbon in crystals, and the detrimental influence of carbon on growth morphology. Coated graphite crucibles reduce these shortcomings for low-temperature growth; however, these coatings deteriorate quickly above $2000\,°C$, regardless of their thickness or deposition process, and thus do not offer a long-term stable growth environment.

There are several reports of crystal growth in boron nitride (BN) crucibles [24.16, 32, 33]. Sizeable transpar-

ent crystals with very low dislocation densities were grown; however, it seems that a BN growth environment produces highly anisotropic growth rates at high temperatures, where the growth rate in the *a*-direction is almost completely inhibited. As a result, coalescence and crystal-size expansion are difficult to achieve.

Compatibility of reactor materials at the high temperatures needed for crystal growth was addressed by *Epelbaum* et al. [24.35]. Crystals were grown from AlN powder with approximately 1% aluminum oxide impurity in a resistively heated reactor at temperatures of 1800–2200 °C using W or graphite heating elements. Different combinations of crucible materials and heating elements yielded results similar to those reported previously [24.36]. Crucibles made of graphite were readily attacked by the Al vapor, while graphite crucibles coated with SiC were unstable at temperatures above 1950 °C, leading to the formation of mixed AlN–SiC crystals varying in color from dark blue to light green. Problems were also associated with the combination of W crucible and heating element, namely degradation of W by aluminum vapor or by oxygen from impurities in the source. The most flexible reactor design was deemed to be a combination of W crucible and graphite heating element.

More recently, efforts with sintered tantalum nitride and tantalum carbide crucibles confirmed that these materials are more stable than any of the aforementioned crucible materials, with crucible lifetimes exceeding 500 h at growth temperatures exceeding 2200 °C [24.31, 37]. Well-faceted crystals with isotropic growth and very low dislocation densities were obtained. These materials have melting points around 3100 °C and 3900 °C, respectively, and thermodynamic calculations [24.34, 38] of the partial pressure of Ta over the solid carbide or nitride have indicated that these materials possess excellent high-temperature stability. Figure 24.6 shows the calculated partial pressures present over several solid crucible materials at 2300 °C in one atmosphere of N_2.

Several groups are developing proprietary processes for fabrication of suitable growth crucibles. Optimization of the sintering process parameters yielded better than 96% dense TaC shapes, which were successfully employed in PVT growth of 38 mm diameter AlN boules [24.31]. Elemental analysis demonstrated that Ta incorporation was below the detection limit (sub-ppm level). However, since TaC appears to possess a larger thermal expansion than AlN, TaC crucibles may exert a compressive stress upon AlN boules during cool-down, leading to the formation of stress-related defects. Thus, use of these crucibles requires that wall contact between the AlN boule and the crucible be avoided. In other work, chemically passivated TaC crucible surfaces were formed by carburization of Ta metal shapes [24.39, 40]. *Mokhov* et al. [24.39] carburized Ta crucibles with 1–2 mm thick walls at 2200–2500 °C in a carbon-containing atmosphere. Carburized crucibles were stable in an atmosphere of Al vapor and N_2 gas at 2300 °C for up to 500 h, after which surface cracks appeared, making them permeable to the vapor. *Hartmann*

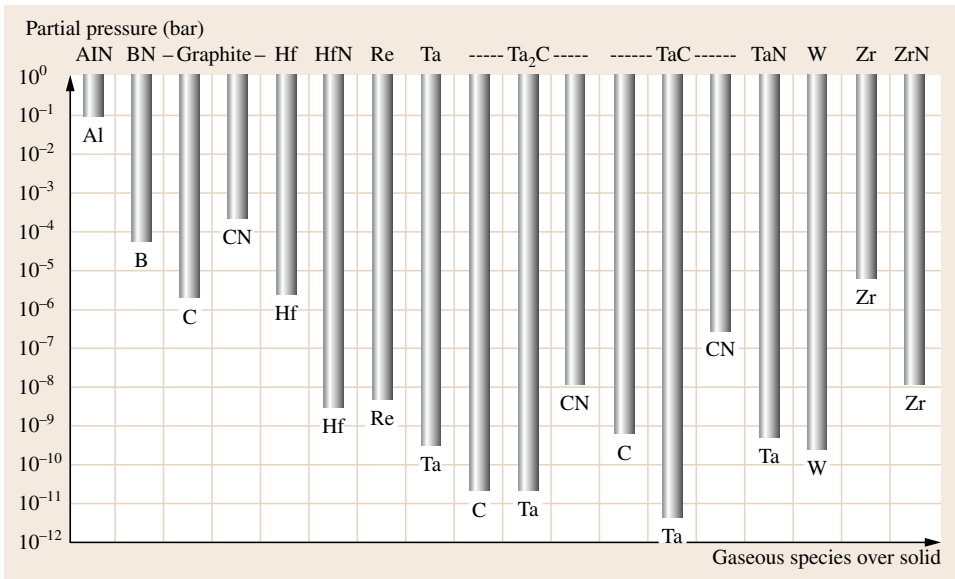


Fig. 24.6 Possible crucible contaminants: partial pressures present over solid crucible materials at 2300 °C in 1 atm nitrogen (after [24.34], with permission)

et al. [24.40] studied the reaction kinetics of Ta carburization, showing that the diffusion-controlled phase transformation follows the sequence $Ta \rightarrow Ta_2C \rightarrow TaC_{1-x}$. Incomplete carburization led to a mechanically stable layered structure of different phases, with Ta_2C at the center and TaC at the surface. When the carburization was allowed to proceed completely to TaC, grain coarsening and anisotropic lattice expansion of the polycrystalline material led to cracking along grain boundaries, rendering fully carburized crucibles unsuitable for PVT growth. Further evaluation of other inert, high-temperature materials may prove fruitful.

24.3 Self-Seeded Growth of AlN Bulk Crystals

Edgar et al. [24.17] reported on AlN crystal growth by sublimation in resistively heated furnaces with W or graphite heating elements. AlN needles and platelets freely nucleated from AlN source material in the cold zone of BN crucibles. Source temperatures were varied from 2000 to 2200 °C and reactor nitrogen pressures ranged from 300 to 800 Torr. Crystals grown in a furnace with W heating elements were either colorless or amber in color, while those grown in a furnace with a graphite heater were colorless. Observed morphologies included needles up to 4 mm in length and 0.5 mm in diameter, and thin plates. The plates were as large as 60 mm^2 and contained growth striations running the length of the crystals along the *c*-direction. These striations appear to be characteristic of crystals grown in BN environments. They are not seen in AlN grown in other types of crucibles [24.17, 33].

AlN boules up to 10 mm in diameter were produced at Crystal IS [24.41] in conical crucibles. No seed crystals were used in the growth process and, typically, several nuclei formed on the crucible walls during the early stages of growth. As the crystal grew, growth competition between different nuclei resulted in single-crystal regions of varying sizes and orientations. A driving rate for growth was set by translation of the crucible relative to the thermal gradient in the reactor. Under adequate growth conditions (e.g., thermal gradient, reactor pressure) the crystal growth rate was equal to the driving rate, which was varied between 0.65 and 0.9 mm/h. Atomic force microscopy (AFM) imaging of the as-grown crystals revealed 0.25 nm high monolayer steps with straight segments. Step flow resulted from screw dislocations intersecting the growing surface. Screw dislocation density was estimated at $5 \times 10^4\ cm^{-2}$.

Wafering of these boules revealed several large grains and polycrystalline regions, or single-crystalline regions exhibiting severe cracking around the periphery [24.15, 42, 43]. Chemomechanical polishing (CMP) was used to obtain surfaces suitable for epitaxial growth. Final etching of vicinal surfaces in a mixture of phosphoric and sulfuric acids or potassium hydroxide solution revealed that the N-terminated face was etched much faster and was rougher than the Al-terminated face.

More recently, growth of single-crystal boules up to 15 mm in diameter and several centimeters in length was reported [24.44]. These were used to prepare 0.5 mm thick wafers which were polished by CMP. Wafers exhibited some color variation, which was attributed to absorption by nitrogen vacancies, but were free of cracks. Synchrotron white-beam x-ray topography (SWBXT) was used to characterize the wafers' defect content. Contrast arising from surface damage was observed near the edges, probably due to imperfect polishing, while a high density of small inclusions was observed near the center. Typical dislocation densities were in the 800–5000 cm^{-2} range; dislocations were distributed inhomogeneously, with higher concentrations near the wafer edge. Narrow x-ray rocking curve widths attested to the high quality of the material obtained.

Schlesser et al. [24.32] and *Schlesser* and *Sitar* [24.16] reported on growth of AlN by vaporization of metallic Al in a nitrogen atmosphere and by sublimation of an AlN source [24.32, 45]. Growth temperatures ranged from 1800 °C to 2300 °C at reactor pressures of 250–750 Torr. Temperature gradients of 10–100 K/cm between the source material and crystal growth region were employed. In Al vaporization experiments, the crystal shape and fastest growth direction was found to depend strongly on the growth temperature: at relatively low temperatures (1800–1900 °C) long needles were grown, temperatures around 1900–2000 °C yielded twinned platelets, while *c*-platelets were formed at temperatures above 2100 °C. These *c*-plates grew at a rate of 5 mm/h in the *c*-plane and 0.2 mm/h along the *c*-axis. Vaporization experiments were performed for 2 h each at a constant growth temperature. Longer growth times did not yield substantially larger crystals. The observed slowdown in growth rate with time was attributed to a decreasing Al flux from the Al source over

time, which was due to the progressive formation of an Al-rich, polycrystalline AlN coating over the molten Al.

In order to overcome problems with the Al source instability in vaporization experiments, crystals were grown for longer periods of time by subliming AlN source material [24.32]. Sublimation yielded a stable Al flux over several days of growth. Experiments were carried out at higher temperatures of 2200–2300 °C in order to obtain vapor pressures of Al above AlN comparable with those above metallic Al in the vaporization experiments. Transparent AlN single crystals with dimensions as large as 13 mm were grown with growth rates exceeding 500 µm/h. These sublimation experiments were performed in BN crucibles and typically yielded fastest growth along the *c*-axis and crystals with surface striations along the *c*-direction, similar to those observed by *Edgar* et al. [24.33].

The natural growth habit of AlN bulk crystals was investigated by *Epelbaum* et al. [24.46]. Crystals were grown in the 2050–2250 °C temperature range using a low temperature gradient of 3–5 K/cm, intended to facilitate free nucleation of separate single crystals under conditions enhancing formation of natural crystal habit planes. A distinct dependence of morphology on growth temperature was observed: crystals grown at 2050 °C were nearly transparent six-sided prismatic needles, 0.1–0.3 mm in diameter and 5–15 mm in length; columnar crystals 3 mm in length and 1.5 mm in diameter characterized primarily by $\{10\bar{1}1\}$ and $\{10\bar{1}2\}$ rhombohedral facets were grown at 2150 °C; finally, thick platelets of dark amber or brownish color grew at 2250 °C. The largest of these latter crystals was approximately $14\times7\times2\,\mathrm{mm}^3$ (Fig. 24.7). Their morphology, orientation, and polarity was studied in greater detail. X-ray diffraction was used to index individual facets and their polarity was confirmed by etching in a molten KOH/NaOH eutectic at 250 °C for 3 min. The Al-polar (0001) and positive rhombohedral faces were characterized by mirror-like facets and transparent material of high crystalline quality, while the N-polar *c*-plane face contained micrometer-sized inclusions and was opaque. Since these freestanding crystals were grown under approximately isothermal conditions, they possessed a zonal structure corresponding to the simultaneous growth on multiple facets. Examination of polished cuts prepared from them revealed that the zones all belonged to the same single crystal, but exhibited different coloration, etching response, and optical properties (see the discussion in Sect. 24.5.2). Structural, optical, thermal, elemental, and electrical characterization results on single crystals and polycrystalline AlN boules were also reported [24.47–49].

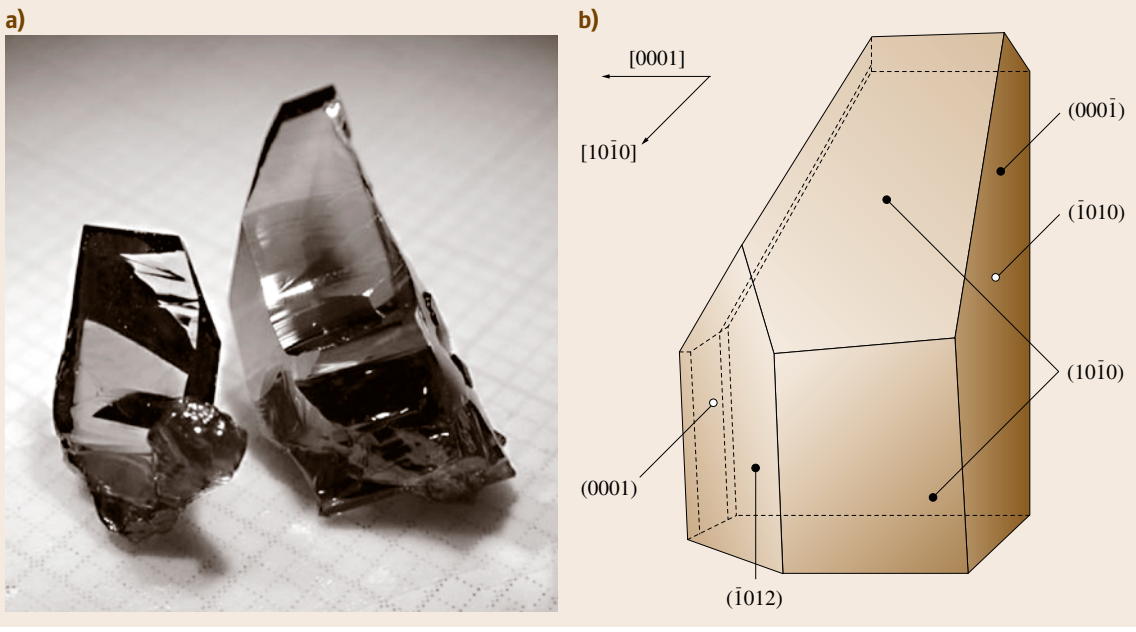


Fig. 24.7 **(a)** Selected crystals grown by spontaneous nucleation at 2250 °C showing typical growth habit (millimeter grid) and **(b)** characteristic growth faces of best formed AlN platelets (after [24.46], with permission of Elsevier)

24.4 Seeded Growth of AlN Bulk Crystals

Seeded growth of AlN on SiC has been studied as a way to exploit the availability of large, high-quality SiC substrates and to control the polarity and orientation of AlN crystals [24.50]. Due to the high process temperatures involved and the difference in thermal expansion between AlN and SiC, the stability of the SiC seeds and the cracking of the AlN layers are important issues that need to be addressed in establishing a reproducible seeded growth process on SiC. In contrast, seeded growth on recently available AlN native seeds eliminates many of the problems associated with heteroepitaxial growth, but is only beginning to be investigated. Techniques to avoid renucleation and maintain stable growth have been developed and led to considerable single-crystal size expansion [24.51, 52]. However, several questions, such as which orientation is most favorable for growth, still need to be addressed.

24.4.1 Growth on SiC Seeds

The growth of AlN crystals seeded on SiC substrates was first reported by *Balkas* et al. [24.36]. Single-crystal platelets were grown in a resistively heated graphite furnace by PVT. Growth temperature was varied from 1900 °C to 2250 °C. SiC-coated graphite crucibles were used in 10–15 h experiments. The source material was 99% dense sintered AlN, chosen to allow controllable source-to-seed separation, which was crucial for good crystal growth. Optimal separation was found to be between 1 and 5 mm. Single-crystal 6H-SiC(0001) substrates $10\times10\,\mathrm{mm}^2$ were used as seeds. Growth in a high temperature range (2100–2250 °C) and a low temperature range (1950–2050 °C) was investigated. Single crystals of ≈ 1 mm thickness that covered the entire SiC seed were grown at 2150 °C and 4 mm separation distance. The growth rate was estimated at 0.5 mm/h. Due to the degradation of the SiC substrates at higher temperatures, isolated nucleation sites were formed on the seeds at temperatures above 2150 °C, and $2\times2\,\mathrm{mm}^2$ hexagonal AlN crystals were grown. The crystals were colored from green to blue, indicating the incorporation of impurities. Secondary-ion mass spectrometry (SIMS) analysis confirmed the presence of Si and C in these crystals. Crystals grown in the low-temperature range were colorless and transparent, but growth rates were significantly lower, 30–50 μm/h. Cracking was always observed in as-grown crystals, due to the thermal expansion coefficient mismatch between SiC and AlN. X-ray diffraction (XRD) patterns confirmed the single-crystal nature of all crystals. Bright-field plan-view transmission-electron microscopy (TEM) and associated selected-area diffraction (SAD) indicated the high quality of the single crystals.

The growth of AlN crystals by sublimation on 6H-SiC seeds was more extensively investigated by *Edgar* et al. [24.17], *Shi* et al. [24.53–55], and *Liu* et al. [24.56–58]. Experiments were carried out in tungsten crucibles placed within the axial temperature gradient of a resistively heated furnace. The growth temperature was typically 1800 °C. SiC wafers (on-axis and 3.5° off-axis) with silicon and carbon terminations were used as substrates. Direct growth [24.53] on as-received Si-terminated SiC resulted in the formation of discontinuous hexagonal subgrains of $1\,\mathrm{mm}^2$ average size. No growth was observed on C-terminated as-received SiC. In order to promote two-dimensional growth on Si-terminated substrates, a 2 μm thick AlN buffer layer was deposited by metalorganic chemical vapor deposition (MOCVD). Continuous growth was achieved by the use of the buffer layer, although cracks formed during cool-down due to stress resulting from the thermal expansion coefficient mismatch. AFM images indicated that AlN grew by the step-flow growth mode.

The initial stages of AlN growth on SiC were studied by *Liu* et al. [24.58]. Fifteen minute growth runs were performed on as-received, on-axis, Si-terminated 6H-SiC(0001) substrates under various temperature and pressure conditions. During the initial stages of growth, AlN nucleated as individual hexagonal hillocks and platelets in an island-like growth mode. Nuclei size and density increased at constant pressure with increased growth temperature in the range of 1800–1900 °C. At constant temperature, growth under reduced pressures yielded coalesced, irregularly shaped platelet crystals. Scanning Auger microprobe (SAM) measurements indicated varying relative compositions of Al, N, Si, and C on different crystal facets of the AlN nuclei. The surface morphology and stress in AlN crystals grown on SiC substrates were also characterized [24.56,57]. AFM images revealed scratches and steps on as-received 6H-SiC substrates, which served as nucleation sites for individual AlN grains grown in a three-dimensional mode. On SiC substrates with an AlN MOCVD epilayer, however, AlN deposited in a two-dimensional growth mode without island formation. Surface mor-

phology varied across the sample, from flat surfaces to regions with large steps (120 nm) separated by large terraces (up to 5 μm). Root-mean-square (RMS) roughness for samples grown with an AlN epilayer was less than 5 nm, compared with 40 nm for crystals grown on as-received substrates. Stress-induced cracks were always observed in the AlN crystals. It was predicted [24.59] that AlN grown on 6H-SiC should be at least 2 mm thick in order to avoid cracking during cool-down from a growth temperature of 2000 °C. Raman spectroscopy revealed that crystals were under compressive stress at the surface and tensile stress (1 GPa) at the interface. Raman spectra indicated improved crystal quality with increasing AlN thickness.

The above method was modified in order to reduce cracking of AlN [24.54, 55]. After deposition of the MOCVD AlN epilayer, an $AlN_{0.8}SiC_{0.2}$ alloy layer was deposited by sublimation from a source mixture of AlN–SiC powders. Pure AlN was then sublimed on the alloy seed as above. The intermediate properties of the alloy layer helped reduce cracking in the overgrown AlN. In addition, the SiC powder source decreased the degradation of the SiC substrates during sublimation growth, allowing for longer growth times. Single-crystal AlN, $4 \times 6 \times 0.5\,mm^3$, was obtained after 100 h of growth. Characterization by XRD and Raman spectroscopy confirmed the high quality of the grown material. Thus, three problems identified with growth of AlN on SiC seeds were addressed by this method: (1) the presence of Si and C in the vapor helped suppress the decomposition at high temperature of the SiC seed, (2) an AlN epilayer promoted two-dimensional growth, and (3) cracking of the AlN bulk layer was greatly reduced by an AlN–SiC alloy interlayer.

Dalmau et al. [24.50, 61] developed a two-step process for deposition of thick AlN layers on SiC, and for reduction of cracks in the grown layers. AlN layers up to 3 mm thick were grown on on-axis and off-axis, (0001)-oriented, Si-face SiC seeds by PVT from an AlN powder source. During the growth, the SiC seeds were gradually decomposed at high temperature, yielding freestanding AlN crystals up to 25 mm in diameter. In other samples, the AlN was delaminated from the SiC seeds. As-grown surfaces of layers grown on on-axis SiC seeds were characterized by sharp hexagonal hillocks, suggesting a dislocation-mediated island growth mode, while layers grown on off-axis seeds exhibited steps aligned perpendicular to the off-axis direction, characteristic of the step-flow growth. Crack-free AlN crystals were obtained from these layers and used to fabricate AlN wafers, as shown in Fig. 24.8. High-resolution rocking curves and reciprocal space maps of the (0002) reflection showed that the full-width at half-maximum intensity (FWHM) ranged from 282 to 1440 arcsec, indicating a tilt distribution in the grown layers caused by strain and/or the formation of low-angle grain boundaries as the AlN coalesced [24.60,62]; nevertheless, these values were comparable to or better than those of the SiC seeds used in these experiments. SWBXT indicated that some strain-free crystals

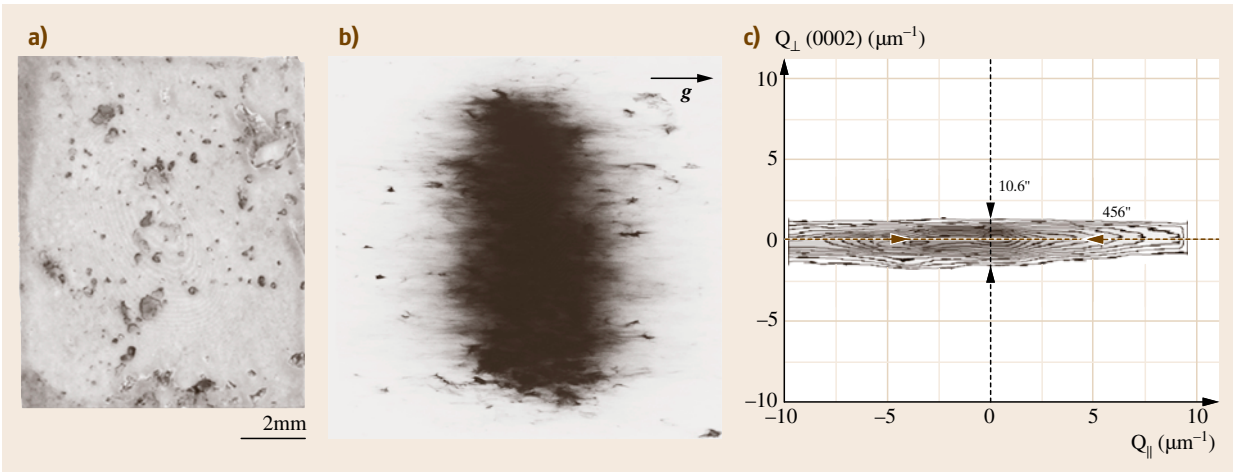


Fig. 24.8 **(a)** Bulk AlN crystal grown by gradually decomposing the SiC substrate; **(b)** transmission topograph ($g = [20\bar{2}1]$) showing inhomogeneous strain and high dislocation density; **(c)** reciprocal space map showing very low triple-axis ω–2Θ scan width (10.6 arcsec) (after [24.60], with permission of Trans Tech)

were obtained, but in all samples the density of dislocations was significantly higher ($> 10^6\,cm^{-2}$) than in self-seeded AlN crystals. Elemental characterization showed impurity concentrations comparable to those found in the AlN source powder (300 ppmw C and 200 ppmw Si), indicating negligible incorporation of C and Si during growth; the low triple axis ω–2θ scan widths typically observed ($\approx$ 11 arcsec) were characteristic of high-purity crystals and consistent with these results.

In other efforts, *Sarney* et al. [24.63] grew bulk AlN on on-axis and 3.5° off-axis, *c*-oriented 6H-SiC seeds. Sublimation from an AlN powder source in N_2 atmosphere was performed in the temperature range 2150–2200 °C with 4 mm separation between the source and seed. The AlN grew well aligned with the substrate. As in previous work [24.36], cracks were observed in the AlN. *Epelbaum* et al. [24.64] studied AlN crystal growth on SiC substrates of different orientations. Layers of 200–500 μm thickness were deposited at seed temperatures around 2000 °C in 350 mbar N_2 pressure. Growth on Si-face, *c*-oriented substrates was characterized by many hexagonal hillocks on the surface. In contrast, 10° off-axis and on-axis, *a*-plane substrates resulted in more stable growth. The smoothest morphology, typical of step-flow growth, was obtained with on-axis, *a*-plane substrates, however, cracks were also observed in the AlN layers. *Epelbaum* et al. [24.65] and *Heimann* et al. [24.66] suggested a possible vapor–liquid–solid mechanism, mediated by the presence of a molten $AlOC_x$ layer on the surface of SiC, during seeded growth on SiC. Finally, successful seeded growth on C-face SiC was reported recently [24.67,68].

24.4.2 Growth on AlN Seeds

Reports on AlN growth on native seeds are limited, as these seeds have only recently become available. Seeded growth of AlN on native seeds by PVT was reported for the first time by *Schlesser* et al. [24.45]. Transparent, single-crystal *c*-platelets prepared by vaporization of Al in N_2 were used as seeds. They were mounted into the top of a BN growth crucible filled with AlN source material. Growth was carried out at 2200 °C with a temperature gradient between the source and seed of approximately 3 K/mm. A small seed, 4 mm tall and 0.5 mm thick, grew over a total of 34 h into a 5 mm tall and 7 mm wide single crystal. Growth rates were highly anisotropic, with the fastest growth direction along the *c*-axis. Also, growth rates on the two *c*-faces of opposite polarity differed by a factor of 2–3, with the Al polarity showing slower and smoother growth. Crystal quality of the grown crystals was characterized by XRD. X-ray rocking curves around the (0002) reflection varied from 25 to 45 arcsec, indicating very high single-crystal quality of the material grown by seeded growth.

Noveski et al. [24.51,69] demonstrated a process for continuous growth of AlN on previously deposited material, resulting in significant expansion of single-crystal grains. Growth was performed in a radiofrequency (RF)-heated reactor at temperatures between 2050 and 2150 °C and pressures of 450–500 Torr, yielding growth rates in the range of 0.1 to 0.3 mm/h. In this process, a starting layer of coalesced polycrystalline AlN was grown into boules up to 38 mm in length and 32 mm in diameter over the course of

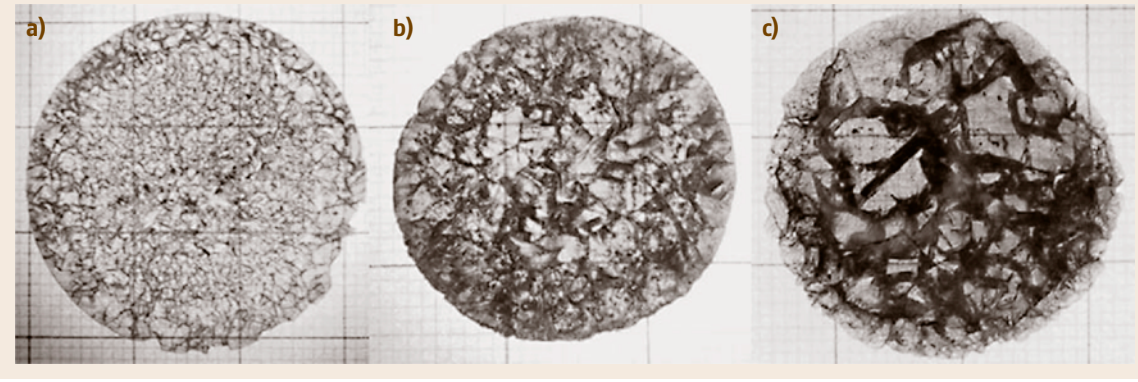


Fig. 24.9a–c Grain evolution observed in different cross-sections of a boule with a diameter of 32 mm: 0.5 mm thick slice, cut after the first 1 mm of growth **(a)**; 1 mm thick slice cut at 22 mm boule length **(b)**; 2 mm thick slice cut at 35 mm boule length, showing centimeter-size grains **(c)** (after [24.51])

several growth runs. Sublimation growth from a presintered AlN source was interrupted several times in order to replenish the source and keep the source-to-seed distance constant. Renucleation of AlN on the previous growth front after exposure of the boules to air was suppressed by using the inverted temperature gradient method. During the early stages of each run, the crystal growth region was maintained in an inverted temperature gradient, effectively desorbing surface contamination and part of the previously grown layer. In this manner, continuous expansion of previously formed single-crystalline grains was achieved (Fig. 24.9). Centimeter-sized, single-crystal grains were observed in polished cross-sections of boules, and epitaxial regrowth was demonstrated regardless of the orientation of individual grains.

In order to overcome problems associated with the formation of cracks in these polycrystalline boules, large single-crystal grains were harvested and used to prepare seeds for subsequent seeded growth [24.52, 70]. To ensure epitaxial regrowth, seeds were etched in a phosphoric and sulfuric acid mixture, followed by dilute hydrofluoric acid, prior to loading into the system, and were maintained in an inverted temperature gradient during the ramp to the growth temperature. Crystal growth was performed in an axial temperature gradient of 5–10 °C/cm, maintaining the source temperature at 2200–2250 °C and reactor pressure at 400–900 Torr. A $(41\bar{5}0)$-oriented seed was expanded from 10 to 18 mm after several consecutive growth runs, representing a 45° crystal expansion angle (Fig. 24.10).

In related work, *Herro* et al. [24.71, 72] investigated seeded growth along the ⟨0001⟩ polar directions. {0001}-Oriented AlN single crystals were successfully grown along both polar directions, but more stable growth results were obtained on N-polar seeds. The growth surface of N-polar crystals was controlled by a single growth center, leading to a mirror-like growth facet. In contrast, the surfaces of crystals grown on Al-polar seeds showed numerous growth centers, leading to a deterioration of crystal quality, even though the same growth parameters were used for both types of seeds. These observations suggest that lower supersaturation is required to obtain stable growth in the Al-polar direction.

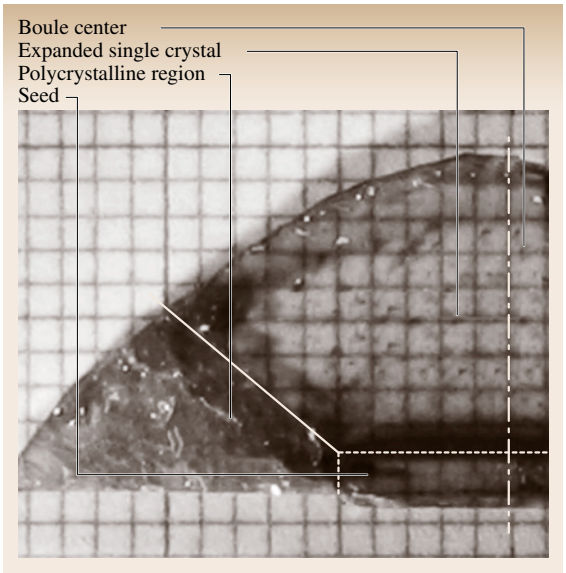


Fig. 24.10 Longitudinal cut of a crystal boule after several growth runs showing the crystal expansion angle (millimeter grid) (after [24.70])

24.5 Characterization of High-Quality Bulk Crystals

As the size of AlN single crystals continues to increase, several characterization techniques are being used to assess the structural and optical properties of large bulk crystals, as well as to determine impurity incorporation, so that the concentration of extended defects and adverse growth contaminants may be minimized by adjusting the growth conditions. Availability of large, strain-free, high-quality bulk crystals has allowed investigators to study the fundamental properties of this material in more detail than has previously been possible with AlN ceramics or thin films. Recent experimental findings have been used to confirm theoretical predictions about the band structure of AlN, leading to revised values for the fundamental bandgap.

24.5.1 Structural Properties

The equilibrium crystal structure (α-phase) of the III-nitrides, AlN, GaN, and InN, is the wurtzite (2H) structure. The stacking sequence of the (0001) close-packed wurtzite planes is ABAB. . ., comprising bilayer sheets of nitrogen and III-metal atoms; this structure

consists of two interpenetrating sublattices that contain the nitrogen and III-metal atoms in tetrahedral coordination. The space group of the wurtzite nitrides is $P6_3mc$, the same as that of the hexagonal (4H and 6H) polytypes of SiC.

X-ray diffraction topography is used to study a crystal's internal diffracting planes in order to discern local changes in the spacing and relative rotation of the planes [24.74]. X-ray topographs, two-dimensional projections of the distribution of diffracted intensity as a function of position in the sample, can be used to map defect structures in large, nearly perfect single crystals and to identify the crystallographic orientations of the diffracting planes. Images are produced by scattering a low-divergence area-filling beam from a set of Bragg planes onto a two-dimensional detector, typically high-resolution x-ray film. In addition, high-resolution x-ray diffraction (HRXRD) is also commonly employed to provide information about the orientation and perfection of single crystals. This technique can be used to generate a reciprocal space map (RSM) representing the two-dimensional intensity contour of the diffracted intensity about a given lattice reflection. These maps provide much more information than typical x-ray rocking curves, since the distribution of lattice tilts (i. e., orientations) and lattice dilations (i. e., d-spacings) can be read independently from the RSM. The lattice dilation distribution is correlated with the concentration of point defects (e.g., vacancies or impurities) in the sampled crystal volume.

SWBXT studies of self-seeded crystals grown by sublimation of AlN powder revealed crystals to be virtually dislocation free [24.37, 60, 73, 75]. Overall dislocation densities were estimated to be around $10^3\,\mathrm{cm}^{-2}$. Defects such as inclusions, growth sector boundaries, and growth dislocations were detected. The presence of Pendellösung fringes in the topographs (Fig. 24.11) was indicative of the high crystalline perfection attained in several samples. Triple-axis x-ray rocking curve FWHM of ω–2θ scans of several large crystals ($\approx 10\,\mathrm{mm}$) were as low as 7.2 arcsec, marginally larger than the theoretical limit of 6 arcsec, indicating a low density of point defects in these samples.

Characterization results reported for bulk single crystals grown at Crystal IS demonstrated that crystals were of high quality. X-ray topographs of an unevenly shaped polished wafer [24.76], approximately $7\times9\,\mathrm{mm}^2$ in size, indicated no significant strain in the wafer and showed an overall dislocation density of $800–1000\,\mathrm{cm}^{-2}$. The density of detected inclusions (presumably oxygen related) was on the order of $10^5\,\mathrm{cm}^{-3}$. FWHM of high-resolution rocking curves ranged from 9 to 12 arcsec, indicating very good crystalline quality. The edge of the wafer in contact with the crucible wall contained cracks and slip bands, probably due to the thermal expansion mismatch between

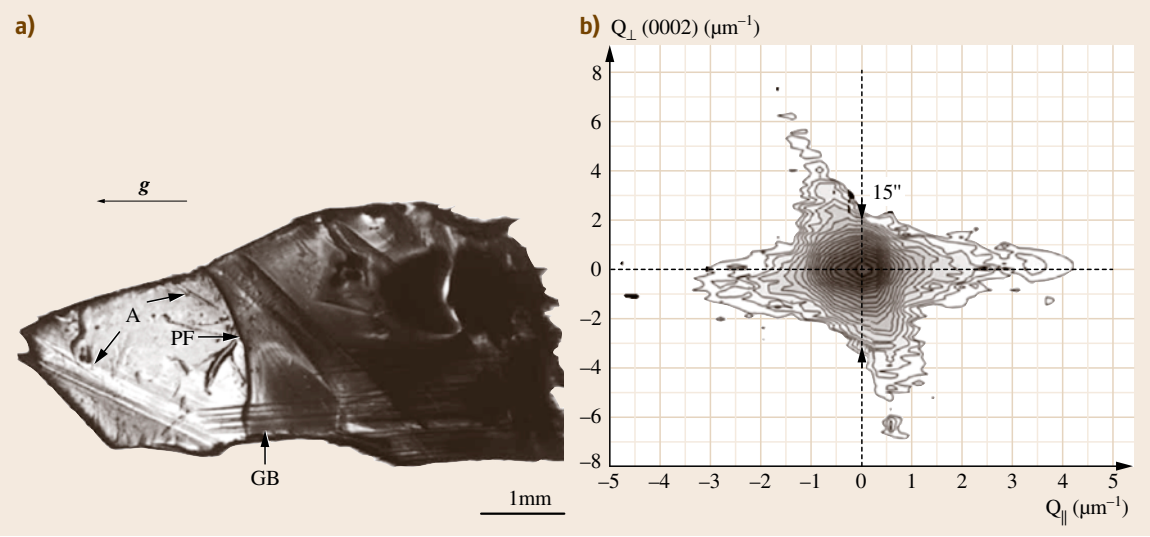


Fig. 24.11 **(a)** Transmission x-ray topograph ($\boldsymbol{g} = [\bar{1}\bar{1}20]$, $\lambda = 0.54$ Å) from a dislocation-free, spontaneously nucleated AlN single crystal (A – surface artifacts, GB – growth bands, PF – pendellösung fringes); **(b)** (0002) reciprocal space map (triple-axis ω–2Θ scan width: 15 arcsec) (after [24.73], with permission)

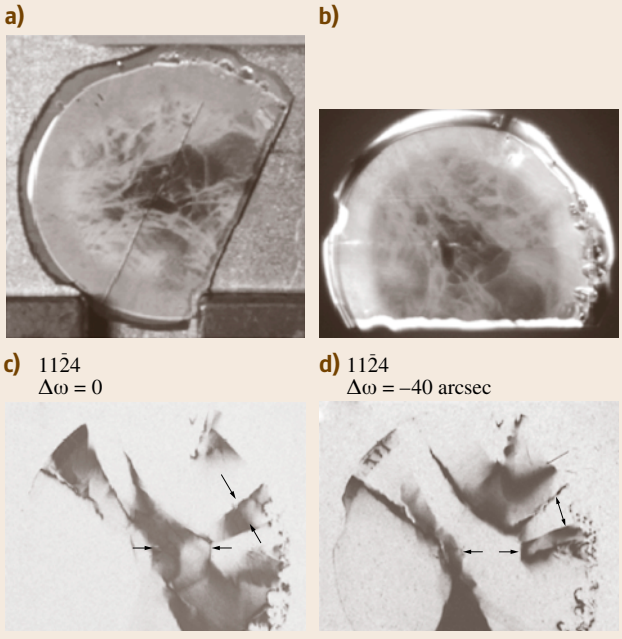


Fig. 24.12 **(a)** Optical image of an AlN substrate. The length of the flat is 22 mm. **(b)** The same substrate taken through crossed polarizers. **(c,d)** Two x-ray topography images of the same substrate taken at an angular distance of 40 arcsec. Small-angle grain boundaries are shown (*black arrows*). $\Delta\omega = 0$ refers to the maximum of the rocking curve. The picture at the right shows the intensity observed at 40 arcsec from the maximum of the rocking curve. Now the areas adjacent to the original black arrows show stronger diffraction intensity. The misalignment between these areas is small, on the order of 40 arcsec (after [24.77], with permission of Wiley-VCH)

the boule and crucible. Figure 24.12 shows a picture of a polished AlN substrate with a flat width of 22 mm, an image of the same substrate taken through crossed polarizers, and x-ray topography images taken at two different rocking angles [24.77]. X-ray topographs revealed the presence of small-angle grain boundaries throughout the wafer and individual dislocations at the wafer edge. No diffraction was observed from inclusions that were optically visible. The nature of these inclusions was not discussed.

Defects in polished AlN wafers were studied by XRD, optical microscopy, etch pit pattern delineation, and AFM [24.78]. A triple-axis rocking curve with a FWHM of 10 arcsec was reported. Figure 24.13 shows an optical image of an AlN surface where chemical etching was used to reveal dislocations (viewed as single dots) and slip bands (viewed as straight lines). These

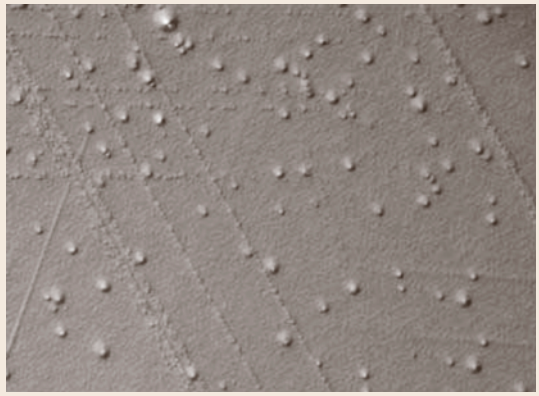


Fig. 24.13 Nomarski image of prismatic slip bands as seen on on-axis oriented AlN after chemical etching (after [24.78], with permission)

slip bands were oriented parallel to the $\langle 1\bar{1}00\rangle$ directions, demonstrating the activation of prismatic glide in AlN single crystals. The density and shape of etch pits in chemically etched AlN were also studied. Etch pit densities for *c*-plane wafers varied from 1×10^3 to $3\times10^4\,\mathrm{cm}^{-2}$, while etch pit patterns were used to distinguish between screw and edge dislocations. In addition, it was shown how subgrain boundaries may propagate as cracks into another grain. Also, etch pits on $\{1\bar{1}00\}$ prismatic planes were reported for the first time; the etch pit density was higher than on basal planes, averaging from 6×10^4 to $4\times10^5\,\mathrm{cm}^{-2}$. AFM images of Al-polar, *c*-plane, epiready substrate surfaces prepared by CMP revealed atomic-level steps for near-on-axis substrates and for off-axis orientations up to 6° off-axis [24.79]. RMS roughness of $5\times5\,\mu\mathrm{m}^2$ scans was as low as 2.15 Å. The presence of shallow pits, whose density decreased with increasing off-axis orientation, was observed on these Al-polar *c*-plane samples. However, the origin of the pits is still not well understood, but may be related to the polishing process. These pits were not observed in AFM scans of substrates with nonpolar orientations.

AFM studies [24.72] of Al- and N-polar *c*-plane AlN surfaces, obtained by seeded growth on AlN seeds, showed a significant difference in the step-and-terrace structures observed on the two different polar surfaces (Fig. 24.14). Single-unit-cell-high steps were observed on both surfaces, but the terrace width on N-polar AlN, 200–250 nm, was much larger than that observed on Al-polar AlN, 50–70 nm. Since seeded growth was

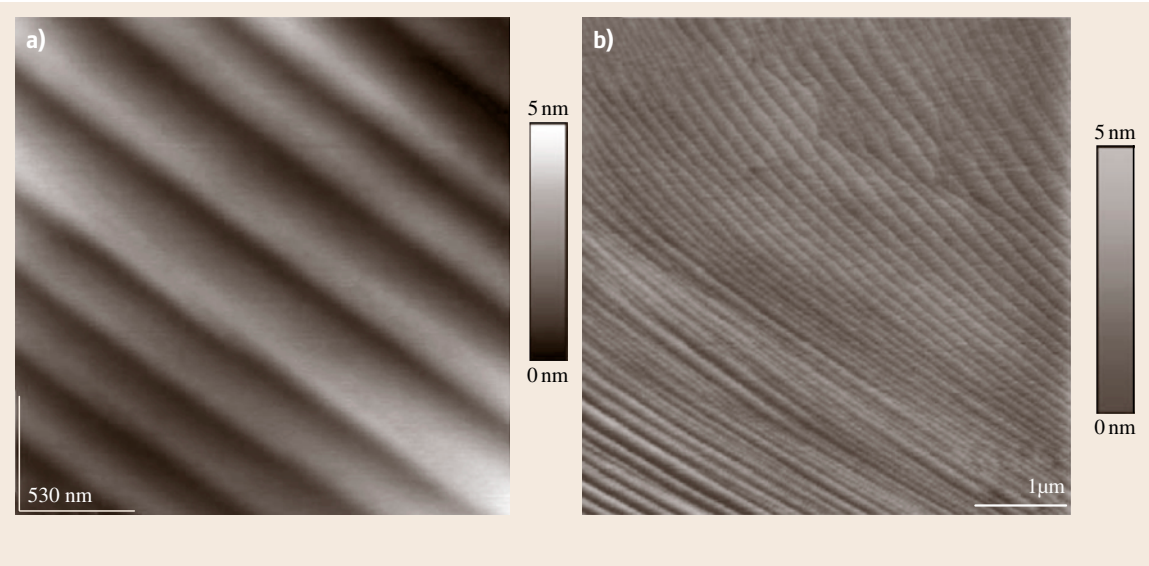


Fig. 24.14a,b AFM micrographs taken on as-grown AlN surfaces: **(a)** N-polar orientation; **(b)** Al-polar orientation. In both cases, single-unit-cell-high steps were observed (after [24.72], with permission)

performed on seeds of both polarities using the same growth conditions, thus ensuring equal supersaturations of Al vapor, these differences were attributed to the surface energy difference of the N- and Al-polar facets.

24.5.2 Fundamental Optical Properties of AlN

AlN has a direct bandgap at the center (Γ-point) of the Brillouin zone exceeding 6 eV. In general, there are still many details concerning the band structure and optical properties of AlN that require further investigation. For example, the band structure parameters near the Γ-point and the fundamental optical transitions were until very recently not well known. In the past, measurements of the bandgap have been performed by optical absorption [24.80–82] and ellipsometry [24.83]. Variations in the measured values were likely due to differences in crystal quality (e.g., impurity and defect concentrations). The room-temperature value commonly quoted in the literature was 6.2 eV. Band-edge luminescence has been investigated using cathodoluminescence (CL) [24.84] and photoluminescence (PL) [24.85].

Recently, though, measurements on high-quality bulk crystals have provided a more complete picture of the band structure. The conduction band has a single minimum (Γ_{7c}) at the Γ-point. The valence band, on the other hand, is split at the Γ-point by the crystal field and the spin–orbit interaction. According to calculations [24.86], the spin–orbit splitting ranges from 11 to 20 meV. The crystal field splitting at the top of the valence band in AlN was predicted [24.87, 88] to be negative, in contrast to the other III-nitrides, but calculated values have ranged widely. However, this information gives a qualitative picture of the valence-band ordering at the Γ-point, and of the associated intrinsic free-exciton transitions. In order of increasing transition energies, these are Γ_{7v} (upper, A-exciton), Γ_{9v} (B-exciton), and Γ_{7v} (lower, C-exciton). The square of the dipole transition matrix elements between the conduction band and the three Γ-point valence states calculated by *Li* et al. [24.89] indicated that the A-exciton transition is nearly forbidden for light polarized perpendicular ($\perp$) to the wurtzite c-axis, while the B- and C-exciton transitions are nearly forbidden for light polarized parallel ($||$) to the c-axis. This picture has recently been confirmed by *Li* et al. [24.89] and optical reflectivity measurements [24.7,90] (Figs. 24.15 and 24.16) which have provided experimental values for the exciton resonances, the crystal field splitting parameter, and the fundamental bandgap of AlN. The fundamental bandgap energy of unstrained AlN was determined by *Chen* et al. [24.7] to be 6.096 eV at 1.7 K, while the crystal field splitting parameter was −230 meV and

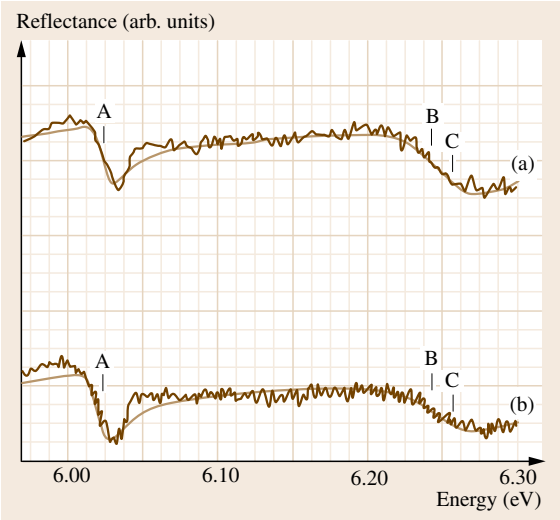


Fig. 24.15 Low-temperature partially polarized optical reflectance spectra from the *m*-face of a bulk AlN crystal with the *c*-axis parallel to the spectrometer slits (*graph* a) and the *c*-axis perpendicular to the slits (*graph* b). *Solid lines* are theoretical fits to the spectra. The bottom of the graph is a (different) finite signal level in each case, to show the features more clearly (after [24.7], with permission of AIP)

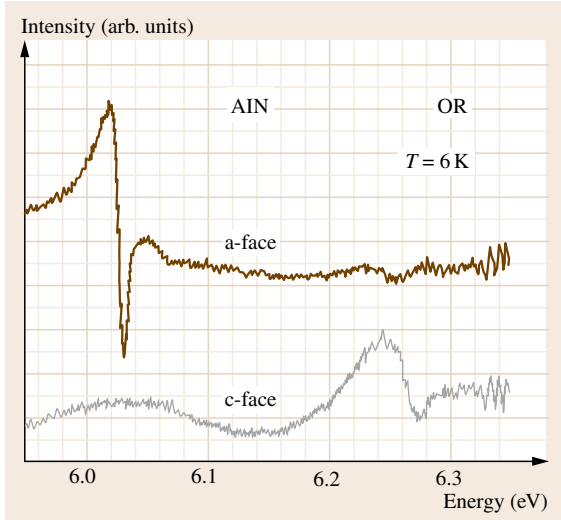


Fig. 24.16 Low-temperature optical reflectivity data at near-normal incidence for AlN samples oriented in two different crystallographic orientations (after [24.90], with permission of APS)

the exciton energies were 6.025, 6.243, and 6.257 eV for the A-, B-, and C-excitons, respectively. Note that the A transition is allowed for light polarized parallel to the *c*-axis. This may explain why earlier absorption measurements consistently resulted in larger values for the bandgap; these measurements were typically performed with light polarized perpendicular to the *c*-axis, and likely probed the B- or C-transitions. These results imply that (0001)-oriented devices grown with AlN or high-Al-content AlGaN alloys will be better edge emitters than surface emitters, and other orientations should be investigated for surface-emitting devices [24.7].

In other studies, the crystalline quality and orientation of a sample oriented with the *c*-axis in the plane of the crystal were evaluated by testing the selection rules for the A_1(TO), E_1(TO), and E_2(high) Raman modes [24.91, 92]. In the $x(zz)x$ geometry, the allowed A_1(TO) and E_1(TO) modes were observed and the forbidden E_2(high) mode was not, while in the $x(zy)x$ geometry, the A_1(TO) mode was suppressed and the E_1(TO) mode was enhanced, confirming the crystal's orientation and high crystalline quality. The superposition of different Raman modes and the presence of quasi-LO modes was observed in the spectra of a randomly oriented sample.

The dependence of phonon spectra on crystal orientation was also observed by *Bickermann* et al. [24.93]. Raman spectra of optical phonons in AlN were taken in backscattering geometry on different well-developed facets of a self-seeded bulk crystal (such as that shown in Fig. 24.7). The results indicated that facets belonging to the same crystal class showed very similar Raman spectra, while the appearance or absence of the A_1(LO), A_1(TO), E_1(LO), and E_1(TO) phonon bands in the spectra could be used to identify the basal *c*-plane facets unambiguously from the prismatic $\{10\bar{1}0\}$ facets (Fig. 24.17). *c*-Plane facets showed, in addition to the E_2 modes, only the A_1(LO) and E_1(TO) bands, while prismatic facets showed the A_1(TO) and both E_1(LO) and E_1(TO) bands. When facets with crystallographic orientations between the basal and prismatic planes were studied, i. e., rhombohedral facets, features corresponding to quasi-LO and quasi-TO phonons with mixed A_1–E_1 symmetry appeared in the spectra.

The zonal dependence of the optical absorption and CL spectra of self-seeded crystals was also investigated [24.94]. Crystals exhibiting natural crystal habits of AlN with well-developed facets [24.46] were selected, cut in different orientations, and polished on both sides. The resulting samples included a number of different zones, which corresponded to volumes of the

crystal grown on a different facet. Thus, differences in impurity incorporation and/or defect formation, as reflected in the optical spectra, were correlated to growth on different facets or polar orientations of AlN. In the near-ultraviolet (near-UV) and visible range, Al-polar zones had the lowest absorption, followed by zones grown in the *r*- and *a*-directions, and finally by N-polar zones. These differences corresponded to differences in crystal coloration, with N-polar zones exhibiting the deepest amber coloration, which is primarily caused by a broad absorption band at 2.8 eV whose origin is still unclear but has in the past been assigned to nitrogen vacancies. In the mid-UV range, the peak position and intensity of the broad absorption bands observed varied depending on the zone. Zones grown on the Al-polar *c*-face exhibited a strong band at 4.6 eV, which was nearly absent in all other samples. Finally, in the 5.0–5.8 eV range, an increase in absorption was observed for zones grown in the *c*-direction regardless of polarity, while zones grown in *r*- or *a*-directions exhibited a local minimum; absorption in this range was attributed to nitrogen vacancies. The CL spectra of bulk crystals and polished cuts also showed intensity variations that were dependent on the investigated area. As shown in Fig. 24.18, *r*- and *a*-plane facets exhibited intense luminescence peaking at 3.8 eV, while this feature was absent on the Al-polar *c*-plane facet, where broad, weak bands at 2.5–2.8, 3.3, and 4.3 eV were present.

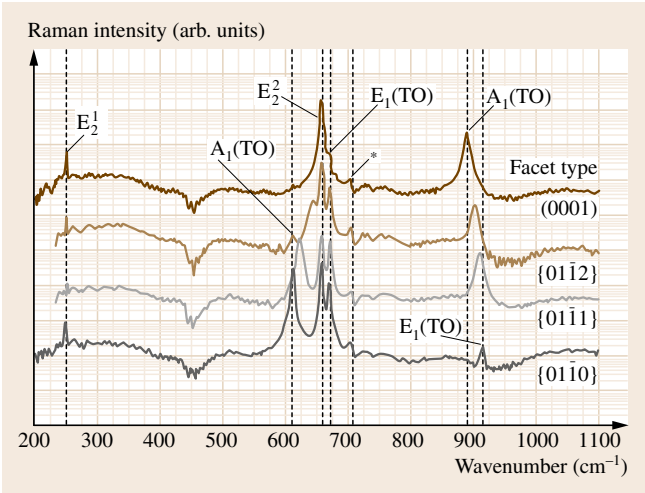


Fig. 24.17 Raman spectra taken in normal incidence on different facets of an AlN single crystal. A logarithmic intensity scale is used to show weak features. The *symbols* denote AlN phonon bands (after [24.93], with permission of AIP)

Optical transitions with energies in the 3–5 eV range are likely due to Al vacancies and their complexes with oxygen.

In other work, *Silveira* et al. [24.84, 95, 96] used CL to study self-seeded AlN crystals and homoepitaxial thin films of AlN grown on these crystals. Both

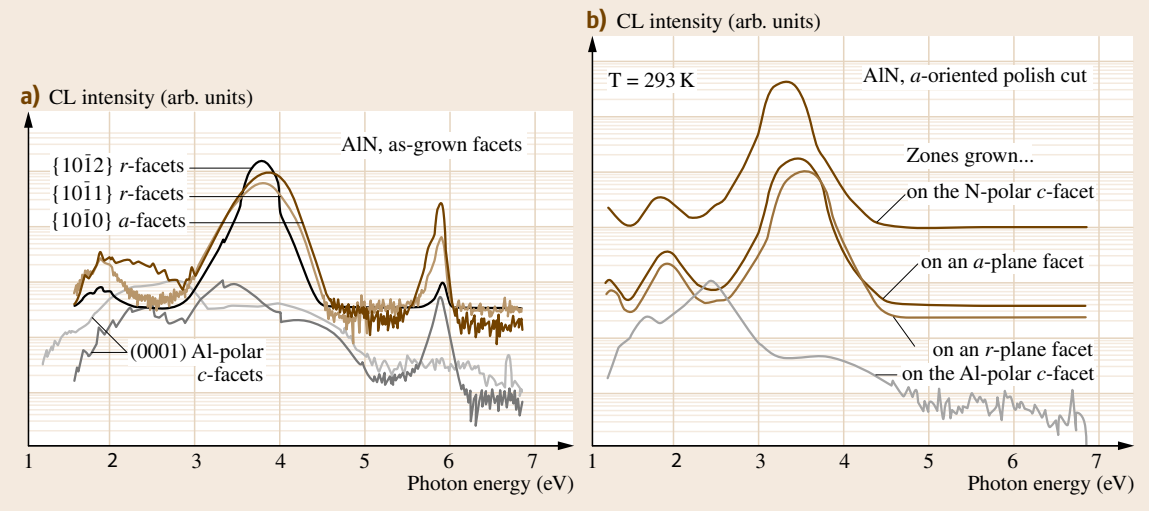


Fig. 24.18a,b Cathodoluminescence spectra of bulk AlN single crystals taken at room temperature. Logarithmic scale is used to show weak features; small jumps in the spectra (*left*) are measurement artifacts. **(a)** Spectra taken on different facet surfaces of an as-grown boule. **(b)** Spectra taken on different zones of an *a*-oriented polished cut (after [24.94], with permission of Wiley-VCH)

c-plane and *a*-plane wafers were cut from bulk crystals and polished by CMP. Strong emission was observed at the near-band-edge (NBE) region around 6 eV, and two additional bands were observed in the energy range between 2 and 5.5 eV. One of these bands (VB), at about 3.5 eV, was attributed to oxygen-related defects, while the second band (UVB), at about 4.4 eV, was tentatively assigned to oxygen-related complexes. The integrated intensity of the NBE emission showed a linear dependence with beam current up to 5 μA, and this band was therefore related to exciton recombination processes. Analysis of the NBE CL spectrum of an *a*-plane sample revealed five transitions in this energy range. Based on the temperature dependence of the NBE spectra, features at 6.026 and 6.041 eV (6 K) were attributed to the free-exciton A- and B-transitions [24.96]. Similar assignments, based on thermal quenching studies, were made for features observed at 6.023 and 6.036 eV in the NBE spectra of a nominally *c*-plane AlN homoepitaxial film [24.84]. However, recent reflectivity measurements [24.90,91] demonstrate that these assignments are likely incorrect.

24.5.3 Impurities

Growth of high-purity AlN is a challenging task. As a result of the high affinity of Al for oxygen (the standard Gibbs free energy of formation of Al_2O_3 at 298.15 K is highly negative, -1.582×10^6 J/mol [24.97]), oxygen is a common contaminant in AlN, and influences, among other things, the lattice parameters, thermal conductivity, luminescence, and defect structure of AlN. Early material property measurements on oxygen-contaminated AlN have been revised as higher-purity single-crystal material has become available. In addition, since commercially available AlN powder contains approximately 1% oxygen impurities, obtaining a high-purity AlN source powder is of interest to the crystal growth community. Calculations by *Karpov* et al. [24.28] have shown that AlN source purification is favorable for obtaining bulk crystals free of Al_2O_3 inclusions. Carbon is also a common contaminant in AlN, while metallic and other impurities are typically found at trace levels. Knowledge of the influence these different contaminants have on the growth process and fundamental properties of AlN is still limited, but recent investigations have provided some valuable data.

Dalmau et al. [24.36] reported that sintering of a commercially purchased AlN source powder at a temperature of 2200 °C resulted in a significant reduction of nearly all impurities, with the largest reductions observed for oxygen and carbon impurities (Table 24.1). Several investigators have incorporated source presin-

Table 24.1 Published GDMS analysis results for AlN (all values in ppmw; *T*: sintering/growth temperature, pressure: system pressure, NA: not available)

Sample	*T* (°C)	Pressure (Torr)	Crucible material	O	C	Si	W	Reference
1. As-received powder	NA	NA	NA	≈ 1000	≈ 3000	200	< 50	[24.37]
2. Sintered powder	2200	400	TaN	≤ 300	≤ 200	200	< 20	[24.37]
3. Self-seeded single crystal	1950/2070*	500/400*	BN	≤ 500	≤ 300	5.5	< 1	[24.91]
4. Self-seeded single crystal	1885/2030*	600/600*	TaN	≤ 1200	≤ 160	130	< 0.05	[24.91]
5. Self-seeded polycrystal	2100	500	TaC	≤ 50	≤ 50	40	< 1	[24.91]
6. Self-seeded polycrystal	2100	500	TaC	≤ 400	≤ 30	40	< 1	[24.91]
7. Self-seeded polycrystal	2250	< 750	W	≈ 86	≈ 100	2.5	7.9	[24.18]
8. Seeded single crystal	2200	400–900	NA	< 100	< 100	80	< 10	[24.52]

* Samples 3 and 4 were grown using a two-stage growth process; temperatures were gradually ramped between the two stages

tering as part of the PVT growth process [24.46, 70, 72]. *Epelbaum* et al. [24.60] identified how low-temperature transport of Al as suboxides during the ramp to growth temperature can lead to poisoning of the AlN seed surface during seeded growth on native seeds. Even when the AlN source is relatively pure (< 300 ppmw O), evaporation of a thin oxide layer on the source may occur at temperatures as low as 1750 °C, leading to an accumulation of aluminum oxynitrides on the seed surface, which make the surface unsuitable for growth. However, the inverted temperature gradient method developed by *Noveski* et al. [24.51, 69] and used by others [24.52, 70–72] during seeded growth on native seeds represents a practical solution to the problem. This surface poisoning does not appear to be a problem during seeded growth on SiC seeds, possibly due to the different growth mechanism involved [24.64, 65].

Bulk AlN with low oxygen content was reported by *Bickermann* et al. [24.18, 98]. Polycrystals were grown in a vertical, cold-wall reactor equipped with W heating elements. Growth was performed in N_2 atmosphere, at pressures below 1000 mbar, using almost sealed crucibles. Source and crystal growth temperatures ranged from 2200 to 2350 °C, and from 2100 to 2250 °C, respectively. Dense, polycrystalline AlN boules up to 15 mm high and 51 mm in diameter were produced with growth rates between 0.2 and 2 mm/h. Boules were composed of *c*-textured crystalline grains, some as large as $5 \times 5\,mm^2$. Although the AlN source material contained significant amounts of various impurities (6000 ppmw oxygen, 300 ppmw carbon, and 500 ppmw metals), as determined by glow discharge mass spectrometry (GDMS), impurity incorporation into grown material was significantly lower (86 ppmw oxygen, 100 ppmw carbon, ≈ 22 ppmw metals). GDMS is a mass-spectrometric technique for the analysis of trace elements in bulk solid samples. It offers several advantages over other trace analysis techniques, including detection limits down to the sub-ppb range, wide dynamic range ($\approx 10^{11}$ range between minor and major components), relative matrix insensitivity, and applicability to a wide variety of materials systems. Table 24.1 shows the results of GDMS analysis on different AlN samples reported in the literature.

A number of researchers have used compositional analysis of AlN crystals together with measurements of optical properties (Sect. 24.5.2) in order to identify impurities that correlate with specific optical transitions. *Slack* et al. [24.99] reported an oxygen-related absorption region between 3.5 and 5.2 eV, with peak positions varying from 4.3 to 4.8 eV depending on the amount of oxygen impurity. These features are likely due to transitions involving Al vacancy–oxygen complexes. The influence of different impurities on the absorption and luminescence spectra of AlN has also been studied by other investigators [24.31, 91, 92, 98]. However, more work is needed before features observed in the absorption and luminescence spectra of high-quality bulk crystals can be unambiguously assigned to specific defect transitions.

24.6 Conclusions and Outlook

AlN crystal growth is a challenging task that has been attempted in the past via a variety of growth methods. Although several issues remain, PVT growth of AlN at high temperatures shows the most promising results and is the only growth technique that can produce high-quality low-dislocation-density crystals. This method has yielded AlN crystals of very high quality and of sufficient size for fabrication of the first devices. The recent demonstration of seeded growth with subsequent crystal-size expansion is certainly a crucial milestone for future development of this technology that will lead to further expansion of single-crystal size. Lifetime and stability of growth crucibles and reactor parts remain a challenge that will need to be addressed in the quest for high-purity crystals and lower production cost. Further research is also needed to improve the understanding of the detrimental effects of various impurities in AlN, so that technologically relevant properties of AlN may be fully exploited by reducing the concentration of adverse growth contaminants.

References

24.1 R. Dalmau, Z. Sitar: Sublimation growth of AlN crystals. In: *Encyclopedia of Materials: Science and Technology*, ed. by K.H.J. Buschow, R.W. Cahn, M.C. Flemings, B. Ilschner, E.J. Kramer, S. Mahajan, P. Veyssière (Elsevier, Oxford 2005) pp. 1–9

24.2 O. Ambacher: Growth and applications of group III-nitrides, J. Phys. D **31**, 2653–26710 (1998)

24.3 R. Gaska, C. Chen, J. Yang, E. Kuokstis, A. Khan, G. Tamulaitis, I. Yilmaz, M.S. Shur, J.C. Rojo, L.J. Schowalter: Deep-ultraviolet emission of AlGaN/AlN quantum wells on bulk AlN, Appl. Phys. Lett. **81**, 4658–4660 (2002)

24.4 L. Liu, J.H. Edgar: Substrates for gallium nitride epitaxy, Mater. Sci. Eng. R **37**, 61–127 (2002)

24.5 B. Monemar: III-V nitrides – important future electronic materials, J. Mater. Sci. **10**, 227–254 (1999)

24.6 L.J. Schowalter, Y. Shusterman, R. Wang, I. Bhat, G. Arunmodhi, G.A. Slack: Epitaxial growth of AlN and $Al_{0.5}Ga_{0.5}N$ layers on aluminum nitride substrates, Appl. Phys. Lett. **76**, 985–987 (2000)

24.7 L. Chen, B.J. Skromme, R.F. Dalmau, R. Schlesser, Z. Sitar, C. Chen, W. Sun, J. Yang, M.A. Khan, M.L. Nakarmi, J.Y. Lin, H.-X. Jiang: Band-edge exciton states in AlN single crystals and epitaxial layers, Appl. Phys. Lett. **85**, 4334–4336 (2004)

24.8 I. Grzegory, J. Jun, M. Boćkowski, S. Krukowski, M. Wróbłewski, B. Lucznik, S. Porowski: III-V-nitrides – Thermodynamics and crystal growth at high N_2 pressure, J. Phys. Chem. Solids **56**, 639–647 (1995)

24.9 F. Briegleb, A. Geuther: Ueber das Stickstoff-magnesium und die Affinitäten des Stickgases zu Metallen, Ann. Chem. **123**, 228–241 (1862)

24.10 G. A. Slack: Aluminum nitride crystal growth, Final Report, Contract No. F49620-78-C-0021 (1980) 1–31

24.11 A. Nikolaev, I. Nikitina, A. Zubrilov, M. Mynbaeva, Y. Melnik, V. Dmitriev: AlN wafers fabricated by hydride vapor phase epitaxy, MRS Internet J. Nitride Semicond. Res. **5S1**, W6.5.1–W6.5.5 (2000)

24.12 R. Dwiliński, R. Doradziński, J. Garczyński, L. Sierzputowski, M. Palczewska, A. Wysmolek, M. Kamińska: AMMONO method of BN, AlN and GaN synthesis and crystal growth, MRS Internet J. Nitride Semicond. Res. **3**, 25.1–25.4 (1998)

24.13 C.O. Dugger: Synthesis of AlN single crystals, Mater. Res. Bull. **9**, 331–336 (1974)

24.14 M. Bockowski: Growth and doping of GaN and AlN single crystals under high nitrogen pressure, Cryst. Res. Technol. **36**, 771–787 (2001)

24.15 J.C. Rojo, G.A. Slack, K. Morgan, B. Raghothamachar, M. Dudley, L.J. Schowalter: Report on the growth of bulk aluminum nitride and subsequent substrate preparation, J. Cryst. Growth **231**, 317–321 (2001)

24.16 R. Schlesser, Z. Sitar: Growth of bulk AlN crystals by vaporization of aluminum in a nitrogen atmosphere, J. Cryst. Growth **234**, 349–353 (2002)

24.17 J.H. Edgar, L. Liu, B. Liu, D. Zhuang, J. Chaudhuri, M. Kuball, S. Rajasingam: Bulk AlN crystal growth: self-seeding and seeding on 6H-SiC substrates, J. Cryst. Growth **246**, 187–193 (2002)

24.18 M. Bickermann, B.M. Epelbaum, A. Winnacker: PVT growth of bulk AlN crystals with low oxygen contamination, Phys. Status Solidi (c) **0**, 1993–1996 (2003)

24.19 P.M. Dryburgh: The estimation of maximum growth rate for aluminum nitride crystals grown by direct sublimation, J. Cryst. Growth **125**, 65–68 (1992)

24.20 L. Liu, J.H. Edgar: Transport effects in the sublimation growth of aluminum nitride, J. Cryst. Growth **220**, 243–253 (2000)

24.21 L. Liu, J.H. Edgar: A global growth rate model for aluminum nitride sublimation, J. Electrochem. Soc. **149**, G12–G15 (2002)

24.22 S.Y. Karpov, D.V. Zimina, Y.N. Makarov, E.N. Mokhov, A.D. Roenkov, M.G. Ramm, Y.A. Vodakov: Sublimation growth of AlN in vacuum and in a gas atmosphere, Phys. Status Solidi (a) **176**, 435–438 (1999)

24.23 A.S. Segal, S.Y. Karpov, Y.N. Makarov, E.N. Mokhov, A.D. Roenkov, M.G. Ramm, Y.A. Vodakov: On mechanisms of sublimation growth of AlN bulk crystals, J. Cryst. Growth **211**, 68–72 (2000)

24.24 V. Noveski, R. Schlesser, S. Mahajan, S. Beaudoin, Z. Sitar: Mass transfer in AlN crystal growth at high temperatures, J. Cryst. Growth **264**, 369–378 (2004)

24.25 B.M. Epelbaum, M. Bickermann, A. Winnacker: Sublimation growth of bulk AlN crystals: Process temperature and growth rate, Mater. Sci. Forum **457-460**, 1537–1540 (2004)

24.26 S.Y. Karpov, A.V. Kulik, M.S. Ramm, E.N. Mokhov, A.D. Roenkov, Y.A. Vodakov, Y.N. Makarov: AlN crystal growth by sublimation technique, Mater. Sci. Forum **353-356**, 779–782 (2001)

24.27 E. Mokhov, S. Smirnov, A. Segal, D. Bazarevskiy, Y. Makarov, M. Ramm, H. Helava: Experimental and theoretical analysis of sublimation growth of bulk AlN crystals, Mater. Sci. Forum **457-460**, 1545–1548 (2004)

24.28 S.Y. Karpov, A.V. Kulik, I.N. Przhevalskii, M.S. Ramm, Y.N. Makarov: Role of oxygen in AlN sublimation growth, Phys. Status Solidi (c) **0**, 1989–1992 (2003)

24.29 Y. Li, D.W. Brenner: First principles prediction of the gas-phase precursors for AlN sublimation growth, Phys. Rev. Lett. **92**, 75503.1–75503.4 (2004)

24.30 Y. Li, D.W. Brenner: Influence of trace precursors on mass transport and growth rate during sublimation deposition of AlN crystal, J. Appl. Phys. **100**, 84901.1–84901.6 (2006)

24.31 R. Schlesser, R. Dalmau, D. Zhuang, R. Collazo, Z. Sitar: Crucible materials for growth of aluminum nitride crystals, J. Cryst. Growth **281**, 75–80 (2005)

24.32 R. Schlesser, R. Dalmau, R. Yakimova, Z. Sitar: Growth of AlN bulk crystals from the vapor phase, Mater. Res. Soc. Symp. Proc. **693**, I.9.4.1–I.9.4.6 (2002)

24.33 B. Liu, J.H. Edgar, B. Raghothamachar, M. Dudley, J.Y. Lin, H.X. Jiang, A. Sarua, M. Kuball: Free nucleation of aluminum nitride single crystals in HPBN crucible by sublimation, Mater. Sci. Eng. B **117**, 99–104 (2005)

24.34 G.A. Slack, J. Whitlock, K. Morgan, L.J. Schowalter: Properties of crucible materials for bulk growth of AlN, Mater. Res. Soc. Symp. Proc. **798**, Y10.74.1–Y10.74.4 (2004)

24.35 B.M. Epelbaum, D. Hoffman, M. Bickermann, A. Winnacker: Sublimation growth of bulk AlN crystals: materials compatibility and crystal quality, Mater. Sci. Forum **389-393**, 1445–1448 (2002)

24.36 C.M. Balkas, Z. Sitar, T. Zheleva, L. Bergman, R. Nemanich, R.F. Davis: Sublimation growth and characterization of bulk aluminum nitride single crystals, J. Cryst. Growth **179**, 363–370 (1997)

24.37 R. Dalmau, B. Raghothamachar, M. Dudley, R. Schlesser, Z. Sitar: Crucible selection in AlN bulk crystal growth, Mater. Res. Soc. Symp. Proc. **798**, Y2.9.1–Y2.9.5 (2004)

24.38 B. Liu, J.H. Edgar, Z. Gu, D. Zhuang, B. Raghothamachar, M. Dudley, A. Sarua, M. Kuball, H.M. Meyer III: The durability of various crucible materials for aluminum nitride crystal growth by sublimation, MRS Internet J. Nitride Semicond. Res. **9**, 6.1–6.11 (2004)

24.39 E.N. Mokhov, O.V. Avdeev, I.S. Barash, T.Y. Chemekova, A.D. Roenkov, A.S. Segal, A.A. Wolfson, Y.N. Makharov, M.G. Ramm, H. Helava: Sublimation growth of AlN bulk crystals in Ta crucibles, J. Cryst. Growth **281**, 93–100 (2005)

24.40 C. Hartmann, J. Wollweber, M. Albrecht, I. Rasin: Preparation and characterization of tantalum carbide as an optional crucible material for bulk aluminum nitride crystal growth via physical vapour transport, Phys. Status Solidi (c) **3**, 1608–1612 (2006)

24.41 L.J. Schowalter, J.C. Rojo, N. Yakolev, Y. Shusterman, K. Dovidenko, R. Wang, I. Bhat, G.A. Slack: Preparation and characterization of single-crystal aluminum nitride substrates, MRS Internet J. Nitride Semicond. Res. **5S1**, W6.7.1–W6.7.6 (2000)

24.42 J.C. Rojo, G.A. Slack, K. Morgan, L.J. Schowalter, M. Dudley: Growth of self-seeded aluminum nitride by sublimation-recondensation and substrate preparation, Mater. Res. Soc. Symp. Proc. **639**, G1.10.1–G1.10.6 (2001)

24.43 J.C. Rojo, L.J. Schowalter, K. Morgan, D.I. Florescu, F.H. Pollack, B. Raghothamachar, M. Dudley: Single-crystal aluminum nitride substrate preparation from bulk crystals, Mater. Res. Soc. Symp. Proc. **680E**, E.2.1.1–E.2.1.7 (2001)

24.44 L.J. Schowalter, G.A. Slack, J.B. Whitlock, K. Morgan, S.B. Schujman, B. Raghothamachar, M. Dudley, K.R. Evans: Fabrication of native, single-crystal AlN substrates, Phys. Status Solidi (c) **0**, 1997–2000 (2003)

24.45 R. Schlesser, R. Dalmau, Z. Sitar: Seeded growth of AlN bulk single crystals by sublimation, J. Cryst. Growth **241**, 416–420 (2002)

24.46 B.M. Epelbaum, C. Seitz, A. Magerl, M. Bickermann, A. Winnacker: Natural growth habit of bulk AlN crystals, J. Cryst. Growth **265**, 577–581 (2004)

24.47 M. Bickermann, B.M. Epelbaum, A. Winnacker: Structural properties of AlN crystals grown by physical vapor transport, Phys. Status Solidi (c) **2**, 2044–2048 (2005)

24.48 M. Bickermann, B.M. Epelbaum, M. Kazan, Z. Herro, P. Masri, A. Winnacker: Growth and characterization of bulk AlN substrates grown by PVT, Phys. Status Solidi (a) **202**, 531–535 (2005)

24.49 M. Bickermann, B.M. Epelbaum, A. Winnacker: Structural, optical, and electrical properties of bulk AlN crystals grown by PVT, Mater. Sci. Forum **457-460**, 1541–1544 (2004)

24.50 R. Dalmau, R. Schlesser, B.J. Rodriguez, R.J. Nemanich, Z. Sitar: AlN bulk crystals grown on SiC seeds, J. Cryst. Growth **281**, 68–74 (2005)

24.51 V. Noveski, R. Schlesser, B. Raghothamachar, M. Dudley, S. Mahajan, S. Beaudoin, Z. Sitar: Seeded growth of bulk AlN crystals and grain evolution in polycrystalline boules, J. Cryst. Growth **279**, 13–19 (2005)

24.52 D. Zhuang, Z.G. Herro, R. Schlesser, B. Raghothamachar, M. Dudley, Z. Sitar: Seeded growth of AlN crystals on nonpolar seeds via physical vapor transport, J. Electron. Mater. **35**, 1513–1517 (2006)

24.53 Y. Shi, Z.Y. Xie, L.H. Liu, B. Liu, J.H. Edgar, M. Kuball: Influence of buffer layer and 6H-SiC substrate polarity on the nucleation of AlN grown by the sublimation sandwich technique, J. Cryst. Growth **233**, 177–186 (2001)

24.54 Y. Shi, B. Liu, L. Liu, J.H. Edgar, E.A. Payzant, J.M. Hayes, M. Kuball: New technique for sublimation growth of AlN single crystals, MRS Internet J. Nitride Semicond. Res. **6**, 5.1–5.6 (2001)

24.55 Y. Shi, B. Liu, L. Liu, J.H. Edgar, H.M. Meyer III, E.A. Payzant, L.R. Walker, N.D. Evans, J.G. Swadener, J. Chaudhuri, J. Chaudhuri: Initial nucleation study and new technique for sublimation growth of AlN on SiC substrate, Phys. Status Solidi (a) **188**, 757–762 (2001)

24.56 L. Liu, B. Liu, Y. Shi, J.H. Edgar: Growth mode and defects in aluminum nitride sublimed on (0001) 6H-SiC substrates, MRS Internet J. Nitride Semicond. Res. **6**, 7.1–7.5 (2001)

24.57 L. Liu, D. Zhuang, B. Liu, Y. Shi, J.H. Edgar, S. Rajasingam, M. Kuball: Characterization of aluminum nitride crystals grown by sublimation, Phys. Status Solidi (a) **188**, 769–773 (2001)

24.58 B. Liu, Y. Shi, L. Liu, J.H. Edgar, D.N. Braski: Surface morphology and composition characterization at the initial stages of AlN crystal growth, Mater. Res. Soc. Symp. Proc. **639**, G3.13.1–G3.13.6 (2001)

24.59 L. Liu, B. Liu, J.H. Edgar, S. Rajasingam, M. Kuball: Raman characterization and stress analysis of AlN grown on SiC by sublimation, J. Appl. Phys. **92**, 5183–5188 (2002)

24.60 B. Raghothamachar, R. Dalmau, M. Dudley, R. Schlesser, D. Zhuang, Z. Herro, Z. Sitar: Structural characterization of bulk AlN single crystals grown from self-seeding and seeding by SiC substrates, Mater. Sci. Forum **527–529**, 1521–1524 (2006)

24.61 R. Dalmau, R. Schlesser, Z. Sitar: Polarity and morphology in seeded growth of bulk AlN on SiC, Phys. Status Solidi (c) **2**, 2036–2039 (2005)

24.62 B. Raghothamachar, M. Dudley, R. Dalmau, R. Schlesser, Z. Sitar: Synchrotron white beam x-ray topography (SWBXT) and high resolution triple axis diffraction studies on AlN layers grown on 4H- and 6H-SiC seeds, Mater. Res. Soc. Symp. Proc. **831**, E8.24.1–E8.24.6 (2005)

24.63 W.L. Sarney, L. Salamanca-Riba, T. Hossain, P. Zhou, H.N. Jayatirtha, H.H. Kang, R.D. Vispute, M. Spencer, K.A. Jones: TEM study of bulk AlN grown by physical vapor transport, MRS Internet J. Nitride Semicond. Res. **5S1**, W5.5.1–W5.5.6 (1999)

24.64 B.M. Epelbaum, M. Bickermann, A. Winnacker: Seeded PVT growth of aluminum nitride on silicon carbide, Mater. Sci. Forum **433–436**, 983–986 (2003)

24.65 B.M. Epelbaum, P. Heimann, M. Bickermann, A. Winnacker: Comparative study of initial growth stage in PVT growth of AlN on SiC and on native AlN susbtrates, Phys. Status Solidi (c) **2**, 2070–2073 (2005)

24.66 P. Heimann, B.M. Epelbaum, M. Bickermann, S. Nagata, A. Winnacker: The initial stage in PVT growth of aluminum nitride, Phys. Status Solidi (c) **3**, 1575–1578 (2006)

24.67 K. Balakrishnan, M. Banno, K. Nakano, G. Narita, N. Tsuchiya, M. Imura, M. Iwaya, S. Kamiyama, K. Shimono, T. Noro, T. Takagi, H. Amano, I. Akasaki: Sublimation growth of AlN bulk crystals by seeded and spontaneous nucleation methods, Mater. Res. Soc. Symp. Proc. **831**, E11.3.1–E11.3.7 (2005)

24.68 S. Wang, B. Raghothamachar, M. Dudley, A.G. Timmerman: Crystal growth and defect characterization of AlN single crystals, Mater. Res. Soc. Symp. Proc. **892**, FF30.06.1–FF30.06.6 (2006)

24.69 V. Noveski, R. Schlesser, J. Freitas Jr., S. Mahajan, S. Beaudoin, Z. Sitar: Vapor phase transport of AlN in an RF heated reactor: Low and high temperature studies, Mater. Res. Soc. Symp. Proc. **798**, Y2.8.1–Y2.8.6 (2004)

24.70 D. Zhuang, Z.G. Herro, R. Schlesser, Z. Sitar: Seeded growth of AlN single crystals by physical vapor transport, J. Cryst. Growth **287**, 372–375 (2006)

24.71 Z.G. Herro, D. Zhuang, R. Schlesser, R. Collazo, Z. Sitar: Growth of large AlN single crystals along the [0001] directions, Mater. Res. Soc. Symp. Proc. **892**, FF21.01.1–FF21.01.6 (2006)

24.72 Z.G. Herro, D. Zhuang, R. Schlesser, R. Collazo, Z. Sitar: Seeded growth of AlN on N- and Al-polar ⟨0001⟩ AlN seeds by physical vapor transport, J. Cryst. Growth **286**, 205–208 (2006)

24.73 B. Raghothamachar, J. Bai, M. Dudley, R. Dalmau, D. Zhuang, Z. Herro, R. Schlesser, Z. Sitar, B. Wang, M. Callahan, K. Rakes, P. Konkapaka, M. Spencer: Characterization of bulk grown GaN and AlN single crystal materials, J. Cryst. Growth **287**, 349–353 (2006)

24.74 M. Dudley, X. Huang: X-ray topography. In: *Encyclopedia of Materials: Science and Technology*, ed. by K.H.J. Buschow, R.W. Cahn, M.C. Flemings, B. Ilschner, E.J. Kramer, S. Mahajan, E. Veyssière (Elsevier, Oxford 2001) pp. 9813–9825

24.75 B. Raghothamachar, W.M. Vetter, M. Dudley, R. Dalmau, R. Schlesser, Z. Sitar, E. Michaels, J.W. Kolis: Synchrotron white beam topography characterization of physical vapor transport grown AlN and ammonothermal GaN, J. Cryst. Growth **246**, 271–280 (2002)

24.76 B. Raghothamachar, M. Dudley, J.C. Rojo, K. Morgan, L.J. Schowalter: X-ray characterization of bulk AlN single crystals grown by the sublimation technique, J. Cryst. Growth **250**, 244–250 (2003)

24.77 L.J. Schowalter, S.B. Schujman, W. Liu, M. Goorsky, M.C. Wood, J. Grandusky, F. Shahedipour-Sandvik: Development of native, single crystal AlN substrates for device applications, Phys. Status Solidi (a) **203**, 1667–1671 (2006)

24.78 R.T. Bondokov, K.E. Morgan, R. Shetty, W. Liu, G.A. Slack, M. Goorsky, L.J. Schowalter: Defect content evaluation in single-crystal AlN wafers, Mater. Res. Soc. Symp. Proc. **892**, FF30.03.1–FF30.03.6 (2006)

24.79 S.B. Schujman, W. Liu, N. Meyer, J.A. Smart, L.J. Schowalter: Atomic force microscope studies on native AlN substrates, Mater. Res. Soc. Symp. Proc. **892**, FF30.05.1–FF30.05.6 (2006)

24.80 J. Pastrňák, L. Roskovcová: Optical absorption edge of AlN single crystals, Phys. Status Solidi (b) **26**, 591–597 (1968)

24.81 W.M. Yim, E.J. Stofko, P.J. Zanzucchi, J.I. Pankove, M. Ettenberg, S.L. Gilbert: Epitaxially grown AlN and its optical band gap, J. Appl. Phys. **44**, 292–296 (1973)

24.82 G.A. Slack, T.F. McNelly: AlN single crystals, J. Cryst. Growth **42**, 560–563 (1977)

24.83 T. Wethkamp, K. Wilmers, C. Cobet, N. Esser, W. Richter, O. Ambacher, M. Stutzmann, M. Cardona: Dielectric function of hexagonal AlN films determined by spectroscopic ellipsometry in the vacuum-UV range, Phys. Rev. B **59**, 1845–1849 (1999)

24.84 E. Silveira, J.A. Freitas Jr., M. Kneissel, D.W. Treat, N.M. Johnson, G.A. Slack, L.J. Schowalter: Near-bandedge cathodoluminescence of an AlN homoepitaxial film, Appl. Phys. Lett. **84**, 3501–3503 (2004)

24.85 E. Kuokstis, J. Zhang, Q. Fareed, J.W. Yang, G. Simin, M.A. Khan, R. Gaska, M. Shur, C. Rojo, L. Schowalter: Near-band-edge photoluminescence of wurtzite-type AlN, Appl. Phys. Lett. **81**, 2755–2757 (2002)

24.86 I. Vurgaftman, J.R. Meyer: Band parameters for nitrogen-containing semiconductors, J. Appl. Phys. **94**, 3675–3696 (2003)

24.87 M. Suzuki, T. Uenoyama, A. Yanase: First-principles calculations of effective-mass parameters of AlN and GaN, Phys. Rev. B **52**, 8132–8139 (1995)

24.88 J.M. Wagner, F. Bechstedt: Properties of strained wurtzite GaN and AlN: Ab initio studies, Phys. Rev. B **66**, 115202.1–115202.20 (2002)

24.89 J. Li, K.B. Nam, L. Nakarmi, J.Y. Lin, H.X. Jiang, P. Carrier, S.H. Wei: Band structure and fundamental optical transitions in wurtzite AlN, Appl. Phys. Lett. **83**, 5163–5165 (2003)

24.90 E. Silveira, J.A. Freitas Jr., O.J. Glembocki, G.A. Slack, L.J. Schowalter: Excitonic structure of bulk AlN from optical reflectivity and cathodoluminescence measurements, Phys. Rev. B **71**, 41201 (2005)

24.91 M. Strassburg, J. Senawiratne, N. Dietz, U. Haboeck, A. Hoffmann, V. Noveski, R. Dalmau, R. Schlesser, Z. Sitar: The growth and optical properties of large, high-quality AlN single crystals, J. Appl. Phys. **96**, 5870–5876 (2004)

24.92 J. Senawiratne, M. Strassburg, N. Dietz, U. Haboeck, A. Hoffmann, V. Noveski, R. Dalmau, R. Schlesser, Z. Sitar: Raman, photoluminescence and absorption studies on high quality AlN single crystals, Phys. Status Solidi (c) **2**, 2774–2778 (2005)

24.93 M. Bickermann, B.M. Epelbaum, P. Heimann, Z.G. Herro, A. Winnacker: Orientation-dependent phonon observation in single-crystalline aluminum nitride, Appl. Phys. Lett. **86**, 131904 (2005)

24.94 M. Bickermann, P. Heimann, B.M. Epelbaum: Orientation-dependent properties of aluminum nitride single crystals, Phys. Status Solidi (c) **3**, 1902–1906 (2006)

24.95 E. Silveira, J.A. Freitas Jr., G.A. Slack, L.J. Schowalter: Cathodoluminescence studies of large bulk AlN crystals, Phys. Status Solidi (c) **0**, 2618–2622 (2003)

24.96 E. Silveira, J.A. Freitas, G.A. Slack, L.J. Schowalter, M. Kneissl, D.W. Treat, N.M. Johnson: Depth-resolved cathodoluminescence of a homoepitaxial AlN thin film, J. Cryst. Growth **281**, 188–193 (2005)

24.97 D.R. Lide (Ed): *CRC Handbook of Chemistry and Physics*, 74th edn (CRC Press, Boca Raton 1993) Chap. 5, p. 5

24.98 M. Bickermann, B.M. Epelbaum, A. Winnacker: Characterization of bulk AlN with low oxygen content, J. Cryst. Growth **269**, 432–442 (2004)

24.99 G.A. Slack, L.J. Schowalter, D. Morelli, J.A. Freitas Jr: Some effects of oxygen impurites on AlN and GaN, J. Cryst. Growth **246**, 287–298 (2002)

25. Growth of Single-Crystal Organic Semiconductors

Christian Kloc, Theo Siegrist, Jens Pflaum

Organic semiconductor crystal growth presents a very different set of challenges than their inorganic counterparts. Although single crystals of organic semiconductors can be grown by the same techniques used for inorganic semiconductors, the weak intermolecular bonds, low melting temperatures, and high vapor pressures and solvent solubilities require specific modifications to crystal growth techniques of these materials. Bulk crystals of only a handful of different materials have been grown from the melt. The Czochralski, Bridgman, and general melt growth techniques are hampered by the high vapor pressure, which causes fast evaporation of the material during the growth process. However, the significant vapor pressure of organic semiconductors makes gas-phase growth methods suitable for most of them. In general, multistep synthesis of organic molecules produces impure materials which need extensive purification. Small crystals, mostly for structure determinations, have been grown from organic solvents. Zone melting has been used for a few materials, but many organic molecules decompose before reaching the melting temperature. The crystal growth of volatile molecules in a stream of flowing gas is therefore a widely used method that combines purification and crystal growth. Although gas-phase grown crystals tend to be small in size, they have high structural quality and superior purity and are therefore preferred for physical property measurements.

25.1 Basics 845
25.2 Theory of Nucleation and Crystal Growth 847
25.2.1 Stability Criteria for Nuclei 847
25.2.2 Thermodynamic Considerations of Crystal Growth 847
25.2.3 Growth Morphology in Relation to Symmetry 848
25.2.4 Structural Defects 848
25.3 Organic Materials of Interest for Semiconducting Single Crystals 848
25.4 Pregrowth Purification 850
25.4.1 Zone Refinement 851
25.4.2 Sublimation and Its Modifications .. 852
25.5 Crystal Growth 854
25.5.1 Melt Growth 855
25.5.2 Growth from the Gas Phase 857
25.5.3 Solvent-Based Growth Methods 862
25.6 Quality of Organic Semiconducting Single Crystals 862
25.7 Organic Single-Crystalline Field-Effect Transistors 863
25.8 Conclusions 864
References 865

25.1 Basics

Most organic molecular crystals are transparent materials that behave like insulators, with electrical resistivities in the range of 10^{13}–$10^{18}\,\Omega\,\mathrm{cm}$ at room temperature. However, some organic molecules with delocalized π-electrons such as conjugated hydrocarbons, phthalocyanines, oligothiophenes, etc. may form colored crystals indicating a small energy gap between the highest occupied (HOMO) and the lowest unoccupied (LUMO) molecular orbitals. Crystals made from such substances often show significant absorption and emission of visible light, and photoconductivity and electrical conductivity, and in general behave more like semiconductors than insulators. Photoconductivity of anthracene, with its three conjugated benzene

rings, intrigued researchers from the beginning of the 20th century [25.1]. The feature that light is emitted from anthracene crystals under the absorption of high-energy radiation such as neutrons or x-rays has been widely used in scintillation detectors [25.2]. Later, research began to explore whether organic semiconductors may be suitable for applications where inorganic semiconductors were already established. Such research required organic semiconductors in thin-film form for applications, and in single-crystal form mostly for basic research. Studies that focus on physical properties resulting from weak intramolecular bonds, high symmetry of molecules, and anisotropy of physical properties require measurements on single crystals. Therefore, many well-established crystal growth methods for inorganic materials have been adapted to the growth of organic semiconductor crystals and are discussed in this chapter.

Semiconductors composed from van der Waals bonded molecules, especially those comprising small organic molecules, may be soluble in numerous organic solvents, even at room temperature. This fact allows for low-temperature processing such as printing, spraying, casting, laminating, etc. to mention just a few. Low-temperature solubility distinguishes significantly organic semiconductors from covalently bonded inorganic semiconductors, which often can only be dissolved in high-temperature fluxes. Organic semiconductors therefore seem to be the perfect components for devices where the active materials, as well as the electrodes and conduction paths, may simply be printed by various techniques. Printing semiconducting elements on plastic foils promises large-scale production of inexpensive electronic devices such as bendable displays, field-effect transistor based circuits or large solar cell arrays [25.3, 4].

The power of organic molecular synthesis and crystal engineering allows the formation of new semiconductor materials through systematic variation of crystalline and molecular structure for structure–properties investigations. Optimization of structural, electrical or optical characteristics through chemical design of molecules may then result in improved electronic devices. Furthermore, new properties may give rise to novel applications and devices. However, understanding the relationship between the molecular composition, the packing of molecules into crystals, and the physical properties of the resulting organic semiconductors still presents a challenge.

Often, studies of physical properties of organic semiconductors were performed on polycrystalline or amorphous thin-film devices due to their ease of fabrication and good control over physical dimensions. However, grain boundaries, inhomogeneous distribution of impurities, and high defect densities make thin-film devices unattractive for studies of intrinsic properties [25.5, 6].

In contrast, single crystals contain only small amounts of impurities and defects, due to the inherent purification during crystallization. Therefore, properties measured on single crystals tend to be more reproducible than those measured on amorphous or polycrystalline thin-film samples.

Historically, properties of inorganic semiconductors, such as silicon, germanium or III–V compounds, have been studied on single crystals or single-crystalline epitaxial thin films. It is therefore reasonable to assume that the intrinsic properties of organic semiconductors can also be studied following the same path. Contrary to inorganic semiconductors, were the growth units are atoms, the growth units in organic crystals are molecules. Such extended moieties, with their internal structure, require reorientation and alignment before incorporation into a crystalline lattice. These processes need to be considered by using a specific crystal growth technique for the growth of a particular organic semiconductor.

In general, organic semiconductors crystallize in low-symmetry unit cells. Therefore, all physical properties are tensorial properties with often large anisotropies and can only be properly evaluated on single crystals. The availability of high-purity and high-quality single crystals of organic semiconductors is thus crucial in exploring the physics of such materials and is very helpful in new material design and in building devices with novel functionality and high performance [25.7, 8].

Single crystals of a series of organic semiconductors have been grown using well-described crystal growth techniques. Examples of monographs focused on the theory and practice of crystal growth are cited at the end of this chapter [25.9, 10]. The weak van der Waals bonds between the growth units (in particular molecules) in organic crystals limit the methods applicable to the preparation of single-crystalline specimens [25.11, 12]. In additional the growth units may decompose relatively easily, thus contaminating the crystals. Since the properties of organic semiconductors, like their inorganic counterparts, are sensitive to low levels of impurities and defects, the growth of high-quality organic semiconductors needs to consider purification, contamination, and defect formation in every step of the preparation process.

In this chapter, we will therefore focus on practical approaches for purification and growth of high-quality molecular semiconductor single crystals. In the past, reviews concentrated either on melt growth [25.12] or gas-phase techniques [25.13, 14]. Here, we attempt to compare different crystal growth techniques in order to suggest their advantages and disadvantages as well as practical criteria for the use of these techniques for organic semiconductors. We focus on technological differences between the growth of inorganic and organic semiconductors. We will further discuss defects and contaminants resulting from the use of particular crystal growth methods.

25.2 Theory of Nucleation and Crystal Growth

The growth kinetics of inorganic as well as organic materials are determined by their inherent parameters, such as the interaction between the individual species/units forming the crystals, and external parameters, such as the growth temperature or adsorption rate. Especially the set of external conditions such as the interaction between a substrate and the initial nucleation layer are often difficult to control, if at all. These parameters are critical for the initial step of nucleation and might even change during growth as a function of temperature.

Furthermore, a fundamental property of organics is the anisotropic extension of the electronic wavefunctions, meaning that the electron distribution shows strong spatial anisotropy of intermolecular overlap, in contrast to inorganic crystals with covalent or ionic bonding. The intention is to correlate the spatial anisotropy of the bonding strength with the tensorial properties, e.g., higher mobility values along certain crystallographic directions.

To characterize the influence of such external parameters on crystal preparation, it is helpful to highlight first the kinetics of crystal formation for the case of an ideal system. In this case it is appropriate to divide the crystal formation into two steps: the initial nucleation and the subsequent growth of the individual nuclei.

25.2.1 Stability Criteria for Nuclei

To initiate volume growth of the intended organic crystal, the formation of the initial nuclei on a given support is the essential step. Beside the optimization of nuclei density in the beginning of crystal formation, an important criterion is the smallest number of organic molecules forming a stable nucleus. As for their inorganic counterparts, stability is governed by the balance between loss in surface energy versus gain in volume energy upon incorporation of an additional molecular building block.

However, besides the van der Waals interaction, which was interpreted on the basis of temporarily fluctuating dipoles by London, the occurring internal degrees of freedom, e.g., the torsion of extended phenyl groups as in the case of 9,10-diphenylanthracene [25.15], might play a considerable role at the early stage of nucleation. Even thermally induced changes of the molecular shape in the gas phase can significantly influence the crystallinity of the molecular systems. For instance, the thermal energy during evaporation is not sufficient to planarize the tetracene backbone of rubrene, which is twisted due to pairwise repulsion of the attached phenyl rings. As a result, thin films of rubrene have proven to be amorphous without any indication of crystallinity [25.16,17]. In contrast, growth from gradient sublimation under a constant gas flow provides sufficient energy to overcome the energy barrier of 210 meV and to planarize the molecule averaged over time [25.16]. In the latter case, rubrene shows defined crystal growth with spatial extensions of its growth planes in the centimeter range.

25.2.2 Thermodynamic Considerations of Crystal Growth

The thermodynamic quantities describing the energetics of crystal growth and especially of nucleation are the sublimation enthalpy and the entropy. Neglecting permanent dipoles, the bonding strength between molecular entities is governed by the weak van der Waals force, resulting in a distribution of sublimation enthalpies from 45 kJ/mol for benzene up to 215 kJ/mol for ovalene [25.18]. Normalizing the heat of sublimation divided by the number of intermolecular contacts reveals an average energy per contact of 50 J/mol for various polyaromatic hydrocarbon crystals, independent of the molecular packing [25.18]. However, for molecules offering additional degrees of freedom, e.g., due to twisted functional groups, the gain in entropy might add a significant amount of energy, determining the final crystalline structure.

25.2.3 Growth Morphology in Relation to Symmetry

In view of the anisotropic physical properties such as the tensor of charge carrier mobility or the optical indicatrix, one of the central aspects of crystal growth is the formation and stability of certain crystallographic facets, planes or axes. Similar to their inorganic equivalents, high-indices surfaces are unstable over time due to their higher growth velocities compared with low-index planes. However, for organic materials the crystal habit, defined as the relative size of the stable faces, proves to be more sensitive to the external growth conditions as a consequence of the weak van der Waals binding energies. Tetracene, and many other oligoacenes grown by plate sublimation, shows a distinct stable crystal habit depending on the environmental conditions. Under vacuum, a preferential growth along the (*ab*)-plane is observed. This mode is determined by the long-range diffusion and the gain of energy by incorporating the individual molecules in this plane under almost equilibrium conditions. In an atmosphere of 400 Torr N_2, however, the mean free path of the sublimed molecule is shorter than the traveling distance in the volume, and the crystal growth is governed by the material transport rather than by the diffusion atop the (*ab*)-crystal surface. The crystals emanating from this growth regime are needle shaped, preferentially oriented with the needle axis along the c^*-direction.

25.2.4 Structural Defects

The growth of organic molecular crystals, occurring in most cases in a temperature range between room temperature up to about 700 K, is accompanied by the formation of structural defects, e.g., vacancies, dislocations, and growth sectors. According to Boltzmann's law, the density of vacancies n in a crystal is a function of the temperature T and the energy, E_v, required to form a vacancy: $n \sim \exp(-E_V/k_B T)$. Possible defects can be characterized by their dimensionality as vacancies (zero-dimensional, 0-D), dislocation lines or screw dislocations (one-dimensional, 1-D), or grain boundaries (two, dimensional 2-D). Even for high-quality anthracene crystals, thermal treatment might result in vacancy densities at room temperature of 10^{14}–10^{16} cm^{-3} after growth. Furthermore, due to the respective packing along the various crystallographic directions, an anisotropic distribution of defects has been observed. Especially in crystals with herringbone-type packing in the (*ab*)-plane and a (001) glide plane, enhanced formation of dislocation lines is observed along the (100)||[010] Burgers vector. The quadratic scaling of the elastic energy with the respective Burgers vector makes the *b*-direction (the shortest distance between adjacent molecules) energetically favorable for the formation of dislocation lines.

In addition, the external conditions during crystal growth may have a significant impact on the defect density [25.19]. In melt-grown crystalline samples, the interaction of the crystal with the walls of the ampoule, especially during the cooling process, might induce dislocation densities three orders of magnitude higher compared with similar crystals grown from gas phase. However, subsequent thermal treatments might decrease the defect density by adding thermal energy to the system during annealing.

25.3 Organic Materials of Interest for Semiconducting Single Crystals

Organic semiconductors represent a large group of solids comprised of organic π-conjugated small molecules, oligomers or polymers. Since polymers are rarely available in single-crystalline form, the materials discussed in this chapter are limited to crystals of small molecules and oligomers.

Organic semiconductors are mostly used as active materials in field-effect transistors, light-emitting diodes or solar cells. These applications determine the selection of molecules of interest for research and production. Figure 25.1 presents examples of molecules with semiconducting properties used for research and applications.

Linear or planar fused-ring compounds, heterocyclic oligomers, and fullerenes are among the most studied molecules with semiconducting properties.

Single crystals of polycyclic aromatic hydrocarbons were among the first reported organic materials exhibiting small but measurable conductivity and photoconductivity. This suggested that these materials contain delocalized π-electrons and belong to the family of semiconducting compounds [25.20, 21].

These early studies required large single crystals for physical measurements. Therefore, the semiconductors selected for these measurements included molecules available in relative large quantity, stable at tempera-

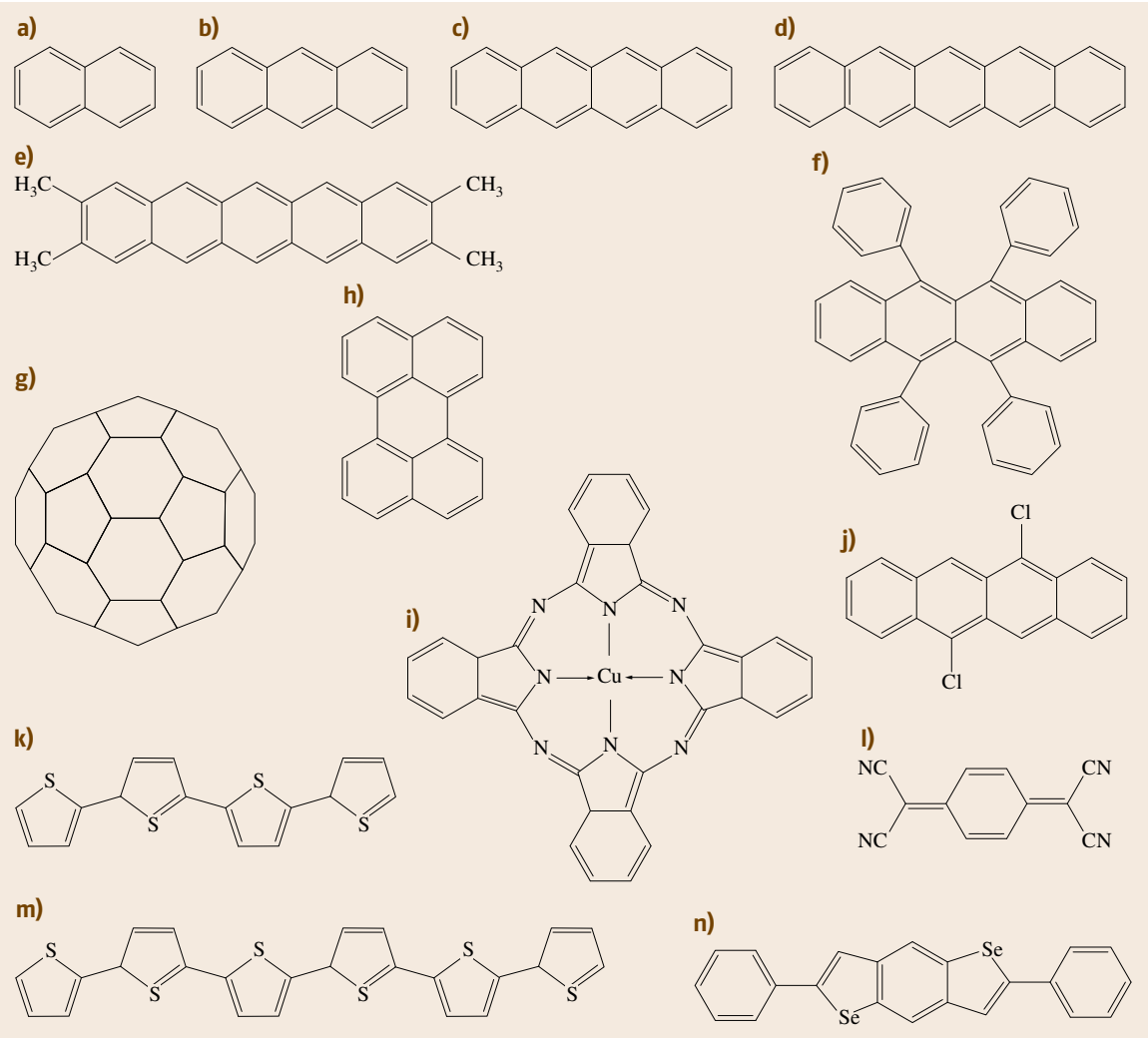


Fig. 25.1a–n Molecules of examples of the most studied organic semiconductors: **(a)** naphthalene, **(b)** anthracene, **(c)** tetracene, **(d)** pentacene, **(e)** 2,3,9,10-tetramethylpentacene (Me_4Pent), **(f)** rubrene, **(g)** fullerene (C_{60}), **(h)** perylene, **(i)** copper phthalocyanine, **(j)** 5,11-dichlorotetracene (DCT), **(k)** α-quaterthiophene (α-4T), **(l)** tetracyanoquinodimethane (TCNQ), **(m)** α-hexathiophene or α-sexithienyl (α-6T), **(n)** 2,6-diphenylbenzo[1,2-*b*:4,5-*b*']diselenophene (DPH-BDS)

tures close to their melting point, and grown in the form of crystalline ingots from the melt. Some materials, such as naphthalene, anthracene, stilbene, terphenyl, diphenylacetylene or quaterphenyl, have been chosen for crystal growth due to their strong scintillation properties [25.22]. Others, such as naphthalene, anthracene, and perylene, were selected for melt growth and time-of-flight measurements [25.12].

Oligothiophenes decompose below their melting temperature and can only be grown from gas phase in the form of small single crystals or thin films. These compounds are widely used in both single-crystal and thin-film forms for field-effect transistors [25.23, 24]. Hydrocarbons, such as rubrene, pentacene, and tetracene, are used to study the physical properties of organic semiconductors and for high-mobility transistors [25.8].

Fullerenes, such as C_{60}, and C_{70}, have received considerable attention due to their spherically delocalized π-electrons, yielding measurable conductivity

and even superconductivity in alkali metal-C_{60} compounds [25.25].

Another group showing promise for practical application are cofacially stacked phthalocyanine systems and, often with central 3d transition-metal atom, porphyrines [25.26]. These compounds are exceptional due to their broad chemical variability and excellent stability. These properties, and the fact that they are available in sufficient quantity and quality, make porphyrines and phthalocyanines prominent candidates for efficient photovoltaic energy conversion.

The observation of light emission from organic diodes and the field effect in transistor configurations stimulated the design and development of many new organic π-conjugated molecules with semiconductor properties [25.27]

Many were synthesized and used only in thin-film field-effect transistors by evaporation or solvent-growth techniques. However, only a limited number of these compounds were grown in single-crystal form and only a few examples are known where the electronic transport properties were optimized.

25.4 Pregrowth Purification

For research purposes, batches of organic semiconductor materials are typically purchased from chemical suppliers. Some special, commercially unavailable molecules are synthesized by individual chemists. In both cases, the syntheses involve multistep organic chemical reactions yielding the expected molecules. Because the yield of an organic synthesis may be low, the desired molecules are often mixed with numerous, not always well-characterized, contaminants. Contaminants may be the molecules introduced as starting material, molecules formed by side reactions or decomposition processes, as well as solvents used in the process. In comparison with classical inorganic semiconductors, such as silicon or GaAs, where 6 N purity or better is available, organic semiconductors are significantly contaminated, with purity in the range of 95–98%. The contaminants are often not well defined and may form by reduction, oxidation, decomposition or photoinduced processes during storage. Therefore, before crystals can be grown, the source materials need to be purified.

The purification methods may be the same as those used for inorganic compounds: zone refining, sublimation or distillation. Additional, due to the solubility of organic semiconductors in organic solvents, recrystallization from organic solvents, or purification by gas- or liquid-phase chromatography, is feasible. The product of such purification requires subsequent removal of traces of solvents. Moreover, some specific contaminants, which are difficult to remove by traditional purification methods, may be altered chemically for effective removal. For instance, removing β-methylnaphthalene and thionaphthalene from naphthalene by fusing naphthalene with molten potassium, which chemically modifies the solid/liquid and solid/gas distribution coefficients, may be an example of chemically altering contaminants prior to removing them via sublimation and zone refining [25.28].

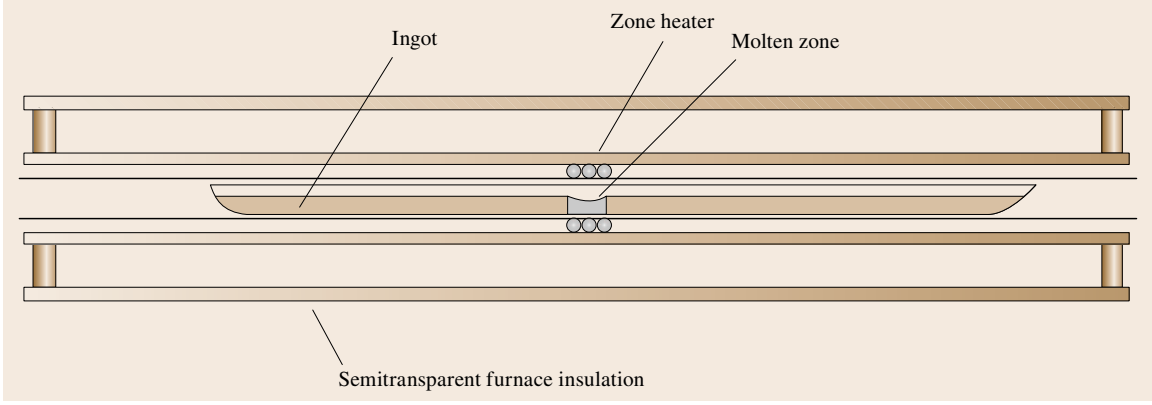


Fig. 25.2 Zone refining with one molten zone in a horizontal arrangement

Organic semiconductors, due to the peculiarity of the bonds, may not only decompose during storage but also dimerize and polymerize, especially if exposed to light. Anthracene is known to form dianthracene under illumination, but this dimer is not very stable and photolitically dissociates back to anthracene [25.29].

Pentacene, which has a mobility larger than $1\,cm^2/(V\,s)$ in both thin-film and single-crystal field-effect transistors, easily oxidizes to 6,13-pentacenequinone [25.30], but also dimerizes and additionally reacts further to form a series of polycondensed aromatic hydrocarbons and undergoes a disproportionation reaction to 6,13-dihydropentacene [25.31].

25.4.1 Zone Refinement

Materials available in larger amounts, which can be melted without decomposition, such as anthracene, naphthalene or perylene, may be purified by repeated zone melting as the technique of choice. Established by *Pfann* for inorganic semiconducting materials [25.32], zone refinement was applied to anthracene [25.33, 34]. In this method, an ingot of about 20–50 cm length is formed and slowly dragged across a cylindrical heating zone of centimeter extension under an inert gas atmosphere. The inert gas on one hand protects the molten material from reaction with air and on the other hand reduces the evaporation of the material from the melted zone. The temperature of the heater is high enough to locally melt the material to form a short molten zone. Outside the heating zone the organic material remains in its solid phase (Figs. 25.2 and 25.3). A zone-refinement apparatus can be realized with an ingot fixed in either horizontal or vertical orientation. The heater moves along the fixed ingot, or alternatively, the ingot moves relative to fixed heater. To allow multiple melting and crystallization of zones along an ingot, a system with numerous heaters may be used (Fig. 25.4).

Due to the slow movement of the molten zone in one direction only, the purified material melts at one end of the zone and crystallizes at the other. Depending on the solubility of the respective impurities in the liquid and solid states, impurities with higher solubility in the melt than in the crystal are moved towards



Fig. 25.3 Zone-refined anthracene. Contamination is moved to both ends of the ampoule, seen as a *dark* and a *light part* at each end of the anthracene ingot. Also, some cracks and crystal segments, formed due to crystal contraction during cooling, are seen

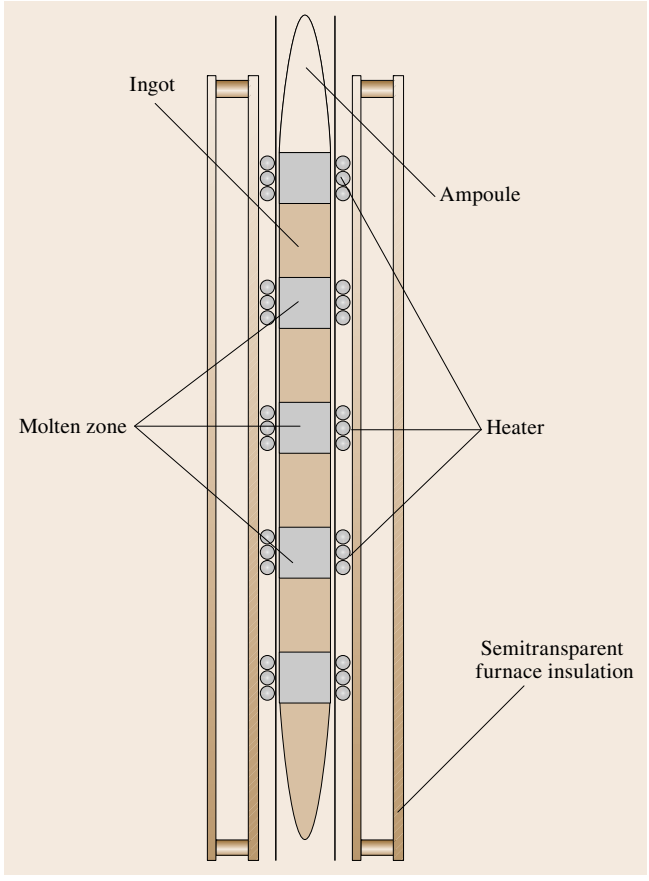


Fig. 25.4 Multizone refining system. To prevent evaporation of material from the melted zone, zone refining is run in vertical orientation. To decrease the time required for the process, a multizone furnace is used ▶

the molten interface, while impurities with lower solubility move to the crystallization interface. Therefore, the former impurities are pulled with the zone whereas the others are transferred to the opposite end of the ingot. Repetition of this process up to several hundred cycles will accumulate impurities on both ends of the ingot and pure material is collected from its central part (Fig. 25.3).

In the case that impurities have equal solubility in the melt and the solid, they cannot be separated via zone melting and need to be removed using other techniques such as sublimation or chemical precipitation. Some success has been reported by using an additional material forming an eutectic with the impurity. In this way the distribution coefficient is changed from an unfavorable value close to 1.0, to a smaller value which simplifies moving the impurities with the eutectic to the end of an ingot. For instance, tetracene, for eutectic zone melting purification, has been mixed with 2-naphthoic acid, while anthracene has been melted with benzoic acid. The zone refinement of such an eutectic mixture allows removing otherwise hard-to-remove impurities [25.35].

The purified material does not need to be removed from the zone-refining apparatus after each run of the molten zone along the ingot. Therefore, the purification process may be automatically repeated many times in the same ampoule [25.36]. Additionally, subsequent purification steps may be performed only on material collected from the central, purest part of the ingots. The purity of substances for which this method has been applied was superior, and low-temperature mobilities, evaluated by the time-of-flight method, were reported to be as high as a few hundred $cm^2/(V\,s)$ at low temperature. Because zone melting requires a large amount of material (on the gram scale) and a specific, noncommercial apparatus, this method is preferred for large-scale purification and has been used only for a limited number of organic semiconductors.

25.4.2 Sublimation and Its Modifications

For studies of new organic semiconductors, laboriously synthesized in only milligram amounts, standard vacuum sublimation (with various modifications) has been commonly used. In this method, material sublimes in vacuum in a temperature gradient between evaporation and deposition zones. If only a very small amount of the material is available, the deposition temperature needs to be significantly lower than the evaporation temperature. Under such conditions, easily evaporated molecules, such as most solvents, evaporate into the vacuum and most of the molecules deposit on some form of cold finger. Heavy molecules do not sublime at all and remain in the evaporation zone.

Vacuum sublimation in a temperature gradient is very efficient, but it often lacks selectivity and most

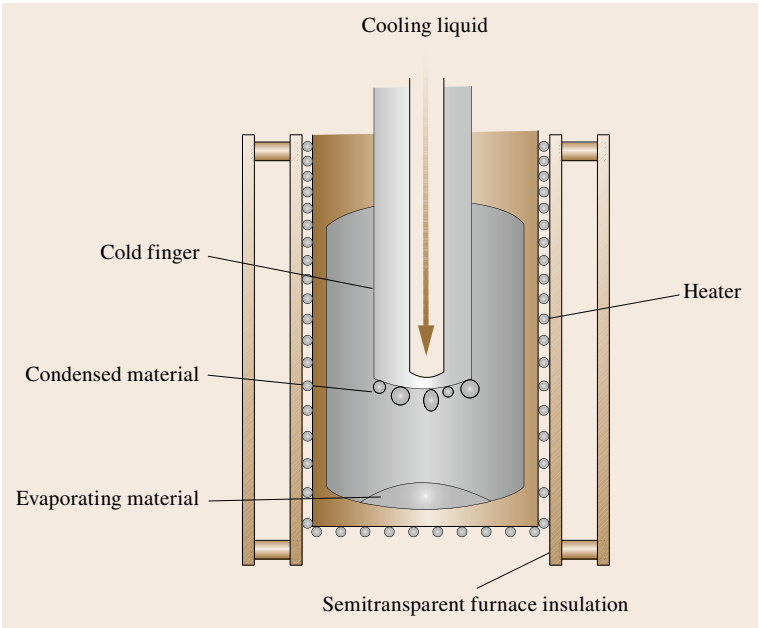


Fig. 25.5 Vacuum sublimation on a cold finger

molecules with comparable properties deposit simultaneously on cold surfaces.

Low-vapor-pressure molecules or solvents may be efficiently removed by sublimation. However, due to the weak van der Waals bonds between molecules, the volatility and evaporation enthalpies of organic molecules with comparable molecular mass are too close for efficient separation. It is worth mentioning at this point that this situation may become even more complex if the molecular species possess a permanent dipole moment, thereby significantly changing the sublimation enthalpies.

To improve the purification of organic semiconductors and change the mass transport kinetics, modified sublimation methods have been proposed. In one case, a carrier gas was introduced into the sublimation apparatus and a long deposition zone with a shallow temperature gradient from the evaporation zone to room temperature was used [25.13,37]. In this way, the heavy impurity molecules, similar to vacuum sublimation, remain in the heating zone and the molecules with high vapor pressure (solvents, etc.) are removed from the deposition zone with the carrier gas stream. The carrier gas transports molecules with different molecular mass to different distances, allowing efficient separation of molecules with different mass.

This method is selective enough that it may even be used for separation of polymorphs or isomers. Polymorphs are crystalline substances formed from the same molecules but which crystallize in different structures and therefore possess different sublimation enthalpies.

Polymorphs of oligothiophenes, hexathiophenes, quaterthiophenes have been separated by this methods for crystal structure determinations.

Another modification of the sublimation technique is step sublimation. Here, the pristine material is placed in a boat at the end of a glass tube that is closed at

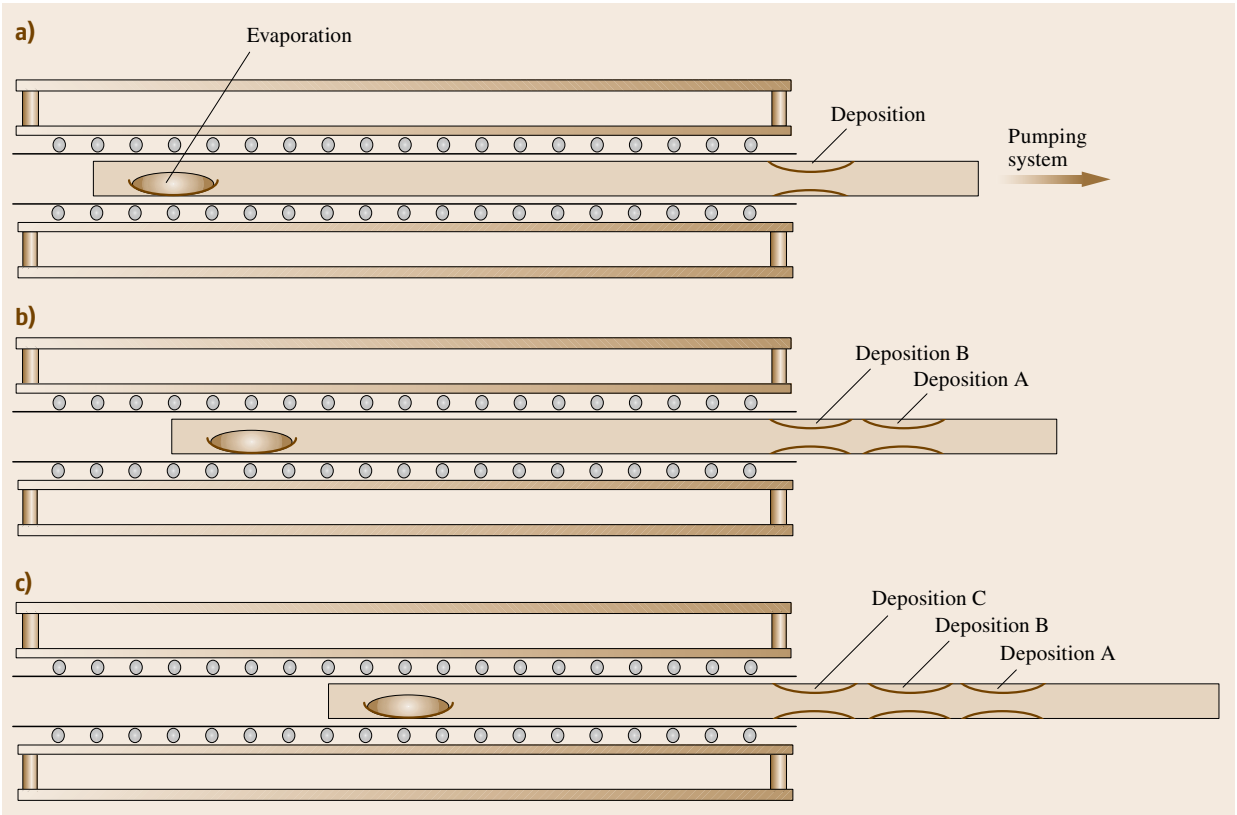


Fig. 25.6a–c The principle of step sublimation. The furnace is kept at constant temperature. The reaction tube is pulled from the furnace in such a way that material from the consecutive processes deposit at the positions marked A, B, C as depicted in (a–c)

one side. Connecting the open side to a pumping system, the tube is evacuated to pressures of 10^{-6} mbar and placed with the closed side into a transparent glass oven. Subsequent stepwise increases of the temperature, with the ingot partially translated out of the heated zone after each new temperature, allows for a detailed analysis of the respective contaminants subliming at different temperatures as well as the determination of the sublimation temperature of the intended material. Furthermore, the open arrangement of the setup allows for in situ optical investigations of the pristine material upon thermal treatment, e.g., for newly synthesized materials, changes between the solid and the liquid at a certain temperature can be observed. The technique can indicate changes in the chemical composition of the material as well as possible phase transitions. Due to its simplicity, this technique is well suited to estimate the thermal stability and sublimation conditions of newly synthesized molecules. Furthermore, this technique enables the purification of lager amounts of material compared with gradient sublimation and is therefore ideal as a prepurification step in combination with zone refinement.

In both of the above-described modifications the purified material needs to be removed after one purification step. For consecutive purification steps, the material needs to be reloaded into a new clean apparatus and the purification process may be repeated. To avoid this laborious and expensive procedure, a vapor zone-refining technique has been developed [25.35]. In this method, tetracene in the form of a long ingot was sublimed in an apparatus similar to a zone-refining system. The temperature, however, was kept below the melting temperature at which tetracene decomposes. Due to the high vapor pressure of tetracene, it evaporates from the short heated zone. Because some impurities may have lower and others higher vapor pressure than tetracene, the impurities are concentrated at both ends of the vapor zone-refining ingot. The efficiency of this purification method was confirmed through liquid-phase chromatography, but no other physical properties sensitive to small quantities of contaminants have been reported.

25.5 Crystal Growth

Organic compounds may be grown from the gas phase, solution or melt. Many well-established methods used for crystal growth of elements, (metals and nonmetals) or compounds (oxides, semiconductors or insulators) may be modified for growth of single-crystal organic semiconductors. The relative weak van der Waals bonds between molecules, the large dimensions of growth units, and the limited thermal stability of organic materials impose specific limitations on the use of these well-established techniques. In comparison with inorganic materials, melting temperatures of organic compounds are relatively low. Many small molecules appear even at room temperature as liquids and cannot be considered as practical semiconductors for room-temperature applications.

Thiophene (C_4H_4S), for example, has a melting temperature of only $-38\,^{\circ}C$ and has not been reported as being used for electronic applications. Both 2,2′-bithiophene ($C_8H_6S_2$) and 2,2′:5′2″-terthiophene are solids at ambient temperatures, with melting temperatures of 32 and 93 °C, respectively. The larger oligothiophenes, i. e., quaterthiophene (four thiophene rings), quinquethiophene (five thiophene rings) [25.38], hexathiophene (sexithiophene, six thiophene rings) [25.24] or the longest synthesized octathiophene (eight thiophene rings), are all solid at room temperature and numerous authors report the use of these oligothiophene for field-effect transistors. The longest oligothiophene, α-8T is difficult to synthesize, as it needs high temperatures for evaporation but is not very stable around the gas-phase growth temperature of 340 °C [25.39]. However the polymer polythiophene, and its derivatives, are soluble and are again very popular as thin-film field-effect-transistor materials.

Similar relations exist in the polycyclic aromatic hydrocarbons. Benzene is a liquid at room temperature; naphthalene is a volatile solid, anthracene melts at 210 °C, but photodimerizes under illumination. The longer hydrocarbons from the acene family, tetracene (naphthacene) and pentacene, are relatively stable solids with excellent semiconducting properties [25.40]. The next in the series, with six (hexacene) and seven (heptacene) conjugated benzene rings, are hard to synthesize and not very stable [25.41]. The polymer, an infinite linear chain of acenes or cyclic polyacenes, has not been synthesized [25.42].

The most frequently used single-crystal growth method for organic semiconductors are the numerous modifications of the vapor growth technique. Most organic molecules possess sufficient vapor pressure that the vapor growth method can be efficiently used. Some materials, such as anthracene, tetracene, pentacene, and

rubrene, have been crystallized in sealed ampoules in the form of needles, platelets or even large bulk single crystals. However, most organic semiconductors have been grown by evaporation and condensation in a carrier gas stream. Oligothiophenes and acenes, for example, have been grown from the vapor phase, and resulting single crystals have been used for physical measurements as well as device preparation. Many organic molecules, designed and synthesized for exploration of their semiconducting properties, have been evaporated during heating and crystallized in the form of small (only a few to tens of micrometers long) crystals. Such small crystals may have sufficient quality that the crystal structure can be determined by diffraction methods (where dimensions of the order of $50 \times 50 \times 5\,\mu m^3$ are needed).

For some applications, such as scintillation detectors, where large crystals of a few cubic centimeters are required, the melt growth techniques are more practical. However, for other applications such as field-effect transistors, large crystals need to be cut and polished before preparing devices on their surfaces. Time-of-flight measurements revealed that the bulk quality of large organic crystals may be superior compared with at their surfaces. Unfortunately, due to the requirement for stability of the material up to the melting point, very few organic semiconductors have been grown from the melt.

Though the large molecules of oligothiophenes, acenes, and many others are excellent organic semiconductors, they have low vapor pressure, making it difficult to use them in gas-phase transport setups, and they often decompose before melting, excluding melt growth techniques. Additionally they show only limited solubility in solvents. These large molecules are sometimes functionalized with long alkane chains to improve solubility, but the substitution creates new molecules and therefore changes the physical properties of the semiconductor. Thus, due to their low solubility, crystals can only be grown from solvents by using high pressures and temperatures in a solvothermal method. However, to date, the quality of solvothermal-grown crystals was not optimized and the quality was insufficient for practical applications.

25.5.1 Melt Growth

Generally, materials that may be purified by zone melting may be crystallized from a melt by either the Bridgman or Czochralski method. In the Bridgman method, the material is melted in a container in a temperature gradient in such a way that crystallization starts at the lowest point of a narrowed ampoule. In most practical Bridgman processes the ampoule is sealed; as a result, the vapor cannot escape from the system. The growth of crystals may be initiated spontaneously or on a small oriented single-crystalline seed.

In the Czochralski method, the material is melted in a crucible at a temperature slightly above the melting point. A seed crystal, which is just below the melting temperature, is pulled from the melt. The crystallization begins on an oriented monocrystalline seed. During the crystal growth process, the melt evaporates from the crucible during the crystal pulling and the vapors continuously escape from the crucible. There-

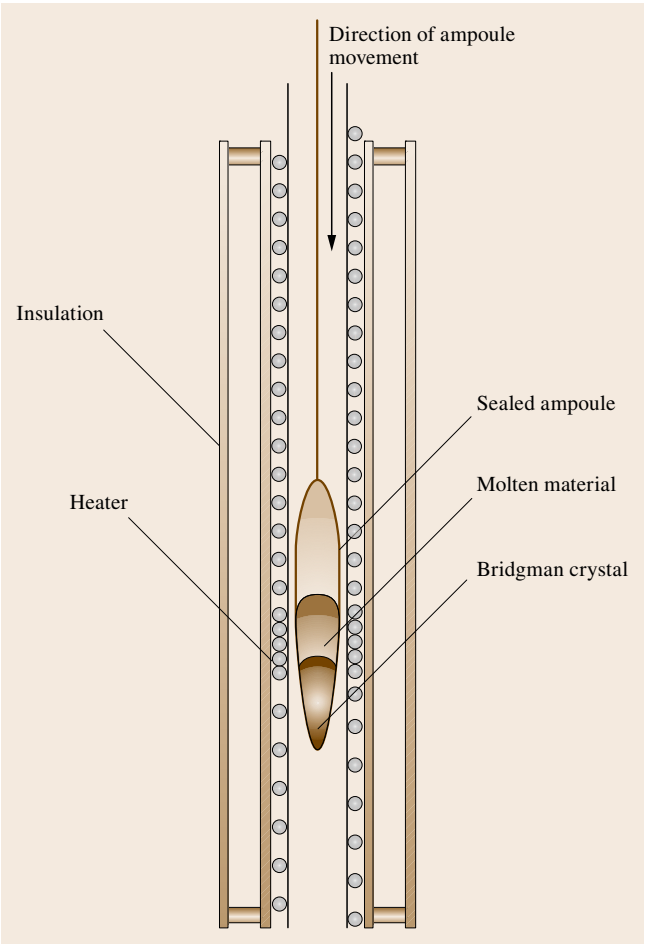


Fig. 25.7 The principle of the Bridgman crystal growth system in a sealed ampoule. A glass ampoule with molten material is moved through a temperature gradient. The crystal nucleates at the tip of the ampoule and grows from the melt when the lower part of the ampoule moves to the colder part of the furnace



Fig. 25.8 Anthracene crystal grown by the Bridgman method inside a glass ampoule; the crystal sticks to the ampoule wall and is shown before removal from the ampoule

fore this method is suitable only for low-vapor-pressure materials.

Organic Semiconductors Grown by the Bridgman Technique

Due to their thermal stability upon melting, low-weight acenes such as naphthalene, anthracene [25.43, 44], 2,3-dimethylnaphthalene [25.45], perylene [25.46], and phenanthrene [25.47] have been grown by the Bridgman technique. Similar to zone refinement, the material is placed in an ampoule sealed under vacuum or at a pressure slightly lower than ambient; for example, 400 Torr of N_2, at room temperature, may be used. In a vertical oven with two different temperature zones, the organic compound is melted in the upper, hotter zone and then slowly lowered into the cooler region for crystallization. Depending on the organic materials, the growth speed can vary over a range from 0.1 mm/h to 0.1 mm/min.

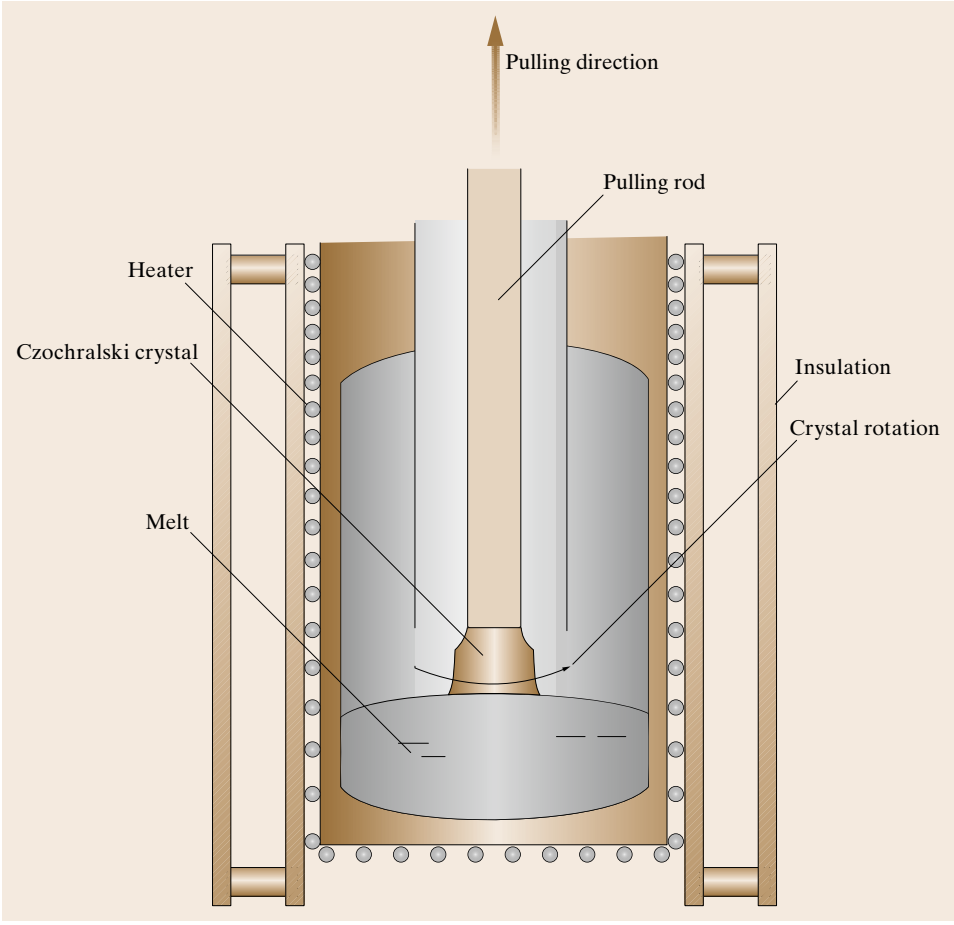


Fig. 25.9 A sketch of the Czochralski apparatus used for the growth of organic material. The pulling rod is slightly cooler than the melt. The heat is removed from the growing crystal through the pulling rod. The crystal is pulled from the melt. The vapor can escape during the growth process through the opening between pulling rod and the ampoule

To avoid possible formation of structural defects caused by mechanical vibrations during the process, the oven is moved instead of the ampoule. The resulting crystals are on the centimeter scale and provide a degree of purity that is as high as the pristine material, and sometimes even better due to the additional refinement cycle during growth.

A schematic diagram of the Bridgman crystal growth apparatus is shown in Fig. 25.7, and an anthracene single crystal grown by this method is shown in Fig. 25.8. A Pyrex or quartz glass ampoule containing a prepurified organic semiconductor is evacuated under vacuum, purged with inert gas, and sealed under vacuum or under reduced inert-gas pressure. The ampoule is heated slightly above the melting point of the material and then lowered through the temperature gradient.

Organic Semiconductors Grown by the Czochralski Technique

Crystals grown by the Bridgman method as well as ingots crystallized during zone refining suffer from cracks and stresses caused by contact with the walls of a container. To avoid this effect, the Czochralski technique was used for benzile, benzophenone, and stearic acid. The scheme of this method is presented in Fig. 25.9. A small seed crystal is slightly immersed into the melt and slowly rotated and pulled from the melt. The melt crystallizes on this seed, forming single crystals with the same orientation as the seed. The high vapor pressure of most organic compounds limits the usability of this method to a few organic semiconductors even though the quality of these crystals compares favorably with the perfection obtained by Bridgman or solution-grown crystals [25.48].

25.5.2 Growth from the Gas Phase

The most popular method of growing single crystals of many organic semiconductors is growth by gas-phase transport. The significant vapor pressure of van der Waals bonded materials [25.49] at moderate temperatures and the possible high purity and quality of vapor-grown crystals favor this method for the growth of single crystals for research purposes.

Even though the gas-phase growth technique is rather simple, the processes involved in evaporation and crystal formation are quite complex. The growth of crystals may be limited by processes occurring in the evaporating material, the gas-phase transport between evaporation and growth zone or on the surfaces of the crystal itself. Crystals may grow close to thermodynamic equilibrium within their own vapor, or far from equilibrium when the gas-phase transported molecules condense very fast or in the presence of an inert gas where molecules diffuse through the surface layer of adsorbed gas.

The growth unit of a molecular crystal is a single molecule, much larger than the growth unit of most inorganic crystals. Therefore, large molecules require additional energy to reorient, or even reconstruct, before incorporation into kinks or steps on the crystal surface.

For some molecules, the required rearrangement has been experimentally observed. Rubrene, which shows the highest charge carrier mobility at room temperature, crystallizes very poorly or as an amorphous layer if the growth temperature is low. The molecules strike a surface and stick to it where they hit, forming an amorphous conglomerate [25.16]. However, by increasing the growth temperature, the crystalline quality of thin films significantly improves [25.16]. To achieve a high enough growth temperature during condensation of rubrene thin film, a semiclosed method, i.e., hot-wall epitaxy, allowing growth at high vapor pressure, was used. Even higher growth temperatures are practical for rubrene and large well-formed rubrene single crystals are routinely obtained.

The presence of inert gas, in either an open or sealed system, radically changes the growth modus. *Horowitz*

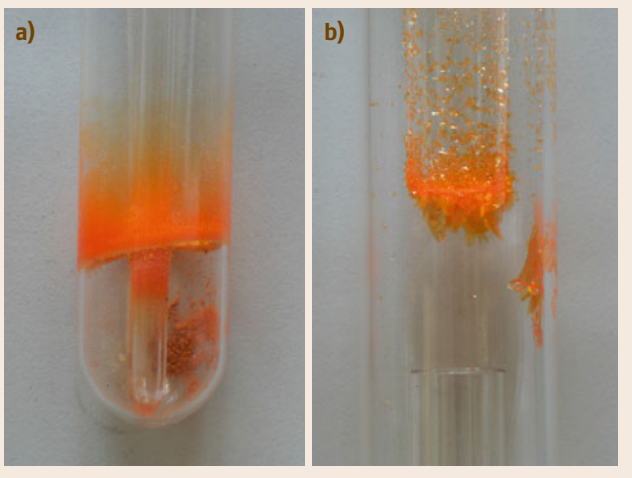


Fig. 25.10a,b α-Hexathiophene grown from the vapor phase. **(a)** Powder evaporated from the lower part of the ampoule, deposited in vacuum on the wall in the form of a fine crystalline powder. No crystals are observed. **(b)** When the ampoule was filled with 1 atm of an inert gas, up to centimeter-size crystals grew at the colder part of the ampoule

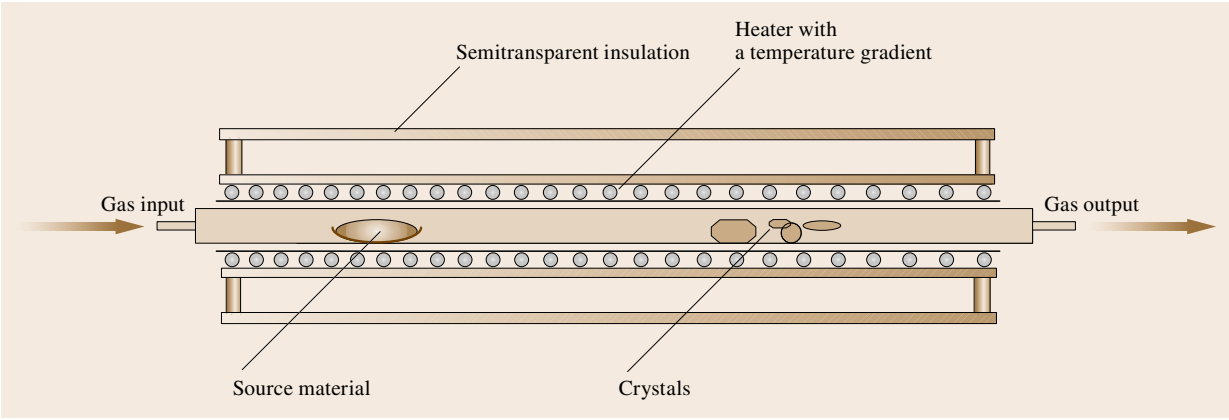
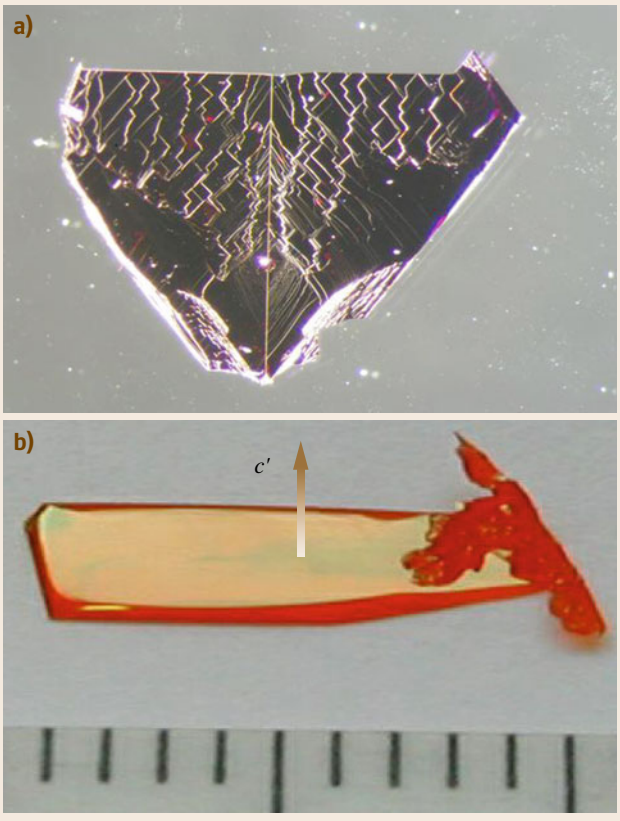


Fig. 25.11 The principle of a vapor-phase transport crystal growth system. The inert gas flows through the reactor, causing transport of molecules from high temperature, where the material evaporates, to the low temperature, where the material deposits. The high vapor pressure impurities are transported with the gas stream out of the furnace and the heavy contaminants remain at the evaporation zone. The presence of an inert gas modifies the surface processes, resulting in spontaneous formation of single crystals



et al. reported α-hexathiophene single crystals grown at a few mbar of argon [25.50].

However, α-hexathiophene, during evaporation in vacuum, deposits as a powder, independent of the temperature gradient. At higher temperature, the vacuum evaporation is very fast and molecules are not able to rearrange before attaching to the growth sides and thus form a powder rather than crystals. After introducing an inert gas into the ampoule or applying a gas flow in an open system, the evaporation rate was significantly reduced, allowing even higher temperatures for evaporation and crystal growth. The molecules gain additional thermal energy, allowing surface diffusion to the nearest growth steps. There the molecules rearrange before forming single-crystalline platelets with well developed faces [25.37]. The same improvement in crystal growth was observed for quaterthiophene [25.51, 52].

At temperatures only slightly lower than the melting point, the occurrence of a rough or even quasiliquid surface layer is assumed. This layer influences the

Fig. 25.12a,b Examples of crystals grown from vapor phase. **(a)** Tetramethylpentacene grown in an inert gas stream: growth steps are visualized due to the use of illumination at shallow angle of incidence. **(b)** Tetracene grown in a closed ampoule: monolayer-high growth steps occur on the crystal surface (steps not visualized) ◀

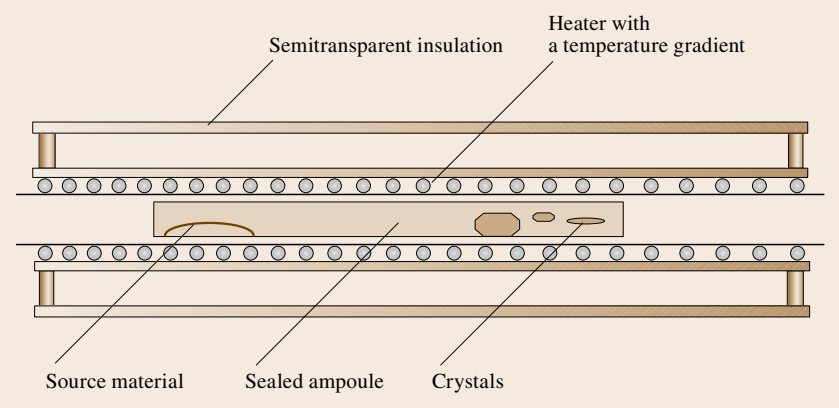


Fig. 25.13 Vapor-phase growth in a sealed glass ampoule. The ampoule may be filled with an inert gas under controlled pressure. The impurities cannot be removed from the ampoule during the growth process

adsorption, migration, surface diffusion, surface rearrangement, and nucleation of molecules and helps in the attachment of molecules to the crystal surface [25.53].

Various modifications of the gas-phase crystal growth technique have been described. They may be divided into processes run in sealed ampoules or in open tubes. Both processes, in a sealed or open tube, may run either in vacuum or in an inert gas atmosphere. In a sealed ampoule, the starting material is enclosed in a glass ampoule and the amount of the material is not changed during the process. However, due to chemical reactions, such as decompositions, photoreactions, polymerization, and others, the chemical composition of the material in a sealed ampoule may change. In an open tube system, a carrier gas is injected through one end of the tube and escapes from the other. The material for crystallization is located in the heated part of the tube, evaporates from there at elevated temperature, and condenses in the colder part of the tube [25.54]. The crystallizing material may undergo similar reactions as in the sealed ampoule. It may further react with the carrier gas and escape with it from the growth tube. The resulting composition and the amount of the material in the system may therefore change during the growth process.

Both variations of gas-phase crystal growth require only small quantities of the starting material. Therefore, many organic compounds have been grown in the form of small needles or platelets. These crystals, while often not large enough for device preparation, are large enough for x-ray diffraction analysis and structure determination. However to grow single crystals large enough for device fabrication, the process parameters need to be further optimized. To keep the temperature gradient between the evaporating and growing material small, sealed ampoules have frequently been used. To lower the evaporation rate and run the growth processes at higher temperatures, an inert gas has been introduced in both sealed and open systems. To purify the material during growth, the open system is preferred, as impurities are carried away from the growing crystal by a stream of inert gas.

Sublimation in sealed ampoules filled with an inert gas has been efficiently used for growth of anthracene, chrysene, diphenyl, *p*-terphenyl, acridine, pyrene, naphthalene, phenanthrene, and benzanthracene. Fluorescence measurements have been performed on such crystals [25.55].

Rubrene and pentacene crystals have been grown in a small temperature gradient formed in a vacuum sealed glass ampoule [25.31, 56]. In both cases growth temperatures were lower than the corresponding temperatures for growth in the gas stream. Also, the crystals produced by vacuum growth were much thicker because the surface migration of adsorbed molecules was limited at lower temperatures. However, the same

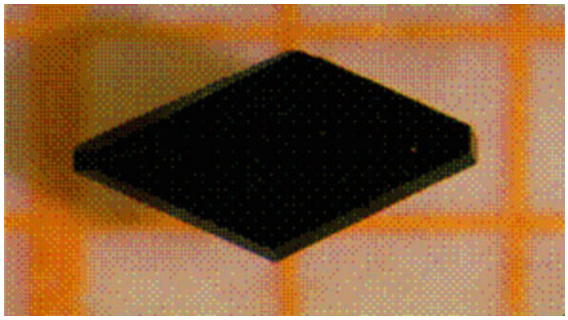


Fig. 25.14 C_{60} crystal grown in a sealed quartz-glass ampoule

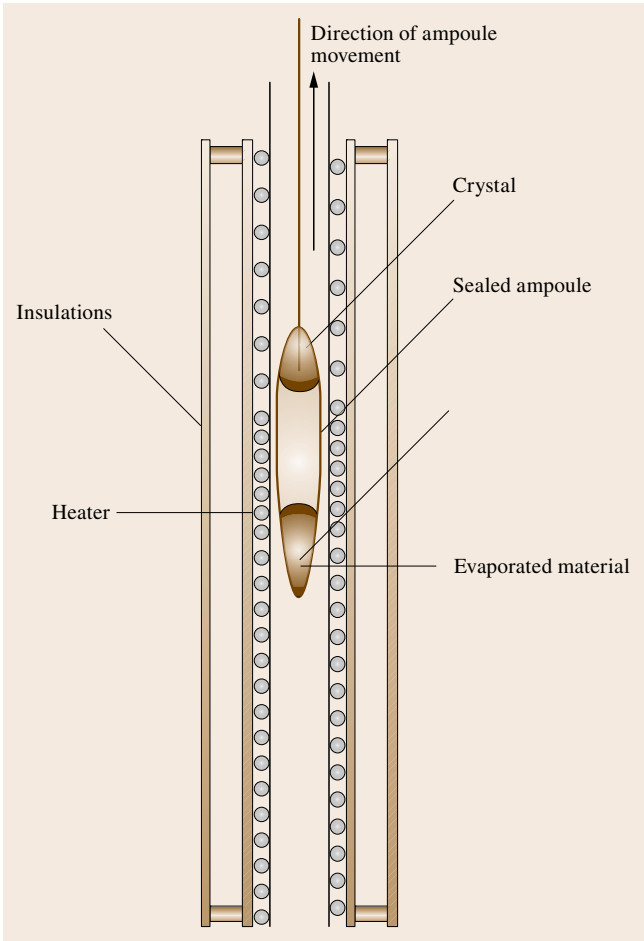


Fig. 25.15 Schematic diagram of the gas-phase growth of crystals while pulling the ampoule through a temperature gradient. Crystal nucleates in the narrow tip of the ampoule during pulling of the ampoule from the high-temperature zone in the lower part of the furnace to the colder, upper part of the furnace



Fig. 25.16 Tetracene crystal formed in the tip of an ampoule while pulling the ampoule through a temperature gradient

growth technique was absolutely inadequate for oligothiophenes, where a gas flow is required to keep a high temperature and to remove impurities from the system.

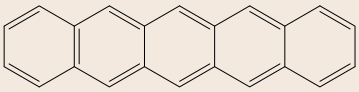
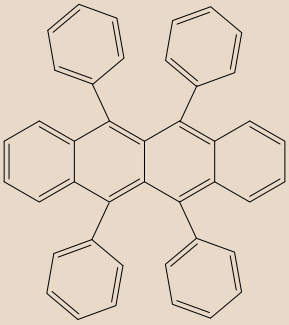
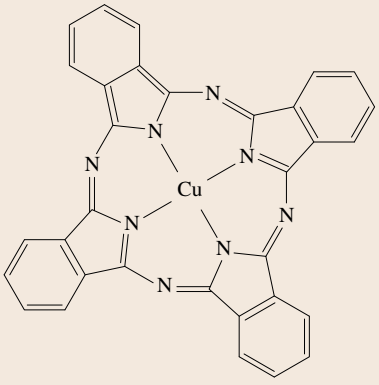
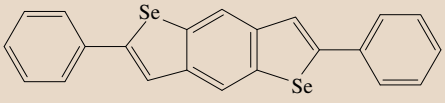
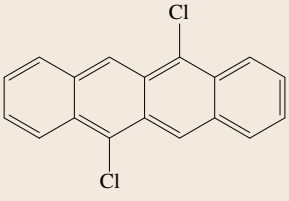
Larger crystals may be obtained from the gas phase by pulling a sealed glass ampoule up through a temperature gradient (the inverse of the Bridgman technique). In this technique, the material evaporates from the lower, hotter part of the ampoule and condenses at a narrow tip of an ampoule pulled into the colder part of the furnace. The conical tip of the ampoule is filled by the growing crystal. Tetracene single crystals have been successfully grown by pulling the ampoule with a speed of 5 mm/day [25.57].

During the growth in a sealed ampoule, even if prepurified materials are used, some impurity molecules may be formed by decomposition, and some impurity molecules intercalated in the source material may be discharged during heating. To avoid contamination of the growing crystals, a part of the vapor may be removed through a small effusion hole placed close to the conical tip of the ampoule. This method, known as semi-open physical vapor transport, has been successfully used to grow nonlinear optical crystals [25.58, 59], but has not been explored for organic semiconductors.

One of the striking features of sublimation-grown crystals is their morphological habit. Many of the polyacenes, rubrene, and perylene derivatives show a preferred two-dimensional growth with aspect ratio between lateral extension and height of the order of 10^2–10^4. Such crystals are most suitable for transport studies carried out in field-effect transistor (FET) geometry by preparing metal contacts by thermal evaporation after growth. Since these measurements are governed by the charge carrier transport along the topmost layers of the crystal surface, contamination after growth by, for instance, photo-oxidation, has to be minimized by sample handling in a glovebox, under controlled lighting, etc.

The results of some field-effect transistor studies on organic single crystals with mobility values equal to or larger than 1 $cm^2/(V\,s)$ are presented in Table 25.1.

Table 25.1 Organic semiconductors with a single-crystal field-effect transistor mobility above 1 $cm^2/(V\,s)$

Structure	Mobility [$cm^2/(V\,s)$]	Reference
 Pentacene	2.2	*Roberson* et al. [25.31]
 Rubrene	13	*Zeis* et al. [25.56]
 Copper phthalocyanine	1.0	*Zeis* et al. [25.60]
 2,6-Diphenylbenzo[1,2-*b*:4,5-*b*′]diselenophene	1.3	*Zeis* et al. [25.61]
 Dichlorotetracene	1.6	*Moon* et al. [25.62]

25.5.3 Solvent-Based Growth Methods

The solubility, vapor pressure, and stability of molecules declines with increasing mass of the organic semiconductor. Therefore melt or gas-phase crystal growth methods are unsuitable for large molecules, since the molecules tend to break apart before melting or evaporation. The only growth method available in such cases is solution growth close to room temperature. In analogy to inorganic materials, the solubility may be increased by high pressure and moderate temperatures below the melting point, similar to quartz crystals, which are grown by the hydrothermal method a few hundred degrees below the melting point of SiO_2.

This concept has been used for organic materials [25.63], where a pressurized solvent (instead of water), was used. With this solvothermal method, it was shown that the practically insoluble material, hexathiophene, is well soluble in benzyl phenyl sulfide sealed in a glass ampoule. During cooling, hexathiophene precipitates to form small platelets. The crystal growth process has not been optimized, and resulting crystals were only a few hundred micrometers in dimensions, insufficient for transistor fabrication or transport measurement.

Small or polar molecules were successfully grown from organic solvents. During solvent evaporation or during cooling of saturated solutions, the material precipitates in the form of crystalline powders or, sometimes, small crystals. This is the method of choice for growth of small crystals for x-ray crystal structure determination. However, the solvent may intercalate or even form ordered mixed crystals. Larger crystals of organic semiconductors, such as anthracene and pyrene, were also grown from solvents by solvent evaporation or by temperature lowering and have been used for semiconducting parameter evaluation. Anthracene and pyrene crystals of a few millimeters, formed by slow evaporation of a solvent, were successfully used for dark conductivity and photoconductivity measurements [25.46].

Anthracene crystals with up to $2\,cm^2$ in area have been grown while suspended in a solvent. The essential feature of this method is the choice of the solvent, ethylene dichloride, with a density that is slightly greater than the density of anthracene at room temperature. Since the density of the solvent decreases faster than the density of anthracene upon heating, it is possible to find a temperature at which both solvent and anthracene density are equal and the crystal can be suspended and grown in solution. Additionally, a layer of xylene (a poor solvent for anthracene) was placed on the top of the anthracene/ethylene chloride solution. Xylene prevents ethylene dichloride from evaporating and further diffuses slowly into the ethylene dichloride and causes a decrease in anthracene solubility, thus creating supersaturation. Under such conditions, crystals can grow undisturbed while suspended in the solvent [25.64].

Further, large crystals of organic materials for nonlinear optics applications have been grown from solvents [25.65]. However, these crystals are transparent large-gap insulators and do not show properties typical of organic semiconductors; they are therefore not discussed in this chapter.

25.6 Quality of Organic Semiconducting Single Crystals

To understand the electronic properties of organic semiconductors, high-quality single crystals are required. In the past the structural quality of gas-phase-grown anthracene and Bridgman-grown 2,3-dimethyl naphthalene were studied with x-ray topography [25.19]. Because anthracene grew in the form of very thin platelets that were strongly warped, x-ray topography was severely hampered. Large, ultrapure Bridgman-grown anthracene as well as 2,3-dimethyl naphthalene single crystals were used for time-of-flight measurement of charge carrier mobilities. The x-ray topographs of these crystals revealed that defects were formed after the crystal growth process, during cooling of the crystals from the growth temperature to room temperature, during removal from ampoules, and during sample preparation for measurements. However, if properly and carefully handled, the quality of cleaved lamellae prepared from Bridgman-grown ingots displayed a highly perfect mosaic with only a few dislocations appearing, mostly at the side where the cleavage process caused stress and glide dislocations [25.19].

Double-crystal x-ray topography was performed on rubrene single crystals grown from the vapor phase [25.66]. In comparison with other organic semiconductors that crystallize in lower symmetries (monoclinic or triclinic), rubrene crystallizes in the orthorhombic system. Besides thin platelets, rubrene forms also thicker crystals suitable for structure analysis. The thermal expansion is not very anisotropic. The rocking curve width of a few crystals (selected

under polarized light from a large batch grown in numerous growth runs) revealed a full-width at half-maximum (FWHM) of the (12 0 0) reflection of 0.013° for the best samples. Such a narrow rocking curve was also observed for the (004) reflection, but the FWHM was twice as large for the (020) reflection. Such a low mosaic spread is among the best exhibited by organic crystals. However, many other measured rubrene crystals displayed larger FWHMs of the order of 0.15°. The mechanism of forming such mosaic spreads in these crystals is not known. Furthermore, it is assumed that both the growth process and, more probably, any temperature gradient formed during the crystal cooling are responsible for defect formation in these crystals, often with an inhomogeneous distribution of dislocations.

Rubrene single crystals show high charge carrier mobility, close to ten times larger than values seen in other organic semiconductors such as tetracene or pentacene. However, the mechanisms by which defects, impurities, and intra- and intermolecular structure impact on charge carrier mobility is not clear as of today.

25.7 Organic Single-Crystalline Field-Effect Transistors

At the foundation of organic semiconductors as an active element of plastic electronics is the ability to use assemblies of molecules in FETs. Charge carrier transport has attracted attention for decades and was often studied using thin-film FET structures. In contrast, only a limited number of groups have focused on intrinsic electronic properties of single-crystal organic semiconductors. While the measurements on thin films, which are the configurations used for applications, are useful and indicate the potential of a particular organic compound, the presence of grain boundaries, impurities, and defects obscures the intrinsic performance that one can expect to achieve from a specific material. The alternative approach for evaluation and selection is the fabrication of an FET structure directly on a single crystal. In this way, the most efficient π-conjugated molecules can be selected from among the many commercially available organic compounds. The latter method allows better evaluation of intrinsic properties of organic semiconductors because the optical, electrical, and other properties are directly dependent on molecular properties of individual molecules that self-assemble (crystallize) on a nanoscale into well-ordered oriented grains, macroscopically defining a single crystal.

FET structures prepared on the natural surfaces of single crystals were described previously [25.8]. Two general variations are used. In the first, the source and drain electrodes, dielectric layer, and gate electrodes are fabricated by different techniques on a silicon wafer or plastic foil, and the single crystal is *stamped* (placed) onto such a device structure. In the second variation, the source and drain contacts are evaporated or printed onto the natural surface of a single crystal, then the dielectric is spun on or evaporated onto the crystal, and finally the gate electrode is fabricated on the dielectric layer. In the first method a strongly doped silicon wafer covered by an insulating layer of silicon oxide (SiO_2) with deposited metallic (mostly gold) electrodes

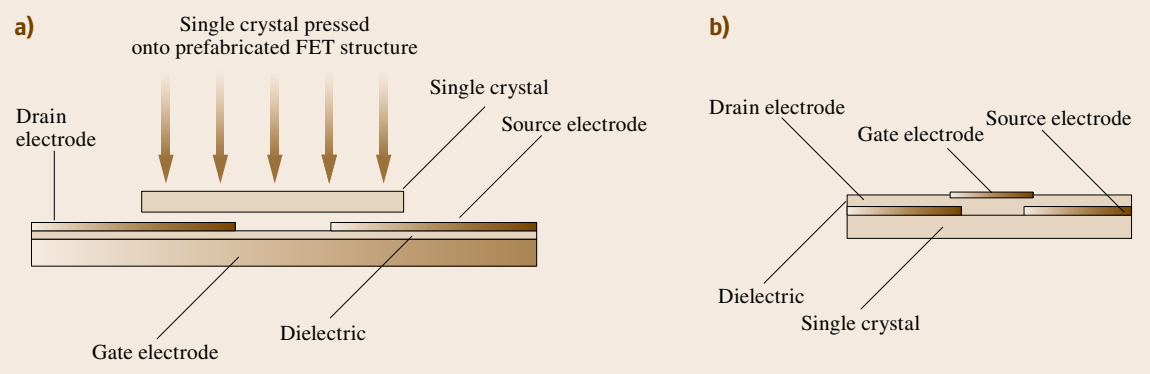


Fig. 25.17a,b Schematic diagram of two types of single-crystal field-effect transistor fabrication. **(a)** The FET electrodes and dielectric are prefabricated and a single crystals is attached by adhesion to the FET structure. **(b)** Electrodes and dielectric are built up step by step on the natural surface of a single crystal

is used as a support for crystals, which are gently affixed by adhesion to form the channel region between the source and gate electrodes. Good adhesion between the prefabricated FET support and crystal is crucial for proper operation of such a device. A similar concept of a prefabricated FET structure has been realized by using either a transparent indium oxide gate on glass or flexible foil and spun-on polymers as a gate dielectric. Again, strong adhesion between the electrodes, polymers, and crystals is crucial and may be controlled through chemical treatment of the polymer. An interesting modification of the last structure is an elastomeric stamp where the gate dielectric is replaced by an air gap. Since no direct contact between the dielectric (here air, inert gas or vacuum) and semiconductor surface occurs, the natural surface of the semiconductor may be studied and effects of the atmosphere on the FET properties may be observed.

For the second method, contact metals for p-type semiconductors are preferably gold or silver or low-work-function metals such as magnesium in the case of n-type materials. The lowest contact resistance on rubrene was obtained with painted contacts from a water-based solution of colloidal graphite. The gate insulation layer may consists of 0.5–2 μm of parylene, prepared from the dimer Parylene N or C. The dimer is evaporated at 160 °C and cracked to a monomer at 680 °C that subsequently polymerizes on the surface of a crystal kept at room temperature. The gate electrode may either be evaporated or painted (colloidal graphite) directly on the parylene layer over the channel area between source and drain contacts.

In both FET structures, the semiconductor properties are tested only in the very thin surface layer of the single crystals (or thin films in a thin-film FET). However, this surface layer may be easily affected by intercalation/adsorption of gases present in the transistor environment. In this way, chemical sensors may be constructed, where the molecules are introduced into the channel area of the FET. Additionally, with the exception of the air-gap structure, the channel area may be modified/affected by the direct contact with a gate dielectric.

The highest FET mobility of 20 $cm^2/(V\,s)$ in p-type rubrene or 1.6 $cm^2/(V\,s)$ in n-type tetracyanoquinodimethane (TCNQ) [25.67] has been obtained in such devices. However, since FET structures probe only the top surface layers, the charge carrier mobility obtained in this way is not necessarily identical to the mobilities measured in the bulk.

The surface charge transport mobility generally decreases with decreasing temperature, an effect attributed to trapping states present at the surface. The bulk charge transport values of electrons and holes may be much higher, as was demonstrated by time-of-flight measurements in naphthalene, anthracene or perylene at low temperatures. In these cases the superior transport properties were attributed to meticulous purification and bulk crystal growth optimization as well as the insensitivity of the bulk properties on chemically poorly defined surface states.

In any case, electronic transport measurements are indispensable tools in evaluating the electronic traps affecting the charge transport in organic semiconductors. Together with optical methods and x-ray topography and diffraction to measure structural quality and elemental/molecular purity, the overall crystal quality of organic semiconductors can be efficiently assessed.

25.8 Conclusions

Single crystals of organic semiconductors have been grown mostly for basic research studies, for structure evaluation as well as for evaluation of maximum performance of organic semiconductors devices. Many purification and crystal growth methods have been applied to organic single crystals. Gas-phase transport is often used for growth of crystals used for field-effect transistors and x-ray structure determinations, whereas the Bridgman method dominates the growth of large crystals. So far, the highest electron and hole mobilities measured by the time-of-flight method have been achieved on crystals purified by extensive zone refining and grown from the melt by the Bridgman method. However, the highest field-effect mobilities have been achieved on crystals purified by sublimation and grown from the vapor phase. The difference in mobilities between the bulk and surface measurements is attributed to different types of defects and contamination in the bulk and on the surfaces. These measurement values still reflect extrinsic effects and do not yet measure the intrinsic properties of organic semiconductor.

As of today, there are not enough studies of quality, purity, defect concentration, and optical and electrical properties on the same material grown by different methods. On the one hand this is a result of the instability of organic compounds and associated changes of

their properties with time, while on the other hand it is challenging to use specific analysis methods for precise characterization of brittle crystals where defects alter with aging. Organic semiconductors need defect and impurity evaluation at part-per-million levels, similar to inorganic semiconductors. Even though organic semiconductors are much less studied than their inorganic counterparts, it seems that organic semiconductors will be an important component of future microelectronics. Organic light-emitting diodes (OLEDs) and displays are already commercially available. However, progress in organic material characterization is needed to guide improvements in purification and crystal growth that will consequently lead to the development of new, better organic semiconductors and higher-performance devices.

References

25.1 A. Byk, H. Borck: Photoelektrische Versuche mit Anthracen, Verh. Dtsch. Phys. Ges. **12**(15), 621–651 (1910)

25.2 J.B. Birks: *Scintillation Counters* (Pergamon, London 1953)

25.3 S.R. Forrest: The path to ubiquitous and low-cost organic electronic applications on plastic, Nature **428**, 911–918 (2004)

25.4 E. Reichmanis, H. Katz, C. Kloc, A. Maliakal: Plastic electronic devices: from materials design to devices applications, Bell Labs Tech. J. **10**, 87–105 (2005)

25.5 G. Horowitz, M. Hajlaoui: Mobility in polycrystalline oligothiophene field-effect transistors dependent on grain size, Adv. Mater. **12**, 1046–1050 (2000)

25.6 T.W. Kelley, C.D. Frisbie: Gate voltage dependent resistance of a single organic semiconductor grain boundary, J. Phys. Chem. B **105**, 4538–4540 (2001)

25.7 N. Karl: Charge-carrier mobility in organic crystals. In: *Organic Electronic Materials, Springer Series in Material Science*, Vol. 41, ed. by R. Farchioni, G. Grosso (Springer, Berlin Heidelberg 2001) pp. 283–326, Part II: Low Molecular Weight Organic Solids

25.8 M.E. Gershenson, V. Podzorov, A.F. Morpurgo: Colloquium: Electronic transport in single-crystal organic transistor, Rev. Mod. Phys. **78**, 973–989 (2006)

25.9 D.T.J. Hurle (Ed.): *Handbook of Crystal Growth* (Elsevier, Amsterdam 1994)

25.10 R.A. Laudise: *The Growth of Single Crystals* (Prentice-Hall, Englewood Cliffs 1970)

25.11 F.R. Lipsett: On the production of single crystals of naphthalene and anthracene, Can. J. Phys. **35**, 284–298 (1957)

25.12 N. Karl: High purity organic molecular crystals. In: *Crystals Growth, Properties and Applications*, Vol. 4, ed. by H.C. Freyhardt (Springer, Berlin Heidelberg 1980) pp. 1–100

25.13 R.A. Laudise, C. Kloc, P.G. Simpkins, T. Siegrist: Physical vapour growth of organic semiconductors, J. Cryst. Growth **187**, 449–454 (1998)

25.14 R.W.I. de Boer, M.E. Gershenson, A.F. Morpurgo, V. Podzorov: Organic single-crystal field-effect transistors, Phys. Status Solidi (a) **201**, 1302–1331 (2004)

25.15 A.T. Tripathi, M. Heinrich, T. Siegrist, J. Pflaum: Growth and electronic transport in 9,10-diphenylanthracene single crystals – An organic semiconductor of high electron and hole mobility, Adv. Mater. **19**(16), 2097–2101 (2007)

25.16 D. Käfer, G. Witte: Growth of crystalline rubrene films with enhanced stability, PhysChemChemPhys **7**, 2850–2853 (2005)

25.17 M.-C. Blüm, E. Ćavar, M. Pivetta, F. Patthey, W.-D. Schneider: Conservation of chirality in a hierarchical supramolecular self-assembled structure with pentagonal symmetry, Angew. Chem. Int. Ed. **44**, 5334–5337 (2005)

25.18 A. Gavezotti, G.R. Desiraju: A systematic analysis of packing energies and other packing parameters for fused-ring aromatic hydrocarbons, Acta Cryst. B **44**, 427–434 (1988)

25.19 H. Klapper: X-ray topography of organic crystals, Growth Cryst. **13**, 109–162 (1991)

25.20 O.H. LeBlanc: Hole and electron drift mobilities in anthracene, J. Chem. Phys. **33**, 626 (1960)

25.21 R.G. Kepler: Charge carrier production and mobility in anthracene crystals, Phys. Rev. **119**, 1226–1229 (1960)

25.22 J.B. Birks: *Scintillation Counters* (Pergamon, London 1953)

25.23 G. Horowitz, D. Fichou, X.Z. Peng, Z.G. Xu, F. Garnier: A field-effect transistor based on conjugated alpha-sexithienyl, Solid State Commun. **72**, 381–384 (1989)

25.24 G. Horowitz, F. Garnier, A. Yassar, R. Hajlaoui, F. Kouki: Field-effect transistor made with a sexithiophene single crystal, Adv. Mater. **8**, 52–54 (1996)

25.25 G.S. Hammond, V.J. Kuck (Eds.): *Fullerenes, Synthesis, Properties, and Chemistry of Large Carbon Clusters* (ACS, Washington 1992)

25.26 F.H. Moser, A.L. Thomas (Eds.): *The Phthalocyanines, Properties* (CRC, Boca Raton 1983)

25.27 A. Facchetti, H.E. Katz, T.J. Marks, J. Veinot: Organic semiconductor materials. In: *Printed Organic and Molecular Electronics*, ed. by D. Gamota, P. Brazis, K. Kalyanasundaram (Kluwer, Dordrecht 2004)

25.28 W. Warta, R. Stehle, N. Karl: Ultrapure, high mobility organic photoconductors, Appl. Phys. A **36**, 163–170 (1985)

25.29 E.A. Chandross, J. Ferguson: Photodimerization of crystalline anthracene. The photolytic disscociation of crystalline dianthracene, J. Chem. Phys. **45**, 3564–3567 (1966)

25.30 O.D. Jurchescu, J. Baas, T.M. Palstra: Effect of impurities on the mobility of single-crystal pentacene, Appl. Phys. Lett. **84**, 3061–3063 (2004)

25.31 L.B. Roberson, J. Kowalik, L.M. Tolbert, C. Kloc, R. Zeis, X. Chi, R. Fleming, C. Wilkins: Pentacene disproportionation during sublimation for field-effect transistors, J. Am. Chem. Soc. **127**, 3069–3075 (2005)

25.32 G. Pfann: Principles of zone-melting, J. Metals **4**, 747–753 (1952)

25.33 K.H. Probst, N. Karl: Energy levels of electron and hole traps in the band gap of doped anthracene crystals, Phys. Status Solidi (a) **27**, 499–508 (1975)

25.34 K.H. Probst, N. Karl: Energy levels of electron and hole traps in the band gap of doped anthracene crystals, Erratum, Phys. Status Solidi (a) **31**, 793 (1975)

25.35 G.J. Sloan, A.R. McGhie: Purification of tetracene: vapor zone refining and eutectic zone melting, Mol. Cryst. Liq. Cryst. **18**, 17–37 (1972)

25.36 M. Brissaud, C. Dolin, J. Le Duigou, B.S. McArdle, J.N. Sherwood: The purification and growth of large ultra-pure plastic single crystals of trimethylacetic acid, J. Cryst. Growth **38**, 134–138 (1977)

25.37 C. Kloc, P.G. Simpkins, T. Siegrist, R.A. Laudise: Physical vapor growth of centimeter-sized crystals of α-hexathiophene, J. Cryst. Growth **182**, 416–427 (1997)

25.38 M. Melucci, M. Gazzano, G. Barbarella, M. Cavallini, F. Biscarini, P. Maccagnani, P. Ostoja: Multiscale self-organization of the organic semiconductor α-quinquethiophene, J. Am. Chem. Soc. **125**, 10266–10274 (2003)

25.39 D. Fichou, B. Bachet, F. Demanze, I. Billy, G. Horowitz, F. Garnier: Growth and structural characterization of the quasi-2-D single crystal of α-octithiophene, Adv. Mater. **8**, 500–504 (1996)

25.40 J. Cornil, J.P. Calbert, J.L. Bredas: Electronic structure of pentacene single crystal: relation to transport properties, J. Am. Chem. Soc. **123**, 1250–1251 (2001)

25.41 W.J. Bailey, C.-W. Liao: Cyclic dienes XI. New syntheses of hexacene and heptacene, J. Am. Chem. Soc. **77**, 992–993 (1955)

25.42 S. Kivelson, O.L. Chapman: Polyacene and a new class of quasi-one-dimensional conductors, Phys. Rev. B **28**, 7236–7243 (1983)

25.43 H. Mette, H. Pick: Elektronenleitfähigkeit von Anthracen-Einkristallen, Z. Phys. **134**, 566–575 (1953), in German

25.44 H. Pick, W. Wissman: Elektronenleitung von Naphthalin-Einkristallen, Z. Phys. **138**, 436–440 (1954), in German

25.45 M. Tachibana, K. Kono, M. Shimizu, K. Kolima: Growth and dislocation characteristics of organic molecular crystals: 2,3-Dimethylnaphthalene, J. Cryst. Growth **198/199**, 665–669 (1999)

25.46 H. Inokuchi: Semi- and photo-conductivity of molecular single-crystals. Anthracene and pyrene, Bull. Chem. Soc. Jpn. **29**, 131–133 (1956)

25.47 B.J. McArdle, J.N. Sherwood: The growth and perfection of phenantrene single crystals, J. Cryst. Growth **22**, 193–200 (1974)

25.48 J. Bleay, R.M. Hooper, R.S. Narang, J.N. Sherwood: The growth of single crystals of some organic compounds by the Czochralski technique and the assessment of their perfection, J. Cryst. Growth **43**, 589–596 (1978)

25.49 C. Kloc, R.A. Laudise: Vapor pressures of organic semiconductors: α-hexathiophene α-quaterthiophene, J. Cryst. Growth **193**, 563–571 (1998)

25.50 G. Horowitz, B. Bachet, A. Yassar, P. Lang, F. Demanze, J. Fave, F. Garnier: Growth and characterization of sexithiophene single crystals, Chem. Mater. **7**, 1337–1341 (1995)

25.51 T. Siegrist, C. Kloc, R.A. Laudise, H.E. Katz, R.C. Haddon: Crystal growth, structure, and electronic band structure of α-4t polymorphs, Adv. Mater. **10**, 379–382 (1998)

25.52 L. Antolini, G. Horowitz, F. Kouki, F. Garnier: Polymorphism in oligothiophenes with an even number of thiophene subunits, Adv. Mater. **10**, 382–385 (1998)

25.53 T. Kuroda: Vapor growth mechanism of a crystal surface covered with a quasi-liquid layer – Effect of self-diffusion coefficient of the quasi-liquid layer on the growth rate, J. Cryst. Growth **99**, 83–87 (1990)

25.54 H. Meng, M. Bendikov, G. Mitchell, R. Helgeson, F. Wudl, Z. Bao, T. Siegrist, C. Kloc, C. Chen: Tetramethylpentacene: Remarkable absence of steric effect on field effect mobility, Adv. Mater. **15**, 1090–1093 (2003)

25.55 L.E. Lyons, G.C. Morris: Photo- and semiconductance in organic crystals. Part III. Photoeffects in dry air with eleven organic compounds, J. Chem. Soc. August, 3648–3660 (1957)

25.56 R. Zeis, C. Besnard, T. Siegrist, C. Schlockermann, X. Chi, C. Kloc: Field-effect studies on rubrene and impurities of rubrene, Chem. Mater. **18**, 244–248 (2006)

25.57 J. Niemax, A.K. Tripathi, J. Pflaum: Comparison of the electronic properties of sublimation- and vapor-Bridgman-grown crystals of tetracene, Appl. Phys. Lett. **86**, 122105 (2005)

25.58 G. Zuccalli, M. Zha, L. Zanotti, C. Paorici: Vapour growth of organic crystals by a semi-open Piz-

zarello (SOP) technique, Mater. Sci. Forum **203**, 35–38 (1996)
25.59 R.S. Fiegelson, R.K. Route, T.-M. Kao: Growth of urea crystals by physical vapor transport, J. Cryst. Growth **72**, 585–594 (1985)
25.60 R. Zeis, T. Siegrist, C. Kloc: Single-crystal field-effect transistors based on copper phthalocyanine, Appl. Phys. Lett. **86**, 022103 (2005)
25.61 R. Zeis, C. Kloc, K. Takimiya, Y. Kunugi, Y. Konda, N. Niihara, T. Otsubo: Single-crystal field-effect transistors based on organic selenium-containing semiconductor, Jpn. J. Appl. Phys. **44**(6A), 3712–3714 (2005)
25.62 H. Moon, R. Zeis, E.-J. Borkent, C. Besnard, A.J. Lovinger, T. Siegrist, C. Kloc, Z. Bao: Synthesis, crystal structure, and transistor performance of tetracene derivatives, J. Am. Chem. Soc. **126**, 15322–15323 (2004)
25.63 A.R. Laudise, P.M. Bridenbaugh, C. Kloc, S.L. Jouppi: Organo-thermal crystal growth of α6 thiophene, J. Cryst. Growth **178**, 585–592 (1997)
25.64 H. Kallman, M. Pope: Preparation of thin anthracene single crystals, Rev. Sci. Instrum. **29**, 993–994 (1958)
25.65 L. Zeng, M. Zha, M. Curti, L. Zanotti, C. Paorici: Solution growth for high anisotropy organic crystals, Mater. Sci. Forum **203**, 39–42 (1996)
25.66 B.D. Chapman, A. Checco, R. Pindak, T. Siegrist, C. Kloc: Dislocations and grain boundaries in semiconducting rubrene single crystals, J. Cryst. Growth **290**, 479–484 (2006)
25.67 E. Menard, V. Podzorov, S.-H. Jur, A. Gaur, M.E. Gershenson, J.A. Rogers: High performance n- and p-type single-crystal organic transistors with free-space gate dielectrics, Adv. Mater. **16**(22/23), 2097–2101 (2004)

26. Growth of III-Nitrides with Halide Vapor Phase Epitaxy (HVPE)

Carl Hemmingsson, Bo Monemar, Yoshinao Kumagai, Akinori Koukitu

III-nitrides can be grown by employing several different techniques, such as molecular-beam epitaxy (MBE), metalorganic vapor-phase epitaxy (MOVPE), halide vapor-phase epitaxy (HVPE), high-pressure solution growth, and sputtering. Each of these are suited for a particular application; the specific property of HVPE is a much larger growth rate, which makes this technique the natural choice for growth of very thick layers that can be used as high-quality native substrates for subsequent growth of device structures using other techniques. Such substrates will be needed for certain devices with high current density or high voltage load, where the high defect density caused by growth on foreign substrates (heteroepitaxy) cannot be tolerated. The HVPE technology is still under development, and below we present the present situation with emphasis on GaN. The thermodynamic limitations of HVPE growth are discussed first, including the high-temperature chemistry in both the source zone and growth zone of a growth reactor. Examples of the design of growth systems are given; in particular, issues such as flow patterns, parasitic growth, and growth rates are discussed. Methods to reduce the defect density for growth on foreign substrates are discussed, as well as various lift-off techniques to prepare free-standing GaN wafers. Common characterization techniques are mentioned, and important physical properties of high-quality GaN wafers are given. The ongoing developments of HVPE growth for AlN and InN are also briefly summarized.

26.1 Growth Chemistry and Thermodynamics . 869
26.2 HVPE Growth Equipment 872
26.3 Substrates and Templates for Bulk GaN Growth 875
26.3.1 Sapphire 875
26.3.2 Silicon Carbide 876
26.3.3 GaAs 876
26.3.4 Lattice-Matched Substrates 877
26.3.5 Growth on Templates 877
26.3.6 Basic 1S-ELO Structures 877
26.3.7 2S-ELO 878
26.4 Substrate Removal Techniques 879
26.4.1 Laser Lift-Off 879
26.4.2 Self-Separation 880
26.4.3 Mechanical Polishing 881
26.4.4 Plasma Etching 881
26.4.5 Chemical Etching and Spontaneous Self-Separation 881
26.5 Doping Techniques for GaN in HVPE 882
26.5.1 n-Type Doping of GaN 882
26.5.2 p-Type Doping of GaN 882
26.6 Defect Densities, Dislocations, and Residual Impurities 883
26.7 Some Important Properties of HVPE-Grown Bulk GaN Material 887
26.8 Growth of AlN by HVPE: Some Preliminary Results 888
26.9 Growth of InN by HVPE: Some Preliminary Results 890
References 891

26.1 Growth Chemistry and Thermodynamics

Commonly, a HVPE reactor for growing group III nitrides (GaN, AlN or InN) consists of two main zones: the source zone for forming chloride gas of a group III metal (Ga, Al or In) and the growth zone where the chloride of a group III metal and NH_3 are mixed to grow the nitride film. Therefore, understanding of the chemistry

at both source zone and growth zone is essential to grow nitrides by HVPE.

In the source zone of a reactor, the group III metal is placed and maintained at a certain temperature. HCl gas is commonly used to form chloride gas of the group III metal. Therefore, the gaseous species formed at the source zone and their equilibrium partial pressures when HCl gas is introduced over the group III metal are important issues. Principally, gaseous species at the source zone are $III \cdot Cl$, $III \cdot Cl_2$, $III \cdot Cl_3$, $(III \cdot Cl_3)_2$, HCl, H_2, and inert gas (IG: N_2, He, Ar, etc.). The following chemical reactions occur simultaneously

$$III(s \text{ or } l) + HCl(g) = III \cdot Cl(g) + \tfrac{1}{2}H_2(g)\,, \quad (26.1)$$

$$III(s \text{ or } l) + 2HCl(g) = III \cdot Cl_2(g) + H_2(g)\,, \quad (26.2)$$

$$III(s \text{ or } l) + 3HCl(g) = III \cdot Cl_3(g) + \tfrac{3}{2}H_2(g)\,, \quad (26.3)$$

$$2III \cdot Cl_3(g) = (III \cdot Cl_3)_2(g)\,. \quad (26.4)$$

Equilibrium partial pressures of the gaseous species in the source zone can be calculated by a thermodynamic calculation [26.1]. It should be noted that a low source-zone temperature, a high HCl input partial pressure or a small surface area of group III metal might cause insufficient reactions in the source zone, i. e., the reactions will be kinetically limited.

Figure 26.1 shows equilibrium partial pressures of the gaseous species P_i in the source zone under a total pressure of the source zone ($\sum P_i$) of 1.0 atm, an input partial pressure of HCl (P^0_{HCl}) of 6×10^{-3} atm, and a mole fraction of hydrogen in the carrier gas (F^0) of 0.0 (inert carrier gas), calculated for Ga, Al, and In source zones. The source-zone temperature ranges from 300 to 1000 °C. In the Ga source zone, the major gaseous species of Ga is GaCl and its equilibrium partial pressure is almost equal to P^0_{HCl} at temperatures above 500 °C. This means that the predominant reaction at the Ga source zone is (26.1), and almost all HCl introduced into the source zone reacts with Ga metal. The In source zone shows the same tendency as the Ga source zone. Only the Al source zone shows a change of the predominant reaction with increase of the source-zone temperature. At low temperatures, the major gaseous species of Al is $AlCl_3$, with an equilibrium partial pressure one-third of P^0_{HCl}, whereas it is AlCl at high temperatures, above 800 °C. Although the carrier gas used in Fig. 26.1 is IG, the equilibrium partial pressures of group III chlorides do not vary when H_2 is used as a carrier gas ($F^0 = 1.0$).

Figure 26.2 shows the values of equilibrium constants K of the growth reactions of GaN, AlN, and InN using $III \cdot Cl$ or $III \cdot Cl_3$ and NH_3 as a function of the reciprocal of the reaction (growth-zone) temperature.

The equilibrium constants can be calculated using thermochemical tables [26.2, 3]. As seen in Fig. 26.1, the group III chloride formed at the source zone is $III \cdot Cl$ (monochloride) when the source-zone temperature is sufficiently high. However, with decreasing

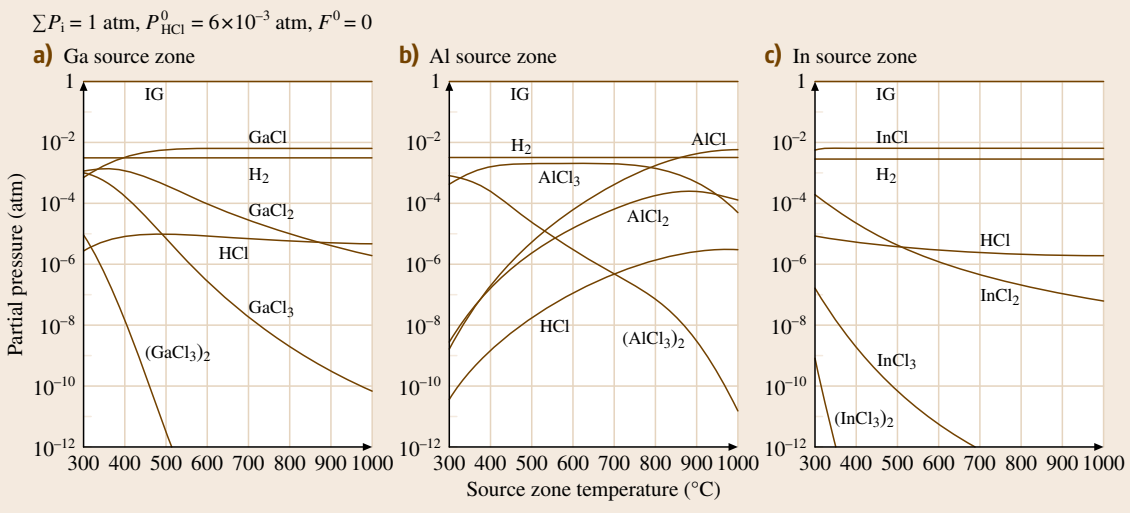


Fig. 26.1a–c Equilibrium partial pressures of gaseous species over group III metals placed in the source zone as a function of temperature calculated for (**a**) Ga, (**b**) Al, and (**c**) In source zones

source-zone temperature, the equilibrium partial pressure of $III \cdot Cl_3$ usually increases. Also, $GaCl_3$, $AlCl_3$, and $InCl_3$ are available commercially in powder form, which makes it possible to sublimate them for growth of nitrides, as an alternative to the use of HCl. Therefore, equilibrium constants of growth reactions using trichlorides are also shown. In the figure, the following order of equilibrium constants K for growing nitrides is seen

$$K_{AlN} \gg K_{GaN} > K_{InN} . \quad (26.5)$$

In general, this order corresponds to the growth rate of nitrides using group III chlorides. For the growth reactions of GaN, the equilibrium constants are close to zero in both reactions using GaCl and $GaCl_3$. Therefore, growth of GaN is possible using GaCl or $GaCl_3$. In the AlN growth, the values of equilibrium constants are extremely large in both reactions using AlCl and $AlCl_3$, indicating high-speed growth of AlN. On the other hand, in the case of InN growth, the value of log K using InCl is significantly small and negative. Consequently, growth of InN is possible only using $InCl_3$ as an In source. Another point expected from the figure is the influence of H_2 on the growth of nitrides, since the growth reactions contain H_2 as a product when monochlorides are used. Therefore, thermodynamic analysis for the growth zone of a HVPE system is meaningful as well as that for source zone, since growth is commonly performed under mass-transportation-limited or thermodynamically controlled conditions.

Thermodynamic analysis of the HVPE growth zone has been performed and reported for GaN [26.4, 5], AlN [26.6], and InN [26.7]. In the literature the influence of various growth conditions on the driving force of growth is described. Here thermodynamic analysis of the conventional GaN growth zone is described as an example. When GaCl formed at the source zone and NH_3 are separately introduced into the growth zone with a carrier gas mixture of H_2 and IG, the following chemical reactions occur simultaneously

$$GaCl(g) + NH_3(g) = GaN(s) + HCl(g) + H_2(g) , \quad (26.6)$$

$$GaCl(g) + HCl(g) = GaCl_2(g) + \tfrac{1}{2}H_2(g) , \quad (26.7)$$

$$GaCl(g) + 2HCl(g) = GaCl_3(g) + H_2(g) , \quad (26.8)$$

$$2GaCl_3(g) = (GaCl_3)_2(g) . \quad (26.9)$$

Equation (26.6) is the main reaction producing GaN growth and the others (26.7–26.9) are secondary reactions. Then, gaseous species coexisting at the growth zone are GaCl, $GaCl_2$, $GaCl_3$, $(GaCl_3)_2$, NH_3, HCl, H_2, and IG. Figure 26.3 shows equilibrium partial pressures of gaseous species at the growth zone as a function of growth-zone temperature. Calculation of equilibrium partial pressures was performed after a procedure developed by *Koukitu* and *Seki* [26.8] for HVPE growth of arsenide and phosphide of Ga and In. The growth conditions are as follows: total pressure of the reactor ($\sum P_i$) of 1.0 atm, input partial pressure of GaCl (P^0_{GaCl}) of 6.0×10^{-3} atm, input V/III ratio ($P^0_{NH_3}/P^0_{GaCl}$) of 50, and mole fraction of hydrogen in the carrier gas (F^0) of 1.0 (H_2 carrier gas). An additional parameter α which denotes the mole fraction of decomposed NH_3 before GaN growth is introduced as follows

$$NH_3(g) \rightarrow (1-\alpha)NH_3(g) + \frac{\alpha}{2}N_2(g) + \frac{3\alpha}{2}H_2(g) . \quad (26.10)$$

The value of α is difficult to determine exactly since it depends on the growth conditions, equipment, and temperature. In Fig. 26.3, the value is fixed at 0.03 according to the literature [26.9], and agreement between the calculated and experimental results [26.4–7]. It is seen that NH_3, GaCl, IG (N_2), and HCl are major gaseous species as well as H_2 used as the carrier gas.

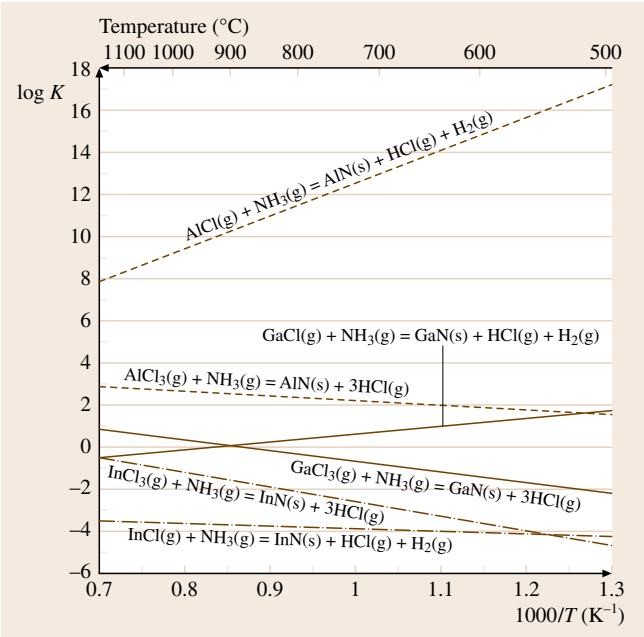


Fig. 26.2 Values of log K as a function of reciprocal of temperature calculated for growth reactions of GaN, AlN, and InN using mono- or trichloride of group III metals and NH_3

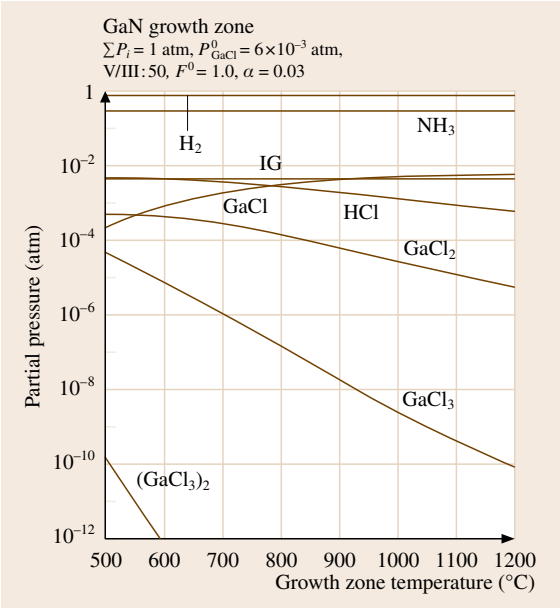


Fig. 26.3 Equilibrium partial pressures of gaseous species over GaN as a function of growth temperature

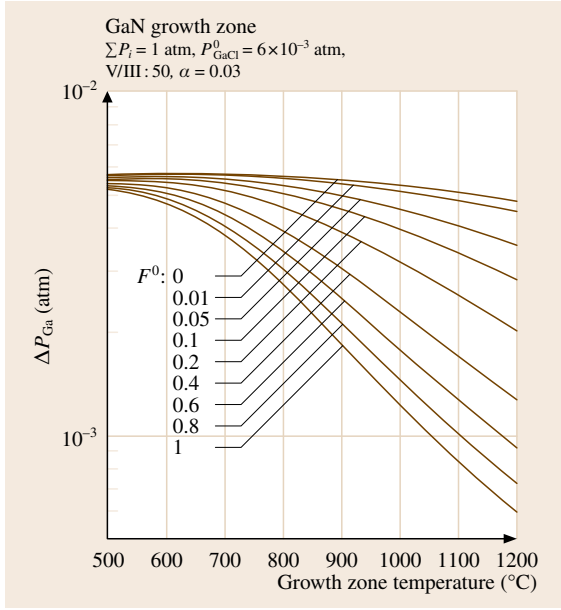


Fig. 26.4 Driving force for growth of GaN as a function of growth-zone temperature calculated for several values of F^0

The equilibrium partial pressure of HCl decreases with increase of growth-zone temperature, while that of GaCl increases with increase of growth-zone temperature and approaches a value nearly equal to P^0_{GaCl}. This means that the growth rate of GaN becomes smaller at high growth temperatures. It is of interest to calculate the driving force for growth as functions of various growth conditions. The driving force ΔP_{Ga} is given by

$$\Delta P_{Ga} = P^0_{GaCl} - \left(P_{GaCl} + P_{GaCl_2} + P_{GaCl_3} + 2P_{(GaCl_3)_2}\right), \quad (26.11)$$

i. e., the difference between the number of Ga atoms put in and the amount of Ga atoms remaining in the vapor phase. Figure 26.4 shows the driving force for GaN growth using GaCl and NH_3 as a function of growth temperature calculated for several values of F^0. It is seen that the driving force decreases with increase of the growth temperature and F^0. Furthermore, the influence of H_2 on the decrease of the driving force is more significant at high growth temperatures. It has also been clarified that the driving force decreases with increase of H_2 in the carrier gas in GaN and InN growths using trichlorides [26.5, 7]. By contrast, growth of AlN using mono- or trichloride of Al does not depend on the presence of H_2, which is due to the extremely large equilibrium constants of the growth reactions, as can be seen in Fig. 26.2. Consequently, for high-speed and high-temperature growth of GaN by HVPE, use of inert carrier gas or mixed carrier gas of H_2 and IG with a small amount of H_2 is quite effective.

26.2 HVPE Growth Equipment

A schematic picture of a typical horizontal hot-walled HVPE growth system, which is the most commonly used geometry, is shown in Fig. 26.5. The reaction chamber is normally a quartz tube that is heated either with a multizone oven or by radiofrequency (RF) induction. The reactor has one low-temperature region where the halides are formed by letting high-purity HCl or Cl_2 gas flow over a melt of a group III metal. The temperature is normally kept about 800–900 °C in this section of the reactor. The precursors are reacting

on the substrate, which is kept at a temperature about 1000–1100 °C. In order to minimize parasitic growth in the inlet of the growth zone and on the walls of the reactor, it is important that the ammonia and the halide are not mixed before they reach the substrate. Inert gases such as nitrogen (N_2), helium (He), argon (Ar) or hydrogen (H_2) and mixtures of these gases are used as carrier gases. In terms of the flow pattern, gases with lighter molecules, such as He or H_2, are more favorable, i. e., the laminar flow condition is obtained more easily.

In HVPE, a huge amount of ammonium chloride (NH_4Cl) is formed downstream of the growth zone due to the reaction between HCl and ammonia. Thus, care has to be taken in order to avoid clogging of the exhaust. The growth system has to be equipped with some type of trap at the outlet. The deposition of ammonium chloride can also be avoided by heating the outlet pipes above ≈ 150 °C. Growth of boules requires very long growth runs, thus it may be necessary to change the trap during the process.

The growth takes place under excess ammonia conditions and in a growth regime where the growth rate is mass transport limited by the vapor pressure of the halide precursor. Thus, in a horizontal system such as shown in Fig. 26.5, it is difficult to achieve a uniform deposition of high-quality material over a large-area substrate since the halide easily becomes depleted over the substrate. Using an inlet geometry where the halide precursor is dispersed uniformly across the deposition zone by a showerhead can solve this problem. The proximity of the showerhead to the susceptor, on which the wafer is placed, minimizes premature reactions between the ammonia and the halide, which leads to good chemical efficiency. A showerhead in combination with rotation of the susceptor is suited to the deposition of uniform layers, allowing scalability to be combined with ease of operation. This type of reactor is normally used commercially in order to produce layers up to typically 300–500 µm. In order to grow thicker layers, this type of reactor is not suitable, mainly because of limitations due to parasitic deposition, which will create particle problems and changes of growth conditions during the growth run.

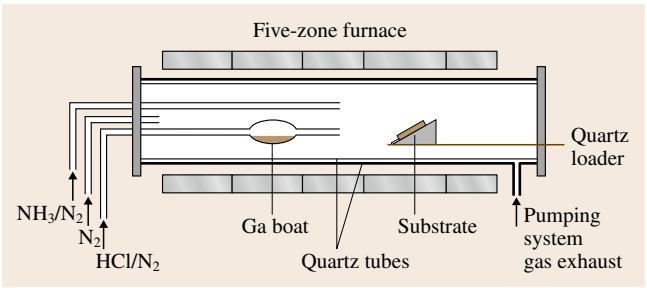


Fig. 26.5 Conventional horizontal HVPE system with a five-zone furnace

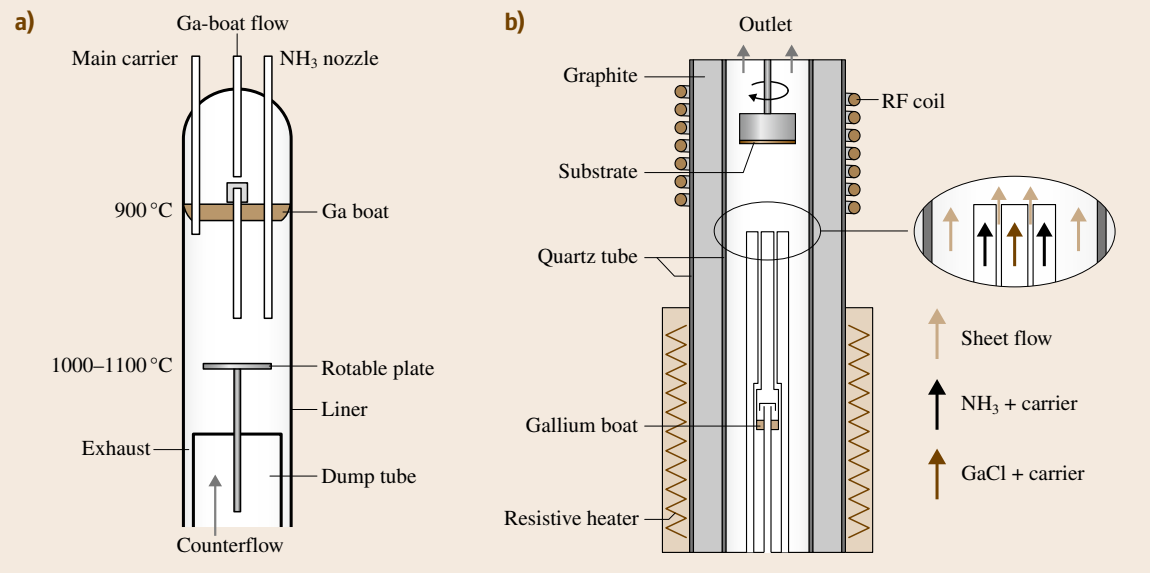


Fig. 26.6 **(a)** Top-fed vertical reactor geometry. The geometry is taken from [26.10] and **(b)** bottom-fed vertical HVPE reactor with a concentric inlet in order to minimize parasitical growth in the inlet

An alternative reactor geometry is a vertical setup, as shown in Fig. 26.6. The precursors can be introduced either from the top (Fig. 26.6a) or from the bottom (Fig. 26.6b). In the geometry where the gases are introduced from the top, the gas flow has to be controlled by adjusting the downward forced-convective flow to balance it with the upward buoyancy-driven convection. The problem with this geometry is a possible particle contamination over the substrate due to particles released from the parasitic growth upstream of the substrate. These particles may fall down and induce defect nucleation centers that degrade the quality of the grown crystal. By introducing the precursors from the bottom, this kind of problems can be minimized since the surface of the growing crystal is facing downwards. Figure 26.6b shows a schematic picture of a hot-walled vertical growth system where the precursors are introduced from the bottom. This system is designed for the growth of boule crystals (layers up to several millimeters). In order to avoid premature reactions between the GaCl and the ammonia, which will cause parasitic deposition at the inlet of the reactor, the inlet is designed with concentric tubes where the GaCl and the ammonia are separated using a sheet flow. In addition to the inlet sheet flow, a sheet flow close to the reactor walls prevents parasitic growth on the walls. The reactor is equipped with rotation of the sample holder, and the distance between the growing surface and the inlet can be kept constant by pulling of the holder.

In a vertical system one problem is to stabilize a high and constant conversion ratio of HCl to GaCl due to the small Ga area. This will affect the reactions (26.1–26.4). A reduction of the GaCl vapor pressure will reduce the growth rate, and the increase of the HCl vapor pressure increases the etching component in the growth process. Thus, it is important to design the Ga container in such a way that the HCl volume over the liquid Ga in the Ga container is kept approximately constant over time. Early work established that the GaCl conversion in a horizontal reactor with a large liquid Ga area was typically stabilized at a high value: the conversion efficiency to GaCl was above 95% [26.9]. By careful design of the Ga container, it has been shown that the conversion efficiency can be up to 98% in a vertical reactor [26.12], which is close to chemical equilibrium at 850 °C [26.13].

To achieve a desirable mass transport behavior, it is important to establish a stable, vortex-free flow field in the reactor. Any recirculating flow can create a nonuniform growth rate over the substrate, less control of the parasitic growth, and increased impurity incorporation. Since the decay of ammonia is a slow process [26.9] which can be accelerated by catalytic effects, a recirculating flow where the gas may be in contact with the walls is especially severe in HVPE, since the parasitic growth on the walls can accelerate the decomposition of the ammonia and, consequently, change the growth conditions. It has been shown that, by minimizing the recirculation flows in the reactor, run-to-run reproducibility is improved drastically [26.14].

The flow pattern in a HVPE reactor is influenced by several mechanisms, such as reactor geometry, heat transfer characteristic, flow boundary conditions, and choice of carrier gases. With respect to recirculation flow, a bottom-fed vertical configuration where the colder gases are flowing upwards towards the normally hotter substrate is preferred because the buoyancy effect has a tendency to stabilize the flow. The use of a hot-walled system will also reduce the recirculation flows generated by natural convection since the precursors are efficiently heated and the thermal gradients are small in such a system. However, since the substrate is oriented perpendicular to the flow direction some care has to be taken in the choice of carrier gases and gas velocities. Figure 26.7 shows an example of modeling using different gas velocities and gas compositions in

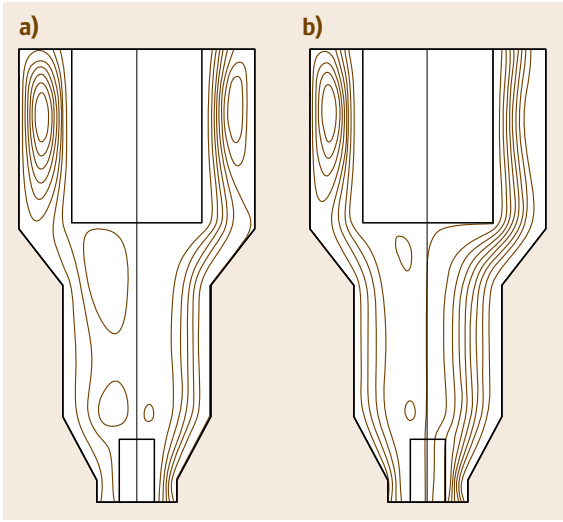


Fig. 26.7 **(a)** Streamline plots using N_2 as a carrier gas. The *left side* shows the streamlines using 0.5 l/min of carrier gas and the *right side* shows the situation when using 5 l/min of carrier gas and **(b)** shows the streamlines using 3 l/min of N_2 (*left side*) and 3 l/min of He (*right side*). The GaCl and NH_3 flow was 20 and 500 ml/min, respectively, in all cases (after [26.11])

a bottom-fed vertical configuration [26.11]. With a low total N_2 carrier gas flow (< 1 l/min), the growth is turbulent, with a vortex pattern in the middle of the substrate. At higher total flow the pattern evolves to an approximately laminar flow in the range 3–10 l/min. N_2 is an attractive choice for carrier gas, since it is inert during the growth conditions, and does not affect the growth chemistry. However, in terms of the flow pattern, gases with lighter molecules, such as He or H_2, are more favorable, i. e., the laminar flow condition can be obtained using lower gas velocities, as clearly shown from Fig. 26.7b.

26.3 Substrates and Templates for Bulk GaN Growth

The ideal way of producing bulk GaN crystals is homoepitaxial growth on a GaN seed crystal. However, due to the lack of commercially available GaN wafers, the use of GaN substrates for HVPE bulk growth is not yet commonly employed. In the few reported experiments on homoepitaxial growth using HVPE, high-pressure grown platelets [26.15] have been used. The dislocation density is low ($< 100\,cm^{-2}$) in this type of substrate; however, the lateral size and thickness are limited to about 1 cm and 100 μm, respectively, and the carrier concentration is very high ($\approx 10^{19}\,cm^{-3}$). The high carrier concentration expands the lattice parameters compared with the relatively low-doped HVPE GaN, which results in stress and cracking problems for layers thicker than ≈ 100 μm [26.16, 17]. Thus, due to the lack of commercial bulk GaN substrates, the growth of bulk crystals is mostly performed on foreign substrates (heteroepitaxy). Several different types of substrate are used or have been used for growth of thick GaN layers using HVPE, such as sapphire (Al_2O_3), SiC, GaAs, Si, MgO, ZnO, TiO_2 and $MgAl_2O_4$ [26.18], to mention a few.

Among these Al_2O_3 is the most commonly employed substrate material for bulk GaN growth, mainly due to the possibility of obtaining large-area sapphire wafers (2 inches) at relatively low cost. Most often, heteroepitaxial growth gives rise to numerous defects such as threading dislocations (TD), stacking faults, voids, and hexagonal pits due to the lattice mismatch and difference in thermal expansion between the substrate and the grown material. Table 26.1 summarizes these properties for some of the most important substrate materials used today. A nonpolar substrate can also give rise to inversion domains and mixed polarities in the grown layer. These defects are detrimental to device performance, causing high device leakage current, short minority-carrier lifetime, reduced thermal conductivity, etc. Other important properties of the substrate that have to be considered are those related to the surface, such as surface roughness, step height, terrace width, and wetting behavior.

26.3.1 Sapphire

Heteroepitaxial growth on sapphire involves several problems. The large difference in lattice constant between sapphire and GaN gives rise to a high density of TDs, and the larger thermal expansion coefficient of sapphire compared with GaN causes a biaxial compressive stress in the GaN layer as it is cooled from growth temperature. For thicker films (> 50 μm), the stress can cause cracking of both the GaN epilayer and the substrate. GaN epitaxy on *c*-plane (0001) sapphire, which is the most common orientation, results in *c*-plane-oriented films, but with a 30° rotation of the in-plane GaN crystal directions with respect to the same directions in the sapphire. Without the in-plane rotation, the lattice mismatch between the GaN and the sapphire is

Table 26.1 Surface lattice parameters and thermal expansion coefficients of some technologically important substrate materials for GaN growth

Substrate	Crystal structure	Growth plane for wurtzite GaN	Surface lattice parameter (Å)	In-plane lattice mismatch to GaN (%)	Thermal expansion coefficient ($10^{-6}\,K^{-1}$)
GaN	Wurtzite	(0001)	3.189		5.6
Al_2O_3	Wurtzite	(0001)	4.758	16.1	7.5
6H-SiC	Wurtzite	(0001)	3.08	3.54	4.2
GaAs	Zincblende	(111)	2.54	20.2	6.03

about 30%. However, the in-plane rotation of the GaN minimizes the lattice difference between the GaN and the sapphire to about 16%. The good morphological, crystallographical, and electrical properties of *c*-plane-grown GaN is mostly responsible for the widespread use of the *c*-orientation.

Nevertheless, in some cases it is beneficial to use growth on planes other than the *c*-plane. In *c*-plane nitrides, we have a built-in electrostatic field in the [0001] direction due to the spontaneous and piezoelectric polarization [26.19]. This field is undesirable for optoelectronics devices since it results in an uncontrollable shift of the emission peak and/or a reduction of the emission efficiency. The influence of this field can be avoided by the use of GaN with other orientations. Thus, other orientations such as *r*-plane ($1\bar{1}02$), *a*-plane ($11\bar{2}0$), and *m*-plane ($10\bar{1}0$) sapphire have been used in order to grow nonpolar *a*-plane GaN [26.20] or to facilitate cleavage of the structure to form edge-emitting lasers [26.21].

By using a miscut sapphire wafer it has been shown that the GaN quality can be improved in MOVPE [26.22, 23]. In HVPE an improvement in the morphology has been observed. Using a slightly miscut *c*-plane substrate with an $\approx 0.3°$ off-orientation against the *a*-plane or the *m*-plane, a reduction in hillocks is observed [26.24]. It has been shown that *a*-plane off-oriented substrates suppress the hillock formation more efficiently than other directions.

Growth on sapphire requires a pretreatment of the sapphire to improve the wetting properties and the crystal quality. One pretreatment step is nitridation, which is done by exposing the sapphire substrate to ammonia at typical growth temperatures (1000–1100 °C). It is believed that a thin AlN or AlN–Al_2O_3 layer forms on the surface, which facilitates nucleation [26.25]. This type of pretreatment is also employed in MOVPE [26.26–29] and MBE [26.30] growth of GaN on sapphire substrates. A second step, which is commonly employed and has been shown to reduce the pit density and improve the crystal structure [26.31, 32] is GaCl pretreatment. The GaCl pretreatment is done just before the growth of GaN commences, by exposing the sapphire to GaCl for $\approx 10–20$ min at the growth temperature. It is believed that the GaCl pretreatment supplies nucleation centers for GaN islands and the promotion of the coalescence of the GaN layer in the early stages of growth.

The crystal quality has been shown to improve by the use of a low-temperature-grown GaN buffer layer (LT-GaN). This technique is used for MOVPE growth of GaN on sapphire and has also been shown to be useful for HVPE growth. This LT-GaN layer greatly improves the surface morphology and reduces the dislocation density of the subsequently grown high-temperature GaN layer. Initially, a thin GaN film on the order of 100 nm is grown at $\approx 550–650$ °C. This layer can serve as a starting layer for growth [26.33]. However, it has been shown that annealing of the LT-GaN layer in ammonia before commencing the high-temperature growth reduces the TD density further [26.34]. Upon annealing of the LT buffer, relatively large grains are formed that can serve as nucleation centers for the subsequent high-temperature growth.

26.3.2 Silicon Carbide

SiC is widely used for growth of device structures using MOVPE and MBE due to the fact that it has several advantages to sapphire such as a smaller lattice mismatch (3.1%), a higher thermal conductivity (3.8 W/cm K), it is conductive, SiC has a polarity which facilitates control of polarity of the GaN, and there is no in-plane rotation between the GaN and the SiC, which makes it possible to cleave the crystal for laser facet formation. However, it has also several disadvantages, i. e., it requires in most cases a buffer layer of AlN or AlGaN due to its poor wetting properties, and the surface roughness is one order of magnitude larger than that of sapphire. The cost of SiC is also much higher than that of sapphire. Most of the above-mentioned favorable properties are not very important for bulk growth and, consequently, SiC substrates are not commonly employed for bulk growth.

26.3.3 GaAs

GaAs is an interesting substrate material since it is brittle and can easily be mechanically removed after growth. It can also be easily removed by etching in aqua regia. Furthermore, it has a thermal expansion coefficient closer to that of GaN than any other foreign substrate material (Table 26.1). GaAs substrates can be used both for growth of zincblende GaN and wurtzite GaN depending on the orientation of the substrate. GaAs(001) gives zincblende GaN while GaAs(111) is used for growth of wurtzite GaN. In principle, zincblende GaN has better electronic properties for device applications, such as isotropic properties, higher mobility, and high optical gain; however, the quality of the zincblende GaN grown on GaAs is very poor due to coexistence between the two phases. Thus, hereafter

we only consider growth of wurtzite GaN grown on GaAs(111).

One problem with growth of GaN on GaAs is the fact that GaAs is decomposed in ammonia ambient at a temperature where the growth of GaN normally takes place (above 1000 °C). This may lead to problems with a degraded GaAs surface before the growth starts and autodoping of As [26.35]. Thus, it is necessary to grow a buffer layer to protect the GaAs surface. One way to do that is to grow a thin protective GaN layer at lower temperatures [26.36, 37]. Using the epitaxial lateral overgrowth (ELO) technique in combination with a low-temperature GaN buffer, 2 inch free-standing GaN layers with a thickness of about 500 μm have been demonstrated [26.28].

26.3.4 Lattice-Matched Substrates

There exist several other potential substrate materials such as $LiAlO_2$, $LiGaO_2$, and $NdGaO_3$ with closer lattice matching to GaN than the substrate materials discussed above. Among these, γ-lithium aluminum oxide ($LiAlO_2$) has shown potential as a substrate material for growth of thick GaN using HVPE [26.38]. The orientation between the $LiAlO_2$ and the GaN is GaN(0001)||$LiAlO_2$(110) and GaN(0001)||$LiAlO_2$(001) with a lattice mismatch of -1.4% and -6.3%, respectively.

Lithium gallate ($LiGaO_2$) has the best lattice matching of all, with only 0.9% lattice mismatch in the basal plane, and has been used for growth of thick GaN [26.39]. However, the poor chemical and thermal stability of these substrate materials in the HVPE growth environment makes the growth conditions very critical. In order to avoid decomposition of the substrate surface before growth, elaborate starting procedures have to be applied, with pretreatment steps and low-temperature GaN buffer layers before growth can commence. However, due to a partial decomposition of the substrate during growth, the grown GaN layer is very often spontaneously separated from the substrate during cooling after growth.

26.3.5 Growth on Templates

A very common growth procedure in HVPE is to start the growth on a starting layer of GaN [26.40], AlN [26.41–43] or ZnO [26.25, 44–46] in order to facilitate the initial nucleation process. The starting layer is normally grown heteroepitaxially with MOVPE (GaN) or by sputtering (AlN, MgO). Among these different types of starting layer, MOVPE-grown GaN is the most frequently used. With the state of the art of the MOVPE GaN heteroepitaxial growth technique today, the starting layers have a TD density typically in the 10^9 cm^{-2} range. In order to reduce the TD density further, the ELO technique can be used. However, this reduction is obtained at the expense of several additional process steps.

26.3.6 Basic 1S-ELO Structures

As mention above, one way to reduce the TD density is the ELO process. This technique has been used in growth of GaAs and has also been successfully used for growth of GaN. A one-step ELO structure (1S-ELO) is fabricated as follows, as depicted in Fig. 26.8: A substrate is covered with a dielectric film (Fig. 26.8a), normally SiN or SiO_2, and patterned by conventional photolithography to form on its whole area a grating of mask-free seeding windows, as shown in Fig. 26.8b. The orientation of the stripes is normally in the {1$\bar{1}$00}

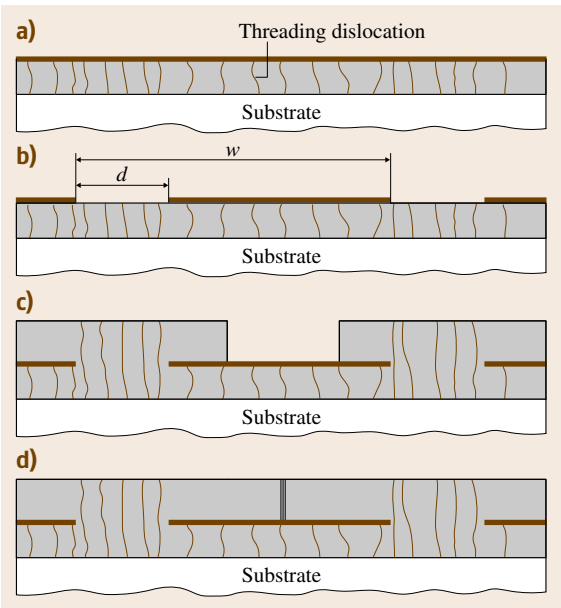


Fig. 26.8a–d Cross-sectional view perpendicular to the [1$\bar{1}$00] direction showing the different steps in the fabrication of a 1S-ELO structure. *Black thin vertical lines* represent threading dislocations. **(a)** Deposition of dielectric film, **(b)** after etching of the dielectric film, where d is the width of the stripes while w is the period of the stripes, **(c)** growth in the lateral direction over the film and **(d)** fully coalesced structure

direction of the GaN layer since it has been shown that lateral expansion is easier in this direction [26.47–50]. The width of the windows (d) in the mask and the periodicity of the lines (w) in the grating is typically about 3 and 10 μm, respectively, and the thickness of the dielectric film is typically about 100 nm. The dielectric is deposited using well-established techniques such as chemical vapor deposition (CVD) or plasma-enhanced CVD (PECVD). Then, an epitaxial layer is deposited on such a substrate. Initially, there is no nucleation on the dielectric stripes; however, as soon as the crystallization front passes the top layer of the mask, growth in the lateral direction over the film starts (Fig. 26.8c), which finally leads to coalescence of the layer, as shown in Fig. 26.8d, and a smooth (0001) surface suitable for further processing is formed.

The basic idea of the ELO technique is that the dielectric mask filters dislocations present in the substrate since defects cannot penetrate through the mask. Thus, in areas above the dielectric stripes where the GaN has grown laterally (wing region), the GaN should be dislocation free. However, in the region where the two laterally grown crystallization fronts meet on the mask, defects are created. Thus, using this technique, two regions with a higher defect density are formed, one in the region without mask and the other in the region where the two laterally growing parts meet on the mask. By using the 1S-ELO technique, the TD density can be reduced by about two orders of magnitude [26.47].

26.3.7 2S-ELO

To reduce the TD density further, double-layer ELO (or 2S-ELO) can be used, where a second dielectric mask layer is processed on a fully coalesced ELO structure. The idea is to cover the remaining regions where the TD is still high with a second dielectric mask. Thus, the remaining TDs are prevented from propagating to the second ELO layer. The mask can either be rotated by 60 or 90° [26.51] in order to keep the orientation along another equivalent $\langle 1\bar{1}00\rangle$ orientation, or be displaced [26.52] from the first array of openings so that the second mask covers the coherent GaN over the window region of the first mask layer. From the theory of image dislocations and image forces [26.53], it is known that dislocations near a free surface bend towards the free surface. In the case of TDs in GaN, they can be bent 90° and start to propagate along the basal plane [26.47, 54, 55]. This phenomenon can be used to reduce the TDs over larger areas. A mask is formed in a similar way as for the conventional ELO process as described above. However, initially during the first step of growth, growth parameters that favor vertical expansion are selected, as shown in Fig. 26.9a. By tuning the process parameters, the stripes will adopt a triangular shape in cross section with $\{11\bar{2}2\}$ lateral facets. Thus, since the TDs are propagating perpendicular to the growing surface, they are bent 90°. This

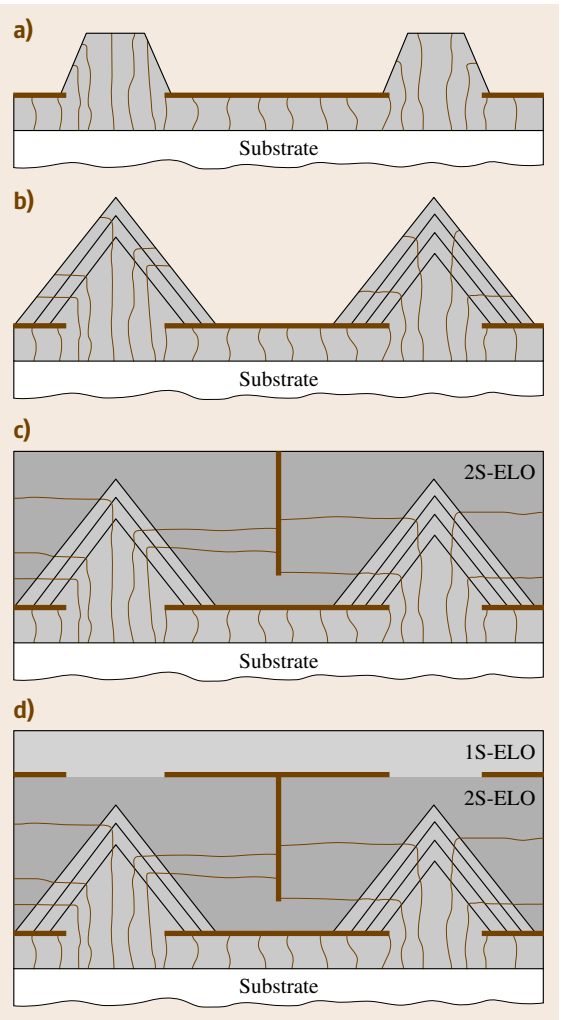


Fig. 26.9a–d Cross-sectional view perpendicular to the $[1\bar{1}00]$ direction showing the different steps in the fabrication of a 2S-ELOG structure **(a–c)** and a layered ELO structure **(d)**. *Black thin vertical lines* represent threading dislocations. **(a,b)** The evolution of the formation of triangular stripes with $\{11\bar{2}2\}$ lateral facets, **(c)** fully coalesced 2S-ELOG structure and **(d)** additional 1S-ELO on 2S-ELO structure

growth mode is kept until the (0001) top facet vanishes completely (Fig. 26.9b). In the second step, the growth condition is changed to promote lateral growth in order to fully coalesce the layer. This can be done either by adding Mg or increasing the growth temperature. The bent TDs from the neighboring window regions meet each other in the middle of the dielectric mask layer, as shown in the Fig. 26.9c. Thus, the TDs pile up above the middle of the mask and start to grow in the *c*-direction.

To further reduce the TDs, a 1S-ELO can be processed on a 2S-ELO with the mask located exactly above the first structure [26.56]. Thus, the TDs originating from the coalesced region on the 2S-ELO structure are efficiently prevented from propagating to the top GaN layer, as shown in Fig. 26.9d. Using this technique with several ELO structures stacked on each other, it has been shown that the TD density can be reduced down to or even below the $10^6\,\mathrm{cm}^{-2}$ range [26.57].

26.4 Substrate Removal Techniques

The development of advanced III-nitride devices, such as laser diodes (LDs) or some high-power lamps for general illumination, will require the growth of device structures on high-quality III-nitride substrates with a low TD density ($< 10^6\,\mathrm{cm}^{-2}$). These types of substrates are very difficult to produce by using heteroepitaxial growth on sapphire or SiC substrates, which is the common technique today. Thus, there is a strong need for free-standing GaN substrates with low TD density in order to fully exploit the III–V nitride materials.

Two major routes have appeared towards the production of bulk GaN wafers. One possibility is growing a thick boule followed by slicing and polishing. The alternative is growing a thick GaN layer on some foreign substrates, followed by substrate removal and proper polishing. Among these, the most attractive way to produce GaN substrates is directly by slicing of a GaN boule and polishing. However, despite many years of development and research, the process control and technical issues are not yet fully solved. Instead, several techniques using thick GaN layers grown by HVPE on foreign substrates followed by substrate removal have been developed.

26.4.1 Laser Lift-Off

The most used substrate material in HVPE is sapphire, which is very hard and chemical inert. This makes it very difficult to remove the substrate mechanically or chemically. Instead, a technique which relies on thermal decomposition of the GaN at the interface between the sapphire and the GaN film has attracted most attention in recent years. Using this so-called laser lift-off process (LLO) [26.58], large-area crack-free GaN substrates up to 2 inches in diameter with a thickness of about 300 µm have been demonstrated [26.59].

The idea behind the LLO process is to irradiate the GaN–sapphire substrate through the sapphire with a laser beam with an energy that is less than the bandgap of sapphire but larger then the bandgap of GaN. Thus, the laser beam will be absorbed at the GaN–sapphire interface, as shown in Fig. 26.10. If the power density of the laser beam is sufficient, a thin layer (of the order 100 nm) of GaN at the interface to the sapphire will decompose into liquid Ga and N_2 gas according to

$$2\mathrm{GaN} \rightarrow \mathrm{N_2(g)} + 2\mathrm{Ga(l)}\,. \qquad (26.12)$$

The decomposition rate of GaN rapidly increases for elevated temperatures [26.60] and a high-power laser beam can easily obtain the onset of thermal decomposition. By scanning the beam, the GaN at the interface can be completely decomposed and, consequently, the GaN layer is delaminated from the sapphire.

Figure 26.11 shows a schematic picture of an LLO setup. It consists of a high-power laser with photon energy larger than the bandgap of GaN (3.43 eV). A suitable energy of 3.49 eV (355 nm) is obtained from the third harmonic of a neodymium-doped yttrium alu-

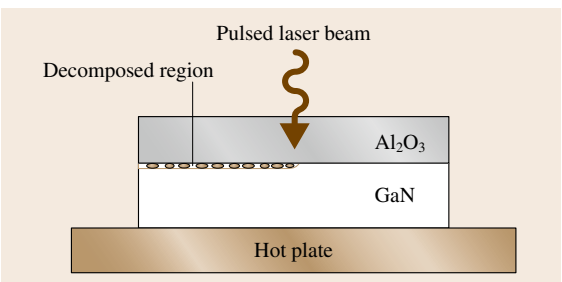


Fig. 26.10 Drawing of the principle of the LLO process

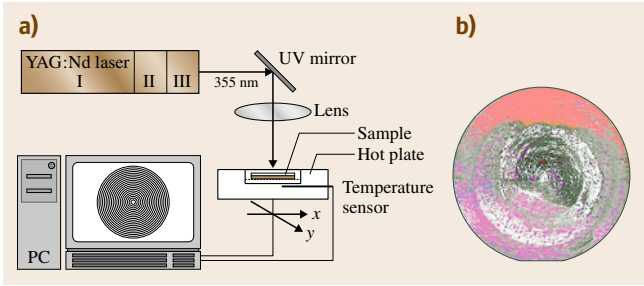


Fig. 26.11 **(a)** Schematic drawing of a laser lift-off setup. The movement of the wafer on the hot plate is done with a computer-controlled x–y stage tool. **(b)** Transmission light image of a 300 μm thick 2 inch free-standing GaN layer. On the backside of the wafer, traces from the laser lift-off process can be observed

minum garnet (Nd:YAG) laser. Another type of laser system that can be used is, for example, a KrF laser with an energy of 5 eV (248 nm). The laser beam is directed and focused on the backside of the sample. In order to reduce the stress due to the difference in thermal expansion coefficients between the substrate and the GaN layer and facilitate the thermal decomposition process, the sample is heated to about 700 °C. The entire sample holder is connected to an x–y stage, which is moved in a controlled fashion via a computer. The laser spot is moved in a spiral pattern from the perimeter to the center of the wafer. An example of a 300 μm thick 2 inch GaN wafer removed from the substrate by this technique is shown in Fig. 26.11b. The wafer is shown in transmitted light with the top surface up, and the spiral pattern from the scanning of the laser beam over the wafer can be observed as a circular pattern on the backside of the wafer. The process is very sensitive to the focusing of the laser beam and the laser output energy. Too high a power density generates cracks in the interface that can propagate through the layer and cause cracking of the wafer, while too small a power density might cause local islands where the layer has not separated. These islands create a strong nonuniform stress in the material during cool down after LLO, which may result in cracking of the layer. Another cause for incomplete separation is parasitic GaN growth on the backside of the substrate. The parasitic GaN absorbs the laser light and prevents the decomposition of the GaN at the interface.

The free-standing layers obtained after LLO are practically strain free. The main problem with free-standing GaN wafers is the substantial bowing of the wafers typically observed. Figure 26.12a shows an example of bowing of a 250 μm thick 2 inch layer residing

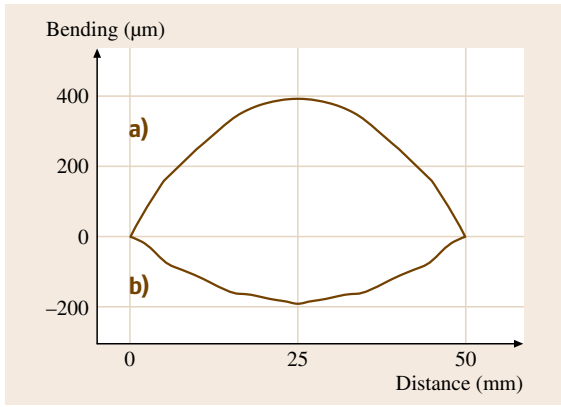


Fig. 26.12a,b Experimentally observed bow for two GaN layers. **(a)** 250 μm thick layer residing on sapphire and **(b)** 300 μm thick free-standing GaN layer. A convex bow of the GaN layer is observed when the GaN layer is residing on sapphire. When the sapphire is removed, the bow switches to a concave bow (after [26.12], with permission from Elsevier)

on sapphire and a 300 μm thick free-standing GaN layer obtained by LLO. As can bee seen, the bowing can be quite large, in this example 400 μm before LLO and 200 μm after LLO. The sign of the bow is changed after LLO. Before LLO, the wafer is convex due to the larger thermal expansion coefficient of the sapphire, while afterwards the layer adopts a concave shape due to the defective interfacial region with large dislocation density and microcracks between the sapphire and the GaN, as shown in Fig. 26.12b. The layer shown in the example has too large a bow for further processing. Thus, in order to reduce the bowing, further processing such as annealing and/or removal of the highly defective region by etching is necessary.

26.4.2 Self-Separation

Many alternative techniques to LLO are under development since the LLO process normally has a relatively low yield. Several of these techniques use the stress that is built up in the GaN layer during cooling due to the difference in thermal expansion of the substrate and the GaN layer. By making a weak link that is provided by cavities between the substrate and the GaN layer, the separation of the substrate and the layer can be done spontaneously during cool down from the growth temperature.

Using ELO structures, voids can intentionally be created. By adjusting the growth process, the size and

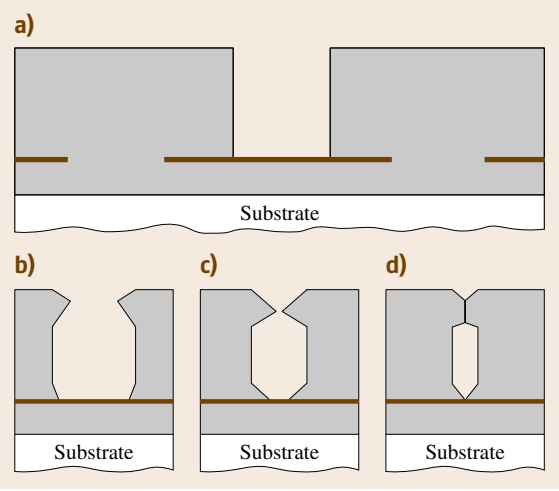


Fig. 26.13a–d Example of using ELO and mass transport in order to create voids at the substrate–GaN interface. **(a)** 1S-ELO structure with not fully coalesced wing region. **(b–d)** Evolution of the void under mass-transport conditions

shape of the voids can be engineered to facilitate separation during cooling [26.54, 61]. Figure 26.13 shows an example of a structure created by using mass transport. A conventional ELO structure with a SiO_2 or SiN mask is used as a starting template. During growth, in the stage when the lateral growth starts, the growth conditions are tuned such that the lateral facet becomes $\{11\bar{2}0\}$ (Fig. 26.13a). The growth is interrupted when the distance between the two lateral facets is a couple of microns. Then, by increasing the temperature to about 1100 °C under ammonia, mass transport will occur, as shown in Fig. 26.13b, c. At the end of the mass transport process, a vertical cavity has been created (Fig. 26.13b), which will facilitate the separation of the GaN layer from the substrate.

One of the more successful techniques that rely on self-separation is the so-called void-assisted separation (VAS) technique. The idea is basically the same as using ELO structures with cavities in the interface. Using this technique, high-quality free-standing substrates of both *c*-oriented [26.62] and *a*-oriented [26.63] GaN have been demonstrated. A thin layer of suitable metal ($\approx$ 20 nm), generally Ti or Al, is deposited onto a thin MOVPE-grown GaN template prepared on a sapphire substrate. Subsequent annealing at $\approx$ 1050 °C of the metal-coated GaN template in a mixture of hydrogen and ammonia causes the metal to break up and form a nanonet-like metal nitride structure with many nanoscale holes with a typical diameter of about 20–30 nm. During the subsequent growth of the thick GaN layer, additional etching of the mask and the underlying GaN occurs, creating multiple voids at the substrate–GaN interface. If these voids exceed a critical size, it is found that the GaN layer is spontaneously separated from the substrate during cooling after growth. For a 250 µm thick GaN layer it was estimated that the critical void size is about 20 µm [26.63]. The nanonet-like metal nitride structure layer also serves as a growth mask, which efficiently blocks the propagation of threading dislocations along the growth axis.

26.4.3 Mechanical Polishing

Using mechanical polishing with diamond slurry, $30 \times 30\,mm^2$ free-standing GaN substrates have been demonstrated from 400–450 µm thick GaN layers [26.64] grown on sapphire. However, this technique will be difficult to use for large-area wafers due to the strong convex bow of the layers that normally occurs after heteroepitaxial growth on foreign substrates. The bow makes it difficult to achieve uniform removal of the substrate by polishing.

26.4.4 Plasma Etching

Free-standing GaN wafers with a thickness of 200 µm and diameter of 30 mm have been demonstrated using reactive-ion etching (RIE) to remove the substrate. The GaN layer was grown on a SiC substrate and the substrate was removed by RIE in an SF_6-containing mixture gas [26.65, 66]. The main disadvantage with this technique is the long plasma processing times. Considering a typical etching rate of $\approx$ 100 nm/min for SiC, for a 300 µm thick SiC substrate an etching time of about 50 h is required.

26.4.5 Chemical Etching and Spontaneous Self-Separation

Sapphire and SiC are very hard and chemically inert and are difficult to etch chemically. However, for other types of substrates, which are softer and less chemically inert, the removal process can be done more easily. Growth of GaN on GaAs(111) has been shown to be a possible route to fabricate free-standing GaN. The substrate can most easily be removed by wet etching in aqua regia after growth. Using GaAs as the substrate, 2 inch free-standing GaN layers with thickness of about 500 µm

have been demonstrated [26.28]. Chemical etching has also shown to be useful for separation of GaN grown on $LiGaO_2$. $LiGaO_2$ can be rapidly etched in a buffered basic solution at 50 °C [26.67] with an etch rate of about 0.25 μm/min.

GaN layers grown on softer and less chemically inert substrates have shown in many cases to be spontaneously separated from the substrate after growth. Examples are HVPE-grown GaN on $NdGaO_3$ [26.68, 69], $LiGaO_2$ [26.39] or $LiAlO_2$ [26.38].

26.5 Doping Techniques for GaN in HVPE

Doping in HVPE can be done either by introducing a diluted dopant gas, mixing of the dopant in the Ga melt or using a separate doping source exposed to HCl in order to form gaseous metal halides.

26.5.1 n-Type Doping of GaN

Nitride semiconductors can easily be n-type doped; in fact they often exhibit unintentional n-type conductivity. This background doping has mainly been attributed to unintentionally introduced impurities, such as oxygen or silicon, which can be introduced from quartz parts within the reactor or from the process gases. For intentional n-type doping, silicon is the most suitable doping element. Silicon can, in principle, act as both an acceptor and a donor, depending on whether it is substituting a gallium atom or a nitrogen atom. However, the silicon atom mainly replaces a gallium atom due to the low covalent radii difference between Si and Ga compared with the radii difference from nitrogen.

Both gaseous sources and solid silicon sources have been used in growth of n-type HVPE GaN. The most commonly used doping gas for n-type doping of MOVPE-grown GaN is silane (SiH_4) or disilane (Si_2H_6). Silane has also been reported to be a useful source for HVPE growth of GaN [26.70]. However, the entrance zone where the Ga boat is situated is rather far away in most HVPE systems, which may results in problems with decomposition of the silane (or disilane) before it reaches the substrate, since the decomposition of the silane (disilane) starts already at temperatures below the temperature of the Ga boat. This problem can be solved by using more stable gases such as dichlorosilane (SiH_2Cl_2) that decomposes at higher temperatures. Using dichlorosilane, doping levels up to 8×10^{18} cm^{-3} have been reported [26.71].

Solid Si can also be used as a Si source by exposing the Si to HCl to form $SiCl_x$. Using this technique, a free electron concentration in GaN up to 10^{18} cm^{-3} has been reported [26.72]. The temperature of the Si source can control the doping level. By changing the temperature in the range 200–400 °C the Si concentration was controlled in the range 1.0×10^{17}–2.5×10^{19} cm^{-3}. However, only 30–50% of the Si atoms were activated as donors.

Bulk growth requires a stable well-controlled doping source. This can be a problem with a solid Si source, as pointed out in [26.71]. These authors observed that controllability was poor using a solid Si source due to changes of the exposed Si area and morphology during growth.

Other n-type dopants that have been used in MOVPE growth of GaN are O, Ge, and Sn. However, there are no reports on intentional doping of HVPE-grown GaN using these dopants.

26.5.2 p-Type Doping of GaN

One of the major challenges associated with growth and development of III–V nitride-based materials is to understand and control the p-type doping. Today, magnesium (Mg) is the only element that has been shown to be a relatively efficient and controllable p-type impurity. Other elements such as Zn and Cd have too large activation energies to be useful as a p-type dopant for GaN due to a very low activation of these dopants at room temperature. Be introduces a shallow acceptor, but suffers from self-compensation problems, so p-type material is not obtained with Be doping [26.73]. However, despite Mg being the most suitable acceptor, it still has a relatively high thermal activation energy ($E_a \approx 0.17$ eV, after [26.74]). The high ionization energy results in only a few percent of the Mg acceptors being ionized at room temperature. One additional problem with Mg doping, which was for a long time the bottleneck for the development of III-nitride technology, is that hydrogen can passivate the Mg dopants by forming an Mg–H complex. The Mg dopant can be activated by removing the hydrogen either by postgrowth annealing in N_2 or an electron irradiation treatment using low-energy electron-beam irradiation (LEEBI) [26.75, 76]. For thick bulk-like material, thermal annealing is the

only useful technique for activation of the acceptors since the penetration depth of low-energy electrons is small. This treatment is normally done in situ, directly after the growth. However, despite the thermal post-growth treatments, the acceptor thermal activation efficiency is still only a few percent. Thus, obtaining a suitably high hole concentration ($> 10^{18}$ cm^{-3} at 300 K) in p-doped GaN using Mg is not an easy task. The upper limit of Mg acceptors that can be incorporated into the lattice is about 10^{20} cm^{-3}, which gives a hole concentration only in the low 10^{18} cm^{-3} range in *c*-plane GaN. Increasing the Mg concentration does not improve the conductivity; in fact, it has been reported that it leads to an even lower hole concentration [26.77]. It has been suggested that the solubility of Mg is limited due to competing formation of Mg_3N_2 [26.78]. Increasing the Mg concentration in GaN beyond this limit may result in precipitation of Mg_3N_2, which leads to a reduction in the hole concentration and a decrease in crystal quality.

Doping of Mg in HVPE can be done by either using a separate boat for the doping species or mixing it with the Ga source. The HCl gas is reacted with the Mg, forming its halide MgCl, which is transported to the growth zone by some suitable carrier gas. A second technique, which has been used both for Zn and Mg doping [26.79], is to thermally evaporate the dopant and transport the species in a suitable carrier gas to the growth zone. To avoid passivation of the acceptors by formation of Mg–H complexes, the rationale would be to avoid using hydrogen as carrier gas. However, it has been suggested that hydrogen is actually beneficial for p-type doping [26.80–83] compared with the hydrogen-free case. It has been proposed that the hydrogen passivates the Mg acceptors during growth and, consequently, represses formation of native donors to compensate for the acceptors. However, despite the technological breakthroughs in growth and development of GaN-based devices, many properties of this material system are not well understood. Doping of bulk growth of GaN using HVPE is not well documented and only a few scientific reports have been presented.

26.6 Defect Densities, Dislocations, and Residual Impurities

Thick HVPE-grown GaN layers are typically developed for the purpose of later use as thick high-quality substrates for epitaxial growth of device structures. Such substrates need lapping and chemical polishing to obtain a suitable surface finish for later epitaxy with other growth techniques. Defects such as minor surface features will be removed during these processing steps, and will therefore not be discussed here. Important problems are wafer bowing, dislocations and stacking faults, impurities, and localized bulk defects.

A major problem already discussed above is the bowing of bulk GaN wafers produced by HVPE on a foreign substrate, which is removed by some lift-off techniques. It is important to reduce the original bowing before lift-off as much as possible; some techniques involving ELO structures with cavities are successful in this respect. Another technique to accomplish this is to grow under conditions where an O-rich defective layer is present close to the substrate. This layer can absorb the deformation during growth and cooling, and give a low-strain (and low-bowing) GaN layer prior to lift-off [26.84]. For substrates suitable for epitaxy the bowing should ideally not be larger than about 10 µm (measured as the elevation of the middle of a 2 inch wafer compared with the perimeter). If the grown free-standing wafer has a substantially larger bowing, the subsequent polishing may produce a variable lattice tilt across the final wafer, i. e., a variable miscut. This in turn might cause a variable growth morphology across the wafer in a later epitaxial growth process for a device structure. If the wafers are prepared from boules, these boules are usually grown with a length of about 10 mm. In this case the memory of a bowing is typically very much reduced, but these properties are not well documented in the literature to date.

A problem related to bowing is cracking. For thick layers on sapphire, cracking typically already occurs in situ during the first tens of microns of growth, due to the tensional strain developed in this initial growth process [26.85]. This cracking helps relax the strain during growth. These cracks typically overgrow (Fig. 26.14) and are generally not seen after growth of a 300 µm layer. Their presence in the interior of the material may well initiate more severe cracking during cool down after growth or during the polishing step. When GaN buffer layers are used for the growth it seems that this initial cracking behavior can be avoided, and the strain in the layer accumulates during growth, increasing the bowing of the wafer. Cracking during cool down is then a more critical issue, depending on the wafer thickness.

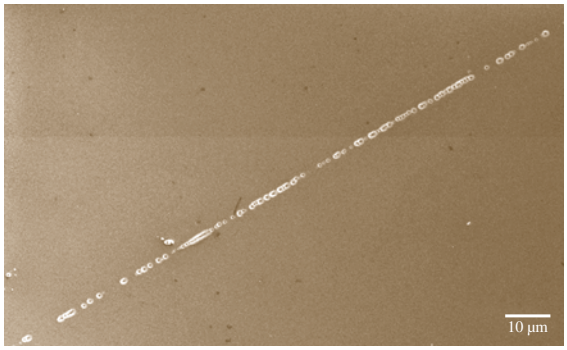


Fig. 26.14 Scanning electron microscopy (SEM) image of a HVPE-grown GaN layer on sapphire, showing an array of pits along a partly overgrown crack

Dislocations threading up through the wafer are severe defects in substrates, since they are typically replicated in the device structure epitaxially grown on top of the wafer. Dislocations are known to have a serious influence on carrier recombination in semiconductors; in GaN it seems that screw dislocations and mixed dislocations are most severe in terms of causing nonradiative recombination [26.86]. The threading dislocation density can be studied in several ways. Upon surface etching they typically form pits, which have a specific shape and size depending on the type of dislocations, and on the etch procedure used. This was studied by *Hino* et al. with HCl etching at 600 °C, where different pit shapes were produced by screw, mixed, and edge dislocations, respectively [26.86].

The dislocation types were established from separate transmission electron microscopy (TEM) studies. Complementary studies by cathodoluminescence (CL) topography reveal a different dark contrast, usually interpreted as due to nonradiative recombination, with strong contrast for screw and mixed dislocations, and quite a weak contrast for edge dislocations [26.86]. Similar results are observed from comparison of a different etching procedure (H_3PO_4 at 180 °C for 45 min) in Fig. 26.15. Here different sizes of pits observed by atomic force microscopy (AFM) (Fig. 26.15a) are observed [26.12]. The large pits are supposed to correspond to dislocations with a screw component, while the small pits correspond to edge dislocations. Figure 26.15b shows a CL topograph of another sample, showing mainly the high-contrast screw and mixed dislocations.

If the etching times are tuned to avoid overlap between different pits, the TD density of a layer can thus be determined by a simple etch pit count, a convenient method for a quick evaluation. The reliability of this technique can be tested by comparison of the dislocation count via etch pits and TEM studies of the same wafer, as reported in [26.86]. Obviously etch pit counting will omit dislocations that are running parallel to the surface, but these are usually not replicated in the overgrown epitaxial structure anyway.

The experience from HVPE growth of thick GaN layers is that the dislocation density is reduced with thickness in a manner that looks like a linear relation in a log–log plot, as seen in Fig. 26.16, where

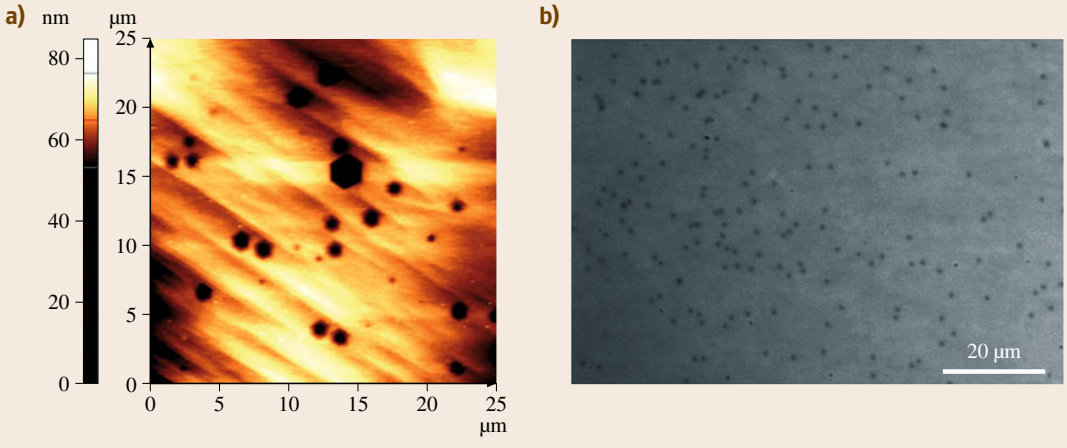


Fig. 26.15 (a) AFM pictures of a 250 µm thick layer after etching in H_3PO_4 at 180 °C for 45 min and (b) CL image of a 400 µm thick layer

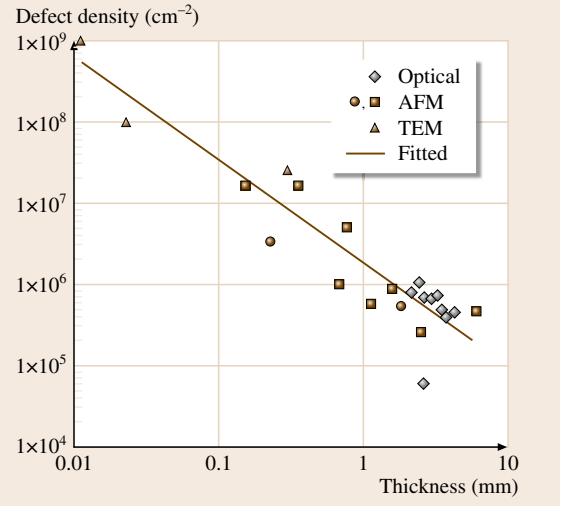


Fig. 26.16 Threading dislocation density as a function of thickness of thick HVPE-grown GaN layers. *Points* labeled (◇), (□), and (△) are taken from [26.89], while (●) from [26.87]

data from different groups are collected. For a thickness of 500 µm the TD density is typically at or below $10^7\,\mathrm{cm}^{-2}$, while for a thickness of several millimeters a TD density of the order of $10^5\,\mathrm{cm}^{-2}$ is expected [26.87]. The mechanism for this has been investigated and suggested to be dislocation annihilation by recombination, driven by the dislocation strain fields and a certain mobility of dislocations at the growth temperature [26.88].

Stacking faults (SFs) are not abundant in GaN grown in the conventional polar (0001) direction. The situation is quite different in the case of growth of nonpolar wafers, such as *a*-plane and *m*-plane GaN on foreign substrates. *a*-Plane GaN can be grown on *r*-plane sapphire, and the defect density in such thick layers has been investigated [26.90]. Apart from dislocations a high density of stacking faults is observed, as shown in Fig. 26.17. These stacking faults thread up through the entire wafer, and are clearly undesirable defects, since they will propagate into an overgrown epitaxial structure [26.91]. The defects are found to be important recombination centers, and have a radiative emission characteristic for each type of SF (Fig. 26.18). This figure shows the low-temperature photoluminescence (PL) spectrum of an *a*-plane GaN layer grown by HVPE, with SF defects as shown in Fig. 26.17. The near-bandgap emission peak (NBE) is due to donor-

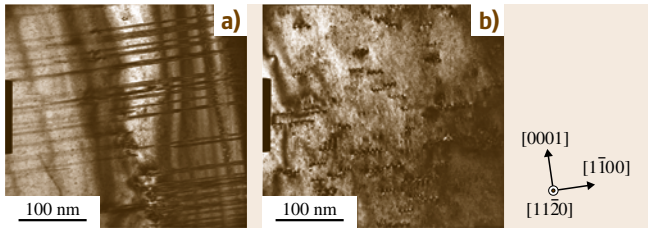


Fig. 26.17a,b Bright-field plan-view TEM images of an *a*-plane GaN film grown by HVPE with an MOVPE-GaN template layer taken close to the [11$\bar{2}$0] zone axis, slightly tilted: **(a)** along the [0001] direction, visualizing stacking faults formed in the basal plane of GaN by parallel lines, and **(b)** around the [0001] direction, visualizing partial dislocations having a nonzero [0001] component

bound excitons, while the broad peak at 3.43 eV is related to basal-plane SFs [26.92].

Growth employing ELO techniques has been attempted to reduce the SF density in thick HVPE GaN layers [26.93]. In this way part of the wafer surface can be free from SFs. However, efficient methods to eliminate these defects over an entire nonpolar wafer have not yet been developed.

X-ray diffraction (XRD) is a standard technique to obtain an overall characteristic of the structural quality of a semiconductor sample. The presence of internal defects such as microcracks and wafer bowing strongly affects the XRD characteristics of thick GaN wafers produced in the way discussed above. The coherence length along the growth direction increases as the TD

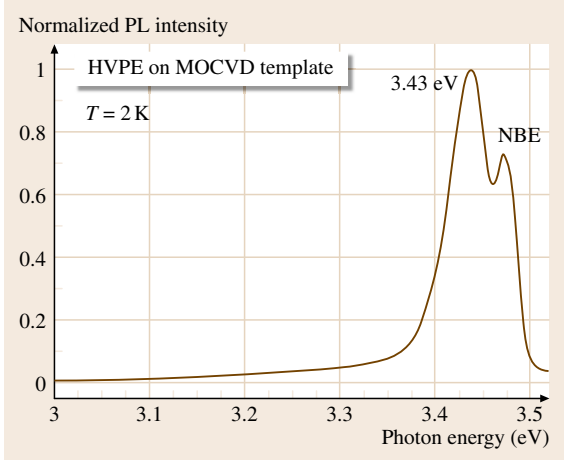


Fig. 26.18 Low-temperature PL spectra of an *a*-plane GaN layer grown by HVPE on an MOCVD-GaN template on *r*-plane sapphire

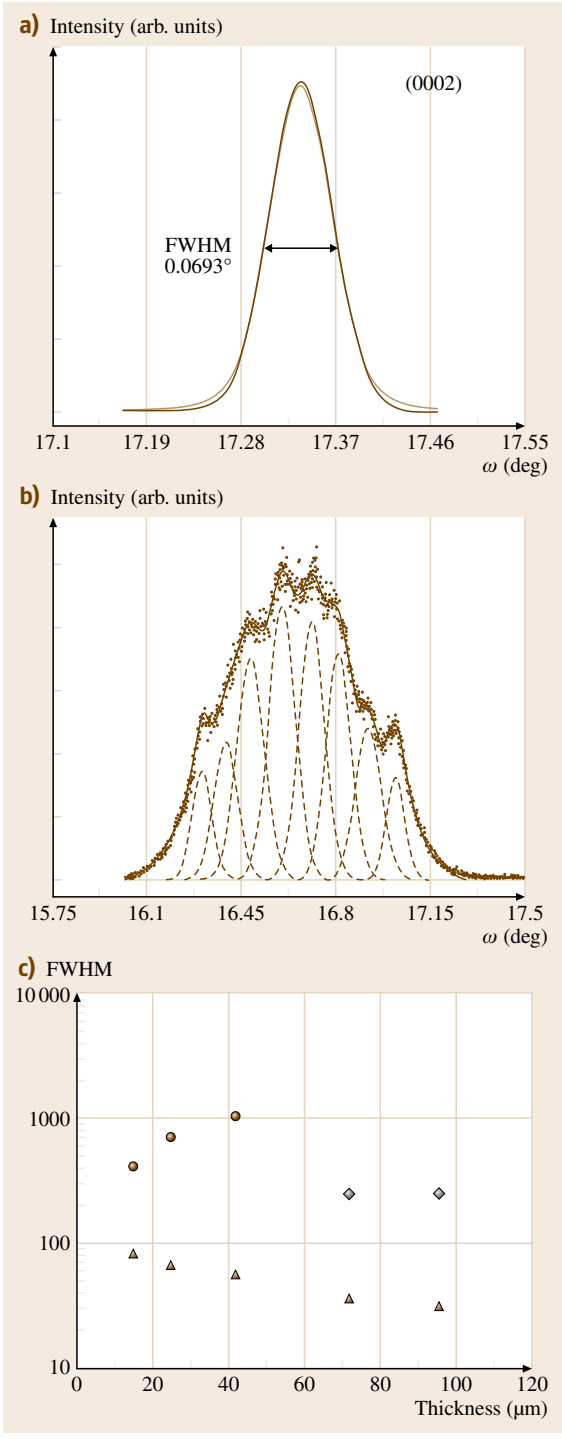


Fig. 26.19a–c Measured XRD line widths versus thickness for HVPE-grown GaN layers on sapphire. **(a)** Shows the line shape of a single rocking curve for a rather thin layer, while a thicker layer in **(b)** shows clear evidence of a mosaic substructure. **(c)** Shows a typical dependence of the line width on thickness for both rocking curve and the radial scan ◀

density is reduced. The full-width at half-maximum (FWHM) value of ω–2θ scans then decreases as the GaN film grows thicker, as seen in Fig. 26.19c for a set of moderately thick HVPE layers on sapphire. These data are consistent with those for another set of much thicker samples (about 300 μm), all having ω–2θ values of about 1 arcmin. The ω-scans show dramatically larger FWHM values, reflecting the presence of domain formation after a certain thickness (Fig. 26.19a,b), the residual bowing, and perhaps to some extent the internal cracks, and these effects are expected to contribute to the lattice tilt of the layers [26.94].

The characteristic XRD data for much thicker free-standing layers typically show much lower line widths. As an example, the FWHM for the ω-rocking curve of a 2 mm thick free-standing layer for the (002) reflection is 187 arcsec and the corresponding 2θ–ω peak has a FWHM of 36 arcsec, measured from the top Ga face [26.12].

Another class of defects of decisive importance for the quality of the material is impurities and point defects such as vacancies and interstitials. Residual impurities are introduced in the material during growth, and the density of such defects is critical mainly in the case of high-resistive material. The two common shallow donors in GaN are Si and O, both of which are easily introduced during growth, for different reasons. The Si contamination may strongly depend on the purity of the ammonia gas used; high-purity ammonia will minimize the Si contamination. There may also be some contribution from the attack on the quartz by parasitic growth upstream and in the growth zone. This process will depend on the proximity of the quartz walls to the substrate during growth. It has been shown that, with extended growth time, Si becomes the dominant residual impurity, while at the beginning of growth O is typically the dominant impurity incorporated. This is natural since O and water vapor are present, e.g., adsorbed or chemisorbed on quartz walls, or on the surface of the Ga source, and will gradually be released during a growth run, so that the amount of O contamination finally de-

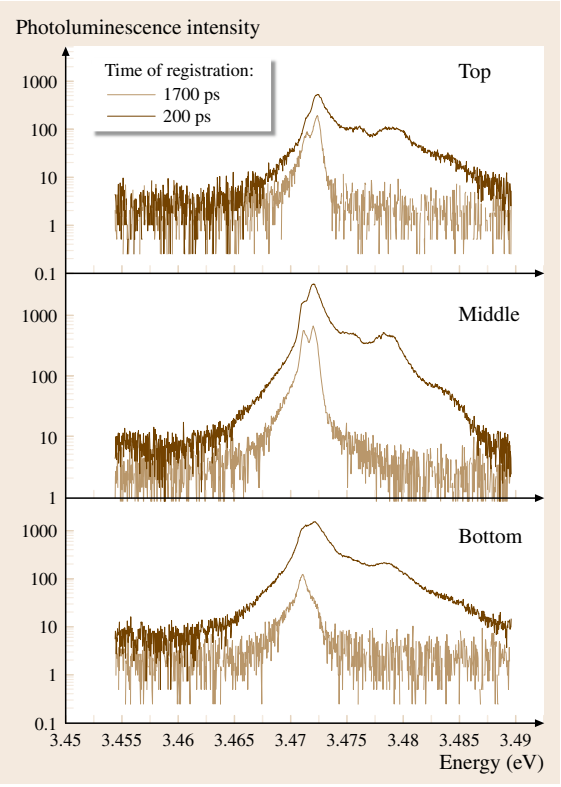


Fig. 26.20 Spatially resolved PL spectra at 2 K measured from different spots at the cross section of a 2 mm thick bulk GaN layer grown by HVPE, measured at two different delay times after the excitation pulse. The lower-energy O-related bound-exciton line (at about 3.471 eV) clearly dominates at the N face, while at the Ga face (grown last) Si is the dominant donor species (the peak at about 3.4725 eV) ◀

creases as the source of O is depleted. O can of course also be introduced via small air leaks in the system. An example is shown in Fig. 26.20, where the PL spectrum from the cross section of a 2 mm thick GaN wafer is dominated by the O bound exciton (BE) spectrum close to the N-side, but dominated by Si at the Ga side (grown last). The ultimate value of Si contamination in a system not used for Si doping is presumably below $10^{15}\,\mathrm{cm}^{-3}$, but this has not been well documented to date.

Other important impurities are metal contaminants, in particular those from the iron group. These create deep levels in GaN, and thus act as compensation centers which decrease the efficiency of doping. The main source of these contaminants are the metal parts of the growth setup (tubing, manifolds, cylinders). Compounds including these metals may transport to the growth zone as particles, although these can be eliminated via particle filters. A more severe process is the transport of chloride molecules of these metals, promoted by the rather high vapor pressure they have already at room temperature. Such contaminants can easily be detected by optical spectroscopy, since these metals have characteristic spectra (typically sharp lines in the range 0.8–1.3 eV) related to the internal transitions in the ions [26.95]. Other important defects are vacancies. In n-type and undoped GaN the main vacancy defect is the V_{Ga}–O complex, with the so-called yellow luminescence (YL) as the optical signature [26.96]. These defects are deep acceptors, and can be eliminated by carefully excluding O from entering the material during growth.

26.7 Some Important Properties of HVPE-Grown Bulk GaN Material

At present, HVPE is the only method that can produce high-purity ($< 10^{16}\,\mathrm{cm}^{-3}$) strain-free GaN material with low dislocation density ($< 10^{6}\,\mathrm{cm}^{-2}$). Such material is therefore the prime choice for establishing the most relevant properties of bulk GaN. Such properties are lattice parameters, thermal expansion coefficients, thermal conductivity, and electron and hole mobilities. The lattice parameters obviously depend significantly on strain [26.97], but also on defect density and doping [26.98, 99], and values in the literature are therefore dependent on the material used. Recent studies on a 2 mm thick nominally undoped, free-standing GaN bulk layer with a residual doping of about $10^{16}\,\mathrm{cm}^{-3}$ and a dislocation density of about $10^{6}\,\mathrm{cm}^{-2}$ probably represent the most accurate values of the lattice parameters for pure bulk GaN (Table 26.2). The lattice parameters as a function of temperature were also measured recently on a free-standing GaN layer, and thermal expansion coefficients were established with improved accuracy [26.100]. The thermal conductivity is another important property that depends strongly on the quality of the material. Early determinations of this quantity on rather defective HVPE GaN layers gave a value of 1.3 W/(cm K) [26.101].

Table 26.2 Some important material parameters for strain-free bulk GaN

Lattice parameter a (Å)	Lattice parameter c (Å) [26.105]	Thermal expansion coefficient α_a (10^{-6}/K) at 300 K	Thermal conductivity 300 K (W/(cm K))	Electron mobility 300 K ($cm^2/(V\,s)$) $n < 10^{16}\ cm^{-3}$	Hole mobility 300 K ($cm^2/(V\,s)$) $p \approx 10^{18}\ cm^{-3}$
3.18943 ±0.00015	5.18501 ±0.00015	4.3	2.3	1350	10

A more recent study on HVPE material with low dislocation density and low doping indicates that the phonon-scattering-limited thermal conductivity at room temperature is much higher, about 2.3 W/(cm K), i. e., considerably better than Si [26.102]. The best electron mobilities in GaN has been obtained in nominally undoped free-standing thick HVPE grown samples; a value of 1350 $cm^2/(V\,s)$ has been reported [26.103]. The hole mobilities have so far been measured only in highly doped and highly defective GaN; no reliable data are available for low-doped HVPE-grown bulk p-GaN to our knowledge. Extrapolated values for such material indicate a limiting hole mobility above 200 $cm^2/(V\,s)$ [26.104], to be confirmed in the future. In Mg-doped epitaxially grown device structures with a typical Mg concentration close to $10^{20}\ cm^{-3}$, the hole mobility is at best about 10 $cm^2/(V\,s)$ [26.104] (see also Table 26.2).

26.8 Growth of AlN by HVPE: Some Preliminary Results

High-quality and large-scale AlN wafers are recently in increasing demand as substrates for ultraviolet (UV) light-emitting devices and high-power high-frequency electronic devices. There have been several reports on growth of AlN by the sublimation–recondensation method [26.106, 107] and by solution growth [26.108]. Although AlN crystals with extremely low dislocation densities can be grown by these methods, expanding the size of the grown crystals is a challenging problem.

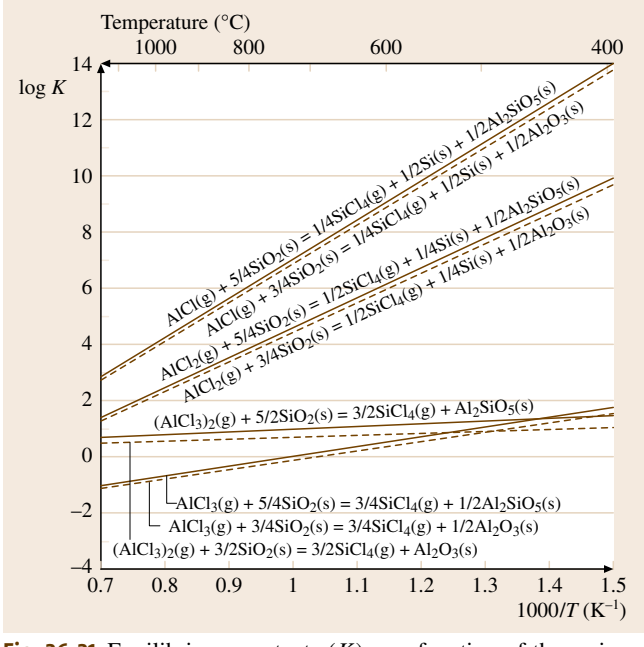


Fig. 26.21 Equilibrium constants (K) as a function of the reciprocal of reaction temperature for reactions between Al chlorides and quartz

On the other hand, high-speed growth of thick AlN layers by HVPE followed by separation of the grown layers from the starting substrates is an interesting approach to prepare AlN wafers. As is widely known, GaN wafers of 2 inch diameter have been mass-produced by HVPE using GaAs [26.109] or sapphire [26.59, 62, 110, 111] as starting substrates. However, investigations concerning HVPE of AlN have been limited [26.1, 112–115] due to the fact that the molten Al or hot AlCl gas reacts violently with the quartz (SiO_2) reactor of the HVPE system, damaging the reactor. On the other hand, there are other Al chlorides such as $AlCl_2$, $AlCl_3$, and $(AlCl_3)_2$. Figure 26.21 shows the values of the equilibrium constants K of the thermodynamically feasible reactions between gaseous AlCl, $AlCl_2$, $AlCl_3$ or $(AlCl_3)_2$ and quartz as a function of the reciprocal of the reaction temperature [26.1]. The following order of the equilibrium constants K of the reactivity of Al chlorides is seen

$$K_{AlCl} > K_{AlCl_2} > K_{(AlCl_3)_2} > K_{AlCl_3}\,. \qquad (26.13)$$

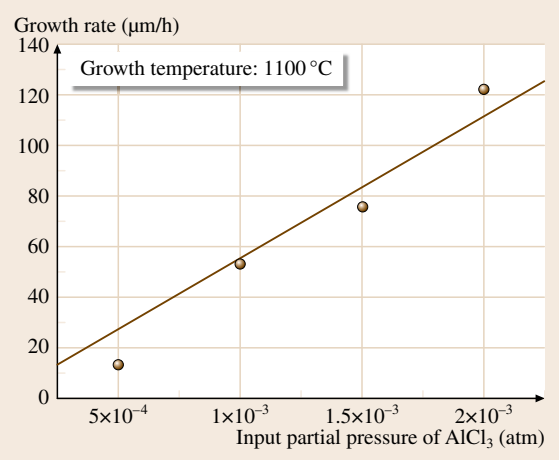


Fig. 26.22 Dependence of AlN growth rate on the $AlCl_3$ input partial pressure at 1100 °C

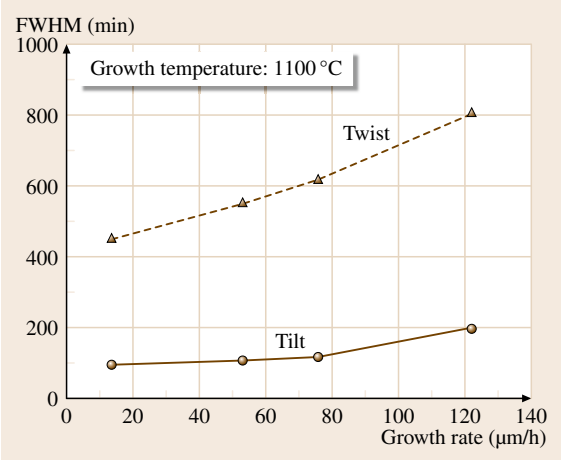


Fig. 26.23 FWHM of XRD rocking curves of the (0002) (tilt component) and the $(10\bar{1}0)$ (twist component) of AlN layers grown at 1100 °C with various growth rates

The reactions between AlCl and quartz have extremely large values of K. On the contrary, reactions between $AlCl_3$ and quartz have small values of K, and negative values of log K at 700 °C or above. Therefore, the reaction between $AlCl_3$ and the quartz reactor is negligible, and $AlCl_3$ is suitable as an Al source in AlN HVPE.

It has already been reported that preferential generation of $AlCl_3$ is possible [26.1] at the Al source zone of a conventional HVPE system by decreasing the source-zone temperature to about 500 °C (Fig. 26.1b). Exploiting this fact, several groups have grown AlN using a conventional hot-walled quartz reactor. In Fig. 26.22, the dependence of AlN growth rate on the $AlCl_3$ input partial pressure is shown [26.114]. Al metal pellets (6 N grade) were placed in the source zone to enlarge the surface area and maintained at 500 °C. $AlCl_3$ was formed by the reaction between the Al metal and HCl gas and mixed with NH_3 in the growth zone where a (0001) sapphire substrate was placed. The input V/III ratio ($NH_3/AlCl_3$) was fixed at 2. Growth was performed at 1100 °C under atmospheric pressure using H_2 as a carrier gas. A linear increase of the growth rate with increase of $AlCl_3$ input pressure is seen in the figure. With an $AlCl_3$ input partial pressure of 2×10^{-3} atm, the growth rate exceeds 100 μm/h. Therefore, high-speed growth of AlN by HVPE is possible just as in the HVPE growth of GaN.

Figure 26.23 shows the FWHM of the x-ray diffraction (XRD) rocking curves of (0002) (tilt component) and $(10\bar{1}0)$ (twist component) of AlN layers grown at 1100 °C with various growth rates [26.114]. Although high-speed growth of AlN is possible at 1100 °C, the FWHM of the (0002) and the $(10\bar{1}0)$ increase with increasing growth rate. In order to grow high-quality AlN layers with a high growth rate, it is considered that a higher growth temperature will be required.

The result of absorption measurements for a 2 μm thick AlN layer grown at 2 μm/h on a sapphire substrate

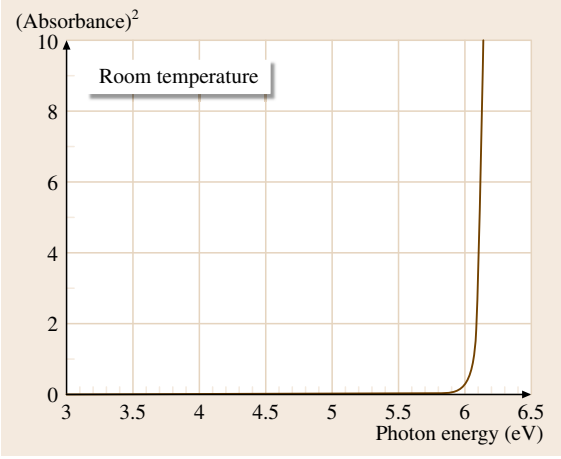


Fig. 26.24 Absorbance squared versus photon energy of an AlN layer measured at room temperature

is shown in Fig. 26.24, where absorbance squared is plotted as a function of photon energy. Extrapolation of the linear region to the horizontal axis gives the bandgap of AlN to be just above 6.0 eV (somewhat influenced by strain).

From the results shown above, the next challenges for AlN HVPE are thought to be high-temperature (> 1100 °C) growth and reduction of dislocation density in the grown layer using AlN templates, ELO structures, etc.

26.9 Growth of InN by HVPE: Some Preliminary Results

Recent progress in the growth of InN by MBE and MOVPE has clarified that the bandgap of InN is around 0.7 eV [26.116–118]. However, growth of thick InN layers remains difficult due to poor thermal stability, low growth rate of InN, and the lack of a suitable substrate material for epitaxy.

Although HVPE is a useful method for high-speed growth of GaN [26.47] and AlN [26.114] without formation of metal droplets, HVPE of InN is complicated: InN growth does not occur when InCl is used as an In source [26.119], while appreciable growth of InN occurs when $InCl_3$ powder is sublimated and transported by a carrier gas other than H_2 [26.119–121]. This is due to the fact that the equilibrium constant of the reaction between $InCl_3$ and NH_3 is larger than that between InCl and NH_3 (Fig. 26.2), and a suppression of InN growth in the presence of H_2 [26.7]. However, in order to grow high-quality InN layers without contamination, formation of $InCl_3$ gas in the source zone of a conventional HVPE system is needed, since commercially available $InCl_3$ powder inevitably contains water due to its hygroscopic nature. According to the thermodynamic analysis of the In source zone, where Cl_2 gas is introduced over the In metal, the equilibrium partial pressure of $InCl_3$ increases with decreasing source-zone temperature [26.122]. Here, it is essential to use Cl_2 instead of HCl to form $InCl_3$ because the reaction between In metal and HCl produces H_2, which suppresses the growth of InN at the growth zone [26.7].

We report preliminary results for successful HVPE growth of InN. Figure 26.25 shows the dependence of InN growth rate on the In source-zone temperature [26.122]. Cl_2 with an input partial pressure of 3.0×10^{-3} atm was introduced over the In metal using N_2 carrier gas, and NH_3 with an input partial pressure of 1.5×10^{-1} atm was separately introduced into the growth zone using N_2 carrier gas. Single-crystalline InN layers *c*-axis oriented without In droplets can be grown on a (0001) sapphire substrate at a growth zone temperature of 500 °C. It is seen that the growth rate increases with decreasing source-zone temperature above 450 °C. This is due to the increase of the $InCl_3$ equilibrium partial pressure at the In source zone. On the other

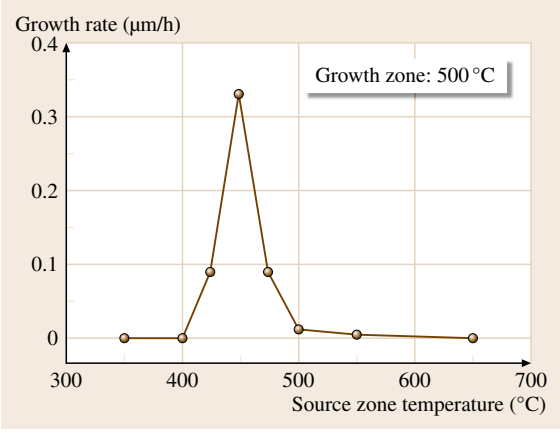


Fig. 26.25 Dependence of InN growth rate on the In source-zone temperature. Growth-zone temperature was fixed at 500 °C

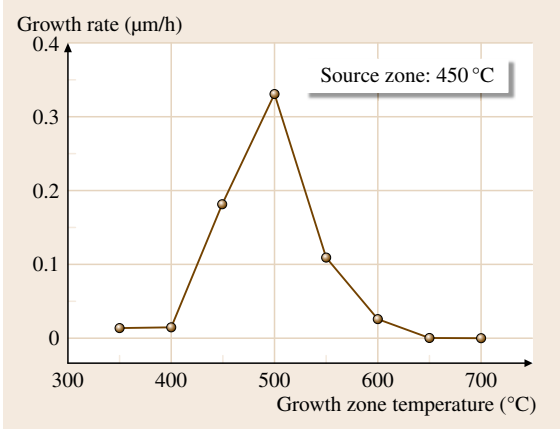


Fig. 26.26 Dependence of InN growth rate on the growth-zone temperature. In source-zone temperature was fixed at 450 °C

hand, with the source-zone temperature below 450 °C, the growth rate dropped rapidly because of insufficient reaction between Cl_2 and In metal.

As for the growth-zone temperature, InN growth is obtained within a narrow temperature range. Figure 26.26 shows the dependence of InN growth rate on the growth-zone temperature. The temperature of the In source zone was fixed at 450 °C. At growth temperature above 500 °C, the growth rate decreases as the growth-zone temperature increases. The growth rate also decreases with decrease of the growth-zone temperature below 500 °C due to insufficient reaction between $InCl_3$ and NH_3. Therefore, either an increase of Cl_2 input into the In source zone or an increase of the total gas flow rate in the reactor will be required to increase the growth rate of InN.

A room-temperature cathodoluminescence spectrum of the InN layer grown at 500 °C is shown in Fig. 26.27. An emission peak is seen at around 0.7 eV. Hall-effect measurements revealed that the InN layer had n-type conductivity with a carrier concentration of $3 \times 10^{19}\,cm^{-3}$ and a carrier mobility of $890\,cm^2/(V\,s)$.

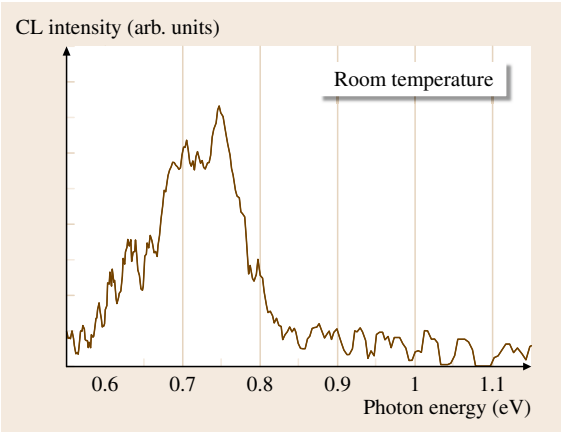


Fig. 26.27 Room-temperature CL spectrum of an InN layer grown at 500 °C by HVPE

The carrier concentration obtained is in agreement with that estimated from the dependence of the bandgap on electron concentration due to the Burstein–Moss effect [26.123].

References

26.1 Y. Kumagai, T. Yamane, T. Miyaji, H. Murakami, Y. Kangawa, A. Koukitu: Hydride vapor phase epitaxy of AlN: thermodynamic analysis of aluminum source and its application to growth, Phys. Status Solidi (c) **0**, 2498–2501 (2003)

26.2 M.W. Chase Jr. (Ed.): *NIST-JANAF Thermochemical Tables*, 4th edn. (National Institute of Standards and Technology, Gaithersburg 1998)

26.3 I. Barin (Ed.): *Thermochemical Data of Pure Substances* (Wiley, New York 1989)

26.4 A. Koukitu, S. Hama, T. Taki, H. Seki: Thermodynamic analysis of hydride vapor phase epitaxy of GaN, Jpn. J. Appl. Phys. **37**, 762–765 (1998)

26.5 Y. Kumagai, K. Takemoto, T. Hasegawa, A. Koukitu, H. Seki: Thermodynamics on tri-halide vapor-phase epitaxy of GaN and $In_xGa_{1-y}N$ using $GaCl_3$ and $InCl_3$, J. Cryst. Growth **231**, 57–67 (2001)

26.6 Y. Kumagai, K. Takemoto, J. Kikuchi, T. Hasegawa, H. Murakami, A. Koukitu: Thermodynamics on hydride vapor phase epitaxy of AlN using $AlCl_3$ and NH_3, Phys. Status Solidi (b) **243**, 1431–1435 (2006)

26.7 Y. Kumagai, K. Takemoto, A. Koukitu, H. Seki: Thermodynamics on halide vapor-phase epitaxy of InN using InCl and $InCl_3$, J. Cryst. Growth **222**, 118–124 (2001)

26.8 A. Koukitu, H. Seki: Thermodynamic analysis of the vapor growth of GaAs: the inert gas-hydrogen mixed carrier system, Jpn. J. Appl. Phys. **16**, 1967–1971 (1977)

26.9 V.S. Ban: Mass spectrometric studies of vapor-phase crystal growth. II. GaN, J. Electrochem. Soc. **119**, 761–765 (1972)

26.10 R.J. Molnar, W. Götz, L.T. Romano, J.M. Johnson: Growth of gallium nitride by hydride vapor-phase epitaxy, J. Cryst. Growth **178**, 147–156 (1997)

26.11 B. Monemar, H. Larsson, C. Hemmingsson, I.G. Ivanov, D. Gogova: Growth of thick GaN layers with hydride vapour phase epitaxy, J. Cryst. Growth **281**, 17–31 (2005)

26.12 C. Hemmingsson, P.P. Paskov, G. Pozina, M. Heuken, B. Schineller, B. Monemar: Growth of bulk GaN in a vertical hydride vapour phase epitaxy reactor, Superlattices Microstruct. **40**, 205–213 (2006)

26.13 V.S. Ban: Mass spectrometric and thermodynamics studies of the CVD of some III–V compounds, J. Cryst. Growth **17**, 19–30 (1972)

26.14 E. Richter, C. Hennig, M. Weyers, F. Habel, J.-D. Tsay, W.-Y. Liu, P. Brückner, F. Scholz, Y. Makarov, A. Segal, J. Kaeppeler: Reactor and growth process optimization for growth of thick GaN layers on sapphire substrates by HVPE, J. Cryst. Growth **277**, 6–12 (2005)

26.15 S. Porowski: High pressure growth of GaN – New prospects for blue lasers, J. Cryst. Growth **166**, 583–589 (1996)

26.16 I. Grzegory, B. Łucznik, M. Boćkowski, B. Pastuszka, G. Kamler, G. Nowak, M. Krysko,

S. Krukowski, S. Porowski: Crystallization of GaN by HVPE on pressure grown seeds, Phys. Status Solidi (a) **203**, 1654–1657 (2006)
26.17 B. Łucznik, B. Pastuszka, I. Grzegory, M. Boćkowski, G. Kamler, E. Litwin-Staszewska, S. Porowski: Deposition of thick GaN layers by HVPE on the pressure grown GaN substrates, J. Cryst. Growth **281**, 38–46 (2005)
26.18 L. Liu, J.H. Edgar: Substrates for gallium nitride epitaxy, Mater. Sci. Eng. Rep. **37**, 61–127 (2002)
26.19 O. Ambacher, J. Majewski, C. Miskys, A. Link, M. Hermann, M. Eickhoff, M. Stutzmann, F. Bernardini, V. Fiorentini, V. Tilak, B. Schaff, L.F. Eastman: Pyroelectric properties of Al(In)GaN/GaN hetero- and quantum well structures, J. Phys. Condens. Matter **14**, 3399–3434 (2002)
26.20 T. Paskova, P.P. Paskov, E. Valcheva, V. Darakchieva, J. Birch, A. Kasic, B. Arnaudov, S. Tungasmita, B. Monemar: Polar and nonpolar GaN grown by HVPE: Preferable substrates for nitride-based emitting devices, Phys. Status Solidi (a) **201**, 2265–2270 (2004)
26.21 W.A. Melton, J.I. Pankove: GaN growth on sapphire, J. Cryst. Growth **178**, 168–173 (1997)
26.22 B. Pécz, M.A. Di Forte-Poisson, F. Huet, G. Radnóczi, L. Tóth, V. Papaioannou, J. Stoemenos: Growth of GaN layers onto misoriented (0001) sapphire by metalorganic chemical vapor deposition, J. Appl. Phys. **86**, 6059–6067 (1999)
26.23 K. Hiramatsu, H. Amano, I. Akasaki, H. Kato, N. Koide, K. Manabe: MOVPE growth of GaN on a misoriented sapphire substrate, J. Cryst. Growth **107**, 509–512 (1991)
26.24 P. Brückner, M. Feneberg, K. Thonke, F. Habel, F. Scholz: High quality GaN layers grown on slightly miscut sapphire wafers, Mater. Res. Soc. Symp. Proc. **892**, 511–516 (2006)
26.25 R.J. Molnar, P. Maki, R. Aggarwal, Z.L. Liau, E.R. Brown, I. Melngailis, W. Götz, L.T. Romano, N.M. Johnson: Gallium nitride thick films grown by hydride vapor phase epitaxy, Mater. Res. Soc. Symp. **423**, 221–226 (1996)
26.26 S. Keller, B.P. Keller, Y.F. Wu, B. Heying, D. Kapolnek, J.S. Speck, U.K. Mishra, S.P. DenBaars: Influence of sapphire nitridation on properties of gallium nitride grown by metalorganic chemical vapor deposition, Appl. Phys. Lett. **68**, 1525–1527 (1996)
26.27 S. Fuke, H. Teshigawara, K. Kuwahara, Y. Takano, T. Ito, M. Yanagihara, K. Ohtsuka: Influences of initial nitridation and buffer layer deposition on the morphology of a (0001) GaN layer grown on sapphire substrates, J. Appl. Phys. **83**, 764–767 (1998)
26.28 K. Motoki, T. Okahisa, S. Nakahata, N. Matsumoto, H. Kimura, H. Kasai, K. Takemoto, K. Uematsu, M. Ueno, Y. Kumagai, A. Koukitu, H. Seki: Growth and characterization of freestanding GaN substrates, J. Cryst. Growth **237–239**, 912–921 (2002)
26.29 M. Ishida, T. Hashimoto, T. Takayama, O. Imafuji, M. Yuri, A. Yoshikama, K. Itoh, Y. Terakoshi, T. Sugino, J. Shirafuji: Growth of GaN thin films on sapphire substrate by low pressure MOCVD, Mater. Res. Soc. Symp. **468**, 69–74 (1997)
26.30 F. Widmann, G. Feuillet, B. Daudin, J.L. Rouviere: Low temperature sapphire nitridation: A clue to optimize GaN layers grown by molecular beam epitaxy, J. Appl. Phys. **85**, 1550–1555 (1999)
26.31 K. Naniwae, S. Itoh, H. Amano, K. Itoh, K. Hiramatsu, I. Akasaki: Growth of single crystal GaN substrate using hydride vapor phase epitaxy, J. Cryst. Growth **99**, 381–384 (1990)
26.32 R.J. Molnar, K.B. Nichols, P. Maki, E.R. Brown, I. Melngailis: The role of impurities in hydride vapor phase epitaxial grown gallium nitride, Mater. Res. Soc. Symp. Proc. **378**, 479–484 (1995)
26.33 J. Lee, H. Paek, J. Yoo, G. Kim, D. Kum: Low temperature buffer growth to improve hydride vapor phase epitaxy of GaN, Mater. Sci. Eng. B **59**, 12–15 (1999)
26.34 P.R. Tavernier, E.V. Etzkorn, Y. Wang, D.R. Clarke: Two-step growth of high-quality GaN by hydride vapor-phase epitaxy, Appl. Phys. Lett. **77**, 1804–1806 (2000)
26.35 H. Tsuchiya, K. Sunaba, M. Minami, T. Suemasu, F. Hasegawa: Influence of As autodoping from GaAs substrates on thick cubic GaN growth by halide vapor phase epitaxy, Jpn. J. Appl. Phys. **37**, L568–L570 (1998)
26.36 F. Hasegawa, M. Minami, K. Sunaba, T. Suemasu: Thick and smooth hexagonal GaN growth on GaAs (111) substrates at 1000 °C with halide vapor phase epitaxy, Jpn. J. Appl. Phys. **38**, L700–L702 (1999)
26.37 Y. Kumagai, H. Murakami, H. Seki, A. Koukitu: Thick and high-quality GaN growth on GaAs (111) substrates for preparation of freestanding GaN, J. Cryst. Growth **246**, 215–222 (2002)
26.38 E. Richter, C. Hennig, U. Zeimer, M. Weyers, G. Tränkle, P. Reiche, S. Ganschow, R. Uecker, K. Peters: Freestanding two inch *c*-plane GaN layers grown on (100) γ-lithium aluminium oxide by hydride vapour phase epitaxy, Phys. Status Solidi (c) **3**, 1439–1443 (2006)
26.39 O. Kryliouk, M. Reed, T. Dann, T. Anderson, B. Chai: Large area GaN substrates, Mater. Sci. Eng. B: Solid-State Mater. Adv. Technol. **66**, 26–29 (1999)
26.40 T. Paskova, S. Tungasmita, E. Valcheva, E. Svedberg, B. Arnaudov, S. Evtimova, P. Persson, A. Henry, R. Beccard, M. Heuken, B. Monemar: Hydride vapour phase homoepitaxlal growth of GaN on MOCVD-grown 'templates', MRS Internet J. Nitrid. Semicond. Res. **5**, W3.14 (2000)
26.41 H. Lee, M. Yuri, T. Ueda, J.S. Harris, K. Sin: Growth of thick GaN films on RF sputtered AlN buffer layer by hydride vapor phase epitaxy, J. Electron. Mater. **26**, 898–902 (1997)

26.42 E. Valcheva, T. Paskova, S. Tungasmita, P.O.Å. Persson, J. Birch, E.B. Svedberg, L. Hultman, B. Monemar: Interface structure of hydride vapor phase epitaxial GaN grown with high-temperature reactively sputtered AlN buffer, Appl. Phys. Lett. **76**, 1860–1862 (2000)

26.43 T. Paskova, E. Valcheva, J. Birch, S. Tungasmita, P.O.Å. Persson, P.P. Paskov, S. Evtimova, M. Abrashev, B. Monemar: Defect and stress relaxation in HVPE-GaN films using high temperature reactively sputtered AlN buffer, J. Cryst. Growth **230**, 381–386 (2001)

26.44 T. Detchprohm, K. Hiramatsu, H. Amano, I. Akasaki: Hydride vapor phase epitaxial growth of a high quality GaN film using a ZnO buffer layer, Appl. Phys. Lett. **61**, 2688–2690 (1992)

26.45 T. Ueda, T.-F. Huang, S. Spruytte, H. Lee, M. Yuri, K. Itoh, T. Baba, J.S. Harris Jr: Vapor phase epitaxy growth of GaN on pulsed laser deposited ZnO buffer layer, J. Cryst. Growth **187**, 340–346 (1998)

26.46 S. Gu, R. Zhang, J. Sun, L. Zhang, T.F. Kuech: The nature and impact of ZnO buffer layers on the initial stages of the hydride vapor phase epitaxy of GaN, MRS Internet J. Nitrid. Semicond. Res. **5**, W3.15 (2000)

26.47 A. Usui, H. Sunakawa, A. Sakai, A.A. Yamaguchi: Thick GaN epitaxial growth with low dislocation density by hydride vapor phase epitaxy, Jpn. J. Appl. Phys. **36**, L899–L902 (1997)

26.48 K. Hiramatsu, H. Matsushima, T. Shibata, N. Sawaki, K. Tadatomo, H. Okagawa, Y. Ohuchi, Y. Honda, T. Matsue: Selective area growth of GaN by MOVPE and HVPE, Mater. Res. Soc. Symp. Proc. **482**, 257–268 (1998)

26.49 G. Nataf, B. Beaumont, A. Bouillé, S. Haffouz, M. Vaille, P. Gibart: Lateral overgrowth of high quality GaN layers on GaN/Al_2O_3 patterned substrates by halide vapour-phase epitaxy, J. Cryst. Growth **192**, 73–78 (1998)

26.50 O. Parillaud, V. Wagner, H.J. Bühlmann, M. Ilegems: Localized Epitaxy of GaN by HVPE on patterned Substrates, MRS Internet J. Nitrid. Semicond. Res. **3**, 40 (1998)

26.51 Y. Zhonghai, M.A.L. Johnson, J.D. Brown, N.A. El-Masrys, J.F. Muth, J.W. Cook Jr, J.F. Schetzina, K.W. Haberern, H.S. Kong, J.A. Edmond: Epitaxial lateral overgrowth of GaN on SiC and sapphire substrates, MRS Internet J. Nitrid. Semicond. Res. **4S1**, G4.3 (1999)

26.52 R. F. Davis, O. H. Nam, T. Zheleva, M. Bremser: Methods of fabricating gallium nitride semiconductor layers by lateral overgrowth through masks, and gallium nitride semiconductor structures fabricated thereby, Patent WO9944224 (1999)

26.53 J. Hirth, J. Lothe: The theory of straight dislocations. In: *Theory of Dislocations* (Wiley, New York 1982) pp. 55–95

26.54 P. Gibart, B. Beaumont, P. Vennéguès: Epitaxial lateral overgrowth of GaN. In: *Nitride Semiconductors, Handbook on Materials and Devices*, ed. by P. Ruterana, M. Albrecht, J. Neugebauer (Wiley, New York 2003) pp. 45–106

26.55 Z. Liliental-Weber, M. Benamara, W. Swider, J. Washburn, J. Park, P.A. Grudowski, C.J. Eiting, R.D. Dupuis: TEM study of defects in laterally overgrown GaN layers, MRS Internet J. Nitrid. Semicond. Res. **4S1**, G4.6 (2000)

26.56 H. Miyake, H. Mizutani, K. Hiramatsu, Y. Iyechika, Y. Honda, T. Maeda: Fabrication of GaN layer with low dislocation density using facet controlled ELO technique, Mater. Res. Symp. Proc. **639**, G5.3.1. (2001)

26.57 S.-I. Nagahama, N. Iwasa, M. Senoh, T. Matsushita, Y. Sugimoto, H. Kiyoku, T. Kozaki, M. Sano, H. Matsumura, H. Umemoto, K. Chocho, T. Mukai: High-power and long-lifetime InGaN multi-quantum-well laser diodes grown on low-dislocation-density GaN substrates, Jpn. J. Appl. Phys. **39**, L647–L650 (2000)

26.58 W.S. Wong, T. Sands, N.W. Cheung: Damage-free separation of GaN thin films from sapphire substrates, Appl. Phys. Lett. **72**, 599–601 (1998)

26.59 M.K. Kelly, R.P. Vaudo, V.M. Phanse, L. Gorgens, O. Ambacher, M. Stutzmann: Large free-standing GaN substrates by hydride vapor phase epitaxy and laser-induced liftoff, Jpn. J. Appl. Phys. **38**, L217–L219 (1999)

26.60 O. Ambacher, M.S. Brandt, R. Dimitrov, T. Metzger, M. Stutzmann, R.A. Fischer, A. Miehr, A. Bergmaier, G. Dollinger: Thermal stability and desorption of group III nitrides prepared by metal organic chemical vapor deposition, J. Vac. Sci. Technol. B **14**, 3532–3542 (1996)

26.61 D. Gogova, A. Kasic, H. Larsson, C. Hemmingsson, B. Monemar, F. Toumisto, K. Saarinen, L. Dobos, B. Pécz, P. Gibart, B. Beaumont: Strain-free bulk-like GaN grown by hydride-vapor-phase-epitaxy on two-step epitaxial lateral overgrown GaN template, J. Appl. Phys. **96**, 799–806 (2004)

26.62 Y. Oshima, T. Eri, M. Shibata, H. Sunakawa, K. Kobayashi, T. Ichihashi, A. Usui: Preparation of freestanding GaN wafers by hydride vapor phase epitaxy with void-assisted separation, Jpn. J. Appl. Phys. **42**, L1–L3 (2003)

26.63 P.R. Tavernier, B. Imer, S.P. DenBaars, D.R. Clarke: Growth of thick (11$\bar{2}$0) GaN using a metal interlayer, Appl. Phys. Lett. **85**, 4630–4632 (2004)

26.64 H.M. Kim, J.E. Oh, T.W. Kang, H.M. Kim, J.E. Oh, T.W. Kang: Preparation of large area free-standing GaN substrates by HVPE using mechanical polishing liftoff method, Mater. Lett. **47**, 276–280 (2001)

26.65 Y.V. Melnik, K.V. Vassilevski, I.P. Nikitina, A.I. Babanin, V.Y. Davydov, V.A. Dmitriev: Physical

properties of bulk GaN crystals grown by HVPE, MRS Internet J. Nitrid. Semicond. Res. **2**, 39 (1997)
26.66 Y. Melnik, A. Nikolaev, I. Nikitina, K.V. Vassilevski, V.A. Dmitriev: Properties of free-standing GaN bulk crystals grown by HVPE, Mater. Res. Soc. Symp. Proc. **482**, 269–274 (1998)
26.67 T.J. Kropewnicki, W.A. Doolittle, C. Carter-Coman, S. Kang, P.A. Kohl, N.M. Jokerst, A.S. Brown, S. April: Selective wet etching of lithium gallate, J. Electrochem. Soc. **145**, L88–L90 (1998)
26.68 O. Oda, T. Inoue, Y. Seki, K. Kainosho, S. Yaegashi, A. Wakahara, A. Yoshida, S. Kurai, Y. Yamada, T. Taguchi: GaN bulk substrates for GaN based LEDs and LDs, Phys. Status Solidi (a) **180**, 51–58 (2000)
26.69 A. Wakahara, T. Yamamoto, K. Ishio, A. Yoshida, Y. Seki, K. Kainosho, O. Oda: Hydride vapor phase epitaxy of GaN on $NdGaO_3$ substrate and realization of freestanding GaN wafers with 2-inch scale, Jpn. J. Appl. Phys. **39**, 2399–2401 (2000)
26.70 R. P. Vaudo, V. M. Phanse, J. Jayapalan, D. Wang, B.J. Skromme: Si-doping of GaN grown on sapphire by HVPE, abstract book, MRS fall meeting, (1997) D16.3
26.71 E. Richter, C. Hennig, U. Zeimer, L. Wang, M. Weyers, G. Tränkle: n-Type doping of HVPE-grown GaN using dichlorosilane, Phys. Status Solidi (a) **203**, 1658–1662 (2006)
26.72 A.V. Fomin, A.E. Nikolaev, I.P. Nikitina, A.S. Zubrilov, M.G. Mynbaeva, N.I. Kuznetsov, A.P. Kovarsky, B.J. Ber, D.V. Tsvetkov: Properties of Si-doped GaN layers grown by HVPE, Phys. Status Solidi (a) **188**, 433–437 (2001)
26.73 C. G. Van de Walle, S. Limpijumnong, J. Neugebauer: First-principles studies of beryllium doping of GaN, Phys. Rev. B **63**, 245205-1–245205-17 (2001)
26.74 W. Götz, N.M. Johnson, J. Walker, D.P. Bour, R.A. Street: Activation of acceptors in Mg-doped GaN grown by metalorganic chemical vapor deposition, Appl. Phys. Lett. **68**, 667–669 (1996)
26.75 H. Amano, M. Kito, K. Hiramatsu, I. Akasaki: p-Type conduction in Mg-doped GaN treated with low-energy electron beam irradiation (LEEBI), Jpn. J. Appl. Phys. **28**, L2112–L2114 (1989)
26.76 S. Nakamura, T. Mukai, M. Senoh, N. Iwasa: Thermal annealing effects on p-type Mg-doped GaN films, Jpn. J. Appl. Phys. **31**, L139–L142 (1992)
26.77 D.P. Bour, H.F. Chung, W. Götz, L. Romano, B.S. Krusor, D. Hofstetter, S. Rudaz, C.P. Kuo, F.A. Ponce, N.M. Johnson, M.G. Craford, R.D. Bringans: Characterization of OMVPE-grown AlGaInN heterostructures, Mater. Res. Soc. Symp. Proc. **449**, 509–518 (1997)
26.78 J. Neugebauer, C.G. Van de Walle: Theory of point defects and complexes in GaN, Mater. Res. Soc. Symp. Proc. **395**, 645–656 (1996)
26.79 A. Usikov, O. Kovalenkov, V. Ivantsov, V. Sukhoveev, V. Dmitriev, N. Shmidt, D. Poloskin, V. Petrov, V. Ratnikov: p-Type GaN epitaxial layers and AlGaN/GaN heterostructures with high hole concentration and mobility grown by HVPE, Mater. Res. Soc. Symp. Proc. **831**, 453–457 (2005)
26.80 J.A. Van Vechten, J.D. Zook, R.D. Horning, B. Goldenberg: Defeating compensation in wide gap semiconductors by growing in H that is removed by low temperature de-ionizing radiation, Jpn. J. Appl. Phys. **31**, 3662–3663 (1992)
26.81 J. Neugebauer, C.G. Van de Walle: Atomic geometry and electronic structure of native defects in GaN, Phys. Rev. B **50**, 8067–8070 (1994)
26.82 J. Neugebauer, C.G. Van de Walle: Hydrogen in GaN: Novel aspects of a common impurity, Phys. Rev. Lett. **75**, 4452–4455 (1995)
26.83 J. Neugebauer, C.G. Van de Walle: Gallium vacancies and the yellow luminescence in GaN, Appl. Phys. Lett. **69**, 503–505 (1996)
26.84 A. Kasic, D. Gogova, H. Larsson, I.G. Ivanov, C. Hemmingsson, R. Yakimova, B. Monemar, M. Heuken: Characterization of crack-free relaxed GaN grown on 2″ sapphire, J. Appl. Phys. **98**, 073525-1–073525-6 (2005)
26.85 E.V. Etzkorn, D.R. Clarke: Cracking of GaN films, J. Appl. Phys. **89**, 1025–1034 (2001)
26.86 T. Hino, S. Tomiya, T. Miyajima, K. Yanashima, S. Hashimoto, M. Ikeda: Characterization of threading dislocations in GaN epitaxial layers, Appl. Phys. Lett. **76**, 3421–3423 (2000)
26.87 R.P. Vaudo, X. Xu, C. Loria, A.D. Salant, J.S. Flynn, G.R. Brandes: GaN boule growth: A pathway to GaN wafers with improved material quality, Phys. Status Solidi (a) **194**, 494–497 (2002)
26.88 M. Albrecht, I.P. Nikitina, A.E. Nikolaev, V.Y. Melnik, V.A. Dmitriev, H.P. Strunk: Dislocation reduction in AlN and GaN bulk crystals grown by HVPE, Phys. Status Solidi (a) **176**, 453–458 (1999)
26.89 CREE homepage: www.cree.com/products/gan_tech.asp (24-Sep 2008)
26.90 T. Paskova, V. Darakchieva, P.P. Paskov, J. Birch, E. Valcheva, P.O.A. Persson, B. Arnaudov, S. Tungasmitta, B. Monemar: Properties of nonpolar *a*-plane GaN films grown by HVPE with AlN buffers, J. Cryst. Growth **281**, 55–61 (2005)
26.91 T. Paskova, R. Kroeger, P.P. Paskov, S. Figge, D. Hommel, B. Monemar, B. Haskell, P. Fini, J.S. Speck, S. Nakamura: Microscopic emission properties of nonpolar *a*-plane GaN grown by HVPE, Proc. SPIE **6121**, 47 (2006)
26.92 P.P. Paskov, T. Paskova, B. Monemar, S. Figge, D. Hommel, B.A. Haskell, P.T. Fini, J.S. Speck, S. Nakamura: Optical properties of nonpolar *a*-plane GaN layers, Superlattices Microstruct. **40**, 253–261 (2006)
26.93 B.A. Haskell, F. Wu, M.D. Craven, S. Matsuda, P.T. Fini, T. Fujii, K. Fujito, S.P. DenBaars, J.S. Speck, S. Nakamura: Defect reduction in $(11\bar{2}0)$ *a*-plane gallium nitride via lateral epitaxial overgrowth by

hydride vapor-phase epitaxy, Appl. Phys. Lett. **83**, 644–646 (2003)
26.94 B. Monemar, T. Paskova, C. Hemmingsson, H. Larsson, P.P. Paskov, I.G. Ivanov, A. Kasic: Growth of thick GaN layers by hydride vapor phase epitaxy, J. Ceram. Process. Res. **6**, 153–162 (2005)
26.95 J. Baur, U. Kaufmann, M. Kunzer, J. Schneider, H. Amano, I. Akasaki, T. Detchprohm, K. Hiramatsu: Characterization of residual transition metal ions in GaN and AlN, Mater. Sci. For. **196–201**, 55–60 (1995)
26.96 K. Saarinen, T. Laine, S. Kuisma, J. Nissilä, P. Hautojärvi, L. Dobrzynski, J.M. Baranowski, K. Pakula, R. Stepniewski, M. Wojdak, A. Wysmolek, T. Suski, M. Leszczynski, I. Grzegory, S. Porowski: Observation of native Ga vacancies in GaN by positron annihilation, Phys. Rev. Lett. **79**, 3030–3033 (1997)
26.97 M. Leszczynski, H. Teisseyre, T. Suski, I. Grzegory, M. Boćkowski, J. Jun, S. Porowski, K. Pakula, J.M. Baranowski, C.T. Foxon, T.S. Cheng: Lattice parameters of gallium nitride, Appl. Phys. Lett. **69**, 73–75 (1996)
26.98 V. Darakchieva, P.P. Paskov, T. Paskova, E. Valcheva, B. Monemar, M. Heuken: Lattice parameters of GaN layers grown on *a*-plane sapphire: Effect of in-plane strain anisotropy, Appl. Phys. Lett. **82**, 703–705 (2003)
26.99 C. G. Van de Walle: Effects of impurities on the lattice parameters of GaN, Phys. Rev. B **68**, 165209-1–165209-5 (2003)
26.100 C. Roder, S. Einfeldt, S. Figge, D. Hommel: Temperature dependence of the thermal expansion of GaN, Phys. Rev. B **72**, 085218-1–085218-6 (2005)
26.101 E.K. Sichel, J.I. Pankove: Thermal conductivity of GaN, 25–360 K, J. Phys. Chem. Solids. **38**, 330 (1977)
26.102 A. Jezowski, P. Stachowiak, T. Plackowski, T. Suski, S. Krukowski, M. Boćkowski, I. Grzegory, B. Danilchecnko, T. Paszkiewicz: Thermal conductivity of GaN crystals grown by high pressure method, Phys. Status Solidi (b) **240**, 447–450 (2003)
26.103 D.C. Look, J.R. Sizelove: Predicted maximum mobility in bulk GaN, Appl. Phys. Lett. **79**, 1133–1135 (2001)
26.104 J.W. Orton, C.T. Foxon: Group III nitride semiconductors for short wavelength light-emitting devices, Rep. Prog. Phys. **61**, 1–75 (1998)
26.105 V. Darakchieva, private communication, 2006
26.106 J.C. Rojo, G.A. Slack, K. Morgan, B. Raghothamachar, M. Dudley, L.J. Schowalter: Report on the growth of bulk aluminum nitride and subsequent substrate preparation, J. Cryst. Growth **231**, 317–321 (2001)
26.107 R. Schlesser, R. Dalmau, Z. Sitar: Seeded growth of AlN bulk single crystals by sublimation, J. Cryst. Growth **241**, 416–420 (2002)
26.108 M. Boćkowski, M. Wróblewski, B. Łucznik, I. Grzegory: Crystal growth of aluminum nitride under high pressure of nitrogen, Mater. Sci. Semicond. Process. **4**, 543–548 (2001)
26.109 K. Motoki, T. Okahisa, N. Matsumoto, M. Matsushima, H. Kimura, H. Kasai, K. Takemoto, K. Uematsu, T. Hirano, M. Nakayama, S. Nakahata, M. Ueno, D. Hara, Y. Kumagai, A. Koukitu, H. Seki: Preparation of large freestanding GaN substrates by hydride vapor phase epitaxy using GaAs as a starting substrate, Jpn. J. Appl. Phys. **40**, L140–L143 (2001)
26.110 S.S. Park, I.-W. Park, S.H. Choh: Free-standing GaN substrates by hydride vapor phase epitaxy, Jpn. J. Appl. Phys. **39**, L1141–L1142 (2000)
26.111 D. Gogova, H. Larsson, A. Kasic, G.R. Yazdi, I. Ivanov, R. Yakimova, B. Monemar, E. Aujol, E. Frayssinet, J.-P. Faurie, B. Beaumont, P. Gibart: High-quality 2″ bulk-like free-standing GaN grown by hydride vapour phase epitaxy on a Si-doped metal organic vapour phase epitaxial GaN template with an ultra low dislocation density, Jpn. J. Appl. Phys. **44**, 1181–1185 (2005)
26.112 A. Nikolaev, I. Nikitina, A. Zubrilov, M. Mynbaeva, Y. Melnik, V. Dmitriev: AlN wafers fabricated by hydride vapor phase epitaxy, Mater. Res. Soc. Symp. Proc. **595**, W6.5 (2000)
26.113 O.Y. Ledyaev, A.E. Cherenkov, A.E. Nikolaev, I.P. Nikitina, N.I. Kuznetsov, M.S. Dunaevski, A.N. Titkov, V.A. Dmitriev: Properties of AlN layers grown on SiC substrates in wide temperature range by HVPE, Phys. Status Solidi (c) **0**, 474–478 (2002)
26.114 Y. Kumagai, T. Yamane, A. Koukitu: Growth of thick AlN layers by hydride vapor-phase epitaxy, J. Cryst. Growth **281**, 62–67 (2005)
26.115 Y.-H. Liu, T. Tanabe, H. Miyake, K. Hiramatsu, T. Shibata, M. Tanaka, Y. Masa: Growth of thick AlN Layer by hydride vapor phase epitaxy, Jpn. J. Appl. Phys. **44**, L505–L507 (2005)
26.116 V.Y. Davydov, A.A. Klochikhin, R.P. Seisyan, V.V. Emtsev, S.V. Ivanov, F. Bechstedt, J. Furthmüller, H. Harima, A.V. Mudryi, J. Aderhold, O. Semchinova, J. Graul: Absorption and emission of hexagonal InN. Evidence of narrow fundamental band gap, Phys. Status Solidi (b) **229**, R1–R3 (2002)
26.117 J. Wu, W. Walukiewicz, K.M. Yu, J.W. Ager III, E.E. Haller, H. Lu, W.J. Schaff, Y. Saito, Y. Nanishi: Unusual properties of the fundamental band gap of InN, Appl. Phys. Lett. **80**, 3967–3969 (2002)
26.118 T. Matsuoka, H. Okamoto, M. Nakao, H. Harima, E. Kurimoto: Optical bandgap energy of wurtzite InN, Appl. Phys. Lett. **81**, 1246–1248 (2002)
26.119 N. Takahashi, J. Ogasawara, A. Koukitu: Vapor phase epitaxy of InN using InCl and $InCl_3$ sources, J. Cryst. Growth **172**, 298–302 (1997)
26.120 L.A. Marasina, I.G. Pichugin, M. Tlaczala: Preparation of InN epitaxial layers in $InCl_3$-NH_3 system, Krist. Tech. **12**, 541–545 (1977)
26.121 N. Takahashi, R. Matsumoto, A. Koukitu, H. Seki: Growth of InN at high temperature by halide vapor

phase epitaxy, Jpn. J. Appl. Phys. **36**, L743–L745 (1997)

26.122 Y. Kumagai, J. Kikuchi, Y. Nishizawa, H. Murakami, A. Koukitu: Hydride vapor phase epitaxy of InN by the formation of $InCl_3$ using In metal and Cl_2, J. Cryst. Growth **300**, 57–61 (2007)

26.123 J. Wu, W. Walukiewicz, S.X. Li, R. Armitage, J.C. Ho, E.R. Weber, E.E. Haller, H. Lu, W.J. Schaff, A. Barcz, R. Jakiela: Effects of electron concentration on the optical absorption edge of InN, Appl. Phys. Lett. **84**, 2805–2807 (2004)

27. Growth of Semiconductor Single Crystals from Vapor Phase

Ramasamy Dhanasekaran

Growth of single crystals from the vapor phase is considered to be an important method to obtain stoichiometric crystalline materials from inexpensive and readily available raw materials. Elements or compounds which are relatively volatile can be grown from vapor phase. Most II–VI, I–III–VI_2, and III–N compounds are high-melting-point materials which may be grown as single crystals by careful use of vapor phase. The chemical vapor transport (CVT) method has been widely used as an advantageous method to grow single crystals of different compounds at temperatures lower than their melting points. This method is quite useful for the growth of II–VI and I–III–VI_2 compounds, which generally have high melting point and large dissociation pressure at the melting point. In addition, they undergo solid-state phase transition during cooling or heating processes, which makes the growth of these compounds by some other methods, such as from the melt, difficult. In addition, the low growth temperature involved reduces defects produced by thermal strain, pollution from the crucible, and the cost of the growth equipment. II–VI compound semiconductors cover a very broad range of electronic and optical properties due to the large range of their energy gaps. These materials in the form of bulk single crystals or thin films are used in light emitters, detectors, linear and nonlinear optical devices, semiconductor electronics, and other devices. The development of growth technology for II–VI compound semiconductors from the vapor phase with the necessary theoretical background is important. I–III–VI_2 chalcopyrite compounds are of technological interest since they show promise for application in areas of visible and infrared light-emitting diodes, infrared detectors, optical parametric oscillators, upconverters, far-infrared generation, and solar energy conversion.

27.1 **Classifications of Vapor Growth** 899

27.2 **Chemical Vapor Transport – Transport Kinetics** 901
27.2.1 Transport Models 901
27.2.2 Physical Chemistry of Chemical Transport Reactions ... 902
27.2.3 Factors Affecting the CVT Reaction 903
27.2.4 Choice of Transporting Agents 904
27.2.5 Advantages and Limitations of CVT Method 904

27.3 **Thermodynamic Considerations** 905
27.3.1 Estimation of Optimum Growth Parameters for the ZnSe–I_2 System by CVT 905
27.3.2 Fluctuations in the Transport Rates 906
27.3.3 Supersaturation Ratios in the ZnS_xSe_{1-x} System 908

27.4 **Growth of II–VI Compound Semiconductors by CVT** 912
27.4.1 Apparatus 912
27.4.2 Preparation of Starting Materials .. 913
27.4.3 Growth of ZnSe Single Crystals 914
27.4.4 Growth of CdS Single Crystals 915

27.5 **Growth of Nanomaterial from Vapor Phase** 916

27.6 **Growth of I–III–VI_2 Compounds** 917
27.6.1 Growth of Undoped and Doped Crystals of $CuAlS_2$ 918
27.6.2 Growth of Undoped and Doped Crystals of $CuAlSe_2$ 919
27.6.3 Growth of $CuGaS_2$-Based Single Crystals ... 921
27.6.4 Growth of $AgGaS_2$ and $AgGaSe_2$ Single Crystals 923

27.7 **Growth of GaN by VPE** 925
27.7.1 Vapor-Phase Epitaxy (VPE) 925
27.7.2 VPE GaN Film Growth 925
27.7.3 Strength of HVPE Method 926
27.7.4 Development of VPE System for the Growth of GaN 926

27.7.5 Growth of GaN by HVPE 927
27.7.6 Characterization of GaN Films 928
27.8 Conclusion 929
References 930

A great deal of interest in these materials is generated by their chalcopyrite structure, which is noncentrosymmetric and makes them useful for second-harmonic generation. III-nitride semiconductors are of great interest to industry and the military due to their optoelectronic and mechanical properties, permitting the development of devices operating in the blue and ultraviolet regions of the spectrum and at high temperatures. Gallium nitride has particularly attracted considerable attention in this regard. Despite the progress recently achieved, some fundamental properties of GaN and its related compounds, such as InGaN and AlGaN, are still not fully understood. Epitaxial methods continue to lead the field of crystal growth by exploring new physics, materials science, and fabrication of novel devices. Good-quality GaN layers have been grown by employing vapor-phase epitaxy systems, the technical details of which are presented in detail herein.

During recent decades, ternary, quaternary, and more recently multinary semiconductor materials have been widely investigated because of their importance for solid-state device applications. However, their crystal growth technology is far from well understood. Due to practical difficulties involved in growing single crystals of most of these materials by melt techniques, regular production of small samples perfect enough and of good enough quality almost always depends upon the availability of vapor-phase (VP) chemical transport reactions (usually *iodine* transport) in closed tubes. One of the common drawbacks of these VP methods is the high level of supersaturation, and hence uncontrolled primary nucleation, which can give rise to many small-sized (often submillimeter) crystals. This high supersaturation is also responsible for various instability patterns (dendrites, overgrowths, etc.) that show up in the final crystals. Crystal growth from the vapor phase is in principle a flexible method of growing single crystals. This potential flexibility has occasionally been exploited, but more often the principles have been poorly understood [27.1]. Preparation of a crystal from the gas phase requires the general reaction

GAS (disordered phase) ⟶
CRYSTAL (ordered phase) .

The gas phase may consist of molecules of the crystal substance, or of its separate constituents, if they are all volatile. Otherwise, the constituents may be reacted with a transporting agent to provide volatile species. In all cases, an inert gas is added to modify the transport kinetics. The basic reaction results in an increase in atomic order.

Important research efforts have been focused on II–VI compounds since the late 1950s. Because of their superiority over rival materials, these compounds are becoming of more importance day by day in research into electronic materials. Many experimental procedures have been improved, and theoretical models have been developed. However, in spite of their positive properties, the crystallographic properties of some II–VI semiconductor materials (e.g., ZnS and ZnSe) have hindered their application in the electronic industry due to polytypism.

Currently, I–III–VI_2 compounds (chalcopyrite ternary semiconductor), such as copper indium diselenide ($CuInSe_2$), copper indium disulfide ($CuInS_2$), and copper gallium diselenide ($CuGaSe_2$), are the most promising low-cost thin-film materials for solar cell applications due to their high absorption coefficient and excellent thermal stability. Photovoltaic (PV) cells based on these materials have potentials to be used on the Earth as well as in various space applications. Scientists from the US National Renewable Energy Laboratory (NREL), have achieved efficiency of about 19.2% with $CuInSe_2$ absorber in laboratory cells. The best efficiency of a thin-film solar cell up to now is 19.5%, by using $Cu(In,Ga)Se_2$ as absorber [27.2], which is comparable to that for polycrystalline Si solar cells. In view of their potential low cost and light weight, these solar cells have been expected to be useful in space applications in addition to the terrestrial domain. Thus, there is strong demand for improvement of the efficiency of PV cells based on these chalcopyrite materials.

The demonstration of blue light-emitting diodes (LEDs) and blue laser diodes (LDs) [27.3] has led to the emergence of III–V nitrides as a suitable material for high-power, high-temperature electronic and optoelectronic device production. The development of

high-quality nitride-based devices is still restricted by the lack of suitable epitaxial substrates materials. Nitride-based structures are most commonly deposited on sapphire (Al_2O_3) substrates. The lattice mismatch of about 15% to GaN causes formation of threading dislocations (TDs) in the sapphire interface and device layers [27.4]. In order to improve GaN epitaxial layers, a two-step deposition process is often applied in both metalorganic chemical vapor deposition (MOCVD) [27.5, 6] and hydride vapor-phase epitaxy (HVPE) [27.7] systems. The application of HVPE technology assures high growth rates of about 500 nm/min for growth of GaN. Hence, sufficiently thick layers can be deposited in a relatively short time. This makes HVPE an advantageous fabrication option for freestanding GaN substrates.

In this chapter, growth of semiconductor single crystals from the vapor phase is explained in general, and the chemical vapor transport technique in particular. Growth of II–VI and I–III–VI_2 compounds is reviewed, and growth of GaN thin films using vapor-phase epitaxy is presented.

27.1 Classifications of Vapor Growth

The growth of crystal from vapor phase can be divided [27.7] into various categories:

1. *Sublimation* or *evaporation*, in which the vapor is obtained from the pure condensed phase at an appropriate temperature;
2. A compound may highly dissociate in the growth system, namely *dissociative sublimation*;
3. If a transporting reaction is used for one or more of the constituents of the crystal, the process is termed either *chemical vapor transport* (CVT) or *physical vapor transport* (PVT), distinguished on the basis of the conditions over the growing crystal. A comparison between PVT, physical vapor deposition (PVD), chemical vapor deposition (CVD), and CVT is shown in Table 27.1

PVT is a closed-tube technique that can be used to grow crystals if the vapor pressure of the material exceeds 10^{-2} Torr at some feasible temperature. Typically in these processes, the source is a solid which must be sublimed (dissociatively or similarly) to provide the vapor. The process by which vapor is obtained from the pure condensed phase at an appropriate temperature and transported to a deposition zone at a lower temperature is called physical vapor transport. The vapor atoms impinge on the substrate surface and become adsorbed, releasing part of their latent heat of condensation and migrating across the crystal surface. They become incorporated into the crystal lattice, releasing their remaining heat of condensation; otherwise they evaporate. This is a relatively high-temperature method.

In the CVT process, as shown in Table 27.1, vapor atoms or molecules are chemically different from those of the growing crystal. Chemical transport reactions are those in which a solid or liquid substance A reacts with a gas to form exclusively volatile products, which in turn undergo the reverse reaction at a different place in the system, resulting in the formation of A. The process appears to be sublimation; however, it does not possess appreciable vapor pressure at the temperatures applied. In addition to a reversible heterogeneous reaction, a concentration gradient must be established. The latter can be the result of a temperature difference, changes in the relative pressures, or the difference in free energy of formation of two substances.

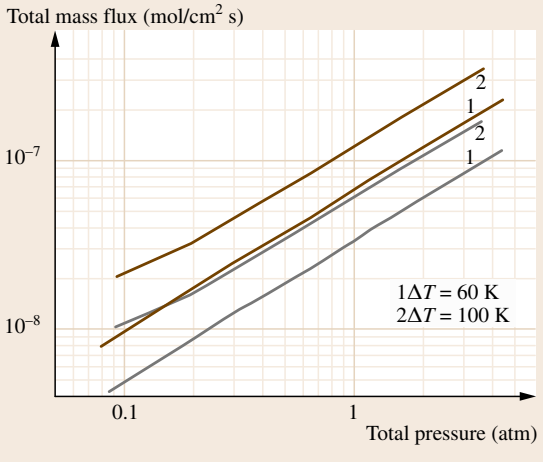


Fig. 27.1 Variation of total mass flux as a function of total pressure in the CdSe–I_2 system for the given two temperature differences between the source zone and growth zone and for the given diameter of 15 cm and length of 14 cm of the growth ampoule

Table 27.1 Comparison between PVT, CVT, PVD, and CVD

Parameters	Physical vapor transport (PVT)	Chemical vapor transport (CVT)	Physical vapor deposition (PVD)	Chemical vapor deposition (CVD)
Growth mechanism and bond energy	Monatomic, associative or dissociative sublimation Direction always from hot to cold ($T_s \rightarrow T_g$)	Reversible chemical reaction migration from hot to cold ($T_s \rightarrow T_g$) as well as from cold to hot ($T_g \rightarrow T_s$) possible	Direction always from hot to cold Nonconformal deposition Highly directional deposition Bonding energy is weak, less than 10 kcal/mol or 0.434 eV/atom	Conformal deposition Multidirectional deposition Bonding energy is strong compared with physical bond, up to 200 kcal/mol
Transport (carrier) gas	Without transport agent or inert gas	Needs a transporting agent such as I_2, Cl_2, etc.	Not necessary	Needs a transporting agent such as nitrogen, argon, etc.
Temperature difference (ΔT)	1–10 K	3–500 K	≈ 50 K to Several 100 K	≈ 50–100 K
Total system pressure (P)	High vacuum (or) inert gas of 0.01–0.5 atm	Up to 3 atm	1 atm	Atmospheric pressure to very low pressure
Thermophysical parameter	Constant	Varying	Constant	Varying
Compressible effect	Insignificant	Significant	Insignificant	Significant
Aspect ratio (l/d)	Typically 5	Typically 10	–	–
Possible flow pattern	Diffusion/advective and solutal convection	Diffusion/advective and thermal convection	Diffusion/advective and solutal convection	Diffusion/advective, thermal convection and laminar for HVPE GaN

The stationary temperature profile (STP) technique has been successfully applied for growing crystals since the growth of crystals by chemical vapor transport was initiated several decades ago. In the STP procedure, the source temperature (T_s) and growth temperature (T_g) are fixed at particular values after keeping a reverse temperature profile for the first few hours in order to clean the crystallization zone. As T_s and T_g are kept at constant values, the supersaturation remains unchanged during the whole growth period. Though this procedure can be adopted to obtain single crystals of many compounds, it may not be the most suitable technique for obtaining large-size single crystals. Also in most cases one ends up with too many crystals as the supersaturation is maintained constant throughout the growth experiment.

In the time-varying temperature profile (TVTP) method, the source temperature is increased linearly with time from a value below the growth temperature, while the growth temperature is kept constant. Hence the supersaturation increases form a negative value (i. e., at $T_s < T_g$) to positive values at which the formation of primary nuclei is possible. After the formation of primary nuclei, although T_s continues to increase, the supersaturation drops due to the decrease of the vaporized mass, which is consumed in producing the first crystal. Then, for a certain length of time depending on the particular vaporization kinetics of the charge, supersaturation remains sufficiently low that the first crystal can be further grown by secondary nucleation. After this, supersaturation increases again, enabling primary nucleation to take place. This TVTP procedure was adopted for growing ternary chalcopyrite crystals. It enables the growth of crystals much larger than those grown by the STP procedure. Also the quality of the crystals has been reported to be superior to those grown by adopting the STP procedure.

One of the drawbacks of the STP procedure is often the onset of constitutional undercooling from the very beginning of the growth process. In this respect, the TVTP procedure is an improvement because, in the first part of the growth period, this cause of instability is avoided. Constitutional undercooling appears as a result of both large supersaturation and the presence of mass convection in the vapor. Supersaturation can practically be reduced by working with small T_s and T_g differences, possibly at temperatures and pressures where thermody-

namics predict low supersaturation. Mass convection, which can be reduced by working at suitably small values of the Grashof number, induces constitutional undercooling through the reduction of the diffusion boundary layer at the growing interface. It is concluded that the time-varying temperature profile method described above can be used to increase the size of the crystals of some ternary compounds. Enlargements of about two- to threefold were obtained by this procedure, as compared with the usual STP technique. Time-varying temperature profile methods have been applied by various researchers to improve the size of CdS [27.8], $CdIn_2S_4$, and $CuInS_2$ [27.9] single crystals grown by CVT technique.

In PVD there is a transfer of subliming molecules/atoms A by (saturated) carrier gas to a colder growth area.

In chemical vapor deposition gaseous compounds of the materials to be deposited are transported to a substrate surface, where a thermal reaction/deposition occurs. Reaction byproducts are then exhausted out of the system.

The other vapor growth methods are:

1. Metalorganic chemical vapor deposition (MOCVD)
2. Vapor-phase epitaxy (VPE)
3. Metalorganic vapor-phase epitaxy (MOVPE)
4. Organometallic vapor-phase epitaxy (OMVPE).

27.2 Chemical Vapor Transport – Transport Kinetics

Crystal growth from the melt using the classical methods of Czochralski, Kyropoulos or Bridgman becomes difficult if the compounds to be grown have high melting points. Additional difficulties arise if the compounds show appreciable dissociation at the melting point or melt only under elevated pressure. To obtain single crystals of such compounds, they are sublimed (either in vacuum or in a stream of carrier gas or vapor of its constituents) and allowed to react in the crystallization chamber [27.10–12]. The temperature required for these processes is high, in the vicinity of the sublimation point. Instead of directly vaporizing a solid at high temperature it may be vaporized at much lower temperature by forming highly volatile chemical intermediates and reacting back the resulting gas mixture at a different temperature, utilizing the temperature dependence of the chemical equilibrium involved [27.12–16]. By properly adjusting the two temperatures, the departure from chemical equilibrium in the vicinity of the growing seeds can be made small enough to avoid nucleation but large enough to make the seeds grow, i. e., appropriate supersaturation can be maintained.

27.2.1 Transport Models

In general transport models have been developed based on the following experimental conditions:

1. The system is one dimensional and the length of the growth ampoule is L units, with the source at $x = 0$, transported to a deposit at $x = L$.
2. The transport mechanism involves a chemical equilibrium which can be written as

$$S_{(s)} + aA_{(g)} = bB_{(g)} + cC_{(g)} + \dots , \qquad (27.1)$$

   associated with an equilibrium constant K and an enthalpy change ΔH, where $S_{(s)}$ is the crystalline source materials, A is the transporting agent, and B and C are the gaseous products.
3. Diffusion is the only means of transport through the vapor phase; turbulent flow and thermal diffusion are ignored.
4. The mean free path is much smaller than the dimension of the system. As a consequence, a total pressure gradient cannot be considered. Impedance to the flow due to total pressure gradients is so small that we can ignore these gradients relative to partial pressure gradients.
5. The surface rate of the reaction is infinitely fast, so local equilibrium is essentially established in the neighborhoods of the source and the substrate.
6. The change of the equilibrium constant upon moving from $x = 0$ to $x = L$, leads to a difference in temperature between the source and growth zones ΔT, which is much smaller than T_g. An equivalent statement is $\Delta T = T_s - T_g \ll (RT_gT_s/\Delta H)$, according to the usual thermodynamic relationship between ΔH and ΔT.
7. $|\Delta H| \gg RT \cong \frac{1}{2}R(T_g + T_s)$. This also implies $\Delta T \ll T_g$.
8. All gases behave ideally.

Following *Schäfer*'s model [27.12], a transport reaction is defined as a reaction of a solid or liquid with a gaseous component in a temperature gradient to form exclusively gaseous products. For chemical transport caused only by diffusion, such as in a sealed silica ampoule, *Schäfer* [27.12] obtained a transport equation for the migration of a solid in a one-dimensional system. *Lever* [27.14] described the chemical transport of a solid involving several simultaneous heterogeneous and homogeneous equilibria [27.17, 18]. *Arizumi* and *Nishinaga* [27.19–21] proposed transport equations for the transport of materials (semiconductors) in closed tubes, assuming a one-dimensional system and considering diffusion and laminar flow as the fundamental transport mechanism (AN model).

Following the model of *Factor* and *Garrett* [27.22, 23] in a one-dimensional transport system, the flux rate J (mol/cm^2 s) of a component i caused by diffusion and Stefan flow can be described. The variation of total mass flux as a function of total pressure in the CdSe–I_2 system for various growth temperatures for given dimensions of the growth ampoule (diameter 15 cm and length 14 cm) is shown in Fig. 27.1.

Using the flux function method of *Richardson* and *Noläng*, it is possible to calculate the net fluxes J_k (mol/cm^2 s) based on an equilibrium model [27.24–26]. The flux function takes into account the Stefan flow, as well as the temperature and total pressure variation of the diffusion coefficient. Thus it becomes possible to compute the transport rates of the simultaneous migration of several condensed phases. A flux function Φ takes into account the temperature dependency of the diffusion coefficient. The advantage of this flux function is that different transport systems with different transporting agents, temperature gradients, and diffusion coefficients can be compared with each other [27.27–29].

27.2.2 Physical Chemistry of Chemical Transport Reactions

Partial Pressure

Consider a closed system containing $n+1$ components, all of which are in chemical equilibrium with one other [27.30]. The temperature is chosen such that only one component is solid, whereas the other n components are in gaseous state. For $n=1$, the trivial case of sublimation of a solid via its gaseous atoms or molecules results. In the following, the case $n=3$ is considered, which applies to the transport of metal chalcogenides by halogens. The equilibriums involved are [27.12]

$$\mathrm{MX_{(s)} + I_{2(g)} \Leftrightarrow MI_{2(g)} + \tfrac{1}{2}X_{2(g)}}\,, \tag{27.2}$$

where M = Cd, Zn and X = S, Se.

A specific example is [27.13, 18, 31]

$$\mathrm{ZnS_{(s)} + I_{2(g)} \Leftrightarrow ZnI_{2(g)} + \tfrac{1}{2}S_{2(g)}}\,. \tag{27.3}$$

In a CVT system, a solid substance MX reacts with a gaseous transporting agent I_2 (chalcogenides) at a higher temperature T_s to form exclusively vapor-phase products MX and $\frac{1}{2}$X at the source zone. The vapor products in turn undergo the reverse reaction at the growth zone at a lower temperature T_g

$$\mathrm{I_{2(g)} \Leftrightarrow 2I_{(g)}}\,. \tag{27.4}$$

The corresponding equilibrium constants of (27.2) and (27.4) are

$$K_{(27.2)} = \frac{p_{\mathrm{MI_2}}\left(\frac{1}{2}p_{\mathrm{MI_2}}\right)^{\frac{1}{2}}}{p_{\mathrm{I_2}}}\,, \tag{27.5}$$

$$K_{(27.4)} = \frac{\mathrm{p_I^2}}{p_{\mathrm{I_2}}}\,, \tag{27.6}$$

respectively.

The total pressure of the system is given by

$$P = p_{\mathrm{I_2}} + p_{\mathrm{I}} + 1.5\,p_{\mathrm{MI_2}}\,. \tag{27.7}$$

The equilibrium constant $K_i(T)$ ($i = 3.2, 3.4$) as a function of temperature T can be evaluated using the relations (27.2) and (27.4–27.6) [27.27–29]

$$\log K_i(T) = a_i - b_i T^{-1} - c_i T^{-2} - d_i \log(T) - e_i T\,. \tag{27.8}$$

If the temperature T and total pressure p are fixed and the value of $K_i(T)$ is known, then the partial pressure of species MI_2, X_2, I_2, and I can be determined by using (27.2) and (27.4–27.8). A graph showing the partial pressure of various gaseous species as a function of total pressure of the CdSe–I_2 system is shown in Fig. 27.2; for ZnSe–I_2 and other systems, refer to literature [27.13, 31–34].

Thermophysical Parameters

The diffusion coefficient of a binary gas mixture is based on the well-known Chapman–Enskog formula [27.29, 32, 35, 36]

$$D_{ij} = 1.858^{-27}\frac{\sqrt{T^3(1/\mathrm{M}_i + 1/\mathrm{M}_j)}}{P\sigma_{ij}^2\Omega_{D_{ij}}}\,. \tag{27.9}$$

In (27.9) σ_{ij} is the characteristic length expressed in Å and Ω_D is the dimensionless diffusion collision integral. The binary collision integral was estimated from individual collision diameters σ_A and σ_B using the expression

$$\sigma_{ij} = \frac{\sigma_i + \sigma_j}{2} , \qquad (27.10)$$

where Ω_D is a function of $k_B T/\varepsilon_{ij}$, where k_B is the Boltzmann's constant, $\varepsilon_{ij} = (\varepsilon_i \varepsilon_j)^{1/2}$, and ε_i and ε_j are the Lennard–Jones energy values for species i and j, respectively. The complete expression for Ω_D can be given as

$$\Omega_D = \frac{A}{T^{*B}} + \frac{C}{\exp(DT^*)} , \qquad (27.11)$$

where $T^* = k_B T/\varepsilon_{ij}$ is the reduced temperature and the values of A, B, C, and D can be calculated from reported data. The diffusion collision integral and diffusion coefficients for various species are presented in Table 27.2.

The molecular viscosity μ and thermal conductivity k_T of the species can be calculated from Chapman–Enskog and Lennard–Jones potential theory [27.29, 37, 38]

$$\mu = 2.669 \times 10^{-26} \frac{\sqrt{MT}}{\sigma_{ij}^2 \Omega_\mu} \ [\mathrm{kg/(m\,s)}] \qquad (27.12)$$

and

$$k_T = 8.324 \times 10^{-22} \frac{\sqrt{(T/M)}}{\sigma_{ij}^2 \Omega_\mu} \ [\mathrm{W/(m\,K)}] , \qquad (27.13)$$

where M is the molecular weight (kg/mol), T is the average temperature (K), σ_{ij} is the collision diameter, and Ω_μ is the viscosity collision integral.

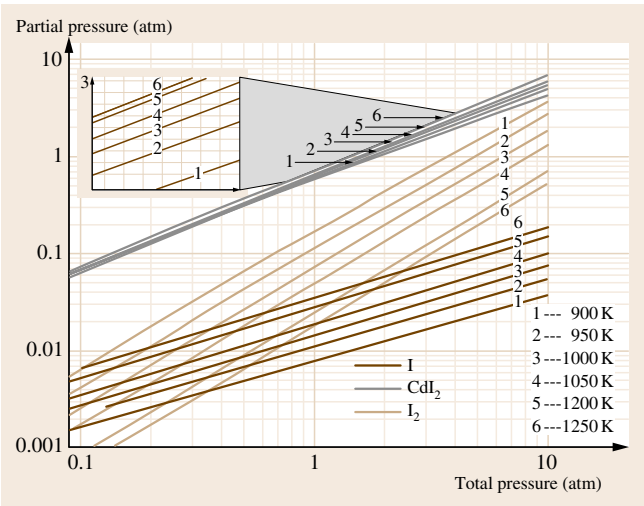


Fig. 27.2 Partial pressures of various gaseous species as a function of total pressure of the CdSe–I_2 system for different temperatures

27.2.3 Factors Affecting the CVT Reaction

Influence of Chemical Parameters on CVT Growth of Crystals

Generally chemical vapor transport reactions depend on chemical parameters such as the free energy change (ΔG), the concentration of the transporting agent (C_T), the temperatures at the source and growth zones (T_s and T_g), etc. [27.29, 39–42]. The free energy change for a reaction depends to a considerable extent on the partial pressures of the chemical species used in the reactions. The amount of material transportation from the source to the growth zone depends strongly on C_T. Also it has been observed by many authors that there is a strong dependence of the size and quality of the resulting crystals on C_T.

Table 27.2 Characteristic length and diffusion collision integral of different species

ij	σ_{ij} (Å)	Ω_{D-ij} at $T = 1173$ K	*ij*	σ_{ij} (Å)	Ω_{D-ij} at $T = 1173$ K
I_2-S_2	4.051	0.914	ZnI_2-Se_2	5.278	0.945
I-S_2	3.538	0.903	ZnI_2-I_2	4.955	0.954
I_2-Se_2	4.189	0.967	Cd-I_2	3.512	0.981
I-Se_2	4.409	0.935	Cd-S_2	3.422	0.914
I_2-I	4.253	0.938	Cd-Se_2	3.762	1.040
Zn-I_2	4.081	1.007	CdI_2-Cd	4.248	0.977
Zn-S_2	4.597	1.175	CdI_2-I_2	5.534	1.262
Zn-Se_2	4.323	0.946	CdI_2-Se_2	5.431	1.232
ZnI_2-S_2	4.673	1.189	CdI_2-S_2	5.072	1.129

If one is concerned only about the rate of transportation and not the quality of the crystals, the absolute values of the temperatures T_s and T_g can be varied over a relatively wide range.

Influence of Geometrical Parameters on CVT Growth of Crystals

The amount of material transported decreases linearly with the length of the tube due to the increase in flow resistance [27.13]. If several seeds are to be formed and to grow in one experiment then the crystallization chamber should not be too small, to avoid intergrowth between the crystals. The distribution of the temperature in the deposition zone must be as uniform as possible in order to avoid reevaporation of crystals from warmer parts during the experiment. The use of a tapered growth zone is advantageous for this purpose, and it induces nucleation at the corner of the tube where the temperature is low. The most important geometrical parameter is the tube cross-section q, which influences the transport rate decisively [27.12, 39, 43, 44].

27.2.4 Choice of Transporting Agents

The choice of transporting agent generally depends on the thermodynamics of the transport reaction and the volatility of the compounds involved [27.1, 22]. In selecting the transporting agents, the following conditions should be taken into consideration [27.40–42, 45–51]:

1. The transporting agent should be chosen such that all species that will be formed by reaction with the solid to be transported have adequate volatility. Moreover there should be good knowledge of the volatility and stability of all the vapor species formed in the reaction and their solubility in the growing crystal.
2. If it is assumed that element M is transported by halogen I through the transport reaction (27.2), the equilibrium constant for this reaction is given by (27.4). To obtain efficient transport, the equilibrium constant for the reactions must not be extreme and should have suitable magnitude at a convenient temperature.
3. The knowledge on the various components of the substances to be transported which have sizable vapor pressures in the temperature range selected for growth.
4. It should be known to the extent of the substance to be transported as undissociated, uncombined molecules in the vapor phase.

27.2.5 Advantages and Limitations of CVT Method

Advantages of Chemical Vapor Transport

1. The growth process is normally carried out at temperatures much lower than the melting point of the material, which is useful for the growth of materials with high melting points and those that exhibit appreciable dissociation at their stoichiometry melting points.
2. Decrease in contamination from the crucible due to the reduced growth temperature.
3. Allotropic crystalline forms can be grown.
4. Good stoichiometry control is possible.
5. Growth of epitaxial layers is possible.
6. In situ chemical vapor cleaning of the substrate/system is possible.
7. The solid–vapor interfaces exhibit higher interfacial morphological stability during growth than in the case of solid–liquid interfaces.

Limitations of Chemical Vapor Transport

1. Thermodynamics and kinetics are complex and poorly understood.
2. Deposition occurs on the substrate as well as on the walls of the container.
3. The reactive gases involved are dangerous in some cases and need special handling procedures.
4. Controlling nucleation is difficult, and growing several crystals due to primary nucleation will result in a decrease in their sizes for a given amount of charge materials.
5. Transporting agents will incorporate into the growing crystals during the growth process and alter the physical properties of the grown crystals.
6. There are difficulties incorporating some doping elements (e.g., Ga, In, Al) into the growing crystals because of their low vapor pressures.

27.3 Thermodynamic Considerations

27.3.1 Estimation of Optimum Growth Parameters for the ZnSe–I_2 System by CVT

The partial pressures inside the tube during growth, the temperature, the iodine concentration, and the tube dimensions have been taken into account for these calculations (Fig. 27.3). The vapor-phase chemical transport of ZnSe with iodine has been considered to consist of three equilibria

$$\mathrm{ZnSe} + \mathrm{I_2} \Leftrightarrow \mathrm{ZnI_2} + \tfrac{1}{2}\mathrm{Se_2}\,, \tag{27.14}$$

$$\mathrm{ZnSe} + \mathrm{I_2} \Leftrightarrow \mathrm{Zn} + 2\mathrm{I} + \tfrac{1}{2}\mathrm{Se_2}\,, \tag{27.15}$$

$$\mathrm{ZnSe} + 2\mathrm{I} \Leftrightarrow \mathrm{ZnI_2} + \tfrac{1}{2}\mathrm{Se_2}\,. \tag{27.16}$$

Neglecting dissociation of ZnSe via

$$\mathrm{ZnSe} \Leftrightarrow \mathrm{Zn} + \tfrac{1}{2}\mathrm{Se_2}\,, \tag{27.17}$$

and dissociation of ZnI_2 via

$$\mathrm{ZnI_2} \Leftrightarrow \mathrm{Zn} + \mathrm{I_2}\,, \tag{27.18}$$

it was assumed that, as a first approximation, the vapor phase contains only four components (I, I_2, ZnI_2, and Se_2) and also the law of mass conservation of iodine at equilibrium was considered

$$\mathrm{I_2} \Leftrightarrow 2\mathrm{I}\,. \tag{27.19}$$

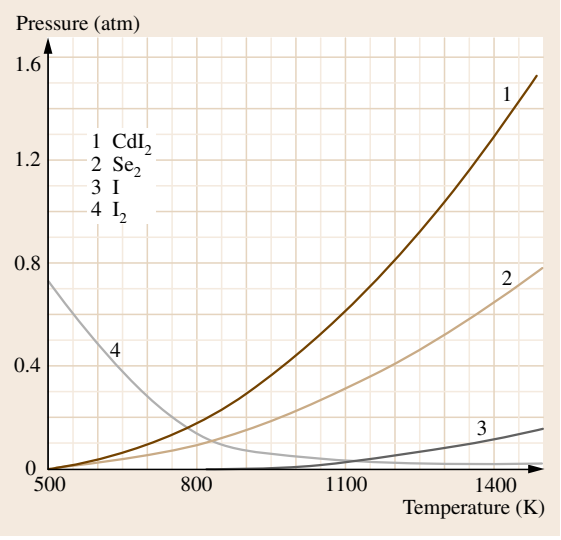


Fig. 27.3 Partial pressures of various species as a function of temperature for various iodine concentration

The partial pressures in terms of initial iodine concentration can be expressed by

$$p^0_{\mathrm{I_2}} = p_{\mathrm{I_2}} + 0.5\,p_{\mathrm{I}} + p_{\mathrm{ZnI_2}}\,. \tag{27.20}$$

The exact stoichiometry of the ZnSe source materials gives the equation

$$p_{\mathrm{ZnI_2}} = 2\,p_{\mathrm{Se_2}}\,, \tag{27.21}$$

where $p^0_{\mathrm{I_2}}$ is the partial pressure of iodine concentration initially taken into account for the calculations, and the other p symbols are the partial pressures of the corresponding components at a given temperature. The equilibrium constants for the reactions (27.14) and (27.19) are given by

$$K_{(27.14)} = \frac{\left(p_{\mathrm{ZnI_2}}\,p^{0.5}_{\mathrm{Se_2}}\right)}{p_{\mathrm{I_2}}}\,, \tag{27.22}$$

$$K_{(27.19)} = \frac{p^2_{\mathrm{I}}}{p_{\mathrm{I_2}}}\,. \tag{27.23}$$

The values can be calculated as a function of temperature from [27.52]

$$K_{(27.14)} = 7.64 - 5849\,T^{-1} - 4154\,T^{-2} - 0.83\log T - 1.5\times10^{-4}\,T\,, \tag{27.24}$$

$$K_{(27.19)} = 4.34 - 7879\,T^{-1} + 4264\,T^{-2} + 0.33\log T + 2\times10^{-5}\,T\,. \tag{27.25}$$

Using (27.20–27.25), the following equation can be derived

$$2\frac{p^2_{\mathrm{I}}}{K_{2.6}} + \left(4\frac{K_{(27.14)}}{K_{(27.19)}}\right)^{\frac{2}{3}} p_{\mathrm{I}}^{\frac{4}{3}} + p_{\mathrm{I}} - 2\frac{CRT}{M} = 0\,, \tag{27.26}$$

where p_{I} is the partial pressure of atomic iodine, C is the initial concentration of iodine, R is the universal gas constant, T is temperature, and M is the molar mass of iodine.

It was assumed that iodine behaves as an ideal gas in these calculations. From (27.26), the partial pressures of the components inside the tube during growth were calculated for iodine concentration in the range 0.5–10 mg/cm^3 and for temperatures in the range 500–1200 °C. The partial pressures of I, I_2, ZnI_2, and Se_2 for temperatures of 500–1200 °C are plotted in Fig. 27.4 for iodine concentration of 2 mg/cm^3.

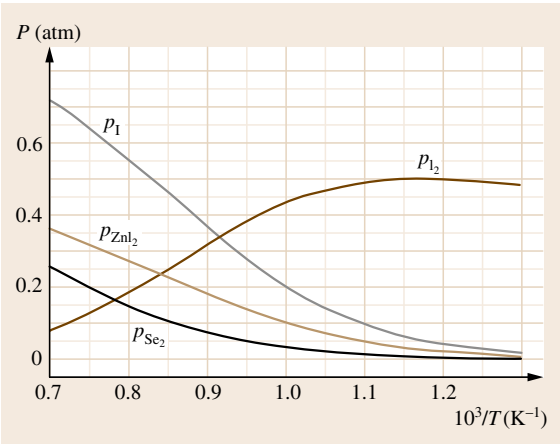


Fig. 27.4 Partial pressure of components for 2 mg/cm^3 iodine

The amount of ZnI_2 formed with respect to the initial concentration of I_2 can be described by the ratio α

$$\alpha = \frac{p_{ZnI_2}}{p^0_{I_2}} \,. \tag{27.27}$$

The variation in the ratio α for different iodine concentrations at different temperatures is shown in Fig. 27.5. The transport rate of ZnI_2 determines the size and quality of the crystal grown at the growth zone. It can be considered as the difference in α between the source and growth zones for given temperature. It can be approximated by

$$\Delta\alpha = \frac{\Delta p_{ZnI_2}}{p^0_{I_2}} \,. \tag{27.28}$$

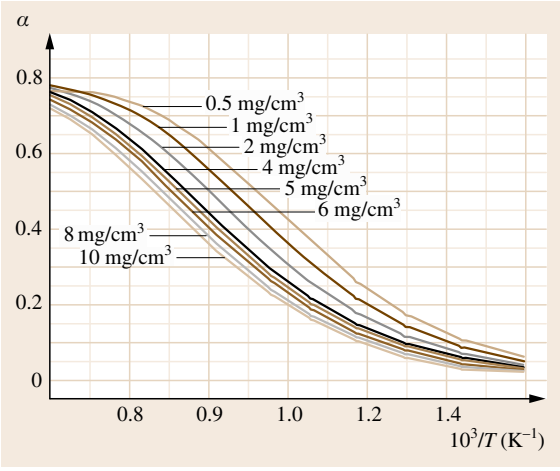


Fig. 27.5 Variation in the ratio α for different iodine concentrations at different temperatures

The temperature difference between two zones was fixed at 50 °C in the calculations. The number of moles of ZnSe transported from the source to the growth end as ZnI_2 in time t is given by

$$n_{ZnSe} \propto \Delta\alpha x t \,. \tag{27.29}$$

The diffusion-limited transport rates (J_D) can be calculated using the formula [27.15, 53]

$$J_D = \frac{2 D_{ZnI_2} p_T}{RTL} \ln\left(\frac{(2p_T - p_{ZnI_2(g)})}{(2p_T - p_{ZnI_2(s)})}\right) \,, \tag{27.30}$$

where D_{ZnI_2} is the diffusion coefficient of the component ZnI_2, p_T is the total pressure at the temperature T, $p_{ZnI_2(g)}$ is the partial pressure of ZnI_2 at the growth zone, $p_{ZnI_2(s)}$ is the partial pressure of ZnI_2 at the source zone, R is the universal gas constant, T is temperature, and L is the distance between the sublimed source and growing crystals in the ampoule.

27.3.2 Fluctuations in the Transport Rates

The iodine concentration of 2 mg/cm^3 is considered for the present investigation. The partial pressure of the components I, ZnI_2, and Se_2 increases with increasing temperature. The partial pressure of I_2 decreases with increasing temperature. The ratio (α) between the partial pressure of ZnI_2 and that of initial iodine pressure is found to decrease with increasing iodine concentration at a given temperature. Also, at higher iodine concentrations, the change in partial pressures of ZnI_2 is found to be minimum. Hence it can be concluded that increase in iodine concentration has little effect on the partial pressure of ZnI_2. From (27.29), the transport rate of ZnI_2 is proportional to the difference in α values of source and deposition zones, i. e., $\Delta\alpha$. The variation of $\Delta\alpha$ with respect to temperature for the various iodine concentrations is shown in Fig. 27.6. For a given iodine concentration the value of $\Delta\alpha$ is found to increase gradually, reach a maximum, and then decrease with increasing temperature. As the iodine concentration increases, the maximum of the curve positions shifts to higher temperatures and also the curves become broadened. From the figure, it can be observed that, for each iodine concentration, there is an optimum temperature region near the peak position where the change in $\Delta\alpha$ is minimum. Hence the fluctuations in transport rates will be minimum in that region. The change in transport rate is proportional to Δp_{ZnI_2}, i. e., the difference between the partial pressures of ZnI_2

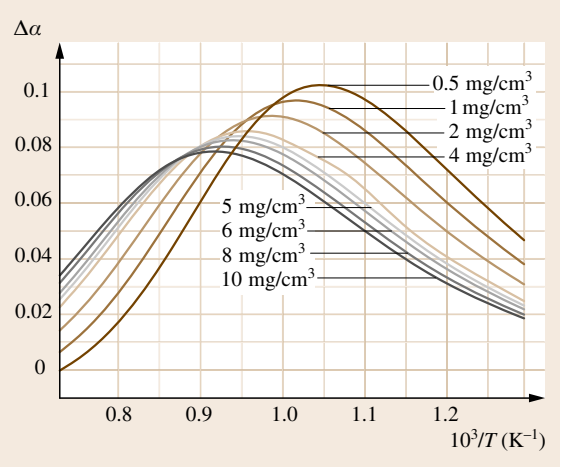


Fig. 27.6 Change in the value of $\Delta\alpha$ with respect to temperature for a given iodine concentration

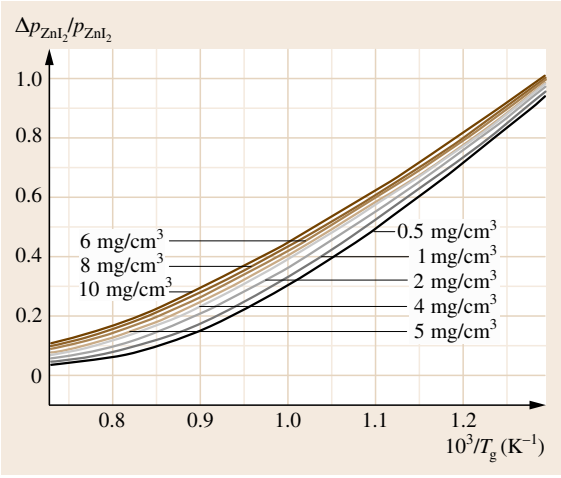


Fig. 27.8 Change in supersaturation ratio as a function of growth temperature for undercooling of 50 K and various iodine concentrations

in the source and deposition zones. So, it can be assumed that, without considering the type of migration along the ampoule, the growth rate is proportional to $\Delta\alpha$.

The fluctuation in transport rates affects the quality of the crystals grown. The fluctuation in transport rates should be minimum to achieve good-quality crystals. Hence it is essential to find the optimum conditions for which the fluctuation is minimum. However a slight drop in temperature at the deposition zone during the growth process causes multinucleation of crystals, which leads to intergrowth and changes in the composition of the crystals. The flow of the material is highly dependent on temperature, and control of temperature at the growth interface is always poorer than the accuracy shown by the temperature controllers in the furnace. Temperature variation up to ±2 K can normally be expected inside the quartz ampoule during the growth process. The fluctuation in transport rates has been calculated for temperature fluctuation up to ±2 K using (27.30), considering an iodine concentration of 2 mg/cm^3 and a constant temperature difference between the two zones of 50 K; the results are shown in Fig. 27.7. It can be observed from the figure that the temperature range of 800–850 °C was found to have minor fluctuations in the transport rates. Somewhere in this temperature range, one can find a line nearly parallel to the x-axis and close to zero on the y-axis, for which the fluctuation in transport rate is expected to be minimum. It was therefore concluded that one could obtain good-quality crystals in the temperature range 800–850 °C.

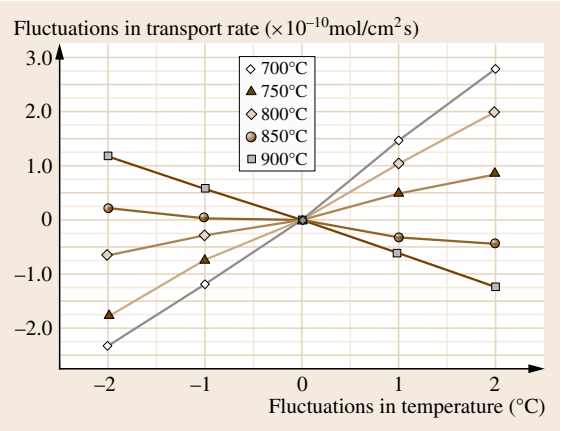


Fig. 27.7 Fluctuation in transport rates at different temperatures for $\Delta T = 50$ °C and for iodine concentration of 2 mg/cm^3

The change in supersaturation ratio $\Delta p_{ZnI_2}/p_{ZnI_2}$ as a function of growth temperature for undercooling of 50 K and various iodine concentrations is shown in Fig. 27.8. It can be seen from the figure that an increase in iodine concentration produces only a small change in supersaturation at given temperature. It can be concluded that the iodine concentration has very little influence on the supersaturation ratio at a given temperature and thus the growth of the crystals.

Nucleation Calculations for the Growth of ZnS_xSe_{1-x} Single Crystals by CVT

The binary nucleation theory was applied to find the critical radius and free energy for the formation of the critical nucleus. The formation and composition of ZnS_xSe_{1-x} single crystals by CVT was found to be affected by the supersaturation ratios of S_2 and Se_2 and hence by the corresponding partial pressure values. The partial pressures of the components in the ZnS_xSe_{1-x}-I_2 system by CVT were found with the thermodynamic model as applied to the case of ZnSe in the previous section.

27.3.3 Supersaturation Ratios in the ZnS_xSe_{1-x} System

The formation of ZnS_xSe_{1-x} by iodine transport may take place by the following chemical equilibrium reactions.

At the source zone

$$ZnS + ZnSe + 2I_2 \Leftrightarrow 2ZnI_2 + \tfrac{1}{2}S_2 + \tfrac{1}{2}Se_2 \,. \quad (27.31)$$

At the growth zone

$$ZnI_2 + xS_2 + (1-x)Se_2 \Leftrightarrow ZnS_xSe_{1-x} \,. \quad (27.32)$$

It is assumed that the vapor phase contains only I, I_2, ZnI_2, S_2, and Se_2. The vapor-phase chemical transport of ZnS and ZnSe with I_2 in a closed tube follows the individual reaction steps as given below

$$ZnS + I_2 \Leftrightarrow ZnI_2 + \tfrac{1}{2}S_2 \,, \quad (27.33)$$

$$ZnSe + I_2 \Leftrightarrow ZnI_2 + \tfrac{1}{2}Se_2 \,. \quad (27.34)$$

Also, considering the mass conservation of iodine at the equilibrium

$$I_2 \Leftrightarrow 2I \,, \quad (27.35)$$

the partial pressures in terms of initial iodine concentration can be given by

$$p^0_{I_2} = p_{I_2} + 0.5\,p_I + p_{ZnI_2} \,. \quad (27.36)$$

The equilibrium constants for (27.33–27.35) are given by

$$K_{(27.33)} = 8.8 - 7539T^{-1} + 8745T^{-2} - 1.19\log T + 2.18\times10^{-6}T \,, \quad (27.37)$$

$$K_{(27.34)} = 7.64 - 5849T^{-1} - 4154T^{-2} - 0.83\log T - 1.5\times10^{-4}T \,, \quad (27.38)$$

$$K_{(27.35)} = 4.34 - 7879T^{-1} + 4264T^{-2} + 0.33\log T + 2\times10^{-5}T \,. \quad (27.39)$$

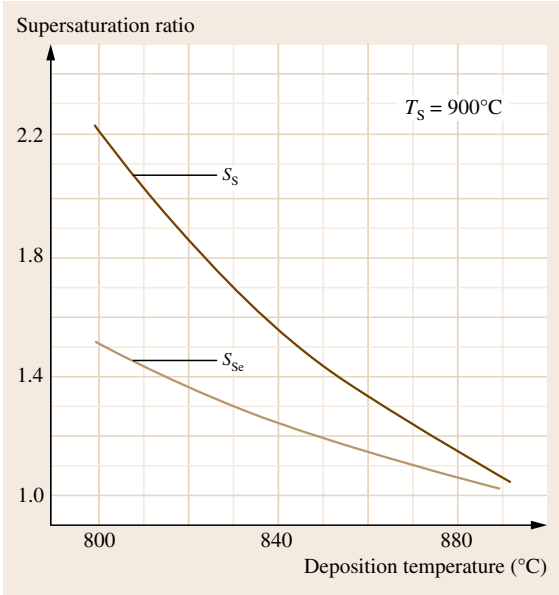


Fig. 27.9 Variation in supersaturation ratios of S_2 and Se_2 with deposition temperature

The partial pressures of the components inside the growth ampoule were calculated using these equations. The partial pressures of S_2 and Se_2 were found to affect the composition of ZnS_xSe_{1-x} even when an ideal solid solution of ZnS and ZnSe (1 : 1) was assumed. Therefore the supersaturation ratios of S_2 and Se_2 have been obtained as a function of deposition temperature for a fixed source temperature and iodine concentration. The supersaturation ratio of the S_2 component in closed-tube vapor transport of ZnS_xSe_{1-x} is given by

$$\frac{p_{S_2}}{p^*_{S_2}} = \frac{(p_{S_2})_s}{(p_{S_2})_d} \,, \quad (27.40)$$

where p_{S_2} is the partial pressure of sulphur at a given temperature, $p^*_{S_2}$ is the equilibrium partial pressure of sulphur, $(p_{S_2})_s$ is the partial pressure of sulphur at the source zone, and $(p_{S_2})_d$ is the partial pressure of sulfur at the deposition zone. Similarly, the supersaturation ratio of selenium can be calculated using

$$\frac{p_{Se_2}}{p^*_{Se_2}} = \frac{(p_{Se_2})_s}{(p_{Se_2})_d} \,. \quad (27.41)$$

Figure 27.9 shows the change in supersaturation ratios of S_2 and Se_2 with respect to varying growth zone temperature for fixed source temperature (900 °C).

Homogeneous Nucleation in the Growth of ZnS_xSe_{1-x} Single Crystals

The spontaneous formation of a nucleus of another supersaturated phase is called homogeneous nucleation. The simple theory of homogeneous nucleation brings out two essential features of the nucleation process: (1) The vapor must be supersaturated with respect to the bulk condensate for small clusters to have any stability; the greater the supersaturation, the smaller the cluster which stands an even chance of increasing in size. (2) The rate of nucleation is strongly dependent on the size of the critical nucleus and hence on the supersaturation. In the present study, binary nucleation theory (capillarity approximation) was applied to the ZnS_xSe_{1-x} system containing 1 : 1 ZnS and ZnSe

$$x\mathrm{ZnS} + (1-x)\mathrm{ZnSe} \Leftrightarrow \mathrm{ZnS}_x\mathrm{Se}_{1-x} \,. \tag{27.42}$$

The free energy of formation of a nucleus is given by

$$\Delta G = -ak_\mathrm{B}T \ln \frac{p_\mathrm{S}}{xp^*_\mathrm{S}} - bk_\mathrm{B}T \ln \frac{p_\mathrm{Se}}{(1-x)p^*_\mathrm{Se}} + \left(aV_\mathrm{ZnS} + bV_\mathrm{ZnSe}\right)^{2/3}(36\pi)^{1/3}\sigma \,, \tag{27.43}$$

where $p_\mathrm{S}/p^*_\mathrm{S}$ is the supersaturation ratio of sulfur, $p_\mathrm{Se}/p^*_\mathrm{Se}$ is the supersaturation ratio of selenium, a the number of ZnS molecules in the nucleus, b is the number of ZnSe molecules in the nucleus, x is the mole fraction of ZnS, $(1-x)$ is the mole fraction of ZnSe, V_ZnS is the molecular volume of ZnS, V_ZnSe is the molecular volume of ZnSe, σ is the interfacial tension (assumed to be constant at 1000 erg/cm^2), k_B is Boltzmann's constant, and T is temperature.

The free energy of formation of a nucleus corresponding to the saddle point can be obtained from

$$\left(\frac{\partial \Delta G}{\partial a}\right)_{T,P} = 0 \,, \quad \left(\frac{\partial \Delta G}{\partial b}\right)_{T,P} = 0 \,. \tag{27.44}$$

Applying this condition to (27.43) yields

$$-k_\mathrm{B}T \ln \frac{p_\mathrm{S}}{xp^*_\mathrm{S}} + \tfrac{2}{3}V_\mathrm{ZnS}(36\pi)^{1/3} \times \sigma\left(a^*V_\mathrm{ZnS} + b^*V_\mathrm{ZnSe}\right)^{-1/3} = 0 \,, \tag{27.45}$$

and

$$-k_\mathrm{B}T \ln \frac{p_\mathrm{Se}}{(1-x)p^*_\mathrm{Se}} + \tfrac{2}{3}V_\mathrm{ZnSe}(36\pi)^{1/3} \times \sigma\left(a^*V_\mathrm{ZnS} + b^*V_\mathrm{ZnSe}\right)^{-1/3} = 0 \,. \tag{27.46}$$

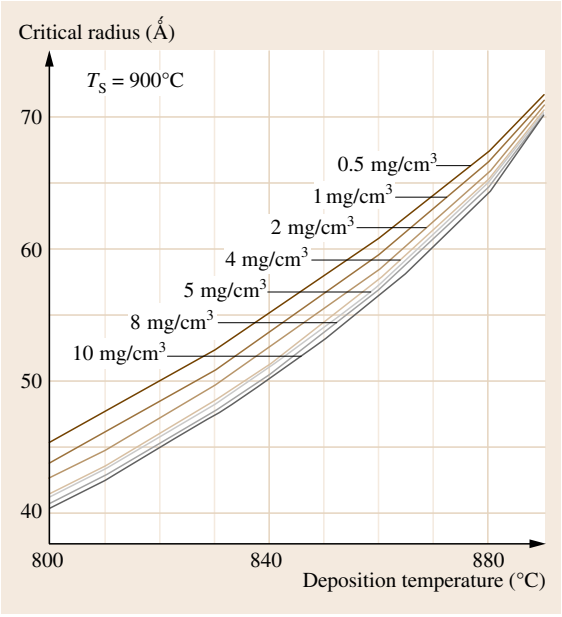


Fig. 27.10 Change in critical radius with deposition temperature

Assuming the shape of the nucleus to be spherical, one has

$$\tfrac{4}{3}\pi r^{*3} = \left(a^*V_\mathrm{ZnS} + b^*V_\mathrm{ZnSe}\right) \,,$$

$$r^* = \left(\frac{3\left(a^*V_\mathrm{ZnS} + b^*V_\mathrm{ZnSe}\right)}{4\pi}\right)^{\frac{1}{3}} \,, \tag{27.47}$$

solving (27.45) and (27.46) to

$$r^* = \frac{2\sigma V_\mathrm{ZnS}}{k_\mathrm{B}T \ln\left(\frac{p_\mathrm{S}}{xp^*_\mathrm{S}}\right)} \,. \tag{27.48}$$

The value of the critical radius has been calculated for iodine concentration of 0.5–10 mg/cm^3 and deposition temperature of 800–890 °C with a constant source temperature of 900 °C. The variation of the critical radius of the ZnS_xSe_{1-x} nucleus is shown in Fig. 27.10 with respect to deposition temperature.

The free energy of formation of the critical nucleus is given by

$$\Delta G^* = \frac{16\pi\sigma^3}{3(\Delta G_v)^2} \,, \tag{27.49}$$

$$\Delta G^* = \frac{16\pi\sigma^3}{3k_\mathrm{B}^2T^2 \ln^2\left(\frac{p_\mathrm{S}}{xp^*_\mathrm{S}}\right)} \,. \tag{27.50}$$

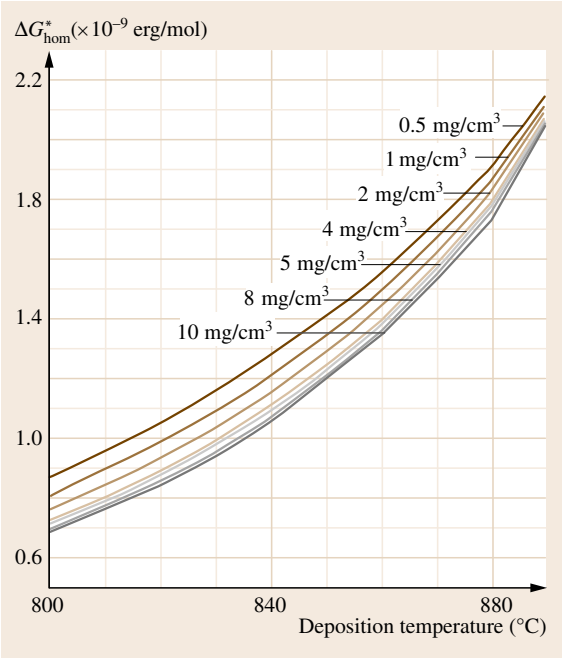


Fig. 27.11 Free energy change for the formation of a critical nucleus with deposition temperature under homogeneous nucleation condition

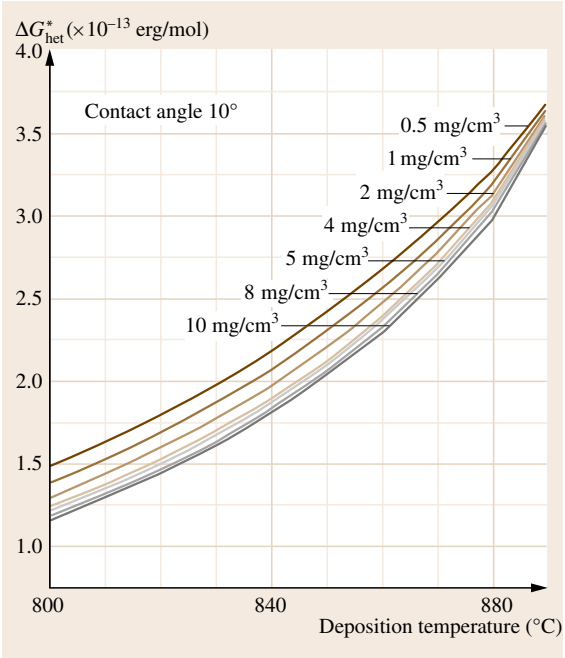


Fig. 27.12 Change in free energy for the formation of a critical heterogeneous nucleus (for contact angle 10°) with deposition temperature

The value of the free energy has been calculated as a function of deposition temperature for various iodine concentrations and is shown in Fig. 27.11.

Heterogeneous Nucleation of ZnS_xSe_{1-x} Single Crystals

The nucleation of a condensed phase on the surface of a foreign body is called heterogeneous nucleation. The nucleation rate depends on the presence of available sites on the surface on which growth can take place to a considerable extent. For example, kinks, steps on a surface, inclusions, etc. facilitate the process of nucleation. In chemical vapor transport, deposition may occur on the ampoule wall so that transported vapor components react to form the crystal. Since the presence of a suitable surface induces nucleation at supersaturations lower than that required for spontaneous nucleation, the free energy associated with the formation of such a critical nucleus must be less than the corresponding free energy change. It is given by

$$\Delta G^*_{het} = \phi(\theta)\Delta G^*_{hom} , \qquad (27.51)$$

where the factor $\phi(\theta)$ is less than 1. In treating such nucleation, a spherical cap-shaped embryo of radius r of solid phase S deposited on a substrate is considered. The contact angle between the cap and the substrate is θ. The ΔG^*_{het} for a critical nucleus is given by

$$\Delta G^*_{het} = \frac{16\pi\sigma^3_{13}\phi(\theta)}{3\Delta G^2_v} , \qquad (27.52)$$

where σ_{13} is the interfacial tension between the vapor and solid

$$\phi(\theta) = \frac{(2+\cos\theta)(1-\cos\theta)^2}{4} . \qquad (27.53)$$

The contact angle θ varies between 0° and 180°. In this case, ΔG^*_{het} has been calculated for θ values of 10°, 30°, and 50° at different deposition zone temperatures, as shown in Figs. 27.12–27.14, respectively.

Variation in Composition with Growth Temperature

In vapor growth, the composition of the growing compound is controlled by the composition of the vapor over it. The undercooling or supersaturation plays the dominant role in determining the composition of the growing crystals. It has been found that the partial pressures of S_2 and Se_2 affect the formation and composition of

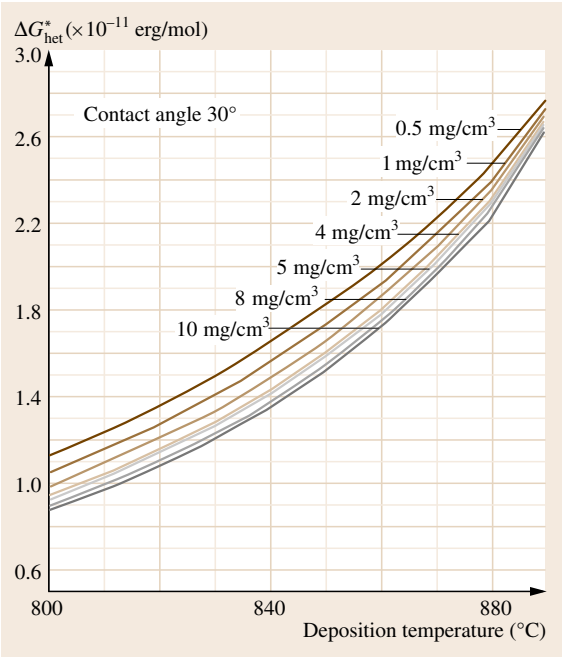


Fig. 27.13 Change in free energy for the formation of a critical heterogeneous nucleus (for contact angle 30°) with deposition temperature

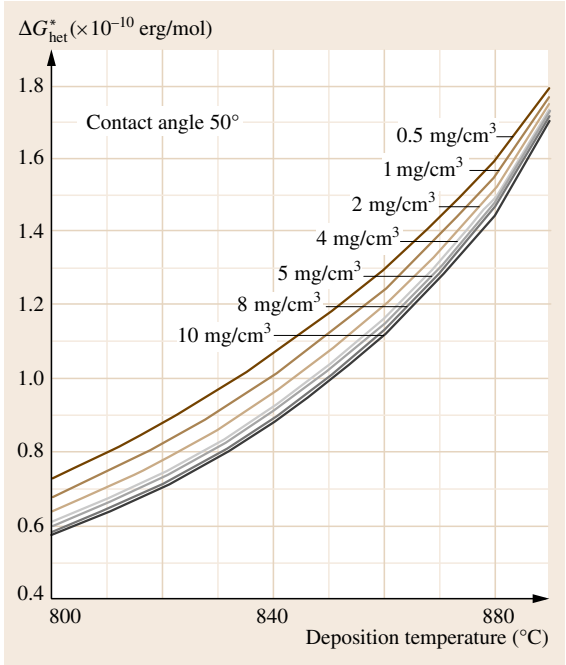


Fig. 27.14 Change in free energy for the formation of a critical heterogeneous nucleus (for contact angle 50°) with deposition temperature

ZnS_xSe_{1-x} even when the ideal solid solution of ZnS and ZnSe was assumed [27.54]. The mole fraction ratio of ZnS and ZnSe is proportional to corresponding partial pressure ratios, given by

$$\frac{x_{ZnS}}{x_{ZnSe}} = \frac{K_{ZnSe}}{K_{ZnS}} \left(\frac{p_{S_2}}{p_{Se_2}} \right)^{1/2} , \qquad (27.54)$$

where K_{ZnS} is the dissociation constant of ZnS, K_{ZnSe} is the dissociation constant of ZnSe, x_{ZnS} is the mole fraction of ZnS, x_{ZnSe} is the mole fraction of ZnSe, and p_i is the partial pressure of the corresponding component ($i = S_2$ or Se_2). By considering this fact, in the present investigation, the supersaturations ratios of S_2 and Se_2 were taken into account for the calculation of the critical radius and free energy of formation. From Fig. 27.9, it was observed that the supersaturation decreases with decreasing undercooling (ΔT). Under conditions of smaller undercooling, the supersaturations of S_2 and Se_2 were found to be close enough; on the other hand, for large undercooling, the difference in the supersaturations of S_2 and Se_2 was large. So one could expect correct stoichiometry of the supersaturated vapor for the case of lower undercooling, resulting in crystal with equal x and $(1-x)$ values for an initial 1 : 1 solid

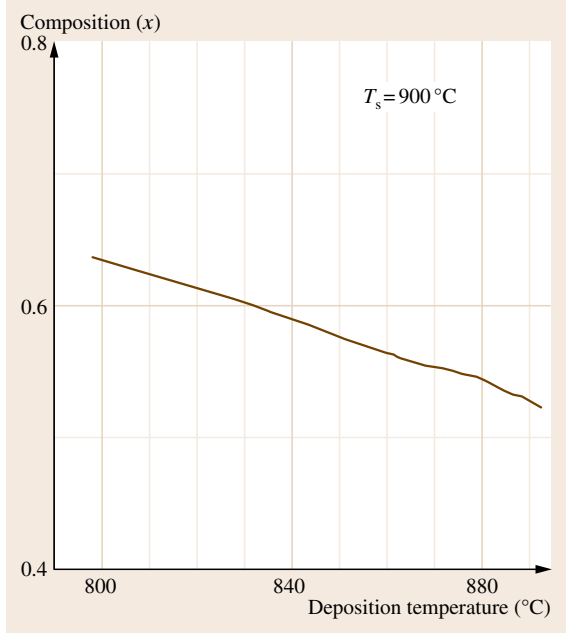


Fig. 27.15 Change in the composition of the grown crystal as a function of deposition temperature

source. For larger undercooling, the crystal would have an S-rich composition as the supersaturation of S will be high compared with that of Se. The calculated change of composition with deposition temperature is shown in Fig. 27.15. As the difference supersaturation ratio of S_2 and Se_2 increases, a crystal with sulfur-rich composition may be obtained.

The deposition temperature was varied from 800 °C to 890 °C for a fixed source zone temperature of 900 °C. The range of iodine concentrations used was 0.5–10 mg/cm^3. The critical radius was found to be high under conditions of smaller undercooling, and remained the same irrespective of iodine concentration. Under conditions of larger undercooling, the critical radius was found to decrease with increasing iodine concentration. The partial pressure of ZnI_2 increased with increasing iodine concentration (and hence supersaturation), resulting in the formation of large number of primary nuclei in the growth zone so that spurious nucleation occurred and hence the size of the critical nucleus decreased. The free energy of formation of a critical nucleus was calculated using (27.49) for different growth zone temperatures and iodine concentrations. As discussed earlier, ΔG^*_{het} was calculated for different contact angles between the substrate or ampoule wall and the crystal using classical nucleation theory. As the contact angle increased, the free energy also increased. The results are similar to that of ΔG^*_{hom} with respect to deposition temperature and iodine concentration.

27.4 Growth of II–VI Compound Semiconductors by CVT

This section deals in detail with the apparatus generally used for growth of II–VI compound single crystals by CVT technique and the preparation of starting materials for the growth process [27.54–68].

27.4.1 Apparatus

Double-zone or multizone furnaces are generally used for crystal growth by CVT technique [27.17, 54–59]. Depending on the required temperature profile and maximum operating temperature, the design and material used in fabrication of these furnaces will be different. Figure 27.16 shows a schematic of a double-zone horizontal furnace.

The muffles are made from ceramic materials or quartz tube of different lengths and diameters depending on the design of the furnace. The gap between the outer casing and muffle is packed with bricks and nonconducting materials such as asbestos powder in order to avoid heat loss. The ampoule is placed above the brick support. The two temperature zones must be considered as two different furnaces, and there is a gap between the two zones called the dead zone, which provides a smooth temperature gradient between the source and growth zone. The length of the dead zone is normally a few centimeters, depending on the required profile. The temperature of each zone is controlled by separate temperature controllers. Each zone has its own temperature sensors. For various regions, the temperature field in a typical cylindrical furnace is not radially symmetrical. If the axis of the furnace is horizontal, then the top part is usually a few degrees hotter then the bottom. If the furnace is set with its axial vertical, this effect is removed as for as the radial distributaries is concerned, but the heat field still depends on the configuration of the heating elements, etc.

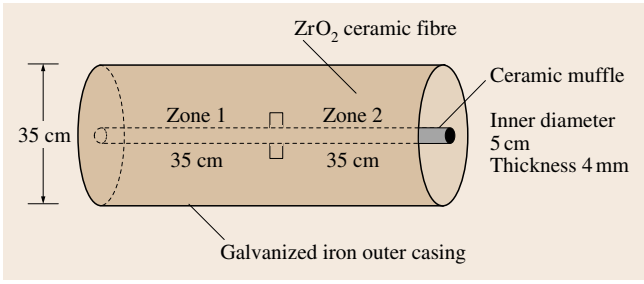


Fig. 27.16 Schematic diagram of a double-zone horizontal furnace for CVT growth

In chemical vapor transport growth, the most common temperature measurement and control techniques are based on thermocouples. Chromel–alumel thermocouples can be used to measure up to 1273 K. The essential requirement for this is purity, which should be 99.999% of the individual metal or alloy. An alumina sheath has to be provided to protect the thermocouple to a considerable extent of its diameter. Generally these temperature sensors will give a very weak signal, on the order of mV. The weak signal will be amplified and used to control the power input of the furnace. The requirements of crystal grower are not fulfilled by

mechanical regulators and on–off controllers and nowadays they have been replaced by electronic controllers. To achieve a stable temperature without a setting error in real systems, proportional–integral–differential (PID) or Eurotherm controllers are used. Since the weak signals obtained from thermocouples are passed to the controllers, they must be carefully shielded. Otherwise stray voltages may be introduced by direct or capacitative coupling. Extension wires used to connect thermocouple outputs to the controller must be prepared from the same alloys with similar thermoelectric characteristics. Such cables are referred to as compensating cables. However these compensating cables can only minimize the error.

The ampoule may be made of any material which does not melt, soften or react appreciably with the species in the system at the operating temperature [27.13]. At temperature up to about 450 °C, Pyrex glass is suitable for many systems. At higher temperature silica is very commonly used, but aluminosilicates can be used as alternatives. Generally a cylindrically shape ampoule is used to grow the crystals, although different shapes of growth and ampoule have been studied. The effect of changing the shape of the growth end of the ampoule has been investigated by many researchers. A rounded end usually results in distributions of crystallites over several centimeters. A tapered, pointed end defines the cold region much better. The next stage was to extend the end of the ampoule by a narrow tube. Nucleation takes place inside the tube at several places, and after a time the crystallites grow together. The final stage of evolution was to provide a crystallite seed, rather than wait for nucleation. A convenient way of doing this is to trap a crystallite at the end of the ampoule by inserting a stopper above it. Generally it is considered that a rounded end to the ampoule gives the lowest possibility of developing unwanted nuclei, assuming that there is initially just one nucleus located centrally at the end of the ampoule.

Vacuum systems are used to evacuate the reaction tubes after filling with the charge materials and transporting agents. This is done for the following reasons:

1. It reduces the chance of explosion of the tube at operating temperature due to the increased vapor pressure of the elements.
2. It enables easy access to the growth zone as the mean free path of the gaseous particles becomes greater than or comparable to the size of the ampoule at lower total pressure.
3. It is advantageous for materials which exhibit a tendency for thermal decomposition and affinity for oxygen.

Oil rotary with diffusion pumps generally provide a vacuum level down to 10^{-6} Torr for loaded transporting agent and feed material within the ampoule.

Before loading the charge materials, the ampoules should be properly cleaned. Cleaning of the ampoule is one of the most important aspects of the growth of crystals by chemical vapor technique. If the ampoules are not cleaned properly, impurities may get into the growing crystal or serve as sites for heterogeneous nucleation and affect crystal quality. The general cleaning procedures include washing and etching (50 : 50 concentrated HNO_3 and 40% HF) and flame polishing. The polycrystalline of the material to be grown is taken in one tube (A) and the other tube (B) is loaded with transporting agent with the use of stopper D while it is cooled with Dewar flask to minimize sublimation of iodine. Then tube A will be cooled while B is heated gently. The iodine which has sublimed from tube B will be condensed in tube A, which will be sealed off in vacuum.

27.4.2 Preparation of Starting Materials

Purification

Whenever the impurity content of the starting elements is higher than desired, a careful check should be made to determine whether a purification step will effectively improve the situation. If one is dealing with an already high-purity semiconductor-grade material, one runs the risk that impurities will be introduced during handling or processing of the material. It is also possible that, even though multiple purification steps may sufficiently decrease certain impurity concentrations, one or two less desirable impurity elements may at the same time be incorporated into the material. Thus, it can occur that, after purification, the overall purity may be better, but the material may be of lesser quality with regards to a specific application. The above comments are not to be taken as a discouragement towards purification steps, but rather as a caution that, during the purification procedure and in the handling of high-purity material in general, great care must be taken to avoid unnecessary contamination. There are two types of purification steps which can often be incorporated during preparation and therefore deserve special mention. The removal of surface oxide is readily achieved by firing the metal compounds, i. e., Zn or Cd, in a stream of pure H_2 just

prior to use. The other step is distillation of the elemental compounds into apparatus.

Preparation of the Starting Compounds

If it is possible to prepare large quantities of the starting compounds in a single sealed system, the chance of obtaining high-purity or controlled impurity-doped material is greatly improved. There are several methods used to prepare ZnSe. In one procedure, ZnO, ZnS, and Se are reacted to yield ZnSe, which probably contains some residual sulfide and oxide.

The most direct method is rapid heating of Zn and Se under argon pressure of 200 atm in an autoclave to the melting point of ZnSe, followed by rapid quenching of the system. The reactor has been designed [27.69] along with a temperature profile for synthesizing ZnSe powder of ≈ 0.9 crystal density from the reaction of 5 N pure elemental zinc and H_2Se in the gas phase by means of H_2 carrier gas. The gas flow rates are: H_2 carrier at 100 cm^3/min, H_2 over zinc boat at 90 cm^3/min, and H_2 mixed with H_2Se at 20 cm^3/min with H_2-to-H_2Se ratio of 40 : 1. The zinc boat is loaded with 10 g zinc before each run, and used entirely to prevent cracking of the quartz upon cooling. ZnSe is controlled as a granular yellow powder both on the liner and attached in a solid chunk to the H_2/H_2Se nozzle. The rate of collection is 1.0 g/h with 50% yield. This powder is then vapor transported under a dynamic vacuum of 10^{-5} Torr out of a furnace at 850 °C using a 20 mm-diameter tube. Again a high-density ZnSe powder is collected at the mouth of the tube furnace while unused Zn and Se are transported further downstream. The approximate weight loss is 10%. All impurities usually detected by spectroscopic analysis are present at less than 0.1 ppm, including copper. This material is then collected and used for crystal growth.

27.4.3 Growth of ZnSe Single Crystals

Increasing attention has been focused on the growth of ZnSe single crystals for application as a substrate for blue light-emitting diodes [27.70, 71]. Growth of ZnSe single crystals was initiated in 1958, but no report of the size of the grown crystals was made in the early literature. The first report on the growth of ZnSe single crystals with mention of their size came from *Nitsche* [27.72], who used the CVT method for growth of these crystals with size of up to $4 \times 4 \times 3$ mm^3. Since 1960 there have been a lot of reports on growth of ZnSe single crystals, mostly by vapor methods and in limited cases by other methods such as melt [27.69, 73], solution [27.74], and solid-state recrystallization [27.75]. The high melting point (1520 °C), multitwin patterns produced during phase transitions from hexagonal to cubic at 1425 °C, and other defects produced at high temperatures have made growth of ZnSe from the melt difficult [27.76]. Attempts have been made by various researchers to use CVT with iodine as a transporting agent to grow ZnSe single crystals with larger size and improved properties suitable for device applications [27.77].

By using seed methods and applying smaller undercooling ($\Delta T = 7$ K), ZnSe single crystals with dimensions of $20 \times 15 \times 15$ mm^3 were grown [27.78]. Later it was shown that the grain size of the grown crystals depends strongly on the undercooling and growth ampoule geometry, and growth of ZnSe with dimensions of $24 \times 14 \times 14$ mm^3 with undercooling as small as 7 °C using an ampoule with a steep conical tip was reported [27.79]. Later there was no further improvement in the size of ZnSe single crystals grown by CVT, and attempts were oriented towards growth of these crystals with more attention to their morphological perfection and improved electrical and optical properties. *Kaldis* [27.80] discussed that the morphology of crystals grown from the vapor phase depends on the mechanism that is rate determining. Very recently, it has been shown that changes in experimental variables such as the system pressure, the temperature conditions, and the concentration of the transporting agent will affect the contribution of mass transport through the convection and diffusion mechanisms and affect the crystallographic perfection and morphological stability of ZnSe single crystals grown by the CVT method [27.81]. The growth aspect of ZnSe single crystals grown by CVT has been studied with special emphasis placed on the formation of different micromorphological patterns formed on the surface of crystals grown under different experimental conditions [27.58].

Pretreatment of starting material for the growth process was carried out by mixing a stoichiometric ratio of ZnSe elements with 5 N purity and loading them into a quartz ampoule. The mixture was heated in vacuum at a temperature of 850 °C for 10 h in order to remove volatile impurities and obtain homogenized polycrystalline ZnSe. The formation of ZnSe was verified by x-ray diffractography. Ampoules with length of 23 cm and diameter of 1 cm were filled with 3 g heat-treated ZnSe polycrystalline powder along with iodine at concentration of 3 mg/cm^3 of the empty space of

the ampoule. The ampoules, cooled by ice, were evacuated to 2×10^{-6} Torr and sealed off. The capsules were placed into a double-zone horizontal furnace controlled by Eurotherm controllers with accuracy of ±0.1 K. PID controllers with accuracy of ±5 K were also used in one of the growth runs. A reverse temperature profile was developed across the ampoule, with the growth zone at high temperature for 24 h to remove powders sticking to the deposition zone of the ampoules and diminish the active sites. Growth runs were carried out for different undercooling (ΔT) values using various compositions of starting materials and ampoule geometries while keeping the temperature of the growth zone constant at 890 °C. Each growth run was carried out for a week. At the end of each growth process, the furnace was slowly cooled to room temperature at a rate of 50 °C/h to prevent thermal strain. The grown crystals have been characterized for their structure and morphology [27.80–85].

27.4.4 Growth of CdS Single Crystals

There has been a long-standing interest in CdS because of its optical and electrical properties. Due to its large bandgap (≈ 2.5 eV) and high quantum efficiency, CdS is used for applications from window material for solar cells to coloring plastics [27.86]. Single crystals of CdS have been grown largely by vapor and in limited cases by melt [27.87], solution, and flux methods [27.88]. Vapor growth of CdS at low temperatures was first achieved by *Nitsche* [27.72], who utilized the chemical vapor technique with iodine as the transporting agent. The growth of CdS by CVT technique was continued by various researchers, and crystals with different morphological habits and sizes were grown under different experimental conditions. *Paorici* [27.89] reported growth of CdS single crystals in the form of hollow prismatic rods in an iodine-rich atmosphere. *Kaldis* [27.90] has extensively studied the growth of CdS single crystals by CVT under different experimental conditions such as source temperature ($750\,°C < T_2 < 1120\,°C$), undercooling ($5\,°C < T < 200\,°C$), and iodine concentration ($0.1\,mg/cm^3 < c < 12\,mg/cm^3$) in order to find suitable conditions for control of nucleation and to improve the size of the grown crystals. These studies showed that, using the vertical pulling method with iodine transport, controlled nucleation was possible only at iodine concentration less than $0.2\,mg/cm^3$ and critical undercooling less than 15 °C. However, applying these conditions resulted in growth of crystals with cadmium deficiency. It was also reported that CdS grown under different experimental conditions exhibited different morphological habits (e.g., hexagonal platelets, hollow conical, and pyramidal) due to random nucleation and when using seed and undercooling of 5 °C. Change in morphology of CdS crystals with change in growth temperature and iodine concentration was also reported by other researchers. *Matsumoto* et al. [27.91] observed that CdS crystals grown at different temperatures and with different iodine concentrations showed different morphological habits such as needles, polyhedron, prisms, pyramids, rods, platelets, dendrites, and irregular shapes. *Attolini* et al. [27.8] improved the perfection of CdS single crystals grown by CVT by adopting the time-increasing supersaturation method, showing that crystals grown under small supersaturation do not exhibit skeletal and hollow forms. Later it was reported that using hydrogen as the transporting agent improved the size of the CdS single crystals and has several other advantages such as better control of nucleation, up to the point of obtaining large crystals and lack of contamination of grown crystals by the transporting agent [27.92]. *Paorici* and *Pelosi* [27.36] extensively studied closed-tube CVT techniques for the Cd:I_2 system from the thermodynamical as well as hydrodynamical point of view and calculated the mass transport rate as a function of overall pressure inside the tube, considering the contribution of thermal convection. *Attolini* et al. [27.93] applied the multidirectional productivity function for predicting the maximum transport efficiency as well as some other CVT features such as the relative importance of the various chemical reactions and the effect of inert gas on transport performance in the CdS:I_2 system.

CdS single crystals grown by CVT in closed tubes using iodine as the transporting agent show different morphological habits and degree of perfection when changing experimental conditions such as the growth temperature and iodine concentration. The growth temperature and iodine concentration have been changed over wide ranges to find empirically the most suitable growth conditions which yield CdS crystals of higher quality and large size. However the optimal growth temperature for a particular concentration of transporting agent for the growth of nearly perfect CdS single crystals remains to be determined. Hence the growth of CdS single crystals under different growth conditions has been studied to proof the agreement of theoretically predicted optimum conditions with experimental observations [27.94].

The experimental details for the growth of CdS single crystals followed at Crystal Growth Centre, Anna

University, are as follows: The starting material was cadmium sulfide of spectroscopic grade (5 N purity). Before use, the powder was heat-treated at 200–300 °C for several hours in vacuum. Three grams of heat-treated powder was filled into quartz ampoule having length of 20 cm and diameter of 1 cm, along with iodine. Due to the high vapor pressure of CdS, the ampoules were made from quartz tubes with thickness of 2 mm for safety reasons. The ampoule, cooled by ice, was evacuated to 2×10^{-6} Torr and sealed off. The capsule was placed into a double-zone horizontal furnace controlled by Eurotherm controllers. A reverse temperature profile was developed across the ampoule over several hours to remove the powder sticking to the tip or deposition zone of the ampoule. The growth temperature (T_g) was varied from 600–950 °C. The concentration of the transporter was varied from 1 to 10 mg/cm^3 and the difference in temperature of the source and deposition was kept constant at ($\Delta T = 50$ K) for all growth runs. Each growth run was carried out for 1 week. After that, the furnace was cooled at room temperature in 20 h.

Crystals grown at different growth temperatures with the same amount of iodine concentration showed different habits and optical quality. The crystals were orange, red, and pale yellow in color, with average dimensions of $3\times2\times1$ mm^3. The experimental results observed are in good agreement with the theoretical calculations. Crystals grown at growth temperature of 750 °C had complete faces, and their habits were mostly pyramidal and platelet. They were found to be more transparent compared with CdS crystal grown at other temperatures for the same transporter concentration. In general, the quality of the grown crystals was found to be good. This could be due to the stability of the flow of the materials transported from the source to the growth zone and the growth at the temperature of 750 °C predicted to be optimum for the iodine concentration of 5 mg/cm^3. At the growth temperature of 600 °C, due to the higher partial supersaturation, more crystals, of smaller size, with needle and irregular habits, and of poor quality were grown. Crystals grown at 950 °C were found to have poorly developed faces in most cases and showed less transparency. The deficiency in the surface perfection and optical quality of CdS crystals grown at 600 °C and 950 °C compared with CdS crystals grown at 750 °C may be due to variations of the transfer rate caused by small fluctuations in the temperature of the deposition zone where the slope of the $\Delta\alpha$ curve is large. Since the optical transmission measurements were carried out for crystalline samples of the same thickness (2 mm) and equally polished surfaces, the difference in transmission could be due to scattering from defect centers. Because of the temperature fluctuation at the growth interface, defects such as precipitates, inclusions, and dislocations may get into the lattice of the growing crystals and affect their optical quality. Figure 27.17 shows some of the CdS single crystals grown at 750 °C for $c = 5$ mg/cm^3 and $\Delta T = 50$ K.

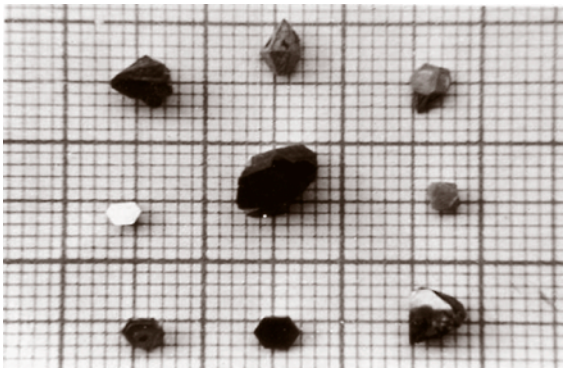


Fig. 27.17 CdS crystals grown at growth temperature of 750 °C

27.5 Growth of Nanomaterial from Vapor Phase

ZnSe can be used in optoelectronic devices such as LED and LDs in the blue wavelength region [27.95]. ZnS:Mn and ZnSe:Mn are known to be good luminescent materials [27.96, 97]. The recent interest in these semiconductors is due to the magnetic properties when transition metals are doped at lower concentrations, forming a separate class of research identified as diluted magnetic semiconductors [27.98]. The sp–d exchange interaction between ZnSe and Mn makes it possible to obtain magnetic character in nonmagnetic semiconductor, as applicable in magnetooptical devices [27.99]. Nanocrystalline growth of ZnS:Mn- and ZnSe:Mn-based semiconductors has attracted substantial interest in recent years [27.100, 101]. Nanocrystals and nanostructures of these materials were grown from aqueous solutions [27.102, 103]. Vapor growth methods such as MOVPE and MOCVD have also been used to synthesize nanostructures of

ZnSe [27.104, 105]. Magnetron sputtering has been used to deposit SiO_2/CdTe/SiO_2 nanocrystalline thin films [27.106]. A few II–VI compound nanocrystallites were grown on glassy matrix [27.107]. Sol–gel synthesis of ZnS was carried out in SiO_2 gels [27.108]. These nanostructures have usually been analyzed by characterizations techniques such as transmission electron microscopy (TEM), photoluminescence, Raman and ultraviolet–visible spectroscopy (UV-vis), etc. Electron spin resonance (ESR) has been used as a tool to analyze paramagnetic impurities in ZnS nanocrystals and quantum dots [27.109].

SiO_2 aerogels were obtained by sol–gel synthesis followed by annealing at high temperatures up to 400 °C. This matrix has been used to deposit nanocrystalline ZnSe:Mn on its pores by the chemical vapor transport method using iodine as transporting agent. ZnSe doped with 0.2 mol % Mn powder synthesized by vapor transport has been used in the experiment. The growth temperature was 800 °C and the temperature difference was 50 K. The experimental procedure has been discussed in detail [27.26]. The characterization details have been reported in the literature [27.104–115].

27.6 Growth of I–III–VI_2 Compounds

Nonvolatile solid substances can be transported through a vapor phase by chemical vapor transport (CVT) when suitable reactive gases are provided in the presence of a temperature gradient, such as when transforming solid substances into gaseous compounds via heterogeneous chemical reactions and vice versa. Vapor-phase chemical transport methods, as first described by *Schäfer* [27.12] and *Nitsche* et al. [27.116], are widely used in closed-tube arrangements for growing crystals. These vapor-grown crystals are often perfect enough and of good enough quality to be used in solid-state physics experiments.

Honeyman and *Wilkinson* [27.117] have grown $CuGaS_2$, $CuAlTe_2$, $AgGaS_2$, $AgAlS_2$, $AgAlSe_2$, and $AgAlTe_2$ single crystals from polycrystalline materials by chemical vapor transport using iodine as the transporting agent to form single crystals. Table 27.3 gives the details of the growth conditions used, such as temperatures, ampoule dimension, and transporting time, and the crystals obtained.

In all cases 5 mg/cm^3 iodine per unit volume of ampoule was used as the transporting agent. The silver compounds required much longer growth times than the copper compounds. This is probably due to the vapor pressure of silver iodide, which is approximately 30 times less than that of copper iodide at the same temperature. The tellurium compounds were also very difficult to grow and gave a low crystal yield. This may be due to the formation of $TeCl_4$, which would prevent the normal iodide vapor transport.

Paorici et al. [27.9] have grown $CuGaS_2$, $CuInS_2$, $CuAlS_2$, and $AgIn_5S_8$ single crystals using a temperature-variation method of the chemical vapor transport technique and iodine as the transporting agent. Larger

Table 27.3 Growth parameters of some I–III–VI_2 compounds by CVT method and their results

Compound	Ampoule diameter (mm)	Length of ampoule (cm)	Source–growth zone temperature (°C)	Transport time	Crystals obtained
$CuGaS_2$	18	20	800–700 850–750	3 days	High yield, yellow–green crystals stable in atmospheres
$CuAlTe_2$	18	20	780–650	5 months	Very low yield, red hexagonal platelets
$AgGaS_2$	18	20	840–740	2 weeks	Moderate yield straw-yellow transparent crystals
$AgAlS_2$	15	14	800–600	3 weeks	Colorless crystals, very unstable in air
$AgAlSe_2$	18	20	750–630	3 months	Low yield, yellow–black crystals
$AgAlTe_2$	18	20	830–630	2 weeks	No crystals

crystals were obtained by means of a time-varying temperature profile method. The principle of the method involves a gradually increase of the source temperature, which allows firstly reduced primary nucleation and secondly the avoidance of constitutional undercooling during the first stages of nucleus growth. The source temperature (at the hot end of the ampoule) T_s is slowly raised as a function of time, while the growth temperature T_g is kept constant. Initially, the ampoule is placed such that T_s is lower than T_g by about 100 °C (temperature inversion). This temperature inversion is a very important feature of the method, because of its cleaning effect on the quartz wall of the deposition zone. After 2–3 days of temperature inversion, T_s is adjusted to about 10 °C lower than T_g. Qualitatively, the growth mechanism can be described as follows. By increasing T_s, when T_s reaches some value, the supersaturation reaches a value for which primary nucleation has a high probability of occurring on some active sites of the quartz walls. If careful quartz treatment is performed, only a few primary nuclei are found. Since now the growth process of these primary nuclei will result in a more probable process, their development into large single crystals is expected. The two alternative methods, i. e., stationary temperature profile (STP) and time-varying temperature profile (TVTP), were used and the sizes of the crystal grown were compared.

27.6.1 Growth of Undoped and Doped Crystals of $CuAlS_2$

$CuAlS_2$ is a wide-bandgap (3.49 eV) member of the ternaries, which has been found to emit strong green and blue photoluminescence (PL) and therefore is considered a candidate material for blue and green light-emitting device realization [27.118,119]. Single crystals were grown by chemical vapor transport technique from polycrystalline $CuAlS_2$, which was prepared by direct melting of the constituent elements in a BN crucible. The resulting crystals, which were typically plate-like with dimensions of $20 \times 10 \times 0.5\,mm^3$, were then annealed in evacuated and sealed quartz ampoules in the presence of 100 mg Zn metal placed at one end of the ampoule with the $CuAlS_2$ crystals placed at the other end. Thermal treatments were carried out for 50 h at different temperatures in the range 973–1173 K.

Shirakata et al. [27.120] have grown $CuAlS_2$ single crystals by chemical vapor transport using iodine as the transporting agent. Growth conditions of source and growth temperatures were 800–650 °C and iodine concentration was $5\,mg/cm^3$. PL measurements were carried out at low temperatures (77 and 10 K). Most of the crystals exhibited a strong, orange PL band peaking at 2.1 eV and weak peaks at 2.9 and 3.55 eV. These results can be explained by considering that a large concentration of antisite disorder defects should be expected in Cu- and Al-rich crystals, being acceptors such as Cu_{Al} defects in Cu-rich samples and donors such as Al_{Cu} defects in Al-rich samples. Thermal treatment in sulfur vapor will result in a decrease of the concentration of sulfur vacancies and an increase of the concentration of the cation vacancies V_{Cu} and V_{Al}. Since the former defects are donor-like while the latter are acceptor-like the degree of compensation under sulfur annealing will be reduced, which was observed experimentally as an increase of *p*-type conductivity. The results for the sharp, near-bandgap PL lines are summarized in Table 27.4, where peak energies and assignment of the exciton PL lines in $CuAlS_2$ crystals are given. The crystals under consideration are as-grown ones of stoichiometric, Al-rich, and Cu-rich compositions as well as crystals annealed in sulfur and in vacuum. Strong lines are indicated by (++), weak lines by (+), and missing lines by (−).

Table 27.4 Summarized PL results on CVT-grown $CuAlS_2$ single crystals

Energy	Crystals					Assignment
	As grown			Annealed		
	Stoichiometric	Al-rich	Cu-rich	In sulfur	In vacuum	
3.376	+	−	+	−	−	−
3.567	+	Broad	+	+	+	−
3.550	++	−	++	++	++	Free exciton
3.540	++	−	++	+	++	Bound exciton
3.532	++	Broad	++	+	++	Bound exciton
3.500	+	−	−	++	−	Bound exciton
3.475	+	−	−	++	−	Bound exciton

Aksenov et al. [27.121] recorded PL spectra for $CuAlS_2$ single crystals doped with Zn by adding metallic zinc into the starting composition of the constituent elements prior to synthesis of the $CuAlS_2$ compound. Zn doping was carried out by using different techniques:

1. Zn dopant was added into the starting composition of constituent elements prior to synthesis of $CuAlS_2$ by direct melting. In this case the concentration of Zn in CVT-grown crystals was found to be equal to the nominal one.
2. Undoped CVT-grown crystals were annealed in evacuated and sealed quartz ampoules in the presence of ZnS and S at 973–1073 K for 60 h, the S pressure being 1–3 atm.
3. The undoped crystals were annealed at 873 K for 20–120 h in the presence of Zn, the Zn metal being placed at one end of the ampoule and the crystals to be doped at the other.

Aksenov et al. [27.122] have grown Cd-doped $CuAlS_2$ single crystals by CVT using iodine as the transporting agent, with grown crystal annealed under different atmospheres such as Cd. Annealing of the crystals in the presence of Cd at 700 °C did not result in any significant change in the PL properties of the crystals, the resulting PL spectrum being essentially the same for as-grown crystals. In the case of annealing at 900 °C for 50 h, an intense yellow–green photoluminescence band peaking at 565 nm was observed. This emission is interpreted as originating form donor–acceptor pair recombination, involving deep levels, formed by Cd-introduced defects.

27.6.2 Growth of Undoped and Doped Crystals of $CuAlSe_2$

$CuAlSe_2$ is one of the wide-bandgap ternary compounds with chalcopyrite-type structure and is promising as an optical application in the blue wavelength region. *Kurposhi* et al. [27.123] have grown single crystals of $CuAlSe_2$ by chemical vapor transport, which were plate-like and transparent with yellowish color. Relatively large single crystals with a well-developed (112) face and typical dimensions of $9\times5\times0.45\,mm^3$ were obtained at source and growth temperatures of 1263 K and 1223 K and iodine concentration of 2–3 mg/cm^3 . It was found that the light transmittance of the crystals decreased with during the days after growth. This may be due to surface oxidation of $CuAlSe_2$ crystals after growth, which is a serious problem for optical applications of this compound.

Chichibu et al. [27.124] have studied the resistivities, carrier concentrations, optical absorption, and PL of undoped and Cd- and Zn-doped $CuAlSe_2$ single crystals grown by CVT. The electrical and optical properties were almost unchanged after annealing under Se pressure. However, resistivity increased about seven orders of magnitude after annealing in vacuum. Resistivity also increased with Cd or Zn doping. The samples showed p-type conduction even with Cd or Zn doping. It was seen in all samples that the reduction of transmittance began from about 2.4 eV. A binding state such as a deep donor level which accompanies a lattice relaxation acts as an optical absorption center that needs more than 2.4 eV for its excitation. The assumed binding state appears to be related to a vacancy at the Se site because the absorption edge was almost unchanged after annealing in a Se atmosphere and shifted after annealing in vacuum. Therefore, taking into account that the absorption edge did not shift with Zn doping but did shift with Cd doping, the binding state may be a complex center consisting of the cation atoms and the nearest X_{Se}, where X is an atom or vacancy.

$CuAlSe_2$ single crystals were grown by CVT method using an ingot synthesized by a melt-grown technique in a rotating horizontal furnace using the elements Cu, Al, and Se with excess Se of 3 mol % form the stoichiometry. A concentration of iodine of 5 mg/cm^3 was used [27.125]. The crystal growth was carried out for 7 days at constant temperature of 850 °C for the source region and 700 °C for the growth zone. As-grown crystals had platelet and needle shape, with typically dimensions of about $9\times6\times0.5\,mm^3$, and showed a greenish yellow color. In PL spectra measured at 80 K, two independent, broad emission bands with peak energies of 1.77 and 1.93 eV were observed.

Prabukanthan and *Dhanasekaran* [27.126] reported the growth of $CuInTe_2$ single crystal by CVT method. A polycrystalline ingot of stoichiometric $CuInTe_2$ was synthesized from copper, indium, and tellurium elements with 4 N purity. The stoichiometric ternary mixture was taken into a quartz ampoule and sealed in a quartz ampoule under vacuum of 2×10^{-6} Torr (0.3 mPa). The ternary mixture was gradually heated to 1323 K at a heating rate of 20 K/h. The ampoule was maintained at this temperature for 2 days until the reaction was complete. Then the furnace was cooled at a rate of 50 K/h. The ampoule was opened and the synthesized polycrystalline $CuInTe_2$ material was analyzed using powder x-ray diffraction (XRD). Single-phase polycrystalline $CuInTe_2$ powder showed a well-defined chalcopyrite structure. Two

grams of synthesized $CuInTe_2$ polycrystalline material and 5 mg/cm^3 of high-purity iodine were taken into a quartz ampoule. The ampoule, cooled by ice, was evacuated to 2×10^{-6} Torr and then sealed off. The ampoule was placed into a double-zone horizontal electrical furnace controlled by Eurotherm temperature controller. During the first stage, the furnace was slowly heated. The temperatures of the source and the growth zones were allowed to reach 873 and 923 K, respectively, in order to remove the material and also to clean the growth zone of the ampoule. The duration was 20 h. After this, the temperatures of the source and growth zones were maintained at 923 and 873 K, respectively. After growth lasting 14 days, the furnace was slowly cooled at a rate of about 20 K/h. When the temperature of the ampoule reached room temperature it was opened to obtain $CuInTe_2$ crystals. The crystals were then cleaned in an ultrasonic bath containing a mixture of acetone and methanol, and then rinsed with deionized water. The $CuInTe_2$ single crystals obtained were black in color with mirror-like upper surface; the maximum dimensions of the crystals obtained was $15\times5\times3$ mm^3. Similarly, single crystals of $CuInTe_2$ were also grown by maintaining source and growth temperatures of 923–823 K and 923–773 K, respectively, for a period of 14 days. The dimensions of the crystals grown at 823 and 773 K were $7\times3\times5$ mm^3 and $4\times3\times3$ mm^3, respectively. The single crystals of $CuInTe_2$ grown at growth zone temperatures of 873, 823, and 773 K are shown in Fig. 27.18a–c. Single-crystal x-ray diffraction studies of $CuInTe_2$ single crystals carried out on crystals grown at different growth zone temperatures indicated tetragonal (chalcopyrite phase) structure.

Gombia et al. [27.127] have grown $CuGaTe_2$ and $CuInTe_2$ single crystals by chemical vapor transport technique and considered thermodynamically the growth parameters. The behavior of all gaseous species, the formation of spurious phases, i. e., liquid Te and solid TeI_4, and transport conditions were discussed. Polycrystalline $CuGaTe_2$ and $CuInTe_2$ ingots were prepared by fusion of the constituents, weighed in stoichiometric ratio. The mixture was sealed in a quartz ampoule under vacuum of 10^{-6} Torr and heated at a rate of about 10 °C/min up to 420 °C (below the Te melting point) for several hours, then kept at a temperature of 900 °C for $CuInTe_2$ and 950 °C for $CuGaTe_2$ for several hours to ensure complete reaction and homogenization. Finally the samples were cooled slowly to 650 °C, annealed at this temperature for 3 days, and quenched to room temperature.

A vapor transport method in a closed tube, using iodine as transport agent and polycrystalline $CuGaTe_2$ and $CuInTe_2$ as the starting source, was employed. To produce single crystals of significant size it is necessary to limit the number of potential sites for crystallization nuclei. Experimentally this can be done by thoroughly cleaning the quartz ampoule and using a low starting temperature gradient to assure a small supersaturation. To ensure the latter condition, a tubular eight-zone furnace permitting different gradients and profiles to establish conditions as close as possible to the theoretical ones was used. Inversion of the temperature profile between the source and crystallization zones reduced the number of nuclei. This process was performed automatically by means of an electronic programmer. The grown crystals were characterized and the resistivity,

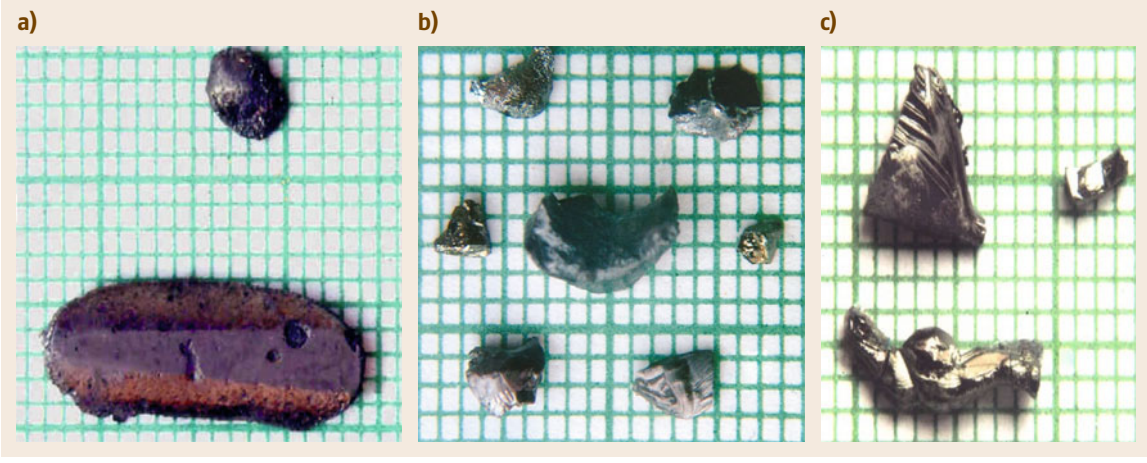


Fig. 27.18a–c $CuInTe_2$ crystals grown at growth temperature of **(a)** 873 K, **(b)** 823 K, and **(c)** 773 K

carrier mobility, and carrier concentration were determined in the temperature range between 80 and 300 K. $CuInTe_2$ crystal grown in this way and annealed under Cd atmosphere changes from p-type to n-type and also exhibits increased mobility.

27.6.3 Growth of $CuGaS_2$-Based Single Crystals

Yu et al. [27.128] have grown $CuGaS_2$ single crystals by two different methods: melt-growth and chemical vapor-phase transport. In the CVT technique iodine was used as a transporting agent. The crystals were synthesized from the constituent elements (Cu, Ga, and S of 6 N purity) in stoichiometric proportions in an evacuated quartz ampoule. The material was held in the temperature range 1050–1100 °C. It was cooled slowly at a rate of 2 °C/h to 700 °C and then cooled at a faster rate to room temperature. Crystals obtained from the melt varied in color from red to yellow–green. The crystals grown form the melt were crushed into powder and used as the initial charge for the vapor transport. This method involved placing the reacted material together with a small amount of iodine in an evacuated quartz ampoule, and heating it in a temperature gradient. The volatile iodine serves as the transporting agent. The temperature difference between the charge and crystallization zones was kept at 50 °C. The temperature of the charge zone was 1000 °C. The grown crystals were homogeneous and showed yellow–green color. The typical crystal dimensions obtained were $1 \times 3 \times 0.4\,mm^3$.

Shirakata et al. [27.129] have grown $CuGaS_2$ single crystal by chemical vapor transport method using iodine as the transporting agent. Stoichiometric quantities of the elements Cu, Ga, and S (6 N) with total weight of 0.5 g were sealed into an evacuated quartz ampoule (10 mm inner diameter, 15 cm length) together with 3–25 mg/cm^3 iodine. The ampoule was placed in a two-zone horizontal furnace with temperature gradient of 900–700 °C and maintained for 4 days. With more than 10 mg/cm^3 iodine all source materials were transported to the other end of the ampoule, and platelike crystals ($5 \times 5 \times 0.2\,mm^3$ typical dimensions) with well-developed (112) plane were grown. With less than 5 mg/cm^3 iodine, some of the source materials remained and crystals were typically yellow–green, but the color became greenish as the quantity of iodine was increased. PL measurements have been carried out on $CuGaS_2$ single crystals at 4.2 and 77 K. At 4.2 K, high-quality single crystals grown by CVT method show sharp PL lines.

Prabukanthan and *Dhanasekaran* [27.130] have grown $CuGaS_2$ (CGS) single crystal by CVT method. Single crystals of CGS were grown by chemical vapor transport method using iodine as the transporting agent. The CGS crystals were grown at three different growth temperatures with 10 mg/cm^3 iodine concentration and temperature difference of 50, 100, and 150 K. The purity of the elements used for these experiments was 4 N. A mixture of the elements Cu, Ga, and S was taken into a quartz ampoule of length 18 cm and diameter 1 cm along with iodine at a concentration of 10 mg/cm^3. The ampoule, cooled by ice, was evacuated to around 2×10^{-6} Torr and sealed off. The ampoule was placed into a double-zone horizontal furnace controlled by temperature controllers with accuracy of ±0.1 K. A reverse temperature profile was developed across the ampoule over several hours to clean the quartz walls of the growth zone. The duration was 20 h [27.131, 132]. After this, the temperatures of the source and growth zones were maintained at 1173 K and 1123 K, respectively. The growth duration was 7 days, after which the furnace was slowly cooled at a rate of about 10 K/h to 773 K and then at the rate of 60 K/h. The CGS single crystals obtained were yellow in color with maximum dimensions of $6 \times 4 \times 6\,mm^3$. Similarly single crystals of CGS have been grown with the same iodine concentration and source zone temperature of 1173 K. Temperature differences of 100 and 150 K were maintained between source and growth zones, i. e., the temperature of the growth zone was maintained at 1073 and 1023 K, respectively. Growth was carried out for a period of 7 days in each case. The CGS single crystals obtained with growth zone temperature of 1073 and 1023 K were orange and green in color, respectively. The maximum dimensions of orange-colored CGS single crystals were $4 \times 2 \times 3\,mm^3$ and of green-colored crystals were $15 \times 0.4 \times 1.2\,mm^3$ (needle like) and $3 \times 2.5 \times 3\,mm^3$.

Single crystals of CGS grown with growth zone temperature of 1123, 1073, and 1023 K are shown in Fig. 27.19. The temperature difference between the source and growth zones affects the quality and color of the resulting crystals. The crystal nucleation rate depends on the magnitude of supersaturation of the gas phase, which is proportional to the temperature difference between the source and growth zones. Normally the temperature difference between the source and growth zones is very low so that the formation of primary nucleation is controlled to form large-size crystals [27.17]. To initiate the crystallization processes, crystal nuclei have to be formed in the crystallization

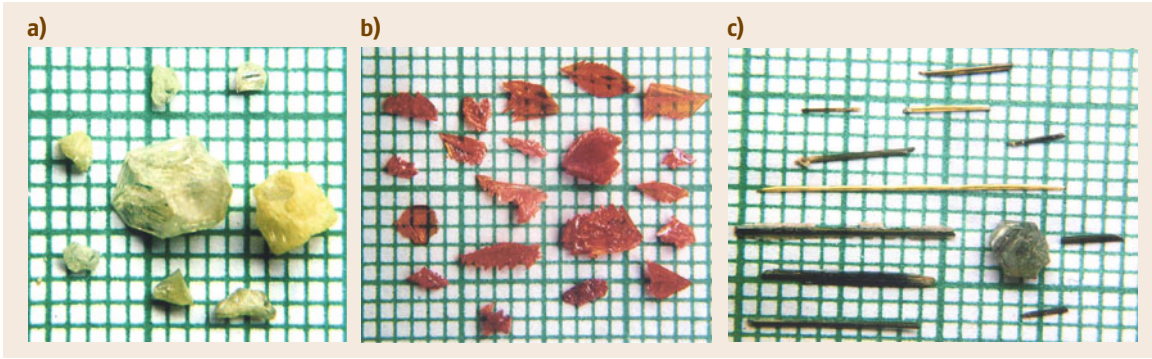


Fig. 27.19a–c As-grown single crystals of $CuGaS_2$ at different growth temperatures: **(a)** 1123 K, **(b)** 1073 K, and **(c)** 1023 K

zone. This is possible only if the gas phase is sufficiently supersaturated (i. e., the gas phase is in the unstable state). In the unstable state of high supersaturation, the rate of crystal nucleation is high and crystal nuclei are formed spontaneously in a short period of time. In the case of our experimental observations at growth temperature of 1023 K, the crystals grown were small in size due to high supersaturation ratio. However, at 1123 K, the crystals grown were larger in size due to the low supersaturation of the gas phase. Under chemical vapor transport conditions, the partial pressures of noble-metal iodides (CuI and GaI_3) are high compared with the partial pressure of sulfur. So controlling the stoichiometric composition is difficult. It is concluded from our experimental observations that, during the growth of CGS single crystal by CVT method with temperature difference between source and growth zones of 50 and 100 K, sulfur may play the main role in the transport process. The formation of other phases such as Cu_2S and Ga_2S_3 takes place during the growth of CGS single crystals at 1123 and 1073 K, respectively. However,when the temperature difference is maintained at 150 K, iodides such as CuI and GaI_3 may be the dominant gas species to from stoichiometric CGS single crystals.

Prabukanthan and *Dhanasekaran* [27.133] have grown Mn-doped $CuGaS_2$ single crystal by CVT method. Stoichiometric compositions of Cu, Ga, and S with 1 mol % Mn as precursor materials were taken into a quartz ampoule with iodine concentration of 10 mg/cm^3 (total weight 1 g, including Mn concentration). The quartz ampoule, cooled by ice, was evacuated to around 2×10^{-6} Torr and sealed off. The ampoule was placed into a double-zone horizontal electrical furnace. The furnace was controlled by Eurotherm temperature programmer and controller. The source and growth zones temperature were 1173 and 1023 K, respectively. The growth period was 7 days. The furnace was slowly cooled at a rate of 10 K/h to 873 K, after which it was cooled rapidly at a rate of 60 K/h. Similar growth conditions were used for growth of 2 mol % Mn-doped $CuGaS_2$ crystals. $CuGaS_2$ single crystals grown with 1 mol % and 2 mol % Mn doping were green and orange in color with dimensions of $2.5\times3\times4$ mm^3 and $4\times3\times3$ mm^3, respectively. Single crystals of 1 mol % and 2 mol % Mn-doped $CuGaS_2$ are shown in Fig. 27.20a,b. The Mn-doped $CuGaS_2$ single crystals were determined to be paramagnetic in nature. The increase of bulk conductivity of the Mn-doped $CuGaS_2$ single crystals at room temperature indicates an increase of hole concentration, and p-type conductivity was also found.

Tanaka et al. [27.134] have grown $CuGaS_{2-2x}Se_{2x}$ single crystal by CVT method. First, in order to prepare $CuGaS_2$ powder, Cu, Ga, and S were weighed in stoichiometric portions and sealed into evacuated silica tubes; then the tubes were heated in a furnace. The temperature was increased gradually to 1200 °C for about 24 h. $CuGaSe_2$ powders were also prepared in a similar way. Subsequently $CuGaS_{2-2x}Se_{2x}$ crystals were prepared by iodine transport method. $CuGaS_2$ and $CuGaSe_2$ powders were weighed in certain proportions, crushed, mixed, and then sealed in evacuated silica tubes (12 mm inner diameter, 10 cm length) with about 18 mg/cm^3 iodine. These ampoules were placed in a two-zone furnace. The source and growth zone temperatures were kept at 850–900 °C and 650–700 °C, respectively. Under these conditions all starting materials were transported by iodine within several days, and crystals of dimensions $3\times10\times0.5$ mm^3 were yielded.

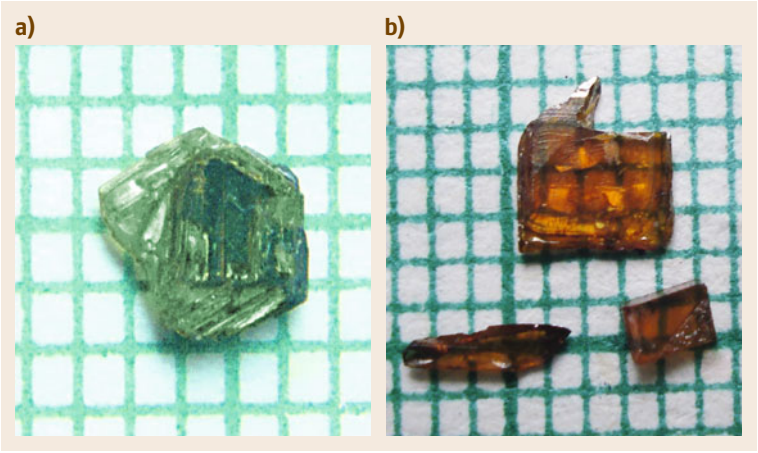


Fig. 27.20a,b As-grown single crystals of **(a)** 1 mol % Mn-doped and **(b)** 2 mol % Mn-doped $CuGaS_2$

The color of the crystals obtained varied continuously with composition: from dark green ($x = 0$), through red, to black ($x = 1$).

Sato et al. [27.135] have grown Fe-doped single crystals of $CuAl_{1-x}Ga_xS_2$ by CVT method using iodine as the transporting agent. Polycrystalline powders of $CuAlS_2$ and $CuGaS_2$ prepared by sintering were used as source materials. The source material and a transporting agent was sealed in vacuum in a silica ampoule with inner diameter of 13 mm and length of 20 cm. The iodine concentration was 25 mg/cm^3. The silica ampoule was placed in a double-zone electrical furnace. Then the temperature of the source and growth zones were kept at 900 °C and 700 °C, respectively. The dimensions of the crystals were $3 \times 4 \times 2$ mm^3. All of these undoped bulk crystals were black. Crystals with composition in the vicinity of $CuAlS_2$ were colored blue when polished to less than 0.5 mm, while those with the composition near $CuGaS_2$ were colored green, indicating the presence of trace impurity of iron. Crystals intentionally doped with Fe were also prepared with Fe concentrations of 0.1 mol % and 0.3 mol %. The grown crystals were characterized by PL. In addition, several researchers have grown $CuGaS_2$ single crystals, described in the literature [27.130, 132].

27.6.4 Growth of $AgGaS_2$ and $AgGaSe_2$ Single Crystals

Prabukanthan and *Dhanasekaran* [27.136] have reported the growth of $AgGaS_2$ single crystal by CVT method. The 1 : 1 : 2 mole ratio of Ag, Ga, and S with excess 0.5% sulfur as precursor materials, and 10 mg/cm^3 of high-purity iodine as the transporting agent, were taken into a quartz ampoule. In order to prevent deviation from stoichiometry resulting from possible volatile loss of sulfur during initial steps, it was found necessary to add excess sulfur. The starting materials were taken into a quartz ampoule (15 mm diameter, 180 mm length) evacuated to 2×10^{-6} Torr and then sealed off. The ampoule was placed into a double-zone (source and growth zones) horizontal electrical furnace. During the first stage the furnace was slowly heated at the rate of 10 K/h. The temperatures of the source and growth zones were allowed to reach 1023 and 1073 K, respectively, in order to clean the wall of the ampoule. The duration was 20 h. After this, the temperature of the source and growth zones were maintained at 1073 and 1023 K, respectively, for the next 15 days, after which the furnace was slowly cooled at a rate of 20 K/h. When the temperature of the ampoule reached room temperature it was opened to obtain yellow-colored $AgGaS_2$ crystals. Similarly single crystals of $AgGaS_2$ were grown with the same iodine concentration and source zone temperature of 1073 K. A temperature differences of 100 K was maintained between source and growth zones, so that the temperature of the growth zone was maintained at 973 K. The growth was carried out for a period of 15 days. The $AgGaS_2$ single crystals obtained were yellow in color. $AgGaS_2$ single crystals grown at growth zone temperatures of 1023 and 973 K are shown in Fig. 27.21a,b. Cut and polished $AgGaS_2$ single crystal grown at 1023 K is shown in Fig. 27.21c. Single-crystal XRD and powder XRD studies indicate that the as-grown $AgGaS_2$ crystals belong to the tetragonal (chalcopyrite) system with (112) plane as the dominant peak. The full width at half-maximum (FWHM) of the x-ray rocking curve

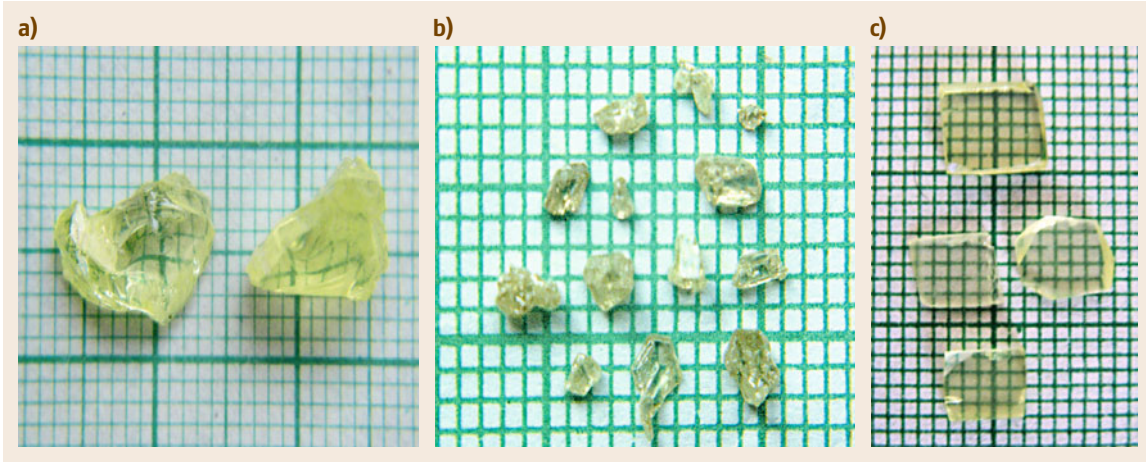


Fig. 27.21a–c $AgGaS_2$ crystals grown at **(a)** 1023 K, **(b)** 973 K, and **(c)** cut and polished $AgGaS_2$ crystals grown at 1023 K

for the as-grown $AgGaS_2$ single crystal was 5 arcsec. The quality of the crystals obtained with both temperature differences (100 and 50 K) between the source and growth zones was found to be good.

Noda et al. [27.137] have measured the transport rate for CVT growth of $AgGaS_2$ single crystal. The transport rate was measured by weighing the total amount of $AgGaS_2$ crystals grown in the growth zone. The important parameters affecting crystal growth were the amount of iodine, source temperature, and the temperature difference between the source and growth zones. The observed transport rate tends to increase with increasing ΔT at fixed T_s, but a higher transport rate does not necessarily mean larger single crystals. The other parameters affecting crystal growth is the presence of a maximum transport rate with increasing T_s at fixed ΔT. This indicates that condensation of the atoms at the growth zone was delayed with increasing growth temperature. All the as-grown crystals were transparent and yellowish in color and had rod and plate morphologies. The rod forms of single crystals were obtained when the growth temperature was more than 1173 K and the transport rate less than 10 mm/day. The biggest plate-type crystal ($7\times5\times2\,mm^3$) was obtained under the conditions of $T_s = 1248$ K and $\Delta T = 75$ K for 1 week. The habit plane of the rod was (112) and the growth direction was nearly in the (112) direction. The PL spectra of the crystals were dependent on the amount of iodine used, and excitonic emission was observed, which means that good-quality crystals were obtained.

Polycrystalline $AgGaS_2$ was prepared by synthesis from its constituent elements Ag, Ga, and S with 5 N purity taken into a quartz tube. Polycrystalline powder (2 g) as a source, was sealed with iodine as the transporting agent at concentration of 5 mg/cm^3 into a quartz ampoule of length 20 cm and inner diameter 1 cm. The as-grown $AgGaS_2$ single crystals were transparent and yellowish in color.

Single crystals of AgGaSSe [27.56] have been successfully grown from 2.5 g polycrystalline powder AgGaSSe as source, sealed with iodine at concentration of 5 mg/cm^3 into a quartz ampoule of length 20 cm and inner diameter 1 cm.

Nigge et al. [27.138] have grown single crystals of $AgGaSe_2$ by CVT method using iodine as the transporting agent. Growth temperature of 770 °C and concentrations of the transporting agent of 1.6–1.7 mg I_2/cm^3 yielded compact single crystals with dimensions up to $8\times5\times5\,mm^3$.

Tafreshi et al. [27.57] have grown single crystals of $Cu_{0.5}Ag_{0.5}InSSe$ for the first time by chemical vapor transport technique using iodine as the transporting agent. A stoichiometric mixture of the constituent elements with 5 N purity was taken, and polycrystalline $Cu_{0.5}Ag_{0.5}InSSe$ ingots were synthesized in a vertical furnace in vacuum at 900 °C. The polycrystalline synthesized powder of 2.5 g together with 5 mg/cm^3 5 N purity iodine was placed in a quartz ampoule with length 16 cm and diameter 1 cm. The ampoule, cooled by ice, was evacuated to 2×10^{-6} Torr and sealed off. The capsule was then placed into a double-zone horizontal furnace controlled by Eurotherm controllers. A reverse temperature profile was developed across the ampoule over several hours to

remove the powder sticking at the tip or deposition zone of the ampoule. The source and growth zone temperatures were kept at 937 °C and 849 °C, respectively. The growth run was carried out for 1 week. After that, the furnace was cooled to room temperature in 20 h. The grown crystals were in the form of small platelets with dimensions of $1 \times 2 \times 0.5\,mm^3$, joined together with mirror-like upper faces. X-ray analysis, surface analysis, and microindentation studies were carried out on the grown crystals to determine structure and lattice parameters, the growth mechanism, and mechanical properties, respectively. $Cu_{0.5}Ag_{0.5}InSSe$ was found to crystallize in tetragonal chalcopyrite structure.

27.7 Growth of GaN by VPE

Epitaxial growth can be achieved by solid-phase, liquid-phase, vapor-phase, and molecular-beam deposition. Vapor-phase growth is by far the most widely used technique for semiconductors. It consists of oriented crystal growth of a material transported from the gas phase onto a suitable solid substrate.

27.7.1 Vapor–Phase Epitaxy (VPE)

VPE systems are particularly employed in mass production of electronic devices because of their proven low cost and high throughput, in addition to their capability to grow advanced epitaxial structures. The fundamental reason for their success is due to the ease of dealing with low- and high-vapor-pressure elements. This is achieved by using specific chemical precursors, in the form of vapor, containing the desired elements. These precursors are brought into the reactor by a suitable carrier gas and normally mix shortly before reaching the substrate, giving rise to the nutrient phase for the crystal growth [27.139]. The release of the gas elements necessary for the construction of the crystalline layer may occur at the solid–gas interface or directly in the gas phase, depending on the type of precursors and the thermodynamic conditions.

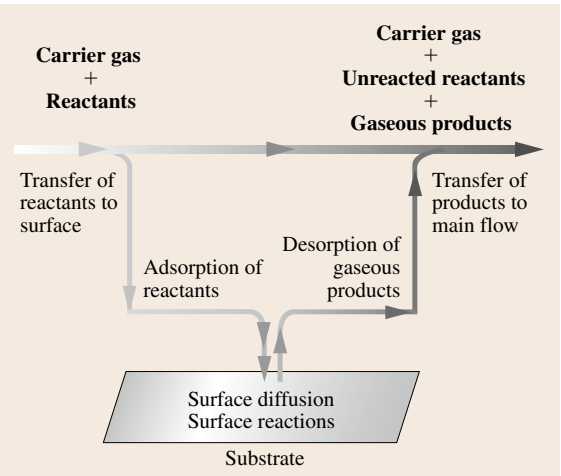


Fig. 27.22 The sequence of steps in a VPE process

In vapor-phase epitaxy with open flow systems a carrier gas containing the reactive species is forced to flow past the substrate crystal. At the crystal surface the species undergo a sequence of chemical reactions leading to extension of the substrate crystal lattice and formation of products which must leave the vicinity in order for the process to continue.

The sequence of steps which is generally assumed to occur is shown schematically in Fig. 27.22. The factors which influence the growth rate and material composition are the vapor pressure and the temperature, both of which can be precisely controlled. Depending upon the sources and the reactor type, one can distinguish between two special cases of VPE, namely hydride vapor-phase epitaxy (HVPE) and metalorganic vapor-phase epitaxy (MOVPE). The former uses inorganic sources and a hot-wall reactor, whereas the latter uses fully or partly organic sources and a cold-wall reactor.

27.7.2 VPE GaN Film Growth

Since the earliest pioneering work on growth of epitaxial films by VPE [27.140] until the early 1980s, VPE was a popular method for the growth of epitaxial layers of gallium nitride [27.141]. However, this technique was largely abandoned in the early 1980s because of its apparent inability to reduce the native defect concentration to nondegenerate levels and thus achieve p-type doping. This was presumed to be due to nitrogen vacancy defects, which would be thermodynamically favored at the high growth temperatures typically used in HVPE GaN growth. This interpretation predominated in spite of reports of nondegenerate films grown by HVPE [27.141] and careful growth stud-

ies which suggested that the incorporation behavior of this donor was inconsistent with a nitrogen vacancy defect [27.142]. With the advent of high-purity source materials and improved heteronucleation schemes, the growth of nondegenerate material has been reported by several groups.

The nature of the chemistry involved in GaN growth by HVPE technique differs from that of other III–V semiconductors. For instance, in GaAs growth by halide vapor-phase epitaxy, which uses the halide of the group V precursor $AsCl_3$ instead of its hydride AsH_3, thermal dissociation of the arsenic compounds results in the formation of As_4 and As_2 molecules, which typically remain volatile and chemically reactive and thus participate in film growth. In GaN HVPE, NH_3 is used as a source of nitrogen rather than nitrogen halide, NCl_3, which is highly explosive and highly unstable. In this process the thermal dissociation of NH_3 results in the formation of N_2 molecules, which are extremely stable and essentially unreactive at temperatures of interest [27.143–145].

Hydride VPE (HVPE) and chloride VPE (Cl-VPE) operate in a very similar manner and can be described by the final reaction as

$$\begin{aligned} &GaCl + NH_3 \rightarrow GaN + HCl + H_2\uparrow , \\ &GaCl_3 + NH_3 \rightarrow GaN + 3HCl . \end{aligned} \qquad (27.55)$$

However, the precursor for generating gallium chloride is different in both techniques. In HVPE of GaN, the gallium source is gallium monochloride (GaCl), which is stable only at temperatures above 600 °C and is produced by the reaction of liquid gallium with HCl gas [27.146–149]. The supply of GaCl is controlled by the gallium cell temperature and the flow rates of HCl gas and H_2 carrier gas. Several researchers have chosen presynthesized $GaCl_3$ instead of HCl gas [27.134, 143–145]. In Cl-VPE, gallium trichloride ($GaCl_3$) is used as the Ga source, due to its high vapor pressure. The use of monohalide (GaCl) or trihalide is the main difference between HVPE and Cl-VPE, respectively.

27.7.3 Strength of HVPE Method

It is important to analyze the importance of HVPE with respect to the other techniques. *Shaw* [27.150] has demonstrated that the Cl-VPE technique is an equilibrium process. The other epitaxial techniques (MOVPE and MBE) operate far from equilibrium conditions [27.151–153]. The near-equilibrium nature arises because of the reversible processes occurring at the interface due to the volatility of group III at the operating temperatures; shift from equilibrium is caused by kinetic factors mainly due to ammonia decomposition. Based on this description it is easy to enumerate the strengths of VPE:

1. In VPE, being a near-equilibrium process, the growth rates are in principle uniquely determined by the mass input rate of the reactants; hence, unlike in nonequilibrium processes (MOVPE and MBE), very high growth rates (> 10 μm/h) can be easily achieved;
2. The lack of carbon incorporation into the film;
3. Cost effectiveness.

In the following, the details of the system and the process of chloride VPE for the growth of GaN layers are described. Furthermore, the optimum conditions for the growth of gallium nitride have been established. Based on our experimental investigations on the influence of the different growth parameters on the quality of the layer, it has been identified that the growth temperature plays a dominant role in the growth of GaN as compared with other parameters such as the flow rate, deposition time, etc.

27.7.4 Development of VPE System for the Growth of GaN

The development of experimental apparatus for the growth of GaN at our university is described [27.153]. The vapor-phase epitaxy (VPE) system mainly consists of a reaction chamber, single-zone furnace, $GaCl_3$ cell assembly, process control, and ammonia gas purifier assembly. The schematic diagram of the system is shown in Fig. 27.23.

As the film growth involves a high-temperature process, the reaction chamber is made out of a quartz tube of length 90 cm, wall thickness 2 mm, and diameter 70 mm. Both ends of the tube are made of stainless steel and the assembly consists of two ports on one end and three ports on the other. Integral structures are made to hold the quartz tube rigidly at either end. One end of the quartz is used for the transport of $GaCl_3$ vapor with nitrogen as carrier gas, and another inlet is used for another stream of nitrogen gas for diluting the reacting species, as the reaction is a dilute reaction. The other end of the reactor tube is used for an ammonia gas input port, exhaust line, and substrate holder setup.

The single-zone furnace consists of heating arrangements surrounded by metal boxes. A ceramic muffle of length 80 cm has been used for winding the heating

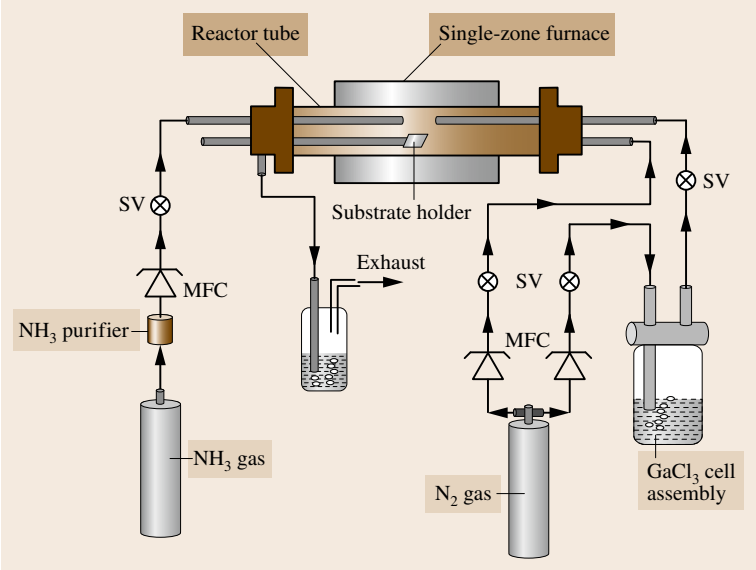


Fig. 27.23 Schematic diagram of the GaN vapor-phase epitaxy system

element (A1 Kanthal wire: SWG 18 type). The windings were done in such a way that the space between them gradually becomes narrow at the ends compared with at the center of the tube in order to compensate for heat losses at the ends of the tube to a certain extent. The windings were insulated by applying a paste of corundum cement and silica gel mixture (the silica gel provides a binding action to the refractory cement). The tube is then packed inside a stainless-steel container using a zirconia-grade fiber blanket of density 128 kg/m^3, which acts as a heat shield. Two thermocouples are used: one to control the furnace temperature, placed at the middle of the ceramic tube, i. e., near the growth zone; and another mounted inside the quartz tube, very close to the boat, so that the growth temperature could be monitored correctly.

The $GaCl_3$ cell assembly is made of quartz tube and a special Teflon assembly. The crystalline $GaCl_3$ in the cell is melted by a liquid-paraffin bath in which it is immersed. An electric heater maintains the paraffin bath at a suitable temperature in the range 80–150 °C. $GaCl_3$ vapor was transported to the reactor by nitrogen carrier gas. The partial pressure of $GaCl_3$ could be controlled by both the $GaCl_3$ cell temperature and the flow rate of the N_2 gas. A mass flow controller and solenoid valves were used to control the flow rate of the carrier gas. A separate nitrogen gas line is used to dilute the ammonia gas to the required partial pressure. This nitrogen gas flow is measured by a float-type flow meter. The flow rate is varied by a needle valve. A computer program controls the temperature of both the furnace and the $GaCl_3$ bath. The entire growth scheme can be preprogrammed. The program also enables the heating and cooling cycle to be programmed and data to be acquired during the growth cycle.

The purifier system consists of molecular sieves, which is a palladium- and silica-based compound, to remove moisture, carbon monoxide, and carbon dioxide form the ammonia gas. The purified ammonia is expected to be of analytical grade. After this online purification of the ammonia gas, its flow is monitored by a gas flow (float-type) meter.

27.7.5 Growth of GaN by HVPE

The experimental conditions for growth of high-quality GaN layers using $GaCl_3$ precursor are discussed in this section. In view of the high-quality GaN growth, it is understood that careful cleaning of substrates prior to loading into the growth furnace is an important issue, because the quality of the grown layer (desired morphology and good optical properties) depends on this process, as does the reproducibility of the results. Sapphire (Al_2O_3(0001)) substrates were degreased in trichloroethylene (TCE), acetone, methanol, and deionized water in sequence for about 10 min. After completing the organic cleaning processes, in order to remove residual damage and scratches on the surface, substrates were chemically etched with $HCl + H_3PO_4$ (3 : 1) solution heated at 80 °C for 15 min. Etched

sapphire substrates were again rinsed thoroughly in deionized water.

A quartz plate of 8 cm^2 area was used as the substrate holder, located at an optimized distance from the $GaCl_3 : NH_3$ mixing zone. Substrates of 1 cm^2 area are used per run and are placed lengthwise along the deposition zone. Considerable variation of the amount and quantity of deposition was observed between layers grown in a single run with respect to the position of the substrate. It was observed that GaN layer always deposits in regions closer to the $GaCl_3 : NH_3$ mixing zone. Initially the substrates are placed close to the mixing zone to find the exact position of uniform deposition. The substrate position has been varied further downstream from the mixing zone. It is observed that the layer thickness decreases rapidly with distance from the mixing zone. Growth ceases completely at distances from 6 to 10 cm downstream of the mixing zone.

After loading the substrates, the reactor was purged with nitrogen gas. Subsequently, the substrate was heated to the desired growth temperature and $GaCl_3$ was supplied using nitrogen carrier gas. The nitrogen source, NH_3, is not stable at high temperature and will thermally decompose to nitrogen and hydrogen gases. At the typical growth temperature (1200 K) the equilibrium value is about 0.1. Hence most of the ammonia will decompose to nitrogen and hydrogen at that elevated temperature in thermodynamic equilibrium. However, it is not easy to reach thermodynamic equilibrium in such an open system. The actual value depends on the NH_3 temperature, partial pressure, residence time, and surface conditions. Both NH_3 partial pressure and residence time can be changed by varying the NH_3 and N_2 flow rates. The H_2 gas, produced from the thermal decomposition of ammonia, will promote the reduction of $GaCl_3$ to GaCl. If hydrogen reduction of $GaCl_3$ is not complete, the remaining $GaCl_3$ can react with ammonia via the following reaction:

$$GaCl_3 + NH_3 \rightarrow GaN + 3HCl\,. \qquad (27.56)$$

No low-temperature buffer layer was used in these experiments. Typical N_2 flow rate for $GaCl_3$ transport was 0.1 l/min. During the process, 1.0–2.0 l/min NH_3 and 1.0–2.0 l/min of N_2 were introduced into the reactor zone. The growth temperature was varied in the range 925–1050 °C. Ambient pressure inside the reactor was maintained at 1 atm for all the experiments.

Under typical growth conditions, reaction (27.56) is thermodynamically favorable. A thick deposition of $GaCl_3$ is always observed on the exhaust side of the reactor, which implies that unreacted GaCl combines with HCl and forms $GaCl_3$, which is a more stable form of gallium chloride at lower temperature (< 600 °C).

27.7.6 Characterization of GaN Films

Following the development of the growth technique described previously, the next most important element aspect is characterization of the materials grown. Characterization of a material can be defined as complete description of its physical and chemical properties. A thorough and extensive characterization of a epilayer is very difficult because this would require a variety of tests using a number of sophisticated instruments. It is obvious that there are no ideal crystals in reality and all crystals grown by any technique contain some defects, impurities, and inhomogeneities. Most physical properties are therefore sensitive to deviation from ideality, and generally the characterization of the grown crystals is necessary.

The assessment of crystalline perfection is essential to interpret the structure-dependent properties. Postgrowth analysis of a epitaxial layer provides information on the processes that occurred during growth. Feedback from the analysis can be used to modify the growth process in order to improve the quality of the layers. Moreover, characterization of the grown epilayers forms an integral part of the growth studies performed by the crystal grower. The demand for layers of the highest quality is increasing, and only systematic characterization enables the crystal grower to optimize growth parameters in order to obtain better results.

An epitaxial layer may be characterized by a description of its chemical composition, its structure, its defects, and the spatial distribution of these three features. It is crucial to know the degree of purity and perfection of epilayers in order to interpret structure-dependent properties and determine whether the material can be successfully employed in experiments or for device fabrication.

GaN, being a technologically important material, has elicited a large number of characterization studies [27.154–159]; further optimization of device performance requires that the fundamental mechanisms upon which these devices operate be better understood. Optimization of GaN growth to reduce defect density is of paramount importance for achieving high-quality GaN layers. The grown epilayers were subjected to the following characterization studies that provide a basic understanding of the GaN material properties:

1. Crystal structure analysis by x-ray powder diffraction and high-resolution x-ray diffraction (HRXRD) techniques
2. Molecular structural analysis by Raman scattering studies
3. Determination of the bandgap of the film by UV–vis absorption spectra
4. Identification of excitonic transitions by both room- and low-temperature photoluminescence (PL) spectra
5. Surface morphology by scanning electron microscope (SEM) studies
6. Electrical transport properties and Hall-effect measurements.

X-ray diffraction was used to determine the crystallinity and orientation of the GaN films. GaN films grown under different experimental conditions were characterized for crystalline quality and phase formation by using powder x-ray diffractometer with Cu K_α radiation; the recorded XRD patterns are shown in Fig. 27.24. It is clear from this figure that films grown at 950 °C and 990 °C exhibit a high degree of *c*-axis orientation nature, which indicating that basal planes of the GaN film and sapphire substrate are parallel to each other. However, the XRD pattern for the film grown at 925 °C shows polycrystalline nature. When the temperature is increased to 950 °C and 990 °C, the polycrystalline nature of the film is suppressed and the single-crystalline nature dominates. It is observed from the XRD results that decomposition of NH_3 is very low at those temperatures and hence the amount of atomic nitrogen for the reaction is also very low.

From XRD analysis, it has been observed that GaN layers are single-phase wurtzite structure. For GaN grown at 925 °C and 950 °C, XRD spectra exhibit a sharp peak of wurtzite GaN (0002) at 34.25°

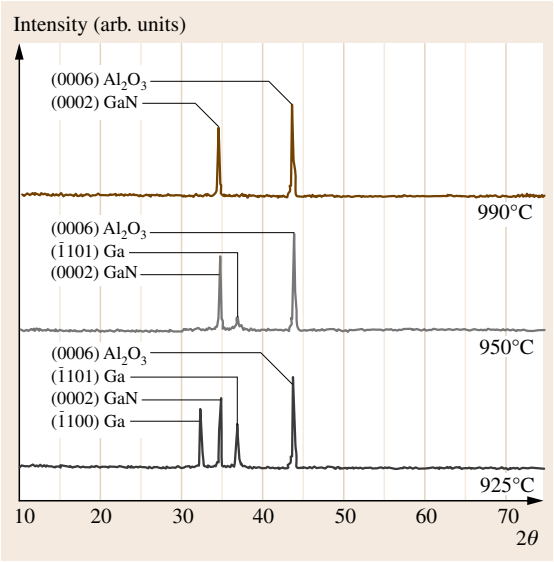


Fig. 27.24 XRD pattern of GaN grown on (0001) sapphire substrate at different growth temperatures

with blunt peaks for GaN ($\bar{1}$011) and GaN ($\bar{1}$100) at $2\theta = 36.60°$ and 32.24°, respectively. However the XRD spectrum for GaN grown at 990 °C shows diffraction only from the *c*-plane of GaN and the sapphire substrate. This indicates that preferentially oriented GaN layer is realized when the growth temperature is kept at 990 °C [27.152]. The lattice parameters have also been calculated from the XRD data as $a = 3.186$ Å and $c = 5.184$ Å, which are in very good agreement with reported values. The results of the other characterization studies are available in the literature [27.160–162]. Single-crystalline GaN nanowires on C-Al_2O_3 substrates have been synthesized by vapor-phase epitaxy process with the help of a Ni catalyst [27.163].

27.8 Conclusion

The growth of single crystals of II–VI and I–III–VI_2 compounds from vapor phase is a field of active research, with many researchers. The theoretical and thermodynamical background for the growth of these crystals have been given. The partial pressures of different components inside the growth ampoule during CVT growth of ZnSe single crystals were calculated using a thermodynamic model. Iodine was considered as the transporting agent. From the calculations, the optimum conditions for the growth of good-quality ZnSe single crystals were determined. The optimum temperature range was found to be 800–850 °C for an iodine concentration of 2 mg/cm^3. The undercooling and hence supersaturation ratios of S_2 and Se_2 were the factors determining the composition of ZnS_xSe_{1-x} single crystals grown in closed-tube vapor transport when ZnS and ZnSe were taken as source materials in 1 : 1 ratio. These values were calculated as a function of deposition

temperature and iodine concentrations. The partial pressures were calculated using a thermodynamic model. The critical radius and free energy of formation were calculated using the supersaturation ratios by classical nucleation theory. Undercooling was found to have an influence on the supersaturations of S_2 and Se_2, and hence on the composition of the resulting crystals. Conditions of larger undercooling were found to favor S-rich composition whereas smaller undercooling was found to favor ZnS_xSe_{1-x} composition near to that of the source. ZnSe:Mn nanocrystals have been synthesized by chemical vapor transport method using iodine as the transporting agent on a matrix of SiO_2 aerogel. The cubic structure has been confirmed based on powder XRD results. The size of the nanocrystals calculated using Debye–Scherrer formula was ≈ 60 nm. This result is supported by TEM and electron diffraction pattern. A well-resolved ESR spectrum containing six lines corresponding to the Mn^{2+} ion in the ZnSe nanocrystal lattice was obtained and attributed to the presence of a low concentration of Mn. The luminescence spectrum shows the band-edge emission at around 466 nm and Mn-related emission at 570 nm. The growth of I–III–VI_2 compounds has been described. Our recent results on vapor-phase epitaxial growth of GaN have been presented.

References

27.1 M.M. Faktor, I. Garrett, R. Heckingbottom: Diffusional limitations in gas phase growth of crystals, J. Cryst. Growth **9**, 3–11 (1971)

27.2 M.A. Contreras, B. Egaas, K. Ramanathan, J. Hiltner, A. Swartzlander, F. Hasoon: Progress toward 20% efficiency in Cu(In,Ga)Se_2 polycrystalline thin-film solar cells, Prog. Photovolt. **7**, 311–316 (1999)

27.3 S. Nakamura, T. Mukai, M. Senon: Candela-class high-brightness InGaN/AlGaN double-heterostructure blue-light-emitting diodes, Appl. Phys. Lett. **64**, 687–1689 (1994)

27.4 T. Lang, M. Odnoblyudov, V. Bougrov, S. Suihkonen, M. Sopanen, H. Lipsanen: Validating gallium nitride growth kinetics using a precursor delivery showerhead as novel chemical reactor, J. Cryst. Growth **292**, 26–32 (2006)

27.5 I. Akasaki, H. Amano, Y. Koide, K. Hiramatsu, N. Sawaki: Effects of ain buffer layer on crystallographic structure and on electrical and optical properties of GaN and $Ga_{1-x}Al_xN$ ($0 < x \leq 0.4$) films grown on sapphire substrate by MOVPE, J. Cryst. Growth **98**, 209–219 (1989)

27.6 M. Sumiya, N. Ogusu, Y. Yotsuda, M. Itoh, S. Fuke, S. Nakamura: Systematic analysis and control of low-temperature GaN buffer layers on sapphire substrates, J. Appl. Phys. **131**, 1311–1319 (2003)

27.7 G.H. Westphal: Convective transport in vapor growth systems, J. Cryst. Growth **65**, 105–123 (1983)

27.8 G. Attolini, C. Paorici, P. Ramasamy: Skeletal and hollow crystals of cadmium sulphide grown under time-increasing supersaturation, J. Cryst. Growth **78**, 181–184 (1986)

27.9 C. Paorici, L. Zanotti, G. Zuccalli: A temperature variation method for the growth of chalcopyrite crystals by iodine vapor transport, J. Cryst. Growth **43**, 705–710 (1978)

27.10 R.F. Lever, G. Mandel: Diffusion and the vapor transport of solids, J. Phys. Chem. Solids **23**, 599 (1962)

27.11 H. Hartmann: Vapor-phase epitaxy of II–VI compounds: A review, J. Cryst. Growth **31**, 323–332 (1975)

27.12 H. Schäfer: *Chemical Transport Reactions* (Academic, New York 1964)

27.13 R. Zuo, W. Wang: Theoretical study on chemical vapor transport of ZnS-I_2 system. Part II. Numerical modelling, J. Cryst. Growth **236**, 695–710 (2002)

27.14 R.F. Lever: Solid transport rate in the vapor-solvent growth system ZnS:I, J. Chem. Phys. **37**, 1078–1082 (1962)

27.15 G. Mandel: Diffusion and the vapor-transport of solids, J. Chem. Phys. **37**, 1177–1198 (1962)

27.16 G. Mandel: Vapor transport of solids by vapor phase reactions, J. Phys. Chem. Solids **23**, 587–598 (1962)

27.17 E. Lendvay: Growth of structurally pure cubic and hexagonal ZnS single crystals, J. Cryst. Growth **10**, 77–84 (1971)

27.18 R. Zuo, W. Wang: Theoretical study on chemical vapor transport of ZnS-I_2 system. Part I: Kinetic process and one-dimensional model, J. Cryst. Growth **236**, 687–694 (2002)

27.19 T. Arizumi, T. Nishinaga: Transport reaction in closed tube process, Jpn. J. Appl. Phys. **4**, 165–172 (1965)

27.20 T. Arizumi, T. Nishinaga: Thermodynamics of vapor growth of ZnSe-Ge-I_2 system in closed tube process, Jpn. J. Appl. Phys. **5**, 21–28 (1966)

27.21 H. Watanabe, T. Nishinaga, T. Arizumi: Vapor transport equations for III–V compound semiconductors, J. Cryst. Growth **17**, 183–188 (1972)

27.22 M.M. Faktor, I. Garrett: *Growth of Crystals from the Vapor* (Chapman and Hall, London 1974)

27.23 K. Noda, N. Mastsumura, S. Otsuka: Chemical-vapor-transport rate of ZnS in closed Tube, J. Electrochem. Soc. **137**, 1281–1294 (1990)

27.24 B.I. Noläng, M.W. Richardson: The transport flux function – A new method for predicting the rate of chemical transport in closed systems: I. Theory, J. Cryst. Growth **34**, 198–204 (1976)

27.25 B.I. Noläng, M.W. Richardson: The transport flux function – a new method for predicting the rate of chemical transport in flosed systems: II. A theoretical study of systems and experimental conditions for the chemical transport of SnO_2, J. Cryst. Growth **34**, 205–214 (1976)

27.26 M.W. Richardson, B.I. Noläng: Predicting the rate of chemical transport using the flux function method, J. Cryst. Growth **42**, 90–97 (1977)

27.27 K. Klosse: A new productivity function and stability criterion in chemical vapor transport processes, J. Solid State Chem. **15**, 105–116 (1975)

27.28 K. Klosse, P. Ullersma: Convection in a chemical vapor transport process, J. Cryst. Growth **18**, 167–174 (1973)

27.29 S.R. Brodkey, H.C. Hershey: *Transport Phenomena. A Unified Approach* (McGraw-Hill, New York 1988)

27.30 R. Nitsche, D.F. Sargent, P. Wild: Crystal growth of quaternary 1_2246_4 chalcogenides by iodine vapor transport, J. Cryst. Growth **1**, 52–53 (1967)

27.31 O. Senthil Kumar, S. Soundeswaran, R. Dhanasekaran: Thermodynamic calculations and growth of ZnSe single crystals by chemical vapor transport technique, Cryst. Growth Des. **2**, 585–589 (2002)

27.32 C. Paorici, C. Pelosi, G. Attolini, G. Zuccalli: Closed-tube chemical-transport mechanisms in the Cd:Te:H:Cl:N system, J. Cryst. Growth **28**, 358–364 (1975)

27.33 C. Paorici, G. Attolini, C. Pelosi, G. Zuccalli: Chemical transport mechanisms in the Cd:Te:H:I system, J. Cryst. Growth **21**, 227–234 (1974)

27.34 C. Paorici, L. Zecchina: The productivity function for multi-reaction chemical vapor transport in closed tubes, J. Cryst. Growth **97**, 267–272 (1989)

27.35 C. Paorici, L. Zecchina: Note on the productivity function in closed tube chemical vaport transport, J. Cryst. Growth **83**, 453–455 (1987)

27.36 C. Paorici, C. Pelosi: Kinetics of vapor growth in the system CdS:I_2, J. Cryst. Growth **35**, 65–72 (1976)

27.37 R.C. Reid, J.M. Prausnitz, T.K. Sherwood: *The Properties of Gases and Liquids*, 3rd edn. (McGraw-Hill, New York 1977)

27.38 K. Böttcher, H. Hartmann, D. Siche: Computational study on the CVT of the ZnSe-I_2 material system, J. Cryst. Growth **224**, 195–203 (2001)

27.39 B.I. Noläng, M.W. Richardson: The transport flux function – A new method for predicting the rate of chemical transport in closed systems: I. Theory, J. Cryst. Growth **34**, 198–204 (1976)

27.40 S. Fiechter, K. Eckert: Crystal growth of HfS_2 by chemical vapor transport with halogen (Cl, Br, I), J. Cryst. Growth **88**, 435–441 (1988)

27.41 O. Senthil Kumar, S. Soundeswaran, D. Kabiraj, D.K. Avasthi, R. Dhanasekaran: Effect of heat treatment and Si ion irradiation on ZnS_xSe_{1-x} single crystals grown by CVT method, J. Cryst. Growth **275**, e567–e570 (2005)

27.42 H. Ogawa, M. Nishio: Epitaxial growth and chemical vapor transport of ZnTe by closed-tube method, J. Cryst. Growth **52**, 263–268 (1981)

27.43 J.O. Hirschfelder, C.F. Curtiss, R.B. Bird: *Molecular Theory of Gases and Liquids* (Wiley, New York 1954)

27.44 F. Rosenberger, M.C. Delong, J.M. Olson: Heat transfer and temperature oscillations in chemical vapor transport crystal growth I, J. Cryst. Growth **19**, 317–328 (1973)

27.45 H. Watanabe, T. Nisi-iinaga, T. Arezume: Vapor transport equations for III–V compound semiconductors, J. Cryst. Growth **17**, 183–188 (1972)

27.46 M. Nishlo, H. Ogawa: Chemical vapor transport in the ZnTe-HCl closed-tube system and its thermodynamic analysis, J. Cryst. Growth **78**, 218–226 (1986)

27.47 M. Lenz, R. Gruehn: Developments in measuring and calculating chemical vapor transport phenomena demonstrated on Cr, Mo, W, and their compounds, Chem. Rev. **97**, 2967–2994 (1997)

27.48 Y.-G. Sha, C.-H. Su, F.R. Szofrari: Thermodynamic analysis and mass flux of the HgZnTe-HgI_2 chemical vapor transport system, J. Cryst. Growth **131**, 574–588 (1993)

27.49 D.W. Mackowski, V.R. Rao, R.W. Knight: Effect of solid phase heat transfer and wall deposition on crystal growth in physical vapor transport ampoules, J. Cryst. Growth **165**, 323–334 (1996)

27.50 A. Nadarajahk, F. Rosenberger, D. Alexander, J. Iwan: Effects of buoyancy-driven flow and thermal boundary conditions on physical vapor transport, J. Cryst. Growth **118**, 49–59 (1992)

27.51 M. Shiloh, J. Gutman: Growth of ZnO single crystals by chemical vapor transport, J. Cryst. Growth **11**, 105–109 (1971)

27.52 H. Hartmann, R. Mach, B. Selle: *Current Topics in Material Science*, Vol. 9, ed. by E. Kaldis (North-Holland, Amsterdam 1982)

27.53 K. Böttcher, H. Hartmann: Zinc selenide single crystal growth by chemical transport reactions, J. Cryst. Growth **146**, 53–58 (1995)

27.54 K. Mochizuki: Vapor growth and stoichiometry control of zinc sulfo-selenide, J. Cryst. Growth **58**, 87–94 (1982)

27.55 O. Senthil Kumar: Growth of pure and doped single crystals and nanocrystals of ZnSe and ZnS_xSe_{1-x} semiconductors by chemical vapor transport and their characterization, Ph.D. Thesis (Anna University, Chennai 2005)

27.56 M.J. Tafreshi: Growth of II–VI. I–III–VI_2 and $CdIn_2S_4$ single crystals by CVT method and their characterizations, Ph.D. Thesis (Anna University, Chennai 1996)

27.57 M.J. Tafreshi, K. Balakrishnan, R. Dhanasekaran: Growth and characterization of pentenary $Cu_{0.5}Ag_{0.5}InSSe$ crystals grown by chemical vapor transport technique, Mater. Res. Bull. **30**, 1371–1377 (1995)

27.58 M.J. Tafreshi, K. Balakrishnan, R. Dhanasekaran: Micromorphological studies on the ZnSe single crystals grown by chemical vapor transport technique, J. Mater. Sci. **32**, 3517–3521 (1997)

27.59 W. Palosz: Vapor transport of ZnO in closed ampoules, J. Cryst. Growth **286**, 42–49 (2006)

27.60 D.W. Greenwell, B.L. Markham, F. Rosenberger: Numerical modeling of diffusive physical vapor transport in cylindrical ampoules, J. Cryst. Growth **51**, 413–425 (1981)

27.61 J.N. Butler, R.S. Brokaw: Thermal conductivity of gas mixtures in chemical equilibrium, J. Chem. Phys. **26**, 1636–1645 (1957)

27.62 G.T. Kim, J.T. Lin, O.C. Jones, M.E. Glicksman, W.M.B. Duval, N.B. Singh: Effects of convection during the physical vapor transport process: application of laser Doppler velocimetry, J. Cryst. Growth **165**, 429–437 (1996)

27.63 B.M. Bulakh, G.S. Pekar: The CdS crystal synthesis from vapors of the component elements, J. Cryst. Growth **8**, 99–103 (1971)

27.64 J.M. Ntep, S. Said Hassani, A. Lusson, A. Tromson-Carli, D. Ballutaud, G. Didier, R. Triboulet: ZnO growth by chemical vapor transport, J. Cryst. Growth **207**, 30–34 (1999)

27.65 G.R. Patzke, S. Locmelis, R. Wartchow, M. Binnewies: Chemical transport phenomena in the ZnO-Ga_2O_3 system, J. Cryst. Growth **203**, 141–148 (1999)

27.66 H. Wiedemeier, W. Palosz: Physical vapor transport of cadmium telluride in closed ampoules, J. Cryst. Growth **96**, 933–945 (1989)

27.67 T. Yamauchi, Y. Takahara, M. Naitoh, N. Narita: Growth mechanism of ZnSe single crystal by chemical vapor transport method, Physica B: Condens. Matter **376/377**, 778–781 (2006)

27.68 C.S. Fang, Q.T. Gu, J.Q. Wei, Q.W. Pan, W. Shi, J.Y. Wang: Growth of ZnSe single crystals, J. Cryst. Growth **209**, 542–546 (2000)

27.69 W.N. Holton, R.K. Watts, R.D. Stinedurf: Synthesis and melt growth of doped ZnSe, J. Cryst. Growth **6**, 97–100 (1969)

27.70 R. Nishizawa, K. Itoh, Y. Okuno, F. Sakurai: Blue light emission from ZnSe p-n junctions, J. Appl. Phys. **57**, 2210–2214 (1985)

27.71 N. Krasnov, Y. Purtov, F. Vaksman, V.V. Serdyuk: ZnSe blue-light-emitting diode, J. Cryst. Growth **125**, 373–374 (1995)

27.72 R. Nitsche: The growth of single crystals of binary and ternary chalcogenides by chemical transport reactions, J. Phys. Chem. Solids **17**, 163–165 (1960)

27.73 P. Rudolph, K. Umetsu, H.J. Koh, T. Fukuda: Growth of twin reduced ZnSe bulk crystals from the melt, J. Cryst. Growth **143**, 359–361 (1994)

27.74 H. Unuma, M. Higuchi, Y. Yamakawa, K. Kodaira, Y. Okano, K. Hoshikawa, T. Fukuda, T. Koyama: Liquid encapsulated flux growth of ZnSe single crystals from Se solvent, Jpn. J. Appl. Phys. **31**, L383–L384 (1992)

27.75 H.H. Woodbury, R.B. Hall: Diffusion of the chalcogens in the II–VI compounds, Phys. Rev. **157**, 641–645 (1967)

27.76 M. Shone, B. Greenberg, M. Kaczenski: Vertical zone growth and characterization of undoped and Na, P and Mn doped ZnSe, J. Cryst. Growth **86**, 132–137 (1988)

27.77 R.N. Bhargava: Materials growth and its impact on devices from wide band gap II–VI compounds, J. Cryst. Growth **86**, 873–879 (1990)

27.78 E. Kaldis: Crystal growth and growth rates of CdS by sublimation and chemical transport, J. Phys. Chem. Solids **26**, 1701–1732 (1965)

27.79 S. Fujita, H. Mimoto, H. Takebe, T. Noguchi: Zno-based thin films synthesized by atmospheric pressure mist chemical vapor deposition, J. Cryst. Growth **47**, 326–334 (1979)

27.80 E. Kaldis: The chemistry of imperfect crystals, preparation, purification, crystal growth and phase theory by F.A. Kruger, J. Cryst. Growth **24**, 24–39 (1974)

27.81 K. Böttcher, H. Hartmann: Zinc selenide single crystal growth by chemical transport reactions, J. Cryst. Growth **146**, 53–58 (1995)

27.82 A.A. Simanovskii, N.N. Sheftal, E.I. Givargizov: Effect of crystallization condition on the morphology of ZnSe crystals, Growth Cryst. **9**, 225–229 (1975)

27.83 I. Nakada, E. Bauser: Origin of multiple steps in vapor growth of $NbSe_4I_{0.33}$, J. Cryst. Growth **96**, 243–257 (1989)

27.84 A.A. Simanovskii, N.N. Sheftal, E. Givargizov: Production of ZnSe single crystals via transport reaction, Growth Cryst. **7**, 224–229 (1969)

27.85 M.H.J. Hottenhuis, C.B. Lucasius: The influence of impurities on crystal growth: In situ observation of the (010) face of potassium hydrogen phthalate, J. Cryst. Growth **78**, 379–388 (1986)

27.86 Z. Sobiesierski, I.M. Dharmadasa, R.H. Williams: Photoluminescence as a probe of semiconductor surfaces: CdTe and CdS, J. Cryst. Growth **101**, 599–602 (1990)

27.87 W.E. Metcalf, R.H. Fahrig: High-pressure, high-temperature growth of cadmium sulfide crystals, J. Electrochem. Soc. **105**, 719–723 (1958)

27.88 M. Rubenstein: Solution growth of some II–VI compounds using tin as a solvent, J. Cryst. Growth **3**, 309–312 (1968)

27.89 C. Paorici: Iodine-doped hollow CdS crystals, J. Cryst. Growth **5**, 315–316 (1969)
27.90 E. Kaldis: Crystal growth and growth rates of CdS by sublimation and chemical transport, J. Cryst. Growth **5**, 376–390 (1969)
27.91 K. Matsumoto, K. Takagi, S. Kaneko: Kinetics of the cubic to hexagonal transformation of cadmium sulfide, J. Electrochem. Soc. **62**, 389–393 (1983)
27.92 G. Attolini, C. Paorici, L. Zanoti: Growth of cadmium sulphide single crystals by vapor-phase hydrogen transport, J. Cryst. Growth **56**, 254–258 (1982)
27.93 G. Attolini, C. Paorici, L. Zecchina: Productivity function for multireactional CVT and its application to iodine transport of cadmium sulphide, J. Cryst. Growth **99**, 731–736 (1990)
27.94 M.J. Tafreshi, K. Balakrishnan, R. Dhanasekaran: Growth, electrical conductivity and microindentation studies of $CuInS_2$ single crystals, J. Mater. Sci. Mater. Electron. **7**, 243–245 (1996)
27.95 S. Itoh, K. Nakano, A. Ishibashi: Raman studies of phosphorus-doped ZnSe, J. Cryst. Growth **214/215**, 1029–1034 (2000)
27.96 E. Chimczak, J.W. Allen: Energy transfer in the electroluminescence of ZnS:Mn and ZnSe:Mn driven by short voltage pulses, J. Phys. D: Appl. Phys. **18**, 951–957 (1985)
27.97 G. Jones, J. Woods: The luminescence of manganese-doped zinc selenide, J. Phys. D: Appl. Phys. **6**, 1640–1651 (1973)
27.98 C. Jin, B. Zhang, Z. Ling, J. Wang, X. Hou, Y. Segawa, X. Wang: Growth and optical characterization of diluted magnetic semiconductor $Zn_{1-x}Mn_xSe$/ZnSe strained-layer superlattices, J. Appl. Phys. **81**, 5148–5153 (1997)
27.99 J.K. Furdyna, N. Samranth: Magnetic properties of diluted magnetic semiconductors: A review, J. Appl. Phys. **61**, 3526–3593 (1987)
27.100 J.F. Suyver, J.J. Kelly, A. Meijerink: Temperature-induced line broadening, line narrowing and line shift in the luminescence of nanocrystalline ZnS:Mn^{2+}, J. Lumin. **104**, 187–196 (2003)
27.101 H. Heulings IV, X. Huang, J. Li, T. Yuen, C.L. Lin: Mn-substituted inorganic-organic hybrid materials based on ZnSe: Nanostructures that may lead to magnetic semiconductors with a strong quantum confinement effect, Nano Lett. **1**, 521–525 (2001)
27.102 C. Wang, W.X. Zhang, X.F. Qian, X.M. Zhang, Y. Xie, Y.T. Qian: An aqueous approach to ZnSe and CdSe semiconductor nanocrystals, Mater. Chem. Phys. **60**, 99–102 (1999)
27.103 C. De Mello Donega, A.A. Bol, A. Meijerink: Time-resolved luminescence of ZnS:Mn^{2+} nanocrystals, J. Lumin. **96**, 87–93 (2002)
27.104 D. Sarigiannis, J.D. Peck, G. Kioseoglou, A. Petrou, T.J. Mountziaris: Characterization of vapor-phase-grown ZnSe nanoparticles, Appl. Phys. Lett. **80**, 4024–4027 (2002)
27.105 X.T. Zhang, K.M. Ip, Z. Liu, Y.P. Leung, Q. Li, S.K. Hark: Structure and photoluminescence of ZnSe nanoribbons grown by metal organic chemical vapor deposition, Appl. Phys. Lett. **84**, 2641–2647 (2004)
27.106 S.K. Bera, S. Choudhuri, A.K. Pal: Electron transport properties of CdTe nanocrystals in SiO_2/CdTe/SiO_2 thin film structures, Thin Solid Films **415**, 68–77 (2002)
27.107 A.A. Lipovskii, E.V. Kolobkova, V.D. Petrikov: Formation of II–VI nanocrystals in a novel phosphate glass, J. Cryst. Growth **184/185**, 365–369 (1998)
27.108 P. Yang, M.K. Lu, C.F. Song, G.J. Zhou, Z.P. Ai, D. Xu, D.R. Yuan, X.F. Cheng: Strong visible-light emission of ZnS nanocrystals embedded in sol–gel silica xerogel, Mater. Sci. Eng. B **97**, 149–153 (2003)
27.109 P.A. Gonzalez Beerman, B.R. McGarvey, S. Muralidharan, R.C.W. Sung: EPR spectra of Mn^{2+}-doped ZnS quantum dots, Chem. Mater. **16**, 915–918 (2004)
27.110 N. Taghavinia, T. Yao: ZnS nanocrystals embedded in SiO_2 matrix, Physica E **21**, 96–102 (2004)
27.111 K. Manzoor, S.R. Vadera, N. Kumar, T.R.N. Kutty: Synthesis and photoluminescent properties of ZnS nanocrystals doped with copper and halogen, Mater. Chem. Phys. **82**, 718–725 (2003)
27.112 C. Liu, J. Liu, W. Xu: The g-factor-shift in ZnS:Mn^{2+} nanocrystals/pyrex glasses composites, Mater. Sci. Eng. B **75**, 78–81 (2000)
27.113 K. Kawano, R. Nakata, M. Sumita: Electron spin resonance study of laser-annealed (Zn,Mn)0 ceramics, Appl. Phys. Lett. **58**, 1742–1745 (1991)
27.114 M. Tanaka: Do triboluminescence spectra really show a spectral shift relative to photoluminescence spectra?, J. Lumin. **100**, 115–126 (2002)
27.115 V.J. Leppert, S. Mahamuni, N.R. Kumbhojkar, S.H. Risbud: Structural and optical characteristics of ZnSe nanocrystals synthesized in the presence of a polymer capping agent, Mater. Sci. Eng. B **52**, 89–92 (1998)
27.116 R. Nitsche, H.U. Bölsterli, M. Lichtensteiger: Crystal growth by chemical transport reactions I. Binary, ternary, and mixed-crystal chalcogenides, J. Phys. Chem. Solids **21**, 199–205 (1961)
27.117 W.N. Honeyman, K.H. Wilkinson: Growth and properties of single crystals of group I-III-VI_2 ternary semiconductors, J. Phys. D: Appl. Phys. **4**, 1182–1185 (1971)
27.118 I. Aksenov, K. Sato: Visible photoluminescence of Zn-doped $CuAlS_2$, Appl. Phys. Lett. **61**, 1063–1066 (1992)
27.119 O. Madelung, V. Rössler, M. Schulz: Optical properties of I-III-VI_2 compounds, Phys. Status Solidi **115**, K113–K118 (1989)
27.120 S. Shirakata, I. Aksenov, K. Sato, S. Isomura: Photoluminescence studies in $CuAlS_2$ crystals, Jpn. J. Appl. Phys **31**, L1071–L1074 (1992)

27.121 I. Aksenov, T. Yasuda, Y. Seawa, K. Sato: Violet photoluminescence in Zn-doped $CuAlS_2$, J. Appl. Phys **74**, 2106–2110 (1993)
27.122 I. Aksenov, T. Yasuda, T. Kai, N. Nishikawa, T. Ohgoh, K. Sato: Visible photoluminescence in undoped and Zn-doped $CuAlS_2$, Jpn. J. Appl. Phys **32**, 1068–1072 (1993)
27.123 N. Kuroishi, K. Mochizuki, K. Kimoto: Surface oxidation of CVT-grown $CuAlSe_2$, Mater. Lett. **57**, 1949–1954 (2003)
27.124 S. Chichibu, M. Shishikura, J. Ino, S. Matsumoto: Electrical and optical properties of $CuAlSe_2$ grown by iodine chemical vapor transport, J. Appl. Phys **70**, 1648–1654 (1991)
27.125 M.-S. Jin, C.-S. Yoon, H.-G. Kim, W.-T. Kim: Growth and characterization of $CuAlSe_2$ single crystals, J. Korean Phys. Soc. **26**, 628 (1993)
27.126 P. Prabukanthan, R. Dhanasekaran: Growth of $CuInTe_2$ single crystals by iodine transport and their characterization, Mater. Res. Bull. **43**, 1996–2004 (2008)
27.127 E. Gombia, F. Leccabue, C. Pelosi, D. Seuret: Vapor growth, thermodynamical study and characterization of $CuInTe_2$ and $CuGaTe_2$ single crystals, J. Cryst. Growth **65**, 391–396 (1983)
27.128 P.W. Yu, D.L. Downing, Y.S. Park: Electrical properties of $CuGaS_2$ single crystals, J. Appl. Phys. **45**, 5283 (1974)
27.129 S. Shirakata, K. Saiki, S. Isomura: Excitonic photoluminescence in $CuGaS_2$ crystals, J. Appl. Phys. **68**, 291–297 (1990)
27.130 P. Prabukanthan, R. Dhanasekaran: Growth of $CuGaS_2$ single crystal by chemical vapor transport and characterization, Cryst. Growth Des. **7**, 618–623 (2007)
27.131 S. Chichibu, S. Shirakata, A. Ogawa, R. Sudo, M. Uchida, Y. Harada, T. Wakiyama, M. Shishikura, S. Matsumoto, S. Isomura: Growth of $Cu(Al_xGa_{1-x})SSe$ pentenary alloy crystals by iodine chemical vapor transport method, J. Cryst. Growth **140**, 388–397 (1994)
27.132 K. Sugiyama, K. Mori, H. Miyake: Growth of epitaxy layer of $CuAlS_2$ on $CuGaS_2$ and characterization, J. Cryst. Growth **113**, 390–395 (1991)
27.133 P. Prabukanthan, R. Dhanasekaran: Influence of Mn doping on $CuGaS_2$ single crystals grown by CVT method and their characterization, J. Phys. D: Appl. Phys. **41**, 115102 (2008)
27.134 S. Tanaka, S. Kawami, H. Kobayashi, H. Sasakura: Luminescence in $CuGaS_{2-2x}S_{e2x}$ mixed crystals grown by chemical vapor transport, J. Phys. Chem. Solids **38**, 680–681 (1977)
27.135 K. Sato, K. Tanaka, K. Ishii, S. Matsuda: Crystal growth and photoluminescence studies in Fe-doped single crystals of $CuAl_{1-x}Ga_xS_2$, J. Cryst. Growth **99**, 772–775 (1990)
27.136 P. Prabukanthan, R. Dhanasekaran: Stoichiometric single crystal growth of $AgGaS_2$ by iodine transport method and characterization, Cryst. Res. Technol. **43**, 1292–1296 (2008)
27.137 Y. Noda, T. Kurasawa, N. Sugai, Y. Furukawa, K. Masumoto: Growth of $AgGaS_2$ single crystals by chemical transport reaction, J. Cryst. Growth **99**, 757–761 (1990)
27.138 K.M. Nigge, F.P. Baumgartner, E. Bucher: CVT-growth of $AgGaSe_2$ single crystals: Electrical and photoluminescence properties, Sol. Energy Mater. Sol. Cells **43**, 335–343 (1996)
27.139 R. Fornari: Vapor phase epitaxial growth and properties of III-nitride materials, Proc. Int. School Cryst. Growth Technol. Important Electron. Mater., ed. by K. Byrappa (2003) pp. 367–390
27.140 H.P. Maruska, J. Tietjen: The preparation and properties of vaporu deposited single crystalline GaN, J. Appl. Phys. Lett. **15**, 327–329 (1969)
27.141 M. Ilemgems: Vapor epitaxy of gallium nitride, J. Cryst. Growth **13/14**, 360–364 (1972)
27.142 W. Seifert, G. Fitzl, E. Butter: Study on the growth rate in VPE of GaN, J. Cryst. Growth **52**, 257–262 (1981)
27.143 R.J. Molnar, W. Gotz, L.T. Romano, N.M. Johnson: Growth of gallium nitride by hydride vapor-phase epitaxy, J. Cryst. Growth **178**, 147–156 (1997)
27.144 H. Lee, J.S. Harris: Observation of superstructure in high-quality pseudomorphic films of NiAl grown on GaAs, J. Cryst. Growth **169**, 689–693 (1996)
27.145 F. Dwikusuma, J. Mayer, T.F. Kuech: Nucleation and initial growth kinetics of GaN on sapphire substrate by hydride vapor-phase epitaxy, J. Cryst. Growth **258**, 65–74 (2003)
27.146 A. Shintani, S. Minagawa: Kinetics of the epitaxial growth of GaN using Ga, HCl and NH_3, J. Cryst. Growth **22**, 1–5 (1974)
27.147 G. Jacob, M. Boulou, M. Furtado: Effect of growth parameters on the properties of GaN:Zn epilayers, J. Cryst. Growth **42**, 136–143 (1977)
27.148 R. Fornari, M. Bosi, N. Armani, G. Attolini, C. Ferrari, C. Pelosi, G. Salviati: Hydride vapor phase epitaxy growth and characterisation of GaN layers, Mater. Sci. Eng. B **79**, 159–164 (2001)
27.149 X. Xu, R.P. Vaudo, C. Loria, A. Salant, G.R. Brandes, J. Chaudhuri: Growth and characterization of low defect GaN by hydride vapor-phase epitaxy, J. Cryst. Growth **246**, 223–229 (2002)
27.150 D.W. Shaw: *Mechanisms in Vapor Phase Epitaxy in Crystal Growth*, ed. by C.H.L. Goodman (Plenum Press, New York 1974) p. 25
27.151 G.B. Stringfellow: Fundamental aspects of vapor growth and epitaxy, J. Cryst. Growth **115**, 1–11 (1991)
27.152 G.B. Stringfellow: Fundamentals of thin film growth, J. Cryst. Growth **137**, 212–223 (1994)
27.153 E. Varadarajan, J. Kumar, R. Dhanasekaran: Fabrication of vapor-phase epitaxy system for the growth of gallium nitride, Proc. 6th Int. Conf. Optoelectron. Photonics **1**, 236–237 (2002)

27.154 I. Akasaki, H. Amano: Widegap column-III nitride semiconductors for UV/blue light emitting devices, J. Electrochem. Soc. **141**, 2266–2269 (1994)
27.155 S. Nakamura, M. Senoh, S. Nagahama, N. Iwasa, Y. Yamada, T. Matsushita, Y. Sugimoto, H. Kiyoku: Large conductance anisotropy in a novel two-dimensional electron system grown on vicinal (111) B GaAs with multiatomic steps, Appl. Phys. Lett. **69**, 3034–3041 (1996)
27.156 I. Akasaki, S. Sota, H. Sakai, T. Tanaka, M. Koike, H. Amano: Shortest wavelength semiconductor laser diode, Electron. Lett. **32**, 1105–1106 (1996)
27.157 S.J. Pearton, J.C. Zolper, R.J. Shul, F. Ren: GaN: Processing, defects, and devices, J. Appl. Phys. **86**, 1–6 (1999)
27.158 H. Morkoc: Comprehensive characterization of hydride VPE grown GaN layers and templates, Mater. Sci. Eng. R **33**, 135–207 (2001)
27.159 R. Fornari, M. Bosi, D. Bersani, G. Attolini, P.P. Lottici, C. Pelosi: Characterization of HVPE GaN layers by atomic force microscopy and Raman spectroscopy, Semicond. Sci. Technol. **16**, 776–782 (2001)
27.160 E. Varadarajan, P. Puviarasu, J. Kumar, R. Dhanasekaran: On the chloride vapor-phase epitaxy growth of GaN and its characterization, J. Cryst. Growth **260**, 43–49 (2004)
27.161 E. Varadarajan, J. Kumar, R. Dhanasekaran: Growth of GaN films by chloride vapor pahse epitaxy, J. Cryst. Growth **268**, 475–477 (2004)
27.162 E. Varadarajan, R. Dhanasekaran, D.K. Avasthi, J. Kumar: Structural, optical and electrical properties of high energy irradiated Cl-VPE grown gallium nitride, Mater. Sci. Eng. B **129**, 121–125 (2006)
27.163 T.I. Shin, H.J. Lee, W.Y. Song, H. Kim, S.-W. Kim, D.H. Yoon: High quality GaN nanowires synthesized from Ga_2O_3 with graphite powder using VPE method, Colloids. Surf. A **313/314**, 52–55 (2008)

Part E Epitaxial

Part E Epitaxial Growth and Thin Films

28 Epitaxial Growth of Silicon Carbide by Chemical Vapor Deposition
Ishwara B. Bhat, Troy, USA

29 Liquid-Phase Electroepitaxy of Semiconductors
Sadik Dost, Victoria, Canada

30 Epitaxial Lateral Overgrowth of Semiconductors
Zbigniew R. Zytkiewicz, Warszawa, Poland

31 Liquid-Phase Epitaxy of Advanced Materials
Christine F. Klemenz Rivenbark, Titusville, USA

32 Molecular-Beam Epitaxial Growth of HgCdTe
James W. Garland, Bolingbrook, USA
Sivalingam Sivananthan, Chicago, USA

33 Metalorganic Vapor-Phase Epitaxy of Diluted Nitrides and Arsenide Quantum Dots
Udo W. Pohl, Berlin, Germany

34 Formation of SiGe Heterostructures and Their Properties
Yasuhiro Shiraki, Tokyo, Japan
Akira Sakai, Osaka, Japan

35 Plasma Energetics in Pulsed Laser and Pulsed Electron Deposition
Mikhail D. Strikovski, Beltsville, USA
Jeonggoo Kim, Beltsville, USA
Solomon H. Kolagani, Beltsville, USA

28. Epitaxial Growth of Silicon Carbide by Chemical Vapor Deposition

Ishwara B. Bhat

The properties of silicon carbide materials are first reviewed, with special emphasis on properties related to power device applications. Epitaxial growth methods for SiC are then discussed with emphasis on recent results for epitaxial growth by the hot-wall chemical vapor deposition method. The growth mechanism for maintaining the polytype, namely *step-controlled epitaxy*, is discussed. Also described is the selective epitaxial growth carried out on SiC at the author's laboratory, including some unpublished work.

28.1 **Polytypes of Silicon Carbide** 941
28.2 **Defects in SiC** 942
28.2.1 Micropipes 942
28.2.2 Screw Dislocations 942
28.2.3 Growth Pits and Triangular Inclusions 943
28.3 **Epitaxial Growth of Silicon Carbide** 944
28.3.1 Substrates for Silicon Carbide Growth 944
28.3.2 How to Control the Polytypes in SiC Homoepitaxy 945
28.3.3 SiC Epitaxial Growth Techniques ... 946
28.3.4 Chemical Vapor Deposition 946
28.4 **Epitaxial Growth on Patterned Substrates** 952
28.4.1 Selective Epitaxial Growth 953
28.4.2 Selective Epitaxial Growth of 4H-SiC Using TaC Mask 954
28.4.3 Orientation Dependence of SiC Selective Growth 956
28.4.4 Effects of Mask-to-Window Ratio ($M:W$) on SiC Selective Growth 957
28.4.5 Effects of C/Si Ratio on SiC Selective Growth 959
28.4.6 Mechanism of Selective Etching and Effect of Atomic Hydrogen 960
28.4.7 Fabrication of 4H-SiC p–n Junction Diodes Using Selective Growth 960
28.5 **Conclusions** 961
References 961

Advanced Si technology has brought about the very large-scale integrated circuits (VLSI) that are available today, and still further development of Si VLSI technology is expected. However, Si is approaching its performance limit due to intrinsic material properties, especially in applications related to high-power, high-temperature, and high-frequency devices. Thus, the development of new materials and technologies useful in this area is crucial.

SiC is a an extremely hard and inert IV–IV compound material having a lot of attractive features, in particular electrical properties which are suitable for advanced electronic devices that cannot be achieved using Si. An appreciation of the potential of SiC for electronics can be gained by examining Table 28.1, which compares the relevant material properties of SiC with Si and GaAs. As can be seen, SiC has large bandgaps (2.4–3.3 eV) [28.1–4], high breakdown fields ($\approx 3\times10^6$ V/cm) [28.5], high saturation electron velocities (2.7×10^6 cm/s) [28.6, 7], and high thermal conductivity (3.2–4.9 W/(cm K)) [28.8]. Owing to these excellent electrical and physical properties, SiC has been regarded as able to function well under high-temperature, high-power, and high-radiation conditions at which conventional semiconductors cannot perform adequately. This ability is expected to enable significant improvements for a wide variety of applications and systems. These applications range from greatly improved high-voltage switching for energy savings in public electric power distribution and electric vehicles, to more powerful microwave electronics for radar and communications, to sensors and controls for cleaner-

Table 28.1 Physical properties of 3C-, 6H-, 4H-SiC, Si, and GaAs at 300 K [28.1]

Properties	3C-SiC	6H-SiC	4H-SiC	Si	GaAs
Crystal structure	ZB	Hex.	Hex.	Dia.	ZB
Lattice constant (Å)	4.36	$a = 3.09$ $c = 15.12$	$a = 3.09$ $c = 10.08$	5.43	5.65
Band structure	Indirect	Indirect	Indirect	Indirect	Direct
Bandgap (eV)	2.4	3.0	3.3	1.11	1.43
Electron mobility ($cm^2/(V\,s)$)	900	350[a] 50[b]	720[a] 650[b]	1400	8500
Breakdown field 10^6 (V/cm)	1.2	2.0	2.4	0.3	0.4
Thermal conductivity (W/(cm K))	3.2	4.9	3.7	1.5	0.5
Saturation drift velocity $\times 10^7$ (cm/s)	2.0	2.0	2.0	1	2
Dielectric constant	9.6	9.7	10	11.8	12.8

[a] mobility along *a*-axis, [b] mobility along *c*-axis

burning more fuel-efficient jet aircraft and automobile engines.

Theoretical simulations have indicated that SiC power metal-oxide semiconductor field-effect transistors (MOSFETs) and diode rectifiers would operate over higher voltage and temperature ranges, have superior switching characteristics, and yet have die sizes nearly 80% smaller than correspondingly rated silicon-based devices [28.9]. Hence, realization of practical SiC power devices will greatly impact the power electronics field.

The development of SiC for electronic applications has been a subject of study for more than 40 years. During the early years, a significant amount of fundamental research was performed, but the development of commercially viable SiC-based devices was limited by the low quality of bulk materials and inadequate epitaxial process. During the late 1980s, significant improvements in bulk and epitaxial process enabled commercial availability of device-quality wafers from Cree Research, Inc. Together, these factors have enabled the fabrication of higher quality device structures and have generated increased research activities in SiC electronic devices. A large number of devices, such as high-voltage Schottky rectifiers [28.10, 11], power metal-oxide semiconductor field-effect transistors [28.9], microwave and millimeter-wave devices [28.12], and high-temperature, radiation-resistant junction FETs (JFETs) [28.13], have been fabricated. However, SiC devices with quality sufficient for large-scale industrial applications were not available until recently. This is primarily due to the fact that the crystal growth and device fabrication technologies for SiC were not sufficiently developed to the degree required for reliable incorporation into electronic systems. Recent commercial availability of SiC Schottky diodes (up to 1200 V and 20 A) from Infineon Technology AG and Cree, Inc., should accelerate the introduction of SiC in commercial systems [28.14]. However, bipolar and power MOSFETs remain commercially elusive.

As for SiC epitaxial growth, homoepitaxial growth of SiC epitaxial layers on SiC substrates has been achieved by so-called *step-controlled growth* [28.15]. The quality of the epilayer and controllability of growth are improving with the improvement of the substrate quality and growth technology. However, abundant defects, including micropipes, screw dislocations, growth pits, step bunching, and 3C inclusions can still be found even in today's commercial wafers. Among these, growth pits, step bunching, and 3C inclusions can be caused by an unoptimized growth process while others are mainly due to defects propagated from the substrate. It is believed that these structural and surface morphological features are the major cause of poor device yield and premature device failure. Thus, these issues have to be addressed in order to advance the widespread commercial introduction of SiC-based systems, especially for high-power applications.

In this chapter, some basic properties of SiC that are relevant for good epitaxial growth are described. Recent progress on thick epitaxial growth as well as on selective growth of SiC will also be described.

28.1 Polytypes of Silicon Carbide

In this section, a concise review of the physical and electrical properties of SiC are presented. This is by no means complete, and further information can be found in the references of this chapter.

SiC has a large number of crystal structures (more than 200) [28.16], which are called polytypes. Considering close-packed structure, each layer of atoms along the *c*-axis can occupy three different positions, denoted by A, B, and C (Fig. 28.1). For SiC, a Si–C pair should be considered as one unit for atoms in close-packed structure. Variation of occupation sites along the *c*-axis brings about different crystal structures. They are usually represented by Ramsdell notation, which is denoted by the number of layers in the unit cell and a crystal system (C for cubic, H for hexagonal, R for rhombohedral). From ABCABCABC... stacking, we generate the 3C-SiC lattice, and from ABABAB... stacking, we generate the 2H-SiC lattice. Depending on the stacking order, the bonding between Si and C atoms in adjacent bilayer planes is of either zincblende (cubic) or wurtzite (hexagonal) nature. Zincblende bonds are rotated 60° with respect to nearest neighbors while hexagonal bonds are mirror images (Fig. 28.2). Each type of bond provides a slightly altered atomic environment, making some lattice sites inequivalent in polytypes. This also results in different ionization energy for dopants when substituted at these two different sites. Bonds in 3C-SiC are all cubic whereas bonds in 2H-SiC are all hexagonal. All of the other polytypes are mixtures of the fundamental zincblende and wurtzite bonds. Some common hexagonal polytypes with more

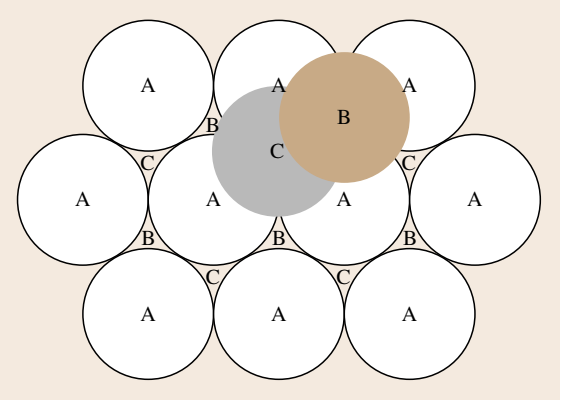


Fig. 28.1 Hexagonal close-packed structure

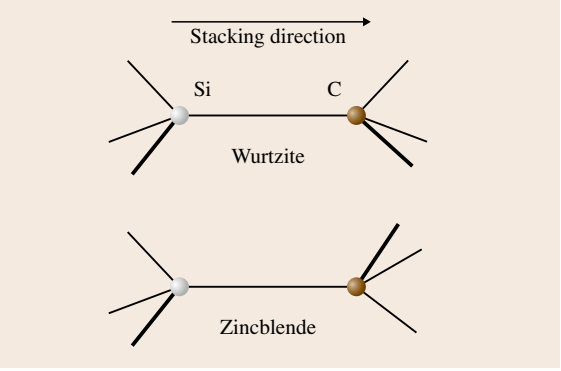


Fig. 28.2 Wurtzite bonding and zincblende bonding between Si and C atoms in adjacent planes. The three tetrahedral bonds are rotated 60° in the cubic case and mirror images in the hexagonal phase

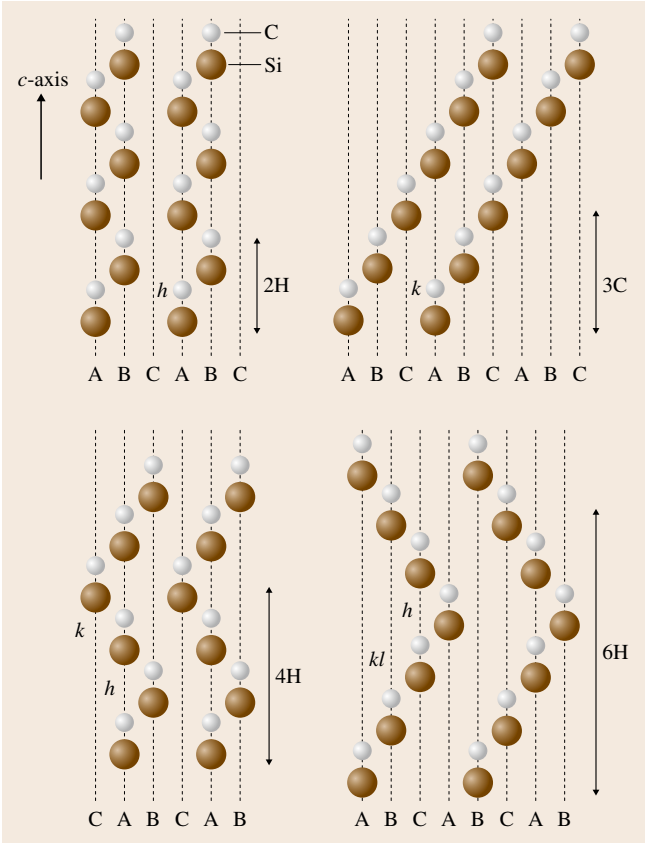


Fig. 28.3 Stacking sequences of different SiC polytypes projected on the [11$\bar{2}$0] plane. Examples of hexagon-stacked bilayers are labeled with *h*, while cubic-stacked bilayers are labeled with *k*

complex stacking sequences are 4H-SiC and 6H-SiC. 4H-SiC is composed equally of cubic and hexagonal bonds, whereas 6H-SiC is two-thirds cubic and one-third hexagonal. Despite the cubic elements, each has overall hexagonal crystal symmetry. The family of hexagonal and rhombohedral polytype is sometimes referred to as α-SiC, whereas 3C-SiC is referred to as β-SiC.

Figure 28.3 shows the stacking sequences for 3C-, 4H-, and 6H-SiC [28.16]. As can be seen, cubic SiC has a lattice constant of $a = 0.4349$ nm at room temperature. For hexagonal SiC, a is approximately 0.3080 nm for all polytypes whereas c varies with the number of layers in the unit cell, one single atomic layer being approximately 0.252 nm for all polytypes.

Why are there so many polytypes? The simplest level of understanding is that the formation energy difference between different polytypes is small. As calculated by *Park* et al. [28.17], the total energy difference for various polytypes is within 4.3 meV/atom. Hence, the temperature and other crystal growth conditions significantly affect the stability of the polytype. The occurrence probability of polytypes depends on the temperature. Generally, 3C-SiC is stable at temperature below 1900 °C, and 6H-SiC is stable at temperature above 1900 °C. A 3C-to-6H solid-phase transformation has been observed at temperature above 2150 °C [28.18, 19]. 4H-SiC also sometimes occurs in the high-temperature region, but the probability is low compared with 6H-SiC [28.20]. The 2H polytype is typically unstable because it can transform to a mixture of 3C and 6H polytypes at typical crystal growth temperatures [28.21]. *Powell* and *Will* have reported that the phase transformation away from 2H polytype can happen at temperatures as low as 400 °C [28.22].

28.2 Defects in SiC

Quality of materials is essential to the performance of the devices. As the development of devices proceed, demands on the quality of the bulk and epitaxial SiC wafers are increasing. Commercially available SiC wafers still contain a large number of various defects, including impurities, micropipes, growth pits, dislocations etc. Understanding the nature and properties of these defects is important to improve both the material quality and device performance. Since structural defects are currently limiting the introduction of commercial SiC devices, these defects are briefly reviewed.

SiC bulk and epitaxial wafers contain a large number of crystal structural defects, including micropipes, screw dislocations, growth pits, triangular inclusions, etc. Table 28.2 summarizes the properties of these defects and their impacts on device operation. More detailed descriptions of some of these defects are given below. Over the last few years, the concentrations of these structural defects have come down significantly, but their density is still high enough to cause problems in devices.

28.2.1 Micropipes

Among the various defects that exist in SiC crystals, screw dislocations lying along the [0001] axis are the most significant and are generally accepted to be one of the major factors limiting the extent of the successful applications of SiC [28.23]. These screw dislocations have been shown to have Burgers vector equal to nc (where c is the lattice parameter and n is an integer), with hollow cores becoming evident with $n \geq 2$ for 6H-SiC and $n \geq 3$ for 4H-SiC. These latter hollow-core dislocations are generally referred to as micropipes. The diameter of micropipes ranges from a few tens of nanometers to several tens of micrometers. Their density has come down in recent years, and micropipe-free wafers have been announced by commercial vendors [28.14]. Figure 28.4 shows an optical microscope picture of a micropipe in a typical 6H substrate used for our epitaxial growth. Using proper growth initiation procedure, it has been possible to close these micropipes during epitaxial growth [28.24]. However, this closure of the micropipe results in a group of elementary screw dislocations in its vicinity.

28.2.2 Screw Dislocations

When the Burgers vector of a SiC screw dislocation is small enough, hollow-core formation is avoided [28.25]. Nevertheless, the screw dislocation possesses many properties similar to micropipes, starting with an undesirable propensity to propagate through the entire thickness of bulk crystals and epilayers. These defects are present in average densities on the order of several thousands to around ten thousand per cm^2 in commercial wafers [28.21]. Because they have not declined in density over time as fast as micropipes, it

Table 28.2 Properties of SiC epilayer extended structural defects [28.29–31]

SiC epilayer defect	Density ($/cm^2$)	Observed defect source	Observed impact on high-field junction	Summary (comments)
Micropipe	< 30 (commercial) < 1 (best)	Substrate micropipes that propagate into epilayer	> 50% breakdown voltage reduction Microplasmas Increased leakage current	Improved in recent years such that the density is less than $\approx 1\,cm^{-2}$ so, large-area power devices possible
Closed-core screw dislocation	≈ 3000 to 10 000	Substrate screw dislocations that propagate into epilayer	≈ 10–30% breakdown voltage reduction Softened breakdown Microplasmas	Density slowly improving, but will be present and affect $\approx 1\,cm^2$ power devices
Triangular 3C inclusions	< 5	Wafer preparation and epitaxial growth process	> 50% breakdown voltage reduction Increased leakage current	Density improving to where these may not be present in most $\approx 1\,cm^2$ power devices
Carrots and comet tails	< 5	Undetermined	Increased leakage current Nonsmooth surface seems likely to impact on Schottky rectifying properties	Density improving to where these may not be present in most $\approx 1\,cm^2$ power devices
Small growth pits	> 3000	Screw dislocations Wafer preparation and epitaxial growth	Nonsmooth surface seems likely to impact on Schottky rectifying properties	Density improving, but screw dislocation density may represent a limiting floor for these defects

would appear that all devices manufactured on mass-produced wafers will contain these defects for the foreseeable future. While not as detrimental to device characteristics as micropipes, experimental evidence is emerging that screw dislocations somewhat negatively impact on the electrical properties of high-field SiC junctions. One study that used x-ray topography to map screw dislocations demonstrated that elementary dislocations are detrimental to the reverse leakage and breakdown properties of low-voltage (< 250 V) 4H-SiC p^+n diodes [28.26]. Similar observations of increased reverse leakage, soft breakdown, and microplasma not associated with micropipes are reported in [28.27, 28]. The physical mechanisms and models for the electrical behavior of these dislocations remain to be further studied.

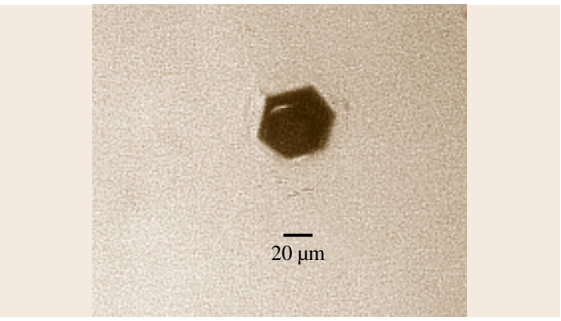


Fig. 28.4 Optical microscope image of a micropipe in a 6H-SiC substrate

28.2.3 Growth Pits and Triangular Inclusions

Besides screw dislocations, other defects, such as growth pits, triangular inclusions, etc., have also been observed in SiC epilayers [28.32, 33]. Unlike micropipes and closed-core screw dislocations, which generally extend through the whole wafer, growth pits and triangular inclusions are primarily present in the epilayer. They are believed to be primarily caused by nonoptimized wafer preparation and epitaxial growth

processing. *Powell* and *Larkin* [28.33] also demonstrated that many morphological imperfections in the as-grown SiC epilayer surface are greatly impacted by surface polishing as well as the epitaxial growth initiation process. However, a recent study by *Schnabel* et al. [28.32], in which electron-beam-induced current (EBIC) measurements were correlated with x-ray screw dislocation mapping and surface growth pit mapping on a 6H-SiC epitaxial layer, revealed that all closed-core screw dislocations on the substrate mapped by x-ray resulted in a corresponding small growth pit on the as-grown epilayer. This suggested that epilayers process improvements may not be able to reduce small growth pit densities below bulk wafer screw dislocation densities.

The quality and smoothness of the semiconductor surface are well known to critically control the electrical properties of Schottky diode junctions. The presence of nonsmooth surface features, such as growth pits and triangular inclusions, could perturb the local electric field and thermionic carrier emission properties, which could result in locally increased current under both forward and reverse bias [28.21]. It is plausible that p–n junction devices are perhaps less affected by SiC surface defects, primarily due to the fact that the peak electric field occurs at the junction buried within the semiconductor. However, p–n junction characteristics can be expected to track surface imperfections in those cases where a surface defect arises due to an extended defect that actually runs through the thickness of the epilayer to intersect the p–n junction. For example, 3C triangular inclusions have been found to greatly increase leakage current and decrease breakdown voltage for kV-class epitaxial p–n junction diodes [28.34].

28.3 Epitaxial Growth of Silicon Carbide

To improve the quality of materials for use in devices and to produce complicated device structures, epitaxial growth techniques are necessary. This section contains a summary of several aspects of SiC epitaxial growth technology, including the SiC growth mechanism, commonly used reactors, SiC precursor sources, substrate materials, and dopant incorporation control. Also discussed are some recent advancements in SiC epitaxial growth.

28.3.1 Substrates for Silicon Carbide Growth

The majority of earlier chemical vapor deposition (CVD) crystal growth research was focused on determining the appropriate processes for obtaining low-defect-density single-crystal SiC films for the advancement of SiC-based devices. The first available substrates for SiC epitaxial growth were mainly small ($\approx 5\,\mathrm{mm}^2$) and irregularly shaped Lely and Acheson-derived SiC substrates that were only suitable for some epilayer physical property studies and limited prototype SiC-based devices. Therefore, dissimilar substrate materials of regular shapes and larger areas were usually chosen for CVD SiC epitaxial growth.

Motivated by the potential for Si–SiC device integration [28.35–37], many workers have attempted to grow SiC heteroepitaxially on Si. Since the growth temperature is limited by the melting point of the Si wafer ($< 1412\,^{\circ}\mathrm{C}$), only cubic SiC can generally be grown on Si substrates, whether the substrate used is (100) or (111). This is because the more stable polytype at these temperatures is cubic. Large thermal and lattice mismatches between Si and SiC have limited the resultant material quality. Many defects such as antiphase boundaries (APBs), stacking-fault (SF) defects, and threading dislocations usually existed in these films and contributed to electrically leaky p–n junctions. APBs are the result of polar SiC growth on nonpolar Si substrate. In addition, other novel substrates such as silicon-on-insulator (SOI) [28.38], twist-bonded universal compliant (UC) substrates [28.38], porous silicon [28.39], and free-standing 3C-SiC (made by removing silicon substrates from thick SiC heteroepitaxial layers) [28.40] have been investigated. Epilayers with improved quality on these substrates have been reported, but p–n junctions built on these layers still show very high leakage current. Recently, a group in Japan has used *undulating* Si substrates to grow thick cubic SiC, followed by the removal of the Si substrates to obtain large-area 3C-SiC wafers [28.41, 42]. Using this undulating Si substrate, they succeeded in reducing the stacking fault density compared with films grown on a planar substrate. However, the large-scale commercial use of this 3C-SiC appears years away, as high-field device performance has remained relatively poor.

TiC has been used as an alternative to Si to grow 3C-SiC, since TiC is more closely lattice-matched to SiC [28.43]. Although 3C-SiC epitaxial layers on TiC

were somewhat superior to those grown on Si, lack of high-quality TiC substrate material and high defect densities in the resulting SiC epitaxial layers have limited advancement of device research using 3C-SiC on TiC substrates.

As (0001)-oriented SiC substrates have become commercially available, more researchers started choosing SiC to grow SiC homoepitaxially. For epitaxial growth on (0001)SiC, typically the Si face has been the preferred surface, partly because of the superior epitaxial surface morphology and well-understood doping behavior compared with the C face. For 6H-SiC, the Si-face substrates are typically polished 3° off-axis from the basal plane, which increases the number of crystallographic steps on the surface to ensure SiC homoepitaxial growth (see the next section). In general, this homoepitaxial growth using off-axis SiC substrates proceeds by a step-controlled crystal growth process, as reported by *Itoh* and *Matsunami* [28.20]. Now the focus of much epitaxial crystal growth research has turned to 4H, mainly because of superior intrinsic properties such as higher bandgap, higher electron mobility, and lower dopant ionization energies. Similar to its off-axis 6H-SiC substrate predecessors, 4H-SiC substrates were initially polished 3° off-axis from the basal plane. However, researchers discovered that, compared with epitaxial growth on 6H-SiC substrates, 4H-SiC growth produces more triangular defects, which were later identified as 3C polytype inclusions [28.44, 45]. With the use of in situ pregrowth surface treatments, the occurrence of these 3C inclusions can be significantly reduced. Subsequently, the incidence of 3C inclusions was eliminated by increasing the 4H step density by using 8° off-axis substrates [28.46].

28.3.2 How to Control the Polytypes in SiC Homoepitaxy

As mentioned in the pervious section, the best way to obtain a high-quality epilayer is *homoepitaxy*, which is effectively free from lattice mismatch between the epilayers and the substrates. To ensure the growth of single polytypes, a method commonly called *step-controlled growth* has been employed in which the substrates are miscut a few degrees off from the (0001)Si face [28.20, 47]. Miscut SiC(0001) crystal surfaces consist of terraces and steps, and these steps reflect the substrate crystal structure, either 4H or 6H. According to the classical growth theory, adsorbed species migrate on the surface and are incorporated into the crystal at steps where the surface potential is low. Another competitive growth process of nucleation takes place on the terraces when the supersaturation is high enough. On the slightly misoriented (0001) plane, the step density is low and vast terraces exist. Then, crystal growth may occur on the terrace through two-dimensional nucleation due to the high supersaturation on the surface. In this case, the polytype of grown layers is determined by the growth conditions, mainly the growth temperature. At temperatures below 1800 °C, 3C-SiC is usually formed because it is stable at low temperature [28.48]. The growth of 3C-SiC can take two possible stacking orders, ABCABC… and ACBACB…, which leads to the formation antiphase boundaries (Fig. 28.5a). On off-oriented substrates, the step density is high and the terrace width is narrow enough for adsorbed species to reach steps. At a step, the incorporation site is uniquely determined by bonds from the step (Fig. 28.5). Hence, homoepitaxy can be achieved through lateral growth from the steps, inheriting the stacking order of the substrate. Hence, epitaxy is usually carried out on (0001) face of SiC (usually Si face) misoriented either 3.5° for 6H or 8° for 4H towards $(11\bar{2}0)$ surface. In recent years, the emphasis has been to use reduced miscut wafers, such as 4°-off (0001) wafers, since they provide several advantages, such as reduction of crystal wastes while slicing wafers from the ingots and reduction of basal plane dislocations [28.49]. It is still possible to replicate substrate polytypes with SiC wafers with smaller offcut, but the optimum growth window for good growth

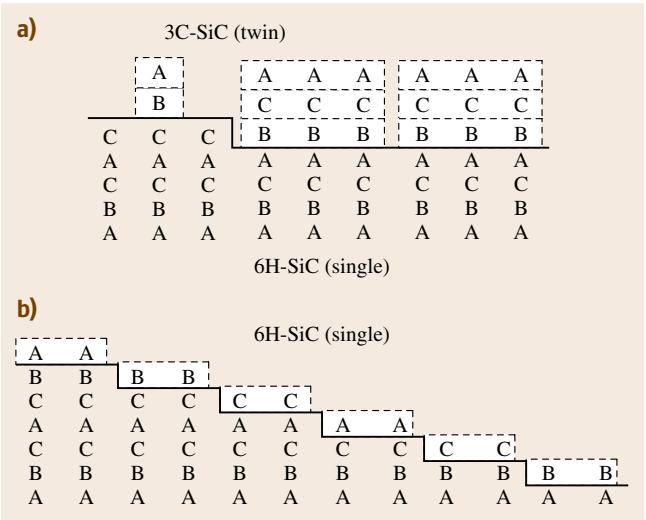


Fig. 28.5a,b Growth modes and polytypes on 6H-SiC substrate. **(a)** 3C-SiC growth by two-dimensional terrace nucleation, **(b)** homoepitaxy of 6H-SiC by step-flow growth (after [28.20])

is much narrower. In addition, increased step bunching is observed when the offcut angle is reduced, thus resulting in increased surface roughness.

28.3.3 SiC Epitaxial Growth Techniques

The purpose of epitaxy is to create a high-quality layer of desired thickness with controlled doping concentration, such as the abrupt p–n junction structure. Various epitaxial growth techniques have been used to achieve this goal. In this section, several important non-CVD epitaxial growth techniques that have been used for growing SiC are presented.

Liquid-phase epitaxy (LPE) is appealing since it is a growth process carried out at or close to equilibrium and thus produces high-quality materials [28.50]. During the LPE process, a SiC wafer, fixed on a graphite holder, is dipped into Si-based melt, which is heated to between 1000 and 2000 °C in a graphite crucible [28.50–54]. Growth takes place due to mass transfer from the crucible acting as the C source to the SiC wafer (seed) in the established temperature gradient. One of the most promising advantages of this method for SiC epitaxial growth is the potential to close micropipes emerging from the substrate. LPE epitaxial layer grows at low supersaturation compared with the physical vapor transport (PVT) growth technique, in which supersaturation is much higher and temperature fluctuations may easily result in local deviations from optimal growth conditions, leading to defect formation. LPE of SiC was shown to be an effective technique to overgrow micropipes in SiC wafers prepared by the physical vapor transport (PVT) technique [28.50–54]. Micropipe closing efficiency of $> 80\%$ has been demonstrated, and the growth rate ranges from several micrometer to millimeter per hour. LPE of SiC requires accurate control of thermal equilibrium conditions to avoid growth of different polytypes at the same time. It is difficult to control the doping concentration by LPE. Also the surface morphology of LPE SiC is rough, and terraces and steps are usually observed on the surface, which needs to be avoided for device fabrication.

Molecular-beam epitaxy (MBE) is an ideal technique for thin epitaxial layer deposition. Gas-source MBE (GSMBE) has been used for SiC homoepitaxial growth [28.55, 56]. It was found that low substrate temperature (< 1000 °C) resulted in deposition of 3C-SiC instead of replication of the stack sequences of the substrate. The growth rate is typically several nm/h. MBE has also been used for growing SiC on Si at relatively low temperature [28.57, 58] to avoid the formation of the voids that are usually observed in Si substrates at the SiC/Si interface when CVD techniques are used. Single-crystal 3C-SiC could be obtained by GSMBE at temperatures as low as 800–900 °C. MBE is suitable for low-dimensional modulation-doped structures or heterostructures of different SiC polytypes in the quantum regime due to its low growth temperature and growth rate. However, the thick epilayers required by high-voltage power device are unlikely to be obtained by MBE.

28.3.4 Chemical Vapor Deposition

The most common epitaxial growth technique for SiC is chemical vapor deposition (CVD), which has the advantages of precise control of the epitaxial layer thickness and impurity doping combined with a reasonable growth rate and good surface morphology. The growth temperatures for typical SiC CVD processes range from 1200 to 1800 °C, while the growth pressures vary from several tens of Torr to atmospheric pressure.

Precursors for SiC CVD Epitaxial Growth

Typical CVD techniques for SiC epitaxial layer growth employ separate sources of Si and C. Silane is the commonly used silicon source, while various choices of hydrocarbons have been used as carbon source. Both are introduced into the reactor with a high-purity H_2 carrier gas. Propane has been the most popular among the hydrocarbon choices, probably because of its association with the first successful demonstration of large-area epitaxial SiC on Si substrates [28.35], while methane, ethylene, and acetylene have been used less extensively. Methane is of interest because of the increased purity available from commercial sources compared with that of propane, although the larger thermal stability results in a smaller C source cracking efficiency [28.59].

Chlorine-based silicon sources, such as SiH_2Cl_2 and Si_2Cl_6, have been used to grow 3C-SiC on Si [28.60, 61]; one advantage is that Cl in the reactor could help to suppress silicon codeposition. Also, as reported by *Yagi* and *Nagasawa* [28.61], the supplied SiH_2Cl_2 is decomposed into $SiCl_2$ and H_2 at the growth temperature. The in situ generated $SiCl_2$ absorption is thought to be self-limited. Thus, atomic-layer epitaxial growth can be achieved by alternating supply of SiH_2Cl_2 and hydrocarbon. Using this method, *Yagi* and *Nagasawa* [28.61] have grown high-uniformity 3C-SiC on 6 inch Si substrates. The thickness deviation of the SiC film (4215 Å in thickness) was less than 1.3% over the substrate. Re-

cently, *Miyanagi* and *Nishino* [28.62] used Si_2Cl_6 as a silicon source material to grow 4H-SiC. Si_2Cl_6 is a safer material than SiH_4, but large numbers of etching pits and scratch-like defects were seen on the resulting epilayers.

Single-source SiC precursors, such as hexamethyldisilane (HMDS) [28.63] and tetramethylsilane [28.64], have also been studied because they usually have much lower cracking temperature than that of multiple-source precursors, which could make lower-temperature ($< 1100\,°C$) SiC CVD possible. However, these chemicals are not available in sufficiently high purity, so their use will not result in layers with low background carrier concentration. Also it is impossible to adjust the C/Si ratio with a single-source precursor, which makes optimization of growth conditions difficult. One possible solution is to use an additional carbon source such as propane to control the C/Si ratio and hence the background doping concentration [28.65]. In addition, a few examples of their use in obtaining reproducible growth of high-quality SiC epitaxial layer have been reported. Hence, use of higher-purity chemicals such as silane and propane offers the best possible routes for growing layers for high-voltage applications. These chemicals can be further purified in situ in the reactor using resin-based purifiers [28.66] .

CVD Reactor Configurations

The most commonly used simple reactor configuration for SiC CVD has been the quartz horizontal reactor operating at atmospheric or low pressure (Fig. 28.6). These reactors can be warm-walled or water-cooled. Researchers from the National Aeronautics and Space Administration (NASA) and Kyoto University have shown that high-quality SiC epilayers can be achieved using this type of reactor [28.33,67]. The gases used are silane (SiH_4) and propane (C_3H_8) with a large amount of H_2 carrier gas. Figure 28.6 shows the schematic of the reactor. The growth rate is determined by the flow of silane gas, whereas the layer quality and the density of *defects* such as cubic SiC inclusions, dopant incorporations etc. are strongly dependent on the growth temperature and the flow rate of propane for a given growth rate. If the silane flow is increased beyond a certain value, the morphology of the grown layer deteriorates quickly. Growth rates of a few μm/h have been obtained using this type of system. *Nakamura* et al. [28.68] reported epitaxial growth in a horizontal cold-wall system with growth rates of up to 6 μm/h at 1500 °C by improving the initial growth conditions. Procedures to minimize doping and thickness nonuniformities include increasing the carrier gas flow (decreasing the residence time of the precursor), reducing the deposition pressure, and tilting the susceptor with respect to the gas flow. More importantly, the limited growth rate and parasitic deposits falling from the ceiling of the reactor wall make it difficult to grow thick ($> 50\,\mu m$) SiC epilayers with good surface morphology.

Vertical cold-wall reactors have also been built and used to grow SiC with high purity and crystal quality [28.69–71]. Precursor gases were introduced from the top of the reactor and the particles falling from the ceiling in the horizontal cold-wall reactor were avoided. The susceptor and attached sample were rotated at up to 1500 rpm to increase uniformity and prevent recirculation of the gases in the chamber. This fast rotation provides a pumping action for the gas flow. A background impurity level below $10^{14}\,cm^{-3}$ was obtained with a growth rate of 5–6 μm/h. Although a similar growth rate was obtained to that achieved in the horizontal cold-wall reactor, longer growth times could be

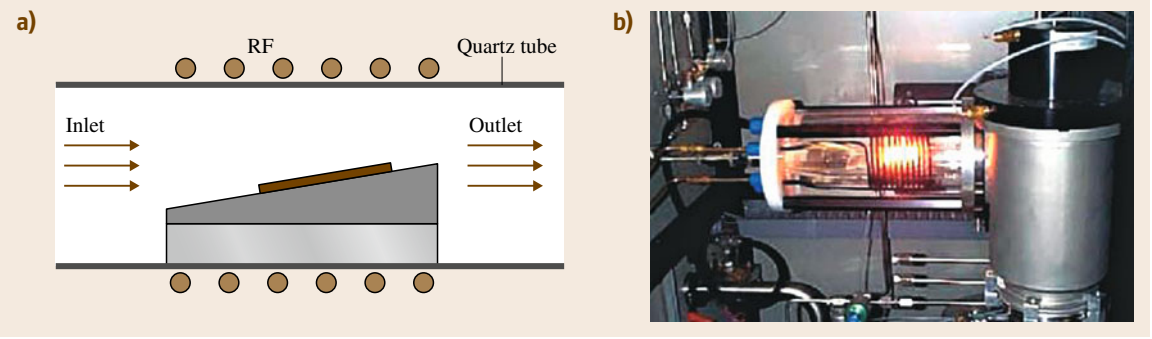


Fig. 28.6a,b Schematic drawing of a typical horizontal cold-wall SiC CVD reactor **(a)** and a horizontal water-cooled cold-wall reactor in operation at Rensselaer Polytechnic Institute (RPI) **(b)** (RF – radiofrequency)

used with the vertical reactor. Thick epilayers up to 50 μm have been obtained using this type of reactor.

In order to reproducibly grow thick, high-quality epilayers for power device applications, horizontal hot-wall reactors were proposed by *Kordina* and coworkers [28.72]. The idea of the hot wall was to obtain very good heating efficiency together with a high cracking efficiency of the precursors since gases could be much more efficiently heated in a hot-wall reactor. Also, since the system is heated more uniformly, Si droplet formation just above the sample surface may be suppressed, and hence a much higher silane flow can be used for growing SiC. This has been discussed as one of the problems that limit the growth rate in cold-wall reactors. Since the reactor walls are all heated (Fig. 28.7), the parasitic deposits on the reactor walls are polycrystalline SiC, which tends to stick to the wall more strongly than the amorphous SiC or byproducts that stick to the reactor wall in cold-wall reactors. Due to all these reasons, it is possible to grow SiC in a hot-wall reactor at a much higher rate and also for longer time without creating the *dusting* and surface morphology degradation that usually occur in cold-wall reactors. Several researchers have adapted this hot-wall process to grow SiC, and currently this appears to be the commonest process to grow SiC epitaxial films. For example, *Kimoto* et al. [28.73] have improved on this process, and have reported very high-purity SiC growth using this type of reactor. Epilayers with 50 μm thickness and n-type background doping in the low $10^{13}\,\mathrm{cm}^{-3}$ range have been achieved reproducibly at 1550 °C and 80 Torr. With additional mechanical rotation, excellent thickness uniformity (1% standard deviation over mean value) and doping uniformity (6% standard deviation over mean value) have been achieved on 2 inch wafers

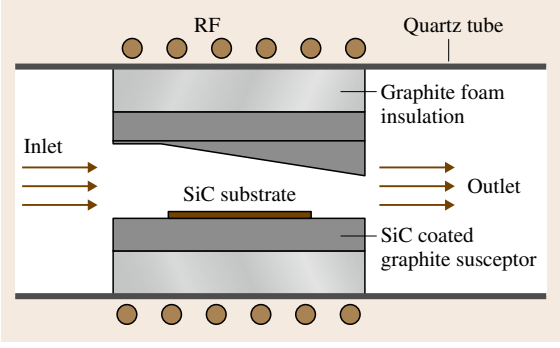


Fig. 28.7 Schematic drawing of a typical horizontal hot-wall SiC CVD reactor. The cross section of graphite wall is rectangular in shape

using a horizontal hot-wall reactor [28.74]. Recently, *Thomas* and *Hecht* [28.75] reported a planetary horizontal hot-wall reactor with handling capacity of seven 2 inch or five 3 inch wafers. High-quality epilayers were grown by optimizing the process conditions. Excellent intrawafer homogeneity (thickness uniformity standard deviation of 2% of mean, doping uniformity standard deviation of 9% of mean) as well as wafer-to-wafer (thickness uniformity standard deviation of 1.6% of mean, doping uniformity standard deviation of 3.3% of mean) on 3 inch wafers have been achieved using this system. These horizontal hot-wall reactors with multiple-wafer capability are becoming industry-standard for growing epitaxial films for commercial production.

The vertical hot-wall reactor (also called the *chimney* CVD reactor) has also been developed as a high-temperature CVD technique in order to increase growth rates further [28.76–78]. The epitaxial growth of SiC in this geometry is investigated mainly for the purpose of growing thick epitaxial layers for high-power applications. In the chimney reactor, the high-temperature (1600–1900 °C) growth process enables epitaxial rates of 10–50 μm/h. Under optimum conditions, mirror-like SiC epilayers with low background doping of low $10^{13}\,\mathrm{cm}^{-3}$ can be obtained. Recently, *Danno* et al. reported fast epitaxial growth (14–19 μm/h) on 4H-SiC(000$\bar{1}$) substrate using a chimney-type reactor [28.79]. High-quality epilayers with 100% micropipe closing have been grown at 1750 °C at C/Si ratio of 0.6. *Fujiwara* et al. reported the reduction of stacking faults in fast epitaxial growth by optimizing initial growth conditions during the heating process [28.80]. Stacking fault density could be dramatically reduced from 1000–9000 cm^{-2} to 0–5 cm^{-2}. The vertical hot-wall reactor has also been used in the author's own laboratory [28.81] for growing thick epitaxial films with high growth rate (> 20 μm/h).

Another type of epitaxial growth, termed *sublimation epitaxy*, was developed to grow bulk-like thick SiC, and was one of the first techniques to produce SiC epitaxial layers. This growth process is based on heating polycrystalline SiC source material to 1700–2000 °C under conditions at which it sublimes into the vapor phase and subsequently condenses onto a cooler SiC seed crystal. This is similar to the bulk growth process. It is possible to achieve high epitaxial growth rate (> 2 mm/h) with a stable mechanism, resulting in high-quality SiC. Thick homoepitaxial growth of 4H-SiC (50–100 μm) [28.82] and 3C-SiC (300 μm) [28.83] with high growth rates of 100 μm/h

and 50 μm/h, respectively, have been demonstrated using this technique. Specular surface and better quality layers (compared with substrate) were obtained by this technique. Recently, *Sveinbjornsson* et al. reported higher field-effect channel mobility ($208\,cm^2/(V\,s)$) in 4H-SiC MOSFETs fabricated on sublimation-grown epilayer compared with that ($125\,cm^2/Vs$) fabricated on a commercial CVD epilayer [28.84]. The mobility enhancement is attributed to better surface morphology of the sublimation epilayer, resulting in less surface scattering and lower density of interface states [28.85] as compared with the reference CVD epilayers. However, good results by sublimation epitaxy can only be obtained when the growth parameters are carefully controlled within a narrow window. One of the remaining challenges is to avoid the introduction of impurities from the growth environment into the epilayers. The purity of the solid polycrystalline SiC source material is the most critical issue in the growth of low-doped SiC by this method.

Recently, a new epitaxial growth process by introducing chlorinated silicon precursors or simply HCl addiction was proposed to achieve high growth rate of SiC [28.86–88]. A high growth rate of 90 μm/h has been obtained using methyltrichlorosilane (MTS) as a precursor [28.86], while growth rates of up to 49 μm/h have been reported using standard silane–propane–hydrogen growth chemistry with incorporation of HCl into the gas mixture [28.87]. No significant difference has been observed in terms of defects, doping uniformity or thickness uniformity compared with the standard process without HCl (or chlorinated silicon precursor). Although the growth mechanism is not fully understood, it is proposed that the addition of chlorine suppresses Si cluster formation in the gas phase, which is thought to be responsible for limiting the growth rate in horizontal cold-wall reactors. Therefore, epitaxial growth with both high growth rate and specular surface morphology is possible using this process. A complete investigation of this process is still ongoing to obtain high-quality SiC epilayers with even higher growth rates.

Doping Incorporation Technology

In order to ensure reproducible and reliable SiC semiconductor device characteristics, well-controlled dopant incorporation must be accomplished. Unlike the doping technology routinely used in the silicon semiconductor industry, SiC cannot be efficiently doped by diffusion at SiC growth temperature due to its low diffusion coefficient. Doping of SiC epitaxial layers of a device structure is accomplished either by flowing a dopant source into the reactor during growth or by implanting the dopant atoms.

Nitrogen is the most common n-type source for in situ doping. Since the atomic size of nitrogen (0.74 Å) is closer to that of carbon (0.77 Å), nitrogen tends to substitute at C sites to a first approximation, consistent with the reported experimental results [28.20]. As discussed previously, the bonding between Si and C atoms in adjacent bilayer planes can be of either zincblende (cubic) or wurtzite (hexagonal) nature. Each type of bond provides a slightly altered atomic environment, making some lattice sites inequivalent in polytypes. In 6H-SiC, three inequivalent sites are available (two cubic sites and one hexagonal site), whereas two inequivalent sites are available in 4H-SiC (one cubic site and one hexagonal site). The ionization energy will be different when a dopant is incorporated into different inequivalent sites. The ionization energies for nitrogen have been reported by several authors, but the values differ a lot. In general, measurements on epitaxial layers with higher donor concentration typically yield lower ionization energy due to Coulombic interactions with neighboring impurities [28.89]. Also, experimentally, it was found that the ionization energies of nitrogen in 4H-SiC are shallower than the corresponding values in 6H-SiC.

In situ nitrogen doping can be realized by passing nitrogen or ammonia into the reactor during the growth. However, control of net dopant incorporation by simply increasing or decreasing the flow of the dopant source is limited in terms of both reproducibility and doping range. This doping range is typically limited to 2×10^{16}–$5\times10^{18}\,cm^{-3}$ for a nitrogen-doped n-type layer. If one increases the nitrogen flow further, either the growth rate is found to reduce or the surface morphology is found to deteriorate significantly [28.90]. So, an alternative method, termed *site-competition growth*, is used to increase the doping concentration [28.91]. It was found that nitrogen incorporation was very sensitive to the C/Si ratio employed during the growth and increased when C/Si decreased for growth on Si-face substrate (Fig. 28.8b). This was explained by site competition between nitrogen and carbon during the growth: since nitrogen and carbon occupy the same sites in SiC, decreasing C/Si will produce more C vacancies in SiC, which will in turn increase nitrogen incorporation. Use of this technique has enabled large expansion of the reproducible doping range, which as a result, now spans from 10^{14} to $5\times10^{19}\,cm^{-3}$.

Phosphorous is another n-type dopant in SiC. However, phosphorous appears to have limited potential as a replacement for nitrogen, especially considering its larger atomic size and similar ionization energy to the nitrogen donor [28.91]. Understanding of the location of phosphorous in the SiC lattice as an isolated impurity, phosphorous-related complexes, and corresponding electronic levels is still poor. Hall measurements on phosphorous-implanted SiC epilayers have yielded two ionization energies: 80 ± 5 and 110 ± 5 meV for 6H-SiC [28.92] and 53 and 93 meV for 4H-SiC [28.93], which were assigned to the hexagonal and quasicubic sites of silicon, respectively. Recent research on phosphorous-implanted SiC indicates that the sheet resistance in high-dose phosphorous-implanted 4H-SiC is as much as an order of magnitude lower than those measured in nitrogen-implanted 4H-SiC with comparable doping and thermal processing [28.94]. Thus, there are some advantages in replacing nitrogen with phosphorous for applications where low sheet resistance is required.

Very little has been reported on in situ doping of phosphorous in CVD. The phosphorous donor ionization energy is also only available on phosphorous-implanted SiC, which generally contains lots of N or Al background. In one report [28.88] on the site-competition effect for phosphorous doping, *Larkin* reported that phosphorous substitutes at the Si site due to its similar atomic size (1.10 Å) to Si (1.17 Å). However, our own experimental results seem to be different from this conclusion, and it appears that phosphorous occupies both Si and C sites [28.95].

Aluminum serves as a shallow acceptor dopant in SiC and can be introduced during growth, or afterwards by implantation. In contrast to nitrogen, the aluminum acceptor resides at the Si lattice sites. Its ionization energy is only weakly dependent on polytype or to lattice sites h, k. The scatter of published data ranges from 190 meV [28.96] to 280 meV [28.97]. The in situ incorporation of Al strongly depends on the C/Si ratio during growth. Increasing C/Si will increase the Al doping concentration.

Boron is another acceptor dopant in SiC. During epitaxial growth, a considerable amount of hole-passivating hydrogen is simultaneously incorporated into the growing B-doped CVD epilayer. Postannealing at 1700 °C in Ar is usually used to dissociate B–H and better activate the B acceptors [28.91]. Although the atomic size of boron (0.82 Å) is closer to that of C (0.77 Å), B–H has an atomic size (1.10 Å) more closely matched with that of Si (1.17 Å) and therefore should occupy Si sites. Experiments have also shown that boron incorporation increases with C/Si [28.91], which is in agreement with the site-competition theory. However, this does not imply that boron substitutes exclusively at Si sites. Experiments have shown that a small amount of boron can also occupy C sites and form an energetically deep complex termed a D-center. The energy level for the boron at the Si site is about 300 meV, as measured from the top of the valence band. The deeper center is about 600–700 meV above the valence band and manifests itself optically by producing donor–acceptor pair spectra at low temperature [28.97]. Its existence was also confirmed by deep-level transient

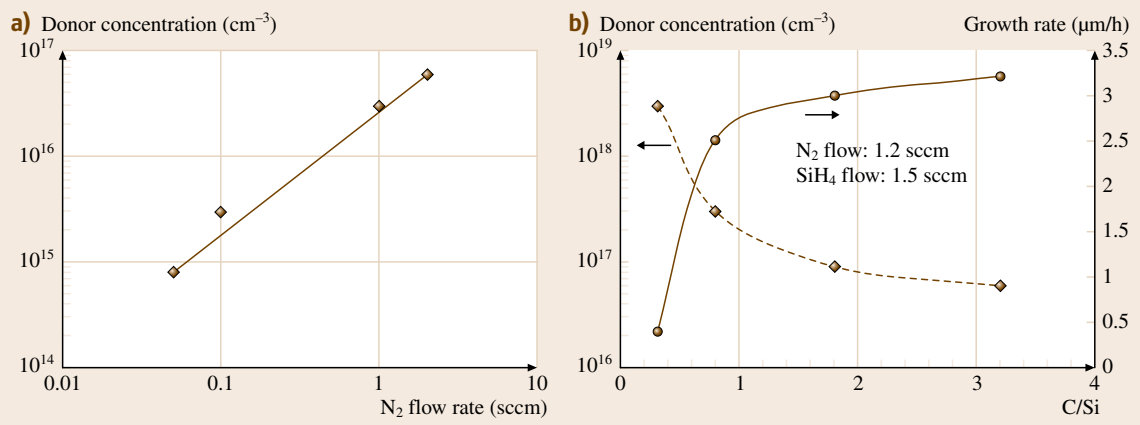


Fig. 28.8 **(a)** Carrier concentration versus N_2 flow for CVD of SiC. Increasing C/Si ratio can decrease the carrier concentration further as shown in **(b)** (after [28.95])

spectroscopy (DLTS) spectra [28.96]. The formation of shallow boron acceptors and deep D-centers can be adjusted during the doping process by the site-competition effect. Use of higher C/Si during growth will reduce the carbon vacancies, thus producing more shallow boron acceptors.

Epitaxial Growth on Nonstandard Crystal Orientations

After the success of epitaxial growth on off-axis (0001)Si-face substrate, growth on many other crystallographic faces of SiC has also been investigated. Most of the epitaxial growth studies on nonstandard crystal planes have focused on 4H-SiC due to its electronic properties advantages over 6H-SiC. Figure 28.9 shows schematics of several selected 4H-SiC lattice planes.

Epitaxial growth on $(000\bar{1})$C-face substrate has been carried out by CVD and compared with growth on (0001)Si face. SiC $(000\bar{1})$C face has a different surface atom configuration from (0001)Si face, and the electronegativity of Si and C atoms is different. This brings about various polarity dependences in chemical reactivity, growth kinetics, impurity incorporation efficiency, thermal oxidation rate, and oxide–SiC interface properties. SiC $(000\bar{1})$C face has shown superior properties of faster oxidation rate [28.98] and low surface roughness [28.96] compared with Si(0001) face. Therefore, it shortens the extremely time-consuming oxidation process on SiC(0001) and it is possible to obtain higher channel mobility of SiC MOSFETs due to reduced surface roughness scattering. Although it was found that the growth window on $(000\bar{1})$C face is narrower and the background doping level is higher compared with growth on (0001)Si face [28.97], high-quality epilayer with a background doping of mid-10^{14} cm^{-3} has been obtained following the development of the hot-wall CVD reactor [28.99]. The nitrogen donor incorporation efficiency has been found to be higher on $(000\bar{1})$C face, while the aluminum acceptor incorporation efficiency on $(000\bar{1})$C is lower compared with on (0001)Si face [28.100–102].

Epitaxial growth of 4H-SiC on $(1\bar{1}00)$ and $(11\bar{2}0)$ faces has also been investigated with the motivation to improve the SiC MOSFET channel mobility [28.103]. Both faces are perpendicular to the (0001) face, as shown in Fig. 28.9b,c, respectively, and no intentional off-angles are required for these faces to realize homoepitaxy of 4H-SiC, owing to the appearance of stacking information on the surface. The surface morphology of epitaxial layers grown on $(1\bar{1}00)$ face was found to be very poor, whereas the resulting SiC$(11\bar{2}0)$

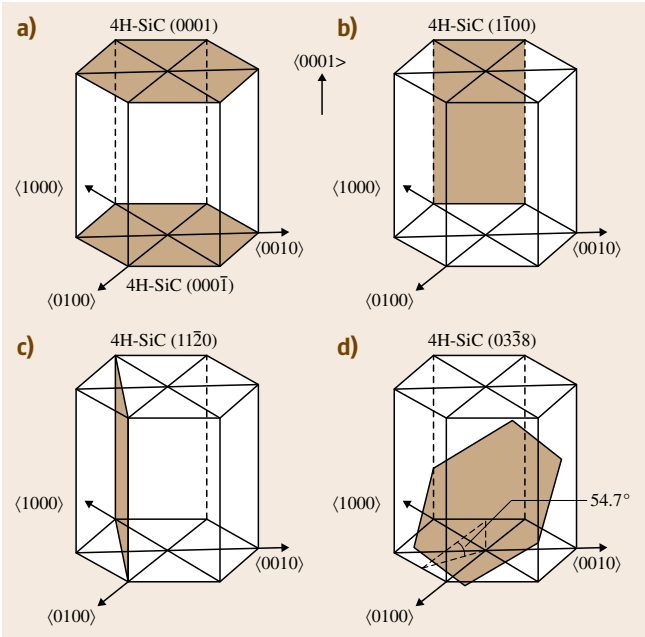


Fig. 28.9a–d Schematic of the selected lattice planes of 4H-SiC. **(a)** 4H-SiC(0001) and $(000\bar{1})$, **(b)** 4H-SiC$(1\bar{1}00)$, **(c)** 4H-SiC$(11\bar{2}0)$, and **(d)** 4H-SiC$(03\bar{3}8)$

epitaxial surface morphology was comparable to or even better than those grown on off-axis (0001)Si face. Although threading screw dislocations and edge dislocations parallel to the *c*-axis are present in $(11\bar{2}0)$ substrate, they are found not to propagate into epilayers. Extremely smooth and micropipe-free layers have been obtained by epitaxial growth on $(11\bar{2}0)$ substrate [28.104, 105]. Growth rates on $(1\bar{1}00)$ and $(11\bar{2}0)$ faces are almost the same as that on off-axis (0001) under the same conditions. The C/Si ratio dependence of dopant incorporation has been observed for epitaxial growth on $(11\bar{2}0)$ substrate [28.102, 105]. When nitrogen was introduced, epitaxial layers grown on $(11\bar{2}0)$ always showed higher donor concentration than on off-axis (0001). Although nitrogen incorporation was suppressed by increased C/Si ratio on $(11\bar{2}0)$, the C/Si dependence was weaker on $(11\bar{2}0)$ epilayers. A background doping concentration of low-10^{14} cm^{-3} for $(11\bar{2}0)$ epilayers can be achieved by increasing the C/Si ratio. In contrast to nitrogen doping, the acceptor (both Al and B) concentration of $(11\bar{2}0)$ epitaxial layers was lower than that of off-axis (0001) epitaxial layers under identical growth conditions.

To avoid propagation of defects along growth direction, SIXON Ltd., Japan, [28.106] developed crystal

growth of 4H-SiC along the $\langle 03\bar{3}8\rangle$ direction which is inclined to the *c*-axis by 54.7° as shown in Fig. 28.9d. During the bulk growth, defects along the $\langle 0001\rangle$ direction propagate diagonally and terminate to the side of ingot. Epitaxial growth on $(03\bar{3}8)$4H-SiC has shown improved surface morphology [28.105, 107]. Microsteps and triangular defects have not been observed on the surface, and almost perfect micropipe closing has been realized in 4H-SiC$(03\bar{3}8)$ epitaxial growth. Growth rate on $(03\bar{3}8)$ is the same as on an off-axis (0001)Si face under the same conditions. Similar dopant incorporation efficiency as that on $(11\bar{2}0)$ has been found for epilayers on $(03\bar{3}8)$. The C/Si ratio dependence of impurity incorporation is intermediate between the case of the (0001)Si face and the $(000\bar{1})$C face. A background doping of low $10^{14}\,\mathrm{cm}^{-3}$ can be achieved on $(03\bar{3}8)$, similar to that on $(11\bar{2}0)$.

Based on the experimental results, impurity incorporation in SiC growth is believed to be dominated mainly by surface bond configuration. Since both Al and B atoms occupy Si sites to form acceptors in SiC, the doping efficiency of these impurities may depend on the number of chemical bonds available from the surface C atoms. On (0001)Si plane, three bonds are available from neighboring C atoms on the surface, while two bonds are available from surface C atoms on $(11\bar{2}0)$ and $(03\bar{3}8)$. On $(000\bar{1})$C face, only one bond is available from the top C atom. This difference may be the reason why the doping efficiency of Al or B on $(11\bar{2}0)$ and $(03\bar{3}8)$ faces is lower than on (0001)Si face but higher than on $(000\bar{1})$C face. In a similar manner, N doping may be influenced by the number of chemical bonds from the surface Si atoms, as N atoms substitute at C sites. Therefore, nitrogen incorporation on $(11\bar{2}0)$ and $(03\bar{3}8)$ faces is more efficient than on (0001)Si face and less efficient than on $(000\bar{1})$C face.

The MOS interface properties of these nonstandard faces have also been studied to explore potential advantages for SiC power MOSFET applications. Although the interface state density (D_{it}) of the 4H-SiC(0001) MOS structure exhibits a rapid increase near the conduction-band edge, those on the other faces exhibit a rather flat D_{it} distribution. $(000\bar{1})$, $(11\bar{2}0)$, and $(03\bar{3}8)$ have about one order of magnitude lower interface density near the conduction-band edge than (0001) [28.108]. As known, the extremely high D_{it} near the band edge causes trapping of electrons induced in the inversion layer and significantly reduces the channel mobility of SiC MOSFETs [28.109]. Planar MOSFETs fabricated on 4H-SiC(0001), $(000\bar{1})$, $(11\bar{2}0)$, and $(03\bar{3}8)$ faces have shown that the effective channel mobility of those nonstandard faces is 2–3 times higher than that on (0001) face. Although the reason for this crystal face dependence is unclear, bond configurations and the polarity of nonstandard surfaces might lead to an intrinsic difference in chemical reactivity during oxidation and to a reduced number of electrically active states near the band edge. Recently, *Kimoto* et al. reported a new oxidation process using N_2O to reduce the interface state density [28.110]. The interface state density near the conduction-band edge was found to be much lower on 4H-SiC$(000\bar{1})$ and $(11\bar{2}0)$ ($\approx 3\times10^{11}\,(/\mathrm{cm}^2\,\mathrm{eV})$) than on 4H-SiC(0001) ($\approx 1\times10^{12}\,(/\mathrm{cm}^2\mathrm{eV})$) with N_2O oxidation. A significant improvement of the channel mobility in SiC MOSFETs fabricated on $(000\bar{1})$ ($> 30\,\mathrm{cm}^2/(\mathrm{V\,s})$), and $(11\bar{2}0)$ ($> 70\,\mathrm{cm}^2/(\mathrm{V\,s})$) epilayers has been achieved [28.111, 112]. 4H-SiC$(000\bar{1})$, $(11\bar{2}0)$, and $(03\bar{3}8)$ faces are promising for MOS-based devices owing to the superior properties of the MOS interface. Note that research on $(03\bar{3}8)$ epitaxial growth and device applications is still limited due to the lack of substrates. All results have been reported by SIXON Ltd. and Kyoto University. Even though these orientations may have better device properties, the lack of availability of these wafers at lower cost may limit widespread use, and most epitaxial work will still be carried out on (0001)Si wafers.

28.4 Epitaxial Growth on Patterned Substrates

Epitaxial growth of SiC provides in situ doping of as-grown layers and better crystal quality as compared with ion implantation. Step-controlled epitaxy has been used at lower temperature (< 1800 °C) for high-quality crystal growth, avoiding SiC sublimation and surface roughening during growth. Therefore, if selective doping of SiC can be achieved via epitaxial growth, then it provides a promising alternative to ion implantation in SiC processing. There are two essential means to realize selective doping by epitaxial growth. One is to apply blanket growth on a trenched substrate, followed by a polishing process to remove excess epilayers on the mesas. The other is to use selective growth with a high-temperature mask that could be selectively re-

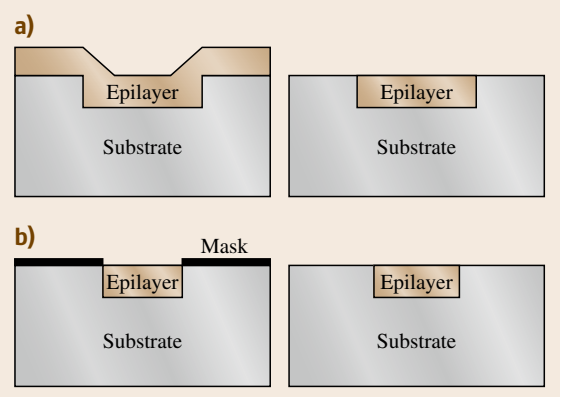


Fig. 28.10a,b Schematic of selective doping of SiC by epitaxial growth. **(a)** Blanket epitaxial growth followed by polishing to remove excess epilayers, **(b)** selective epitaxial growth followed by mask removal

moved after growth. These two processes are illustrated schematically in Fig. 28.10.

A few trials of homoepitaxial CVD growth of SiC on a trenched substrate have been reported. *Nordell* et al. [28.113] investigated the growth behavior at various C/Si ratios and temperatures. It was found that a low C/Si ratio gave smooth growth and small differences in growth rates between different lattice planes. A larger C/Si ratio gave more faceted growth, and the growth rate was lower in the $\langle 1\bar{1}00\rangle$ direction than in the $\langle 11\bar{2}0\rangle$ direction. *Chen* et al. [28.114] also carried out homoepitaxial CVD growth on trenched 4H-SiC substrate. Similar growth behavior was observed near trenches. It was found that the growth rate on trench side walls was usually lower than that on the bottom of a trench and on the top surface, and this difference became smaller with decreasing C/Si ratio. Growth on mesas oriented parallel to the substrate miscut direction showed clear step-flow growth, while growth on mesas oriented perpendicular to the miscut direction revealed the formation of (0001) plane. These studies focus more on crystal growth behavior; applications on device fabrication have hardly been reported.

Epitaxial growth on patterned substrates, specifically, 4H-SiC mesas, has been carried out at NASA [28.115–118]. 4H-SiC substrates were patterned with a series of mesas of various shapes and sizes (such as squares and hexagons) by dry etching techniques. When epitaxial growth is carried out on these substrates, step-free surfaces are obtained provided that the mesas do not contain any screw dislocations. Such techniques have been used to provide step-free large-size mesas up to $200\,\mu m \times 200\,\mu m$. Such mesas have been used for growth of cubic SiC or hexagonal GaN layers. The results from these studies have been reviewed before [28.117] and will not be repeated here.

28.4.1 Selective Epitaxial Growth

Selective epitaxial growth is a well-established technique for Si [28.119] and GaN [28.120, 121]. However, only a few works have been reported on selective growth of SiC. This is not surprising since high growth temperature above 1450 °C is generally required to grow high-quality epilayers of SiC by chemical vapor deposition. This high growth temperature makes it a challenge to identify an appropriate mask for selective epitaxial growth of SiC.

Several groups [28.122, 123] have demonstrated low-temperature ($\approx$ 1000–1200 °C) selective deposition of 3C-SiC on Si substrate using SiO_2 and Si_3N_4 as the mask. Two conflicting requirements became apparent: high growth temperatures were needed to produce the best crystal quality 3C-SiC films, but low growth temperatures were needed to minimize damage to the mask. Polycrystalline 3C-SiC was usually deposited in unmasked window when the temperature was lowered to avoid significant damage to the mask. In addition, delamination of dielectric mask was often observed. To improve selectivity, HCl was sometimes added to the carrier gas [28.124]. Lateral epitaxial overgrowth (LEO) has also been studied, and it was found that defect density in the LEO region was significantly reduced compared with films grown directly on Si substrate [28.125, 126].

Selective growth at higher temperature requires masks that can withstand the growth temperature of $> 1500\,°C$. One such mask is graphite. Recently, homoepitaxial selective growth of SiC has been reported using graphite mask [28.127–129]. *Chen* et al. investigated selective homoepitaxial growth of 4H-SiC on off-axis (0001) and $(11\bar{2}0)$ substrate at 1500 °C [28.128]. Polycrystalline 3C-SiC was observed on the graphite mask, and laterally overgrown polytype was identified as 3C-SiC in contrast to the 4H-SiC grown in window openings. Local epitaxy and lateral epitaxial overgrowth of SiC were even studied by using physical vapor transport (PVT) [28.129]. A lateral/vertical growth rate ratio of 6 was achieved. It was found that dislocations in the substrate propagated only into epilayers grown above the seed regions but not into the lateral overgrown region. The apparent disadvantage of the graphite mask is that the mask itself could act as

a carbon source during high-temperature SiC epitaxial growth. This results in local variation in the C/Si ratio, which affects local crystal growth behavior and the doping concentration of grown layers. Also, polycrystalline SiC deposition on the mask interferes with the lateral growth. Because of these limitations, it is better to identify another mask that will withstand the high growth temperature but that will not cause contamination of the layer itself.

28.4.2 Selective Epitaxial Growth of 4H-SiC Using TaC Mask

At RPI, we have used TaC as the high-temperature mask for growing SiC selectively. Some salient features of this selective growth will now be presented, followed by some device results.

The mask to be used for selective epitaxial growth of SiC essentially needs to be stable under high temperature (> 1400 °C) in hydrogen ambient. Silicon oxide and silicon nitride are commonly used masks for selective growth of silicon and III–V compound semiconductors [28.119, 130, 131]. However, they are etched very quickly in hydrogen ambient under high temperatures and can be used only at relatively low temperature (≈ 1000 °C). TaC is a well-known refractory material with high melting point and high chemical resistance. TaC-coated components have been used with success in conventional vapor-phase epitaxy (VPE) of SiC [28.132]. In addition, TaC has been successfully used as a coating of the graphite susceptor in SiC epitaxy [28.95, 133].

A TaC mask was prepared by converting Ta to TaC in a CVD reactor. Specifically, high-purity Ta metal (99.999%) was first evaporated by electron-beam evaporation and patterned. Ta-coated SiC wafers were then placed in the CVD reactor, and the chamber was pumped down to 5×10^{-6} Torr using a turbo pump be-

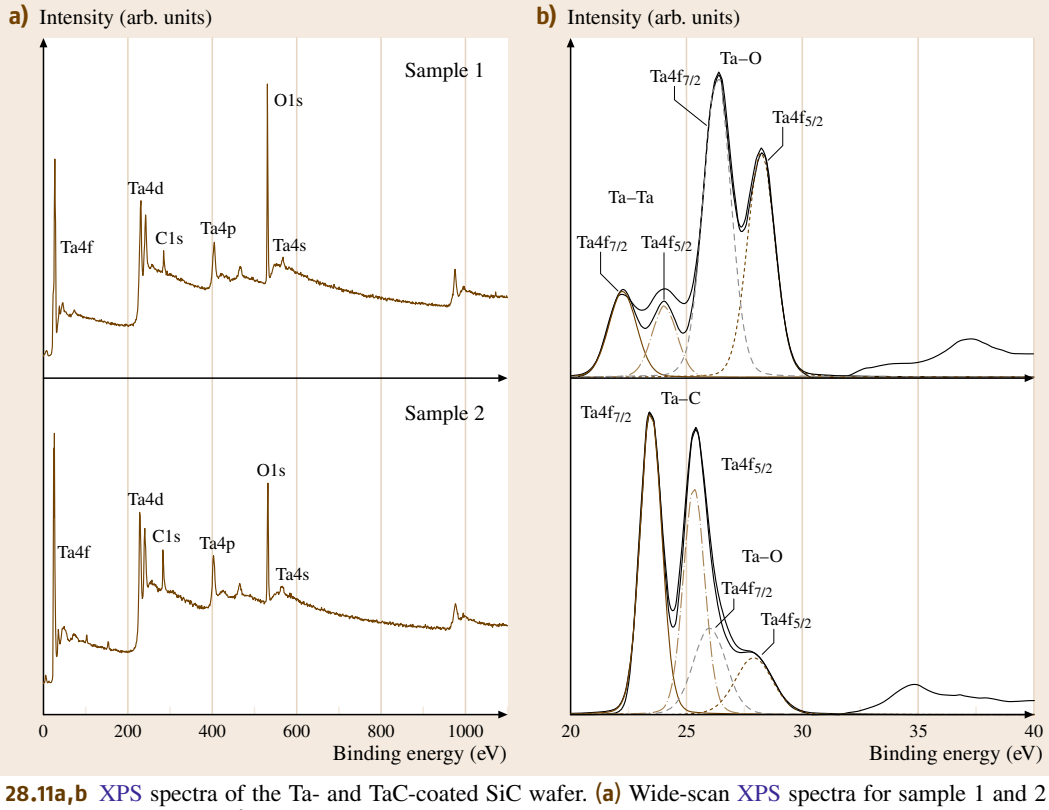


Fig. 28.11a,b XPS spectra of the Ta- and TaC-coated SiC wafer. **(a)** Wide-scan XPS spectra for sample 1 and 2 which have as-deposited 600–700 Å Ta film on the SiC. Sample 2 has been kept in C_3H_8/H_2 ambient at 1300 °C for 15 min. **(b)** XPS spectra from Ta4f for sample 1 and 2. They are fitted with Gaussian peaks which are assigned to Ta ($Ta4f_{7/2}$: 22.4 eV, $Ta4f_{5/2}$: 24.0 eV) Ta_2O_5 ($Ta4f_{7/2}$: 26.3 eV, $Ta4f_{5/2}$: 28.2 eV), TaC ($Ta4f_{7/2}$: 23.5 eV, $Ta4f_{5/2}$: 25.3 eV)

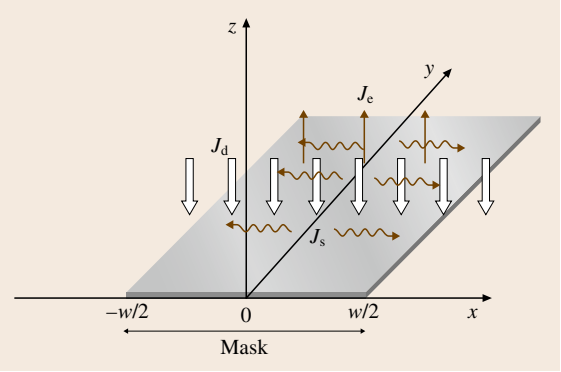


Fig. 28.12 Schematic of reactant species motion on the mask surface, taking into account surface diffusion

fore the susceptor was heated up. The wafers were then kept at 1300 °C in 180 ppm C_3H_8 diluted in H_2 ambient under 100 Torr pressure for 15 min. After the carburization process, the color of the mask changed from grey to golden yellow. X-ray photoelectron spectroscopy (XPS) has been used to confirm the formation of TaC, as show in Fig. 28.11. Sample 1 has as-deposited Ta on the surface whereas the carburization process was carried out on sample 2. Figure 28.11a shows wide-scan XPS spectra of the samples. The main peaks correspond to tantalum (Ta4s, Ta4p, Ta4d, and Ta4f), carbon (C1s), and oxygen (O1s). It is clear that the carbon fraction (18 and 31.5% for samples 1 and 2, respectively) increases after the carburization process. Also notice that some oxygen is present on the top surface of the films and that the amount of oxygen decreases after the carburization process. The same analysis was carried out for both samples at a depth of 100 Å below the surface (materials near the surface were removed by Ar^+ ion sputtering). The analysis shows that the amount of oxygen decreases significantly with depth. It is likely that the oxygen near the surface of the film is from natural oxidation.

Figure 28.11b shows high-resolution XPS spectra from Ta_{4f} for samples 1 and 2. They are fitted with six Gaussian peaks, which are assigned to Ta ($Ta4f_{7/2}$: 22.2 eV, $Ta4f_{5/2}$: 24.0 eV), Ta_2O_5 ($Ta4f_{7/2}$: 26.2 eV, $Ta4f_{5/2}$: 28.0 eV) and TaC ($Ta4f_{7/2}$: 23.4 eV, $Ta4f_{5/2}$: 25.4 eV). The binding energies are close to those reported elsewhere [28.134, 135]. Particularly, comparing the results with the work by *Gruzalski* and *Zehner* [28.134], who determined core-level binding energies of TaC_x over the range $0.5 < x < 1.0$, the carburized film here corresponds in composition to $TaC_{1.0}$.

The growth selectivity with a TaC mask is significantly dependent on the growth conditions. Polycrystalline film deposition occurs on the mask under nonoptimized conditions. The polycrystalline deposition on the masks is closely related to the surface concentration of the reactant species. Figure 28.12 shows a schematic diagram of the motion of reactant species on the mask region, taking account of surface diffusion. The reactant species arrive on the mask region with a flux density of J_d, migrate on the mask surface during a mean surface lifetime of τ_s, and then desorb from the mask surface and re-evaporate with a flux density of J_e. In general, the surface concentration of reactant species on the SiC surface could be assumed to be negligibly small due to the homoepitaxial incorporation of the species.

However, the surface concentration on the mask area cannot be neglected because the reactant species arriving on the mask surfaces are difficult to be incorporated into adsorption sites. Thus, the reactant species that arrive on the mask within a diffusion length (λ_s) of the edge of the window opening are incorporated into the substrate during epitaxial growth, and the surface concentration distribution across the mask is dependent

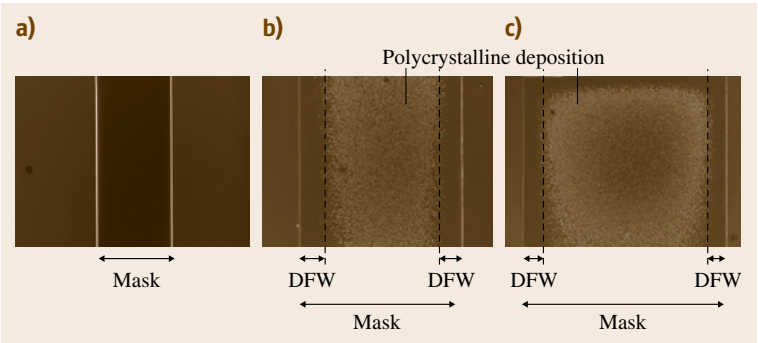


Fig. 28.13a–c SEM viewgraph of SiC polycrystal deposition on TaC mask at 1833 K. Flow rate is 2.24 sccm for both SiH_4 and C_3H_8. Growth pressure is 80 Torr. Width of the mask is **(a)** 100 μm, **(b)** 500 μm, **(c)** 1000 μm, while $M : W = 1$

on the surface diffusion length, which determines the profile of polycrystalline deposition.

Figure 28.13 shows the polycrystalline growth on a mask and the defect free width (DFW) when the mask widths are very large; this experiment gives an approximate surface diffusion length of the growth species on the TaC mask.

28.4.3 Orientation Dependence of SiC Selective Growth

A circular pattern was first used to study the orientation dependence of the selective growth of SiC. The circular pattern consists of 5 μm wide mask windows spaced every half degree as spokes of a wheel. The patterned sample was then carburized and SiC was grown in the CVD reactor. The flow rates were 1.2 and 1.2 sccm for C_3H_8 and SiH_4, respectively, using H_2 as the carrier gas. The epilayers were grown at 1550 °C under 80 Torr pressure, which would result in nominal planar growth rate of 3–4 μm/h. The growth lasted for 1 h.

Figure 28.14 shows tilted top views of selectively grown SiC window stripes along different directions. When the window stripes are parallel to the $\langle 11\bar{2}0\rangle$ miscut direction, the growth on the exposed area followed the substrate orientation, and the top surface was smooth and specular (Fig. 28.14a). However, when the window stripes were aligned along $\langle 1\bar{1}00\rangle$, the growth on the window stripes developed (0001) facet (Fig. 28.14c). For window stripes along a direction between $\langle 11\bar{2}0\rangle$ and $\langle 1\bar{1}00\rangle$, (0001) facet intersected the 8° off (0001) fronts and the extent of (0001) facet depended on the angle between the stripe orientation and the $\langle 11\bar{2}0\rangle$ miscut direction.

To explain the formation of the (0001) facets, the effect of substrate offcut orientation has to be taken into account. As mentioned above, off-axis 4H-SiC(0001) 8° miscut towards $\langle 11\bar{2}0\rangle$ was used in this work. When the stripe direction is along $\langle 11\bar{2}0\rangle$ miscut, there is no restriction on the step-flow growth. New steps are continuously available and facet develops starting from the edges of the selective epitaxial layer. However, when the selective growth opening is along the $\langle 1\bar{1}00\rangle$ direction, step flow was restricted within the opening window and pure step-flow growth makes all steps to move out of the edge, as depicted in Fig. 28.15. Cross-sectional scanning electron microscopy (SEM) of selectively grown films in $\langle 1\bar{1}00\rangle$ strip openings indicated good agreement of w/h ratio with the schematic shown in Fig. 28.15. When the growth opening window is aligned between $\langle 1\bar{1}00\rangle$ and $\langle 11\bar{2}0\rangle$ with an angular displacement larger than 20° from these two orientations, step-flow growth is dominant, although partially restricted due to the angu-

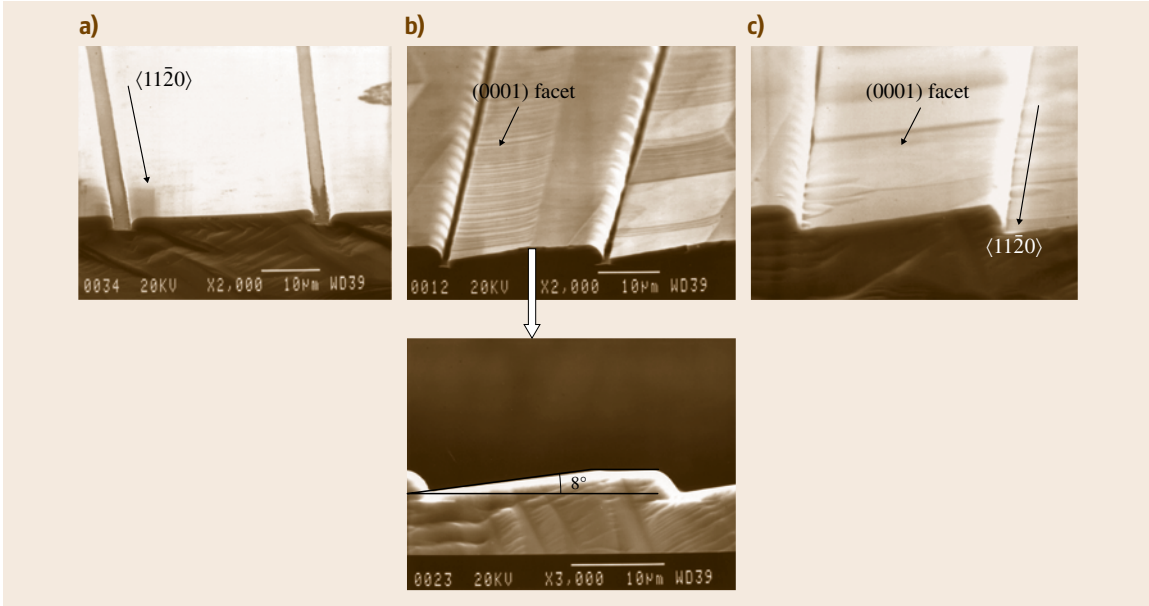


Fig. 28.14a–c Top view of the selective growth of 4H-SiC when window openings are along: **(a)** $\langle 11\bar{2}0\rangle$ miscut direction, **(b)** direction between $\langle 11\bar{2}0\rangle$ and $\langle 1\bar{1}00\rangle$, **(c)** $\langle 1\bar{1}00\rangle$ direction

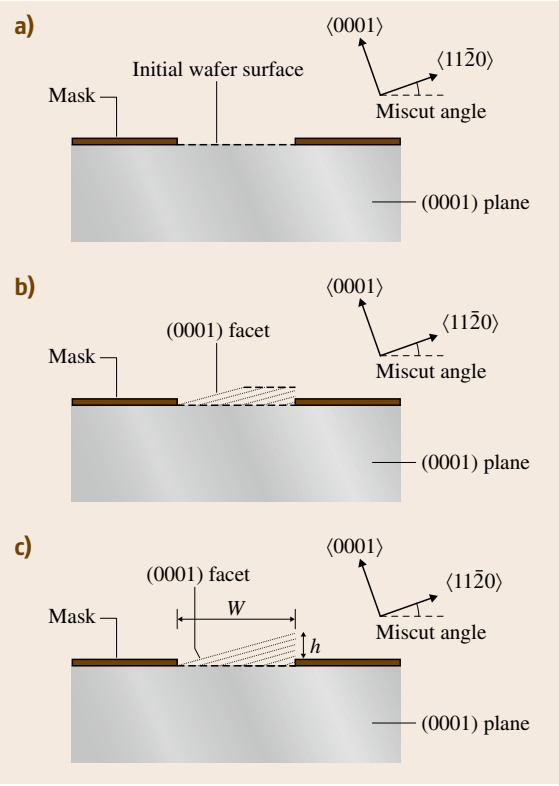


Fig. 28.15a–c Schematic images of the (0001) facet formation on 4H-SiC off (0001) axis towards ⟨11$\bar{2}$0⟩ substrate: **(a)** after selective growth, **(b)** after selective growth for a short time, **(c)** after selective growth for a longer time

lar displacement between step orientation and opening window orientation. Therefore, (0001) facet was formed within the growth window, whereas the percentage of the window occupied by (0001) facet does not increase significantly with increasing angular displacement from ⟨11$\bar{2}$0⟩.

The morphology of growth on (0001) facet was rougher, whereas smoother surface was observed on 8° off-axis growth front (Fig. 28.14a–c). It is likely that some 3C-SiC may have also nucleated on (0001) facet at relatively low temperature (≈ 1550 °C). Similar facet formation was also reported by *Chen* et al. [28.136] during SiC deposition on mesa structures of 4H-SiC(0001) substrate. Since step-flow growth dominated on the off-axis SiC surface, the flat and specular epilayers without 3C-SiC were grown on the off-axis surface. Therefore, when selective epitaxial growth on planar off-axis substrate is designed for device fabrication, growth

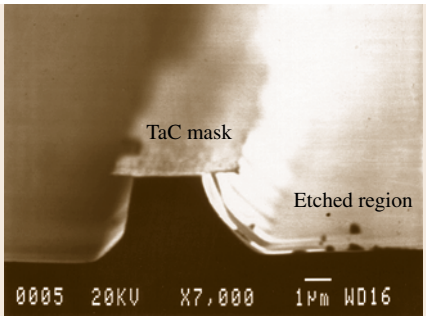


Fig. 28.16 In situ etching, instead of growth, occurs if SiH_4 flow is reduced by half compared with that used for Fig. 28.14. Note that the mask is intact after etching. SiH_4 flow rate: 0.6 sccm

window openings should be aligned along the miscut orientation.

It is worth mentioning that the TaC mask can also act as an in situ etching mask instead of a selective growth mask. When the silane flow rate was reduced to half that used in Fig. 28.14 under otherwise identical conditions, 3 μm/h etching was obtained in unmasked region (Fig. 28.16). The mask itself was not etched, and etching of SiC under the mask left the mask hanging over the edge of the mesa. The mask peeled off during dicing for SEM observation, indicating that it was intact after etching. In situ etching studies using various gases have been carried out previously [28.95], and it was pointed out that the etch rate increases with increasing temperature under otherwise identical conditions. On the other hand, reactive atomic hydrogen is concluded to play a key role in etching of SiC. Therefore, the most plausible reasons for selective etching of SiC are: (1) the local temperature of the window opening region is higher than the nominal measured temperature of the susceptor since the conditions resulting in the etching of TaC-coated wafer are still within the growth window for a bare SiC substrate in our horizontal cold-wall CVD system, and (2) Ta at high temperature may produce atomic hydrogen that may enhance the etching rate of SiC.

28.4.4 Effects of Mask-to-Window Ratio (*M* : *W*) on SiC Selective Growth

As mentioned previously, selective in situ etching occurred with lower SiH_4 flow, even though the same conditions result in growth when a bare SiC substrate is used. It is evident that the mask itself has an influence on the selective growth and/or etching. In order

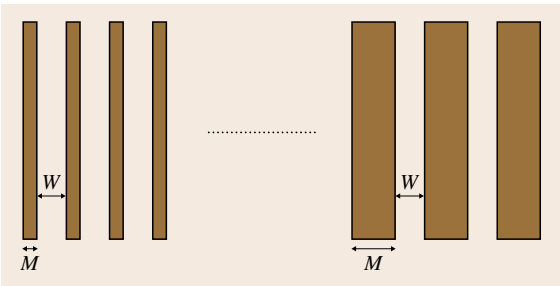


Fig. 28.17 Schematic of the linear pattern with varied mask (M) and window opening (W) width. M and W varied from 2 to 1000 μm. Pitch width (P) = mask width (M) + window opening width (W)

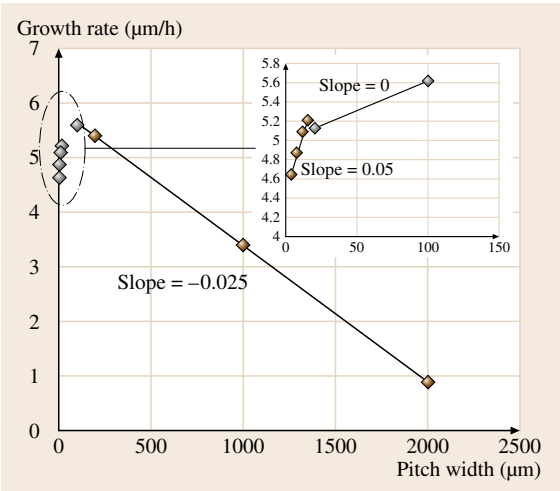


Fig. 28.18 Plot of selective growth rate as a function of pitch width. Pitch width (P) = mask width (M) + window width (W). $M : W = 1$. Flow rate is 2.24 sccm for both SiH_4 and C_3H_8. Growth temperature and pressure are 1833 K and 80 Torr, respectively. The *insert* shows an expanded plot for pitch width ≤ 100 μm

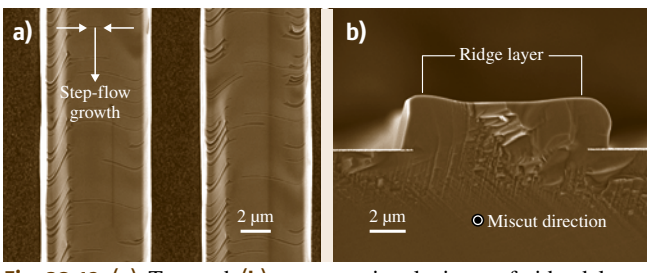


Fig. 28.19 **(a)** Top and **(b)** cross-sectional views of ridged layer grown an 4H-SiC(0001) substrate miscut towards ⟨11$\bar{2}$0⟩ direction. Stripes are along ⟨11$\bar{2}$0⟩ miscut direction

to identify the effects of the mask during the process, a linear pattern with varied mask and window opening width (Fig. 28.17) was made on the same substrate. This assures that the local conditions, such as temperature, precursor flow, pressure etc., for each window opening are the same. Therefore, different growth and/or etching behaviors, if any, are basically due to the existence of the mask. The growth was carried out on such a patterned substrate at temperature of 1560 °C under 80 Torr while the flow rate was kept at 2.24 sccm for both SiH_4 and C_3H_8. Figure 28.18 shows a plot of selective growth rate versus pitch width (pitch width = mask width (M) + window width (W)) when the mask width-to-window width ratio ($M : W$) was kept at 1. As can be seen, the selective growth rate increases with increasing pitch width when the pitch width is below 100 μm, indicating that the growth process rather than etching is dominant under these conditions and is enhanced by diffusion of species from the mask.

The enhanced growth due to the supply of the reactants from the mask is also illustrated by the ridge growth at the edges of the mask, as shown in Fig. 28.19. Since the window stripes were patterned along the ⟨11$\bar{2}$0⟩ miscut direction, miscut steps were provided continuously. Excess species supplied laterally from the mask could be easily incorporated at step sites near the edge. Therefore, the step-flow growth velocity became higher than that at the center area of the window opening. Figure 28.20 shows a schematic diagram of the vicinal surface and ridge growth due to the diffusion of species from the mask to the window. Step-flow growth occurs not only along but also perpendicular to the miscut direction.

However, the selective growth rate decreases with further increasing of the pitch width (≥ 200 μm). The growth rate reduces from 5.5 to 0.9 μm/h when the pitch width increases from 200 to 2000 μm. As is well known, both growth and etching process exist during SiC epitaxy and the etching process could be dominant under certain circumstances (e.g., higher temperature or lower precursor flow). In this experiment, the growth conditions were identical for all window openings since they were patterned on the same substrate and growth was carried out in the same run. It is believed that the decreased growth rate with increasing mask width is due to the enhanced etching by the mask. The enhanced etching process is probably caused by the production of atomic hydrogen by tantalum at high temperature, similar to the well-known hydrogenation catalysis by metals such as palladium [28.137]. Therefore, a larger area of the mask results in more atomic hydrogen and thus more

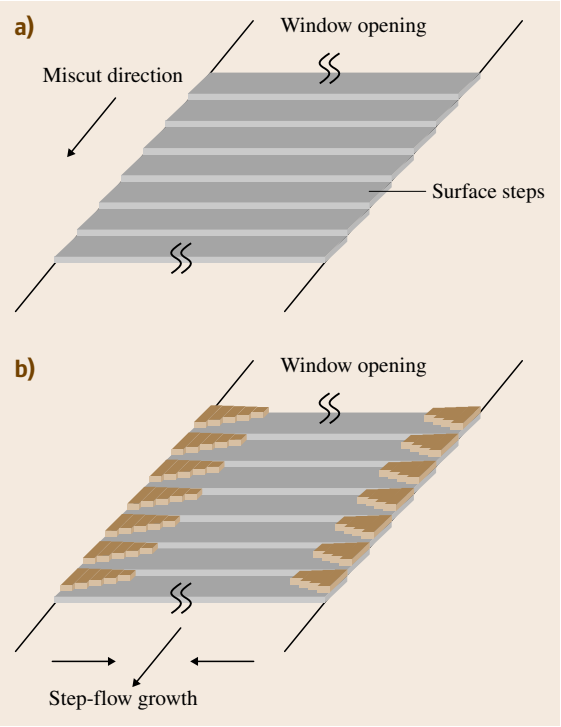


Fig. 28.20a,b Schematic of (a) (0001) vicinal surface and (b) ridge growth of the edge of the mask. Note that step-flow growth is along the directions parallel and perpendicular to miscut direction due to excess supply of species from the mask to the edge of window openings

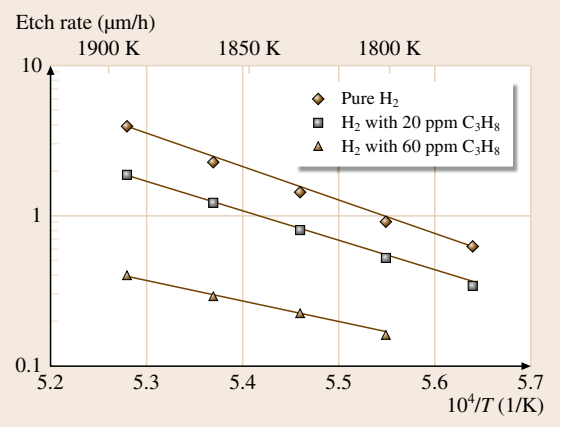


Fig. 28.21 Arrhenius plot of the etch rate of 4H-SiC as a function of temperature at different C_3H_8 flows. Reactor pressure is 100 Torr

etching of SiC in the vicinity. It is worth mentioning that significant etching of about 30 μm in 30 min has been obtained when growth was carried out on a patterned substrate with > 90% of the surface covered by the mask [28.90].

Based on the studies of growth rate as a function of mask layout, it is evident that the growth process is dominant and that growth is enhanced by reactant diffusion from the mask when the mask is narrow (< 100 μm in this study). This increase in growth rate is limited by the surface diffusion rate of reactant species on the mask. However, the etching process competes with the growth process when the mask area becomes larger, and the growth rate decreases (or even etching occurs) with further increases in mask width.

28.4.5 Effects of C/Si Ratio on SiC Selective Growth

It has been found from in situ etching study of SiC [28.95] that adding a small amount of C_3H_8 increases the hydrocarbon pressure and hence suppresses the etching of SiC. Figure 28.21 shows the variation of etch rate of a bare 4H-SiC substrate at different C_3H_8 flows, for etching carried out at temperature range of 1800–1900 K in hydrogen ambient. Therefore, changing the C_3H_8 flow during the growth with fixed SiH_4 flow would change the formation of hydrocarbon in the chamber and hence the etching of SiC. Figure 28.22 shows the dependence of selective growth rate on C/Si ratio at different pitch widths and $M : W$ ratios. When the C/Si ratio is low (= 1), the etching process is dominant and no mask-enhanced growth is observed for narrow mask width (≤ 100 μm), as observed previously. The selective growth rate decreases with increasing mask width, and almost no growth is obtained when the mask width was increased to 1000 μm. On a nonmasked wafer, such growth conditions would result in about 3 μm/h growth rate. With increasing of the C/Si ratio, as expected, the growth rate increases for all investigated pitch widths. Mask-enhanced growth for pitch width ≤ 100 μm is observed for C/Si ratio of both 3 and 6, and the growth rate saturates with further increasing of the mask width.

Decreased growth rate with increasing $M : W$ ratio for pitch width of 500 μm is obtained for a C/Si ratio of 1 and 3, as shown in Fig. 28.22. However, mask-enhanced growth, instead of etching, is achieved for pitch width of 500 μm for a C/Si ratio of 6, indicating

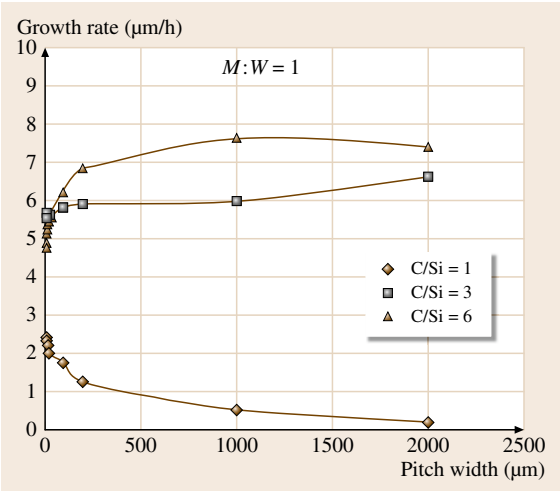


Fig. 28.22 Plot of selective growth rate as a function of pitch width at various C/Si ratios. Pitch width P = mask width (M) + window width (W). $M : W = 1$. Flow rate of SiH_4 is kept at 2.24 sccm. Growth temperature is 1813 K. Growth pressure is 80 Torr

that the etching process during epitaxy is suppressed by additional C_3H_8 flow.

28.4.6 Mechanism of Selective Etching and Effect of Atomic Hydrogen

It is worth pointing out that growth is obtained (Fig. 28.23) for extreme $M : W = 1000\,\mu m : 5\,\mu m$ at a C/Si ratio of 6 with SiH_4 flow of 2.24 sccm, while selectivity is insignificantly deteriorated. It is evident from the experiment that in situ selective etching is enhanced by atomic hydrogen produced by the mask under high temperature, which could be suppressed by increasing the C_3H_8 flow. Increasing the C_3H_8 flow is believed to be the most effective way to suppress in situ etching of SiC using a TaC mask without greatly deteriorating selectivity.

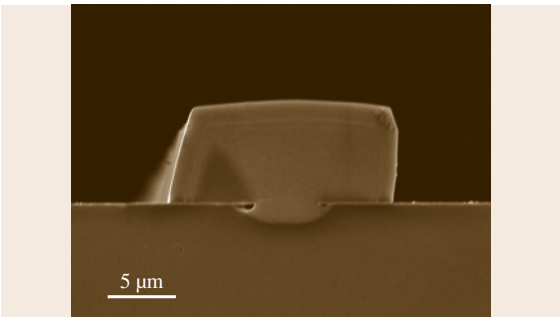


Fig. 28.23 Cross-sectional view of selective growth with $M : W = 1000\,\mu m : 5\,\mu m$ at C/Si = 6. Flow rate of SiH_4 is kept at 2.24 sccm. Growth temperature is 1813 K. Growth pressure is 80 Torr

28.4.7 Fabrication of 4H-SiC p–n Junction Diodes Using Selective Growth

To illustrate the efficacy of selective growth for device fabrication, p–n junction diodes have been fabricated using selectively grown SiC. The starting wafer is commercial 8° off (0001)Si face, p-epitaxial layer grown on p^+ 4H-SiC substrate from CREE Research Inc. The nominal thickness and Al doping of the p-epilayer are 12 μm and $9.3 \times 10^{15}\,cm^{-3}$, respectively. Fabrication was started by cleaning the wafers using a standard solvent degrease, Piranha clean, and RCA clean. Alignment marks were then trenched using CHF_3/O_2 plasma through a titanium/nickel transfer mask while the metal mask was prepared using a lift-off process. Next, refill regions were formed by reactive ion etch (RIE) through an oxide mask. In this step, ≈ 600 Å tantalum was first deposited using an e-beam evaporator and a masking oxide was then deposited, patterned, and etched using a combination of dry and wet processes to open the refill window. Two etch steps followed to form refill trench. Tantalum and SiC trench were etched using CF_4/O_2 and CHF_3/O_2 plasma, respectively. The etched trenches were about 1.5 μm deep. After the trench etching, the masking oxide was stripped using buffered oxide etch (BOE). Since both tantalum and SiC are inert to BOE at room temperature, it is safe to use BOE for oxide removal. Next, the wafer was loaded into the horizontal cold-wall reactor and tantalum film was then converted to tantalum carbide by exposing the wafer in propane/hydrogen ambient at 1300 °C for 15 min as described previously. Epitaxial growth of SiC was carried out at temperature in the range of 1500–1600 °C. Silane, propane, and nitrogen were used as the precursors with hydrogen as the carrier gas. The flow rates of silane, propane, nitrogen, and hydrogen were kept at 2.2, 3.7, 8sccm, and 12.5 slm, respectively, during the growth. The RIE-etched trenches were refilled by nitrogen-doped n-type epitaxial film grown by selective epitaxy. The doping concentration was measured by mercury probe capacitance–voltage (C–V) using an epilayer grown on planar substrate under the same conditions. The TaC mask was then removed after selective growth using wet etchant. Subsequently, diodes were fabricated using standard contact procedure.

The forward and reverse current–voltage (I–V) characteristics of a square-trench (250 μm × 250 μm) refilled diode were first compared with those of a mesa etched PIN circular diode. Similar I–V characteristics were observed for both diodes, indicating that damage from the RIE etching might have been cured during epitaxial growth and that the junction interface is as good as that in a PIN diode fabricated by planar epitaxial growth. The difference in the forward I–V characteristic at higher current is possibly due to the higher series resistance of the p-type base of the trench refilled diode.

28.5 Conclusions

In this chapter, some basic properties of SiC and its epitaxial growth process have been described. Most of the early epitaxial growth was carried out using propane and silane in a horizontal cold-wall reactor. In recent years, hot-wall reactors have been developed for SiC growth, allowing much higher growth rate with very good surface morphology and very low background doping concentration. High-voltage (> 10 kV) power devices have been demonstrated. Epitaxial growth of SiC on bulk SiC substrates has advanced significantly during the last decade, and commercial SiC devices have been introduced by several manufacturers. Further refinement of the basic reactor geometry and the growth process will be necessary to fully exploit the advantages of SiC over Si in devices. One such improvement may be the introduction of chlorine-containing precursors in addition to the more conventional silane and propane precursors. Some aspects of selective growth of SiC using TaC masks developed at the author's laboratory (mostly unpublished) are also reviewed.

References

28.1 T.P. Chow: SiC and GaN high voltage power switching devices, Mater. Sci. Forum **338–342**, 1155–1160 (2000)

28.2 R.G. Humphreys, D. Bimberg, W.J. Choyke: Wavelength modulated absorption in SiC, Solid State Comm. **39**, 163–167 (1981)

28.3 W.J. Choyke, L. Patrick: Exciton recombination radiation and phonon spectrum of 6H-SiC, Phys. Rev. **127**, 1868–1877 (1962)

28.4 W.V. Münch, I. Pfaffeneder: Breakdown field in vapor grown silicon carbide p-n junctions, J. Appl. Phys. **48**, 4831–4833 (1977)

28.5 D.K. Ferry: High field transport in wide band gap semiconductors, Phys. Rev. B1 **12**, 2361–2369 (1975)

28.6 R.P. Joshi: Monte Carlo calculations of the temperataure and field dependent electron transport parameters for 4H-SiC, J. Appl. Phys. **78**, 5518–5521 (1995)

28.7 E. Moruan, O. Noblanc, C. Dua, C. Brylinski: SiC microwave power devices, Mater. Sci. Forum **353–356**, 669–674 (2001)

28.8 G.A. Slack: Thermal conductivity of pure and impure silicon, silicon carbide, and diamond, J. Appl. Phys. **35**, 3460 (1964)

28.9 M. Bhatnagar, B.J. Baliga: Comparison of 6H-SiC, 3C-SiC and Si power devices, IEEE Trans. Electron. Dev. **40**(3), 645–655 (1993)

28.10 T. Kimoto, T. Urushidani, S. Kobayashi, H. Matsunami: High voltage SiC Schottky barrier diodes with low on-resistances, IEEE Electron. Dev. Lett. **14**, 548–550 (1993)

28.11 D. Alok, B.J. Baliga, P.K. Mclarty: A simple edge termination for silicon carbide devices with nearly ideal breakdown voltages, IEEE Electron. Dev. Lett. **15**, 394–395 (1994)

28.12 R.J. Trew, J.-B. Yan, P.M. Mock: The potential of diamond and SiC electronic devices for microwave and millimeter wave power applications, Proc. IEEE **79**(5), 598–620 (1991)

28.13 J.M. McGarrity, F.B. McLean, W.M. DeLancey, J. Palmour, C. Carter, J. Edmond, R.R. Oakley: SiC JFET radiation response, IEEE Trans. Nucl. Sci. **39**(6), 1974–1981 (1992)

28.14 See for example, http://www.cree.com/ and http://www.infineon.com/

28.15 H. Matsunami, T. Kimoto: Step controlled epitaxial growth of SiC: High quality homoepitaxy, Mater. Sci. Eng. **R20**(3), 125–166 (1997)

28.16 W.J. Choyke, G. Pensl: Physical properties of SiC, MRS Bull. **22**(3), 25–29 (1997)

28.17 C.H. Park, B.H. Cheong, K.H. Lee, K.J. Chang: Structural and electronic propertires of cubic, 2H, 4H and 6H SiC, Phys. Rev. B **49**(7), 4485–4493 (1994)

28.18 W.S. Yoo, H. Matsunami: Polytype-controlled single crystal growth of silicon carbide using 3C-6H solid state phase transformation, J. Appl. Phys. **70**(11), 7124–7131 (1991)

28.19 W.S. Yoo, H. Matsunami: Solid state phase transformation in cubic silicon carbide, Jpn. J. Appl. Phys. Part I (regular papers and short notes) **30**, 545–553 (1991)

28.20 A. Itoh, H. Matsunami: Single crystal growth of SiC and electronic devices, Crit. Rev. Solid State Mater. Sci. **22**(2), 111–197 (1997)

28.21 P.G. Neudeck: Electrical impact of SiC structural defects on high electric field devices, Mater. Sci. Forum **338–342**, 1161–1166 (2000)

28.22 J.A. Powell, H.A. Will: Low temperature solid state phase transformations in 2H SiC, J. Appl. Phys. **43**(4), 1400–1408 (1972)

28.23 M. Dudley, X. Huang: Characterization of SiC using synchrotron white beam x-ray topography, Mater. Sci. Forum **338–342**, 431–436 (2000)

28.24 I. Kamata, H. Tsuchida, T. Jikimoto, K. Izumi: Structural transformation of screw dislocation via thick 4H-SiC epitaxial growth, Jpn. J. Appl. Phys. **39**, 6496–6500 (2000)

28.25 P. Pirouz: On micropipes and nanopipes in SiC and GaN, Philos. Mag. A **78**, 727–736 (1998)

28.26 P.G. Neudeck, H. Wei, M. Dudley: Study of bulk and elementary screw dislocation assisted reverse breakdown in low-voltage (< 250 V) 4H-SiC pn junction diodes: DC properties, IEEE Trans. Electron. Dev. **46**(3), 478–484 (1999)

28.27 U. Zimmermann, A. Hallen, A.O. Konstantinov, B. Breitholtz: Investigation of microplasma breakdown in 4H SiC, Mater. Res. Soc. Symp. Proc. **512**, 151–156 (1998)

28.28 A.O. Konstantinov, Q. Wahab, N. Nordell, U. Lindefelt: Study of Avalanche breakdown and impact ionization in 4H SiC, J. Electron. Mater. **27**(4), 335–341 (1998)

28.29 P.G. Neudeck, J.A. Powell: Performance limiting micropipe defects in SiC wafers, IEEE Electron. Dev. Lett. **15**, 63–65 (1994)

28.30 W. Si, M. Dudley, R. Glass, V. Tsvetkov, C. Carter Jr: Hollow core screw dislocations in 6H-SiC single crystals: A test of Frank's theory, J. Electon. Mater. **26**, 128–133 (1997)

28.31 W. Si, M. Dudley: Experimental studies of hollow core screw dislocations in 6H- and 4H-SiC single crystals, Mater. Sci. Forum **264–268**, 429–432 (1998)

28.32 C.M. Schnabel, M. Tabib-Azar, P.G. Neudeck, S.G. Bailey, H.B. Su, M. Dudle, R.P. Raffaelle: Correlation of EBIC and SWBXT imaged defects and epilayer growth pits in 6H-SiC Schottky diodes, Mater. Sci. Forum **338–342**, 489–492 (2000)

28.33 J.A. Powell, D.J. Larkin: Process induced morphological defects in epitaxial CVD silicon carbide, Phys. Status Solidi (b) **202**, 529–548 (1997)

28.34 T. Kimoto, N. Miyamoto, H. Matsunami: Performance limiting surface defects in SiC epitaxial pn junction diodes, IEEE Trans. Electron. Dev. **46**(3), 471–477 (1999)

28.35 S. Nishino, J.A. Powell, W. Will: Production of large area single crystal of 3C-SiC for semiconductor devices, Appl. Phys. Lett. **42**, 460 (1983)

28.36 S. Nishino, K. Matsumoto, Y. Chen, Y. Nishio: Epitaxial growth of 4H-SiC by sublimation close space technique, Mater. Sci. Eng. B **61/62**, 121–124 (1999)

28.37 H. Nakazawa, M. Suemitsu, S. Asami: Formation of high quality SiC on Si(001) at 900 °C using monomethylsilane gas source MBE, Mater. Sci. Forum **338–342**, 269–272 (2000)

28.38 M.E. Okhuysen, M.S. Mazzola, Y.-H. Lo: Low temperature growth of 3C-SiC on silicon for advanced substrate development, Mater. Sci. Forum **338–342**, 305–308 (2000)

28.39 M.-A. Hasan, A. Faik, D. Purser, D. Lieu: Heteroepitaxy of 3C-SiC on Si (100) using porous Si as a compliant seed crystal, Tech. Dig. Int. Conf. SiC Relat. Mater. ICSCRM2001 (Tsukuba 2001) pp. 492–493

28.40 Y. Ishida, K. Kushibe, T. Takahashi, H. Okumura, S. Yoshida: 3C-SiC homoepitaxial growth by chemical vapor deposition and Schottky barrier junction characteristics, Mater. Sci. Forum **389–393**, 275–278 (2002)

28.41 H. Nagasawa, K. Yagi, T. Kawahara: 3C-SiC heteroeptaxial growth on (001) Si undulant substrates, J. Cryst. Growth **237–239**, 1244–1249 (2002)

28.42 H. Nagasawa, K. Yagi, T. Kawahara, N. Hatta, G. Pensl, W.J. Choyke, T. Yamada, K.M. Itoh, A. Schoner: *Silicon Carbide: Recent Major Advances* (Springer, Berlin, Heidelberg 2004) p. 207

28.43 F.R. Chien, S.R. Nutt, J.M. Carulli Jr., N. Bunchan, C.P. Beetz Jr., W.S. Yoo: Heteroepitaxial growth of beta SiC films on TiC substrates: Interface structure and defects, J. Mater. Res. **9**(8), 2086–2095 (1994)

28.44 C. Hallin, A.O. Konstantinov, O. Kordina, E. Janzen: Mechanism of cubic SiC nucleation on off-axis substrates, Proc. 6th Int. Conf. SiC Relat. Mater. 1995, Inst. Phys. Conf. Ser. **142**, 85–88 (1996)

28.45 J.A. Powell, D.J. Larkin, P.B. Abel, L. Zhou, P. Pirouz: Effect if tilt angle on the morphology of SIC epitaxial films grown on vicinal (0001) SiC substrates. In: *Silicon Carbide and Related Materials*, Inst. Phys. Conf. Ser., Vol. 142 (1995) pp. 77–80

28.46 V.F. Tsvetkov, S.T. Allen, H.S. Kong, C.H. Carter Jr.: Recent progress in SiC crystal growth, Proc. 6th Int. Conf. SiC Relat. Mater. 1995, Inst. Phys. Conf. Ser. **142**, 17–22 (1996)

28.47 D.J. Larkin: An overview of SiC epitaxial growth, MRS Bulletin **22**(3), 36–41 (1997)

28.48 V. Heine, C. Cheng, R.J. Needs: The preference of SiC for growth in the metastable cubic form, J. Am. Ceram. Soc. **74**, 2630–2633 (1991)

28.49 K. Wada, T. Kimoto, K. Nishikawa, H. Matsunami: Epitaxial growth of 4H-SiC on 4° off-axis (0001) and (000-1) substrates by hot wall CVD, Mater. Sci. Forum **527–529**, 219–222 (2006)

28.50 S. Rendakova, V. Ivantsov, V. Dmitriev: High quality 6H- and 4H-SiC pn structures with stable elelctric breakdown grown by liquid phase epitaxy, Mater. Sci. Forum **264–268**, 163–166 (1998)

28.51 D.H. Hofmann, M.H. Muller: Prospects of the use of liquid phase techniques for the growth of bulk silicon carbide crystals, Mater. Sci. Eng. B **61/62**, 29–39 (1999)

28.52 R. Yakimova, M. Syväjärvi, S. Redankova, V.A. Dimitriev, A. Henry, E. Janzen: Micropipe healing in liquid phase epitaxial growth of SiC, Mater. Sci. Forum **338–342**, 237–240 (2000)

28.53 A. Tanaka, T. Ataka, E. Ohkura, H. Katsuno: Growth modes of silicon carbide in low-temperature liquid phase epitaxy, Jpn. J. Appl. Phys. **43**(11A), 7670–7671 (2004)

28.54 O. Filip, B. Epelbaum, M. Bickermann, A. Winnacker: Micropipe healing in SiC wafers by liquid-phase epitaxy in Si–Ge melts, J. Cryst. Growth **271**, 142–150 (2004)

28.55 T. Hatayama, S. Nakamura, K. Kurobe, T. Kimoto, T. Fuyuki, H. Matsunami: High-temperature surface structure transitions and growth of alpha-SiC (0001) in ultrahigh vacuum, Mater. Sci. Eng. B **61/62**, 135–138 (1999)

28.56 S. Nakamura, T. Hatayama, T. Kimoto, T. Fuyuki, H. Matsunami: Growth of SiC on 6H-SiC $\{01\bar{1}4\}$ substrates by gas source molecular beam epitaxy, Mater. Sci. Forum **338–342**, 201–204 (2000)

28.57 T. Sugii, T. Aoyama, T. Ito: Low-temperature growth of beta-SiC on Si by gas-source MBE, J. Electrochem. Soc. **137**(3), 989–992 (1990)

28.58 H. Nakazawa, M. Suemitsu, S. Asami: Formation of high quality SiC on Si (001) at 900 °C using monomethylsilane gas-source MBE, Mater. Sci. Forum **338–342**, 269–272 (2000)

28.59 C. Hallin, I.G. Ivanov, T. Egillson, A. Henry, O. Kordina, E. Jansen: The material quality of CVD grown SiC using various precursors, J. Cryst. Growth **183**, 163 (1998)

28.60 Y. Gao, J.H. Edgar: Selective epitaxial growth of SiC: Thermodyanamic analysis of the Si-C-Cl-H and Si-C-Cl-H-O systems, J. Electrochem. Soc. **144**(5), 1875–1880 (1997)

28.61 K. Yagi, H. Nagasawa: 3C-SiC growth by alternate supply of SiH_2Cl_2 and C_2H_2, J. Cryst. Growth **174**, 653–657 (1997)

28.62 T. Miyanagi, S. Nishino: Hotwall CVD growth of 4H-SiC using Si2Cl6-C3H8-H2 system, Mater. Sci. Forum **389–393**, 199–202 (2002)

28.63 C. Sartel, V. Souliere, Y. Monteil, H. El-Harrouni, J.M. Bluet, G. Guillot: Epitaxial growth of 4H-SiC with hexamethyldisilane, Mater. Sci. Forum **389–393**, 263–266 (2002)

28.64 R. Rodriguez-Clemente, A. Figueras, S. Garelik, B. Armas, C. Combescure: Influence of temperature and tetramethylsilane partial pressure on the beta SiC depositin by cold wall chemical vapor deposition, J. Cryst. Growth **125**, 532–542 (1992)

28.65 T. Hatayama, H. Yano, Y. Uraoka, T. Fuyuki: High purity SiC epitaxial growth by chemical vapor deposition using CH_3SiH_3 and C_3H_3 sources, Mater. Sci. Forum **527–529**, 203–206 (2006)

28.66 See for example, http://www.saespuregas.com/

28.67 H. Matsunami, T. Kimoto: Step controlled epitaxial growth of SiC: High quality homoepitaxy, Mater. Sci. Eng. **R20**(3), 125–166 (1997)

28.68 S. Nakamura, T. Kimoto, H. Matsunami: Fast growth and doping characteristics of SiC in a horizontal cold wall CVD, Mater. Sci. Forum **389–393**, 183–186 (2002)

28.69 R. Rupp, A. Wiedenhofer, P. Friedrichs, D. Peters, R. Schorner, D. Stephani: Growth of SiC epitaxial layers in a vertical cold wall reactor suited for high voltage applications, Mater. Sci. Forum **264–268**, 89–96 (1998)

28.70 C. Sartel, J.M. Bluet, V. Souliere, I. El-Harrouni, Y. Monteil, M. Mermoux, G. Guillot: Characterization of homoepitaxial 4H-SiC layer grown from silane/propane system, Mater. Sci. Forum **433–436**, 165–168 (2003)

28.71 B. Thomas, W. Bartsch, R. Stein, R. Schorner, D. Stephani: Properties and suitability of 4H-SiC epitaxial layers grown at different CVD systems for high voltage applications, Mater. Sci. Forum **457–460**, 181–184 (2004)

28.72 O. Kordina, C. Hallin, A. Henry, J.P. Bergman, I. Ivanov, A. Ellison, N.T. Son, E. Janzen: Growth of SiC by hot-wall, CVD and HTCVD, Phys. Status Solidi (b) **202**, 321–334 (1996)

28.73 T. Kimoto, S. Nakazawa, K. Fujihira, T. Hirao, S. Nakamura, Y. Chen, H. Matsunami: Recent achievement and future challenges in SiC homoepitaxial growth, Mater. Sci. Forum **389–393**, 165–170 (2002)

28.74 A. Shoner, A. Konstantinov, S. Karlsson, R. Berge: Highly uniform epitaxial SiC-layer growth in a hot wall CVD reactor with mechanical rotation, Mater. Sci. Forum **389–393**, 187–190 (2002)

28.75 B. Thomas, C. Hecht: Epitaxial growth of n-type 4H-SiC on 3, wafers for power devices, Mater. Sci. Forum **483–485**, 141–146 (2005)

28.76 A. Ellison, J. Zhang, J. Peterson, A. Henry, Q. Wahab, J.P. Bergman, Y.N. Makarov, A. Vorob'ev, A. Vehanen, E. Janzen: High temperature CVD growth of SiC, Mater. Sci. Eng. B **61/62**, 113–120 (1999)

28.77 H. Fujiwara, K. Danno, T. Kimoto, T. Tojo, H. Matsunami: Fast epitaixal growth of thick 4H-SiC with specular surface by chimney-type vertical hot-wall chemical vapor depositon, Mater. Sci. Forum **457–460**, 205–208 (2004)

28.78 E. Janzén, J.P. Bergman, Ö. Danielsson, U. Forsberg, C. Hallin, J. ul Hassan, A. Henry, I.G. Ivanov, A. Kakanakova-Georgieva, P. Persson, Q. ul Wa-

hab: SiC and III-nitride growth in a hot-wall CVD reactor, Mater. Sci. Forum **483–485**, 61–66 (2005)
28.79 K. Danno, T. Kimoto, K. Asano, Y. Sugawara, H. Matsunami: Fast epitaxial growth of high-purity 4H-SiC(0001) in a vertical hot-wall chemical vapor deposition, J. Electron. Mater. **34**(4), 324–329 (2005)
28.80 H. Fujiwara, T. Kimoto, T. Tojo, H. Matsunami: Reduction of stacking faults in fast epitaxial growth of 4H-SiC and its impacts on high-voltage Schottky diodes, Mater. Sci. Forum **483–485**, 151–154 (2005)
28.81 I. Bhat, Canhua Li: High growth rate epitaxy of SiC in a vertical hotwall reactor, unpublished
28.82 M. Syvajarvi, R. Yakimova, H. Jacobsson, M.K. Linnarsson, A. Henry, E. Janzén: High growth rate epitaxy of thick 4H-SiC layers, Mater. Sci. Forum **338–342**, 165–168 (2000)
28.83 T. Furusho, T. Miyanagi, Y. Okui, S. Ohshima, S. Nishino: Homoepitaxial growth of cubic silicon carbide by sublimation epitaxy, Mater. Sci. Forum **389–393**, 279–282 (2002)
28.84 E.O. Sveinbjornsson, H.O. Olafsson, G. Gudjonsson, F. Allerstam, P.A. Nilsson, M. Syvajarvi, R. Yakimova, C. Hallin, T. Rodle, R. Jos: High field effect mobility in Si face 4H-SiC MOSFET made on sublimation grown epitaxial material, Mater. Sci. Forum **483–485**, 841–844 (2005)
28.85 D. Ziane, J.M. Bluet, G. Guillot, P. Godignon, J. Monserrat, R. Ciechonski, M. Syvajarvi, R. Yakimova, L. Chen, P. Mawby: Characterizations of SiC/SiO_2 interface quality toward high power MOSFETs realization, Mater. Sci. Forum **457–460**, 1281–1286 (2004)
28.86 R.C. Glass, P. Lu, J.H. Edgar, O.J. Glembocki, P.B. Klein, E.R. Glaser, J. Perrin, J. Chaudhuri: High-speed homoepitaxy of SiC from methyltrichloro-silane by CVD, Int. Conf. Silicon Carbide Relat. Mater. (Pittsburgh 2005)
28.87 R. Myers, O. Kordina, Z. Shishkin, F. Yan, R.P. Devaty, S.E. Saddow: Effects of HCl addictive on the growth rate of 4H-SiC in a hot wall CVD reactor, Int. Conf. Silicon Carbide Relat. Mater. (Pittsburgh 2005)
28.88 A. Veneroni, F. Omarini, M. Masi: Silicon carbide growth mechanisms from SiH_4, $SiHCl_3$ and nC_3H_8, Cryst. Growth Technol. **40**(10/11), 967–971 (2005)
28.89 G. Pensl, W.J. Choyke: Electrical and optical characterization of SiC, Physica B **185**, 264–283 (1993)
28.90 R. Wang, I. Bhat, unpublished results
28.91 D.J. Larkin: SiC dopant incorporation control by site competetion CVD, Phys. Status Solidi (b) **202**, 305–320 (1997)
28.92 T. Troffer, C. Peppermuller, G. Pensi, K. Rottner, A. Schoner: Phosphorus-related donors in 6H-SiC generated by ion implantation, J. Appl. Phys. **80**(7), 3739–3743 (1996)
28.93 M.A. Capano, J.A. Cooper Jr., M.R. Melloch, A. Saxler, W.C. Mitchel: Ionization energies and electron mobililties in phosphorous and nitrogen implanted SiC, J. Appl. Phys. **87**(12), 8773–8777 (2000)
28.94 S. Rao, T.P. Chow, I. Bhat: Dependence of the ionization energy of phosphorous donor in 4H-SiC on doping concentration, Mater. Sci. Forum **527–529**, 597–600 (2006)
28.95 R. Wang: SiC epitaxial growth for power device applications. Ph.D. Thesis (Rensselaer Polytechnic Institute, Troy 2002)
28.96 M.H. Anikin, A.A. Lebedev, A.L. Syrkin, A.V. Suvorov: Investigation of deep levels in SiC by capacitance spectroscopy methods, Sov. Phys. Semicond. **19**, 69–71 (1985)
28.97 W. Suttrop, G. Pensi, P. Lanig: Boron related deep centers in SiC, Appl. Phys. A **51**, 231–237 (1990)
28.98 A. Golz, G. Horstmann, E. Stein von Kamienski, H. Kurz: Oxidation kinetics of 3C, 4H and 6H silicon carbide, Proc. Sixth Int. Conf. Silicon Carbide Relat. Mater. (1996) pp. 633–636
28.99 K. Wada, T. Kimoto, K. Nishikawa, H. Matsunami: Improved surface morphology and background doping concentration in 4H-SiC $(000\bar{1})$ epitaxial growth by hot-wall CVD, Mater. Sci. Forum **483–485**, 85–88 (2005)
28.100 T. Yamamoto, T. Kimoto, H. Matsunami: Impurity incorporation mechanism in step-controlled epitaxy growth temperature and substrate off-angle dependence, Mater. Sci. Forum **264–268**, 111–116 (1998)
28.101 U. Forsberg, Ö. Danielsson, A. Henry, M.K. Linnarsson, E. Janzén: Nitrogen doping of epitaxial silicon carbide, J. Cryst. Growth **236**(1–3), 101–112 (2002)
28.102 U. Forsberg, Ö. Danielsson, A. Henry, M.K. Linnarsson, E. Janzén: Aluminium doping of epitaxial silicon carbide, J. Cryst. Growth **253**(1–4), 340–350 (2003)
28.103 T. Kimoto, T. Yamamoto, Z.Y. Chen, H. Matsunami: 4H-SiC $(11\bar{2}0)$ epitaxial growth, Mater. Sci. Forum **338–342**, 189–192 (2000)
28.104 T. Kimoto, K. Hashimoto, K. Fujihira, K. Danno, S. Nakamura, Y. Negoro, H. Matsunami: Epitaxial growth and characterization of 4H-SiC$(11\bar{2}0)$ and $(03\bar{3}8)$, Mater. Res. Soc. Symp. Proc. **742**, 3–13 (2003)
28.105 Z. Zhang, Y. Gao, A.C. Arjunan, E.Y. Toupitsyn, P. Sadagopan, R. Kennedy, T.S. Sudarshan: CVD growth and characterization of 4H-SiC epitaxial film on $(11\bar{2}0)$ as-cut substrates, Mater. Sci. Forum **483–485**, 113–116 (2005)
28.106 K. Nakayama, Y. Miyanagi, H. Shiomi, S. Nishino, T. Kimoto, H. Matsunami: The development of 4H-SiC $\{03\bar{3}8\}$ wafers, Mater. Sci. Forum **389–393**, 123–127 (2002)
28.107 T. Kimoto, K. Danno, K. Fujihira, H. Shiomi, H. Matsunami: Complete micropipe dissociation in 4H-SiC (03-38) epitaxial growth and its impact on reverse characteristics of Schottky barrier diodes, Mater. Sci. Forum **433–436**, 197–200 (2003)

28.108 T. Kimoto, K. Danno, K. Fujihira, H. Shiomi, H. Matsunami: SiC epitaxy on non-standard surfaces, Mater. Sci. Forum **433–436**, 125–130 (2003)

28.109 E. Arnold, D. Alok: Effect of interface states on electron transport in 4H–SiC inversion layers, IEEE Trans. Electron. Dev. **48**, 1870–1877 (2001)

28.110 T. Kimoto, Y. Kanzaki, M. Noborio, H. Kawano, H. Matsunami: Interface properties of metal–oxide–semiconductor structures on 4H-SiC {0001} and $(11\bar{2}0)$ formed by N_2O oxidation, Jpn. J. Appl. Phys. **44**(3), 1213–1218 (2005)

28.111 K. Fukuda, J. Senzaki, K. Kojima, T. Suzuki: High inversion channel mobility of MOSFET fabricated on 4H-SiC $C(000\bar{1})$ face using H_2 post-oxidation annealing, Mater. Sci. Forum **433–436**, 567–570 (2003)

28.112 T. Kimoto, H. Kawano, J. Suda: 1200V-class 4H-SiC RESURF MOSFETs with low on-resistances, Proc. 17th Int. Symp. Power Semicond. Devices IC's (2005) pp. 159–162

28.113 N. Nordell, S. Karlsson, A.O. Kenstantinov: Growth of 4H and 6H SiC in trenches and around stripe mesas, Mater. Sci. Forum **264–268**, 131–134 (1998)

28.114 Y. Chen, T. Kimoto, Y. Takeuchi, R.K. Malhan, H. Matsunami: Homoepitaxy of 4H-SiC on trenched (0001) Si face substrates by chemical vapor deposition, Jpn. J. Appl. Phys. **43**(7A), 4105–4109 (2004)

28.115 P.G. Neudeck, J.A. Powell, G.M. Beheim, E.L. Benavage, P.B. Abel, A.J. Trunek, D.J. Spry, M. Dudley, W.M. Vetter: Enlargement of step-free SiC surfaces by homoepitaxial web growth of thin SiC cantilevers, J. Appl. Phys. **92**, 2391–2400 (2002)

28.116 P.G. Neudeck, A.J. Trunek, D.J. Spry, J.A. Powell, H. Du, M. Skowronski, N.D. Bassim, M.A. Mastro, M.E. Twigg, R.T. Holm, R.L. Henry, C.R. Eddy Jr.: Recent results from epitaxial growth on step free 4H-SiC mesas, Mater. Res. Soc. Symp. Proc. **911**, B08–03 (2006)

28.117 P.G. Neudeck, A.J. Powell: Homoepitaxial and heteroepitaxial growth on step-free SiC mesas. In: *Silicon Carbide: Recent Major Advances*, ed. by W.J. Choyke, H. Matsunami, G. Pensi (Springer, New York 2003) p. 179

28.118 N.D. Bassima, M.E. Twigg, M.A. Mastro, C.R. Eddy Jr., T.J. Zega, R.L. Henry, J.C. Culbertson, R.T. Holm, P. Neudeck, J.A. Powell, A.J. Trunek: Dislocations in III-nitride films grown on 4H-SiC mesas with and without surface steps, J. Cryst. Growth **304**, 103–107 (2007)

28.119 M.R. Goulding: Selective epitaxial growth of silicon, Mater. Sci. Eng. B **17**(1–3), 47–67 (1993)

28.120 D. Kapolnek, S. Keller, R. Vetury, R.D. Underwood, P. Kozodoy, S.P. Den Baars, U.K. Mishra: Anisotropic epitaxial lateral growth in GaN selective area epitaxy, Appl. Phys. Lett. **71**(9), 1204–1206 (1997)

28.121 O. Nam, T.S. Zheleva, M.D. Bremser, R.F. Davis: Lateral epitaxial overgrowth of GaN films on SiO_2 areas via metalorganic vapor phase epitaxy, J. Electron. Mater. **27**(4), 233–237 (1998)

28.122 Y. Ohshita: Low temperature and selective growth of β-SiC using the $SiH_2Cl_2/i{-}C_4H_{10}/HCl/H_2$, Appl. Phys. Lett. **57**(6), 605–607 (1990)

28.123 J.H. Edgar, Y. Gao, J. Chaudhuri, S. Cheema, P.W. Yip, M.V. Sidorov: Selective epitaxial growth of silicon carbide on SiO_2 masked Si(100): The effects of temperature, J. Appl. Phys. **84**(1), 201–204 (1998)

28.124 K. Teker: Selective epitaxial growth of 3C-SiC on patterned Si using hexamethyldisilane by APCVD, J. Cryst. Growth **257**(3/4), 245–254 (2003)

28.125 S. Nishino, C. Jacob, Y. Okui, S. Ohshima, Y. Masuda: Lateral over-growth of 3C-SiC on patterned Si(111) substrates, J. Cryst. Growth **237–239**(2), 1250–1253 (2002)

28.126 A.R. Bushroa, C. Jacob, H. Saijo, S. Nishino: Lateral epitaxial overgrowth and reduction in defect density of 3C-SiC on patterned Si substrates, J. Cryst. Growth **271**(1/2), 200–206 (2004)

28.127 E. Eshun, C. Taylor, M.G. Spencer, K. Kornegay, I. Ferguson, A. Gurray, R. Stall: Homoepitaxial and selective area growth of 4H and 6H silicon carbide using a resistively heated vertical reactor, Mater. Res. Soc. Symp. **572**, 173–178 (1999)

28.128 Y. Chen, T. Kimoto, Y. Takeuchi, H. Matsunami: Homoepitaxial mesa structures on 4H-SiC (0001) and $(11\bar{2}0)$ substrates by chemical vapor deposition, J. Cryst. Growth, **254**, 115–122 (2003)

28.129 Y. Khlebnikov, I. Khlebnikov, M. Parker, T.S. Sudarshan: Local epitaxy and lateral epitaxial overgrowth of SiC, J. Cryst. Growth **233**, 112–120 (2001)

28.130 R. Zhang, I. Bhat: Atomic force microscopy studies of CdTe films grown by epitaxial lateral overgrowth, J. Electron. Mater. **30**(11), 1370–1375 (2001)

28.131 B.A. Haskell, T.J. Baker, M.B. McLaurin, F. Wu, P.T. Fini, S.P. DenBaars, J.S. Speck, S. Nakamura: Defect reduction in *m*-plane gallium nitride via lateral epitaxial overgrowth by hydride phase epitaxy, Appl. Phys. Lett. **86**(11), 111917–1–111917–3 (2005)

28.132 A.A. Burk Jr., M.J. O'Loughlin, H.D. Nordby Jr.: SiC epitaxial layer growth in a novel multi-wafer vapor-phase epitaxial (VPE) reactor, J. Cryst. Growth **200**, 458–466 (1999)

28.133 L.B. Rowland, G.T. Dunne, J.A. Freitas Jr.: Initial results on thick 4H-SiC epitaxial layers grown using vapor phase epitaxy, Mater. Sci. Forum **338–342**, 161–164 (2000)

28.134 G.R. Gruzalski, D.M. Zehner: Defect states in substoichiometric tantalum carbide, Phys. Rev. B **34**(6), 3841–3848 (1986)

28.135 A.K. Dua, V.C. George: TaC coatings prepared by hot filament chemical vapour deposition: Characteri-

zation and properties, Thin Solid Films **247**, 34–38 (1994)
28.136 Y. Chen, T. Kimoto, Y. Takeuchi, H. Matsunami: Selective homoepitaxy of 4H-SiC on (0001) and (11$\bar{2}$0) masked substrates, J. Cryst. Growth **237–239**, 1224–1229 (2002)
28.137 Y. Fukai: *The Metal-Hydrogen System*, 2nd edn. (Springer, Berlin, Heidelberg 2005)

29. Liquid-Phase Electroepitaxy of Semiconductors

Sadik Dost

The chapter presents a review of the growth of single-crystal bulk semiconductors by liquid-phase electroepitaxy (LPEE). Following a short introduction, early modeling and theoretical studies on LPEE are briefly introduced. Recent experimental results on LPEE growth of GaAs/GaInAs single crystals under a static applied magnetic field are discussed in detail. The results of three-dimensional numerical simulations carried out for LPEE growth of GaAs under various electric and magnetic field levels are presented. The effect of magnetic field nonuniformities is numerically examined. Crystal growth experiments show that the application of a static magnetic field in LPEE growth of GaAs increases the growth rate very significantly. A continuum model to predict such high growth rates is also presented. The introduction of a new electric mobility in the model, i. e., the *electromagnetic* mobility, allows accurate predictions of both the growth rate and the growth interface shape. Space limitation required the citation of a limited number of references related to LPEE [29.1–73]. For details of many aspects of the LPEE growth process and its historical developments, the reader is referred to these references and also others cited therein.

29.1 **Background** 967
29.1.1 Liquid-Phase Electroepitaxy 968
29.1.2 Natural Convection 970
29.1.3 Applied Magnetic Fields 970
29.1.4 Observation of Growth Rate 970
29.2 **Early Theoretical and Modeling Studies** .. 971
29.2.1 Peltier-Induced Growth Kinetics: Electromigration Mechanism 971
29.2.2 A One-Dimensional Model 973
29.2.3 Source-Current-Controlled (SCC) Growth 975
29.3 **Two-Dimensional Continuum Models** 977
29.4 **LPEE Growth Under a Stationary Magnetic Field** 978
29.4.1 Experiments 979
29.5 **Three-Dimensional Simulations** 981
29.5.1 Simulation Model 982
29.5.2 Numerical Method 983
29.5.3 Effect of Magnetic Field Strength .. 984
29.5.4 Evolution of Interfaces 989
29.5.5 Effect of High Electric and Magnetic Field Levels 990
29.6 **High Growth Rates in LPEE: Electromagnetic Mobility** 992
29.6.1 Estimation of the Electromagnetic Mobility Value 993
29.6.2 Simulations of High Growth Rates in a GaAs System 994
References 996

29.1 Background

Liquid-phase electroepitaxy (LPEE) is a solution growth technique by which layers of single crystals are grown at relatively low temperatures. It has great potential for producing high-quality, thick crystals of compound and alloy semiconductors. The LPEE growth technique was developed through the use of electric current for dopant modulation in LPE [29.1], and thereafter became a solution growth technique for growth of binary and ternary semiconductor crystals [29.1–11].

Growth in LPEE is initiated and sustained by passing an electric current through the substrate–solution–source system while the overall furnace temperature is kept constant. Since growth takes place at constant furnace temperature, LPEE has a number of advantages

Table 29.1 Potential applications of alloy semiconductors [29.12]

Semiconductor alloy	Applications
$Ga_{0.96}In_{0.04}As$	Substrates lattice matched to blue diodes and lasers (ZnSe)
$Ga_xIn_{1-x}As$, $InAs_{1-x}P_x$	Substrates suitable for OEICs operating in the 1.3–2 μm region
$Ga_xIn_{1-x}P$, $GaAs_{1-x}P_x$, $Al_xGa_{1-x}As$	Substrates for diodes and lasers operating in the visible range
$Hg_{1-x}Cd_xTe$, $Ga_{1-x}In_xSb$, $InAs_xSb_{1-x}$	Substrates for mid- and far-infrared detectors and lasers
$Si_{1-x}Ge_x$	Substrates for n-channel field-effect transistors (FETs) and efficient optoelectronic devices, solar cells, photodetectors
$Cd_xZn_{1-x}Te$	Substrates for γ- and x-ray detectors

such as steady and controlled growth rate, controlled doping, improved surface morphology and defect structure, low dislocation density, and improved electronic characteristics. In addition, the method is suitable for growing ternary and quaternary alloy crystals with desired compositions. This feature of LPEE has attracted interest in the growth of high-quality semiconductor crystals since the availability of such thick alloy substrates may solve the problems arising from lattice mismatch encountered in the integration of different material layers, and may open new horizons in the fabrication technology of optoelectronic devices and integrated circuits (OEICs). Due to the technological importance of LPEE, a number of experimental and modeling studies have been carried out in recent years.

Alloy semiconductors, such as GaInAs, GaInSb, GaInP, and CdZnTe, grown on commercially available GaAs, GaSb, GaP, and CdTe substrates, are of interest as lattice-matched substrates for novel semiconductor devices in optoelectronics (see [29.12] for more information). For instance, $Ga_{0.47}In_{0.53}As$ ternary alloy grown epitaxially on the lattice-matched InP substrate has been used as an active layer in lasers and photodetectors in optical communication systems [29.12–14]. It is a very good candidate for high-speed transistors because of its high carrier mobility. GaInAs epitaxial layers grown on GaAs substrates have also been used for high-electron-mobility transistors (HEMT) structures with significantly improved performance, and for strained-layer lasers, modulators, and detectors operating in the near-infrared region [29.15]. For this ternary material, however, only thin layers can be grown due to the lattice mismatch. As a result, many problems have been observed in lasers fabricated on such substrates, which are therefore restricted to the 0.8–1.1 μm region [29.16].

High-performance semiconductor lasers operating in the 2–5 μm range are highly desirable in optical-fiber communication systems employing low-loss fluoride-based fibers, laser radar, remote sensing of atmospheric gases, and molecular spectroscopy [29.17–19]. The availability of InAsP, GaInAs, and GaInSb substrates with desired thicknesses and quality would overcome this difficulty. These materials and many other desired alloy semiconductors either cannot be grown commercially, or are grown with inadequate thickness and quality, or cannot be grown reproducibly. LPEE has proven to have the potential for growing such crystals with the desired properties. The alloy materials that can be grown by LPEE are summarized in Table 29.1.

Semiconductors grown by LPEE show advantages over crystals grown by melt growth techniques, namely, lack of detectable electron traps [29.20], low vacancy densities [29.21], low dislocation densities [29.22], and high luminescence efficiency [29.23]. The distinct feature of the LPEE growth process is its capability to grow crystals with uniform crystal compositions. For example, millimeter-thick ingots of GaInAs [29.23–27], AlGaSb [29.28], and AlGaAs [29.29–32] exhibit remarkable compositional uniformity.

The above-mentioned features along with its low hardware cost make LPEE quite attractive for growth of high-quality alloy semiconductors in the form of both bulk crystals and buffer layers. However, reproducible growth of such crystals requires good understanding and control of the key mechanisms governing this process.

29.1.1 Liquid-Phase Electroepitaxy

In a typical LPEE growth system, graphite electrodes are placed at the top and bottom of the growth cell (Fig. 29.1). The substrate is placed at the bottom of the solution and the source material is placed between the solution and the upper electrode. The liquid contact zone located below the substrate provides a uniform, low-resistance electrical contact between the lower face of the substrate and the lower electrode, which is essential for satisfactory growth. The boron nitride *jacket* around the horizontal sandwich layers forms the cell

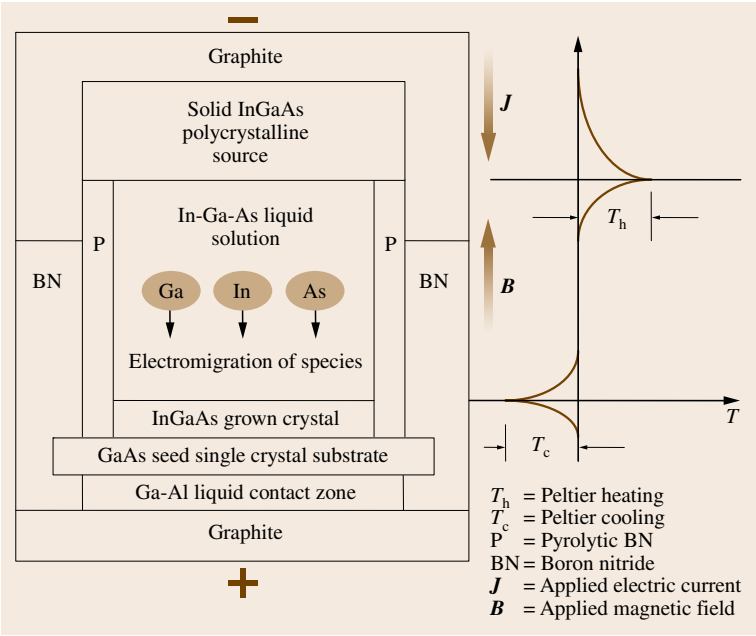


Fig. 29.1 Schematic view of an LPEE crucible for a GaInAs system. Note that the temperature distribution shown is not the actual one; it describes symbolically the Peltier cooling/heating at the interfaces

and acts as both a heat conductor and an electrical insulator. The growth temperature is typically in the range of 650–900 °C, depending on the material to be grown. After the system reaches thermodynamic equilibrium, the electric current is turned on and growth is initiated. During the growth process, the furnace temperature is kept constant. The applied electric current is the sole external driving force and the controlling element of the growth, and makes it possible to achieve a high growth rate and precise control of the process. The electric current passes through the lower electrode, contact zone, and substrate, but may bypass the source material into the upper electrode. A static magnetic field may also be used in LPEE. We discuss below some of the factors playing roles in the LPEE growth process.

Thermoelectric Effects

In a well-designed LPEE apparatus, vertical and horizontal external temperature gradients are effectively minimized. Thermal effects that may lead to temperature gradients in the solution may then be assumed to be solely due to the Peltier cooling/heating at the solid–liquid interfaces and the Joule heating in the grown crystal.

Peltier Cooling/Heating is a thermoelectric effect caused by the electric current passing across the solution–substrate (growth interface) and the substrate–contact zone interfaces. The electric current causes heat absorption or evolution at the interfaces, depending on the direction of the electric current and type of electrical conductivity of the crystal (n-type or p-type). In an equilibrated LPEE system with a positive polarity of the n-type lower electrode crystal, Peltier cooling occurs at the growth interface and is accompanied by Peltier heating at the substrate–contact zone interface. Thus, heat transport across the substrate affects the amount of cooling at the growth interface. Indeed, the amount of cooling at the growth interface increases with increasing substrate thickness. If the current passes through the solution–n-type source (dissolution) interface, Peltier heating occurs at this interface.

Being a semiconductor, the substrate has high electrical resistivity. The electric current passing through the substrate induces Joule heating proportional to the square of the current density and electrical resistivity (Joule heating produced in the solution and graphite electrodes is at least an order of magnitude lower because of the low electrical resistivity). The effect of Joule heating in the substrate increases with increasing substrate thickness and becomes significant for bulk crystals. A one-dimensional model presented in [29.32] suggests that the Joule heating may present itself as a thermal limiting factor (barrier) in the growth of very thick crystals, particularly in the growth of high-resistivity materials.

Growth Mechanisms

The main growth mechanism of LPEE is the transport mechanism known as *electromigration*. In the growth of compound and alloy semiconductors, the solutions are metallic conductors. In such solutions, electromigration takes place due to electron momentum exchange and electrostatic field forces [29.5, 9]. Under the influence of the electric field induced by the applied electric current, solute species migrate towards the anode with a velocity proportional to the solute mobility and electric field. Thus, when the substrate has positive polarity, the solution becomes supersaturated with solute near the substrate–solution interface, resulting in epitaxial growth.

The combined effect of Peltier cooling/heating and Joule heating results in an axial temperature gradient in the solution. This temperature gradient supersaturates the solution in the vicinity of the growth interface, leading to a further contribution to epitaxial growth. This is the second main growth mechanism of LPEE. Either electromigration or Peltier cooling can become dominant, depending on the particular growth conditions [29.8, 9, 33]. However, these contributions can be affected by the presence of natural convection in the solutions, as shown numerically in [29.34].

A typical growth rate in the LPEE growth of GaAs at a $3\,A/cm^2$ electric current density is about 0.5 mm/day. For the growth of thick crystals (several millimeters), mass transport in the liquid solution is mainly due to electromigration. The contribution of molecular diffusion is very small, as shown experimentally in [29.26, 27], and also numerically in [29.35, 36]. The growth rate increases with increasing electric current density. However, at higher electric current densities, for instance $10\,A/cm^2$ or higher, the growth becomes unstable [29.26, 27].

29.1.2 Natural Convection

The effect of natural convection has been observed in various experiments [29.26, 27, 37, 38]. It enhances the overall transport processes, and thus increases the growth rate, which is desirable. However, convection often has an adverse influence on growth kinetics, and on the structure and quality of grown crystals [29.37]. It has been observed that convective flow, resulting from both thermal and solutal gradients, leads to the growth of GaAs/GaInAs layers with nonuniform thickness profiles [29.8, 10, 26, 27]. Furthermore, convection has been found to limit the maximum achievable thickness in bulk crystal growth experiments [29.23], due to the loss of surface quality caused by unstable growth conditions [29.26, 27].

In the growth of alloy semiconductors, convection adds another dimension to the difficulty of the problem. In most alloys, the densities of the components are significantly different. This difference gives rise to inhomogeneity in the composition of the liquid solution during growth. In other words, gravity makes it difficult to maintain the solution with a uniform liquid composition. Less dense components move upwards, leading to the depletion of the required component(s) in the vicinity of the growth interface. This results in unsatisfactory growth. For example, in the case of GaInP, phosphorus, with the smallest density, tends to float.

29.1.3 Applied Magnetic Fields

In order to suppress convection, a static, external applied magnetic field has also been used in LPEE [29.26, 27]. As we will see later, the application of a vertical static magnetic field (perfectly aligned with the growth direction and the applied electric field) indeed suppresses convection significantly. However, it was also observed, unexpectedly, that the applied magnetic field increases growth rate very significantly. For instance, a field of 4.5 kG increases the growth rate about tenfold. Experimental [29.26, 27] and modeling [29.35, 36, 40, 41] studies have shown that the growth rate is also proportional to the intensity of the applied magnetic field; however its contribution to mass transport is about twice that of the applied electric current.

29.1.4 Observation of Growth Rate

One of the most significant advantages of the LPEE growth technique is the possibility of monitoring in situ the evolution of the growth interface. Although the subject of this chapter is the modeling and numerical simulations of the LPEE growth process, due to its significance we wanted to mention a great experimental technique developed in [29.74]. The technique is based on resistance measurements of the growth cell during LPEE growth. When scaled with the use of the technique of dopant modulation by current pulses (time markers) [29.1], the in situ monitoring allows the study of growth rate (averaged over the cross-section area of the crystal).

The literature on the experimental studies carried out on LPEE growth of various semiconductors is rich (for a detailed account of the subject, see [29.41]). In the following sections, we first present a short re-

view of the early modeling and theoretical studies. Then, due to its significance, we give a short summary of the results of the recent experimental study of [29.26], carried out for LPEE growth of GaInAs under a strong static magnetic field. We also present a summary of the three-dimensional simulations carried our for LPEE growth of binary systems. Finally, a continuum model developed to predict the high growth rates observed in the LPEE growth of GaAs is introduced.

29.2 Early Theoretical and Modeling Studies

A number of conceptual/modeling studies have been carried out to have a better understanding of the relative contributions of electromigration, Peltier cooling, diffusion, and convection. These early studies contributed significantly to understanding of the LPEE growth process. Here, we present a summary of some of those early contributions.

29.2.1 Peltier-Induced Growth Kinetics: Electromigration Mechanism

An analytical treatment of the Peltier-induced growth kinetics in the LPEE growth of GaAs was presented in the absence of the effect of natural convection [29.10]. In this model, the growth rate was examined by considering diffusion and electromigration of As in a Ga-rich solution (Fig. 29.2). The mass balance for the solution and the grown layer is written as

$$\rho_L C_L(T_0)\, L = \rho_S C_S R(t) + \rho_L \int_R^L C(x,t)\,\mathrm{d}x\ . \quad (29.1)$$

The distribution of solute $C(x,t)$ in the solution is expressed by writing the conservation of mass for the ionized species as

$$\frac{\partial C}{\partial t} = D_C \frac{\partial^2 C}{\partial x^2} - Z_{\mathrm{eff}}\mu_E \frac{\partial}{\partial x}(EC)\ , \quad (29.2)$$

where

$$\mu_E = \frac{FD_C}{RT} \quad (29.3a)$$

and

$$Z_{\mathrm{eff}} = Z - Z_0 \frac{\sigma^{-1}(C) - \sigma^{-1}(0)}{C\sigma^{-1}(0)}\ , \quad (29.3b)$$

and μ_E, F, and σ_E are the electric mobility, the Faraday number, and the conductivity of the solution, respectively, Z and Z_0 represent the valances of solute and solvent ions, Z_{eff} is the effective charge of solute species, and D_C is the diffusion coefficient. Differentiating (29.1) with respect to time and using (29.2), we obtain the growth rate as

$$V(t) = \rho_L \frac{D_C\,(\partial C/\partial x)|_{x=R} - \mu_E Z_{\mathrm{eff}} E(R) C_L(T_1)}{\rho_S C_S - \rho_L C_L(T_1)}\ . \quad (29.4)$$

As can be seen, the calculation of the growth rate requires the electric field intensity E to be known, defined by the charge distribution in the solution and the solute concentration $C(x,t)$. Since the Ga (or Ga-rich) solution exhibits metallic properties, the participation of free electrons in the electric conductivity is much greater than that of the ionized solute (arsenic in this case) atoms. One may then assume that the electric field intensity E is constant across the solution and its value can be estimated from the expression $J = \sigma_E E$, which is simply the constitutive equation used for the electric

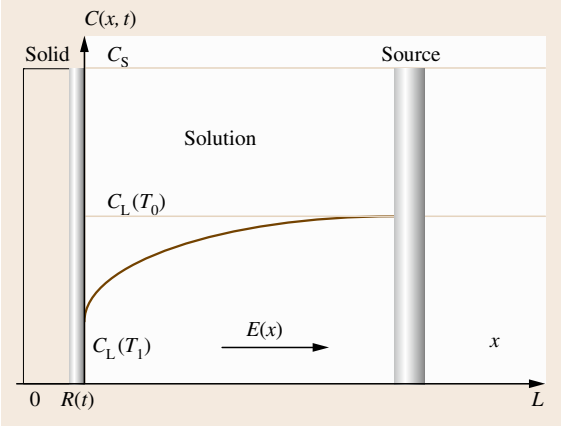


Fig. 29.2 Distribution of the solute concentration $C(x,t)$ in the solution (liquid) and solid: C_L = equilibrium composition of the solution, R = thickness of the grown layer, L = solution height, t = time, E = electric field intensity. In this setup electric current bypasses the source material (distribution of arsenic concentration in the solution after a very long time; after [29.10])

current with the conductivity σ_E of the solution [29.41]. In this case, the growth expression reduces to that given in [29.41, 63] with the assumption $E = Z_{eff}E$. Then, (29.2) reduces to the one-dimensional mass transport equation, which can be deduced from that given in [29.41, 63] as

$$\frac{\partial C}{\partial t} = D_C \frac{\partial^2 C}{\partial x^2} - \mu_E E \frac{\partial C}{\partial x} \,. \tag{29.5}$$

Equation (29.2) can be solved numerically under the following conditions (in the absence of Peltier effect at the source)

$$\begin{aligned} C(x,0) &= C_L(T_0)\,, \\ C(R,0) &= C_L(T_1)\,, \\ C(L,t) &= C_L(T_0)\,, \\ \left.\frac{\partial C}{\partial x}\right|_{x=L} &= 0\,. \end{aligned} \tag{29.6}$$

One can see that, in order to calculate the growth rate in (29.4), one must know the values (or functions) of $D_C(T)$, $C_L(T)$, $\Delta T \equiv T_1 - T_0$, $\sigma_E(C)$, and also Z_{eff}. Some of these values can be determined experimentally (such as $D_C(T)$, $\sigma_E(C)$, and Z_{eff}) and some of them (such as $C_L(T)$ and $\Delta T \equiv T_1 - T_0$) can be estimated through calculations (or numerical simulations). These values were estimated in [29.10] as follows.

The temperature difference $\Delta T \equiv T_1 - T_0$ was estimated directly by taking into account the fact that the growth of an epitaxial layer without the source on the solution surface occurs until the following condition is fulfilled (Fig. 29.3)

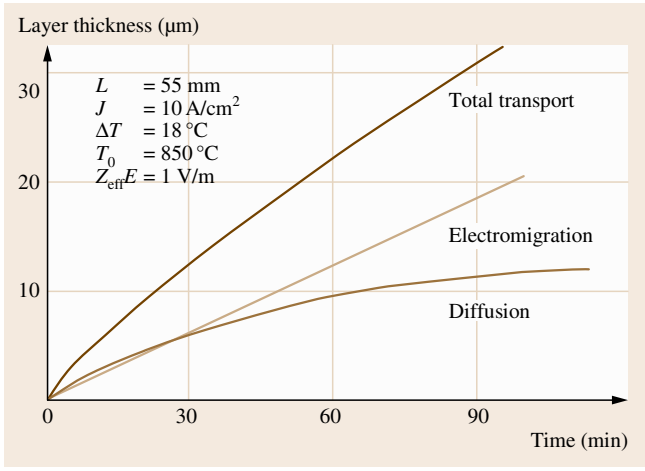


Fig. 29.4 Layer thickness versus time, and the relative contributions of electromigration and diffusion (after [29.10])

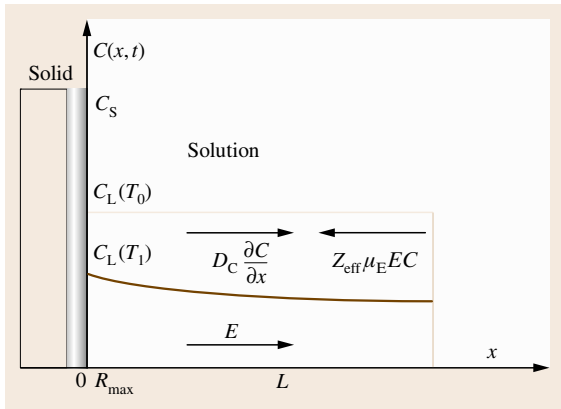


Fig. 29.3 Distribution of arsenic concentration in the solution after a very long time (after [29.10])

$$D_C \frac{\partial C}{\partial x} = Z_{eff}\mu_E EC\,, \tag{29.7}$$

which means that the diffusion, electromigration, and electrotransport streams balance each other. Solving (29.7) and substituting into (29.2) yields (see [29.10] for details)

$$C_L(T_1) = \frac{C_L(T_0) - (C_S\rho_S R_{max})/(\rho_L L)}{1 - (\mu_E L Z_{eff} E)/(2D_C)}\,, \tag{29.8}$$

where R_{max} is the maximum thickness of the layer. Equation (29.8) and the exact knowledge of the liquidus curve $C_L(T)$ will determine $\Delta T \equiv T_1 - T_0$.

The electric conductivity of the Ga solution and the parameter Z_{eff} were estimated in [29.10] as follows. The product EZ_{eff}, which is linearly dependent on current density, was treated as the parameter to fit the experimental data of the growth rates obtained (see [29.10] for the experimental data) as

$$\frac{J}{Z_{eff}E} = \text{const.}, \quad \text{at } T_0 = \text{const.} \tag{29.9}$$

It follows that the fitting parameter $Z_{eff}E$ has to be proportional to the current density J. Agreement within $\pm 20\%$ between the calculated and measured values can be achieved, as suggested in [29.10] (Fig. 29.4). Actually in the growth of very thick crystals (during prolonged growth periods), as will be seen later [29.26], this agreement is very close, within a very small margin.

Once the values of $Z_{eff}E$ are known from the fitting procedure, the electrical conductivity σ_E, the effective charge Z_{eff}, and the electric field intensity E can be

estimated. Using $J = \sigma_E E$, and (29.3b) we obtain

$$\sigma^{-1}(C) = \sigma^{-1}(0)\left(1+\frac{ZC}{Z_0}\right)\frac{1+(1-\Pi)^{1/2}}{2} \tag{29.10}$$

and

$$Z_{\text{eff}} = Z - Z_0\frac{\left(1+\frac{ZC}{Z_0}\right)\left[1+(1-\Pi)^{1/2}\right]-2}{2C} \tag{29.11a}$$

with

$$\Pi \equiv \frac{4Z_{\text{eff}}EC}{Z_0\sigma^{-1}(0)J\left(1+\frac{ZC}{Z_0}\right)^2}\,. \tag{29.11b}$$

Using (29.10) and (29.11a,b) the calculated values of Z_{eff} are tabulated in Table 29.2.

These results showed that mass transport in the LPEE growth of GaAs is due to both diffusion and electromigration of solute (As) in the liquid towards the seed substrate. The high value of the effective charge, estimated by fitting the theoretical values to those measured ones, justifies the conclusion that *the migration of arsenic species in the liquid solution is realized mainly due to collisions with electrons flowing across the solution*.

Indeed, this conclusion given in [29.10] for the mechanism of electromigration established the understanding of the electromigration process. As we will discuss it later, the high growth rates achieved under an applied magnetic field in the LPEE growth of GaAs [29.26] can only be explained by such a mechanism, as suggested in [29.61–63]:

> *The resistance during the collision of electrons with the species of the solution determines the mobility of the species and in turn the growth rate. This resistance is very much reduced under an applied static magnetic field due to the possibility that the charged species are aligned along the magnetic field lines (which are almost uniform along the growth direction in the growth system used in [29.26]), and leads to a very high mobility.*

Thus, the mass transport due to electromigration increases tremendously and the total mobility of species depends not only on the electric mobility coefficient which is measured in the absence of an applied magnetic field, but also on the magnetic field intensity and a new material coefficient that is called the *magnetic mobility* in [29.61–63]. This understanding supports the earlier definition of electromigration in LPEE.

Table 29.2 Estimated values of electrical conductivity and effective charge [29.10]

T_0 (°C)	$C_L(T_0)$ (at. %)	$(Z_{\text{eff}}E/J)\times10^3$ (Ω cm)	$\sigma^{-1}(C)\times10^5$ (Ω cm)	Z_{eff} (As^{3-})
750	1.38	−1.2	5	−24
800	2.23	−1.2	5.2	−23
850	2.75	−1.2	5.5	−22

29.2.2 A One-Dimensional Model

Based on the conservation of species mass, a one-dimensional model for the LPEE growth process was given in [29.8, 9], where the contributions of the Peltier effect at the solid–solution interfaces and that of solute electromigration in the solution to the overall growth process were defined. According to this one-dimensional model, the contribution of electromigration to growth is dominant in the absence of convection, and the contribution of the Peltier effect can be dominant in the presence of convection. (The relative contributions of electromigration and the Peltier effect have been determined more clearly through two-dimensional numerical simulation models developed by the author; the reader is referred to [29.34, 48–50] for details.)

The one-dimensional mass transport equation was written as

$$\frac{\partial C}{\partial t} + V^g\frac{\partial C}{\partial x} = D_C\frac{\partial^2 C}{\partial x^2} - \mu_E E\frac{\partial C}{\partial x}\,. \tag{29.12}$$

The following boundary conditions were considered

$$-D_C\left.\frac{\partial C}{\partial x}\right|_0 + \mu_E E C_L = (C_S - C_L)V^g\,, \tag{29.13}$$

$C = C_0$ at $t = 0$ for all x, and
at $t > 0$ for $x = \infty$ (absence of convection), or
$C = C_0$ at $t > 0$ for $x > \delta$ (presence of convection),
$C = C_L$ at $t > 0$ and $x = 0$ (growth follows the liquidus line).

Equation (29.12) was solved analytically with the assumption of a small growth velocity so that the second term on the left-hand side of (29.12) was neglected. The growth velocity was obtained for two cases: (i) for an infinitely long boundary layer ($\delta = \infty$, no convection), and (ii) for a finite boundary layer (with convection),

which are given respectively as

$$V_{\mathrm{T}}^{\mathrm{g}} = \frac{\Delta T_{\mathrm{p}}}{C_{\mathrm{S}} - C_{\mathrm{L}}} \left.\frac{\mathrm{d}C}{\mathrm{d}T}\right|_{\mathrm{L}} \left(\frac{D_{\mathrm{C}}}{\pi t}\right)^{1/2} + \mu_{\mathrm{E}} E \frac{C_{\mathrm{L}}}{C_{\mathrm{S}} - C_{\mathrm{L}}} \tag{29.14}$$

and

$$V_{\mathrm{T}}^{\mathrm{g}} = \frac{\Delta T_{\mathrm{p}}}{C_{\mathrm{S}} - C_{\mathrm{L}}} \left.\frac{\mathrm{d}C}{\mathrm{d}T}\right|_{\mathrm{L}} \frac{D_{\mathrm{C}}}{\delta} + \mu_{\mathrm{E}} E \frac{C_{\mathrm{L}}}{C_{\mathrm{S}} - C_{\mathrm{L}}} \,. \tag{29.15}$$

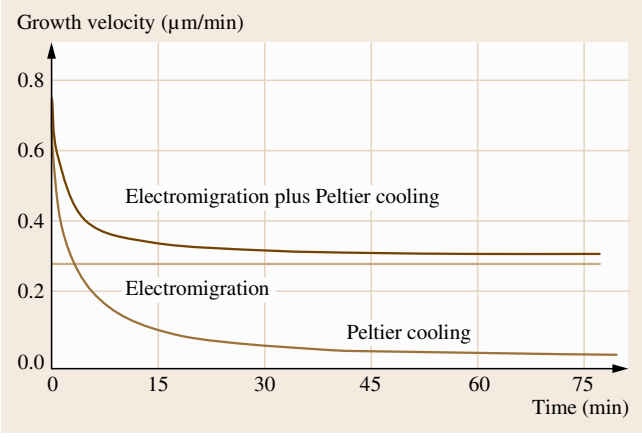


Fig. 29.5 Growth velocity of GaAs calculated from (29.14) (after [29.8, 9])

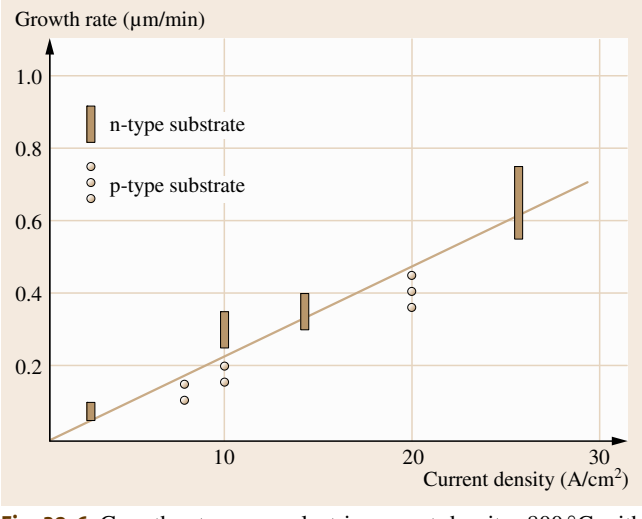


Fig. 29.6 Growth rate versus electric current density: 800 °C with a substrate thickness of 300 μm (after [29.8, 9])

In (29.14) and (29.15) the first terms represent the contribution of the Peltier effect and the second terms represent the contribution of electromigration to the growth velocity. Both terms depend linearly on the electric current through ΔT_{p} and E, respectively. Equation (29.14) was solved for LPEE growth of GaAs from a Ga/As solution at 800 °C growth temperature and using $J = 10\,\mathrm{A/cm^2}$, $\Delta T_{\mathrm{p}} = -3\,^{\circ}\mathrm{C}$, $D_{\mathrm{C}} = 6.0 \times 10^{-5}\,\mathrm{cm^2/s}$, and $\mu_{\mathrm{E}} E = 10^{-5}\,\mathrm{cm/s}$. The results are plotted in Fig. 29.5.

Equation (29.15) was also solved for various boundary layer thicknesses. It was shown that, as the boundary layer gets thinner, the contribution of Peltier cooling to the growth rate increases. The contribution of Peltier cooling to the growth rate also increases with increasing Peltier cooling at the growth interface (see [29.8, 9] for details).

According to the model presented above the relative contributions of Peltier cooling at the growth interface and electromigration of solute species in the liquid towards the interface depend on the experimental conditions. On the basis of this model, a quantitative criterion was given in [29.8, 9] to determine the relative contributions of the Peltier effect and electromigration. A critical substrate thickness d_{c} was defined, for which the contributions of the Peltier effect and electromigration are equal. When the substrate thickness is greater than the critical thickness, the Peltier effect dominates, and when the thickness is smaller than the critical thickness, electromigration dominates. Their conclusion then was that, in the growth of thick crystals and in the presence of significant convection, electromigration is dominated by Peltier cooling. On the other hand, with thin substrates and in the absence of significant convection, electromigration dominates electroepitaxial growth.

In order to verify the predictions of the one-dimensional model, specific LPEE experiments were devised in [29.8, 9]. Under specific growth conditions, using n- and p-type seed substrates, it was shown that the growth in the case of the p-type substrate was smaller than in the case of the n-type substrate. From the difference in growth rates, it was concluded that the contribution of Peltier cooling to the growth rate is less than 15%. The almost linear relationship between growth rate and electric current density observed experimentally is consistent with theoretical predictions (Fig. 29.6).

It was shown experimentally that the growth rate is also proportional (almost linearly) to current density for all growth temperatures used, and that, for a given cur-

rent density, the growth rate increases with temperature. Results are summarized in Fig. 29.7 for LPEE growth of GaAs on a 0.3 mm thick n-type substrate.

Another important issue is the selection of a proper solution height when an LPEE crucible is designed since it influences the growth rate, among of course other growth parameters. LPEE experiments designed for the growth of GaAs at 800 °C using an n-type substrate showed that growth rate is linearly proportional to solution height up to a certain height (about 10 mm), above which the growth rate remains constant. The results of experimental measurements in [29.8, 9] are presented in Fig. 29.8. Naturally, the relative contribution of the Peltier effect to the growth rate varies with solution height due to the contribution of convection in the solution. Experiments carried out in [29.8, 9] (at 25 A/cm^2 electric current density and 900 °C) show that the contribution of Peltier cooling increases with solution height (Fig. 29.9).

29.2.3 Source-Current-Controlled (SCC) Growth

The source-current-controlled (SCC) method is a version of LPEE with the difference that the furnace temperature is lowered gradually during growth similar to in liquid-phase epitaxy (LPE) while the electric current is simultaneously used to generate a temperature gradient and supply additional solute to the liquid [29.64–67]. In this setup the applied electric current passes through the source, the solution, and then through the graphite on top, but bypasses the substrate (Fig. 29.10). Due to the passage of electric current through the source the temperature T_1 just above the

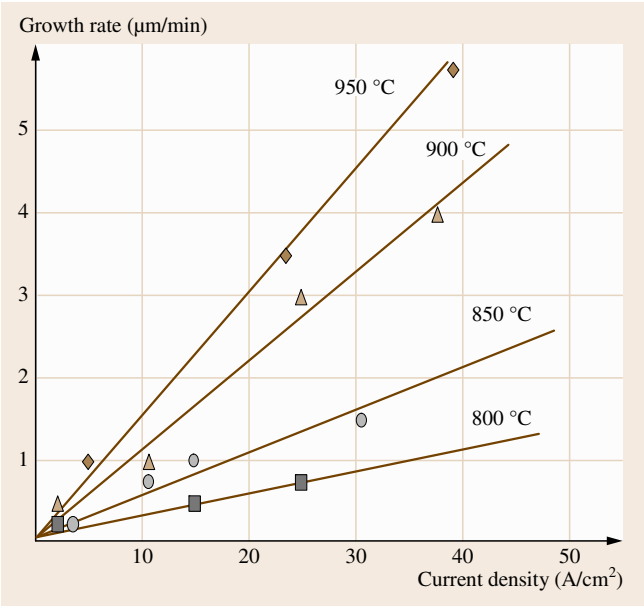


Fig. 29.7 Growth rate versus current density at various growth temperatures (after [29.8, 9])

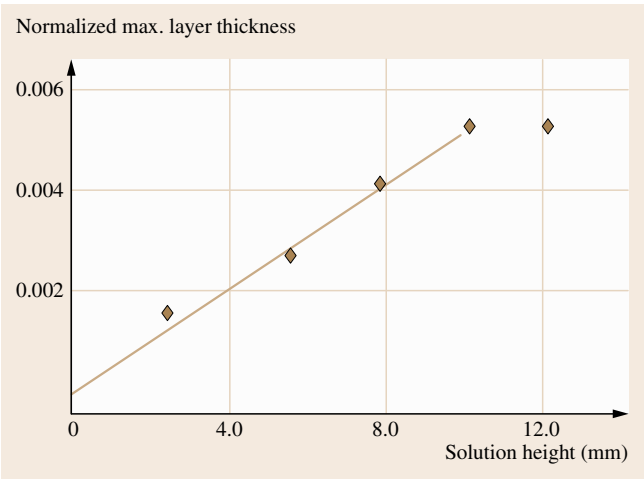


Fig. 29.8 Normalized maximum GaAs layer thickness as a function of solution height under the experimental conditions of 800 °C growth temperature, 0.3 mm thick n-type substrate (after [29.8, 9])

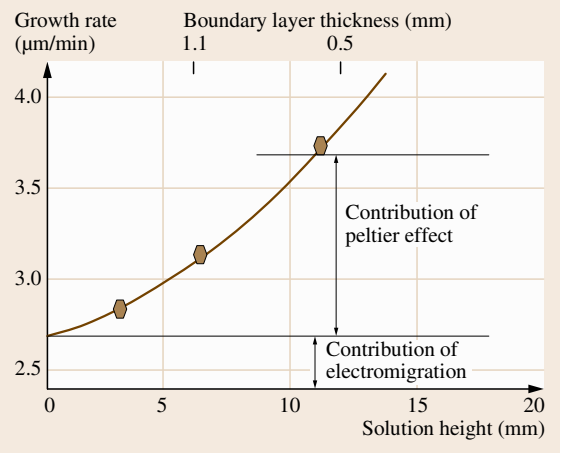


Fig. 29.9 Growth rate of GaAs from a Ga/As solution (at 900 °C and 25 A/cm^2) as a function of solution height. Substrates were Cr-doped and 0.3 mm thick. The estimated boundary layer thicknesses are also indicted at the *top* (after [29.8, 9])

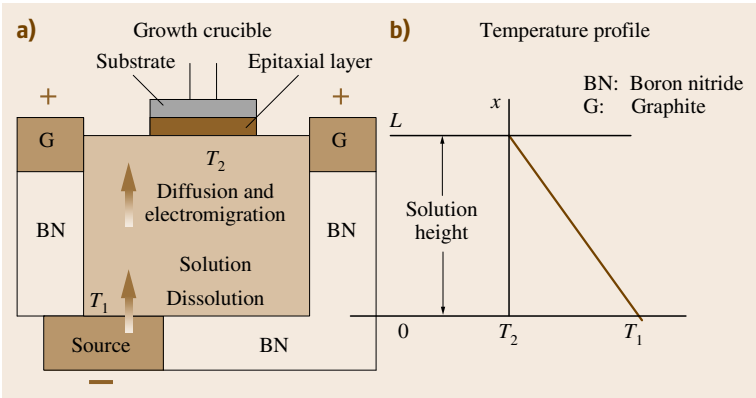


Fig. 29.10a,b Schematic view of the SCC (LPEE) growth crucible **(a)** domain and temperature profile **(b)** used in the model (after [29.64])

source is higher than that (T_2) just below the substrate. This temperature difference generates a temperature gradient between the source and the substrate. For this system, the thickness of the grown layer is calculated by solving the one-dimensional mass transport equation given in (29.5) (where we assume the mobility to be positive for current flow from source to substrate, opposite to the sign convection used in [29.64]: $\mu_E \equiv -\mu$) under the boundary conditions

$$
\begin{aligned}
C(0,t) &= C_0 - (R_0/m_0)t\,,\\
C(L,t) &= C_L - (R_L/m_L)t\,,\\
C(x,0) &= C_0 + (C_L - C_0)(x/L)\,,
\end{aligned}
\qquad (29.16)
$$

where C_0 and C_L are the initial solution concentration in the vicinity of the growth interface and the source, respectively, and R_0 and R_L represent, respectively, the cooling rates at the growth and dissolution interfaces. The solution height is denoted by L, and m_0 and m_L are the slopes of the liquidus curves near the growth and dissolution interfaces, given by

$$
m_0 \equiv \frac{1}{w_L}\left.\frac{dT}{dX^L}\right|_{x=0}\,,
$$

and

$$
m_L \equiv \frac{1}{w_L}\left.\frac{dT}{dX^L}\right|_{x=L}\,, \qquad (29.17)
$$

where X^L represents the atomic fraction of the solute, and w_L is the solution density. Through an approximate analytical solution to (29.5), an expression for the layer thickness was given as

$$
L = M_t/C_S\,, \qquad (29.18)
$$

where

$$
\begin{aligned}
M_t = {} & D_C\left(\frac{\mu E}{2D_C} - \frac{1}{L}\right)\left(C_0 - \frac{R_0 t}{2m_0}\right)t\\
& + \frac{D_C}{L}\exp\left(\frac{\mu E}{2D_C}\right)\left(C_L - \frac{R_L t}{2m_L}\right)t\\
& - \left[\frac{\pi}{L}\sum_{n=1}^{\infty}\frac{nT_n(0)}{A} + \frac{2}{L}\sum_{n=1}^{\infty}\frac{BC_L - C_0}{A}\right]\\
& \times\left[\exp\left(-D_C A t\right) - 1\right]\\
& + \left(\frac{\pi}{L^3}\sum_{n=1}^{\infty}\frac{2n^2\pi}{A^2}\right)\left(\frac{R_0}{m_0} - B\frac{R_L}{m_L}\right)\\
& \times\left[t + \frac{1}{D_C A}\exp\left(-D_C A t\right) - \frac{1}{D_C A}\right]
\end{aligned}
\qquad (29.19)
$$

and C_S is the concentration of C atoms per unit volume of the grown layer. For an $A_xB_{1-x}C$ system, C_S is given by $C_S = 4/d^3$, where d is the lattice constant of the ternary compound. The layer thickness for diffusion- and electromigration-limited growth in a temperature-graded solution can be calculated using (29.18) and (29.19) [29.64].

The thickness of the grown layers of an $In_{0.53}Ga_{0.47}As$ system was calculated in [29.64] and various numerical data were given for the dependence of concentration on growth time, layer thickness as a function of temperature and cooling rate, the relative contributions of electromigration and diffusion to growth rate, and the composition of the grown crystal along the growth direction. These calculations were made using the value $\mu E = 0.1$–0.001 cm/min for the mobility of As in the Ga/As solution. It was stated in [29.64] that *the real value of μ can be determined through a comparison of experimental layer thicknesses with computed ones*. Indeed, as shown

in [29.26, 62, 63] the mobility was calculated using experimental results of LPEE of a GaInAs system with and without the application of an external magnetic field.

The above analysis was extended in [29.68, 69] to a $Ga_xIn_{1-x}As$ system to determine the composition variation in the grown crystals. In this model, for the first time, phase equilibrium between the crystal and the solution is maintained while having consistency between the transported and incorporated mass or solute atoms at the growth interface. The comparison of experiments with computed results revealed that in the Ga/In/As solution the diffusion coefficient of Ga is about twice that of As, and the electric mobility of Ga is larger than that of As. The above results were instrumental in the development of future two-dimensional (2-D) and three-dimensional (3-D) numerical models and simulations for such systems.

29.3 Two-Dimensional Continuum Models

As mentioned earlier, the growth process of LPEE is quite complex and involves the interactions of various thermomechanical and electromagnetic fields. These include fluid flow, heat and mass transfer, electric and magnetic fields, various thermoelectric effects and their interactions in the liquid phase, and heat and electric conduction with various thermoelectric effects in the solid phase. In addition, the moving growth and dissolution interfaces with possible finite mass transport rates complicate the process further. One-dimensional and simple models are not sufficient for a full understanding of the various aspects of the LPEE growth process. To gain a better understanding of the growth process of LPEE, over the past 10 years a number of numerical simulation modeling studies have been carried out by the author's research group [29.34–36, 39–41, 46, 48–50, 61–63, 70–73].

For the first time, a two-dimensional computer simulation model for the LPEE growth process of GaAs was introduced in [29.70]. This simulation model was based on the rational mathematical model given for a binary system in [29.71]. The objective of this diffusion model was to examine the relative contributions of electromigration and Peltier cooling without introducing the additional complexity of natural convection. The model includes heat transfer, diffusive mass transport, electromigration, and Peltier and Joule effects. The governing equations are solved numerically using a finite volume method. Simulations are presented for three different growth cell configurations to investigate: (i) temperature and concentration distribution in the growth cell, (ii) the effect of applied electric current density and substrate thickness, and (iii) the contribution of electromigration and Peltier cooling to the overall growth rate.

Based on the simplifying assumptions used in this work, the simulation results showed that the magnitude of the relative temperature at the growing interface is controlled mainly by Peltier cooling for thin substrates (less than 2 mm) and small electric current densities (less than $20\,A/cm^2$). As expected, Joule heating becomes significant only for thick substrates and high electric current densities. For all configurations investigated, electromigration is found to be the dominant growth mechanism. In critical regions of the growth cell, relatively small changes in the configuration are found to have a significant impact on the process, and on the degree of nonuniformity of the grown crystal.

This diffusion model has been followed by a number of numerical simulation models specific to particular growth cell configuration. As an extension of the diffusion model in [29.70], the effect of natural convection in LPEE was introduced for the first time in [29.34]. In this work, the effect of thermosolutal convection in LPEE growth of GaAs was investigated through a two-dimensional numerical simulation model that accounts for heat transfer and electric current distribution with Peltier and Joule effects, diffusive and convective mass transport including the effect of electromigration, and fluid flow coupled with temperature and concentration fields. Simulations were performed for two growth cell configurations and the results are analyzed to determine growth rates, substrate shape evolution, and relative contributions of Peltier cooling and electromigration. The simulations predicted and helped explain a number of experimentally observed features, which previous diffusion-based models failed to reproduce. As we will see later in detail, in general, electromigration is found to be the dominant growth mechanism, but the contribution of Peltier cooling to the overall growth rate is found to be significantly enhanced by thermosolutal convection in the solution, and Peltier cooling can in fact become the dominant growth mechanism for certain growth conditions and growth cell configuration. The overall growth rate is found to increase with increasing

furnace temperature and applied electric current density. This thermosolutal convection model predicts an increased nonuniformity of the grown layers compared with the pure diffusion model in [29.70]. The shape of the grown layers is also shown to be very sensitive to changes in growth cell configuration.

The LPEE growth of ternary alloys was numerically simulated in [29.50] using a diffusion model for the growth of AlGaAs, and in [29.73] including the effect of convection in growth of GaInAs. The growth of $Al_xGa_{1-x}As$ is considered from a Ga-rich solution. The solution is dilute, with 0.345% Al and 2.445% As. The growth temperature is 850 °C, the electric current density is 10 A/cm^2, and the solid composition is up to $x = 0.4$. Simulations are carried out in the absence of convection [29.50].

In the simulations carried out for LPEE growth of $Ga_xIn_{1-x}As$ ($x = 0.94$), the computational domain covered one-half of the crucible geometry, assuming symmetry of the geometric and boundary conditions with respect to the y-axis [29.73]. The initial temperature was chosen as 780 °C, corresponding to the experimental growth conditions. The solution compositions, determined from the Ga/In/As phase diagram for growth at 780 °C, were assumed to be uniformly distributed in the liquid zone. In this experimental setup the Ga/In/As solution is nondilute, with 29.85% Ga and 7.07% As.

Two-dimensional simulation models have also been developed for LPEE growth of crystals under magnetic fields [29.72]. The feasibility of using a magnetic field for suppressing convection in LPEE was first studied through a model for the growth of GaAs in [29.49]. The LPEE growth process of GaAs was numerically simulated under an applied static magnetic field using the finite element method based on the penalty function formulation [29.49]. It was found that this formulation is more robust and efficient than a mixed velocity–pressure formulation. The results of these early simulations have shown that the effect of natural convection can be reduced significantly by the application of an external static magnetic field. For the crucible selected, the uniformity of grown layers improves with increasing magnitude of the applied magnetic field. Results also showed that complete elimination of natural convection in the liquid phase requires the application of a very large magnetic field (about and more than 20 kG). However, this prediction is numerical, based on the model assumptions and simplifications made, and as we will see later in growth of bulk crystals by LPEE, the strong interaction between the applied magnetic and electric fields does not allow the use of a magnetic field intensity above a critical (maximum) value. For instance, this value was about 4.5 kG in LPEE growth of GaAs in experiments [29.26], and growth at higher field intensities led to unstable growth.

However, this early simulation model in [29.49] shed light on a number of issues in LPEE growth under magnetic field and laid the foundation for further experimental and numerical simulation studies in LPEE. It also provided a valuable insight into the use of the finite element technique for future studies. (A comprehensive review of the two-dimensional simulations carried out for LPEE can be found in [29.41].)

29.4 LPEE Growth Under a Stationary Magnetic Field

In spite of many significant advantages, LPEE has suffered historically from mainly three *shortfalls* towards its commercialization. The first is the achievable crystal thickness, which is relatively small, on the order of a few millimeters. This is mainly due to the combined effect of Peltier and Joule heating in the system, leading to higher temperature gradients and relatively strong natural convection in the liquid solution zone that cause unsatisfactory and unstable growth. This puts a limit on the achievable crystal thickness, particularly in the growth of bulk crystals, and providing less useful material. The second issue in LPEE has been its low growth rate. The growth rate in LPEE is almost linearly proportional to the applied electric current density, and increases with increasing electric current density. For instance, it is about 0.5 mm/day at 3 A/cm^2. For higher electric current density levels, the growth rate will increase, but in the growth of thick (bulk) crystals the combined effect of temperature gradients and natural convection may lead to unstable growth. The third shortfall is the need for a single-crystal seed of the same composition as the crystal to be grown. Small compositional differences, on the order of 4% depending on the crystal lattice parameters, can be tolerated, but higher compositional differences may lead to unsatisfactory growth.

The first two shortfalls of LPEE have recently been addressed in [29.26]. By optimizing the growth param-

eters of LPEE, and also using a static external applied magnetic field, a number of thick, flat GaAs single crystals and $In_{0.04}Ga_{0.96}As$ single crystals of uniform compositions were grown, and the growth rate of LPEE was increased more than tenfold for a selected electric current density. The crystals grown under magnetic field or no magnetic field were all single crystals, and the results were reproducible in terms of crystal thickness, growth rate, and compositional uniformity. The addressing of the third shortfall has been attempted in [29.42–45] by utilizing the liquid-phase diffusion (LPD) technique.

A comprehensive experimental study of LPEE growth of GaAs and $Ga_{0.96}In_{0.04}As$ single crystals has been carried using the facility in the Crystal Growth Laboratory (CGL) of the University of Victoria. The LPEE experiments under no magnetic field have led to the growth of a large number of GaAs and $Ga_{0.96}In_{0.04}As$ single crystals of thicknesses up to 9 mm. It was possible to apply electric current densities of 3, 5, and 7 A/cm^2. The corresponding growth rates in these experiments were about 0.57, 0.75, and 1.25 mm/day, respectively. Growth interfaces were very flat, and the growth experiments were reproducible in terms of crystal thickness and growth rate. Experiments at higher electric current intensities were not successful.

Experiments at the 3, 5, and 7 A/cm^2 electric current density levels were repeated under various applied static magnetic field levels, starting at 3 A/cm^2 electric current density and 20 kG magnetic field level (based on an earlier initial numerical estimation in [29.49]). The LPEE experiments at the 4.5 kG and lower magnetic field levels were successful, but those under higher magnetic field levels were not. These experiments indicate that for the LPEE system used in [29.26] the 4.5 kG field level is the maximum (*critical*) field intensity above which the growth is not stable. The numerical simulations conducted under the same conditions yielded a lower *critical* magnetic field level of 2.0–3.0 kG [29.35]. In addition, the experimental LPEE growth rates under a magnetic field are much higher than those under no magnetic field. For instance, as we will see later, the growth rate at 4.5 kG magnetic field level was about ten times higher than that under no magnetic field (at $J = 3\,A/cm^2$). The experiments performed at the $B = 1.0$ and 2.0 kG field levels (at $J = 3\,A/cm^2$) were also successful, and the growth rates were also higher at 1.62 and 2.35 mm/day, respectively. Experiments showed that the application of an external magnetic field is very beneficial in increasing the growth rate in LPEE to a level competitive with other bulk crystal growth techniques.

At the higher magnetic field levels (even at the $J = 3\,A/cm^2$ electric current density level), and the higher electric current density levels ($J = 10\,A/cm^2$ or higher), the experiments did not lead to successful growth, but showed very interesting outcomes. Although very thick crystals were grown, even up to a 9 mm thickness, the growth processes were unstable and led to uneven grown crystals. From visual inspection of the grown crystals, the adverse effects of natural convection and strong electromagnetic interactions were obvious, causing either one-sided growth or, particularly in four experiments, to holes in the grown crystals [29.27]. It was considered that such growth (one-sided and with holes) is because of strong and unstable convection in the liquid zones (solution and contact zones) due to the strong interaction between the magnetic field and the applied electric current. Such predictions were confirmed qualitatively by numerical simulations [29.35, 36].

29.4.1 Experiments

In the initial LPEE experiments, a 20 kG magnetic field level was used based on the predictions in [29.49]. It was realized that this level of magnetic field was very strong, and the growth results were not successful. The applied magnetic field intensity was gradually lowered, and successful growth was first achieved at 4.5 kG.

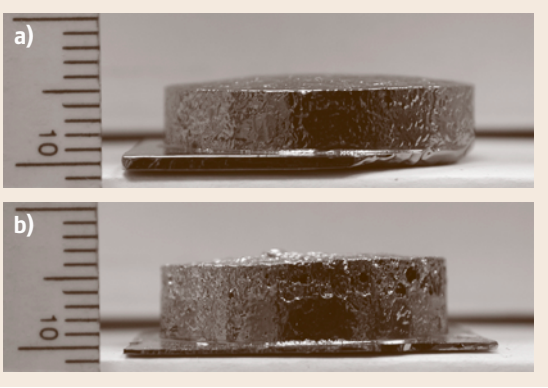


Fig. 29.11a,b Two sample GaAs crystals grown without magnetic field. **(a)** All the material put into the solution well was depleted. **(b)** The growth has been stopped before the depletion of the solution in order to measure the growth rate accurately, and the upper part is the secondary growth during cooling (after [29.26])

A number of experiments were performed at this level. Experiments were also performed at 1.0 and 2.0 kG field levels to study the effect of the applied magnetic field on the growth rate. Details of the experimental results can be found in [29.26].

In the LPEE setup used, the grown crystal and the liquid solution could not be separated at the end of an experiment. Therefore, a secondary growth (like an LPE growth) occurs during the cooling period in the experiments that were stopped earlier (before depleting all the solution put in the growth well). Some experiments were stopped before depleting the solution for the purpose of determining the growth rate accurately. Most of the crystals were grown under low current density levels (3, 5, and 7 A/cm^2). Two sample GaAs crystals are shown in Fig. 29.11.

Attempts at these electric current density levels failed. This may be attributed to the strong convection

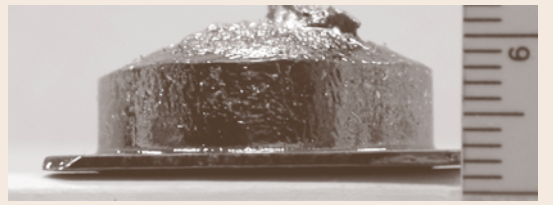


Fig. 29.13 Sample GaAs crystal grown at the $J = 3$ A/cm^2 electric current density and $B = 4.5$ kG magnetic field level (after [29.26])

in the solution at these levels of applied current during the prolonged growth periods in growth of *bulk* crystals. It must be mentioned that it is possible to use higher electric current densities (higher than 7 A/cm^2) in the growth of thin layers, as reported in the literature (e.g., [29.47]).

Experiments were conducted for various growth periods (from 1 to 8 days) at a temperature of 800 °C. The results are summarized in Fig. 29.12. As can be seen, the average thickness of the grown crystals is proportional to the applied electric current density. As expected, the thickness increases with time. It was concluded previously that the growth rate in LPEE is a linear function of the applied electric current density [29.12, 23]. The results shown in Fig. 29.12a indicate that this is approximately the case at the low electric current density levels, but that there is slight deviation from linearity (with a higher rate) at the higher electric current density levels. This deviation can be attributed to the enhanced natural convection in the solution. The increase of electric current density up to 7 A/cm^2 in the growth of *bulk* crystals by LPEE has been a significant contribution. This was possible due to the novel design features of the LPEE setup in [29.26].

Crystals were grown at 3 A/cm^2, without magnetic field, for various periods of time to determine the growth rate. Crystals were grown with thicknesses between 1.5 and 4.5 mm, with an average growth rate of 0.57 mm/day, as shown in Fig. 29.12b. In one of the experiments a thickness of 4.5 mm was achieved in 8 days. A number of crystals were also successfully grown under the electric current densities of 5 and 7 A/cm^2. The growth rates were 0.75 mm/day (2.25 mm thickness in 3 days) and 1.25 mm/day (3.75 mm thickness in 3 days), respectively. It must be mentioned that some of the growth thicknesses were not representative for calculating the growth rate since in such experiments the source material put into the well was completely depleted before stopping the growth (Fig. 29.12a). Those

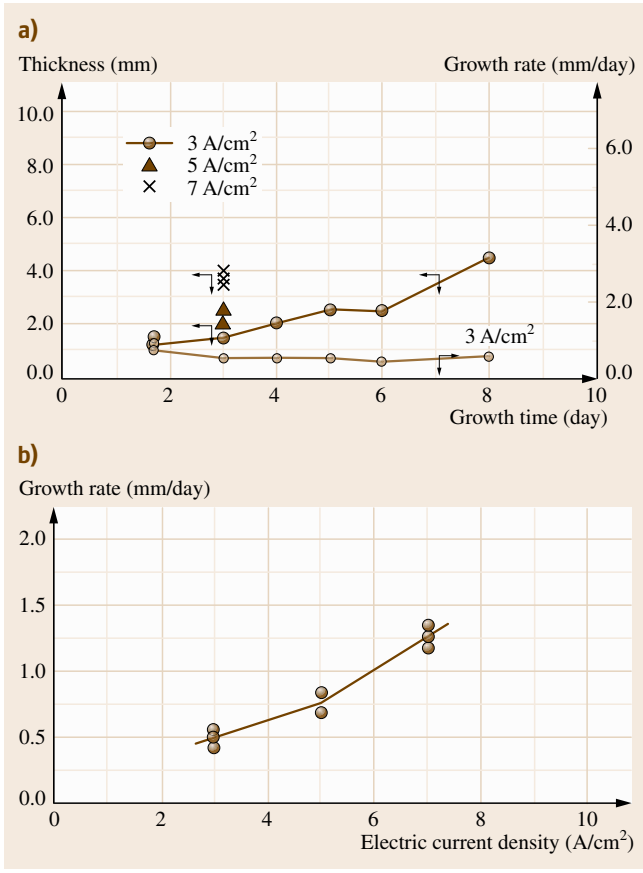


Fig. 29.12a,b Summary of the LPEE growth rates **(b)** and thickness **(a)** in the absence of applied magnetic field (after [29.26])

experiments were not included in the calculation of growth rates.

As mentioned earlier, in order to suppress the natural convection in the liquid solution for the purpose of prolonging and stabilizing the LPEE growth process for growing bulk single crystals (thicker crystals), an applied static magnetic field was used. A sample grown GaAs crystal is shown in Fig. 29.13.

The static applied magnetic field induces a magnetic body force acting on the moving particles of the liquid solution. The combined effect of the magnetic and gravitational body forces suppresses convection and prolongs growth. This beneficial effect of an applied magnetic field was the initial intention of the research program at UVic CGL. This goal was successfully achieved, by growing thick single crystals. However, the unexpected effect (a very *positive* effect of course) of the applied magnetic (at 4.5 kG and lower field levels) was the significant increase in the growth rate (about ten times at the 4.5 kG level, Fig. 29.14). The average growth rates were calculated at specific electric current density levels based on the selected representative experiments, those that were stopped deliberately before depleting the source material. This increase in the growth rate was almost the same at each of three electric current density levels, namely about 6.1, 7.8, and 10.5 mm/day at $J = 3$, 5, and 7 A/cm^2. Such a drastic increase in the growth rate elevates the LPEE growth process to the category of a bulk growth. Growth rates at the $B = 1.0$ and 2.0 kG levels were also higher, about 1.62 and 2.35 mm/day, respectively. Results show that the growth rate is also proportional to the applied magnetic field level (Fig. 29.15).

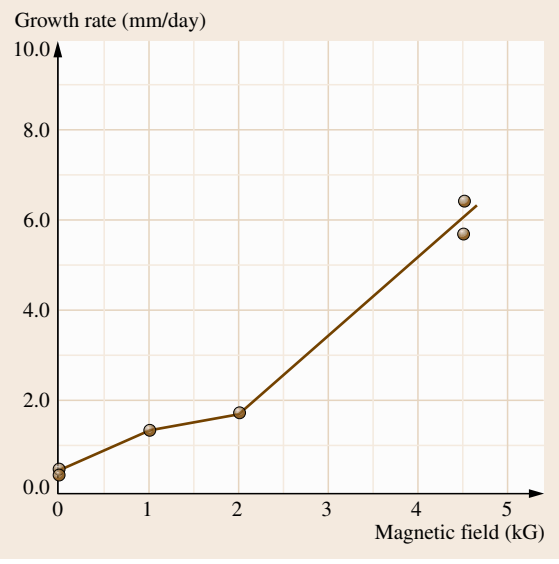


Fig. 29.15 Growth versus magnetic field intensity at $J = 3$ A/cm^2 (after [29.26])

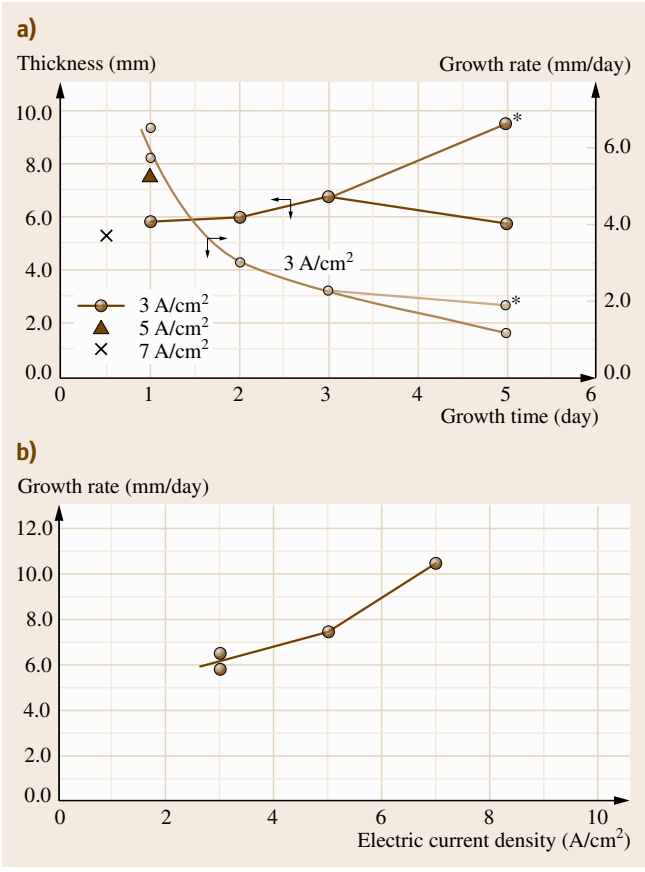


Fig. 29.14 Summary of the growth rates at the $B = 4.5$ kG magnetic field level (after [29.26])

29.5 Three-Dimensional Simulations

The earlier two-dimensional simulation results have shown that the level of applied magnetic field has a significant effect on natural convection in the solution, both in intensity and structure [29.46]. A stronger applied magnetic field leads to weaker convection in the solution, and more uniform interfaces. These